U.S. DEPARTMENT OF ENERGY

Office of ENERGY EFFICIENCY & RENEWABLE ENERGY

Materials

FY 2020 Annual Progress Report

Vehicle Technologies Office

(This page intentionally left blank)

Disclaimer

This report was prepared as an account of work sponsored by an agency of the United States government. Neither the United States government nor any agency thereof, nor any of their employees, makes any warranty, express or implied, or assumes any legal liability or responsibility for the accuracy, completeness, or usefulness of any information, apparatus, product, or process disclosed or represents that its use would not infringe privately owned rights. Reference herein to any specific commercial product, process, or service by trade name, trademark, manufacturer, or otherwise does not necessarily constitute or imply its endorsement, recommendation, or favoring by the United States government or any agency thereof. The views and opinions of authors expressed herein do not necessarily state or reflect those of the United States government or any agency thereof.

Acknowledgements

First and foremost, the Principal Investigators from industry, academia, and the National Laboratories who supplied the content of these reports are to be acknowledged and commended. It is their work that moves our nation forward to improved and more affordable transportation, as well as increased energy security.

Thank you to the project managers at the National Energy Technology Laboratory for continued support administering these projects.

We would also like to acknowledge Energetics for their help in preparing and publishing this report.

Gurpreet Singh
Acting Program Manager
Materials Technology Program
Vehicle Technologies Office

Jerry L. Gibbs
DOE Technology Manager
Propulsion Materials
Vehicle Technologies Office

Sarah Kleinbaum
DOE Technology Manager
Multi-Material Joining
Lightweight Materials
Vehicle Technologies Office

H. Felix Wu, Ph. D
DOE Technology Manager
Carbon Fiber and Polymer Composites
Lightweight Materials
Vehicle Technologies Office

Acronyms and Abbreviations

symbols

α	activation length
Δ$	difference in costs
Δkg	difference in weight
ε	strain
ϵ^{DIC}	strain obtained from digital imaging correlations
ϵ_V^S	volumetric solute size misfit
Φ	diameter
ϕ_n	mode-I fracture toughness
γ	austenite formation
φ	equivalence ratio
λ	deformation (when referring to a change in dimension)
λ	wavelength (when referring to vibration)
μ	coefficient of friction
μin	microinch
μm	micrometer
Θ	designation used for microscale intermetallic precipitates mostly located at the grain boundaries in the as-cast state of Al
Θ′	designation for nanoscale intermetallic precipitates present in the grain interiors of cast-Al alloy
ρ	density
σ	stress (or strength, when referring to physical properties)
τ	time (when used in the kinetic equation for irreversible chain scission)
τ_y	yield stress
τ_{10}	a compositional phase of a ternary intermetallic, such as aluminum (Al)–silicon (Si) light alloy reinforced with a cast-iron insert (e.g., Al–iron [Fe]–Si)
Ψ	loss coefficient defined as $\Psi = \Delta U/U$
Ψ_m	energy of morphed networks
$\Psi_0, \Psi_\infty, \Psi_m, \Psi_d, \Psi_M$	energy at different states (virgin state, aged state, morphed state, deactivated state, and total matrix) when referring to a polymer matrix
0D	Zero-dimensional (component described by a single mean value)
16Mo3	a EN10028 specified pressure vessel grade chrome molybdenum steel alloy for use in elevated working temperatures
1D	One-dimensional

1-ID	designation for the beamline at the Advanced Photon Source located at Argonne National Laboratory
2D	two-dimensional
3D	three-dimensional
3M	Minnesota Mining and Manufacturing Company (company's former name)
304	steel containing chromium (between 18% and 20%) and nickel (between 8% and 10.5%)
310	a medium carbon austenitic stainless-steel for high-temperature applications such as furnace parts and heat-treatment equipment
316L	the low carbon version of 316 stainless-steel commonly used in chemical and petrochemical industry, in food processing, pharmaceutical equipment, medical devices, in potable water, wastewater treatment, in marine applications and architectural applications near the seashore or in urban areas
347	a niobium stabilized chromium-nickel austenitic stainless-steel with corrosion resistance similar to 304/304
38MnVS6	a grade of micro-alloyed medium carbon steel for applications demanding high mechanical properties and smooth surfaces
4140	a low alloy steel containing chromium, molybdenum, and manganese
5xxx	series designation for Al alloyed with magnesium
6xxx	series designation for Al alloyed with magnesium and silicon
7xxx	series designation for Al alloyed with zirconium

A

Å	angstrom
A206	Al alloy significantly stronger than the premium quality alloys used for automotive castings with mechanical properties approaching some grades of ductile iron and having excellent high-temperature tensile and low cycle fatigue strength
A316L	a chromium-nickel- molybdenum austenitic stainless-steel developed to provide improved corrosion resistance to Alloy 304/304L in moderately corrosive environments
A319	Al alloy having a composition of 6% Si and 3.5% Cu alloy with 1.0 Fe maximum that has excellent casting and machining characteristics and very good corrosion resistance and weldability
A356	Al alloy with greater elongation, higher strength, and considerably higher ductility than Alloy 356 because of lower Fe content that is typically used for airframe castings, machine parts, truck chassis parts, aircraft and missile components, and structural parts requiring high-strength
A365	a primary die-casting alloy (Al-Si_9-Mg-Mn) widely used to manufacture automotive parts
AA	aluminum alloy
AA	Aluminum Association (when used with a series)

AA3003	Al alloy with moderate strength, which can be increased by cold working, and good corrosion resistance
AA5083	Al alloy with Mg and traces of Mn and Cr that is highly resistant to attack by seawater and industrial chemicals
AA5182	wrought Al alloy with good corrosion resistance and weldability containing 4.5% Mg, 0.35% Mn, and the balance Al
AA6016	Al alloy with the highest ductility among the 6000-series alloys containing AlSi1.2, Mg.4
AA6022	heat treatable low Cu precipitation hardenable Al sheet alloy containing 0.8% to 1.5% Si, 0.45% to 0.70% Mg, and 0.25% zinc (Zn)
AA6061	precipitation hardening Al alloy containing 0.8% to 1.2% Mg and 0.4% to 0.8% Si as its major alloying elements
AA6063	Al alloy consisting of Al, Mg, and 0.5Si used for pipe, railings, furniture, architectural extrusions, irrigation pipes, and transportation
AA6111	wrought Al alloy that is a heat treatable and possesses high-strength and excellent stretch-forming characteristics containing 0.6% to 1.1% Si, 0.5% to 1.0% Mg, 0.1% to 0.45% Mn, 0.5% to 0.9% Cu, and 0.15% Zn
AA7075	Al alloy with strength comparable to many steels, good fatigue strength, and average machinability
ABAQUS	software suite for finite element analysis and computer-aided engineering
ABL	acrylonitrile-butadiene-lignin
ACEC	Advanced Combustion Engine and Emission Control
ACMZ	designation for Al alloys containing aluminum, copper, manganese, and zirconium
ACN	acrylonitrile
ACP	Advanced Carbon Products
AC-STEM	aberration-corrected scanning transmission electron microscope (or microscopy)
AET	Applied Engineering & Technology Integration, Inc.
AFA	Alumina-Forming Austenitics - Al_2O_3-forming austenitic alloys
Ag	silver
AHSS	advanced high-strength steel
Al	aluminum
Al/θ'	designation for the Al_2Cu interface
Al-Fe-Si	aluminum-iron-silicon
Al-G	aluminum graphene
Al_2Cu	aluminum-copper (2:1)
Al_4C_3	aluminum carbide
Alloy 31V	an iron-nickel-chromium-molybdenum alloy with the addition of nitrogen

Alloy 206	an aluminum-copper alloy used in high-performance aerospace, combat, and tactical vehicle applications because of its durability
Alloy 319	a 6% Si and 3.5% Cu alloy with 1.0 Fe maximum with excellent casting and machining characteristics
Alloy 356	a cast-Al alloy consisting of 6.5 to 7.5% Si, 0.6% Fe, 0.25% Cu, 0.2 to 0.45% Mg, 0.25% Ti, 0.35% Xn and 0.35% Mn typically heat-treated to improve its strength characteristics used for aircraft parts, pump housings, impellers, high velocity blowers and structural castings
Alloy 418	a martensitic chromium-tungsten-nickel stainless grade that is ideal for high stress components up to 649°C
Alloy 422	a hardenable, martensitic stainless-steel designed for service temperatures as high as 1200 ˚F
Alloy 751	a precipitation hardenable nickel-chromium alloy, used mainly for the exhaust valves of internal combustion engines
Alloy 380	one of the most commonly specified aluminum alloys with the best combination of casting, mechanical, and thermal properties that exhibits excellent fluidity, pressure tightness, and resistance to hot cracking and used for a wide variety of products including chassis for electronic equipment, engine brackets, gearbox cases, household furniture, power, and hand tools
Alloy 626	anickel-based superalloy that possesses high-strength properties and resistance to elevated temperatures
Alloy 2618	a high-strength aluminum alloy which contains both copper and magnesium with good machinability and resistance to atmospheric attack typically used in aerospace and defense components
Al_3Ni	nickel aluminide
Al_2O_3	aluminum oxide (or alumina)
$Al(OH)_3$	aluminum hydroxide
AlSiCu	aluminum-silicon-copper alloy is a cast-Al alloy widely used due to its high castability and low-density
AlTi	aluminum-titanium alloy
ALWF	aluminum warm forming
AM	additive manufacturing or additive manufactured (when referring to processes)
AM60	a castable magnesium alloy with excellent ductility, superior energy absorbing properties, and good strength and castability
AMC	Al matrix composites
AMIPC	additively manufactured interpenetrating phase composite
ANL	Argonne National Laboratory
ANSYS	industry-standard code based on finite element modeling
AP	atmospheric plasma

APS	Atmospheric Plasma Solutions (when referring to a company providing treatment of Mg)
APS	Advanced Photon Source (when referring to materials characterization)
APS-U	Advanced Photon Source Upgrade
APT	atom probe tomography
Ar	argon
Arconic	company specializing in lightweight metals engineering and manufacturing
ARM200CF	an atomic resolution transmission electron microscope operating at a maximum accelerating potential of 200kV
Arplas	company with innovative welding applications for the automotive industry based on the principle of applying the minimum possible energy (heat) to the parts to be joined while still reaching a full structural weld
ASCENDS	Advanced data SCiENce toolkit for Non-Data Scientists
ASM	American Society of Metals
ASTM	American Society for Testing and Materials
ASTM A956	ASTM test standard for Leeb hardness testing of steel products
ASTM B117	ASTM test standard for salt spray test used to produce relative corrosion resistance information on metals and coated metals
ASTM B646	ASTM standard practice for fracture toughness testing of aluminum alloys
ASTM D1735	ASTM test standard for testing water resistance of coatings in an apparatus similar to that used for salt spray testing
ASTM E8-16a	ASTM standard test method for tension testing of metallic materials
ASTM E561	ASTM standard test method for KR curve determination
ASTM E1820	ASTM test standard for measurement of fracture toughness plane stress / plane-strain
ASTM G85	ASTM test standard for cyclic acidified salt fog (spray) testing
at.%	atomic percent
at. fr.	atomic fraction
ATI	Allegheny Teledyne Incorporated
AZ21	Mg alloy with 2% Al and 1% Zn
AZ31B	most widely available Mg grade alloy, high-strength-to-weight ratio with a composition of 2.5% to 3.5% Al and 0.7% to 1.3% Zn
AZ61	Mg alloy with 92% Mg, 5.80 - 7.20% Al, 0.40 - 1.50% Zn, 0.15% Mn and 0.10% Si
AZ80	Mg alloy with 91%Mg, 7.80 - 9.20% Al, 0.20 - 0.80% Zn, 0.12% Mn, and 0.10% Si
AZS312	A brittle Mg alloy with Mg, Al, Zn and Si components

B

BASF	Badische Anilin und Soda Fabrik (German for "Baden Aniline and Soda Factory")
Bcc or bcc	body-centered cubic
Bi	bismuth
BIW	body-in-white
BJ	binder-jetting
BJAM	binder jet additive manufacturing
BMW	Bayerische Motoren Werke AG; a German luxury automobile, motorcycle, and engine manufacturing company
BP	budget period
BR	Bayesian ridge
BSE	backscattered electron

C

^{0}C	degrees Centigrade
C	carbon
C44	elastic moduli (parameter used in modeling)
Ca	calcium
CA50	the 50% mass burned crank angle location
CAD	computer-aided design
CAE	computer-aided engineering
CALPHAD	CALculation of PHAse Diagrams
CCT	cyclic corrosion testing
Cd	cadmium
Ce	cerium
CEM	computational electromagnetics model (or modeling)
CF	carbon fiber
CF8C-Plus	cast stainless-steel developed to provide higher temperature capability and reliability for advanced diesel engine components
CFD	computational fluid dynamics
CFRC	carbon fiber-reinforced composite
CFRE	carbon fiber-reinforced epoxy
CFRP	carbon fiber-reinforced polymer
CFTF	Carbon Fiber Technology Facility
CGMD	coarse-grained molecular dynamic
CHONS	carbon-hydrogen-oxygen-nitrogen-sulfur

CHT	conjugate heat transfer
cm	centimeter
cm^2	square centimeter
CNP	carbon nanoparticle
CNP-OH	carbon nanoparticle that is hydroxyl-terminated
Co	cobalt
CO_2	carbon dioxide
COMSOL	a cross-platform finite element analysis, solver, and multiphysics simulation software that allows conventional physics-based user interfaces and coupled systems of partial differential equations
CONVERGE	computational fluid dynamic software by Convergent Science Inc. with autonomous meshing capabilities that eliminates the grid generation problems from the simulation process
COST507	(European) Cooperation in Science and Technology 507
CPEC	close proximity electromagnetic carbonization
cP(s)	centipoise(s)
Cr	chromium
CR	compression ratio
$CrO_2(OH)_2$	dihydroxy(dioxo)chromium
Cr_2O_3	chromium oxide
CRADA	Cooperative Research and Development Agreement
CRS	cold-rolled steel
C-RTM	compression resin transfer mold (or molding)
CT	computed tomography
CTP	coal tar pitch
CTPM	coal tar pitch mesophase
Cu	copper
CuCl	copper chloride

D

d	sliding distance (when referring to friction testing)
DataHUB	data-centric architecture for data storage
dBA	decibels, A weighted
DC	direct current (when referring to electricity)
DC	Dow Corning (when referring to adhesives)
DCB	double cantilever beam
DED	direct energy deposition

DFT	density functional theory
DI	direct injection (when referring to internal combustion engines)
DIC	digital image correlation
DICTRA	DIffusion-Controlled TRAnsformations in multi-component systems, a software diffusion module within Thermo-Calc for accurate simulation of diffusion-controlled reactions in multi-component alloy systems
DL	difunctional linker
DMA	dynamic mechanical analysis
DOE	U.S. Department of Energy (when referring to the agency)
DP	dual phase
DP500	dual phase steel that possesses good formability and weldability which is suitable for car safety components such as reinforcements
DP590	dual phase steel with low tensile strength (590 MPa) and low yield frequently used in automotive body structure applications requiring high-energy absorption
DP980	dual phase steel consisting of a ferrite matrix containing a hard second phase
DSA	dynamic strain aging
D_x	density of reactants
D_y	final relaxed density
Dy	dysprosium

E

e.g.	abbreviation meaning “for example”
E	stiffness or Young’s modulus
EBSD	electron backscatter diffraction
E-coat or e-coat	electrophoretic coating
ECorr	corrosion potential
EDS	energy-dispersive spectroscopy
EDX	energy-dispersive x-ray
E-EGR	electric exhaust gas recirculation
EELS	electron energy-loss spectroscopy
EERE	Office of Energy Efficiency and Renewable Energy
EFP	E-Form Plus
EGR	exhaust gas recirculation
EIS	electrochemical impedance spectroscopy
EPIKOTE™	EPIKOTE™ Resin 05475 with EPIKURE Curing Agent 05443: a system with low viscosity, a relatively long injection window, excellent wetting and adhesion to CFs, and superior thermal and mechanical performance

Epot	potential energy (parameter used in modeling)
Er	erbium
ESE Carbon	ESE Carbon company – supplier of carbon fiber composites and other services for tailored-fiber placement, high-pressure resin infusion, engineering design, and analysis
ESM	electrochemical strain microscopy
et al.	abbreviation meaning "and others"
EV	electric vehicle (when referring to types of vehicles)
EWI	Edison Welding Institute

F

F	deformation gradient tensor
F_N	force normal to a plane
FADI-AMT LLC	a limited liability company that does testing of automotive materials; the name is a composite of the first name of the company's president (Fadi Abu-Farha) and the abbreviation for automotive materials testing
FaST	Friction-stir assisted Scribe Technique
FBJ	friction bit joining
FCA US LLC	Fiat Chrysler Automobiles U.S. Limited Liability Company
FCC or fcc	face-centered cubic
FDS	flow drill screw
Fe	iron
Fe_3C	iron carbide (or Cementite)
FeCu	iron-copper alloy used for many applications due to its high-strength and electric and thermal properties
FE	finite element
FEA	finite element analysis
FEM	finite element method (or model)
FEV	Forschungsgesellschaft für Energietechnik und Verbrennungsmotorenles
FIB	focused ion beam
FLTM	Ford Laboratory Test Method
FOM	figure of merit
FSE	friction-stir extrusion
FSI	friction-stir interlocking
FSP	friction-stir processing
FSPR	friction self-piercing riveting
FSSW	friction-stir spot welding (or weld)

FSW	friction-stir welding (or weld)
FY	fiscal year

G

g	gram(s)
G	graphene
Ga	gallium
g/cc or g/cm^3	grams per cubic centimeter
G/D (band)	The G band is a result of in-plane vibrations of SP2 bonded carbon atoms whereas the D band is due to out-of-plane vibrations attributed to the presence of structural defects
Gd	gadolinium
GG-MIT	Grossman Group at Massachusetts Institute of Technology
GM	General Motors LLC
Gmsh	an open-source 3D finite element mesh generator with a built-in CAD engine and post-processor that provides a fast, light, and user-friendly meshing tool with parametric input and advanced visualization capabilities
GMW14872	GM procedure for an accelerated laboratory corrosion test method to evaluate assemblies and components using a combination of cyclic conditions (salt solution, various temperatures, humidity, and ambient environment) to accelerate metallic corrosion
G-NAC	GTEKT North American Corporation
GNP	graphene nano particles (or powders)
GP	Guinier-Preston
GPa	gigapascals
GROD	grain reference orientation deviation
g/s or g/sec	grams per second
GTN	Gursoon-Tvergaard-Needleman
GT-POWER	simulation software by Gamma Technologies Inc. used to predict engine performance quantities such as power, torque, airflow, volumetric efficiency, fuel consumption, turbocharger performance and matching, and pumping losses

H

h or hr	hour(s)
H13	a Cr, molybdenum, vanadium hot work tool steel with high hardenability and excellent toughness
H_2O	water
HAADF	high-angle annular dark-field
HCF	high cycle fatigue
HCP	hexagonal close packed

HD	heavy-duty
HDDE	heavy-duty diesel engine
HDG	hot-dip galvanized (or hot-dip galvanizing)
HDGE	hot-dip galvanized E-coated
HEXM	high-energy x-ray microscope
Hf	hafnium
HIP	hot isostatic pressing
HiSiMo	high silicon molybdenum
HK30Nb	a grade of cast stainless-steel with a composition of 25% Cr, 21% Ni, 1.75% Si, 1.5% Mn, and trace amounts of C, P, S, and Mo
Ho	holmium
HP-RTM	high-pressure resin transfer molding
HRB	Hardness Rockwell – B scale
HSA	high-strength aluminum
HSLA	high-strength low alloy
HSLA 340	steel intended for general presswork, bending, and forming
HT	heat-treated
HTC	heat transfer coefficient when referring to material properties
HTC	high-temperature carbonization when referring to carbon fiber

I

i.e.	abbreviation for “id est,” a Latin phrase meaning “that is”
i3	five-door urban electric vehicle
i8	coupe with an advanced plugin hybrid drivetrain
i_{corr}	corrosion current density
I	electrical current (when referring to mathematical equations)
ICME	integrated computational materials engineering
IE	Erichsen Index
ImageJ	a Java-based software program by the National Institutes of Health used for image analysis and processing
IM	intermetallic
IMC	intermetallic compound
IMP	intermetallic particle
in.	inch
in situ	onsite or in place
INL	Idaho National Laboratory

J

JOEL JEM-2200FS	a state-of-the-art analytical electron microscope equipped with a 200kV field emission gun and an in-column energy filter that allows a zero-loss image resulting in clear images with high contrast manufactured by JOEL Ltd.

K

K	degree Kelvin
k	thermal conductivity (when used in heat transfer equations)
k	abbreviation for 1000
Kα	refers to incident X-rays from aluminum, magnesium and manganese that are monochromatic with an accurately known magnitude used in X-ray photon spectroscopy
k_B	the Boltzmann constant
K_s	rate of chain scission
K_{s0}	the Arrhenius rate factor
K_{TH}	threshold stress intensity
keV	kiloelectron volt
kg	kilogram
kg/m^3	kilograms per cubic meter
kJ	kilojoules
kJ/mol	kilojoules per mole
kN	kilonewton
kN/mm	kilonewton per millimeter
k_p	parabolic rate constant which describes the isothermal oxidation kinetics during high-temperature dwells
K-S	Kolmogorov-Smirnov
Ksi, ksi, and kpsi	kilopound per square inch
KUKA	Keller und Knappich Augsburg
kV	kilovolt
kW	kilowatt
kWh/kg	kilowatt-hour per kilogram
kWh/lb	Kilowatt-hour per pound

L

l	length
LAMMPS	Large-scale Atomic/Molecular Massively Parallel Simulator
Ll_2	designation for the major strengthening phase precipitates of Al alloys

L&L Products	technology driven business-to-business company with unique expertise in static sealing, acoustics, vibration reduction, structural reinforcements, and composite components
Lb	pound(s)
LCF	low cycle fatigue
LCCF	low-cost carbon fiber
LD	light-duty
LDH	layered double hydroxide
Li	lithium
LightMAT	Lightweight Materials Consortium
LIMS	Liquid Injection Molding Simulation
LLC or LCC	Limited Liability Company
LMP	Larson Miller Parameter
LNF	designation for the 260-horsepower direct injection turbo Ecotech engine
LOOCV	Leave One Out Cross-Validation
lp	lattice parameter (used in modeling)
LPBF	laser powder bed fusion
LR	linear regression
LS-DYNA	advanced, general-purpose, multiphysics simulation software package
LSP	laser surface processing
LTC	low temperature carbonization
Ltd.	limited

M

m	meter
m^2	square meter
M	molar
Magna	Magna International Inc.
MAT	material
*MAT233	a LS-DYNA material model for hexagonal closed packet metals capable of describing the yielding asymmetry between tension and compression for such materials
*MAT36	a more accurate LS-DYNA material model that considers planar anisotropy (i.e., R0, R45, and R90 are required) with increased accuracy accompanied by an increase in computational speed
MATLAB	MATrix LABoratory, a multi-paradigm numerical computing environment and programming language
MAS	micro-alloyed steel

MD	medium-duty or molecular dynamic, depending on the report
MD/MC	Molecular Dynamic/Monte Carlo
meV	millielectron volt(s)
Mg	magnesium
$MgCO_3$	magnesium carbonate
MgO	magnesium oxide
Mg_2Si	magnesium silicide
$Mg(OH)_2$	magnesium hydroxide
MIC	maximal information coefficient
min	minute(s)
mJ	milli-Joules
mJ/m^2	milli-Joules per square meter
MKT	Ford Motor Company's designation for "MarK Touring" series of Lincoln makes
mL/h	milliliter per hour
ML	machine-learning
m/min	meters per minute
mm	millimeters
mm^3/Nm	cubic millimeters per nanometer
mm/sec	millimeters per second
MMC	metal matrix composites
Mn	manganese
Mo	molybdenum
MOBNI4	Mobility Ni alloys kinetics database (Thermo-Calc Software) version 4
MOOSE	multiphysics object-oriented simulation environment
MPa	megapascals
mpg	miles per gallon
MRD	multi-ring-domed
ms	milliseconds
MSI or Msi	million pounds per square inch
MSU	Michigan State University
mT	metric ton
MTS	Material Testing Systems
MTU	Michigan Technological University
MUD	multiples of uniform distribution
$mV_{OCP,AA}$	millivolts of open-circuit potential for aluminum alloy

N

n	the nonlinear exponent from a Ramberg-Osgood material law
N	nitrogen
N	number of surviving chains (when referring to the kinetics equation of polymer chain scission)
N_f	number of cycles to failure
NaCl	sodium chloride
Nb	niobium
Nd	neodymium
NEISS	non-equilibrium interfacial solute segregation
NETL	National Energy Technology Laboratory
Ni	nickel
NiCr	nickel-chromium
NiO	nickel (II) oxide
nm	nanometer(s)
Nm	Newton meters
NN	nearest neighbor
N/m	newtons per meter
N/mm	newtons per millimeter
N/mm^2	newtons per square millimeter

O

O	oxygen
O_2	diatomic oxygen
OCP	open-circuit potential
OEM	original equipment manufacturer
OH^-	hydroxide ion
O-octo	O-terminated octopolar
ORNL	Oak Ridge National Laboratory
OSU	The Ohio State University
OT	octet-truss

P

P (or p)	pressure
P^{DIC}	reaction force from digital image correlations
PAA	polyphthalamide
PA-6	polyamide 6 (or nylon 6)

PA-66	polyamide 66 (or nylon 66)
PACE	Partnership on Advanced Combustion Engines
PAN	polyacrylonitrile
PAPSC	Pressure-Assistant Precision Sand-Casting
Pb	lead
PBCM	process-based cost model
PBO	poly(p-phenylene-2,6-benzobisoxazole
PCC	Pearson's correlation coefficient
PE	polyethylene
PEL	potential energy landscape
pH	quantitative measure of the acidity or basicity of aqueous or other liquid solutions
p-k_p	a parameter "p," the proportion of the oxide scale, which spalls at each cycle, and the parabolic rate constant, "k_p" used for determining oxide growth and spallation kinetics
PLC	Portevin–Le Chatelier
PM10	particulate matter smaller than 10 micrometers
PMC	polymer matrix composite
PNNL	Pacific Northwest National Laboratory
POSCO	current company name for Pohang Iron and Steel Company
PP	polypropylene (when referring to polymers)
PP	petroleum pitch (when referring to biomass)
PPA	polyphthalamide
PPG	Pittsburgh Plate Glass
ppm	parts per million
PPM	Pinetree POSCO Mg (when referring to a source of magnesium)
PPM	petroleum pitch mesophase (when referring to biomass)
PPR	Park–Paulino–Roesler
ps	picoseconds
PTFE	polytetrafluoroethylene
PyCALPHAD	an open-source Python library for designing thermodynamic models, calculating phase diagrams and investigating phase equilibria within the CALPHAD method

Q

q	heat flux (when used in heat transfer equations)
QSP	quasistatic pole
QUAKERDRAW® 450 MAG	a metal drawing and forming fluid produced by Quaker-Houghton for use with magnesium

R

r	radius
R^2	coefficient of determination
Ra	the arithmetic average of the absolute values of the profile height deviations from the mean line, recorded within the evaluation length for surface roughness
RAMACO	Ramaco Carbon LLC
RAV4 EV	a "zero emission," plugin, all-electric vehicle produced by Toyota from 1997 to 2003, which was powered by an advanced nickel-metal hydride (NiMH) battery pack with a 27 kWh capacity
R&D	research and development
RDS	rivet delivery system
RE	rare-earth
ReaxFF	reactive force field
ReaxFF MD	reactive force field molecular dynamics
RF	random forest (when referring to machine-learning models)
RH	relative humidity
RiskPy	a Python library for automated risk analysis
RIVTAC®	a high-speed process supplied by Bollhoff for joining Al, steel, plastics, and non-ferrous metals, as well as for mixed joints, multilayer joints, and hybrid joints of these materials
Rotacast®	Nemak-owned technology to gravity fill a mold by the use of a pouring ladle located at the mold
rpm or RPM	revolution(s) per minute
RR	Rolls Royce
RR350	an alloy that evolved from a World War II aircraft application by Rolls Royce (RR)
RSR	resistance spot rivet (or riveting)
RSW	resistance spot weld (or welding)
RT	room temperature
RTM	resin transfer mold (or molding)
RVE	representative volume element

S

s	seconds
SA	simulated annealing
SAE	Society of Automotive Engineers

SAE J175	SAE Recommended Practice for Wheels—Impact Test Procedure—Road Vehicles that provides minimum performance requirements and related uniform laboratory test procedures for evaluating axial (lateral) curb impact collision properties of all wheels intended for use on passenger cars and light trucks
SAE J328	SAE Recommended Practice for Wheels—Passenger Car and Light Truck Performance Requirements and Test Procedures that provides minimum performance requirements and uniform procedures for fatigue testing of wheels intended for normal highway use and temporary use on passenger cars, light trucks, and multipurpose vehicles
SAE J2334	SAE Surface Vehicle Standard used when determining corrosion performance for a particular coating system, substrate, process, or design and can be used as a validation tool as well as a development tool
SAE J2522	SAE Recommended Practice for Dynamometer Global Brake Effectiveness defining an Inertia Dynamometer Test procedure that assesses the effectiveness behavior of a friction material with regard to pressure, temperature and speed for motor vehicles fitted with hydraulic brake actuation with the main purpose of comparing friction materials under the most equal conditions possible
SAE J2530	SAE Recommended Practice for Aftermarket Wheels Performance Requirements and Testing Procedures that provides performance and sampling guidelines, testing procedures and marking requirements for aftermarket wheels used on cars, light trucks and multipurpose vehicles
SAE J2562	SAE Recommended Practice for Biaxial Wheel Fatigue Test that provides uniform laboratory procedures for biaxial fatigue testing of wheels intended for normal highway use and temporary use on passenger car vehicles and light trucks
SBIR	Small Business Innovative Research
SBR	styrene-butadiene rubber
S-C	semi-coherent
SCC	stress corrosion cracking
SCE	saturated calomel electrode
SECCM	scanning electrochemical cell microscopy
SEM	scanning electron microscope (or microscopy)
SFE	stacking fault energy(ies)
SHR	strain-hardening rate
ShAPE™	Shear-Assisted Processing and Extrusion
Si	silicon
SiC	silicon carbide
SiO_2	silicon oxide
s-k_p	simple kp for oxide growth kinetics that gives a parabolic fit up to 100h or less
SL	scribe length (when referring to a friction-stir welding process)
SLA	scalable multi-material stereolithography

SLPS	supersolidus liquid-phase sintering
Sm	samarium
SNL	Sandia National Laboratories
SPR	self-pierce riveting or self-piercing rivet
sR or sr	steradian or square radian
Sr	strontium
SRI	Southern Research Institute
SRS	strain-rate sensitivity
SStAC	Stainless-Steel Alloy Corrosion (the name of a simulation tool)
STEM	scanning transmission electron microscope (or microscopy)
SVM	support vector machine regression

T

t	time
t10	the time it takes an alloy-oxide interface to reach 10 wt.%
T	temperature
T_g	glass transition temperature
T4	temper designation for Al that is solution heat-treated and naturally aged to a substantially stable condition
T5	temper designation for Al that is cooled from an elevated temperature shaping process then artificially aged
T6	temper designation for Al that is heat-treated at a temperature between 325˚F and 400˚F to increase the strength
T7	temper designation for Al that is solution heat-treated and then artificially overaged
Tb	terbium
TCMG5	Thermo-Calc Magnesium version 5 - a Thermo-Calc thermodynamic database for Mg-based alloys used for calculating phase diagrams and thermodynamic properties, and for predicting phase equilibria and simulating solidification processes for a wide range of magnesium alloys
TCNI8	Thermo-Calc Nickel version 8 - a Thermo-Calc thermodynamic database for Ni-based superalloy phases within a 25-element framework plus argon and hydrogen for the gas phase only
TCT	twist compression testing
TD	transverse direction
TEM	transmission electron microscope (or microscopy)
TFP	tailored-fiber placement
Thermo-Calc	software package for thermodynamic
Ti	titanium

Ti-6Al-4V	a Grade 5 alloy consisting of a two-phase α+β titanium alloy with aluminum as the alpha stabilizer and vanadium as the beta stabilizer
TiB_2	titanium boride
TiO_2	titania
Tl	thallium
TL	trifunctional (cross) linker
Tm	thulium
TMPTA	trimethylolpropane triacrylate
TP	thermoplastic
TPI	TPI Composites, Inc.
TS	thermoset

U

u_0	vibration amplitude (for ultrasonic welding)
U	stored energy
ΔU	change (dissipation) of energy
UD	unidirectional
UD-CCM	University of Delaware Center for Composite Materials
UF	University of Florida
UIUC	University of Illinois at Urbana-Champagne
UM	University of Michigan-Dearborn
UP	University of Pennsylvania
U.S.	United States
USAMP	U.S. Automotive Materials Partnership
USW	ultrasonic welding
UTS	ultimate tensile strength
UV	ultraviolet
UW	University of Wyoming

V

V	vanadium
V	voltage (when referring to electricity)
V	wear volume (when referring to friction testing)
Vf	volume fraction
VFAW	vaporizing foil-actuator welding
vol%	volume percent

vs.	versus
V_{SCE}	voltage of the saturated calomel electrode
VTO	Vehicle Technologies Office

W

W	watts
WARP3D	an open-source code for 3D nonlinear analysis of solids
WC	tungsten carbide
WDS	wavelength dispersive spectroscopy
W/mK	watts per meter degree Kelvin
WRI	Western Research Institute
wt%	percent by weight

X

XFEM	extended finite element method
XPS	x-ray photoelectron spectroscopy
XRD	x-ray diffraction

Y

Y	yttrium
YAG	yttrium-aluminum-garnet
Yb	ytterbium
YS	yield strength

Z

ZAXME11100	magnesium alloy with a composition of Mg-1.0Zn-1.0Al-0.5Ca-0.4Mn-0.2Ce by weight percent
ZEK100	magnesium alloy composed of zinc, rare-earth (RE) elements, and Zr
ZFEM	complex-variable (Z) finite element method
ZK60	magnesium wrought alloy consisting of primary matrix α (Mg) and the eutectic
Zn	zinc
ZPPR	complex-valued cohesive model designation
Zr	zirconium
ZX21	magnesium alloy consisting of Mg–2Zn–1Ca
ZX30	magnesium alloy consisting of Mg-3Zn-0.2Ca

Executive Summary

The Materials Technology subprogram supports the Vehicle Technologies Office's (VTO's) mission to accelerate the deployment of clean energy technology toward achieving net-zero emissions in the transportation sector. The Propulsion Materials research portfolio seeks to develop higher performance materials that can withstand increasingly extreme environments and address the future properties needed for a variety of high-efficiency powertrain types, sizes, fueling concepts, and combustion modes. The Lightweight Materials research portfolio enables improvements in fuel economy by providing properties that are equal to or better than traditional materials at a lower weight. Because it takes less energy to accelerate a lighter object, replacing cast-iron (Fe) and traditional steel components with lightweight materials—such as advanced high-strength steels (AHSS), magnesium (Mg) alloys, aluminum (Al) alloys, and fiber-reinforced polymer composites—can directly reduce a vehicle's fuel consumption. By 2025, the Materials Technology research activities seek to enable a 25% weight reduction of the glider for light-duty (LD) vehicles including body, chassis, and interior as compared to a 2015 baseline at no more than a $5/lb-saved increase in cost.

Propulsion Materials

In fiscal year (FY)-2020, the Propulsion Materials portfolio included research in four main areas: (1) use of multiscale modeling to predict corrosion and oxidation of engine components and the material properties needed for future engines; (2) development of new lightweight alloys for high-temperature engine components; (3) additive manufacturing (AM) of powertrain alloys; and (4) lightweight high-efficiency engines for medium-duty (MD) vehicles. In addition to these four main thrusts, work was completed on several exploratory projects in novel materials, coatings, processing techniques, and characterization methods relevant to propulsion materials.

The environment within an engine and exhaust system during operation is extremely harsh, with high temperatures and pressures, combustion, and corrosive exhaust gases. This environment corrodes components, including engine intake and exhaust valves, valve seats, and exhaust manifolds. Three projects aim to develop practical and accurate models that can rapidly evaluate corrosion/oxidation of materials—such as stainless-steel, nickel-chromium (NiCr) based alloys, and cast-Fe—and predict the components performance. These new models will help decrease the time and cost of development as materials are selected for new engines that operate at higher temperatures.

Automotive applications need low-cost, lightweight, high-temperature alloys to enhance efficiencies in systems such as internal combustion engines. One project focuses on increasing the compositional range of the Al-Fe-silicon (Si) system via alloy design and non-equilibrium processing, such as AM. Another effort seeks to develop a fundamental understanding of the features that impart thermal stability to cast-Al precipitate microstructures, such as those found in Al-Cu and ACMZ alloys. Some components, such as exhaust valves, are exposed to even higher temperatures and the development of lower cost, improved wrought-processed Ni-based alloys is needed to achieve the combination of yield and fatigue strengths, oxidation resistance, and cost specific to the operating characteristics and lifetime expectations. Pistons in heavy-duty (HD) diesel engines also have unique requirements and researchers are investigating existing commercial alloys, new developmental alloys, and alloys combined with thermal barrier coatings to enable increased operating temperature while requiring only moderate cost increases. Lastly, corrosion-resistant coatings are also being evaluated to determine whether the operating temperatures of alloys can be increased by improving cyclic oxidation resistance without impacting the alloy high cycle fatigue behavior.

AM offers unprecedented possibilities to fabricate unique and complex near net-shape components leading to significant savings by decreasing tooling and materials cost, accelerating prototype development, offering unique properties, and increasing system efficiency through advanced designs not achievable via conventional fabrication processes. In-depth understanding of the relationship between microstructure and processing

parameters could result in unique microstructures and enhanced or geometrically tailored properties for a wide range of powertrain materials and components. Work in this area addresses the specific challenges and opportunities associated with AM for future LD and HD engine components. Key factors, such as cost, influence of feedstock characteristics, volatilization of species, cooling rates, non-equilibrium phases, materials properties, non-uniform geometry-dependent thermal history, thermal cycling, etc., are assessed for existing and new materials via both modeling and experimental studies.

While the market share of battery electric vehicles is increasing, most MD vehicles are projected to contain conventional or hybrid internal combustion engines well beyond 2030. Improvements in engine efficiency and reductions in powertrain weight have strong leverage to reduce vehicle related CO_2 emissions for decades to come. Two new projects will use advanced materials and weight savings technologies to demonstrate greater than 15% weight reduction of the baseline engine while increasing efficiency. Approaches being investigated include development of new high-strength and heat-resistant materials that can be incorporated with novel metal casting and AM processes to produce highly durable engine structures to maximize performance of the materials and systems with minimum mass and cost.

Lightweight Materials

In FY-2020, the lightweight materials portfolio included research in these three areas: (1) improving the properties and manufacturability of light metals, such as AHSS, Al alloys, and Mg alloys; (2) reducing the cost of carbon fibers (CFs) and developing Integrated Computational Materials Engineering (ICME) frameworks for manufacturing of polymer composites; and (3) developing novel joining methods to enable multi-material systems.

Substitution of light metals for mild steel can result in weight savings of 25% to 60% per component, which increases fuel efficiency. However, there are several challenges to the increased use of light metals including material cost, room temperature formability, and corrosion mitigation. One project is working to lower the cost of Al castings to be more competitive with cast-Fe by using novel processing methods to break up the detrimental iron-intermetallic phases that can form in less expensive secondary Al alloys. Similarly, the use of high-performance Mg alloys in the automotive industry is currently limited due to the addition of costly rare-earth (RE) elements, need for high-temperature forming, and difficulties in corrosion mitigation. Two projects in this report aim to eliminate the need for RE additives—one through alloy development and the other through a novel solid-phase processing method—while an additional project seeks to validate methods of preventing Mg corrosion.

Polymer composites also have the potential to reduce component weight by more than 60%. One of the main barriers to widespread implementation is the high cost of CF, which is due in large part to the cost of input material (precursor) and the CF conversion process. In addition to a successfully commercialized plasma oxidation technology, one project is addressing this challenge by developing higher throughput, low temperature carbonization of CF, thus further lowering manufacturing costs and increasing production rates. Two projects are investigating potential low-cost CF alternative precursors utilizing ICME models to guide their research to meet DOE's cost targets (no more than $5 per pound). Another challenge to implementation of polymer composites is related to the time required to manufacture components. One project demonstrated cradle-to-grave by integrating manufacturing with structural performance using ICME framework for high-volume production for underbody assembly utilizing a fast-cure resin via the developed ICME frameworks to reduce cycle time (less than three minutes). Several other projects are tackling the challenge of manufacturing automotive components such as doors, wheels, and seat backs using low-cost, high-throughput manufacturing methods.

The most effective way to reduce the overall weight of a vehicle is to tailor the material selection to each component's needs. However, joining dissimilar materials to create a multi-material structure is a significant challenge. In FY-2020, the Joining Core Program continued its efforts to address specific challenging material pairs including Mg-CFRP, CFRP-steel, and Mg-steel, as well as addressing galvanic corrosion in joints. The methods developed in the Joining Core Program include ultrasonic welding, novel methods for mechanical fastening, overmolding, adhesives, and friction-stir-welding. Solid-state welding, including an impact welding process investigated by one project, allows for joining materials with vastly different melting temperatures, which is not possible with fusion welding. Another two projects incorporate fasteners into welding processes, both solid-state and fusion, in order to provide a strong spot joint comparable to resistance spot welds in steel-to-steel joints. Research on adhesives addresses concerns with the coefficient of thermal expansion (CTE) mismatch seen in dissimilar material joints, as well as predictive modeling of environmental damage. Additional modeling work includes two projects that model the effect of galvanic corrosion on a wide variety of joining methods and material combinations to predict the effect on joint strength and fatigue life and one project that predicts failure of Al to steel joints.

Table of Contents

List of Figures

List of Tables

Vehicle Technologies Office Overview

Vehicles move our national economy. Annually, vehicles transport 11 billion tons of freight—about $35 billion worth of goods each day[1]—and move people more than 3 trillion vehicle-miles.[2] Growing our economy requires transportation, and transportation requires energy. The transportation sector accounts for about 30% of total U.S. energy needs[3] and the average U.S. household spends over 15% of its total family expenditures on transportation, making it the most expensive spending category after housing.[4]

The Vehicle Technologies Office (VTO) funds a broad portfolio of research, development, demonstration, and deployment (RDD&D) projects to develop affordable, efficient, and clean transportation options to tackle the climate crisis and accelerate the development and widespread use of a variety of innovative transportation technologies. The research pathways focus on electrification, fuel diversification, vehicle efficiency, energy storage, lightweight materials, and new mobility technologies to improve the overall energy efficiency and affordability of the transportation or mobility system. VTO leverages the unique capabilities and world-class expertise of the National Laboratory system to develop innovations in electrification, including advanced battery technologies; advanced combustion engines and fuels, including co-optimized systems; advanced materials for lighter-weight vehicle structures; and energy efficient mobility systems.

VTO is uniquely positioned to accelerate sustainable transportation technologies due to strategic public-private research partnerships with industry (e.g., U.S. DRIVE, 21st Century Truck Partnership) that leverage relevant expertise. These partnerships prevent duplication of effort, focus DOE research on critical RDD&D barriers, and accelerate progress. VTO focuses on research that supports DOE's goals of building a 100% clean energy economy, addressing climate change, and achieving net-zero emissions no later than 2050 to the benefit of all Americans.

Annual Progress Report

As shown in the organization chart (below), VTO is organized by technology area: Batteries & Electrification R&D, Materials Technology R&D, Advanced Engine & Fuel R&D, Energy Efficient Mobility Systems, and Technology Integration. Each year, VTO's technology areas prepare an Annual Progress Report (APR) that details progress and accomplishments during the fiscal year. VTO is pleased to submit this APR for Fiscal Year (FY) 2020. In this APR, each project active during FY 2020 describes work conducted in support of VTO's mission. Individual project descriptions in this APR detail funding, objectives, approach, results, and conclusions during FY 2020.

[1] Bureau of Transportation Statistics, Department of Transportation, Transportation Statistics Annual Report 2018, Table 4-1. https://www.bts.gov/tsar.
[2] Transportation Energy Data Book 37th Edition, Oak Ridge National Laboratory (ORNL), 2019. Table 3.8 Shares of Highway Vehicle-Miles Traveled by Vehicle Type, 1970-2017.
[3] Ibid. Table 2.1 U.S. Consumption of Total Energy by End-use Sector, 1950-2018.
[4] Ibid. Table 10.1 Average Annual Expenditures of Households by Income, 2016.

Organization Chart

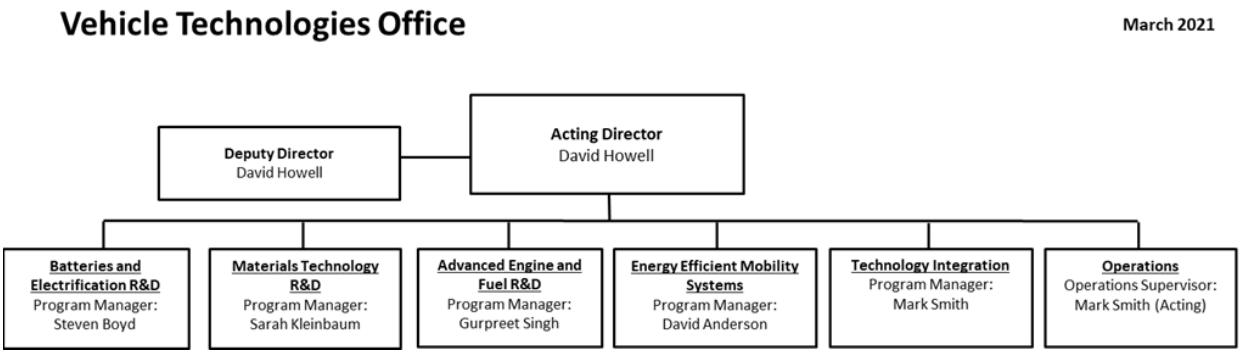

Materials Technology Program Overview

Introduction

The Materials Technology subprogram supports vehicle lightweighting and improved propulsion (powertrain) efficiency through early-stage research and development (R&D) to increase understanding of novel materials and by engaging industry to further develop and deploy technologies into more fuel-efficient LD and HD vehicles. Research activities that have a high degree of scientific or technical uncertainty are often led by National Laboratories or their academic partners. As materials discoveries mature into promising technologies, material manufacturers, automotive original equipment manufacturers (OEMs), and suppliers are consulted and engaged to test feasibility in relevant automotive applications in preparation for market realization.

The Propulsion Materials portfolio is closely aligned with other VTO subprograms to identify critical materials needs for next-generation high-efficiency powertrains for both HD and LD vehicles. Strategies for achieving high-efficiency powertrains include improved powertrain thermal efficiency, increased power density resulting from high-strength and lightweight materials, and petroleum displacement through fuel substitution strategies. The Propulsion Materials portfolio features a National Laboratory consortium that targets critical engine components based on thermal loading and structural requirements and utilizes an ICME approach to link advanced characterization to high-performance computing methods to accelerate development of new material families. In FY-2020, a collaboration with the Advanced Engine and Fuels subprogram resulted in two new projects that will concurrently improve engine efficiency and target a 15% weight reduction of powertrain components.

The Lightweight Materials team works closely with industry through the U.S. DRIVE partnership to understand LD vehicle structural weight reduction goals and to identify technical challenges that prevent the deployment of lightweight materials. The most promising and likely approach for lightweighting is a multi-material structure, which focuses on the use of the right material for the application. The Lightweight Materials research portfolio addresses significant technology gaps for each family of structural materials: Mg, AHSS, Al, and polymer composites. Gaps include raw material costs, formability, manufacturing cycle time, ability to model and predict failure, and corrosion mitigation. In addition, research efforts investigate dissimilar material joining in order to enable the reliable assembly of these multi-material systems.

Goals

The Materials Technology subprogram supports the VTO's mission to accelerate the deployment of clean energy technology toward achieving net-zero emissions in the transportation sector." Lighter vehicles with more efficient engines reduce fuel use, decrease greenhouse gas emissions, and save consumers money. The structural and powertrain systems that we target to improve are limited by materials performance. By improving the properties of powertrain and structural materials, we can enable a significant improvement in fuel economy for future vehicles. Increasing the strength and oxidation resistance of high-temperature materials will enable new combustion strategies while improving properties in structural materials, such as stiffness, strength, joinability, and crash energy absorption—all with lower cost—will accelerate the deployment of lightweight materials in the automotive market. The specific performance and cost targets for the Materials Technology subprogram are to:

- Enable a 25% weight reduction for LD vehicle gliders including body, chassis, and interior as compared to a 2015 baseline at no more than a $5/lb.-saved increase in cost by 2025.
- Validate a 25% improvement in high-temperature (300°C) component strength relative to components made with 2010 baseline cast-Al alloys (A319 or A356) for improved efficiency LD engines by 2025.

State-of-the-Art

Automakers are seeking to improve fuel economy while maintaining or improving vehicle performance and safety. Reducing the weight of the vehicle's structure improves fuel economy and reduces the demand on the vehicle's powertrain, allowing for further fuel savings. For structural components, the market is shifting from traditional steel components to lighter weight materials, such as AHSS, Al alloys, Mg alloys, and CF composites. Lighter structures allow for downsized powertrains with smaller engines or battery packs, while maintaining or improving vehicle performance.

In order to meet property requirements in increasingly severe combustion environments, new cast-Al alloys are needed. This is due, in part, to inadequate thermal performance, as well as very high peak cylinder pressures in advanced engine applications. Moreover, inadequate databases, modeling, and design tools are significant barriers for further development of new materials. By evaluating existing computational tools and identifying gaps that must be overcome to achieve seamless integration across multiple-length scales and increasing understanding of the basic behavior of the material (e.g., effects of solute at the atomistic level, microstructural development, microstructure/property relationships, fracture and failure mechanisms, durability, temperature dependent behavior, etc.), more accurate design tools and predictive models can be established. High-quality, consistent, and accessible databases are needed to support this development.

AHSS is the most mature lightweight material in terms of widespread use in industry due to its compatibility with existing manufacturing infrastructure and vehicle materials. Application of third generation high-strength steel has the potential to reduce component weight by up to 25%, particularly in strength-limited designs. However, technical challenges remain to improve weldability and weight reduction is dependent on the ability to maintain stiffness at reduced gauges. Al continues to see steady growth in market share in the automotive industry despite issues of material cost, room temperature (RT) formability, and limitations within the existing manufacturing infrastructure. This is due to the 40% weight savings that can be achieved with Al along with the well-established domestic supply chain. Mg has the potential to significantly reduce vehicle component weight by 55% or greater; however, there are several significant technical barriers preventing increased use of this material in vehicle designs. Mg has high raw material costs and price volatility, relatively low specific stiffness, difficulty in forming sheet at low temperatures, low ductility of finished components, and a limited alloy set, among other challenges. CF and other polymer composites have the potential to reduce component weight by more than 60%. The main barriers to widespread use are the high cost to manufacture the CF, lack of high-volume composite manufacturing methods, and a need for reliable predictive tools for both part design and performance prediction.

When combinations of the above lightweight materials are used, the resulting multi-material structures have challenges of their own. Traditional joining methods used in automotive assembly, such as resistance spot welding and riveting, are inefficient for joining of dissimilar metals and for some combinations, infeasible. In the near-term, friction-stir scribe welding and resistance spot riveting are showing promising advances for joining of AHSS and Al (the more mature lightweight metals). An additional challenge posed by multi-material structures is the increased risk of corrosion due to galvanic coupling. As the barriers to introduction of Mg and CF are overcome, breakthroughs in joining technology will also be necessary.

Program Organization Matrix

The Materials Technology subprogram is led by Acting Program Manager, Gurpreet Singh.

- Propulsion Materials focuses on:
  - High-Temperature Materials (Jerry Gibbs) – which includes research on the material characteristics that influence temperature dependent behavior, as well as alloy development.
- Lightweight Materials consists of three research portfolios:
  - Light Metals (Sarah Kleinbaum / Jerry Gibbs) – which includes research on property improvement and processing advances for AHSS, Al, and Mg.
  - Polymer Composites (Felix Wu) – which includes research on low-cost production of CF, novel processing methods for polymer composites, and predictive performance models of CF and other fiber-reinforced or hybrid composites.
  - Joining of Dissimilar Materials (Sarah Kleinbaum) – which includes research on solid-state, mechanical, and chemical joining methods, as well as galvanic corrosion mitigation.

All of the activities within the Materials Technology subprogram utilize computational methods for material discovery, prediction of structure, understanding failure mechanisms including corrosion, and the effects of processing on properties.

(This page intentionally left blank)

I Propulsion Materials

I.1 Modeling of Powertrain Materials

I.1.1 Multi-Scale Modeling of Corrosion and Oxidation Performance and Their Impact on High-Temperature Fatigue of Automotive Exhaust Manifold Components (Ford Motor Company)

Mei Li, Principal Investigator
Ford Motor Company
2101 Village Road
Room 2014
Dearborn, MI 48124
E-mail: mli9@ford.com

Jerry L. Gibbs, DOE Technology Manager
U.S. Department of Energy
E-mail: jerry.gibbs@ee.doe.gov

Start Date: October 1, 2018 End Date: September 30, 2021
Project Funding: $1,840,000 DOE share: $1,260,000 Non-DOE share: $580,000

Project Introduction

Corrosion and oxidation of exhaust manifold components made from cast-Fe or steel under typical service conditions can be very severe and are a chief concern within the automotive industry, yet an understanding remains elusive as of today [1]. This is partly due to the lack of knowledge regarding the failure in structural components having been built upon either corrosion/oxidation or mechanical loads independently. In real applications, however, materials are susceptible to experiencing corrosion/oxidation in synergy with mechanical loads, which is more severe than the effects produced by these two mechanisms independently.

In this project, it is proposed to develop a multi-scale computational model to predict:

1. The oxidation/corrosion performance of two different categories of iron-based materials used for exhaust manifold in Advance Combustion Engine and Emission Control (ACEC) gas compositions at two different temperatures (e.g., 805°C and 1050°C). This model, spanning from the atom level to the microstructure level, aims to study the oxidation/corrosion susceptibility of materials of interest to ACEC gas, as well as the diffusion-controlled growth of oxidation/corrosion production.
2. The lives of exhaust manifold components, based on a comprehensive database of high-temperature corrosion/oxidation and fatigue durability data, and a thorough and detailed investigation of the physical mechanisms that cause damage in high-temperature fatigue, with special consideration of the synergy effects of corrosion/oxidation.

Objectives

- To develop multi-scale computational models capable of predicting the location and extent of high-temperature corrosion/oxidation of automotive exhaust manifold materials (e.g., cast steels, Ni-resistant, cast-iron) in ACEC gas compositions for temperatures up to 1050°C.
- To conduct static and thermal cycling corrosion/oxidation trials in controlled atmosphere and demonstrate the model capable of predicting the corrosion/oxidation performance of the exhaust manifold materials exposed to high temperatures and realistic combustion gases to within 10% of experimental measurements.

- To develop a robust computational model to predict the high-temperature fatigue life of the material under corrosive/oxidizing conditions, and demonstrate the model is capable of predicting the corrosion/oxidation-fatigue performance of exhaust manifold materials exposed to high temperatures and realistic environment to within 10% of experimental measurements.
- To demonstrate the predictive utility of the developed corrosion/oxidation-fatigue model in accelerating the development of new exhaust manifold alloys.

Approach

- Develop a multi-scale simulation method that integrates atomistic and mechanistic models to understand the influence of composition, microstructure, and environment on the corrosion/oxidation performance of iron-based materials in combustion gases.
- Validate the corrosion/oxidation performance models using static and thermal cyclic corrosion/oxidation trials in controlled, realistic combustion gases.
- Develop and validate the corrosion/oxidation-fatigue model for exhaust manifold components.
- Demonstrate success of the project by quantifying the acceleration of developing new exhaust manifold alloys with computational tools.

Results

In FY 2020, the progress in both simulations and experiments were made for the assessment of corrosion/oxidation performance of high silicon molybdenum (HiSiMo)-type cast-Fe alloys in an exhaust gas environment.

Experimentally, the oxidation performance of HiSiMo-type alloys under static and cyclic oxidation conditions were quantified using weight changes, scanning electron microscope (SEM), and transmission electron microscope (TEM). Four different HiSiMo-type alloys with Cr and Al as alloying elements were cast and their chemical compositions are listed in Table I.1.1.1. All these alloys exhibit the typical as-cast-Fe microstructures that consist of an Fe matrix, graphic nodules, and Mo-rich eutectics.

Table I.1.1.1. Studied Chemical Composition of HiSiMo-Type Alloys in Weight Percent

Alloy Designation	Ci	Si	Mn	Mo	Ni	Cr	Al	Fe
HiSiMo	3.20	4.30	0.32	0.78	0.20	0.05	N/A	Bal.
HiSiMo-0.5Cr	3.13	4.70	0.30	0.80	0.15	0.52	N/A	Bal.
HiSiMo-0.9Cr	3.11	4.60	0.30	0.86	0.15	0.90	N/A	Bal.
HiSiMo-3Al	2.90	2.70	0.30	0.70	0.09	0.10	3.0	Bal.

First, the cyclic oxidization trials were conducted for those HiSiMo-type alloys in dry air and wet air with 10 vol% water vapors to record the mass changes, which are always used to represent the degree of oxidation. The temperature region was selected from RT to 800°C with a cycle time of 0.1 h. The mass change curves for the four alloys in experiments conducted at Oak Ridge National Laboratory (ORNL) are shown in Figure I.1.1.1(a). The equipment for cyclic oxidation trials are well described in Pinto *et al.* [2]. The mass of the base HiSiMo alloys gradually increases after a rapid mass gain stage. The two-stage oxidation process that is characterized by the two different slopes in the mass change curves relates to the oxidation reaction and continuous transportation of oxidation products to the interior of the metal. For the alloys with the additions of Cr or Al, the masses are constant after the occurrence of oxidation reactions, which indicates the formation of protective scales. This indicates that the alloying elements of Cr and Al can significantly enhance the oxidation resistance of HiSiMo-type alloys. In addition, Figure I.1.1.1(b) illustrates SEM imaging of the oxidation layers formed after 750°C static oxidation trials in combustion gas for 100 h to further demonstrate the merits of the

addition of Cr and Al in improving the oxidation performance of HiSiMo-type alloys. In terms of oxidation layer thickness, HiSiMo-3Al shows the greatest oxidation resistance, followed by the alloys with a CR alloying, while the thickest oxidation layers were developed in base HiSiMo alloys. This agrees well with the results of the cyclic oxidation trials.

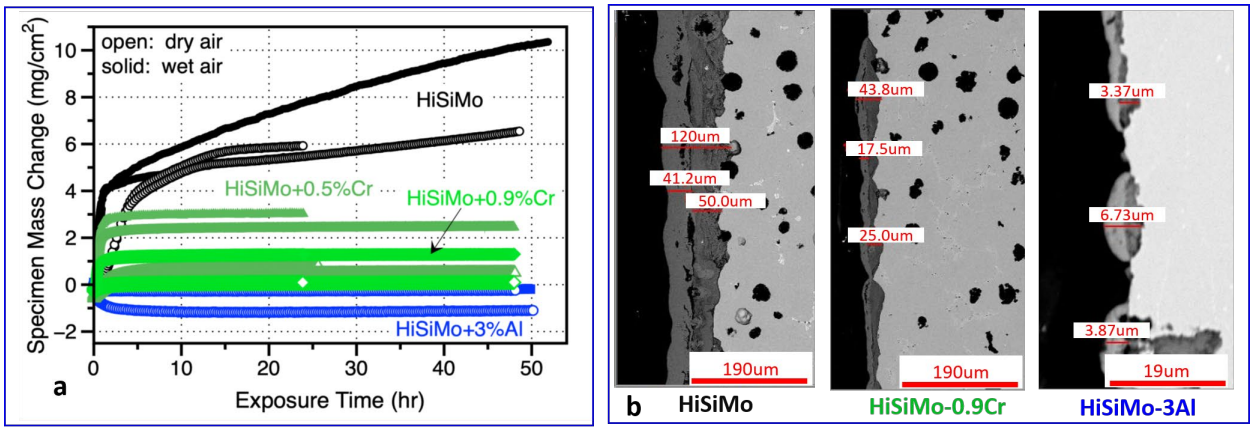

Figure I.1.1.1. (a) Mass changes during cyclic oxidation trials. (b) Oxidation layer structures and thicknesses of static oxidation trials for HiSiMo-type alloys. Source: ORNL and Missouri Science and Technology.

To reveal the involved oxidation reactions, TEM was employed to further investigate the details of oxidation products that show multilayer structures in the SEM imaging. Figure I.1.1.2 shows the TEM results of the oxidation scale in HiSiMo-0.9Cr statically oxidized in combustion gas at 750°C for 100 h. Region A was determined as the alloy matrix since no oxygen (O) was detected in the energy-dispersive spectrometer analysis. Next to region A, a very thin layer with a thickness of 100 µm was observed, labeled as region B, which mainly consists of nano-crystalline Cr-Si oxides with very small amount of Fe. The formation of these nano-crystalline Cr-Si oxides result from the migration of Cr to metal surface and the sequential reactions with combustion gas species. Such layers are absent in the TEM results of base HiSiMo alloys. Therefore, it is inferred that the segregation behavior of Cr contributes to the formation of Fe-dilute layers to reduce oxidation reactions. In addition to the layer with nano-crystalline Cr-Si oxides, another two oxidation layers were observed in TEM imaging. Region C shows a mixture of amorphous Si and pure Fe-O phases, while region D is composed of pure Fe-O and complex Fe-Si-O crystalline phases with sizes of 100–200 µm, as can be observed in Figure I.1.1.2. These experimental results would be used to validate the simulation results.

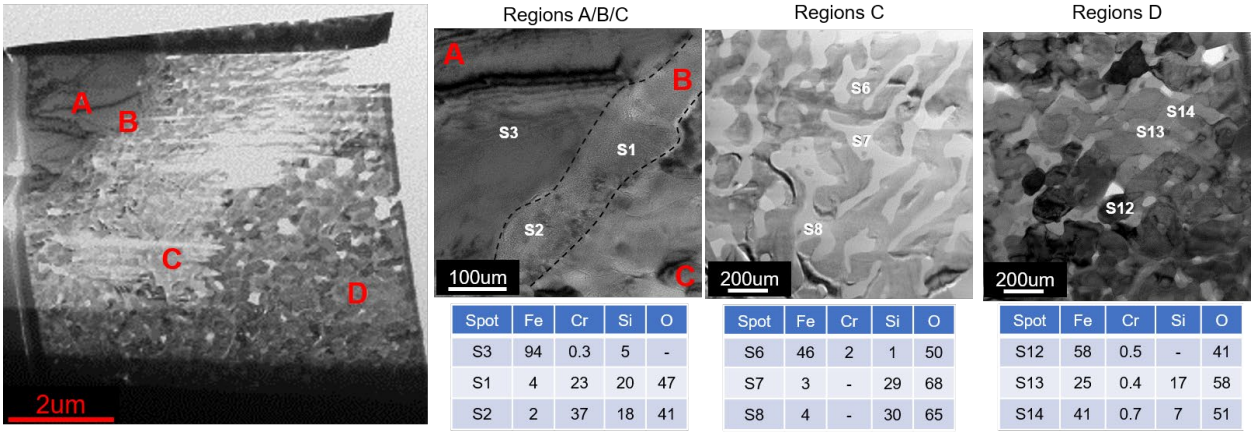

Spot	Fe	Cr	Si	O
S3	94	0.3	5	-
S1	4	23	20	47
S2	2	37	18	41

Spot	Fe	Cr	Si	O
S6	46	2	1	50
S7	3	-	29	68
S8	4	-	30	65

Spot	Fe	Cr	Si	O
S12	58	0.5	-	41
S13	25	0.4	17	58
S14	41	0.7	7	51

Figure I.1.1.2. TEM imaging and energy-dispersive spectrometer analysis of the oxidation layers formed after 750°C static oxidation trials for HiSiMo-0.9Cr in combustion gas for 100 h. Source: Ford.

A multi-scale simulation framework that includes a reactive force field molecular dynamic, ReaxFF MD [3], and a diffusion-controlled phase-transformation DICTR simulation are proposed to study the reaction and diffusion-dominated processes, respectively, as observed in oxidation trials of HiSiMo-type alloys. The efforts were mainly made to develop a robust ReaxFF MD by integrating with density function theory (DFT) and potential energy landscape (PEL) methods in FY 2020.

The initial status shown in Figure I.1.1.3 illustrates the basic settings for ReaxFF MD simulation. Metallic atoms were arranged as a body-centered cubic (bcc) structure in the middle of simulation boxes with dimensions of 30Å×30Å×100Å, while gas species including 50 H_2O molecules and 50 O_2 molecules were introduced into the simulation boxes from the top and the bottom. The employed force fields that describe the interactions between metal-metal, metal-gas, and gas-gas were obtained from Shin *et al.* [4]. ReaxFF MD simulations were then performed for pure Fe and Fe50at%-Cr25at%-Al25at% with a constant size, temperature, and pressure ensemble to study the influence of alloying elements and temperatures on oxidation dynamics. After 0.5 ns and 1 ns simulation time, additional sets of O_2 and H_2O molecules were added to the simulation boxes to maintain the pressures. Figure I.1.1.3 shows the configuration snapshots at three simulation times. This indicates that the metal surfaces were able to capture gas species under the employed force fields to form oxidation layers and that the thickness increased with simulation time evolving.

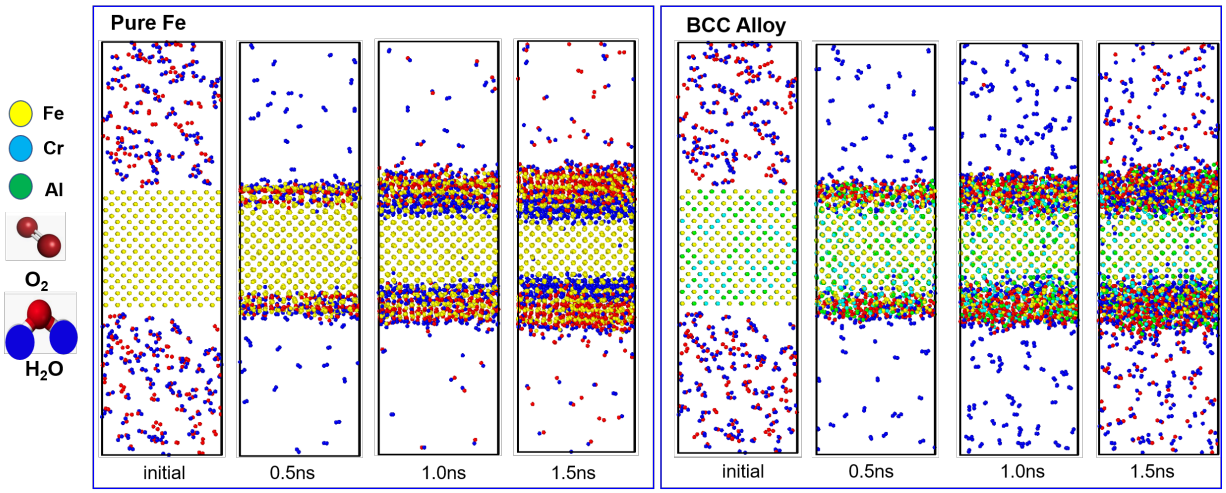

Figure I.1.1.3. Configuration evolution results in ReaxFF MD simulation of oxidation reactions for pure Fe and the bcc alloy in the gas system consisting of H_2O and O_2 molecules. Source: The Ohio State University.

The configuration results, however, cannot provide quantitative comparisons between pure Fe and the bcc alloy to determine the advantages of alloying elements. Instead, through the systematic studies, several insights were achieved by correlating the reduced oxidation phenomena with stresses-related quantities. The simulation box was equally divided into 100 bins along the long axis and the stress in each bin was derived using the canonical ensemble over all the atoms/molecule within the bin. Figure I.1.1.4 shows the ReaxFF MD simulated stress results for the bcc alloy to illustrate these correlations. First, the distribution of O at outer part of metals agrees with the stress profile well and is referred to as the stress gradient. This results from the segregation of alloying elements, including Cr and Al, into a metal surface under the reactive force fields. Second, it is easily inferred that the summation of stresses can be used to represent the thickness of oxidation scales. Third, the stress peak determines the adsorption of the H_2O molecule to a metal surface, and thus determines the remaining H_2O molecule in the gas environment as well. Fourth, the diffusivity of O and H decreases within the stress drop regime, which is due to highly disordered O and H distribution driven by the reactive force field.

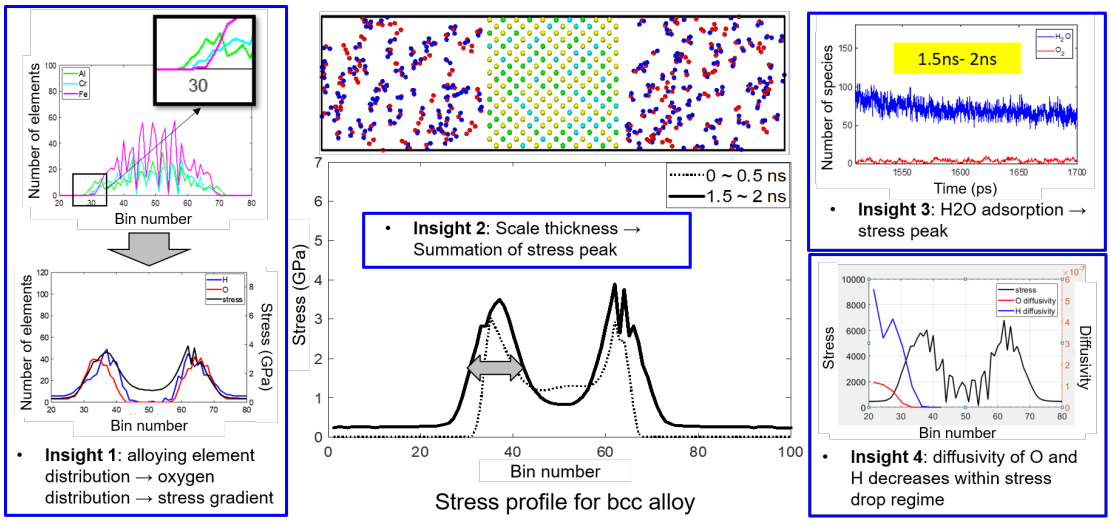

Figure I.1.1.4. Correlations between stress results in ReaxFF MD simulations and reduced oxidation phenomena to quantify oxidation performance. Source: The Ohio State University.

The ReaxFF MD simulation results at 0.5 ns in terms of stress gradient, peak stress, and summation of stresses for pure Fe and the bcc alloy at 800K and 1500K are listed in Table I.1.1.2. The data indicate that the increasing of temperature results in increases of peak stress, stress gradient, and summation of stresses, as well as the reduction of oxidation resistance for both pure Fe and the bcc alloy. On the other hand, the bcc alloy always has a smaller peak stress, stress gradient, and summation of stresses than that of pure Fe, which associates the reduced oxidation phenomena, including more remaining H_2O in gas, lower O distribution at the outer part of the metal matrix, and thinner oxidations scale. Based on these observations in the ReaxFF MD simulation, it is thus concluded that the better anti-oxidation performance of the bcc alloy with additions of Cr and Al, compared to pure Fe, is resulted from mechanical properties, chemical species adsorption, and transport properties, which are directly related to the stress gradient, peak stress, and summation of stresses, respectively.

Table I.1.1.2. The ReaxFF MD Simulation Results for bcc Alloy and Pure Fe at 0.5 ns in Terms of Peak Stress, Stress Gradient, and Summation of Stresses

Metals	Peak Stress (GPa)	Stress Gradient (GPa/Å)	Summation of Stresses (GPa)
Bcc Alloy at 800K	3.9	0.45	76.2
Pure Fe at 800K	5.8	1.13	126.6
Bcc Alloy at 1500K	4.4	0.60	111.5
Pure Fe at 1500K	6.0	1.20	148.6

In the ReaxFF MD simulation, the reactive force fields between the exhaust gas species and oxidation products are excluded since they are not available in the current database. These force fields, however, play an important role in determining the stabilities of oxidation products and the following reaction dynamics once all the metallic atoms at the surface transform to corresponding oxides. DFT calculations were conducted to investigate the adsorption energies of exhaust gas species that include CO, CO_2, H_2O, and O_2 on the surfaces of Fe_2O_3, Cr_2O_3, and Al_2O_3. Figure I.1.1.5(a) shows a representative DFT investigation for Fe_2O_3. A structure of H_2O on a specific surface position in a Fe_2O_3 slab was created and fully relaxed to achieve the ground state. Following that, the adsorption energy was calculated with reference to the ground energies of H_2O and Fe_2O_3. The position dependent adsorption energies of different gas species on the Fe_2O_3 slabs are also shown in Figure I.1.1.5(a). These adsorption energies will be converted to Gibbs free energy to parameterize the reactive force fields between exhaust gas species and oxidation products.

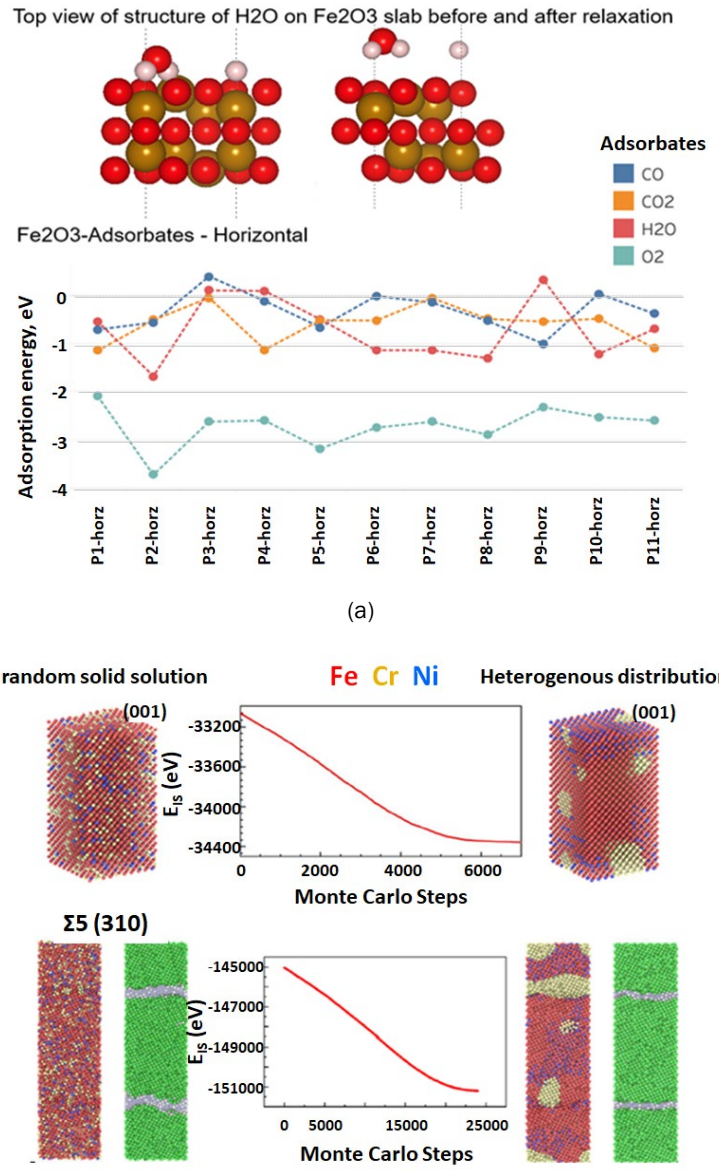

Figure I.1.1.5. (a) DFT calculation of adsorption energy of exhast gas species on the Fe oxide surface. (b) A PEL simulation of segregated structures on surface and grain boundaries. Sources: The Ohio State University and University of Michigan.

Finally, PEL modeling was employed to create heterogenous metal structures in contrast to random solid solutions that are generally used in a ReaxFF MD simulation. The formation of heterogenous structures relates to the migration of solute atoms to their energetic favored positions. Such a solid-state diffusion process is hard to be tackled by a MD method due to the timescale limitation. The heterogenous structures for austenitic steels with additions of Ni and Cr were created using the interatomic potential developed by Bonny *et al.* [5], because it provided a stable and segregated structure after thousands of Monte Carlo Steps, as shown in Figure I.1.1.5(b). Cr segregated to metal surfaces or grain boundaries with decreasing energies. PEL modeling with the activation-relaxation technique [6] also reveals that the peaks of probability distribution functions for mitigation of Cr at both surfaces and grain boundaries locate at a lower energy position than Fe, which indicates that Cr has a higher mobility at surfaces and grain boundaries. The segregated structure will be integrated with a ReaxFF MD simulation.

Conclusions

Static and cyclic oxidation trials were performed for HiSiMo-type alloys in the selected environment. Base HiSiMo alloys exhibited much higher mass increases after both static and cyclic oxidation trials than the alloys with additions of Cr or Al, which indicates a higher degree of oxidation. Oxidation products with multilayer structures were observed in SEM and TEM characterizations which revealed that the unique segregation behavior of alloying elements that results in the formation of Fe-dilute layers contributes the enhanced oxidation resistance. The experimental results demonstrate the merits of alloying element and will be used to validate the simulation results.

ReaxFF MD simulations were employed to study the oxidation reactions of pure Fe and bcc alloys in the selected environment. The correlations between stress related quantities and reduced oxidation phenomena were successful established. It is thus concluded that the bcc alloy with addition of Cr and Al have merits over pure Fe in terms of peak stress, stress gradient, and summation of stresses. In addition, DFT was employed to investigate the surface coverage of exhaust gas species on Cr/Al/Fe oxides surface and PEL was used to understand the segregation of alloying elements, which will provide more reliable force field and more realistic metal structures, respectively, to increase the robustness of ReaxFF MD simulation.

Key Publications

Three publications are under preparation and will be submitted in FY 2021:

1. "First principle study of surface properties and adsorption of exhaust gas species on fe/cr/al oxides."
2. "Molecular dynamic simulation of the effects of Cr and Al on oxidation performance of bcc iron using a Reactive Force Field."
3. "Potential Energy Landscape Evaluation of Migration Mechanisms of Cr and Ni in Austenitic Steels."

References

1. Ekström, M., 2015, "Oxidation and corrosion fatigue aspects of cast exhaust manifolds," Doctoral dissertation, KTH Royal Institute of Technology, Stockholm, Sweden. Available at: http://kth.diva-portal.org/smash/get/diva2:810259/FULLTEXT01.pdf (last accessed 2 December 2020).
2. Pint, B. A., I. G. Wright, and P. F. Tortorelli, 2002, "Effect of cycle frequency on high-temperature oxidation behavior of alumina-forming alloys," *Oxid. Met.,* Vol. 58, pp. 73–101.
3. Zou, C., Y. K. Shin, A. C. T. van Duin, H. Fang, and Z.-K. Liu, 2015, "Molecular dynamics simulations of the effects of vacancies on nickel self-diffusion, oxygen diffusion and oxidation initiation in nickel, using the ReaxFF reactive force field," *Acta Mater.*, Vol. 83, pp. 102–112.
4. Shin, Y. K., H. Kwak, A. V. Vasenkov, D. Sengupta, and A. C. T. van Duin, 2015, "Development of a ReaxFF reactive force field for Fe/Cr/O/S and application to oxidation of butane over a pyrite-covered Cr_2O_3 catalyst," *ACS Catal.*, Vol. 5, No. 12, pp. 7226–7236.
5. Bonny, G., N. Castin, and D. Terentyev, 2013, "Interatomic potential for studying aging under irradiation in stainless steels: The FeNiCr model alloy," *Model. Simul. Mat. Sci. Eng.*, Vol. 21, No. 8, Art. 085004.
6. Cances, E., F. Legoll, M.-C. Marinica, K. Minoukadeh, and F. Willaime, 2009, "Some improvements of the activation-relaxation technique method for finding transition pathways on potential energy surfaces," *J. Chem. Phys.*, Vol. 130, Art. 114711.

I.1.2 Lightweight High-Temperature Alloys Based on the Al-Fe-Si System (University of Florida)

Michele V. Manuel, Co-Principal Investigator
University of Florida
549 Gale Lemerand Drive
Gainesville, FL 32611
E-mail: mmanuel@mse.ufl.edu

Richard G. Hennig, Co-Principal Investigator
University of Florida
549 Gale Lemerand Drive
Gainesville, FL 32611
E-mail: rhennig@ufl.edu

Jerry L. Gibbs, DOE Technology Manager
U.S. Department of Energy
E-mail: jerry.gibbs@ee.doe.gov

Start Date: October 1, 2016 End Date: December 31, 2020
Total Project Funding: $1,102,082 DOE share: $991,873 Non-DOE share: $110,209

Project Introduction

Automotive applications need low-cost, lightweight, high-temperature alloys to enhance efficiencies in systems such as internal combustion engines. The aluminum-iron-silicon (Al-Fe-Si) system provides an opportunity to develop such a material, as it comprises three of the lowest cost elements abundant in nature. Specifically, the τ_{11}-$Al_4Fe_{1.7}Si$ (previously called τ_{10}) ternary intermetallic phase is a lightweight and low-cost phase with promising mechanical properties at high temperatures. However, the τ_{11}-$Al_4Fe_{1.7}Si$ phase has an extremely small compositional range, which should be expanded to use this alloy at a commercial scale. To increase this compositional range, the equilibrium phase boundaries can be manipulated and expanded via alloy design and non-equilibrium processing, while the parts can potentially be fabricated by AM.

Objectives

The objective of this project is to expand the phase boundaries of τ_{11}-$Al_4Fe_{1.7}Si$ via alloy design and AM to exploit the non-equilibrium nature of the total melting and solidification process. Additions of a quaternary solute X to the Al-Fe-Si ternary system will be examined. It is expected that the alloys produced will have superior tensile strength of competing intermetallic systems and have a density comparable to titanium (Ti)-Al alloys.

Approach

An integrated computational approach was used that spans electronic structure calculations to thermodynamic models that are paired with strategic experiments for alloy characterization, which thereby assists with the validation process to produce revolutionary automotive components superseding current commercial and research-grade high-temperature alloys.

The project is being conducted in three budget periods:

Budget Period 1: Candidate solute elements were identified that have the potential to increase the compositional range over which the τ_{11}-$Al_4Fe_{1.7}Si$ phase is stable. Ternary and quaternary alloys were cast via arc-melting. The Go/No-Go milestone decision was to deliver alloys that have the potential to display a stable τ_{11} Al-Fe-Si-X phase. This deliverable was achieved through the experimental demonstration of the desired τ_{11} phase in the Al-Fe-Si-X alloy system (where X = Ni).

Budget Period 2: For the candidate solute elements, the compositional range of the τ_{11} phase was expanded by computationally evaluating its energetic and thermodynamic stability. The Go/No-Go milestone decision was to create a list of chemistries suitable for powder processing via three-dimensional (3D) printing. This deliverable was achieved through computational prediction and experimental demonstration of the desired τ_{11} phase in the Al-Fe-Si-X alloy system (where X = copper [Cu], manganese [Mn], nickel [Ni], and zinc [Zn]).

Budget Period 3: The stability of τ_{11}-Al_4 (Fe, Mn)$_{1.7}$Si was studied by DFT calculations. Experimentally these calculations were validated, and its phase boundary was determined. Al-Fe-Si-Mn powder were processed by AM to determine optimum printing parameters to fabricate specimens for mechanical and microstructural characterization. The Go/No-Go milestone decision will be based on the production of mechanical test samples using AM. Argon-atomized Al-Fe-Si-Mn alloy powders were fabricated and the components for mechanical testing will be produced by 3D laser printing.

Results

Previous experimental results showed that the addition of Mn to the Al-Fe-Si stabilizes the τ_{11}-$Al_4Fe_{1.7}Si$ phase. To determine the stability and preferential behavior of Mn to substitute on a particular sublattice in the τ_{11} phase, DFT calculations were performed. For Al, six Al atoms were substituted in the 6h Wyckoff position with Mn, for Fe, three atoms were substituted in the 6h position, and for Si, one Si atom was substituted in the 2a position. Three different calculations for Mn substitution in τ_{11} phase were performed. To determine the energy cost or gain associated with the substitution, the energy of all possible competing phases was considered. The competing phases determine the relevant chemical potentials of the elemental components. This analysis required the construction of a quaternary convex hull using the DFT calculated energies. Four pure elemental phase, 27 binary phases, and 34 ternary phases of Al, Fe, Si, and Mn competing phases were included. The structures were obtained from the Inorganic Crystal Structure and Materials Project Databases. Figure I.1.2.1 shows the quaternary convex hull diagram for the Al-Fe-Mn-Si system. The τ_{11} phase (orange circle) lies on the convex hull and its four competing phases in the tetrahedron (blue circles). The calculated hull distance for Mn was –5, 129, and 36 meV for substitutions on the Al, Fe, and Si sites, respectively. The calculation showed that the Mn solubility is energetically favorable in the τ_{11} structure. As the hull distance for Mn in the Fe site is below the convex hull, this suggests that Mn will substitute Fe atoms in the τ_{11} phase. These results were used to guide the choices of diffusion couples and alloy fabrication. As discussed below, the main result of the DFT calculations is that Mn preferentially substitutes for Fe, which is consistent with the experimental results.

The calculated hull distance showed that Mn is completely soluble in τ_{11}. However, the convex hull distance predicts only the enthalpy contribution to the free energy, but not the contribution from the entropy. Thus, the ideal solution model was used to estimate the configurational entropic contribution to the energy to calculate the Gibbs free energy.

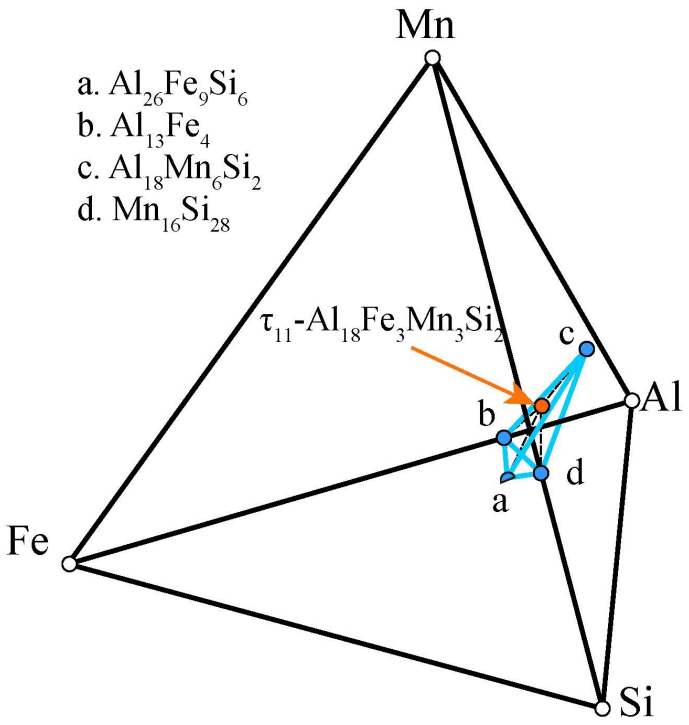

Figure I.1.2.1. DFT calculated quaternary convex hull diagram. The blue dots represent the four competing phases of the τ11 phase. The orange dot represents the τ11 phase with the addition of Mn in the Fe sites. Increase in Mn content in τ11 decreased the hull distance, indicating that the addition of Mn stabilizes the τ11 phase [1]. Source: University of Florida.

Figure I.1.2.2 shows the calculated Gibbs free energy curve at 1,000°C. With the increase in Mn content, the Gibbs free energy of τ_{11} decreased, thus further stabilizing the phase. Higher Mn contents increase the disorder in the system, which in turn increases the entropic contribution, and hence, minimizes the Gibbs free energy of the τ_{11} phase. We also studied the other competing phases listed in Figure I.1.2.1, and how the addition of Mn destabilizes or stabilizes those competing phases. The experimental results showed a similar stabilization of the τ_{11} phase from the arc-melted Al-Fe-Si-Mn alloy cast in the laboratory.

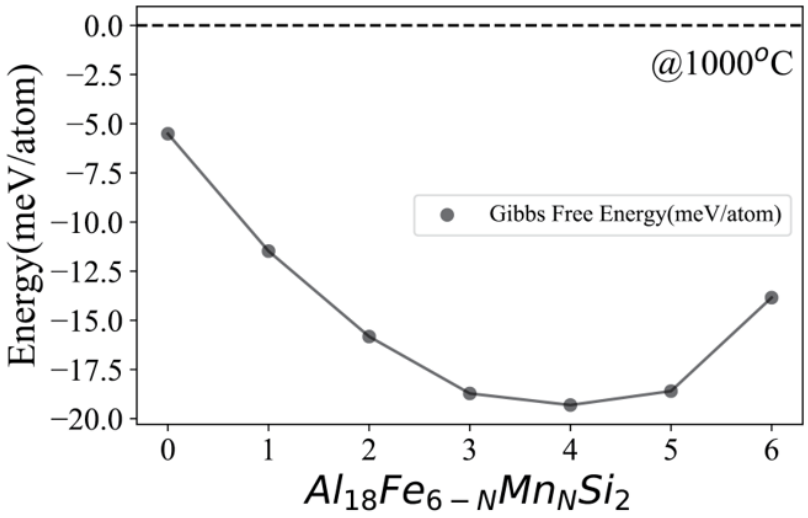

Figure I.1.2.2. Gibbs free energy curve for the τ11 phase with the addition of Mn at 1000°C with a corresponding increase in Mn in the Fe site decreased the Gibbs free of the τ11, thereby stabilizing the phase [1]. Source: University of Florida.

Cluster expansion and Monte Carlo simulations were utilized in another approach to investigate and predict the phase stability of the τ_{11} phase. These simulations aim to calculate entropic contributions, which are more accurate estimates than values obtained from simple solution models. The formation energy of the τ_{11} structures as a function of composition was calculated using DFT as implemented in the Vienna Ab initio Simulation Package. Developing a surrogate model using cluster expansion requires structures and their formation energy with varying composition and atomic environment. These formation energies are shown in Figure I.1.2.3.

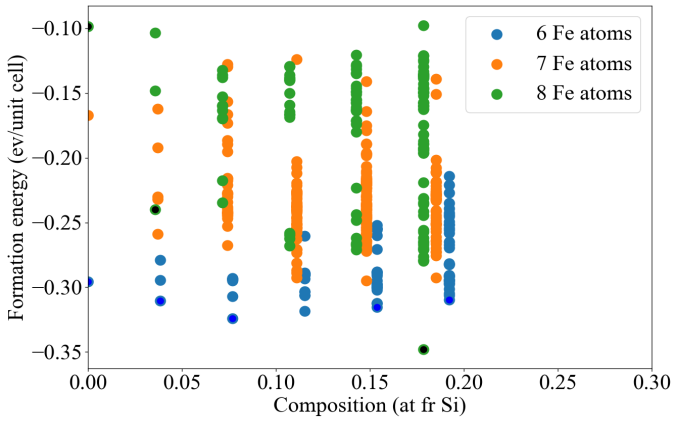

Figure I.1.2.3. DFT formation energies of the τ_{11} phase. Each point represents a structure with a particular composition and atomic environment symmetrically distinct from the other structures [2]. Source: University of Florida.

These structures and formation energies were then used to construct a cluster expansion-based surrogate model. The surrogate model can be used to perform lattice Monte Carlo simulations to calculate the free energy, which in turn can be used to calculate the phase stability. In the case of the τ_{11} phase, the clusters in the structures get excessively distorted during the DFT relaxations. As a result, the surrogate model fitted to this data fail to predict the formation of energy with a high accuracy. Nevertheless, a surrogate model can be fit to a subset of structures, as shown in Figure I.1.2.4, and generate a pseudo-ternary surrogate model for the τ_{11} phase. The fitness of this surrogate model can be measured by calculating the Leave One Out Cross-Validation score (LOOCV). Lower values of the LOOCV score indicate better predicted formation energies by the surrogate model [3],[4].

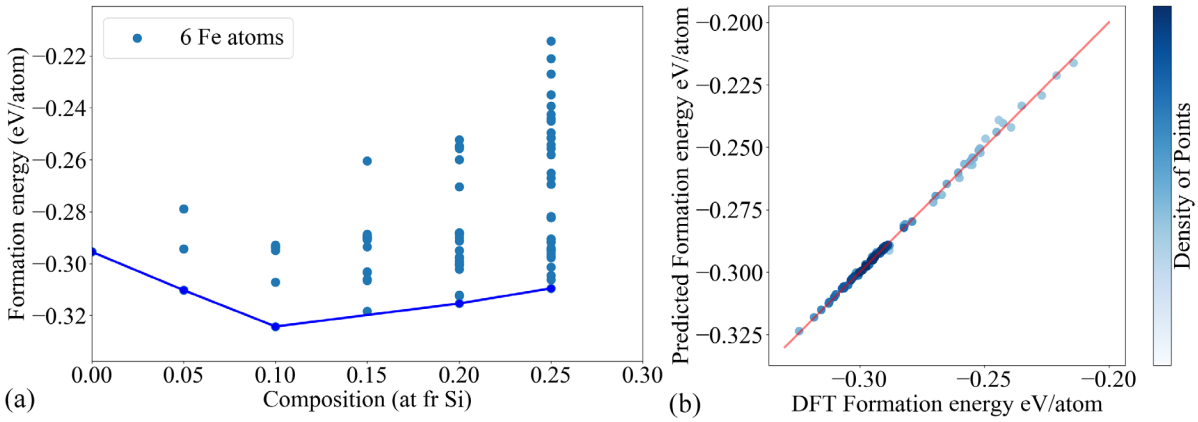

Figure I.1.2.4. (a) DFT formation energy of a subset of τ_{11} structures. The blue line represents the convex hull line. (b) Formation energy predicted by the cluster expansion surrogate model shown in comparison to DFT formation energy [2]. Source: University of Florida.

This pseudo-ternary surrogate model was then utilized to perform lattice Monte Carlo simulations. The output of these simulations is the free energy curves for the pseudo-ternary τ_{11} phase, as shown in Figure I.1.2.5. The 'CLEX' line represents the 0 K free energy curve predicted by the cluster expansion surrogate model, which is similar to the convex hull line in Figure I.1.2.4(a).

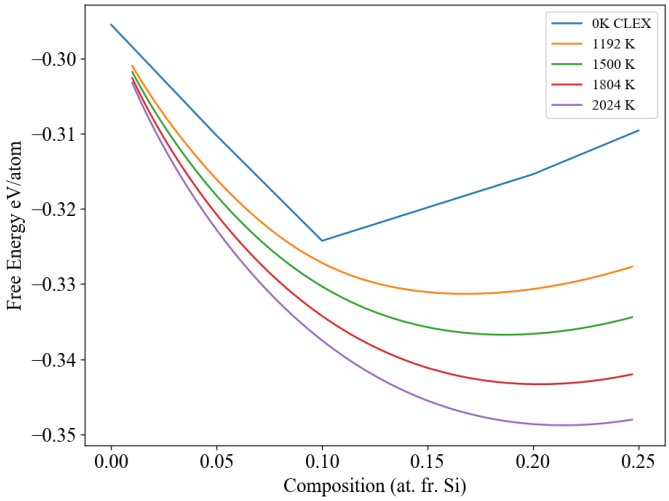

Figure I.1.2.5. Pseudo-ternary free energy curves for the τ_{11} phase at 23% of Fe as a function of the composition of Si at various temperatures [2]. Source: University of Florida.

Experimentally, Al-Fe-Si-Mn alloys were prepared by arc-melting in a water-cooled Cu hearth under an argon atmosphere. Followed by a heat-treatment at 800°C, the alloy samples were analyzed using SEM, in combination with backscattered electron (BSE) imaging, electron dispersive spectroscopy (EDS), and electron probe microanalysis. The data was used to determine the entire compositional range of the τ_{11} phase at 800°C in composition space. Figure I.1.2.6 shows the phase boundary of the τ_{11} phase at 800°C with 4.5 at% Mn and the most recently published phase diagram reported in the literature is shown at the right for comparison. These results confirmed the stabilization of τ_{11}-$Al_4Fe_{1.7}Si$ by the addition of Mn to the Al-Fe-Si system as predicted by the DFT calculations. A continuous solid solution from the τ_{11} phase with 3 at% Mn and τ_8-Al_9Mn_3Si was confirmed by diffusion couples, and equilibrated alloys. The optimal composition for Al-Fe-Si-Mn was used for 3D printing the single phase of τ_{11}.

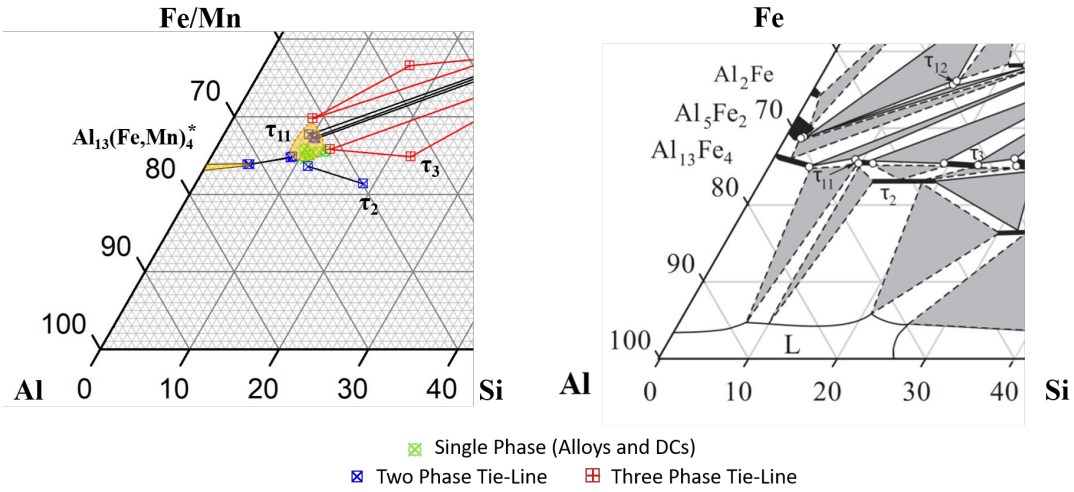

Figure I.1.2.6. Experimentally measured composition of $\tau_{11}Al_4(Fe, Mn)_{1.7}Si$ at 800 °C with 4.5 at% Mn on the left, shown against a published Al-Fe-Si phase diagram at 800 °C [5] for comparison [1]. Source: University of Florida.

To minimize a trial-and-error approach to determine the optimal printing parameters for the 3D printing of the τ_{11} powders, DFT calculations were used to determine the reflectivity of the alloy at various laser wavelengths. Figure I.1.2.7 shows the calculated reflectivity from DFT as a function of electromagnetic wavelength. These calculations revealed higher laser absorption near 1 µm and higher reflectivity between 2 µm and 10 µm. Guided by the DFT calculation, prefabricated τ_{11} powders were shipped to Fraunhofer USA to print bulk samples using a Direct Energy Deposition (DED) system. Fraunhofer USA's DED system has a laser with a wavelength of 1 µm, a wide range of power options (up to 16 kW) and cameras for process viewing and melt pool size control. The ability to control various processing parameters allows for the experimentation within a wide processing window to determine optimal processing parameters for 3D printing. Figure I.1.2.7 also shows the results obtained from the 3D printer trials with the DED from Fraunhofer USA. Preliminary trails using the DED illustrated the ability to successfully melt the powders and produce bulk samples, although some delamination and cracking were observed in the fabricated specimens. A second set of trials with the DED system will be carried out with a smaller laser spot size to help reduce stress, and therefore cracking and delamination.

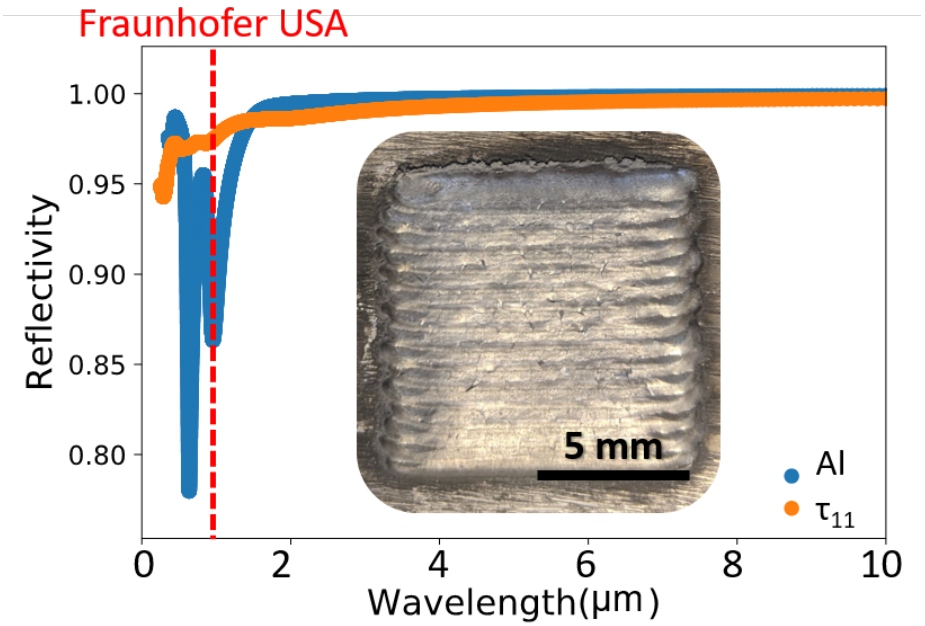

Figure I.1.2.7. DFT calculated reflectivity of pure Al (blue) and the τ_{11} phase (orange). Both τ_{11} and Al have high reflectivity in the infrared region. The inset image is a representative example of a τ_{11} processed using DED [6].
Source: University of Florida.

Conclusions

In this budget period, investigations were performed to study the stability of Al-Fe-Si-Mn alloys and explore the optimal laser printing parameters using a DED system to fabricate the components for mechanical testing and microstructural characterization. The main conclusions drawn from this budget period are as follows:

- Computationally, the stability of τ11-Al4 (Fe, Mn)1.7Si was studied by DFT calculations. These calculations reveal that Mn solubility is energetically favorable in τ11 structure and suggest the complete miscibility between Fe and Mn.
- Experimental results confirmed the stabilization of τ11-Al4 Fe1.7Si by the addition of Mn as predicted by the DFT calculations and the phase boundary of τ11-Al4 (Fe, Mn)1.7Si at 800°C was determined.
- Al-Fe-Si-Mn powders were successfully melted using a DED system resulting in solid specimens. A new set of parameters is being tested to obtain optimal printing conditions to fabricate specimens for mechanical testing.

References

1. Soto-Medina, S., B. Rijal, R. G. Hennig, and M. V. Manuel, M. V., 2021, "Study of the solubility of Mn in the τ_{11}-$Al_4Fe_{1.7}Si$ phase at 800°C," Manuscript in preparation.
2. Hire, A. C., B. Rijal, S. Soto-Medina, R. G. Hennig, and M. V. Manuel, 2021, "Energetic and entropic calculation of τ_{11}-$Al_4Fe_{1.7}Si$ phase and competing phases using cluster expansion and Monte Carlo," Unpublished work.
3. M. Stone, 1974, "Cross-validatory choice and assessment of statistical predictions," *J. R. Stat. Soc. Series B Stat.*, Vol. 36, No. 2, pp. 111–147.
4. van de Walle, A., and G. Ceder, 2002, "Automating first principles phase diagram calculations," *J. Phase Equilibria Diffus.,* Vol. 23, No. 4, Art. 348.
5. Marker, M. C. J., B. Skolyszewska-Kühberger, H. S. Effenberger, C. Schmetterer, and K. W. Richter, 2011, "Phase equilibria and structural investigations in the system Al-Fe-Si," *Intermetallics*, Vol. 19, No. 12, pp. 1919–1929.
6. Rijal, B., S. Soto-Medina, A. C. Hire, R. G. Hennig, and M. V. Manuel, 2021, "DFT calculation of reflectivity of $Al_4Fe_{1.7}Si$ phase," Unpublished work.

Acknowledgements

The authors also acknowledge Dr. Anil Sachdev at General Motors for his valuable knowledge gleaned from many discussions.

I.1.3 Machine-Learning and Supercomputing to Predict Corrosion/Oxidation of High-Performance Valve Alloys (Oak Ridge National Laboratory)

Dongwon Shin, Principal Investigator
Oak Ridge National Laboratory
1 Bethel Valley Road
Oak Ridge, TN 37831
E-mail: shind@ornl.gov

Jerry L. Gibbs, DOE Technology Manager
U.S. Department of Energy
E-mail: jerry.gibbs@ee.doe.gov

Start Date: October 1, 2018 End Date: September 30, 2021
Project Funding: $500,000 DOE share: $500,000 Non-DOE share: $0

Project Introduction

Although it is practically and technologically important, there is presently no established modeling approach that can accurately predict the high-temperature oxidation behavior of multi-component structural alloys due to the inherent complexity. There are physics-based modeling approaches that can predict high-temperature oxidation; however, the lack of fundamental oxidation kinetics data, such as mobilities of metal cations in oxides and O permeabilities within the alloy matrix, hampers accurate quantitative prediction from physics-based simulations.

Objectives

Machine-Learning

This project aims to develop practical and accurate machine-learning (ML) models that can rapidly predict high-temperature oxidation kinetics of multi-component NiCr-based alloys as a function of alloy chemistry and operation temperature. These models will be trained with ORNL's highly consistent and well-curated cyclic oxidation experimental dataset for various model and commercial NiCr-based alloys, which has been developed over the past two decades.

Supercomputing

Our goal in this work is performing a series of large-scale atomistic simulations based on the reactive force field (ReaxFF) method on DOE supercomputers to supplement scarce fundamental experimental data pertinent to high-temperature oxidation kinetics. The main barrier of such atomistic simulations is developing high-fidelity interatomic potentials of multi-component systems, which takes years of iterative effort. This task's primary objective is to develop a new data analytics framework designed to significantly accelerate interatomic potential development of multi-component systems relevant to NiCr alloys oxidation with the objective of reducing interatomic potential development intervals from years to months.

Approach

Machine-Learning

Two characteristic oxidation models—a simple parabolic law (s-k_p) and a statistical cyclic oxidation model (p-k_p)—that take eventual spallation of the protective oxide into account are chosen to quantitatively represent the high-temperature oxidation. The correlations between the input features in the dataset—in this case, the elemental compositions of each alloy and the relevant oxidation temperature and atmosphere—and k_p was evaluated by the Pearson correlation coefficient (PCC). Five representative ML algorithms were used: (1) linear regression (LR); (2) Bayesian ridge (BR); (3) k-nearest neighbor (NN); (4) random forest (RF); and (5) support vector machines (SVM) regression were used. ASCENDS [1],[2], the open-source data analytics front-end developed by ORNL, was supported by the VTO Propulsion Materials Program and employed to

perform correlation analysis and ML training. The coefficient of determination (R^2) was used to represent the accuracy of each ML model.

Supercomputing

The overall workflow is presented in Figure I.1.3.1. The high-throughput data population of ReaxFF simulations in body-centered cubic Cr was performed via high-performance computing using the Theta supercomputer at the Argonne Leadership Computing Facility. Approximately 100,000 potentials were sampled based on a design of experiment approach in and 18-dimensional parameter space. ReaxFF simulations were performed for each potential to derive properties, such as temperature-dependent lattice parameters, potential energy, and elastic modulus.

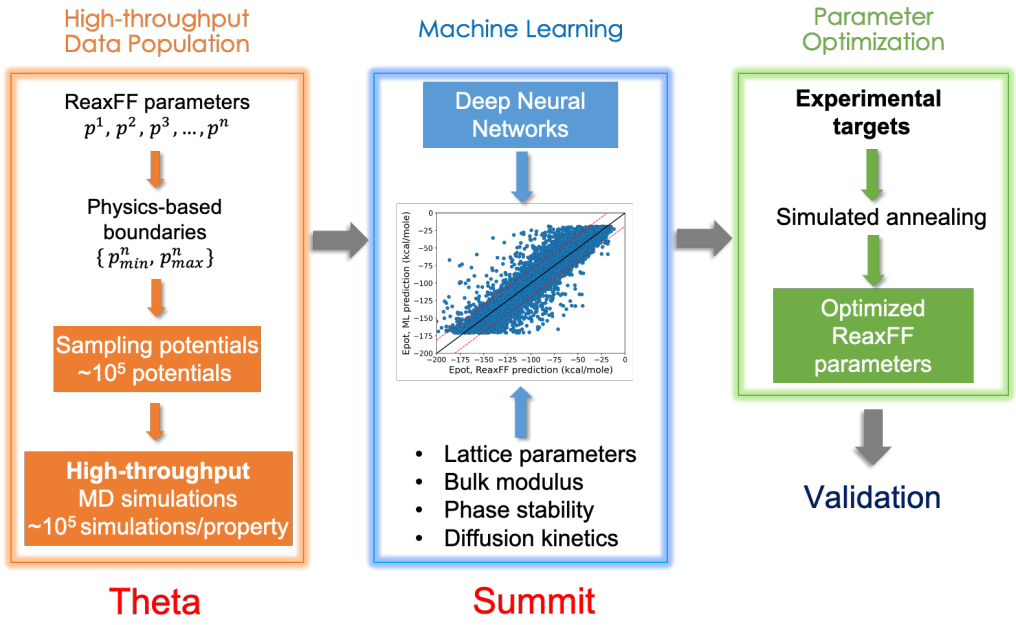

Figure I.1.3.1. Schematic showing the framework for developing new ReaxFF interatomic potentials optimized to experimental targets properties by utilizing ML models and simulated annealing method. Source: ORNL.

In parallel, ReaxFF was developed for Ni/Cr/O/H by employing the conventional approach; the model parameters are manually optimized using single parameter-based parabolic extrapolation method to reproduce DFT data and available experimental data.

Results

Machine-Learning

Figure I.1.3.2 presents the correlation coefficients determined by the PCC method in different cyclic oxidation atmospheres. PCC analysis correctly identified the generally expected impactful features on k_p, such as the oxidation temperature (T) and the contents of Cr and Al, which is in good agreement with trends observed by experiments. Based on these results, features were selected to train ML models and evaluate their performance.

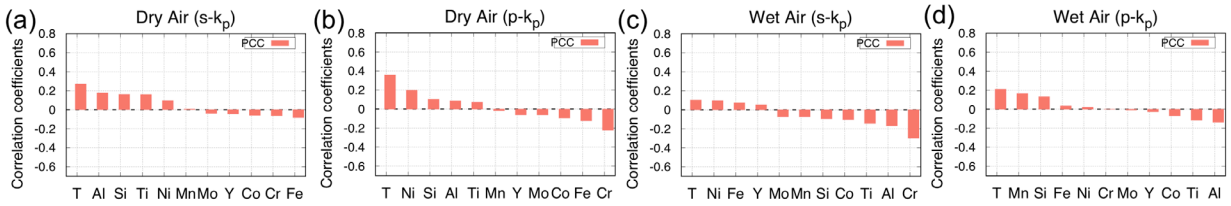

Figure I.1.3.2. Correlation analysis between input features and k_p (both s-k_p and p-k_p models) using the PCC method at difference atmospheres. Source: ORNL.

Figure I.1.3.3 shows the performance of five ML models as a function of the numbers of top-ranking features determined by PCC. In all cases, increasing the top-ranking features from 2 to ~4 can increase the accuracy of these models. However, considering more features in training does not considerably improve the accuracy. The highest accuracy of these models is generally in the order of SVM>BR>RF≈NN>LR (dry air) and SVM>BR≈LR>NN>RF (wet air). For both wet air and dry air datasets, fitting experimental data with the s-k_p or p-k_p model does not significantly affect the performance of the ML models.

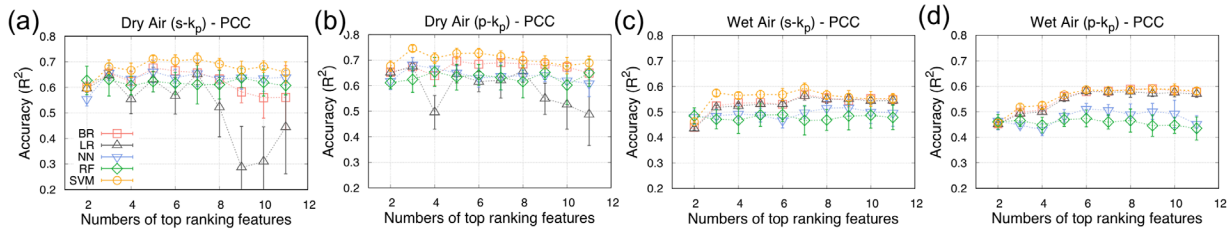

Figure I.1.3.3. Accuracy of ML models as a function of the number of top-ranking features. Source: ORNL.

Figure I.1.3.4 compares experimental and ML-predicted k_p from the SVM models at different atmospheres with s-k_p and p-k_p. For most of the data, the difference between experimental and ML-predicted k_p are within one order-of-magnitude, which can be considered as good agreement from the perspective of high-temperature oxidation. Compared results from dry air exposure with these from wet air exposure, the predicted k_p in dry air are in a slightly better agreement with the experimental k_p than their counterparts in wet air, which can be attributed to the more complex oxidation behavior of multi-components alloy in wet air atmosphere, leading to larger variations of the experimental results.

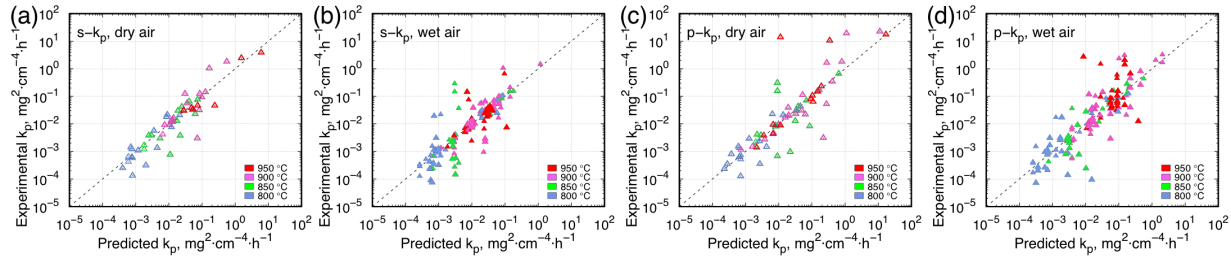

Figure I.1.3.4. Experimental vs. predicted k_p using (a, b) the s-k_p and (c, d) the p-k_p procedures in dry and wet air. Source: ORNL.

While the demonstrated ML workflow can predict the oxidation kinetics of the NiCr alloys with some accuracy, the features used within are simple elemental compositions and temperature that cannot efficiently represent the underlying mechanisms. At least three simultaneous physical processes are occurring during cyclic oxidation of the studied alloys in a wet atmosphere. The time during which a continuous, protective, thermally grown Cr_2O_3-based scale is maintained on the surface of the alloys corresponds to the alloy oxidation lifetime. It is a function of growth rate of the protective Cr_2O_3 scale, the volatilization of the Cr_2O_3 oxide into $CrO_2(OH)_2$ and the spallation of the Cr_2O_3 scale. Further, a loss of Cr in the underlying alloy will be characteristic of all three processes. In the literature, for Ni-based materials, it is commonly accepted that when the Cr concentration at the alloy-oxide interface reaches 10 wt.%, the Cr_2O_3 cannot be maintained [3]. Therefore, the physics-based simulations in this study are predicting the time to 10 wt.% (henceforth named t10) using a CALculation of PHAse Diagrams (CALPHAD)-based thermodynamic and kinetic model [4]. This approach considers all three processes in addition to the composition and constitutional phases of each studied alloy at the considered temperature. For each alloy at each condition, t10 will be used as an input parameter for the next round of ML model training to predict oxidation lifetime of the alloys. Examples of calculated t10 for selected commercial alloys as a function of temperature and atmosphere are presented in Figure I.1.3.5.

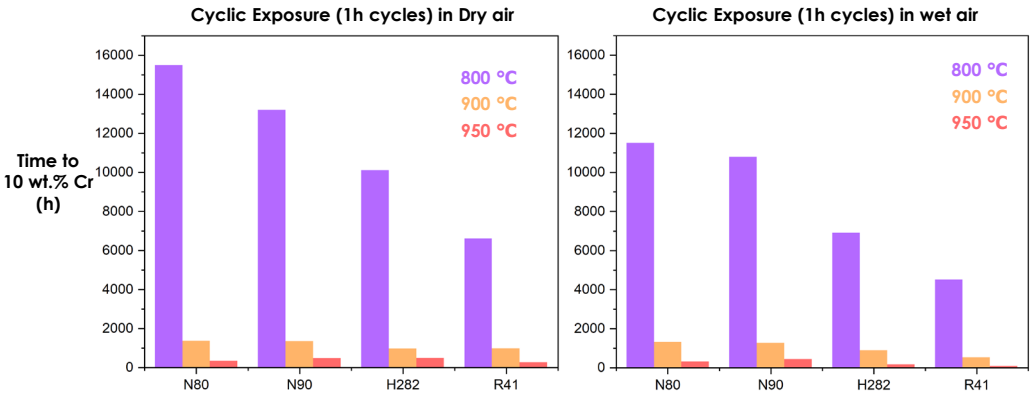

Figure I.1.3.5. Time in hours to reach 10 wt% Cr calculated for selected commercial alloys and 800°C, 900°C, and 950°C in dry and wet air. Source: ORNL.

Supercomputing

Neural network models were trained with the large input dataset from FY 2019 high-throughput ReaxFF simulation results, using the Summit supercomputer at the Oak Ridge Leadership Computing Facility. Deep neural network architecture was employed to derive high-fidelity ML models. Approximately 5,000 different neural networks were searched for each material property of interest to find the ML models with high accuracy in predictions. Figure I.1.3.6 shows the predictions of properties in body-centered cubic Cr using the trained ML models. The ReaxFF results shown were not used in training and, thus, validate the accuracy of the ML models in describing the landscape of the ReaxFF parameter space. Initial work based on a simulated annealing (SA) approach was performed to find the optimized 18 ReaxFF model parameters that minimized the error between the experimental and simulation results. The SA-optimized ReaxFF parameters will be validated using actual ReaxFF simulations to see if a data analytics-driven approach can be used to rapidly identify model parameter sets that can replicate experiments.

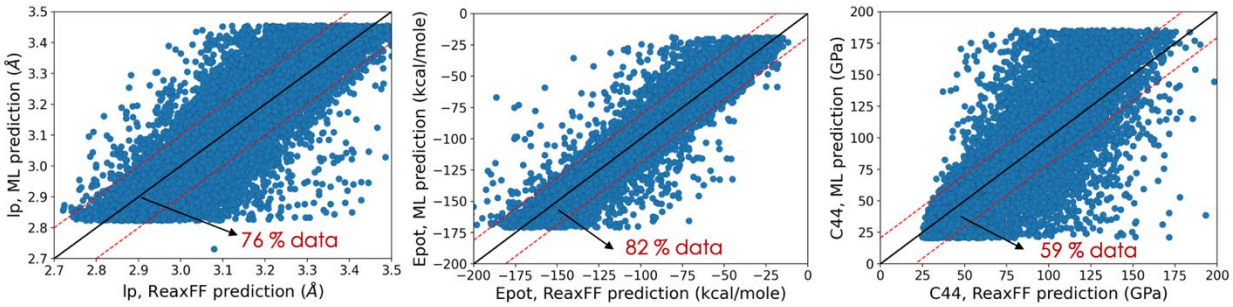

Figure I.1.3.6. Parity plots showing the comparison between ML-predicted values and ReaxFF predicted lattice parameters (lp), potential energy (Epot), and elastic moduli (C44). Source: ORNL.

Additionally, MD simulations were performed for the initial corrosion of rock-salt NiO(111), NiO(001), and a-Cr_2O_3(0001) surfaces to validate the manually developed Ni/Cr/O/H force field. In NiO, the most stable configuration is known to be the O-terminated octopolar (O-octo) structure for the (111) surface. From the MD simulation of O-octo surface with high-temperature water at 600 K, two dissociation configurations were observed, as shown in Figure I.1.3.7(a). A water molecule is first adsorbed on the subsurface Ni and dissociated by transferring H to either the surface O or the second subsurface O (e.g., a deeper penetration of H). The dissociation can occur with and without water assistance. In the period of 100 ps simulation time, the O-octo surface was covered by dissociated water molecules at 0.18 monolayer coverage. On the other hand, the (001) planar surface is less reactive than the O-octo(111) surface and only one water surface was dissociated.

As shown in the snapshots in Figure I.1.3.7(b), the dissociation follows the (1-4) dissociation mechanism in the simulation. OH species are observed to adsorb on the Cr top site diffuses along the surface by proton transfer between OH and an adsorbed water. With the higher water density of 0.5 g/cm^3, the dissociated water coverage is about 0.25 ML at 600 K and 0.47 ML at 1000 K, indicating that surface hydroxylation is accelerated at high-temperature.

One of the large-scale simulations of interest in this study is the diffusion of metal and O in oxide in the presence of vacancies, which will provide an atomic level insight of oxidation initiation, diffusion in grain boundaries, vacancy clustering, etc. As a preliminary study, vacancy diffusion simulations of rock-salt structured NiO were performed with 0.5%-Ni vacancy concentration at 1200, 1500, and 1800 K. The large-scale simulations were performed on both the Roar supercomputer (Penn State University) and Theta (Argonne Leadership Computing Facility). During the period of simulation time, Ni moves to neighboring vacancy sites. Using the trajectories collected for 500 ps, the mean square displacements were calculated and the diffusion constant of Ni at each temperature was obtained from the slope of the averaged mean square displacement using Einstein's relation. As shown in Figure I.1.3.7(c), the diffusion constants estimated from ReaxFF are placed in between the experimental values [5],[6]. Since the experimental range is very broad and the vacancy concentration should be much lower than the simulation condition, our predictions on the diffusion constants are currently in qualitative agreement. More refined simulations that are closer to the real experiments will be performed in FY 2021.

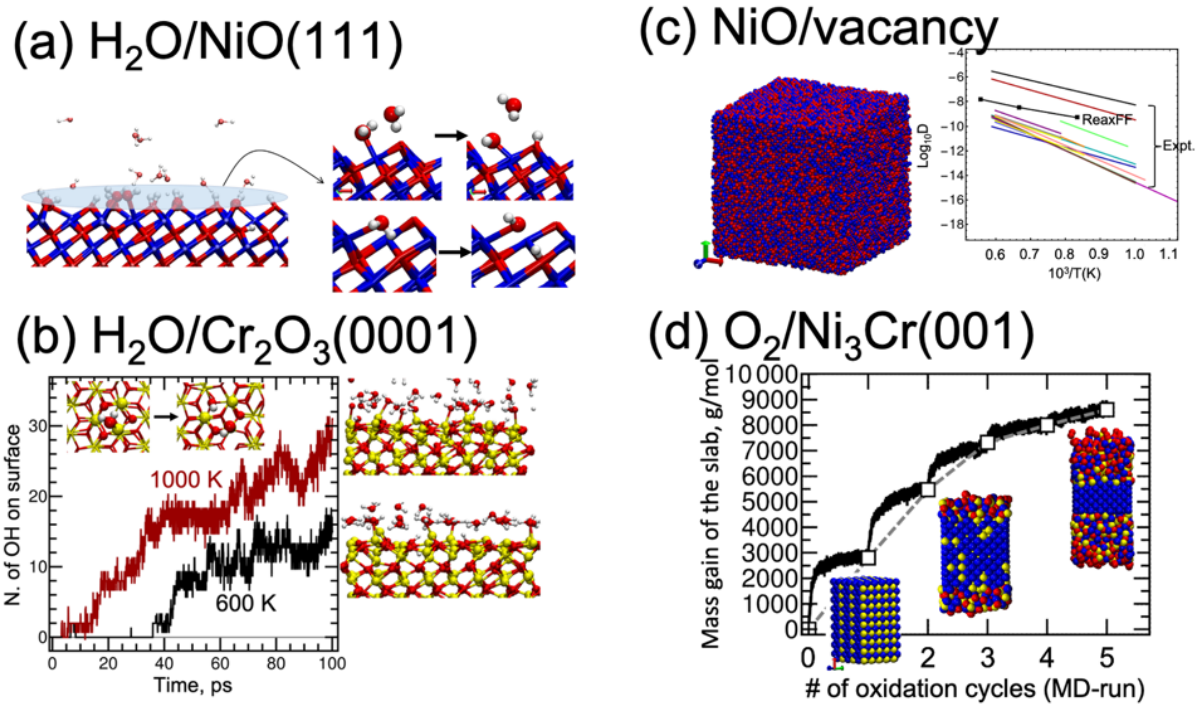

Figure I.1.3.7. Applications of the ReaxFF Ni/Cr/O/H force field. (a) and (b) Initial corrosion of NiO(111,O-terminated octopolar structure) and Cr_2O_3(0001) surface with high-temperature water. (c) Diffusion of Ni in NiO with 0.5%Ni-vac. at T=1200 K, 1500 K, 1800 K. (d) Oxidation of Ni_3Cr at 1200 K using a hybrid MD/Monte Carlo (MC) simulation method. Source: ORNL.

The alloy oxidation process in Ni_3Cr in gaseous O_2 was also investigated. O transport from gas phase to metal surface and the diffusion to subsurface layers can be observed by performing MD simulation. However, metal diffusion—in particular, the interlayer diffusion responding to a given environment in a defect-free slab—is expected to be the slow dynamic on very long-time scales. To overcome this, a hybrid MD/MC simulation method was used. A Ni_3Cr(001) slab was generated by adding a vacuum space to a Ni_3Cr supercell cleaved

along the (001) plane and performed a MD simulation at 1200 K under a gaseous O_2 environment. O transported from the gas phase to the alloy surface and formed Ni-rich oxide layers on the surface. The Cr to Ni %-ratio is 26:74 in the oxide layers and 25:75 in the center layers, indicating there is no significant diffusion between the layers, and thus, no change in the composition. Then, MC simulation employing the Metropolis acceptance criterion was used to swap over Ni and Cr metal components. Since Cr oxide is more stable than Ni-oxide, eventually the surface that was mainly covered by Ni-oxide becomes the Cr-rich oxide. After the first cycle of MD/MC run, the Cr:Ni %-ratio is 46:54. Multiple cycles of MD/MC simulations were performed until the oxidation curve (mass profile) is saturated, as observed in Figure I.1.3.7(d). As the oxidation proceeds, the Cr-rich alloy-oxide (Cr>25%) is formed on the surface and a pure Ni meal region is formed in the center layers. This agrees with the experimental observation, which is Cr oxide in the shell and Ni metals in the core [7].

Conclusions

Machine-Learning

We established a data analytics workflow that can rapidly and accurately predict cyclic oxidation of NiCr-based alloys from ML models trained with the highly consistent and well-curated oxidation dataset at ORNL. Correlation analyses can correctly identify the impactful features on a parabolic rate constant of k_p, which is consistent with trends reported in the literature. The ML-predicted k_p are in good agreement with the experiments from the perspective of high-temperature oxidation. The current work demonstrates that ML is a promising approach to predict high-temperature oxidation behavior of multi-component alloys.

Supercomputing

We demonstrated the feasibility of significantly accelerating the development of high-fidelity multi-component ReaxFF potentials by exploiting modern data analytics and supercomputing. From the high-throughput 100,000 ReaxFF simulation results of multiple materials properties, ML models have been successfully trained, and then used within the SA method to rapidly optimize 18 model parameters to reproduce real experimental data. Manually trained ReaxFF Ni/Cr/O/H potential was used to run large-scale simulations on DOE supercomputers. Preliminary results are qualitatively in good agreement with experiments, where available. More refined ReaxFF simulations will be performed in FY 2021 as an effort to supplement scarce fundamental data pertinent to oxidation kinetics of high-temperature alloys.

Key Publications

1. Sengul, M. Y., Y. Song, N. Nayir, Y. Gao, Y. Hung, T. Dasgupta, and A. C. T. van Duin, 2020, "An initial design-enhanced deep learning-based optimization framework to parameterize multi-component ReaxFF force fields," *Npj Comput. Mater.*, in revision.

References

1. Lee, S., J. Peng, A. Williams, and D. Shin, 2020, "ASCENDS: Advanced data SCiENce toolkit for non-data scientists," *J. Open-Source Softw.*, Vol. 5, No. 46, Art. 1656.
2. Peng, J., S. Lee, A. Williams, J. A. Haynes, and D. Shin, 2020, "Advanced data science toolkit for non-data scientists—A user guide," *CALPHAD*, Vol. 68, Art. 101733.
3. Duan, R., A. Jalowicka, K. Unocic, B. A. Pint, P. Huczkowski, A. Chyrkin, D. Grüner, R. Pillai, and W. J. Quadakkers, 2016, "Predicting oxidation-limited lifetime of thin-walled components of NiCrW alloy 230," *Oxid. Met.*, Vol. 87, pp. 11–38.
4. Pillai, R., A. Jalowicka, T. Galiullin, D. Naumenko, M. Ernsberger, R. Herzog, and W. J. Quadakkers, 2016, "Simulating the effect of aluminizing on a CoNiCrAlY-coated Ni-base superalloy," *CALPHAD*, Vol. 53, pp. 62–71.
5. R. Morlotti, "Determination of diffusion coefficient of cation vacancies in nickel oxide," 1969, *J. Phys. Sci. A*, Vol. 24, pp. 441–443.

6. Peterson, N. L., and C. L. Wiley, 1985, "Point defects and diffusion in NiO," *J. Phys. Chem. Solids*, Vol. 46, No. 1, pp. 43–52.

7. Bohra, M., P. Grammatikopoulos, R. E. Diaz, V. Singh, J. Zhao, J. F. Bobo, A. Kuronen, F. Djurabekova, K. Nordlund, and M. Sowwan, 2015, "Surface segregation in chromium-doped NiCr alloy nanoparticles and its effect on their magnetic behavior," *Chem. Mater.*, Vol. 27, No. 9, pp. 3216–3225.

Acknowledgements

The author would like to thank J. Peng, R. Pillai, M. Romedenne, B. Pint, G. Muralidharan and J. A. Haynes of ORNL for their support on developing ML framework for predicting alloy oxidation. The author would also like to acknowledge A. van Duin, Y. Shin, Y. Gao of Penn State, and N. S. H. Gunda and S. Lee of ORNL for developing data analytics workflow and high-throughput ReaxFF simulations.

I.1.4 Multi-Scale Development and Validation of the Stainless-Steel Alloy Corrosion Tool for High-Temperature Engine Materials (University of Florida)

Michael Tonks, Principal Investigator
University of Florida
158 Rhines Hall
Gainesville, FL 32611
E-mail: michael.tonks@ufl.edu

Jerry L. Gibbs, DOE Technology Manager
U.S. Department of Energy
E-mail: jerry.gibbs@ee.doe.gov

Start Date: October 1, 2018 End Date: December 31, 2021
Project Funding: $617,474 DOE share: $492,474 Non-DOE share: $125,000

Project Introduction

The environment within an engine cylinder during operation is extremely harsh, with high temperatures, combustion, and corrosive exhaust gases. This environment corrodes engine components, including exhaust valves and exhaust valve seats. Current engine materials, such as stainless steels, resist corrosion during normal operation. However, as new engines are pushed to higher temperatures, the material can undergo microstructure evolution that sensitizes the material to corrosion, resulting in premature failure.

Companies that design and build engine parts do not typically employ models of corrosion; rather, they employ standard temperature ranges and allowable fuels for which each alloy can be employed when making material selection decisions for a specific part and customer. These standards are based on conservative physical properties of the alloy and on successful deployment history. This reliance on conservative standards can result in over-design and increased cost. In addition, if a new advanced engine design results in conditions significantly different from the deployment history, these standards may not be applicable. This can lead to a vastly increased time and cost of development.

Objectives

The goal of this project is to create a simulation tool to assist in part design, reducing costs by eliminating the need for conservative material selection, and enabling alloy optimization to improve corrosion resistance. Thus, it will help reduce costs for existing engines and will assist in the material and engine design for the engines of the future, reducing development time by years. To meet our stated goal, we will develop the Stainless-Steel Alloy Corrosion (SStAC) tool, which will:

- Model corrosion of valve steels in an engine environment at temperatures up to 800°C.
- Be able to run in one dimension for a fast estimate of the corrosion rate and in two or three dimensions for more detailed simulations that represent any part of the geometry and predict the precise location and rate of corrosion and its impact on the mechanical and thermal behavior.
- Be implemented using the Multiphysics Object-Oriented Simulation Environment (MOOSE).
- Couple a corrosion model that describes the fundamental mechanisms of corrosion (including the impact of the microstructure and alloy composition) with mechanics and thermal transport models.

At the completion of the project, the SStAC tool will be able to predict the corrosion rate of engine valves with no more than 10% error.

Approach

The SStAC tool is being developed using a combination of macroscale model development, mesoscale, and atomic-scale simulations to define the impact of microstructure on alloy corrosion and an experimental campaign to inform and validate the models. This work is being carried out during three budget periods (BPs). BP 1 ended in February 2020 and our primary focus was the development of an initial corrosion model. BP 2 focused on the creation of the SStAC tool using the MOOSE framework. BP 3 will begin in March 2021 and will be the completion and preliminary validation of the SStAC tool. The tasks for BP 2 are:

- **Task 2.1 – Second Experimental Campaign:** The corroded samples from the first campaign are being characterized. Also, additional samples are being corroded after thermal annealing. Engine testing will also be carried out.
- **Task 2.2 – Mesoscale Model Development:** The phase-field model is being coupled with the electric potential and a mechanics model. DFT and MD simulations are being used to calculate critical material properties in the alloy and oxide phases.
- **Task 2.3 – Implementation of the SStAC Tool Using MOOSE:** The SStAC tool is being implemented in MOOSE, coupling the corrosion tool (defining the oxide growth with the extended finite element method [XFEM]) with mechanics and thermal transport. The numerical capability of the corrosion tool will be evaluated at the end of the performance period.

Results

Task 2.1 – Second Experimental Campaign

Samples of 21-2N and 23-8N valve steel alloys, which primarily vary in their manganese (Mn), chrome (Cr), and nickel (Ni) compositions, were exposed to atmospheric carbon dioxide (CO_2) gas at 700°C and time-lapse corrosion data were collected. Samples were characterized before and after corrosion by various techniques, such as SEM and scanning transmission electron microscopy (STEM). The composition of these two alloys is presented in Table I.1.4.1.

Table I.1.4.1. Chemical Composition of the Two Different Alloys 21-2N and 23-8N Studied in Weight Percent (wt%) With Fe In Balance.

	Cr	Mn	Ni	C	Mo	Si
21-2Ni-8.5Mn	20.25	8.5	2.13	0.55	0.5	0.25
23-8Ni-1.5Mn	23	1.5	8	0.38	0.5	1

The studied samples were removed from the furnace after 50, 100, 275, 500, and 1,000 hours. Mass variation data points are shown in Figure I.1.4.1. 21-2Ni-8.5Mn alloy data points showed a parabolic behavior up to 1,000 hours (weight gain = $A \cdot t^b$ where t is the time and b = 0.49 with a slope of 3.02×10^{-6} mg cm^{-2} s^{-1}). The second alloy, 23-8Ni-1.5Mn, showed significant standard deviation that resulted from scattered weight changes in the population of samples up to 1,000 hours. For this alloy, some spallation has likely occurred at exposure times greater than 500 hours resulting in weight loss. To obtain more information about the oxide composition and thickness formed on both alloys, surface and cross-sectional characterization were done. Figure I.1.4.2 shows a surface view of the 23-8Ni-1.5Mn corroded up to 275 hours in CO_2 at 700°C. Heterogeneous oxide formation on the surface of the sample with islands and porous structure with grain boundaries can be observed in Figure I.1.4.2(a). Elemental composition of the selected area in Figure I.1.4.2(b) was done by EDS maps, as shown Figure I.1.4.2(c). The islands are rich in Fe oxide meaning that Fe has reached the surface and the substrate grain boundaries are rich in Mn oxide, probably induced by fast migration of Mn through the substrate grain boundaries. This surface characterization confirmed the scattered mass variations shown in Figure I.1.4.1 are due to non-homogeneous oxide formation leading to potential spallation at later exposure times. Surface characterization of 21-2Ni-8.5Mn showed homogenous and protective oxide, which reflects the small standard deviation of weight gain up to 1,000 hours.

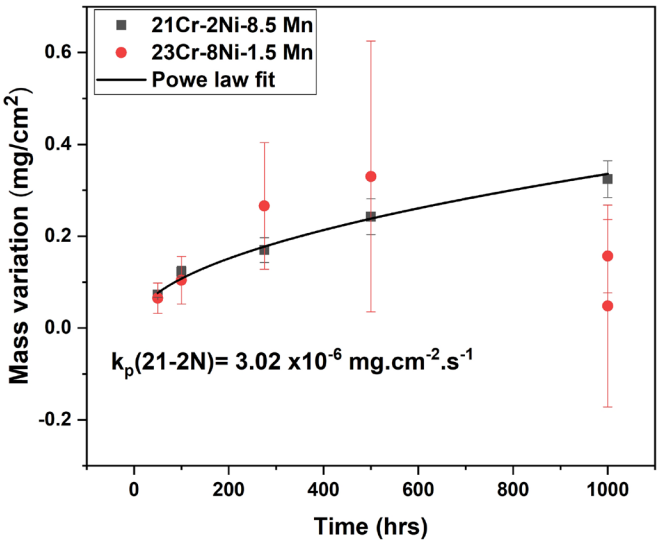

Figure I.1.4.1. Mass variation changes of both 23-8Ni-1.5Mn and 21-2Ni-8.5Mn alloys following atmospheric corrosion in CO_2 at 700°C up to 1,000 h. Source: University of Wisconsin–Madison.

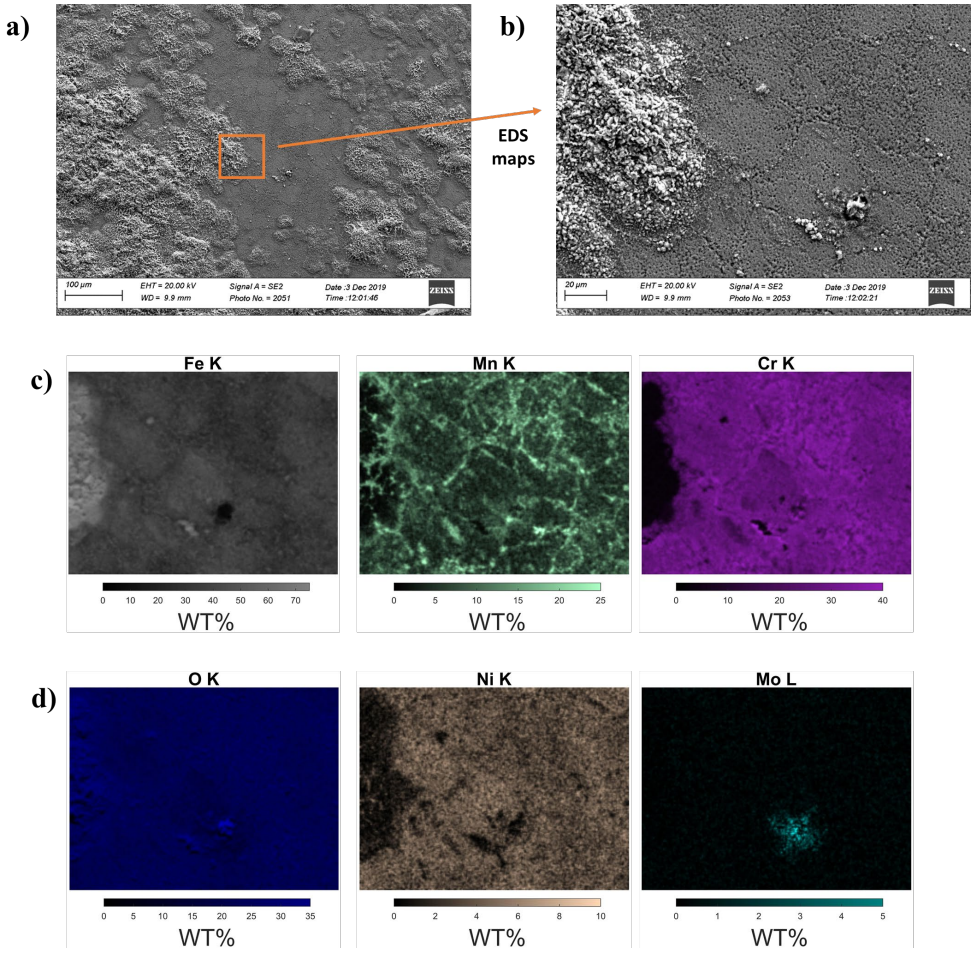

Figure I.1.4.2. SEM-EDS surface characterization of the 23-8Ni-1.5Mn sample after 275 hours in CO_2 at 700°C. (a) Heterogeneous oxide formation on the surface. (b) Area selected for EDS. (c) EDS maps of the selected area for Fe, Mn, and Cr. (d) EDS maps of the selected area for O, Ni, and molydbdenum (Mo). Source: University of Wisconsin–Madison.

Cross-sectional analysis of the oxide thickness and composition was done on all corroded 21-2Ni-8.5Mn samples using a focused ion beam (FIB) to lift-out 20×20 µm samples for SEM-EDS characterization. SEM-EDS maps on 21-2Ni-8.5Mn corroded for 500 hours at 700°C are shown in Figure I.1.4.3. The STEM-EDS maps were used to measure the oxide layer thicknesses.

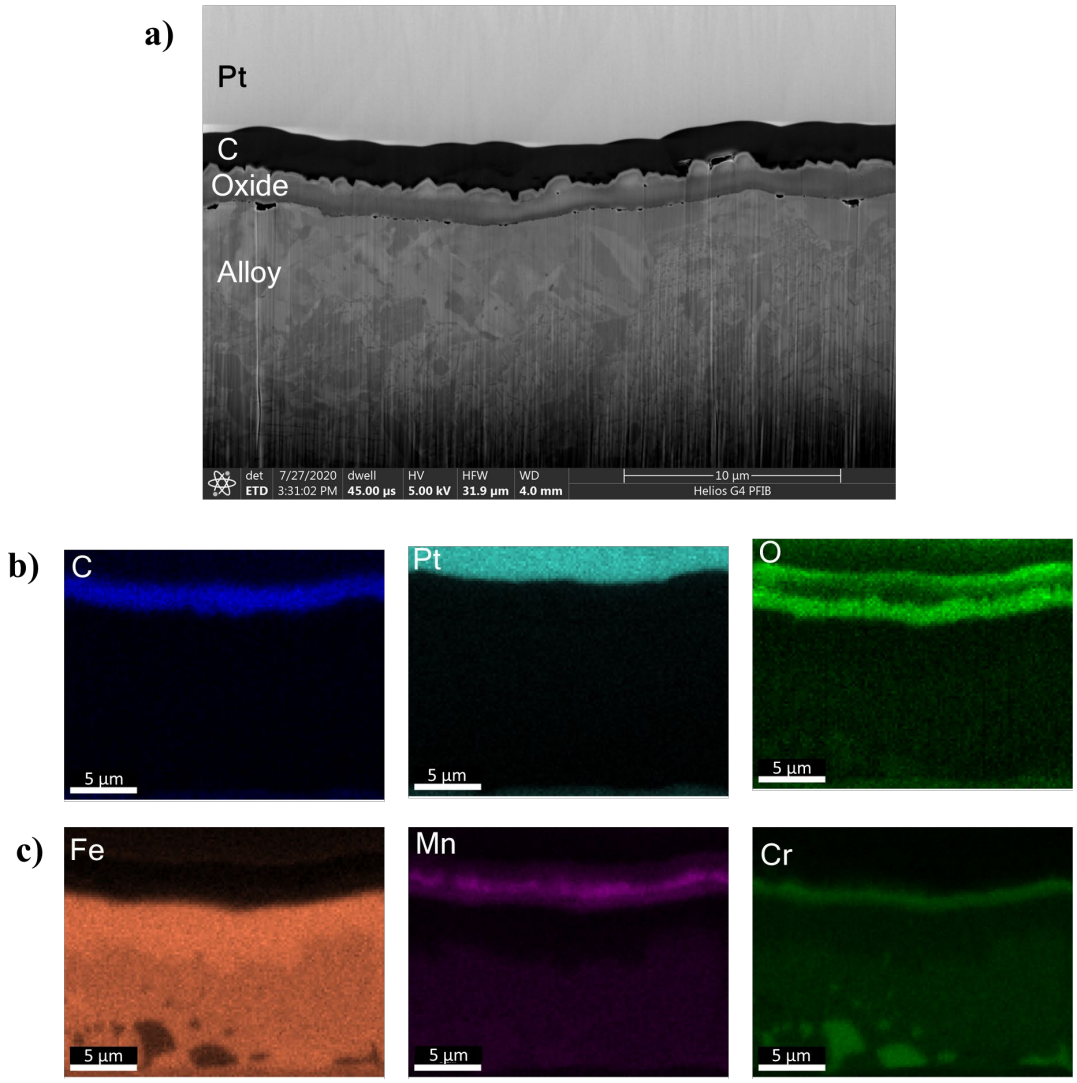

Figure I.1.4.3. SEM-EDS cross-sectional characterization of the 21-2Ni-8.5Mn sample after 500 h in CO_2 at 700°C. (a) The SEM image of the cross-section. (b) The EDS maps for C, Pt, and O. (c) The EDS maps for Fe, Mn, and Cr. Source: University of Wisconsin–Madison.

Carbon (C) and platinum (Pt) layers were deposited to protect the oxide layer from ion damage while doing the cross-section thinning process in the FIB. EDS maps show Mn oxide forms at the oxide\gas interface, a thin Cr oxide layer forms next, and an inner MnCr oxide spinel forms at the oxide\alloy interface. In addition, the substrate ahead of the oxide is enriched in Fe and depleted in Cr and Mn. The C and platinum (Pt) were deposited on the surface to prepare for characterization. A summary of an average total oxide thicknesses of all time-lapse 21-2Ni-8.5Mn alloy samples measured over 1000 hours by STEM-EDS is presented in Figure I.1.4.4.

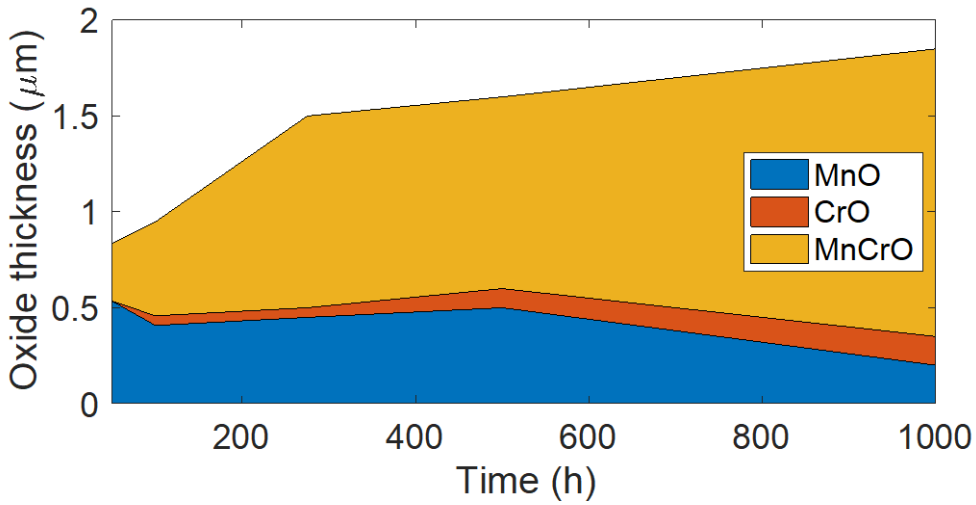

Figure I.1.4.4. Oxide thickness versus time in 21-2Ni-8.5Mn samples exposed to CO_2 at 700°C measured using STEM-EDS. Source: University of Florida.

Task 2.2 – Mesoscale Model Development

A mesoscale model of the valve steel corrosion was developed to provide a tool to model more of the basic physics occurring during the corrosion, including charge transport, formation of multiple oxide phases, lattice strains, and the impact of grain boundaries. It has been implemented using the finite element method using MOOSE. In the mesoscale model, the oxide layer formation is represented using the phase-field method, in which variable fields represent the phases and element compositions within the material. These variable fields evolve to minimize the overall free energy of the system. A coupled-current condition is assumed within the material, which forces the net electric charge transported through the oxide during any given time increment to be zero [1]. It also ensures that no sudden charge redistribution takes place in the metal oxide system, consistent with the assumption that growth is approximately a steady state phenomenon [2]. This allows inclusion of the impact of the electric potential on the ion transport and oxide growth.

A phase-field model was developed that includes variables to represent the critical phases observed in the experiments, mainly the metal alloy phase, the spinel phase, and the Mn oxide phase. Variables were added to describe the voids that form at the metal/oxide interface, and the open volume surrounding the valve. In addition, there are variables describing the local molar fractions of Mn, Cr, O, and vacancies.

The predictions of the model in simplified one-dimensional (1D) domains were explored, as shown in Figure I.1.4.5. A 1D system was modeled that initially has a region of alloy phase on the left and the open volume filled with gas on the right, as shown in Figure I.1.4.5(a). Also, there is an initial void in the alloy and initial layers of the spinel and MnO phases between the metal and the gas-filled volume. The chemical potential (μ) for Mn and Cr is fixed on the left boundary, allowing additional metal atoms to enter the system. The values of μ for O are fixed on the right boundary, allowing O atoms to enter the system. Depending on the relative values of μ for the various elements, different oxide layers will grow. When all the chemical potential values at the boundary are equal, the void and oxide phases grow at equally, with the void ending at the metal/oxide interface, as observed in Figure I.1.4.5(b). When the chemical potential of Cr is higher than the other elements, the spinel phase grows faster than the void and MnO, as can be seen in Figure I.1.4.5(c). The spinel phase also grows faster when the O chemical potential is higher, as shown in Figure I.1.4.5(d). When the chemical potential of Mn is higher, the MnO phase grows faster, as can be seen in Figure I.1.4.5(e).

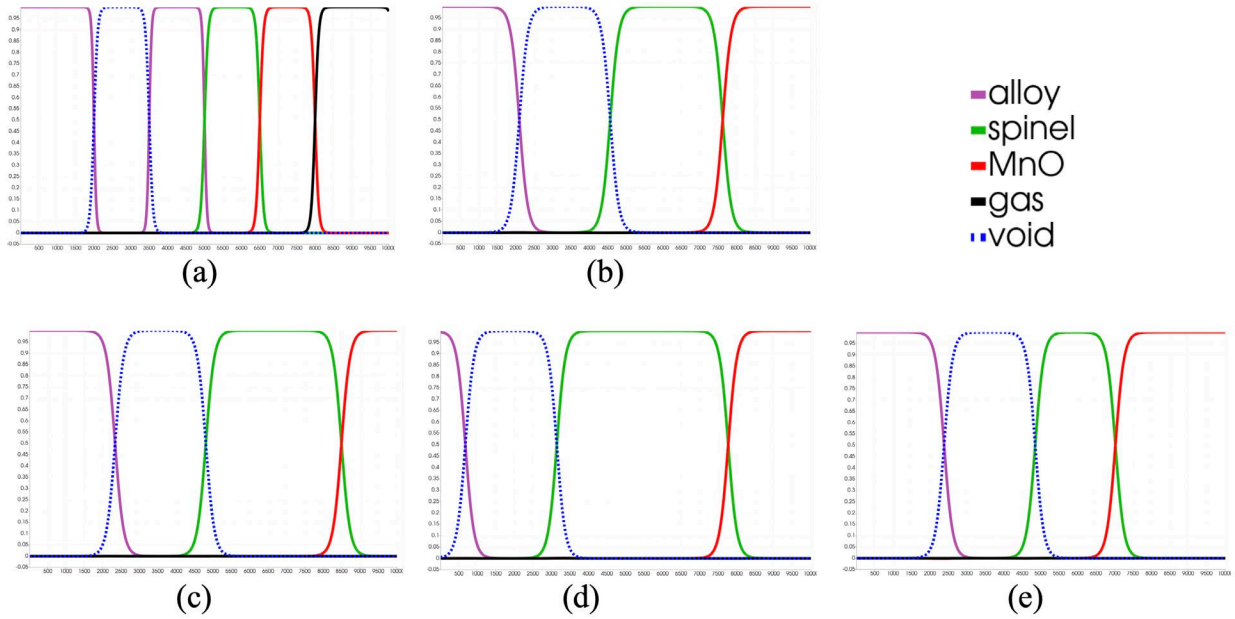

Figure I.1.4.5. Simulation of oxidation using the mesoscale model in a 1D domain. (a) The initial condition of the order parameters. (b)-(e) The equilibrium states of the simulation with different boundary conditions (BCs) for the μ values (e.g., the equilibrium state refers to when the non-linear residual is decreased down to 10^{-8}). Source: University of Florida.

Close collaboration with the experimental campaign has helped to guide the scope of the atomistic calculations. In BP 2, focus was shifted from investigating the properties of the bulk alloy system to probing more dynamic behavior in the microstructures that develop during the corrosion process. Using atomistic simulation techniques, the fundamental mechanisms of the microstructural evolution can be isolated and provide insights regarding which reaction pathways are most energetically favorable. Vacancy formation and migration energies in the alloy and oxide phases are essential to determine the diffusivity of each phase. Due to the layering of each phase near the surface, diffusivity between phases is a key factor in understanding the overall corrosion process.

Table I.1.4.2 enumerates the vacancy formation energy of each species in each of the phases detected by EDS mappings of samples from the experimental campaign. The relatively low formation energy of Mn vacancies in the MnO phase is consistent with the experimental finding that this layer forms rapidly at the surface. This low activation energy indicates that diffusion pathways involving Mn in the MnO phase are readily traversable at elevated temperature. In the $MnCr_2O_4$ (spinel) phase, Mn vacancies have a lower formation energy than the Cr vacancies, but both are well below the formation energy of the O vacancies. From these findings, we can assume that the dominant diffusion mechanism is cation vacancy mediated in both the oxide and spinel phases. Vacancy formation energies in the bulk alloy phase are more evenly distributed, indicating that preferential migration of the alloy components is unlikely below the surface layers.

Table I.1.4.2. Vacancy Formation Energy of Each Species in the Alloy and Oxide Phases Calculated using DFT simulations as Reported in eV

	Mn	Cr	O	Fe
MnO	0.1130	-	4.9274	-
$MnCr_2O_4$	3.5411	3.9278	5.4733	-
FeCrMn	2.5323	2.0881	-	2.2769

In addition to static vacancy defects, migration pathways were calculated using the nudged elastic band method. Combined results from MD and DFT calculations show that in the alloy phase, migration barrier heights are similar in magnitude to the vacancy formation energy and are insensitive to the migrating defect's local chemical environment. In the spinel phase, migration pathways are made more complicated by the structure's symmetry. Unlike the close packed face-centered cubic structure of the alloy phase, cations in the spinel lattice have multiple possible migration pathways. We chose to focus on the migration of Mn as it exhibits a lower vacancy formation energy. Through an exhaustive search of possible Mn migration pathways, we were able to conclude that the path between the 16C and 32E Wyckoff positions has the lowest barrier height. Figure I.1.4.6 depicts the cubic spline interpolation of intermediate images along that path. Each point corresponds to the energy of the image relative to the energetically equivalent endpoints. The observed barrier height is approximately 0.65 eV, which is significantly lower than the cation's vacancy formation energy. This finding suggests that the 16C to 32E migration pathway is instrumental to diffusion both within the phase and between the alloy and oxide phases.

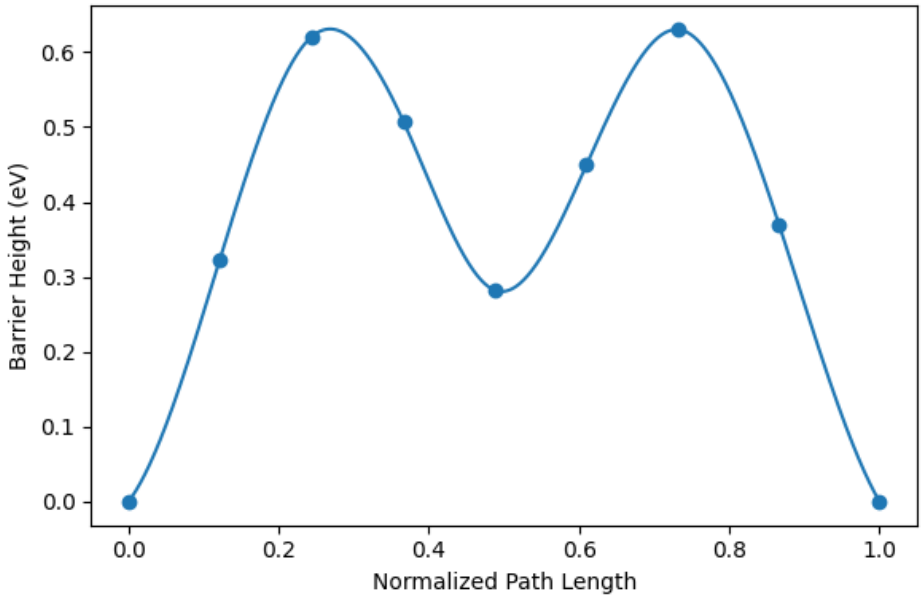

Figure I.1.4.6. Cubic spline interpolation of the Mn 16C -> 32E migration energy barrier in $MnCr_2O_4$ calculated using DFT and MD simulations. Source: University of Florida.

Task 2.3 – Implementation of the SStAC Tool Using MOOSE

The Coupled-Current Charge Compensation corrosion model was adapted for the corrosion of steel 21-2N and implemented in the finite element-based environment MOOSE. Only one oxide scale is considered for the moment. From preliminary experimental data and thermodynamics consideration, the main oxide growing in the conditions of interest is a Cr-Mn spinel of stoichiometry close to $MnCr_2O_4$. This spinel is modeled as a p-type semi-conductor, meaning that it can be thought of as a fixed lattice of O^{2-} anions with cation vacancies (V''_{Mn} and V''_{Cr}) diffusing through balanced by electron holes h^+. This mechanism leads to an outward oxide growth. The metal/oxide interface displacement is neglected.

To model the moving oxide surface, the XFEM module in MOOSE was used. XFEM can be used to model moving interfaces between materials. To model the outward oxide growth, the mesh was artificially extended on the right side of the domain to leave some space for the oxide to grow into it. Using this method, the implementation of the outward spinel oxide growth on top of the 21-2N alloy was successful, as shown in Figure I.1.4.7.

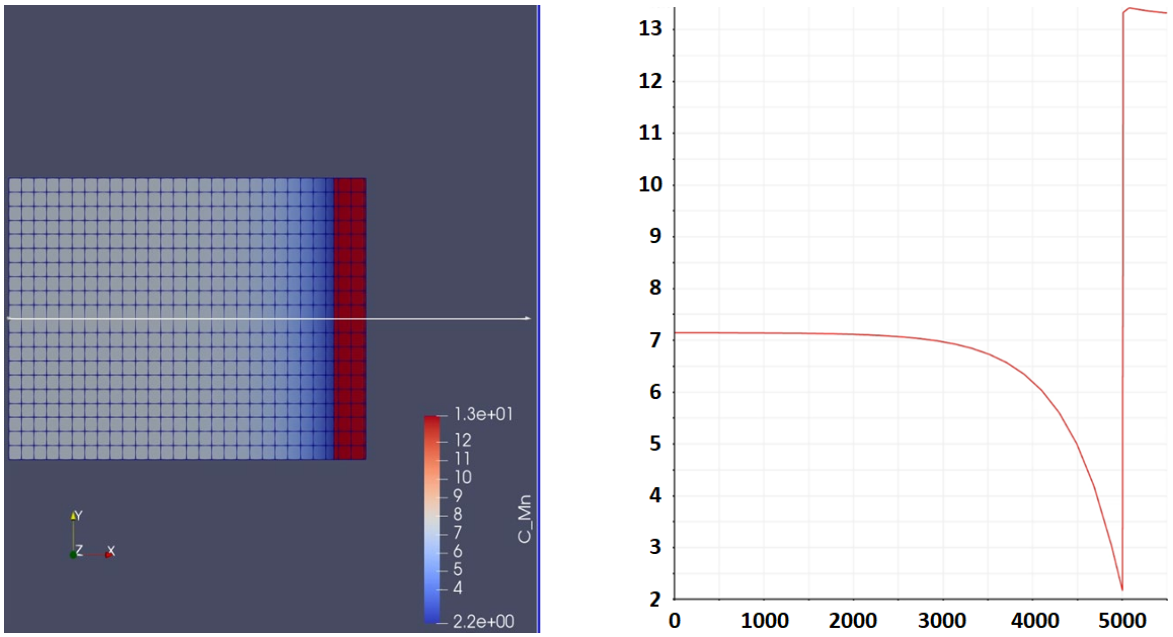

(a) (b)

Figure I.1.4.7. 2D simulation results showing (a) the Mn concentration profile in the metal (blue) and in the oxide (red) and (b) the Mn concentration profile near the oxide/metal interface along the white line shown in part (a).
Source: University of Wisconsin–Madison.

The model runs on a two-dimensional mesh although it currently only works for planar interfaces, with no two-dimensional variations of the parameters. Ongoing work is focused on implementing non-planar XFEM interface movement in a three-dimensional mesh. On a theoretical point of view, the model must also be modified to better account for the limitation of the oxidation rate caused by the slow diffusion of Mn in the metal. Being able to model several oxide layers simultaneous growth or shrinkage as a function of exposure time is also conceivable.

Conclusions

The objective of this project was to develop the SStAC tool for predicting the corrosion of 21-2N and 23-8N stainless-steel engine valves during engine operation. In the second BP, testing was completed in a CO_2 environment and some of the corroded samples were characterized. These results have indicated that Mn plays a major role in resisting oxidation and that MnO and a Mn-Cr-O spinel are the primary oxide phases formed. The development of a mesoscale oxidation model, which will be used to determine the impact of alloying elements and microstructure on the overall oxidation rate, was continued in the second BP. A phase-field model was developed that includes the primary oxide phases observed in the experiments. Atomic-scale simulations found that the Mn formation energy in the Mn oxide phase is much lower than in all other phases, providing a possible reason for why the MnO forms first.

References

1. Fromhold, A. T., Jr., and E. L. Cook, 1968, “Kinetics of oxide film growth on metal crystals: Electronic and ionic diffusion in large surface-charge and space-charge fields,” *Phys. Rev.*, Vol. 175, No. 3, pp. 877–897.
2. Fromhold, A. T., Jr., 1969, “Parabolic oxidation of metals,” *Phys. Lett. A*, Vol. 29, pp. 157–158.

Acknowledgements

All the work summarized in this report is due to the hard work of our research team composed of members from the University of Florida, University of Wisconsin–Madison, Tenneco, and Idaho National Laboratory.

I.2 Solid-State Processing and Metal Matrix Composites

I.2.1 Direct Extruded High-Conductivity Copper for Electric Machines (Pacific Northwest National Laboratory)

Glenn Grant, Principal Investigator
Pacific Northwest National Laboratory
902 Battelle Boulevard
Richland, WA 99352
E-mail: glenn.grant@pnnl.gov

Jerry L. Gibbs, DOE Technology Manager
U.S. Department of Energy
E-mail: jerry.gibbs@ee.doe.gov

Start Date: October 1, 2017 End Date: December 31, 2020
Project Funding: $1,150,000 DOE share: $600,000 Non-DOE share: $550,000

Project Introduction

The focus of this project is to develop and demonstrate a high-power induction motor that utilizes a rotor "squirrel cage" (shorting bars plus end cap assembly) made with a new high-conductivity, Cu-C composite material fabricated by Shear-Assisted Processing and Extrusion or ShAPE™—a new manufacturing process being developed at PNNL. In this rotor, shown in Figure I.2.1.1, the shorting bars are linear blade-like parts that run the height of the rotor from end cap to end cap. The bars allow for current to flow between the end caps during motor operation. Higher conductivity in this bar will allow for greater torque to be generated, which can lead to potential improvements in performance or downsizing and lightweighting opportunities, depending on product drivers. The project is a 50/50 cost share with General Motors (GM) and will develop a motor application relevant to their commercial transportation market.

Figure I.2.1.1. Induction motor rotor and an example of a shorting bar. Source: PNNL.

Objectives

The objectives of this project are to: (a) develop Cu-C composites with higher conductivity than annealed Cu; and (b) develop a shear-assisted extrusion process as a method to fabricate the composites.

Approach

While Cu-C composites are well-known in the research world for their enhanced conductivity and ampacity, scalable methods to fabricate composite conductors have been elusive. The ShAPE™ equipment comprises of a rotating tool with a through-cavity and an extrusion container. The billet to be processed is inserted into the stationary extrusion container and the flat face of the rotating die is abutted against it. Owing to the intense shear and frictional heat, the billet material at the tool interface is plasticized and flows through the cavity in the tool to form the extrudate.

In FY 2019, ShAPE was used to manufacture Cu-C composite wires using monolayer graphene, based on previous work suggesting that the electrical performance of Cu/graphene (G) was dependent on additive defect density [1]. Low-defect density G procured as sheets that were chemically vapor-deposited on C110000 Cu alloy foils were consolidated with a solid Cu billet and extruded to form wires using the ShAPE™ process. Cu alloy foils without G were also extruded into wires to manufacture the control samples. The composition of the different samples manufactured in FY 2019 is provided in Table I.2.1.1, which also shows the electrical conductivity of the Cu-C composite wires measured using the four-point probe method. Results show a progressive increase in the conductivity of the wires with an increase in G content. The highest conductivity of 104.8% International Annealed Copper Standard (IACS), corresponding to an increase of 4%, was measured for wires with 6-ppm graphene.

In order to understand the conducitivity enhancement mechanisms, it was essential to determine the location of the G material in the Cu microstructure. Therefore, in FY 2020, advanced microstructural characterization was performed using TEM and atom probe tomography (APT) to evaluate the Cu-G microstructure. For the TEM and APT analysis, Cu-G composite samples with 6-ppm G were obtained from the vicinity of a grain boundary using FIB milling, after which they were imaged.

Table I.2.1.1. Electrical Conductivity of the Cu-C Composite Wires Measured by Four-Point Probe Method

Sample	G Content (ppm)	Electrical Conductivity (%IACS)	Property Improvement with Respect to Control
A (control sample)	0	100.75 ± 0.002	–
B	1.5	103.57 ± 0.001	2.8%
C	2	103.83 ± 0.002	3.1%
D	6	104.80 ± 0.003	4.0%

Results

While the TEM analysis did not provide detailed understanding of G in the Cu microstructure, the APT analysis clearly showed the morphology of the C in the form of G at the Cu grain boundaries. Of the six needles obtained from the FIB samples, two samples contained C that was imaged. Of the two APT samples with carbon, Sample 2 demonstrated a higher C concentration and was hypothesized to be closer to the grain boundary than Sample 1, as shown in Figure I.2.1.2. Table I.2.1.2 provides the elemental composition of the two APT samples.

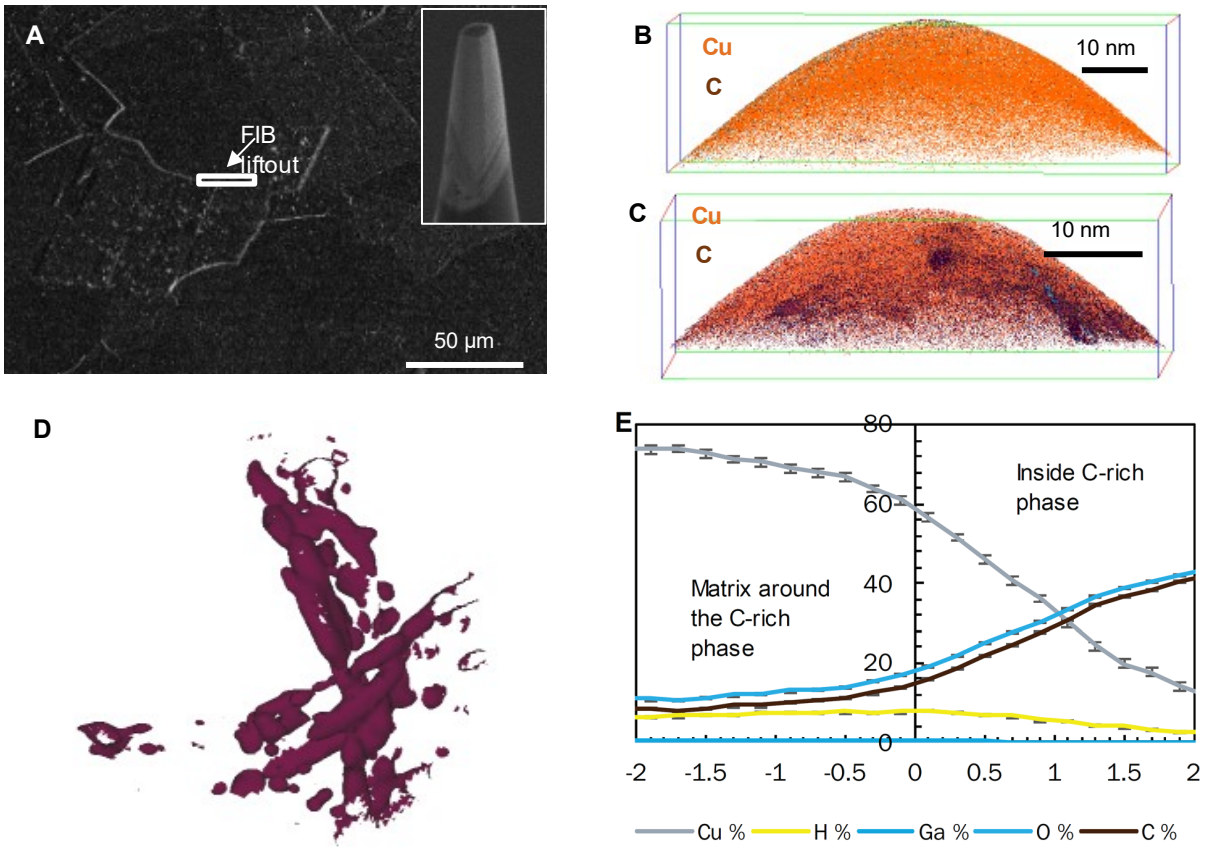

Figure I.2.1.2. (a) FIB lift-out location in the Cu-G composite microstructure at a grain boundary. (b) Side view of Sample 1 of the 6 FIB needles showing insignificant C enrichment. (c) Side view of Sample 2 of the 6 FIB needles showing significant C and O enrichment. (d) Top view of the iso-concentration surface created to delineate the carbon-enriched region from the surrounding Cu matrix. (e) The composition of the sample on the carbon-rich and Cu-rich sides. Source: PNNL.

Table I.2.1.2. Composition of the FIB Needles Obtained from the Cu-G Composite Determined Using APT

Sample	Cu	H	Ga	O	C
1	97.15 ± 0.14	0.96 ± 0.01	0.35 ± 0.01	1.20 ± 0.01	0.34 ± 0.01
2	93.74 ± 0.10	2.09 ± 0.01	0.93 ± 0.01	1.89 ± 0.01	1.34 ± 0.01

It is interesting to note that in addition to Cu and carbon, the APT analysis showed the samples contained statistically significant quantities of hydrogen (H), gallium (Ga), and O. The Ga can be introduced during the FIB process and the H can be introduced from the APT chamber. On the other hand, the O may be introduced either during the G manufacturing or when the samples were handled during the billet precursor assembly prior to the ShAPE™ process. In either case, it is evident that despite the presence of O, possibly at the interface between the Cu and the G (in the form of carbon), the Cu-G composites that were demonstrated increased electrical conductivity by 4%.

Conclusions

In FY 2019, ShAPE™ technology was used to fabricate Cu-C composite wires with 2.5 mm diameter and > 1 m length. Monolayer G with low-defect-density was used to manufacture the composite wires instead of reduced G oxide or graphite. Extrusion tools and dies, as well processing parameters, were determined to achieve fully compacted microstructures with adequate G distribution and no porosity. Electrical conductivity of the composite wires increased as a function of G content at RT as verified by third-party testing. At elevated temperatures, resistivity of the composite wires lower than the control sample, as well as that of pure Cu.

Mechanical testing demonstrated that the composite wires behaved like annealed pure Cu samples, plausibly owing to the very low G quantities used in the fabrication process. This project leverages a new manufacturing process to produce high-conductivity wire by an unconventional method involving high-shear and plastic deformation. This technology could be disruptive to the way automotive traction drives are constructed, sized, or powered. The high-conductivity wire for stator winding could spill over into permanent magnet motor space where there are also strong incentives to improve motor performance.

In FY 2020, TEM and APT analysis was performed on Cu-G composites with 6-ppm graphene. APT analysis showed that only the FIB needles obtained from closer to the grain boundary showed significant C enrichment. The C was co-located with O in the FIB needles, possibly at the interface between the Cu and the C. Despite the presence of O at the interface, the conductivity of the Cu-G sample showed an improvement.

Key Publications

1. Li, X., B. Gwalani, N. Overman, G. Grant, and K. Kappagantula, 2020, "Manufacturing bulk-scale copper-graphene composites with enhanced conductivity," manuscript in preparation.
2. Li, X., C. Zhou, N. Overman, N. Canfield, X. Ma, K. Kappagantula, J. Schroth, and G. Grant, 2020, "Meter-long copper-carbon composite wire with a uniform carbon dispersion made by friction extrusion," manuscript in preparation.
3. Kappagantula, K., X. Li, W. Choi, and G. Grant, 2021, "A manufacturing perspective on the development of ultra-high-conductivity metal composites," TMS 2021, Orlando, FL, USA, accepted for presentation.
4. Kappagantula, K., X. Li, and G. J. Grant, 2020, "Development of ultraconductive materials using solid-phase processing," Invited Lecture at Chemical Engineering Department Seminar, Ohio University, Athens, OH, USA.
5. Kappagantula, K., X. Li, C. Zhou, H. Wang, J. G. Schroth, and G. J. Grant, 2019, "Solid-phase processing of conductive copper/graphene alloys via ShAPE™ approach," *MS&T 2019*, Portland OR, USA.
6. Li, X., N. L. Canfield, J. T. Darsell, C. Zhou, H. Wang, J. G. Schroth, and G. J. Grant, 2019, "ShAPE: A novel solid-phase processing of making bulk size metal matrix composite without agglomeration," *MS&T 2019*, Portland OR, USA.
7. Li, X., G. J. Grant, C. Zhou, H. Wang, T. A. Perry, and J. G. Schroth, 2019, "Copper-graphite composite wire made by ShAPE," *TMS 2019*, San Antonio TX, USA.
8. Li, X., N. R. Overman, T. J. Roosendaal, M. J. Olszta, C. Zhou, H. Wang, T. A. Perry, J. G. Schroth, and G. J. Grant, 2019, "Microstructure and mechanical properties of pure copper wire produced by ShAPE," *JOM*, Vol. 71, No. 12, pp. 4799–4805.

References

1. Kappagantula, K., and F. Kraft, 2017, "Ultraconductive Metal Composite Forms and the Synthesis Thereof," U.S. Patent US20190267153A1.

I.2.2 Metal Matrix Composite Brakes Using Titanium Diboride (Pacific Northwest National Laboratory)

Glenn Grant, Co-Principal Investigator
Pacific Northwest National Laboratory
902 Battelle Boulevard
Richland, WA 99352
E-mail: glenn.grant@pnnl.gov

Merritt Osbourn, Co-Principal Investigator
Arconic Technical Center
100 Technical Drive
New Kensington, PA 15069
E-mail: merritt.osbourn@arconic.com

Jerry L. Gibbs, DOE Technology Manager
U.S. Department of Energy
E-mail: jerry.gibbs@ee.doe.gov

Start Date: September 1, 2017 End Date: June 30, 2021
Project Funding: $660,800 DOE share: $300,000 Non-DOE share: $360,800

Project Introduction

Currently, no viable, cost-competitive alternative to cast-Fe brake rotors exists for the automotive market. While in past years many weight savings materials and designs have been developed for other parts of a vehicle, the brake assembly remains tied to nearly fifty-year-old technology, as shown in Figure I.2.2.1. Metal-matrix composites (MMCs) present an opportunity to replace cast-Fe brakes in certain vehicles. By replacing cast-Fe rotors with lighter weight MMCs, the opportunity exists to reduce the unsprung weight of the brake assembly and adjacent components, such as suspension arms and springs. A 50% savings in mass in a rotating and unsprung location can lead to a 0.25–0.35 mpg fuel savings in a mid-sized car. In addition, Al MMC brakes can provide combinations of high-friction coefficients, particularly heat transfer characteristics, and increased wear life that can favorably affect system life-cycle costs. A 50% increase in wear life can double the interval between rotor change-outs and can affect the economics for those vehicles sensitive to down time. Lower wear also means fewer wear particles are generated during braking. These wear particles are the second-largest source of particulate emissions from a vehicle. “In urban areas, around 55% of total non-exhaust PM10 (particulate matter smaller than 10 micrometers) emissions is from brake wear” [1].

Al MMC brake rotors were investigated in past DOE-funded programs during the early 2000s. A commercial application of Al MMC silicon carbide (SiC) rotors was implemented in a limited number of Plymouth Prowler vehicles in 1998, while numerous manufacturers have implemented Al MMC rotors and drums in limited production vehicles (e.g., Toyota RAV4-EV, GM EV1, Lotus Elise, Volkswagen Lupo). But in all cases, cost avoidance could not be fully demonstrated when replacing the cast-iron-equivalent part.

Figure I.2.2.1. Conventional brake design utilizing an Al caliper and a cast-Fe brake disc. Source: PNNL.

The current automotive landscape has changed in the last ten years, however. The changes that have been made may provide opportunities to look again at Al MMC brakes. One of the significant changes comes from electric/hybride vehicles. Energy harvesting in electric/hybrid vehicle operation decreases the amount of energy that must be dissipated by the mechanical brakes by as much as 40%. This can allow for much lower front brake temperatures, enabling the use of lighter weight, lower melting temperature alloys as rotors. Also, cast-Fe rusts and the friction coefficent of rusty surfaces is not consistent, making it difficult to manage in brake-by-wire systems tasked with balancing mechanical brake force with energy harvesting. Consumers demand a smooth stop (i.e., driver feel and noise, vibration and harshness issues). As such, corrosion-resistant and low-wear alloys (e.g., Al MMCs) may provide better control. Another factor is the coming change in duty cycle for a vehicle. The next-generation of personal transportation vehicles may need drastically improved durability and longer maintenance intervals if they are to be used in new mobility strategies like 24/7 ride-sharing or fleet ownership scenarios.

Barriers to more widespread use of MMCs for vehicle lightweighting include: (1) the costs of the feedstock, especially the insoluble reinforcement (e.g., particle, whisker, or fiber) usually SiC; (2) the cost of combining the reinforcement with the matrix in production, which requires cost and effort to ensure the SiC particles are "sized" or coated correctly to promote wetting in molten Al; and (3) the cost of shaping/machining MMC components. One of the concepts to address these barriers is to develop an alternative reinforcing particle. Titanium diboride (TiB_2) reinforcement offers an opportunity to improve wear-resistance at a lower particle loading because of improved C-Al bonding. SiC reinforcement is costly when prepared for inclusion in an Al composite (i.e., particle-size fraction constraints, SiO_2 coating, etc.). TiB_2 has much improved wetting with Al allowing for finer particle-size and better homogeneity, which may prove to provide a lower cost overall due to the lower amount of particle loading required and reduced compositing time for the same friction and wear performance.

Recent improvements to the TiB_2 production process by Arconic may make it a more viable technical ceramic for MMCs than in the past. This LightMAT-funded project will utilize TiB_2 as a substitute for more traditional MMC efforts using SiC to improve performance, wear life, and cost in brake rotors.

Objectives

The objective of the project is to reduce the weight of brake rotors by > 50% over current cast-Fe materials, and at the same time, improve brake performance, wear life, and life-cycle costs over traditional cast-Fe systems. The project will develop an Al MMC material that shows appropriate wear-resistance, friction coefficient, and tribologic properties, and shows a potential for a cost/benefit ratio appropriate for commercial development.

Approach

The overall approach to the work will be to cast TiB_2-reinforced Al brake rotors in several different reinforcement loadings and test for friction and wear performance. The data will be compared to a large DOE-generated database of properties developed on Al-SiC (and other) MMC brake materials in the early 2000s.

The project proceeds through six tasks. The first task involved the production of a 60 vol.% reinforced master alloy produced at the Arconic Technology Center. This master alloy is produced by liquid Al infiltration of a TiB_2 preform.

In the second task, the master alloy and a A356 ingot were combined in a crucible at appropriate ratios to produce 5, 10, and 15 vol.% reinforced melts. A series of stir casting trials were initiated to establish mixing times, melt temperatures, mixing paddle geometry, and mixing paddle speeds. Figure I.2.2.2(a), (b), and (c) show the stir casting equipment, star-design mixing impeller, and close-up of the process, respectively. After determining final stir casting parameters, melts were poured into open steel book molds to produce rectangular castings approximately 10 in. × 7 in. × 1 in., as can be seen in Figure I.2.2.3(a). As-cast plates were hot-rolled at 450°C for two passes with an approximate 30% reduction, then solutionized, and heat-treated to T7.

The as-cast and rolled plates were then machined to subscale rotors for wear-testing, as shown in Figure I.2.2.3(b). Gravity cast plates show some variability in porosity, but the small variations are not expected to affect the friction testing significantly. Approximately three rotors from each particle loading have been fabricated for wear-testing.

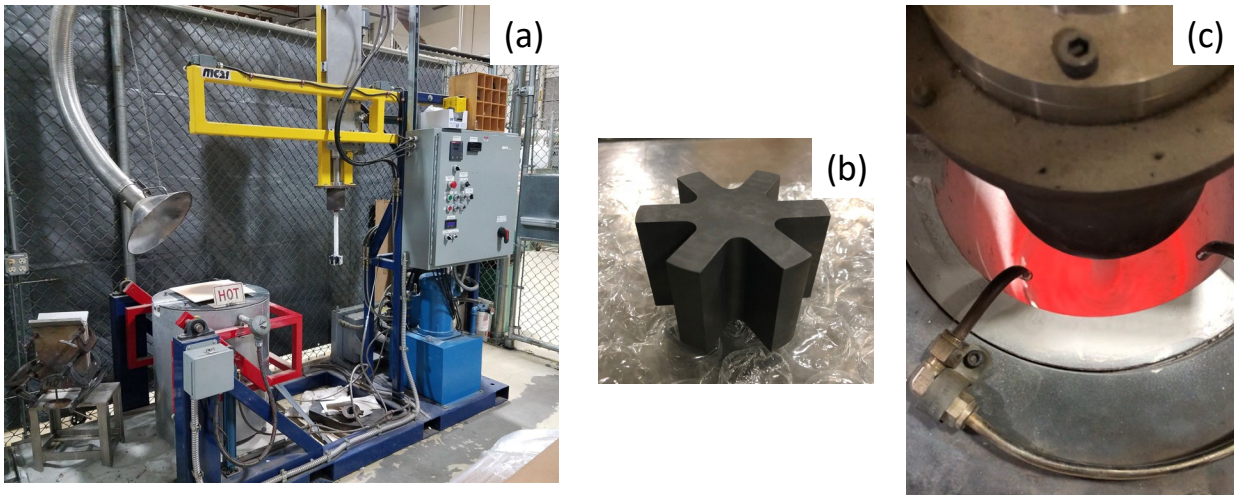

Figure I.2.2.2. (a) Tilt-pour stir casting equipment at PNNL used for the casting trials; (b) star-design bladed impeller installed in mixer head; and (c) close-up of the stir casting process. Source: PNNL.

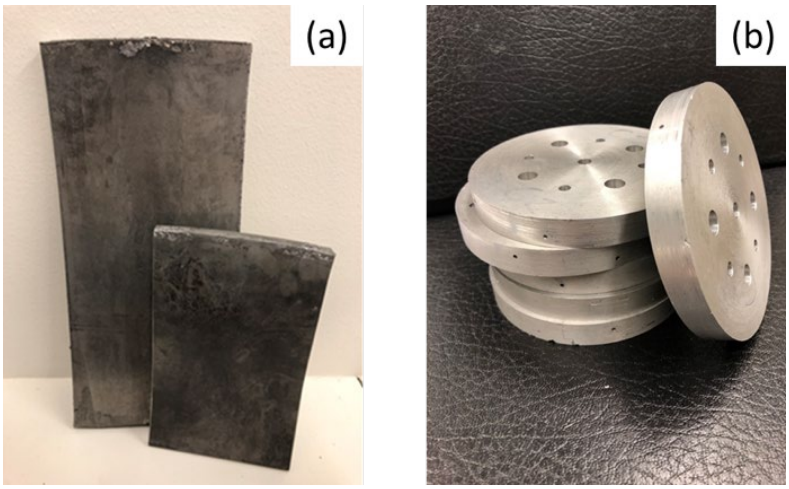

Figure I.2.2.3. (a) Gravity cast plates of 5, 10, and 15 vol % TiB_2-reinforced A356 alloy; and (b) subscale rotors ready for friction/wear-testing. Source: PNNL.

Wear-testing is comprised of mounting the subscale rotors on an instrumented brake testing rig, as shown in Figure I.2.2.4, which is capable of rotating the rotor or pad holder, as shown in Figure I.2.2.5, and applying clamping loads appropriate for automotive braking conditions. This rig is a reduced-scale brake dynamometer and is based on the brake inertia dynamometers employed in Society of Automotive Engineers (SAE) standard J2522 for testing the effectiveness of friction material with regard to pressure, temperature, and speed [2]. However, in our rig, the pad holder rotates and the rotor is stationary, as can be seen in Figure I.2.2.4(b). There is no flywheel between the spindle and pad holder, yet deceleration behavior can be simulated by controlling the speed of the spindle. Several energy profiles can be investigated including low temperature, low load continuous torque tests, and high load and high-temperature transients. After testing, the data on loads, torque, power, and temperature are compiled and friction coefficients are calculated and correlated to test conditions. During the tests, the rotors are paired with several different pad compositions to measure the effect and optimize the friction pair.

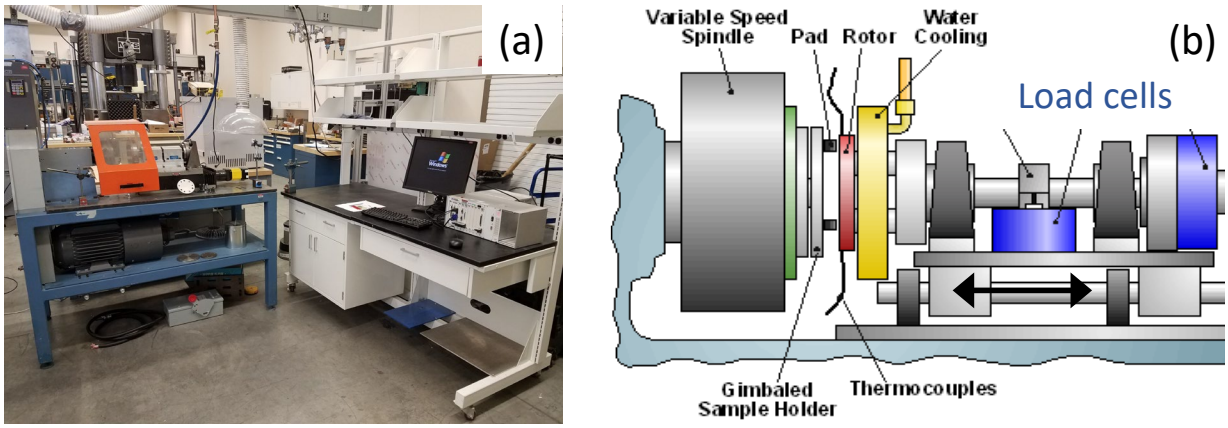

Figure I.2.2.4. (a) Brake friction pair test stand at PNNL and (b) schematic of the test setup with corresponding locations of the pads, rotor, load cells, and other measurement equipment. Source: PNNL.

In FY 2020, pad materials were sourced and machined to fit in the pad holder, as shown in Figure I.2.2.5. Pad materials were selected to have a range of properties that may produce different behaviors when applied against Al MMC rotors. Pads include examples of the original Plymouth Prowler units that were specified by Chrysler for the Al/SiC MMC rotors used in the 1980s, pads designed to run against SiC ceramic brakes found

in several high-performance cars, phenolic pads used against cast-Fe rotors in racing applications, and a conventional phenolic used in a mid-sized sedan.

Figure I.2.2.5. Brake pad holder and tested subscale brake rotor. Source: PNNL.

After testing, rotors and pads are measured and weighed to establish mass gain or loss and the rotor wear tracks are analyzed for geometry. The transfer layer usually formed on the rotor is also analyzed for chemistry and pad reactions.

Results

The final task of this project, friction pair testing, originally scheduled for the first and second quarters of FY 2020, was significantly delayed by the COVID-19 pandemic and limited access to laboratory test equipment. Nonetheless, we were able to complete sourcing and machining of all pad materials, prepare the computer control algorithms for the brake test frame, and develop a test plan consistent with industry accepted procedures. The final friction pair testing is planned for the first two-quarters of FY 2021.

During FY 2020, a literature review was performed to determine the testing procedures for the friction pair. Based on SAE J2522 and available literature [3],[4], the testing procedure can be divided into five segments: (1) green coefficient of friction (μ); (2) burnishing; (3) sensitivity analysis; (4) fade; and (5) recovery. First, contact of unworn pads and rotors happens in the green μ segment. Constant load is applied to reach a stable temperature and friction coefficient. Then, a transfer layer is established in the burnishing step. Load follows a step function in each cycle, which replicates the snub braking conditions. Sensitivity analysis consists of various speed and loads to establish the change in the friction coefficient with respect to the load at a given speed. During the fade segment, temperature increases, and the friction coefficient decreases in each cycle by applying almost full stops at a constant high load. During recovery, snub braking is performed at a constant low load to lower the temperatures and stabilize the friction coefficient. While these segments are important in assessing the performance of the friction pair, another important feature is the specific wear rate of each component. Specific wear rate is a commonly reported property in the literature and can be easily benchmarked against the values available for other MMC rotors. Specific wear rate (mm^3/Nm) can be calculated from volume changes using Equation (1).

$$Wear\ rate = \frac{V}{F_N d} \quad (1)$$

where V is the wear volume, F_N is the normal force, and d is the sliding distance. Wear volume can be found from dimensional changes in the components, topographical measurements of the wear track on the rotor, and interrupted mass measurements of the pads.

Table I.2.2.1 summarizes the testing plan developed for the friction pair. Parallel to the standard, tests will start with green friction coefficient and burnishing segments. Next, sensitivity and fade tests will provide the change

in the friction coefficient with speed, pressure, and temperature. Wear tests at two different temperatures will result in the wear rates for highway and city driving conditions, with the low temperature-low load corresponding to highway and high-temperature-high load corresponding to city conditions.

Table I.2.2.1. Testing Plan for the Friction Pairs

Test Segment	Initial Brake Temperature (°C)	Speed (m/s)	Pressure (MPa)	Cycle	Final Brake Temperature (°C)
Green μ	25	–	increasing	5	100
Burnishing	100	4	varying	5	–
Sensitivity	25	1–4	0.4–0.7	1 (each)	–
Fade	25	4	0.9	10	–
Wear (Low T)	25	4	0.4	10	200
Wear (High T)	25	1	0.8	10	600

As the wear tests will last longer than the other segments (e.g., ~600 s/cycle), maintaining a stable friction coefficient and final brake temperature are critical. In order to maintain a steady state temperature during the tests, the rotors will be cooled with water, as observed in Figure I.2.2.4(b) above. Friction coefficients will also be monitored during the wear tests through online measurements of the normal forces and torques. A stable friction pair results in an almost constant friction coefficient with time, whereas large fluctuations are observed for an unstable friction pair, as illustrated by Figure I.2.2.6. After satisfying the conditions for a stable friction pair, wear rates and friction coefficients will be benchmarked against the large dataset generated by DOE projects on Al/SiC MMCs in the early to mid-2000s and the values available in the literature for Al/SiC and other MMCs.

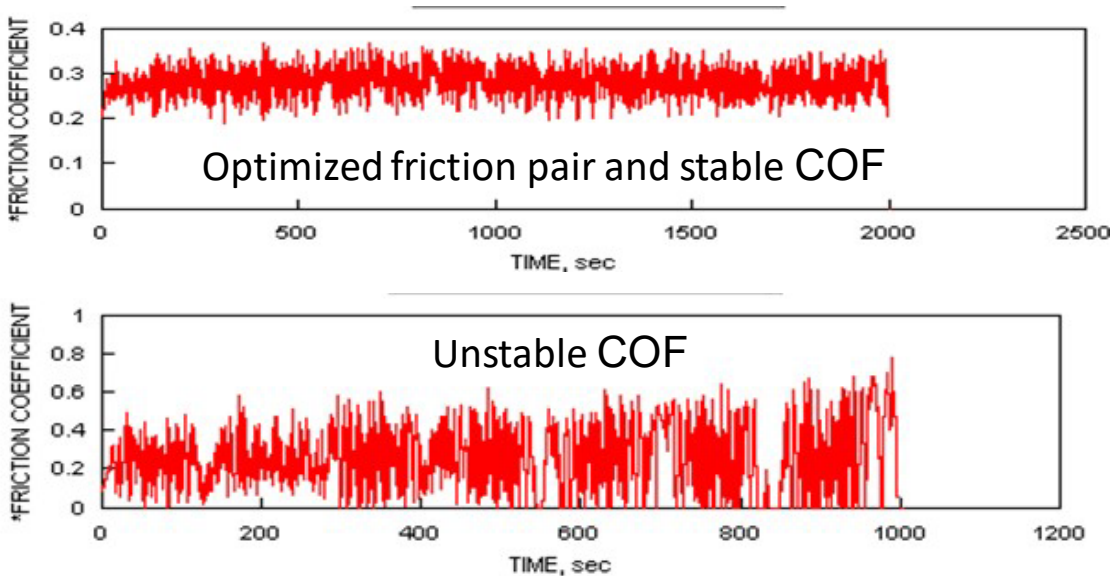

Figure I.2.2.6. Change in the friction coefficient with time for stable vs unstable friction pairs. Source: PNNL.

Conclusions

Future vehicle platforms have created opportunities to re-evaluate Al MMC brakes. Lightweight brake rotors have an opportunity to contribute to vehicle lightweighting efforts and offer the possibility of a 50% weight savings in rotating and unsprung mass in some vehicle applications. This project investigates a potentially lower cost reinforcement than the more traditional SiC by fabricating TiB_2 reinforced subscale brake rotor components. The stir-cast rotors will be tested for wear and tribologic performance according to the testing

plan developed for the reduced-scale dynamometer test setup. Specific wear rates and friction coefficients obtained from the tests will be compared to a large dataset of performance characteristics generated by DOE projects on Al/SiC MMCs in the early to mid-2000s, and the results will be available in the literature. The results of this work will inform an opportunity for lightweighting this important contributor to vehicle mass.

References

1. Halonen, A., 2016, "Is now the time for lightweight brakes?" *The Brake Report*. Available at: https://thebrakereport.com/is-now-the-time-for-lightweight-brakes/ (accessed December 2, 2020).
2. SAE, 2014, "Dynamometer global brake effectiveness," *SAE International*, J2522_201409, Ground Vehicle Standard. Available at: https://doi.org/10.4271/J2522_201409 (accessed December 2, 2020).
3. Jang, H., K. Ko, S. J. Kim, R. H. Basch, and J. W. Fash, 2004, "The effect of metal fibers on the friction performance of automotive brake friction materials," *Wear*, Vol. 256, No. 3–4, pp. 406–414.
4. Cho, M. H., S. J. Kim, D. Kim, H. Jang, 2005, "Effects of ingredients on tribological characteristics of a brake lining: An experimental case study," *Wear*, Vol. 258, No. 11–12, pp. 1682–1687.

I.3 Powertrain Materials Core Program

I.3.1 Cost-Effective Lightweight Engine Alloys – Thrust 1

I.3.1.1 New Aluminum Alloys with Improved High-Temperature Performance (1A/1B)

I.3.1.1.1 Fundamental Studies of Complex Precipitation Pathways in Lightweight Alloys (Task 1A1) (Oak Ridge National Laboratory)

Dongwon Shin, Co-Principal Investigator
Oak Ridge National Laboratory
1 Bethel Valley Road
Oak Ridge, TN 37831
E-mail: shind@ornl.gov

Amit Shyam, Co-Principal Investigator
Oak Ridge National Laboratory
1 Bethel Valley Road
Oak Ridge, TN 37831
E-mail: shyama@ornl.gov

Jerry L. Gibbs, DOE Technology Manager
U.S. Department of Energy
E-mail: jerry.gibbs@ee.doe.gov

Start Date: October 1, 2018 End Date: September 30, 2023
Project Funding: $350,000 DOE share: $350,000 Non-DOE share: $0

Project Introduction

Engineering of key interfaces between the Al matrix and strengthening precipitate phases to increase the temperature capability of lightweight Al alloys is a key scientific driver for this task. By explicitly utilizing modern materials science research capabilities (i.e., advanced characterization and computation at DOE facilities), the ORNL team is significantly accelerating and promoting understanding of interfacial structures in Al-Cu and Al-Ni alloys. The understanding gained in the fundamental studies within this task are being applied in other program tasks to guide the design of advanced lightweight Al alloys capable of even higher temperatures to enable automotive propulsion with higher efficiencies and reduced environmental impact.

Objectives

Al-Cu Alloys

The focus of the fundamental studies in this subtask was the determination of the interfacial structures in the {110} semi-coherent Al/θ' (Al_2Cu) interface and their role in the segregation of Cu to these principle precipitate growth interfaces. The goals of this investigation were to identify the defects present in this semi-coherent interface, the atomic arrangements of these defects, and most importantly, the role of the defects in the incorporation of Cu into and out of the strengthening precipitates. These interfacial structural units regulate the boundary mobility, a key factor in precipitate stability and resultant coarsening. Motivation is that increased stability and coarsening resistance of strengthening precipitates at elevated temperatures result in superior high-temperature mechanical properties of lightweight alloys.

Al-Ni Alloys

This subtask aims to investigate the largely unknown interfacial structures of Al/Al_3Ni in Al-Ni-X alloys near the eutectic composition; therefore, a fundamental study is required to understand the stability and coarsening behavior of the Al_3Ni phase within an Al matrix. To predict interfacial energies between the matrix and Al_3Ni,

the goal of this work is modeling interface structures within the context of first principles DFT studies based on prior orientational relationship reported in the literature [1].

Approach

Al-Cu Alloys

Aberration-corrected STEM and first principles calculations were used to accurately determine the atomic structure of the highly mobile, semi-coherent precipitate interfaces that control the precipitate evolution process in the Al-Cu system. In fcc materials, such as Al, the geometrically necessary dislocations prefer to be perfect edge dislocations with a <110> line direction on {111} glide planes. Viewing these dislocations along a <110> direction provides a clear view parallel to the line direction of the atomic arrangements in the interface.

Al-Ni Alloys

Supercell models of the Al/Al_3Ni interface between the alloys have been constructed. Orientation relationships observed between the fcc-Al matrix and Al_3Ni precipitates during directional solidification [1] were replicated at the interface in the supercell models. Multiple supercell models were enumerated to find optimized geometry at the interface, which minimizes the interfacial strain and energy. Due to the large size of supercells and the number of possible structures that need to be constructed to simulate the Al/Al_3Ni interface, it was essential to perform DFT interface calculations on a supercomputer. The Summit supercomputer at the Oak Ridge Leadership Computing Facility was extensively used to reduce the timeframe of these massive calculations.

Results

Al-Cu Alloys

High-angle annular dark-field (HAADF) images of the Al/θ'-Al_2Cu interfaces were recorded using an aberration-corrected Nion UltraSTEM200™ STEM (i.e., the highest spatial resolution microscope at ORNL). Figure I.3.1.1.1.1 and Figure I.3.1.1.1.2 are HAADF images showing that the semi-coherent {110} interface is not a simple combination of abrupt terminations of the two phases. The brightest features in these images are columns of Cu atoms and the less intense features are columns of Al.

Figure I.3.1.1.1.1 shows a periodic defect structure at the interface consisting of two alternating units. In the first unit, 2 cAl unit vectors match 1.5 cθ' unit vectors, while in the second, 3 cAl unit vectors match with 2 cθ' unit vectors. These two units will be referred to as 2Al:1.5θ' and 3Al:2θ'. The dislocations that loop the precipitate plates are contained within these interfacial structural units. The interfacial dislocations identified in these two alternating interfacial structural units are not the compact dislocations deduced from the original studies of this precipitate. Instead, Figure I.3.1.1.1.1(a) shows that they have the same atomic structure as perfect edge dislocations with b = a/2 <110> laying on {111}-type glide planes in the Al matrix. The misfit strain remaining at the interface is only +0.25%. The very small residual strain at this semi-coherent interface is of the same magnitude as the misfit strain present at the coherent interface (-0.25%). Thus, the observed interfacial dislocation array nearly accommodates all the misfit strain, leaving a small amount of residual strain to interact with matrix dislocations along this semi-coherent interface.

The compositional sensitivity of HAADF imaging reveals that there are columns of Cu and Al atoms missing in the interface based on expected atom positions in the bulk Al and θ' structures, as can be seen in Figure I.3.1.1.1.1(b). In the smaller 2_{Al}:$1.5_{\theta'}$ unit, an Al column from θ' and an Al column from the Al matrix would share nearly the same space. The top schematic (and image) shows only one Al column is present. In the larger 3_{Al}:$2_{\theta'}$ unit, a Cu column from θ' and an Al column from the Al matrix would share nearly the same space. The bottom schematic (and image) shows that the Cu column is missing. The lineal atom density of a Cu column in this projection is half that for an Al column, so the local composition in the interface region, before solute segregation effects are considered, maintains the θ' Al_2Cu stoichiometry.

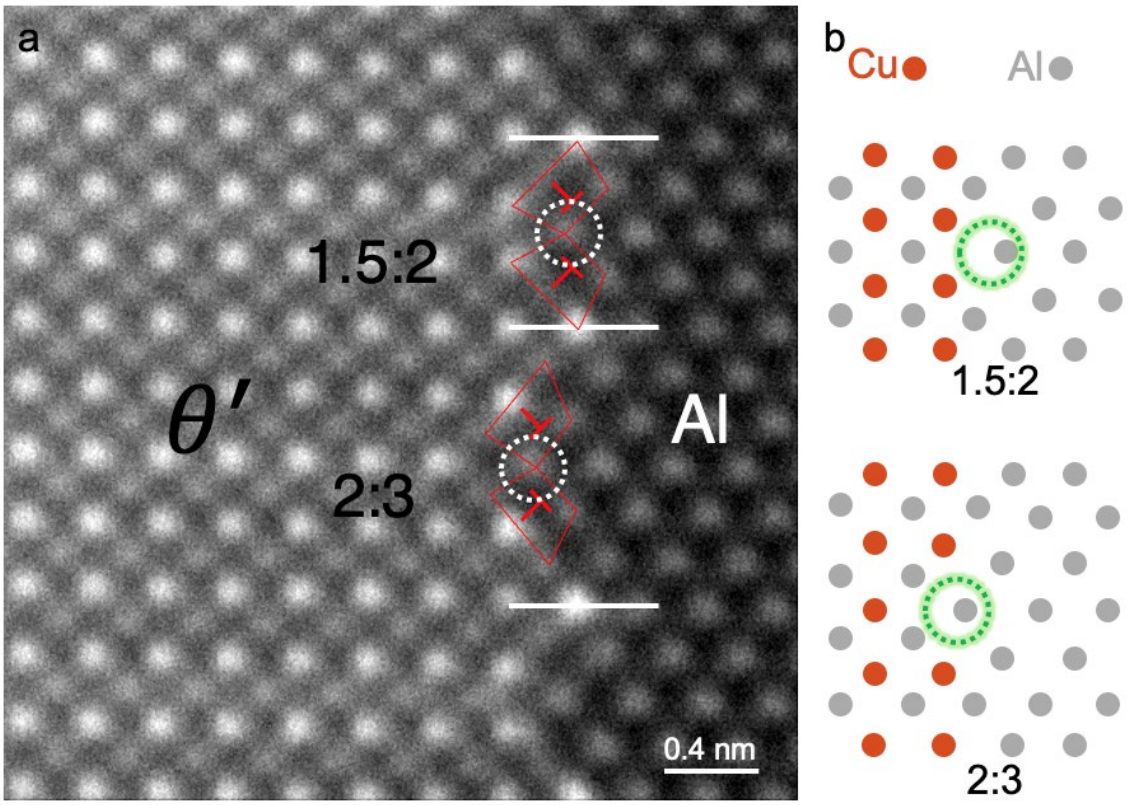

Figure I.3.1.1.1.1. HAADF image of the semi-coherent {110} Al/θ' interface as viewed along the <110> direction. (a) The interface is composed of arrays of dislocations (cores outlined in red) laying on {111}-type glide planes in the Al matrix. (b) Schematics show atomic arrangements in two defect structural units along the interface. Circles indicate regions in units where single Al columns are present and where two columns would exist in an interface produced by merging two bulk structures. Source: ORNL.

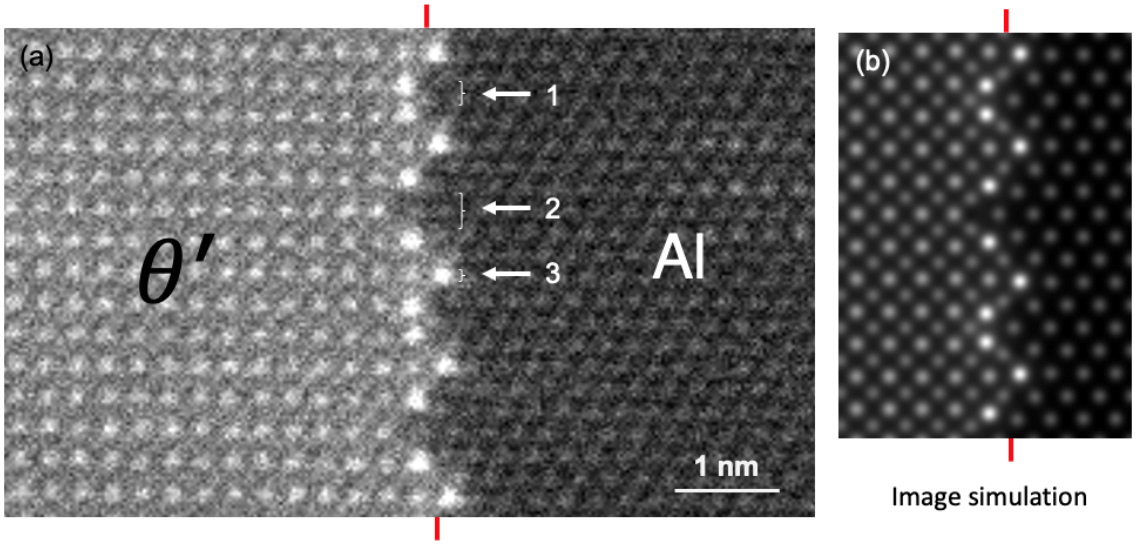

Figure I.3.1.1.1.2. HAADF image and simulated image of Cu segregation to semi-coherent {110} interface in the <-110> projection. (a) Image showing Cu filling the vacant sites at 1 in θ' near the missing Al column position, Cu filling the vacant sites at 2 in θ' near the missing Cu column position, and Cu substituting for Al at 3 in the Al. (b) Simulated HAADF image assuming that Cu fills all of the vacant sites in sites 1 and 2 and that Cu replaces all of the Al in site 3. Source: ORNL.

First principles theory was used to compute the equilibrium structure of the {110} semi-coherent interface and to calculate the Cu segregation energies using large supercells—up to 850 atoms—constructed with the experimentally observed periodicity in which 10 c_{Al} units are matched to 7 $c_{\theta'}$ units. Dislocations present in the calculated relaxed structure, as observed in Figure I.3.1.1.1.3, are located by identifying the extra plane of atoms associated with these edge dislocations. The observed segregation sites all sit on the compressed side of the dislocation cores where one would expect to find the smaller Cu atom. Calculations of the Cu segregation energies involved comparing the total energy of the two systems, one with a Cu solute atom in an Al site away from the interface and the other with that Cu solute atom located at various sites in the interfacial region. Moving a Cu solute atom to one of the three experimentally observed Cu segregation sites reduced the energy of the system between 0.31 to 0.44 eV.

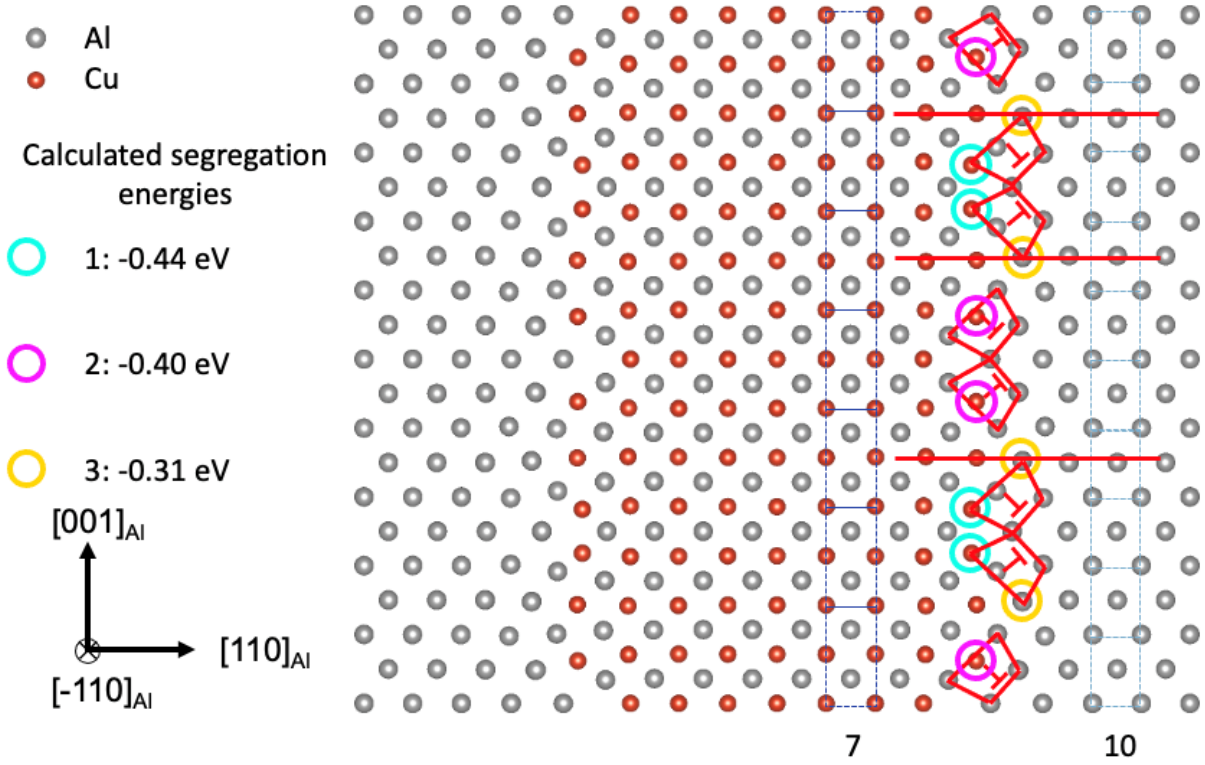

Figure I.3.1.1.1.3. <110> projection of a DFT supercell used to investigate structure and Cu segregation energetics at the {110} semi-coherent interface. The computed dislocation structure matches those seen experimentally. Three observed segregation sites (circled) are located on the compressed side of the edge dislocation cores. Calculated Cu segregation energies to these sites indicate that these are energetically favorable. Source: ORNL.

Al-Ni Alloys

Figure I.3.1.1.1.4 illustrates examples of the enumerated interface models and the orientation relationship between the Al matrix and the Al_3Ni precipitate. As shown in Figure I.3.1.1.1.4, large supercell models with 200-400 atoms were used for the preliminary interfacial energy calculations.

The termination planes at the Al/Al_3Ni interfaces from the literature were high-index low-symmetry planes. Several Al/Al_3Ni interface supercell models with high-symmetry termination planes were enumerated, as illustrated in Figure I.3.1.1.1.5. Supercells with larger matrix and precipitate size when compared to the Al/Al_2Cu models were constructed with up to 700 atoms in the supercell.

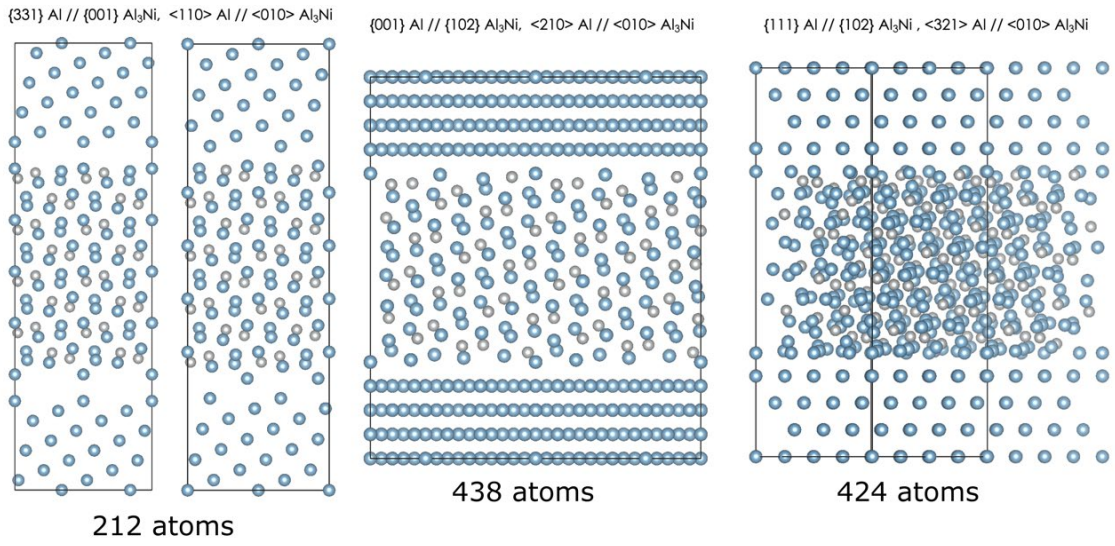

Figure I.3.1.1.1.4. Selected supercell models to represent the Al/Al_3Ni interface configuration. Orientation relationships from literature were used to enumerate the Al/Al_3Ni supercell models. Source: ORNL.

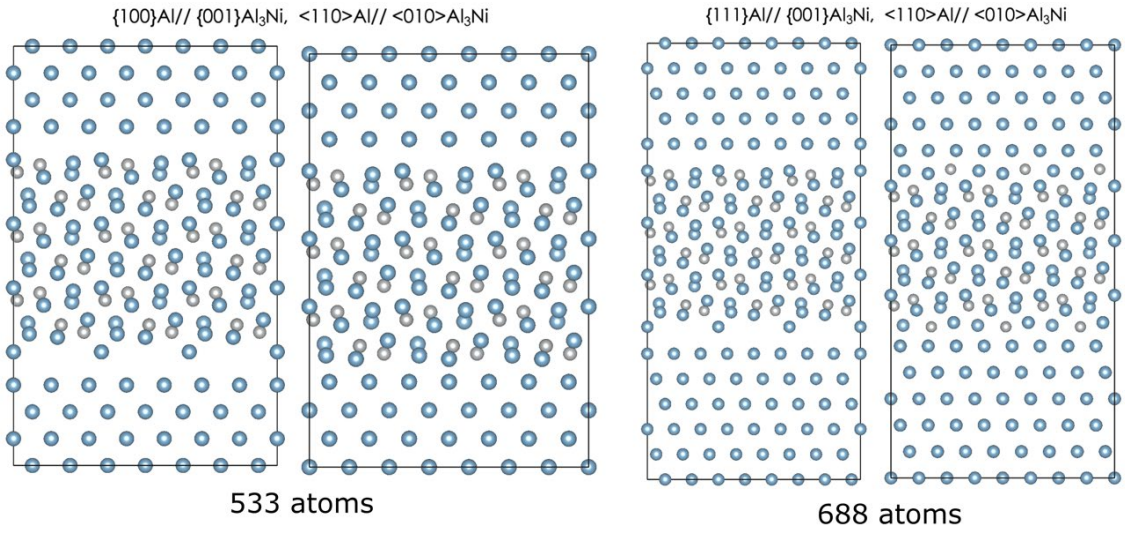

Figure I.3.1.1.1.5. (a) HR-STEM results showing a single layer of Al_3Zr at the interface between the Al matrix and the Al_2Cu θ′ precipitate. (b) Full nucleation of Al_3Zr $L1_2$ on θ′ precipitate. (c) "Ghost" layers of Al_3Zr ($L1_2$ structure) near the θ′ precipitates after higher temperature aging. Source: ORNL.

First principles-based calculations were performed using DFT high-performance computing employing the Summit supercomputer. Large-scale DFT simulations were required to relax the interfacial strain and calculate the energy of the constructed supercells, which contain up to 700 atoms. We estimate that working on graphics processing unit computing at Summit reduced the computational time by a factor of 10 while also reducing the computation cost (node hours) when compared to more traditional supercomputing systems. This economy of node hours will be even more important as this study progresses toward future more advanced simulations where even larger supercells will be necessary

Preliminary DFT analysis in the Figure I.3.1.1.1.6 suggests that the interface energies of the supercells from literature are much higher when compared to the low index interfaces. Figure I.3.1.1.1.6 also shows that the low index interfaces have comparable energetics to the Al/Al_2Cu semi-coherent interfaces, for which interface engineering has had significant influence previously in this program.

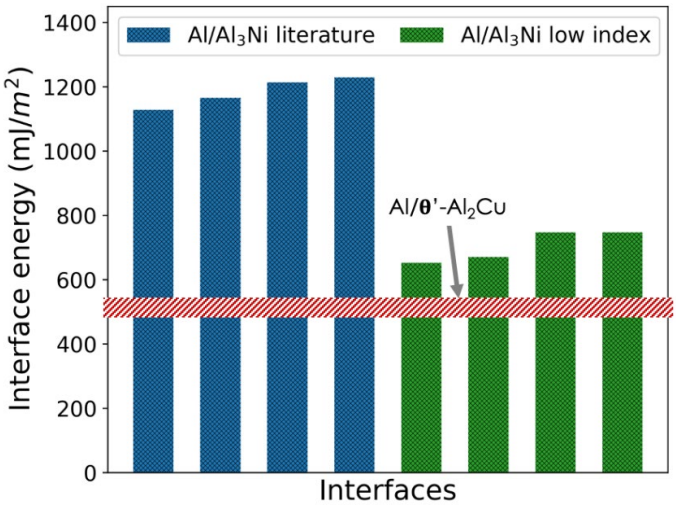

Figure I.3.1.1.1.6. Interface energies of the constructed Al/Al_3Ni supercell models calculated using DFT compared to the energies of the Al/θ'-Al_2Cu interfaces previously analyzed in this subtask. Source: ORNL

Conclusions

Al-Cu Alloys

STEM and DFT investigations identified the interfacial defect units, the interfacial defect unit structures, and most importantly, the role of the defect units in the incorporation of Cu into and out of the precipitates. The agreements between various aspects of the computed and observed structures leads us to conclude that we have accurately determined the essential atomic structure features of this semi-coherent interface, which result in the exceptional increase—and then decrease—in strength of these materials. Precipitation-hardened Al alloys all rely on metastable phases that grow, dissolve, or transform at elevated temperatures. Knowing the atomic arrangements in the principle growth interfaces will enable guided modifications of interfacial arrangements with the aim to precisely control the structures that are critical for enhanced thermal stability of strengthening precipitates in alloys.

Al-Ni Alloys

Our team was successful in constructing supercell models with Al/Al_3Ni interface for the first time using experimental observations in the literature. We have also constructed multiple large supercell models with up to 700 atoms in the supercell, which have high-symmetry and low index termination planes at the interface. DFT high-performance computing analysis using the Oak Ridge Leadership Computing Facility's Summit supercomputer showed that interfaces from the literature have high-energy, whereas low index interfaces were more energetically favorable. Experimental analysis planned in the subtask will refine the interface orientations of Al matrix and Al_3Ni precipitates.

Key Publications

1. Samolyuk, G. D., M. Eisenbach, D. Shin, Y. N. Osetsky, A. Shyam, and J. R. Morris, 2020, "Equilibrium solute segregation to matrix-θ′ precipitate interfaces in Al-Cu alloys from first principles," *Phys. Rev. Mater.*, Vol. 4, Art. 073801.
2. Peng, J., S. Bahl, A. Shyam, J. A. Haynes, and D. Shin, 2020, "Solute-vacancy clustering in aluminum," *Acta Mater.*, Vol. 196, pp. 747–758.
3. Poplawsky, J. D., B. K. Milligan, L. F. Allard, D. Shin, P. Shower, M. F. Chisholm, and A. Shyam, 2020, "The synergistic role of Mn and Zr/Ti in producing θ′/$L1_2$ co-precipitates in Al-Cu alloys," *Acta Mater.*, Vol. 194, pp. 577–586.
4. Chisholm, M.-F., D. Shin, G. Duscher, M. P. Oxley, L. F. Allard, J. D. Poplawsky and A. Shyam, 2020, "Atomic structures of interfacial solute gateways in Al-Cu alloys," submitted for publication.

References

1. Cantor, B., and G. A. Chadwick, 1974, "The growth crystallography of unidirectionally solidified Al-Al_3Ni and Al-Al_2Cu eutectics," *J. Cryst. Growth.*, Vol. 23, pp. 12–20.
2. Shyam, A., S. Roy, D. Shin, J. D. Poplawsky, L.F. Allard, Y. Yamamoto, J. R. Morris, B. Mazumder, J. C. Idrobo, A. Rodriguez, T. R. Watkins, and J. A. Haynes, 2019, "Elevated temperature microstructural stability in cast-Al-Cu-Mn-Zr alloys through solute segregation," *Mater. Sci. Eng. A*, Vol. 765, Art. #138279, 23 September 2019.
3. Poplawsky, J. D., B. K. Milligan, L. F. Allard, D. Shin, P. Shower, M. F. Chisholm, and A. Shyam, 2020, "The synergistic role of Mn and Zr/Ti in producing $\theta'/L1_2$ co-precipitates in Al-Cu alloys," *Acta Mater.*, Vol. 194, pp. 577–586.

Acknowledgements

The authors acknowledge the efforts of M. Chisholm, H. Gunda, R. Michi, J. Poplawsky, S. Bahl, L. Allard, and J. A. Haynes for their contributions to this research effort.

I.3.1.1.2 New Higher Temperature Performance Alloys (Task 1A2) (Oak Ridge National Laboratory)

Amit Shyam, Co-Principal Investigator
Oak Ridge National Laboratory
1 Bethel Valley Road
Oak Ridge, TN 37831
E-mail: shyama@ornl.gov

Dongwon Shin, Co-Principal Investigator
Oak Ridge National Laboratory
1 Bethel Valley Road
Oak Ridge, TN 37831
E-mail: shind@ornl.gov

Jerry L. Gibbs, DOE Technology Manager
U.S. Department of Energy
E-mail: jerry.gibbs@ee.doe.gov

Start Date: October 1, 2018 End Date: September 30, 2023
Project Funding: $375,000 DOE share: $375,000 Non-DOE share: $0

Project Introduction

Mechanisms that lead to improved thermal stability and other favorable attributes in lightweight Al alloys are emphasized in this task. Attributes are associated with mechanical and thermal properties of interest for powertrain components, such as LD pistons and turbo compressors. An ICME approach was applied to understand and elucidate mechanisms of interest. This section covers FY 2020 efforts for Task 1A2, "New Higher Performance Aluminum Alloys," as a part of Thrust 1A for "New Aluminum Alloys with Improved High-Temperature Performance."

Objectives

This task focuses on a fundamental understanding of the features that impart thermal stability to cast-Al precipitate microstructures. This is a low technology readiness level subtask to develop improved scientific understanding of these alloys and key phenomena and to suggest pathways for improved high-temperature performance Al-Cu and other Al alloys. These pathways include the identification of potential mechanisms for further improvement of thermal stability of favorable precipitates.

Approach

In this task, the emphasis is on the establishment of microstructure and mechanical property associations of interest by linking experimental and simulation results. The approach relies on an interplay between advanced characterization and theoretical calculations that help to establish and understand the mechanisms that in turn are utilized to develop improved high-temperature Al alloys that meet or exceed targeted industry needs.

Within the precipitation-hardened alloys, there remains an emphasis on utilizing the non-equilibrium interfacial solute segregation (NEISS) mechanism and associated co-precipitate formation to improve the chemistry, heat treatments, and elevated temperature capability of ACMZ alloys and variants. For the dispersion-hardened alloys in development, the chemistries to be examined comprise alloys with improved elevated temperature properties, including alloys in the Al-Ni system. Neutron diffraction techniques are being applied to understand the deformation mechanisms in Al-Cu alloys of interest.

Results

Thermal Stability Mechanisms

Our team investigated the NEISS mechanism in order to extend the temperature limits of Al-Cu alloys and in particular the temperature limit of the ACMZ family of cast high-temperature alloys [1]. Figure I.3.1.1.2.1 is an illustration of key results suggesting the NEISS mechanism in ACMZ alloys through APT results. Figure I.3.1.1.2.1(a) shows that the θ' precipitate was sliced and viewed along the <110> direction in this APT data rendition. Two-dimensional contour plots further reveal the solute segregation profiles in the exposure conditions following aging at 300°C for 2100 h, as observed in Figure I.3.1.1.2.1(b), and 350°C 2000 h, as can be seen in Figure I.3.1.1.2.1(c). For solutes that have equilibrium segregation, increasing time does not lead to changes in solute concentration and increasing temperature leads to a decrease in solute concentration at the interfaces. For solutes that have non-equilibrium segregation, increasing temperature and time leads to an increase in solute concentrations. These observations show that Si reaches equilibrium concentrations at 300°C and Mn segregation remains non-equilibrium at 300°C, but equilibrium is reached at 350°C; Ti and Zr remain non-equilibrium segregants at 350°C as well. Interestingly, the potency of individual elements to stabilize the strengthening precipitates diminishes severely when segregation levels become non-equilibrium.

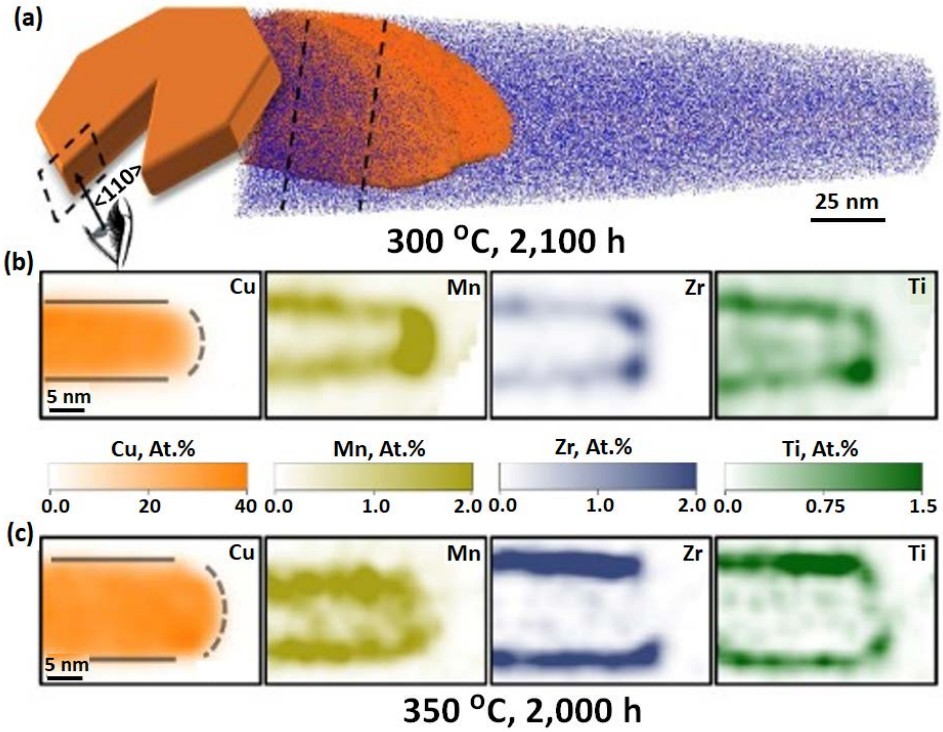

Figure I.3.1.1.2.1. Segregation of key solutes on the interface of a strengthening precipitate in an ACMZ alloy. (a) View of observation direction in a θ' precipitate platelet by APT. (b) Segregation profiles following aging at 300°C after 2,100 h. (c) Segregation profiles following aging at 350°C after 2,000 h [1]. Source: ORNL.

If non-equilibrium solute segregation is allowed to proceed for extended periods at elevated temperature (e.g., Zr segregation after extended exposure at 350°C), it is reasonable to expect that a compound may form at the critical interfaces. Indeed, Figure I.3.1.1.2.2 shows the formation of the $Al_3(TiZr)$ phase on the coherent interface of the θ' precipitate after an extended 2,000 h exposure at 350°C. The atom tomography line profile indicates the formation of the trialuminide phase with ~25 at% (Ti+Zr) on the coherent interface. In addition, it was shown that the ratio of Ti to Zr in the trialuminide phase was close to what is expected from simple Vegard's law-based strain energy minimization calculations.

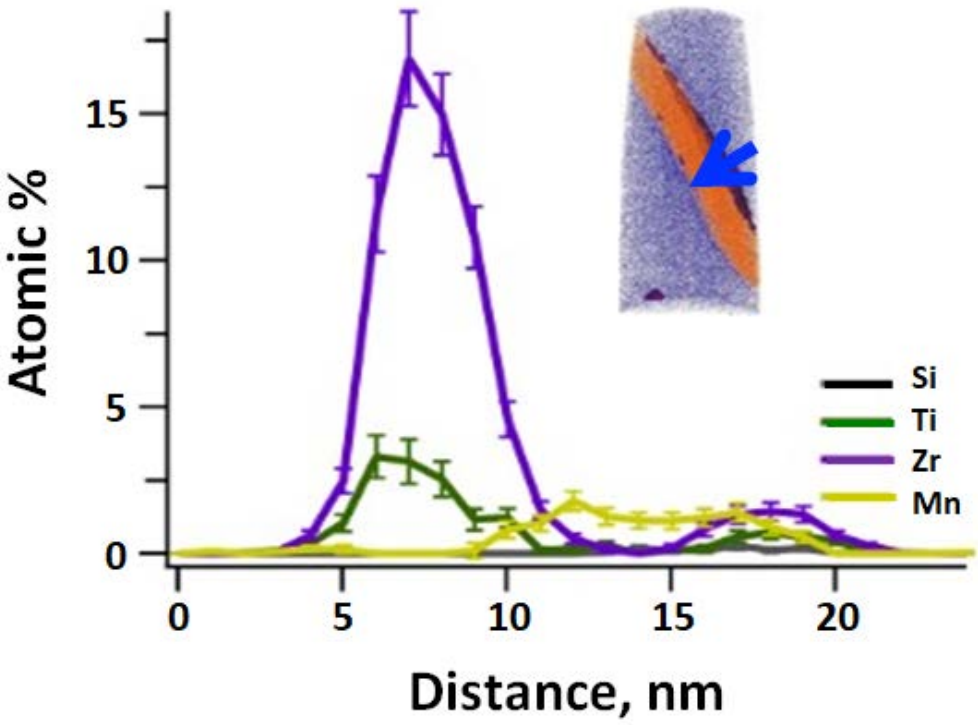

Figure I.3.1.1.2.2. APT demonstrating the formation of $Al_3(TiZr)$ phase on the coherent interface of the θ' precipitate after extended exposure at 350 °C [1]. Source: ORNL.

The underlying reasons for the thermal stability resulting from segregation of solutes are related to solute drag (kinetic effect) and reduction in interfacial energy (thermodynamic effect) as has been reported earlier [2],[3]. DFT calculations show that the interfacial energy of the $L1_2$ Al_3Zr or Al_3Ti layer on the coherent interface of the θ' precipitate was close to zero.

The low interfacial energy implies a low driving force available for coarsening and explains the thermal stability of ACMZ alloys under non-equilibrium segregation conditions. The results of the DFT calculations that were performed on the Summit supercomputer are shown in Figure I.3.1.1.2.3.

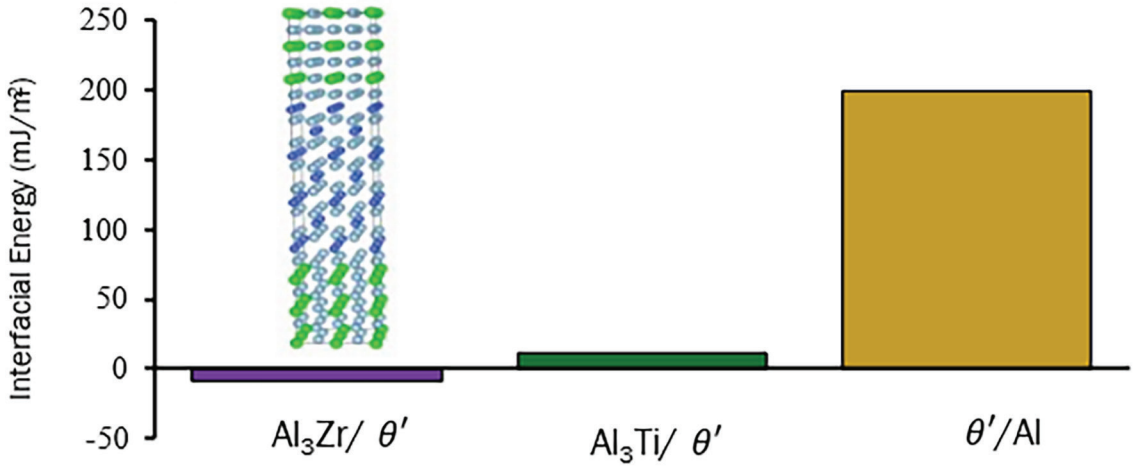

Figure I.3.1.1.2.3. DFT calculations showing the interfacial energy values of a θ' /L12 (Al3X) co-precipitate layer compared to the interfacial energy of the coherent interface of the same precipitate [1]. Source: ORNL.

Neutron Diffraction of Al-Cu Alloys

The strain-hardening rate in Al-Cu alloys was determined to be strongly orientation-dependent, which was modeled based on load-sharing between the precipitates and the matrix. As shown in Figure I.3.1.1.2.4, certain grain orientations (e.g., <002>) were more efficient at transferring load to the precipitate and had a lower strain-hardening rate in the matrix. Conversely, other grain orientations (e.g., <111>) did not transfer load to the precipitate as efficiently and they led to a higher strain-hardening rate in the matrix.

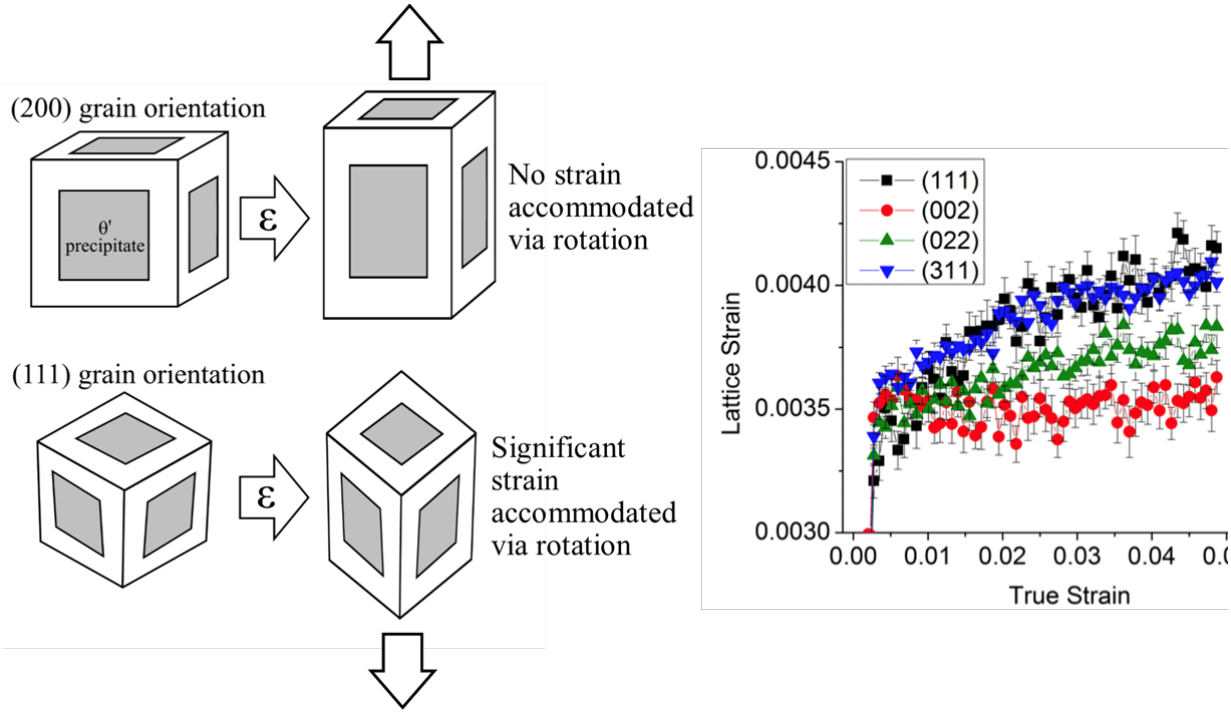

Figure I.3.1.1.2.4. Orientation dependence of strain-hardening in an Al-Cu alloy. Source: ORNL.

By utilizing a model developed by Hosford *et al.* [4], the deformation behavior of individual precipitates was described. Figure I.3.1.1.2.5 shows the measurement (e.g., lattice strains from neutron diffraction on x-axis) with the applied bulk stress (on the y-axis) for a θ′ precipitate in an Al-Cu alloy. The precipitates are in the (422) grain orientation plotted against measured stress versus lattice strain data for (211) oriented precipitates, which are in a grain close to the (422) orientation. These orientations are not the same due to the tetragonal crystal structure of θ′, but they are very close—the true orientation of θ′ precipitates within the (422) grain orientation is approximately (423). Note the close match between the experimental data and the model prediction with only inputs in the model from the measured specimen tensile stress-strain curve and the compliance matrix from literature.

Crystallographic orientation-dependent strain-hardening can also be predicted with the developed model, as shown in Figure I.3.1.1.2.6. The comparison of predicted average instantaneous matrix strain-hardening rate versus experimentally determined average instantaneous strain-hardening rate using a power law fit, both measured from 0.5-3.5% strain is performed in this figure. A y=x line has also been included to display theoretically expected predictions. Crystallographic orientations are labeled with their Miller indices. These results support the development of improved ductility and low cycle fatigue resistant Al alloys for cylinder head and other internal combustion engine applications.

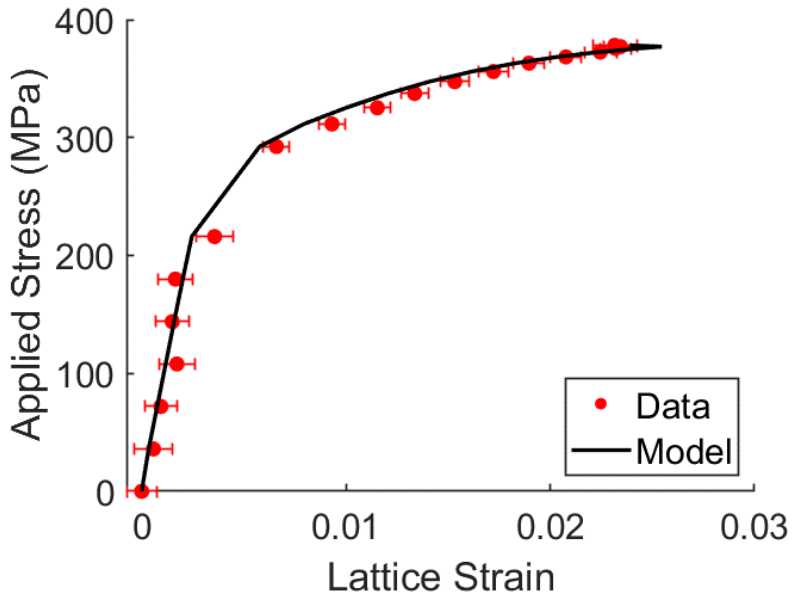

Figure I.3.1.1.2.5. Measurement (from neutron diffraction) and model prediction of the tensile behavior of a θ′ precipitate. Source: ORNL.

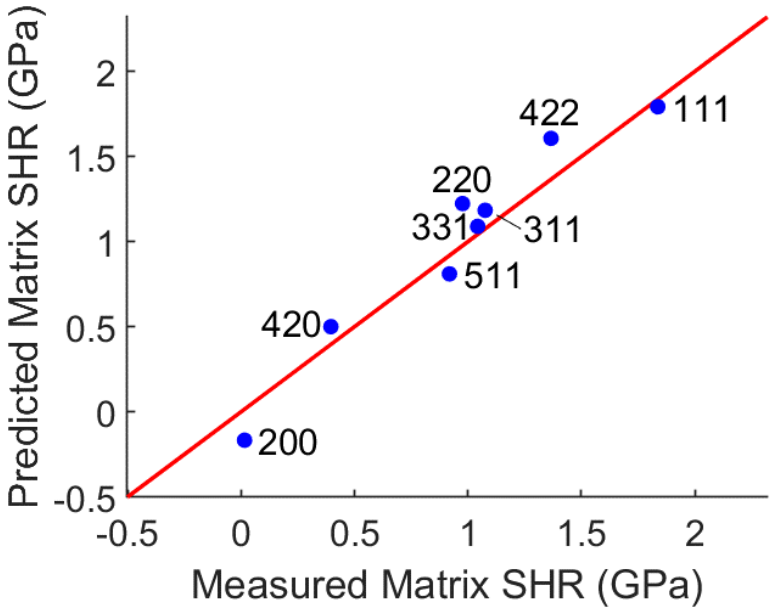

Figure I.3.1.1.2.6. Comparison of predicted (from model) and measured (from neutron diffraction) matrix strain-hardening rate (SHR) in an Al-Cu alloy. Source: ORNL.

Conclusions

Thermal Stability Mechanisms

Our team demonstrated that solute segregation to heterophase interfaces in a $\theta'(Al_2Cu)$ phase strengthened Al alloy can be applied to continuously stabilize this microstructure at elevated temperature. We termed this mechanism, NEISS, and describe the utility of this approach to stabilize microstructures at elevated homologous temperature. In particular, it is proposed that the NEISS mechanism is a knob that can be applied to continuously rejuvenate precipitation-hardened microstructures at elevated homologous temperatures for improved high-temperature alloy design.

Neutron Diffraction

In this work, our team applied *in situ* neutron diffraction of Al-Cu alloys under load to investigate both the precipitate-dislocation interactions and strain-hardening mechanisms as a function of crystallographic orientation. A precipitate rotation-based strain accommodation mechanism was identified that determines the crystallographic orientation-dependent strain-hardening behavior in a primarily θ′ rich microstructure. Finally, the rotation of plate shaped precipitates and associated crystallographic orientation-dependent strain-hardening during early-stage plastic deformation is described via a quantitative model.

Key Publications

1. Poplawsky, J. D., B. K. Milligan, L. F. Allard, D. Shin, P. Shower, M. F. Chisholm, and A. Shyam, 2020, "The synergistic role of Mn and Zr/Ti in producing θ′/$L1_2$ co-precipitates in Al-Cu alloys," *Acta Mater.*, Vol. 194, pp. 577–586.
2. Samolyuk, G. D., M. Eisenbach, D. Shin, Y. N. Osetsky, A. Shyam, and J. R. Morris, 2020, "Equilibrium solute segregation to matrix-θ′ precipitate interfaces in Al-Cu alloys from first principles," *Phys. Rev. Mater.*, Vol. 4, Art. 073801.
3. Milligan, B., D. Ma, L. F. Allard, A. Clarke, and A. Shyam, 2020, "Crystallographic orientation-dependent strain-hardening in a precipitation-strengthened Al-Cu alloy," *Acta Mater.*, in revision.
4. P. Shower, J.D. Poplawsky, S. Bahl and A. Shyam, 2020, "The role of Si in determining the stability of the θ′ precipitate in Al-Cu-Mn-Zr alloys" *J. Alloys Compd.*, in revision.

References

1. Poplawsky, J. D., B. K. Milligan, L. F. Allard, D. Shin, P. Shower, M. F. Chisholm, and A. Shyam, 2020, "The synergistic role of Mn and Zr/Ti in producing θ′/L12 co-precipitates in Al-Cu alloys," *Acta Mater.*, Vol. 194, pp. 577– 586.
2. Shyam, A., S. Roy, D. Shin, J. D. Poplawsky, L.F. Allard, Y. Yamamoto, J. R. Morris, B. Mazumder, J. C. Idrobo, A. Rodriguez, T. R. Watkins, and J. A. Haynes, 2019, "Elevated temperature microstructural stability in cast-Al-Cu-Mn-Zr alloys through solute segregation," *Mat. Sci. Eng. A–Struct*, Vol. 765, Art. #138279, 23 September 2019.
3. Shower, P., J. R. Morris, D. Shin, B. Radhakrishnan, J. D. Poplawsky and A. Shyam, 2019, "Mechanisms for stabilizing θ′(Al2Cu) precipitates at elevated temperatures investigated with phase-field modeling" *Materialia*, Vol. 6, Art. 100335.
4. Hosford, W. F., and R. H. Zeisloft, 1972, "The anisotropy of age-hardened Al-4 pct Cu single crystals during plane-strain compression," *Metall. Trans. A.*, Vol. 3, pp. 113–121.

Acknowledgements

The authors acknowledge the efforts of M. Chisholm, H. Gunda, R. Michi, J. Poplawsky, S. Bahl, L. Allard, R. Michi, B. Milligan, P. Shower, T. Watkins, D. McClurg, S. Hawkins and J. A. Haynes for their contributions to this research effort.

I.3.1.1.3 Properties of Cast-Al-Cu-Mn-Zr (ACMZ) Alloys (Task 1B) (Oak Ridge National Laboratory)

Amit Shyam, Co-Principal Investigator
Oak Ridge National Laboratory
1 Bethel Valley Road
Oak Ridge, TN 37831
E-mail: shyama@ornl.gov

J. Allen Haynes, Co-Principal Investigator
Oak Ridge National Laboratory
1 Bethel Valley Road
Oak Ridge, TN 37831
E-mail: haynesa@ornl.gov

Jerry L. Gibbs, DOE Technology Manager
U.S. Department of Energy
E-mail: jerry.gibbs@ee.doe.gov

Start Date: October 1, 2018 End Date: September 30, 2023
Project Funding: $325,000 DOE share: $325,000 Non-DOE share: $0

Project Introduction

The primary focus of this task is higher temperature cast-Al alloys to fit near-term transportation sector opportunities. Precipitation-hardened alloys are the most common lightweight alloys used for cylinder heads and blocks in internal combustion engines. The fundamental efforts in this task will focus on improving the intermediate temperature (e.g., < 150°C) ductility and low cycle fatigue (LCF) of ACMZ variants by controlling both the intragranular and intergranular precipitates. Efforts are also underway in trying to understand the corrosion behavior of ACMZ variants. These alloys are applied in powertrain applications (e.g., cylinder head, piston, turbocharger, etc.) for boosted engines with higher power density.

Objectives

This task focuses on a fundamental understanding of the factors that affect the low to intermediate temperature (e.g., < 150°C) ductility, LCF life, and corrosion behavior of cast ACMZ alloys. This is a mid-Technology Readiness Level (TRL) task to understand and suggest pathways for further improvement in ductility of the higher Cu content alloys (5 wt% Cu) at ambient temperature. The LCF life is targeted to be above the baseline performance of commercial cast 319 Al alloys and equal to or above that of commercial cast A356 + 0.5Cu Al alloys. Following are the key objectives in this task:

- Identified microstructural features that determine the relevant mechanical properties of cast-Al alloys for high-efficiency automotive engine applications.
- Improved features by alloy chemistry and/or processing modifications.
- Published scientific studies that further advance materials technology for lightweight, cost-effective, higher temperature alloys, particularly within the automotive sector.

Approach

The equilibrium θ-Al_2Cu and metastable equilibrium θ′-Al_2Cu are the two major types of intermetallic precipitates in the microstructure of the ACMZ family of cast-Al alloys. The θ precipitates are microscale in size and mostly located at the grain boundaries in the as-cast state. The θ′ precipitates are nanoscale-sized and present in the grain interiors. Most of the strength in the ACMZ alloys is derived from the nanoscale θ′ precipitates, while the θ precipitates do not significantly contribute to strengthening. At the same time, the

brittle θ precipitates tend to fracture under mechanical load, which can impact the overall fracture behavior during monotonic tensile and cyclic deformation of ACMZ alloys. The LCF behavior of an alloy is commonly thought to be correlated with alloy ductility. To better understand the effect of θ precipitates on both the ductility and LCF behavior of ACMZ alloys, a series of five ACMZ alloys with Cu content ranging between 6.0 to 9.0 wt.% (e.g., 6.0, 6.6, 7.3, 8.0, and 9.0 wt.% Cu) were fabricated via gravity sand-casting. These alloys were solution-treated at 540°C for 5 h, quenched in water at 80°C, and subsequently aged at 240°C for 5 h, which is the standard precipitation strengthening treatment for cast ACMZ alloys. The volume fraction of θ precipitates in the as-aged microstructure increases, but that of θ′ precipitates within the grain bodies remains constant, with an increase in Cu content between 6.0 to 9.0 wt.%. The higher Cu content is beneficial as it improves the hot-tearing resistance of ACMZ alloys [1]. Room and elevated temperature tensile tests were performed to measure the ductility of the alloys. LCF tests were performed in the temperature range of 150 to 250°C and compared to the baseline performance of A356 + 0.5Cu and 319 Al alloys. The present approach relies on microstructural characterization by SEM and electron backscatter diffraction (EBSD), combined with finite element simulations of the major microstructural features to understand the fracture behavior of ACMZ alloys under monotonic tensile and LCF loading.

Results

This study identified previously that the RT ductility of as-aged ACMZ alloys with 6.0 to 9.0 wt.% Cu decreased monotonically with an increase in Cu content, while the yield strength remained the same. The increase in size and volume fraction of θ precipitates with increasing Cu content made monotonic tensile crack initiation and propagation easier, as fracture of the larger intermetallic precipitates located along the alloy grain boundaries led to a decrease in the ductility. FY 2020 studies demonstrated that the LCF life of ACMZ alloys in the temperature range of 150 to 250°C is almost insensitive to the Cu content, as shown in Figure I.3.1.1.3.1. The specimens tested at 150°C were in the as-aged condition. An additional preconditioning heat-treatment at 250°C for 100 h was given after aging the specimens tested at 250°C. The 319 and A356 + 0.5 Cu are commercial alloys. This result is significant because the generally expected relationship of an improvement in LCF life with ductility is not followed in the current ACMZ alloy microstructures [2]. Furthermore, the LCF life of ACMZ alloys was shown to be comparable or better than the baseline A356 + 0.5Cu and 319 Al alloys.

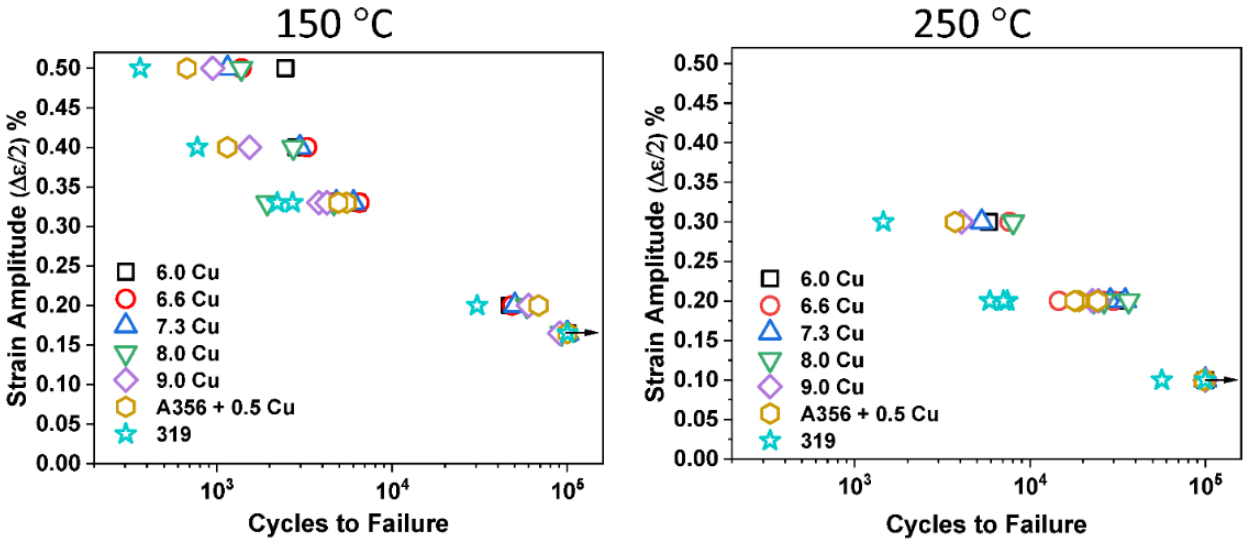

Figure I.3.1.1.3.1. LCF life of ACMZ alloys with 6.0 to 9.0 wt%. Cu at (a) 150°C and (b) 250°C. Source: ORNL.

Porosity is a common defect in cast alloys that can impact both tensile and fatigue behaviors. The pore size distribution was characterized with X-ray tomography and found to be similar among the extreme cases of 6.0 to 9.0 wt.% Cu ACMZ alloys, as shown in Figure I.3.1.1.3.2.

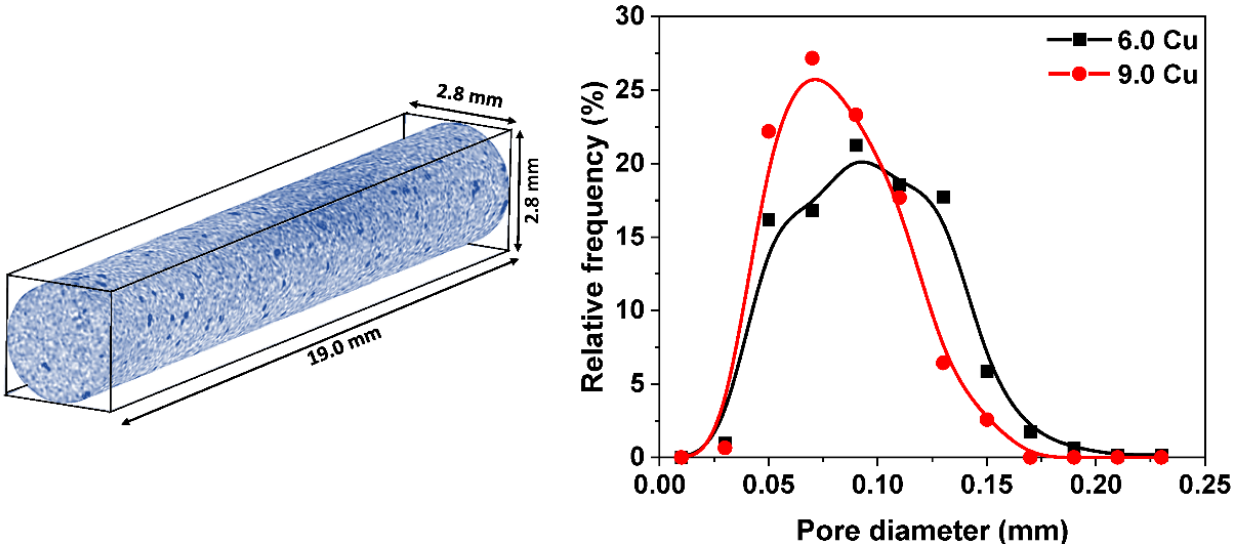

(a) (b)

Figure I.3.1.1.3.2. (a) A three-dimensional reconstruction of X-ray tomography measurement showing spatial distribution of pores in ACMZ alloy with 6.0 wt.% Cu; and (b) a comparison of pore size distribution between ACMZ alloys with 6.0 and 9.0 wt.% Cu. Source: ORNL.

The examination of fracture surfaces, as shown in Figure I.3.1.1.3.3 explains the insensitivity of LCF life to the Cu content. The fatigue cracks initiated at near surface pores in the test specimens, unlike the tensile tests where the cracks initiate at fractured grain boundary θ precipitates within the volume of the test specimens. The nominal load applied during LCF is insufficient to fracture the θ precipitates and initiate a crack. The fatigue crack initiation lifetime was similar for all the Cu contents due to the similar pore size distributions and negligible impact of θ precipitates. The θ precipitates also do not significantly influence the fatigue crack propagation as evidenced by the limited presence of the precipitates in the fatigue crack propagation region, as observed in Figure I.3.1.1.3.3. In contrast, the significant impact of θ precipitates on monotonic tensile crack propagation can be seen by their widespread presence on the tensile rupture region that is equivalent to the case of monotonic tensile loading. Since both fatigue crack initiation and propagation are largely unaffected by the θ precipitates, the total LCF life is similar for 6.0 to 9.0 wt.% Cu ACMZ alloys. Taken together, it can be concluded that the ductility and LCF life are separately controlled by grain boundary θ precipitates and near surface pores, respectively. As a result, ductility and LCF life are poorly correlated for the microstructures of the tested cast ACMZ alloys. This was a somewhat unexpected conclusion, based on the previously discussed general anticipation of ductility affecting alloy fatigue life.

EBSD was used to experimentally validate the damage potential of grain boundary θ precipitates and pores in monotonic tensile and LCF loading. Figure I.3.1.1.3.4 shows grain reference orientation deviation (GROD) maps from the gauge sections of fractured monotonic tensile and LCF specimens of ACMZ alloy with 9.0 wt.% Cu tested at 250°C. A higher GROD value implies higher plastic strain concentration and consequently, greater damage accumulation. Pores create even higher strain concentration than grain boundary θ precipitates in monotonic tensile and LCF loading with the difference between pores and precipitates more pronounced in the latter case. This observation confirms that pores are more damaging than θ precipitates.

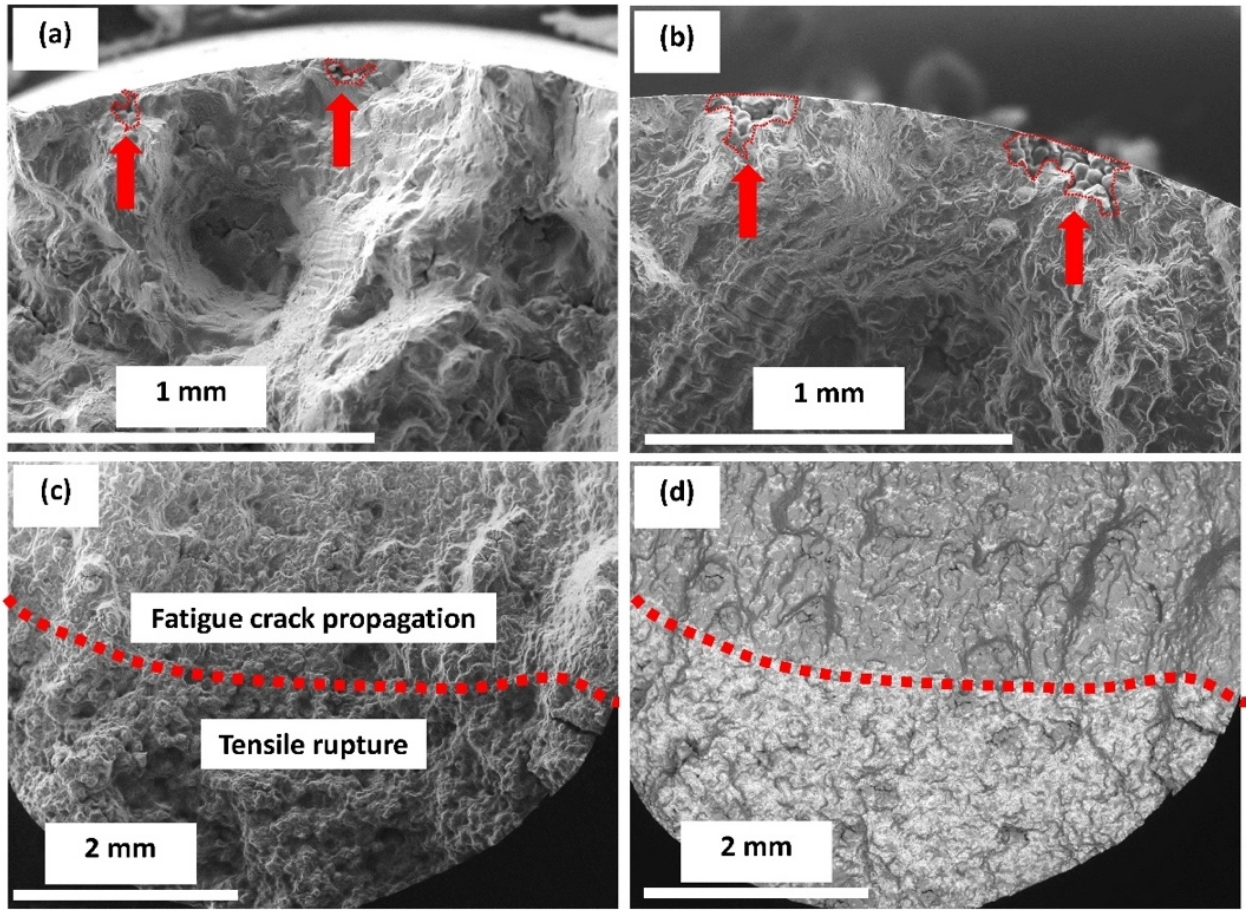

Figure I.3.1.1.3.3. Fracture surfaces after LCF tests at 250°C of (a) 6.0 wt.% Cu and (b) 9.0 wt.% Cu alloys. Lower magnification fracture surfaces of 9.0 wt.% Cu alloy in (a) secondary electron and (b) backscatter electron modes, respectively, showing that, compared to tensile rupture, fatigue crack propagation is insensitive to θ precipitates (regions of brighter contrast). Source: ORNL.

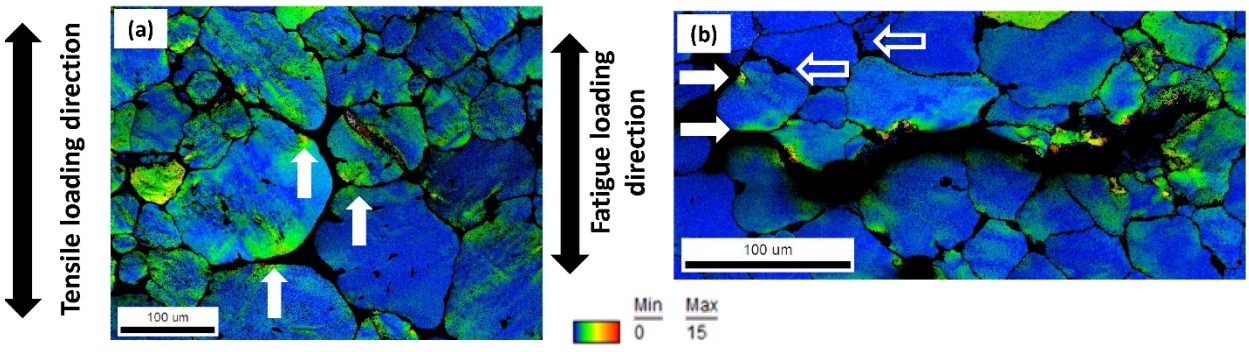

(a) (b)

Figure I.3.1.1.3.4. EBSD derived GROD maps from gauge sections of fractured (a) tensile and (b) LCF specimens of ACMZ alloy with 9.0 wt.% Cu tested at 250°C. Solid arrows in (a) and (b) indicate strain concentration at pores. Open arrows in (b) indicate the absence of strain concentration at grain boundary θ precipitates. The GROD values range between 0 to 15°. Source: ORNL.

Finite element modeling was used to simulate the damage potential of pores and grain boundary θ precipitates under monotonic tensile loading and were compared with EBSD observation. SEM micrographs of a large pore and θ precipitates, as shown in Figure I.3.1.1.3.5, are used as input microstructures for simulations. The θ precipitates were modeled as purely elastic with 120 GPa modulus and 710 MPa fracture strength. The α-Al and θ′ precipitates were modeled as a single elasto-plastic entity obeying the power law derived from the experimental stress-strain curves. Observations from these simulations were that cracks initiate at the edges of the pore at 0.86% nominal tensile strain due to high strain concentration. Significantly, no crack initiation is predicted to occur at the θ precipitates until at least 3.3% simulated nominal tensile strain. The finite element simulations corroborate the EBSD observation that large pores are more damaging than θ precipitates.

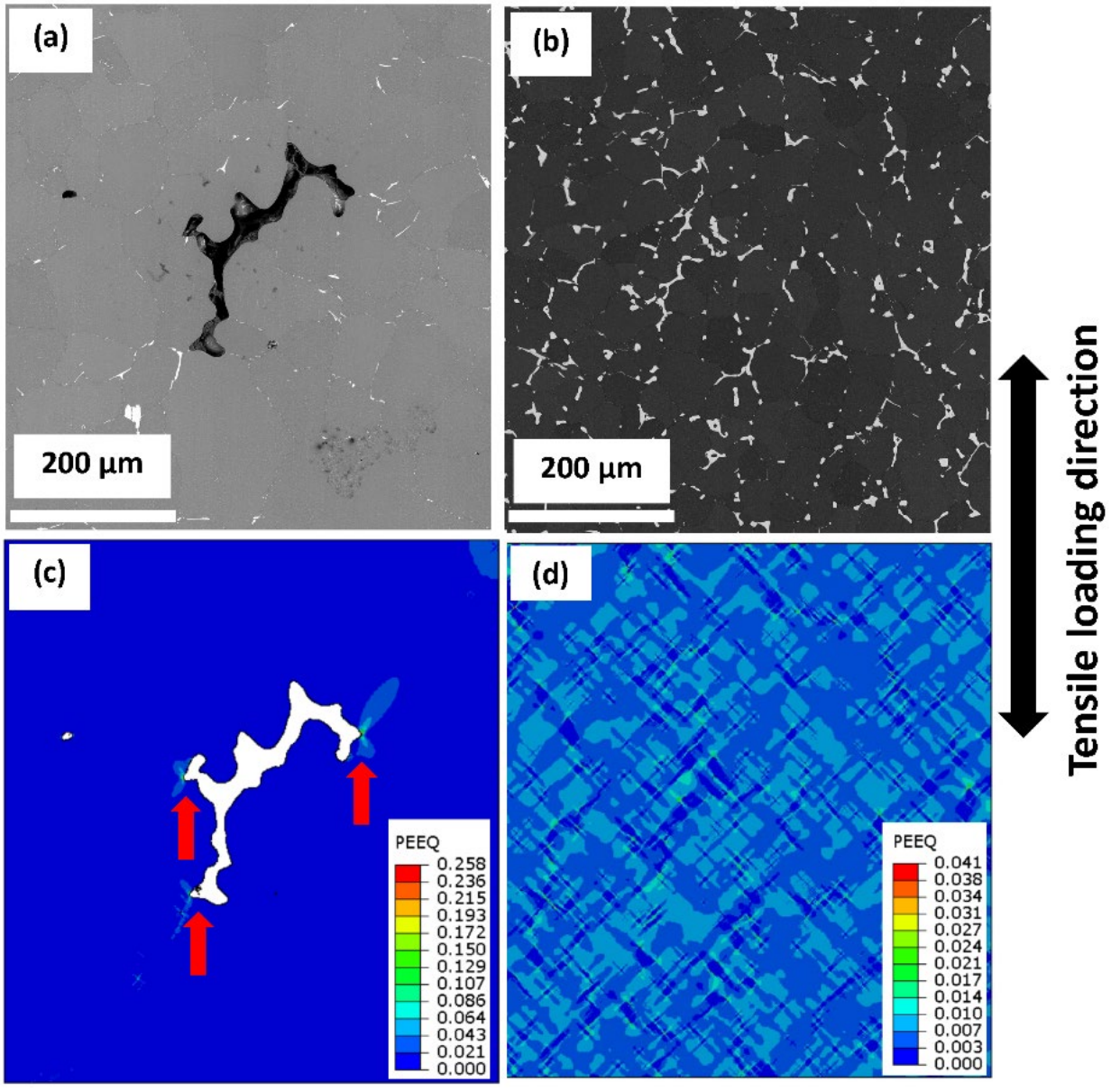

Figure I.3.1.1.3.5. SEM micrographs of (a) a large pore and (b) grain boundary θ precipitates in a 9.0 wt.% Cu alloy. For reference, (c) and (d) are equivalent plastic strain maps corresponding to (a) and (b), respectively, at 0.86% nominal tensile strain in simulation. The red arrows in (c) indicate crack initiation sites at the pore. Source: ORNL.

Higher strain concentration at the pores lead to fatigue crack initiation at these sites. Although, the pores are more damaging than the θ precipitates, their effect on ductility in monotonic testing is limited due to their lower number density. Despite the lower strain concentration at the θ precipitates, the higher nominal stress reached in the monotonic tensile test eventually fractures a large number of θ precipitates to create a volumetric 'domino effect' that leads to the formation of a macrocrack. This effect is ultimately responsible for the monotonic decrease in the ductility of ACMZ alloys as Cu content is increased.

Conclusions

The following are the major conclusions resulting from this subtask research effort:

- The LCF life at 150°C and 250°C of ACMZ alloys with 6.0 to 9.0 wt.% Cu is comparable to commercial baseline alloys A356 + 0.5Cu and 319 Al alloys.
- Grain boundary θ precipitates form the weak links in the microstructure that affect the ductility, but not the LCF life, which is mainly controlled by porosity in the cast ACMZ alloys. As a result, ductility and LCF life are poorly correlated in the current ACMZ alloy microstructures.
- The LCF life can be improved by reducing porosity in cast ACMZ alloys, particularly near the surface.

Key Publications

1. Bahl, S., X. Hu, K. Sisco, J. A. Haynes, and A. Shyam, 2020, "Influence of copper content on the high-temperature tensile and low cycle fatigue behavior of cast-Al-Cu-Mn-Zr alloys," *Int. J. Fatigue*, Vol. 140, Art. 105836.
2. Bahl, S., X. Hu, E. Hoar, J. Cheng, J. A. Haynes, and A. Shyam, 2020, "Effect of copper content on the tensile elongation of Al-Cu-Mn-Zr alloys: Experiments and finite element simulations," *Mater. Sci. Eng. A*, Vol. 772, Art. 138801.
3. Milligan, B. K., S. Roy, C. S. Hawkins, L. F. Allard, and A. Shyam, 2020, "Impact of microstructural stability on the creep behavior of cast-Al-Cu alloys," *Mater. Sci. Eng. A*, Vol. 772, Art. 138697.
4. Shyam, A., S. Roy, D. Shin, J. D. Poplawsky, L. F. Allard, Y. Yamamoto, J. R. Morris, B. Mazumder, J. C. Idrobo, A. Rodriguez, T. R. Watkins, and J. A. Haynes, 2019, "Elevated temperature microstructural stability in cast-Al-Cu-Mn-Zr alloys through solute segregation," *Mater. Sci. Eng. A*, Vol. 765, Art. 138279.
5. Sabau, A. S., B. K. Milligan, S. Mirmiran, C. Glaspie, A. Shyam, J. A. Haynes, A. F. Rodriguez, J. A. Gonzales Villarreal and J. Talamantes, 2020, "Grain refinement effect on the hot-tearing resistance of higher temperature Al-Cu-Mn-Zr alloys," *Metals*, Vol. 10, No. 4, Art. 430.

References

1. Sabau, A. S., S. Mirmiran, C. Glaspie, S. M. Li, D. Apelian, A. Shyam, J. A. Haynes, and A. F. Rodriguez, 2018, "Hot-tearing assessment of multi-component nongrain-refined Al-Cu alloys for permanent mold castings based on load measurements in a constrained mold," *Metall Mater Trans B*, Vol. 49, No. 3, pp. 1267–1287.
2. Suresh, S., 1998, *Fatigue of Materials*. Cambridge University Press, New York, NY, USA.

Acknowledgements

The authors acknowledge the efforts of S. Bahl, D. Shin, K. Sisco, A. Sabau, R. Michi, J. Poplawsky, D. McClurg, S. Hawkins, X. Hu, J. Cheng and Larry Allard for their contributions to this research effort.

I.3.2 Cost-Effective Higher Temperature Engine Alloys – Thrust 2

I.3.2.1 Advanced Affordable Wrought Engine Alloys (2A/2B)

I.3.2.1.1 Development of Oxidation-Resistant Valve Alloys for 900–950˚C (Task 2A1) (Oak Ridge National Laboratory)

Govindarajan Muralidharan, Co-Principal Investigator
Oak Ridge National Laboratory
1 Bethel Valley Road
Oak Ridge, TN 37831
E-mail: muralidhargn@ornl.gov

Bruce Pint, Co-Principal Investigator
Oak Ridge National Laboratory
1 Bethel Valley Road
Oak Ridge, TN 37831
E-mail: pintba@ornl.gov

Jerry L. Gibbs, DOE Technology Manager
U.S. Department of Energy
E-mail: jerry.gibbs@ee.doe.gov

Start Date: October 1, 2018 End Date: September 30, 2023
Project Funding: $400,000 DOE share: $400,000 Non-DOE share: $0

Project Introduction

Improving the engine efficiencies of passenger and commercial vehicles is a major goal of the DOE-EERE VTO. One potential approach to achieving improved engine efficiency, while reducing emissions, is through retaining more heat in the exhaust gas. This approach has been projected to increase exhaust gas temperatures from a current value of 760°C to values of at least 870°C and very likely reach as high as 1,000°C in the longer term [1],[2]. High-performance exhaust valves, currently used at temperatures up to ~760°C, are fabricated using Ni-based alloys, such as commercial Alloy 751. Other higher performance Ni-based alloys primarily developed for aerospace applications have the potential to operate at temperatures of 1,000°C with the desired strength, but may be both too expensive for automotive applications and also extremely difficult to forge into valves via the existing manufacturing infrastructure.

Objectives

The primary objective of this project is the development of cost-effective advanced alloys for exhaust valves, capable of operating at temperatures up at least 900°C, and up to 950°C. These alloys should have the appropriate combination of oxidation resistance and high-temperature mechanical strength required for the most-rigorous exhaust valve applications in both automotive and HD diesel engines. In collaboration with a recently established cooperative research and development agreement (CRADA) partner Federal Mogul Powertrain/Tenneco, this project aims to demonstrate the suitability of one downselected alloy for use in exhaust valves by fabricating and testing prototype valves using an industrially produced heat in FY 2021.

Approach

Table I.3.2.1.1.1 shows the targeted strength, fatigue life, oxidation resistance, and cost targets of materials needed for exhaust valves in next-generation high-efficiency engines. Two parallel approaches were pursued in the design strategy: (1) chromia-forming, lower cost, higher strength Ni-based alloys; and (2) more-oxidation-resistant alumina-forming Ni-based alloys. The principal approach to achieving Ni-based alloys with adequate high-temperature mechanical strength in either approach is through the use of γ’ precipitates for strengthening

in a γ-matrix. In addition to controlling the volume fraction of γ', a fine distribution of these precipitates must be achieved for optimum strengthening. One or more carbide phases, such as $M_{23}C_6$, MC, and M_7C_3 may also be present for grain size control. Because at 900°C and above, diffusion rates can be significant, the key challenge in achieving the long-term mechanical properties is to ensure that the γ' precipitates remain stable over the anticipated lifetime of the alloys with relatively low rates of coarsening. While it was anticipated that the alumina-forming alloys could achieve the targeted strength and oxidation resistance at temperatures up to 950°C, it is likely that oxidation-resistant coatings would be needed at temperatures greater than 900°C to protect the higher strength chromia-forming alloys from the combustion environment. Another task within this research thrust (e.g., Task 2A3) is pursing development of oxidation-resistant slurry aluminide and thermal-spray coatings for the chromia-forming alloys in this project.

Table I.3.2.1.1.1. Target Properties and Metrics

Property	Final Target
Yield Strength	≥ 50 Ksi at 950°C.
Fatigue Life	Fatigue life of new alloys > fatigue life of Alloy 751 at 900–950°C at 30–50 Ksi.
Oxidation Resistance	Mass change ≤2X commercial alumina-forming alloys at 950°C.
Cost	≤ 1.25X of 751.

The approach used in this task to develop the two classes of alloys is outlined below:

- **Chromia-forming alloys**: Previous work at ORNL has shown that the strengths in the heat-treated condition of new, lower cost ORNL alloys are superior to that of Alloy 751 at temperatures of 870°C and beyond [3],[4]. This subtask will identify alloys that can maintain their long-term strength at 900°C and above. Microstructural evolution will be evaluated in a select group of alloys fabricated at the laboratory-scale. Larger-sized heats will be fabricated by an industrial partner, and high-temperature fatigue properties of those heats will be evaluated. Prototype exhaust valves will be fabricated using one or more downselected alloys, based upon the measured properties of the industrial heats. These prototype exhaust valves will be evaluated on a testing rig and/or in engine-tests by the CRADA partner in its commercial facilities. Advanced characterization is being used to study γ'-precipitate evolution in the various alloys to determine how this behavior affects high-temperature mechanical properties. Advanced modeling will be used to predict microstructural evolution and will be validated to enable longer term predictions of alloy strength stability.
- **Alumina-forming alloys**: The primary challenge in this class of alloys is achieving high-temperature mechanical properties while maintaining the excellent oxidation resistance provided by the alumina scale. Alumina-forming alloys are generally lower strength than chromia-forming ones. Computational thermodynamics will be used to design alloys with desired γ' contents while also achieving good alumina scale formability at the targeted temperature of 950°C. Kinetic modeling will be used to design alloys with appropriate γ' sizes. Modeling will be validated using TEM, APT, and ultra-small-angle/small-angle scattering in FY 2021.

Results

Chromia-forming alloys: In FY 2020, results from uniaxial fatigue tests at 900°C, 200 MPa from laboratory-scale heats of ORNL Alloys 16, 161, 163, 200, and 41M3 showed several alloys (i.e., 16, 200, and 41M3) with higher cycles to failure than commercial vacuum-induction melting/vacuum Alloy 751. However, ORNL alloy heats of Alloys 161 and 163 exhibited lower-than-expected fatigue lives than the commercial vacuum-induction melted/vacuum–arc-refined Alloy 751. Because all ORNL laboratory-scale heats showed higher yield strengths than Alloy 751 at 900°C, it was particularly surprising that Alloys 161 and 163, which had better yield and tensile strengths than Alloy 751, did not perform better in these fatigue tests. To understand whether rapid coarsening of the strengthening precipitate γ' at 900°C was the result of poor fatigue properties of Alloys 161 and 163, fatigue-tested specimens were cross-sectioned, and γ' precipitate sizes were examined

using backscattered electron micrography. Figure I.3.2.1.1.1 shows a comparison between the microstructures of commercial Alloy 751 and ORNL Alloys 161 and 200. Note that the γ' volume fraction is lower and the γ' sizes are clearly larger in Alloy 751 than in ORNL Alloys 161 and 200. It was thus concluded that factors other than strength, such as processing-induced defects at or near the surface, could have resulted in premature crack initiation, thereby contributing to the lower fatigue life of Alloys 161 and 163.

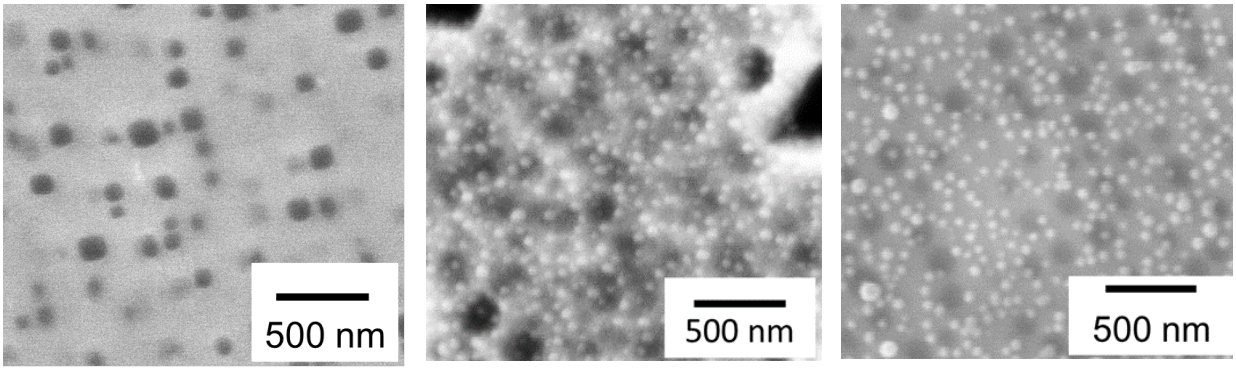

(a) (b) (c)

Figure I.3.2.1.1.1. BSEM images from fatigue-tested specimens: (a) Alloy 751; (b) ORNL Alloy 161; and (c) ORNL Alloy 163. Source: ORNL.

One alloy—ORNL Alloy 161 (nominal composition: 49Ni-26Fe-17.5Cr-1Co-1Mo-1.7Al-3.6Ti-0.4C, in all weight percentage) [1]—was downselected for initial scale-up using vacuum-induction melting. This work was performed by ATI Specialty Metals.[5] Figure I.3.2.1.1.2(a) shows an image of the vacuum-induction melted and cast ingot that cracked during subsequent forging and hot rolling while Figure I.3.2.1.1.2(b) shows that the same alloy could be rolled successfully by modifying the processing parameters (heat M2045).

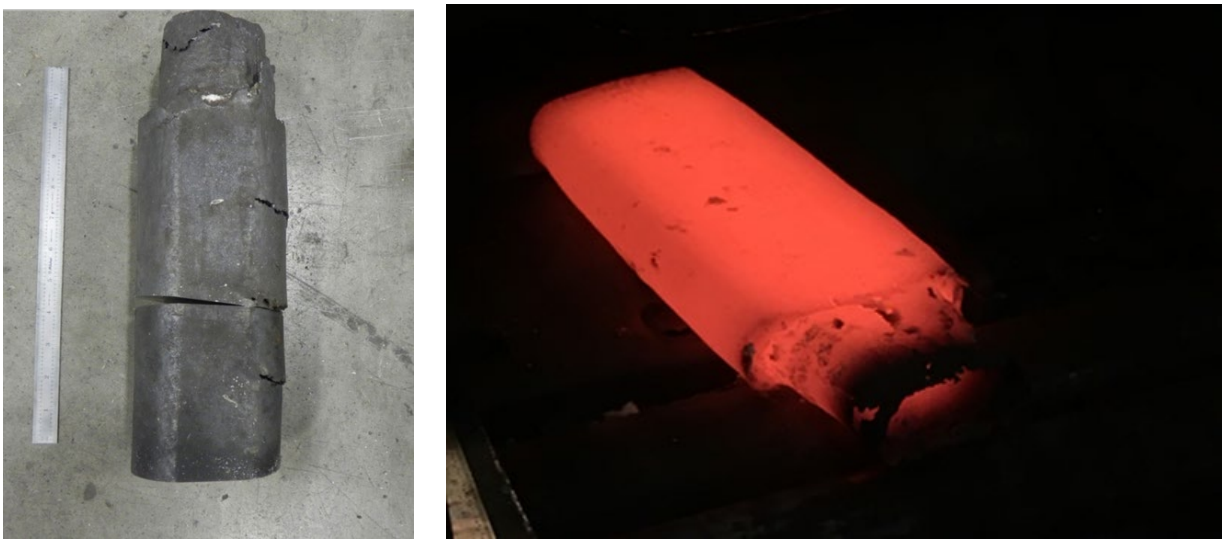

(a) (b)

Figure I.3.2.1.1.2. (a) Vacuum-induction melting and processing of Alloy 161 Ingot cracked in Trial #1. (b) Alloy was forged and rolled successfully without cracking In Trial #2. Source: ORNL.

[5] ATI Specialty Metals website. https://www.titaniummanufacturers.com/ati-specialty-metals/.

Figure I.3.2.1.1.3(a) shows an BSE diffraction pattern from Alloy heat M2045 in the aged condition. From this image, it was concluded that there was no indication of a strongly preferred orientation in the solution-annealed and aged condition, and the grain size was estimated to be about 141 µm. Figure I.3.2.1.1.3(b) shows a high-magnification scanning electron micrograph of the specimens shown in Figure I.3.2.1.1.3(a), which confirms the presence of very fine γ' precipitates in the aged condition in M2045.

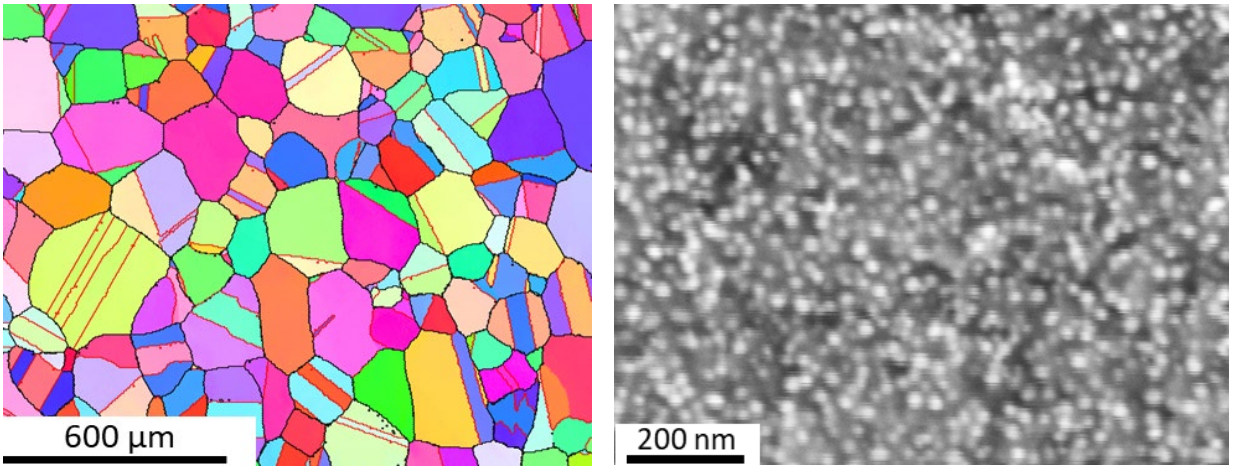

Figure I.3.2.1.1.3. (a) BSE diffraction pattern from M2045 in the aged condition showing grain size and grain orientations. (b) BSE microscope image showing the presence of very fine γ' precipitates. Source: ORNL.

Figure I.3.2.1.1.4 shows a comparison of the yield strengths of laboratory-scale heats of ORNL Alloy 161, Alloy 41M3, Alloy 200, baseline Alloy 751, and aged M2045. Note that all ORNL-developed alloys have higher yield strength than baseline Alloy 751 at temperatures greater than ~760°C, and the properties of the industrial-scale heat are consistent with properties of the equivalent laboratory-scale heat.

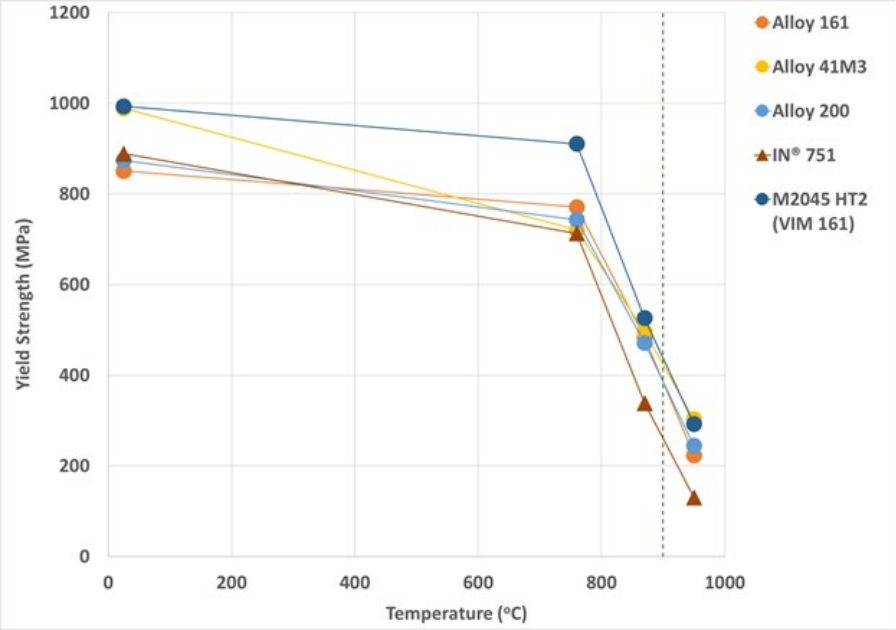

Figure I.3.2.1.1.4. Tensile testing of industrial-scale heat of ORNL Alloy 161 (M2045) shows yield strengths consistent with other laboratory-scale heats. Source: ORNL.

Figure I.3.2.1.1.5 shows results from fully reversed (R = -1) uniaxial fatigue tests on M2045 at 900°C, onducted at 5 Hz. Tests have been carried to lifetimes greater than 25 million cycles, revealing the stability of the microstructure to greater than 2,500 hours at this temperature. These results show the benefit of lower defects and lower residuals achieved through vacuum-induction arc-melting and holds promise of successful scaling up and transitioning of alloys to the end application. Additional alloys are being scaled-up and will be tested in follow-on work, in consultation with the CRADA partner.

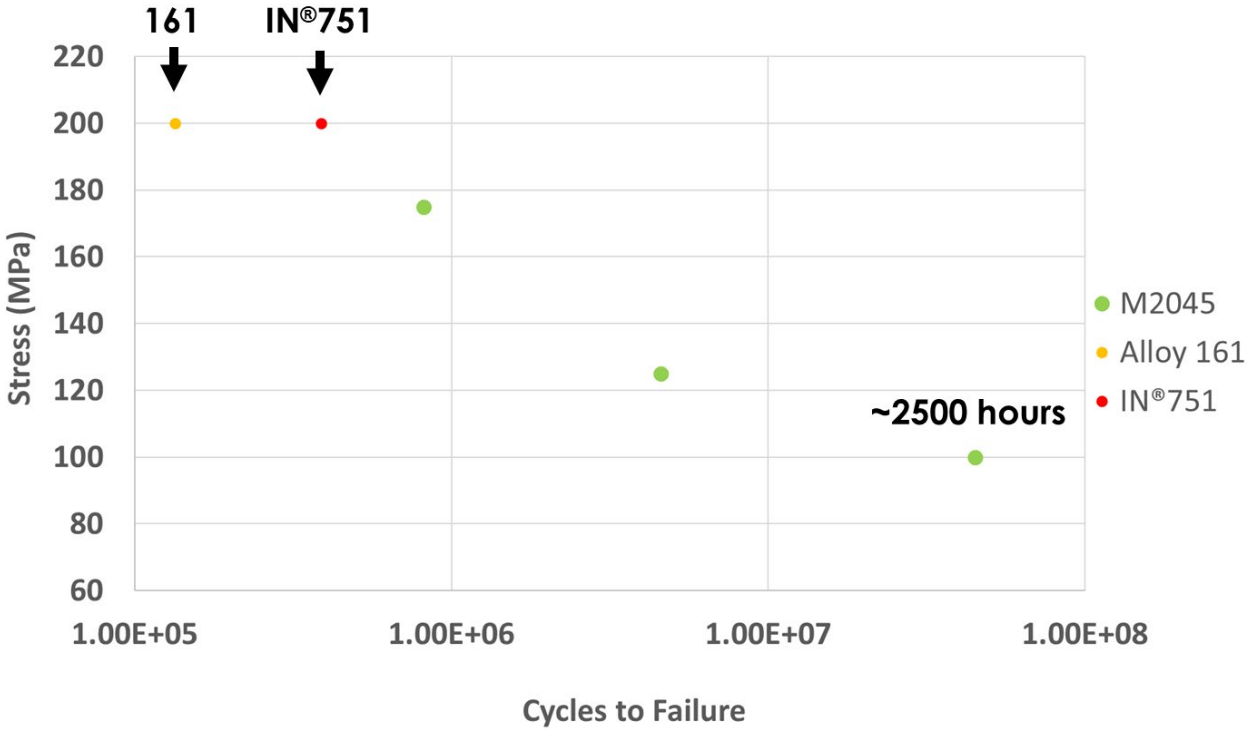

Figure I.3.2.1.1.5. Results from fully reversed uniaxial testing of industrial-scale heat of ORNL Alloy 161 (M2045) at 900°C and 5 Hz shows properties consistent with long-term stability of microstructure. Source: ORNL.

Alumina-forming alloys: Figure I.3.2.1.1.6(a) compares the mass change as a function of a number of one-hour cycles at 950°C in-air plus 10% water-vapor environment for several new ORNL alloys developed in FY 2020 to that of alumina-forming commercial alloy Haynes 214 and chromia-forming alloy Udimet 520. The ORNL alumina formers show oxidation behavior comparable to that of the commercial 214 alloy. All alumina formers shown in the figure show oxidation behavior far superior to that of the chromia-former Udimet 520. Figure I.3.2.1.1.6(b) shows the cross-section of a sample from ORNL Alloy 5B tested for 950 1-h cycles with mass change shown Figure I.3.2.1.1.6(a). Note the presence of a thin oxide scale, rich in Al, confirming the formation of an Al-rich oxide in this condition.

Figure I.3.2.1.1.7 compares the yield strengths at 950°C of the new ORNL alloys developed this year with those of commercial chromia-former Udimet 520 and commercial alumina-former Haynes 214. Note that significant improvements have been achieved in yield strengths measured at 950°C and that the FY 2020 targets were successfully exceeded while achieving good oxidation resistance at 950°C in-air plus 10% water-vapor environment. Although further improvements are needed to attain the targeted yield strength values for this project, the improvements in yield strength are substantial, and scale-up of one alumina-forming alloy is planned for this year. The improvements achieved this year suggest that the alloy development strategy is appropriate and will continue to be used to explore further improvements with the ultimate target of achieving the yield strength of the high-strength chromia-forming alloys at this temperature.

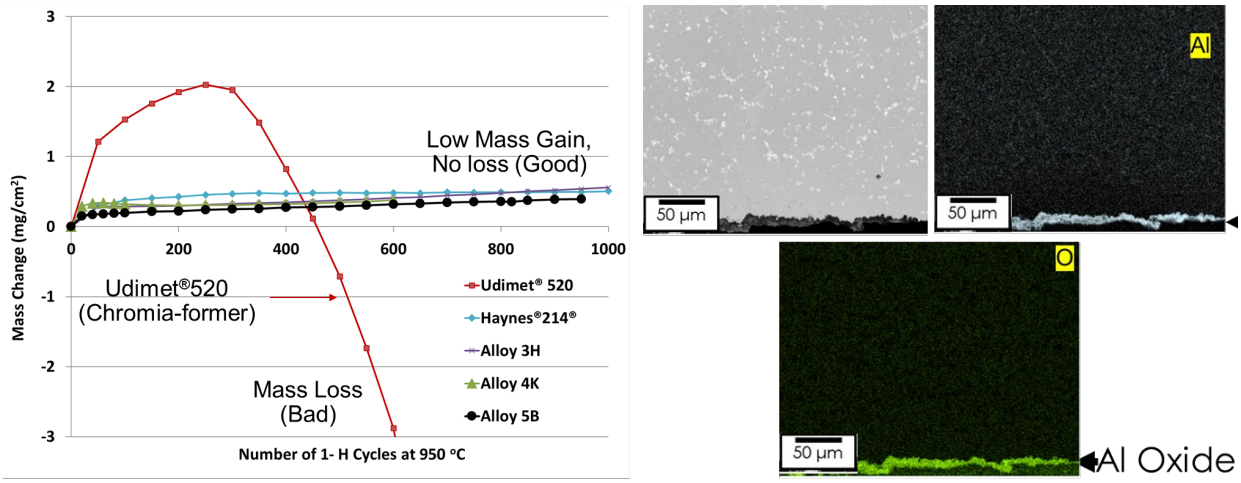

(a) (b)

Figure I.3.2.1.1.6. (a) Newly designed alumina-forming alloys showed oxidation behavior comparable to commercial alumina-forming Ni-based alloys at 950°C, in-air + 10% water-vapor. (b). Cross-section of a sample from ORNL Alloy 5B tested for 950 1-Hr cycles showing presence of a thin Al-rich oxide scale. Source: ORNL.

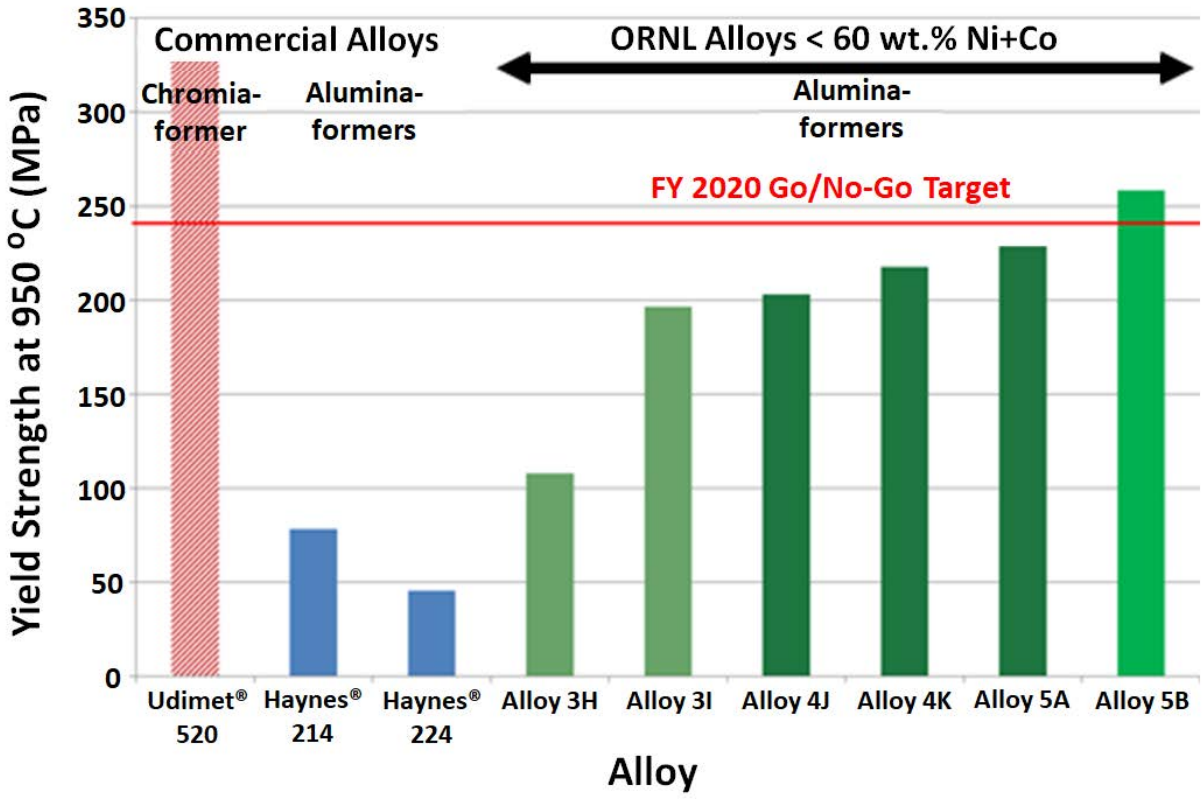

Figure I.3.2.1.1.7. Yield strength of best new alumina-forming alloy exceeded FY 2020 target at 950°C. Source: ORNL.

Conclusions

A new lower cost chromia-forming alloy developed at ORNL has been successfully produced in industrial-scale heat. High-temperature tensile testing of industrially produced material shows tensile properties consistent with properties obtained from laboratory-scale heat. High-temperature fatigue testing indicates microstructural stability to at least 2,500 hours at 900°C. Additional chromia-forming ORNL alloys will be scaled-up in FY 2021 with guidance from CRADA partner Federal Mogul Powertrain/Tenneco. New ORNL alumina-forming alloys have been developed with promising yield strengths at 950°C, and scale-up of one alloy composition is planned for FY 2021.

Key Publications

1. Muralidharan, G., and B. Pint, 2020, "Alumina-forming creep resistant Ni-based alloys," U. S. Patent No. 10,745,781, August 18, 2020.

References

1. DOE Vehicle Technologies Office, 2013, "LD Vehicles Technical Requirements and Gaps for Lightweight and Propulsion Materials," DOE VTO Workshop Report No. DOE/EE-0868, February 2013.
2. DOE Vehicle Technologies Office, 2013, "Trucks and HD Vehicles Technical Requirements and Gaps for Lightweight and Propulsion Materials," DOE VTO Workshop Report No. DOE/EE-0867, February 2013.
3. Muralidharan, G., "Low-cost FeNiCr alloys for high-temperature valve applications," U. S. Patent No. 9,605,565, March 28, 2017.
4. Muralidharan, G., "Low-cost, high-strength FeNiCr alloys for high-temperature exhaust valve applications," U. S. Patent No. 9,752,468 B2, September 5, 2017.

Acknowledgements

The authors would like to acknowledge S. Shukla, J. Chiles, D. T. Pierce, D. Leonard, J. Poplawsky, J. A. Haynes, T. Muth, T. R. Watkins, D. Erdman, K. Hedrick, J. Moser, C. Hawkins, G. Cox, K. Hanson, D. Moore, C. Carmichael, I. Stinson, G. Garner, T. Lowe, and T. Geer from ORNL; M. Frith, J. Ilavsky, S. Lapidus, and D. Singh from Argonne National Laboratory (ANL); and B. Gwalani, A. Devraj, and L. Kovanik from PNNL for their support in this work.

I.3.2.1.2 Higher Temperature Heavy-Duty Piston Alloys (Task 2A2) (Oak Ridge National Laboratory)

Dean Pierce, Co-Principal Investigator
Oak Ridge National Laboratory
1 Bethel Valley Road
Oak Ridge, TN 37831
E-mail: piercedt@ornl.gov

Govindarajan Muralidharan, Co-Principal Investigator
Oak Ridge National Laboratory
1 Bethel Valley Road
Oak Ridge, TN 37831
E-mail: muralidhargn@ornl.gov

Jerry L. Gibbs, DOE Technology Manager
U.S. Department of Energy
E-mail: jerry.gibbs@ee.doe.gov

Start Date: October 1, 2018 End Date: September 30, 2023
Project Funding: $200,000 DOE share: $200,000 Non-DOE share: $0

Project Introduction

Quench and tempered 4140 martensitic steel and micro-alloyed 38MnVS6 steel are the primary materials used in pistons for heavy-duty diesel engines (HDDEs). A major pathway to increasing the efficiency of internal combustion engines involves increasing both the peak cylinder pressure and combustion gas temperatures. However, these piston materials are operating at their limits of mechanical and thermal loading in current HDDEs. The 4140 and micro-alloyed steel alloys are limited to an operating temperature of ~500°C. As such, current piston materials are a major barrier to increasing engine efficiency for the long-haul freight industry.

Objectives

The objectives of this project are to investigate existing commercial alloys, as well as alloys being developed at ORNL, for use in HDDE pistons. Alloys that have the potential to enable increased operating temperatures and cylinder pressures, but require only moderate increases in materials and manufacturing costs over 4140 steels, are of particular interest. Specifically, the new alloys must meet the unique combinations of requirements for HDDE pistons, including high-temperature strength, high cycle fatigue strength, cyclic oxidation resistance in a combustion environment, wear-resistance, machinability, friction weldability, and microstructural stability. These phenomena can act synergistically to cause failure or to create cost or manufacturing barriers. The targeted peak piston operating temperature within this task is > 600°C. Further key targets include ultimate tensile strength (UTS) levels of approximately 525 MPa at peak temperature and acceptable oxidation resistance at > 600°C.

Approach

Four major groups of alloys are being investigated to identify materials that are suitable from a performance and cost perspective for use in next-generation HDDE pistons: (1) commercial martensitic stainless steels; (2) ORNL low-cost low Cr developmental alloys with superior elevated temperature strength; (3) ORNL developmental alloys with medium levels of Cr and improved oxidation resistance; and (4) advanced high Cr developmental alloys for operation at 650 to 700°C.

Results

Commercial Alloys

Two commercial baseline alloys were selected for evaluation of mechanical and oxidation properties in the first stage of this project: (1) martensitic stainless-steel Alloy 418 (Fe-0.15C-0.25Mn-0.25Si-13Cr-2Ni-3W wt.%); and (2) martensitic stainless-steel Alloy 422 (Fe-0.23C-0.75Mn-0.35Si-1Mo-11.5Cr-0.8Ni-1W wt.%). These alloys continue to be subjected to relevant elevated temperature tensile tests at 600, 650, and 700°C. The additional testing has primarily focused on acquiring additional elevated temperature strength data after long-term aging for 500 hours (h) at 600 and 650°C to further understand the effects of aging on longer term mechanical properties. Both Alloy 422 and Alloy 418 steels retain significant strength advantages over 4140 in the as-tempered condition, as shown in Figure I.3.2.1.2.1(a), with Alloy 422 possessing the highest elevated temperature strength. Both Alloy 422 and Alloy 418 show modest strength loss with aging. The strength levels of Alloy 422 steel are likely sufficient to enable piston operation at 600°C peak surface temperatures, and possibly higher, although engine testing is needed to verify.

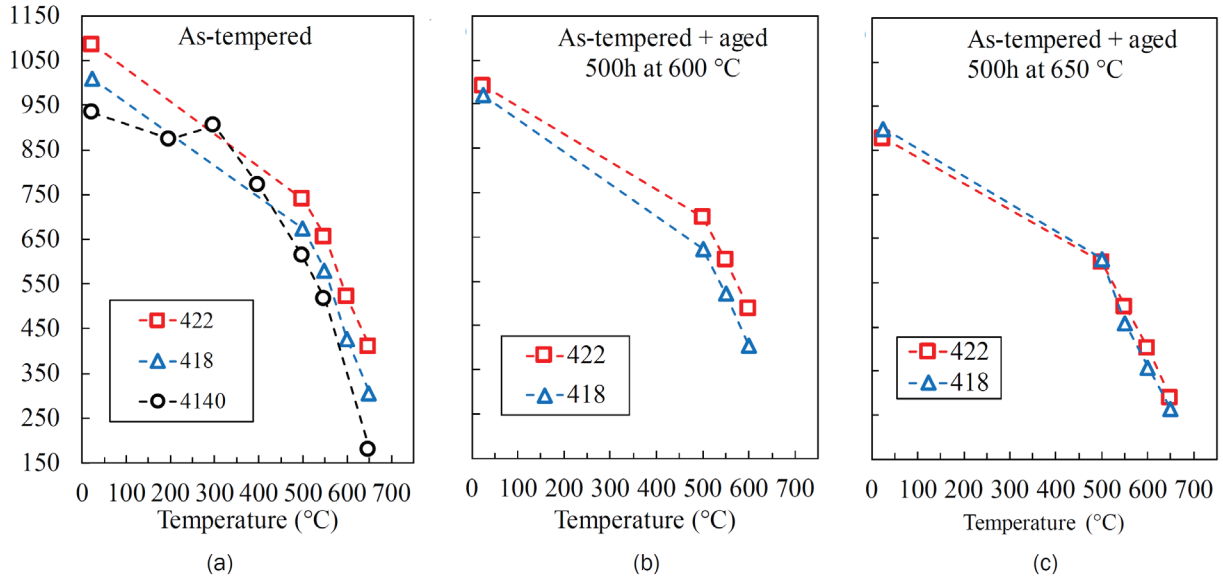

Figure I.3.2.1.2.1. UTS vs. test temperature of 422, 418, and 4140 in the: (a) as-tempered; (b) as-tempered plus aged 500 h at 600°C: and (c) as-tempered plus aged 500 h at 650°C conditions. Source: ORNL.

Oxidation testing of Alloy 422 and Alloy 418 has been conducted from 250 to 1,000 h at temperatures of 550°C, 600°C, and 650°C, as shown in Figure I.3.2.1.2.2(a) through (c). In FY 2020, cyclic oxidation testing of commercial Alloy 418 and Alloy 422 steels focused on temperatures ranging from 550°C to 650°C and longer term testing to 500 h and 1,000 h has been conducted relative to initial tests in FY 2019, which were conducted for 250 h. Alloy 418 and Alloy 422 steels exhibit relatively low-mass gain—relative to lower Cr Alloys T22 and T91—in the first 250 h of testing at 550, 600, and 650°C. Longer term oxidation testing at 550°C indicates break-way oxidation in Alloy 422 occurs after ~300 h, while Alloy 418 continues to exhibit relatively low-mass gain. The balance of strength and oxidation resistance of Alloy 418 and Alloy 422 make them potential candidates for piston materials in next-generation HDDEs.

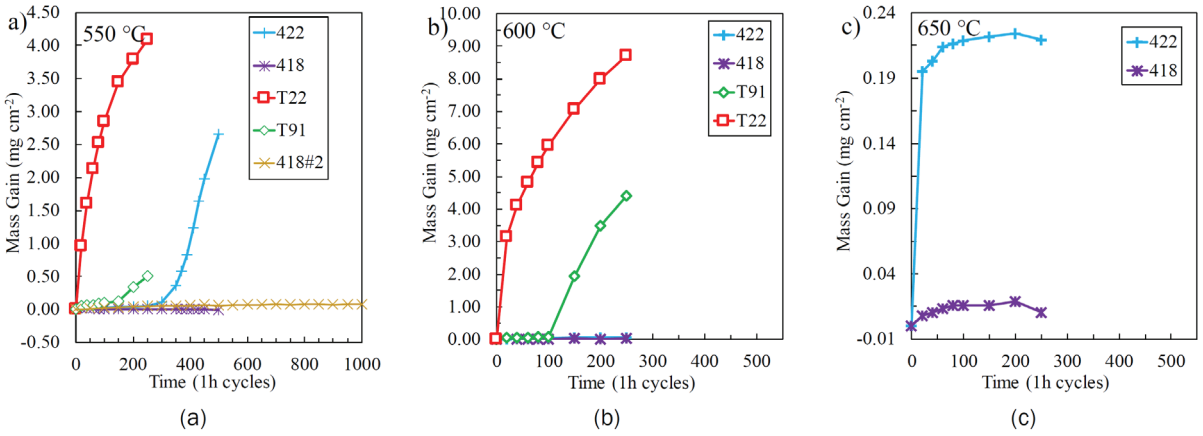

Figure I.3.2.1.2.2. Oxidation mass change vs time (1 h cycles) in-air plus 10% H_2O at temperatures of: (a) 550; (b) 600; and (c) 650 °C. Source: ORNL.

Low-Cost Medium Cr Alloys

Alloy design efforts to achieve acceptable oxidation resistance at medium levels of Cr are continuing to reduce alloy cost as compared to higher Cr alloys, such as Alloy 418 and Alloy 422 (12 weight percentage Cr). Reducing Cr, a relatively high cost element, directly lowers the raw material cost and may allow alternative alloying strategies. These alloy design efforts have thus far been able to achieve oxidation resistance similar to Alloy 422 at significantly lower levels of Cr. Figure I.3.2.1.2.3(a) shows the mass gain due to oxidation of medium Cr developmental Alloys A, B, C, and D, along with Alloy 418 and Alloy 422, during cyclic oxidation of 1 h cycles at 550°C in an atmosphere of air and 10% water-vapor. Medium Cr Alloys C and D exhibit less mass gain relative to Alloy 422 after 1,000 h of cyclic oxidation testing. Cross-sections of the oxide layers are shown in Figure I.3.2.1.2.3(b), (c), (d), and (e). Medium Cr Alloys A and B show thick multilayer oxide scales, whereas Alloys C and D show regions of very thin oxide (green arrow) near thicker Fe oxide nodules (red arrow). Refinement of the alloy composition is ongoing to further improve the oxide resistance and to suppress the tendency for the growth of Fe oxide nodules.

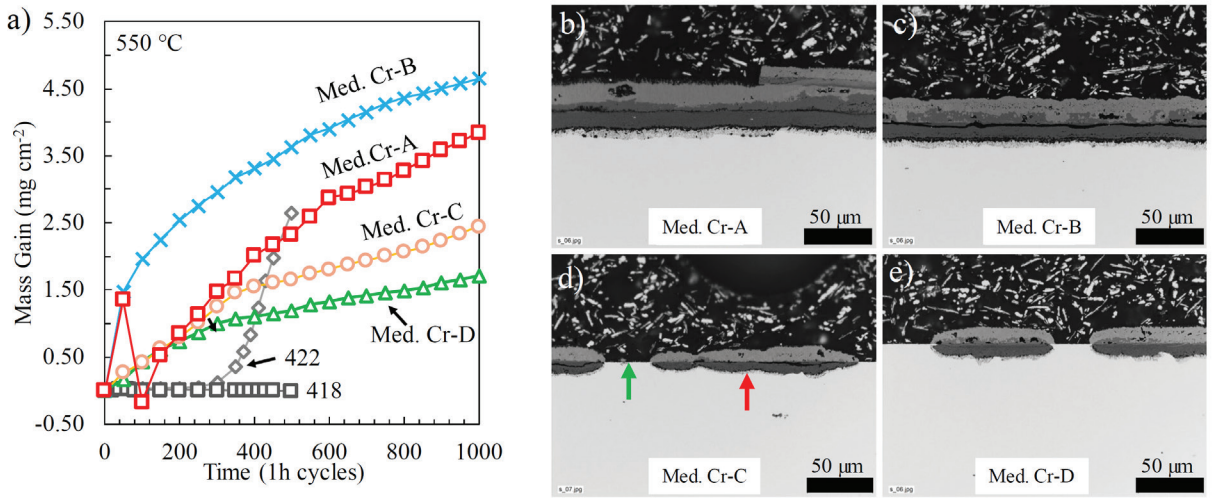

Figure I.3.2.1.2.3. Results of oxidation testing of select medium Cr Alloys and Alloy 418 and Alloy 422. (a) Mass change of medium Cr alloys vs time (1 h cycles) in-air and 10% water-vapor at 550°C. Cross-sectional optical micrographs after 1,000 h of oxidation testing for alloys: (b) Med. Cr-A; (c) Med. Cr-B, (d) Med. Cr-C; and (e) Med. Cr-D. Source: ORNL.

The elevated temperature UTS of these medium Cr alloys is compared in Figure I.3.2.1.2.4 in the (a) as-tempered and (b) as-tempered plus aged 500 h at 600°C conditions. The UTS of the medium Cr developmental alloys exceeds that of Alloy 422 and Alloy 418 in the as-tempered condition, but drops below Alloy 422 in the aged condition, while remining above Alloy 418. Alloy development strategies are currently being explored to reduce microstructural aging and softening so the medium Cr developmental alloy strength at elevated temperatures remains above the higher cost of Alloy 422.

High Cr Martensitic Steels

Alloy design concepts for advanced high Cr martensitic steels have been developed for higher operating temperatures ~650 to 700°C. These steels are designed to possess advanced strength and cyclic oxidation resistance at 650 to 700°C. High Cr-A steel exemplifies the high-strength levels of these alloys, with UTS levels near 550 MPa at 650°C, which is similar to medium Cr-A, as shown in Figure I.3.2.1.2.4(a). High Cr steels are currently undergoing long-term aging for 500 h at 600°C to evaluate their resistance to softening and oxidation at 650°C. Additional alloying modifications are under consideration to achieve target strength levels at 700°C.

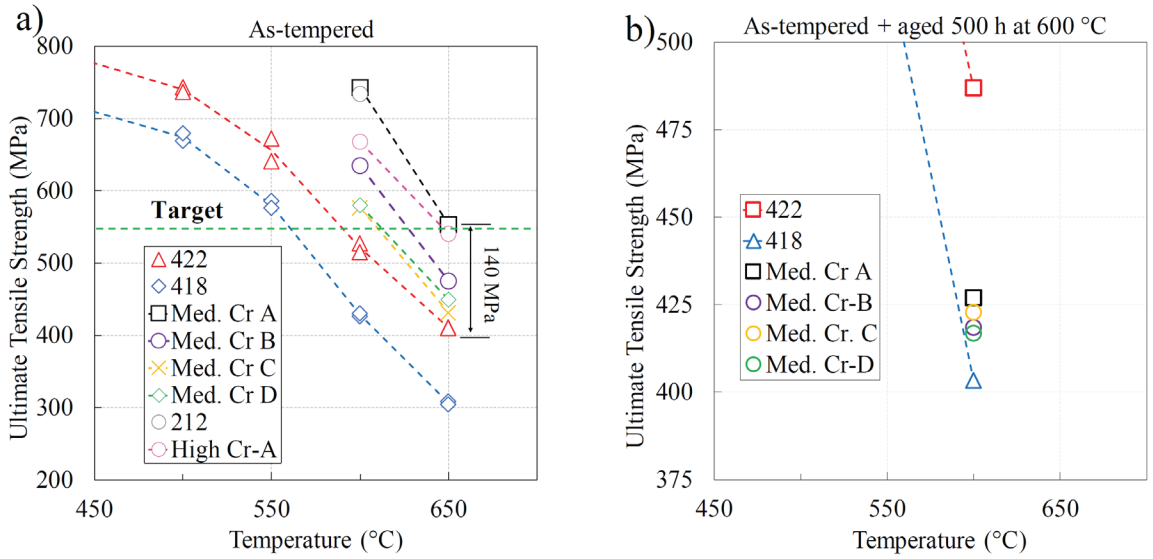

Figure I.3.2.1.2.4. UTS of commercial alloys 418, 422, as well as developmental alloys HTCR-Plus, HTC-OR, and BCO: (a) as-tempered; and (b) aged at 600°C for 500 hours at test temperatures of 500°C, 550°C, 600°C, and 650°C. Source: ORNL.

Low Cr Martensitic Steels

Alloy design concepts for alloys with lower Cr levels for lower cost applications are also under development. These steels, targeted for operation at 550 to 600°C, show very high levels of strength compared to baseline commercial Alloy 422. For instance, the UTS of low Cr Alloy 212 exceeds 700 MPa at 600°C, which is far superior to the target of 525 MPa. Alloy development is ongoing to further improve the balance of elevated temperature strength and oxidation resistance of these developmental alloys.

Conclusions

Multiple high-temperature steel alloy development concepts were investigated. These concepts target low, medium, and high Cr alloys with a variety of cost and performance ranges. Alloy design strategies have been developed to optimize strength and oxidation resistance characteristics that address the demanding combination of properties and performance requirements of pistons for future advanced HDDEs. Several alloys within the groups of steels being investigated show significant promise to improve performance over

current and candidate materials for HDDE pistons. Further metallurgical and manufacturing development of select alloys within these groups, as well as industrial collaboration, will be sought in Year 3 of this task.

Key Publications

1. Pierce, D., G. Muralidharan, L. Allard, J. Poplawsky B. Pint, and J. A. Haynes, 2021, "Martensitic stainless steels for next-generation diesel engine pistons," in preparation.

Acknowledgements

The following ORNL personnel are acknowledged for their contributions to this project: L. Allard, T. Muth, J. Poplawsky, J. A. Haynes, B. Pint, C. Carmichael, I. Stinson, H. Wang, E. Cakmak, K. Hedrick, G. Garner, and Y. Yamamoto.

I.3.2.1.3 High-Temperature Coatings for Valve Alloys (Task 2A3) (Oak Ridge National Laboratory)

Sebastien Dryepondt, Co-Principal Investigator
Oak Ridge National Laboratory
1 Bethel Valley Road
Oak Ridge, TN 37831
E-mail: dryepondtsn@ornl.gov

Beth Armstrong, Co-Principal Investigator
Oak Ridge National Laboratory
1 Bethel Valley Road
Oak Ridge, TN 37831
E-mail: armstrongbl@ornl.gov

Jerry L. Gibbs, DOE Technology Manager
U.S. Department of Energy
E-mail: jerry.gibbs@ee.doe.gov

Start Date: October 1, 2018 End Date: September 30, 2023
Project Funding: $175,000 DOE share: $175,000 Non-DOE share: $0

Project Introduction

As described in Report No. I.3.2.1.1 entitled, "Development of Oxidation-Resistant Valve Alloys for 900–950˚C Use," ORNL is designing lower cost, higher strength oxidation-resistant NiFeCr-based valve alloys for operating in temperatures up to approximately 950°C. Such NiFeCr-based alloys have excellent mechanical properties up to 950°C, but as chromia-forming alloys, their oxidation resistance above 900°C is marginal or inadequate in some environments. Another route to enabling an alloy with excellent higher temperature strength to meet environmental resistance requirements in highly oxidizing environments is to apply cost-effective oxidation-resistant coatings—typically alumina-forming coatings for temperatures above 900°C—on high-strength chromia-forming valve alloys. Thus, in this task, ORNL is developing diffusion aluminide and overlay MCrAlY coatings in collaboration with both academic and industrial partners. Previous coating studies by this ORNL task team clearly demonstrated that the cyclic oxidation resistance of commercial valve alloy 31V (57Ni-23Cr-13Fe-2Mo-2.3Ti-1.3Al-0.9Nb) can be significantly improved with an aluminide or thermally sprayed MCrAlY type coating without impacting the high cycle fatigue (HCF) behavior of the underlying alloy [1]. A coupled thermodynamic and kinetics model is used in the present study to optimize the coating fabrication process for ORNL's new high-strength NiFeCr-based alloys to predict coating and substrate microstructure evolution during coating deposition/diffusion and to estimate the in-service coating lifetime at specific temperatures. Experimental validation of the coating's performance on these new alloys include oxidation testing in combustion-relevant environments (e.g., 10% water-vapor) at 900°C and 950°C and HCF testing at 900°C.

Objectives

The main objectives of this task are to develop and validate cost-effective oxidation-resistant alumina-forming coatings to improve the durability of high-strength valve alloys. Oxidation and HCF testing will be performed to demonstrate the superior performance of coated versus bare specimens and to support the development of a lifetime prediction tool for coated components based on a coupled thermodynamic and kinetics model.

Approach

The first slurry coatings fabricated at ORNL were thin and quite inhomogeneous in thickness due to poor wetting of the coating on the new family of high-strength NiFeCr-based alloys. Commercial Al slurries were

also purchased from Ceral, Inc., but the alloy substrates also did not wet well with the commercial slurry systems. Optimization of slurry coatings was, therefore, conducted at ORNL through modifications of both the slurry chemistry and the heat-treatment procedure used for the coated coupons. In addition, in collaboration with Flame Spray, Inc., a flame spray slurry aluminide coating was deposited on both Alloy 31V and one of ORNL's high-strength alloy compositions and evaluated along with ORNL's slurry coatings. To assess the performance of these new commercial slurry coatings, as well as commercial thermally sprayed NiCoCrAlYHfSi coatings (e.g., Amdry 386, deposited by Stony Brook University's Thermal-Spray Laboratory using high velocity O fuel spraying), oxidation, and fatigue testing was carried out at 900–950°C. Extensive microstructural characterization was also performed to validate the coupled thermodynamic and kinetics model as a tool to predict coated component microstructure evolution and lifetime.

Results

ORNL Slurry Coating Optimization

A series of Al-rich coatings was prepared on three Ni-based alloys—two ORNL alloys [Alloy 2686 and Alloy 2687] and one commercial alloy [Alloy 31V]—utilizing ORNL's Al slurry dip-coating approach. The chemical compositions of these substrates are reported in Table I.3.2.1.3.1 in weight percentages (wt.%).

Table I.3.2.1.3.1. Substrate Chemical Composition in Weight Percent

Substrate	Ni	Fe	Cr	Ti	Al	Mo	C	Others
ORNL 2687	47	27	18	3.8	1.8	1.2	0.03	1 Co
ORNL 2686	39.8	34.6	19.2	3	1.2	1.2	0.03	0.9 Co
Pyromet 31V	57	13.6	22.7	2.3	1.3	2	0.04	0.9 Nb, 0.2 Si

Two Al slurries were considered, the baseline Al-based slurry formulation and the baseline slurry with the addition of Al chloride as an activator. All substrates were double-dipped from the same batch of one of the two slurries to ensure excess concentration of Al was present on the surface. Some of the Alloy 2687 coupons were solution-annealed at 1,121°C for 4 hours (h) to assess the impact of the substrate chemical homogeneity on the diffusion coating quality. Coupons were annealed for 4 h at 1,121°C followed by 4 h at 800°C in vacuum (~10^{-6} Torr) using a Brew furnace. Examples of the resulting coating cross-sectional microstructures for Alloy 2687, Alloy 2686, and Alloy 31V are shown in Figure I.3.2.1.3.1. Overall, coating thickness and homogeneity was superior for the Alloy 2687 coupons as compared to the Alloy 2686 and Alloy 31V coupons. The use of an activator successfully led to a thicker coating for the Alloy 2687 annealed coupon, as observed in Figure I.3.2.1.3.1(a) and (h), but not for the Alloy 2686 and Alloy 2687 as-fabricated coupons. As can be seen in Figure I.3.2.1.3.1(h), the coating thickness on Alloy 2687 was ~30 µm and is expected to significantly improve the alloy cyclic oxidation resistance at 900°C and 950°C. The reasons for the variable thickness of the as-deposited slurry coatings on the three alloys will be the subject of further investigation.

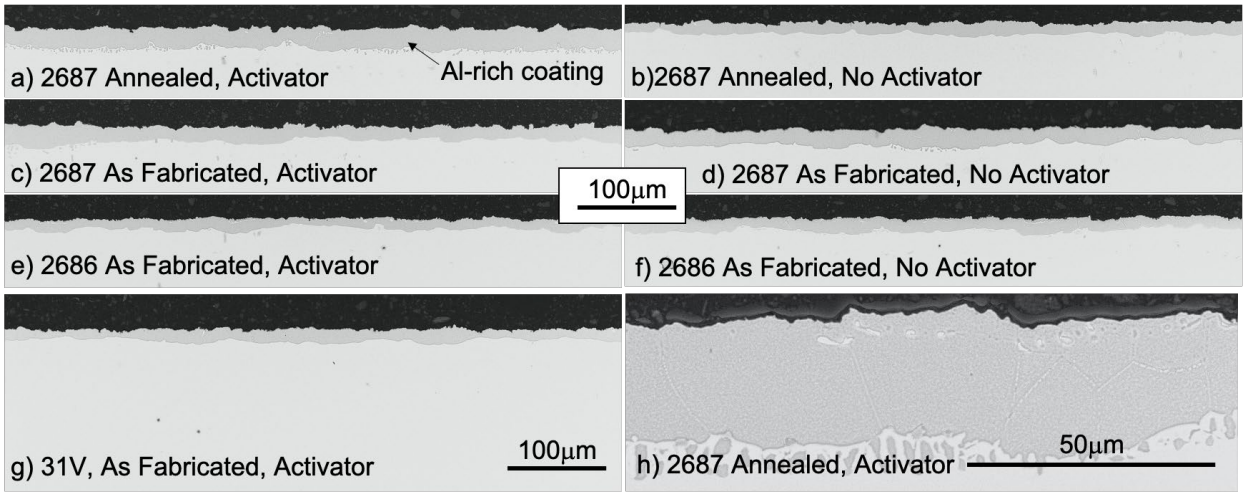

Figure I.3.2.1.3.1. ORNL slurry aluminide coatings after annealing for 4 h at 1,121°C and 4 h at 800°C. (a) Annealed Alloy 2687 coupon with Al chloride activator added to the baseline slurry. (b) Annealed Alloy 2687 coupon added to the baseline slurry. (c) As-fabricated Alloy 2687 coupon added to the slurry with an activator. (d) As-fabricated Alloy 2687 coupon added to the baseline slurry. (e) As-fabricated Alloy 2686 coupon added to the slurry with an activator. (f) As-fabricated Alloy 2686 coupon added to the baseline slurry. (g) 31V coupon with the activator. (h) Higher magnification of (a). Source: ORNL.

Flame Spray, Inc., Slurry Coating Testing and Characterization

Slurry aluminide coatings of both 20 and 40 μm thicknesses were deposited by Flame Spray, Inc., on the Pyromet 31V and ORNL 2687 alloys using the heat-treatment recommended by ORNL for 4 h at 1,121°C, followed by 4 h at 800°C. Figure I.3.2.1.3.2 compares the cyclic oxidation behavior for 1 h cycle lengths at 900°C shown in Figure I.3.2.1.3.2(a) and (c) and 950°C shown in Figure I.3.2.1.3.2(b) and (d), in-air and 10% water-vapor for the bare and Flame Spray, Inc., slurry coated alloys. For Alloy 31V, a substantial decrease of the oxidation mass gain was observed for the coated specimens at 900°C and 950°C in comparison with the bare alloy. Both the 20 μm-thick and 40 μm-thick aluminide coatings remained protective for the entire duration of these rigorous tests for 1,000 h at 900°C and 500 h at 950°C. The cyclic oxidation resistance for Alloy 2687 was also significantly improved by the aluminide coating. At 900°C, the thinner coating was protective for ~600 h, after which gradual mass losses were observed. By comparison, the bare alloy began rapid spallation of the chromia scale after 200 cycles. The 40 μm coating performed better with slight mass losses only at the very end of the 1,000 h test. At 950°C, severe mass losses were measured for the bare 2687 sample prior to 100 cycles, while very limited mass changes were observed for the 40 μm coated specimens to 500 cycles. Coating degradation was, however, observed after 400 h for the 20 μm-thick coating with significant mass losses. Degradation of the thinner coating on Alloy 2687 is likely due to the higher Ti concentration in this alloy, 3.8 wt.% versus 2.3 wt.% for Alloy 31V, with Ti diffusing to the coating surface and affecting both the growth and adherence of the oxide scale, particularly at 950°C where Ti likely has high mobility in the aluminide.

Detailed characterization of the as-coated Alloy 31V and 2687 specimens was performed with electron microprobe analysis using both EDS and wavelength dispersive spectroscopy (WDS). Quantified element distribution maps were acquired with EDS and WDS combined with precise determination of the chemical composition of the coatings and interdiffusion zones. Figure I.3.2.1.3.3 shows the BSEM images and EDS element mapping of the as-received Flame Spray, Inc., aluminide coatings on the substrates for Alloy 31V and Alloy 2687. Similar coating thicknesses of about 40 μm were observed on both. The interdiffusion zone on both alloys mainly consisted of Cr, Fe, and Mo with a low fraction of dispersed TiNb-rich carbides in Alloy 31V and Ti-carbides in the case of Alloy 2687.

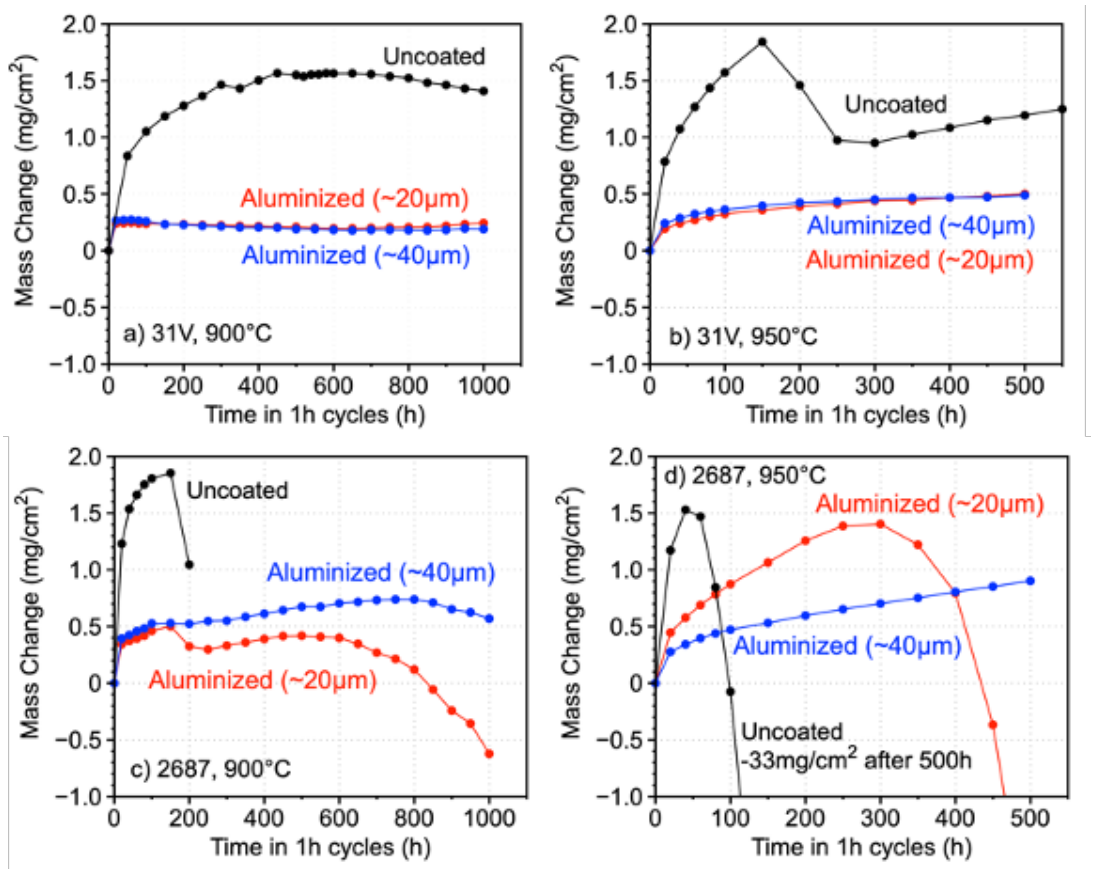

Figure I.3.2.1.3.2. 1 h cyclic oxidation behavior in-air and 10% water-vapor of bare alloy and Flame Spray, Inc., slurry aluminide coated alloy. (a) Alloy 31V at 900°C. (b) Alloy 31V at 950°C. (c) Alloy 2687 at 900°C. (d) Alloy 2687 at 950°C. Source: ORNL.

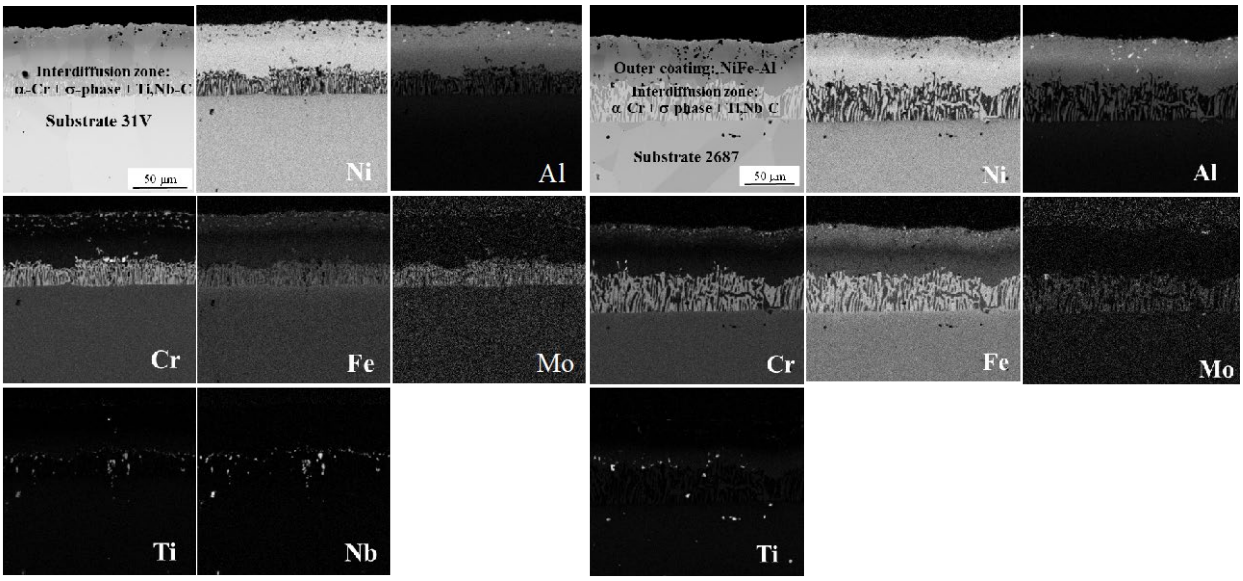

Figure I.3.2.1.3.3. Microstructure of the as-deposited Flame Spray, Inc., slurry aluminide coating of: (a) Alloy 31V; and (b) Alloy 2687. Source: ORNL.

Coupled Thermodynamic-Kinetic Modeling

The degradation of the slurry-deposited coatings with a 40 μm coating thickness provided by Flame Spray, Inc., during high-temperature exposure was simulated with a coupled thermodynamic-kinetic model [2]. The measured concentrations for the coating-substrate systems were used as input for the models. Thermodynamic and kinetic data for all relevant phases (e.g., β-Bcc, α-Bcc, γ-fcc, γ′-fcc, and σ-phase) was considered and extracted from commercially available databases (e.g., TCNI8 and MOBNI4). The model provided element concentrations and phase distributions across the thickness of the coating and into the substrate as a function of time and temperature.

Figure I.3.2.1.3.4(a) and (b) highlights the good agreement between observed and calculated phase distribution for the Alloy 31V coupon exposed for 1,000 1 h cycle at 900°C in-air and 10% water-vapor. A complete depletion of the β-(NiFe)Al was predicted by the model, which agrees with the experimental observation. Additionally, the model was able to predict the observed phase distribution in terms of the type of phases and depths of different diffusion zones as marked by dotted lines on the micrograph and on the calculated phase distribution. An enrichment of α-Cr phase in the three-phase region (γ+γ'+α-Cr) was observed underneath the external alumina scale that was predicted by the model. This was followed by a three-phase region (γ+γ'+σ) extending into the alloy up to a depth of about 120 μm from the oxide-coating interface.

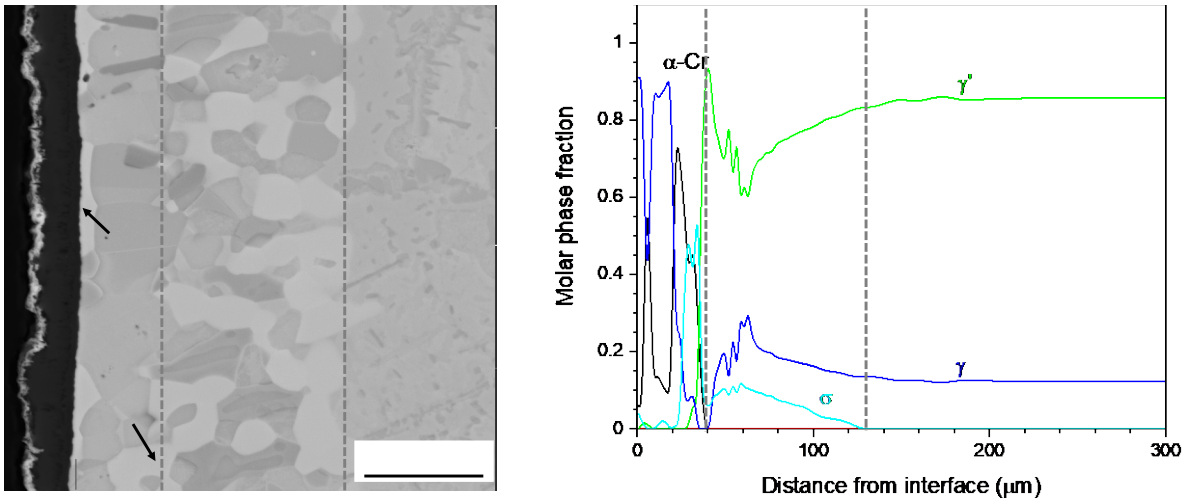

(a) (b)

Figure I.3.2.1.3.4. (a) BSEM image of the cross-section of the aluminized, slurry-deposited Alloy 31V specimen. (b) Calculated phase distribution for the same specimen exposed for 1,000 h at 900 °C in-air and 10% water-vapor in 1 h cycles. Source: ORNL.

HCF of Coated Alloy 2687

A set of Alloy 2687 fatigue specimens was coated using the Flame Spray, Inc., slurry and a commercial MCrAlY (e.g., Amdry 386, Ni-22Co-17Cr-12Al-0.5Hf-0.5Y-0.4Si) coating deposited by Stony Brook University. HCF testing was conducted at 900°C at 20 Hz and applied stresses of 125 MPa or 150 MPa with a 0.1 load ratio. As can be seen in Table I.3.2.1.3.2, the numbers of cycles to failure (defined as Nf) with a maximum stress of 125 MPa were very similar for the slurry aluminide and MCrAlY coatings, but at 150 MPa, Nf was higher for the MCrAlY coating in comparison with the slurry aluminide coating. Such Nf variation of less than a factor of two are expected for the HCF tests. Overall, these results are consistent with HCF data generated on ORNL's high-strength alloys at 900°C. HCF testing of bare Alloy 2687 using the same conditions and same heat-treatment as for the coated specimens is planned for next year. In addition, microstructure characterization was conducted on the MCrAlY coated HCF specimens after rupture. Coating cracking was only observed in the vicinity of the fracture surface, highlighting good ductility of the MCrAlY coating at 900°C.

Table I.3.2.1.3.2. HCF Results at 900°C for Coated Alloy 2687 Specimens

	Cycles to Failure (Nf)	
Stress (MPa)	150 MPa	125 MPa
MCrAlY	8,772,961	16,404,255
Slurry Aluminide	4,761,576	15,193,547

Conclusions

ORNL is developing and characterizing cost-effective, oxidation-resistant, alumina-forming coatings for a new family of lower cost, higher strength NiFeCr-based valve alloys. Significant improvement was achieved in ORNL aluminide slurry dip-coating homogeneity by adding an activator. Aluminide coatings deposited on valve alloys by Flame Spray, Inc., exhibited superior cyclic oxidation resistance in comparison with bare alloys at 900°C and 950°C in combustion-relevant closely controlled laboratory test environments. A coupled thermodynamic and kinetics model was used to predict the coating and substrate microstructure evolution at 900°C and 950°C during oxidation. The phase distribution prediction was consistent with the phase distribution observed after testing. This model will be key to develop lifetime predictive tools for coated valve components. Commercial slurry aluminide and MCrAlY coatings were deposited on fatigue specimens machined from high-strength ORNL valve Alloy 2687. The HCF data generated at 900°C were consistent with data for the bare alloy. These results indicate that low-cost coatings are a promising route for increasing the allowable temperature of high-strength valve alloys.

Key Publications

A journal article is under internal review and will be submitted early 2021.

References

1. Dryepondt, S., S. J. Jones, Y. Zhang, P. J. Maziasz, and B. A. Pint, 2015, "Oxidation, creep, and fatigue properties of bare and coated 31V alloy," *JOM*, Vol. 67, No. 1, pp. 68–76.
2. Pillai, R., W. Sloof, A. Chyrkin, L. Singheiser, and W. J. Quadakkers, 2015, "A new computational approach for modeling the microstructural evolution and residual lifetime assessment of MCrAlY coatings," *Mater. High Temp.*, Vol. 32, No. 1–2, pp. 57–67.

Acknowledgements

The authors would like to acknowledge M. Stephens, T. Lowe, and V. Cox for assisting with the experimental work. They also would like to acknowledge M. Lance for generating the electron microprobe analyses data.

I.3.2.1.4 Development of Cast, Higher Temperature Austenitic Alloys (Task 2B1) (Oak Ridge National Laboratory)

Michael P. Brady, Co-Principal Investigator
Oak Ridge National Laboratory
1 Bethel Valley Road
Oak Ridge, TN 37831
E-mail: bradymp@ornl.gov

Yukinori Yamamoto, Co-Principal Investigator
Oak Ridge National Laboratory
1 Bethel Valley Road
Oak Ridge, TN 37831
E-mail: yamamotoy@ornl.gov

Jerry L. Gibbs, DOE Technology Manager
U.S. Department of Energy
E-mail: jerry.gibbs@ee.doe.gov

Start Date: October 1, 2018 End Date: September 30, 2022
Project Funding: $275,000 DOE share: $275,000 Non-DOE share: $0

Project Introduction

Automotive exhaust components are anticipated to experience temperatures of ≥ 900–950°C in the near future to reach efficiency targets. The cast alloys currently used for turbocharger housings and exhaust manifolds are at their upper-temperature limit for creep and/or oxidation resistance. Therefore, new, cost-effective alloys will be required to meet these increasing operating temperature requirements.

Objectives

The goal of this subtask is to increase the upper-temperature oxidation limit to ≥ 900–950°C for next-generation cast austenitic stainless-steel exhaust gas components. Candidate alloys will utilize an Fe(Ni) base with ≤ 25–30 weight percent (wt.%) Ni to remain cost-competitive. They will also minimize the use of other costly alloying additions, such as Mo, Nb, W, etc. The cast stainless alloys being developed in this subtask are referred to as Alumina-Forming Austenitics (AFA) and have the distinction of being designed to form an alumina (Al_2O_3) protective oxide scale on the surface during oxidation, rather than the chromia (Cr_2O_3) oxide scales that form on most commercial stainless alloys. Alumina scales are typically slower growing and more protective than chromia scales, particularly at higher temperatures, but alloy design and the casting of Al-containing stainless alloys can be challenging.

Approach

Leveraging recent ORNL alloy development successes for wrought 25Ni-base AFA alloys for use up to 850–900°C and cast 35Ni-base AFA alloys for use up to 1,150°C, designing the exploration of second generation cast AFA alloys with ≤ 25 wt.% Ni has been pursued for use in exhaust components. Alloy design, development, and refinement in this Thrust 2 subtask are being guided by Thrust 4 activities, including advanced characterization of nano-microscale strengthening precipitates (e.g., Thrust 4A), as well as computational activities including CALPHAD and ML for alloy design, which is co-supported by Thrust 4B: Advanced Computation. In FY 2020, the focus was on characterization of initial trial commercial castings of downselected laboratory-scale alloys designed based on CALPHAD approaches. Expanded efforts were also initiated for ML prediction of creep-rupture lifetimes using the ORNL legacy wrought AFA creep dataset. This included an exploration of methodologies to extend the ML prediction capability to design of new AFA alloys

with improved creep properties. The use of ML approaches to supplement state-of-the-art CALPHAD-based alloy design is of great interest given the complexity of developmental engineering alloys such as AFA, which cover an enormous composition space, typically with well over ten intentional alloying additions to be considered, along with multiscale and multiphase microstructures.

Results

Oxidation, creep, and tensile testing, along with thermophysical properties evaluation, were performed for trial commercial heats of the FY 2019 downselected AFA5 alloy designed by CALPHAD methods and based on Fe-17Cr-22Ni-4Al-0.6Nb-0.5C wt.%. Exploratory commercial scale-up casting of AFA5 was completed through a commercial foundry (MetalTek International, Waukesha, WI) by air induction melting with an Ar cover gas. Three different forms of ingots were delivered—plate, keel block, and round bar—totaling approximately 36 kg. The first commercial heat was out of specification at ~20 wt.% Cr, which aids oxidation resistance at the expense of creep resistance. The second commercial heat came in on target at ~16.5 to 17.5 wt.% Cr. Studying trial commercial heats in the earlier stages of alloy design efforts is critical, as the higher levels of impurities, reduced elemental specification control, and typically coarser microstructures encountered in commercial processing as compared to laboratory-scale arc-casting can result in degraded properties. A basis for further alloy design to increase tolerance to commercial scale processes can then be pursued.

Oxidation evaluation under an aggressive condition of one-hour (h) cycles to 950°C in-air with 10% H_2O to simulate engine exhaust gas conditions indicated low-mass gains through 1,000 one-hour cycles. This was consistent with protective alumina formation by a laboratory-scale arc-cast heat and both commercial heats of AFA5, as can be seen in Figure I.3.2.1.4.1. The presence of a continuous alumina scale was confirmed by cross-sectional analysis (not shown). In contrast, the Fe-35Ni-25Cr wt.%-based commercial cast chromia-forming Alloy HP, which is more costly from a raw material standpoint than AFA5 due to its higher Ni levels, exhibited a transition to oxide scale spallation and mass loss after ~400 one-hour cycles, with extensive mass loss in excess of 35 mg/cm^2 after 1,000 one-hour cycles. Other lower Ni and Cr benchmark commercial cast chromia-forming alloys HK30Nb (e.g., Fe-20Ni-25Cr-based), 1.4826 (e.g., Fe-22Ni-12Cr-based), and CF8C plus (e.g., Fe-11Ni-18Cr-based) exhibited worse oxidation resistance than Alloy HP (data not shown).

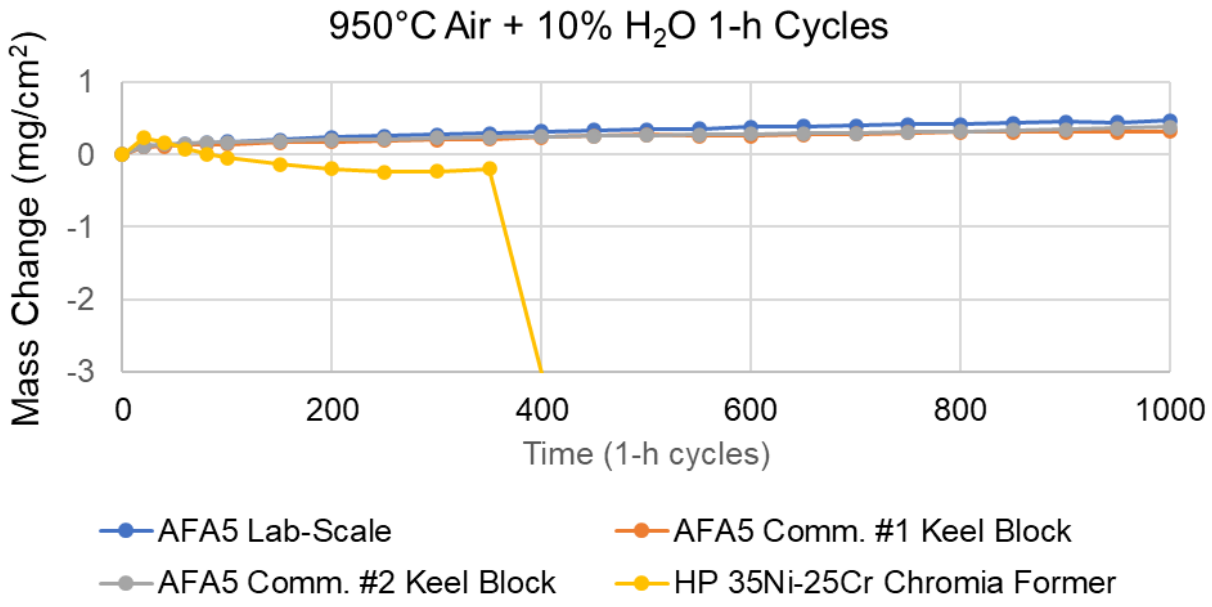

Figure I.3.2.1.4.1. Specific mass change after cyclic oxidation with one-hour cycles at 950°C in-air with 10% H_2O. Source: ORNL.

Mechanical properties of the two commercially produced cast AFA5 heats were compared with the laboratory arc-cast AFA5 alloy and commercial cast chromia-forming alloys HK30Nb, 1.4826, and CF8C. The creep-rupture lives of the alloys tested at 900°C and 50 MPa are summarized in Figure I.3.2.1.4.2. The laboratory-scale heat made via arc-melting achieved more than an 1,100 h creep-rupture life, significantly superior to those of the reference commercial cast chromia-forming stainless steels. The first commercial heat (e.g., Comm. #1), however, exhibited creep-rupture lives between 340-510 h which, although promising, were significantly lower than that of the laboratory-cast AFA5. The first commercial heat did not meet the compositional specification containing 20 wt.% Cr, instead of the 17 wt.% Cr target. This was expected to reduce the amount of $M_{23}C_6$ strengthening precipitates, but may explain its lower creep-rupture life performance. The second commercial heat (e.g., Comm. #2) evaluated in three different product forms (e.g., rod, keel block, plate) that met the targeted 17 wt.% Cr range showed inconsistent creep-rupture lives ranging from ~8 to 780 h. The results indicated that factors other than Cr level are degrading creep behavior relative to the laboratory-scale arc-cast AFA5.

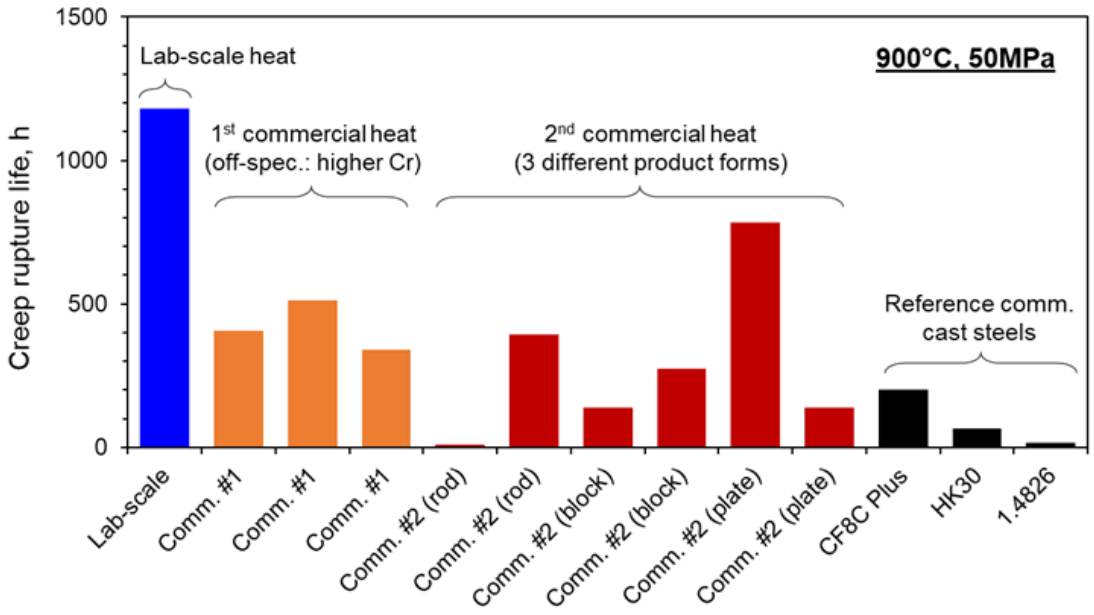

Figure I.3.2.1.4.2. Comparison of creep-rupture lives of cast AFA5 alloys and reference alloys tested at 900°C and 50MPa. Source: ORNL.

One possible explanation for the inconsistent mechanical properties in the trial commercial cast AFA heats is the level of Y. These Y additions were made to all exploratory cast AFA alloys to optimize oxidation resistance. However, past work at ORNL for wrought AFA alloys has observed that elevated levels of Y can result in significantly reduced ductility. This phenomenon is further complicated by the difficulty in controllably adding Y in the ~0.001 to 0.05 wt.% range of interest due to its high O affinity. Creep-rupture life at 900°C and 50 MPa and RT plastic tensile elongation plotted as a function of analyzed Y contents in the heats are shown in Figure I.3.2.1.4.3. The commercial cast alloys showed Y levels in the range of 0.054 to 0.074 wt.%, whereas the laboratory-scale arc-cast AFA5 had 0.04 wt.% Y. As shown in Figure I.3.2.1.4.3(a), the creep-rupture lives generally decreased with increasing Y content. The higher Y content also generally showed lower tensile ductility at RT, as shown in Figure I.3.2.1.4.3(b). Although these trends are not definitive given the limited range of Y contents assessed and considering other composition and cast microstructure variations among the heats, they do support the possibility that high Y levels may degrade mechanical properties. Preparation of several laboratory-scale AFA5 heats containing a range of Y contents, as well as procurement of a trial commercial heat of AFA5 with no Y additions, are currently in progress in order to validate the proposed degradation mechanism, as well as to evaluate the potential impact of reduced Y or Y-free AFA5 on oxidation resistance.

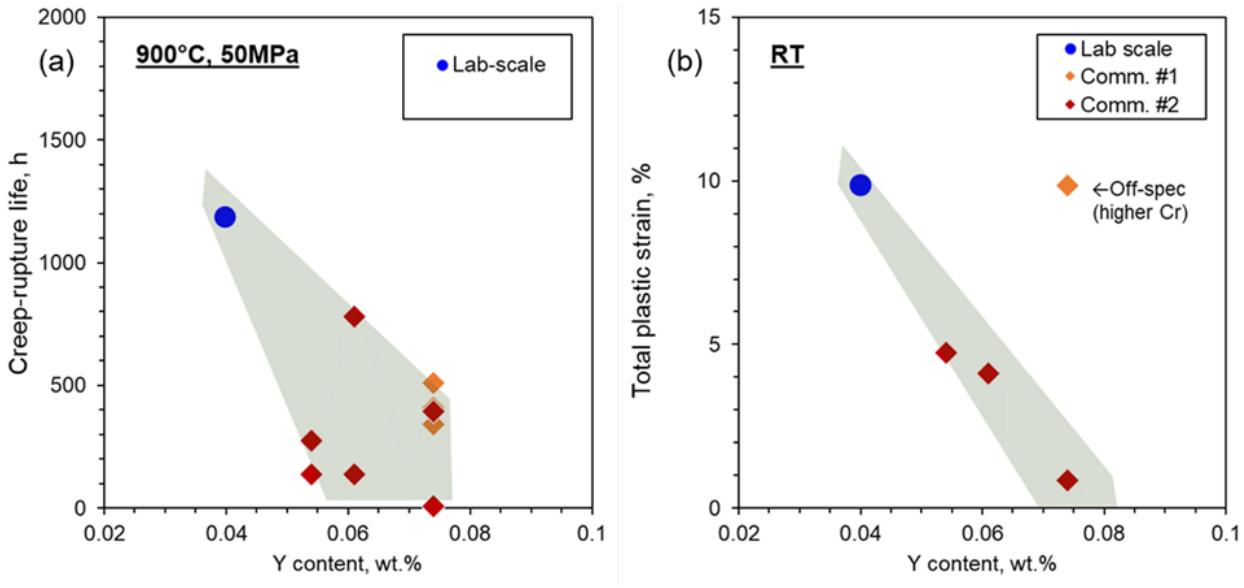

Figure I.3.2.1.4.3. The effect of yttrium (Y) content on: (a) creep-rupture lives tested at 900°C and 50MPa; and (b) RT ductility of cast AFA5 alloys. Source: ORNL.

The other key activity performed in FY 2020 was proof-of-principle work devoted to the development and assessment of ML-assisted approaches to the design of new alloys with greatly improved creep resistance. The goal was to further accelerate the state-of-the-art alloy design approaches based on CALPHAD and ICME used thus far in the project. The effort leverages legacy ORNL creep data for developmental wrought AFA alloys, with 96 unique AFA compositions and 216 creep tests obtained over the past decade where select alloys were tested under multiple creep conditions.

The adopted data analytics workflow is shown in Figure I.3.2.1.4.4. The workflow is divided into two parts: (Part 1) training and evaluation of ML models to identify the highest fidelity models to predict AFA creep resistance based on the ORNL wrought AFA creep dataset and (Part 2) prediction and ranking of the creep resistance of 2,000,000 generated hypothetical AFA compositions to identify candidate alloys with improved creep resistance for experimental validation. In Part 1, the ORNL wrought AFA composition-Larson Miller Parameter (LMP) experimental creep-rupture dataset was augmented by computational thermodynamic calculation of phase equilibria features for each alloy (i.e., phase fraction, phase compositions, and phase supersaturations). This provided an improved mechanistic basis for ML prediction of LMP beyond simple bulk alloy composition correlations. The global dataset was split into a training dataset (e.g., 72% of the available AFA LMP data), a validation dataset (e.g., 18% of the available AFA LMP data) based on the *k*-fold cross-validation (k=5), and a test dataset (e.g., 10% of the available AFA LMP data). Five widely used ML models were trained with different numbers of top-ranking composition and phase equilibria related features determined by maximal information coefficient (MIC) and PCC, respectively: (1) LR; (2) BR; (3) *k*-NN; (4) RF; and (5) SVM regression. The performances of the obtained ML models were then evaluated using the test dataset. The complete dataset was randomly shuffled 10 times, resulting in 10 groups of training-validation-test datasets. The ML training (using the training + validation datasets) and evaluation (using the test dataset that was not included in the training) was performed for each group to minimize uncertainty.

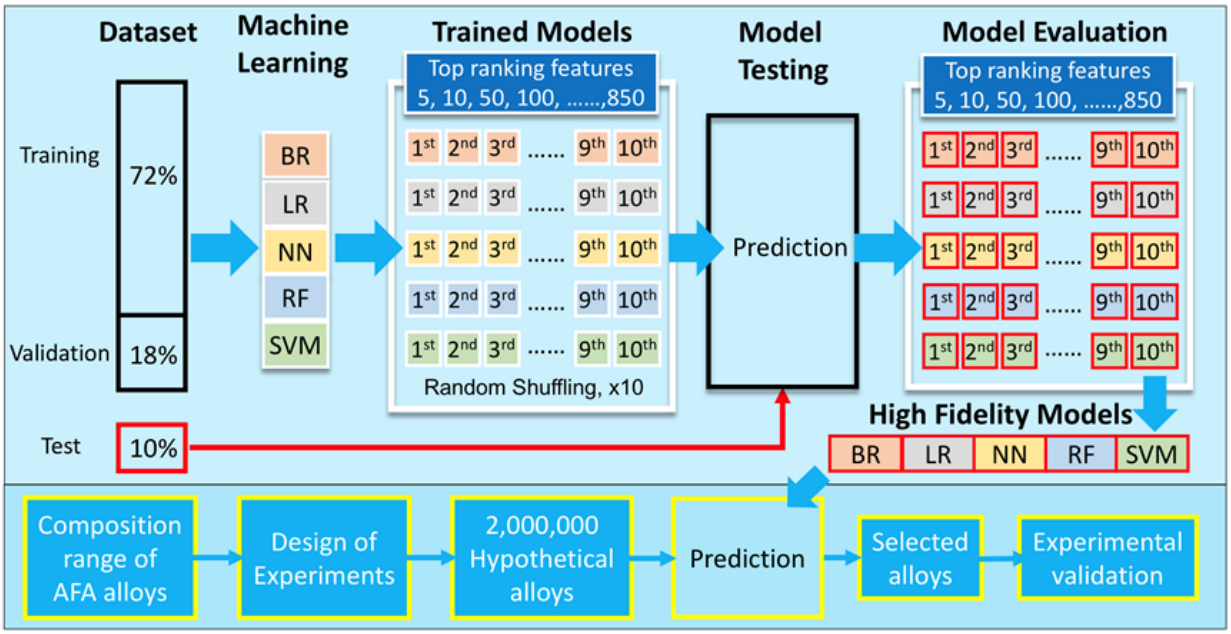

Figure I.3.2.1.4.4. ML-assisted workflow to design AFA alloys with improved creep resistance. Source: ORNL.

Based on the method above, Figure I.3.2.1.4.5(a) and (b) show the accuracy of ML models as a function of the top-ranking features from MIC and PCC in training and evaluation from one of the 10 groups as an example. In ML training, RF, BR, and SVM models exhibited good accuracy (e.g., > 0.8) regardless of the number of features used in training and outperformed NN and LR. The performance of these models in prediction were then further evaluated using the test dataset. As shown in Figure I.3.2.1.4.5(c), RF, BR, and SVM demonstrated very high accuracy in prediction (e.g., ~0.9). For the models trained with features ranked by the PCC correlation analysis, as shown in Figure I.3.2.1.4.5(d), RF outperformed other models with the highest accuracy of 0.9. Both the BR and SVM models exhibited lower accuracy than their counterparts in Figure I.3.2.1.4.5(c). Assessment of the results from 10 groups of datasets revealed that RF, SVM, and BR models trained with the top-200 features from the MIC analysis exhibited the best performance in predicting creep resistance via LMP values. In the next step, RF, SVM, and BR models were trained with the top 200 features from MIC analysis using the complete dataset (e.g., training + validation + test datasets), and these high-fidelity models will be used in FY 2021 to predict the LMP values for 2,000,000 generated hypothetical AFA alloys with the associated computational thermodynamic phase equilibria calculations in Part 2 of the workflow, as can be seen in Figure I.3.2.1.4.4. The predicted LMP values of the 2,000,000 hypothetical AFA alloys will be collated and ranked across the downselected high-fidelity ML models from Part 1 of the workflow, with several top ranked alloys to be manufactured and experimentally evaluated for creep resistance. A second iteration of ML will then be pursued, employing more advanced feature-LMP correlation approaches [5] than the current bivariate (zero-order) MIC and PCC techniques that can potentially consider partial correlation (first-order) to identify and relate the key composition-phase equilibria feature sets that influence creep-rupture life to feed into the ML models for improved LMP predictive capability more effectively.

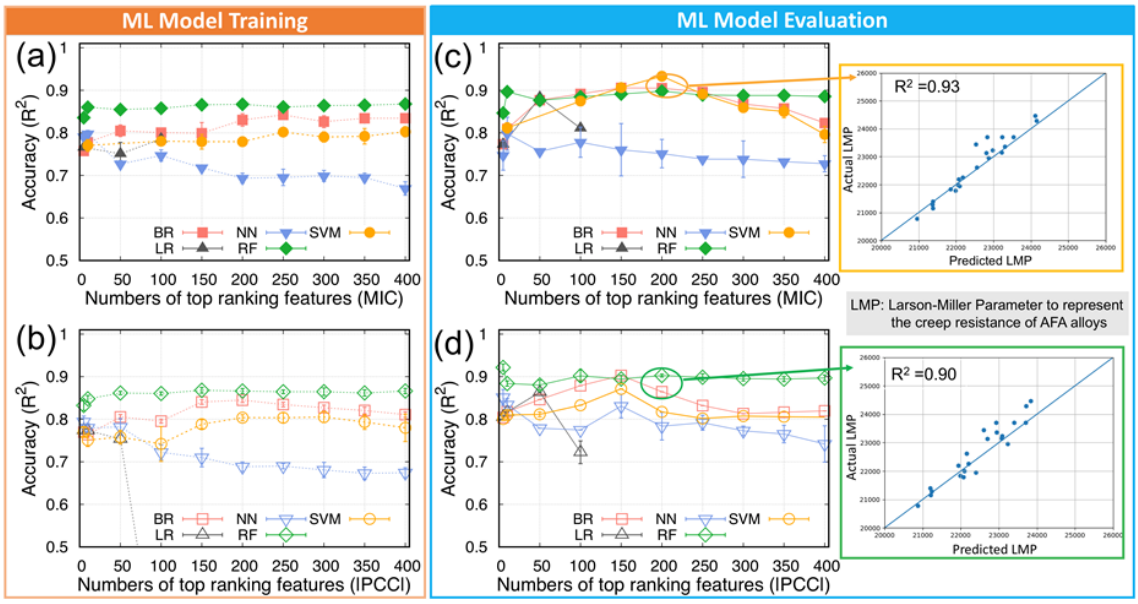

Figure I.3.2.1.4.5. Performance of BR, LR, NN, SVM, and RF models in model training using the training + validation datasets for (a) and (c) MIC and (b) and (d) PCC with evaluations using the test dataset from one of 10 groups. Source: ORNL.

Conclusions

Initial trials of developmental AFA5 alloy cast commercial heats have shown good oxidation resistance, superior to cast chromia-forming benchmark alloys, which is consistent with protective alumina formation. However, mechanical properties in the commercial heats were inconsistent with reduced creep-rupture lives—albeit with still generally better values than those seen with the cast chromia-forming benchmarks—and lower RT tensile ductility as compared to laboratory-scale arc-cast AFA5. The detrimental impacts appear to result, at least in part, from relatively high levels of Y additions in the commercial heats used to optimize oxidation resistance. A systematic series of laboratory-scale arc-cast AFA alloys with varying levels of Y, as well as a commercial Y-free heat of AFA 5, are in progress to confirm this hypothesis and provide a basis for further scale-up of AFA5. New alloy design methodologies for further improvements in creep resistance based on ML techniques have also been initiated. Thus far, the adopted ML-assisted workflow strategy has shown good capability to accurately predict LMP values from the legacy ORNL wrought AFA creep dataset.

Key Publications

1. Peng, J., Y. Yamamoto, M. P. Brady, S. Lee, J. A. Haynes, and D. Shin, 2020, "Uncertainty quantification of machine-learning predicted creep property of alumina-forming austenitic alloys," *JOM*. Available at: https://doi.org/10.1007/s11837-020-04423-x.

References

1. Freedman, D. A., 2009, *Statistical Models: Theory and Practice*. Cambridge University Press, New York, NY, USA.
2. Tipping, M. E., 2001, "Sparse Bayesian learning and the relevance vector machine," *J. Mach. Learn. Res.*, Vol. 1, pp. 211–244.
3. Altman, N. S., 1992, "An introduction to kernel and NN nonparametric regression," *Am. Stat.*, Vol. 46, No. 3, pp. 175–185.
4. Breiman, L., 2001, "Random forests," *Mach. Learn.*, Vol. 45, No. 1, pp. 5–32.
5. Cortes, C., and V. Vapnik, 1995, "Support vector networks," *Mach. Learn.*, Vol. 20, No. 3, pp. 273–297.

Acknowledgements

The authors would like to acknowledge G. A. Cox, D. T. Moore, D. C. Heidel, K. O. Hanson, G. Garner, M. S. Stephens, T. Lowe, T. Jordan, C. S. Hawkins, J. L. Moser, and K. L. Hedrick for their assistance with the experimental work. The authors also acknowledge Drs. A. Devaraj, B. Gwalani, and L. Kovarik for their collaborative support on the detailed alloy microstructure under Thrust 4A; Drs. J. Peng, D. Shin, and S. Lee of ORNL for leading the ML efforts; and Dr. G. Muralidharan of ORNL for his alloy design insights.

I.3.2.1.5 Selective Material Processing to Improve Local Properties (Task 2B2) (Oak Ridge National Laboratory)

Glenn Grant, Co-Principal Investigator
Pacific Northwest National Laboratory
902 Battelle Boulevard
Richland, WA 99352
E-mail: glenn.grant@pnnl.gov

Saumyadeep Jana, Co-Principal Investigator
Pacific Northwest National Laboratory
902 Battelle Boulevard
Richland, WA 99352
E-mail: saumyadeep.jana@pnnl.gov

Jerry L. Gibbs, DOE Technology Manager
U.S. Department of Energy
E-mail: jerry.gibbs@ee.doe.gov

Start Date: July 1, 2019 End Date: September 30, 2021
Project Funding: $300,000 DOE share: $300,000 Non-DOE share: $0

Project Introduction

The project goal is to develop advanced hybrid manufacturing processes to locally improve the performance of parts and assemblies through selective microstructure modification. The concept includes the notion that, in general, strength requirements of an assembly are often driven by a limited number of highly loaded small areas on a complex part. Failure in these areas can drive global component section thickness or strength requirements leading to excessive and unnecessary part weight. If just those selected areas could be improved to the strength, or more importantly the fatigue and toughness requirements, then overall material and/or cost-savings could be achieved.

This concept of applying a secondary process to selective areas to locally improve the properties where they are needed could allow for using lower cost materials to achieve properties that meet or exceed the current state-of-the-art materials. The added cost of the secondary process is offset by the lower base material cost, with the balance designed to achieve a total cost of no more than 10% higher than the current production process.

Selective area modification could also enable new high-performance alloys, local up-alloying, and improve the performance of parts made by advanced manufacturing techniques such as laser or friction additive processes. In many cases, advanced alloys are designed to gain, for instance, higher temperature performance, but often at the expense of another property, such as castability, fracture toughness, or fatigue performance. For these new alloy opportunities, local property improvement through selective processing and engineering could enable economical and better bulk material performance, while still addressing the extreme performance requirements in localized areas.

The project will investigate and demonstrate advanced processes such as friction-stir processing (FSP), cold spray, and others that have the potential to product enhanced properties on local areas of complex propulsion material castings, forgings, or AM materials. FSP, for example, has been shown to provide dramatic improvements in fatigue performance to cast materials across a wide range of alloy systems [1],[2], as observed in Figure I.3.2.1.5.1.

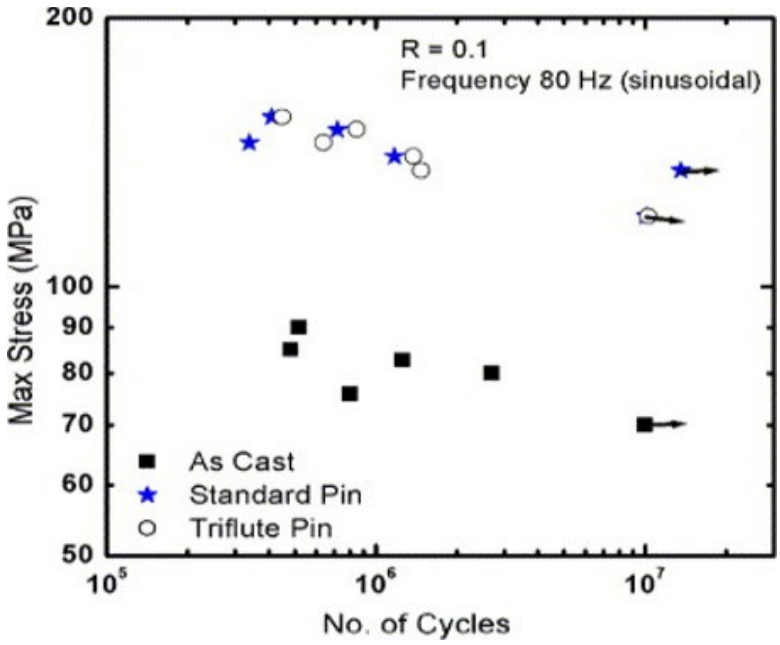

Figure I.3.2.1.5.1. Previous fatigue testing results showing that significant improvements in fatigue performance can be achieved when applying FSP to cast-Al alloys. (2015 DOE VTO Annual Merit Review, "Tailored Materials for Improved Internal Combustion Engine Efficiency," pm048_grant_2015_o.pdf). Source: PNNL.

Local property improvements can be especially important in enabling new high-performance alloys. In some cases, alloys designed for higher temperature operation arrive at their performance through complex alloy chemistries that can show coarse second-phase precipitates or have castability issues leading to near surface casting defects. FSP has been shown to be able to refine microstructure, heal casting defects, improve alloy homogeneity, and produce a wrought microstructure.

Objectives

This project will investigate and demonstrate advanced processes, such as FSP, cold spray, and others that have the potential to produce enhanced properties on local areas of complex powertrain material castings, forgings, or AM materials. In some cases, it is expected that local secondary processing can enable lower cost ferrous and non-ferrous alloys to achieve properties that meet or exceed the current state-of-the-art advanced materials. Additionally, local processing of next-generation materials may push these materials to achieve extraordinary local properties.

Approach

The project's overall approach will be to demonstrate through several solid-phase processing tecniques that local property improvements can contribute to the goals of increased materials strength and performance to enable increased engine efficiency. The approach is divided into the three tasks outlined in Table I.3.2.1.5.1.

Table I.3.2.1.5.1. Project Task Descriptions

	Task Description
Task 1	Demonstrate local property improvements to cast engine alloys.
Task 2	Develop a hybrid manufacturing process where FSP/cold spray is used to locally improve cast, forged, or AM parts composed of newly developed alloy concepts.
Task 3	Develop methods to locally alloy with FSP and/or cold spray to enable high-performance surfaces on lower cost bulk materials.

Task 1 will demonstrate that FSP as a process is capable of improving the microstructure and performance of Al materials in blocks and cylinder heads, as observed in Figure I.3.2.1.5.2(a). This task focuses on improving the local microstructure and performance of areas within a casting that will undergo drilling and threading operations to receive threaded fasteners using the setup shown in Figure I.3.2.1.5.2(b). It will also demonstrate the concept of improving the microstructure, healing potential casting defects near cast-in holes, and provide data on the pullout strength of fasteners threaded in these holes. The concept is to process the region where a threaded hole will be drilled and tapped such that the microstructure created by FSP provides greater reliability for the later fastening operation. The requirement for casting integrity around fastener areas can be a driver of cost forcing complex die design and higher cost alloys.

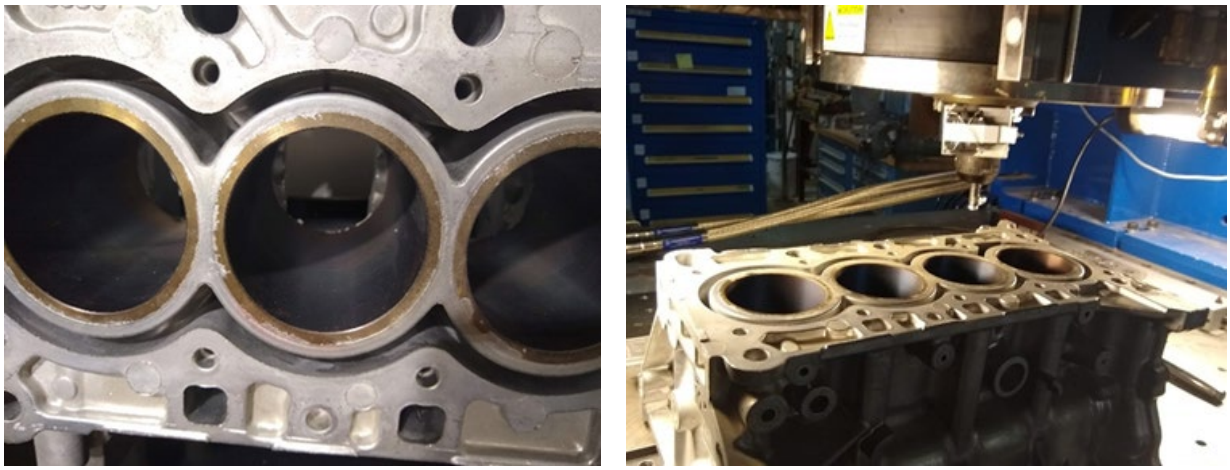

(a) (b)

Figure I.3.2.1.5.2. (a) Deck surface of an as-cast-Al block showing cast-in holes for head bolts above and below the interbore area. (b) Block positioned in FSP machining center showing the processing tool mounted in tool holder. Source: PNNL.

Just prior to drilling and tapping, a secondary operation such as FSP, may be able to allow either lower cost alloys, lower cost die design, or allow new alloys without as much consideration given to alloy fluidity and casting integrity around areas that will be later machined, such as features like threaded holes, an even deck, or sealing surfaces. The deliverables of this task will be reports documenting microstructure, mechanical properties, and threaded fastener pullout strength as a function of processing parameters.

The experimental approach involves casting plates in book molds that have replacable core pins mounted on one wall of the mold as shown in Figure I.3.2.1.5.3(a) and the experimental plan shown in Figure I.3.2.1.5.3(b). These pins are designed to produce coupon-sized examples of the types and geometries of defects seen around cast-in holes, including pin holes, blow outs, and shrinkage pores. In addition, uncoated H13 core pins or used core pins with failed coatings will be used to simulate soldering defects seen when pin coatings break down. Different pins will reflect a variety of conditions, including differing thermal conductivity and coating effects. Castings will be analyzed destructively to see which pin condition(s) creates the defect styles most commonly seen in production, with consultation from vehicle manufacturers. From this information, the pin condition will be downselected and a population of castings will be made with similar conditions.

Half of this population will be subjected to FSP using a narrow tool plunge and retract technique illustrated schematically in Figure I.3.2.1.5.4. This will produce a fine-grained microstructure and heal defects within a narrow region lining the hole. All plates will be drilled and tapped using standard procedures and and cut into individual coupons that can be tested on a bolt retention test rig at PNNL.

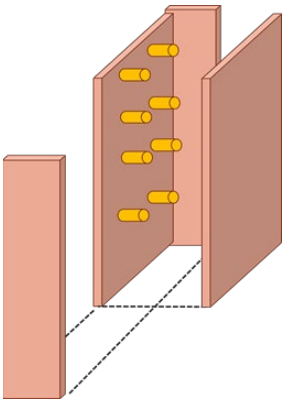

(a)

Experimental Plan:

- Initial trials use a heterogeneous set of core pins to create different defect styles
- Core pins with and without coatings, and core pins of different cooling rates and the potential for shrinkage porosity
- Downselection of core pin with representative defects
- Casting trials with downselected core pins
- Samples are then cut from cast plate for drilling and tapping for fasteners
- A population of plates will be friction-stir processed prior to drilling and tapping to test efficacy of selective processing
- Processed and unporcessed samples will be subjected to bolt retention testing to quantify performance.

(b)

Figure I.3.2.1.5.3. Casting mold design for generating different defects around core pins using (a) a steel book mold with core pins to create cast-in holes and (b) the details of the experimental plan. Source: PNNL.

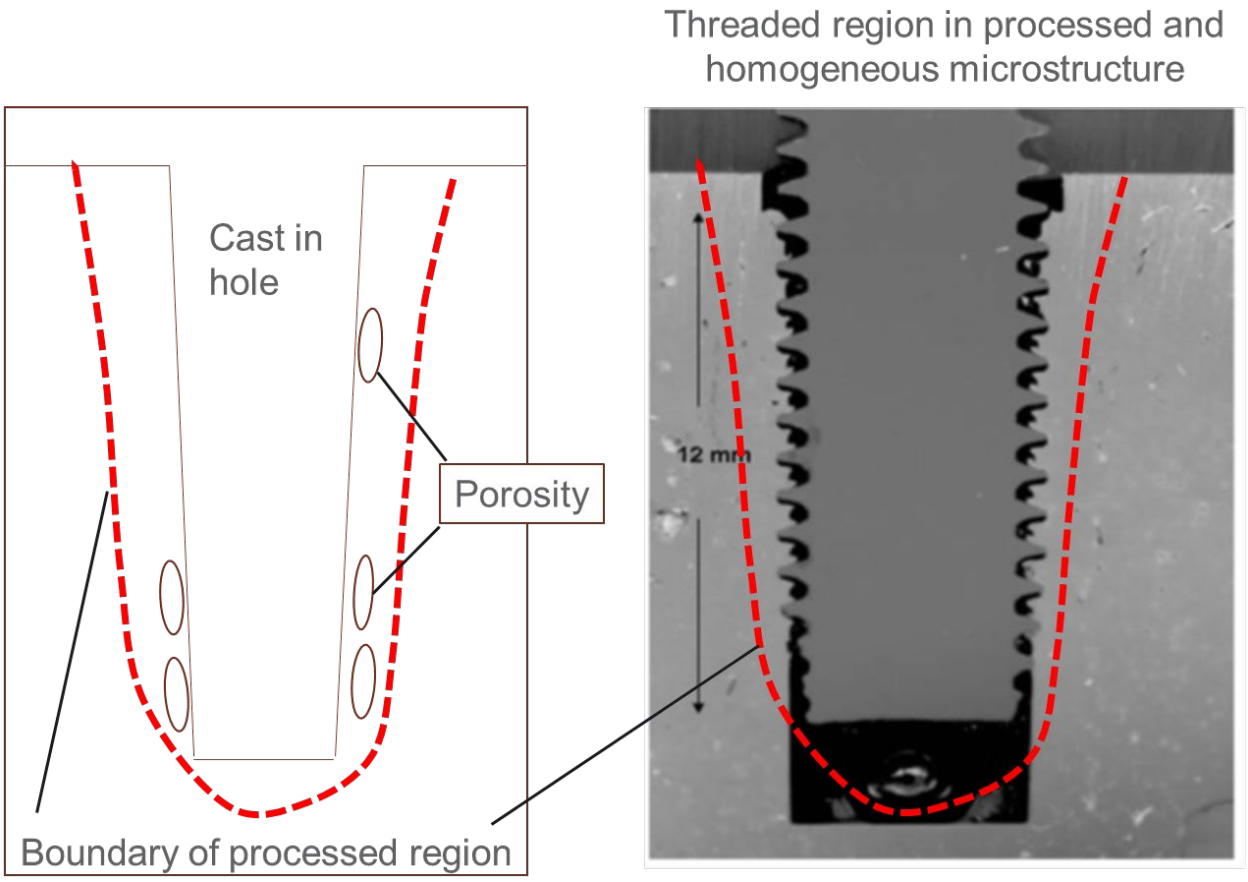

Figure I.3.2.1.5.4. Schematic diagram of FSP region healing porosity in the area later threaded for a fastener. Source: PNNL.

Table I.3.2.1.5.2 outlines applications potentially targeted for this project. FY 2019 and FY 2020 material and application focus areas are highlighted with an asterisk.

Table I.3.2.1.5.2. Targeted Applications of Selective Processing

Application	Technical Barrier	Material	Process Method
***Engine Block and Cylinder Head**	Cast microstructural defects. Head bolt thread failure/pullout from block.	Al	Selective FSP
***Engine Block and Cylinder Head Deck Surface**	Deck surface near cylinder bore, strength/creep at high-temperature.	Al	FSP and selective alloying through FSP
***Cylinder Head**	Head bolt boss strength.	Al	Selective FSP
Piston	Cast or forged piston and ring failures due to overloading/heating associated with advanced combustion schemes.	Al Al MMC	Selective FSP Selective friction adhesive
Crankshaft	Fatigue limit failures in fillet areas and oiling holes.	Steel, cast, and forged	Selective FSP
Shaft (Camshaft and Countershaft)	Flexural fatigue and surface hardness failures.	Steel, cast	Selective FSP Cold spray
Valve and Valve Seat/Bridge Area	Low oxidation resistance and premature failure when operated at high-pressure/temperatures.	Steel	Cold spray and FSP

Beginning in late FY 2020 and early FY 2021, our focus will broaden to include modification of block areas near the top deck sealing surface where local stresses and high-temperature can cause issues with creep and mechanical overload. In addition, several areas focusing on Al pistons will be considered for selective property improvement. This work will be the focus of a CRADA effort under negotiation for FY 2021.

As advanced cast alloys are developed by ORNL and others. Components like pistons may require variable microstructures and local properties to optimize performance. For example, local properties of piston bowl rims or top ring lands may require additional alloy homogenization or microstructure optimization to achieve higher properties than the bulk material in order to avoid premature failure due to fatigue or local softening. In another example, it is anticipated that FSP may be a high-value-added processing method for local areas of parts made by conventional casting/forging methods, or even advanced techniques like laser AM to improve a common shortcoming of these materials with respect to anisotropic fracture toughness and fatigue strength. We anticipate the task will be highly coordinated with ORNL and result in development and delivery of new materials that are hybrids of several advanced manufacturing processes.

In out years, the project will focus on the notion of using selective processing to create local compositional gradients or local alloying by cold spray and FSP. These two solid-phase alloying processes are currently being investigated in programs at PNNL as a way to produce local alloy chemistries and functionally graded materials. We propose to leverage this work and develop multi-material structures, different from coatings, that can produce high-performance local regions on potentially lower cost bulk substrates. High peak cylinder pressure piston tops on lower cost Al pistons are one example of the concept.

Results

Project work during FY 2020 focused on Task 1, which involved demonstration of local property improvements to cast engine alloys. Efforts focused on a demonstration of defect elimination by FSP at the coupon-level. Efforts were also directed at casting mold design for molds with replaceable core pins and towards upgrading out-threaded fastener pullout strength test equipment.

COVID-19 restrictions significantly slowed progress during the latter half of FY 2020, thereby preventing greater progress on the casting trials due to limited access to laboratory casting equipment. However, FSP trials were able to be completed on at least one alloy casting without core pin defects. This work has demonstrated defect healing and porosity elimination by FSP in flat plate castings of a strontium-modified A356 alloy. These book mold castings have small secondary dendrite arm spacing and are representative of the kinds of casting microstructures seen in production cylinder heads. These regions were processed using a tool pin producing a processed depth of approximately 0.22 in., as can be seen in Figure I.3.2.1.5.5. The macrograph shows the processed region free of volumetric indication. Adjacent to the processed region, several areas of porosity can be observed. The hydrostatic state of stress and complete dynamic recrystallization induced by FSP closes porosity.

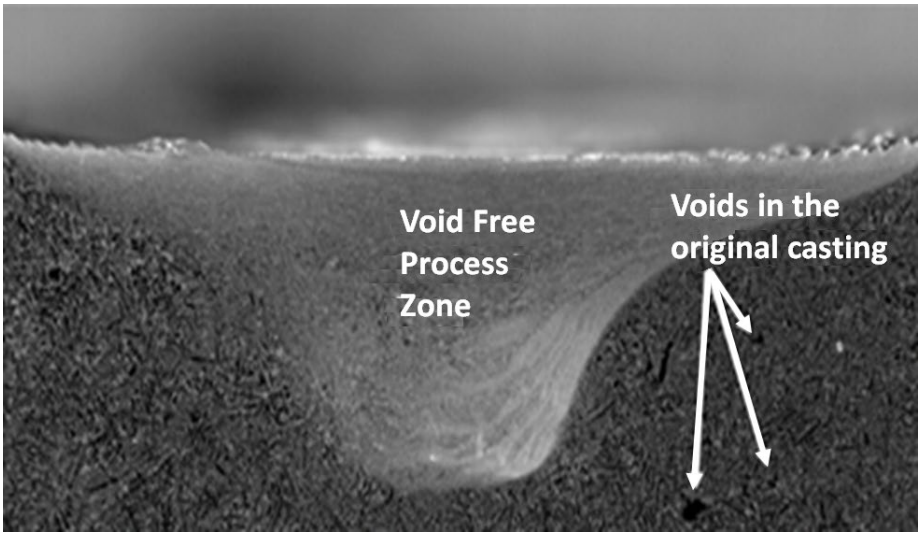

Figure I.3.2.1.5.5. Macrograph cross-section of an FSP processed region showing complete healing of casting porosity in the processed region. Source: PNNL.

The project is also obtaining a quantity of Alloy 380 and Alloy 319, which will be the alloys used in the cast-in hole trials. Also, during FY 2020, work continued modifying a test rig to test the pullout strength of a threaded fastener. The rig shown in Figure I.3.2.1.5.6 uses an RS Technologies Torque-Tension measuring system with an Altas-Copco Nutrunner electric-drive torque wrench mounted in a frame that captures a small section of Al casting in which there is a threaded hole. A bolt is inserted in the threaded hole and the instrumented torque wrench records the torque required to either fail the fastener or the threads in the casting. The frame also incorporates a load cell so that the clamp force can be recorded. This device is used to quantify the effects of casting defects near threaded holes and will be used to quantify the advantage of producing a friction processed region in the area that will be threaded for a fastener.

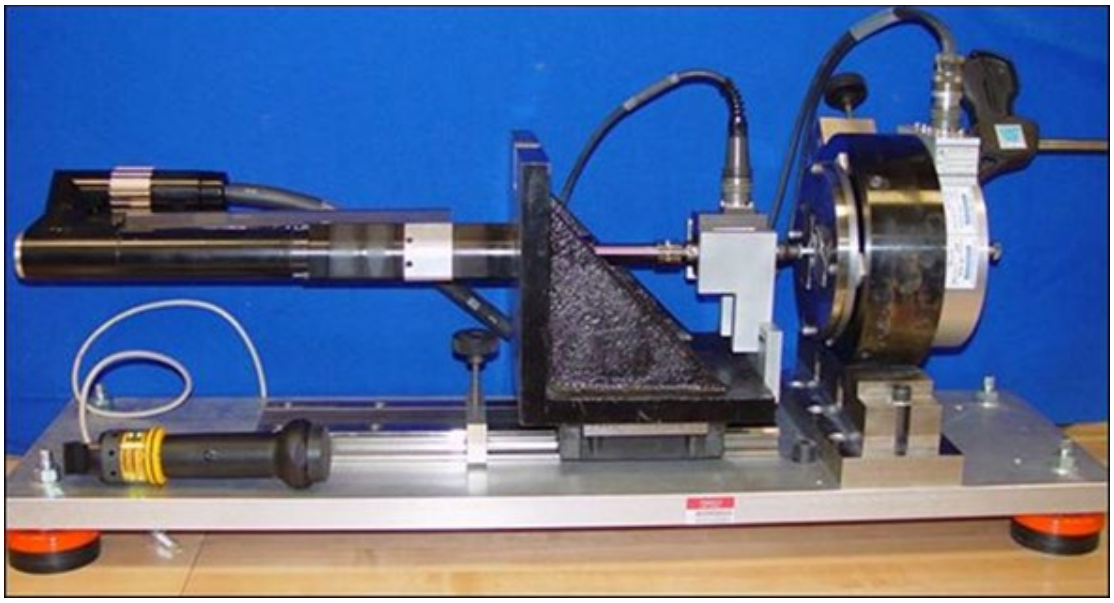

Figure I.3.2.1.5.6. Torque-Tension Measuring rig used to quantify the thread pullout performance of an FSP region. Source: PNNL.

Conclusions

During FY 2020, FSP trials were completed on at least one alloy casting without core pin defects. This demonstrated defect healing and porosity elimination by FSP in flat plate castings of a strontium-modified A356 alloy. Casting dies were also designed to allow the casting of coupons that will display different types of casting defects around core pins. These coupons will be subjected to FSP and tested for pullout strength of a threaded fastener. During FY 2020, a test rig was also modified for measuring threaded fastener pullout strength in these specific geometries. Core pin castings trials will begin in FY 2021.

References

1. Jana, S., R. S. Mishra, J. B. Baumann, and G. J. Grant, 2010, "Effect of FSP on fatigue behavior of an investment cast-Al-7Si-0.6 Mg alloy," *Acta Mater.*, Vol. 58, No. 3, pp. 989–1003.

2. Jana, S., R. S. Mishra, and G. J. Grant, 2016. Friction-Stir Casting Modification for Enhanced Structural Efficiency: A Volume in the Friction-Stir Welding and Processing Book Series, Elsevier, Oxford, UK.

Acknowledgements

The project has benefitted greatly from discussions with B. Carlson and Q. Wang from GM R&D. In addition, GM provided experimental materials including unmachined four-cylinder blocks, crankshafts, and base alloy materials.

I.3.3 Additive Manufacturing – Thrust 3

I.3.3.1 Development of Higher Temperature Alloys for Additive Manufacturing (3A/3B)

I.3.3.1.1 Fundamental Development of Lightweight Alloys for Additive Manufacturing (Task 3A1) (Oak Ridge National Laboratory)

Amit Shyam, Co-Principal Investigator
Oak Ridge National Laboratory
1 Bethel Valley Road
Oak Ridge, TN 37831
E-mail: shyama@ornl.gov

Alex Plotkowski, Co-Principal Investigator
Oak Ridge National Laboratory
1 Bethel Valley Road
Oak Ridge, TN 37831
E-mail: plotkowskiaj@ornl.gov

Jerry L. Gibbs, DOE Technology Manager
U.S. Department of Energy
E-mail: jerry.gibbs@ee.doe.gov

Start Date: October 1, 2018 End Date: September 30, 2023
Project Funding: $425,000 DOE share: $425,000 Non-DOE share: $0

Project Introduction

Automotive companies look to apply the immense interest and technical potential for AM in powertrain applications. Al alloys with improved specific strength are an obvious starting point for applying AM to lightweight engine applications. The primary focus in this task are higher temperature Al alloys in the following families: (1) precipitation-hardened alloys (e.g., Al-Cu-Mn-Zr, Al-Cu-Mn-Zr-type alloys); (2) dispersion-hardened alloys (Al-Ce-Mn); and (3) a combination of the two concepts (e.g., ACMZ + Ce). The primary applications are higher temperature, lightweight powertrain components, such as cylinder heads, pistons, turbochargers, etc. Smaller-bore pistons are a specific target application for AM to enable higher-efficiency internal combustion engines. Higher power density, lightweight, and boosted engine components will be targeted with the newly developed alloys and AM processes.

Objectives

The objective is to fabricate Al alloys via laser AM with yield strengths over the temperature range of 250–400°C, which exceed existing high-volume wrought commercial Al piston alloys by at least 35% while maintaining adequate ductility, fatigue resistance, and 250°C strength for lightweight piston applications.

Approach

A number of studies using laser powder bed AM were performed in FY 2020 to investigate AM of new ORNL-designed Al alloys, including alloys in the Al-Ce-Mn, Al-Cu-Ce, Al-Ce-Ni, and ACMZ systems. The research approach included advanced characterization of the alloy microstructures, including high-resolution scanning transmission electron microscopy (HR-STEM) and APT, measurement of mechanical properties (e.g., tensile and creep) at elevated temperatures, and thermodynamic and kinetics modeling. These activities resulted in numerous key scientific findings and the publication of three peer-reviewed journal articles in FY 2020. Additional publications are in progress and planned for FY 2021. A number of additional new alloys have been identified to expand on existing research. Fabrication of these alloys and subsequent characterization is planned for FY 2021.

Results

At the beginning of FY 2020, two manuscripts were completed and submitted related to the project team's research on AM of an Al-10Ce-8Mn weight percent (wt.%) alloy (see Key Publications section). Key results of the first study published in *Acta Materialia* [1] are shown in Figure I.3.3.1.1.1. The high solidification rates in the AM were found to produce unique metastable microstructures in the AM material, as well as unique solid-state phase transformations during thermal exposure. The heterogeneous microstructure was characterized to identify specific non-equilibrium phases and to relate the mechanical properties to the microstructure and processing of the alloy. The alloy was found to have exceptional high-temperature properties, particularly following long-term thermal exposure (e.g., 200 hours [h] at 400°C) and compared favorably with high-performing wrought Al alloys, such as Alloy 2618.

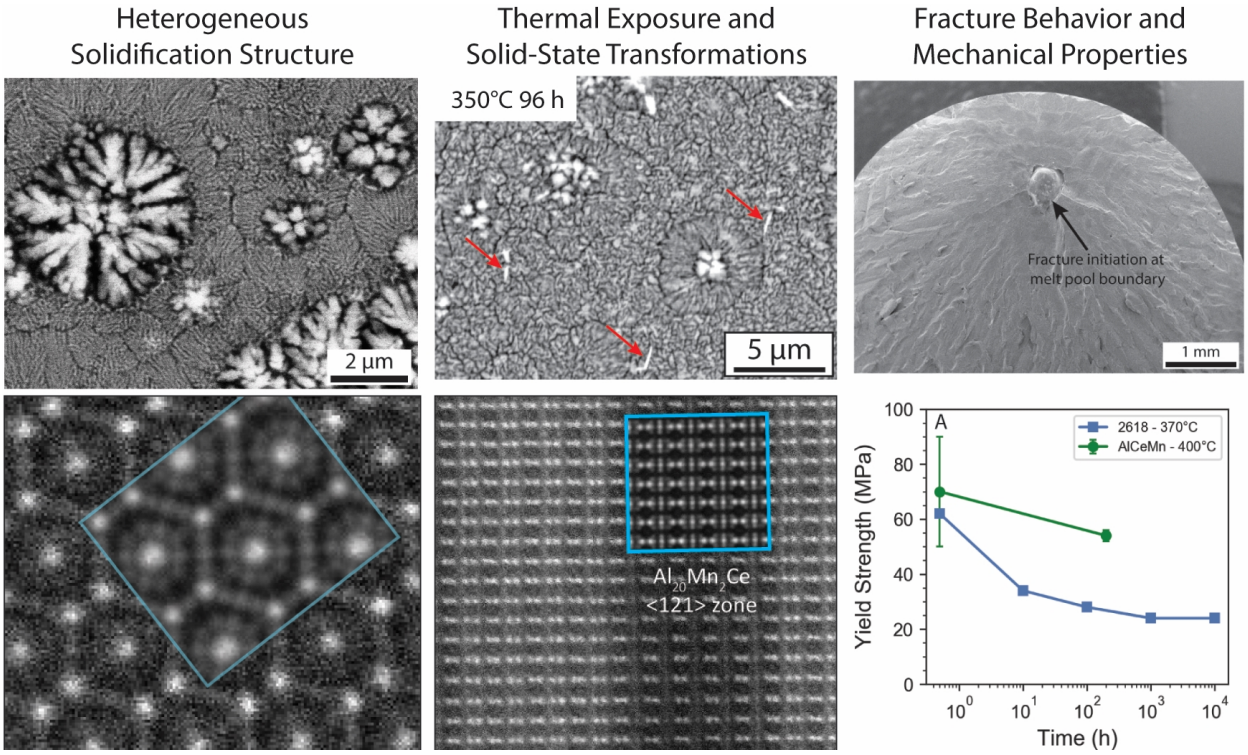

Figure I.3.3.1.1.1. Key results of a study of the microstructure and mechanical properties of an AM Al-10Ce-8Mn alloy, showing the heterogeneous solidification microstructure, examples of atomic-scale STEM of non-equilibrium intermetallic phases, a representative fracture surface showing initiation at a melt pool boundary, and yield at 400°C as a function thermal exposure time compared to Alloy 2618. Source: ORNL.

To help further understand the non-equilibrium phase formation during solidification and thermal exposure of the AM Al-Ce-Mn alloy microstructure, the initial work was followed by a casting study of similar compositions. Through these experiments and a series of targeted DFT calculations, the project team was able to refine the thermodynamic database for the Al-Ce-Mn system. The refined thermodynamic database was then used to perform nucleation-rate calculations for key ternary intermetallic compounds as a function of local undercooling, as observed in Figure I.3.3.1.1.2. These calculations showed that the high surface energy of the equilibrium phase (e.g., $Al_{10}Mn_2Ce$) allowed its nucleation to be suppressed for a wide range of compositions when the cooling rate and, therefore, the undercooling are high. Instead, for high cooling rates, the $Al_{20}Mn_2Ce$ metastable intermetallic phase is favored. These results helped to explain the complex metastable phase formation observed in the AM samples and why the resulting microstructures are so different from conventional processing. These results were published this year in the *Journal of Alloys and Compounds* [2].

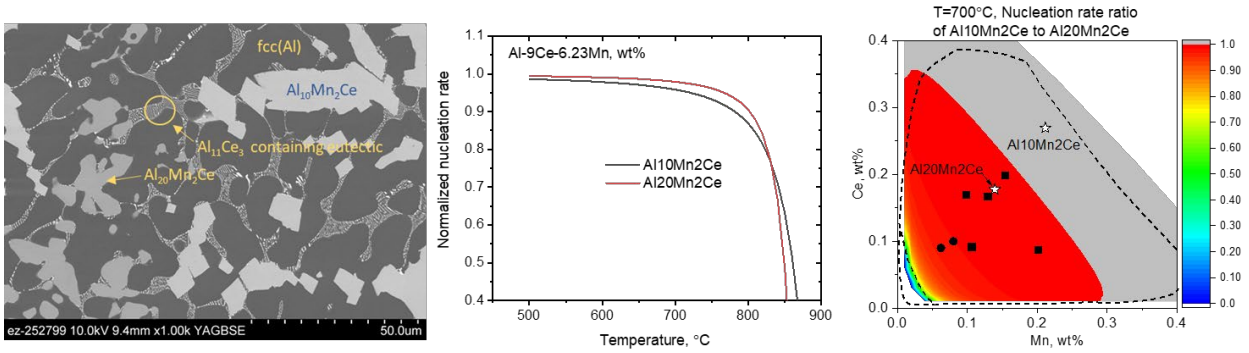

(a) (b) (c)

Figure I.3.3.1.1.2. Summary of key results for the thermodynamic assessment of the Al-Ce-Mn system showing: (a) the cast microstructure for an Al-Ce-Mn alloy with complex nucleation competition between the $Al_{10}Mn_2Ce$ and $Al_{20}Mn_2Ce$ primary intermetallic phases; (b) a comparison of the computed nucleation rates for these two ternary intermetallics as a function of nucleation temperature; and (c) the Al-rich corner of the ternary phase diagram showing the increased composition range in which non-equilibrium nucleation of the $Al_{20}Mn_2Ce$ intermetallic is favored for a nucleation temperature of 700°C. Source: ORNL.

Significant characterization and analysis were performed for an additively manufactured ACMZ alloy, as can be seen in Figure I.3.3.1.1.3. Compared to similar cast compositions, the microstructure of this AM ACMZ shows a highly refined eutectic solidification microstructure consisting of fcc-Al and Al_2Cu θ intermetallic particles. The θ phase exhibits a much finer and more uniform distribution than for similar alloy compositions when cast, in which case these intermetallic particles are found primarily along grain boundaries and have been shown to be the limiting factor for cast alloy ductility [3]. The as-fabricated AM samples also exhibited an extremely fine distribution of θ' precipitated within the fcc-Al matrix, suggesting an effective *in situ* heat-treatment caused by the rapid and repeated thermal cycles during the layer-by-layer powder bed laser AM process. These differences in microstructure result in an increase in both strength and ductility compared to peak-aged cast ACMZ alloys, and a similar retention of properties after prolonged thermal exposure. A manuscript detailing these results was published this year in *Materialia* [4].

The microstructure of the AM alloys, including ACMZ, were also analyzed using APT to evaluate the nanoscale distribution of elements within and around different phases in the unique, rapidly solidified microstructures. These APT analyses of as-fabricated ACMZ samples, which can be seen in Figure I.3.3.1.1.4, revealed a slight enrichment of 0.2 at.% Mn and 0.1 at.% Zr inside the θ', but no segregation at the matrix/θ' interfaces. However, a matrix composition of ~0.3 at.% Zr indicated significant Zr supersaturation and, thus, a strong potential for Al_3Zr precipitation upon aging. If this occurs, then the Al_3Zr would likely provide additional strengthening during high-temperature exposures. Similar data was collected for the Al-Ce-Cu- and Al-Ce-Ni-based alloys to aid in phase identification and identify the segregation of specific elements between phases. Additional publications, including these results to help understand phase stability and phase transformations during AM, are planned for FY 2021.

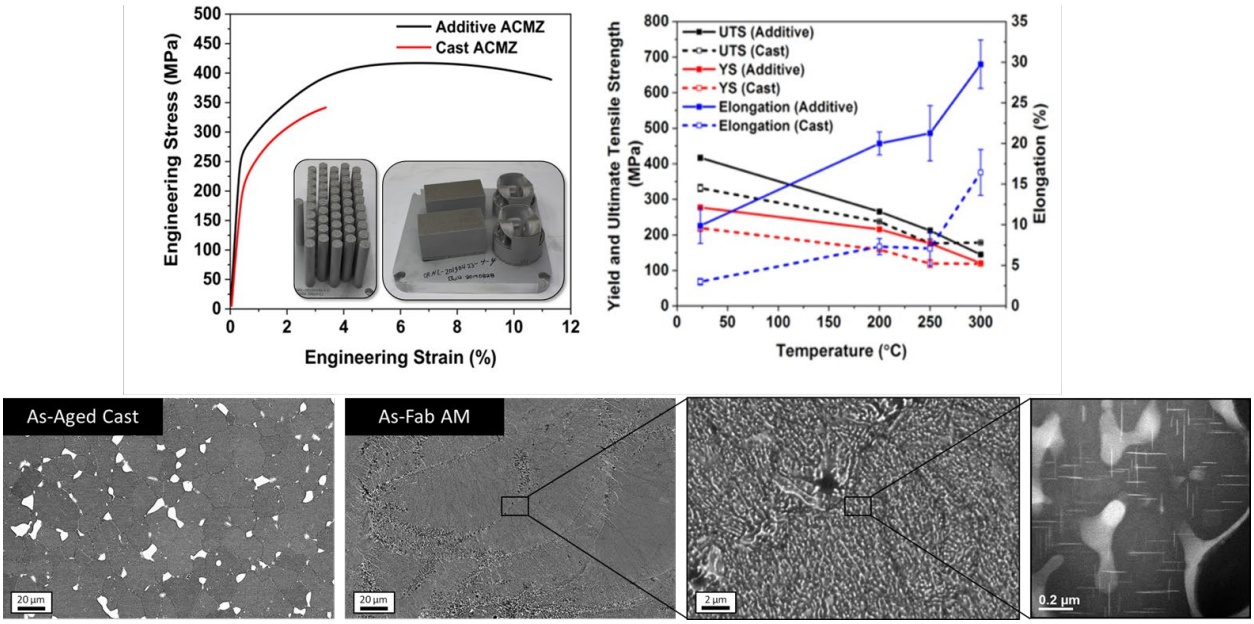

Figure I.3.3.1.1.3. Representative microstructural characterization of an AM ACMZ alloy showing a highly refined solidification microstructure as compared to a similar cast alloy. Representative tensile curves show that the AM alloy exhibits both higher strength and ductility than the cast counterpart, and retains a high fraction of these properties following prolonged thermal exposure (up to 200 h at 300°C). Source: ORNL.

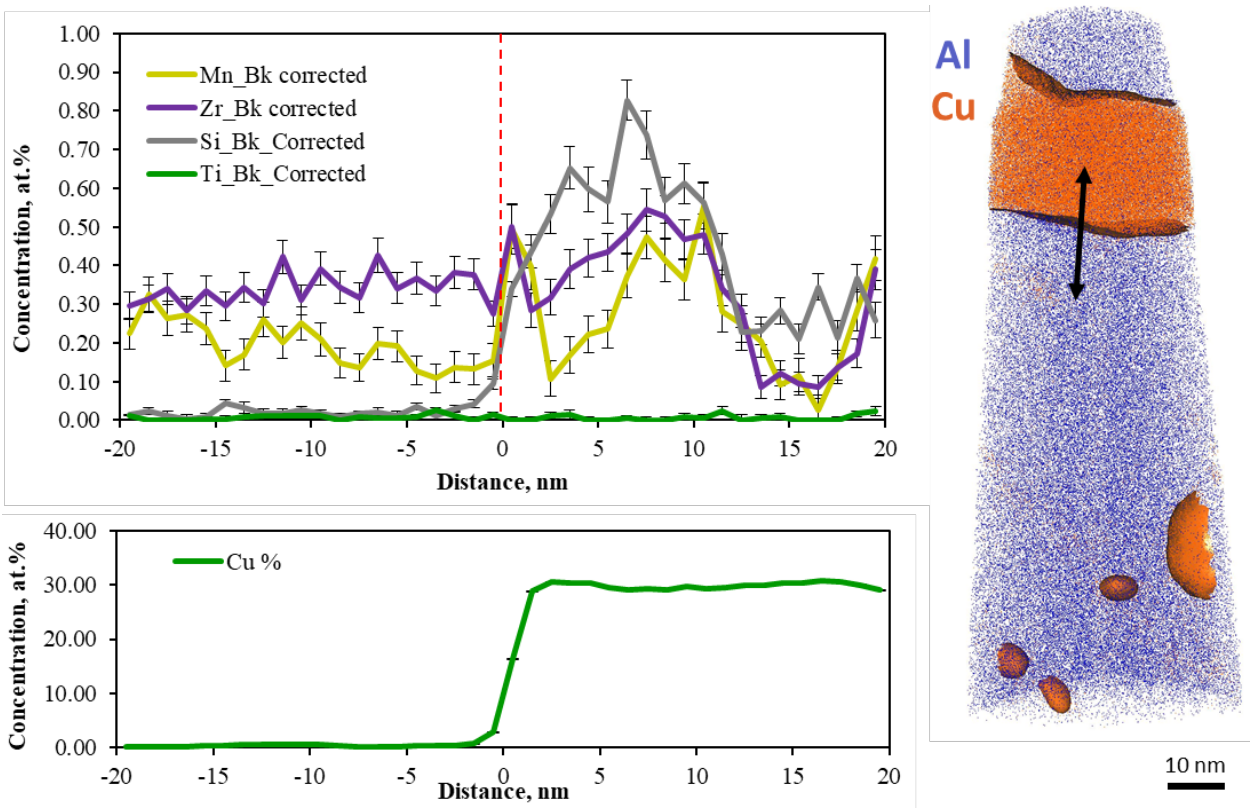

Figure I.3.3.1.1.4. APT of the as-fabricated AM ACMZ microstructure. The APT reconstruction and composition profile across an interface between the fcc-Al matrix and a Cu-rich intermetallic. Although little segregation is observed to the interface, significant Zr supersaturation is shown in the Al matrix. Source: ORNL.

The project team has also investigated the high-temperature properties of a promising AM Al-Ce-Ni-Mn alloy. Stress-jump creep tests were performed at multiple stresses at the same temperature. Creep load was increased when a steady state creep rate was measured at that stress level. Creep data collected for the AM Al-Ce-Ni-Mn following a 450°C, 2 h stress relief anneal are summarized in Figure I.3.3.1.1.5 at a few representative temperatures and compared with similar data for cast ACMZ and RR350 alloys. The minimum creep rates are well below the already very high-performing cast ACMZ and RR350 cylinder head alloys, and diffusional creep appears to be absent, despite grain refinement during the additive process. Thus, preliminary creep testing indicates that some of the printed Al alloys appear to have remarkable creep resistance at quite extreme temperatures for Al-based alloys. This will be studied in more detail in FY 2021.

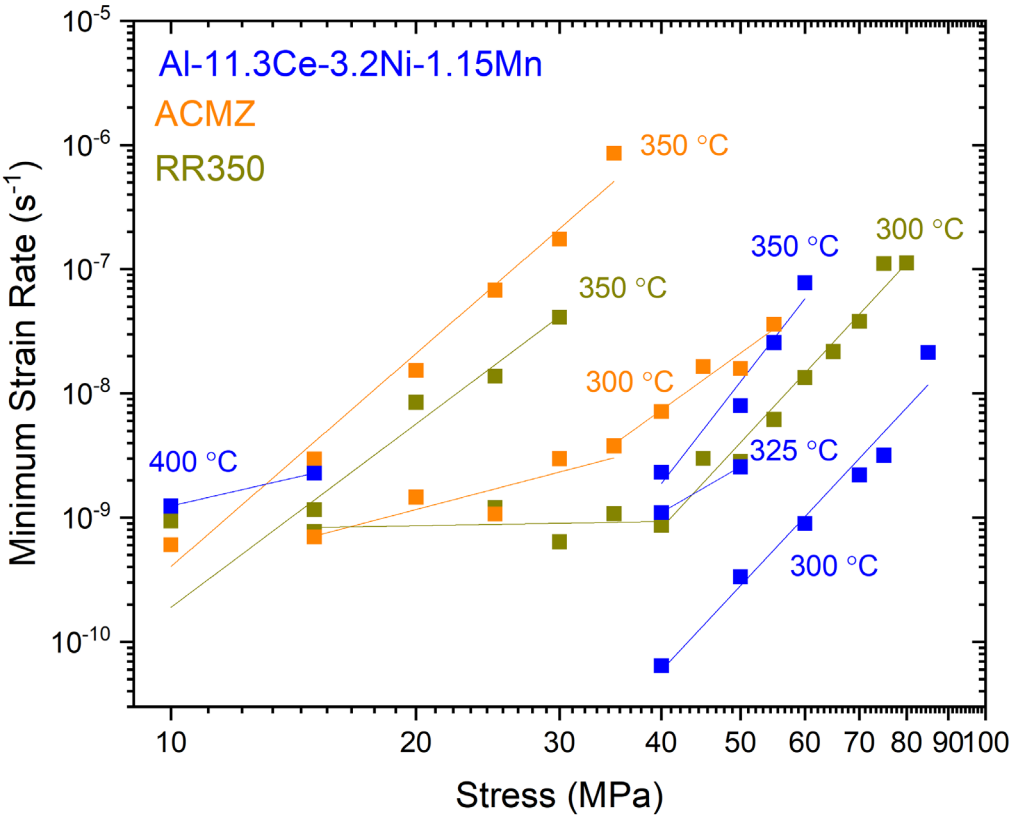

Figure I.3.3.1.1.5. Minimum strain-rate for tensile creep tests as a function of applied stress and temperature for the AM Al-11.3Ce-3.2Ni-1.5Mn (wt.%) alloy as compared to cast and aged ACMZ and RR350 cast alloys. Source: ORNL.

Finally, several new alloys were designed and procured for AM. Originally, four alloy compositions were selected and planned for fabrication before the end of FY 2020. However, delays in procurement caused by COVID-19 have postponed fabrication. In particular, the alloy supplier was not able to procure sufficient quantities of Er and Hf to cast an alloy intended for investigating the formation of core-shell $L1_2$ precipitates. Within the last few weeks prior to this report's writing, the project team decided to cancel the order for that alloy and replace it with a different alloy with more-conventional alloy additions. A eutectic Al-Cu variant of ACMZ was instead selected. The team's prior research on printed ACMZ has shown that the extremely refined eutectic Al_2Cu θ intermetallic structure in the AM state enables the alloy to retain ductility where a similar volume fraction of θ in a cast structure limits ductility due to the size and location of the intermetallic particles. There is, therefore, an opportunity to investigate extremely high-volume fractions of finely dispersed reinforcing intermetallic phases by printing alloys with compositions near their eutectic points. The final alloy was therefore selected to investigate the potential of this alloy design philosophy for the Al-Cu binary eutectic reaction, as described in Table I.3.3.1.1.1.

Table I.3.3.1.1.1. Summary of New Al Alloys and Status for AM

Alloy Designation	Status	Al	Cu	Ce	Ni	Mn	Zr	Er	Hf	Si	Fe
FY 2020-01	Atomized, ready for AM	Bal.	9	6	-	-	3	-	-	<0.1	<0.1
~~FY 2020-02~~	Cancelled	~~Bal.~~	~~9~~	~~6~~	-	-	~~1~~	~~1~~	~~1~~	~~<0.1~~	~~<0.1~~
FY 2020-03	Cast, ready for atomization	Bal.	-	9	4	0.5	1	-	-	<0.1	<0.1
FY 2020-04	Atomized, ready for AM	Bal.	15	-	-	0.5	1	-	-	<0.1	<0.1
FY 2020-05	Purchase orders in progress	Bal.	32.7	-	-	0.5	1	-	-	<0.1	<0.1

Overall, two of the project team's original alloy compositions have been successfully atomized and screened and are ready for fabrication. The third alloy has been cast and is ready for atomization. To replace the cancelled alloy, the project team is in the process of finalizing a purchase order for alloying. The lead time is expected to be approximately 1-2 weeks for casting of the final alloy. The schedule currently places AM of all alloys in the first quarter of FY 2021.

Conclusions

The research in this subtask during FY 2020 has shown that AM of Al alloys offers the potential to form novel and beneficial microstructures that cannot be achieved through conventional processing. These microstructures, formed as a result of the very high cooling and solidification rates characteristic of laser powder bed AM of Al alloys, potentially offer significant benefits in terms of mechanical properties, especially for high-temperature applications. A fundamental understanding of phase-transformation phenomena that result within these microstructures and the relationships between microstructure evolution and mechanical properties is critical for the development of new alloys that use these mechanisms to achieve unprecedented performance in Al alloys. The research in this task resulted in several new alloy compositions that are well-suited for AM and exhibit exciting mechanical properties that are competitive with, or better than, existing high-performance Al alloys used in powertrain applications. Advanced characterization, additional experiments, and modeling of thermodynamics and kinetics of phase transformations in these alloys has helped us understand the critical mechanisms and non-equilibrium behavior of the alloys during processing and the consequences of these unique microstructural features on alloy properties. Based on this information, the project team can make better decisions about appropriate chemistry selection for the next-generation of Al alloys for AM.

Key Publications

1. Plotkowski, A., K. Sisco, S. Bahl, A. Shyam, Y. Yang, L. Allard, P. Nandwana, A. Marquez Rossy, and R. R. Dehoff, 2020, "Microstructure and properties of a high-temperature Al-Ce-Mn alloy produced by additive manufacturing," *Acta Mater.*, Vol. 196, pp. 595–608.
2. Yang, Y., S. Bahl, K. Sisco, M. Lance, D. Shin, A. Shyam, A. Plotkowski, and R. R. Dehoff, 2020, "Primary solidification of ternary compounds in Al-rich Al-Ce-Mn alloys," *J. Alloys Compd.*, Vol. 844, Art. 156048.
3. Shyam, A., A. Plotkowski, S. Bahl, K. Sisco, L. F. Allard, Y. Yang, J. A. Haynes, and R. R. Dehoff, 2020, "An additively manufactured Al-Cu-Mn-Zr alloy microstructure and tensile mechanical properties," *Materialia*, Vol. 12, Art. 100758.
4. Bahl, S., *et al.*, 2021, "Strain-rate sensitivity in an additively manufactured Al-Cu-Ce alloys," in preparation.
5. Plotkowski, A., *et al.*, 2021, "Additive manufacturing of Al-Cu-Ce alloys," in preparation.

References

1. Plotkowski, A., K. Sisco, S. Bahl, A. Shyam, Y. Yang, L. Allard, P. Nandwana, A. Marquez Rossy, and R. R. Dehoff, 2020, "Microstructure and properties of a high-temperature Al-Ce-Mn alloy produced by additive manufacturing," *Acta Mater.*, Vol. 196, pp. 595–608.
2. Yang, Y., S. Bahl, K. Sisco, M. Lance, D. Shin, A. Shyam, A. Plotkowski, and R. R. Dehoff, 2020, "Primary solidification of ternary compounds in Al-rich Al-Ce-Mn alloys," *J. Alloys Compd*., Vol. 844, Art. 156048.
3. Bahl, S., X. Hu, E. Hoar, J. Cheng, J. A. Haynes, and A. Shyam, 2020, "Effect of copper content on the tensile elongation of Al-Cu-Mn-Zr alloys: Experiments and finite element simulations," *Mater. Sci. Eng. A*, Vol. 772, Art. 138801.
4. Shyam, A., A. Plotkowski, S. Bahl, K. Sisco, L. F. Allard, Y. Yang, J. A. Haynes, and R. R. Dehoff, 2020, "An additively manufactured Al-Cu-Mn-Zr alloy microstructure and tensile mechanical properties," *Materialia*, Vol. 12, Art. 100758.

Acknowledgements

The authors acknowledge the contributions of the ORNL team members for this subtask: R. Dehoff, S. Bahl, R. Michi, Y. Yang, and L. Allard.

I.3.3.1.2 Hybrid Manufacturing of Additive Manufactured Interpenetrating Phase Composites (AMIPC) (Task 3A2) (Oak Ridge National Laboratory)

Derek Splitter, Principal Investigator
Oak Ridge National Laboratory
2360 Cherahala Boulevard
Knoxville, TN 37932
E-mail: splitterda@ornl.gov

Jerry L. Gibbs, DOE Technology Manager
U.S. Department of Energy
E-mail: jerry.gibbs@ee.doe.gov

Start Date: October 1, 2018 End Date: September 30, 2023
Project Funding: $220,000 DOE share: $220,000 Non-DOE share: $0

Project Introduction

This work seeks to understand how the combination of metal AM with metal casting via a new process termed "PrintCasting" can be used to create multi-material composite structures that increase energy absorption and prevent failures of the ring-land area of automotive pistons without significantly affecting overall weight or thermal conductivity of the component. A key advantage of PrintCasting is that it leverages AM control over the mesostructure of the reinforcing phase. Therefore, the geometry and spatial distribution of the reinforcing constituent can be precisely controlled to create composites with geometries that realize improved energy absorbing behavior, as well as other tailored properties. It has been demonstrated that high levels of energy absorption can be achieved by creating a reinforcement geometry that converts the applied tensile load into local compression of the more-brittle cast matrix. The printed reinforcement geometry is patterned with a topology designed to be bending-dominated, which, upon axial loading, collapses, and compresses the lightweight alloy matrix trapped between. The project has the potential to provide solutions to overcome key barriers related to localized piston damage related to knock or pre-ignition in high-efficiency turbocharged, spark-ignited engines.

Objectives

This project aims to create AM metal-metal composites with high-energy absorption. Potential broader applications include energy absorption under tensile loading for scenarios that include impulse loading, blast containment, and load-bearing structures, all of which are conditions relevant to automotive pistons in boosted, spark-ignited engines that are prone to knock/pre-ignition. The project objective is to understand the geometric factors, bonding, material selection, and processing aspects that enable development of multi-material hybrid systems suitable to high-demand applications.

Approach

A powerful feature of metal AM is its ability to directly print net-shaped composites with a high-level of architectural complexity. In general, this local control over composition is achieved by changing the feedstock composition and geometry that is printed. However, rapid mixing of some constituents inside the melt pool can lead to the formation of undesirable, brittle intermetallic compounds making it challenging to print metallic composites. This project approaches composite fabrication by printing composite skeleton or lattice structures for mechanical reinforcement via a laser powder bed AM of 316L austenitic stainless-steel or Ti64 Ti-based alloy. Subsequently, the printed lattice is overcast with a lower-melting-point lightweight alloy—in this study, a cast-Al Alloy A356. Lightweight cast Alloy 356 has lower ductility due to porosity and experiences brittle failure under tension, but undergoes very large plastic deformation under compression. Conversely, the AM 316L or Ti64 reinforcement lattice can achieve very high-strength and tensile ductility.

The A356/316L or Ti64/Al material systems are known to form brittle Fe-Al or Ti-Al intermetallic compounds when fused together [1]. This effect motivated the design of the novel PrintCasting hybrid-processing strategy. This approach combines AM with casting to eliminate liquid-phase mixing of the two alloys, thus avoiding intermetallic formation, as highlighted in Figure I.3.3.1.2.1.

The resulting part is an interpenetrating phase composite in which the two constituents form continuous and interconnected networks but do not fuse and form Al-based intermetallics at the interfaces. An interpenetrating morphology can enable unique mechanical and thermal properties in a nonlinear blending manner from each of the constituents to the overall behavior of the composite [2]-[5]. More specifically, it has been shown that fracture toughness can be increased by interconnecting the more ductile phase in a brittle/ductile system which further improves energy absorption.

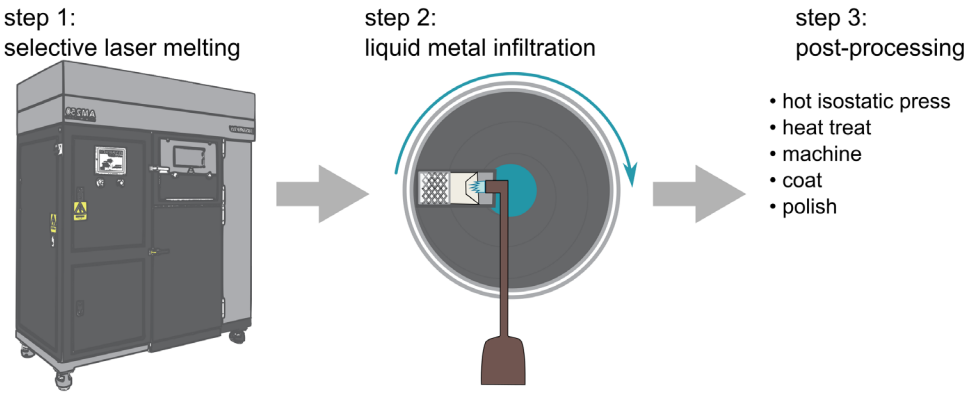

Figure I.3.3.1.2.1. Process for synthesizing AM interpenetrating phase composites using the PrintCasting technique. The model is printed using a selective laser melting process, filled with liquid metal using centrifugal casting, and then post-processed to optimize the properties. Source: ORNL.

Results

FY 2020 progress consisted of the completion of simulations and experiments coupling detailed finite element analysis (FEA) simulations with digital image correlation (DIC) measurements, novel lattice geometry modifications, hot isostatic pressing (HIP) of 316L/A356 samples and preform fabrication and infiltration of Ti64 preforms with Al356 using updated lattice geometries.

The most significant FY 2020 project output centered on defining a simulation approach that was published (see Cheng *et al.* in the Key Publications section). In this effort, mechanical DIC testing was coupled to detailed FEA simulations of AM 316L stainless-steel preforms infiltrated with A356 via vacuum casting. The approach explored bonding- and interface-effects between the two constituents and the associated global and local mechanical behaviors. Once calibrated, the FEA simulation tool was used to explore the effects of lattice geometry and materials performance to down-select geometries of interest for mechanical testing.

The developed simulation framework employed three domains: (1) the AM printed lattice (i.e., 316L stainless-steel); (2) the infiltrated alloy (i.e., Al A356); and (3) an interface between the two. The interface enables tuning of the mechanical bonding of the constituents and overall local and global behaviors. The result of this approach is conceptualized in Figure I.3.3.1.2.2(a), where the measured DIC and corresponding FEA of the samples are compared, and the resultant performance of 20% and 50% A356 samples are shown in Figure I.3.3.1.2.2(b) with excellent overall agreement between the simulation and measurements.

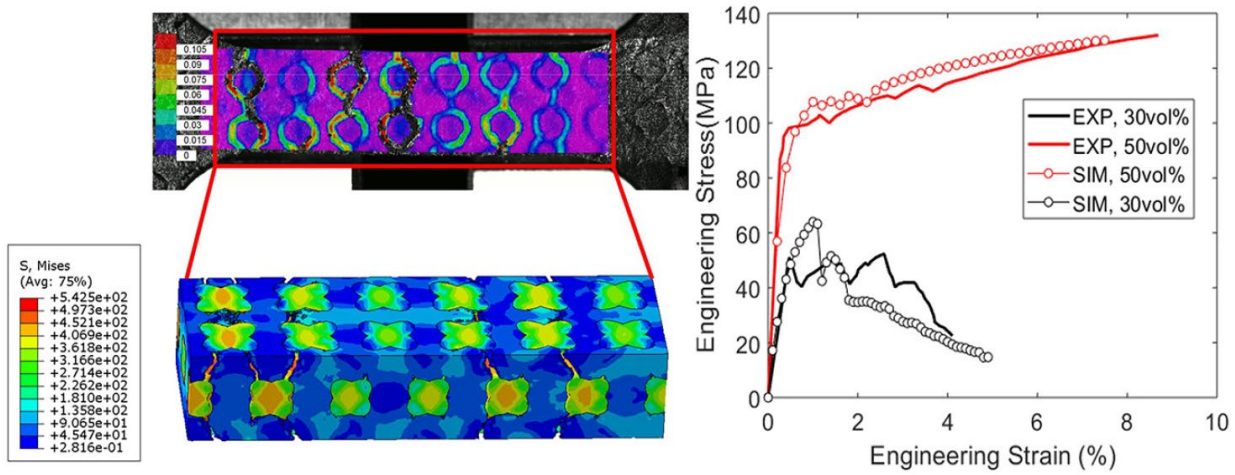

Figure I.3.3.1.2.2. (a) DIC measurements and associated FEA model of the 50% volume faction PrintCast composite uniaxial tension test sample. (b) The macroscopic tensile performance of samples for 20 and 50% volume fraction 316L stainless-steel in measurements (lines) and simulation (dots) showing excellent overall agreement in stress-strain behavior. Source: ORNL.

Additional work is currently underway to evaluate both HIP and non-HIP samples to fully probe the simulation-interface capabilities and performance. The HIP postprocessing of samples (e.g., a process often used with some cast racing-engine components) was completed in FY 2020, and the resultant analysis of the material and its performance and associated FEA simulation validation are planned for FY 2021.

Figure I.3.3.1.2.3 shows a marked difference in the material's tensile performance as a function of the 316L reinforcement volume fraction. The increase in absorbed energy was found to not be a linear relationship where a step change was observed in the energy absorption and associated tensile load of the PrintCast material at approximately 30% volume fraction reinforcement for 316L stainless-steel in a body-centered cubic (Bcc) lattice geometry.

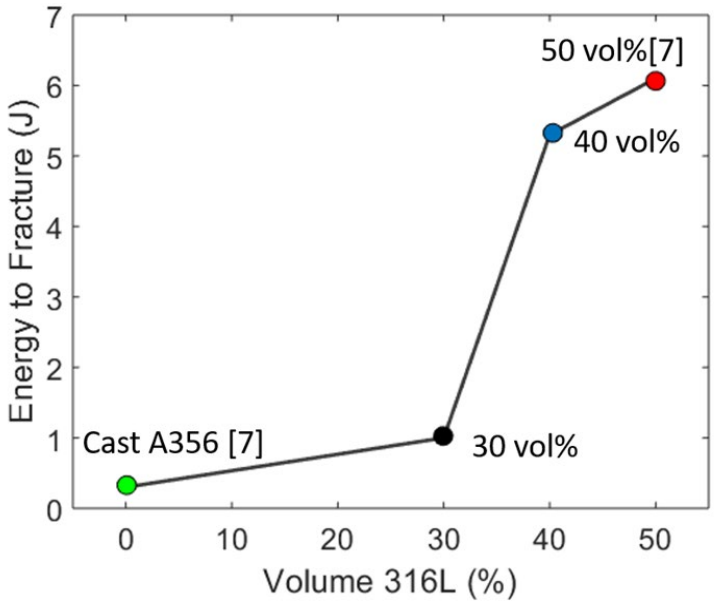

Figure I.3.3.1.2.3. Energy to failure calculated from the measured stress-strain curves for PrintCast. Source: ORNL.

The source of the measured five-times increase in energy absorption from 30% to 40% reinforcement volume fraction was explored in the FEA simulation. The localized stress state in the reinforcement was found to exceed the UTS of 316L stainless-steel. The energy to fracture step change corresponds with a localized (i.e., non-distributed load in the material) to delocalized stress state (i.e., load shared more uniformly throughout the material). Moreover, regardless of the load being localized or delocalized, the highest stress concentration location was near the nodes of the lattice structure. Therefore, in localized loading, the node locations can become overloaded and fail prematurely resulting in low energy absorption.

Using this information, a parametric study was conducted to ascertain the effect of lattice-node geometries, as shown in Figure I.3.3.1.2.4, which significantly modified stress-riser affects across various geometries. It was found that the fillet design could be used to maintain constant cross-sectional area and stress state in the Bcc lattice orientation. Using the understanding provided by the simulations, a series of preforms were designed and are ready for manufacture in FY 2021 to demonstrate the performance differences of the adapted geometries. As shown in Figure I.3.3.1.2.4, the fillets range from no modification (nominal), to a radiused fillet that maintains constant cross-sectional area (left middle), to an undercut (right middle), and a sphere (right). All geometries are designed to maintain a constant volume fraction of reinforcement, but vary the geometry and associated local cross-sectional area.

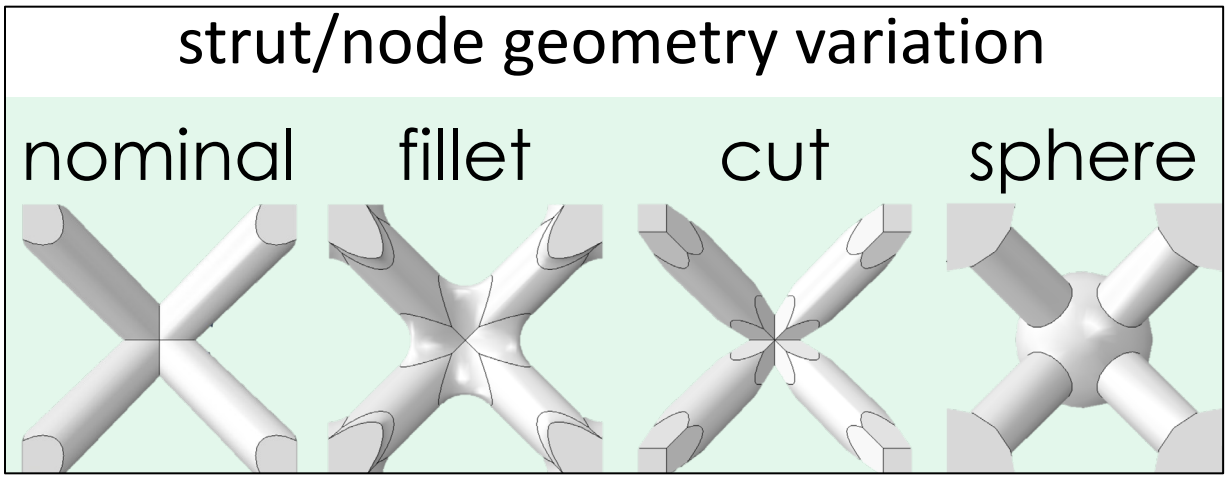

Figure I.3.3.1.2.4. Unit-cell geometries explored for stress optimization at the node interface. Source: ORNL.

Lastly, samples with Ti64 reinforcement were produced in both Bcc, as shown in Figure I.3.3.1.2.5(a), and octet-truss (OT), as shown in Figure I.3.3.1.2.5(b), lattice geometries to evaluate composites with further weight reductions. Both geometries were infiltrated with Al356 and DIC tensile bars were fabricated from the composites. The performance of a PrintCast material system, combining two lightweight materials (Al and Ti) with differing strengths and cost is of direct interest for lightweighting and associated performance improvements in automotive pistons and powertrain components due to high-strength and lightweight. Conversely, conventional and or monolithic Ti components would be prohibitive due to cost and conventional fabrication challenges.

(a) (b)

Figure I.3.3.1.2.5. PrintCast DIC dog-bone samples of Ti64/A356 constituents in: (a) the bcc; and (b) OT geometries. Source: ORNL.

Conclusions

Research and analysis to understand the properties and potential of PrintCast metal-metal composites continued, and an effort to understand lattice parameters and design was conducted to assess how lattice geometry can affect the localized-to-delocalized stress state behavior. The coupled approach of simulations and targeted experiments is systematically addressing the fundamental tradeoffs in the material performance of various PrintCast metal-metal composites systems with novel reinforcement geometries, reinforcement volumes, and materials combinations. The goal is to research and demonstrate potential breakthrough approaches for more robust materials solutions for automotive pistons and other associated high-demand powertrain components in advanced, higher-efficiency engines with extreme operating conditions, including pre-ignition and knock.

Key Publications

1. Cheng, J., M. Gussev, J. Allen, X. Hu, A. R. Moustafa, D. A. Splitter, and A. Shyam, 2020. "Deformation and failure of PrintCast A356/316 L composites: Digital image correlation and finite element modeling," *Mater. Des.*, Vol. 195, Art. 109061.
2. Pawlowski, P. E., A. Shyam, D. A. Splitter, A. M. Elliott, and Z. C. Cordero, UT-Battelle, LLC, 2019, "Additive manufactured interpenetrating phase composite," U.S. Patent Application 16/389,280.

References

1. Hofmann, D. C., J. Kolodziejska, S. Roberts, R. Otis, R. P. Dillon, J.O. Suh, Z. K. Liu, and J. P. Borgonia, 2014, "Compositionally graded metals: A new frontier of additive manufacturing," *J. Mater. Res.*, Vol. 29, No. 17, pp. 1899–1910.

2. Moustafa, A. R., R. B. Dinwiddie, A. E. Pawlowski, D. A. Splitter, A. Shyam, and Z. C. Cordero, 2018. Mesostructure and porosity effects on the thermal conductivity of additively manufactured interpenetrating phase composites," *Addit. Manuf.*, Vol. 22, pp. 223–229.

3. Pawlowski, A. E., Z. C. Cordero, M. R. French, T. R. Muth, J. K. Carver, R. B. Dinwiddie, A. M. Elliott, A. Shyam, and D. A. Splitter, 2017, "Damage-tolerant metallic composites via melt infiltration of additively manufactured preforms," *Mater. Des*., Vol. 127, pp. 346–351.

4. Cheng, J., M. Gussev, J. Allen, X. Hu, A. R. Moustafa, D. A. Splitter, and A. Shyam, 2020, "Deformation and failure of PrintCast A356/316 L composites: Digital image correlation and finite element modeling," *Mater. Des*., Vol. 195, Art. 109061.

5. Poole, L. L., M. Gonzales, M. R. French, W. A. Yarberry III, A. R. Moustafa, and Z. C. Cordero, 2020, "Hypervelocity impact of PrintCast 316L/A356 composites," *Int. J. Impact Eng*., Vol. 136, Art. 103407.

Acknowledgements

The authors would like to acknowledge the efforts of X. Hu, A. Shyam, J. Cheng, J. Allen, M. Gussev, and A. Moustafa from Rice University; and Z. Cordero from Rice University/Massachusetts Institute of Technology for their contributions to this research effort.

I.3.3.1.3 Fundamentals of Austenitic Alloy Processing by Additive Manufacturing (Task 3B1) (Oak Ridge National Laboratory)

Sebastien Dryepondt, Co-Principal Investigator
Oak Ridge National Laboratory
1 Bethel Valley Road
Oak Ridge, TN 37831
E-mail: dryepondtsn@ornl.gov

Peeyush Nandwana, Co-Principal Investigator
Oak Ridge National Laboratory
1 Bethel Valley Road
Oak Ridge, TN 37831
E-mail: nandwanap@ornl.gov

Jerry L. Gibbs, DOE Technology Manager
U.S. Department of Energy
E-mail: jerry.gibbs@ee.doe.gov

Start Date: October 1, 2018 End Date: September 30, 2023
Project Funding: $200,000 DOE share: $200,000 Non-DOE share: $0

Project Introduction

AM is an attractive and potentially lower cost solution to design complex high-efficiency, high-temperature combustion engine components. High-temperature austenitic steels, such as 310-type HK30Nb (Fe-25Cr-20Ni-1.4Nb-0.3Mo-0.2Mn-0.2C) or 347-type CF8C+, are required for components like turbocharger housings and exhaust manifolds, but AM work on austenitic steels has so far been limited to a few lower temperature stainless steels, such as alloys 304 and 316L. For higher temperature intermediate-stress applications, Ni-based Alloy 625 is currently the material of choice, but the alloy cost might be prohibitive for automotive engine components. There is, therefore, a need to assess the AM production of high-temperature austenitic steels, optimize their fabrication parameters, and generate the high-temperature data required to qualify the alloys for component operation.

Objectives

The objective is to fabricate high-temperature austenitic steels by AM and characterize them for internal combustion engine applications. Castable and weldable austenitic steels currently used for engine components are obvious candidates. However, the ultimate goal is to develop steels specifically designed for AM processing in order to take full advantage of the thermal profiles offered during AM fabrication—in particular, very fast-cooling rates during melt pool solidification leading to unique non-equilibrium microstructures.

Approach

This project aims to characterize austenitic steels fabricated by AM, with a focus on laser powder bed fusion (LPBF) methods, for powertrain components operating at 600-900°C. Initial work in FY 2019 was conducted on Alloy 316L as the AM reference stainless-steel due to powder availability. However, current and future research is focused on higher temperature austenitic steels, such as 310-type HK30Nb or 347-type CF8C+. After optimization of the AM fabrication parameters, in-depth microstructure characterization will be performed and tensile, creep, fatigue, and oxidation data will be generated at temperatures up to ~900°C. Once relationships between AM-specific microstructural features and the resulting properties are established and understood, thermodynamic and kinetics modeling tools will be used to develop advanced high-temperature, high-performance AM austenitic steels.

Results

Density measurement and microstructure characterization of small, printed cubes were used to optimize the LPBF fabrication parameters of 310-type HK30Nb steel. Rods and rectangular plates were then fabricated for characterization of alloy microstructure and mechanical properties. Very few defects were observed. Figure I.3.3.1.3.1(a) shows an example of a typical "lack of fusion" type void at a melt pool boundary. Figure I.3.3.1.3.1(b) through (d) highlight the presence of fine equiaxed or elongated cellular structures, with walls containing high dislocation densities. These cellular structures, attributed to the very fast-cooling rates during printing, have also been observed in LPBF 316L steels [1],[2], but the high Nb, Cr, and C concentrations in the HK30Nb steel led to an additional phenomenon: the formation of Cr and Nb-rich nano precipitates, likely carbides, within the cell walls.

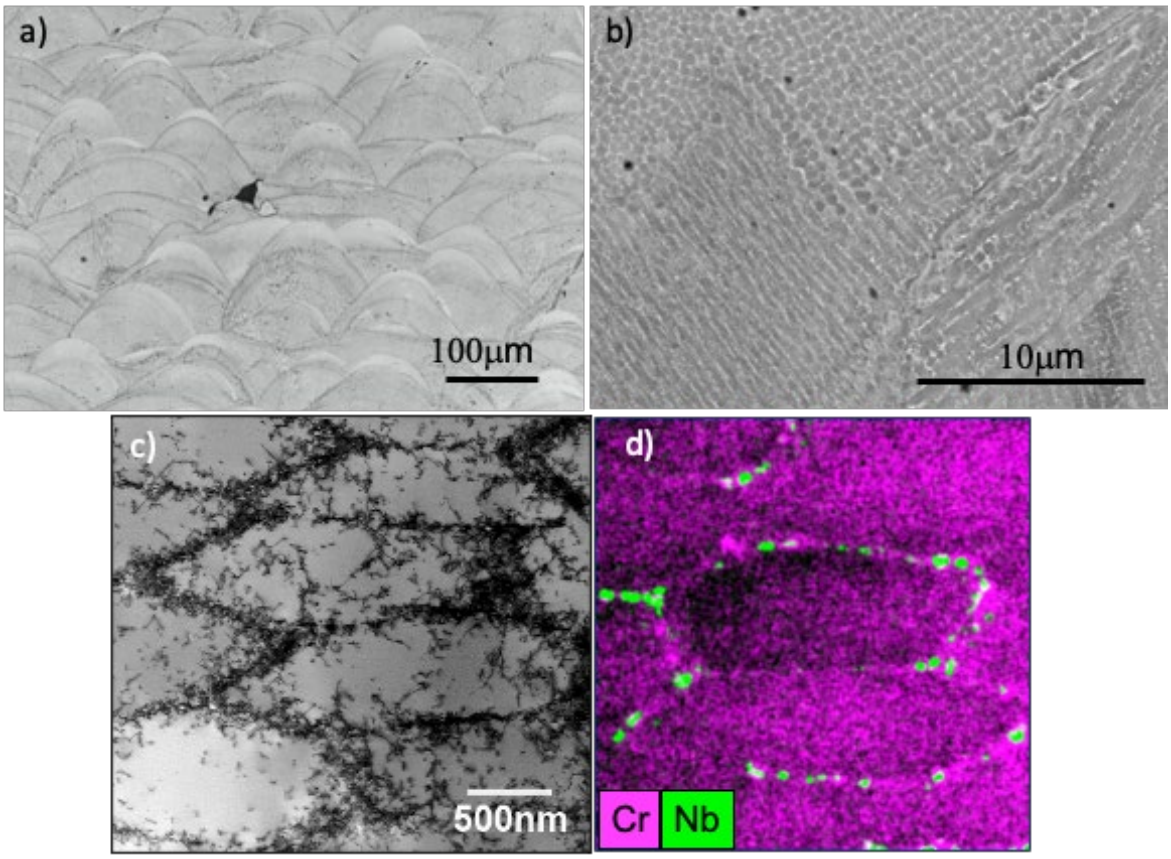

Figure I.3.3.1.3.1. HK30Nb steel microstructure: (a) etched optical micrographs showing melt pool boundaries and one lack of fusion type defect; (b) etched SEM image highlighting the presence of cellular structures; (c) TEM image; and (d) combined Cr and Nb chemical maps showing the presence of nanoscale Nb- and Cr-rich precipitates in the high-dislocation-density cellular structure walls. Source: ORNL.

As can be seen in Figure I.3.3.1.3.2(a) and (b), the tensile properties at 20°C to 900°C of the HK30Nb steel along and perpendicular to the build direction were quite similar, except for slightly higher deformations at rupture at all temperatures perpendicular to the build direction and a higher yield strength in the same direction at RT. Figure I.3.3.1.3.2(a) and (b) also highlight the superior yield strength of the LPBF HK30Nb steel in comparison with cast HK30Nb and advanced 310-type wrought HR3C (Fe-25Cr-20Ni-0.4Nb-0.2N) steel at 20-900°C. The deformation at rupture of the LPBF HK30Nb was only slightly lower compared to the deformation at rupture of HR3C and similar to the deformation of cast HK30Nb at temperature below 800°C.

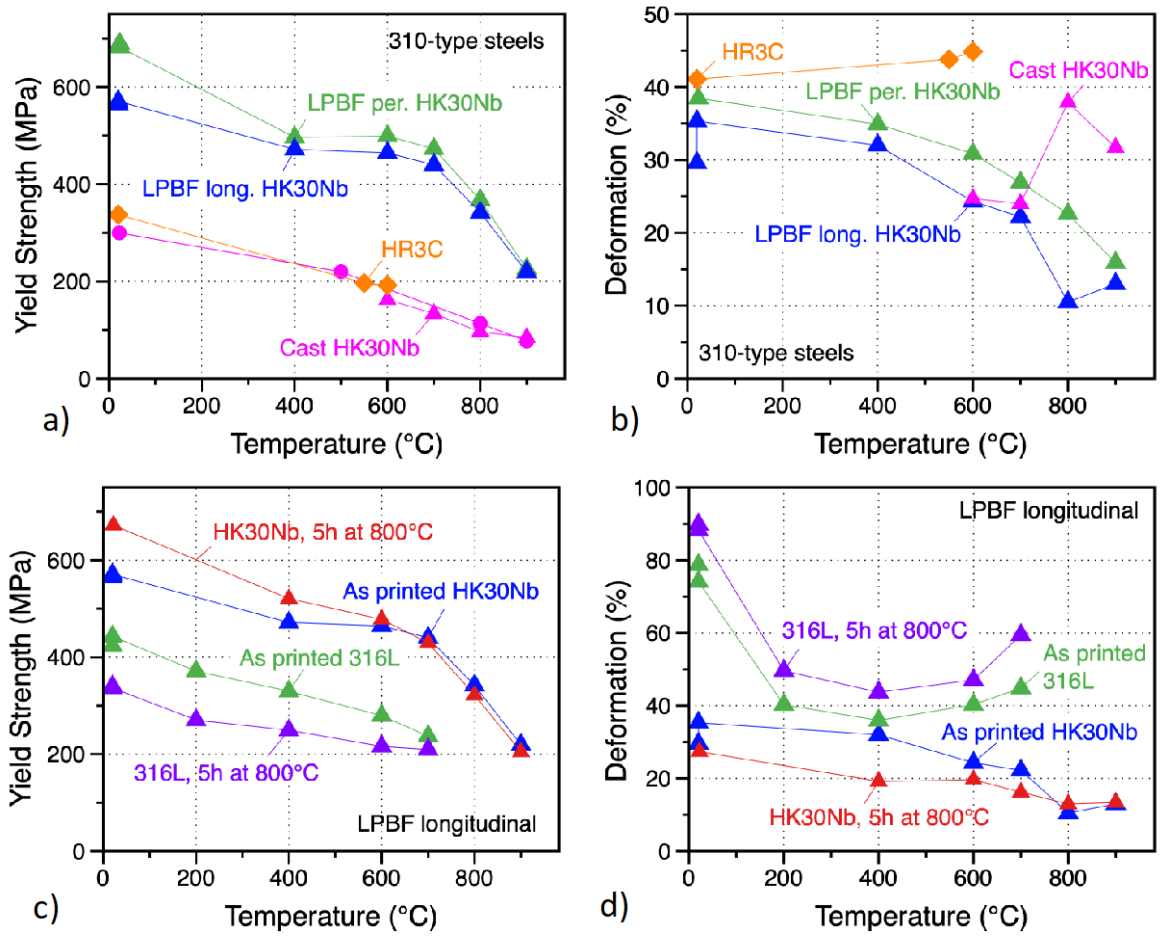

Figure I.3.3.1.3.2. Comparison of the as-printed LPBF HK30Nb tensile properties along and perpendicular to the build direction with the tensile properties of cast HK30Nb and wrought HR3C: (a) yield strength; and (b) deformation at rupture. Effect of annealing for 5 h at 800 °C on the tensile properties of LPBF 316L and LPBF HK30Nb steels: (c) yield strength; and (d) deformation at rupture. Source: ORNL.

Initial assessment of the printed HK30Nb high-temperature stability was conducted by annealing the alloy for 5 h at 800°C, the heat-treatment of interest for stress relief. Figure I.3.3.1.3.3 shows that this heat-treatment resulted in the growth of some precipitates, but also nucleation of new (Ni,Si)-rich precipitates, primarily at the grain boundaries. Further, the cellular structure was preserved after annealing for 5 h at 800°C, contrary to what was previously observed for LPBF 316L steel. The impact of the microstructure evolution on the tensile properties along the build direction for the LPBF HK30Nb and LPBF 316L steels can be seen in Figure I.3.3.1.3.3(c) and (d). For LPBF HK30Nb steel, yield strengths were similar before and after annealing except for a higher yield value at RT after annealing, while the heat-treatment led to a decrease of the yield strengths for the LPBF 316L steel at 20-700°C. In addition, annealing for 5 h at 800°C resulted in a slight decrease of the deformation at rupture for the LPBF HK30Nb steel, but an increase of the deformation for the LPBF316L steel.

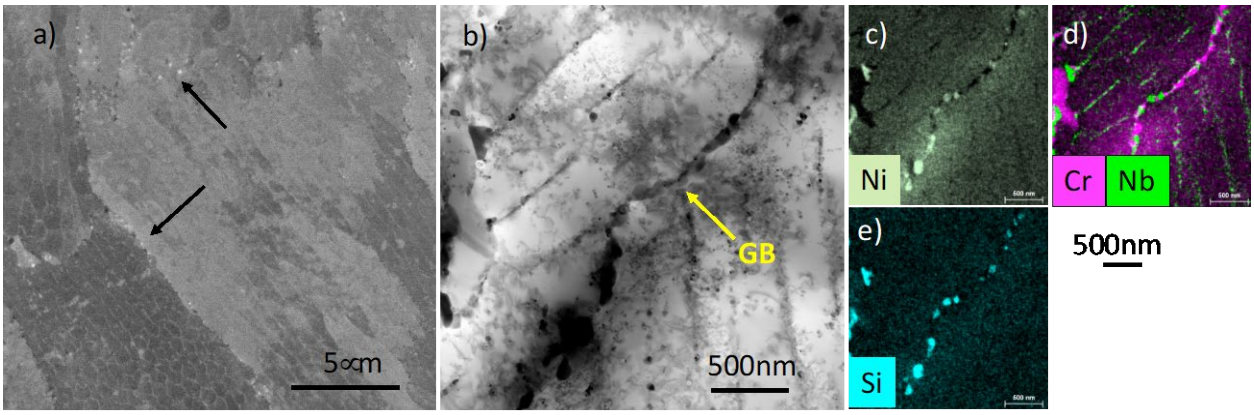

Figure I.3.3.1.3.3. Microstructure of the LPBF HK30Nb steel after 5 h at 800°C, showing the growth and nucleation of new precipitates at grain boundaries. (a) SEM micrograph with black arrows showing coarser precipitates. (b)TEM. (c), (d), and (e) Chemical maps highlighting Nb-, Cr-, and (Ni,Si)-rich nanoprecipitates. Source: ORNL.

The creep behavior of LPBF HK30Nb steel along and perpendicular to the build direction was evaluated at 700°C to 900°C, with lifetimes varying from 35 h to 2,700 h. Figure I.3.3.1.3.4 shows that the creep lifetime along the build direction of the LPBF HK30Nb steel was roughly five-times longer at 750°C, 100 MPa, compared with the lifetime of cast HK30Nb steel. This superior creep behavior for LPBF steel was also observed at 700 and 800°C. However, at 900°C and with an applied stress of 50 MPa, similar lifetimes were observed for the LPBF and cast HK30Nb steels. The superior creep strength of the LPBF steel at < 900°C comes from the cellular structure and presence of nanocarbides. These microstructural features are likely unstable at 900°C. Testing perpendicular to the build direction resulted in a significant decrease of creep lifetime compared to the lifetime along the build direction, but creep strength was still superior to the creep strength of the cast HK30Nb, as observed in Figure I.3.3.1.3.4. Extensive microstructure characterization of creep specimens will be conducted in FY 2021 to understand this anisotropic creep behavior. Initial thermodynamic and kinetics calculations indicating that the intercellular regions solidified last during laser powder bed printing were in good agreement with both the observed microstructure and the presence of nanocarbides in the cellular walls. Further simulations will be performed in FY 2021 to predict the evolution of the microstructure after long-term high-temperature exposures.

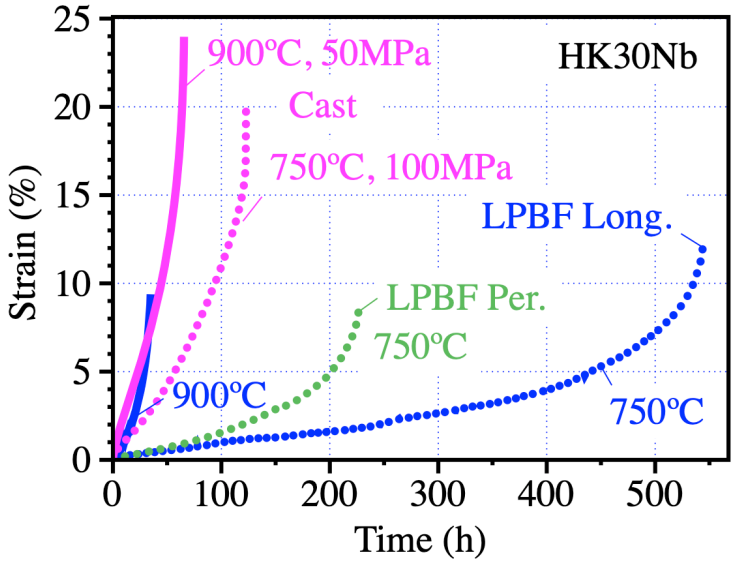

Figure I.3.3.1.3.4. Comparison of the creep properties of LPBF HK30Nb steel—along and perpendicular to the build direction at 750 and 900°C to the creep properties of cast HK30Nb. Source: ORNL.

Conclusions

Alloy HK30Nb, a higher temperature austenitic steel that had not been printed previously, was successfully fabricated by LPBF. Very rapid cooling rates during printing led to the formation of cellular structures with high-dislocation-density and numerous nanoprecipitates within the cell walls. These resultant printed structures contained few significant defects, and the microstructural features resulted in very high tensile and creep strengths in comparison with cast HK30Nb. Additional microstructure characterization is needed to elucidate the reason for lower creep lifetime perpendicular to the build direction and to assess the long-term high-temperature stability of this non-equilibrium LPBF steel. The superior properties of LPBF steels should further increase the potential for new, higher-efficiency engine components enabled by advanced designs only possible via AM. CF8C+, a 347-type steel strengthened by nano carbonitrides, will be fabricated by LPBF in FY 2021. The ultimate goal of the project is to develop an LPBF-specific austenitic steel with oxidation resistance superior to conventional 310-type steels and creep resistance superior to 347-type steels at temperatures greater than 700°C.

Key Publications

1. Dryepondt, S., P. Nandwana, P. Fernandez-Zelaia, and F. List III, 2020, "Microstructure and high-temperature tensile properties of 316L fabricated by LPBF," *Addit. Manuf.*, accepted for publication.
2. Fernandez-Zelaia, P., Y. Lee, Q. Campbell, S. Dryepondt, M. M. Kirka, and A. Marquez Rossy, 2020, "Microstructural digital image correlation: Statistical estimation of strain using spatial correlation functions," *Acta Mater.*, under revision,

References

1. Wang, Y. M., T. Voisin, J. T. McKeown, J. Ye, N. P. Calta, Z. Li, Z. Zeng, Y. Zhang, W. Chen, T. T. Roehling, R. T. Ott, M. K. Santala, P. J. Depond, M. J. Matthews, A. V. Hamza, and T. Zhu, 2018, "Additively manufactured hierarchical stainless steels with high-strength and ductility," *Nat. Mater.*, Vol. 17, pp. 63–73.
2. Liu, L., Q. Ding, Y. Zhong, J. Zou, J. Wu, Y. L. Chiu, J. Li, Z. Zhang, Q. Yu, and Z. Shen, 2018, "Dislocation network in additive manufactured steel breaks strength–ductility trade-off," *Mater. Today*, Vol. 21, pp. 354–361.

Acknowledgements

The authors acknowledge the contributions of the following ORNL team members for this subtask: K. Unocic, R. Kannan, Y. Lee, K. Hedrick, T. Lowe, and S. Hawkins.

I.3.3.1.4 Ferritic Alloys for Heavy-Duty Pistons via Additive Manufacturing (Task 3B2) (Oak Ridge National Laboratory)

Peeyush Nandwana, Co-Principal Investigator
Oak Ridge National Laboratory
1 Bethel Valley Road
Oak Ridge, TN 37831
E-mail: nandwanap@ornl.gov

Amy Elliott, Co-Principal Investigator
Oak Ridge National Laboratory
1 Bethel Valley Road
Oak Ridge, TN 37831
E-mail: elliottam@ornl.gov

Jerry L. Gibbs, DOE Technology Manager
U.S. Department of Energy
E-mail: jerry.gibbs@ee.doe.gov

Start Date: October 1, 2018 End Date: September 30, 2023
Project Funding: $225,000 DOE share: $225,000 Non-DOE share: $0

Project Introduction

AM has garnered interest from the automotive sector due to its immense potential in unlocking novel designs and net-shaping capabilities, as well as offering the opportunity to print complex parts from classes of alloys that were previously considered difficult to fabricate. One of the limitations of AM is that it can be cost-prohibitive for very large volumes and low-cost-margins, such as those required in passenger vehicles. HD engines, such as those used in freight trucks, can become early adopters of AM technologies due to their relatively lower manufacturing volumes and comparatively higher cost margins compared to passenger vehicles. The costs can be further reduced by using binder jet additive manufacturing (BJAM), a powder bed-based AM technology that deposits green parts without the need for specialized build chambers or power sources, such as a laser or an electron beam source. The green parts can then be subjected to sintering for full densification to near-net-shaped geometries that can be subsequently machined to the required surface finish. The potential to scale-up the operation arises from the fact that BJAM can have significantly larger build chambers compared to other powder bed AM technologies. A further advantage is that conventional powder metallurgy and metal-injection-molding industries have already set the precedent for conducting sintering operations at scales that are economically viable for HD engine parts. The primary focus of this task is the fabrication of ferritic alloys via BJAM to enable advanced pistons for HD truck applications.

Objectives

The objective is to fabricate a ferritic/martensitic steel via BJAM, followed by sintering and post-sintering heat treatments to achieve higher room- and elevated temperature tensile strengths compared to 4140 and micro-alloyed steels (MAS), which are the current commonly used alloys for HD pistons. An additional objective is to evaluate the oxidation behavior of the printed tool steel alloys to determine suitability for piston fabrication.

Approach

The focus in FY 2020 was the development of appropriate HIP and heat-treatment cycles to improve the strength of binder jet printed H13 steel to enable achievement of superior high-temperature tensile strength. Further, the impact of heat treatments on microstructure evolution was determined and associated with the resulting tensile behavior. Extensive thermodynamic and kinetic calculations were conducted to rationalize the

microstructure evolution during heat treatments, as well as during tensile testing. Finally, oxidation studies were conducted, and the results showed that the mass gain for H13 was about half that of Alloy 4140 during a 1,000 h exposure at 600°C. Key findings have been published in a journal article (see Key Publications section); several others are currently in preparation.

Results

In the beginning of FY 2020, the project team submitted a manuscript detailing the sintering conditions and the impact of binder saturation on resulting distortion, densification, and microstructure evolution of H13 steels. In summary, the project team identified the process window for sintering of H13 and highlighted the need for post-sintering heat treatments because supersolidus liquid-phase sintering (SLPS) results in solute segregation. Further, the project team showed that the phenomenological sintering models, while applicable to systems with limited to no solubility, such as tungsten carbide-cobalt, have limitations for monolithic alloys. The solute segregation closer to smaller prior austenite grains was proof that new grains nucleate during cool down from the liquid-phase during SLPS, as opposed to the existing theory that SLPS only results in grain growth [1]. Figure I.3.3.1.4.1 shows a summary of EBSD images and associated EDS maps highlighting the segregation of vanadium in smaller grains after SLPS of H13 samples at 1,300 and 1,400°C.

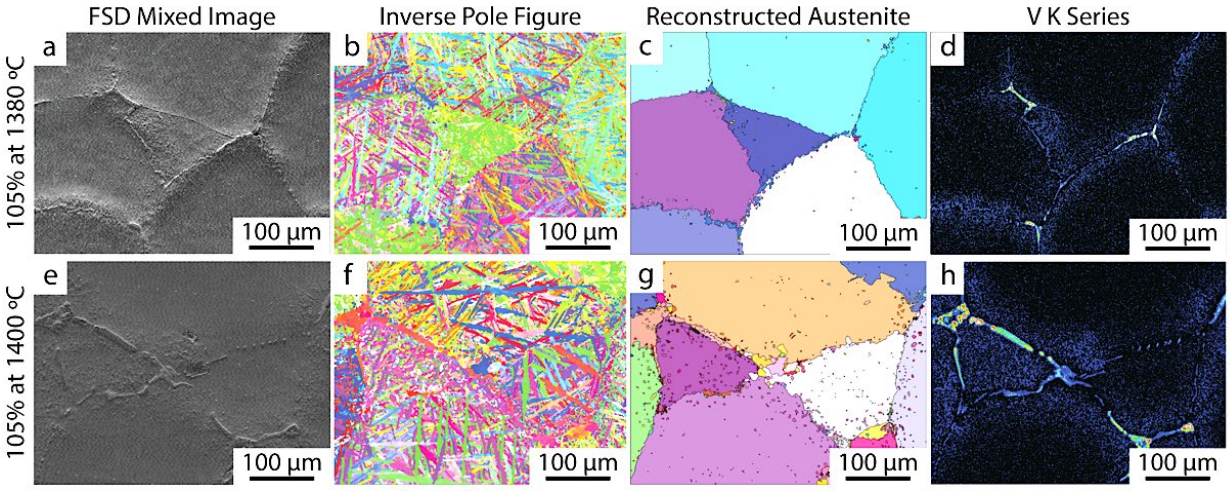

Figure I.3.3.1.4.1. (a) and (e) The forward-scatter detector image showing the grain structure. (b) and (f) The inverse pole figure showing the martensite. (c) and (g) Reconstructed austenite. (d) and (h) The associated energy-dispersive spectroscopy maps showing V segregation within finer grains in H13 samples sintered at 1380 and 1400°C [2]. Source: ORNL.

To mitigate the porosity inherent to BJAM-sintered samples and homogenize their microstructure, the samples were subjected to HIP at 1,190°C at a pressure of 100 MPa for 8 h followed by furnace cooling. Following HIP, the samples were austenitized at 982°C, followed by double-tempering at 550°C. Samples were subsequently air-cooled to RT. The austenitizing and double-tempering schedules were derived from the standard H13 heat treatments designed for tooling applications [3]. Thus, there is a need to develop more-specific heat treatments for printed piston applications. These initial heat treatments were used to determine baseline material properties. Tensile testing was conducted at room and elevated temperatures, with a heating rate of 10°C/min followed by a 30-minute soak for high-temperature testing. A manuscript summarizing these findings is currently under preparation.

Figure I.3.3.1.4.2 shows the superior yield strength (YS) and UTS of BJAM H13, which is identified as 8580 in Figure I.3.3.1.4.2, in as-sintered and sintered HIP, and heat-treated (HIP+HT), where HT is heat-treated conditions compared to 4140 and MAS alloys at all temperatures. Note that the YS of 8580 HIP+HT is higher than that of as-sintered 8580 from RT up to 400°C, beyond which it drops below the YS of the as-sintered condition. Further, the UTS of 8580 HIP+HT is comparable to the conventionally fabricated H13. The HIP+HT postprocessing, in addition to increasing the YS and UTS compared to as-sintered H13, also significantly improved the elongation at all temperatures (possibly by reducing defects and modifying microstructure). While the elongation of the sintered 8580 HIP+HT is lower than that of wrought 4140 and MAS alloys, it is considered more than sufficient for piston applications. Also note that while the YS and UTS of the 8580 HIP+HT piston drops from 1,400 MPa to ~800 MPa on increasing the temperature from 400 to 600°C, it is significantly higher than that of 4140 and MAS alloys at these temperatures. Studies are currently underway to determine the impact of long-term thermal exposures on the high-temperature tensile properties of H13. This is because the tempering of martensite during long-term exposures will determine the upper-temperature limit of this material for prolonged exposure that is encountered in piston applications.

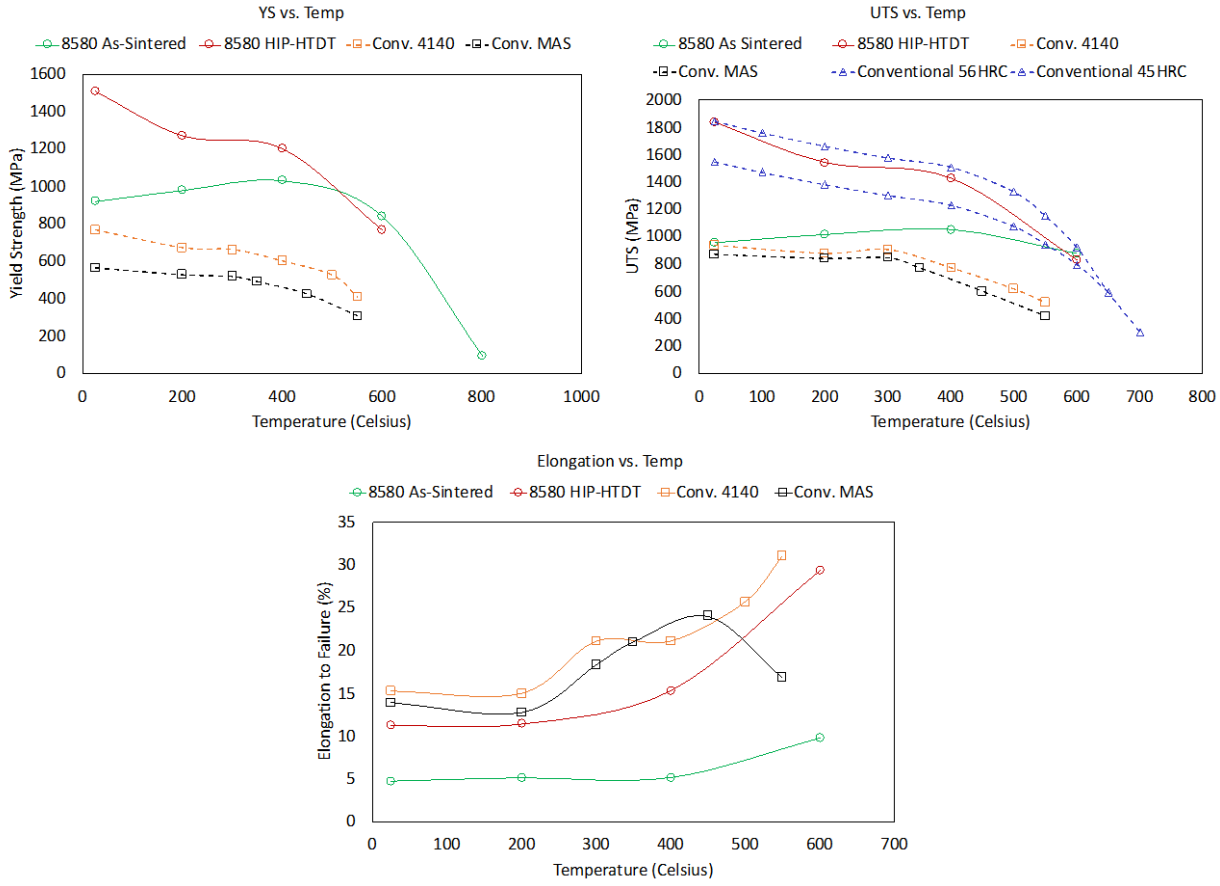

Figure I.3.3.1.4.2. (a) the room- and high-temperature YS; (b) UTS; and (c) elongation of BJAM H13 in the as-sintered and HIP+HT conditions in comparison with 4140 and MAS alloys, the current HD piston materials. The reference data for 4140 and MAS has been adopted from Pierce *et al.* [4]. UTS data for conventional H13 has been adopted from Harvey [5]. Source: ORNL.

The RT microstructures for as-sintered and BJAM H13 HIP+HT show notable differences at all length scales. At lower magnification, the as-sintered microstructure shows the prior unmelted powder particles embedded within the liquid channels that solidified upon cool down from the SLPS regime, as observed in Figure I.3.3.1.4.3(a). On the other hand, the HIP+HT microstructure consists of uniformly distributed

martensite, as can be seen in Figure I.3.3.1.4.3(d). Higher magnification images show the grain boundaries decorated with carbides in the as-sintered H13 that explain the lower-elongation for the as-sintered samples, as shown in Figure I.3.3.1.4.3(b). Finally, the higher magnification images also show the presence of a bainitic microstructure in as-sintered H13, shown in Figure I.3.3.1.4.3(c), while the HIP+HT condition has fine carbides uniformly dispersed in the martensitic matrix, as seen in Figure I.3.3.1.4.3(f).

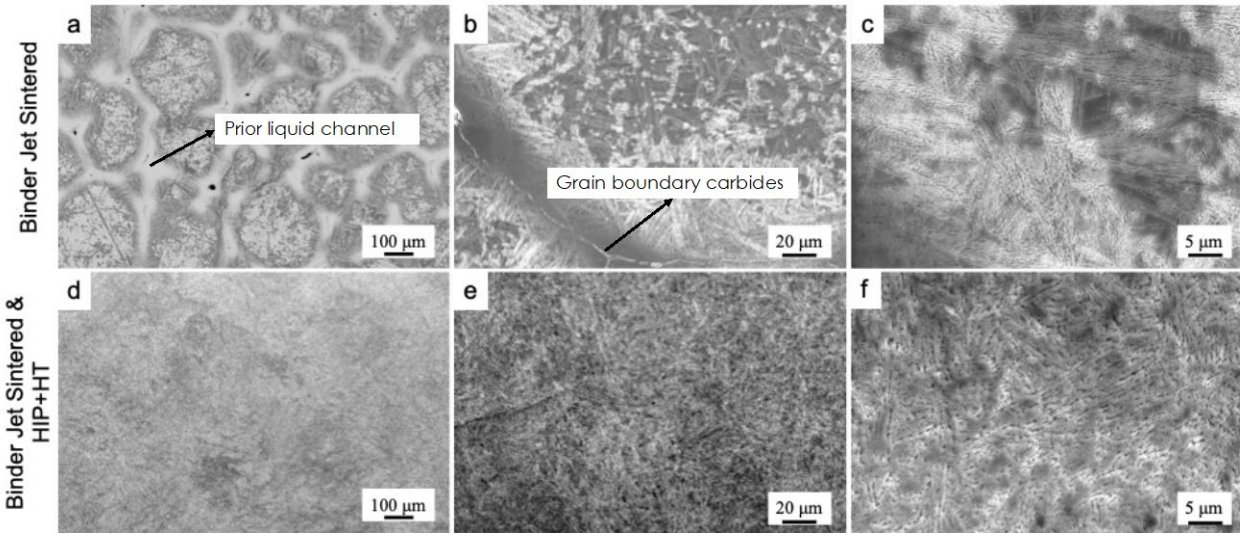

Figure I.3.3.1.4.3. The microstructure of BJAM H13 in as-sintered (a–c) and HIP+HT conditions (d–f). Source: ORNL.

While the microstructures in as-sintered and HIP+HT conditions explain the differences in RT strength and elongation, they do not provide insights on the changes occurring in strength as a function of temperature, especially the loss of strength between 400°C and 600°C. To understand these changes, coupons were extracted from the tensile samples and subjected to rigorous microstructure analysis. Further, DICTRA simulations were conducted to determine the formation of carbides during the ramp-up and soaking prior to high-temperature testing.

The microstructure is predominantly a mixture of martensite and bainite at all temperatures in the as-sintered condition, whereas the HIP+HT conditions have a mix of carbides and martensite. Based on the DICTRA simulations in Figure I.3.3.1.4.4, it can be seen that the as-sintered sample (blue curve) only begins to show the formation of M_6C carbides at 400°C whereas, for HIP+HT (red curve), the carbides are present all the way from RT to 600°C—thus explaining the higher strength of HIP+HT condition. Note that the carbide distributions are shown as a function of the distance from the grain boundary, and only the M_6C carbides are shown for brevity because they are the phase believed to contribute to strengthening of the material. By contrast, the as-sintered sample contained a significant volume fraction of embrittling M_7C_3 carbides at the grain boundary (not shown). In the as-sintered condition, the YS reaches a peak at 400°C that is in line with the DICTRA simulations that reveal the precipitation of the strengthening M_6C that drops in volume fraction on increasing the temperature to 600°C. Further, for HIP+HT, the M_6C carbide volume fraction initially drops at 200°C and then slightly increases at 400°C before dropping off at 600°C. This observation is in line with the observed tensile behavior of the HIP+HT samples—which lends further credence to the hypothesis that M_6C is the key strengthening phase. The relatively similar carbide levels at 200°C and 400°C explain the plateau in the YS in that temperature range. In summary. in the case of the HIP+HT sample, the initial drop in carbide volume fraction at 200°C, combined with martensite tempering, results in the initial drop in YS, which plateaus at 400°C. Finally, at 600°C, the combined effect of martensite tempering and carbide volume fraction reduction results in a precipitous drop in strength.

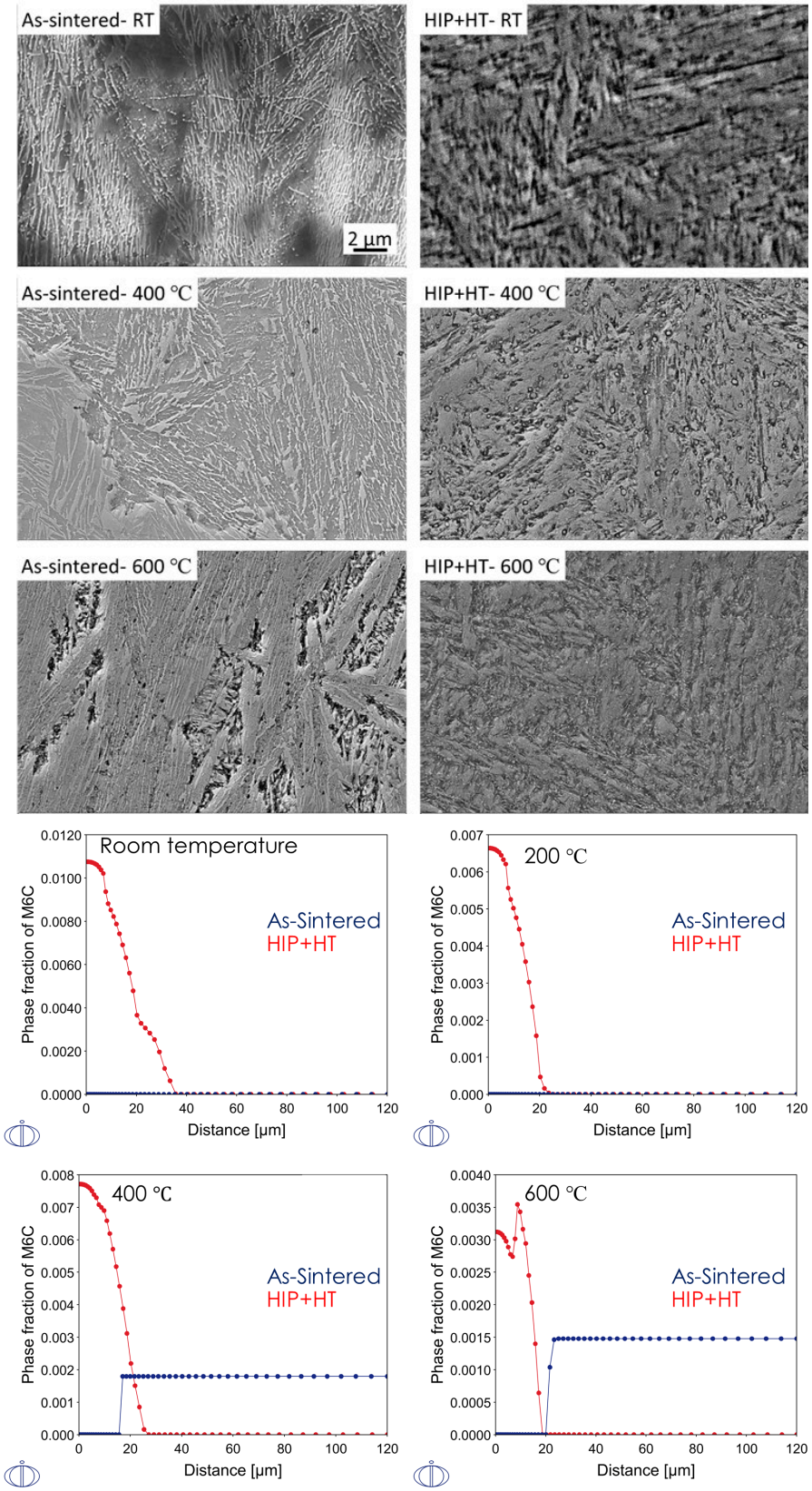

Figure I.3.3.1.4.4. The microstructure of BJAM H13 in an as-sintered and HIP+HT conditions after tensile testing at various temperatures along with the DICTRA simulations showing the evolution of M_6C carbides. Source: ORNL.

Finally, one-hour cyclic oxidation testing was conducted at 550°C in-air + 10% H_2O on BJAM HIP+HT samples for 1,000 h. The sample exhibited a protective oxidation behavior for ~200 h followed by significant mass gains. The weight gain per unit area of BJAM HIP+HT H13 was about half that of wrought 4140 alloy after 1,000 hours due to the higher Cr content, 5.0 wt.% versus 1.0 wt.%, and the retardation of fast-growing Fe-rich oxide formation. Although both alloys experienced substantial mass gains during long-term cyclic oxidation at 550°C, neither exhibited spallation after 1,000 cycles. The 4140 steels are not intended for piston environments above 500°C. Other research within this program (Task 2A2) suggests the possibility of minor alloying additions to steels with moderate Cr levels can improve oxidation behavior; thus, slight modification of the H13 alloy might be effective to improve environmental resistance at higher temperatures, as observed in Figure I.3.3.1.4.5.

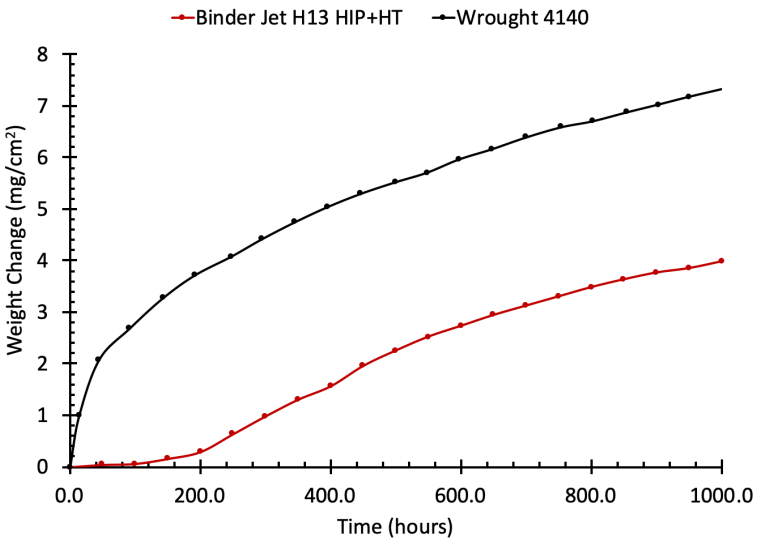

Figure I.3.3.1.4.5. Cyclic oxidation (one-hour cycles) mass gains comparing a BJAM HIP+HT H13 alloy with a wrought 4140 alloy at 550oC in-air + 10% H_2O. Source: ORNL.

Conclusions

Research on BJAM H13 in FY 2020 has shown that BJAM is a viable technique to fabricate complex tool steel components, possibly including HD pistons. While H13 has been historically used as a tool steel material, the near net-shape potential offered by BJAM can help minimize machining to a level necessary to achieve final surface finish, compared to the extensive machining required while using forging blanks. Minimizing potential machining operations can help mitigate some of the gap between the difficult-to-machine H13 compared to 4140 that can be readily machined. The initial high-temperature tensile properties and oxidation behavior of BJAM H13 suggest this material has promise for use as an advanced piston alloy. However, the impact of long-term thermal exposure on elevated properties needs to be determined along with HCF behavior to further qualify this material for deeper investigation for HD pistons.

Key Publications

1. Nandwana, P., K. Rangasayee, and D. Siddel, 2020, "Microstructure evolution during BJAM of H13 tool steel," *Addit. Manuf.*, Vol. 36, Art. 101534. Available at: https://doi.org/10.1016/j.addma.2020.101534 (last accessed 21 January 2021).

References

1. German, R. M., 1997, "Supersolidus liquid-phase sintering of prealloyed powders," *Metall. Mater. Trans. A.*, Vol. 28, pp. 1553–1567.

2. Nandwana, P., K. Rangasayee, and D. Siddel, 2020, "Microstructure evolution during BJAM of H13 tool steel," *Addit. Manuf.*, Vol. 36, Art. 101534. Available at: https://doi.org/10.1016/j.addma.2020.101534 (last accessed 21 January 2021).

3. Hudson Tool Steel Corporation, 2021, “H13 Tool Steel,” Available at: https://www.hudsontoolsteel.com/technical-data/steelH3 (last accessed 21 January 2021).

4. Pierce, D., A. Haynes, J. Hughes, R. Graves, P. Maziasz, G. Muralidharan, A. Shyam, B. Wang, R. England, and C. Daniel, 2019, “High-temperature materials for HDDEs: Historical and future trends,” *Prog. Mater. Sci.*, Vol. 103, pp. 109–179. Available at: https://doi.org/10.1016/j.pmatsci.2018.10.004 (last accessed 21 January 2021).

5. Harvey, P. D., 1982, *Engineering Properties of Steel*, American Society for Metals, Metals Park, OH, USA.

Acknowledgements

The authors acknowledge the contributions of the ORNL team members for this subtask: R. Kannan, D. Siddel, A. Rossy Marquez, K. Hedrick, D. Pierce, and S. Dryepondt.

I.3.4 Advanced Characterization and Computational Methods – Thrust 4

I.3.4.1 Advanced Characterization (4A)

I.3.4.1.1 Overview of Advanced Characterization Within the Powertrain Materials Program (Task 4A1) (Oak Ridge National Laboratory)

Thomas R Watkins, Co-Principal Investigator
Oak Ridge National Laboratory
1 Bethel Valley Road
Oak Ridge, TN 37831
E-mail: watkinstr@ornl.gov

Jerry L. Gibbs, DOE Technology Manager
U.S. Department of Energy
E-mail: jerry.gibbs@ee.doe.gov

Start Date: October 1, 2019 End Date: September 30, 2023
Project Funding (FY 2020): $425,000 DOE share: $425,000 Non-DOE share: $0

Project Introduction

This report describes the activities performed during the second year of the Advanced Characterization activity under Thrust 4A within the VTO Powertrain Materials Core Program (PMCP). The goal of the PMCP, which was launched in October 2018, is to accelerate development and delivery of new, cost-effective advanced alloy solutions, via a modern ICME approach. The properties of these new materials are targeted to enable improvements in engine efficiency, weight reductions, and durability enhancement over the full range of on-road vehicle classes (e.g., Classes 1-8). Five materials development thrusts are included in the PMCP: Thrust 1: Cost-effective, Lightweight (i.e., Aluminum Alloys) Engine Alloys; Thrust 2: Cost-effective, Higher Temperature Engine Alloys (i.e., Nickel- and Iron-based Alloys); Thrust 3: AM of New Powertrain Alloys; Thrust 4: Advanced Characterization and Computational Methods; and Thrust 5: Exploratory Research for Powertrain Material. This project is Thrust 4 and addresses the advanced characterization needs of the various tasks within these three materials development thrusts. Advanced characterization activities include STEM, APT, synchrotron x-rays, neutron scattering, and others.

The advanced characterization thrust is a multi-laboratory effort involving ANL, PNNL, and ORNL. ORNL and PNNL conducted the advanced electron microscopy and APT studies. Synchrotron x-rays and neutrons were used for diffraction, tomography, and small-angle scattering, conducted at ANL's Advanced Photon Source and at ORNL's Spallation Neutron Source (SNS), respectively. ANL's and PNNL's advanced characterization activities are reported elsewhere. This report only discusses ORNL's advanced characterization activities under Thrust 4A.

Objective

The overall objective of the advanced characterization activity is to use experimental techniques to accelerate alloy design and the TRL, and to support the advanced predictive ICME efforts in Thrust 4B.

Approach

The approach in this thrust is to leverage the unique combinations of materials science capabilities at three National Laboratories in advanced characterization, as well as expertise in advanced computation, alloy design, synthesis, and processing. The PMCP Thrusts 1–3 all propose, compete, and share costs via ORNL program funds for PMCP-funded access to advanced characterization capabilities and modern computational tools and expertise. Often both are applied, such as combining advanced microscopy with APT (PNNL) and ML to understand cast–alumina-forming alloys exhibiting a promising combination of creep and oxidation

resistance for exhaust components in Thrust 2. That is, the experimental data are used to inform and train ML models. Similarly, advanced microscopy (ORNL and PNNL), APT (PNNL), and x-ray scattering at the synchrotron (ANL) testing results were integrated to understand the size, distribution, and shape of γ' precipitates within alumina-forming Ni-based alloys under Thrust 2. This is a key aspect of the PMCP, distinguishing it from VTO's current portfolio, and increasing the opportunity for fundamental research with the mission of accelerating key discoveries into targeted new materials that enable design of advanced internal combustion engines with more extreme operating conditions and higher efficiencies. In addition to the two projects just mentioned, Table I.3.4.1.1.1 provides a snapshot of the breadth of advanced characterization projects funded in FY 2019 and FY 2020. The Results section focuses on describing selected in-depth STEM and APT studies at ORNL.

Table I.3.4.1.1.1. Thrust 4A Funded Advanced Characterization Projects in FY 2019 and FY 2020

Thrust	Task	Description	Tool
1. Cost-Effective, Lightweight Higher Temperature Engine Alloys	Fundamental studies of complex precipitation pathways	*In situ* loading neutron data analysis	SNS
2. Cost-Effective Higher Temperature Engine Alloys	Development of cast, higher temperature alloys	Measure the O concentrations in Ni- and Fe-based alloys at the oxide/alloy interfaces	APT Thermodynamic Calcs
3. Additive Manufacturing of New Powertrain Alloys	Fundamental of austenitic alloy processing by AM	Electron microscopy to understand carbide disappearance	JEOL JEM-2200FS Aberration-Corrected STEM

Results

Many important materials properties depend strongly on local atomic arrangements and compositions. Advanced characterization and computation undergird the PMCP's three alloy development thrusts, each with multiple subtasks providing needed information and insight into the structure and composition of new, developmental materials. Two foundational advanced microstructural characterization techniques are electron microscopy and APT.

Electron microscopy analyzes the local structure, atomistic arrangements, and compositions in advanced alloys. A key method for imaging to the atomic level is aberration-corrected STEM (AC-STEM) combined with electron energy-loss spectroscopy (EELS) measurements. With the successful correction of lens aberrations, AC-STEM has become the dominant microscopy technique used today in material research, due to the extremely high-resolution and the availability of simultaneous imaging and spectroscopic modes. Like a SEM, an incident probe is scanned across a sample. However, with AC-STEM, the sample is thin enough so that the beam is transmitted. A HAADF detector collects Rutherford scattering from the atomic nuclei, producing an image with strong sensitivity to atomic number Z. Simultaneously, an EELS can provide elemental maps and electronic structure information.

One of several such instruments at ORNL is the JEOL JEM-2200FS AC-STEM, which utilizes primarily HAADF imaging in scanning transmission mode to elucidate the structures of materials at the sub-Ångström level (e.g., 0.07 nm). For example, in a crystalline structure, columns of atoms with a higher average atomic number appear in brighter contrast than those with a lower atomic number, allowing the crystal structures of various phases in a material to be determined when the images are matched to crystal structure models and/or image simulations. The electron microscope also uses an x-ray detector so that x-rays from the same or comparable areas can be collected to map the distribution of elements within the various microstructural features being imaged. These methods continue to be used in the project areas described in the next section.

STEM and Advanced Photon Source Characterization of New Cast High-Temperature Al-Cu-Mn-Zr Alloys (Thrust 1 Advanced Characterization Needs)

Thrust 1 is developing cost-effective, high-temperature, cast-Al alloys with extremely stable microstructures. One task studies the fundamental precipitation pathways of precipitation-hardened Al alloys. Another task is developing new higher performance Al alloys capable of operating temperatures exceeding 400°C. Engineering of key interfaces to increase the temperature capability of lightweight aluminum alloys are being studied in the former. In the latter, new high-performance alloys are being tailored for targeted engine applications at even higher operating temperatures.

Prior program work developed a new family of ACMZ alloys that exhibit extremely stable strengthening precipitates (e.g., Al_2Cu, θ′ structure) over time at very high, homologous temperatures (e.g., $\leq$350°C). The effect of crystallographic orientation of precipitates in Al-Cu alloys on strain-hardening is being studied via methods of neutron diffraction and STEM. As a lead-in to these studies on ORNL's ACMZ alloys, preliminary work was conducted on the commercial Al-Cu Alloy 206 after systematic aging treatments. Neutron diffraction results obtained during *in situ* deformation testing showed significant anisotropy with distribution of the Al_2Cu precipitates. The θ′ precipitates are present as high-aspect-ratio faceted platelets arrayed on the three crystallographic cube planes within an Al matrix. The observed anisotropy was hypothesized to be due to looping of dislocations around the high-aspect-ratio θ′ precipitates, which would manifest in the microstructure as a rotation of the θ′ precipitates away from the ideal 90° orientation. The precipitate rotation under load was modeled analytically in this work, and the STEM experimental results shown in Figure I.3.4.1.1.1 clearly validated the predicted precipitate rotations. This supports the precipitate rotation hypothesis and explains the hardening behavior that was observed *in situ* in loading neutron diffraction studies. The overall implications of the present work and for upcoming studies of the more advanced ACMZ alloys are to better understand the strain-hardening behavior of lightweight, high-temperature alloy systems with high-aspect-ratio strengthening precipitates [1].

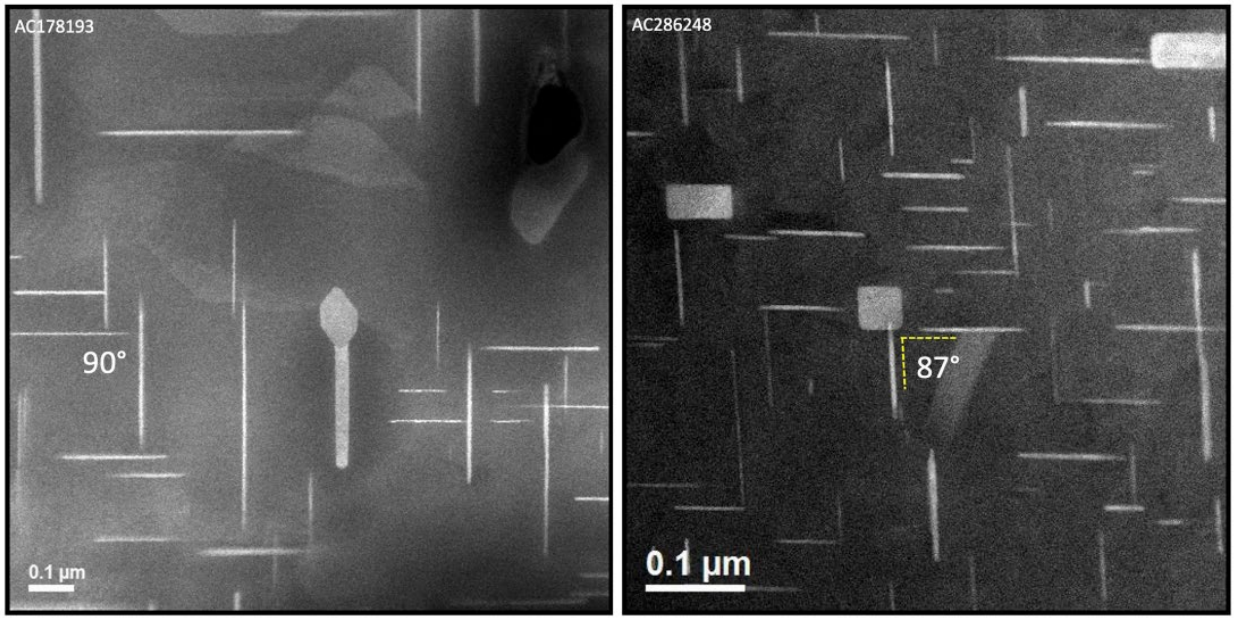

(a) (b)

Figure I.3.4.1.1.1. HAADF images where the thin θ′ precipitates are shown along a cube edge crystallographic direction (i.e., <001> zone axis orientation). (a) The undeformed sample showing the two precipitate habits at precise right angles. (b) The rotation of θ′ precipitates in the ACMZ alloy are clearly shown. Source: ORNL.

Understanding and controlling the interfaces between the Al matrix and the θ' precipitates is critical to the design of lightweight alloys that retain their strength to even higher temperatures. The semi-coherent interface structures that develop on the minor face of the θ' platelet precipitates within ACMZ alloys aged at 240°C were closely examined via STEM. Previous experimental and theoretical investigations of the Al/θ' semi-coherent interfaces concentrated on planar (001) coherent and {100} semi-coherent (S-C) interfaces. However, it was discovered in this work that the {100} S-C interface rarely exhibits extended planar regions and does not appear to have a typical periodic interface structure. The bottom section of the interface in Figure I.3.4.1.1.2 shows the most commonly observed structure in S-C {100} interfaces. This interface segment is observed to be composed of steps with terraces containing compact, perfect a<001> dislocation cores. Additionally, this boundary often contains regions that appear compositionally disordered, as can be seen in the top section of the interface in Figure I.3.4.1.1.2. What is actually seen is a superposition of the anti-phase domains of the ordered Al_2Cu θ' phase that complicates the interpretation of the microscopy images of this interface.

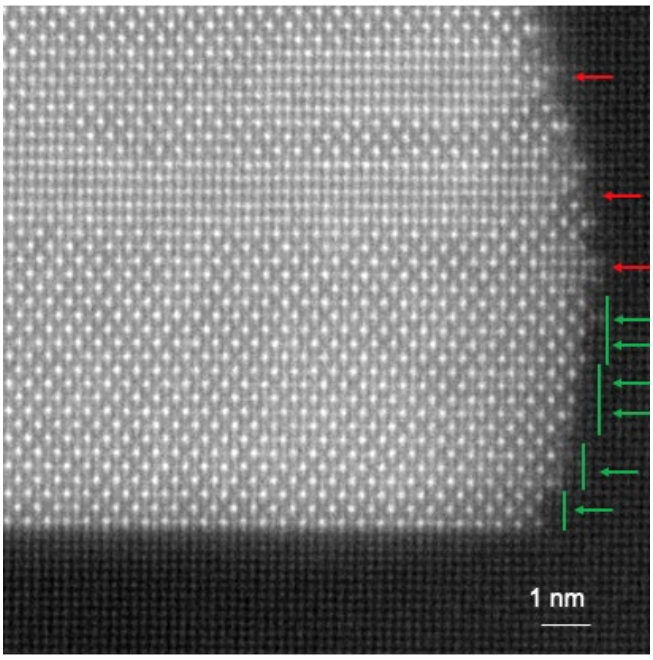

Figure I.3.4.1.1.2. HAADF image of θ' (Al2Cu) precipitate in Al. The images of <010> θ' projections often contain regions that appear to be compositionally disordered, as exemplified in the top left region of the image and these regions are a superposition of anti-phase domains of the ordered Al2Cu θ' phase. The {100} interface rarely has extended straight/planar regions and does not appear to have a periodic interface structure. The bottom section of the interface in the image shows this interface segment is composed of steps with θ' terraces that contain compact, perfect a<001> dislocation cores (green arrows). Source: ORNL.

However, there are regions of this interface without anti-phase domains where the atomic structure can be clearly determined. Figure I.3.4.1.1.3(a) shows one such S-C interface containing a {101} facet in a<010> projection. In each of the 3Al:2θ' unit segments of the interface, a dislocation core structure similar to what has been calculated for this interface [2],[3] can be seen Figure I.3.4.1.1.3(b). The presence of compact, perfect a<001> dislocation cores are identified. Another dislocation should be expected in the 2Al:1.5θ' unit segments of the interface, but that core is not as reproducible as what was computed using first principles calculations. The computed a<001> interfacial dislocation core in these segments is predicted to be composed of a continuous (001) Al plane with two (001) Cu planes on the θ' side of the interface that end at the interface, as seen in Figure I.3.4.1.1.3(c). The experimentally observed dislocation core in the 2Al:1.5θ' unit segments of the interface exhibit these main characteristics, but the atomic configurations in the core are more diverse than what has been computed for an ideal, periodic, planar boundary consisting only of 2Al:1.5θ' structural units.

The other notable feature of this interface in Figure I.3.4.1.1.3(a) are the Cu-enriched columns on the matrix side of the interface that are not directly associated with the dislocation core. These fingers of Cu segregation have been interpreted to be evidence of a transitional θ'' phase forming at the interface [4]. The expected periodicity of the Cu-rich planes in θ'' were not observed. Instead, the Cu-rich planes extending into the Al matrix typically match the spacing of the structural units that comprise the interface. DFT calculations performed on the 3Al:2θ' unit supercells of the (100) semi-coherent interface identify these sites by the orange arrows in Figure I.3.4.1.1.3(a) as the preferred Cu segregation site [3]. Again, the observed Cu-rich sites in these (100) semi-coherent interfaces are calculated to be where Cu segregates in this interface. The defects present in this S-C interface, their structure, and most importantly their role in the incorporation of Cu into and out of the strengthening precipitates have been identified. These interfacial structural units regulate the boundary mobility, a key factor in understanding the stability of these precipitates at elevated temperatures.

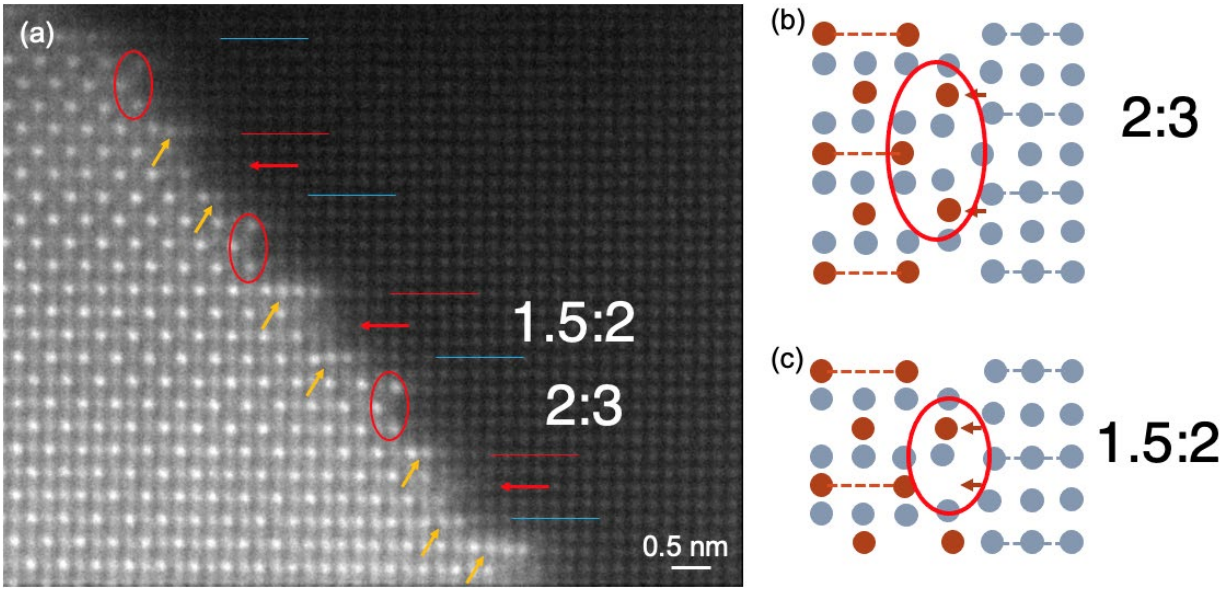

Figure I.3.4.1.1.3. (a) HAADF image of a {101} facet of the semi-coherent interface seen in a <010> projection. Extra Cu columns (segregation sites) are observed at the interface by the orange arrows. (b) In each of the 3Al:2θ' unit-cell segments of the interface, a dislocation core denoted by the red ellipse structure similar to that calculated for this interface [2],[3] is seen. The red arrows in the schematics identify the extra planes associated with the dislocation cores. (c) Another dislocation should be in the smaller 2Al:1.5θ' unit-cell segments of the interface denoted by the red arrows in (c), but that core is not as reproducible as the one computed using first principles calculations. Source: ORNL.

Precipitation-hardened Al alloys all rely on metastable phases that grow, dissolve, or transform at elevated temperatures. Understanding the atomic structure of the principal growth interfaces is an important step towards enhancing precipitate stability. Through composition and heat-treatment, these insights will enable guided modifications of interfacial arrangements with the aim to precisely control the structures that are critical for enhanced thermal stability of the strengthening precipitates in Al alloys.

APT is a microscopy technique that can reconstruct the 3D atomic locations within a small volume of material (~100 × 100 × 100 nm^3) with <1 nm resolution and 10 ppm sensitivity. Therefore, APT is a good technique to measure matrix compositions, precipitate contents, and interfacial segregation profiles at extremely high-resolution. In this thrust, APT was used to better understand the nanostructures of advanced high-temperature Al alloys with various micro-alloying additions after various thermal exposures to develop low-cost, oxidation-resistant materials for exhaust manifolds and turbo housings, and to accelerate fundamental understanding and development of new lightweight alloys for AM methods.

The hardness of Al-Cu alloys relies on a θ' rich microstructure; however, θ' is a metastable phase that can rapidly coarsen and transforms to θ at temperatures ≥ 250°C. This transformation softens Al-Cu alloys, preventing them from having adequate strength for most higher temperature applications. The ACMZ family of alloys are lightweight Al-Cu alloys with Mn and Zr additions (and intentionally low Si content) that retain hardness after lengthy exposures to 350°C. APT was used to quantify matrix compositions, θ' compositions, and interfacial solute segregation to θ' interfaces within ACMZ alloys to better understand its high-temperature microstructural stability. The APT data clearly revealed that Mn and Zr segregation behaviors to specific θ' interfaces are critical for the thermal stability of ACMZ [5],[6] and that they both work synergistically to stabilize θ' at higher temperatures. These additions are synergistic because Zr is an ineffective stabilizer without Mn addition, while Zr further improves the thermal stability of θ' when added in addition to Mn. APT and STEM results showed that additions of Mn, which is more mobile in Al than Zr, stabilize the θ' surfaces for a long enough period of time to allow for the slower diffusing Zr to segregate to θ' interfaces and eventually form a highly stable $L1_2$ structure. Formation of the interfacial $L1_2$ structure further improves the thermal stability of θ'. Figure I.3.4.1.1.4 shows experimental data evidencing this conclusion and a schematic of this process.

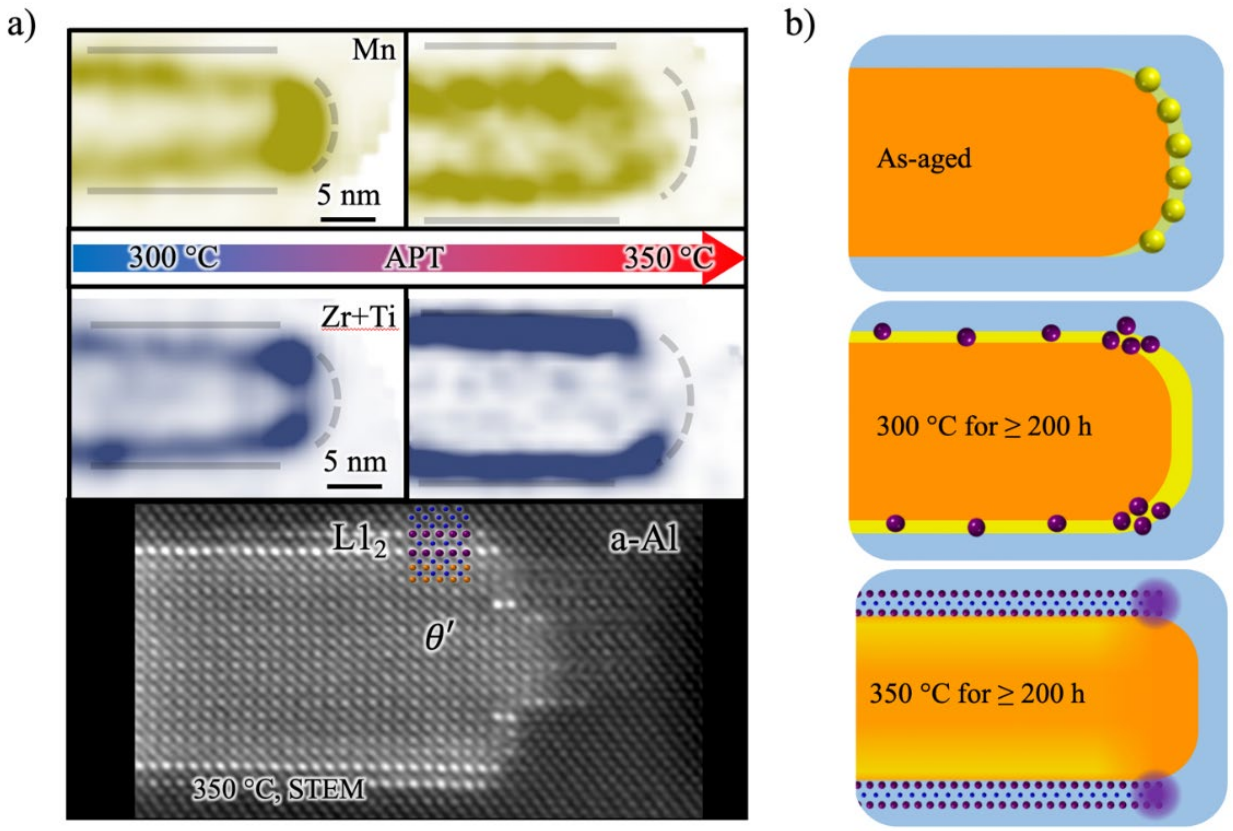

Figure I.3.4.1.1.4. (a) Top: APT 2D composition profiles of the θ' particle cross-section in Al after exposure to the indicated temperature for 2,000 hr. Coherent and semi-coherent interfaces are labeled by solid and dotted lines, respectively. Bottom: STEM image of θ' after a 350°C exposure with $L1_2$ $Al_3(Ti,Zr)$ at the coherent interface. (b) A schematic showing the Mn and Zr interfacial segregation and phase formation behaviors in the as-aged microstructure and lengthy exposures to 300 and 350°C. The earlier Mn segregation stabilizes θ' for a long enough time for the slower diffusing Zr to segregate to the coherent interfaces and eventually form an $L1_2$ structure. This figure contains data from reference [5]. Source: ORNL.

STEM and APT of Higher Temperature (Ni-Based) Alloys (Thrust 2 Higher Temperature Engine Alloys)

The Thrust 2 alloy development tasks investigate cost-effective higher temperature engine alloys (e.g., Ni- and Fe-based alloys) and the mechanisms that determine strength, microstructural stability, and oxidation resistance. Two example efforts are discussed below. In the first effort, new, cost-effective (e.g., lower Ni-based) alumina-forming alloys for 900-950°C are being developed. The second effort seeks to understand oxidation behavior of various commercial automotive exhaust valve alloys during high-temperature oxidation with laboratory-based cyclic oxidation testing in simulated exhaust environments. Advanced characterization is essential to developing an understanding of both.

Although Ni-based alloys have good high-temperature tensile and fatigue properties, they are expensive. New novel compositions with reduced Ni content are being explored, such as precipitation-strengthened superalloys with increased Fe content. These new higher temperature, lower cost alloys are being developed for exhaust valves in both automotive gasoline and HDDEs. The high-temperature fatigue properties of these superalloys depend on volume fraction, particle-size distribution, morphology (i.e., cubic vs. spheroidal) and an anti-phase boundary-fault energy of the reinforcing γ' phase (nominally, Ni_3Al). The current advanced characterization study analyzes the microstructure of a novel NiFeCr-based superalloy developed at ORNL after solutionizing and heat-treatment at 800°C for 4 hours. Electropolished thin-foil samples were characterized in the JEOL JEM-2200FS AC-STEM, with HAADF images in particular showing details of the γ' structure and distribution within the matrix, γ, as observed in Figure I.3.4.1.1.5. Understanding the γ/γ' morphology, size distribution and volume fraction is key in understanding the high-temperature mechanical properties, particularly fatigue, of these novel precipitation-strengthened Fe and Ni containing superalloys.

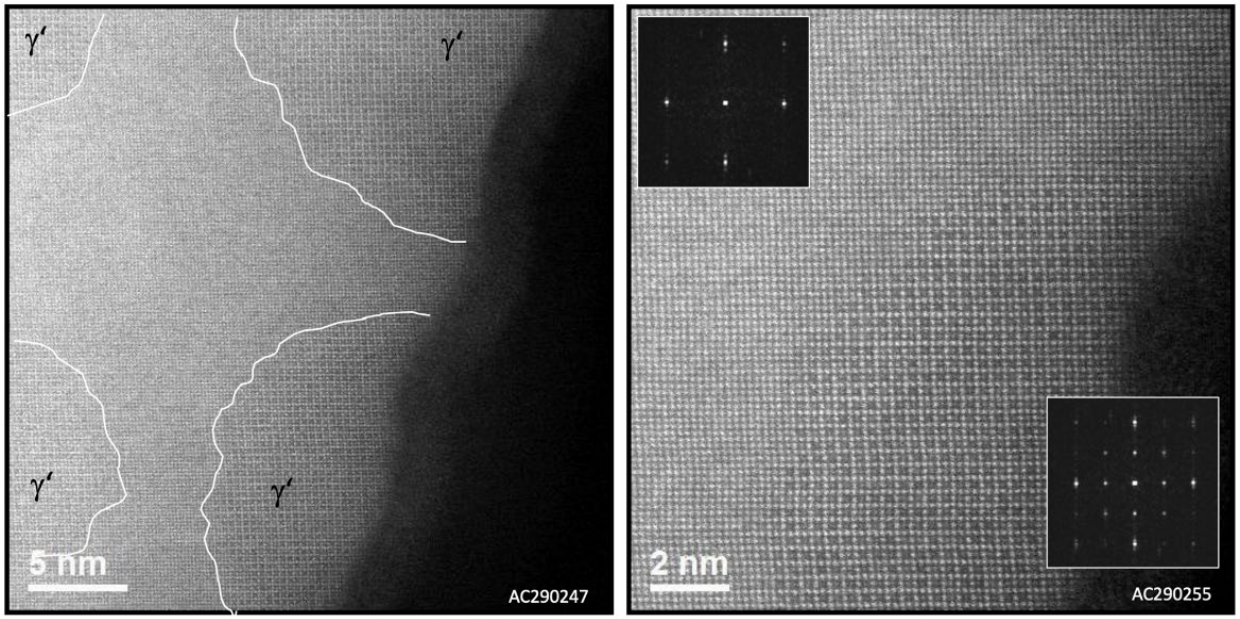

(a) (b)

Figure I.3.4.1.1.5. (a) HAADF image of a NiCrFe thin alloy foil in <001> zone axis orientation, showing several ordered γ' precipitates in the disordered γ matrix. (b) At higher magnification, the atomic columns are clearly revealed, and the insert diffractograms from the matrix and precipitate show the additional periodicities resulting from the doubling of the unit-cell size in the γ'. These precipitates are generally spheroidal, with a distinct interface between precipitate and matrix. Source: ORNL.

Currently, the design and optimization of austenitic Ni and Fe alloys with high creep strength and oxidation resistance for high-temperature applications are based primarily on experimental know-how and oxidation maps empirically developed in the early 1970s. The transition from protective to non-protective oxidation (and vice-versa) in these alloys is an extremely important phenomenon for the practical use of these materials. The O-solubility in the alloys plays a crucial role in controlling this transition. Available experimental results suggest the critical Cr/Al concentrations responsible for a protective oxide scale morphology may be strongly affected by both the influences of major (e.g., Ni, Fe, Al, and Cr) and minor (e.g., C, Mn, Mo, N, Nb, Si, Ti, and V) alloying additions on O-solubility in the alloys.

Figure I.3.4.1.1.6(a) shows the APT atom map of Ni200 oxidized at 1,000°C for 48 hours with O and Ni ions displayed as blue and green dots, respectively, with no evidence for O supersaturation within the metal a few nanometers from the oxide/metal interfaces for these alloys. A comparison between the O concentration, as shown in Figure I.3.4.1.1.6(b), within a few nanometers and about 1 mm from the NiO/Ni interface, as observed in Figure I.3.4.1.1.6(c) and (d), shows that both values were below the noise level of APT (e.g., ≤ 10 ppm). These values are significantly lower than that reported in the literature (450 ppm at 1,000°C) or expected based on theoretical calculations (e.g., Sievert's law). The hypothesis is that O is segregated to the alloy grain boundaries. This will be the focus of future investigations.

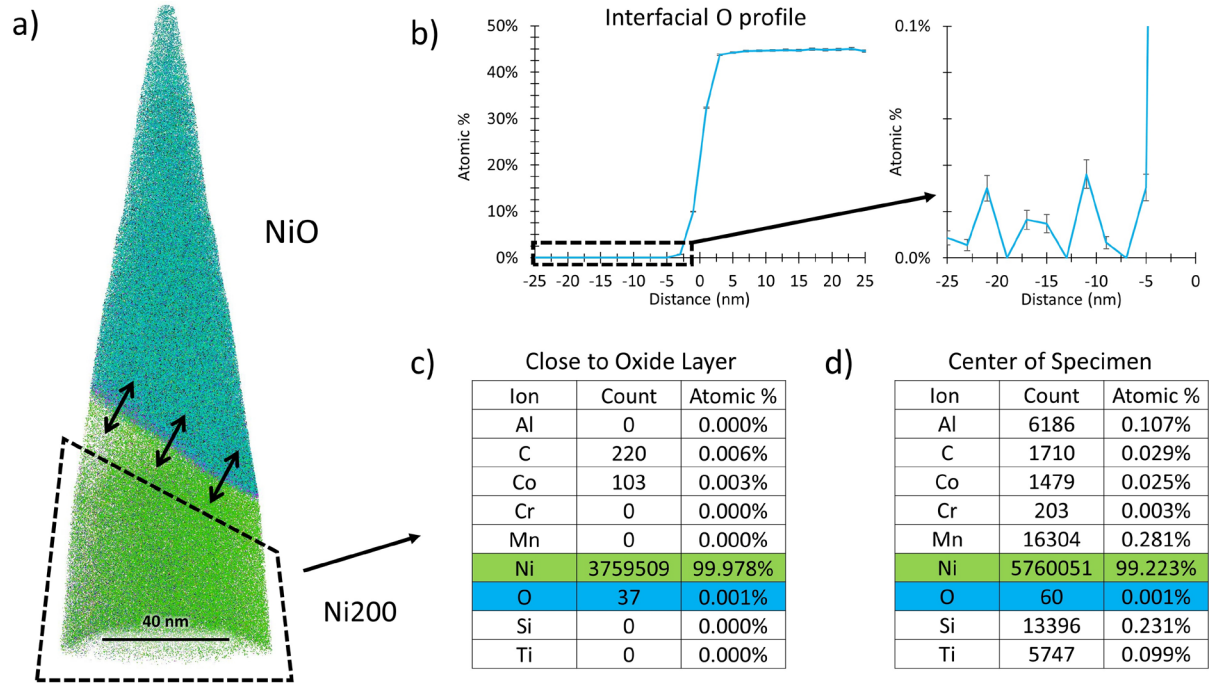

c) Close to Oxide Layer

Ion	Count	Atomic %
Al	0	0.000%
C	220	0.006%
Co	103	0.003%
Cr	0	0.000%
Mn	0	0.000%
Ni	3759509	99.978%
O	37	0.001%
Si	0	0.000%
Ti	0	0.000%

d) Center of Specimen

Ion	Count	Atomic %
Al	6186	0.107%
C	1710	0.029%
Co	1479	0.025%
Cr	203	0.003%
Mn	16304	0.281%
Ni	5760051	99.223%
O	60	0.001%
Si	13396	0.231%
Ti	5747	0.099%

Figure I.3.4.1.1.6. (a) An APT atom map of oxidized Ni200 with O and Ni ions displayed as blue and green dots, respectively. (b) O profile at the NiO/Ni interface showing O contents at the noise level within nanometers of the interface. (c) Composition close to the oxide layer containing a larger volume and more atoms to increase the compositional measurement sensitivity. (d) Composition in the center of the oxidized specimen (~1 mm from the Ni/NiO interface). Source: ORNL.

Systematic measurements to quantify O concentrations beneath an external oxide scale have never been attempted before and the results will provide valuable information on the role of alloy composition on O-solubility. The measured O-solubility combined with the CALPHAD data for the diffusion of alloying elements in the alloys will serve as an input for Wagner's model of internal oxidation. The envisaged approach can be employed to construct oxidation maps for high-temperature alloy systems in a wide temperature range. This will assist alloy designers and engineers in the selection, development, and optimization of novel high-temperature materials, components, and applications.

STEM and APT of Newly Designed High-Temperature Aluminum Alloys (Thrust 3 Additive Manufacturing)

Thrust 3 investigates AM of various key classes of powertrain alloys. Two directions are discussed below. The first direction focuses on the development of a promising new family of Al-Cu-Mn-Zr-Ce alloys for AM processing methods. The second direction focuses on AM technologies to fabricate austenitic steels for piston, turbocharger, and exhaust applications at 600-850°C, with the new manufacturing methods leading to locally tailored properties, microstructure, and/or chemistry.

The Al-Ce-Mn alloy system has been designed for the laser powder bed AM process, and the resultant structure and properties are being investigated to enable further refinement of alloy and AM process design. After LPBF, the system demonstrates fascinating new microstructures, including complex intermetallic dispersions on a very fine-scale, due to the very rapid solidification processes experienced by aluminum alloys in LPBF. The as-built material exhibited a variety of non-equilibrium phase compositions and morphologies [7], that then evolved further with additional time and heat-treatment. After 350°C for 96 hours, one alloy exhibited nascent plate structures beginning to form in the eutectic regions. After another 96 hours treatment at 400°C, the presence of a plate phase-dominated the eutectic region, as can be seen in the inset of Figure I.3.4.1.1.7(a). The plate morphology of one of the crystals in the inset shown in Figure I.3.4.1.1.7(a) is primarily composed of a previously unknown crystal structure in the Al-Ce-Mn system, layered internally with a small volume fraction of previously identified $Al_{20}Mn_2$ Ce phase. The small area outlined in red over some dark bands is shown reoriented in Figure I.3.4.1.1.7(b). The known $Al_{20}Mn_2Ce$ phase is on the left of Figure I.3.4.1.1.7(b), and the prior unknown phase crystal structure, labeled $Al_{51}Mn_7Ce_4$, is on the right. The $Al_{51}Mn_7Ce_4$ phase was identified based on a comparison to crystallographic information from an Al-Mo-La alloy. The observed areas of both these phases are shown in matching color boxes in Figure I.3.4.1.1.7(c) with simulated structures from both the $Al_{20}Mn_2Ce$ and the normalized $Al_{51}Mn_7Ce_4$ phases shown in the insets. The match between the observed results and the database simulation is excellent.

The addition of Mn to an Al-Ce-Ni ternary eutectic alloy designed for AM was found to further improve elevated temperature properties of this material. The goal of this study was to use AC-STEM combined with EELS measurements to identify the phases present in the alloy, as well as other microstructural features that play a role in this enhanced alloy.

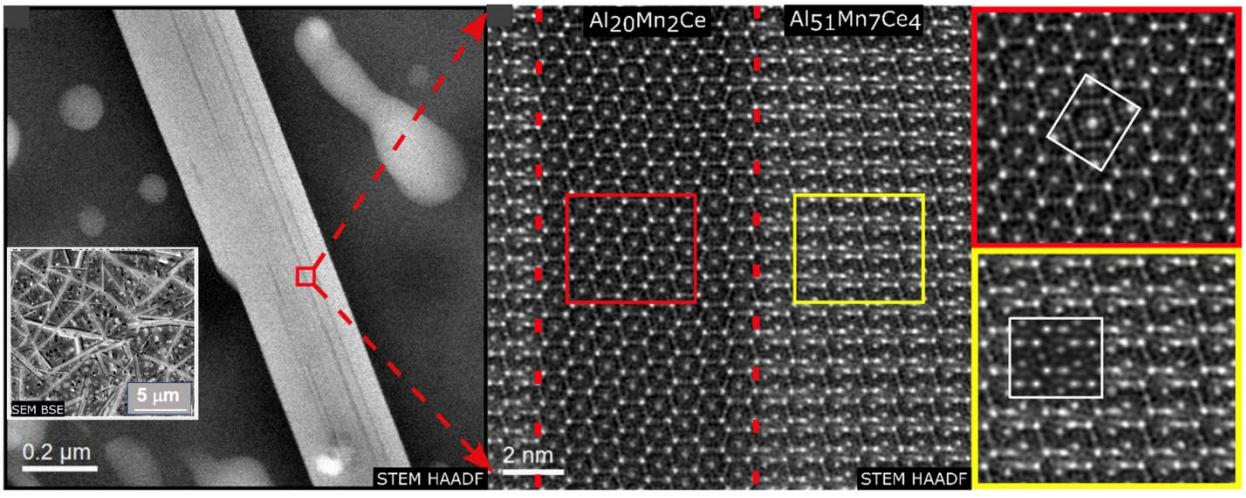

Figure I.3.4.1.1.7. (a) A STEM HAADF micrograph of region within an Al-C-Mn alloy after 96 h at 400°C; inset is a lower magnification view from a SEM. (b) Enlarged view of precipitate shows of two phases. (c) Each phase is enlarged further from (b) showing that the simulated atomic structures (white insets) match the observed results. Source: ORNL.

The microstructures of the Al-Ce-Ni-Mn alloy were found to be composed of a distribution of at least four intermetallics in an Al matrix, as can be seen in Figure I.3.4.1.1.8. The expected $Al_{11}Ce_3$ and Al_3Ni intermetallic phases were found to be present although the volume fraction of the Al_3Ni was relatively small. In addition to these phases, two other phases containing all four elements were found. One of the phases contained Al, Mn, Ce, and small amounts of Ni, while the other contained Al, Ni, Ce, and small amounts of Mn. These phases have been tentatively identified as $Al_{20}Mn_2Ce$ and $Al_{23}Ni_6Ce_4$, although additional work is needed to confirm this identification and the variability of the elemental stoichiometry.

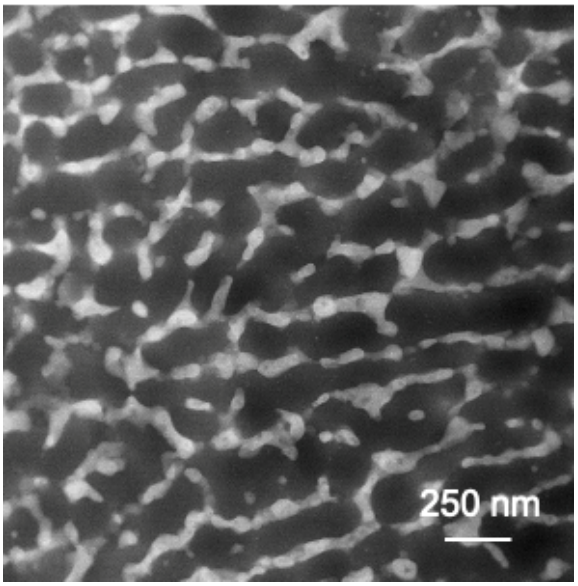

Figure I.3.4.1.1.8. HAADF image of the additive Al-Ce-Ni-Mn alloy. The microstructure consists of cells of Al-rich matrix (e.g., the dark regions) separated by strings of alternating intermetallic phases. Source: ORNL.

EELS and atomic resolution imaging conclusively identified the two-component phases present in the alloy, $Al_{11}Ce_3$ and Al_3Ni, as seen in Figure I.3.4.1.1.9. Additional work to confirm the identity of additional unknown phases is continuing.

These dispersion-strengthened, printed Al-Ce-Ni-Mn alloys are being investigated to address the need for lightweight structural materials for elevated temperature applications as an alternative to precipitation-hardened aluminum alloys, such as the commercial cast Alloys 319 or 356 or the advanced cast-Al alloy ACMZ. It has been demonstrated that relatively large volume fractions of intermetallic particles in the Al matrix are possible via AM. It is now necessary to demonstrate how well distributed these phases are, and how stable the dispersions strengthened microstructures are against coarsening or transforming to other phases over time at elevated temperatures. Once the phases present in the alloy are conclusively determined, investigations of the: (a) correlation between resultant microstructures and mechanical properties; (b) thermal stability of the microstructures; and (c) crystallography of the microstructures formed will follow.

APT was used to identify phase compositions in AM Al-Cu-Ce, Al-Cu-Ce-Zr, Al-Cu-Ce-Zr-Mn, Al-Ce-Ni-Mn, Al-Ce-Mg-Zr, and ACMZ. By comparison, the AM versions of the ACMZ alloys (designed by this VTO-funded program) are much harder than cast ACMZ. Preliminary studies have shown that these alloys retain a higher hardness after lengthy thermal exposures to extreme temperatures. The mechanisms behind the higher hardness and better thermal stability of AM alloys are not yet well understood, but there is evidence that they are linked to the unique as-printed microstructure and ability to supersaturate the matrix allowed by the fast-cooling rates found in AM processes. These unique microstructures contain several phases that are difficult to identify, making compositional measurements from APT important for phase identification. APT is also being used to discover solute segregation to precipitate interfaces, which could also contribute to thermal stability.

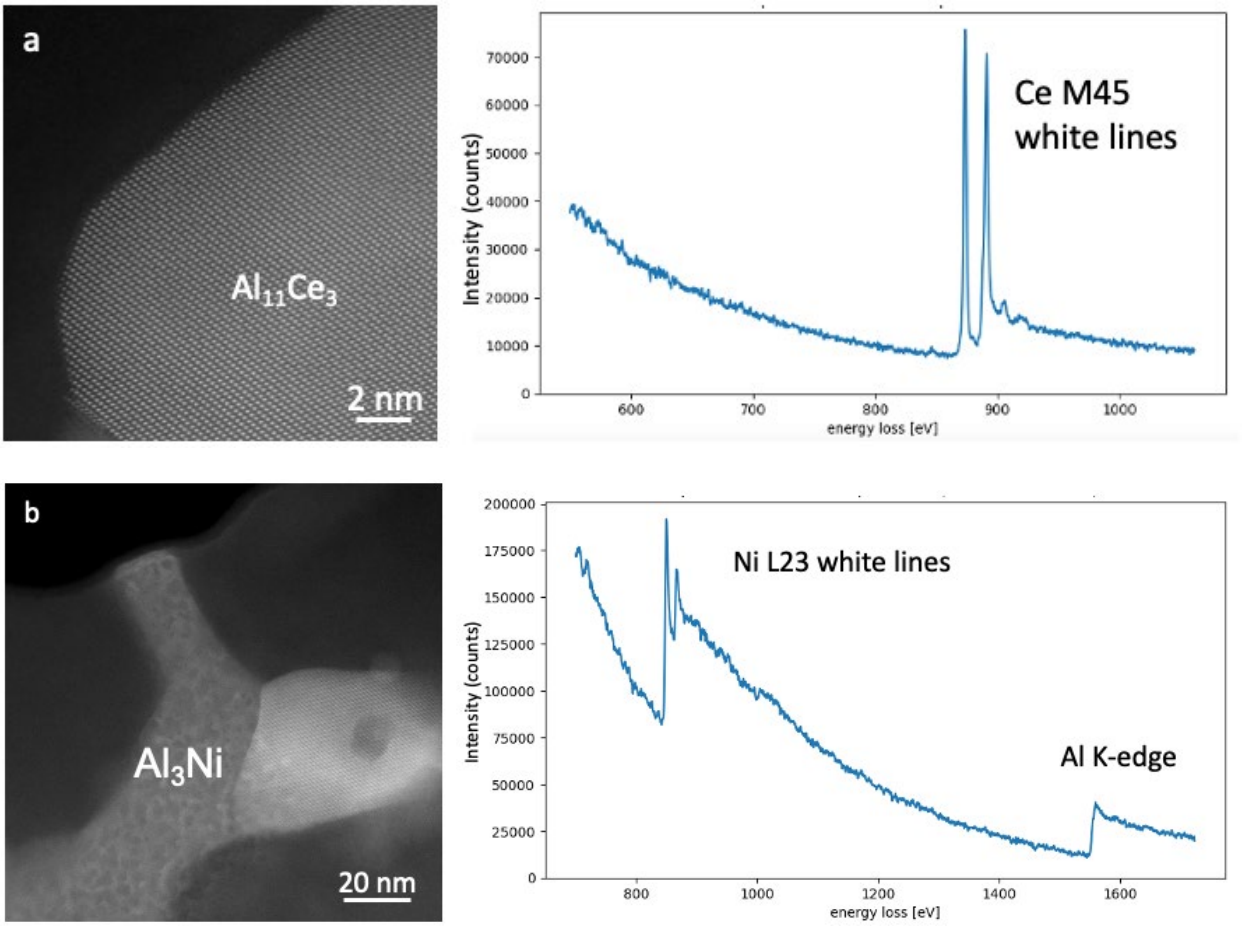

Figure I.3.4.1.1.9. HAADF images and EEL spectra of intermetallics in an additive Al-Ce-Ni-Mn alloy. (a) Al11Ce3 phase. (b) Al3Ni phase. Source: ORNL.

STEM of High-Temperature Stainless Steels Printed via LPBF AM

In another Thrust 3 task, the microstructure of a heat-treated, high-temperature austenitic steel Fe-25Cr-20Ni-1.4Nb-0.2C (HK30Nb) fabricated by LPBF process was characterized by STEM to identify nanoscale precipitates within subgrain cell boundaries. The subgrain structure was maintained through heat-treatment with a high-density of fine cellular structure showing three types of carbides at these subgrain boundaries. First, the initial nanosized carbides were identified as Nb_3Cr_3C based on high-resolution STEM imaging. These grew slightly from ~2 to ~5 nm after 5 hours of exposure to 700°C. The second type of carbides were identified as $Cr_{23}C_6$ using HR-STEM but were much larger (~10-30 nm) as shown in Figure I.3.4.1.1.10. The third carbide type was ~40 nm in size and was speculatively identified as NbC based on the energy-dispersive x-ray spectroscopy results. A structural analysis will be performed to confirm the phase identification. These results support and begin to explain the outstanding creep behavior of these printed alloys, suggesting that the extended creep lifetime of the LPBF HK30Nb steel at 700°C was due to the presence of the printed subgrain structure, which was likely stabilized by these nanosized carbides.

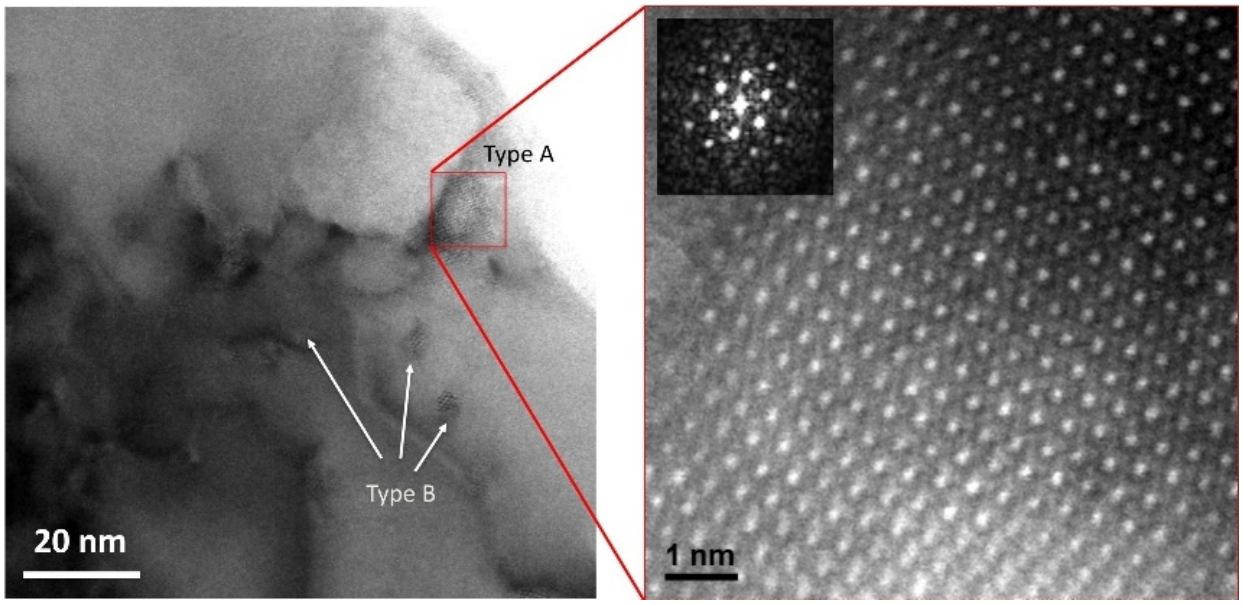

Figure I.3.4.1.1.10. (a) Bright-field STEM image and (b) high-resolution HAADF-STEM image with fast Fourier transform (inset) highlighting $Cr_{23}C_6$ carbide (Type A) at the subgrain boundary in LPBF Hk30Nb after exposure for 5 hours at 700°C. Type B was identified as Nb_3Cr_3C. Source: ORNL.

Conclusions

In FY 2020, the advanced characterization activity at ORNL within the PMCP provided detailed characterization of a wide range of materials and phenomena, using advanced microscopy capabilities. This report provides representative examples of electron microscopy and APT results, which contribute to the design and compositional development of newly developed advanced alloys and processing methods (with superior targeted properties at more extreme stresses and temperatures) in multiple categories, including cast high-temperature Al alloys, printed high-temperature Al alloys, wrought NiFeCr alloys, and printed high-temperature stainless steels (among others).

Key Publications

1. Milligan, B. K., D. Ma, L. F. Allard, A. Clarke, and A. Shyam, 2020, "Crystallographic orientation-dependent strain-hardening in a precipitation-strengthened Al-Cu alloy," *Acta Mater.*, submitted.
2. Poplawsky, J. D., B. K. Milligan, L. F. Allard, D. Shin, P. Shower, M. F. Chisholm, and A. Shyam, 2020, "The synergistic role of Mn and Zr/Ti in producing θ′/L12 co-precipitates in Al-Cu alloys," *Acta Mater.*, Vol. 194, pp. 577–586.

References

1. Milligan, B. K., D. Ma, L. F. Allard, A. Clarke, and A. Shyam, 2020, "Crystallographic orientation-dependent strain-hardening in a precipitation-strengthened Al-Cu alloy," *Acta Mater.*, submitted.
2. Kim, K., B.-C. Zhou, and C. Wolverton, 2019, "Interfacial stability of θ'/Al in Al-Cu alloys," *Scripta Mater.*, Vol. 159, pp. 99–103.
3. Shin, D., A. Shyam, S. Lee, Y. Yamamoto, and J. A. Haynes, 2017, "Solute segregation at the Al/ θ'-Al_2Cu interface in Al-Cu alloys," *Acta Mater.*, Vol. 141, pp. 327–340.
4. Bourgeois, L., N. V. Medhekar, A. E. Smith, M. Weyland, J.-F. Nie, and C. Dwyer, 2013, "Efficient atomic-scale kinetics through a complex heterophase interface," *Phys. Rev. Lett.*, Vol. 111, Art. 046102.

5. Poplawsky, J. D., B. K. Milligan, L. F. Allard, D. Shin, P. Shower, M. F. Chisholm, and A. Shyam, 2020, "The synergistic role of Mn and Zr/Ti in producing θ′/L12 co-precipitates in Al-Cu alloys," *Acta Mater.*, Vol. 194, pp. 577–586.

6. Shyam, A., S. Roy, D. Shin, J. D. Poplawsky, L. F. Allard, Y. Yamamoto, J. R. Morris, B. Mazumder, J. C. Idrobo, A. Rodriguez, T. R. Watkins, and J. A. Haynes, 2019, "Elevated temperature microstructural stability in cast-Al-Cu-Mn-Zr alloys through solute segregation," *Mater. Sci. Eng. A*, Vol. 765, Art. 138279.

7. Sisco, K., L. F. Allard, A. Shyam, A. Plotkowski, R. Dehoff, Y. Yang, S. Bahl, and S. Babu, 2020, "Non-equilibrium solid-state transformations in additively manufactured ternary Al-Ce-Mn," *Microsc. Microanal.*, submitted.

I.3.4.2 Advanced Computation (4B)

I.3.4.2.1 Modeling of Light-Duty Engines (Task 4B4) (Oak Ridge National Laboratory)

Charles E. A. Finney, Principal Investigator
Oak Ridge National Laboratory
1 Bethel Valley Road
Oak Ridge, TN 37831
E-mail: finneyc@ornl.gov

Jerry L. Gibbs, DOE Technology Manager
U.S. Department of Energy
E-mail: jerry.gibbs@ee.doe.gov

Start Date: October 1, 2019 End Date: September 30, 2023
Project Funding: $150,000 DOE share: $150,000 Non-DOE share: $0

Project Introduction

Internal combustion engines power the vast majority of vehicles in LD applications and are projected to remain the primary powerplant for automotive propulsion for at least the next 20 years [1], even accounting for the heavy current emphasis on electrification. Automotive LD engines have evolved significantly over the past several decades [2] with specific power and emissions output targets being driven by fuel economy and pollutant emissions regulations, such as the Corporate Average Fuel Economy standards [3]. This rapid evolution has been enabled by advances in combustion control and boosting (e.g., turbocharging). This has allowed smaller, lighter engines to outperform their predecessors. However, the consequence of increased specific output via intensified combustion is more extreme engine operating conditions, resulting in both higher temperatures and pressures experienced by engine materials. An initial study performed by ORNL in 2018 identified several potential advantages to higher performance materials that enable even higher specific engine output [4].

As in cylinder temperatures continue to increase, they are presently nearing the practical operating limit for common commercial alloys used in the pistons, valves, and cylinder heads. A projection of advanced LD engine performance into the coming decades has identified potential temperature ranges in the cylinder environment [5], but the required materials properties to operate in these environments are still unknown. This project seeks to inform materials selection and development by using a computational approach to estimate the thermomechanical environment at intensified operating conditions, as well as the resulting stresses, fatigue, and creep experienced by the respective materials in key engine components.

The primary focus is on higher temperature cast-Al and wrought steel alloys, particularly for use in the pistons, valves, and cylinder head. More advanced versions of these alloys are anticipated to be critical in allowing the continued development of high-efficiency internal combustion engines. The fundamental efforts in this project seek to predict the thermomechanical materials environment at projected future operating conditions. The required performance and properties can help guide alloy selection or alloy development targets for future boosted engines with higher power densities and superior efficiencies.

Objectives

This project focuses on understanding the thermal and mechanical stresses experienced by engine cylinder component materials at extreme operating conditions. Key targets are LCF and creep in alloy materials in the piston, valves, and cylinder head. This low-to-mid-TRL study will provide insight into projected operating conditions and suggest the needs and targets for future materials research.

Approach

This project uses a computational approach to model combustion and heat transfer for LD internal combustion engine speeds and loads. Computational models are constructed based on measured design data, and limited validation data are used to tune and calibrate the models to match experimental engine performance. Once the combustion models are validated at known conditions and performance characteristics, operating points at intensified combustion regimes are simulated, and cylinder pressure and cylinder heat flux maps are calculated. These combustion outputs are then used as BCs for a mechanical loading model to evaluate the stresses and other materials responses to the combustion conditions. A multi-year plan beginning in FY 2019 provides for the first year to set up and validate the model components and for the exploration of potential operating scenarios using the models in following years.

The target engine platform is a GM 2.0L turbocharged direct-injected LNF "EcoTec" engine, rated at 260 bhp, 260 ft-lb in stock trim. The engine is used by complementary activities funded by the VTO in the Partnership on Advanced Combustion Engines (PACE) program, which provides experimental validation data at a limited set of operating points. Both programs have the same computational models but use them differently based on programmatic goals.

The two computational models for combustion are for a low-dimensional treatment and a high-dimensional treatment. Here, low-dimensional means that the properties of a component volume might be described by a single, mean value (0D), or simply along a characteristic length (1D), without accounting for radial and circumferential variations. Whereas the high-dimensional (3D) treatment accounts for all variations with very fine (0.5–4.0 mm) spatial resolution. Both models use design and operating data measured at ORNL. The low-dimensional model is implemented in GT-POWER, an industry-standard system-level simulation suite with components catered for internal combustion engine modeling. The GT-POWER model incorporates high-fidelity geometry surface data of the pistons, valves, and head as measured for use in conjugate heat transfer (CHT) modeling to solve for materials temperatures. The high-dimensional model is implemented in CONVERGE, an industry-standard CFD code with high-fidelity combustion and fluid dynamics models. The CONVERGE model also uses the measured geometry data for CHT modeling.

The structural model for thermally and mechanically induced stresses in the materials is implemented in ANSYS, an industry-standard code based on finite element modeling. The code uses a solid model based on the same surfaces used in the combustion models. Cylinder heat flux maps and cylinder pressures from the high-dimensional combustion model are used as BCs. Additionally, the cooling surface thermal conditions are specified, or calculated using the CFD code. The relevant materials thermal and physical properties for each component are also included.

Results

In FY 2020, the following major activities were accomplished:

- Completed setup of the GT-POWER model, with detailed CHT treatments in the piston, valves, and head.
- Completed setup of the CONVERGE model.
- Completed setup of the ANSYS model.
- Obtained validation data from PACE activities.
- Began tuning of the CONVERGE model to match the experimental data.

A major task of the ANSYS setup was a simplification of surfaces for better handling within the software. One example of this simplification is seen in Figure I.3.4.2.1.1 which shows an exhaust valve with both the original and grouped, or simplified, surface features. The internal resolution of the component is retained and the simpler topology improves model performance.

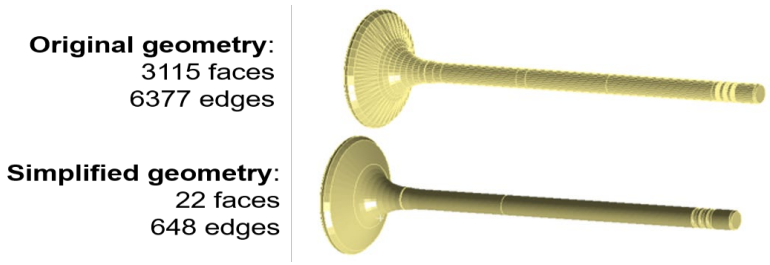

Figure I.3.4.2.1.1. Virtual simplification of a valve surface, with fewer resultant features, to aid FEA. Source: SimuTech.

Acquisition of the experimental validation data was delayed because of workplace restrictions during the COVID-19 pandemic, but several load points at an engine speed of 2,000 rpm were provided. The project will extend its focus to engine speeds of 5,000 rpm or higher. This is outside the range of current PACE targets but is where engine operation currently faces the greatest materials challenges. Because of the high temperatures sustained by the engine at the highest engine speeds and loads, engine control strategies often compromise engine performance to protect the materials in certain engine components [4].

With the validation in place, two load points at 2,000 rpm were selected for CFD model calibration: 4 bar and 22 bar indicated mean effective pressure. The higher load-point is of most interest to this project because of the more intense combustion conditions. This baseline simulation was tuned using a fully iterative CHT solution in which materials temperatures and thermal BCs are solved rather than being estimated. In this iterative process, multiple consecutive engine cycles were simulated, with the first cycle being the most inaccurate because initial BCs were estimations. Over the course of several ensuing engine cycles, the engine conditions, including materials temperature distributions, converged to a steady state value.

Figure I.3.4.2.1.2 shows the cylinder pressure trace during combustion for the first cycle of the 22 bar indicated mean effective pressure case, with only assumed BCs, compared with the distribution (e.g., ±2 standard deviations) of experimental data. In the first cycle while the combustion phasing, measured by the crank angle of 50% fuel mass burned (CA50), was close, the simulation's peak pressure was somewhat lower than the experimental mean because the equivalence ratio (φ) from initial conditions was 1.09 instead of the target 1.00. With multiple-cycle convergence, the target equivalence ratio and pressure trace will be converged upon. This simulation model validation process is ongoing.

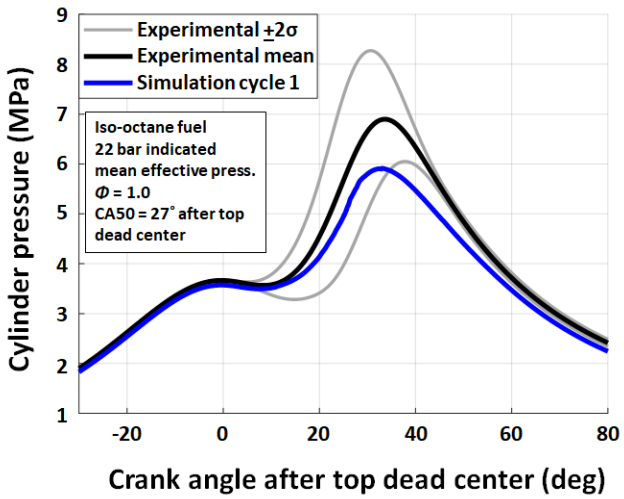

Figure I.3.4.2.1.2. Experimental and simulated cylinder pressure traces used to validate the CFD model. Source: ORNL.

Conclusions

In this first year of model development, multiple components were assembled and have undergone individual refinement before being fully integrated. The integrated set of models will permit estimation of combustion heat fluxes, resultant temperatures, and thermal and mechanical stresses in cylinder components in a variety of operating conditions and strategies. This knowledge will inform future materials selection and development for the next-generation of LD internal combustion engines.

References

1. Reitz, R. D., H. Ogawa, R. Payri, T. Fansler, S. Kokjohn, Y. Moriyoshi, A. K. Agarwal, D. Arcoumanis, D. Assanis, C. Bae, K. Boulouchos, M. Canakci, S. Curran, I. Denbratt, M. Gavaises, M. Guenthner, C. Hasse, Z. Huang, T. Ishiyama, B. Johansson, T. V. Johnson, G. Kalghatgi, M. Moike, S. C. Kong, A. Liepertz, P. Miles, R. Novella, A. Onorati, M. Richter, S. Shuai, D. Siebers, W. Su, M. Trujillo, N. Uchida, B. M. Vaglieco, R. M. Wagner, and H. Zhao, 2019, "The future of the internal combustion engine," *Int. J. Engine Res.*, Vol. 21, No. 1, pp. 3–16.
2. Splitter, D., A. Pawlowski, and R. Wagner, 2016, "A historical analysis of the co-evolution of gasoline octane number and spark-ignition engines," *Front. Mech. Eng.*, Vol. 1, Art. 16.
3. U. S. National Highway Traffic Safety Administration (NHTSA) website, n.d., "Corporate average fuel economy." Available at: www.nhtsa.gov/laws-regulations/corporate-average-fuel-economy. Accessed 2 December 2020.
4. Mills, Z. G., C. E. A. Finney, K. D. Edwards, and J. A. Haynes, 2019, "Benefits of higher temperature operation in boosted SI engines enabled by advanced materials," *Proceedings of the 2018 Fall Technical Conference of the ASME Internal Combustion Engine Division*, 4–7 November 2018, San Diego, CA, USA. Paper ICEF2018-9739.
5. U. S. Department of Energy Vehicles Technologies Office website, 2013, "Light-duty vehicles technical requirements and gaps for lightweight and propulsion materials." Available at: www1.eere.energy.gov/vehiclesandfuels/pdfs/wr_ldvehicles.pdf. Accessed 2 December 2020.

Acknowledgements

Co-investigators include Z. G. Mills and F. D. F. Chuahy of ORNL. Consulting contributors include J. A. Haynes and G. Muralidharan of ORNL. Experimental validation data were provided by V. B. Colomer and D. A. Splitter of ORNL.

I.3.5 Exploratory Research for Powertrain Materials – Thrust 5

I.3.5.1 Advanced Anticorrosion Coatings on Lightweight Magnesium Alloys by Atmospheric CO_2 Plasma Treatment (5A) (Oak Ridge National Laboratory)

Gyoung Gug Jang, Co-Principal Investigator
Oak Ridge National Laboratory
1 Bethel Valley Road
Oak Ridge, TN 37831
E-mail: jangg@ornl.gov

Michael Brady, Co-Principal Investigator
Oak Ridge National Laboratory
1 Bethel Valley Road
Oak Ridge, TN 37831
E-mail: badymp@ornl.gov

Jiheon Jun, Co-Principal Investigator
Oak Ridge National Laboratory
1 Bethel Valley Road
Oak Ridge, TN 37831
E-mail: junj@ornl.gov

Jerry L. Gibbs, DOE Technology Manager
U.S. Department of Energy
E-mail: jerry.gibbs@ee.doe.gov

Start Date: April 1, 2019 End Date: March 31, 2020
Project Funding: $157,500 DOE share: $150,000 Non-DOE share: $7,500

Project Introduction

This one-year exploratory research effort, in collaboration with an industrial partner, was funded under Thrust 5 of the VTO Core Powertrain Materials Program. The goal was to develop a novel atmospheric plasma (AP)-based surface treatment for corrosion protection of lightweight Mg alloys. All tasks were successfully completed at the end of FY 2020. Based on the promising results, follow-up funding was awarded by the DOE Technology Commercialization Fund Program under the title: *Expansion of Atmospheric CO_2 Plasma Conversion Coatings on Lightweight Magnesium Alloys*.

The poor corrosion resistance of Mg is one of the major bottlenecks limiting broad application of Mg alloys for lightweight vehicle frame and powertrain components. Due to its high chemical reactivity and the unprotective porous oxides of Mg, various corrosion mitigation strategies for Mg, such as alloying and protective coating, are required for vehicle applications. However, due to marginal corrosion mitigation using current alloying strategies, protective coatings are still considered as the most cost-effective way to improve that resistance.

Recently, a new coating approach described corrosion-protective carbonate layers growing from a microstructured surface of Mg by electron beam-excited CO_2 [1]. Wang *et al.* demonstrated that the naturally formed oxide/hydroxide film on Mg was carbonized into a smooth, compact $MgCO_3$ protective surface layer via reaction with CO_2 species activated by either the high-energy electron beam or glow discharge. This

innovative and early-stage discovery needs to be further studied and developed for lower cost processes amenable to high-volume vehicle production.

Objectives

Inspired by $MgCO_3$ layer formation with excited CO_2 under electron beam or plasma irradiation, this project proposed to develop an anticorrosion treatment for Mg alloys via a cost-effective atmospheric (open to air), RT CO_2 plasma techniques. The aim was to demonstrate the formation of a protective $MgCO_3$ surface layer with greater than 10-fold reduction in the corrosion rate on Mg alloys by the AP treatment and to conduct the evaluation for powertrain components using advanced characterization and corrosion tests.

Approach

The atmospheric CO_2 plasma treatment was used to form an $MgCO_3$ protective layer on a bare Mg substrate in a custom-designed gas-enriched chamber. Proof-of-principle assessments were pursued with an industrial partner—Atmospheric Plasma Solutions (APS), Inc. Cary, NC—to evaluate the potential of this concept to form the engineered $MgCO_3$ layer. APS has successfully developed a commercialized AP technology for rapid, low-cost, open-air (i.e., with no vacuum chamber required) removal of paints containing organics and inorganics to prepare surfaces for recoating. Their approach uses a non-thermal but chemically active plasma of atomic nitrogen and O from air to react with the surface. Surfaces can be treated manually or with an automated batch of continuous systems. Using CO_2 rather than air as the source feedstock gas gives a potential to use the AP approach as a method to introduce activated CO_2 into the naturally formed Mg oxide/hydroxide layer on Mg surface and produce the protective $MgCO_3$ layer to provide corrosion resistance, as shown in Figure I.3.5.1.1.

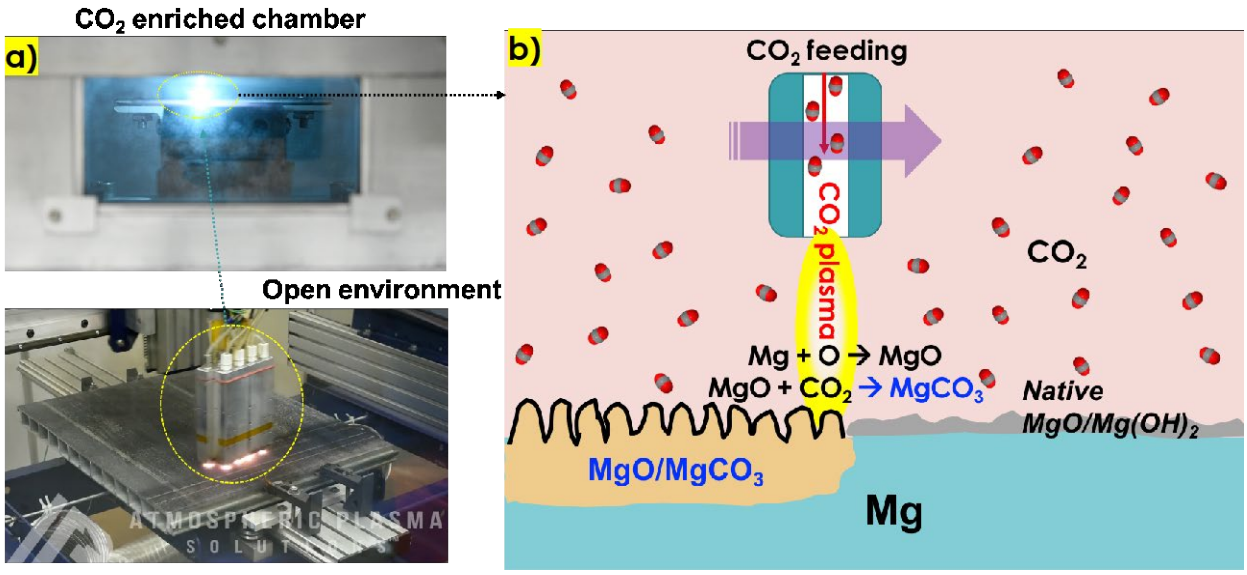

Figure I.3.5.1.1. (a) The open environment system for the inline CO_2 AP treatment on a Mg specimen inside a CO_2-enriched chamber. (b) The described approach wherein the CO_2 plasma converts a Mg surface to an $MgO/MgCO_3$ intermixed protective layer. Source (a) APS; (b) ORNL.

Results

CO_2 AP treatment formed a superhydrophobic $MgO/MgCO_3$ particle mixture layer with a 1–2 μm thickness, as shown in the SEM image of Figure I.3.5.1.2(a). The CO_2 AP beam appears to ablate a portion of the Mg surface within the direct exposure area, and the evaporated Mg species possibly deposit on the surface around the cavities as nanoparticle agglomerations. Also, the cross-sectional TEM image in Figure I.3.5.1.2(b) shows that the microstructured conversion layer formed on the Mg surface as a single entity. The as-received CO_2 AP-treated Mg specimen exhibited superhydrophobic surface characteristics with a water droplet contact angle of 150 degrees, resulting in excellent water repellency, as compared to the untreated bare Mg specimen (i.e.,

600-grit polished), which wetted readily, as shown in Figure I.3.5.1.2(c). A thin layer of air was observed to be trapped at the AP-treated Mg surface when immersed in an aqueous salt solution, as can be seen in Figure I.3.5.1.2(d). When a superhydrophobic surface is immersed in water, it appears shiny due to the total internal reflection of light from the thin layer of air (plastron) trapped on the surface, as can be seen in Figure I.3.5.1.2(e) [2].

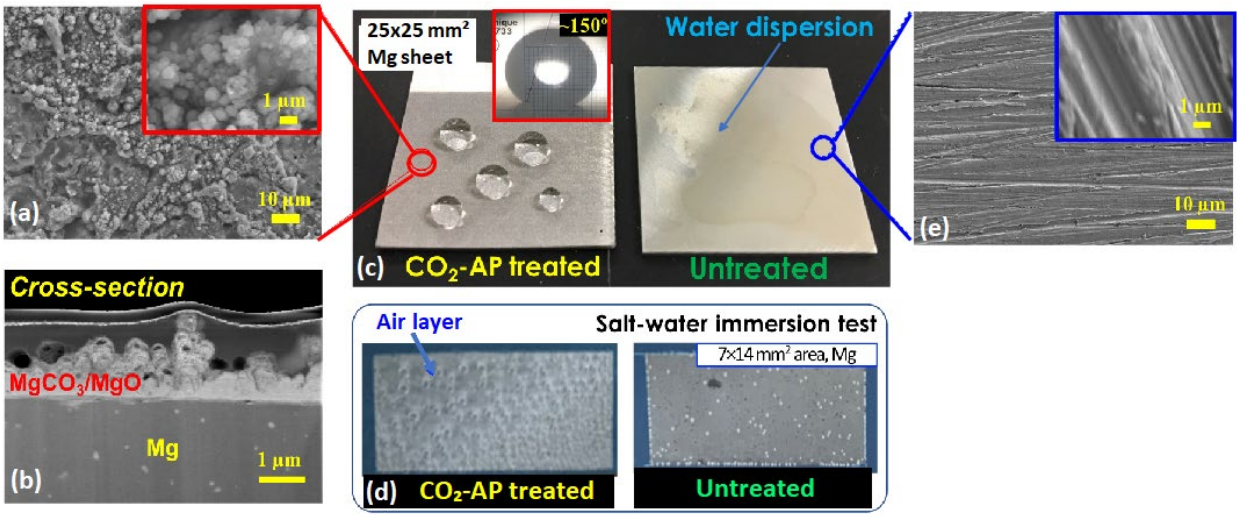

Figure I.3.5.1.2. (a) SEM and (b) cross-sectional TEM images showing a CO_2 plasma-driven protective layer that consisted of particle deposition on a dense layer. The CO_2 AP-treated Mg surface showing (c) superhydrophobicity and (d) immersed samples under 3.5 wt.% NaCl solution. (e) The superhydrophobic surface with a shiny appearance due to the total internal reflection of light from the thin air layer. Source: ORNL.

The CO_2 AP-treated surface exhibited significant corrosion protection. Figure I.3.5.1.3(a) shows the surfaces of a Mg specimen (~1 cm^2) exposed to 3.5 wt.% NaCl solution for 20 h. The CO_2 AP-treated surface has a much smaller area of corrosion attack than does the untreated Mg. An H-collection test showed that the CO_2 AP treatment (i.e., five-times sweep) significantly reduced the corrosion rate by ~5.5 times as compared with the untreated Mg sample. Note that this simple test was used as a screening test to simulate a highly aggressive environment. The results of H-collection agreed with the subsequent electrochemical corrosion rate measurement supported by the data in Figure I.3.5.1.3(b). The CO_2 AP sample exhibited lower corrosion current density (i_{corr}), which was four orders of magnitude less than a bare Mg sample. The low current of CO_2 AP sample in the first cycle was attributed to the superhydrophobic characteristics. Even after the second cycle of measurement, the corrosion current is still 10 times lower in the CO_2 AP-treated Mg than the bare Mg (i.e., one cycle) [3].

The reasons behind this significant corrosion mitigation effect appear to be multifaceted and are associated with the non-wetting surface properties, chemical composition, and crystalline changes (e.g., $MgCO_3$/MgO mixture) resulting from the CO_2 AP treatment. In general, a superhydrophobic surface can be attributed to two types of features: (1) nanoscale surface roughness and (2) low surface energy material coatings, such as C and fluorine. Figure I.3.5.1.2 previously showed that nanoscale roughness was formed by nanoparticle and pillar agglomeration on the surface. It suggests that the plasma ablated a portion of Mg away during the process, and the evaporated Mg particles, possibly oxidized to MgO, deposited on the surface thereby resulting in nanopillars. Then, the chemically active CO_2 plasma molecules adsorbed on the MgO nanoparticle surfaces simultaneously during multiple treatments under a CO_2-enriched environment. In principle, $MgCO_3$ can be formed via the chemical reaction $MgO + CO_2 \rightarrow MgCO_3$. The standard enthalpy of formation of $MgCO_3$ is -1095.8 kJ mol^{-1} (i.e., the exothermic reaction is thermodynamically favorable even at RT). Also, the MgO particles have diverse basic sites where acidic CO_2 molecules can be chemically or physically adsorbed on the surface, resulting in various carbonate surface species including bicarbonate, bidentate, and unidentate

carbonates [4]. The theoretical CO_2 uptake capacity of MgO is 109% (e.g., 1.09 g of CO_2 per gram of MgO sorbent). When the size of MgO is at the nanoscale, the mesoporous MgO can show an adsorption capacity of 8–10 wt.% at 25–30°C [4],[5]. We also considered that heat generation could be another factor to accelerate CO_2 adsorption at the surface. Even though AP is a cold plasma, substrate temperature could elevate to as high as 200°C during the treatment with plasma. We also found that the superhydrophobicity of the treated surfaces is robust enough to not be destroyed by masking tape, as can be seen in Figure I.3.5.1.4(a). The low mechanical durability of many superhydrophobic surfaces has been a critical limitation in expanding its application. It appears the deposited nanoparticles had fused to each other resulting in strong bonding and subsequent durability.

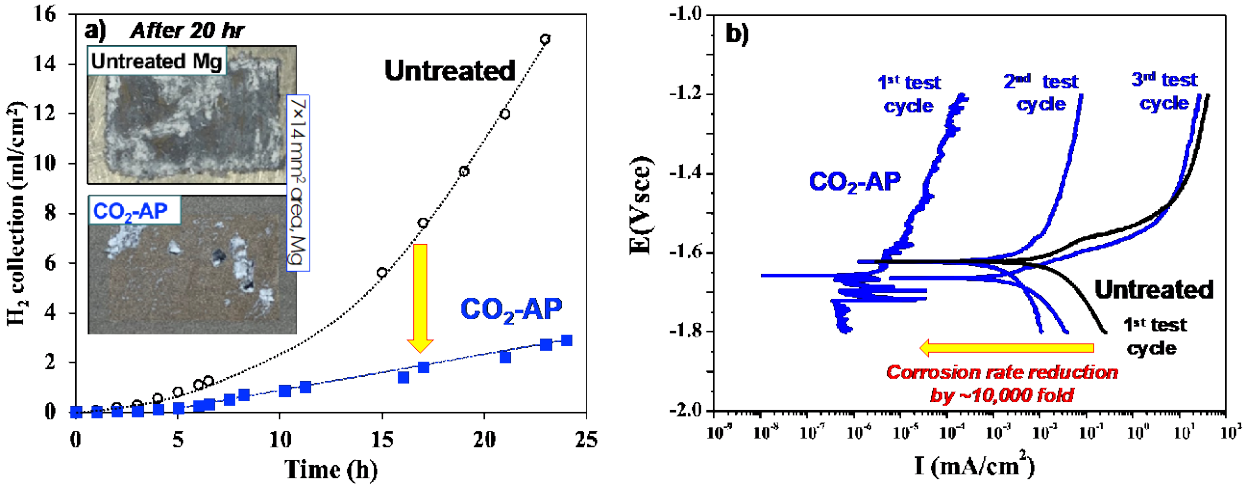

Figure I.3.5.1.3. (a) H-collection test on CO_2 AP-treated surface in 3.5 wt.% NaCl. Inset pictures are corroded Mg and CO_2 AP-treated Mg surfaces after 20 hours. (b) Electrochemical corrosion rate measurement on the surface in 3.5 wt.% NaCl solution. Source: ORNL.

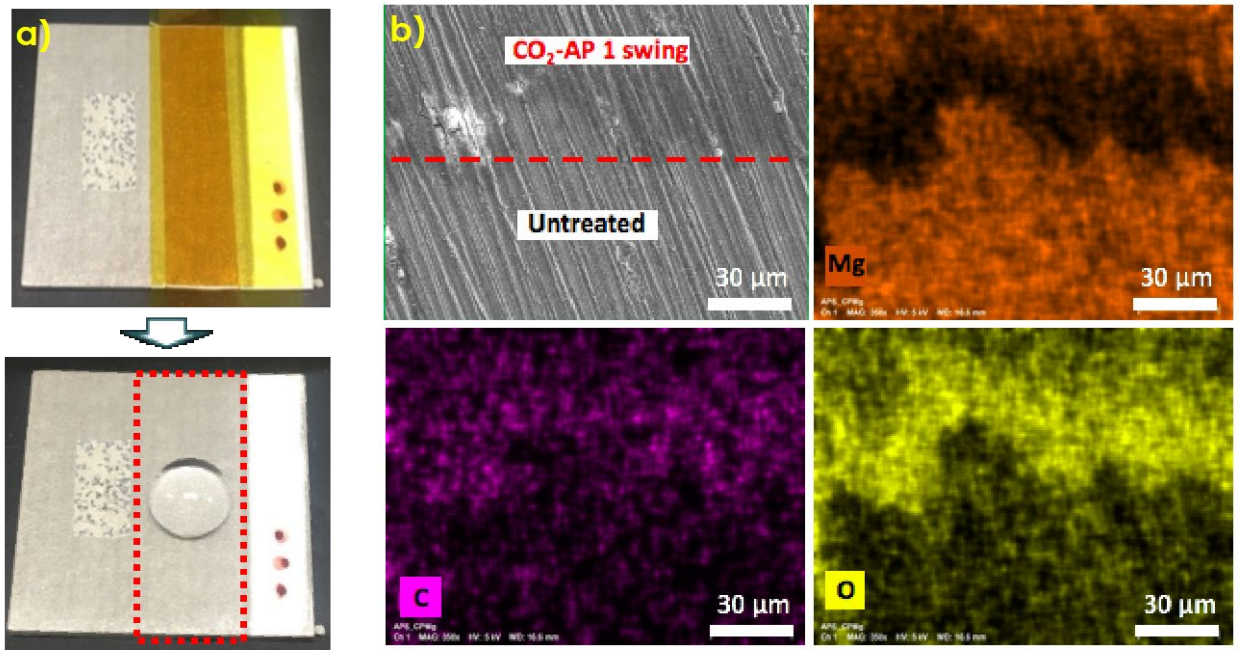

Figure I.3.5.1.4. (a) Durability test on the superhydrophobic surfce of a five-times sweep Mg sample. (b) SEM-energy-dispersive x-ray images of CO_2 AP-treated Mg surface. Source: ORNL.

The CO_2 AP-treated surface adsorbs C species. Figure I.3.5.1.4(b) shows the top surface coated with CO_2 AP-treated Mg. The treated surface had more O and C components suggesting that the plasma converts MgO and that the MgO adsorbs CO_2 or possibly C (e.g., volatile organic carbons) from the environment. Surface films after CO_2 AP treatment were further characterized by cross-sectional HAADF-STEM with energy-dispersive x-ray analyses, as observed in Figure I.3.5.1.5. Results indicated that the chemically converted nanoparticle agglomerations formed rod-like nodules on a dense layer formed on the Mg substrate. The STEM and energy-dispersive x-ray semiquantitative elemental mapping of the structured layer with 1–2 μm thickness indicates that three major elements, Mg, O, and C, are well dispersed throughout the layer, verifying the likely coexistence of MgO and $MgCO_3$. Note that the interphase between the dense film and Mg appears to be a single layer without defective cracks. The presence of MgO could be associated with the small amount of air in the CO_2-enriched chamber, as well as direct CO_2 conversion into CO and O_2. Non-thermal plasma reactors at low temperature and atmospheric pressure dissociate CO_2 into CO and O_2 [6]. The surface carbonization was analyzed by x-ray photoelectron spectroscopy (XPS), as shown in Figure I.3.5.1.6, also revealing Mg, O, and C. The treated sample shows a distinct C-carbonate peak at 292 eV and a broad C-C peak fraction at 285 eV, while the untreated sample has a relatively low C-carbonate peak, which is very similar to a previous result [7]. Note that all carbon-related peaks in the reference sample disappear after 15 sec Ar-sputtering. However, trace C still presents in the CO_2 AP-treated sample after 5,000 sec Ar-sputtering. The carbonation on the untreated surface could be caused by atmospheric CO_2 adsorption. It was reported that pure Mg surfaces rapidly form ~2 nm oxide/hydroxide films after only 10 s, and the air-formed oxide/hydroxide films on Mg adsorb a significant amount of C from ambient to form $MgCO_3$ [7]. Upon exposure to the ambient atmosphere, the thin oxide/hydroxide film Mg surface picks up volatile organic carbons to form predominantly bidentate-bound carboxylate salts, which cause a significant surface change from hydrophilic to hydrophobic [7]. In addition, another reported XPS study on CO_2 carbonization on MgO particles confirmed that the formation of carbonate species on MgO particle increases significantly with an increase in the CO_2 concentration [8].

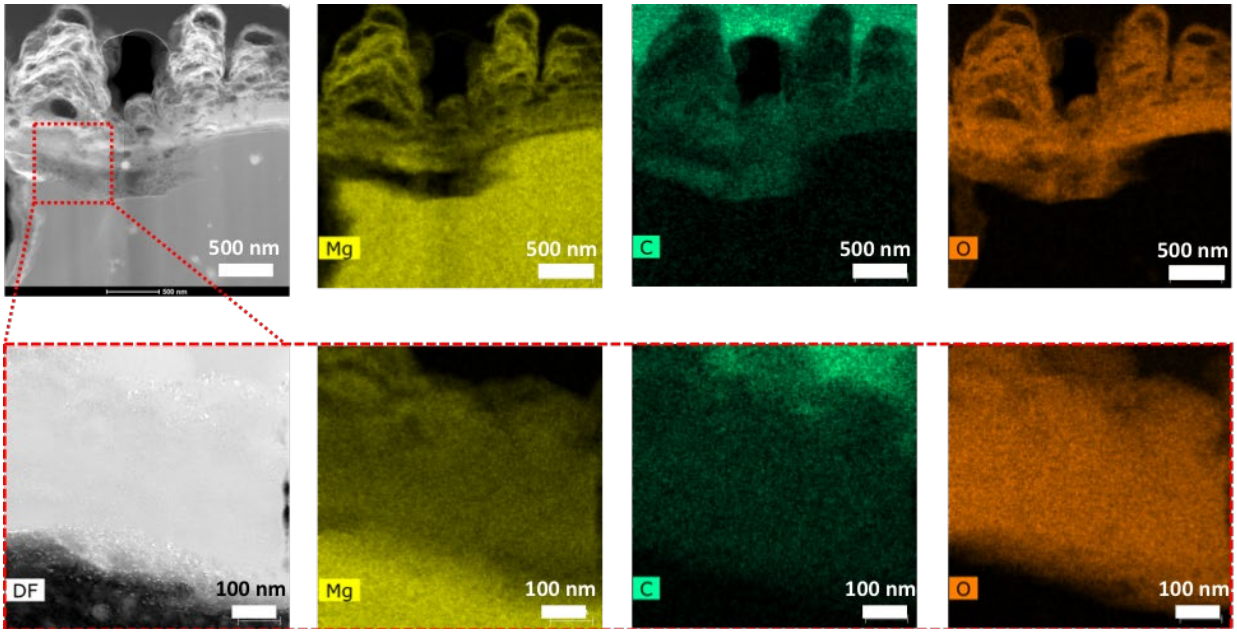

Figure I.3.5.1.5. High-magnification cross-sectional HAADF-STEM images of CO_2 AP-treated Mg along with energy-dispersive x-ray elemental mapping showing the distribution of Mg, C and O in the treated layer (C: 15.5 atomic %, O: 53.0 %, and Mg: 26.5 % in the zoom-in image). Source: ORNL.

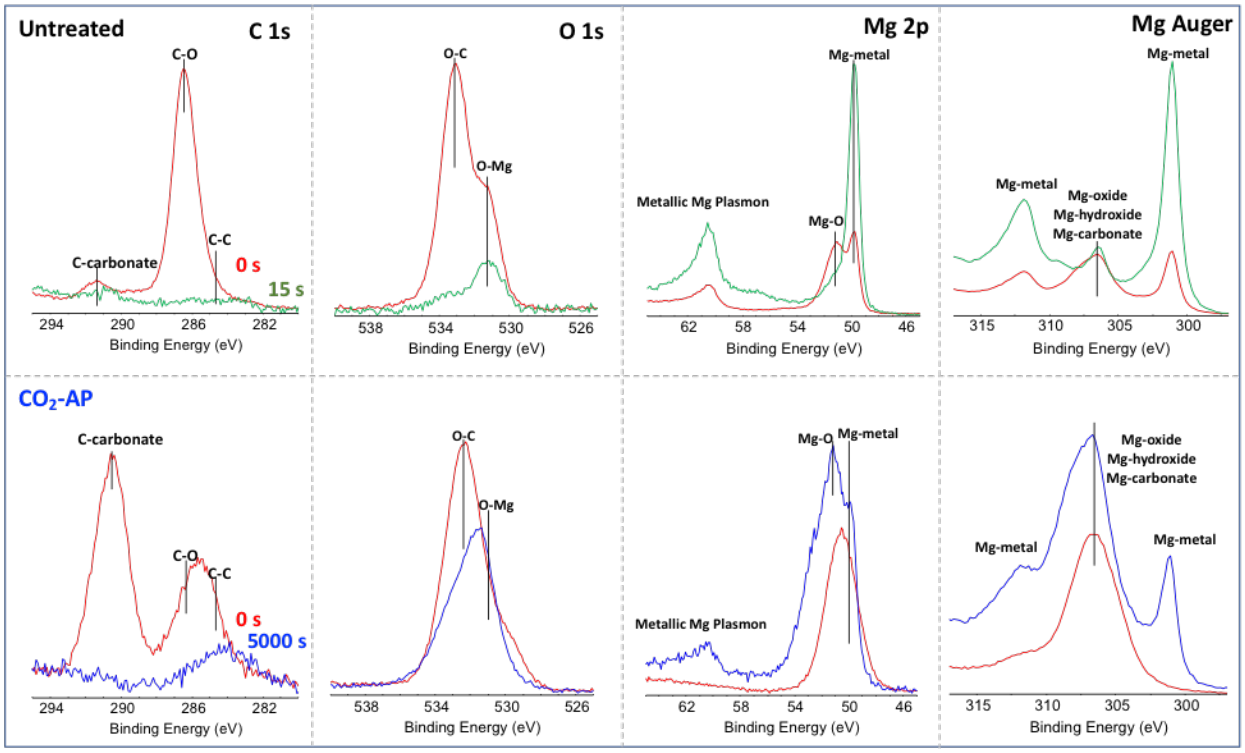

Figure I.3.5.1.6. XPS patterns for the CO_2 AP-treated Mg compared to untreated Mg. Source: ORNL.

Two O 1 s peaks are easily distinguished in the XPS spectra of two comparable samples, as observed in Figure I.3.5.1.6. From the literature, it is known that the peaks related to MgO have binding energy at approximately 530.0–531.0 eV, MgOH have binding energy at approximately 530.0–533.2 eV, and $MgCO_3$ present peaks in the range of 533.2–533.5 eV [8]. Similarly, a strong O-C peak in O 1 s spectra of the treated sample was present after the long-time sputtering while the O-C peak from the untreated sample disappeared spontaneously after the short time sputtering. The two Mg spectra (e.g., Mg 2p and Mg auger) indicate CO_2 AP-formed thick $MgCO_3$/MgO films.

Conclusions

CO_2 AP treatment has demonstrated the formation of an effective anticorrosion layer on a bare Mg surface. This treatment resulted in a more than tenfold reduction in the corrosion current density i_{corr} (i.e., the corrosion rate) compared to untreated Mg specimens. In addition, the H-collection test showed that the AP treatment reduced the corrosion rate by ~5.5 times on Mg specimens in a very aggressive immersion test. The significant corrosion mitigation effect was associated with the formation of $MgCO_3$ and MgO layer and superhydrophobic surface features. Detailed surface characterization results, such as XPS, SEM and TEM- energy-dispersive x-ray analyses, suggested protective, non-wettable $MgCO_3$ layer formation, but more experiments and characterization for duplication and evaluation of other Mg alloy types, as well as scale-up, are required. These technical questions will be further studied in a follow-on project awarded by the DOE Technology Commercialization Fund Program.

Key Publications

1. Election Decision for Invention Disclosure ID# 201904507, DOE S# S-161,923, “Advanced Anticorrosion Coatings on Lightweight Magnesium Alloys by Atmospheric CO_2 Plasma Treatment.”

References

1. Wang, Y., B. Liu, X. Zhao, X. Zhang, Y. Miao, N. Yang, B. Yang, L. Zhang, W. Kuang, J. Li, E. Ma, and Z. Shan, 2018, “Turning a native or corroded Mg alloy surface into an anticorrosion coating in excited CO_2,” *Nat. Commun.*, Vol. 9, Art. 4058.

2. Panchanathan, D., A. Rajappan, K. K. Varanasi, and G. H. Mckinley, 2018, "Plastron regeneration on submerged superhydrophobic surfaces using *in situ* gas generation by chemical reaction," *ACS Appl. Mater. Interfaces*, Vol. 10, No. 39, pp. 33684-33692.
3. Jang, G.G. 2019, "Advanced Anticorrosion Coatings on Lightweight Magnesium Alloys by Atmospheric CO_2 Plasma Treatment" *DOE VTO Materials 2019 Annual Progress Report*, pp.160-169.
4. Hu, Y., Y. Guo, J. Sun, H. Li, and W. Liu, 2019, "Progress in MgO sorbents for cyclic CO2 capture: A comprehensive review," *J. Mater. Chem. A*, Vol. 7, pp. 20103–20120.
5. Ho, K., S. Jin, M. Zhong, A. Vu, and C. Lee, 2017, "Sorption capacity and stability of mesoporous magnesium oxide in post-combustion CO_2 capture," *Mater. Chem. Phys.*, Vol. 198, pp. 154–161.
6. Mei, D., and X. Tu, 2017, "Atmospheric pressure non-thermal plasma activation of CO_2 in a packed-bed dielectric barrier discharge reactor," *ChemPhysChem*, Vol. 18, No. 22, pp. 3253 –3259.
7. Fotea, C., J. Callaway, M. R. Alexander, 2006, "Characterization of the surface chemistry of magnesium exposed to the ambient atmosphere," *Surf. Interface Anal.*, Vol. 38, pp. 1578–1587.
8. Rheinheimer, V., C. Unluer, J. Liu, S. Ruan, J. Pan, and P. J. M. Monteiro, 2017, "XPS study on the stability and transformation of hydrate and carbonate phases within MgO systems," *Materials*, Vol. 10, No. 1, Art. 75.

Acknowledgements

The authors acknowledge the efforts of M. Chisholm, N. S. Harsha Gunda, R. Michi, J. Poplawsky, S. Bahl, L. Allard, and J. A. Haynes for their contributions to this research effort.

This research used the Center for Nanophase Materials Sciences resources at ORNL, which is a U.S. DOE Office of Science User Facility. D. Leonard at ORNL conducted the TEM/ energy-dispersive x-ray analysis, and H. Meyer at ORNL performed the XPS analysis.

I.3.5.2 Novel Materials for Polymer Composite Engine Blocks (5B) (Oak Ridge National Laboratory)

Amit K. Naskar, Co-Principal Investigator
Oak Ridge National Laboratory
1 Bethel Valley Road
Oak Ridge, TN 37831
E-mail: naskarak@ornl.gov

Vlastimil Kunc, Co-Principal Investigator
Oak Ridge National Laboratory
1 Bethel Valley Road
Oak Ridge, TN 37831
E-mail: kuncv@ornl.gov

Brian Knouff, Co-Principal Investigator
Oak Ridge National Laboratory
1 Bethel Valley Road
Oak Ridge, TN 37831
E-mail: knouffbj@ornl.gov

Jerry L. Gibbs, DOE Technology Manager
U.S. Department of Energy
E-mail: jerry.gibbs@ee.doe.gov

Start Date: April 1, 2019 End Date: March 31, 2020
Project Funding: $150,000 DOE share: $150,000 Non-DOE share: $0

Project Introduction

This PMCP—Thrust 5 research effort conducted preliminary R&D to evaluate and advance novel polymer matrix composite (PMC) systems for LD internal combustion engine block applications, targeting reductions of 40% in component weight, 30% in vehicle emissions, and 50% in engine noise (e.g., NVH) relative to conventional metal castings. Although PMC engine blocks are expected to exhibit promising results, no PMC systems are specifically designed for this application. Thermomechanical properties of most polymer materials and second-phase reinforcements are not well-suited to engine block requirements. Typical PMC materials are particularly challenged by elevated temperature creep and fatigue, as well as by demands on efficient heat transfer. A PMC engine block will likely need to contain or include some metallic or ceramic structures, primarily in areas of high wear. This one-year exploratory effort was focused on tuning and developing a tough, temperature-resistant PMC material system for future lightweight engine block applications.

Experiments with PMC engine blocks focused primarily on race-car requirements and leveraged existing products, such as Torlon® or Bakelite® polymers, with commercially available fibers [1]. An engine block not only has to withstand demanding operating temperatures, but must also enable the combustion heat to transfer away from the engine cylinders. The measurement of this ability to conduct heat is called thermal conductivity and is defined by Fourier's Law: $q=k\Delta T$, where q is the heat flux (flow of energy per unit time per unit area) and k is the thermal conductivity (usually expressed in units of watts per meter-Kelvin (W/mK). Systematic R&D of composites and constituent materials are needed to realize the potential benefits of PMC engine blocks for passenger vehicles with long-term service requirements and cost limitations.

Objectives

This one-year exploratory project addresses current issues with Bakelite® embrittlement during continued thermal exposure and debonding from metal inserts. The objective of this effort is to develop lightweight composite materials with high toughness, acceptable temperature resistance, cost-affordability, and rapid heat-dissipation through a percolated network of thermally conducting reinforcing fibers, while also maintaining adhesion to metals. For proper development and design of the materials, this project also aims to develop the working environments of the PMC blocks that include the temperature profile or envelope during operation, mechanical loads, and vibrational analyses. The initial targets include fabrication of PMCs using CFs and demonstration of acceptable performance, such as 100 MPa mechanical strength equivalent, as well as the demonstration of composite thermal stability up to 200°C.

Approach

The approach is to design a lightweight composite material system capable of satisfying engine block operation requirements—at minimum potential cost and manufacturing complexity—comprising a suitable polymer, a fiber reinforcement, a particulate phase with a tailored interface, and toughening agents and additives. Thermosetting networked polymers offer the greatest potential for creep and fatigue resistance. While phenolic resins, such as Bakelite®, have been evaluated in engine block applications, there are a variety of other potentially suitable candidates, including high-temperature epoxies, polyimides, bis-maleimides [2], cyanate esters [3], and benzoxazines [4]. However, many of these chemistries are currently cost-prohibitive because high-temperature formulations are produced in small volumes, primarily for the aerospace industry. Variant phenolic resin chemistries that were developed earlier by ORNL may offer the potential for rapid manufacturing and high-service loads above their glass transition temperature (T_g), while being strengthened with a moderate volume fraction of second-phase reinforcement. These variant phenolic resins are rubber-toughened novolac and a sustainable lignin derivative: acrylonitrile-butadiene-lignin polymer [5],[6].

Reinforcements evaluated in previous studies included low-cost glass fibers and polyacrylonitrile-based CFs. While these reinforcements are readily available and well understood, their low-thermal conductivity (i.e., 2–13 W/mK) [7],[8] and limited mechanical properties are not ideal for engine block applications. Composites containing pitch-based CFs [9], with a thermal conductivity exceeding 800 W/mK, and even higher mechanical stiffness than polyacrylonitrile CF, offer greater freedom to tailor composite thermomechanical properties; thus, they were selected for evaluation in this project. The thermomechanical property dependence on fiber loading, aspect ratio, orientation, and presence of additional fillers' required assessment. It has also been reported that nanomaterials like G can be used in the sizing of CFs or added to the base polymer to provide better thermomechanical properties [10],[11]. Further improvements to the selected composite's thermomechanical properties may be made through the toughening of the matrix. Tailored chemistry between functionalized high-performance thermoplastics reacted with thermosetting resins has been reported to increase the overall fracture toughness and T_g while decreasing thermal expansion [12],[13]. Also, while not part of this one-year project, joining to metallic components would need to be considered in future applications to enable a multi-material system.

The ORNL Manufacturing Demonstration Facility has demonstrated significant advancements in high-rate deposition and high-quality component production using AM, which gives the unique capability to fabricate complex and variably sized parts in a relatively short time, and this includes both polymeric and metallic AM. This ability is useful when fabricating prototypes because it alleviates the need for die-cast tooling for any metal parts or inserts that may be required in this or future projects that include more complex metal/polymer hybrid systems. Most importantly, for this project application, AM can fabricate complex shapes of variable size, which will be crucial to optimize the design and capability of internal metallic components. Our research plan included the following steps:

- Evaluation and downselection of base polymer chemistries. Multiple polymers were physically evaluated to obtain experimental data for the most promising crosslinked, amorphous, and semicrystalline chemistries, as well as their suitability for engine block use, cost, and manufacturing considerations.

- Identification and evaluation of fiber and particulate reinforcements, including CF and graphene. Ongoing and potential efforts on cost-reduction and physical property improvement were evaluated.
- Development with downselected polymer matrices, reinforcements with compatible sizing, and selected tougheners or modifiers.
- Identification of technical challenges and opportunities.
- Identification of cost and manufacturing challenges and opportunities.

Results

Resin Selection and Modification

The team concluded an investigation of different candidates for the matrix material, including a variety of thermosetting networked polymers and semicrystalline and amorphous thermoplastics. Thermosetting phenolics were selected as the base chemistry for development, mainly due to the reduced cost. The early-stage data addressed issues with Bakelite® embrittlement during continued thermal exposure and debonding from metal inserts. Rubber- toughened phenolic resins, based on an equal mass mixture of rubber and resin, displayed continuity in both the rubber and phenolic phases. A representative morphology was observed by TEM, as can be seen in Figure I.3.5.2.1.

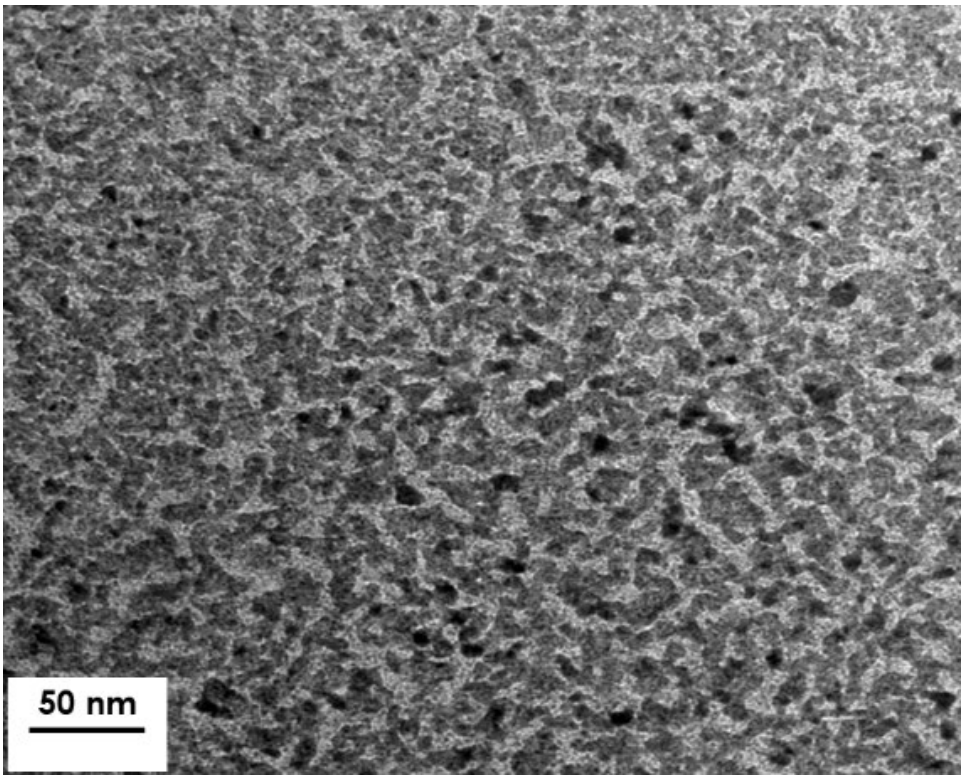

Figure I.3.5.2.1. Transmission electron micrograph of a phenolic resin, toughened with an equal mass of rubber, where both rubber (light color) and phenolic resin (dark color) phases form a co-continuous structure. Source: ORNL.

The toughened composition with the tensile stress-strain profile shown in Figure I.3.5.2.2(a) was further used for CFRC manufacturing. The processability and heat-dissipation rate still needs to be optimized. The processability (moldability) of the composites will be analyzed by melt rheology and RT dynamic performance of the composites. ORNL's recent work shows toughened resin from the modified phenolics. The data, shown in Figure I.3.5.2.2(b) meets initial milestones for the project by developing a protocol for resin-composite fabrication from a selected, toughened polymer. With 12 wt.% CF, the toughened composition exhibits 1.6% strain to failure, as shown in Figure I.3.5.2.2(c).

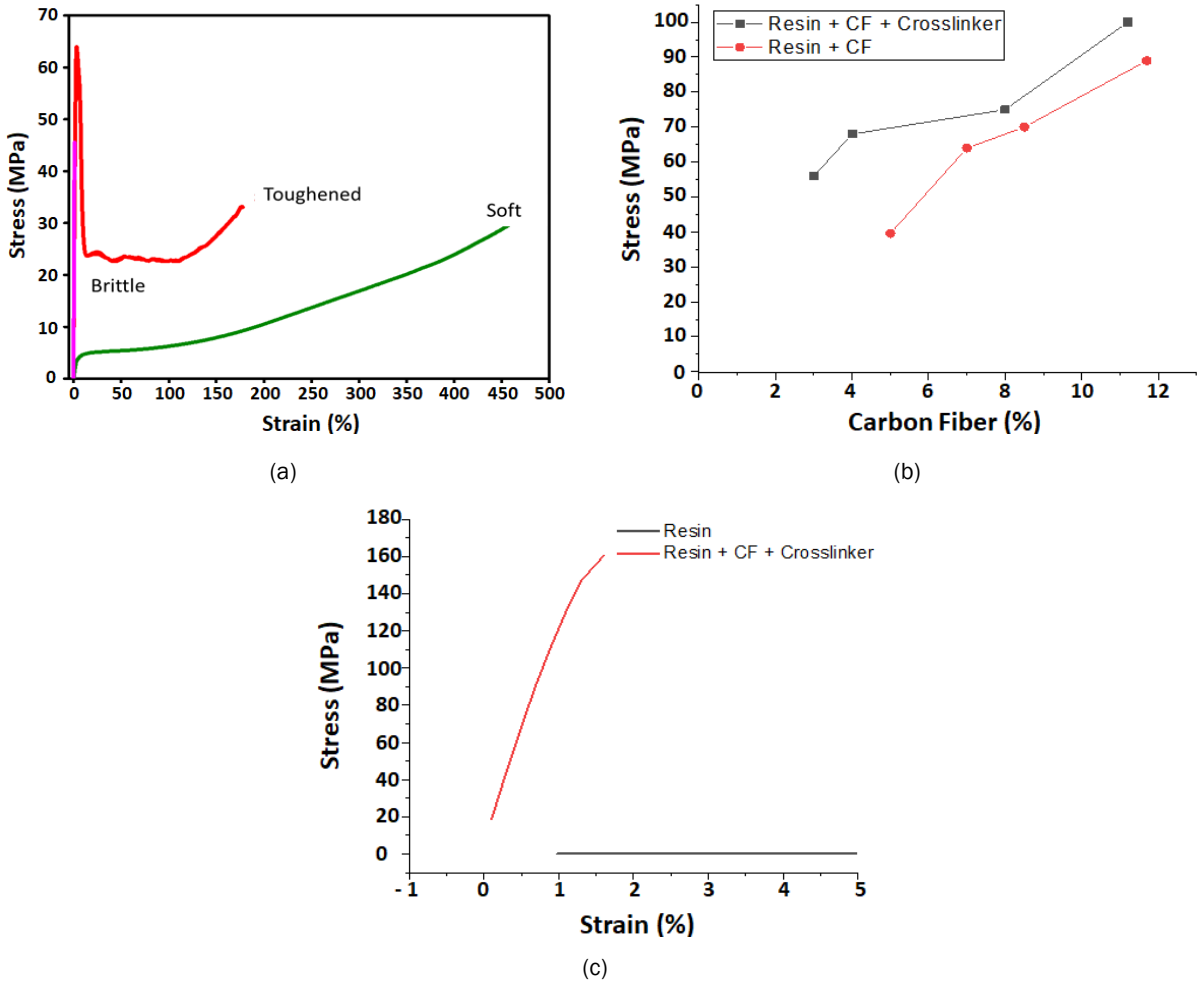

Figure I.3.5.2.2. (a) Temperature-resistant phenolics are the preferred material for engine block applications; however, these compositions are very brittle (magenta-colored data). (b) Use of a crosslinker (both matrix and fiber surface modifier) changes the in-failure mode from fiber/matrix debonding to fiber breakage; therefore, use of 4–12 wt% CFs delivered compositions with 60–100 MPa tensile strength. (c) With 12 wt.% CF, the toughened composition exhibits 1.6% strain to failure. Source: ORNL.

Because phenolic resins are expensive in the current market, an alternative cross-linkable phenolic oligomer alloy—acrylonitrile-butadiene-lignin (ABL), previously developed at ORNL—was studied. The cost of this partially renewable material can be less than $1.5/lb. However, the least expensive material may not have good thermomechanical or dimensional stability. Therefore, crosslinking and nano-reinforcement chemistry were developed for this resin system. The mechanical properties of the resin systems are displayed in Figure I.3.5.2.3. The dispersion of hydroxyl-terminated carbon nanoparticle (CNP-OH) in ABL does not affect either the strength or the modulus of the ABL resin. However, crosslinking the ABL resin using a new crosslinking chemistry involving a difunctional linker (DL) doubled the tensile strength, as shown in Figure I.3.5.2.3(a), and modulus, as shown in Figure I.3.5.2.3(b). Dispersing the nanoparticle at that crosslinking stage does not further enhance the tensile strength but significantly enhances the tensile modulus (~70%). In addition, the dynamic crosslinking (e.g., crosslinking under shear mixing) of the components (e.g., rubber or the toughening agent and the resin) was significantly influenced by the time of the mixing cycle. Crosslinker types affecting the T_g of the toughening agent were studied. The addition of a crosslinker could effectively increase the T_g by 5°C to 8°C, while enhancing the toughness significantly (50%). This is a key finding for resin and future nanocomposite development work.

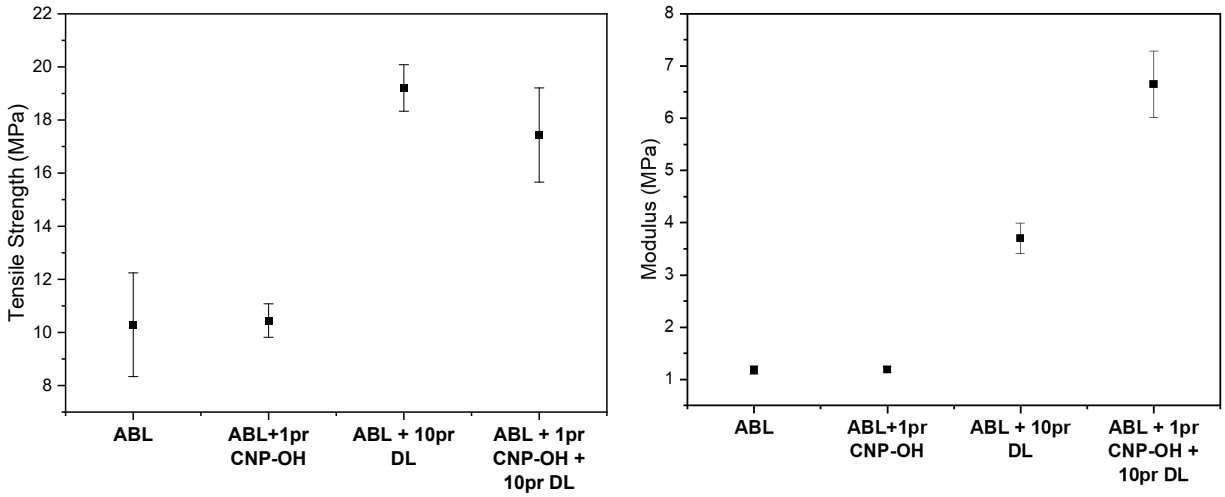

Figure I.3.5.2.3. Mechanical properties for (a) tensile strength and (b) modulus of a renewable variant of toughened phenolic resin. Source: ORNL.

Performance of Composites of the Resin

To understand the use of the resins as a composite matrix with the appropriate chemistry of the interfacial bonding, the same crosslinker was deployed as the interfacial bond promoter without the use of a conventional sizing agent. CFs usually contain aromatic or graphitic chemical structures that give them their exceptional mechanical strength and resistance to chemical degradation. However, this also makes them inert to chemical functionalization that enables primary or secondary interactions that can help improve fiber-matrix adhesion. Composites created from such fibers, therefore, usually have lower-than-expected tensile strength. The approaches to enhance interactions between a reinforcing fiber and matrix can be broadly classified as (a) covalent bonding between the fiber and matrix; (b) dipole interactions including H bonding between compatible fiber-matrix systems; (c) diffusion and entanglement of polymeric chains of the fiber and matrix; and (d) mechanical interlocking. In cases where covalent bonding, dipole interactions, or entanglements are not possible, the inherent surface roughness of these fibers can be used to introduce and enhance mechanical interlocking. The strength of a fiber-reinforced composite is ultimately linked to the strength of the interphase, the three-dimensional region encompassing the two-dimensional interface and a finite volume of fiber and matrix.

Based on the protocol developed in the bench-scale process using a hand-laying method, composite laminate containing 12% CFs were prepared with resultant unidirectional renewable composite tensile properties, as shown in Figure I.3.5.2.4(a). The interfacial engineering using a varied resin crosslinker itself as a coupling agent works well to increase the mechanical properties by about 25–50%. The role of the CNP with strength enhancement of the composite is not very significant compared to an optimal system that uses a trifunctional crosslinker (TL) (Bar 5). Nonetheless, CNP does provide some strength enhancement for composition with a difunctional crosslinker (DL + CNP, Bar 3, vs. DL alone in Bar 2). However, hydroxyl-terminated CNP (CNP-OH, Bar 4) did not give a significant strength enhancement. Thus, a resin chemistry was deployed, and a composite fabrication protocol was developed with potential to provide a good engine block grade, low-cost, partially renewable composite.

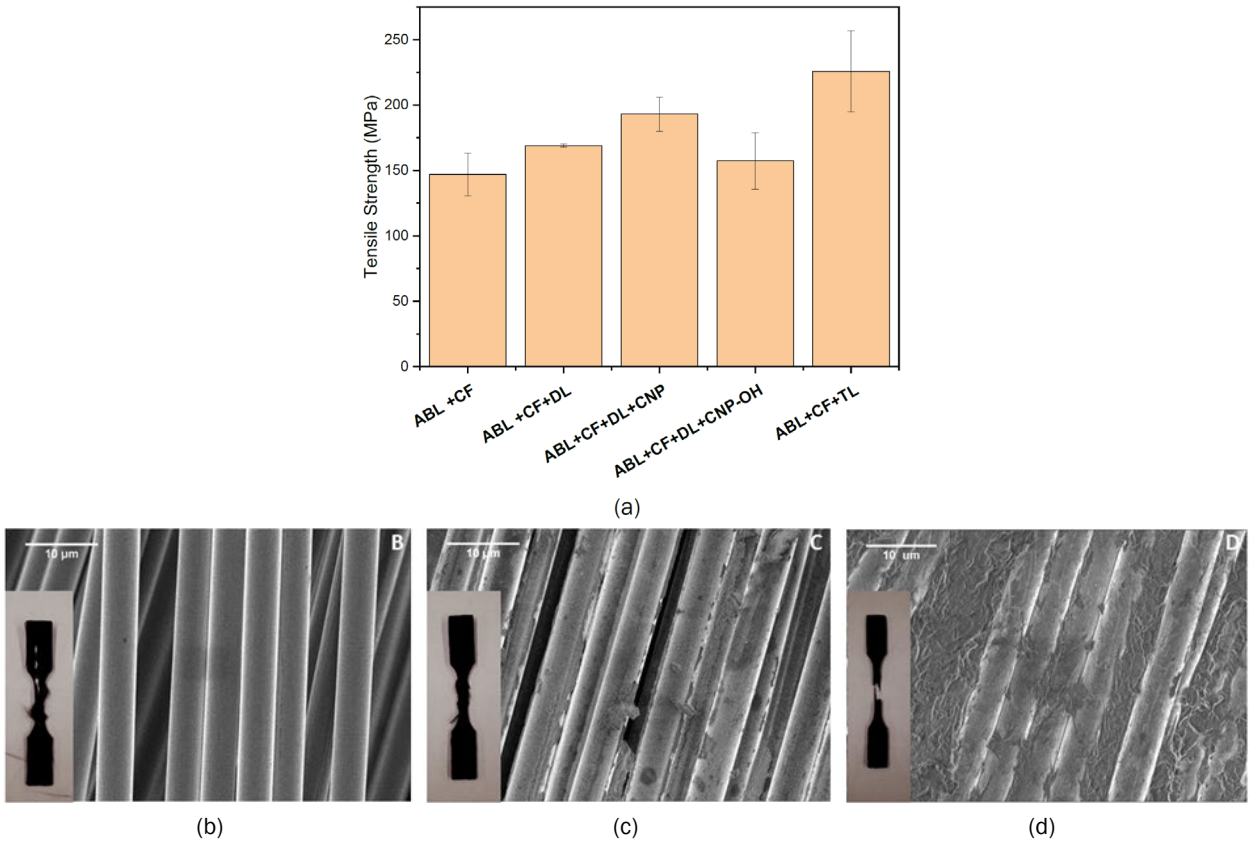

Figure I.3.5.2.4. (a) Tensile strength of unidirectional renewable composite containing ~12% CF. (b) Fractured interface of control ABL + CF composite showing bare fibers, indicating poor interfacial adhesion. (c) ABL + CF + DL composite fractured surface, showing remnants of elastomer on CFs indicating better interfacial adhesion. (d) ABL + CF + TL showing the best interfacial adhesion and inset images showing the sample failing by fiber fracture. Source: ORNL.

SEM images of the failed surface showed bare fibers in the control composites (ABL + CF), as observed in Figure I.3.5.2.4(b), with increasing amounts of elastomer adhering to the interface with treatments of DL, as observed in Figure I.3.5.2.4(c), and treatments of TL, as can be seen in Figure I.3.5.2.4(d), respectively. ABL-CF-TL composites were also found to fail by fiber fracture (see inset failed specimen images), further confirming superior interfacial adhesion. By using traditionally functionalized CFs, not only was mechanical interlocking enhanced by allowing the above crosslinkers to create an interphase by interdiffusion and subsequent crosslinking, but the possibility of covalent bonding between the fiber and the matrix was also enabled. The development of an interphase, as evidenced by the images of fracture surfaces in Figure I.3.5.2.4(b)-(d), avoids the sharp boundaries, heterogeneities, and discontinuity of an interface, thus allowing for better transfer of load from the matrix to the fiber.

The thermal degradation characteristics of the resin and composite systems were analyzed by thermogravimetry (under nitrogen), and the data shown in Figure I.3.5.2.5 suggest no degradation up to 200°C and only 3–5% mass loss in the composite at 300°C. These data confirm the preliminary feasibility of the usage of this product for engine block materials. The processability of the chopped fiber composite and mechanical properties of the aged materials need to be tested in future research. The char forming characteristics in this resin are visible from the >30% charred residue, even in neat ABL resin at 600°C. The crosslinked composites exhibit even more charred residue as compared to the control composite. The charring behavior of this toughened resin is important for its thermal-oxidative resistance should they become exposed to air. The charred layer acts as a barrier to O and protects the underlying polymer material.

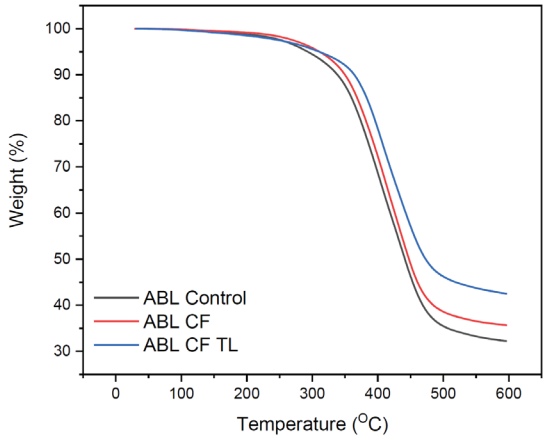

Figure I.3.5.2.5. Thermogravimetric analysis of the neat resin and its two composites. Source: ORNL.

Parametric Studies and Virtual Simulations

A single-cylinder piston two-stroke engine, as observed in Figure I.3.5.2.6, was purchased from Pegasus Aeronautics to develop the process parameters that will be used as a starting point to develop design standards for future PMC applications for internal combustion engines. These parameters are expected to vary as we delve into automotive engines, but this was chosen as a starting point to analyze an engine system in the exploratory program.

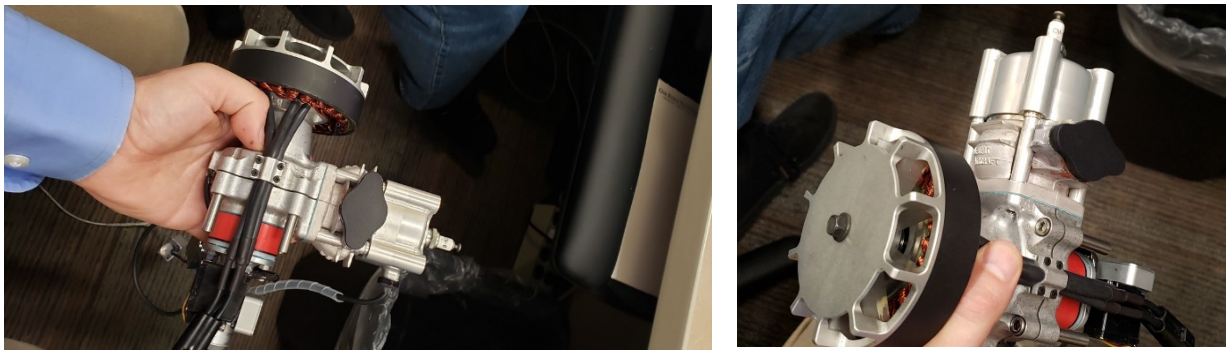

Figure I.3.5.2.6. The single-cylinder two-stroke GE35 engine was purchased for parametric studies and for the engine operation for temperature, mechanical, and vibrational analyses. This is a steppingstone to larger automotive engines. Source: ORNL.

Computer-aided design files were also obtained from Pegasus Aeronautics. The geometry of the GE-35 engine is shown in Figure I.3.5.2.7. In future work, these geometries will be meshed and preprocessed for FEA, which will be used to determine the appropriate BCs (i.e., loads and constraints) of the current engine design. Once completed, these BCs will be used to aid in the design and optimization of the composite engine block and other appropriate components. Components that will be considered for composite designs include the cylinder block, crankcases (e.g., rear and front), throttle body, water jacket, generator drive cover, and gear-train box.

It must be stressed that the design must be developed with processing in mind. The best design cannot be used if it cannot be fabricated into a functional part. For the components mentioned, injection-molding of CFRCs (e.g., gear-train box, water jacket, drive cover) and compression molding for higher temperature applications (e.g., crankcases and cylinder blocks) are being considered. Each of these processes and associated materials offer a different set of material properties that will be used in the optimization.

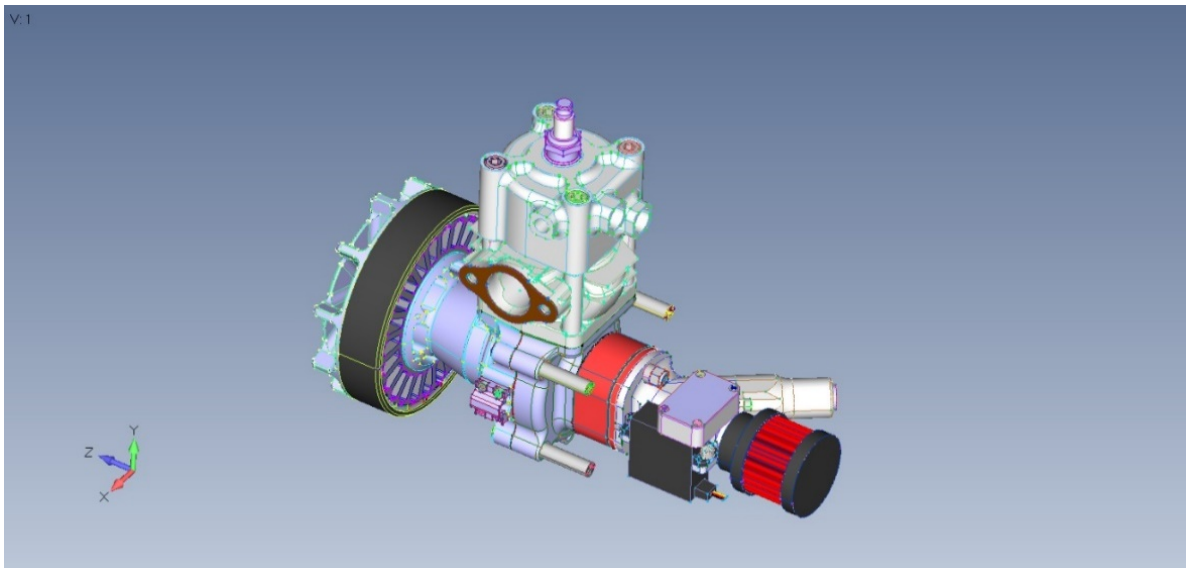

Figure I.3.5.2.7. Computer-aided design geometry of the Pegasus GE-35 engine that has been imported into a preprocessor for FEA. Source: ORNL.

Conclusions

In this one-year exploratory project, methods to toughen phenolic resins were identified and prepared as a renewable variant that is tough and provides an excellent matrix for superior fiber-reinforced composite performance. An appropriate fiber-matrix bonding methodology has been developed for the specific resin systems. Composites were fabricated from toughened phenolic resin systems that demonstrated greater than 100 MPa strength equivalent in the composite materials. In future work, the rheological and mechanical properties of discontinuous fiber composites need to be developed using the established methodology, and mechanical property retention after thermal aging needs to be assessed. The composite itself does not show any significant mass loss, as measured by thermogravimetry when scanned at 10°C/min until 250°C. A single-cylinder, two-stroke engine has been obtained and will be used as a starting point to develop design standards for future PMC applications to internal combustion engines. Future work should consist of FEA to determine the appropriate BCs (e.g., loads and constraints) of the current engine design and parameters considered for property optimization of the composite material.

Key Publications

1. Naskar, A. K., V. Kunc, and B. Knouff, 2019, "Novel materials for polymer composite engine blocks," Informal presentation at EERE Vehicle Technologies Program Annual Merit Review, June 13, 2019.
2. Naskar, A. K., V. Kunc, and B. Knouff, 2020, "Novel materials for polymer composite engine blocks," Informal presentation at EERE Vehicle Technologies Program Annual Merit Review, June 3, 2020.

References

1. Magda, M., 2015, "Plastic race engine returns as Polimotor 2 project underway," *Enginelabs*, 29 May 2015. Available at: https://www.enginelabs.com/news/plastic-race-engine-returns-as-polimotor-2-project-underway/, accessed 2 December 2020.
2. Sava, M., I. Sava, V. Cozan, and F. Tanasa, 2007, "Preparation and polymerization of bismaleimide compounds," *J. Appl. Polym. Sci.*, Vol. 106, No. 4, pp. 2185–2191.
3. Hamerton, I., and J. N. Hay, 1999, "Recent developments in the chemistry of cyanate esters," *Polym. Int.*, Vol. 47, No. 4, pp. 465–473.

4. Yagci, Y., B. Kiskan, and N. N. Ghosh, 2009, "Recent advancement on polybenzoxazine—A newly developed high-performance thermoset," *J. Polym. Sci. A1*, Vol. 47, No. 21, pp. 5565–5576.

5. Tran, C. D., J. Chen, J. K. Keum, and A. K. Naskar, 2016, "A new class of renewable thermoplastics with extraordinary performance from nanostructured lignin-elastomers," *Adv. Funct. Mater.*, Vol. 26, No. 16, pp. 2677–2685.

6. Naskar, A. K., J. K. Keum, and R. G. Boeman. 2016, "Polymer matrix nanocomposites for automotive structural components," *Nat. Nanotechnol.*, Vol. 11, No. 12, pp. 1026–1030.

7. Katzman, H. A., P. M. Adams, T. D. Le, and C. S. Hemminger, 1994, "Characterization of low-thermal conductivity pan-based carbon fibers," *Carbon*, Vol. 32, No. 3, pp. 379–391.

8. McIvor, S. D., M. I. Darby, G. H. Wostenholm, B. Yates, L. Banfield, R. King, and A. Webb, 1990, "Thermal conductivity measurements of some glass fiber- and carbon fiber-reinforced plastics," *J. Mater. Sci.*, Vol. 25, No. 7, pp. 3127–3132.

9. Huson, M. G., 2017, "High-performance pitch-based CFs," In: Bhat, G., (Ed.), *Structure and Properties of High-Performance Fibers*, pp. 31–78, Oxford: Woodhead Publishing.

10. Saleem, H., A. Edathil, T. Ncube, J. Pokhrel, S. Khoori, A. Abraham, and V. Mittal, 2016, "Mechanical and thermal properties of thermoset–graphene nanocomposites," *Macromol. Mater. Eng.*, Vol. 301, No. 3, pp. 231–259.

11. Di Pasquale, G., O. Motto, A. Rocca, J. T. Carter, P. T. McGrail, and D. Acierno, 1997, "New high-performance thermoplastic toughened epoxy thermosets," *Polymer*, Vol. 38, No. 17, pp. 4345–4348.

12. Chen, H., V. V. Ginzburg, J. Yang, Y. Yang, W. Liu, Y. Huang, and B. Chen, 2016, "Thermal conductivity of polymer-based composites: Fundamentals and applications," *Prog. Polym. Sci.*, Vol. 59, pp. 41–85.

13. Lin, C. H., J. C. Chen, C. M. Huang, and T. Y. Juang, 2014, "High-performance thermosetting films based on an amino-functionalized poly(ether sulfone)," *J. Appl. Polym. Sci.*, Vol. 131, No. 21, 5 November 2014.

Acknowledgements

The authors would like to acknowledge the guidance provided by Dr. R. Davies, ORNL Sustainable Transportation Program deputy director; Mr. F. Xiong; and Dr. N. Kanbargi for leading the laboratory work with the preparation and testing of composite specimens.

I.3.5.3 Novel Aluminum Matrix Composite for Powertrain Applications (5C) (Oak Ridge National Laboratory)

Zhili Feng, Principal Investigator
Oak Ridge National Laboratory
1 Bethel Valley Road
Oak Ridge, TN 37831
E-mail: fengz@ornl.gov

Jerry L. Gibbs, DOE Technology Manager
U.S. Department of Energy
E-mail: jerry.gibbs@ee.doe.gov

Start Date: April 1, 2019 End Date: June 30, 2020
Project Funding: $100,000 DOE share: $100,000 Non-DOE share: $0

Project Introduction

This one-year exploratory research effort at ORNL began in April 2019 as the result of an award under Thrust 5 of the VTO PMCP.

There are several fundamentally distinctive ways to strengthen materials for elevated temperature service. Solid solution strengthening and precipitation-aging hardening are commonly used in a variety of Al alloys, stainless steels, and nickel-based superalloys. Dispersion strengthening presents an additional attractive strengthening strategy by dispersing fine particles that are thermally stable, nearly insoluble, and exhibit very low diffusivity in the matrix to enhance elevated temperature strength. Well-known examples include oxide-dispersion-strengthened steels and nickel alloys that can have even higher high-temperature strength than precipitation-based counterparts. Dispersion strengthening has also been extensively investigated and developed for Al alloys to enhance elevated temperature strength, largely for aerospace and automotive applications [1]. MMCs are one of the examples of dispersion strengthening that have been used commercially in the automotive market for nearly 20 years, including in powertrain applications, such as cylinder liners, pistons, and connecting rods [2]. As the automotive industry is highly sensitive to cost, wider application of MMCs will require performance improvements coupled with novel or innovative process improvements to substantially reduce overall cost.

For the same volume fraction, it is well-accepted that nanosized particles are much more effective than micron-sized particles in strengthening materials due to reduced interparticle spacing and the Orowan hardening effect [3]. However, achieving the uniform dispersion of nanosized particles in a molten metal and subsequent solidified metal matrix has proven extremely difficult. Due to the surface tension effect and density differences, nanosized oxide particles have a much greater tendency to agglomerate and float to the surface during metal casting. Attempts to apply external energy fields—such as ultrasonic energy and electromagnetic energy—to break down the agglomerates and mix the nanoparticles uniformly in the molten metal have been experimentally evaluated at laboratory-scale with limited success; thus, they have had little opportunity to demonstrate potential success in larger-quantity production. For other functional additives, chemical reactions with the molten matrix material during casting or liquid metal infiltration decompose or degrade the additives and cause weak bonding between the additives and the matrix. Therefore, the solid-state-based dispersion processes proposed here offer a new processing route to engineer and synthesize stronger and lighter MMCs for a number of applications, including powertrain components.

As part of the DOE VTO PMCP Thrust for Emerging Concepts (Thrust 5), ORNL and PNNL jointly explored the technical feasibility of using FSP, friction-stir extrusion (FSE), and Shear-Assisted Processing and

Extrusion (ShAPE™), to produce Al matrix composites (AMCs) for powertrain applications. Although the FSP/E and ShAPE™ processes share the same fundamental principles of solid-state material processing that rely on frictional heating and extensive shear-dominated deformation to mix, consolidate, and produce materials, the capabilities and equipment at ORNL and PNNL differ. This collaborative effort enables the two National Laboratories to combine their collective and complementary expertise and equipment capabilities to effectively carry out the proposed research to achieve the proposed project goals. This report primarily describes the associated research efforts at ORNL.

Objectives

The goal of the joint research is to demonstrate the technical feasibility of using FSP/E and ShAPE™ processes to produce AMCs with additions of graphene, other forms of carbon, and other nanosized additives, such as carbide, ceramic, and oxide particles, to significantly improve the strength of Al-based alloys at elevated temperatures relevant to automotive-powertrain applications. The research targets a minimum of 20% increase in strength at RT and 300°C, compared to baseline 7xxx series alloys, or alternatively, ORNL's ACMZ family of alloys.

Approach

The feasibility of a novel solid-state processing route to synthesize MMC materials for powertrain applications was investigated. The effort aimed to combine several innovations in FSP and FSE patented by ORNL [4]–[7] to stir, consolidate, and extrude powders, chips, and other feedstock materials into useable product forms. Past ORNL research [8],[9] shows that FSP and FSE are highly effective uniformly to disperse high-volume fractions of nanosized additives in the metal matrix, which potentially overcomes a major technical barrier in synthesizing nanocomposites via processing by casting methods [10].

This exploratory effort focused on Al-based MMCs for potential powertrain applications in cylinder liners, pistons, driveshafts, and connecting rods. Candidate nano-additives included ceramic-based, carbon-based, and other types of functional additives. The primary objective was to incorporate purposely designed nano-additives into the matrix by the proposed solid-state processing routes to determine whether such additions can significantly enhance static and creep strength, wear-resistance, friction reduction, and thermal conductivity of ACMZ cast alloys and 7xxx Al alloys. The synthesized materials were tested for their materials properties and compared to key reference materials. One potential scale-up approach is friction-stir AM, which is under development at ORNL for high-temperature materials for nuclear industry applications.

Research included the following activities:

- Potential nano-additives were identified and selected for MMCs that may lead to creep strength, wear-resistance, and thermal-property improvement.
- Matrix materials having the most impact for powertrain applications with the proposed MMC approach were selected. Materials included two emerging high-strength Al alloys—ORNL's ACMZ Al alloy, and the 7xxx series alloy, which is the highest-strength wrought Al alloy for automotive applications, as well as Alloy 6061.
- Design, engineering, and processing were enhanced for nano-additives for simultaneous strength, wear-resistance, and thermal-property improvement.
- A friction-stir-based process was developed and refined to produce sample materials for testing and evaluation.
- The microstructure, mechanical property, and functional properties were characterized on the MMC samples and baseline reference materials to determine the feasibility for property enhancement.
- Potential scale-up production approaches were identified for complexity and cost.

Results

A high-throughput rapid-processing method was developed and used to add nano-additives to the Al matrix based on the FSP and FSE process systems available at ORNL. Figure I.3.5.3.1 shows the basics of the process. Machined AA6061 or AA7075 chips and powders were mixed with additives as the initial feedstock matrix materials. Solid-state FSP was used to consolidate the feedstock material to form fully dense, consolidated MMC. Ceramic-, intermetallic-, and carbon-based additives, in the range of 3–10 wt%, were used in this exploratory project. Fully consolidated MMC material blocks were fabricated and were further characterized and tested.

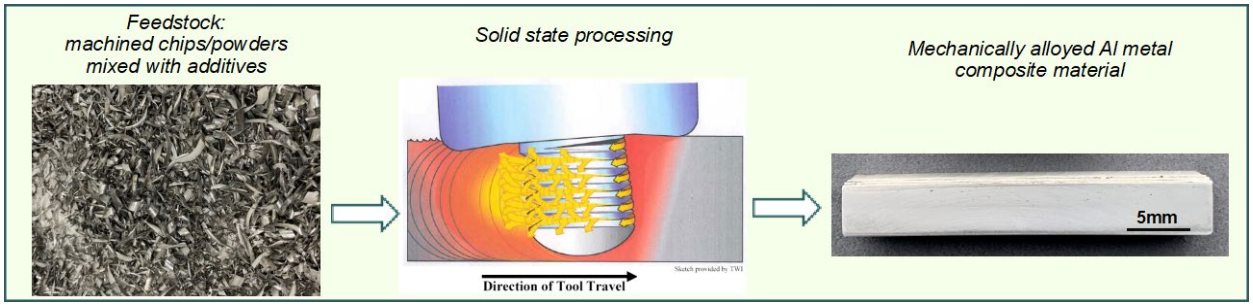

Figure I.3.5.3.1. Basic friction-stir based solid-state MMC fabrication approach. Source: ORNL.

Figure I.3.5.3.2 shows the processed Al matrix with nano-additives in the processed region. Approximately 3–4 in. long × 1.5–2 in. wide × 0.25 in. thick AMC material blocks were produced for testing and evaluation.

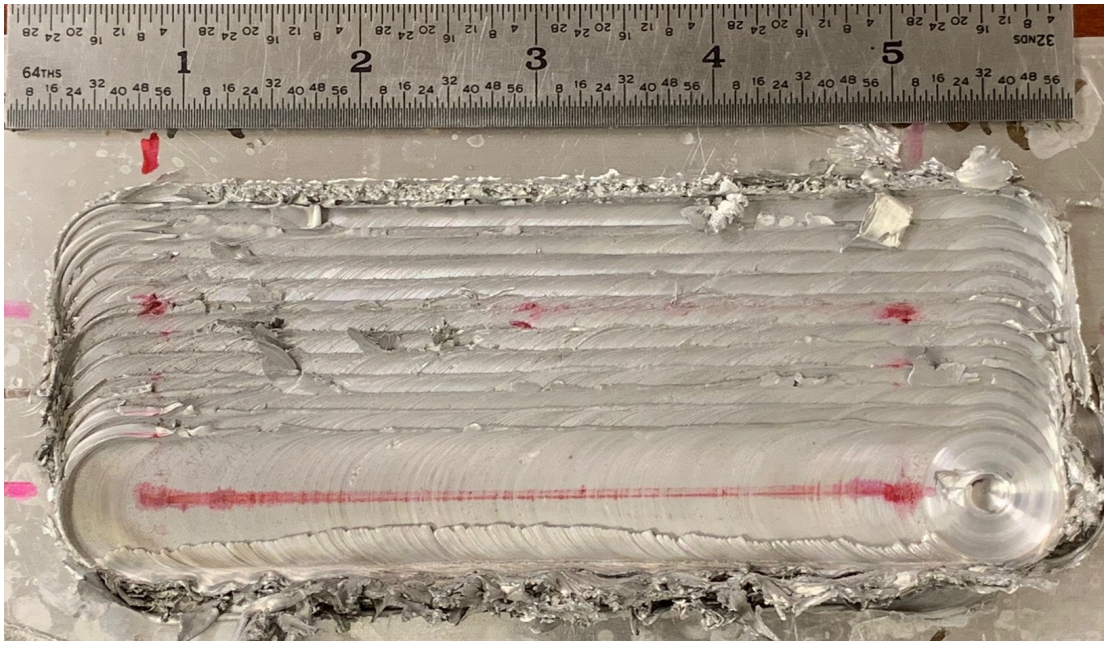

Figure I.3.5.3.2. Friction-stir-processed AA6061 block with nano-additives in the processed region. Source: ORNL.

The microhardness measurement results of different nano-additive Al composites with AA7075 as the matrix material are shown in Figure I.3.5.3.3. Four different nano-additives are shown: 3%wt. carbon, and three different intermetallics (IM) at the same 5 wt%. The process is far from optimized in this exploratory study, so the results presented in the figure only represent preliminary results. Microhardness was measured on the as-processed conditions, which is expected to be between the O and T4 condition. The results presented in Figure I.3.5.3.3 clearly show a significant increase in microhardness when nano-additives were added to the

matrix material by the solid-state processing in this study. For C additives, 15% increase in microhardness was achieved. For IM additives, all three additives meet or exceed the targeted 20% increase in strength identified for this exploratory study. Increases in the microhardness from 20% to 50% were obtained, with the IM-C additive reaching a 50% increase over the reference AA7075 without additives. Similarly, increases from 20–30% in hardness and strength were achieved for the AA6061 matrix material [11].

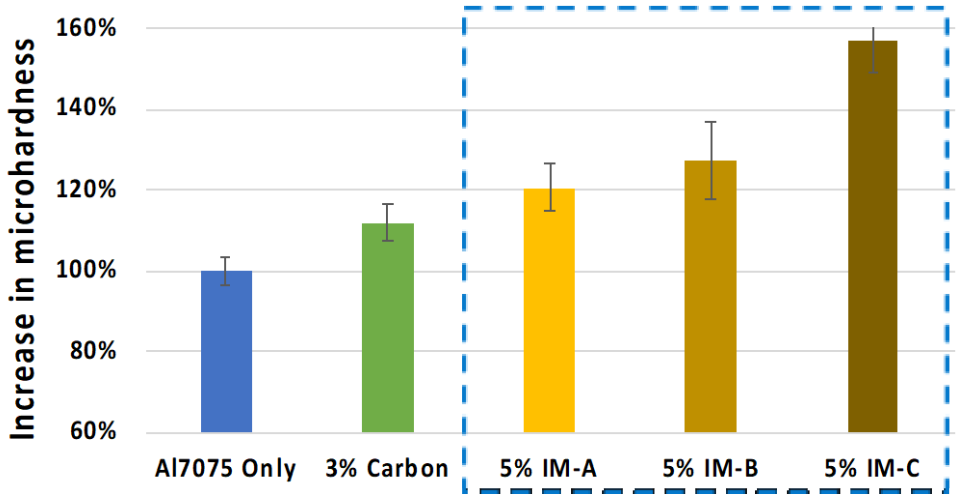

Figure I.3.5.3.3. Microhardness results by adding different IMs and C to AA7075 matrix. Source: ORNL.

Figure I.3.5.3.4 shows an example of IM nano-additives in AA6061 MMC produced by solid-state FSP. Fairly uniform distribution of intermetallic particles was observed. The sizes of the IM particles were in the range of 100 nm to sub-microns.

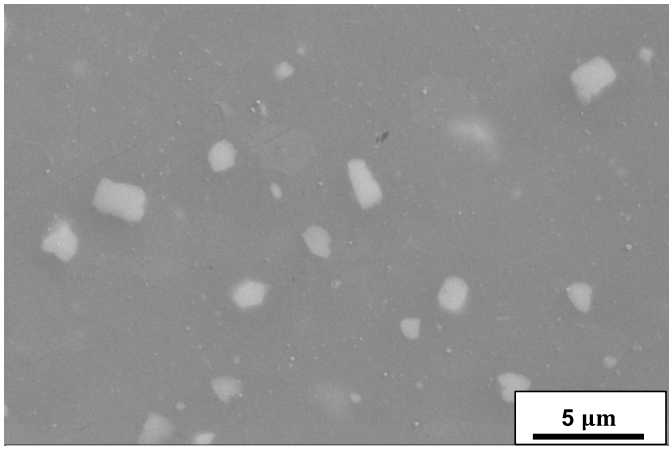

Figure I.3.5.3.4. Distribution of IM nano-additives in AA6061 matrix. Source: ORNL.

ORNL and PNNL maintained close collaboration on the selection of matrix materials and additives. The research at ORNL focused on the FSP/FSE high-throughput route, whereas the research conducted at PNNL focused on ShAPE™ to effectively utilize the capabilities and equipment at the two National Laboratories. ORNL also provided three different ACMZ alloy variants to PNNL as a matrix material to explore the possibility to further enhance the performance of ACMZ alloys through the addition of nano-additives.

Conclusions

Our exploratory research project successfully demonstrates the feasibility of solid-state material processing with mechanical alloying to synthesize stronger and lighter Al metal composite materials for engine and body structures:

- Up to 50% hardness increase was achieved for AA7075-based MCMs with 5%wt. intermetallic additives.
- Up to 25% hardness increase was achieved for AA6061-based MCMs with 5%wt. SiC or intermetallic additives.
- Baseline process condition was established for high-throughput FSP synthesis of Al MCMs.

Key Publications

1. Feng, Z., 2019, "Novel Al matrix composites for powertrain applications," 2019 VTO Annual Merit Review, VTO Powertrain Emerging Technologies, 10–13 June 2019, Arlington, VA, USA.
2. Feng, Z., 2020, "Novel Al matrix composites for powertrain applications," 2019 VTO Annual Merit Review, VTO Powertrain Emerging Technologies, June 2020, online virtual meeting, USA.

References

1. Bloch, E. A., 1961, "Dispersion-strengthened aluminum alloys," *Metallurgical Reviews*, Vol. 6, No. 1, pp. 193–240.
2. Hunt, W. H., and D. B. Miracle, 2001, "Automotive applications of metal matrix composites," in: Miracle, D. B, and S. L. Donaldson (eds.), *ASM Handbook*, Vol. 21. OH: ASM International, pp. 1029–1032.
3. Kouzeli, M., and A. Mortensen, 2002, "Size-dependent strengthening in particle-reinforced Al," *Acta Mater*., Vol. 50, pp. 39–51.
4. Feng, Z., S. A. David, and D. A. Frederick, 2011, "Friction-stir method for forming structures and materials," U.S. Patent No. 8061579 B2, November 22, 2011.
5. Manchiraju, V. K., Z. Feng, A. David, and Z. Yu, 2017, "Providing plastic zone extrusion," U.S. Patent No. 9,616,497 B2, April 11, 2017.
6. Manchiraju, V. K., Z. Feng, A. David, and Z. Yu, 2014, "System for and method of plastic zone extrusion," European Patent No. EP2777837A1, October 15, 2014.
7. Manchiraju, V. K., and Z. Feng, 2015, "提供塑形区挤出 (translated to 'Providing plastic zone extrusion,'" Chinese Patent No. CN102371286B, July 29, 2015.
8. Qu, J., H. Xu, Z. Feng, D. A. Frederick, L. An, and H. Heinrich, 2011, "Improving the tribological characteristics of aluminum 6061 alloy by surface compositing with sub-micro-size ceramic particles via friction-stir processing," *Wear*, Vol. 271, No. 9–10, pp. 1940–1945.
9. Yu, Z., Z. Feng, V. Manchiraju, and S. A. David, 2013, "Friction-stir extrusion of Al alloys," in: Marquis, F. (ed.), *Proceedings of the 8th Pacific Rim International Congress on Advanced Materials and Processing (PRICM 8)*, 4–9 August 2013, Waikoloa, HA, USA.
10. Yang, Y., J. Lan, and X. Li, 2004, "Study on bulk Al matrix nanocomposite fabricated by ultrasonic dispersion of nanosized SiC particles in molten Al alloy," *Mat. Sci. Eng. A–Struct.*, Vol. 380, No. 1–2, pp. 378–383.
11. Feng, Z., 2019, "Novel aluminum matrix composite for powertrain applications," DOE VTO FY 2019 Annual Progress Report.

Acknowledgements

The principal investigator would like to recognize S. Zhang, Y. Li, and D.A. Frederick of ORNL for their support and assistance with this project.

I.3.5.4 High-Strength Aluminum Graphene Composite for Powertrain System (Pacific Northwest National Laboratory)

Xiao Li, Principal Investigator
Pacific Northwest National Laboratory
902 Battelle Boulevard
Richland, WA 99352
E-mail: xiao.li@pnnl.gov

Jerry L. Gibbs, DOE Technology Manager
U.S. Department of Energy
E-mail: jerry.gibbs@ee.doe.gov

Start Date: April 1, 2019 End Date: March 31, 2020
Project Funding: $100,000 DOE share: $100,000 Non-DOE share: $0

Project Introduction

The next-generation of powertrain material demands high-strength and lightweight. Al and its alloys, with a density of approximately one-third that of steel and cast-iron, has the potential of reducing weight by at least 40% in properly designed structures and components for powertrain systems. Barriers to the use of Al include limited strength, fatigue performance, lack of formability, and joining and corrosion issues. For example, the failure of an Al connecting rod-like the one shown in Figure I.3.5.4.1—usually called 'throwing a rod'—is one of the most common causes of catastrophic engine failure in vehicles, frequently putting the broken rod through the side of the crankcase and thereby rendering the engine irreparable.

Figure I.3.5.4.1. Al connecting rod for a 4-stroke engine failed by fatigue, which subsequently impacted the crankshaft and caused catastrophic engine damage. Source: Wikipedia.

The application of an Al-G composite can have outstanding mechanical properties and can be a promising candidate material for next-generation powertrain components if manufacturing methods can be developed to take full advantage of the novel composite. Recent work on manufacturing bulk size (e.g., >100 mm) graphene-reinforced metal matrix material has been limited by two major issues: (1) an agglomeration of particles using powder metallurgy or melting process methods due to poor particle dispersion and (2) high processing temperatures are too high causing weak formation of Al-carbide intermetallics, which degrade the quality of the composite. To achieve the best mechanical properties, G must be homogeneously dispersed in the metal matrix without significant detrimental thermal effects.

As part of the DOE VTO Core Powertrain Materials Program, PNNL is exploring the technical feasibility of using FSP and ShAPE™—an advanced scalable form of friction extrusion—to produce AMCs for powertrain applications. Whereas FSP and ShAPE™ share the same fundamental principles of solid-phase material processing described by extensive shear-dominated deformation, they can be applied differently for either selective-local reinforcing or to produce a bulk structure, respectively.

Objectives

This conceptual project is being worked on in collaboration with ORNL, which is conducting complementary experiments using friction extrusion techniques to screen the material performance impact of adding other dispersion phases, besides C, to Al. The goal is to demonstrate the potential of using friction-stir-based processes to produce AMCs with additions of graphene, other forms of C, and other nanosized additives, such as carbide oxide particles to significantly improve the strength of Al-based alloys under elevated temperatures relevant to powertrain applications. The goal is to achieve a minimum of 20% increase in strength at RT and 300°C, as compared to the baseline 7xxx series alloys, or alternatively relative to ORNL's new ACMZ alloy).

Approach

ShAPE™ is a novel manufacturing process with a significant difference from the traditional process of extrusion, where the die rotates against the billet so that frictional heat softens the material, as shown in Figure I.3.5.4.2. The high-shear deformation leads to a refined grain structure and highly textured crystallographic orientation, which enables improved strength and ductility. In addition, ShAPE™ perfectly addresses the two challenges discussed above: (1) it is a solid-phase processing that mixes, consolidates, and extrudes material with the aid of high-shear deformation; and (2) compared to melting methods, the processing temperature of ShAPE™ is much lower. Thus, thermal degradation can be largely reduced or even avoided.

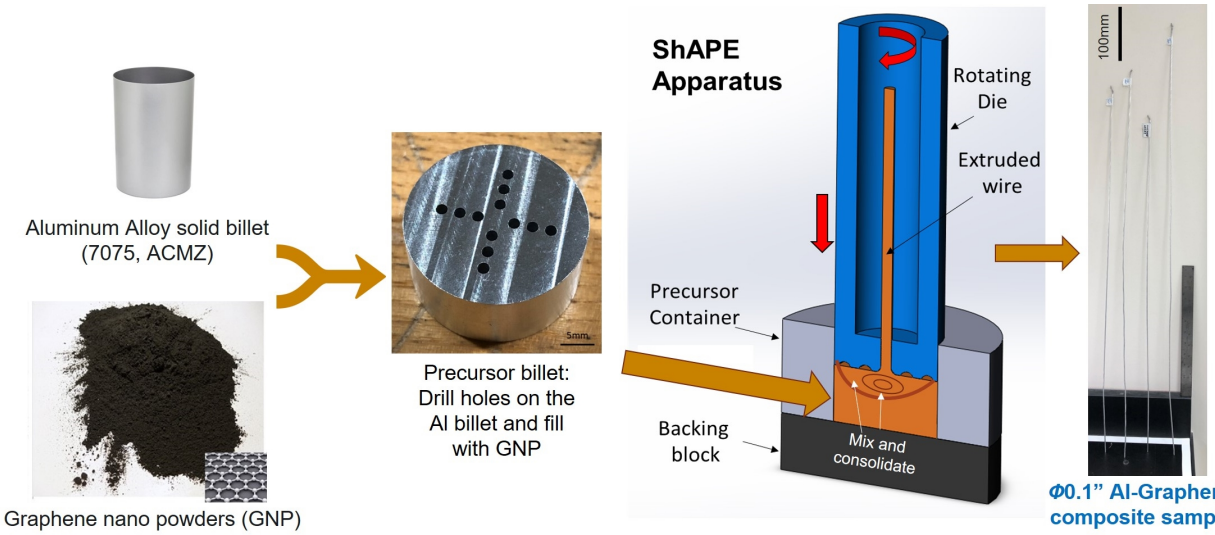

Figure I.3.5.4.2. Schematic diagram of the ShAPE™ process. Source: PNNL.

To demonstrate the ability for ShAPE™ to mix and homogenously distribute G throughout an Al matrix in the experimental setup, a series of Al-G composite wires were produced using the following procedure:

- Machine an Al alloy to a cylindrical billet with a 1 in. diameter and a 0.5 in. length.
- Drill a pattern of holes with a 0.45 in. depth across the billets, in which the G nano-powder was filled, as shown previously in Figure I.3.5.4.2.
- Load the precursor billet into the ShAPE™ machine and process it.
- Control the process temperature via active chilling by applying water around the billet on the container and helium gas to increase the convective heat transfer around the die face, as shown in Figure I.3.5.4.3.

- Use a scroll-face die design tool with a 1 in. outside diameter and 0.1 in. hole diameter; thus, the extrusion ratio is 100:1, as can be seen in the inset in Figure I.3.5.4.3.

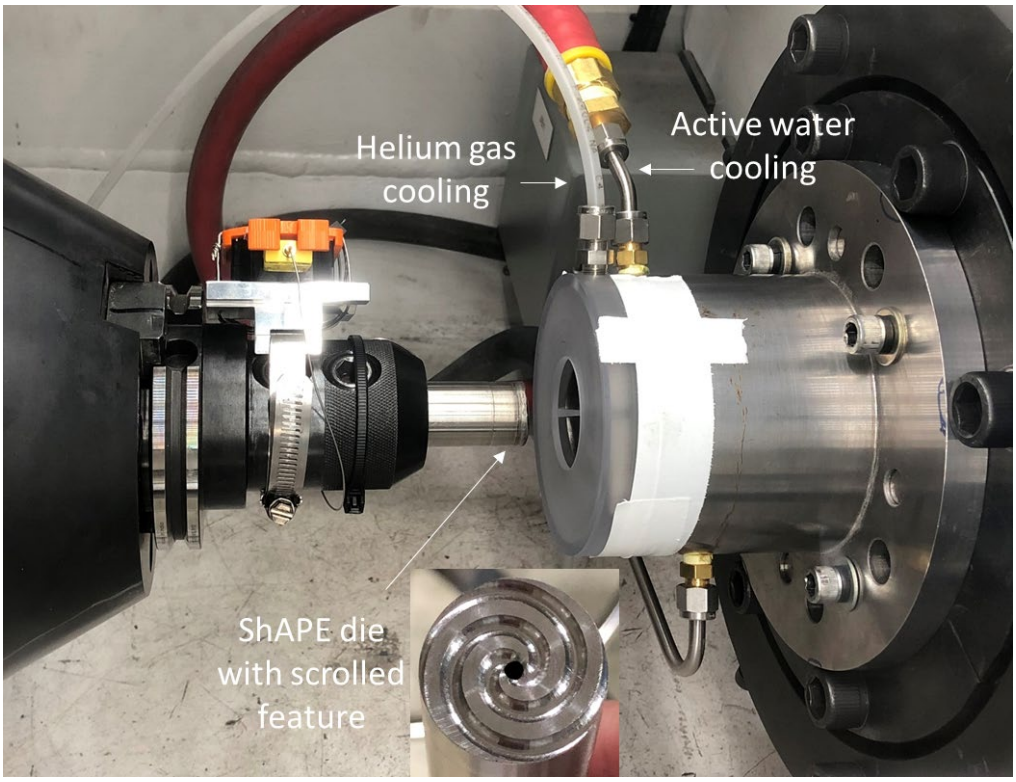

Figure I.3.5.4.3. Experimental setup of ShAPE™ process. Source: PNNL.

Results

Through a design of experiment approach, effective processing parameters were determined to be as follows:

- ACMZ alloy – 150 rpm die rotational speed and 4 mm/min die feed rate
- AA7075 – 100 rpm die rotational speed and 1 mm/min die feed rate were selected.

High-quality Al-G composite wires with about a 1-meter length, sound straightness, and a smooth surface were produced as can be seen in Figure I.3.5.4.4(a). The cross-sections of the composite wires were inspected by an optical microscope. The results indicate the wires are void-free, uniform, and have no obvious phase segregation. Figure I.3.5.4.4(b) shows the cross-section of the AA7075-G ShAPE™ processed wire.

Electron microscopy was utilized to further analyze the distribution of the G in the composite wire. Figure I.3.5.4.5(a) is a BSE image; the gray area is Al and white regions are Cu in the ACMZ alloy. The EDS image is shown in Figure I.3.5.4.5(b) from the same area, which indicates the G addition was very uniformly dispersed in the metal matrix. In addition, the grain size of AA7075 was refined to ~7 µm, while the particle-size of the G powder was refined to sub-micron.

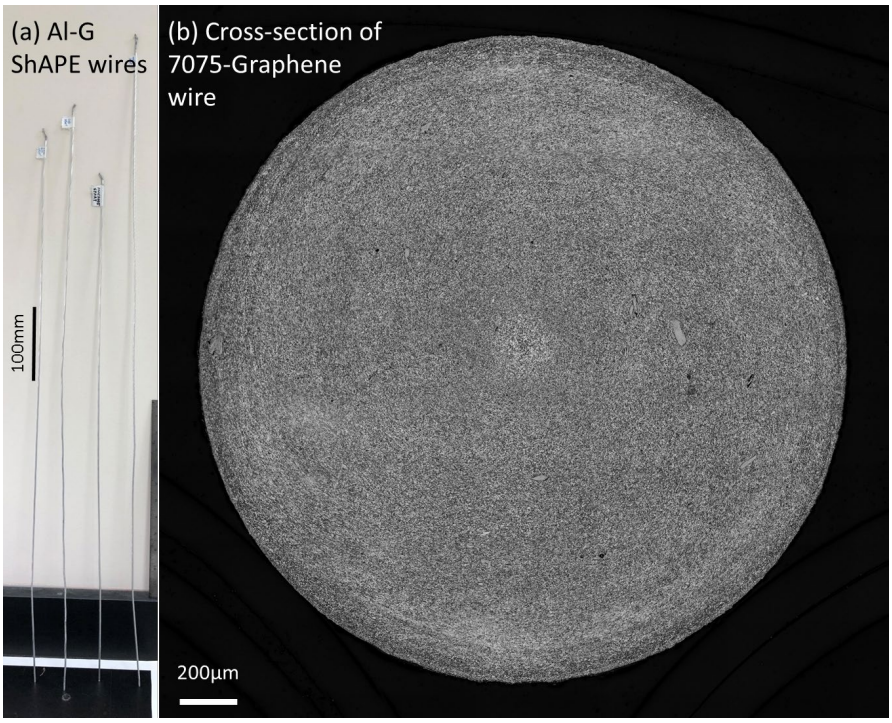

Figure I.3.5.4.4. (a) Al-G composite wires produced by ShAPE™; and (b) a cross-section of 7075 G ShAPE™ wire. Source: PNNL.

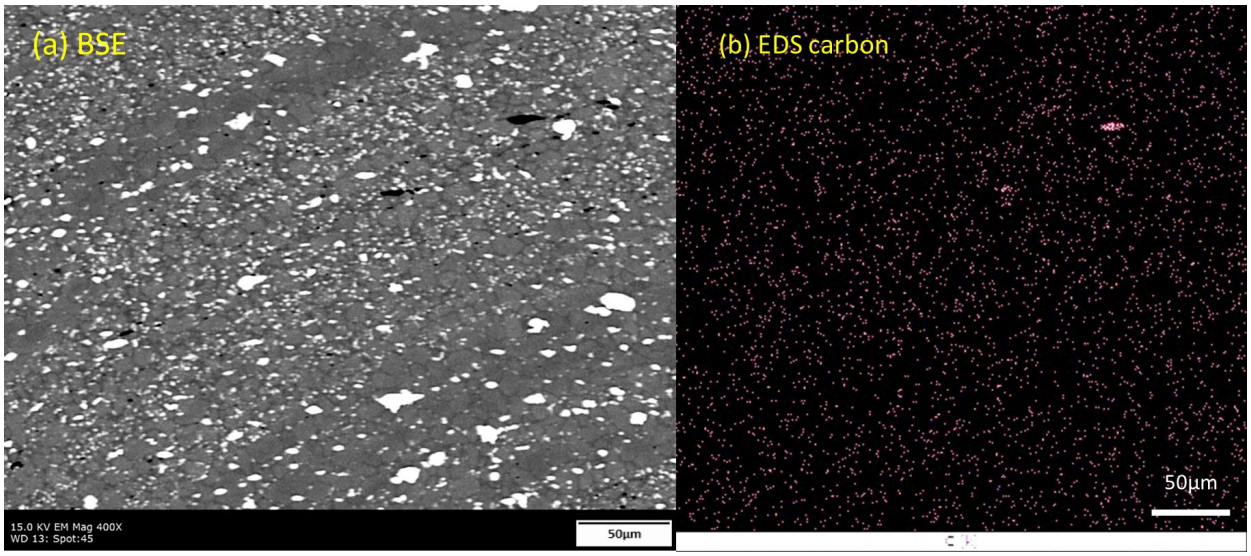

Figure I.3.5.4.5. (a) BSE image of Al-G ShAPE™ wire. (b) EDS image shows uniform C dispersion. Source: PNNL.

Figure I.3.5.4.6 shows the die face temperature at the location where shear deformation occurs, which is the peak temperature achieved during processing. This temperature profile confirms adequate thermal management was achieved, while the processing temperature of ShAPE™ was maintained in the 350–400°C range, which is much lower than that of other compositing processes (e.g., melting [> 600°C] or sintering [450–600°C]). XRD analysis was applied on the Al-G ShAPE™ samples and the results indicated that the brittle carbides (e.g., Al_4C_3) were not formed during the ShAPE™ process. Thus, the quality of the G is maintained, and the formation of brittle Al-carbides is avoided.

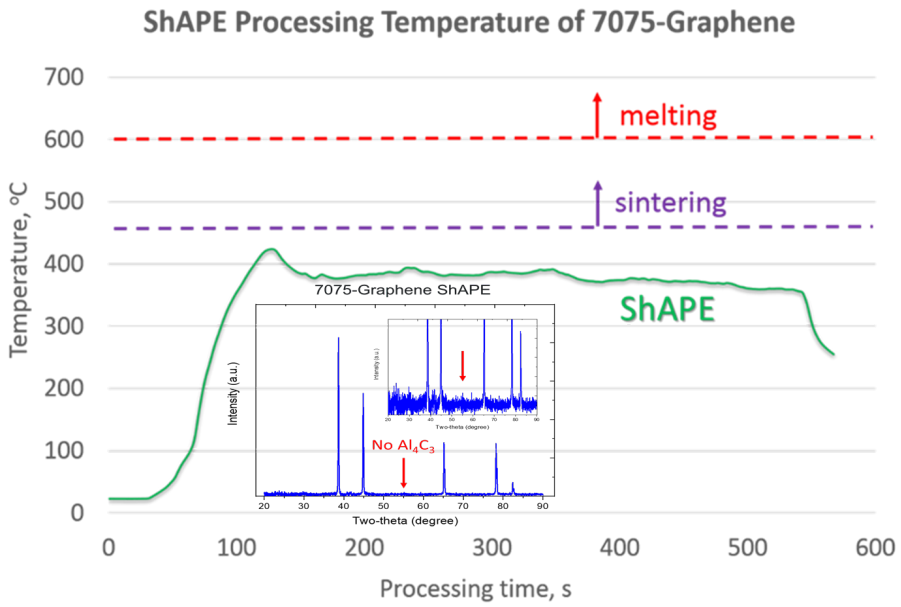

Figure I.3.5.4.6. ShAPE™-processing temperature of making 7075-G composite, as compared to other processes. Inset: XRD results show no carbide was formed during ShAPE process. Source: PNNL.

The RT tensile test results of the 7075 ShAPE™ sample, the 7075-0.08wt%G ShAPE™ sample, and the 7075-0.1wt%G ShAPE™ sample are presented in Figure I.3.5.4.7(a). Also, the ultimate strength and ductility of three Al alloys that are commonly used in powertrain system are given in the plot to compare with the ShAPE™ samples. The as-extruded 7075 ShAPE™ sample has the same ductility, but slightly lower strength compared to commercial 7075-T73. When a tiny amount of G was added, the ductility was improved nearly two times the strength also increased by 10%; thus, the toughness was largely increased compared with the sample without graphene. In Figure I.3.5.4.7(b), 300°C tensile curves of 7075-G ShAPE™ sample and commercial 7075-T73 sample are presented. Compared to the commercial 7075-T73, the Al-G wire has a slightly lower strength, but the ductility improved by 30%. This indicates that the Al-G composite made by ShAPE™ has better high-temperature performance and possible better creep resistance at an elevated temperature. The effect of post-heat-treatment on Al-G composite has not been studied, so it is reasonable to assume the best mechanical performance has not been reached yet.

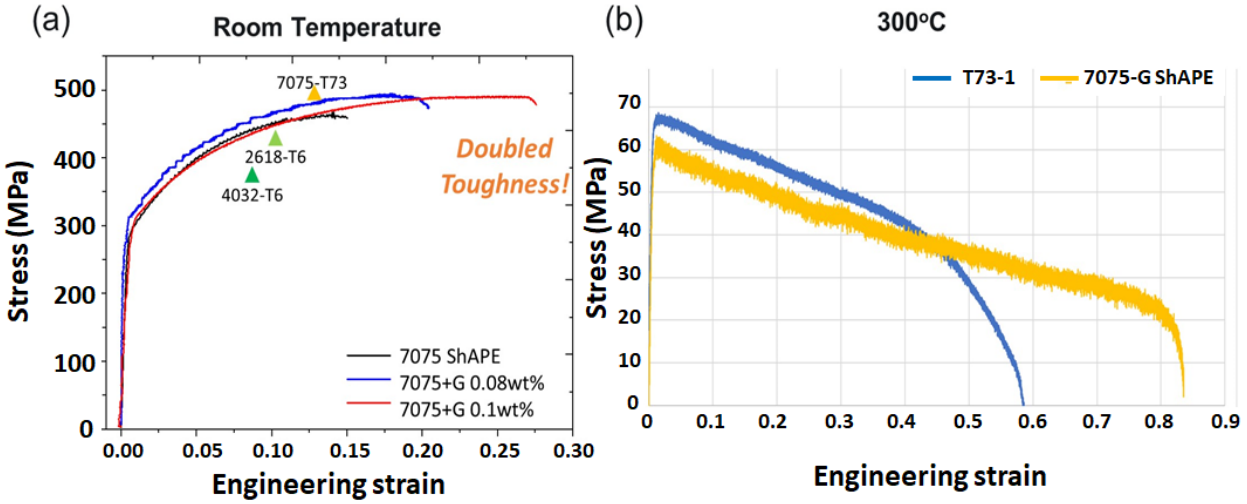

Figure I.3.5.4.7. Mechanical properties of 7075-G composite at (a) RT; and (b) 300°C, as compared to other Al alloys used in powertrain systems. Source: PNNL.

The reason that the Al-G ShAPE composite has better mechanical properties is complex. It can be explained by at least the following aspects: (1) despite having G or not, ShAPE™ samples have a refined grain size of 2–3 µm compared to commercial 7075 at ~50 µm, as observed in Figure I.3.5.4.8(a); (2) compared to the 7075 sample, the 7075-G sample developed a stronger <111> texture, which indicates good interfacial bonding between Al (face-centered cubic) and graphene; and (3) as can be seen in Figure I.3.5.4.8(b), the TEM EDS results show that the G is distributed on the grain boundaries and attached with precipitates. With a homogenized G dispersion, the improved interfacial bonding between the Al matrix and the precipitate could be the reason that the 7075-G ShAPE™ samples had a high ductility. Further study needs to be carried out to reveal the interfacial strength of metal-graphene.

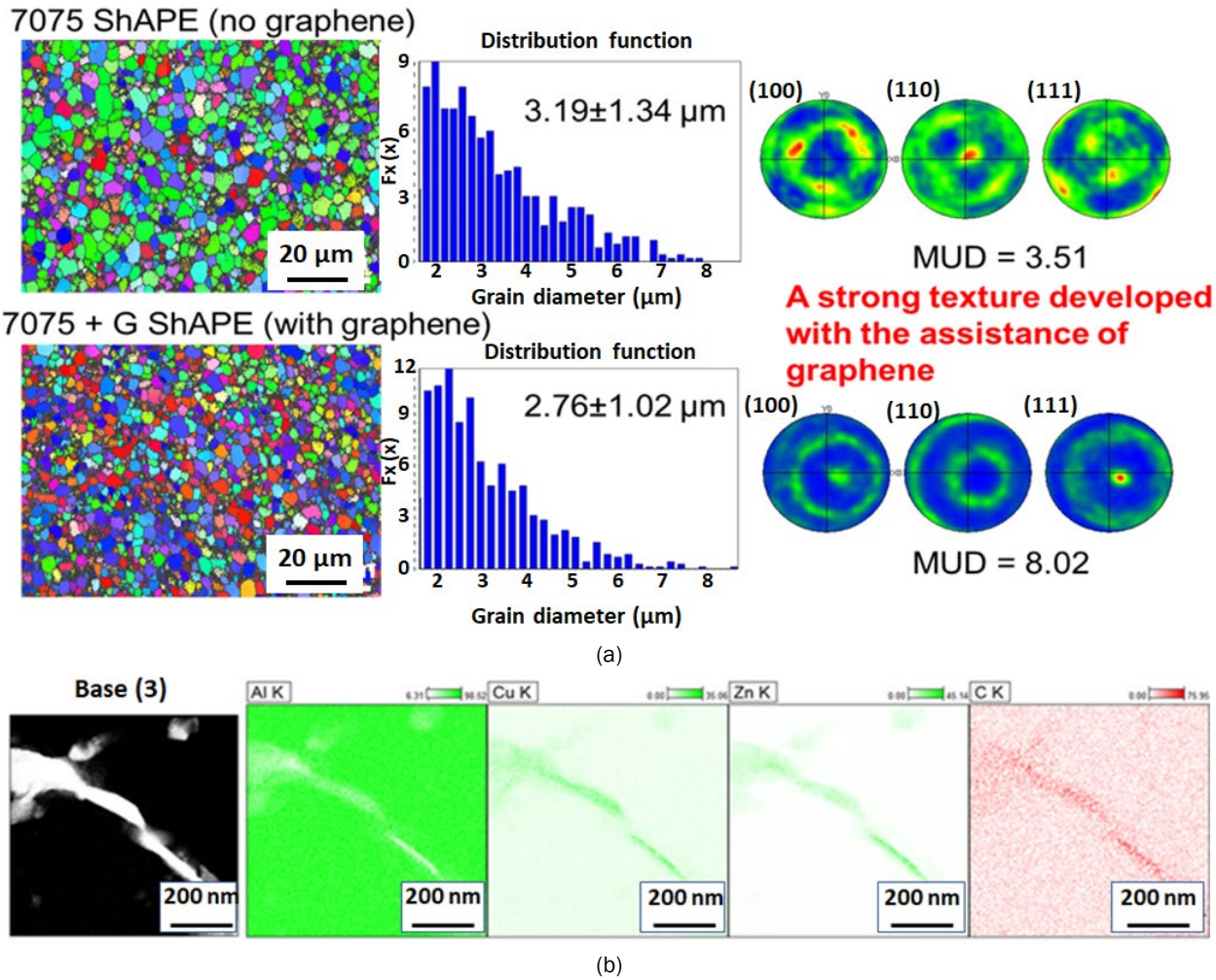

Figure I.3.5.4.8. (a) EBSD results of the 7075 and 7075-G ShAPE samples, from left to right: grain structure, grain size distribution, and crystallographic orientation; and (b) TEM EDS analysis on Al-G sample. Source: PNNL.

Conclusions

ShAPE™ can successfully produce an Al-G composite by mixing and extruding an Al alloy with G via high-shear deformation. The high-shear deformation not only uniformly disperses the additional material, but also leads to a refined grain structure and highly textured crystallographic orientation, which enables outstanding strength and ductility.

With the successful completion of the concept trials, it was demonstrated that void-free uniformly dispersed Al-G composite can be achieved by ShAPE™. Mechanical properties of the composite material showed 100% increased ductility and toughness at RT and 30% improvement at elevated temperature, compared with commercial AA7075 alloy. Phase identification proved definitively that Al-carbide formation, and other intermetallics, were avoided during the process.

To obtain an in-depth understanding of the complex strengthening mechanisms is critical to the yet-to-be-optimized strength. Future proposed efforts aim to experimentally investigate the effect of: (1) G content; (2) Al-G interfacial strength; and (3) post-heat-treatment conditions.

Key Publications

1. Li, X., 2019, "Shear-Assisted Processing and Extrusion (ShAPE™): A novel solid-phase processing of making bulk size metal matrix composite without agglomeration," *Multifunctional Ceramic- and Metal Matrix Composites: Processing, Microstructure, Properties and Performance*, *Materials Science & Technology 2019*, 29 September–3 October 2019, Portland, OR, USA.
2. Li, X., 2020, "7075 Aluminum Graphene Composites Made by Shear-Assisted Processing and Extrusion," *Solid-State Processing of Metals and Composites, Materials Science & Technology 2020,* 2–6 November 2020, virtual.

References

1. Li, X., D. Baffari, and A. P. Reynolds, 2018, "Friction-stir consolidation of aluminum machining chips," *Int. J. Adv. Manuf. Tech.*, Vol. 94, No. 5–8, pp. 2031–2042.
2. Hwang, J., T. Yoon, S. H. Jin, J. Lee, T.-S. Kim, S. H. Hong, and S. Jeon, 2013, "Enhanced mechanical properties of graphene/copper nanocomposites using a molecular-level mixing process," *Adv. Mater.*, Vol. 25, No. 46, pp. 6724–6729.
3. Sun, Y., C. Zhang, B. Liu, Q. Meng, S. Ma, and W. Dai, 2017, "Reduced graphene oxide-reinforced 7075 AMCs: Powder synthesis and mechanical properties," *Metals*, Vol. 7, No. 11, Art. 499.
4. Renguo, G., L. Chao, Z. Zhanyong, C. Runze, and L. Chunming, 2012, "Study on preparation of graphene and Al-graphene composite," *Rare Metal Mat. Eng.*, Vol. 41, pp. 607–611.

Acknowledgements

This research was supported by the Powertrain Material Core Program of DOE's VTO. The authors are grateful for the efforts of Darrell Herling for project management, Xiaolong Ma for microstructural characterization, Tim Roosendaal for mechanical testing, and Anthony Guzman for preparation of the metallographic specimens. Pacific Northwest National Laboratory is operated by Battelle Energy Alliance, LLC, for DOE under maintenance and operations contract DE-AC06-76101830.

I.3.5.5 Development of High-Temperature Sample Environment for Advanced Alloy Characterization Using High-Energy X-ray Techniques (Argonne National Laboratory)

Andrew Chuang, Principal Investigator
Advanced Photon Source
Argonne National Laboratory
9700 S. Cass Avenue
Lemont, IL 60439
E-mail: cchuang@anl.gov

Jerry L. Gibbs, DOE Technology Manager
U.S. Department of Energy
E-mail: jerry.gibbs@ee.doe.gov

Start Date: May 1, 2020 End Date: September 30, 2021
Project Funding: $150,000 DOE share: $150,000 Non-DOE share: $0

Project Introduction

The High-Energy X-Ray Microscope (HEXM) is a long beamline that has been approved and will be built as a part of the Advanced Photon Source Upgrade (APS-U) project. The APS-U project will increase the brightness of the APS high-energy X-ray beams by two orders of magnitude, enabling researchers to make groundbreaking discoveries and innovations that create new products and industries. HEXM will investigate structure and evolution within bulk materials, often in extreme environments, with both the enhanced high-energy X-ray scattering techniques used today (e.g., at 1-ID of APS) and with novel coherence-based techniques enabled by the low-emittance APS-U multi-bend-achromat lattice.

Advanced material characterization plays an important role in the alloy development process. It allows researchers to connect process parameters to performance by providing detailed information on the underlying microstructure. Among existing techniques, high-energy X-ray imaging has the unique combination of being: (1) fast; (2) nondestructive; (3) multiscale (mm to sub-micron); and (4) well-suited to *in situ* studies, such as mechanical and thermal loading. The context for this research will be ***in situ* studies of microstructure evolution (i.e., defect/secondary phase formation and/or annihilation)** in select engineering alloys at **elevated temperatures** by high-energy X-ray imaging techniques. In order to have mechanistic understanding of the microstructures that govern the performance of materials at the mesoscale, direct observation of microstructure changes under in-service conditions (e.g., at elevated temperatures and/or under external load) are needed. To perform theoretical computations to model such processes, both images of the secondary phases and porosity, and microstructure information (e.g., crystal structure, texture) are required. The ultimate goal is for real-time monitoring of microstructure with sub-micron resolution at service environments (i.e., in terms of temperature and external load).

Objectives

The objective of this work will be the continued improvement of a high-temperature sample environment that was developed in the first year of the project. A high-temperature heating apparatus utilizing induction technology was developed to use at a new high-energy X-ray beamline that provides zoom-in and zoom-out X-ray imaging capability of mm-sized specimens with sub-micron resolutions. In the second year, we plan to integrate the heating device with a small load frame to study the material under thermal-mechanical load. The proposed setup enables the investigation of material deformation under high-temperature, similar to the environment in the hot-section of an engine.

The impact of the present work contributes at both the engineering and basic materials science levels. As an example, Figure I.3.5.5.1 shows a 3D crack morphology in a Ti alloy. The specimen with a cross-section of 2 mm × 2 mm was machined from an actual part and fatigued to initiate a crack. The X-ray tomography technique was used to monitor the growth of the crack as the number of cycles advanced to simulate the material under service-loading conditions. The fatigue life of a material is determined by its ability to hinder the initiation of a crack and the subsequent growth of cracks once a small crack is initiated. The local microstructure and environmental factors play a critical role in affecting these processes, as well as fatigue lifetime. Current techniques provide imaging resolutions of 1~3 µm and can be employed at ambient temperatures. To further obtain the mechanistic understanding of these phenomenon under in-service conditions requires information at elevated temperatures. The development and utilization of a rapid, nondestructive heating cell to work in conjunction with a load frame and X-ray imaging tool with sub-micron spatial resolution and large field-of-view in millimeter range can fill the gap and will have a very substantial impact on alloy characterization and development. Various alloy systems (e.g., Al- or Fe-based) used in a vehicle powertrain can benefit from the successful development of the current project.

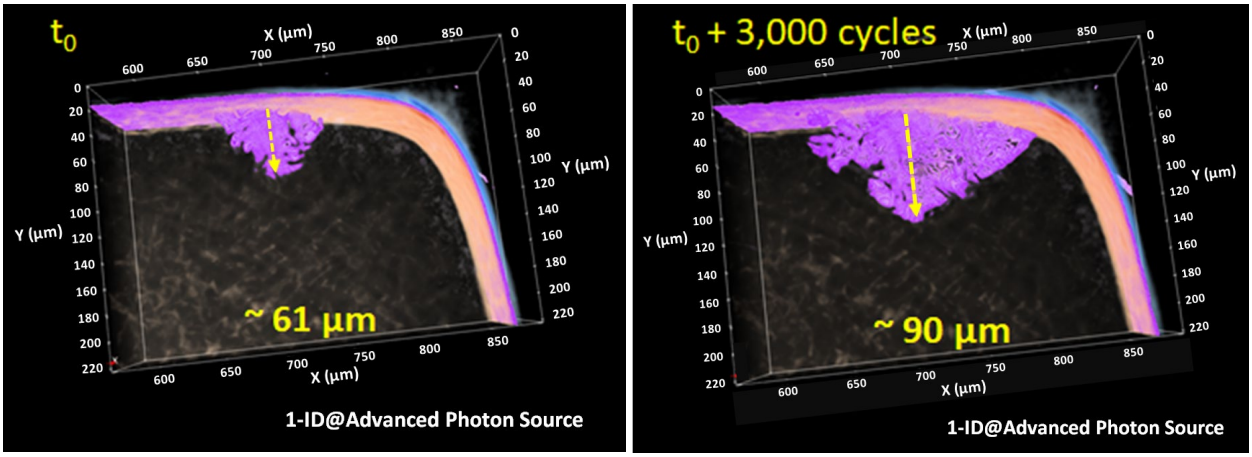

(a) (b)

Figure I.3.5.5.1. The images compare 3D morphology of a fatigue crack inside a Ti alloy where the specimen undergoes tensile cyclic loadings at ambient temperature. The 3D images were generated by X-ray tomography and show (a) the crack grows perpendicular to the loading direction, which (b) extends 30 µm after 3,000 cycles. Source: ANL.

Approach

The project intends to develop a high-temperature environmental cell that can be used in conjunction with the high-resolution full-field X-ray imaging instrument that is part of a newly constructed HEXM beam line in the APS-U Project. The imaging instrument will use 40~120 keV synchrotron X-rays to provide the real-time zoom-in and zoom-out capability to study materials at different length scales (e.g., from millimeter to sub-micron). The spatial diffraction limit for the imaging system is expected to be 100 nm at the sample. The instrument can zoom-out to characterize the material with up to a 4-mm large field-of-view and a resolution of ~2 µm. After identifying the region of interest, the instrument can zoom-in to study detailed features with resolution down to ~100 nm.

In FY 2019, a heating device was developed that utilized induction technology to achieve a heating/cooling rate of 25°C/sec. The system has a closed-loop temperature controller to precisely control the temperature within ± 3°C at 1200°C. To continue development of the characterization capability, we propose to integrate a small load frame to the system to study the material under thermal-mechanical load, as shown in Figure I.3.5.5.2. The proposed load frame can perform uniaxial tension, compression, and fatigue of millimeter-size specimens suitable for a high-energy X-ray experiment and is also portable and can be used among different beamlines/facilities. The capability can simulate the thermal-mechanical environment, similar to those in the hot-section of an engine block.

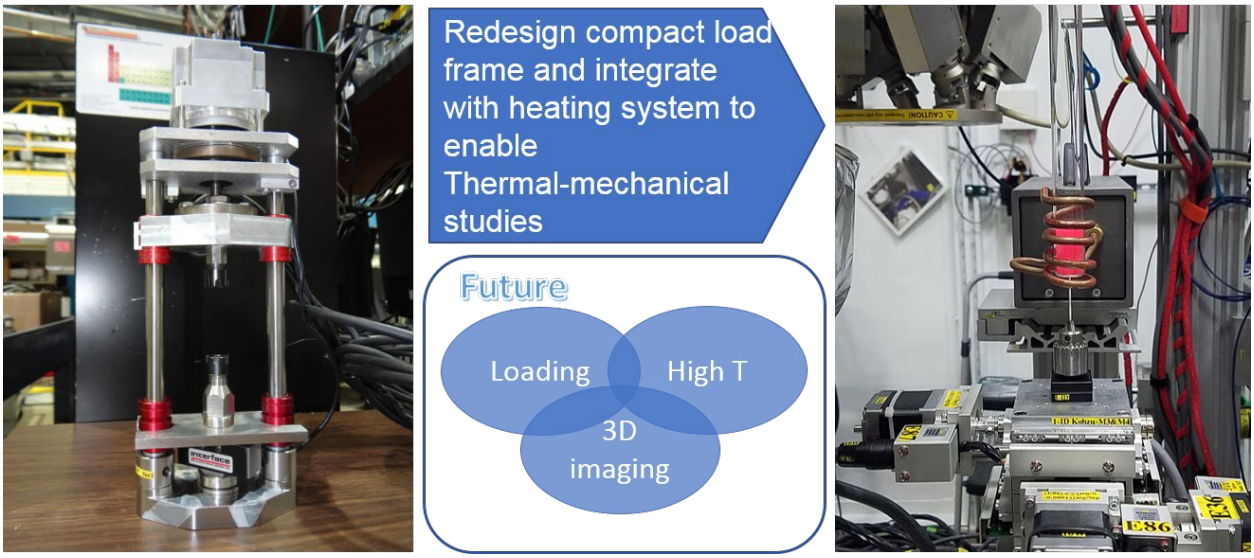

Figure I.3.5.5.2. Integration of a small, portable load frame into a system to study material under thermal-mechanical load that can perform uniaxial tension, compression, and fatigue of a millimeter-size specimen suitable for high-energy X-ray experiments among different beamlines/facilities. Source: ANL.

Results

In FY 2019, we successfully developed the heating apparatus that has the heating/cooling rate of up to 25°C ~30°C/sec with a proportional–integral–derivative close-loop temperature control. The temperature can be controlled precisely to ± 3°C at 1200°C. The second generation design, as shown in Figure I.3.5.5.3(a), was used in a pilot experiment at the end of 2019 to study steel at an elevated temperature. A high-energy tomography experiment was conducted at 900°C with ~1.2 µm/pixel image resolution. The image quality shown in Figure I.3.5.5.3(b) is comparable to the regular RT measurement.

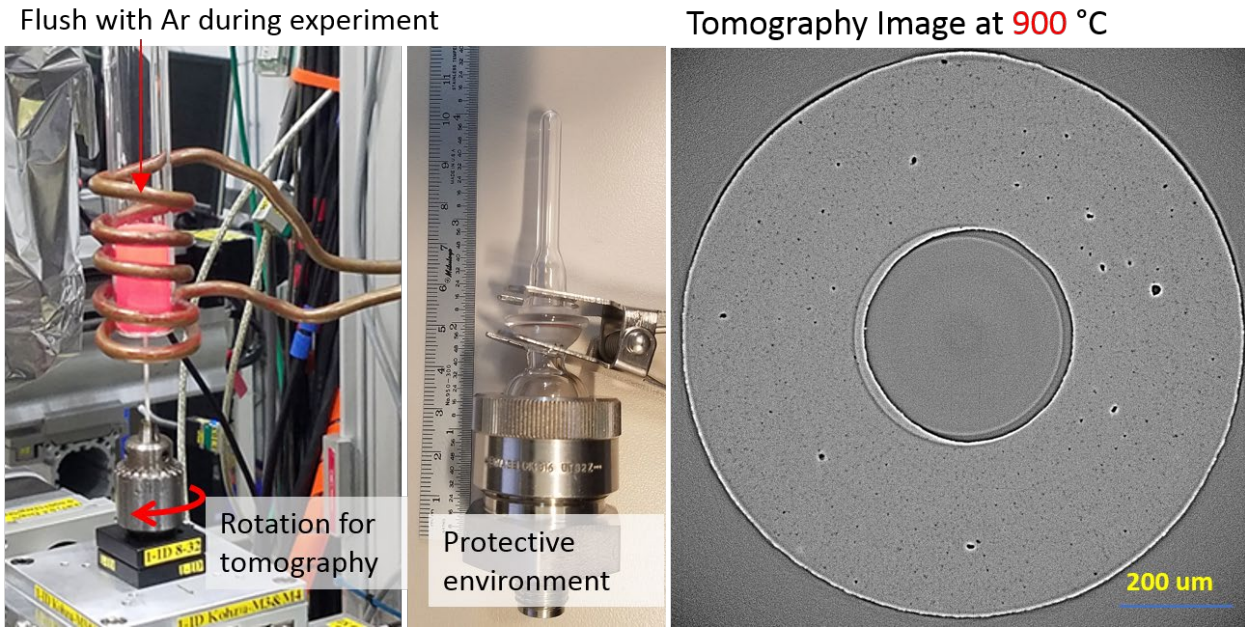

(a) (b)

Figure I.3.5.5.3. (a) X-ray imaging experiment at elevated temperature showing the environmental cell used to protect the specimen from oxidation. (b) Tomography image collected at 900 °C. Source: ANL.

In FY 2020, we planned to integrate the heating mechanism developed in FY 2019 with a compact load frame system to enable a thermal-mechanical experiment. The tasks consist of modifying the existing equipment by: (1) enlarging the post-spacing and length of the post; and (2) evaluating the feasibility of an in-grip rotation system to rotate the specimen. The initial estimated cost of modification is within the scope of the budget. Due to the pandemic situation that shut down ANL since March 2020, the laboratory is only operating under limited-operation mode, where only essential operation is permitted. These tasks were delayed due to the limited access to the laboratory facilities. We continued to work with the vendors to finalize the modification and started the procurement process at the end of 2020.

Conclusions

We have successfully developed the heating apparatus that has the heating/cooling rate of 25 ~ 30°C/sec with a proportional–integral–derivative close-loop temperature control. The temperature can be controlled precisely at 1000 ~ 1200°C range. High-temperature tomography has been demonstrated at 900°C with comparable image quality to the RT measurement. The integration of heating apparatus and compact load frame is underway.

Key Publications

1. Chuang, A., and P. Kenesei, 2020, “High-temperature cell for high-energy X-ray imaging applications,” (in preparation).

Acknowledgements

The author would like to acknowledge the members of the APS Material Physics and Engineering Group in the X-ray Science Division at ANL for their assistance during the development of this device. The author also thanks Dr. Dileep Singh of the Applied Materials Division at ANL for his fruitful discussion and guidance during the project. This project used APS resources at ANL, a DOE Office of Science User Facility operated for the DOE Office of Science by ANL under Contract No. DE-AC02-06CH11357.

I.4 Lightweight High-Efficiency Engines for Medium-Duty Vehicles

I.4.1 Next-Generation High-Efficiency Boosted Engine Development (Ford Research and Advanced Engineering)

Michael Shelby, Principal Investigator
Ford Motor Company
Research and Innovation Center
2101 Village Road
Dearborn, MI 48121
E-mail: mshelby@ford.com

Jerry L. Gibbs, DOE Technology Manager
U.S. Department of Energy
E-mail: jerry.gibbs@ee.doe.gov

Start Date: October 1, 2019 End Date: December 31, 2022
Project Funding: $10,000,000 DOE share: $7,566,730 Non-DOE share: $2,433,270

Project Introduction

The next-generation high-efficiency engine development project is a 39-month DOE-EERE VTO-funded R&D project that combines advanced combustion system technologies, thermal management strategies, and advanced materials to demonstrate a boosted gasoline engine with peak efficiency exceeding the best of today's hybrid engines, as shown in Figure I.4.1.1. While the market share of battery electric vehicles is increasing, most LD vehicles are projected to contain conventional or hybrid internal combustion engines well beyond 2030. Improvements in engine efficiency and reductions in powertrain weight have strong leverage to reduce vehicle related CO_2 emissions for decades to come. This project develops engine efficiency and weight-saving technologies that enable competitive, profitable internal combustion engines, targeting the highest production volume powertrains.

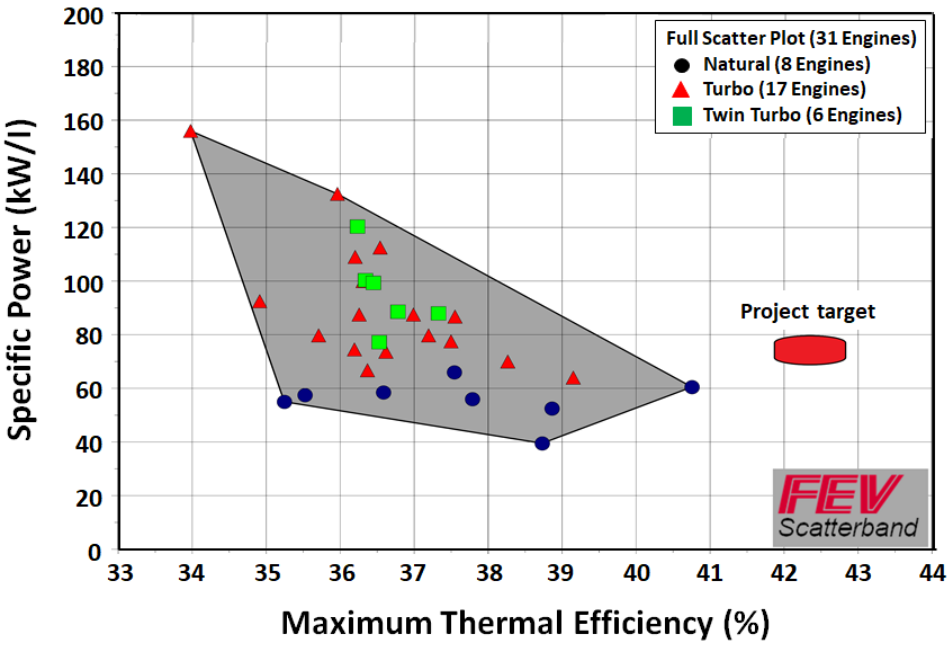

Figure I.4.1.1. Specific power vs. maximum efficiency. Source: FEV, Ford.

The project team consists of Ford Motor Company, FEV North America, and ORNL. Each partner brings different strengths to this collaboration, and the combined knowledge in powertrain, combustion, component design, analytical development, and AM will ensure a successful project.

Objectives

The objective of this project is to develop an engine with advanced combustion technologies capable of achieving ≥ 23% fuel efficiency improvement relative to a baseline 2016-model-year 3.5L V6 EcoBoost F150. The engine will be compliant with applicable U.S. Environmental Protection Agency emissions standards and the fuel economy improvement will be demonstrated via engine dynamometer testing coupled to vehicle drive-cycle simulations. Advanced materials and weight-saving technologies will also be used to demonstrate the capability of ≥ 15% weight reduction of the baseline engine. These targets are particularly challenging given that the baseline engine is already a lightweight downsized boosted engine.

FY 2020 concept design and analysis objectives are as follows:

- Develop initial requirements and assumptions for each engine system based on the overall project goals
- Build a combustion computational fluid dynamics model to evaluate combustion concepts
- Develop several concepts, including two combustion systems, coatings, advanced cooling systems, and other technologies
- Design and build a single-cylinder engine.

Approach

To achieve the goals of the project, work will be divided into several overlapping workstreams as illustrated in Figure I.4.1.2. The technology selection process will be strongly guided by analytical tools, including three-dimensional (3D) flow and combustion modeling, as well as structural and thermal analysis. Key items related to engine efficiency, outlined in the blue dotted circles of Figure I.4.1.2, will be demonstrated and developed using single-cylinder research engines. The final status of the fuel economy and weight targets will be demonstrated via dynamometer testing of a complete multicylinder engine, circled in yellow on the figure, along with regulatory drive-cycle simulations.

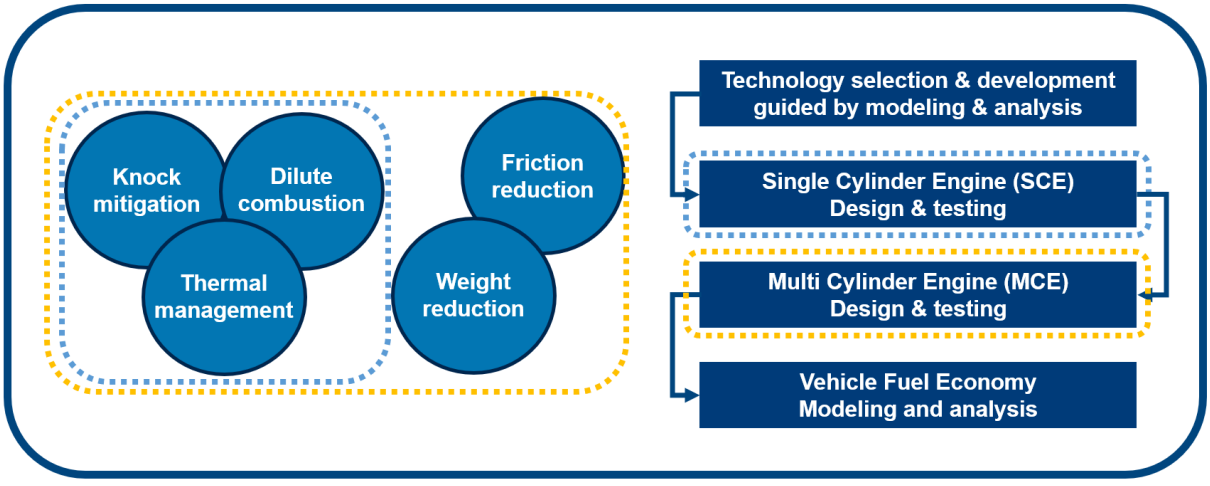

Figure I.4.1.2. The project development approach and work streams. Source: Ford.

This report will emphasize the materials aspects of the project. A second report has been prepared for the Advanced Engine and Fuel Technologies annual report focusing on the combustion and efficiency portions of the project.

Results

Work during this reporting period has been focused in three areas: (1) modeling of the combustion system for improved dilution tolerance and knock mitigation; (2) designing and manufacturing of two single-cylinder engines intended to demonstrate the capabilities of the combustion system; and (3) designing long lead components and major subsystems of the multicylinder engine.

In the course of these efforts, material selection and advanced manufacturing techniques have played a key role in solving the following four design challenges: (1) how to reduce the mass and improve the function of the cylinder head, (2) how to design a prechamber ignition system with limited package space and challenging loading and thermal BCs, (3) whether low-thermal inertial coatings can be used to improve thermal efficiency while avoiding a knock penalty, and (4) whether composites can be used to reduce the oil pan mass and provide rapid low-cost prototype parts. The body of this report contains one section discussing each of these four questions.

Weight Savings and Functional Improvements via Additive Manufacturing of Cylinder Head Cores

A conventional Al cylinder head casting, shown in Figure I.4.1.3, is made from an assembly of 11 complex sand cores: (1) intake port; (2) exhaust port; (3) upper water jacket; (4) lower water jacket; (5) top; (6) chamber (bottom); (7) oil drain; (8) intake side; (9) exhaust side; (10) front; and (11) rear. These sand cores, as shown in Figure I.4.1.4, require parting lines, draft angles, and minimum thickness. AM enables the cylinder head designer to eliminate these design constraints facilitating weight reductions and functional improvements.

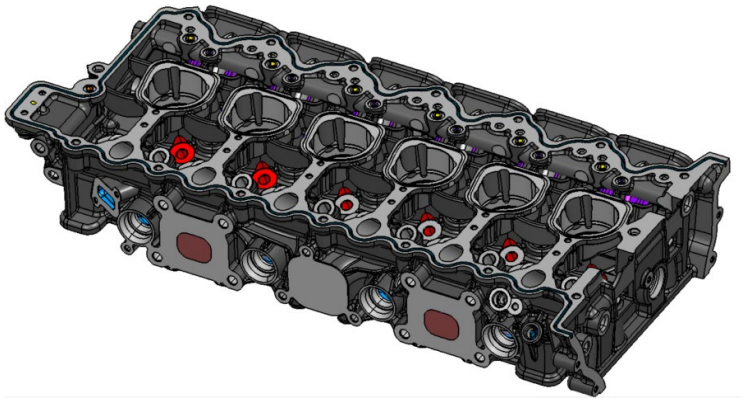

Figure I.4.1.3. Cylinder head made of AS7GU-T64-Al. Source: Ford.

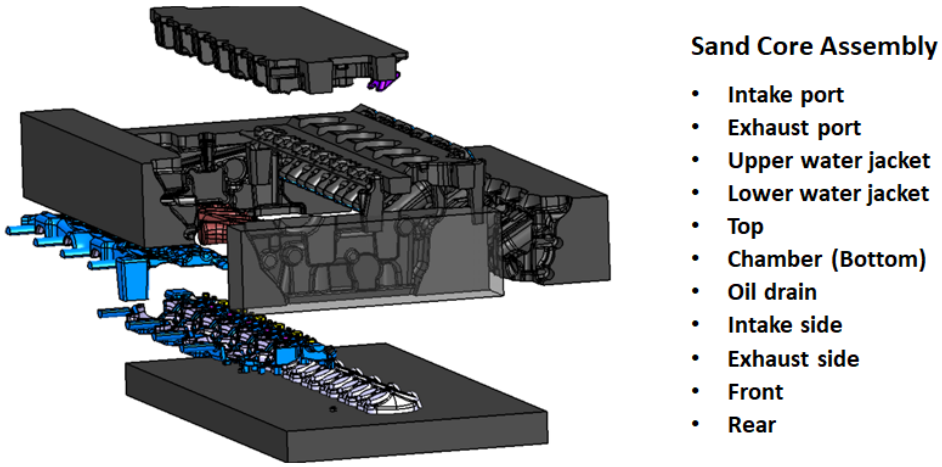

Figure I.4.1.4. Cylinder head sand core assembly showing the 11 sand cores. Source: Ford.

Conventionally manufactured cylinder head water jacket cores require draft angles of three degrees, as can be seen in Figure I.4.1.5. The draft angle is necessary to form a parting line for the top and bottom of the pattern tools. This often results in undesirable sharp edges and thicker cross-sections. The printed cores do not require draft angles to form a parting line. As a result, improved fillets and reduced cross-sections can be achieved.

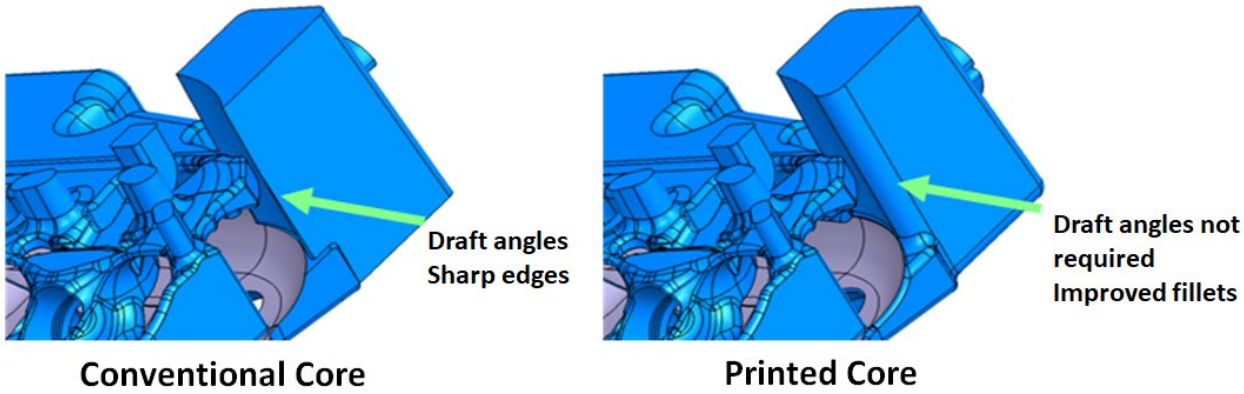

Figure I.4.1.5. Cylinder head water jacket for a conventional core and a printed core. Source: Ford.

Similarly, the cylinder head side cores (e.g., top, bottom, oil drain, intake side, exhaust side, front, rear) require draft angles of three degrees, as observed in Figure I.4.1.6. The printed cores enable the backside of features, such as bosses and flanges, to be "cored-out," resulting in reduced wall thickness and mass.

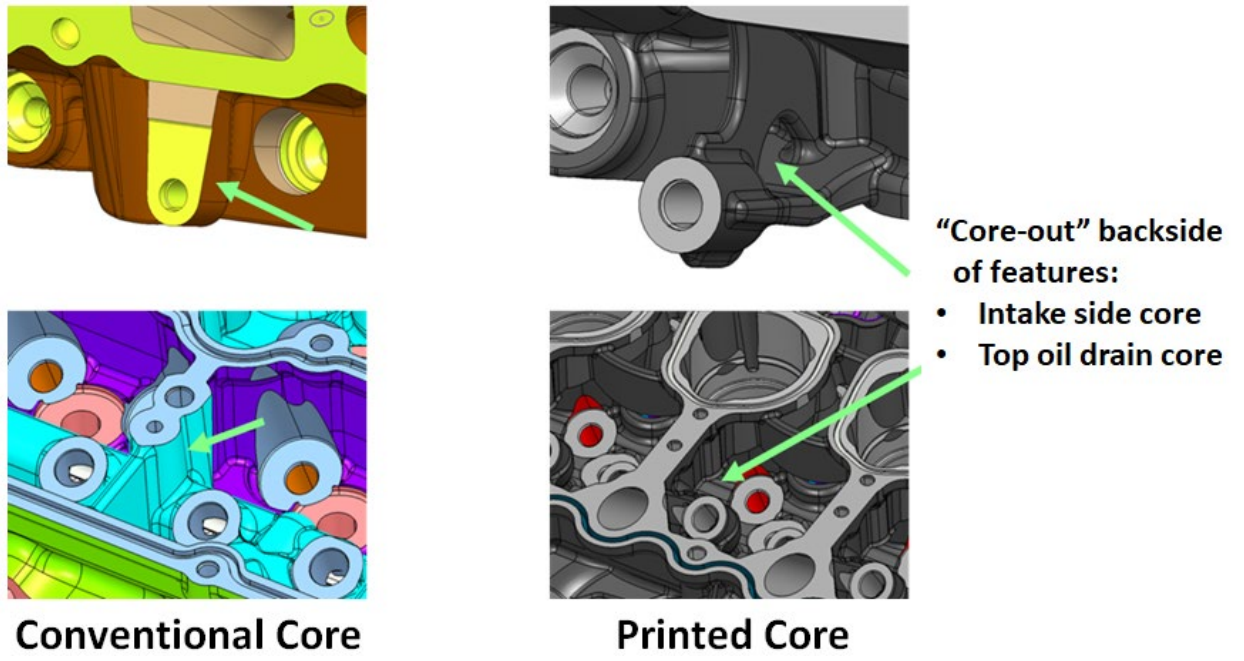

Figure I.4.1.6. Cylinder head side cores. Source: Ford.

Another potential key benefit for the application of printed cores is core consolidation, as can be seen in Figure I.4.1.7. The cylinder head manufacturing team will investigate consolidation of the lower and upper water jackets and exhaust port cores. The objective of this study is to reduce part complexity and assembly cost while increasing quality and robustness.

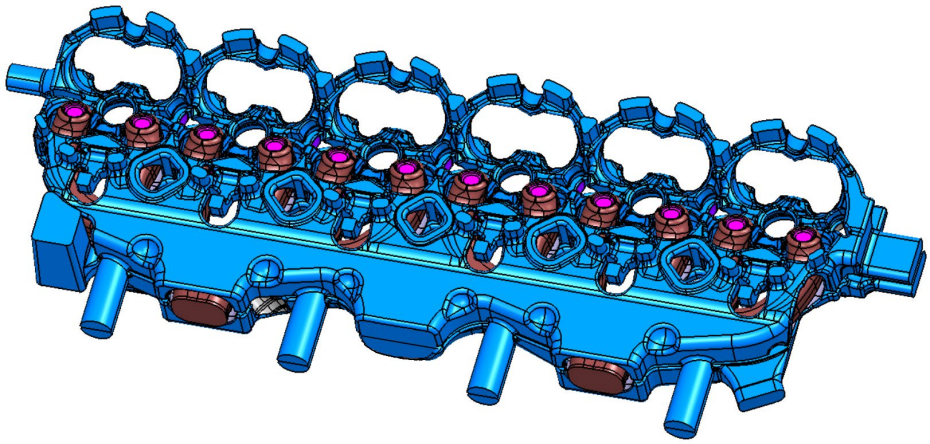

Figure I.4.1.7. Core consolidation of the lower water jacket, the upper water jacket, and exhaust ports. Source: Ford.

Last, the cylinder head printed cores will enable functional improvement opportunities by a better thermally managed cylinder head. By using printed cores instead of conventionally manufactured ones, the draft angle and parting lines are not required around the secondary spark plug positioned between the exhaust valves as shown in Figure I.4.1.8. As a result, the cross-sectional area for coolant flow in the critical exhaust bridges was increased by 34%.

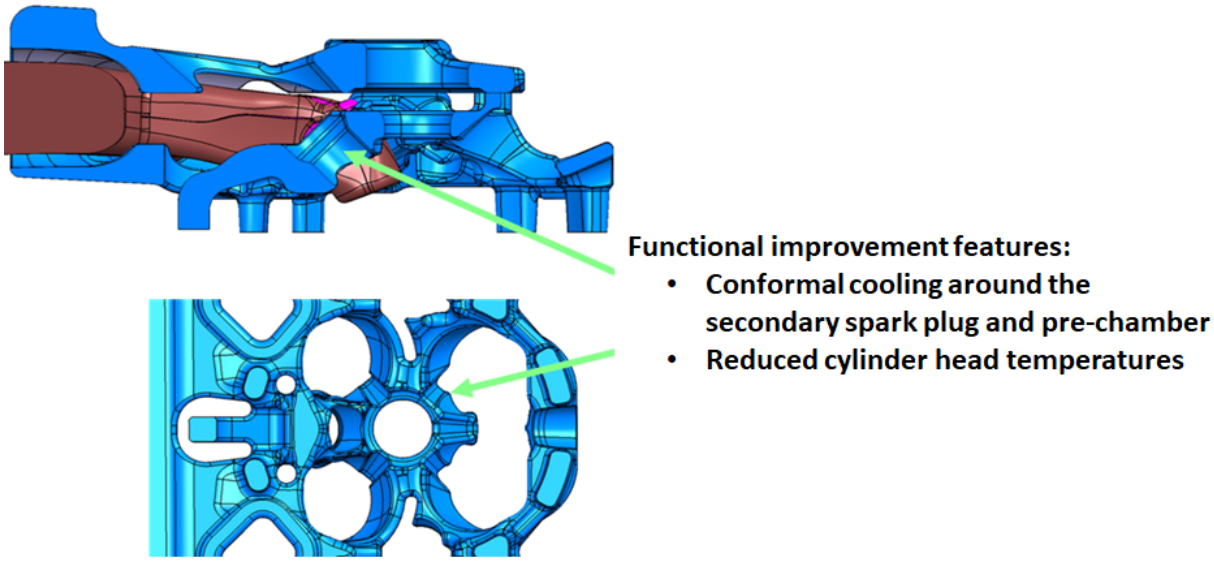

Figure I.4.1.8. Secondary spark plug and prechamber cooling improvements. Source: Ford.

In summary, AM cores in place of conventional cores has the following benefits:

- Reduced weight (~5%)
- Eliminated draft angles and parting lines
- Consolidated casting cores (reduced complexity/cost)
- Functional improvement (reduced knock at stoichiometric air-to-fuel ratios)
- Improved targeted cooling (conformal)
- Reduced cylinder head temperatures.

Material Considerations for Design of a Prechamber Ignition System

To meet the challenging engine efficiency target, an active prechamber ignition system was selected for this engine. This type of ignition system places a small combustion volume separate from the main combustion chamber. Air and fuel injectors are installed into this small chamber so that the residual mass fraction can be controlled separately from the main chamber. This allows an easily ignited mixture to be burned in the prechamber, sending hot reactive jets of gas into the main chamber. These act as a distributed, high-energy ignition source for the main combustion chamber, facilitating efficient dilute combustion.

An active prechamber ignition system presents several challenges. An additional spark plug, fuel injector, and air injector must be packaged into the already crowded center of the cylinder head. The prechamber is also subject to cyclical high pressures and temperatures that present material selection challenges.

To address the packaging challenges, our team has elected to produce the prechamber ignition system body with an AM process. This facilitates complex geometric features that enable improved packaging and function. The materials available for AM are expanding but remain more limited than conventional manufacturing processes. Both the prechamber insert and clamp were printed at the Ford Advanced Manufacturing Center using 8620 steel powder on a LPBF technology metal 3D printing machine, as observed in Figure I.4.1.9. Final machining will be completed at the Ford Research and Innovation Center machine shop. This material was selected for its mechanical strength at elevated temperatures.

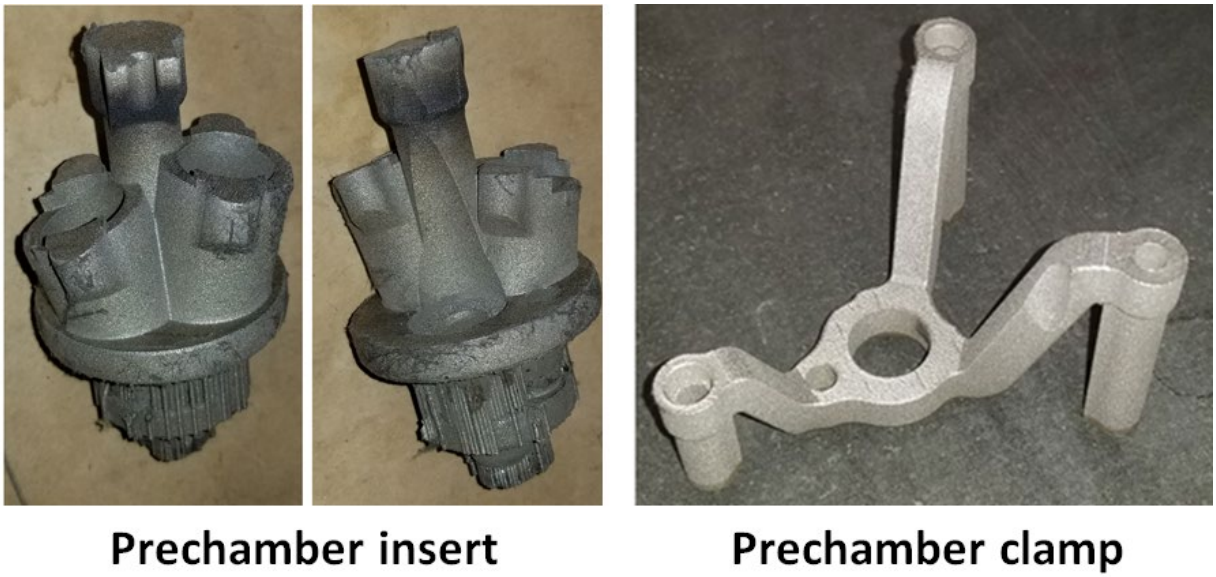

Figure I.4.1.9. Printed prechamber insert and clamp. Source: Ford.

Additional 45-degree angled structural supports to the upper prechamber insert overhangs, required during printing, will be removed before final machining as can be seen in Figure I.4.1.10. The prechamber nozzle will be machined from 16Mo3 tool steel, which offers very good strength and wear-resistance at elevated temperatures.

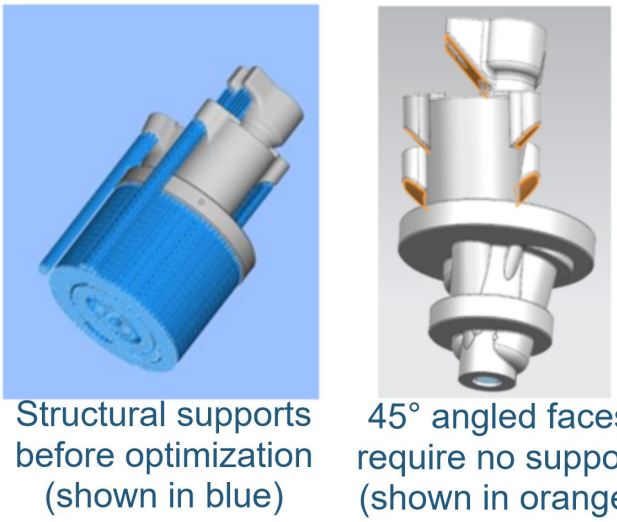

Figure I.4.1.10. Prechamber printing structural supports. Source: Ford, FEV.

Evaluation of a Low-Thermal Inertia Thermal Barrier Coating

Thermal "swing coatings" were investigated because of their potential to reduce heat losses from the combustion chamber without degrading knock performance. Typical thermal barrier coatings present a hotter surface to the combustion gases to reduce heat losses, but the hotter surface also transfers more heat to the charge during the intake and compression strokes, leading to an increased tendency to knock. A coating with a very low heat capacity can follow the charge temperature throughout the cycle, providing reduced heat losses in the expansion stroke without excess heating during intake. Such coatings typically have very high porosity.

A piston and set of valves shown in Figure I.4.1.11 were coated by Adiabatics in the fourth quarter of 2019 and were tested on a surrogate single-cylinder engine to evaluate the impact on heat losses and knock. Published literature [1] describes the Adiabatics coatings as hollow aluminosilicate particles held in a binder of either organic polysilazane or metal phosphate.

Steady state fuel consumption testing conducted on both coated and uncoated hardware showed a relative improvement in indicated thermal efficiency (ITE) of around 0.7% at a light load, and decreasing to -1.9% at a high load.

Figure I.4.1.11. Coated piston and valve hardware before testing. Source: Ford.

A breakdown of the fuel consumption differences using correlations to other measured data showed that small penalties (~0.1%) were seen due to CO emissions, burn duration, and dilution. Considering the variability between operating conditions, these are likely not statistically significant. There was also a modest penalty (0.24%) due to increased hydrocarbon emissions. This represents a 10–20% increase in hydrocarbon emissions, which is similar to results reported in the literature for similar coatings. This is often attributed to surface roughness or open porosity in the coating. Finally, the high loads showed relative losses of up to 2.0% due to combustion phasing from knock.

There was no independent measurement of the impact of reduced heat losses. However, the difference between measured ITE increase and the sum of the breakdown of the fuel consumption components should have mostly represented any heat losses. Any errors in measurements or changes in compression ratio also could show up in this difference. Assuming this represents the heat losses, the results showed that, throughout the load sweep, the change in ITE due to heat losses ranged from -0.6 to +2.0%, with an average of +1.0%.

Knock-limited data, from load and speed sweeps, showed CA50 retarded by 0.7–4.1 crank angle degrees with the coated parts, with an average of 2.2 crank angle degrees. Correcting for this level of increased knock tendency with compression ratio (CR) would require a reduction of roughly 0.5 ratio. This change would offset even the best estimate of efficiency gain due to the coating.

In effect, the coated engine was acting like it had a 0.5 higher CR. This result prompted a question as to whether the CR for the coated parts was incorrect. If the thickness of the coating was delivered as specified, it would increase the CR by less than 0.2 points. This was partially corrected for by adjusting the deck height of the engine to match the squish height between the piston and the head of the baseline engine. The actual CR of the engine was not measured due to concerns that the oil used to measure the volume would negatively impact the coating. An additional check on CR was performed by comparing compression strokes in motoring cycles. These compression trends suggest a negligible difference in CR.

A cursory inspection of the coated parts showed the coating to be intact after the testing was completed, demonstrating the basic durability of the coating, as shown in Figure I.4.1.12. The coated valves showed discoloration, but no significant deposits. The piston, however, showed significant, but fairly typical deposits. For comparison, the uncoated cylinder head had deposits in only some places. Further analysis of the deposit and coating thicknesses is planned.

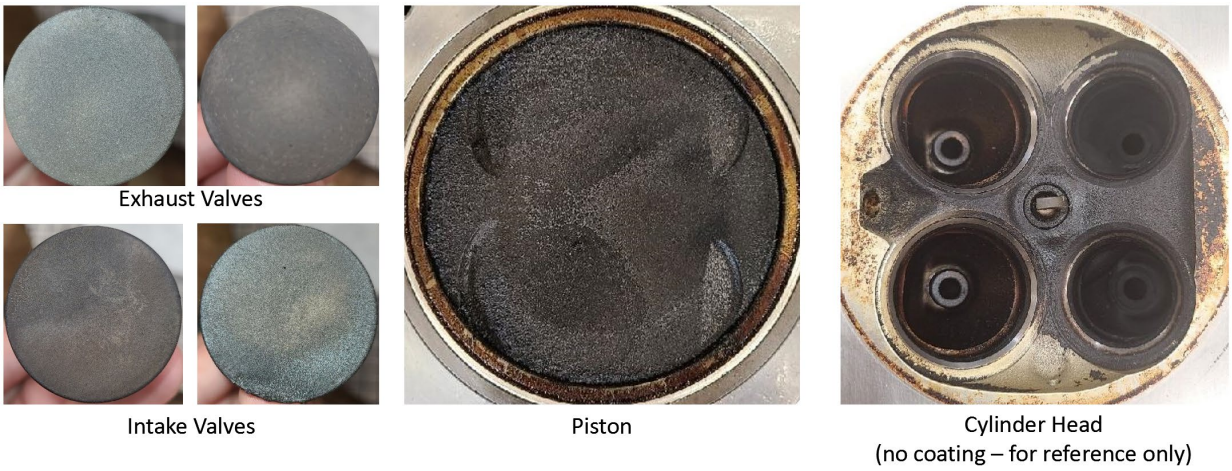

Figure I.4.1.12. Coated hardware after testing. Source: Ford.

The current plan is not to pursue this coating on the single-cylinder engine hardware because of the knock penalty. Whether this, or a similar coating would be beneficial in select parts of the combustion chamber, or other engine surfaces, is under consideration.

Composite Oil Pan

As a part of the weight reduction target for this project, a composite oil pan is being designed as a demonstration component. The oil pan was chosen because it has several design requirements that, if satisfied, will demonstrate suitability of the chosen material and process to other components. The pan must be lightweight, easy to manufacture, and be durable to the chemical, thermal, and mechanical BCs present on the engine. The oil pan is also long and has a deep draw, which are challenging for some manufacturing processes.

The engine oil pan is being designed assuming a composite material can be used to provide structural capabilities needed for the powertrain system and reduced mass compared to conventional materials. The single piece component, as shown in Figure I.4.1.13, is designed for an oil capacity of six quarts and a complete perimeter seal. In addition, it is a structural component of the powertrain with mounting features where the engine assembly and transmission are attached. This mounting interface enhances the stiffness of the powertrain assembly for superior NVH characteristics. A further structural feature is to provide a mounting location for the vehicle air-conditioning compressor. Providing a mounting boss directly on the pan saves weight by eliminating the need for a bracket and additional fasteners.

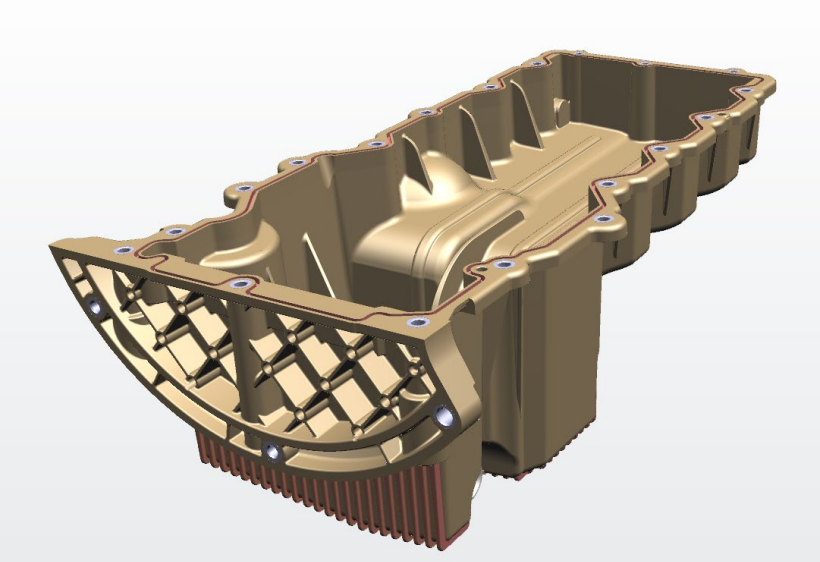

Figure I.4.1.13. Composite oil pan. Source: Ford.

Multiple molding processes were evaluated for the composite oil pan design, including injection-molding, compression molding, blow molding, and thermoforming. These processes were evaluated for tooling costs, component durability, material capability, material properties, design complexity, sealing, and material recyclability. Extrusion compression molding was chosen as the best match to meet the form, function, and weight reduction goals. It also more easily supports prototype timing and costs.

For extrusion compression molding, pellets of thermoplastic material reinforced with fibers are fed into a hopper for a low sheer extruder, which is used to plasticate the composite material into a “charge.” The charge is then transferred to a fast-acting press for the compression/consolidation process. The use of AM to fabricate the tooling will be the prime path.

The extrusion compression molding process (low sheer) combined with longer initial fiber length (10 mm pellets), will result in fibers with larger aspect ratios compared to short fiber (1-2 mm) thermoplastics used in injection-molding processes. This will result in improved mechanical performance (stiffness and strength) of the molded part. These pellets may not be available commercially; therefore, ORNL may need to make them for the project. For fabrication of these pellets, one possible source is the Institute for Advanced Composites Manufacturing Innovation and Michigan State University Scale-up Research Facility in Michigan. CF will be used as a reinforcement with (30–40% weight percent) in a thermoplastic matrix of polyamide "nylon." Material supplier partners will be contacted to explore the availability of the compounded material and narrow the selection of the polyamide (i.e., PA-6, PA-66, etc.). ORNL has long-standing relationships with multiple material suppliers, such as Plasticomp, Celanese, BASF, and Mitsubishi Chemicals.

Another possibility is to use Solvay's Amodel® polyphthalamide, which has a heat-deflection temperature of 282°C. This product is good for the application but will require a metal tool, which can also be fabricated using AM. A glass and CF hybrid will be investigated, but the hybrid is a short fiber thermoplastic. To obtain long fiber reinforcement, Solvay recommends coupling this bulk material with their Evolite composite tape. The tape comprises unidirectional fiber (either glass or carbon) in the same polyphthalamide matrix. These tapes could be strategically placed into the tool during molding to provide efficient stiffening and strengthening of critical areas in the oil pan. The determination of the geometry of the tapes and their placement locations would be made from the design optimization.

The goal is to have at least three-degree draft angles to enable separation of the pan from the tool after molding. It may be possible to include inserts in the molding process; however, they will likely be pressed in post-molding.

Conclusions

Simultaneously meeting the fuel economy and weight targets of this project presents several materials-related challenges. In the first year of this project, we have reduced the mass of the cylinder head using innovative casting and manufacturing techniques. Advanced materials and manufacturing techniques have been applied to solve thermomechanical and packaging issues related to the prechamber ignition system. A low-thermal-capacity thermal barrier coating has been explored analytically and experimentally to quantify the impact on engine thermal efficiency and knock tendency. Finally, a rapid-prototype compression-molded oil pan has been designed to meet functional, structural, and weight targets. These efforts directly support the single-cylinder engine and multicylinder engine development tasks of the project.

References

1. Andrie, M., S. Kokjohn, S. Paliwal, L. S. Kamo, *et al.*, 2019, "Low heat capacitance thermal barrier coatings for internal combustion engines," SAE Technical Paper 2019-01-0228, Warrendale, PA, USA.

Acknowledgements

The author would like to thank our partners at FEV North America (led by M. Case) and ORNL (led by B. Knouff) for their collaboration and support, as well as our National Energy Technology Project Manager, R. Nine, for his continued guidance.

I.4.2 Low-Mass and High-Efficiency Engine for Medium-Duty Truck Applications (General Motors)

Qigui Wang, Co-Principal Investigator
General Motors, LLC.
30003 Fisher Brothers Road
Warren, MI 48093
E-mail: qigui.wang@gm.com

Ed Keating, Co-Principal Investigator
General Motors, LLC.
28755 Louis Chevrolet Road
Warren, MI 48093
E-mail: ed.keating@gm.com

Jerry L. Gibbs, DOE Technology Manager
U.S. Department of Energy
E-mail: jerry.gibbs@ee.doe.gov

Start Date: October 1, 2019 End Date: December 31, 2023
Project Funding: $2,384,143 DOE share: $1,847,314 Non-DOE share: $536,829

Project Introduction

Today's transportation vehicle customers demand that manufacturers produce engines with lower weight and improved efficiency to reduce fuel consumption, emissions, and costs associated with vehicle use, while maintaining or even increasing engine performance. Developing the next-generation of high-efficiency, very-low-emission internal combustion engines requires a combination of new combustion strategies, advanced materials, and new materials processing techniques to further increase engine efficiency and reduce weight. The expected national economic, environmental, and energy security benefits of these next-generation engines and materials would be significant because most vehicles sold over the next two decades will still include an internal combustion engine. The availability of advanced lightweight engine designs will provide a significant positive impact on the fuel efficiency, environmental impact, and competitiveness of the U.S. auto industry [1].

Objectives

The objective of this collaborative project between GM, ORNL, The Ohio State University (OSU), Michigan Technological University (MTU), and Eck Industries, Inc. (Eck), is to develop an advanced MD truck engine equipped with advanced materials and combustion technologies capable of ≥ 10% fuel efficiency improvement and approaches capable of ≥ 15% engine-weight reduction when compared to the 2015 GM L96 VORTEC 6.0L V8 Port Fuel Injected engine, compliant with applicable U.S. Environmental Protection Agency emission standards with performance demonstrated via simulation coupled with engine dynamometer tests.

Approach

This project is proposed as a large-scale engine design and demonstration enabled by an advanced materials and manufacturing development program, with a comprehensive plan spanning a period of four years. The project begins with engine architecture design and analysis activity, advanced materials and manufacturing process development, and downselection. It culminates in an engine test cell evaluation with optimal materials and manufacturing solutions supporting final vehicle simulation. The final engine test will verify engine weight reduction and performance to the objectives of the funding opportunity announcement [1].

Several advanced combustion technologies will be investigated including stoichiometric combustion; increased CR; aggressive exhaust gas recirculation (EGR) dilution and load-point optimization with a focus on an optimal cylinder deactivation; advanced valve train phasing and lift strategies; advanced fuel system strategies including "ultra" high-pressure direct injection (DI); advanced ignition systems including prechamber spark plug; advanced EGR dilution systems including electric-EGR (E-EGR); Atkinson or Miller cycle strategies; variable induction system strategies; and combustion chamber cooling strategies.

In this project, high-strength and heat-resistant materials will be developed and incorporated with novel metal casting and AM processes to produce highly durable engine structures to maximize performance of the materials and systems with minimum mass and cost. The opportunity to include advanced materials and manufacturing in conjunction with high potential combustion systems and engine technologies also creates the chance to revisit the most appropriate engine specification to realize the desired efficiencies while reducing engine-weight cost-effectively. A focus will be on the most cost-effective solution to promote wide market acceptance using the right materials in the right place and right process for the right parts. Single material and multi-material solutions for key engine components, such as head and block, will be investigated to achieve weight reduction and performance requirements. Furthermore, ICME and computer-aided engineering (CAE) tools will be fully used during the entire program to accelerate both the new material and manufacturing process development and optimization, as well as the complete engine design and manufacturing [2],[3].

The project is planned for two phases over four BPs separated by distinct go/no-go decision points as follows:

- Phase 1—Technology R&D:
    - **Budget Period 1**: Identification of potential engine architecture designs and initial verification coupled with advanced technologies for combustion systems, materials and manufacturing concepts for weight-saving and performance-improvement through simulations and development.
    - **Budget Period 2:** Evaluation of proposed individual technology concepts using current equivalent architecture of GM development engines in conjunction with advanced materials and manufacturing process development of high-value weight reduction and performance improvement strategies for components and subsystems.
- Phase 2—Technology Validation and Demonstration:
    - **Budget Period 3**: Design, procure, manufacture, assemble, and perform initial developmental testing of a proposed MD truck engine capable of meeting requirements.
    - **Budget Period 4:** Demonstration of performance and weight reduction to meet requirements using engine test cell and vehicle simulations.

Results

Task 1.1. Layout and Performance Simulation of Engine Architectures (Normally Aspirated Large-Displacement and Downsized Boosted Small-Displacement Concepts)

Work during FY 2020 was focused on the evaluation of normally aspirated large-displacement and downsized boosted small-displacement engine concepts relative to the project objectives using simulation tools.

Subtask 1.1.1—Approximate overall engine displacement, cylinder size, and number of cylinders for peak efficiency at high-fuel-usage MD truck engine operating points has been determined for both engine concepts. Constraints include meeting peak-power and torque targets of the model year 2015 base engine. The baseline 2015 GM MD truck engine has been simulated using the Phase 2 Greenhouse Gas Emission Model simulation tool with results transferred to a GM internal vehicle model. The simulation results identified the top 14 points representing 95% of fuel used during the test cycle, as shown in Table I.4.2.1.

Table I.4.2.1. Operating Points Weighted by Fuel Usage

Engine Speed (rpm)	Engine Brake Torque (Nm)	Fraction of Total Fuel (%)
2000	367.6	22.08
1750	236.3	20.51
1750	472.7	18.92
1500	315.1	7.31
2000	105.0	5.02
2500	420.2	4.70
1000	420.2	4.56
2000	577.7	4.22
2200	212.7	2.22
1300	154.9	1.76
2800	577.7	1.34
1500	52.5	1.23
2000	10.5	1.09
1000	10.5	0.66

Subtask 1.1.2—A basic layout of concept engines in a current MD truck has been accomplished to understand packaging opportunities and challenges. Both engine concepts shown in Figure I.4.2.1 have been successfully packaged in the target MD truck.

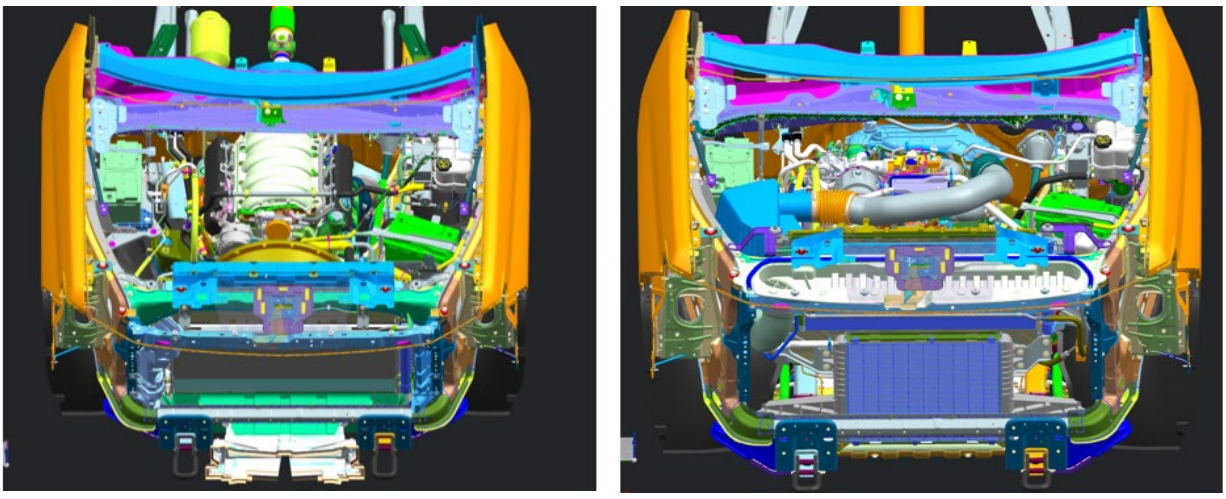

(a) (b)

Figure I.4.2.1. (a) A normally aspirated large-displacement V8 engine. (b) A downsized boosted small-displacement L6 engine packaged in the target vehicle engine compartment. Source: GM.

Subtask 1.1.3—An approximate weight and cost of an engine assembly has been determined for both engine concepts. Best opportunities for weight reduction and cost reduction were identified.

Subtask 1.1.4—Opportunities to implement a high-value combustion system technology into both engine concept layouts have been explored and design studies have been completed to package this technology into both engine concept layouts. The list of high-value combustion system technologies is shown in Figure I.4.2.2.

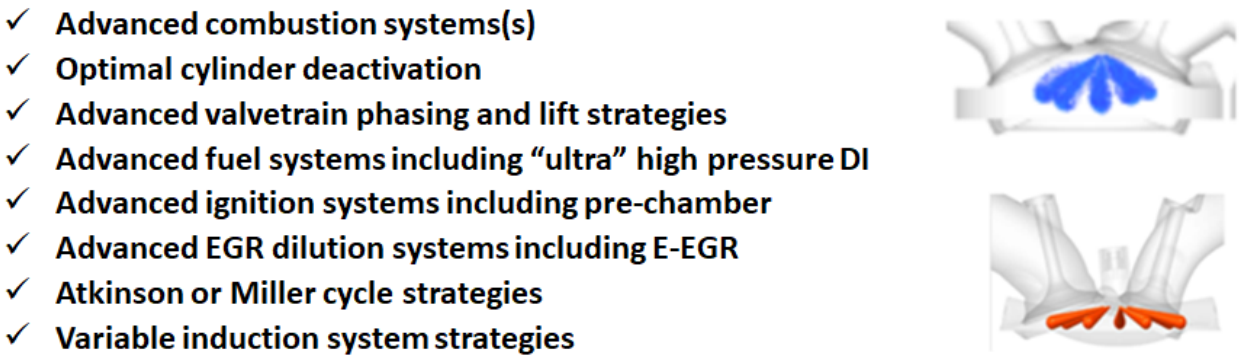

Figure I.4.2.2. High-value combustion technologies. Source: GM.

Subtask 1.1.5—One-dimensional (1D) simulation models of both engine concepts have been developed to establish initial performance predictions. These models have been correlated using results obtained from the engine testing of similar engine configurations. Basic model representations (for illustration purposes only and the content is not intended to be read) are shown in Figure I.4.2.3.

Subtask 1.1.6—The correlated 1D engine concept models have been used to execute the optimization of the boosting system (on the boosted concept), induction system, exhaust system, and valve events to investigate opportunities for improved performance at high-fuel-usage MD truck operating points and full load.

The normally aspirated large-displacement V8 engine 1D model was used to complete an engine displacement sweep to investigate best performance and fuel consumption. Engine displacements from 6.0L to 8.0L were initially investigated for performance and fuel consumption. The trend was that simulated engine fuel efficiency improved with increased engine displacement. This basic study did not account for resulting mass and size differences.

The downsized boosted small-displacement L6 engine 1D model was used to complete an engine displacement investigation for this concept to investigate the best performance and fuel consumption. A maximum downsized boosted displacement of 3.0L has been investigated. In addition, a second displacement of 3.7L that is less stressed and uses a simplified turbocharger installation was also investigated.

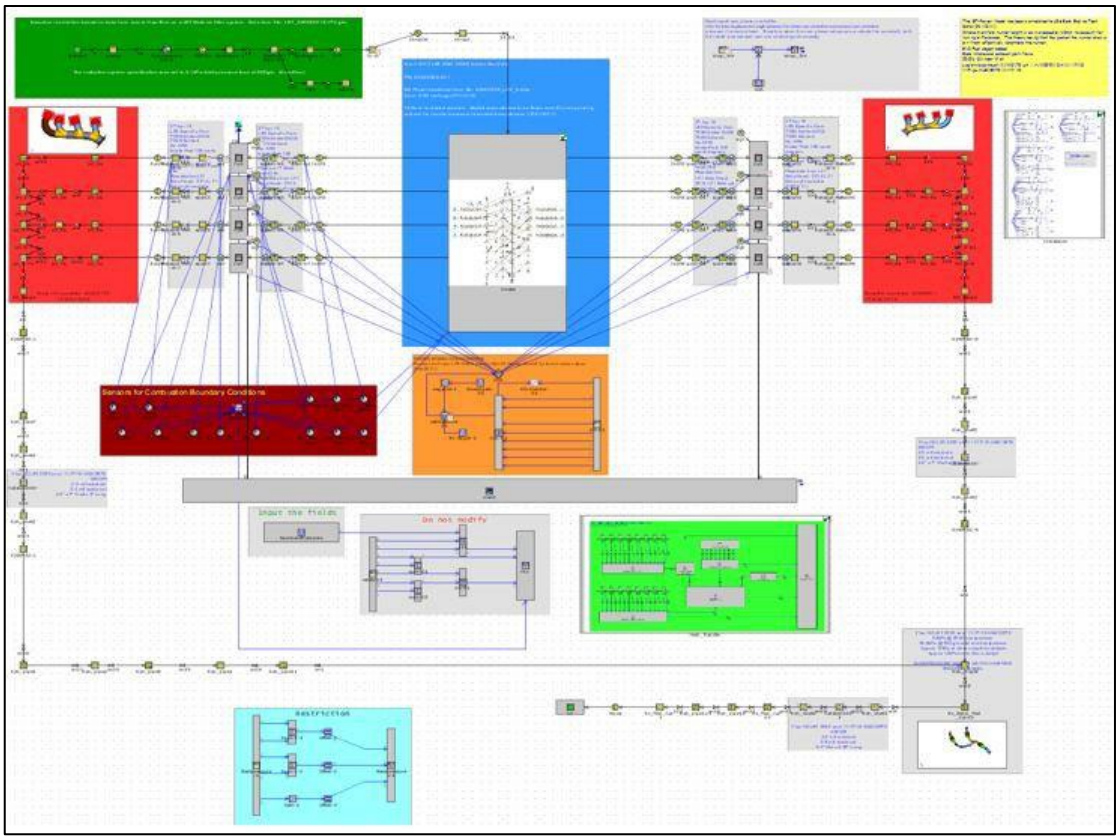

(a)

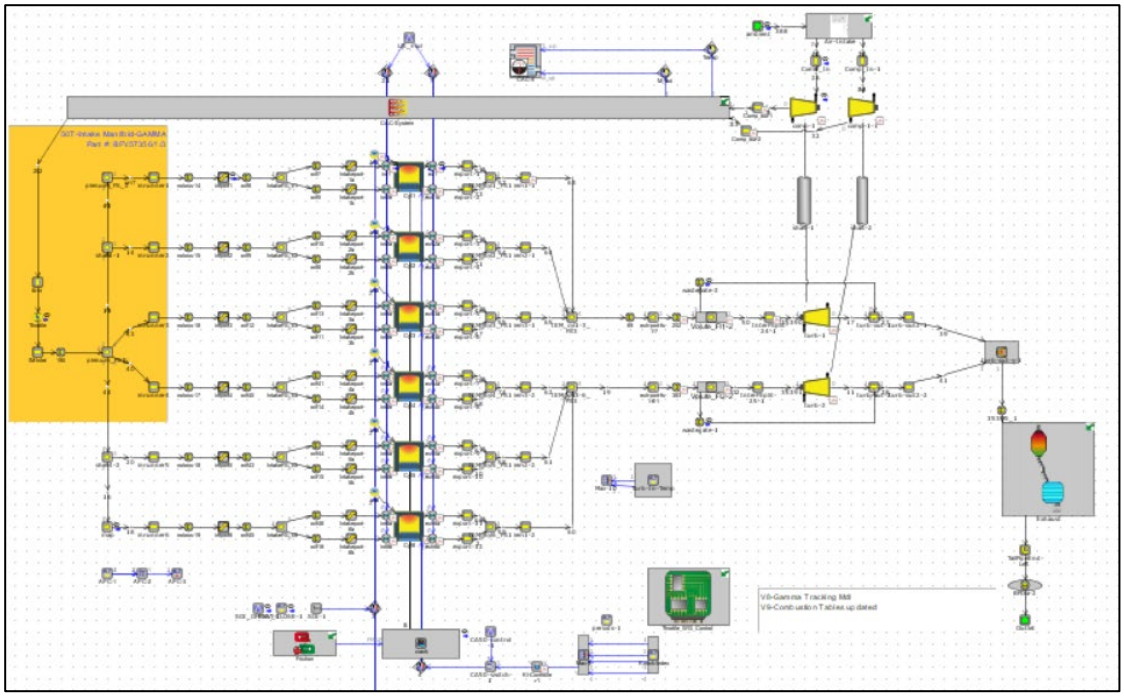

(b)

Figure I.4.2.3. 1D simulation model representations of: (a) a normally aspirated large-displacement V8 engine; and (b) a downsized boosted small-displacement L6 engine. (**FOR ILLUSTRATION PURPOSES ONLY**). Source: GM.

Subtask 1.1.7—A 3D computational fluid dynamics (CFD) analysis was employed to create and evaluate potential combustion system design and technology enhancements that will improve net-specific fuel consumption at high-fuel-usage MD truck operating points and/or full load performance. Initial 3D CFD combustion models of both engine concepts have been developed to establish a baseline and to assess opportunities for improvement. An example of the simulation results for flame propagation is shown in Figure I.4.2.4.

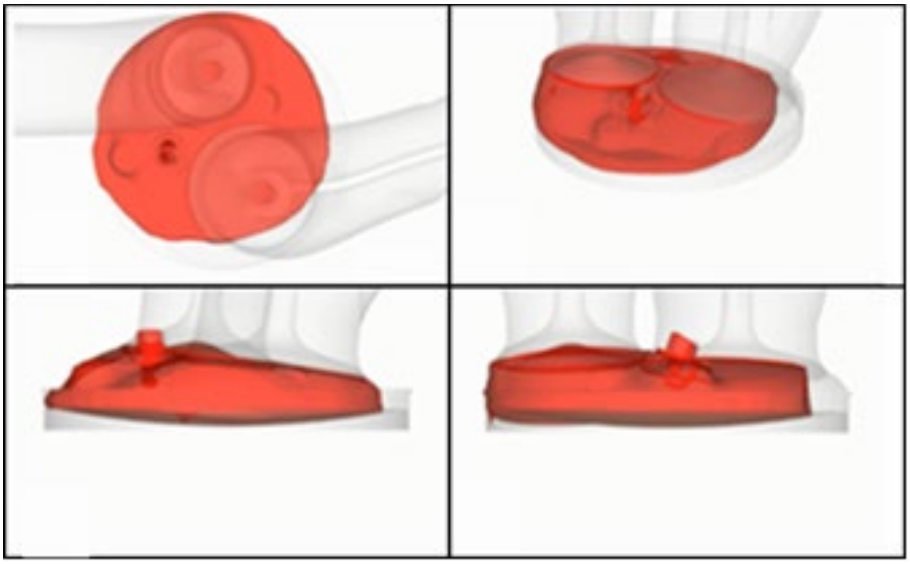

(a)

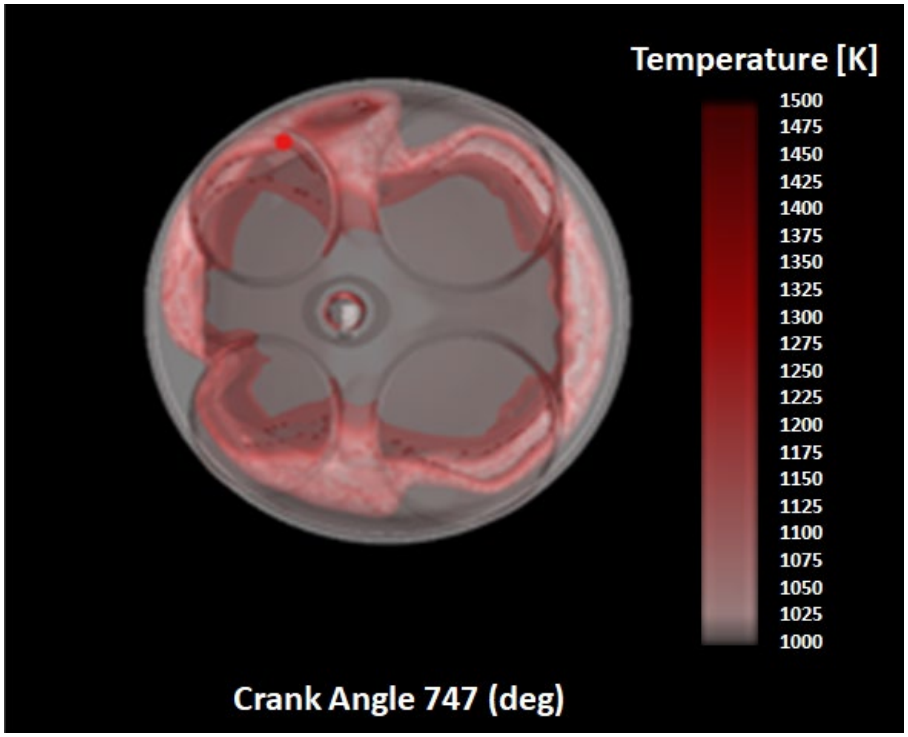

(b)

Figure I.4.2.4. A 3D CFD simulation of the flame propagation of (a) a normally aspirated large-displacement V8 engine. (b) A downsized boosted small-displacement L6 engine. Source: GM.

Task 1.2. Weight-Saving Material and Manufacturing Technology Selection and Development

Work during FY 2020 was focused on the selection and development of new materials and manufacturing solutions for key engine components identified relative to the project objectives using both simulation tools and preliminary experiments. Based on mass-saving opportunities and high engine performance requirements, several key engine components have been identified, including a cast-Al engine block, a cast-Al head, a cast-steel and nodular Fe crankshaft, and a piston fabricated with AM. Table I.4.2.2 shows the materials and manufacturing technology solutions and Figure I.4.2.5 gives the mass-saving potential opportunities for these key engine components.

Table I.4.2.2. Materials and Manufacturing Solutions for Key Engine Components

2015 VORTEC 6.0L VI PFI Engine (L96 Baseline) – HT3500		MAS Reduction and Performance Enhancement Opportunities	
Key Parts	Materials	Advanced Materials and Manufacturing	
		Option 1	Option 2
Engine block	Cast-iron	Cast high-strength high-temperature Al	Multi-materials
Cylinder head	Cast-Al	Cast high-strength high-temperature Al	Multi-materials
Crankshaft	Cast nodular iron	High-strength cast-steel	High-strength high-modulus nodular iron
Piston	Hypereutectic Al	High-strength high-temperature Al for AM	High-entropy alloys for AM
Exhaust manifold	Cast ductile iron	High-temperature cast-steel	- - - - -

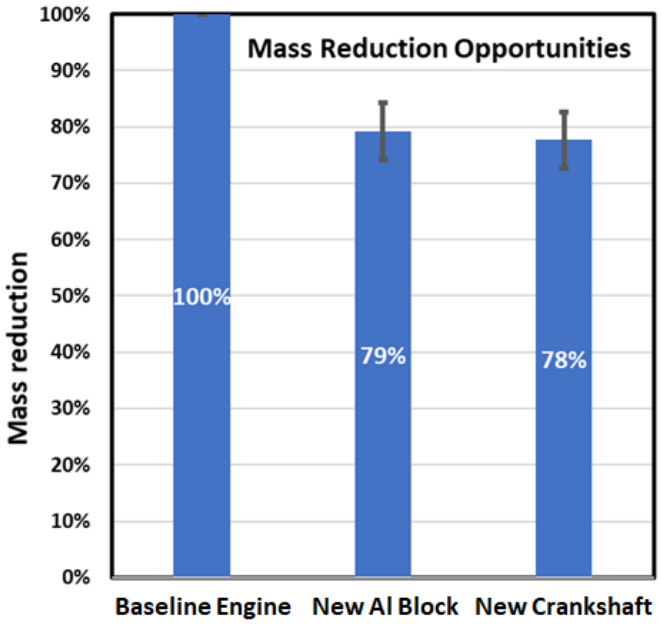

Figure I.4.2.5. Mass-saving potential for the key components. Source: GM.

Subtask 1.2.1—Mechanical and thermomechanical property requirements for key engine components. The targeted mechanical and thermomechanical property requirements have been developed for key engine components based on the required fuel efficiency improvement (i.e., at least 10% more than the 2015 baseline engine) and CAE durability analyses. Table I.4.2.3 shows an example of the targeted properties defined for the cast-Al engine block.

Table I.4.2.3. Baseline and Targeted Material Properties for the Cast-Al Engine Block

Component	Property	Baseline (GM L96 Engine)	Cost Lightweight Alloy Targets	Key Properties (must meet)
Engine Block	RT Performance	@25C (cast-iron)	@25C	---
	UTS (MPa)	265	> 280	Key
	YS (MPa)	240	> 240	Key
	Elongation (%)	0.5	> 1	---
	Density (g/cm^3)	7.2	< 3.5	Key
	Fatigue Strength (MPa)	76	100	Key
	Hot-Tearing Resistance	Excellent	Excellent	Key
	High-Temperature Performance*	@300C	@300C	---
	UTS (MPa)	222	145	Key
	YS (MPa)	200	100	Key
	Fatigue Strength (MPa)	64	48	Key

Subtask 1.2.2—Single material and multi-material solutions for head and block with CAE analysis. A study of several comparable GM cast-Al V8 cylinder heads was conducted. An equivalent architecture GM production head of an L8T engine—the successor to the project baseline engine 2015 L96 engine—was selected for new alloy and novel casting process investigation. Cast-in-place intake and exhaust valve seats have been proposed to replace press-in-place valve seats to enlarge the design space for the high-performance combustion design in the cylinder head.

Single lightweight material (e.g., cast-Al) and multi-material solutions for the engine block have been extensively explored with new designs and comprehensive CAE analyses. A single piece cast-Al block has been iteratively designed using the state-of-the-art GM CAE durability Level 2 and Level 3 analyses, as well as a damage accumulation analysis with nodal-based materials properties from the casting process simulation, as observed in Figure I.4.2.6.

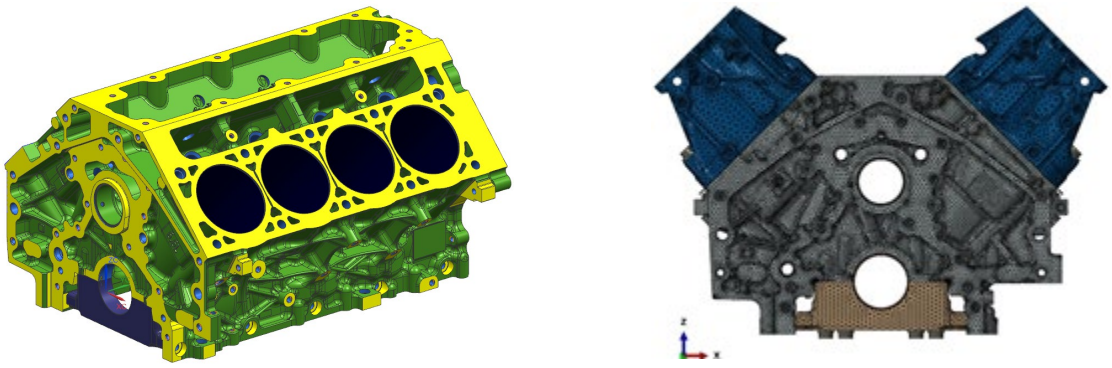

(a) (b)

Figure I.4.2.6. (a) Single piece cast-Al block design. (b) Meshed-assembled modes for CAE analysis. Source: GM.

A study of raising the camshaft bore on durability of the cast-Al block was also conducted. It was found that the safety factors of the block were improved by 10%, particularly for hot-spot areas such as bulkhead breath window high stress regions, when the camshaft bore is raised by 25 mm. This provides a design opportunity of using lightweight cast-Al alloys in MD truck engine applications. Meanwhile, the NVH analysis has been conducted with the newly designed cast-Al block and the results have also been compared with the current cast-Fe block. As expected, the cast-Al engine block has very marginally higher noise levels (~2 dBA) than an Fe block due to its reduced mass.

Multi-material options for the L8T V8 engine block have been explored to further reduce mass while maintaining the needed performance and durability. A split engine block design has been completed and is show in Figure I.4.2.7. The engine block is split from the main crank journal centerline. The upper portion is cast-Al and the lower portion is a combination of Fe main-cap inserts overcast with Mg or Fe main-cap inserts molded over with polymer. A complete CAE durability and damage accumulation analysis was used to determine the best combination of the multi-material split block.

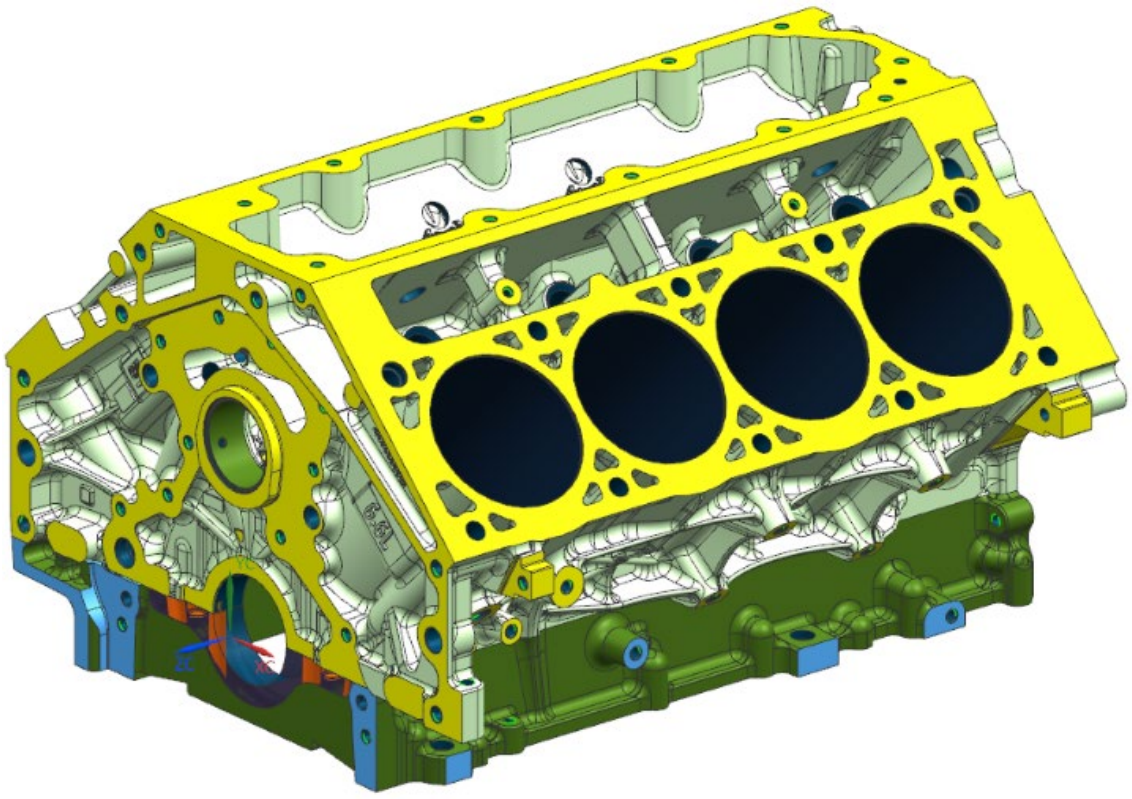

Figure I.4.2.7. A new split engine block design of cast-Al (upper portion) and a combination of Fe main-cap inserts overcast with Mg or Fe main-cap inserts molded over with polymer (lower portion). Source: GM.

Subtask 1.2.3—Material solutions for high-performance pistons. The AM process was selected to make the L8T V8 engine piston in Phase 1. Three alloys have been chosen to print the piston, including the ACMZ alloy [4], the Al-Ce-Ni-based alloy [5], and the light high-entropy alloy [6]. The ORNL team has developed a printable Al-Ce-Mn alloy with a thermally stable microstructure and attractive mechanical properties up to 400°C. Figure I.4.2.8 shows an example of the UTS of this alloy (as-printed) compared to a current automotive piston cast-Al alloy and the RT Vickers hardness pyramid number (HV) after a 200-hour thermal exposure at various temperatures as compared to ACMZ alloy.

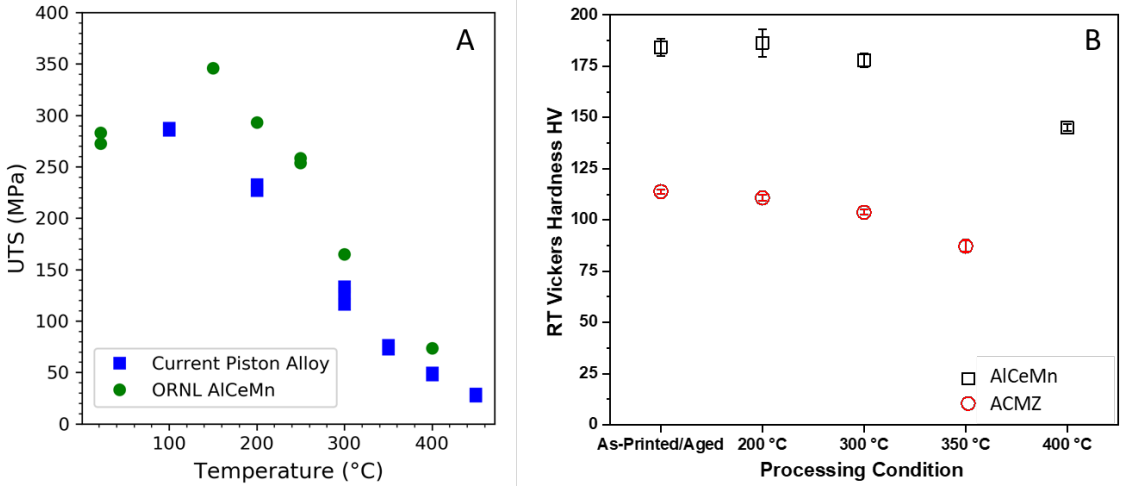

Figure I.4.2.8. Mechanical properties of the ORNL Al-Ce-Mn alloy fabricated with AM compared with cast-Al and ACMZ alloys currently used in piston manufacture. Source: ORNL.

Subtask 1.2.4—Advanced casting process solutions for high-performance castings. Alternate chilling methods have been investigated with A356-T6 alloy for driving thermal gradients and solidification. An experimental ablation cell shown in Figure I.4.2.9(a) was manufactured, and a standard step plate was ablated along with a control sample, as observed in Figure I.4.2.9(b). The ablated casting shows elongation more than doubling with a roughly 10% increase in tensile strength.

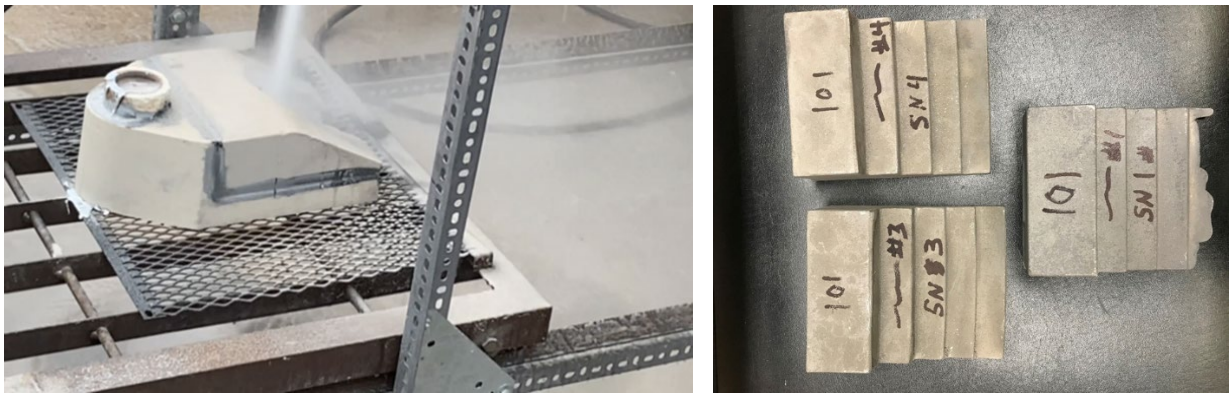

(a) (b)

Figure I.4.2.9. (a) Prototype ablation cell. (b) Step plates. Source: Eck.

Further studies were conducted at Eck using a variety of chill types and sizes along with two pieces using nanocoated filters to understand how small amounts of nanoparticles impact strength and elongation. Mechanical property testing and microstructure evaluation indicate that thermal conductivity and thermal capacity of the chill system plays an important role in dendrite arm spacing and mechanical properties.

Extensive casting simulations were started at Eck to determine the gating and chilling systems to produce a quality Al cylinder head. Initially, those simulations looked at a full-deck chill. All those scenarios showed mid-head porosity, as shown in Figure I.4.2.10(a), due to the in-gates passing through the chill, resulting in reduced feeding to the midsection of the head. More simulations were then conducted with different chill and riser configurations, such as a reduced chill profile confined to the combustion chambers, shown in Figure I.4.2.10(b), and added code risers, shown in Figure I.4.2.11(a). The simulation results are quite promising and removed much of the porosity, as shown in Figure I.4.2.11(b).

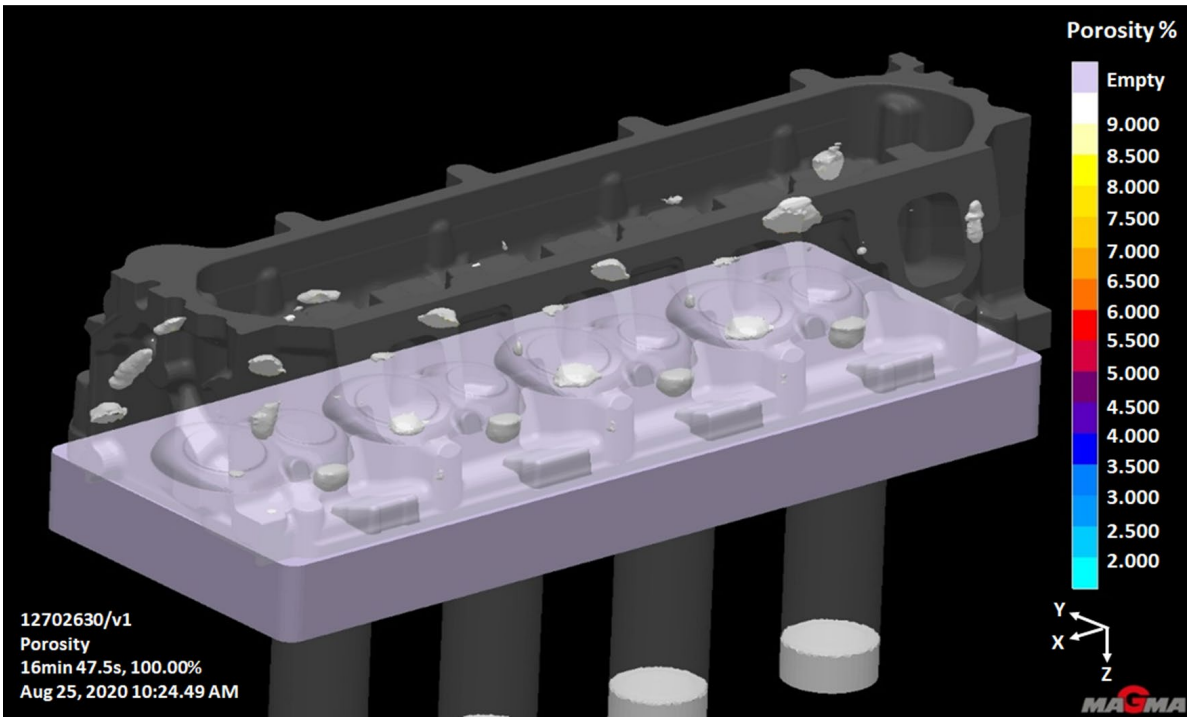

(a)

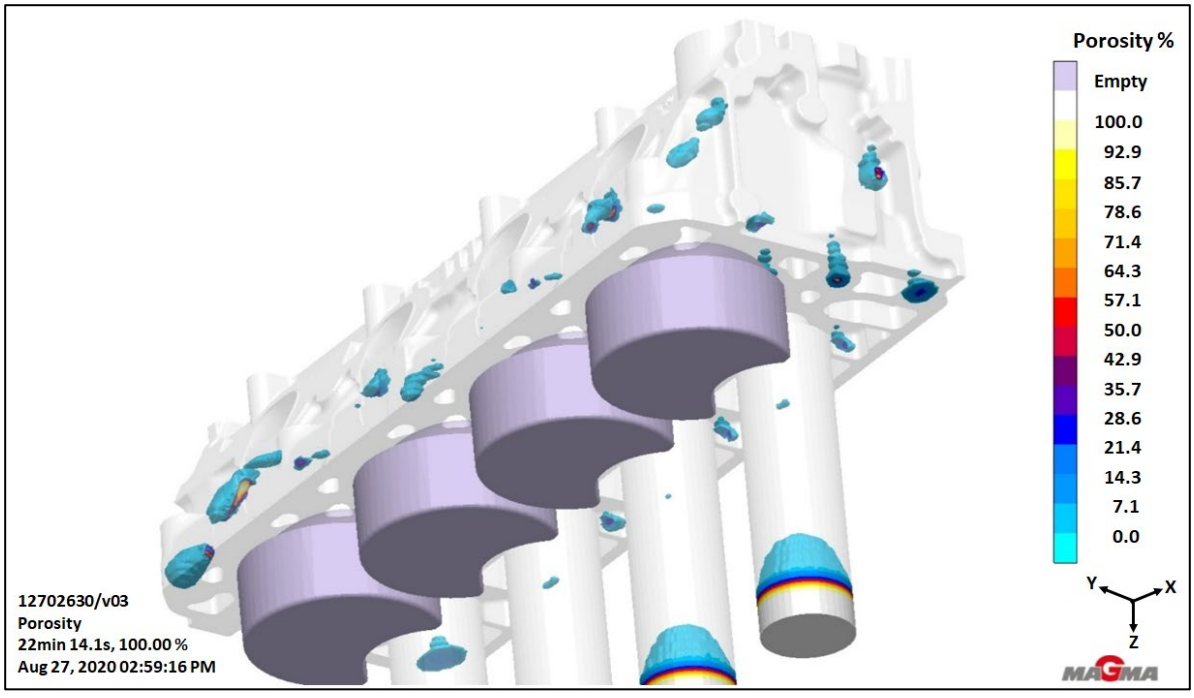

(b)

Figure I.4.2.10. (a) Simulation with a large deck face chill. (b) A chill profile confined to the combustion chambers. Source: Eck.

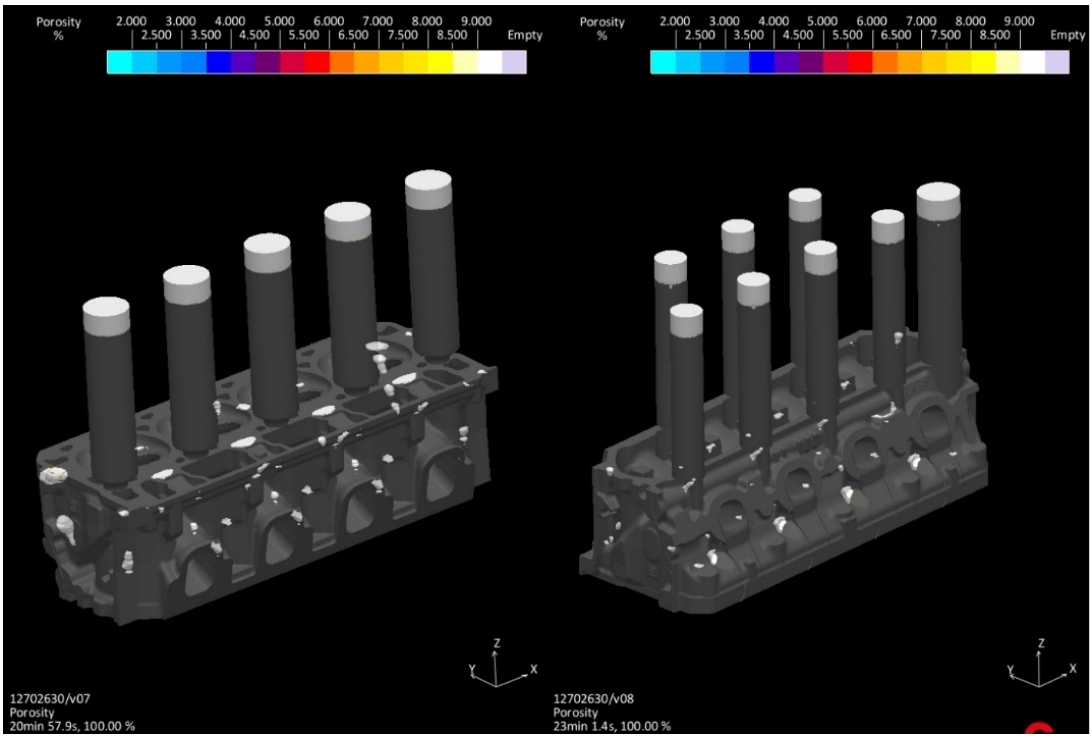

(a)

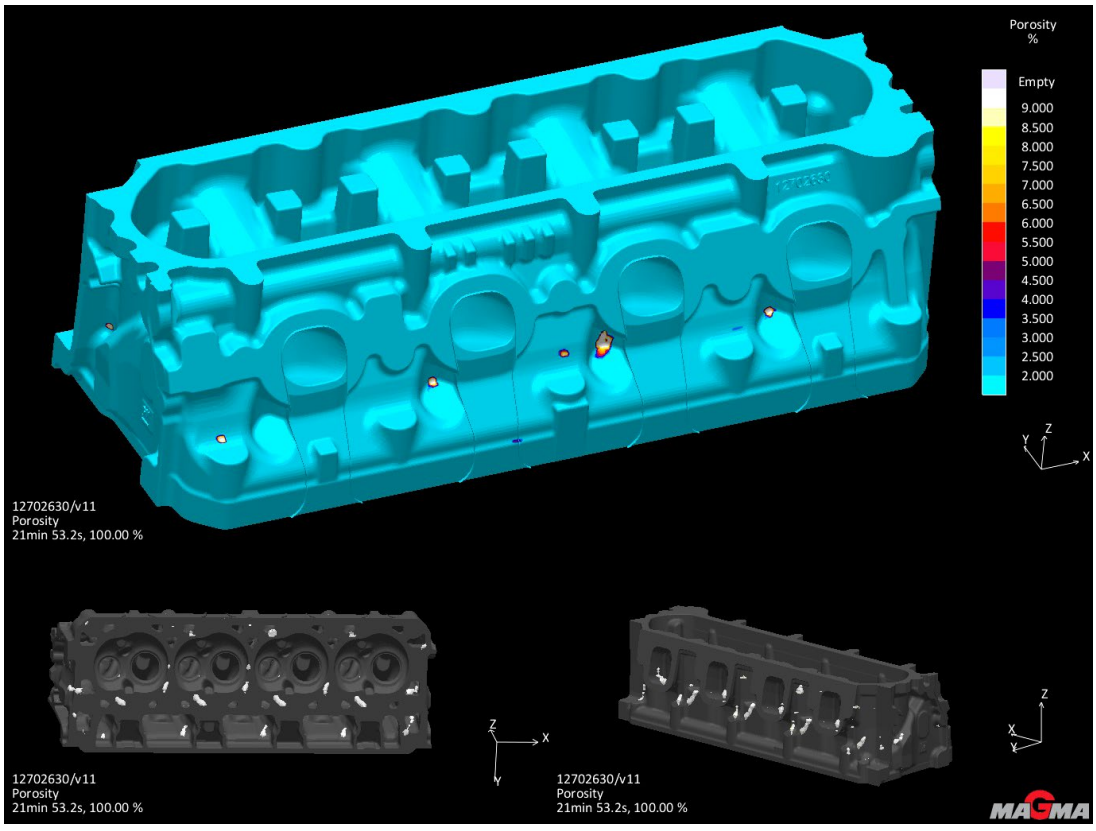

(b)

Figure I.4.2.11. (a) Simulation with code risers. (b) Simulation results showing reduced porosity. Source: Eck.

Work on overcasting cylinder valve seats was started at OSU by designing a sand-casting pattern for the overcasting experiments. Casting simulation was used in-mold filling to optimize the pattern design to minimize turbulence and improve metal-front uniformity, as observed in Figure I.4.2.12(a). The finally optimized pattern has been fabricated for ongoing overcasting experiments, as shown in Figure I.4.2.12(b), and subsequent heat-treatment will be performed to evaluate the interface bonding with the production-steel-based valve seats with and without coating.

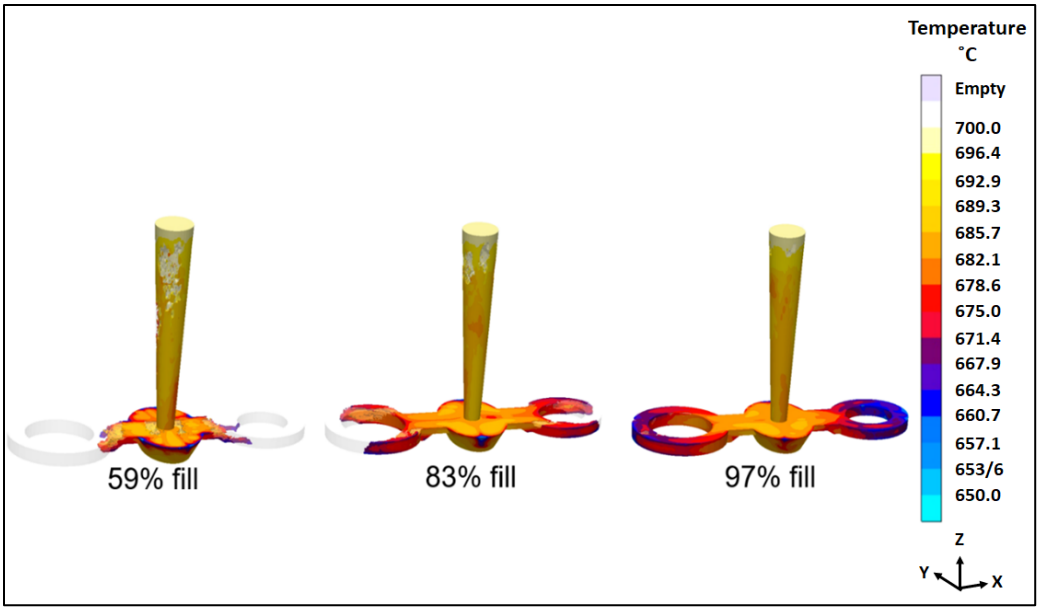

(a)

(b)

Figure I.4.2.12. (a) A mold filling simulation for a 319 Al alloy in overcasting sand cavity simulated with sodium silicate bonded sand for three fill percentages showing the temperature distribution during filling. (b) The sand-casting pattern made of polylactic acid polymer with steel valve seats. Source: The Ohio State University.

Subtask 1.2.5—Cost-effective high-strength/high-modulus ferrous material solutions for the crankshaft. Iterative design of a cast-steel hollow crankshaft with center webs, shown in Figure I.4.2.13(a), and without center webs, shown in Figure I.4.2.13(b) in the main journals was completed for the Phase 1 platform L8T V8 engine. A full CAE analysis has been conducted for both designs. The calculated fatigue reserve factors on the fillets and lightening and oil holes in both designs have met the design and performance requirements. The overall fatigue reserve factors of both cast-steel designs are better than those of a production V8 forged-steel crankshaft and still saves 0.15 Kg in mass.

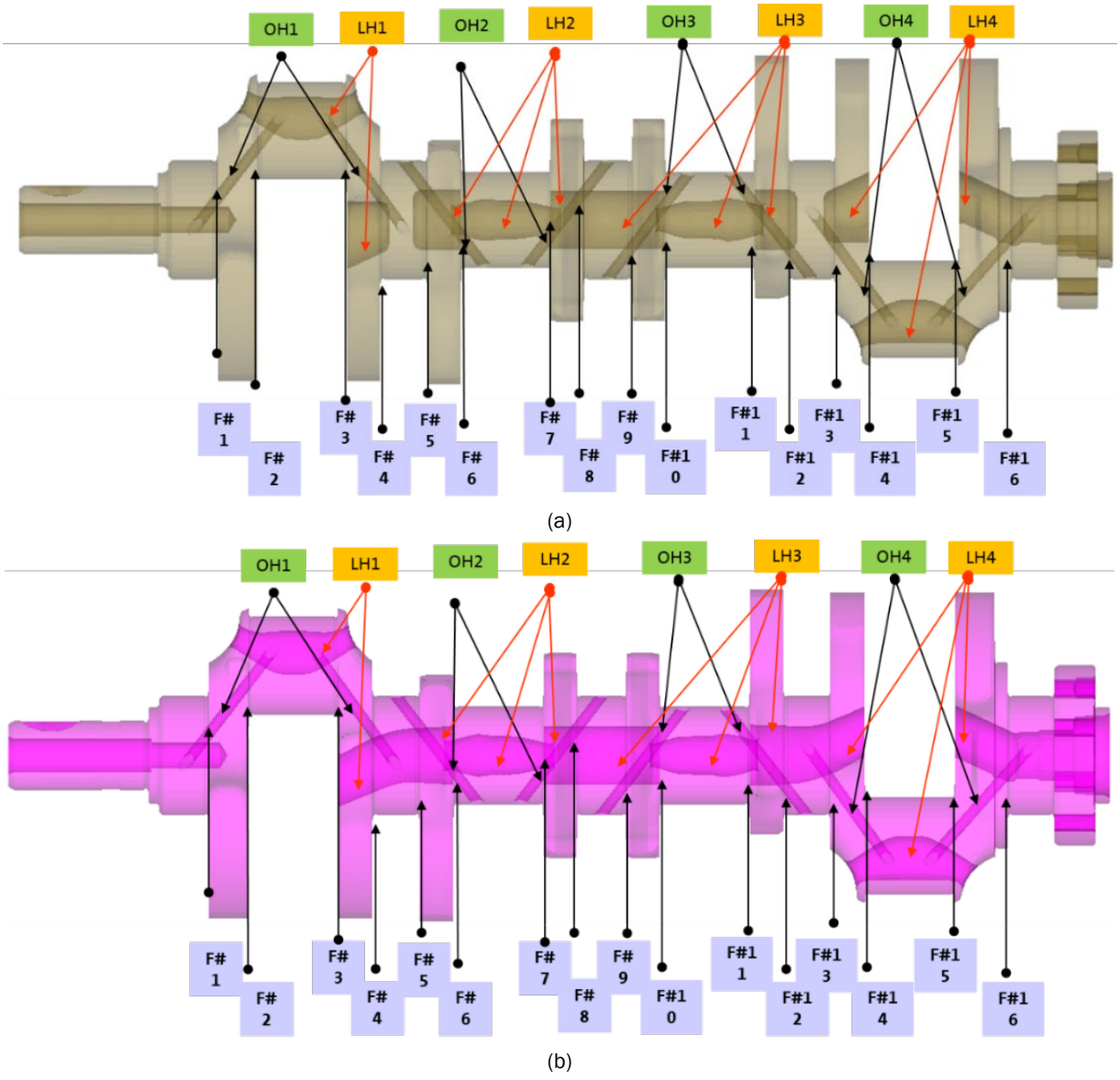

Figure I.4.2.13. Cross-section of cast-steel designs together (a) with numbering of fillets (F#), lightening holes (LH) and oil holes (OH) with webs at main journals; and (b) without webs at the main journals. Source: GM.

The design of the nodular Fe crankshaft was close to completion at the end of FY 2020 with high-strength and high-modular, ductile Fe alloy, as observed in Figure I.4.2.14. Because of the design (i.e., external dimensions) constraints of the existing L8T platform engine, the new nodular Fe crank must be designed as a solid piece to be able to achieve the same performance as the forged-steel crank. Nevertheless, the newly designed nodular Fe crank is still about 0.2 kg lighter than its forged-steel counterpart.

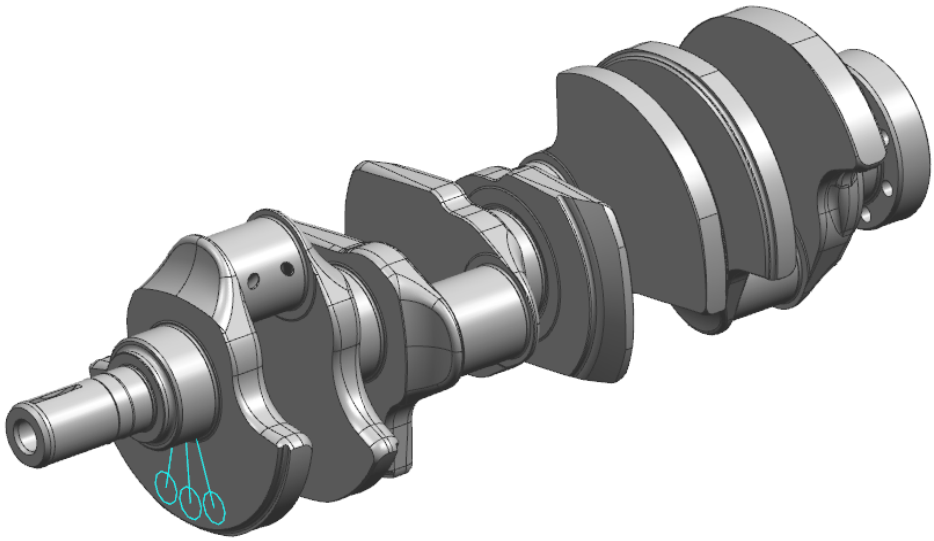

Figure I.4.2.14. New nodular Fe crankshaft design. Source: GM.

Leveraging prior DOE and GM work [7] on cast-steel crankshaft development to identify alloy system and casting strategies, MTU continued prototype crankshaft casting. Three potential alloy chemistries, shown in Table I.4.2.4, were selected for coupon-level comparison of as-cast mechanical properties and shrinkage tendency to allow for final alloy selection. The GM34 CrMoV chemistry is based on a pending GM patent application. The DOE-optimized alloy represents the most promising chemistry based on previous work completed by GM. The DOE-optimized alloy with Ce is a cerium-added variant of the DOE-optimized alloy and is included to study the potential microstructural refinement effect of cerium.

Table I.4.2.4. Selected Alloy Composition for Coupon-Level Comparison

Alloy	C	Si	Mn	P	S	Cr	Ni	Mo	Cu	Ti	V	Al	Ce
GM 34 CrMoV	0.38	0.40	0.90	0.03 max	0.050	1.10	0.25 max	0.30	0.20 max	0.03 max	0.10	0.030	---
DOE-Optimized Alloy	0.30	0.50	1.10	0.03 max	0.050	0.35	0.25 max	0.20	0.20 max	0.03 max	0.08	0.030	---
DOE-Optimized Alloy + Ce	0.30	0.50	1.10	0.03 max	0.050	0.35	0.25 max	0.20	0.20 max	0.03 max	0.08	0.030	0.030

The test coupon mold was developed using Altair Inspire Cast casting simulation software to minimize predicted porosity and ensure good mold filling characteristics (e.g., filling time, metal flow). The first casting trial using the initial mold design resulted in castings containing macroscopic centerline-shrinkage porosity, so insulating riser sleeves were added at the midpoint and bottom of each bar, as shown in Figure I.4.2.15, to minimize shrinkage porosity in the sections between the riser sleeves from which tensile specimens are extracted.

A heat of the DOE-optimized alloy was poured into three variants of the multiple riser sleeve mold, which are shown schematically in Figure I.4.2.15, to compare the effect of varying the cooling rate. The baseline mold (standard mold) consisted of just the additional riser sleeves, while a second mold utilized steel chills, which were 0.75 in. thick on the first and third bars and 0.375 in. thick on the second and fourth bars, centered between the riser sleeves. A high-conductivity chromite facing sand was used in a third mold.

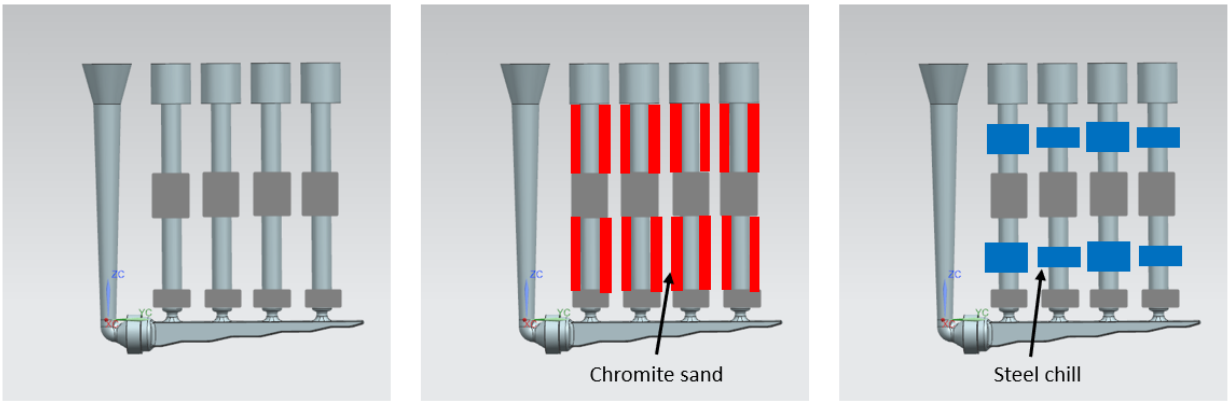

Figure I.4.2.15. Schematic illustration of the three multiple riser sleeve mold variants.
Source: Michigan Technological University.

Multiple transverse and longitudinal sections were extracted from each casting type, from within the regions between the riser sleeves, and no macroporosity was evident. The longitudinal sections were then metallographically prepared for microscopic analysis (up to 500× optical magnification), which showed little to no porosity. Tensile specimens were machined according to ASTM E8-16a Specimen 3 for each casting from the two bars closest to the sprue and tested to failure. The results are shown in Table I.4.2.5. All specimens, regardless of which casting they were extracted from, had low total elongation, which was confirmed via SEM fractographic analysis to be caused by shrinkage porosity. The chromite facing sand specimens were similar in strength and elongation to the standard mold, while the chilled specimens showed a higher elongation on average. Fractographic analysis of the fracture surface of two chilled specimens, 3/4-Bar 1-Upper and 3/4-Bar 1-Lower, with significantly different total elongation, showed that the specimen with lower-elongation, specimen 3/4-Bar 1-Lower, exhibited significantly more shrinkage porosity on the fracture surface.

Developing a high-strength, high-modulus, castable, cost-effective quality ductile Fe for a lightweight crankshaft application in a MD combustion engine began at MTU. A comprehensive literature search was conducted to understand the influencing factors on the elastic modulus of ductile iron. Empirical data in the literature show that the elastic modulus decreases significantly with increasing graphite fraction and with decreasing nodularity. Therefore, one potential strategy for increasing the elastic modulus is to reduce the amount of graphite in the microstructure by reducing carbon; however, castability (i.e., fluidity/mold filling, shrinkage tendency, and hot-tearing susceptibility) has been shown to degrade with decreasing C content. Because the matrix phase—usually pearlite, ferrite, or some combination of both—makes up the majority of the microstructure by volume, it is desirable to find an alloying scheme to increase the matrix elastic modulus, thereby reducing the extent to which C content must be reduced in order to achieve the target elastic modulus. The data available in the literature also indicate that cobalt is the most promising element for increasing the elastic modulus of ferrite when practicality (e.g., cost) is considered. Si has been shown to significantly decrease the elastic modulus of ferrite, so, given its relatively high concentration in ductile iron, it is desirable to evaluate the viability of reducing its concentration. The available published data are for binary iron-based solid solutions, however, so the combined effect of cobalt and Si additions on the elastic modulus of Fe needs to be studied to isolate the solid solution effects from graphite effects, as well as in ductile Fe alloys to understand their overall effects. To search for additional potential alloying schemes to increase the ductile-iron-matrix elastic modulus, first principles calculations (i.e., DFT) is being employed to simulate the combined effects of various unlike solute elements on the elastic modulus of iron.

Table I.4.2.5. Physical Properties for Different Mold Types

Mold Type	Specimen ID*	0.2% YS (MPa)	UTS (MPa)	Total Elongation (%)	Notes
Chills	3/4-Bar-1-Upper	555	703	1.9	
	3/4-Bar-1-Lower	521	522	0.6	
	3/8-Bar-2-Upper	543	730	2.5	
	3/8-Bar-2-Lower	545	711	2.2	
	Average	**541**	**667**	**1.8**	
	St. Dev.	14	97	0.8	
Chromite Facing Sand	Bar-1-Upper	548	641	1.0	
	Bar-1-Lower	550	661	1.5	
	Bar-2-Upper	558	647	1.1	
	Bar-2-Lower	512	533	0.9	
	Average	**542**	**621**	**1.1**	
	St. Dev.	20	59	0.3	
Standard	Bar-1-Upper	538	618	1.0	Fractured outside gauge.
	Bar-1-Lower	571	596	0.7	Fractured outside gauge.
	Bar-2-Upper	541	670	1.4	Fractured outside gauge.
	Bar-2-Lower	528	559	1.0	
	Average	**545**	**611**	**1.0**	
	St. Dev.	19	46	0.3	

* Bar 1 is closest to the sprue; Bar 2 is the next bar away from the sprue. “Upper” indicates the region between the top two riser sleeves, while “Lower” indicates the region between the bottom two riser sleeves. The chill thickness for each chilled specimen is indicated by the fraction in the specimen ID.

Subtask 1.2.6—Material and manufacturing solutions for other engine components. A study has been carried out in exploring the opportunities to reduce mass of other engine parts using lightweight materials. As shown in Figure I.4.2.16, mass reduction options have been evaluated for the oil pan, pickup tube assembly, oil pan cover, and engine block valley cover. The mass savings and weight reduction rate vary from 14% to 86%, depending upon the part geometry and material used.

Pan-Oil		Volume	Material	Density	Mass kg	Mass lbs	Weight Reduction
L8T Baseline	12696279/002	2151640	Aluminum	2710	5.83	12.86	
Option One		2151640	PF-1110	2050	4.41	9.72	24%
Option One		2151640	PF-6510	1700	3.66	8.06	37%
Option Two Pan	BGA46055	1967156	PF-6510	1700	3.34	7.37	
Brkt-Oil Filter		127574	Aluminum	2710	0.35	0.76	
Over Mold Total					3.69	8.13	37%
Option Three Pan	BGA48315	1952397	PF-6510	1700	3.32	7.32	
RearBrkt/Oil Filter		629837	Aluminum	2710	1.70	3.76	
Over Mold Total					5.02	11.08	14%

PickUpTube-Asm		Volume	Material	Density	Mass kg	Mass lbs	Weight Reduction
L8T Baseline	12619979/003	80820	Mix-Steel	7842	0.63	1.40	
Option One		80820	PA66	1070	0.09	0.19	86%
Option Two	BGB46970	189445	PA66	1070	0.20	0.45	68%

Cover-Oil Pan		Volume	Material	Density	Mass kg	Mass lbs	Weight Reduction
L8T Baseline	12630766/003	16676	Aluminum	2760	0.05	0.10	
Option One		16676	PA66	1070	0.02	0.04	61%

Cover-Valley		Volume	Material	Density	Mass kg	Mass lbs	Weight Reduction
L8T Baseline	12700640/002	411294	Aluminum	2620	1.08	2.38	
Option One		411294	PF-6510	1700	0.70	1.54	35%
Option Two Cover	BGB41214	365333	PF-6510	1700	0.62	1.37	
FuelPumpBrkt		32469	Aluminum	2620	0.09	0.19	
Over Mold Total					0.71	1.56	34%

(a)

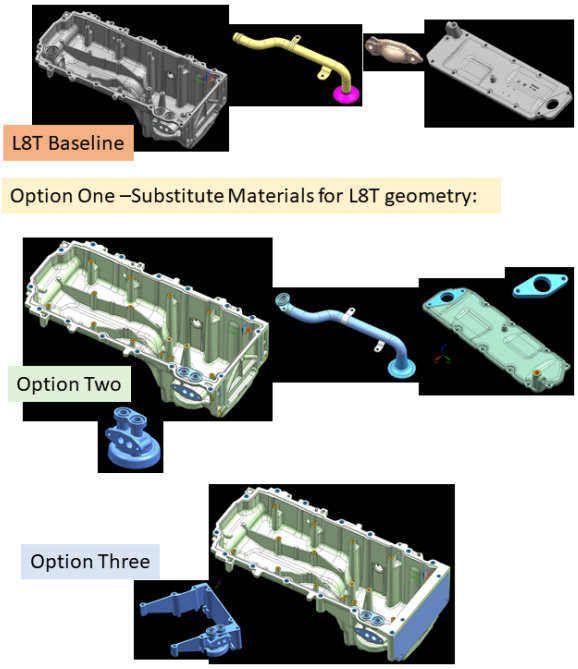

(b)

Figure I.4.2.16. Mass reduction opportunities evaluated for oil pan, pickup tube assembly, oil pan cover, and engine block valley cover. Source: GM.

Conclusions

After simulation of baseline engine operating points weighted by fuel usage, both normally aspirated large-displacement V8 and downsized boosted small-displacement L6 engine concepts have been virtually evaluated relative to the project objectives with advanced combustion technologies. The simulated engine fuel efficiency is found to improve with increased engine displacement. Both engine concepts have been successfully packaged in the target MD truck engine compartment.

Advanced materials and manufacturing solutions that reduce mass and improve engine performance have been explored and virtually evaluated. Lightweight engine blocks and cost-effective crankshafts have been iteratively designed and validated in CAE durability analyses. A new sand-casting process for head and block, overcasting head valve seats, and new crankshaft materials were also evaluated through simulations and experiments.

References

1. DOE-EERE, 2019, “Fiscal Year 2019 advanced vehicle technologies research funding opportunity announcement,” DE-FOA-0002014, Washington, D.C., USA. Available at: https://eere-exchange.energy.gov/FileContent.aspx?FileID=25f7a4dd-9874-4aee-9606-2ab52fe9cc18. Accessed 9 December 2020.
2. Pollock, T. M., J. E. Allison, D. G. Backman, M. C. Boyce, M. Gersh, E. A. Holm, R. LeSar, M. Long, A. C. Powell IV, J. J. Schirra, D. D. Whitis, and C. Woodward, 2008, “ICME: A transformational discipline for improved competitiveness and national security,” The National Academies Press, Washington, D.C., USA.
3. Wang, Q. G., P. Jones, Y. Wang, and D. Gerard, 2011, “Advances in computational tools for virtual casting of aluminum components,” in: Allison, J. E., P. M. Collins, and G. Spanos (eds.), *Proceedings of the 1st World Congress on ICME*, TMS 2011, pp. 217–222.

4. ORNL, 2018, “ORNL-developed alloy promises better fuel economy,” Available at: https://www.ornl.gov/blog/eesd-review/ornl-developed-alloy-promises-better-fuel-economy. Accessed 9 December 2020.

5. Plotkowski, A., O. Rios, N. Sridharan, Z. Sims, K. Unocic, R. T. Ott, R. R. Dehoff, and S. S. Babu, 2017, “Evaluation of an Al-Ce alloy for laser additive manufacturing,” *Acta Mater.*, Vol. 126, pp. 507–519.

6. Luo, A. A., W. Sun, and X. Huang, 2018, “High-entropy AlCrTiV Alloys”, U.S. Patent Application, US 2018/0119255.

7. Huff, R. K., 2016, “Development of high-performance cast crankshafts,” DOE-EERE Vehicle Technologies – Annual Merit Review, 9 June 2016, Project ID: PM 065. Available at: https://www.energy.gov/sites/prod/files/2016/06/f33/pm065_huff_2016_o_web.pdf. Accessed 9 December 2020.

Acknowledgements

The Principal Investigators would like to thank DOE-EERE VTO for the opportunity to work on this important project, especially Mr. K. Howden and Mr. J. Gibbs at DOE for their project oversight. The Principal Investigators are also very grateful to Mr. S. Campbell (contract manager at GM) and the GM project and management team, Dr. A. Shyam, and his team at ORNL, Prof. A. Luo and his team at OSU, Prof. P. Sanders, and his team at MTU, and Mr. D. Weiss and his team at Eck Industries, Inc., for their extreme support and dedication to the project.

I.4.3 Lightweight and Highly Efficient Engines Through Al and Si Alloying of Martensitic Materials (Oak Ridge National Laboratory)

Yong-Ching Chen, Co-Principal Investigator
Cummins
Cummins Technical Center
1900 McKinley Avenue
Columbus, IN 47201
E-mail: yong-ching.c.chen@cummins.com

Dean Pierce, Co-Principal Investigator
Oak Ridge National Laboratory
1 Bethel Valley Road
Oak Ridge, TN 37831
E-mail: piercedt@ornl.gov

Jerry L. Gibbs, DOE Technology Manager
U.S. Department of Energy
E-mail: jerry.gibbs@ee.doe.gov

Start Date: May 1, 2019 End Date: April 30, 2021
Project Funding: $472,690 DOE share: $380,000 Non-DOE share: $92,690

Project Introduction

This is a joint 2-year project between ORNL and Cummins to develop and engine test a new steel alloy for pistons in diesel engines. The project brings expertise from both organizations to enable rapid development and specific optimization of the alloy's properties for the unique requirements of the piston application. The project is split into a beginning, Phase 1, focused on laboratory-scale alloy development, and Phase 2, focused on scaling the developed alloy, manufacturing a piston from the new alloy, then engine testing the piston. Work in both phases of the project will be completed jointly by Cummins and ORNL, but ORNL will execute the majority of the alloy development in Phase 1 while Cummins will be responsible for the majority of the work relating to piston manufacture and engine testing in Phase 2. The majority of Phase 1 work has been completed, and the project is currently transitioning into Phase 2.

The current piston materials for medium and HDDEs are quenched and tempered 4140 martensitic steel and grade 38MnVS6 MAS. These materials are cost-effective and have high-strength and acceptable oxidation resistance at temperatures up to 500°C. A primary pathway to increase the efficiency of internal combustion engines involves increasing both peak cylinder pressure and combustion gas temperature. However, 4140 and MAS are currently operating at their temperature limits, which prevents further increases in efficiency by increasing combustion gas temperatures and pressures. Thus, new piston materials are required to overcome this barrier to increasing medium and HD diesel engine efficiency. Additional barriers to implementing new piston materials are cost and manufacturability. Some commercially available candidate materials that may possess the necessary elevated temperature properties are too expensive or have poor weldability and/or machinability resulting in additional costs and technical barriers.

Objectives

The objectives of this project are to develop and engine test new steel alloys for pistons. A new steel alloy must exhibit sufficient fatigue strength and oxidation resistance to be able to operate at peak temperatures of 600°C for extended periods of time. Furthermore, elevated temperature strength, oxidation resistance, and thermal conductivity are often in conflict with one another, and significant attention in this project is focused

on how to balance these properties. An alloy must also be friction weldable to a piston-skirt material of 4140 or MAS and have reasonably good machining characteristics. In addition, the raw material cost of the new steel can only be incrementally greater than 4140 or MAS. The steel must also have a high TRL to enable the alloy to be scaled and implemented in a relatively rapid timeframe, meaning the alloy should be similar enough to existing materials that it can be manufactured and processed with existing processes and equipment at steel mills and piston manufacturers. Therefore, while innovative alloying strategies are being pursued in this project, radical departures from current or candidate materials are avoided in this two-year project. Cummins and ORNL have defined internal targets for strength, thermal conductivity, oxidation resistance, and cost for the new alloys.

Approach

This project is focused on the development of new alloys for piston materials. We have selected 4140 as the baseline alloy along with one additional commercial alloy, designated alloy "C," with higher heat resistance that may be suitable for 600°C operation in piston materials. These baseline alloys are used to evaluate performance improvements of the new developmental alloys. This project uses computational alloy design to identify alloy chemistries that have the necessary mechanical and oxidation properties for piston applications operating at 600°C. Once alloy compositions have been identified, the alloys are arc-melted, processed by hot rolling, heat-treated, tested, and characterized. Testing includes elevated temperature tensile testing, oxidation testing, thermal diffusivity measurements, and measurements of the CTE for select alloys. Samples were also aged at high temperatures for long periods of time to simulate heat exposure due to engine operation, and then tensile tested at elevated temperatures to evaluate the resistance to aging. Microstructures were characterized by optical microscopy.

An iterative alloy development process was used, in which small batches of material are melted and tested, and these results fed into the development of the next batch of alloys. This process has resulted in an improved understanding of alloying effects on properties relevant to piston materials, continuous optimization, and downselection of promising alloy chemistries and processing routes. The same tests were performed on Alloy 4140 and Alloy C as were used in the developmental alloys to assess any improvement over the commercial alloys. CFD software was employed to evaluate how properties such as thermal conductivity affect piston temperatures to evaluate how predicted surface temperatures will change from alloy to alloy.

For the final phase of this project, a suitable developmental alloy will be downselected and scaled to make a round bar of suitable diameter for piston manufacture and engine testing. The piston of the new material will be engine-abuse tested to identify operational limits of the new alloy and its durability. After engine testing, the piston will be evaluated to further characterize the materials resistance to aging and oxidation in a combustion atmosphere.

Results

The data generated in this project are proprietary and only relative improvements to Alloy C are provided. Cummins and ORNL melted and tested a total of 24 developmental steels with varied compositions in the first 1.5 years of this project. We also evaluated different processing routes to improve the mechanical properties. Each alloy was subjected to elevated temperature mechanical testing, oxidation testing, and thermal conductivity testing. Some alloys were subjected to additional tests to measure coefficients of thermal expansion and heat capacity. A large database of elevated temperature properties has been developed from the developmental alloys. Several of the new alloys exhibit elevated temperature properties that are far superior to 4140 and Alloy C, including an alloy designated X, and in some cases at significantly lower cost than Alloy C.

The following important results and achievements have occurred in this project in FY 2020:

- 24 developmental alloys have been tested, and a large database of elevated temperature material properties has been developed to provide a deep understanding of alloying and processing effects on properties of these steels.

- A 53% increase in elevated temperature strength at 600°C relative to Alloy C has been achieved in developmental Alloy X after long-term aging, demonstrating significantly higher elevated temperature strength and heat resistance.
- Developmental Alloy X is expected to have a 20% lower cost than Alloy C.
- Developmental Alloy X exhibits similar oxidation resistance to Alloy C, despite significantly lower cost and higher strength and significantly improved oxidation resistance over 4140.

Cummins and ORNL will be downselecting an alloy to manufacture pistons for engine testing, which is scheduled to occur in the next phase of this project. This process of downselecting the alloy is expected to be complete in the first quarter of FY 2021.

Conclusions

In FY 2020, Cummins and ORNL-developed numerous steel alloys with the intent to improve properties over current commercial piston alloys and commercially available candidate piston materials. We have developed alloys with superior strength, oxidation resistance, thermal conductivity, and lower cost than 4140, MAS, and candidate commercial alloys for next-generation pistons operating at peak temperatures of 600°C. Several alloys exhibit properties relevant to piston materials that are significantly improved over existing commercial alloys, and one or more of these will be downselected for piston manufacture and engine testing in the next phase of this project.

Acknowledgements

The following ORNL personnel are acknowledged for their contributions to this project: G. Muralidharan, A. Haynes, T. Muth, B. Pint, I. Stinson, G. Cox, D. Moore, D. Heidel, H. Wang, A. Trofimov, K. Hedrick, and G. Garner. The following Cummins personnel are acknowledged for their contributions as well: C. Trobaugh, Q. Ma, J. Zhou, H. Savage, B. Wang, and W. D. McNulty.

II Lightweight Materials

II.1 Automotive Metals

II.1.1 Non-Rare-Earth Mg Bumper Beam (Pacific Northwest National Laboratory/ Magna R&D CRADA)

Scott Whalen, Principal Investigator
Pacific Northwest National Laboratory
902 Battelle Boulevard
Richland, WA 99352
E-mail: scott.whalen@pnnl.gov

Tim Skszek, Co-Principal Investigator
Magna Services of America, Inc (Magna R&D)
750 Tower Dr.
Troy, MI 48098
E-mail: tim.skszek@magna.com

Sarah Kleinbaum, DOE Technology Manager
U.S. Department of Energy
E-mail: sarah.kleinbaum@ee.doe.gov

Start Date: January 1, 2019 End Date: September 30, 2022
Project Funding: $2,005,000 DOE share: $1,005,000 Non-DOE share: $1,000,000

Project Introduction

A lightweight bumper beam made from Al or Mg offers a 25% to 60% weight savings, respectively, as compared to a high-strength steel state-of-the-art component. For a new CRADA between PNNL and Magna R&D, this lightweight bumper beam was chosen as the component to target because its geometry is fairly simplistic for demonstrating direct manufacturing capability utilizing a novel advanced extrusion process developed by PNNL called ShAPE™. The bumper component offers commercial value by providing mass reduction in the front of the vehicle along with ride and handling benefit.

Preliminary experiments performed at PNNL demonstrated the ability to ShAPE™ fabricate non-RE Mg tubing with high-strength, improved ductility, and energy absorption. ShAPE™ has shown that extruded ZK60 and AZS312 tubing with a 7.5-mm diameter and 0.75-mm-wall thickness have a similar energy absorption to AA6061-T6, which can be attributed to significant grain refinement, breakdown, and dispersion of second phases, as well as the ability to eliminate anisotropy in compressive/tensile strength [1],[2],[3]. This enables Mg to be considered as an option for further mass reduction, beyond what can be achieved with Al; however, early market penetration using Al is a near-term opportunity. Al bumpers represent approximately 54% of the North American LD vehicle market. Should this research effort be successful in providing a 30% mass reduction at equal cost relative to Al bumpers, it is anticipated that 25% market penetration would be realized over the next five years and 50% market share by 2030. All Al automotive bumpers are sourcing from the tier network of vendors, thereby providing resourcing opportunity based on equal performance, reduced mass, and cost equivalent lower than Al bumpers. Since inception of the project, funding and scope have expanded to include the use of ShAPE™ to extrude Al products from less expensive feedstock such as scrap or castings consisting of primary and secondary Al.

Objectives

The goal of this Magna R&D/PNNL CRADA is to demonstrate the feasibility of using PNNL's ShAPE™ technology for producing non-RE Mg alloy and Al alloy tubular extrusions, which can be used in the fabrication of automotive sub-assemblies, such as bumper beams and battery trays.

Approach

The scope of this work focuses on two discrete thrusts: (1) using the ShAPE™ process to extrude circular cross-sections from Mg and Al alloy solid billets to determine if the process can be used to manufacture Al components and is scalable and (2) using the ShAPE™ process to extrude rectangular cross-sections from non-RE Mg alloy and Al alloy billets using a port hole bridge die approach. As a step toward rectangular cross-sections, round tubing will first be extruded using a port hole bridge die approach integrated into the ShAPE™ process. Magna is primarily responsible for supplying feedstock material, tool fabrication, process modeling, and testing. PNNL is primarily responsible for tool design and integration, process development, microstructural characterization, publication, project reporting, and limited mechanical testing. Figure II.1.1.1 shows PNNL's first-of-a-kind ShAPE™ machine.

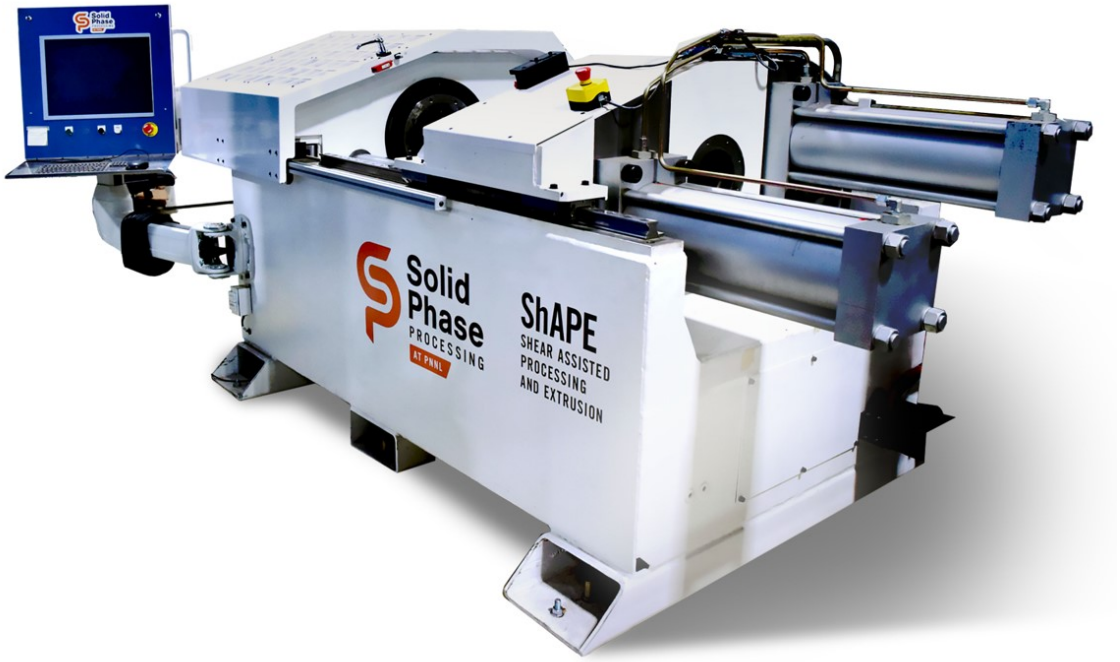

Figure II.1.1.1. ShAPE™ machine installed in PNNL's Solid-Phase Processing Laboratory. Source: PNNL.

Unlike conventional indirect extrusion where the die is pressed against the billet using a strictly linear motion, the ShAPE™ extrusion process superimposes a rotational shear force by spinning the die, as observed in Figure II.1.1.2. The ShAPE™ process is described in detail elsewhere [3]; however, the basic operation for extruding round tubular profiles is briefly described here for convenience. Contact between the billet and rotating die generates frictional heating at the die/billet interface along with adiabatic heating within a thin layer of deforming material below the die face. The extent of heat generation and depth of the deformation zone is controlled by regulating rotational speed, motor torque, and ram speed. As a result, the heat required to soften the material is entirely derived by the process and billet pre-heating in a separate furnace is not required. As temperature increases, material plastically flows inward toward the extrusion orifice through individual spiral grooves machined into the die face. Upon exiting the grooves, the flow streams consolidate prior to entering the extrusion orifice where the material then flows between the mandrel and die-bearing surface to form a tube.

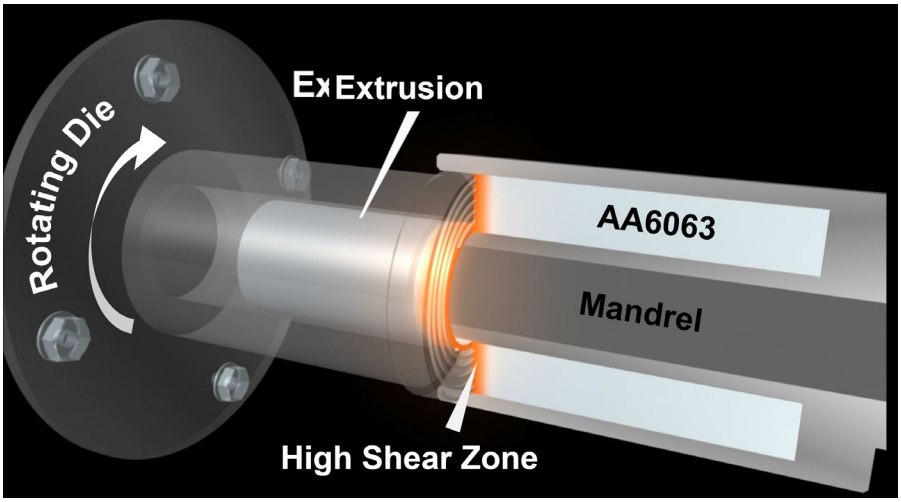

Figure II.1.1.2. Schematic of ShAPE™ tooling and process. Source: PNNL.

Results

The primary goal in FY 2020 was to demonstrate that the ShAPE™ process was scalable and capable of extrusion speeds fast enough to indicate potential for industrial relevance. To accomplish this, tooling and process parameters were developed for extruding AA6063-T5 billets at the maximum ram speed of the ShAPE™ machine—0.38 m/min. The tooling and die set produced a thin-walled tube having a 12-mm outer diameter with inner diameters of 8 mm and 10 mm giving an extrusion ratio of 11.8 and 20.6, respectively. The resulting extrusion velocity (i.e., the speed at which the extrusion exits the die) for the 2-mm-wall thickness was 4.5 m/min and 7.8 m/min for the 1-mm-wall thickness. Numerous extrusions were performed at speeds ranging from 0.75 m/min to 7.8 m/min. Figure II.1.1.3 shows examples of the 1-mm and 2-mm-wall thickness tubes extruded by ShAPE™.

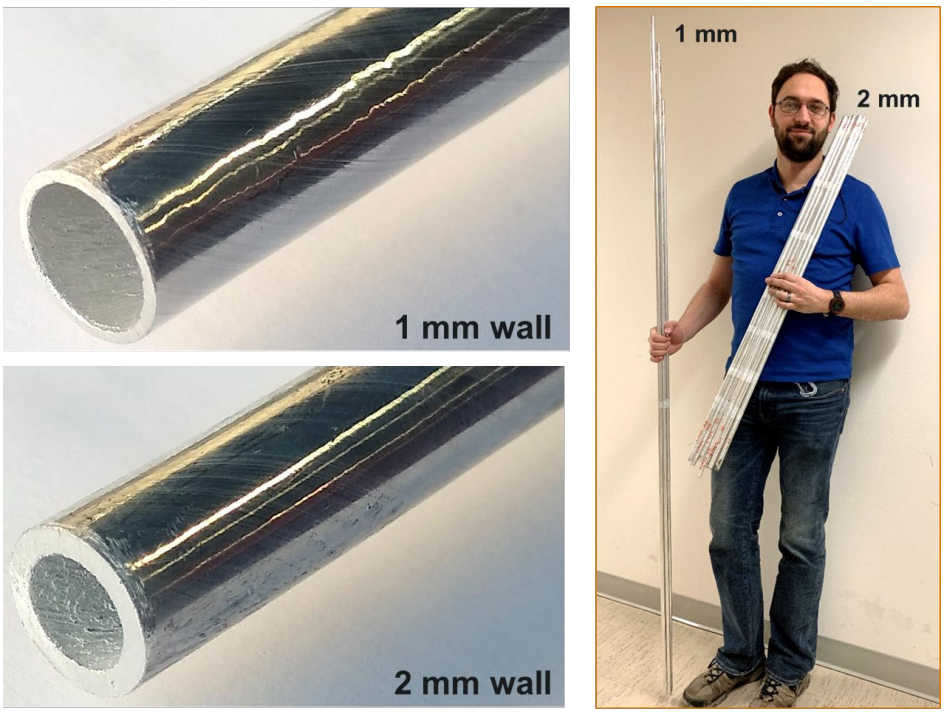

Figure II.1.1.3. Examples of AA6063-T5 tubing extruded by ShAPE™. Source: PNNL.

After extrusion, 150-mm-long sections were cut from the tubes and artificially aged at 177°C for 8 hours. This heat-treatment results in a T5 temper since no solution heat-treatment or water quench occurred before artificial aging. The 150-mm-long specimens were fitted with tapered pugs on each end per ASTM E8 and pulled in an MTS 810 load frame with a 50-kN load cell at a rate of 2.3 mm/min, with a 50-mm extensometer measuring the gauge length. Tensile tests were performed for 1 mm thick tubes extruded at 0.71, 0.94, 1.4, 2.8, and 4.5 m/min and for 2 mm thick tubes extruded at 1.2, 1.6, 2.5, 4.9, and 7.8 m/min. Three replicates were tested for each wall thickness and extrusion speed for 48 total specimens. The tensile test results are shown in Figure II.1.1.4 and compared to the ASTM B221M-13 minimum standard [4] and American Society of Metals (ASM) Typical Values [5] for AA6063 tubes of this size in the T5 and T6 conditions. Tubes that are 1-mm and 2-mm-thick are not differentiated in the plot because no statistical difference in performance between the two-wall thicknesses was observed. The 0.2% YS, ultimate strength, and elongation at the break are shown from left to right. This data shows that yield and ultimate strength for ShAPE™ extruded AA6063 in the T5 condition are significantly higher than conventionally extruded AA6063 in the T5 condition. In fact, yield and ultimate strength for ShAPE™ extruded AA6063 in the T5 condition exceed that of the ASTM minimum standard for the T6 condition and are on par with ASM typical values for T6. As such, extrusions may be fabricated with significantly improved mechanical properties yielding near-T6 properties with only a T5 heat-treatment, thus entirely bypassing the solution heat-treatment and water quenching steps. Elongation is on par with the standards and the large spread in the data is likely due to issues with the mandrel fixturing. Tabular data reporting the average values ± 1 standard deviation is shown in Table II.1.1.1.

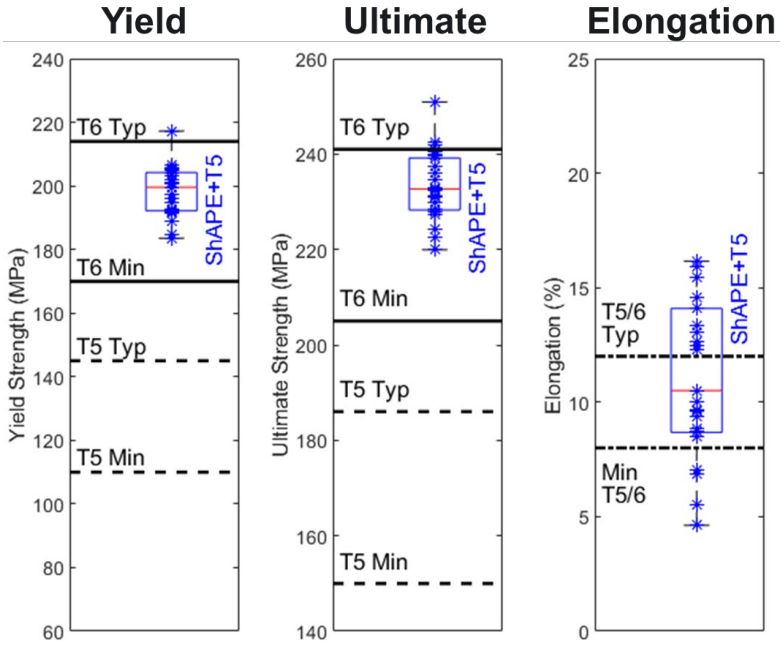

Figure II.1.1.4. Tensile properties of 1 mm and 2 mm thick AA6063-T5 tubing extruded by ShAPE™. Source: PNNL.

Table II.1.1.1. Tensile Properties of 1 mm and 2 mm Thick AA6063-T5 Tubing Extruded by ShAPE™ Compared to the Relevant ASTM [4] and ASM [5] Standards

	ShAPE + T5 Heat-Treated	T5 Min [4]	T5 Typ [5]	T6 Min [4]	T6 Min [5]
YS (MPa)	198.3 ± 15.5	110	145	170	214
Ultimate Strength (MPa)	233.5 ± 14.0	150	186	205	241
Failure Elongation (%)	11.0 ± 6.9	8	12	8	12

The ability to obtain T6 properties with a T5 heat-treatment results from solutionizing occurring *in situ* to the extrusion process due to the extreme shear conditions inherent to ShAPE™. SEM backscattered electron (BSE) imaging in Figure II.1.1.5 shows microstructure for as-ShAPE™ Extruded and ShAPE™ Extruded + T5 at exit velocities of 1.2, 2.5, 4.9, and 7.8 m/min (left to right). It is observed that neither grain size nor the size and distribution of the Mg_2Si second-phase precipitates are appreciably affected by extrusion speed, which explains why the tensile properties are also not a function of the extrusion speeds investigated.

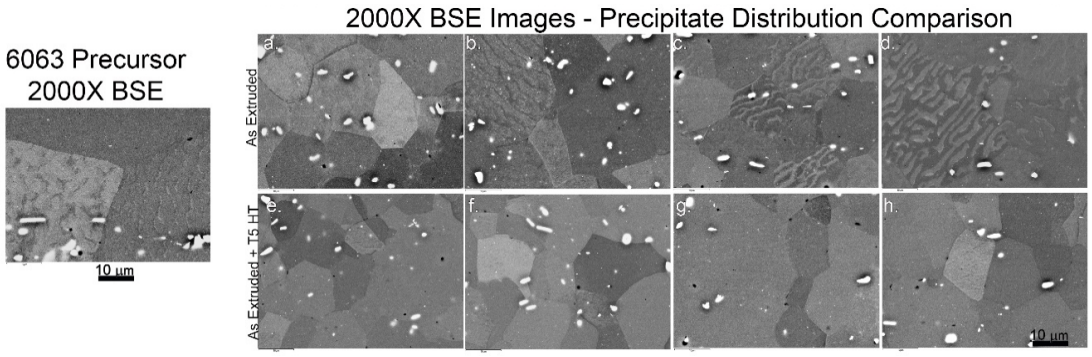

Figure II.1.1.5. Microstructure for As-ShAPE™ Extruded and ShAPE™ Extruded + T5 at exit velocities of 1.2, 2.5, 4.9, and 7.8 ms/min from left to right respectively. Source: PNNL.

Conclusions

Tooling and process parameters were developed for ShAPE™ extrusion of AA6063 billets into round, thin wall tubing. ShAPE™ extrusion of 12-mm diameter tubing with 1-mm and 2-mm-wall thickness was performed at the maximum ram speed of the ShAPE™ machine, which resulted in an extrusion speed of 7.8 m/min. Tensile properties of ShAPE™ extruded AA6063 heat-treated to the T5 condition exceed the ASTM and ASM standards for conventionally extruded AA6063 in the T5 condition and were on par with the T6 properties. In FY 2021, the project will transition to the use scrap as feedstock and development of a port hole bridge die approach for ultimately extruding non-circular cross-sections.

Key Publications

1. Taysom, B. S., S. Whalen, Md. Reza-E-Rabby, M. DiCiano, and T. Skszek, "Shear-Assisted Processing and Extrusion of thin-walled AA6063 tubing," Submitted to *TMS 2021 Light Metals*.

References

1. Lavender, C., V. Joshi, G. Grant, S. Jana, S. Whalen, J. Darsell, and N. Overman, 2019, "System and process for formations of extrusion products," U.S. Patent No. 10,189,063, January 29, 2019.
2. Whalen, S., V. Joshi, N. Overman, D. Caldwell, C. Lavender, and T. Skszek, 2017, "Scaled-up fabrication of thin-walled Mg ZK60 tubing using ShAPE™," *Magnesium Technology 2017*, Part of the Minerals, Metals & Materials Series. Springer, New York, NY, USA. pp. 315–321.
3. Whalen, S., N. Overman, V. Joshi, T. Varga, D. Graff, and C. Lavender, 2019, "Mg alloy ZK60 tubing made by ShAPE," *Mat. Sci. Eng. A*, Vol. 755, No. 7, pp. 278-288.
4. ASTM B221M-13, 2013, "Standard Specification for Aluminum and Aluminum – Alloy Extruded Bars, Rods, Wires, Profiles, and Tubes (Metric)," Table 2.
5. ASM Handbook, Vol 2b, 2011, "Properties and Selection of Aluminum Alloys, Typical Mechanical Properties," Table 4–6, p. 395.

Acknowledgements

PNNL and Magna R&D thank the Vehicle Technologies LightMAT Program for supporting this project.

II.1.2 Low-Cost Magnesium Sheet Component Development and Demonstration Project (Fiat Chrysler Automobile, U.S., LLC)

Randy Gerken, Principal Investigator
Fiat Chrysler Automobile, U.S., LLC
800 Chrysler Drive, CIMS: 485-00-15
Auburn Hills, MI 48326
E-mail: randy.gerken@fcagroup.com

Sarah Kleinbaum, DOE Technology Manager
U.S. Department of Energy
E-mail: sarah.kleinbaum@ee.doe.gov

Start Date: October 1, 2016 End Date: February 28, 2021
Project Funding: $2,045,227 DOE share: $1,431,659 Non-DOE share: $613,568

Project Introduction

The value of the Low-Cost Magnesium Sheet Project to OEMs lies in the potential availability of a lower cost, more formable Mg sheet alloy, and reduced cost of using a Mg sheet in automotive applications due to: (a) improved formability at reduced temperatures; and (b) improved corrosion protection and reduced coating costs as a result of improved forming lubricant and coating technologies.

Objectives

The objective of this project is to research, develop, and demonstrate at least one large, challenging Mg sheet component on a model year 2013 or newer vehicle at a manufacturing cost of less than $2.50 per pound of weight saved.

Approach

The U.S. Automotive Materials Partnership, LLC (USAMP), has employed a technical approach that integrates experimental, computational, and data tools that can accelerate the development and deployment cycle of low-cost Mg sheets. To accomplish the project objective, USAMP proposed to research, develop, test, and evaluate at least one Mg alloy and commensurate processing suitable for rolling automotive appearance grade sheet, and forming inner and outer door panels based on the 2013 Ford Fusion to validate the results.

This 52-month project consists of the following seven research activities conducted concurrently over three BPs: (1) technical cost guidance to identify key cost drivers associated with current Mg component production; (2) material characterization and modeling studies; (3) rolling trials on ingots; (4) pretreatment, coating application, and lubrication studies; (5) forming studies; (6) scaling to warm forming of large components; and (7) joining studies. Public data and experimental results developed on the project are archived in the DataHUB repository by the LightMAT Consortium.

The project progressed in FY 2020 in the following three thrust areas:

1. Virtual development of new Mg sheet alloys with leading-edge modeling techniques that range from design and characterization to their deployment into complex automotive manufacturing systems and developing the business case.
2. Achieving the practical understanding of Mg sheet alloys with the development of detailed material property data at elevated temperatures, and their implementation in computational modeling tools for validation on intermediate size and scale to the demonstration automotive panels.

3. Improvement of downstream rolling and joining processes, pretreatments, high-temperature lubricants, and corrosion coatings to enable greater use of existing Mg alloy sheet materials.

The Low-Cost Magnesium Sheet Project participants are listed below (Henkel and Xtalic completed their sub-awards this year):

- Sub-awardees: Applied Engineering & Technology (AET) Integration, Inc.; Fuchs Lubricants Co.; Henkel Corporation; PPG Industries, Inc.; Quaker-Houghton Chemical Corporation; Vehma International of America, Inc.; Xtalic Corporation; The Ohio State University (OSU); University of Florida (UF); University of Illinois at Urbana-Champaign (UIUC); University of Michigan (UM); and University of Pennsylvania (UP).
- Vendors: Bucciero & Associates, LLC; Camanoe Associates; M-Tech International, LLC; Pinetree POSCO Mg (PPM); Korea Magnesium Industry; Edison Welding Institute (EWI); FADI-AMT LLC; and Inal Tech, Inc.
- DOE National Laboratories: PNNL and ORNL.

Table II.1.2.1 lists the completion status of the project's 11 milestones at the end of FY 2020.

Table II.1.2.1. Status of Project Tasks and Milestones at the End of FY 2020

BP	Milestone Number	Milestone Type	Task	Description	Status
1	1	Go/No-Go	**Task 0:** Project Management/Contracting	100% of purchase orders issued to subs.	Complete
	2	Technical	**Task 1:** Technical Cost Guidance	Baseline cost model for Mg sheet complete.	Complete
	3	Technical	**Task 2:** Alloy and Sheet Processing Development	New Mg alloy sheet composition(s) identified.	Complete
2	4	Technical	**Task 2:** Alloy and Sheet Processing Development	Constitutive model for textured Mg alloy completed and ideal texture suggested.	75%*
	5	Technical	**Task 2:** Alloy and Sheet Processing Development	Forming analysis completed on medium sheet.	90%
	6	Technical	**Task 3:** Sheet Coatings and Lubricant Evaluation and Development	Forming lubricant composition identified.	Complete
	7	Go/No-Go	**Task 5:** Mg alloy Sheet Production	Manufacture and deliver experimental medium-width sheets.	Complete
3	8	Technical	**Task 3:** Sheet Coatings and Lubricant Evaluation and Development	Evaluation of corrosion protection coating completed.	90%
	9	Technical	**Task 5:** Mg alloy Sheet Production	Delivery of wide sheet.	Complete
	10	Technical	**Task 6:** Mg alloy Large Body Component Production	Mg alloy panels formed to specifications.	25%
	11	Technical	**Task 7:** Component(s) Demonstration	Final delivery and performance evaluation completed.	Complete

NOTE: "*" Milestone expected to be achieved in BP3.

Results

To date, the USAMP has achieved seven of the 11 defined project milestones, and expects to achieve the remaining four milestones when the project concludes in February 2021. Highlights and representative results are summarized in this section.

Development of Technical Cost Model

Camanoe Associates improved the process-based cost models (PBCMs) needed to conduct a complete cost-estimate of Mg door production during the reporting period. PBCMs of coil pretreatment, part production, assembly, and paint are used for both the Mg doors, as shown in Figure II.1.2.1. However, costs related to coil production could not be calculated with greater specificity as information is lacking on the production process, so the team will attempt to further engage material suppliers in the final year. Thus, those costs are presently being estimated through discussions with industry experts and review of published information. The lightweighting cost of the Mg doors and parts is calculated by dividing the difference in cost between the Mg and steel designs by the difference in weight (Δ$/Δkg). The project has a lightweighting cost target of $11/kg for the complete door assembly and $5/kg for individual parts.

Steel	Cold rolled	Galvanization	Stamping	N/A	Conventional	Conventional
Approach	*Approximate Supplier Cost*	*Approximate Supplier Cost*	*PBCM*	*N/A*	*PBCM*	*PBCM*
Mg	Twin roll casting	Coating	Warm Forming & Casting	N/A	Include Mg RSW	Conventional + pretreatment
Approach	*Estimate*	*PBCM*	*PBCM*	*N/A*	*PBCM*	*PBCM*

Figure II.1.2.1. Comparative analysis scope and approach for modeling and cost-estimation. Source: Camanoe Associates.

Preliminary cost modeling indicates that the Mg door cost is significantly under the $11/kg cost target for several scenarios of coil production cost. Furthermore, the three largest Mg parts are under the $5/kg part cost target for a low-production cost scenario: door inner, door outer, and window surround (60% of total part costs). The uncertainty in the coated Mg alloy sheet is a key driver of the results.

Alloy Development and Modeling Studies

The university team of UF, UM, and UIUC continued their development and evaluation of USAMP Experimental Alloy 3 binary and ternary Mg alloys using guidance from the ICME models developed based on the energy landscape computations of a range of elemental solutes systematically identified by the team.

OSU demonstrated a new sheet alloy, ZAXME11100 (USAMP Alloy 2 Plus - Mg-1.0Zn-1.0Al-0.5Ca-0.4Mn-0.2Ce by weight), which offers both excellent ductility (31% tensile elongation) and RT formability (7.8 mm Erichsen Index (IE)) in the solution-treated condition (T4), combined with a high YS (270 MPa) upon post-forming aging treatment (T6).

Development of Experimental Alloy 2-Plus

OSU developed a new "USAMP Alloy 2 Plus" sheet alloy, ZAXME11100 (Mg-1.0Zn-1.0Al-0.5Ca-0.4Mn-0.2Ce, wt. %), for RT forming applications [1]. Their initial evaluations of this new Mg alloy indicate it is comparable to 6000 series aluminum alloys (AA6016 and AA6061), and hence, shows high potential for RT forming of automotive panels. Based on the solidification path and phase formation temperatures calculated for the new alloy, as shown in Figure II.1.2.2, a multistage homogenization process was developed to sequentially dissolve all intermetallic phases at each stage and achieve maximum dissolution of all alloying elements.

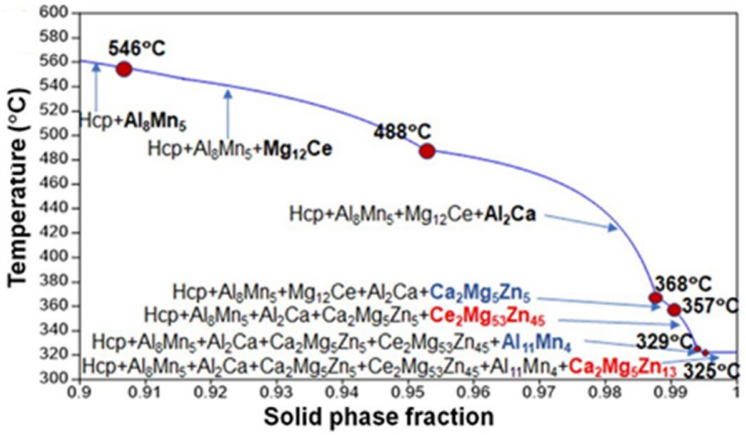

Figure II.1.2.2. Calculated solidification path for USAMP Alloy 2 Plus. Source: The Ohio State University.

Figure II.1.2.3(a) shows uniformly fine grains (i.e., < 10 mm), while Figure II.1.2.3(b) shows weak split basal texture in the USAMP Alloy 2 Plus in the T4 condition (after solution treatment at 480°C for 1 h).

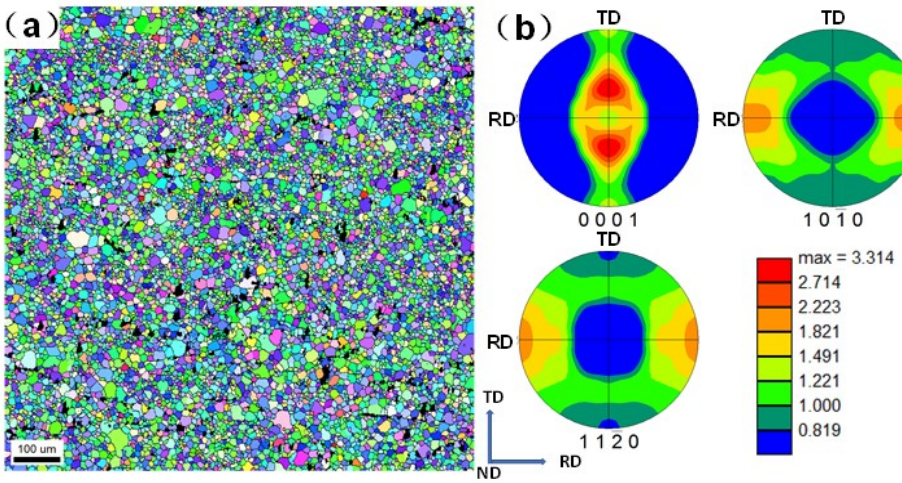

Figure II.1.2.3. Characterization of the microstructure of the USAMP Alloy 2 Plus after solution-treated (T4) at 480°C for 1 hour: (a) EBSD inverse pole figure map; and (b) texture pole figures. Source: The Ohio State University.

Figure II.1.2.4 compares the RT formability (e.g., Erichsen cupping test, 1 mm sheet, and 20 mm punch diameter) test results of Alloy 2 Plus with commercial AZ31 alloy, the presently most formable Mg sheet alloys (ZEK100 and E-form Plus [EFP]) and 6xxx AA (6061-O and 6016-T4). Among all Mg alloys, USAMP Alloy 2 Plus shows the highest formability (i.e., IE value of 7.8 mm), which is comparable to commercial 6xxx AA (7.6 to 10 mm) used in the automotive industry.

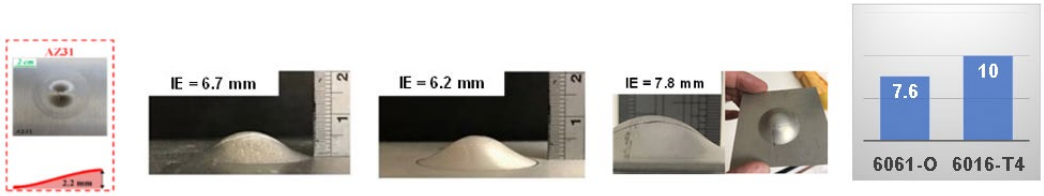

Figure II.1.2.4. Formability (Erichsen cupping test) results at RT of Alloy 2 Plus in comparison with commercial Mg alloys AZ31, ZEK100, and EFP, as well as Al alloys. Source: The Ohio State University.

Figure II.1.2.5 plots IE value vs. YS at RT for AZ31 [2] and various alloys evaluated by USAMP. Compared to commercial AZ31B alloy, ZEK100, EFP, and USAMP Alloy 2, all show improved RT formability, but with slightly reduced YS. The new sheet alloy, ZAXME11100 (USAMP Alloy 2 Plus), offers both excellent ductility (31% tensile elongation) and RT formability (7.8 mm EI) in the solution-treated condition (T4), but with an extraordinary high YS (270 MPa) upon post-forming aging treatment (T6). For age-hardening Alloy 2 Plus, AA6061 and AA6016 alloy, the IE was measured at T4 temper, while the YS is tested at T6 conditions. The excellent combination of strength and formability of this new Mg alloy, comparable to those of 6xxx sheet aluminum alloys (AA6016 and AA6061), clearly shows potential for RT forming of automotive applications.

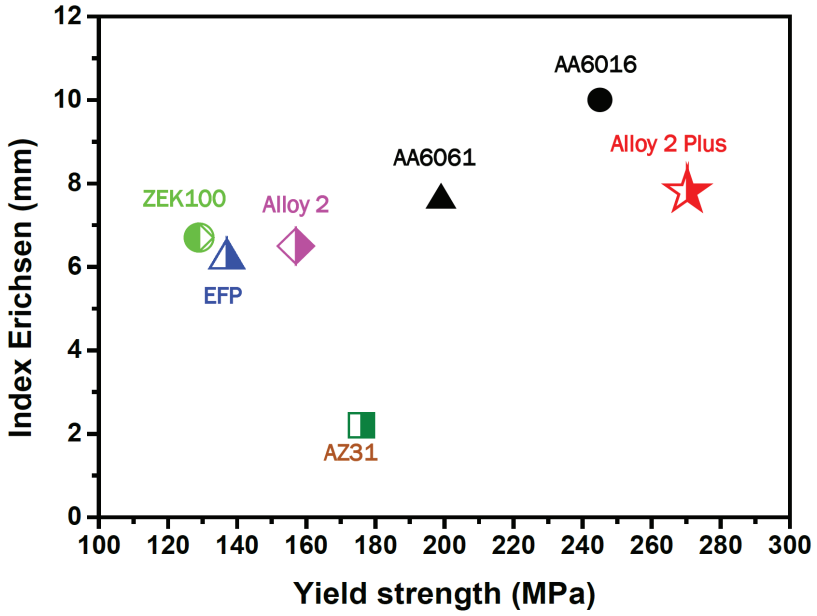

Figure II.1.2.5. RT formability (i.e., values [3]) vs. YS of various new Mg alloys evaluated by USAMP, in comparison with commercial Mg alloy AZ31B [2] and AA 6061 [4] and 6016 [5]. Source: The Ohio State University.

In FY 2021, the lab-scale study of USAMP Alloy 2 Plus will be continued with an emphasis on optimizing heat-treatment conditions for mechanical property and formability of Alloy 2 Plus at RT; and studying the influence of various heat treatments on microstructure, texture, recrystallization, and grain growth of Alloy 2 Plus sheet.

Predictive Modeling to Compute the Energy Landscape for Solutes and Support Alloy Development

ICME-based Approach

The low ductility of Mg alloys at RT is a direct consequence of the anisotropic response of the hexagonal close packed (hcp) crystal structure to loading, where the slip of basal dislocations occurs at a much lower critical stress as compared to non-basal dislocations. Deformation of polycrystalline Mg is therefore dominated by basal slip, resulting in too few independent slip systems available at low temperatures for appreciable ductility. A promising approach for improving the ductility of Mg is adding solutes that interact with dislocations to potentially reduce the difference in the stresses required to move basal and non-basal dislocations. UIUC has used DFT to compute inputs for solid solution strengthening models of $\langle c+a \rangle$ edge and screw dislocations, and $(10\bar{1}2)$ and $(10\bar{1}1)$ twinning dislocations in Mg. The key inputs to the solution strengthening models are [6],[7],[8]: (a) accurate dislocation geometries for computing solute-dislocation interaction energies from either direct substitution of solutes into core sites, or from the local strain and slip distributions in the dislocation cores; (b) solute volumetric size misfits that determine the interaction strengths of solutes with the dislocation strain field; and (c) solute chemical misfits that determine the interaction strengths of solutes with either stacking faults or twin boundaries.

UIUC has completed all the DFT calculations needed to predict the interaction energies of 63 different solute species with $(10\bar{1}1)$ twinning edge, $(10\bar{1}2)$ edge, and $\langle c+a \rangle$ edge dislocations in Mg using approximate interaction models. A key finding is that both the solute-dislocation interactions and the changes in yield stress scale as second-order polynomials in the volumetric solute size misfit ϵ_V^s, as shown in Figure II.1.2.6. These scaling relations allow UIUC to efficiently compute the effects of a large number of different solute species on the mechanical properties of Mg, and also show that solutes with large mismatch in size with Mg (either undersized or oversized) are the most effective at strengthening the individual deformation modes.

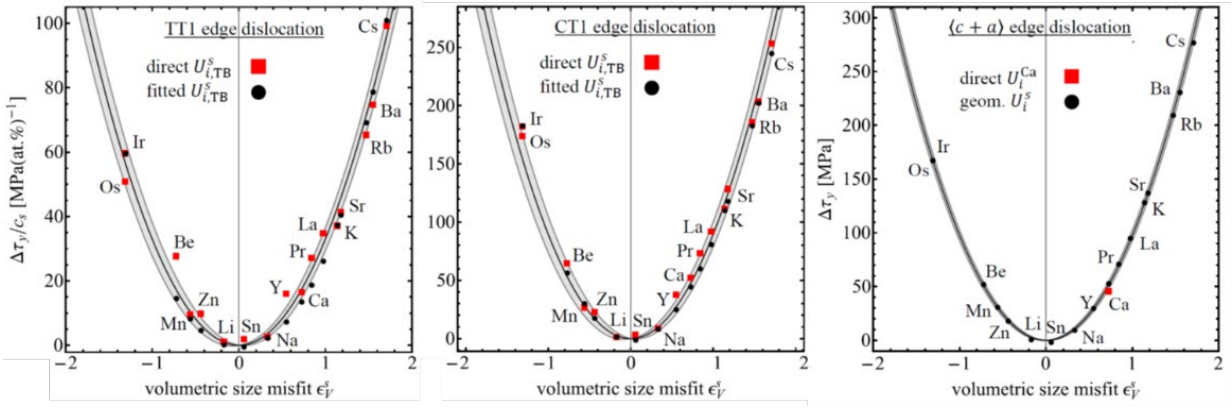

Figure II.1.2.6. Changes in yield stress vs. solute size misfit. Source: University of Illinois at Urbana–Champaign.

UIUC has combined their solid solution strengthening predictions with solubility limits from alloy phase diagrams to determine which solutes have the greatest potential for improving the mechanical properties of Mg alloys through solution strengthening. While large or small solutes are the most effective strengtheners in Mg, these solutes generally have low solubilities, which limits their overall effectiveness at strengthening the different deformation modes. UIUC has computed solubility limits for twelve binary Mg alloys using the COST507 thermodynamic database [9] and the Pycalphad code [10], and they extracted solubility limits for 44 other binary Mg alloys from literature. It was found that the RE solutes Gd, Tb, Dy, Nd, Ho, Er, Tm, Yb, and Sm are the most promising for increasing the strength and ductility of hcp Mg, with the solutes listed in decreasing order of effectiveness. The non-RE solutes Y, Sc, Pb, Ca, Ag, Bi, Tl, Zn, Li, Ga, Al, and Cd are also promising for increasing the strength and ductility of hcp Mg, with the solutes listed in decreasing order of effectiveness.

Solubility analysis was extended to eight assessed ternary Mg alloy systems in the COST507 database. Solubility limits were computed for Mg-Al-Cu, Mg-Al-Li, Mg-Al-Mn, Mg-Al-Si, Mg-Al-Zn, Mg-Cu-Si, Mg-Cu-Y, and Mg-Cu-Zn by scanning the temperature-composition space for each alloy to determine the maximum solubility of each solute in the hcp phase of Mg. Since large solutes are the most effective strengtheners in Mg, it is generally expected that in the most promising ternary alloys, the smaller of the two solutes will increase the solubility of the larger solute. Pycalphad calculations for these ternary systems show that in the Mg-Al-Li system, Al increases the solubility of Li and Li increases the solubility of Al. Adding a small amount of Li to Mg-Al can increase the yield stress of the non-basal deformation modes by up to 25% while reducing the ratios of the non-basal to basal yield stresses by up to 10%. For the other seven ternary systems, the addition of a second solute either has a negligible effect on the solubility of the second solute or reduces the solubility depending on the alloy.

Development of Experimental Alloy 3

The UF-led development of a viable USAMP Experimental Alloy 3 consisted of an investigation of binary and ternary alloys with a range of alloying elements of Ca (from 0.1 – 1 wt %) and Zn (from 0 – 4 wt %). Progress and accomplishments are summarized below.

Mg-Ca and Mg-Sn Solute Strengthening Model and DFT Experimental Validation

A heat-treatment schedule that removed the Mg_2Ca and Mg_2Sn precipitates in the microstructure of recrystallized sheets of Mg – 0.2Ca and Mg – 1.5Sn (at. %) cold worked up to 15 and 20% thickness reduction was identified. SEM and energy-dispersive spectroscopy performed on heat-treated (500°C/24 hrs) Mg – 1.5Sn and Mg – 0.2Ca samples showed evidence of a small amount of Mg_2Sn and Mg_2Ca phase around grain boundaries, respectively, as shown in Figure II.1.2.7. However, no Mg_2Sn and Mg_2Ca particles were observed in the grains after heat-treating at 500°C for 24 hours. Heat-treated Mg-1.5Sn and Mg-0.2Ca samples were shipped to PNNL in January 2020. Finally, four sheets—two as-rolled and two completely recrystallized of Mg-0.2Ca and Mg-1.5Sn with 15% cold worked—were shipped to PNNL in March 2020 for further testing.

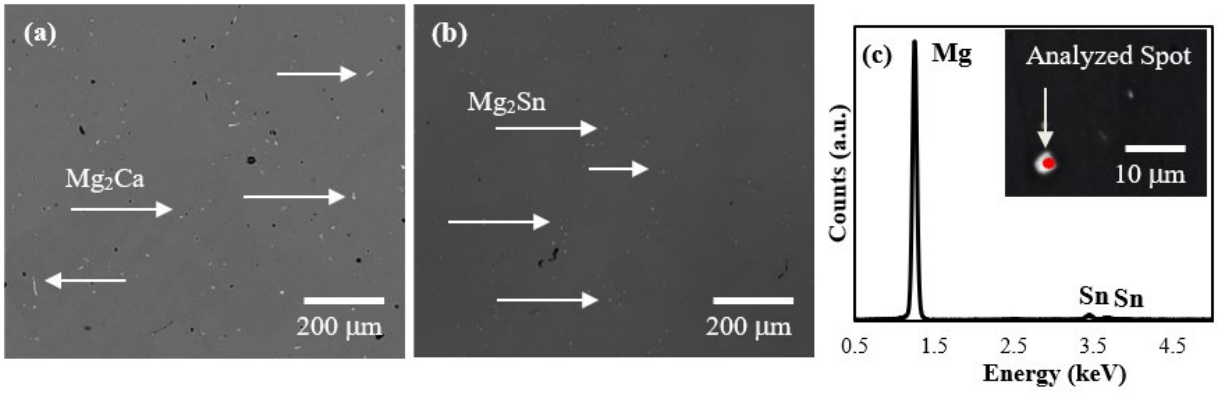

Figure II.1.2.7. BSE image of (a) Mg-0.2Ca and (b) Mg-1.5Sn (at.%) sheets heat-treated at 500°C for 24 hours showing the distribution of the second-phase; and (c) energy-dispersive spectroscopy spectrum of the second-phase indicating that it is Mg_2Sn. Source: University of Florida.

Mg-Ca and Mg-Sn Solute Strengthening Model and DSA Experimental Validation

Dynamic strain aging (DSA) experiments on Mg-0.1Ca, Mg-0.35Ca, Mg-0.1Ca-0.5Zn, and Mg-0.35Ca-0.5Zn (wt.%) alloys at 200, 250, and 300°C have been completed. It is hypothesized that deformation of Mg-Ca-based alloys, under conditions at which DSA occurs, can enhance formability via texture modification. DSA is commonly observed as serrated flow curves during high-temperature compression testing and under conditions at which the strain-rate sensitivity (SRS) is negative [11]. Mg-0.1Ca and Mg-0.1Ca-0.5Zn were characterized by positive values of SRS; thus, no DSA occurs at the tested conditions. This can be related to the low amount of Ca in the Mg matrix of 0.1 wt.%. On the other hand, compositions of higher amounts of Ca (i.e., 0.35Ca wt.%) were characterized by negative SRS at 200 and 250°C from 10^{-2} to 10^{-3} s^{-1}. These results correlate to findings that demonstrate that increasing the solute content broadens the range of conditions at which DSA occurs [11].

Static recrystallization experiments on samples of Mg-0.35Ca and Mg-0.35Ca-0.5Zn displaying DSA behavior have been completed. These samples were initially compressed under DSA conditions and then heat-treated at 450°C for various times and water quenched. The average grain size of as-deformed and annealed samples is summarized in Table II.1.2.2. EBSD will be performed on recrystallized samples in FY 2021 to measure texture strength and characterize "RE – type" texture development of these alloys.

Table II.1.2.2. Average Grain Size of as-deformed and Annealed Samples of Mg-0.35Ca and Mg-0.35Ca-0.5Zn Compressed Under DSA and Non-DSA Conditions

Composition (wt.%)	Conditions	Temperature (°C)	Strain-Rate (s^{-1})	Strain (%)	Average Grain Size (μm)			
					As-Deformed	Annealed at 450°C		
						15 min.	30 min.	45 min.
Mg – 0.35Ca	DSA	200	10^{-3}	15	1343 ± 360	351 ± 123	249 ± 201	–
			10^{-2}	15	1289 ± 454	289 ± 131	303 ± 159	–
		250	10^{-3}	25	1267 ± 403	–	249 ± 108	291 ± 104
			10^{-2}	25	1499 ± 549	–	206 ± 102	335 ± 107
	No DSA	300	10^{-2}	25	1586 ± 365	–	247 ± 108	336 ± 100
Mg – 0.35Ca –0.5Zn	DSA	200	10^{-3}	15	762 ± 162	312 ± 122	243 ± 169	–
		250	10^{-3}	15	856 ± 305	346 ± 190	389 ± 242	–
	No DSA	300	10^{-3}	15	993 ± 367	317 ± 165	405 ± 192	–

Recrystallization, Texture, and Grain Growth Studies of New Alloys

UM continued the development of a Mg-Zn-Ca alloy (Alloy 3) with a weak crystallographic texture by exploring the texture evolution and microstructure evolution that occurs during plane-strain compression of unalloyed Mg, Mg-Ca binaries, and Mg-Zn-Ca ternary alloys. Table II.1.2.3 shows the six alloys that were subjected to a 10-pass plane-strain compression test using a Gleeble Thermomechanical simulator to mimic the rolling process. EBSD and optical microscopy were used to characterize the microstructure and texture evolution in the as-deformed and annealed conditions, as shown in Figure II.1.2.8.

The ternary alloys behaved differently than the unalloyed and binary specimen during both deformation and annealing. The microstructure of all three ternary alloys shows serrated grain boundaries, evidence of grain boundary bulging, and necklace structures of fine grains along grain boundaries—features of discontinuous dynamic recrystallization [12]. No such structures were observed in the unalloyed and binary samples. Texture analysis of the as-deformed condition (measured using EBSD) show a strong basal texture in the unalloyed Mg and Mg-Ca binaries. The ternary alloys had much weaker deformation textures and a tendency for spreading in the transverse direction (TD). EBSD grain orientation spread analysis demonstrated the unalloyed, binary alloys, and ZX21 alloy were partially recrystallized in the as-deformed state. Very little recrystallization (< 1%) was observed in the deformed 3 wt% Zn alloys.

Table II.1.2.3. Alloy Name, Composition, and the Solution Treatment Temperature and Duration Used for the Six Alloys Studied

Alloy Name	Zn Content (wt.%)	Ca Content (wt.%)	Solution Treatment Temperature (°C)	Solution Treatment Duration
Unalloyed	0	0	n/a	24 hours
X0	0	0.1	500	24 hours
X1	0	0.5	500	24 hours
ZX21	1.8	0.5	350	24 hours
ZX30	3	0.1	350	24 hours
ZX31	3	0.5	350	24 hours

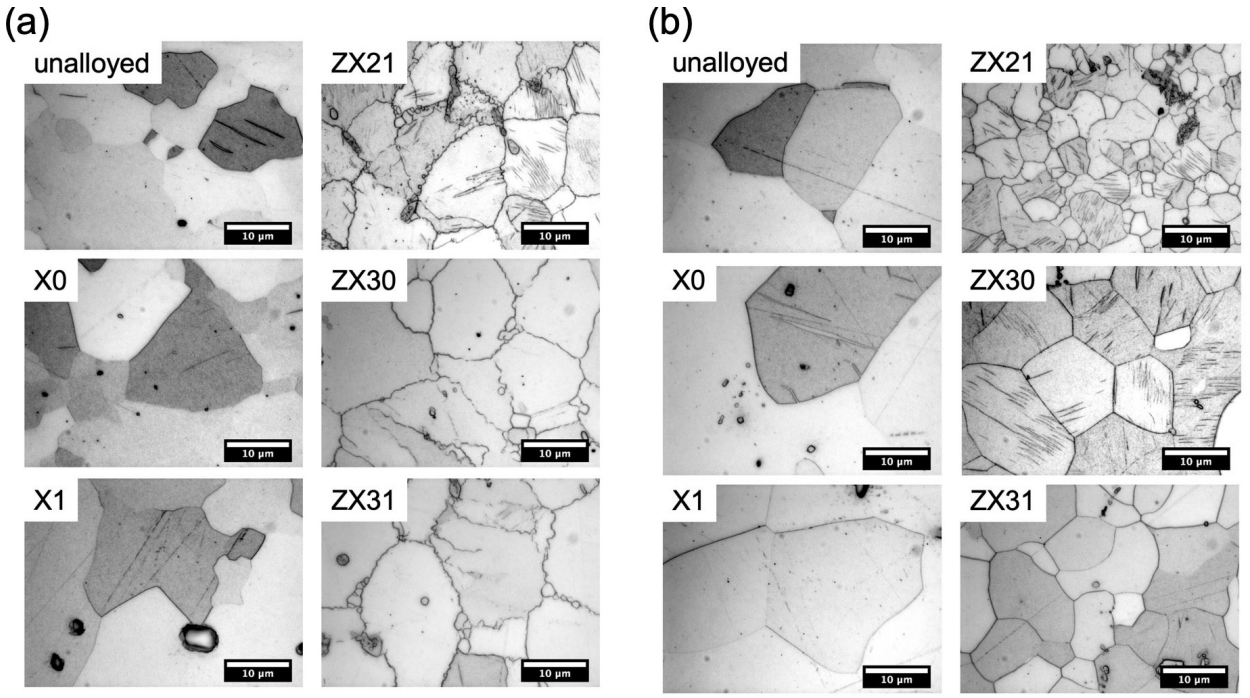

Figure II.1.2.8. Optical micrographs of the alloys studied in the (a) as-deformed and (b) annealed conditions. The rolling direction is vertical. Source: University of Michigan.

Little texture evolution occurred during the 30-minute post-deformation annealing treatment at 350°C in the unalloyed and binary alloys, though some grain growth did occur. Static recrystallization led to a dramatic change in texture in the alloys containing 3 wt% Zn. Though formability has not yet been assessed in these materials and texture alone does not control formability, the non-basal textures observed in the annealed ZX30 and ZX31 alloys show promise in developing a Mg sheet with high formability and reduced in-plane anisotropy.

Determine Constitutive Behaviors of Mg Alloys

The activities for PNNL at the mesoscale consisted of two tasks: (1) microstructure-based ductility and formability predictions; and (2) small-scale *in situ* experiments for model input and validations. These two tasks aim at establishing the fundamental relationships between alloy compositions and microstructural attributes, which are in turn determined by processing, to the deformation fundamentals of the different slip and twin systems for the currently available alloys and the new Mg alloy compositions to be identified in the program, thereby providing the quantitative multiscale linkages for sheet formability simulations. Key accomplishments are summarized below.

Materials

Two binary Mg alloys—Mg-0.2Ca (at. %) and Mg-1.5Sn (at. %)—were received from UF, denoted as Batch #1 (not to be confused with similar designations for four EFP Mg sheet batches being evaluated for formability). In March 2020, UF sent a new batch of binary Mg alloys (i.e., Batch #2), as shown in Table II.1.2.4.

Table II.1.2.4. The Binary Mg Alloy Samples of Batch #1 and Batch #2

Batch #	Composition (at.%)	Cold-rolled	Recrystalized
1	Mg-0.2Ca	20% reduction	400° for 120 hours
1	Mg-1.5Sn	20% reduction	500° for 24 hours
2	Mg-0.2Ca	15% reduction	400° for 120 hours
2	Mg-1.5Sn	15% reduction	500° for 24 hours

In situ Neutron Diffraction

In situ neutron diffraction has been widely used to investigate the mesoscopic characteristics, such as lattice strain evolution of individual hkl diffraction, peak intensity changes by grain reorientation, and peak broadening resulting from local strain during plastic deformations. Two samples cut from recrystallized Batch #1 Mg alloys were used for *in situ* neutron diffraction tensile test carried out at RT with a strain-rate of 10^{-6} s^{-1} at the VULCAN Diffractometer of SNS at ORNL. Representative neutron diffraction spectra from Bank 1 and Bank 2 for recrystallized Batch #1 Mg-0.2Ca sample were obtained.

In situ Synchrotron X-ray Diffraction

Synchrotron X-ray diffraction (XRD) is a powerful and efficient technique to investigate the deformation behaviors of bulk materials under *in situ* loading, due to its good penetration ability and flexible set up with loading and heating equipment. Various challenges with using lab-based XRD systems motivated PNNL to apply for using the exceptionally high-intensity X-rays at the APS at ANL with a high penetrating power, which is suitable to capture real-time crystallographic changes occurring in the 1.2 mm thick Mg alloy plates during tensile deformation without needing to interrupt the tests for data collection. Hence, all Batch #2 samples were investigated by Synchrotron XRD at the beamline 11-ID-C at the APS. Spotty patterns of diffraction rings observed indicated the grain size is relatively large compared to the beam size (0.2 mm). Other information collected or calculated included the integrated XRD spectrum and the lattice strain calculated using the lattice spacing, which indicates the development of elastic intragranular strain-induced by slips or twinning during the deformation. Due to the small beam size of synchrotron and relatively large grain size, the texture measured by XRD was not successful.

Additional analysis of texture of an as-rolled condition, as well as deformation texture, will be conducted in FY 2021 by EBSD technique. The SEM backscattered imaging will be used to reveal key features of the microstructure before and after tensile deformation. This information will be passed on to Task 1 focused on microstructure-based mesoscale modeling capability to predict the ductility and formability of a wrought Mg sheet with the grain-level deformation heterogeneities induced by texture, grain size, critical resolved shear stress (influenced by alloy chemistry) by accounting for different slip and twinning modes. The critical resolved shear stresses for different slip and twin systems for these alloys will be obtained by the *in situ* neutron diffraction measurements as a part of Task 2 in conjunction with DFT modeling from University of Illinois. The *in situ* data will be used in conjunction with an elastic-viscoplastic self-consistent model that will be developed to fully understand the deformation mechanisms under different conditions and to quantify the critical resolved shear stress of the available slip and twinning modes, as well as the elastic and plastic strains for various grain families in alloys of different compositions.

Material Property Measurements for Modeling Formability of EFP

While focused material testing and texture characterization was continued due to the sourcing of a new batch (Batch #4) of wide width EFP Mg alloy sheets from PPM (required for warm forming the demonstration automotive door panels in FY 2021), the emphasis in FY 2020 technical effort shifted to development and optimization of the material cards (MAT233) for FEA using LS-DYNA, and their validation in baseline warm forming simulations of medium size parts such as a cross-form, which incorporates similar draw depths as the demonstration door inner and outer panels. The Data Fit/Modeling team generated the representative hardening curves and material cards to capture the force-displacement response obtained from various mechanical tests for different mesh sizes, and also generated regularized forming limit diagrams for enabling simulations over a

range of temperatures and strain rates. Validation of these material cards was carried out over two rounds of cross-form experiments conducted at EWI to identify a warm forming process window for the Batch #1 and #4 alloys, and comparison to ZEK100 alloy, which was a major achievement in FY 2020. The ongoing improvement and application of material cards for final door forming simulations and correlation with warm forming experiments will be the emphasis for FY 2021. Selected accomplishments are summarized below.

PNNL and FADI-AMT completed a comprehensive test matrix of elevated temperature tension tests on Mg EFP sheet (Batch #1) corresponding to more than 100 tests. The test matrix comprised three temperatures (i.e., 150°C, 200°C, and 250°C), four strain rates (i.e., 0.004/s, 0.01/s, 0.1/s, and 0.5/s), and three in-plane directions (i.e., 0° (rolling direction [RD]), 45° and 90° TD, and at least three repeats for each test condition). Sample strain was captured using the DIC technique to provide high spatial and temporal resolution results and potentially capture any subtleties, such as micro-yielding, that were first reported by PNNL during RT testing of this alloy in previous fiscal years. Digital image correlation-based high-resolution data was also necessary to support the mesh regularization in finite element modeling being performed by project partners (i.e., Inal Tech and Vehma) to enable accurate stamping simulations of the prototype Mg door. After completion of the test matrix, the team analyzed the mechanical behavior of Mg EFP sheet (i.e., in-plane anisotropy, YS, work hardening and ductility) as a function of the test parameters and vendor's material batch, and the implications for stamping operations.

Figure II.1.2.9 shows the effect of strain-rate and in-plane orientation on the stress-strain curves at 250°C. The data shows that the stress for the initial work hardening rate at 0.5/s (e.g., the highest strain-rate used in this work) was significantly greater than that at 0.004/s (e.g., the slowest strain-rate used in this work) irrespective of the in-plane orientation. Further, the anisotropy at this temperature seems to be more evident at the higher strain-rate than at the lower strain-rate. The data also shows that following necking (e.g., maximum in the stress-strain curve), the rate of softening was also greater at the higher strain-rate than at the lower rate.

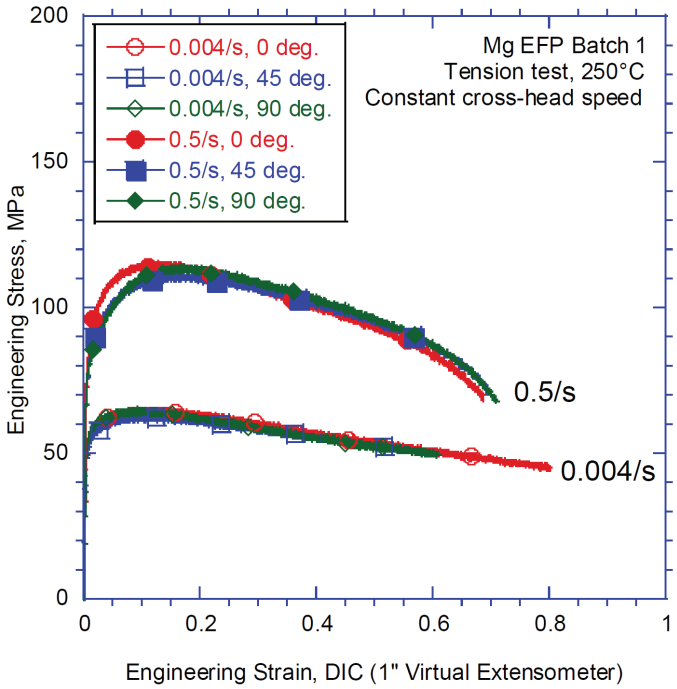

Figure II.1.2.9. Engineering stress-strain curve of Mg EFP (Batch #1) at 250 °C showing the effect of strain-rate on the flow curves along different in-plane orientations. Source: PNNL.

Figure II.1.2.10 shows the effect of temperature on the stress-strain curves in 0 degree, and that post-necking softening in Mg EFP under the current test conditions seems to be relatively temperature independent. Plastic deformation in Mg is known to be a complex interplay between the original sheet texture and the activation of different slip and twinning systems as a function of temperature and strain rates. Further, there is also a likelihood of Mg EFP undergoing dynamic recrystallization at high temperatures. Therefore, the mechanical test data needs to be analyzed in combination with microstructure (e.g., twin volume fraction, recrystallization) texture analysis and modeling to understand this alloy's behavior that will then be leveraged for successful stamping of a door panel.

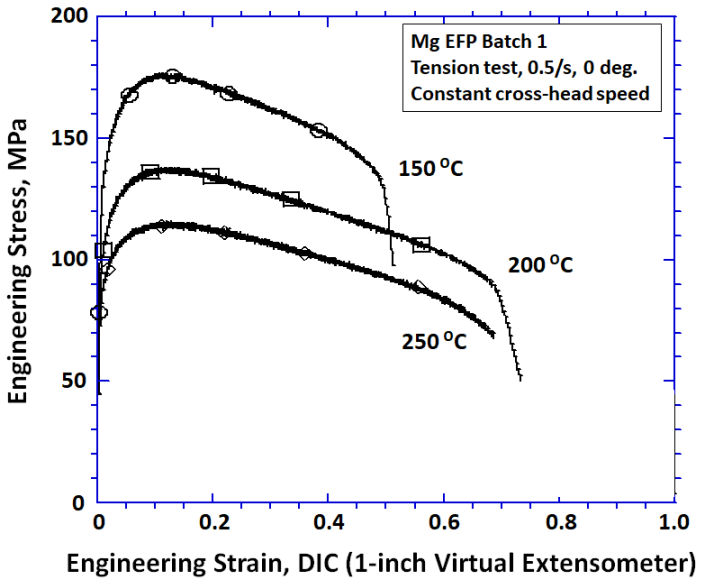

Figure II.1.2.10. Engineering stress-strain curve of Mg EFP (Batch #1) at 0.5/s and in RD showing the effect of test temperature. Source: PNNL.

ICME Modeling of EFP Formability

The UP and Inal Tech, Inc. are developing ICME methods coupled with experimental studies combining data from several batches of EFP and data tools to simulate thermomechanical processing for improved and cost-effective formability. A continuum model is being developed for textured Mg polycrystalline sheet materials that deform by slip and twinning mechanisms to be used in simulations of warm forming. Primary features of the anisotropic elastic-plastic model account for a continuous evolution of (i) the evolution of the anisotropy differential (e.g., strength in the principal direction of anisotropy relative to the strength in the TD); (ii) the strength differential (e.g., tension/compression asymmetry); and (iii) the evolution of the material-symmetry (e.g., the rotation of the orthotropic triad that characterizes the symmetry of the microstructure). For non-uniform deformations, such as those found in forming a car door panel, those properties will vary continuously throughout a component.

In the first part of the work, the ICME framework has been developed to generate a continuum model that is based on the LS-DYNA *MAT233 material card. The *MAT233 material card is based on an orthotropic yield criterion for hcp metals that was proposed by Cazacu *et al.* [13]. This framework employs already existing codes/models/subroutines based on the works of Inal *et al.* [14], Lévesque *et al.* [15], and Kohar *et al.* [16],[17]. The *MAT233 and *MAT36 cards, for 200°C, have been developed for EFP Batch #3, based on mechanical testing results (in the form of uniaxial tension along RD, TD, and 45° direction) shown in Figure II.1.2.11(a) provided by FADI-AMT, interrupted strain EBSD measurements (performed by Inal Tech Inc.) shown in Figure II.1.2.11(b), and virtual testing performed by the calibrated crystal plasticity model resulting in the pole figure in Figure II.1.2.11(c).

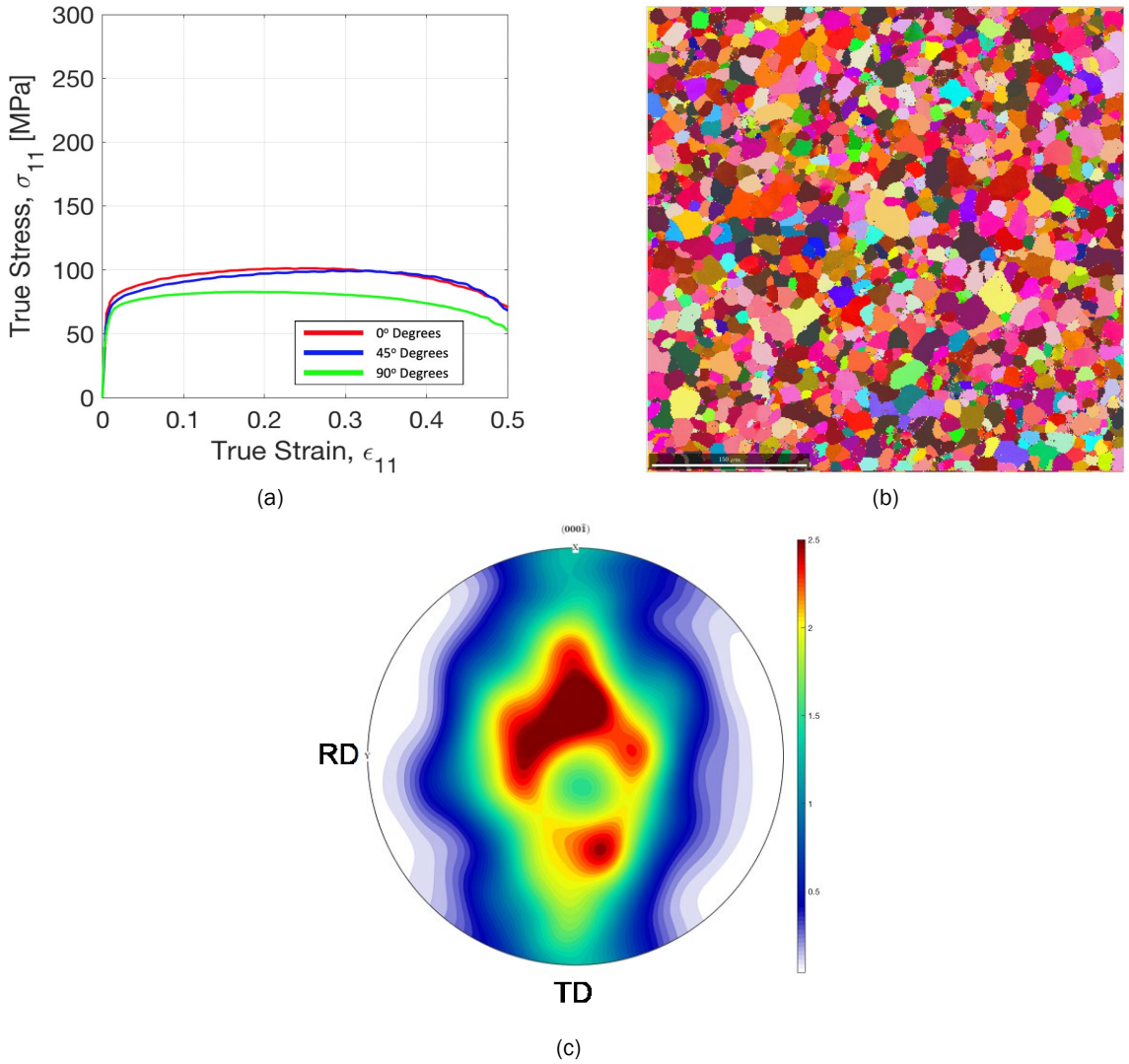

Figure II.1.2.11. (a) Uniaxial stress-strain curves. (b) Initial EBSD. (c) Pole figure. Source: Inal Tech Inc.

In the second part, the ICME framework has been developed for Batch #1 EFP alloy to generate a continuum model that is based on the *MAT233 material card in LS-DYNA. The experimental uniaxial tensile testing of Batch #1 for EFP that was obtained by PNNL, as well as the EBSD measurements obtained by UM, were used to generate this material card. The ICME framework was used to create the *MAT233 material card at a temperature of 200°C, and a strain-rate of 0.01/s. The ICME framework was employed to provide stress-strain curves for plane-strain tensile in the RD, biaxial tension, and uniaxial compression in the RD and simple shear in the RD. All these curves were employed to develop the *MAT233 card.

In the third part, the experimental uniaxial tensile testing of Batch #1 EFP that was obtained by PNNL was used to generate the material card for EFP; the *MAT233 material card for three temperatures (e.g., 150°C, 200°C, 250°C) and three strain rates (e.g., 0.01/s, 0.1/s, 0.5/s) for three different mesh sizes (e.g., 6.0 mm, 3.0 mm, 1.5 mm). This process required mesh regularization through the inverse finite element method and was performed on two different developer versions of LS-DYNA (DEV142332 and DEV148991) due to numerical instabilities encountered with the earlier versions of LS-DYNA.

The method of inverse finite element method is used to identify the stress-strain response for EFP for use in warm forming simulations. All simulations were analyzed using a developer version of the nonlinear explicit dynamic formulation of the commercial finite element software LS-DYNA – DEV148991. A prescribed velocity profile that matched the experimental ramp-up to a constant velocity of the apparatus was prescribed to the pulling nodes, as shown in Figure II.1.2.12.

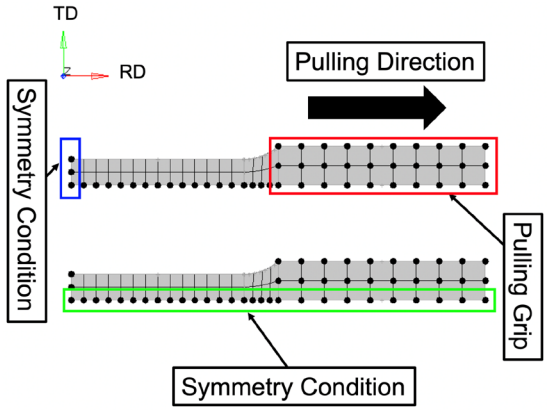

Figure II.1.2.12. BCs of the finite element model. Source: Inal Tech Inc.

Figure II.1.2.13(a) and Figure II.1.2.13(b) present the comparison between simulation and experimental stress-strain responses of EFP for various conditions. Good correlation is achieved through the inverse finite element method. It should be mentioned that for the case of 0.1s-1 strain-rate and the 250°C simulation, the calibration is not as good as the others. This is because the numerical instability (overshooting) problem. Based on the models that were constructed, the *MAT233 material card was not correctly identifying/selecting the correct curves for interpolation for the lowest strain-rate curves.

The fourth part of this work is the development of enhanced finite element software for simulations of forming that account for the effects of rotations of the material-symmetry axes that characterize anisotropy. These effects result from texture (microstructural) evolution. The model builds on the work of Pan and Bassani [18], which was applied to steel alloys, and the collaboration between Inal and Bassani that utilizes polycrystalline simulations, which was applied to an Al alloy [16]. This task necessarily followed the development of the *MAT233 material card outlined above, which was required for the first simulations of door panel stamping. This enhanced material model based on Batch #1 property data is referred to as *MAT233+, since it is also based on the Cazacu *et al.* [13] orthotropic yield criterion for hexagonal closed packed metals. This is not a built-in material model in LS-DYNA but requires a user-defined material subroutine that was developed in previous work. Using *MAT233+, forming limits for off-axis strain states can be computed using Marciniak and Kuczynski calculations, which were carried out for other constitutive models that include anisotropy and tension-compression asymmetries associated with non-Schmid slip non-associated flow effects [19].

In FY 2021, polycrystalline simulations partly fit to available experimental data for EFP will be used to determine the parameters that determine the material-symmetry rotations in the plastic flow relations, and the simulations for Batch #1 will be carried out. The deliverable user material model for *MAT233+ will enhance the capabilities for the forming simulations that will be provided to the door product and forming process modelers and others at the end of this project. The final step is to build the finite element user material model designated as *MAT233+, to extend the Cazacu-Plunkett-Barlat flow rule to account for material-symmetry rotations (microstructural rotations) for Batch #1.

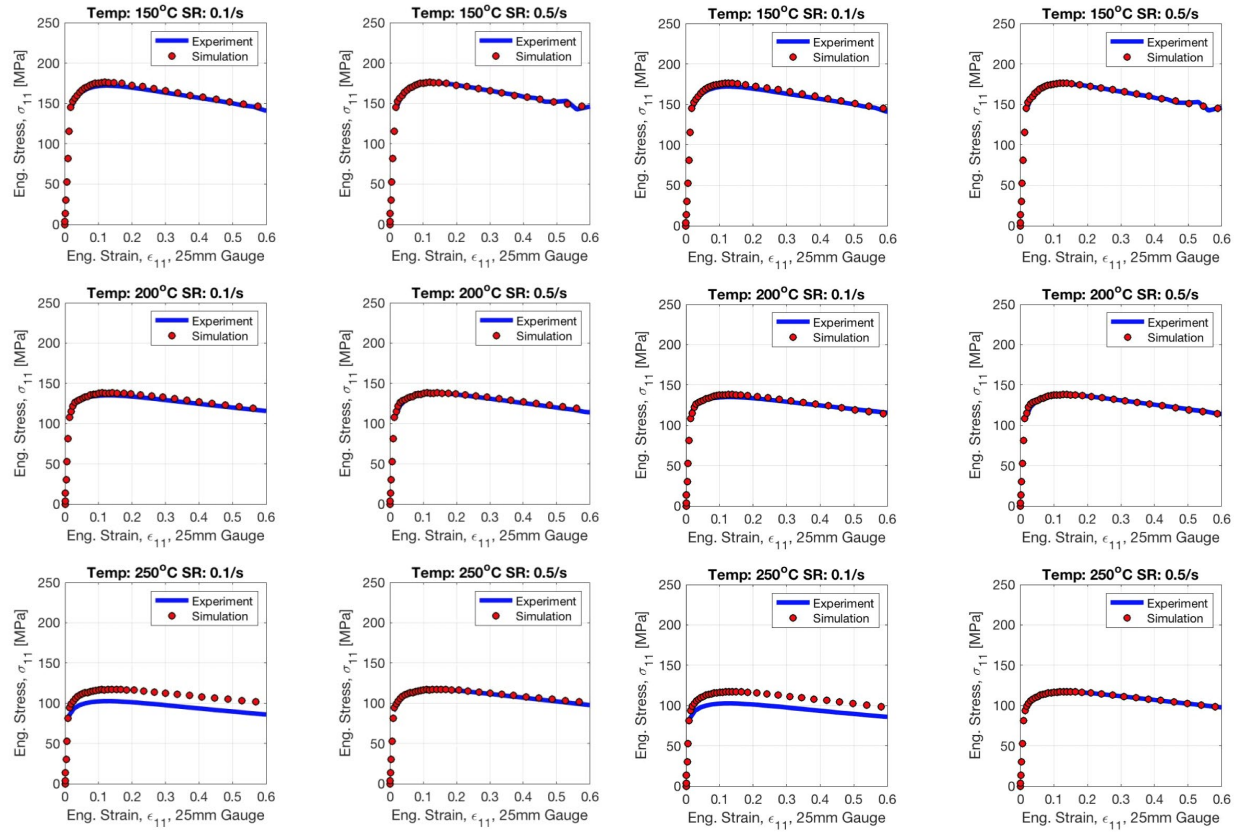

Figure II.1.2.13. Comparison between simulation and experimental stress-strain responses of EFP for various conditions for: (a) the 3mm mesh size; and (b) the 1.5mm mesh size. Source: Inal Tech Inc.

Coil-applied Anticorrosion Treatments

During FY 2020, Xtalic and Henkel completed their respective subtasks and met key deliverables for pursuing coil-applied coatings to protect the Mg sheet from corrosion prior to being formed. They collaborated with other task members to deposit their pretreatments on EFP sheet blanks for producing a "Mini-Door" (i.e., a dimensionally scaled-down component with selected door features that has coil pretreatment [Henkel], forming lubricant [Quaker or Fuchs], welding [AET], and corrosion pretreatment and paint [PPG]). In November 2019, Henkel deoxidized and applied process "D" to EFP panel sections of the Mini-Door to be distributed to the appropriate lubricant supplier.

In addition to the Mini-Door parts, Henkel deoxidized and applied process "D" coil pretreatment to approximately 100 8" x 12" EFP panels and shipped to Task 3 members for subsequent oil application and/or testing. EFP panels with Henkel pretreatment "D" were tested side-by-side with a Zn treatment produced by Xtalic, and electrogalvanized steel panels supplied by ACT Test Panels, LLC, as a control in a modified version of ASTM D 2247 –"Standard Practice for Testing Water Resistance of Coatings in 100% Relative Humidity" [20].

Humidity Testing and Results

Henkel performed humidity testing in a 100% relative humidity chamber at 100°F for periods of 24 h, 48 h, and 72 h. The samples were tested in triplicate with untreated cut edges. The coupons were visually evaluated and photographed, and glow discharge optical emission spectroscopy was performed to measure surface oxidation.

The results suggest EFP Mg with Xtalic Zn coating and Henkel pretreatment process "D" coated Mg both fall short in providing corrosion protection compared to galvanized steel. After 72 hours of humidity exposure, Henkel pretreatment process "D" showed oxidation of the underlying Mg, indicating the protection is limited to < 72 hours of 100% relative humidity. The Xtalic Zn coating showed surface variation where some areas have very little degradation where other areas had a deep layer of oxidation trough the Zn layer in into the underlying Mg. In addition, both Henkel process "D" and Xtalic Zn coating had changes in surface texture that may be difficult to correct during body-in-white pretreatment in the OEM paint shop, creating challenges for use in the Class A areas of an automobile. The testing indicated that both Henkel pretreatment process "D" and Xtalic Zn treatment can provide limited short-term protection, but neither could match the humidity corrosion resistance of galvanized steel.

E-Coated Lap-Shear Joints in B117 Salt Spray Corrosion Testing

EFP lap-shear coupons were e-coated (BASF Cathogard 800) and tested in ASTM B117-19 "Salt Fog" [21] environment for 30 days to evaluate for weakness in corrosion resistance in the region of the adhesive joint. Triplicate lap-shear coupons were tested using EFP with different surface conditions.

Figure II.1.2.14 shows example results Henkel captured on one such set of lap-shear coupons. Coupons with process "D" showed corrosion undercutting from the edges but no increased corrosion associated with the adhesive joint. EFP coupons with pretreatment process "D" demonstrated significantly better resistance to corrosion than those without it.

With the completion of this task, Henkel has demonstrated its coil pretreatment process "D" includes deoxidizing and cleaning products that effectively removed Mg oxides/hydroxide followed by pretreatment that has helped increase corrosion resistance in 100% humidity testing and salt fog testing.

(a) (b) (c)

Figure II.1.2.14. Example results of Henkel tests on lap-shear joints in corrosion testing, showing the: (a) initial condition with solvent cleaned before being e-coated; (b) post testing condition; and (c) post testing condition with loose material removed. Source: Henkel.

Lubricant Development and Testing

Fuchs and Quaker-Houghton have completed their development and optimization of lubricants for the Mg sheet-forming process, delivering Renoform 1102 ALWF and QUAKERDRAW® 450 MAG, respectively. Both lubricants were evaluated in cross-form tests conducted at EWI at the end of FY 2019 on two batches (Batches #1 and #3) of the AZ21 EFP sheet with Henkel pretreatment "D" and Xtalic's Zn-coated blanks. The Fuchs lubricant was more successful in forming acceptable parts over a broader range of forming conditions and was selected for a new round of cross-form stamping conducted in FY 2020 on the EFP Batch #4 sheets sourced from PPM. The USAMP team plans to use it for the demonstration door panel forming trials in early FY 2021. Renoform 1102 ALWF is designed for application and submission as a dry or drying film through the blank heating oven and then into the stamping die as a dry film.

Joining Process Evaluation and Development

Most of AET's efforts in FY 2020 focused on RSW weldability studies and weld process optimization of AZ21 sheet material in bare and pretreated conditions, both with and without forming lubricants, as well as Arplas and laser welding of bare AZ21 sheet material without forming lubricants.

RSW weldability evaluations conducted to date (including previous research periods) showed:

- The 50-mm radius F-type electrode was successful in welding all coating/lubricant combinations being considered except for Henkel process "D" pretreated material and bare AZ21 Batch #3 with Fuchs lubricant.
- The multi-ringed domed (MRD) electrode was successful in welding AZ21 in all coating/lubricant configurations being considered in this project, including the Henkel pretreated materials and Fuchs lubricated materials.
- Neither the 6-mm ball, nor the 6-mm truncated electrodes, were successful in welding AZ21 in any of the evaluated coating/lubricant configurations and are no longer being considered for additional evaluation or development going forward.

Once the optimum electrode types had been evaluated for each coating/lubricant combination, AET conducted studies to optimize weld parameters to achieve good welds for all three lubricant choices with a single set of process parameters for each coating/electrode configuration shown in Table II.1.2.5.

Table II.1.2.5. Coating/Electrode/Lubricant Combinations Investigated in FY 2020

Coating	Electrode	Lubricant		
Bare AZ21 Batch #3	F-type and MRD	No lube		
	MRD	No lube	Fuchs lube	
Henkel Process D	MRD	No lube	Fuchs lube	Quaker lube
Xtalic Zn Plate	F-type and MRD	No lube	Fuchs lube	Quaker lube

Figure II.1.2.15 shows an example of optimizing the weld current process window for the Xtalic Zn plate pretreatment for all three lubricant choices using an MRD electrode at 1,200 lb. weld force and 50 ms weld time. Figure II.1.2.15(a) shows experimental weld data produced over a relatively wide range to identify an acceptable process window for each lubricant configuration. Figure II.1.2.15(b) shows a narrowed process window that is suitable for producing good welds for all three lubricant configurations. The hollow data points indicate the occurrence of weld expulsion while the highlighted area in Figure II.1.2.15(b) indicates the optimized weld current range. Note that it was not possible to develop a similar optimized process range for all coating/electrode/lubricant combinations evaluated as part of the study.

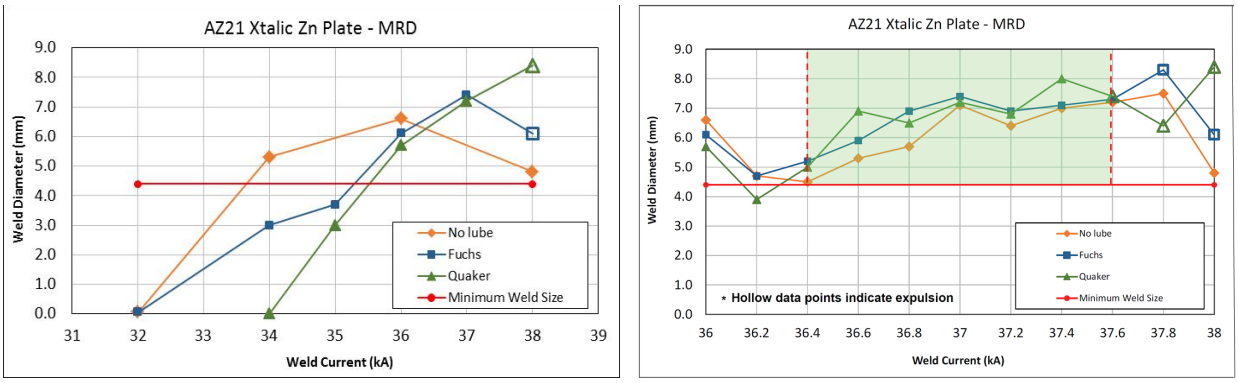

(a) (b)

Figure II.1.2.15. Example of process optimization efforts for welding of AZ21 plated with: (a) Xtalic Zn plating; and (b) MRD electrodes. Source: AET.

For bare AZ21 Batch #3 with no lube, two F-type electrode life studies were conducted at weld parameters from within the optimized process range for that combination. In both cases, the electrodes achieved a life of ~200 good welds (with only acetone cleaning prior to start of the test), which was substantially better than the 15-20 good welds observed in earlier studies.

AET continued investigating modifications to the Arplas welding process to produce welds without visible surface welding cracks. This was accomplished by substantially reducing heat input. However, reducing the heat input enough to eliminate visible surface cracks resulted in substantially reduced weld strength and still did not eliminate internal cracks. Consequently, AET is no longer evaluating Arplas welding.

AET analyzed laser welds produced on bare AZ21 Batch #3 with no lubricant to identify any trends affecting weld depth and width because of weld speed and power. Work continued to optimize laser welds produced for bare AZ21 Batch #3 with no lubricant and the addition of 0.1 mm shims between the sheets near the weld to produce a slight gap similar to what is seen in a typical production application. Figure II.1.2.16(a) shows a cross-section of a weld produced at 800 W and 2.2 m/min, while Figure II.1.2.16(b) shows a cross-section of a weld produced at 1000 W and 4.0 m/min. Smaller welds with higher penetration were achieved at the higher power setting and weld speed.

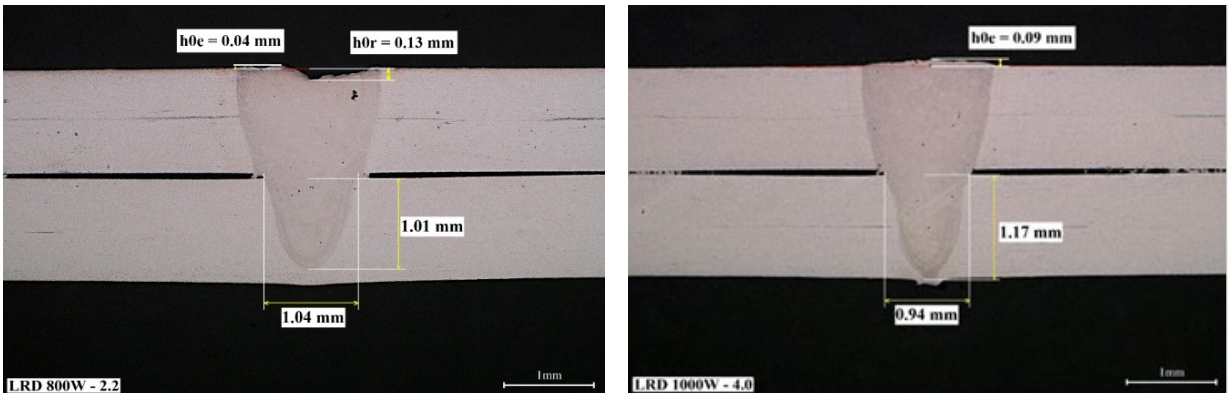

(a) (b)

Figure II.1.2.16. Laser weld cross-sections at: (a) 800 W at 2.2 m/min; and (b) 1000 W at 4.0 m/min. Source: AET.

Preparing for E-coating of Mini-Door Panels

A typical pretreatment line sequence is shown in Figure II.1.2.17. The following sections summarize progress made in FY 2020 in metal treatment to the cleaning and pretreatment of EFP.

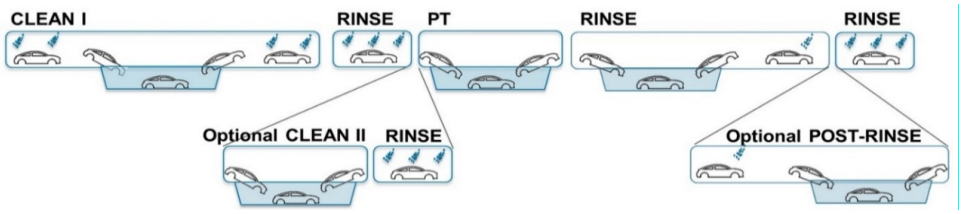

Figure II.1.2.17. A typical automotive pretreatment sequence, prior to electrocoat. Source: PPG.

Multi-metal Couples Joined Using Rivets + Adhesive Prior to Cleaning

The goal of this subtask was to determine the level of galvanic corrosion in multi-metal couples of EFP, cold-rolled steel (CRS), hot-dip galvanized e-coated (HDGE), and/or AA6111. The best cleaning and pretreatment processes were examined with systems that protect all metals. In this work, couples that were joined with adhesive and rivets prior to cleaning and pretreatment were evaluated. In Figure II.1.2.18, the visual evaluation of the multi-metal couples following corrosion testing are shown, with the three-week corrosion results for the CRS containing couples and the six-week corrosion results of the remaining adhesive and rivet couples. The pretreatment system for couples containing CRS requires pretreatment (PT) 1, while EFP requires treatment with a cleaning (C) 2 or C2.4 type bath to achieve corrosion protection. Images of CRS/EFP were taken after three weeks of corrosion testing, while the images of the other couples were taken after six weeks of corrosion testing. In these couples, the substrate that will corrode more is on the bottom for easier visualization. Based on the corrosion results, it appears that the pretreatment process of C2 or C2.4 followed by PT 1 is the most promising solution for mixed substrates thus far.

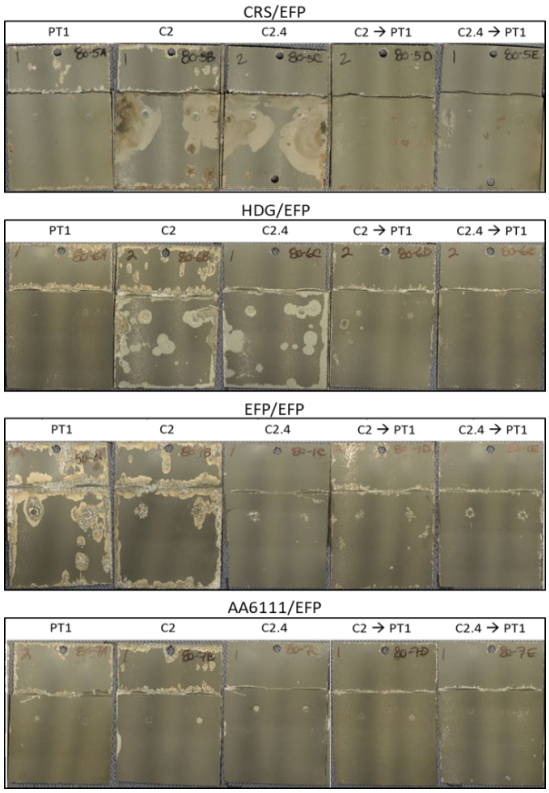

Figure II.1.2.18. EFP/other substrate couples bonded using rivets and adhesive after cyclic corrosion testing. Source: PPG.

PPG Coating Compatibility with Quaker Panels

The goal of this work is to test the best PPG cleaning and pretreatment processes, a two-step process (e.g., C1 followed by C2.4) and a three-step process (e.g., C1, then C2.4, and followed by PT8) on panels received from Quaker (e.g., Henkel/Quaker and Xtalic/Quaker), as well as an as-received EFP control. The panels were subjected to cyclic corrosion testing and evaluated after C1 to determine water break performance and the amount of exposure time to C1 in order to be cleaned showing that the Xtalic/Quaker samples required the most amount of cleaning, followed by Henkel/Quaker, and then EFP as-received. The two-step cleaning and pretreatment process provides sufficient protection and would be more desirable than a three-step process.

Panels were pretreated with either a two- or three-step process, then e-coated, and subjected to ASTM G-85 A2 filiform corrosion testing for three or six weeks. For Henkel coil pretreated samples and the as-received EFP, the two-step cleaning and pretreatment process appears to provide sufficient protection and is more desirable than a three-step process. Cross-hatch testing was completed on the Quaker EFP panels. There were no differences between the Quaker (e.g., Henkel/Quaker and Xtalic/Quaker) EFP and the as-received EFP control with the two-step process.

Additionally, the two-step process above and an additional PPG cleaning and pretreatment process (e.g., C1, then C2.4, followed by PT1) were evaluated on Xtalic/Quaker EFP panels to address the loss in corrosion performance due to surface blistering. The Xtalic/Quaker EFP panels went through three weeks of corrosion testing and will undergo three additional weeks of testing. Results indicate that the panels do not experience the same amount of surface blistering previously seen, and the least amount of blistering was observed with the new three-step process (e.g., C1, then C2.4, followed by PT1).

Optimization of Pretreatment Formulations

The goal of this work is to evaluate existing and improved PPG cleaning and pretreatment processes on different substrates to be used on a multi-metal system. Three PPG cleaning and pretreatment processes were evaluated (e.g., C1 followed by C2.4, C1 followed by C2.21, and C1 followed by PT1). EFP and AA6111 panels pretreated with C2.4 and C2.21 performed the best, while panels pretreated with PT1 performed the worst. CRS panels pretreated with C2.4 performed the worst and were removed from testing after three weeks.

Processes using two cleaning steps and a pretreating step can adequately protect rivet- and adhesion-joined and unjoined EFP, AA6111, HDGE, and CRS substrates in the same line. The compatibility assessment found that the cleaning and pretreatment processes provided corrosion protection on Xtalic/Quaker and Henkel/Quaker EFP comparable to bare EFP. Progress was made on the optimization of novel cleaning solutions to provide a compact process for treating EFP along with AA6111 and CRS.

Production of Large Automotive Body Components

During FY 2020, Vehma participated in two rounds of cross-form testing at EWI and conducted correlation studies using LS-DYNA simulations with the MAT233 (delivered by Inal Tech) material card to calibrate and prepare for door simulations. Vehma performed the cross-form die simulation correlation analysis. Due to the plastic behavior of the material model, the strain values did not correlate between Argus measurements and simulation. The results and concerns were reviewed with the USAMP team and it was agreed to move forward with door outer simulations using the best setting of the cross-form simulations. Vehma performed the door outer panel forming simulations. Low Class A surface strains were achieved on the door outer panel. The simulation results, concerns, product modifications, and the die changes were reviewed with USAMP after which die modifications were kicked off, as shown in Figure II.1.2.19 and Figure II.1.2.20.

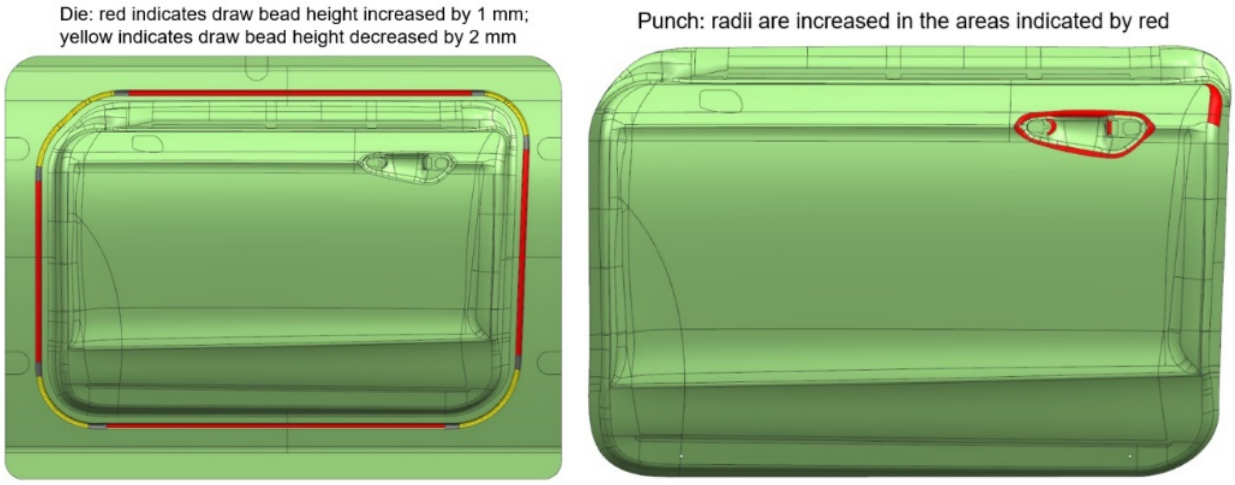

(a) (b)

Figure II.1.2.19. Door product modifications showing: (a) a draw bead changes; and (b) radii changes in the door handle area. Source: Vehma.

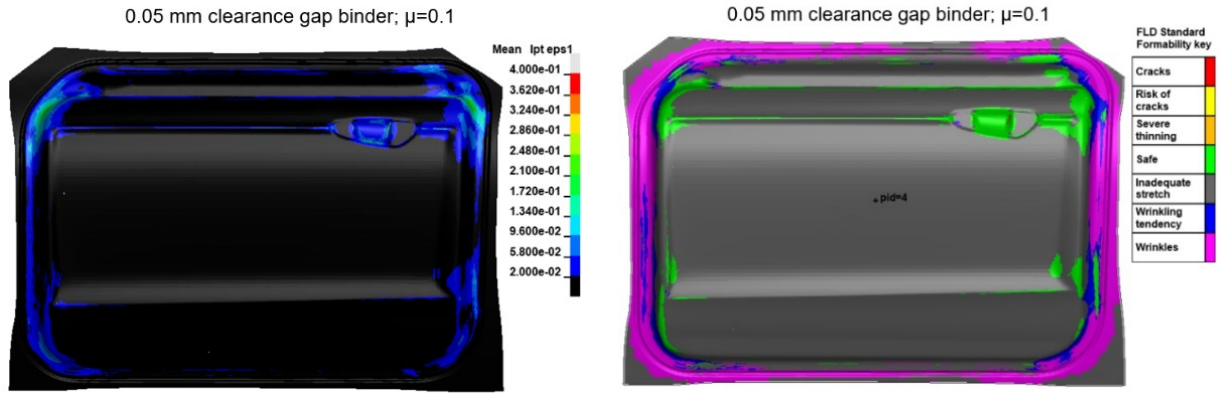

(a) (b)

Figure II.1.2.20. Simulation results predicting: (a) a major strain and (b) a FLD chart showing an acceptable product can be stamped. Source: Vehma.

Demonstration of Components

Tensile testing of coupons cut from cross-form warm-stamped samples was completed and the results used to generate Batch #3 EFP CAE material properties, as shown in Figure II.1.2.21. Vehma and USAMP decided to use the worst-case properties from these tests in CAE simulations of the door assembly with EFP inner and outer panels. Vehma performed a door CAE performance analysis, as shown in Figure II.1.2.22, and concluded that the door will achieve all engineering requirements at a mass of 10.14 kg using a 1.2 mm EFP inner and a 1.1 mm EFP outer stamping. The CAE analyses performed were stiffness and modal, denting and oil canning, check over and sag, and NHTSA Laboratory Test Procedure for Side Impact Protection – FMVSS 214S (Static). The door panels achieve a 62% mass savings relative to the steel baseline panels. With no Nitto patch to enhance stiffness, the outer stamping will need to be 1.25 mm thick and the mass savings are reduced by 150g (to 60%).

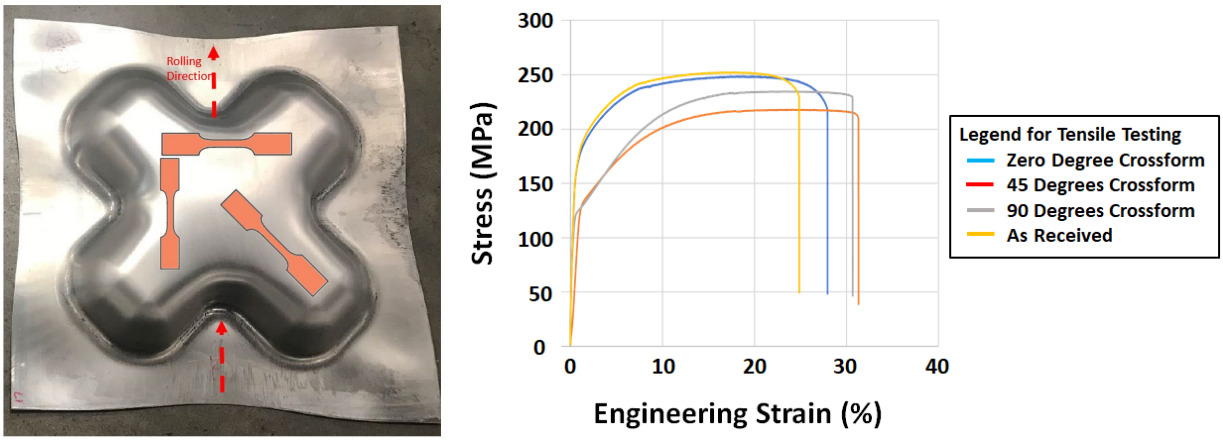

(a) (b)

Figure II.1.2.21. (a) Warm-stamped cross-form part showing material property measurement directions. (b) The stress-strain curve for 90-degree sheet orientation used for CAE. Source: Vehma.

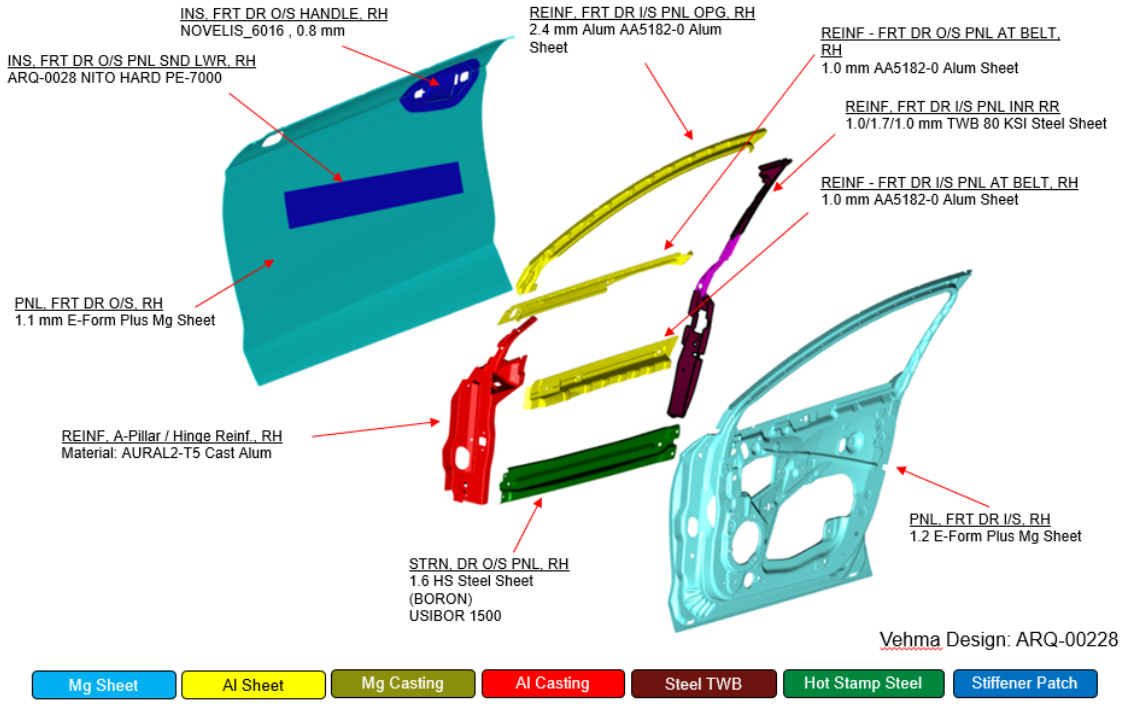

Figure II.1.2.22. Demonstration door computer-aided design bill of materials. Source: Vehma.

In FY 2021, Vehma will perform door outer panel die modifications and prepare the die for manufacturing door outer panels at Promatek. Vehma will perform door inner forming simulations, die modifications, and then manufacture door inner panels at Promatek. Finally, Vehma will conduct simulations to evaluate the MAT233+ card when delivered by Inal Tech.

Conclusions

During FY 2020, USAMP's university team has nearly completed computational modeling studies to predict elemental solutes for viable binary and ternary alloy chemistries that are free of RE elements. Constitutive material characterization and DFT studies for these novel alloys will be completed in FY 2021.

Material property testing and texture characterization of four batches of EFP (AZ21) Mg sheet were completed. Material cards were developed for baseline FEA formability simulation studies using Batch #1 property measurements and characterization data. An initial version of material card MAT233 was applied in warm forming simulations of the cross-form and good correlation was obtained with experimental parts. A second round of warm forming trials on the cross-form confirmed that EFP Batch #4 is closer in formability to Batch #1. The data were utilized in ICME-based crystal plasticity material models and LS-DYNA material cards were developed for modeling formability over a range of forming temperatures, strains, and FEA mesh sizes. The application of MAT233 for simulations of door outer and inner panels is in progress and will be used to drive die modifications prior to warm forming trials on the demonstration parts in FY 2021. An enhanced constitutive model for Mg Sheet with evolving anisotropy is in development and will be delivered in FY 2021 as a MAT233+ card for comparison to forming predictions obtained with the baseline MAT233 card. Initial performance analysis indicates the Mg door panels achieve a 62% mass savings relative to the steel baseline panels.

The coatings research team has completed development and evaluation of low-cost coil-applied pretreatments, and a warm forming lubricant was selected for scale application in planned door panel forming demonstrations. The corrosion coatings team will conduct evaluation of fabricated “mini-door” samples incorporating feasible joining process(es) in FY 2021. Preliminary cost modeling indicates that the Mg door cost is significantly under the $11/kg cost target for several scenarios of coil production cost. The technical cost model will be further refined in FY 2021 to estimate the impact of these technological advances relative to the project goals of demonstrating a low-cost Mg sheet alloy.

Key Publications

1. Cuadrado, W., and M. V. Manuel, 2020, “Connecting dynamic strain aging to deformation processing in magnesium-calcium-based alloys,” *TMS Annual Meeting*, 23–27 February 2020, San Diego, CA, USA.
2. Berman, T. D., and J. E. Allison, 2020, “Relating texture and thermomechanical processing variables in Mg-Zn-Ca alloys,” *TMS Annual Meeting*, 23–27 February 2020, San Diego, CA, USA.
3. Shi, R., J. Miao, T. Avey, and A. A. Luo, 2020, “A new magnesium sheet alloy with high tensile properties and RT formability,” *Sci. Rep.*, Vol. 10, No. 1, pp. 1–10.
4. Shi, R., J. Miao, Z. Li, and A. A. Luo, 2019, “A new magnesium sheet alloy and its multistage homogenization for simultaneously improved ductility and strength at RT,” *Scr. Mater.*, Vol. 171, pp. 92–97.

References

1. Shi, R., J. Miao, T. Avey, and A. A. Luo, 2020, “A new magnesium sheet alloy with high tensile properties and RT formability,” *Sci. Rep.*, Vol. 10, No. 1, pp. 1–10.
2. Chaudry, U. M., T. H. Kim, S. D. Park, Y. S. Kim, K. Hamad, and J.-G. Kim, 2018, “On the high formability of AZ31-0.5 Ca magnesium alloy,” *Materials*, Vol. 11, No. 11, Art. 2201.
3. Berman, T. D., and J. E. Allison, 2020, unpublished research, UM, Ann Arbor, MI, USA.
4. Ozturk, F., E. Esener, S. Toros, and C. R. Picu, 2010, “Effects of aging parameters on formability of 6061-O alloy,” *Mater. Des.*, Vol. 31, pp. 4847–4852.
5. Hirth, S. M., G. J. Marshall, S. A. Court, and D. J. Lloyd, 2001, “Effects of Si on the aging behavior and formability of aluminum alloys based on AA6016,” *Mater. Sci. Eng. A*, Vol. 319–321, pp. 452–456.
6. Yasi, J. A., L. G. Hector Jr., and D. R. Trinkle, 2010, “First principles data for solid solution strengthening of magnesium: From geometry and chemistry to properties,” *Acta Mater.*, Vol. 58, No. 17, pp. 5704–5713.

7. Ghazisaeidi, M., L. G. Hector Jr., and W. A. Curtin, 2014, “Solute strengthening of twinning dislocations in Mg alloys,” *Acta Mater.*, Vol. 80, pp. 278–287.

8. Buey, D., L. G. Hector Jr., and M. Ghazisaeidi, 2018, “Core structure and solute strengthening of second-order pyramidal < c+ a> dislocations in Mg-Y alloys,” *Acta Mater.*, Vol. 147, pp. 1−9.

9. Ansara, I., A. T. Dinsdale, and M. H. Rand, eds., 1998, *COST 507: Thermodynamical Database for Light Metal Alloys, Vol. 2*, EUR 18499, Office for Official Publications of the European Communities, Luxembourg, Belgium.

10. Otis, R., and Z.-K. Liu, 2017, “pycalphad: CALPHAD-based computational thermodynamics in python,” *J. Open Res. Software*, Vol. 5, No. 1, p. 1.

11. Wang, T., L. Jiang, R. K. Mishra, and J. J. Jonas, 2014, “Effect of Ca addition on the intensity of the RE texture component in extruded magnesium alloys,” *Metall. Mater. Trans. A*, Vol. 45, No. 10, pp. 4698–4709.

12. Humphreys, F. J., and M. Hatherly, 2004, *Recrystallization and Related Annealing Phenomena*, *2nd ed.*, Elsevier, Amsterdam, Netherlands.

13. Kohar, C. P., A. Brahme, F. Hekmat, R. K. Mishra, and K. Inal, 2019, “A computational mechanics engineering framework for predicting the axial crush response of Al extrusions,” *Thin Wall. Struct.*, Vol. 140, pp. 516–532.

14. Inal, K., R. K. Mishra, and O. Cazacu, 2010. “Forming simulation of aluminum sheets using an anisotropic yield function coupled with crystal plasticity theory,” *Int. J. Solids Struct*., Vol. 47, No. 17, pp. 2223–2233.

15. Lévesque, J., K. Inal, K. W. Neale, and R. K. Mishra, 2010, “Numerical modeling of formability of extruded magnesium alloy tubes,” *Int. J. Plast.*, Vol. 26, No. 1, pp. 65–83.

16. Kohar, C. P., A. Brahme, J. Imbert, R. K. Mishra, and K. Inal, 2017, “Effects of coupling anisotropic yield functions with the optimization process of extruded aluminum front rail geometries in crashworthiness,” *Int. J. Solids Struct.*, Vol. 128, pp. 174–198.

17. Kohar, C. P., J. L. Bassani, A. Brahme, W. Muhammad, R. K. Mishra, and K. Inal, 2019, “A new multiscale framework to incorporate microstructure evolution in phenomenological plasticity: Theory, explicit finite element formulation, implementation and validation,” *Int. J. Plast*., Vol. 117, pp. 122–156.

18. Bassani, J., and H. Pan, 2012, “A phenomenological model for microstructural evolution during plastic flow.” *CR Mec*., Vol. 340, pp. 369–377.

19. Racherla, V., and J. L. Bassani, 2007, “Strain burst phenomena in the necking of a sheet that deforms by non-associated plastic flow,” *Model. Sim. Mat. Sci. Eng.*, Vol. 15, pp. S297–S311.

20. ASTM International, 2015, Standard Practice for Testing Water Resistance of Coatings in 100% Relative Humidity, ASTM D2247-15, West Conshohocken, PA, USA.

21. ASTM International, 2019, *Standard Practice for Operating Salt Spray (Fog) Apparatus*, ASTM B117-19. West Conshohocken, PA, USA.

Acknowledgements

This project is a continuing collaboration with many researchers from Ford Motor Company, Fiat Chrysler Automobiles US LLC, GM, and sponsor/support/subrecipient/vendor organizations. The contributions of the following USAMP task leaders to this report are gratefully acknowledged: Leland Decker and Aslam Adam (FCA); Bita Ghaffari and Mei Li (Ford Motor); Lou Hector, Arianna Morales, and Anil Sachdev (GM R&D); Jon Carter and Manish Mehta (M-Tech International LLC); and Gloria Bucciero (Bucciero and Associates).

II.1.3 New Technologies for High-Performance Lightweight Aluminum Castings (National Energy Technology Laboratory/General Motors)

Paul D. Jablonski, Co-Principal Investigator
National Energy Technology Laboratory
1450 Queen Ave SW
Albany, OR 97321
E-mail: paul.jablonski@netl.doe.gov

Qigui Wang, Co-Principal Investigator
General Motors
30003 Fisher Brothers Road
Warren, MI 48093-2350
E-mail: qigui.wang@gm.com

David Weiss, Co-Principal Investigator
Eck Industries
1602 North 8th Street
Manitowoc, WI 54220
E-mail: david.weiss@eckindustries.com

Sarah Kleinbaum, DOE Technology Manager
U.S. Department of Energy
E-mail: sarah.kleinbaum@ee.doe.gov

Start Date: December 27, 2019 End Date: December 27, 2021
Project Funding: $500,000 DOE share: $500,000 Non-DOE share: $0

Project Introduction

Lightweight Al shape castings have widespread applications for structural components in the automotive, aerospace, and general engineering industries due to their excellent castability, corrosion resistance, and high-strength-to-weight ratio in a heat-treated condition. In the automotive industry, cast-Al alloys have been increasingly used to replace cast-Fe and steel in vehicle applications, such as engine blocks, cylinder heads, intake manifolds, brackets, housings, chassis, transmission parts, and suspension systems to reduce mass. Currently, over 400 lbs of Al alloys are used in a vehicle, among which near 300 lbs are Al shape castings [1]. As many of the Al shape castings used in automobiles involve cyclic loading, fatigue properties of the castings are critical to their success. The increasing use of lightweight Al cast components in critical structures requires improved integrity, with more reliable and quantifiable performance. These goals are made more challenging by the complexity of shape casting processing, which involves many competing mechanisms, multiphysics phenomena, and potentially large uncertainties.

The understanding of mechanical performance of Al castings was summarized by Wang *et al.* [2],[3] who discussed the roles of porosity, oxide films, dendrite arm spacing, intermetallic and Si particles, and matrix strength in tensile fracture and fatigue crack initiation and propagation. One of the conclusions is that casting defects (e.g., porosity, oxides) are major microstructural heterogeneities that cause a significant reduction in the tensile and fatigue resistance of Al castings. Recent research results [4],[5] corroborate these findings. Under static loading, the volume fraction of defects dominates the tensile behavior. In dynamic loading, however, it is the defect size that controls fatigue performance. Reducing defect size increases fatigue properties. When the defect sizes are smaller than a critical size (e.g., ~50 μm), the eutectic particles and

persistent slip bands in the Al matrix become fatigue crack initiation sites with a significant increase of fatigue life. To improve strength and fatigue performance of cast-Al alloys, casting defects should be minimized, and eutectic particles should be refined and uniformly distributed in the microstructure. In Al castings, the size and population of multiscale defects and microstructure constituents depend not only upon the alloy composition and melt quality, but also the casting process—including mold filling and solidification conditions.

Recently, there has been significant effort in developing high-temperature cast-Al alloys for high-performance cylinder head applications. The newly developed cast-Al alloys have shown significant improvement in tensile strengths at both room and elevated temperatures. The comparison of low cycle and HCF properties to those of a production alloy does not show significant improvements, which limits the application and implementation of the new high-temperature Al alloys. Fatigue resistance of Al castings is strongly dependent on microstructure (e.g., columnar grains) and particularly defects such as porosity, oxides, and inclusions. The microstructure constituents and multiscale defects in Al castings are much more dependent upon the casting process than on alloy composition or heat-treatment. This remains the biggest challenge for implementing any new high-performance Al alloys for improved engine efficiency and mass reduction.

For instance, in cylinder head casting, a gravity-poured semi-permanent mold casting process is commonly used for mass production. Because of gravity pouring, a significant amount of Al oxides are produced and entrapped in the head casting during mold filling. The entrained oxides provide heterogeneous nucleation substrates for porosity and large eutectic particle formation during solidification. Furthermore, as liquid metal is introduced from the deck face and the riser is the last to fill in the gravity-poured semi-permanent mold head casting process, the riser feedability and microstructure soundness is poor, not to mention the resulting low metal yield. Rotacast® is considered as a premium casting process for making premium cylinder head casting. However, it is a very costly process—more than 50% more expensive than gravity-poured semi-permanent casting. In Rotacast® heads, oxides are unavoidable due to gravity pouring of liquid metal into the Rotacast® pour ladle, and the casting quality is not much better than that of semi-permanent mold cast heads. Therefore, this project proposes to develop a novel casting process, Pressure-Assistant Precision Sand-Casting (PAPSC) [6],[7], for producing flawless cast-Al cylinder heads with minimum manufacturing and energy costs.

Objectives

The objective of this collaborative project between National Energy Technology Laboratory (NETL), GM, and Eck Industries, Inc., is to develop a novel and cost-effective precision sand-casting process to produce high-quality and high-performance cast-Al cylinder heads with minimum porosity and oxides.

Approach

The proposed approach is to leverage GM, Eck, and NETL's experience in producing high-quality metal castings through various microstructure control and defect elimination technologies, as well as comprehensive quantification of microstructure characteristics and mechanical properties. The project begins with the new precision sand-casting process technology development and demonstration at NETL. The validated new precision sand-casting process technologies will be used to make high-quality prototype cylinder head castings for thorough microstructure quantification and mechanical property evaluation. The final engine test will verify the cylinder heads made by the newly developed casting process technologies have superior performance in comparison with the current production heads. Four tasks have been proposed to achieve the objectives of the project:

- Task 1: Novel precision sand-casting process development.
- Task 2: Prototype casting of cylinder heads using the novel precision casting process.
- Task 3: Comprehensive evaluation of microstructure and mechanical properties of the head castings.
- Task 4: Cylinder head component and Dyno durability testing.

Results

Task 1. Novel Precision Sand-Casting Process Development

Work during FY 2020 was focused on the development of the novel precision sand-casting process. However, much of the laboratory progress was delayed by the COVID-19 virus and associated laboratory closures so much of what is discussed here outlines the plans of work yet to be performed. The new PAPSC [4],[5] casting process is proposed to make a high premium cast-Al cylinder head. As illustrated in Figure II.1.3.1, two heads may be made in a production mold with a deck face metal chill and precision sand core boxes for enhanced productivity. Unlike a conventional gravity-poured semi-permanent mold casting, the head cavity will be bottom filled using low pressure or pumping mechanisms in the new process. After filling and roll over, the head casting will be solidified under low pressure applied to the riser with sand core pistons. The deck face chill will be extracted when it is thermally saturated and replaced with water spray to enhance cooling. The timing of chill extraction and pressurization profile during solidification may be optimized to deliver the best quality casting.

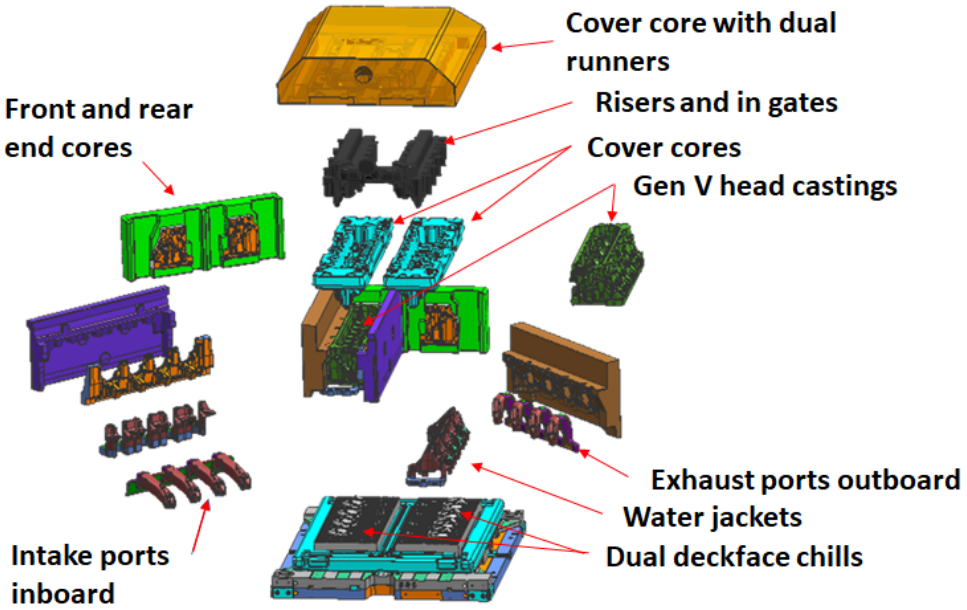

Figure II.1.3.1. New PAPSC process for manufacturing a cast-Al head. Source: GM.

In another version, the deck face chill will be water-cooled, which will be made of cast-Fe with protruding fins in a water-cooled cavity. The first evaluation of this approach will be to cast a simple Al plate against the water-cooled chill. Figure II.1.3.2 shows a photo of the pattern being used to form the chill plate. The fins protrude into a lower recess, which will be plumbed for water-cooling. The simple plate casting will be formed on the upper side of the finned half of the chill. Critical variables include water temperature and water flow rate delay time before the start of water flow. Once the parameters are well-defined and good microstructural control is achieved, another chill will be made with an upper surface that forms the cylinder head deck surface and combustion chambers. Figure II.1.3.3 shows a photo of the pattern being used to form the casting side of the combustion chamber/deck face chill plate before finishing.

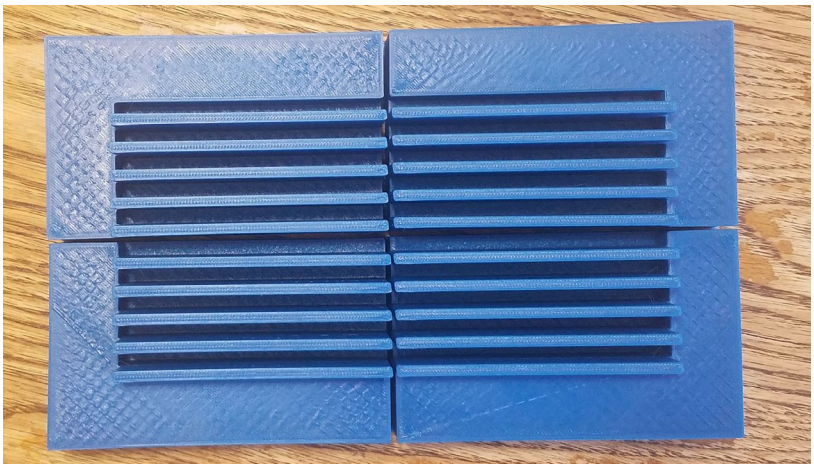

Figure II.1.3.2. Water-cooled chill pattern. Source: NETL.

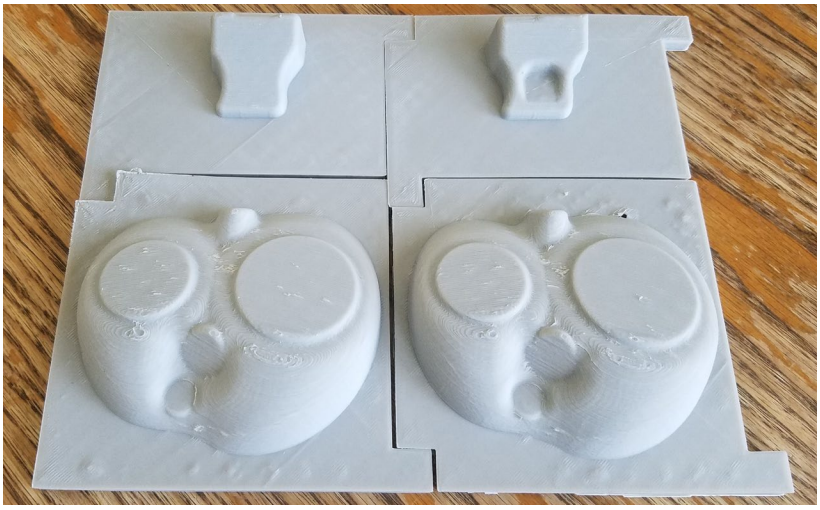

Figure II.1.3.3. Water-cooled deck face chill patter and combustion chamber on the deck face side. Source: NETL.

Task 2. Prototype Casting of Cylinder Heads Using the Novel Precision Casting Process

Eck Industries Inc. will produce prototype cylinder head castings using the novel precision casting process technologies to be developed. Eck has done a lot of advanced work in cast-Al, such as ultrasonic degassing and grain refinement, nano-metal matrix composites, etc. A recent relevant project is DOE contract DE-AC05-000R22725, subcontract 4000022893, "Development of an Advanced Squeeze Casting Process for the Production of High Integrity Truck Components." Eck has advanced equipment and facilities in melting, melt quality control, casting process development and validation, heat-treatment, tensile testing, and nondestructive tests, including four available low pressure permanent mold machines and three air set molding lines, ultrasonic degasser, dye penetrant, and digital radiography.

The cylinder head selected for this project is a V8 engine head, as shown in Figure II.1.3.4, which is made of a 319-T7 alloy using state-of-the-art semi-permanent mold casting. Figure II.1.3.5 shows a comparison of the simulated oxides in the baseline head and those predicted in the head made by the novel PAPSC process. Figure II.1.3.5(a) shows the number of oxides predicted in the baseline head is much more than that in the novel cast head as the mold filling in the new PAPSC process is much more quiescent, as seen in Figure II.1.3.5(b). After solidification, the microstructure in the new head, particularly near the deck face, is finer than that of the baseline head, as shown in Figure II.1.3.6. As a result, the predicted porosity in the novel casting head is also much lower than that observed in the baseline head, as shown in Figure II.1.3.7.

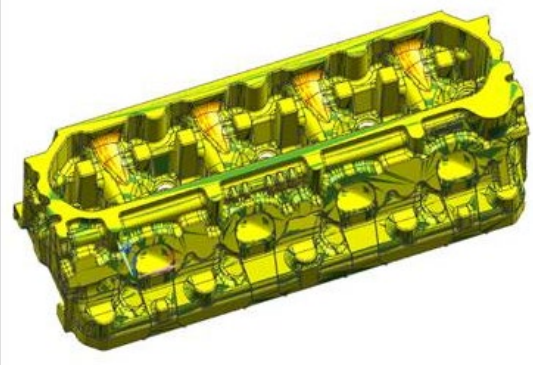

Figure II.1.3.4. A typical V8 engine cylinder head. Source: Eck Industries, Inc.

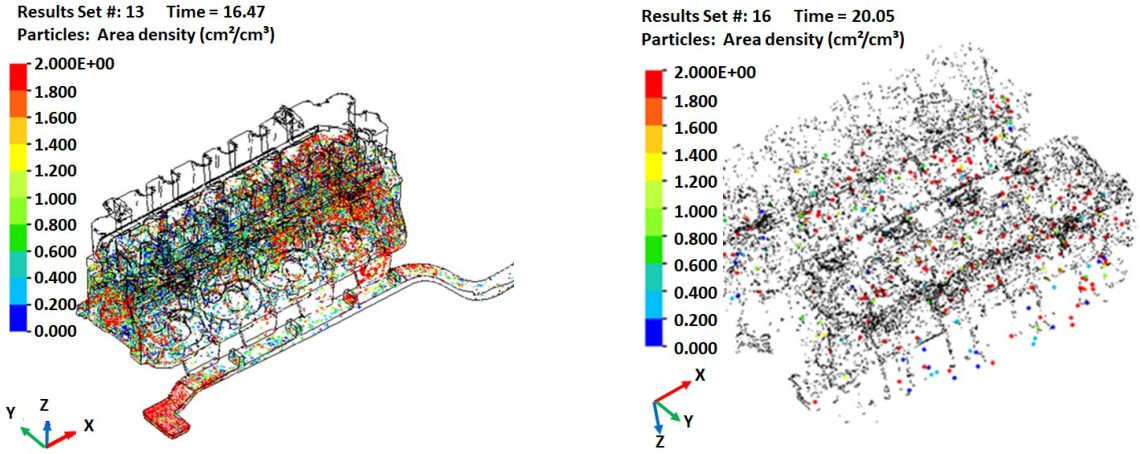

(a) (b)

Figure II.1.3.5. A comparison of the simulated oxides in: (a) the gravity-poured semi-permanent mold baseline cast head; and (b) the head made by the novel casting process. Source: Eck Industries, Inc.

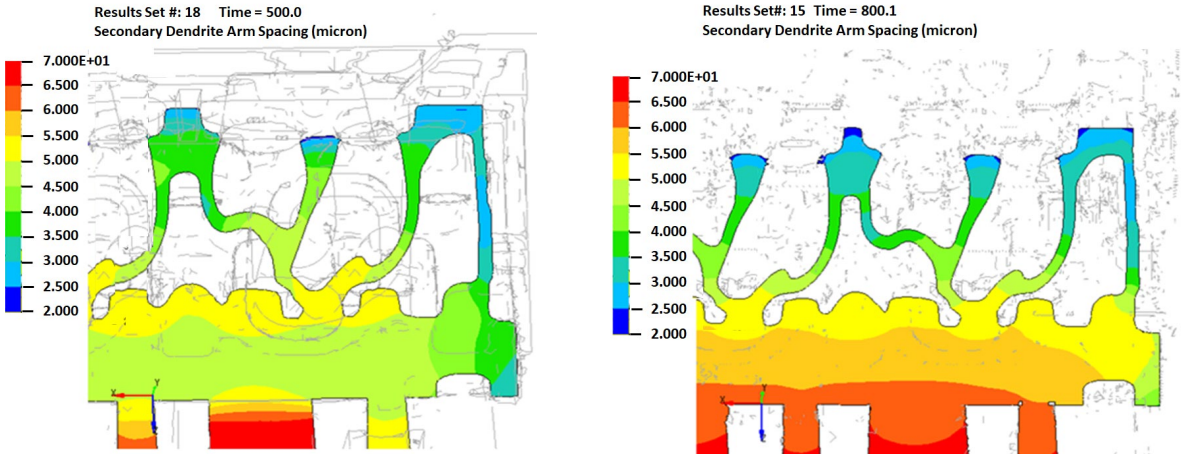

(a) (b)

Figure II.1.3.6. A comparison of the simulated secondary dendrite arm spacing in: (a) the gravity-poured semi-permanent mold baseline cast head; and (b) the head made by the novel casting process. Source: Eck Industries, Inc.

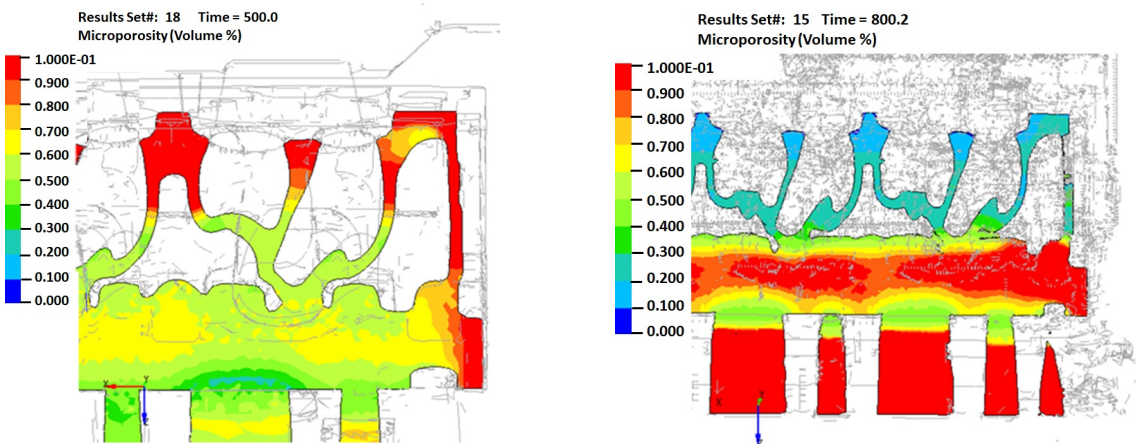

Figure II.1.3.7. A comparison of the simulated microporosity in: (a) the gravity-poured semi-permanent mold baseline cast head; and (b) the head made by the novel casting process. Source: Eck Industries, Inc.

Table II.1.3.1 summarizes the oxides, secondary dendrite arm spacing, microporosity and macroporosity simulated in the controlled locations in the baseline head and the head made by the novel casting process. As expected, the novel casting process produces much better casting quality in comparison with the baseline head.

Table II.1.3.1. Comparison of the Casting Quality Predicted in Two Heads

Casting Quality Comparison		SPM	PS (Chill+Spray)
Oxides (cm^2/cc)	CC1	2	0
	CC2	63	0
	RP	< 1	0
Secondary Dendrite Arm Spacing (μm)	CC1	29.8	25.5
	CC2	29.7	25.3
	RP	42.6	47.1
Microporosity (vol%)	CC1	0.16	0.01
	CC2	0.12	0.01
	RP	0.04	0.05
Microporosity Max. Size (μm)	CC1	695	346
	CC2	646	312
	RP	479	639
Macroporosity (vol%)	CC1	0.00	0.00
	CC2	0.00	0.00
	RP	0.00	0.00

CC1 = combustion chamber location 1; CC2 = combustion chamber location 2; RP = rocker pedestal location; SPM = semi-permanent mold; PS = pressure spray

Conclusions

Novel casting process was simulated with a V8 cylinder head. The results of the head made by the novel casting process show the refined microstructure and the reduced porosity in comparison with the baseline head made by the state-of-the-art semi-permanent mold casting process.

References

1. Metallic Material Trends in North American Light Vehicles - Automotive Right-Weighting, 2015, Ducker Worldwide, March 2015.
2. Wang, Q. G., D. Apelian and J. R. Griffiths, 1998, in: Tiyrakioglu, M., and J. Campbell (eds.), Advances in Aluminum Casting Technology: Proceedings from Materials Solutions Conference ’98 on Aluminum Casting Technology, ASM International, pp. 217–223.
3. Wang, Q. G., 2003, “Microstructural effects on the tensile and fracture behavior of aluminum casting alloys A356/357,” Metall. Mater. Trans. A, Vol. 34, pp. 2887–2899.
4. McDowell, D. L., K. Gall, M. F. Horstemeyer, and J. Fan, 2003, “Microstructure-based fatigue modeling of cast A356-T6 alloy,” Eng. Fract. Mech., Vol. 70, No. 1, pp. 49–80.
5. Houria, M. I., Y. Nadot, R. Fathallah, M. Roy, and D. M. Maijer, 2015, “Influence of casting defect and SDAS on the multiaxial fatigue behavior of A356-T6 alloy including mean stress effect,” Int. J. Fatigue, Vol. 80, pp. 90–102.
6. Cogan, C., Q. Wang, and M. Meyer, 2018, “Method of Manufacturing Metal Castings,” Patent Application US20180016666.
7. Walker, M., J. Carter, and Q. Wang, 2017, “Mold Assembly and Method for Manufacturing Metal Castings,” Patent Application US20190134704.

Acknowledgements

NETL would like to acknowledge the valuable assistance of Mr. E. Argetsinger, Dr. M. Detrois, and Mr. J. Mendenhall.

II.1.4 Low-Cost Corrosion Protection Techniques for Magnesium Alloys (Pacific Northwest National Laboratory)

Aashish Rohatgi, Co-Principal Investigator
Pacific Northwest National Laboratory
902 Battelle Boulevard
Richland, WA 99352
E-mail: aashish.rohatgi@pnnl.gov

Saumyadeep Jana, Co-Principal Investigator
Pacific Northwest National Laboratory
902 Battelle Boulevard
Richland, WA 99352
E-mail: saumyadeep.jana@pnnl.gov

Sarah Kleinbaum, DOE Technology Manager
U.S. Department of Energy
E-mail: sarah.kleinbaum@ee.doe.gov

Start Date: December 1, 2018 End Date: December 31, 2020
Project Funding: $350,000 DOE share: $350,000 Non-DOE share: $0

Project Introduction

Mg alloys, because of their excellent strength-to-weight ratio, have tremendous weight reduction potential. However, poor corrosion resistance of Mg alloys, especially in chloride-containing environment, hinders greater use of Mg alloys. The challenge associated with corrosion of Mg alloys becomes more difficult to manage in a multi-material scenario, which is applicable for the automotive sector, due to issues of galvanic coupling. Surface coating-based corrosion mitigation strategies provide an effective and economical method of corrosion protection in Mg alloys, by placing a physical barrier between the corrosive environment and the Mg alloy substrate. Some of the coating technologies used for the protection of Mg alloys from corrosion include: (1) chemical conversion coatings; (2) anodizing; (3) organic coatings; and (4) electroplating. However, there are a number of concerns with existing coating technologies used for Mg alloys (e.g., Cr-based conversion coatings have serious environmental impacts, porous nature of the anodizing coating in Mg alloys needs additional sealants, organic coatings suffer from poor adhesion issues together with environmental concerns, electroplated coatings have increased risk of galvanic corrosion in the event of any damage to coating, etc.).

Development of non-chemical surface treatment technologies toward corrosion mitigation in Mg alloys could be an environment-friendly alternative. Use of laser-based methods is a potential non-chemical approach to enhance corrosion resistance in Mg alloys. The current project investigates the effect of a new type of laser surface processing (LSP), which involves use of a relatively low (~hundreds of mJ) energy laser pulse, on corrosion behavior of a commercial Mg alloy. The underlying mechanism of corrosion protection, especially for longer duration testing in LSP-treated Mg alloys, has been determined through microstructural characterization, electrochemical tests, and surface chemical analysis.

Objectives

The objective of this project is to understand the mechanism(s) behind the corrosion protection behavior exhibited by a surface-modified commercial AZ31B sheet. Preliminary surface processing experiments that involved the use of lasers on a commercial AZ31B Mg sheet indicated substantial improvement in corrosion resistance based on results obtained in salt fog corrosion tests. Experiments performed in FY 2019 revealed a continuous surface film on the laser-processed surface that was hypothesized to play a role in providing

corrosion protection. Therefore, the objective in FY 2020 was to understand the structure and chemistry of this film to elucidate the underlying mechanism of corrosion protection.

Approach

In the present study, a commercially available 1 mm thick AZ31 Mg sheet alloy was processed (one sheet face only) using a neodymium-doped yttrium-aluminum-garnet (Nd:YAG) pulsed-laser (pulse duration 6-8 ns) with a spot size of ~500 microns. LSP was performed at three different energies of ~100 mJ (LSP Sample 1), ~200 mJ (LSP Sample 2), and ~300 mJ (LSP Sample 3) corresponding to a power of ~1, ~2, and ~3 W, respectively. During LSP, the workpiece was kept in a sample holder under deionized water confinement without any protective layer. The laser-scan head scans the top surface of the work material in a zig-zag pattern to create a large-processed area.

Corrosion behavior of LSP coupons was determined by ASTM B117 method and electrochemical tests. Electrochemical tests were performed at RT using 5% NaCl aqueous solution as the electrolyte and employing a three-electrode cell setup containing a graphite counter electrode, a saturated calomel electrode as a reference electrode, and test specimens as the working electrode. Microstructural information from LSP-treated AZ31 (LSP Sample 2) and non-LSP base metal (BM) was obtained through imaging studies on transverse cross-section coupons on a JEOL JSM-7600F SEM using the backscattered electron imaging using a Low-Angle Backscattered Electron detector. Low-kV imaging (5 keV) was employed at a short working distance (e.g., 8 mm) to minimize the interaction volume and probe very near the surface. Upon preparation of an electron transparent lamella using cross-section lift-out technique utilizing FIB milling, subsequent analysis was performed on a JEOL ARM 200CF aberration Cs-corrected TEM at an accelerating voltage of 200 kV. TEM selected area diffraction and STEM was performed using annular dark-field and bright-field to understand the crystallographic orientation and microchemistry of the near surface region. Chemical analyses in STEM mode were conducted using EDS with a JEOL Centurio EDS detector (0.9-sR solid collection angle). Finally, the characterization data was used to develop and test a hypothesis for the corrosion protection observed in laser-surface-modified Mg sheets.

Results

ASTM B117 corrosion test data for LSP and BM samples were reported in our FY 2019 report. LSP coupons showed a very slight increase in weight (~2% to 3%) while the BM showed severe corrosion, and an order-of-magnitude larger weight gain (~20%) due to the build up of corrosion products. In FY 2020, grazing incidence x-ray diffraction (GI-XRD) was carried out to gain further insight in the corrosion behavior of coupons after long-term (56 days) exposure to continuous salt fog testing. The improved corrosion resistance of LSP coupons was independently confirmed through GI-XRD since the x-ray peak intensity of $Mg(OH)_2$ (corrosion product) was noted to be weaker in LSP condition, as observed in Figure II.1.4.1(a), in comparison to BM, as observed in Figure II.1.4.1(b). In addition to ASTM B117 testing, electrochemical impedance spectroscopy (EIS), which provides information about the electrochemical nature of various physical phenomena occurring at the corrosion coupon/electrolyte interface, was conducted on LSP-treated AZ31 and BM.

Figure II.1.4.2(a) summarizes the Nyquist plots for all specimens (e.g., BM and LSP Samples 1, 2, and 3) obtained through the EIS test. The presence of characteristic capacitive loops and inductive loops could be noticed in the Nyquist plot. The Nyquist plots very clearly show that the LSP-treated AZ31 surface has a much higher corrosion resistance in comparison to the BM surface, since the capacitive loops associated with the LSP samples are larger in diameter as compared to BM samples indicating a higher polarization resistance. Data from the EIS test was additionally plotted in the phase angle Bode diagram, as shown in Figure II.1.4.2(b), which confirms the capacitive nature of the electrical double layer forming on the surface. The more negative values of phase angles in the midfrequency range (e.g., 10–1000 Hz) imply greater capacitive nature of the film. Typically, an ideal capacitor exhibits a phase angle of -90 degrees. As evident from Figure II.1.4.2(b), LSP-3 shows the most negative phase angle of ~-70 degrees around 100 Hz, while the BM specimen has a phase angle of -55 degrees at the same frequency range. Other LSP-treated samples (e.g., LSP-1 and LSP-2) show similar phase angles as the LSP-3 specimen in the midfrequency range, and thus, no

meaningful difference could be observed between various LSP conditions. Collectively, more negative values of phase angles in the midfrequency range for the LSP-treated AZ31 surface are an indication of the higher capacitive performance of the LSP specimens over the BM specimen. This higher capacitive behavior of LSP specimens is indicative of their better corrosion resistance than BM specimen.

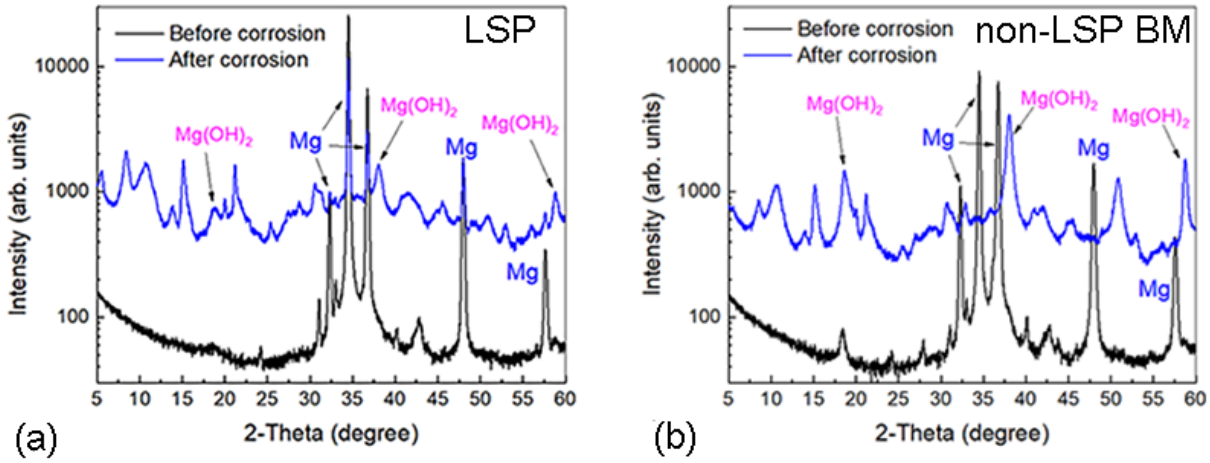

Figure II.1.4.1. GI-XRD data showing improved corrosion resistance in: (a) the LSP sample; and (b) the BM sample. Source: PNNL.

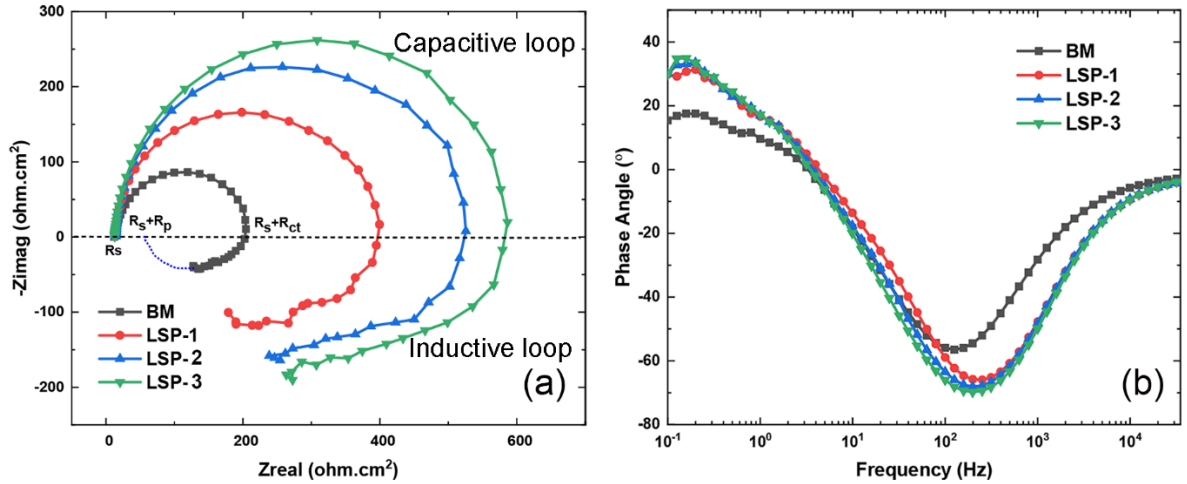

Figure II.1.4.2. (a) Nyquist plot and (b) Bode plot for LSP and BM samples indicating improved corrosion resistance. Source: PNNL.

Extensive SEM imaging of the LSP-treated surface along the through-thickness direction at high-magnification was carried out during FY 2019. The resulting microstructural analysis revealed the presence of a porous surface film measuring ~0.5 µm in thickness that formed during laser treatment. By contrast, the BM surface was devoid of any such features. In FY 2020, the near surface region, including the surface film, was analyzed in greater detail. Apart from the surface film with finger-like features, a second, thin contiguous interlayer that measured ~tens of nm thick between the underlying AZ31 matrix and the outer finger-like film was noted. This thin interlayer appeared to be dense in nature and continuously following the laser treated surface, which appears to contain multiple peaks and troughs. Additionally, the presence of a few very bright particles that are almost randomly located could be noticed within the AZ31 matrix in both the BM and LSP-treated condition.

EDS analysis indicated these particles to be rich in Al and Mn and are thus believed to be Al-Mn intermetallic particles (IMPs) with the possibility of several chemical stoichiometries.

To learn further details about the LSP surface, chemical analysis was carried out in STEM mode. Low-magnification STEM-EDS elemental maps from LSP AZ31 showed a uniform bulk alloy composition across the sample, while the top surface film appeared to be Mg- and O-rich, and the distribution of Al-Mn IMPs confirmed the dark contrast observed in the bright-field TEM images, as observed in Figure II.1.4.3(a). Combined elemental maps of Mn/Al/Mg and Mn/Al—where Mn-Blue, Al-Red, and Mg-Green—were also produced to illustrate the location of each element signal with respect to one another. STEM-EDS elemental maps suggest a very slight Al enrichment at the interface between the O-rich outer film with finger-like features and the bulk. The enrichment of the Al appears in a greater detail near the surface as a distinct, thin interlayer ~20 nm thick, as shown in the elemental map in Figure II.1.4.3(b). In summary, EDS analysis together with SEM and STEM imaging confirmed formation of Mg/Al-based mixed-metal oxide surface film on LSP-treated AZ31 sheet. An independent confirmation of the surface chemistry was made by carrying out XPS analysis as well.

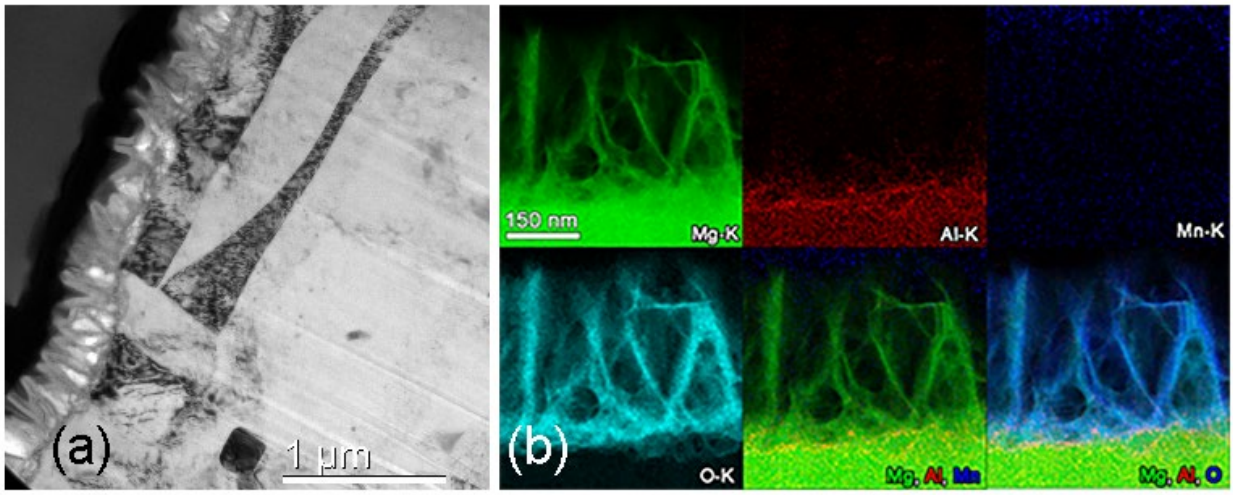

Figure II.1.4.3. (a) Bright-field TEM image of LSP sample and (b) STEM-EDS elemental mapping of the surface of the AZ31 sheet after LSP. The surface film appears to be rich in O. Source: PNNL.

Exposure of LSP-treated corrosion coupons to a salt fog environment results in the formation of a surface film that is uniform and compact in nature. In contrast, the surface film forming on the BM had a mixed appearance with sharp discontinuities that resembled “mud cracking” morphology, as observed in

(a) (b) (c)

Figure II.1.4.4(a). Representative SEM images of the LSP-treated AZ31 corrosion sample surface are shown in

(a) (b) (c)

Figure II.1.4.4(b) and (c), respectively. The surface film that is present on an LSP-treated sample after corrosion had a characteristic “plate-like” morphology, which is typical of layered double hydroxide (LDH) compounds. LDHs are represented by a general formula of $[M_{1-x}^{2+}M_x^{3+}(OH)_2][A^{n-}]_{x/n}\cdot mH_2O$, where M^{2+} and M^{3+} are divalent and trivalent metal cations, respectively, and A^{n-} is the interlayer anions of a valence of n. Based on the morphological evidence presented in Figure II.1.4.4, we hypothesize that a Mg^{2+}/Al^{3+}-type of LDH surface film is forming during a corrosion test and plays a major role in providing improved corrosion resistance in LSP-treated AZ31.

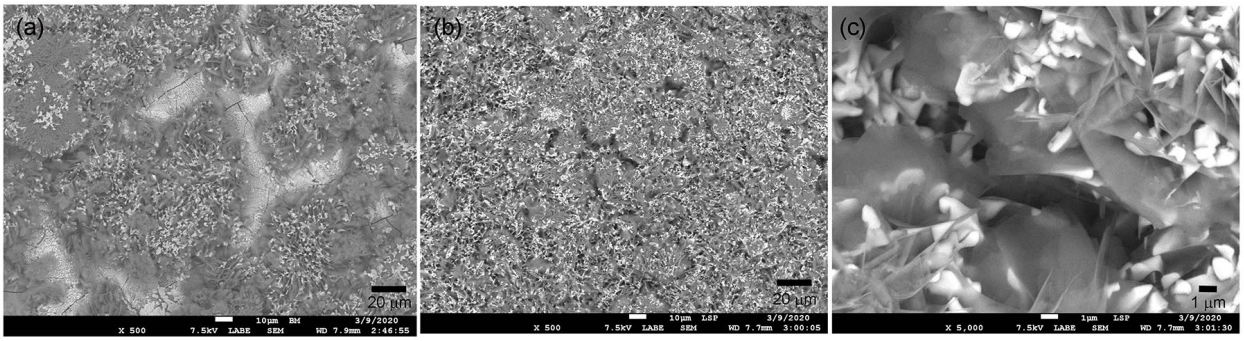

(a) (b) (c)

Figure II.1.4.4. SEM images showing the morphology of AZ31 coupon surface after corrosion testing. (a) BM and (b) and (c) LSP indicating the formation of an LDH-type film. Source: PNNL.

To test our proposed hypothesis, the effectiveness of LDH compounds-based surface films as an alternative to laser-based surface processing for improving the corrosion resistance of AZ31 alloy was investigated. A hydrothermal co-precipitation method was employed to coat AZ31 coupons with Mg-Al-based and Mg-Zn-based LDH coatings. Corrosion behavior of these LDH-coated AZ31 coupons was evaluated through an ASTM B117 test for up to ~1000 h (i.e., ~six weeks). Of the coating chemistries explored, coatings based on Mg-Al and Mg-Zn LDH performed the best and showed < 1% of total weight gain. In comparison, the uncoated AZ31 BM showed up to 2% weight gain. Surface appearance of the coated AZ31 coupons as a function of test duration is summarized in Figure II.1.4.5. Based on the macroscopic images, formation of a uniform coating could be noticed in the as-fabricated coupons (t = 0 h). During ASTM B117 corrosion testing, the appearance of both the LDH surface coatings (i.e., Mg-Al or Mg-Zn based) changed in a very uniform manner and localized corrosion debris formation was not observed.

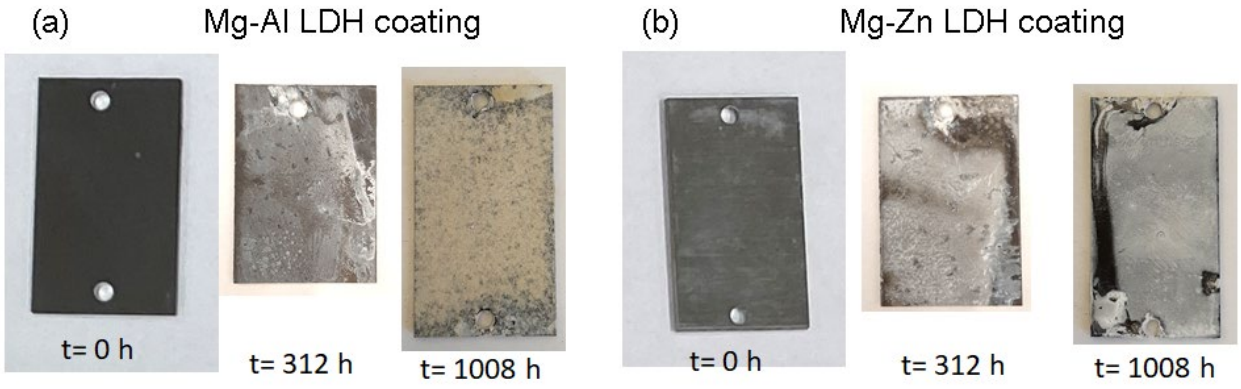

Figure II.1.4.5. Macroscopic images of hydrothermally coated AZ31 coupons, before and after ASTM B117 test: (a) Mg-Al LDH; and (b) Mg-Zn LDH. Source: PNNL.

Conclusions

LSP results in significant enhancement of corrosion resistance relative to non-LSP BM in an AZ31 Mg alloy as evident by (1) an order-of-magnitude lower weight gain by LSP coupons in ASTM B117 testing and (2) significantly higher polarization resistance of LSP coupons as was observed in the larger capacitive loop diameter seen during EIS testing. Lower weight gain in LSP samples implies a lower amount of corrosion products (i.e., less corrosion). Likewise, higher polarization resistance in LSP samples implies a lower corrosion current (i.e., lower corrosion rate). TEM and EDS analysis shows that LSP results in an outer ~0.5-µm-thick, porous, mixed-metal (Mg, Al) oxide surface film with finger-like features that is growing atop a dense ~20-nm-thick Al-rich oxide layer integral with the BM. Additionally, LSP leads to substantial

refinement in the size and number density of Al-Mn intermetallic particles in the near surface region of AZ31. Based on the analytical and electrochemical characterization, improved corrosion resistance of LSP processed AZ31 Mg is attributed to the insulating barrier effect of the Mg/Al-type of LDH film that is formed when the LSP-induced mixed Mg-Al-oxide layer reacts with the chloride-containing environment. Additionally, a reduction in size and density of Al-Mn IMPs results in a lower cathode to anode ratio within the Mg matrix, thus it reduces the propensity for localized microgalvanic corrosion and related pit formation. The effectiveness of LDH-type of surface coating in improving the corrosion resistance of Mg AZ31 alloy was confirmed by coating AZ31 samples with hydrothermally produced LDH coatings that too showed better corrosion resistance than uncoated BM.

Acknowledgements

The technical contribution of PNNL staff for performing this research is gratefully acknowledged. We also recognize Mr. R. Seffens for carrying out the corrosion test, Mr. A. Schemer-kohrn for the SEM imaging, and Dr. D. Edwards for the TEM imaging. The technical contribution of PNNL staff for performing this research is gratefully acknowledged: Mr. R. Seffens for carrying out the corrosion test, Mr. A. Schemer-Kohrn for the SEM imaging, Drs. D. Edwards and M. Olszta for the TEM imaging, Dr. M. Engelhard for the XPS analysis, Dr. M. Bowden for the XRD analysis, and Dr. S. Nune for preparing the hydrothermal LDH coatings. A portion of this work was performed using the Environmental Molecular Sciences Laboratory (EMSL), a national scientific user facility sponsored by DOE's Office of Biological and Environmental Research and located at PNNL. Technical support provided by external collaborators is also acknowledged: Laser processing was performed at University of Iowa by Dr. A. Samanta and Prof. H. Ding and electrochemical testing was performed at Oregon State University by P. Murkute and Prof. O. B. Isgor.

II.1.5 Reducing Mass of Steel Auto Bodies Using Thin Advanced High-Strength Steel with Carbon-Reinforced Epoxy Coating (Idaho National Laboratory/ Oak Ridge National Laboratory)

Gabriel Ilevbare, Co-Principal Investigator
Idaho National Laboratory
2351 N. Boulevard
Idaho Falls, ID 83401
E-mail: gabriel.ilevbare@inl.gov

Brian Knouff, Co-Principal Investigator
Oak Ridge National Laboratory
1 Bethel Valley Road
Oak Ridge, TN 37831
E-mail: knouffbj@ornl.gov

Sarah Kleinbaum, DOE Technology Manager
U.S. Department of Energy
E-mail: sarah.kleinbaum@ee.doe.gov

Start Date: April 1, 2018 End Date: March 31, 2020
Project Funding: $639,000 DOE share: $300,000 Non-DOE share: $339,000

Project Introduction

Diversitak, a company based in Detroit, MI, has developed a proprietary, low specific gravity, carbon fiber reinforced epoxy (CFRE). Preliminary testing on this new material conducted in collaboration with ArcelorMittal Steel Company proved out the concept. A thin layer of this CFRE was applied to a stamped sheet of steel with residual stamping oils from a mill, in a time corresponding to automotive processing (e.g., ~15 sec), and processed following automotive e-coat procedures (phosphating + 175–200°C heating), to complete the curing. No problems with adherence or performance were noted. While the CFRE does add weight to a thin gauge steel panel, it weighs much less than what is displaced by using thicker conventional mild steel gauges. The application of the coating showed a significant increased dent resistance, oil canning resistance, and part stiffness.

This project was designed to mature this new technology to near manufacturing readiness to reduce the weight of a vehicle and lower the cost of weight reduction. The process involves the use of thinner gauge steels than are currently used, stiffened by CFRE application on one side. The collaborative development team included two industrial manufacturers: Diversitak and ArcelorMittal Steel Company; LightMAT; and two National Laboratories: ORNL and INL. The team developed a new manufacturing process to reduce the weight of a vehicle and lower the cost of weight reduction. This team also developed a better understanding of how to apply the coating and how it will perform in-service. The team also performed an in-depth study to determine the long-term durability of the materials manufactured using this technology and well-known automotive industry-standard tests.

Objectives

Recent steel industry advances have led to the development of AHSS, which can be of a thinner gauge, and thus lighter than conventional sheet steels, while supporting vehicle structural functions. Thinner gauge steel panels are subject to inherent sheet-forming defects that limit their applicability. Those defects can result in an increased potential for denting, vibration at high vehicle speeds, and “oil canning” (e.g., waviness in the steel

sheet). Those defects are caused by residual stresses, which are induced during coil production and tend to become more exaggerated as the strength level of the rolled sheet is increased to meet the need for a thinner—and thus lighter—sheet. Conventional autobody sheet steel averages 1.1 mm thick, ranging from 0.65 to 2.5 mm depending on the location, but typical exterior panels are often 0.75 mm thick. Reducing total body panel thickness from 0.75 mm to 0.55 mm could reduce body mass from 130 to 95 kg (27%) for an average vehicle [1].

The goal of this work is to develop CFRE technology so that AHSS body panels may be reduced in thickness from 0.75 to 0.55 mm to reduce component mass. To accomplish this goal, the optimal reinforcement fiber length and fiber concentration was determined. Following that phase, the CTE in all three directions was determined to feed into manufacturing models and methods for rapidly and inexpensively applying the coating was determined. This was followed by panel-level evaluations of the coating and steel combination.

Approach

This was a two-year effort. ORNL's tasks included optimization and selection of the best CFRE material. This included a determination of the optimal fiber length, optimal fiber concentration, and a determination of the optimal coating thickness for best vehicle structural function and performance at the least cost. ORNL, along with the suppliers, developed a durable CFRE application process (e.g., gun material, design, robotic dispensing process) and identified the adhesion stability of the CFRE during process holding. An approach to ensure that application/curing timing conformed to conventional assembly line speed and plant cycle times was determined. ORNL also determined the CTE of the material in all three directions and performed all material scanning electron microscopic analysis.

INL performed characterization of corrosion properties of steel panels coated with the optimized CFRE. These tests included coupons and body panels. Diversitak produced different epoxy formulations and determined the physical and chemical properties that are critical to mixing with CFs and produced a stable coating that can be cured in the time range to support automotive assembly processing (e.g., ~10–15 secs). They also mixed different amounts and types of CF with a range of epoxy formulations and measured the cured coating properties. ArcelorMittal characterized several AHSS attributes (i.e., metallurgy heat-treatment for required AHSS properties versus sheet thickness, state of internal stress, and adhesion of the CFRE to the steel as a function of sheet rolling and stamping preparation).

Results

Results reported previously in the FY 2019 annual report focused on corrosion testing and included results from the SAE J2334 "Laboratory Cyclic Corrosion Test (April 2016)", the Ford Laboratory Test Method (FLTM) BQ 104-02, Humidity Resistance test (constant humidity of 95% at 38°C for 24 h), and the FLTM BQ 104-07 Environmental Test cycles (Procedure 11). Details of the test procedure can be obtained from the VTO 2019 Materials Annual Progress Report, which focused on the results of the lap-shear tests to test coating bond strength and flexural strength of the coating metal system before and after the corrosion evaluation [2]. A brief description of results from corrosion resulting from the presence of a scribe line to simulate coating damage from the J2334 corrosion test were also included. In the current report, more detailed results from that evaluation are discussed, which had not been completed prior to the FY 2019 deadline. For these tests, the thickness of the AHSS plate material was irrelevant, so no mention will be made regarding its thickness. The J2334 test coupons were DP500 steel plates measuring 10.16 cm × 30.48 cm (4 in. × 12 in.) and were coated with 0.5 mm thick CFRE. The SAE J2334 test was comprised of a humid cycle (50°C at 100% relative humidity for 6 h), a salt fog application cycle (0.25 h), and a dry-off cycle (60°C at 50% relative humidity, 17.75 h) for a total of 24 h comprising one test cycle. The fog atomization was adjusted to generate a condensate collection rate of 2 mL/h to 4 mL/h, as stipulated in SAE J2334, with the fog collection defined in ASTM D1735-14, "Standard Practice for Testing Water Resistance of Coatings Using Water Fog Apparatus." The testing solution was 0.5% NaCl, 0.1% CaCl2, and 0.075% NaHCO3. The first two cycles were conducted in a Q-Fog Salt Fog Chamber, while the final dry-off cycle was conducted in a humidity chamber where the humidity was generated using deionized water.

Undercoating Corrosion Evaluation

For the undercoating corrosion evaluation, the coating was removed to determine if any corrosion has occurred under the coating. The coating was removed in three areas along the scribe line of the J2334 coupons by bending the coupon past 90 degrees. This typically allowed for an approximate 1/4-in. width of coating to be broken off down from each side of the apex of the bend. The metal to coating adhesion was very good. Figure II.1.5.1 shows the coupon after being bent back on itself in a U-shape to facilitate the removal of the coating. A plastic paint scraper was used after bending to remove as much CFRE coating as possible without further damage to the coupon. Figure II.1.5.2 shows the same panel when it was re-flattened after breaking off the coating in three areas. The presence of the e-coat seemed to prevent the easy removal of the CFRE coating suggesting an improvement in the coating adhesion. Areas that had more e-coating on top of the CFRE coating inhibit the cracking/flaking/tearing of the CFRE coating compared with areas that seemed to have less e-coating. In some cases, success in removing coating from the specimens even after the coupon was bent onto itself, as observed in Figure II.1.5.1, and then re-flattened was limited, as seen in Position C in Figure II.1.5.2. After coating removal, each exposed scribe area was examined under a microscope at 50X.

Figure II.1.5.1. Specimen J148 shown bent on itself to remove coating at Area C. Previously bent areas shown at Areas A and B. Source: INL.

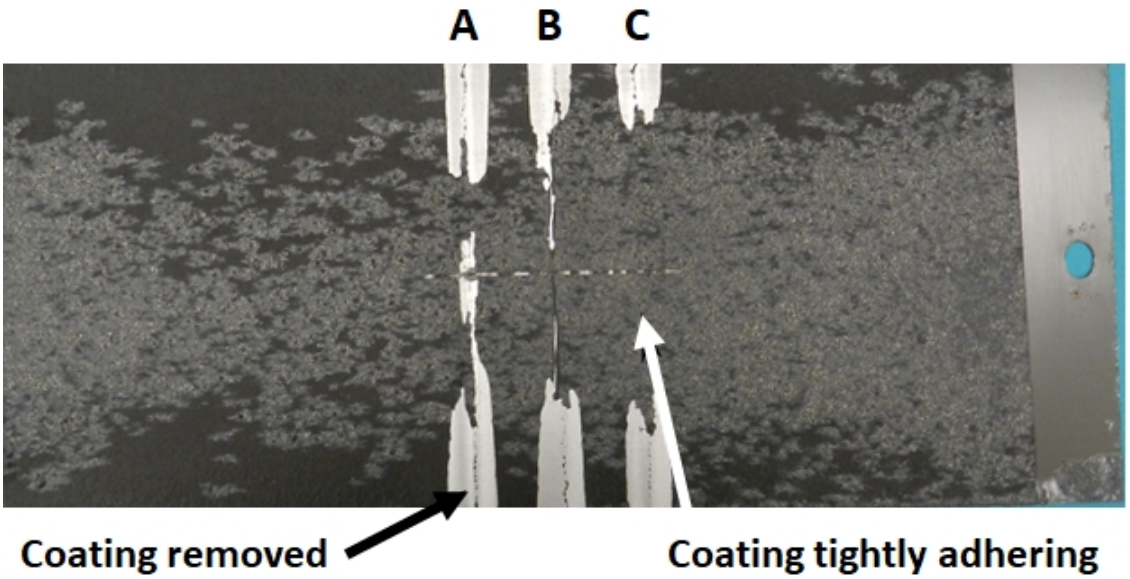

Figure II.1.5.2. Specimen J148 shown after being bent back into a U-shape and then re-flattened. The coating in the middle areas did not delaminate completely after bending. The horizontal scribe line is visible in this photo. Source: INL.

Prior to breaking the coating off, there was no indication of corrosion under the coating. There were no loose or delaminated areas on the steel surface, nor in areas where the coating appeared to have lifted off the surface. However, after removing the coating, an indication of corrosion migrating under the coating from the edge of the scribe line was observed.

Figure II.1.5.3 and Figure II.1.5.4 show the baseline (e.g., not exposed to environment) specimens at 50X and 200X magnification with some of the CFRE coating removed. The CFRE coating is the black portion on the left side of Figure II.1.5.4, while the right side shows the BM condition after the coating was removed. These were then compared with specimens exposed to a corrosive environment.

Figure II.1.5.5 shows coupon J103, which was exposed to test procedure J2334 for four cycles. Very minimal corrosion was observed on the coupon. The corrosion appears as light-gray semi-circles radiating out from the edge of the scribe line, which penetrated about 0.2 mm underneath the coating from the edge of the scribe line. The black regions in the middle of the shiny portion in the picture are coating remnants that did not come off the surface. Figure II.1.5.6 shows that the corrosion became more visible at eight cycles, which penetrated about 0.3 mm underneath the coating from the edge of the scribe line on this coupon. Figure II.1.5.7, Figure II.1.5.8, and Figure II.1.5.9 show increasing corrosion at 20, 30, and 40 cycles, respectively. Corrosion penetrated approximately 0.9 mm underneath the coating from the edge of the scribe line at 20 and 30 cycles. The corrosion was also more continuous along the scribe line in these photos. The maximum penetration distance of 1.7 mm was measured on a 40-cycle coupon. No pitting corrosion was observed on any of the specimens up to a magnification of 200X. For the final analyses, the corrosion layer was chemcially cleaned away to provide direct examination of the BM to determine the extent of corrosion.

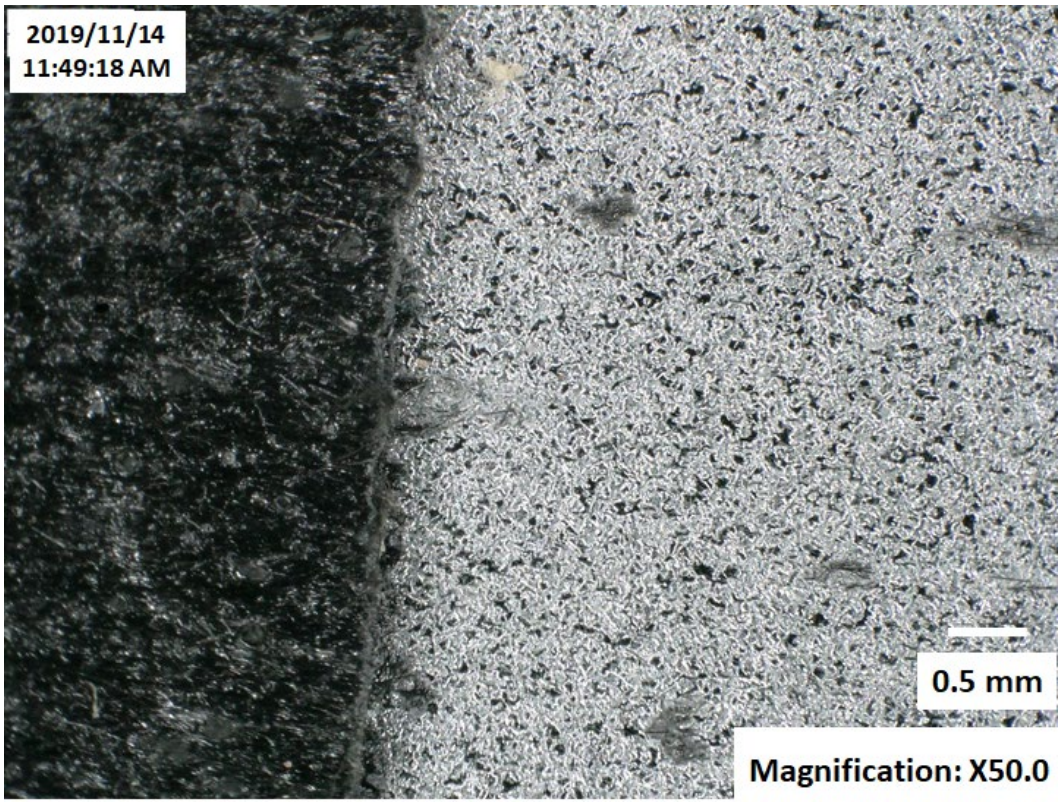

Figure II.1.5.3. Unexposed baseline coupon (not exposed to environment) showing no corrosion under the coating at 50X. Source: INL.

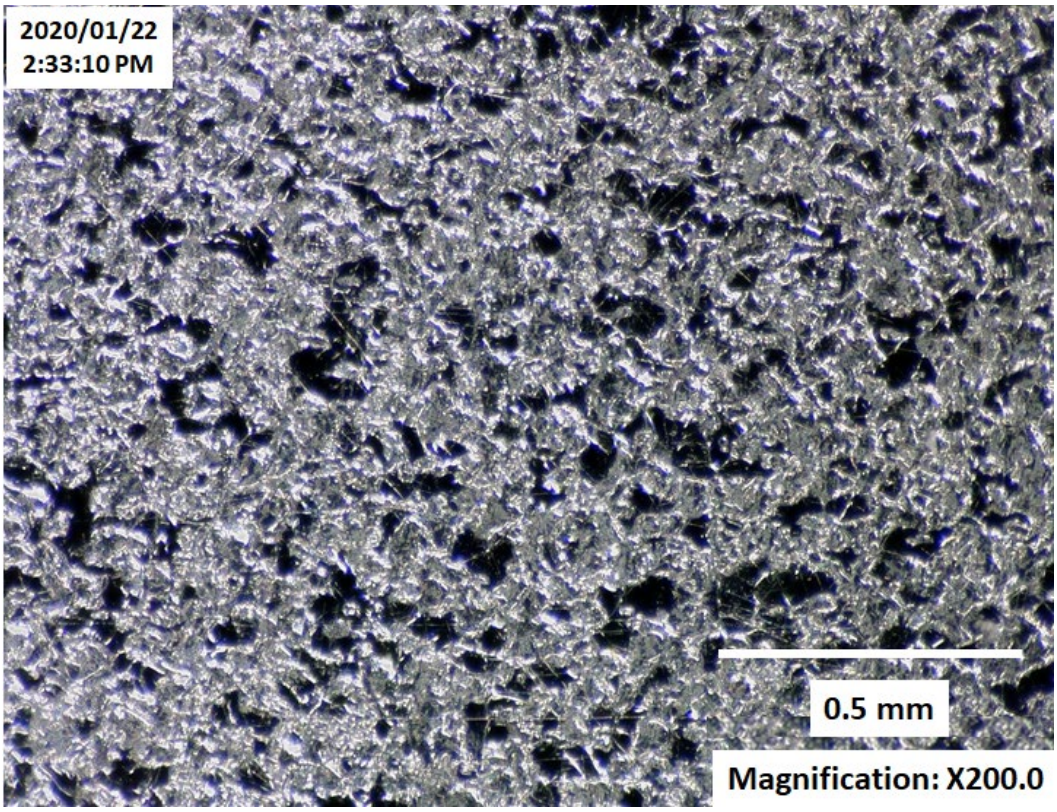

Figure II.1.5.4. Unexposed baseline coupon (not exposed to environment) showing no corrosion under coating at 200X. Source: INL.

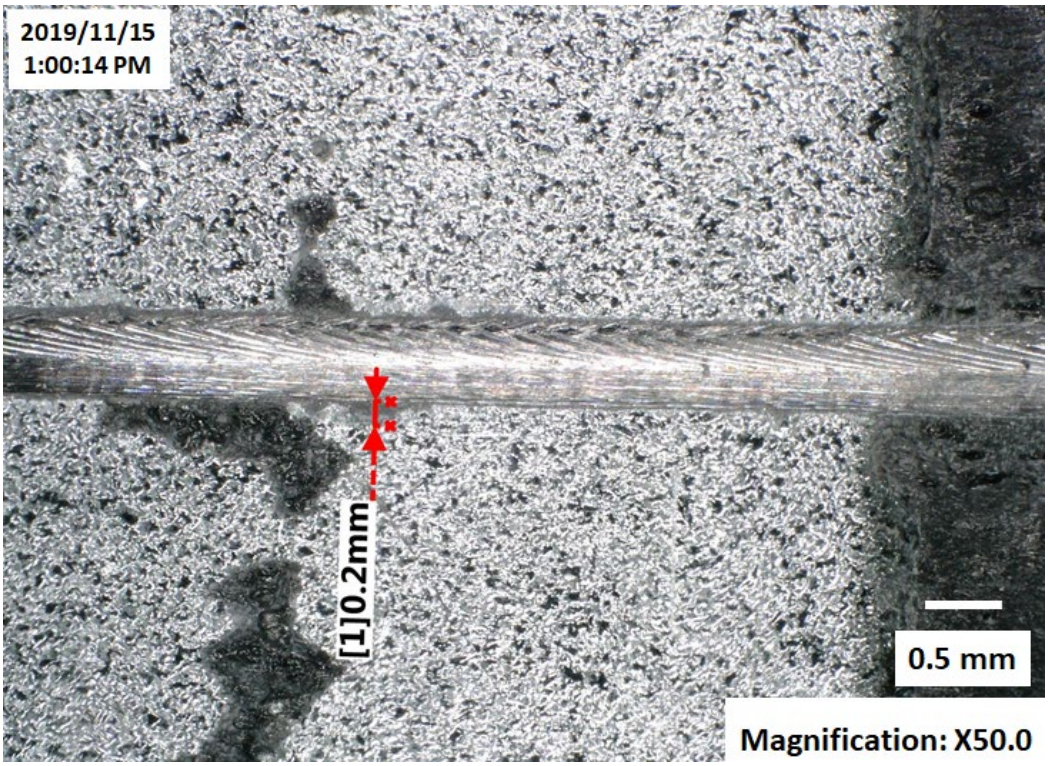

Figure II.1.5.5. Coupon J103 after four cycles at 50X. Source: INL.

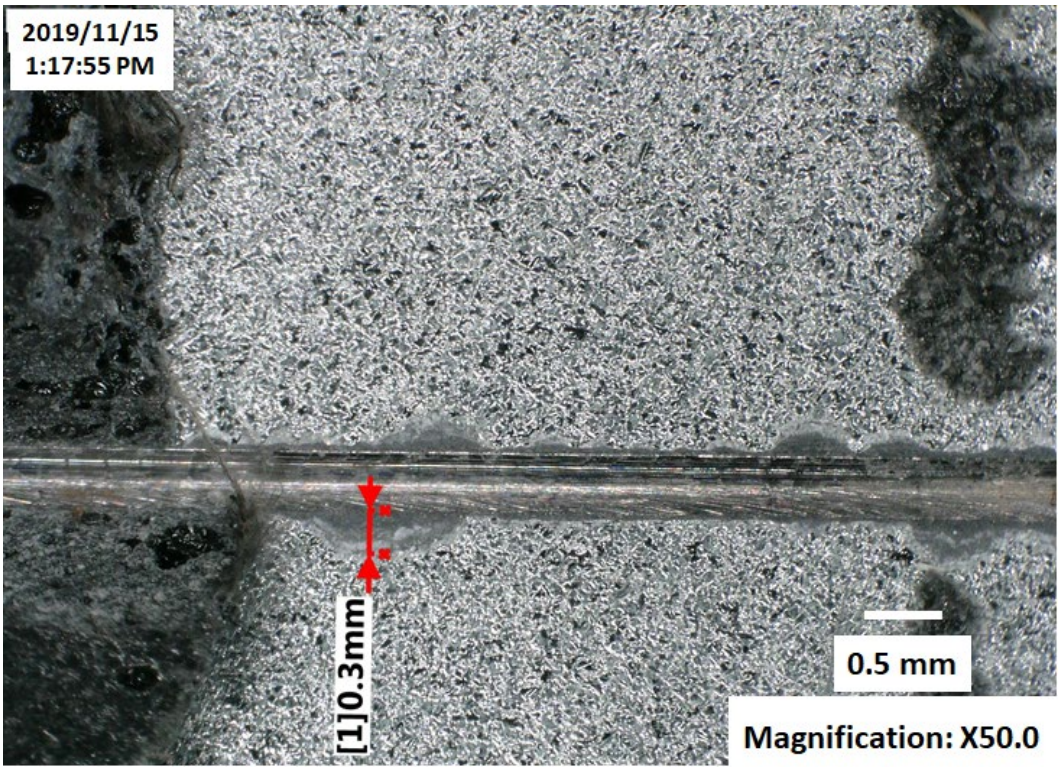

Figure II.1.5.6. Coupon J106 after eight cycles at 50X. Source: INL.

Figure II.1.5.7. Coupon J111 at 20 cycles at 50X, showing more continuous corrosion along the scribe line. Source: INL.

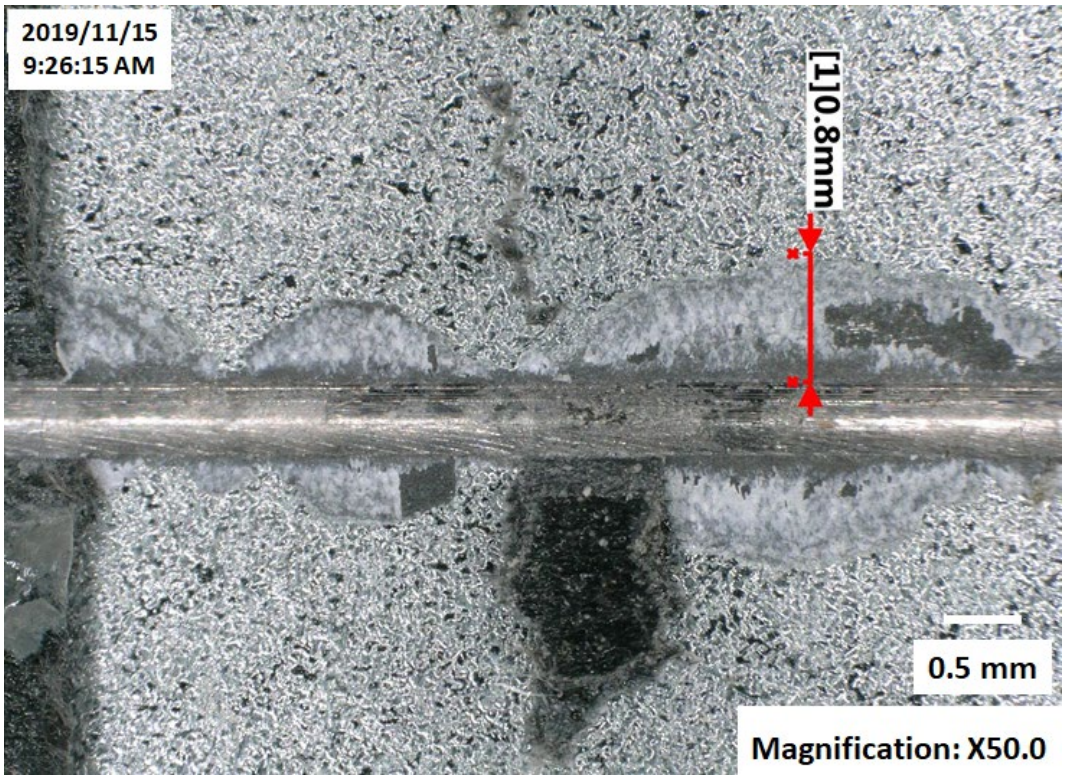

Figure II.1.5.8. Coupon J118 at 30 cycles at 50X, showing more continuous corrosion along the scribe line. Source: INL.

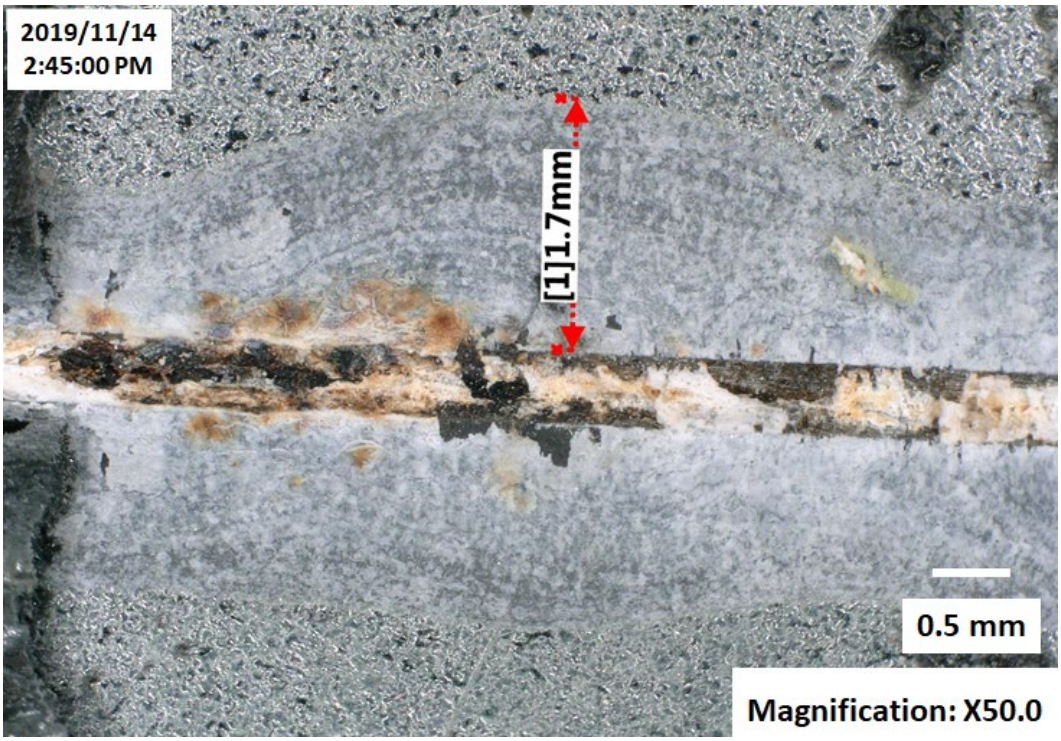

Figure II.1.5.9. Coupon J124 at 40 cycles at 50X, showing more continuous corrosion along the scribe line. Source: INL.

Figure II.1.5.10 and Figure II.1.5.11 display the “as-found” corrosion and “after cleaning” of coupon J124 that was exposed for 40 corrosion cycles. The corrosion was more difficult to remove after 40 cycles, and this is why some small spots of corrosion product remain after the cleaning process. Out of caution, the cleaning was discontinued to prevent significant damage (e.g., removal) to the BM. Figure II.1.5.12 shows coupon J124 after cleaning at a magification of 200X. The photograph shows that the surface resembled those of the other test coupons that were examined. The surface was etched darker where the corrosion was located and scratched by the applicator are evident; however, there is no evidence of pit initiation. The BM texture is the same as an untested baseline sample shown in Figure II.1.5.4 above.

Figure II.1.5.10. Coupon J124, 40 cycles, after coating removal (50X). Source: INL.

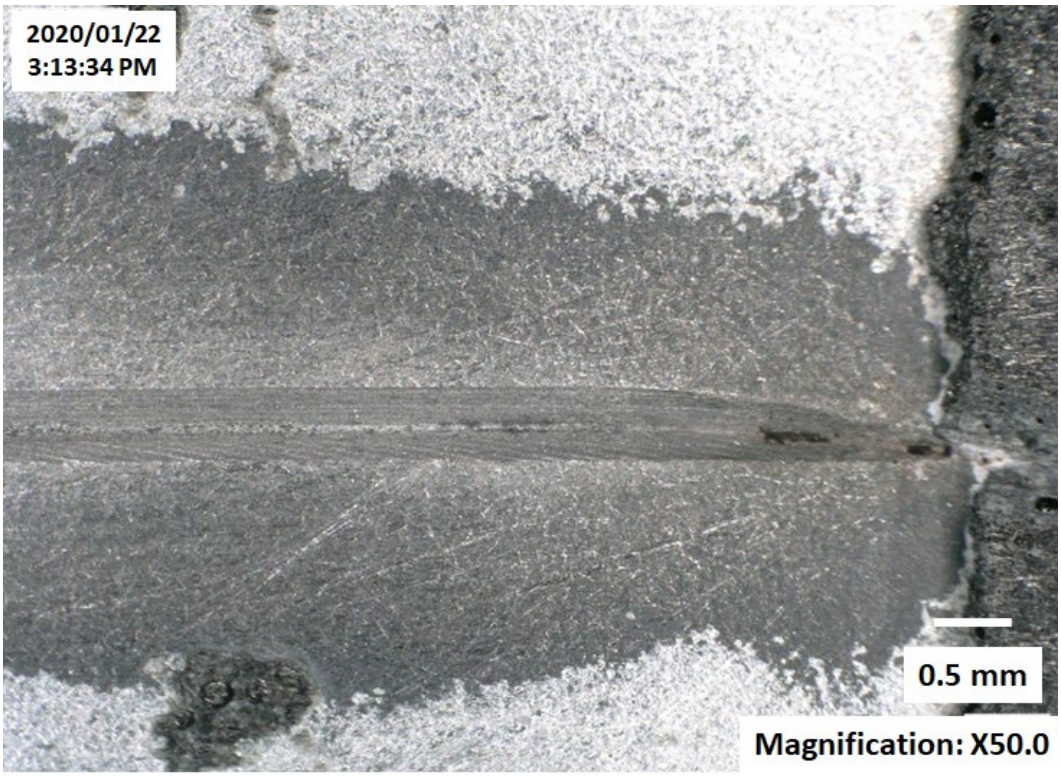

Figure II.1.5.11. Coupon J124, at 40 cycles, after corrosion was cleaned off surface (50X). Source: INL.

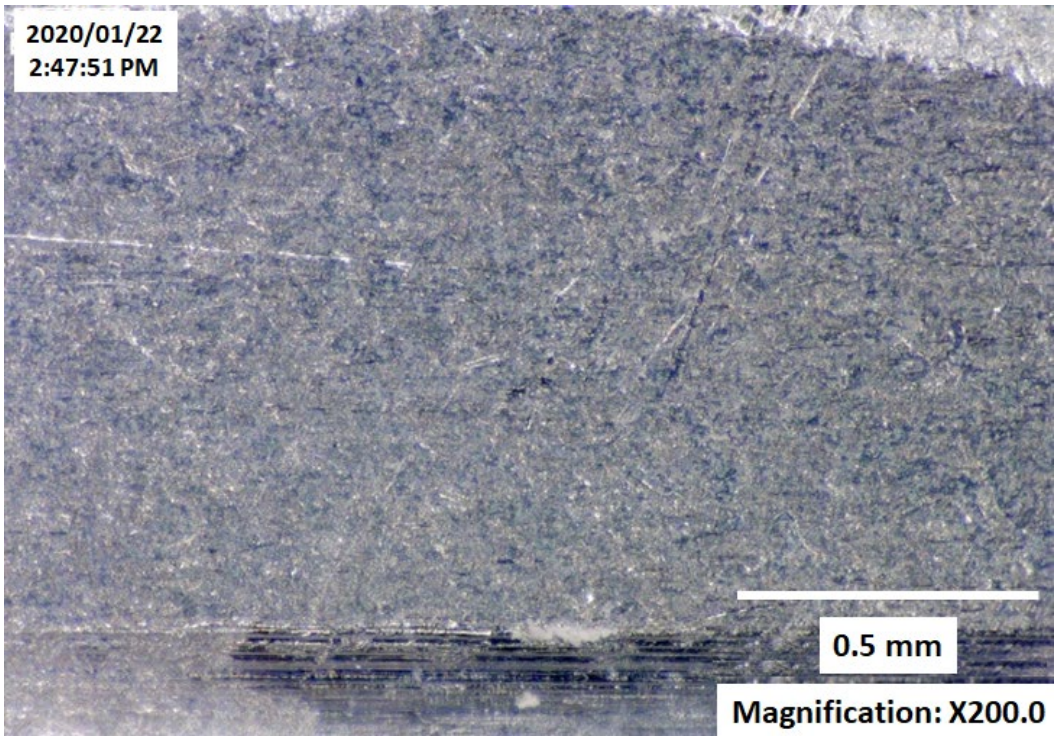

Figure II.1.5.12. Coupon J124, at 40 cycles, after corrosion was cleaned off surface (200X). Source: INL.

Conclusions

Due to the fact that corrosion was only observed on the corrosion evaluation coupons with the scribe line (Test SAE J2334), the implications from this observed corrosion were considered to be minimal to the performance of the coating. It is believed that corrosion initiated on the bare metal in the scribe line and continued under the coating. Interestingly, the coating did not show any signs of blistering, or creepback. This is likely due to the coating thickness and strength, and the fact that corrosion was minimal. The scribe line test is an aggressive test which is usually utilized on exterior surfaces to simulate coating damage. However, it did reveal that corrosion could occur if a cut or a discontinuity were to exist on a coated surface, and if that surface were to be exposed to a corrosive enviroment.

It is recommended that longer term testing be conducted to determine the true rate of corrosion under the film, and to determine whether corrosion accelerates at time periods longer than the 40 cycles studied here. Additional testing of different coating thicknesses for longer time periods may also be useful in determining whether the coating is prone to creepback at any time longer than the 40 cycles tested here as the coating thickness varies. The coating thickness tested here was approximately 0.5 mm. It may also help to further validate what the optimum CFRE thickness that should be applied to the door panels.

Key Publications

1. Sadagopan, S., M. Kuo, M. Lizak, R. Robison, R. Eadara, T. Brewer, J. M. Joseff, C. D. Warren, and G. Ilevbare, 2018, "Door Lightweighting Using Ultra-Thin AHSS Reinforced with Low-Density CFRE Materials," *Proceedings of the 17th Annual Great Design in Steels Conference*, 16–19 May 2018, Detroit, MI, USA.

References

1. Singh, H., and G. Coates, 2014, "Lightweighting with AHSS: Minimum Thickness Study & Application Guidelines, Version 5.0," *Proceedings of the 13th Annual Great Design in Steels Conference*, May 14, 2014, Livonia, MI, USA.
2. U.S. Department of Energy, 2020, "Materials 2019 Annual Progress Report," VTO, DOE-EERE, DOE/EE-1990, pp. 234–240.

Acknowledgements

The significant technical contributions of the following individuals are acknowledged and appreciated: T. Yoder, INL; and S. Li and P. Danquah, Diversitak.

II.1.6 Reducing the Weight of Vehicle Components Via Lost Foam Casting of Ductile and Austempered Ductile Iron (Skuld LLC)

Sarah Jordan, Principal Investigator
Skuld LLC
1509 Blatt Boulevard
Gahanna, OH 43230
E-mail: sjordan@skuldllc.com

Jerry L. Gibbs, DOE Technology Manager
U.S. Department of Energy
E-mail: jerry.gibbs@ee.doe.gov

Start Date: July 1, 2019 End Date: June 30, 2020
Project Funding: $200,000 DOE share: $200,000 Non-DOE share: $0

Project Introduction

This was a Phase I Small Business Innovation Research project to address casting defects intended for automotive lightweighting. DOE seeks to develop material lightweighting technologies for automotive applications because the vehicle weight directly impacts the amount of energy required. Due to both fuel efficiency standards, as well as the move to electric vehicles, there is a need to lightweight nearly every component possible. For electric vehicles, the weight impacts the needed battery size as well as the vehicle range. Lightweighting efforts reduce the needed battery size, which can further reduce the necessary vehicle weight in a virtuous cycle.

This project seeks to address lightweighting for castings by using ductile iron. Nearly 600 pounds of a vehicle's weight consists of castings with about half of that consisting of Fe or steel [1]. DOE has aggressive goals for Fe components [2], which include reducing the weight of steering knuckles by 25–35% and the weight of brakes by 50% by 2025. In addition, there is a goal to increase the castability of Fe to 2.5 mm +/- 0.75 mm by 2050.

There are two primary methods to achieve the lightweighting of Fe and steel components. The first is to replace them with alternate low-density materials, such as Al or Mg. This has the drawback of adding cost, as well as the fact that there is a point of diminishing returns as those materials do not have as high a strength, which means that thicker sections are required.

The other alternative is to develop improved ferrous alloys. Ductile Fe is 10% less dense than steel. It is also known to have the lowest cost specific strength (e.g., strength normalized to density). This is particularly true for its heat-treated version, austempered ductile iron. When designed properly, austempered ductile Fe castings can take advantage of the fact that it is about 2.3 times stiffer than Al and that even with a density 2.5 times that of Al, a weight reduction is still possible when switching from Al to austempered ductile iron.

The problem is that historically ductile Fe has not been formed in section thicknesses under 6.35 mm (0.25 in.). Instead, the casting is solidified to become primarily massive Fe carbide, Fe_3C, a.k.a white iron. This carbide material is hard and brittle and does not have the desired material properties of ductile Fe. Much research has been conducted on this issue such that some foundries are now capable of achieving 3 mm. The Lightweight Innovations For Tomorrow consortium has developed a sand-casting process that is able to achieve 1 mm [3]. However, the use of sand, whether green sand or resin-bonded sand, introduces another issue, which is tolerance control. Due to mold wall movement during casting, sand-casting typically has a tolerance variation greater than 0.75 mm, which is an issue if the starting dimension is only 1 mm.

Skuld LLC has developed a new alloying process that has shown to be capable of achieving 1.5 mm ductile Fe in production parts using the lost foam casting process. Using a proprietary combination of commercial raw materials, the thermodynamics are shifted so that ductile Fe forms, rather than massive carbides. Through the use of non-detectable amounts of barium and bismuth, which have the correct atomic diameter, such that the basal planes are shifted to prefer graphite nodules and austenite to solidify while achieving the same nodule count and form as in standard ductile iron. In addition, Skuld LLC has developed a process capability to injection mold foams as thin as 0.7 mm while manufacturer limitations have been indicated to be 6 mm.

This project seeks to show that the Skuld LLC process can address the current problems with casting thin-walled ductile Fe so that it can be used as a lightweighting material for Al thicker than 3.8 mm, as well as cast-Fe and steel.

Objectives

The objectives of this project were as follows:

- To develop a method of smoothing the surface of the foam to minimize surface defects.
- To determine the dimensional control for lost foam in thin-walled sections.
- To determine the fluidity length of ductile Fe in lost foam.
- To show that imperfections can be eliminated including carbides, high nodule count, and other microstructural defects in lost foam and to compare the same heats to resin-bonded sand.

Approach

To study roughness, a variety of coatings were applied to different foam densities (e.g., 0.477, 1.23, and 3.335 lb./ft^3) and measured using a profilometer. The low-density foams were also measured using a confocal laser microscope and measured three-dimensionally due to frequent issues with “out of range” results with the profilometer. The intermediate density coated and uncoated foam were cast in ductile Fe and the resulting casting roughness was measured for comparison to the starting roughness.

Using a 100-lb furnace and a Flowtret inoculation system, 16 heats were cast in a variety of chemistry ranges to cover the three primary grades of ductile iron: 65-45-12, 80-55-06, and 100-70-03. For all heats except for Heat 1, samples were cast in both lost foam and in resin-bonded sand. In Heat 1, only lost foam samples were produced. The lost foam samples were machined in expanded polystyrene foam in thicknesses of 1, 1.5, 2, 3, 4, and either 6 or 6.35 mm. Lost foam samples were produced in a variety of lengths to test fluidity and to produce tensile samples. The resin-bonded samples were manually produced from standard commercial keel block and wing mold samples with a variety thicknesses ranging from 0.38 to 9.91 mm. Heats 9 through 13 had two sets of samples cast as there were two coating thicknesses used at 25,575 and 7,425 cP viscosity, respectively. For the ceramic refractory lost foam coating, Polycap 367 coating was used for Heats 1–3 and FoamKote 7600 was used for Heats 4–16. Standard commercial pyrolite refractory downsprue, Foam Lok 70-12-11 adhesive, and Accucast ID40 ceramic mold beads were used for the mold process.

To determine the dimensional control in thin sections, the machined expanded polystyrene samples were measured in three locations per sample to obtain an average value and compared to the nominal per the Computer Numerical Control drawing. Only Heats 3–16 were considered due to known defect issues during pouring.

Fluidity is the ability of molten metal to flow through the gating system and fill the cavity of the casting mold prior to solidification. The purpose for this part of the project was to determine how large a component is feasible and for gating design. The amount of superheat is a critical parameter so the tap temperature (e.g., temperature when the metal is poured out of the furnace) and the pour temperature (e.g., temperature in the ladle just before pouring) were measured. After solidification, the length of the resulting casting was measured from the ingate to the end of the casting. There were difficulties machining an Archimedes spiral in foam and having sufficient structural integrity during the coating process. Therefore, for Heats 1–8, a spoked

arrangement of 280-mm samples was used with two samples of each thickness. For Heats 9–16, the samples were primarily intended for tensile specimens and were only 235 mm in length.

To determine if the process eliminated imperfections, microstructural analysis was done to the lost foam and resin-bonded sand samples. Nodules were evaluated in the unetched condition at 100X. Then samples were etched with 4% nital to examine pearlite and ferrite. Finally, a 10% ammonium persulfate solution was used to reveal massive carbides. X-ray analysis, hardness testing, and tensile testing were also conducted on the lost foam samples.

Results

The goal for minimizing roughness was to ensure that surface roughness was no more than 5% of the sample thickness. For a 1-mm sample, this means that the roughness must be below 984 µin Ra. The uncoated foam had an Ra of 230–250 µin and the resulting casting averaged 273 µin. The best coating method was an acrylic sealer, which resulted in a foam smoothness of 65 µin and an as-casting roughness of 178 µin—an improvement of 30% in the final casting surface. More importantly, it eliminated the foam bead appearance that makes lost foam castings look like styrofoam cups and achieved an appearance closer to traditional investment casting. The as-cast surface is shown in Figure II.1.6.1. Although it eliminated the foam bead appearance, it did not eliminate the blow hole or blow vents (horizontal lines). However, those can be removed with hot wax and emery paper prior to casting. See key publications for details on the roughness results.

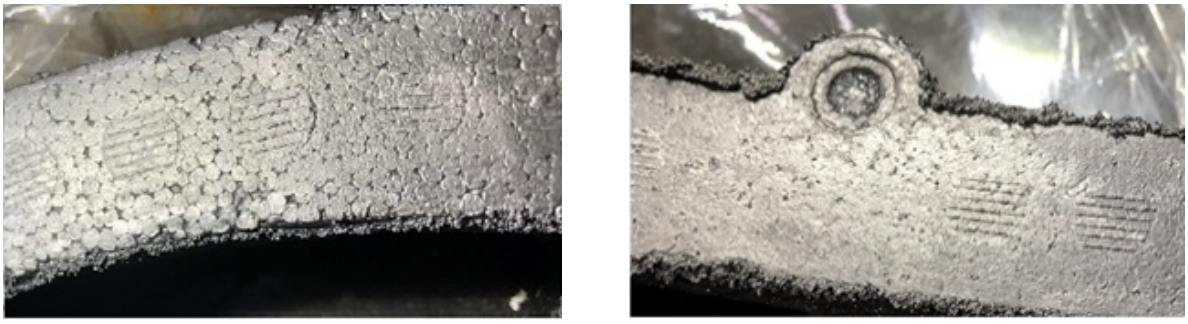

(a) (b)

Figure II.1.6.1. Photographs of the cast surface: (a) uncoated; and (b) improved with acrylic coating. Source: Skuld LLC.

Normal lost foam maintains a dimensional control of +/-0.003 inch per inch. This compares to sand-casting, which is +/-0.030 to 0.050 inch per inch and lost wax investment casting at +/-0.002. However, those tolerances have been determined over larger lengths than being considered in thin-walled sections. The target for this project was that variations be no greater than 5% of the nominal thickness. Table II.1.6.1 shows the results. The 2-sigma (two standard deviations) of the results are also shown as that is the typical amount used for quoting a tolerance range.

In general, the tolerance control is higher than the typical lost foam measurement of +/0.003 inch per inch. However, those measurements are made over a much longer distance. It appears likely that part of the variation is due to mold wall movement due to pressure as the results are generally larger than nominal. This may have been exacerbated compared to production processes as the molds were made through manual compaction. Finally, the resultant measurements were compared to the Computer Numerical Control nominal rather than a one-to-one comparison with the resulting foam, so it is not clear what part of the tolerance is consumed by the foam's dimensional accuracy versus what is consumed by the pouring portion of the process.

Table II.1.6.1. Measured Tolerance Results Comparing to Nominal Thickness

Thickness	Number of Samples	Average Measured Thickness (mm)	% Variation of Nominal	2 Sigma Tolerance Range (mm)
1 mm (0.0394 in.)	31	1.04	3.90%	0.16
1.5 mm (0.0591 in.)	36	1.57	4.83%	0.22
2 mm (0.0787 in.)	38	2.07	3.70%	0.20
3 mm (0.1181 in.)	37	3.15	4.91%	0.20
4 mm (0.1575 in.)	38	4.05	1.13%	0.30
6 mm (0.2362 in.)	28	6.15	2.45%	0.24
6.35 mm (0.25 in.)	10	6.57	3.45%	0.15

The fluidity was measured with the minimum, maximum, and average shown in Table II.1.6.2. The length of the fluidity runners were insufficient to determine the maximum distance in all, but the 1-mm samples filled the entire length of the fluidity pattern and likely would have had greater results than the maximum length of pattern. The average fluidity is a function of thickness as expected. Fluidity was not found to be correlated to pour temperature as it appears to involve other phenomena, such as distance from the downsprue and time between taking the pour temperature and completing the pouring.

Table II.1.6.2. Measured Fluidity Results Where * Indicates Maximum Length of Pattern

Thickness	Minimum Fluidity (in.)	Maximum Fluidity (in.)	Average Fluidity (in.)
1 mm/0.0394 in.	0.50	8.94	3.20
1.5 mm/0.0591 in.	0.94	11.00*	5.68
2 mm/.787 in.	1.75	11.00*	7.50
3 mm/0.1181 in.	5.25	11.00*	8.93
4 mm/0.1575 in.	4.63	11.00*	9.43
6 mm/0.2362 in.	9.25*	9.25*	9.25
6.35 mm/0.25 in.	5.63	11.00*	10.42

A range of chemistries were cast to investigate proof-of-concept for the standard ductile Fe grades (e.g., 65-45-12, 80-55-06, 100-70-03). In addition, in some cases intentionally high levels of carbide-inducing elements were added to determine the impact. The expectation was not to test for process capability or with the expectation that all samples would be free of carbides, but rather to get a general understanding of the range where carbide-free microstructures can be produced. The microstructure was examined after etching to evaluate pearlite, ferrite, and for massive carbides. Figure II.1.6.2 shows a typical carbide-free structure. Of the 16 heats, five had carbides in samples above 3 mm. For those remaining, seven resulted in a no bake, two lost foam, and two with both mold types had carbide-free microstructures under 3 mm.

This was unexpected as the authors background is in lost foam casting. The expectation was that the no bake would be a control sample that would show carbides in the same heat and section thickness while the lost foam did not due to the more insulating nature of the mold material. The fact that the no bake was as good or better indicates that the inoculation practice was insufficient, the time to pour and amount of cooling after tapping left insufficient superheat to vaporize the foam, or that the lost foam is not as insulative as expected. The thinnest carbide-free samples in lost foam were at 1 mm, which is the thinnest tested, and 0.76 mm in the no bake samples. Additional details are being reported at the upcoming American Foundry Society Metalcasting Congress.

In the majority of prior work, unusual alloying methods are utilized which lead to microstructures that do not match standard ductile Fe ane, which cannot be presumed to match typical ductile Fe properties. A common approach to prevent massive carbides is to increase the number of nucleation sites. This prevents carbides but results in high nodule counts, often over 2000 nodules/mm^2 which is ten times more than normal [4]. The method used here to prevent massive carbides does not rely on significantly greater number of nucleation sites but rather on adjusting the crystal structure. The nodules were characterized in the research. For the samples not found to be fully carbidic, nodule counts were typical of standard ductile Fe with an average of 178 nodules per mm^2 and a maximum of 300.

Figure II.1.6.2. Micrograph etched at 1.5 mm thickness showing typical bullseye ferrite and no carbides at 100X. Source: Skuld LLC.

Of the lost foam samples, 71 were sent for x-ray analysis. Those with obvious physical defects, such as cold shuts or mispours, were not tested. Of the samples sent, none showed massive carbides in the x-ray analysis. However, 15.6% of the samples showed some porosity or shrinkage, with the remaining 84.4% showing either no or negligible porosity/shrinkage. In cases where the microstructure revealed carbides—but the x-ray analysis did not—two primary reasons were determined to be the cause. First, if the material is fully carbidic, it will be of uniform density so x-ray analysis will not show a density difference. Second, very fine carbides do not necessarily show up through an x-ray because this is more of a macroscopic nondestructive testing method.

In lost foam, tensile tests are typically made using a no bake keel block mold with 0.5-in. round sample, which does not account for either thickness and chill nor process differences. Sixty samples were tensile tested, of which 33 were lost foam at 3 mm thickness or thinner, 22 were 4- or 6-mm lost foam, and five samples were 0.5 in. (12.7 mm) keel block samples. The lost foam samples did not pass the ductile Fe mechnical values for the given grades. There were a variety of reasons for this, including casting defects such as slag, cold shot defects, and graphite floatation. This is largely a function of the non-production setting, including but not limited to the use of a Flowtret system, small ladle size, and lack of spectrometer during casting.

Two hundred twenty lost foam samples were tested for hardness per ASTM A956 and converted to Brinell. Typically, foundries rely on Brinell hardness testing as a nondestructive test means to show that the material has the required strength. However, for thin-walled sections, Brinell is not feasible due to the bulging of the material, so rebound testing was used. Of the samples without carbides, 47% tested in the expected range, 44% were lower, and 9% were higher. For carbide samples where one would expect high-hardness readings, only 18% tested high, 58% tested in range, and 25% were low.

Conclusions

This project showed the surface roughness of the lost foam can be improved with coatings on the foam prior to casting, resulting in a 30% improvement in the surface roughness of the casting as well as the elimination of the foam bead appearance. This should be studied further in particular as to its potential impact on improving fatigue properties.

The dimensional control measurements show that lost foam can currently meet DOE's 2050 goal for Fe castings. The goal is achieving 2.5+/-0.75 mm. Lost foam is capable of preventing defects at 1 mm with an average variation of 0.039 mm from nominal. In addition, it can currently achieve tolerance control of +/-0.16 mm at 1-mm thickness. Potentially, this could be reduced further if one removed foams of unacceptable variation. The study only compared the results to nominal-machined dimensions and did not analyze the variation in the intermediate foam step.

The fluidity was determined for 1 mm to reach a maximum of 8.94 mm and was higher than 11 mm for thicknesses of about 1.5 mm. This indicates that large thin-walled sections are feasible with proper gating and sufficient superheat.

Samples found to be free of carbide were as thin as 0.76 in no bake and 1 mm in lost foam. Lost foam potentially could have been even less if there was sufficient superheat and if samples thinner than 1 mm had been produced. Eighty-four percent of samples did not exhibit porosity or shrinkage as determined by x-ray analysis, but the method used was limited in its ability to distinguish small carbides or fully carbidic material.

The methodology used showed that it is capable of eliminating defects including massive carbides, porosity, and high surface roughness. In addition, based on the fluidity measurements, large production parts are feasible. Based on the use of typical scrap and variations seen in chemistry, the process appears feasible with standard production practices once commercialized. Additional research to model the chemistry solidification, as well as the unexpected results in the no bake samples, is needed. Research is also needed to ensure an adequate method of nondestructive testing for carbides and to ensure mechanical properties are met. In addition, the project had an original goal to fully determine the necessary process control parameters, as well as to model when carbides will form. That was not feasible as the use of a Flowtret system for Mg inoculation was found to give erratic recovery rates and the small size of the furnace and ladle gave times and temperatures not reflective of production scale processes.

Key Publications

1. Jordan, S., M. DeBruin, C. Brown, and H. Gasvoda, 2020, *Design Considerations for Lightweighting with Ductile Iron Castings,* No. 2020-01-0656. SAE Technical Paper.
2. Jordan, S., M. DeBruin, A. A. Luo, and E. Cinkilic, 2021, Thin-Walled Ductile Iron with Carbide-Free Microstructure Down to Under One Millimeter in Lost Foam and No Bake Casting, American Foundry Society Metalcasting Congress, forthcoming.

References

1. Leider, N., 2014, "Automotive castings in ample supply," *Metal Casting Design & Purchasing,* March/April 2014.
2. U.S. Department of Energy, 2013, Workshop Report: Light-Duty Vehicles Technical Requirements and Gaps for Lightweight and Propulsion Materials, February 2013.
3. Stein, R. E., *et al.*, 2017, "Ductile iron alloys and materials including a thin wall layer of a ductile iron alloy." U.S. Patent Application No. 16/348,723, filed November 15, 2017.
4. Fraś, E., M. Górny, and H. Lopez, 2014, "Thin wall ductile iron castings as substitutes for aluminum alloy castings," *Arch. Metall. Mater.,* Vol. 59, No. 2, pp. 459–465.

Acknowledgements

The authors acknowledge OSU Lightweight Materials and Manufacturing Research Laboratory for providing the experimental foundry facility and Worcester Polytechnic Institute's Surface Metrology Laboratory for assistance in the 3D surface metrology measurements. They also acknowledge the following M. DeBruin from Skuld LLC; Dr. A. Luo, K. Kushner, C. Ridgeway, T. Avey, and J. Meier from OSU; and Dr. C. Brown and H. Gasvoda from Worcester Polytechnic Institute.

II.1.7 Overcoming the Barriers to Lightweighting by Enabling Low-Cost and High-Performance Structural Automotive Aluminum Castings (Pacific Northwest National Laboratory/Eck Industries)

Aashish Rohatgi, Co-Principal Investigator
Pacific Northwest National Laboratory
902 Battelle Boulevard
Richland, WA 99352
E-mail: aashish.rohatgi@pnnl.gov

David Weiss, Co-Principal Investigator
Eck Industries, Inc.
1602 North Eighth Street
Manitowoc, WI 54220
E-mail: david.weiss@eckindustries.com

Jerry L. Gibbs, DOE Technology Manager
U.S. Department of Energy
E-mail: jerry.gibbs@ee.doe.gov

Start Date: July 25, 2018 End Date: February 26, 2021
Project Funding: $500,000 DOE share: $250,000 Non-DOE share: $250,000

Project Introduction

The U.S. transportation industry is the biggest user of Al castings. In 2015, 17.84 million light vehicles (e.g., cars and trucks) were sold [1]. A typical vehicle contains ~400 lbs Al (~73% as castings), which represents a number that is expected to rise as high as ~500 lbs in 2025 [2]. Considering that a typical full-size sedan weighs anywhere between 2000–3000 lbs, greater use of low-cost and high-performance Al castings can contribute significantly to cost-effective vehicle weight reduction. However, cost and mechanical performance of Al castings are two key long-standing industry challenges that need to be overcome to enable greater weight reduction in mass-market vehicles. In other words, if the cost of Al castings could be reduced, and their mechanical performance enhanced, even greater market penetration (e.g., by replacing ferrous components) is possible.

One way to lower the cost of Al castings is to use "secondary" Al alloys (i.e., those produced from recycled Al), due to their ~16% lower cost than the "primary" Al produced via electrolytic reduction of alumina. However, many secondary Al alloys allow up to 0.60% Fe (as compared to 0.1-0.2% Fe in primary Al alloy) leading to the formation of iron-intermetallic phases in the microstructure. These intermetallics are detrimental to the tensile properties and elongation of the castings in comparison with the primary Al alloy. Thus, to keep costs low, Al may be skipped in favor of cheaper, but heavier, cast-iron. Further, irrespective of the choice of primary vs. secondary Al alloy, Al castings are often subjected to long-duration heat treatments, such as solutioning and aging, to improve their strength and ductility. Such heat treatments further add to the overall cost of the castings. Thus, techniques need to be developed that can help lower the cost of Al castings and enhance their performance (e.g., by enabling secondary Al alloys to overcome mechanical property limitations and by lowering the cost of heat treatments).

Objectives

The goal of this project is to develop strategies to help lower the cost of Al castings by enabling secondary Al alloys to overcome the mechanical property limitations and by lowering the cost of heat treatments. We propose to use two different processing techniques to achieve this goal. The first is an ultrasonic technique that enhances the mechanical properties by processing the molten secondary Al alloy, while the second uses a PNNL proprietary technique (in development) to shorten the solutionizing duration of the Al alloy. Thus, the project objectives are to:

- Develop process parameters for the ultrasonic technique leading to improvement in mechanical properties of the selected secondary Al alloy (i.e., containing "high" Fe %).
- Develop an alternate heat-treatment (with a shorter duration and/or lower temperature) leading to similar mechanical properties as the conventional heat-treatment for the selected Al alloy.

Approach

Eck Industries has identified A356 Al and A206 Al as alloys of interest for the purpose of ultrasonic process development and alternate heat-treatment development, respectively. The standardized chemistry of these alloys is listed in Table II.1.7.1 [3]. Both alloys were cast by Eck, and the subsequent experiments using these alloys are described in further detail in this report.

Table II.1.7.1. Standardized Compositions of the A356.0 Al and A206.0 Al Alloy

Alloy	Composition (wt.%)			
A356.0 Al	6.5 to 7.5% Si	0.25 to 0.45% Mg	0.2% Fe	0.2% Cu
A206.0 Al	4.2 to 5.0% Cu	0.15 to 0.35% Mg	0.2 to 0.5% Mn	0.15 to 0.3% Ti

Ingots of alloy A356 were cast with Fe < 0.1 wt.% and 0.9 wt.% to mimic primary (e.g., low Fe content) and secondary (e.g., high-Fe content) version of this alloy, respectively. In FY 2019, a benchtop setup for ultrasonic treatment of the melt was developed at PNNL, and the first set of ultrasonic treatment experiments were completed for the low Fe alloy. In FY 2020, the high-Fe alloy was processed using the same procedures previously developed. Ultrasonic impulses were applied in the melt using a Ti-6Al-4V probe. The key variable studied was ultrasonic power, keeping the treatment time and temperature constant at 2 min and ~620°C, respectively. The as-cast samples were polished by traditional metallography techniques and analyzed by optical and SEM. Backscatter mode was used for the SEM imaging, while EDS was used for composition analysis. ImageJ software was used to analyze the SEM images to quantify the microstructural features, such as the size and volume fraction of the dendrites and intermetallics.

The A206 Al alloy was permanent mold cast in the form of tensile samples seen in Figure II.1.7.1. In FY 2019, some as-cast tensile bars were cut into ~1/2 in. thick sections, which are shown schematically as blue cylinders in Figure II.1.7.1(a). The samples were subjected to standard T4 heat-treatment, which comprises pretreatment of ~510°C with a 1.5 h ramp to the pretreatment temperature, followed by solution treatment for 12 h at ~525°C, followed by water quenching and RT aging for 5 days. For some T4 samples, the solution heat-treatment was interrupted at 2, 4, and 8 hours. T4 heat-treated samples were further subjected to a T7 heat-treatment at 200°C for 4 h. The heat-treated samples were characterized by hardness measurements (HRB: 1/16 in. Rockwell spherical indenter, 100 kg load) to evaluate the influence of heat-treatment on the mechanical properties. Figure II.1.7.1(b) summarizes the results of the standard treatment. In FY 2020, the as-cast samples were solutionized by a PNNL proprietary electrical-heating setup for various times and temperatures, water quenched, and subjected to the regular T7 treatment. Hardness was used as a metric to compare the standard heat-treatment against PNNL's proprietary heat-treatment approach. As the standard treatment involves pretreatment and higher solutionization temperatures, some as-cast samples were solutionized in a regular furnace at similar times and temperatures of the PNNL treatment. This enabled a direct comparison between the two heat treatments. Finally, the samples were characterized by SEM with the procedure described for the A356 alloy.

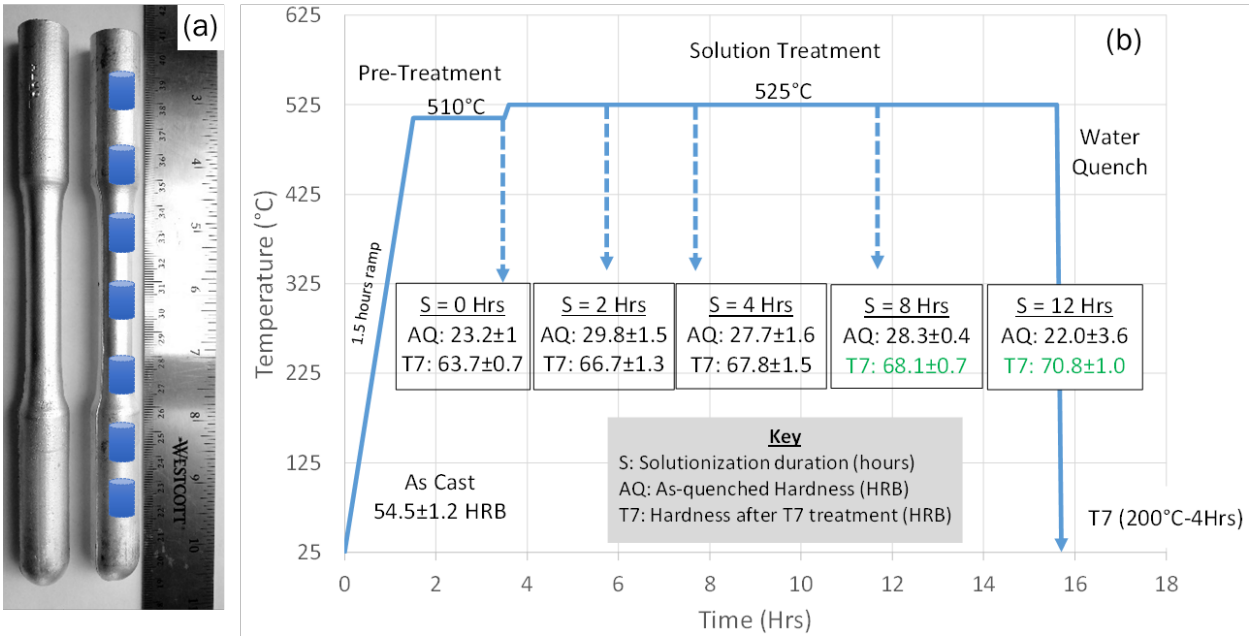

Figure II.1.7.1. (a) As-cast A206 Al alloy tensile bars where the blue cylinders schematically show samples that were machined from the tensile bars for heat-treatment experiments. (b) Standard heat-treatment procedure implemented in the experiments during FY 2019 and resulting hardness values. Source: PNNL.

Results

In FY 2019, the effects of ultrasonic treatment were investigated in the low Fe alloy. The microstructure contained primary Al-dendrite phase, the Si-eutectic phase, and the intermetallic compounds, such as Mg_2Si and Chinese-script-like phases of composition $Al_8Mg_3FeSi_6$ identified by EDS. Some of these phases in an ultrasonically treated sample had smaller sizes when compared to the control sample with no ultrasonic treatment, although scatter in the data made it difficult to ascertain clear trends. Effects of ultrasonication on high-Fe alloy was the focus in FY 2020. Figure II.1.7.2(a) and Figure II.1.7.2(b) show the microstructure of the high-Fe alloy before and after ultrasonication, respectively, at maximum power (50 W). Figure II.1.7.2(c) shows the low Fe sample after ultrasonication at 50 W. Microstructures of high-Fe samples are quite different than low Fe alloy in both control and ultrasonicated samples. For example, in the high-Fe case, ultrasonication does not appear to change the dendrite or intermetallic sizes, and the latter have a needle-like morphology, ~25 µm long on average. Intermetallic volume fraction increases with ultrasonication. On the other hand, the low Fe sample has a smaller dendrite and intermetallic volume fraction, and the intermetallics seem restricted to short lengths (~4 µm on average) in inter-dendritic spaces.

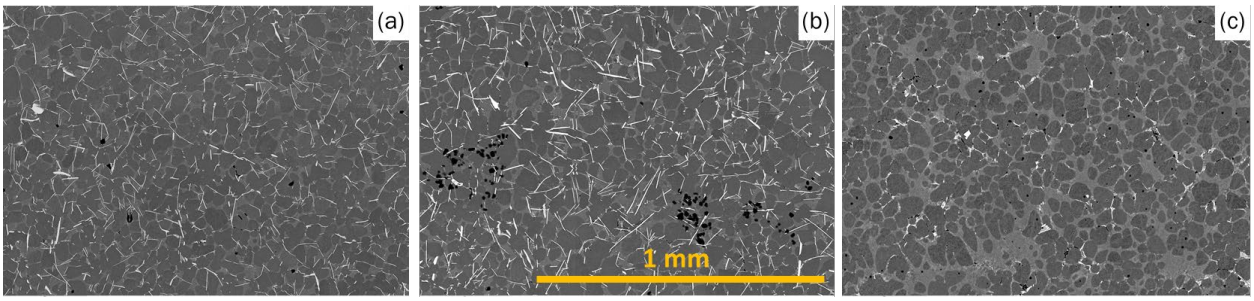

Figure II.1.7.2. As-cast SEM microstructure of A356 Al alloy for: (a) the high-Fe sample without ultrasonication; (b) the high-Fe sample with ultrasonication; and (c) the low Fe sample with ultrasonication. Source: PNNL.

Under the test conditions employed in this work, the morphology of the intermetallics seems to be independent of the ultrasonic treatment in both low- and high-Fe alloys. High-magnification SEM images and EDS analyses identified the intermetallics in the high-Fe samples as β-type Al_5FeSi precipitates, as seen in Figure II.1.7.3(a). These precipitates are detrimental to ductility due to their needle-like shapes [4]. Intermetallics in low Fe are α-type $Al_8Mg_3FeSi_6$ precipitates, as observed in Figure II.1.7.3(b), parallel to the observation in the literature [5]. The precipitate morphology can also be affected by the cooling rate. However, because the experimental procedures for both the low- and high-Fe cases were the same, the cooling rate is expected to be the same, and the presence of β-type precipitates is associated with the high-Fe content. A possible remedy to avoid the long, needle-like β intermetallics in the casting may be to apply ultrasonic treatment to the alloy in the semi-solid region and/or apply higher power than used in the current work. We anticipate that high-power and/or ultrasonication in semi-solid-state will fracture the long, needle-like β intermetallics and this size refinement may reduce their deleterious effect on the mechanical properties of the casting [4].

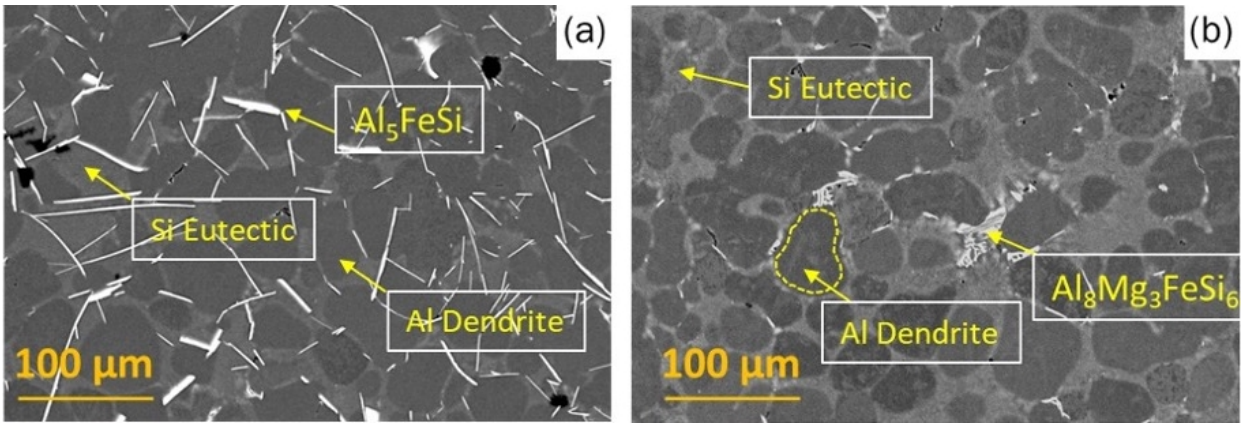

Figure II.1.7.3. As-cast SEM microstructure of A356 Al alloy: (a) without ultrasonication; and (b) with ultrasonication. Source: PNNL.

Quantitative analysis of the microstructures of the high-Fe samples show a slight increase in dendrite and intermetallic sizes with the ultrasonication, as observed in Figure II.1.7.4(a). The dendrite size plotted in Figure II.1.7.4 was determined according to the procedures described in the literature [4]. For high-Fe samples, intermetallic size was the longest dimension of the β needles. The same image analysis for low Fe samples also shows a slight increase and then a decrease in the dendrite size with higher ultrasonication powers. On the other hand, intermetallic size in low Fe samples, defined as the diameter of the circle fitting to the average area of the precipitates, slightly decreases with ultrasonication, as observed in Figure II.1.7.4(b). It is important to note that some of these measurements are within the error included in image analysis. This leads to inconclusive results on the relationship between the ultrasonication and microstructure development, especially for the dendrite size.

As part of the second objective of the project, microstructure and hardness of the A206 alloy are compared for the conventional and PNNL heat-treatment procedures. As detailed in the approach section, the conventional heat-treatment procedure had two variations. The first corresponds to the standard treatment employed by the Eck Industries and heat-treatment industry in general. This treatment was replicated at PNNL, and the results were shown in Figure II.1.7.1(b) above. The second variety, referred to as “furnace” from this point on in the text, serves as a more-direct comparison to PNNL’s modified heat-treatment as times and temperatures are closer. When compared to the standard, PNNL’s modified solutionizing heat-treatment at 500°C for 2 h yields similar or higher hardness in both, as-solutionized and in T7 states shown in Table II.1.7.2. Further, the PNNL method’s hardness values (“2 h” in Table II.1.7.2) are almost identical to the standard with a total processing time of 11.5 h (Standard “8 h” in Table II.1.7.2), indicating that the new method being developed is about six times more efficient than the standard method in terms of the processing time.

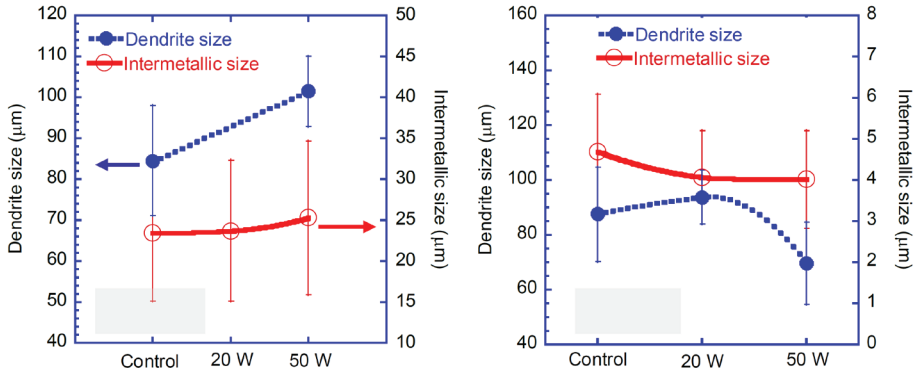

Figure II.1.7.4. Plots summarizing the quantitative image analysis results for (a) high Fe and (b) low Fe. Error bars are median absolute deviation. Source: PNNL.

Table II.1.7.2. Comparison of PNNL and Standard Heat Treatments

Heat Treatment	Ramp Time (h)	Soak Time (h) and Temperature (°C)	Total Process Time (h)	Hardness (Solutionized) HRB	Hardness (T7 Aged) HRB
Standard"0 h"	1.5	2 h at 517 °C	3.5	23.2 ± 1.5	63.7 ± 0.7
Standard "8 h"	1.5	2 h at 510 °C + 8 h at 522 °C	11.5	28.3 ± 0.4	68.1 ± 0.7
Standard "12 h"	1.5	2 h at 510 °C + 12 h at 522 °C	15.5	22.0 ± 3.6	70.8 ± 1.0
PNNL "2 h"	0.1	2 h at 500 °C	2.1	29.1 ± 3.0	68.0 ± 0.6

Microstructural analysis of the T7 heat-treated samples in Figure II.1.7.5 also confirms the efficiency of PNNL's method relative to the standard for solutionizing the large Al_2Cu precipitates in the starting as-cast microstructure. The SEM images in Figure II.1.7.5(a-c) show that while none of the heat treatments completely solutionized the Al_2Cu precipitates, the undissolved volume fraction of Al_2Cu (the bright phase) is comparable. The major difference in these images is that while the standard treatments appear to be more successful in dissolving precipitates along the grain boundaries, the PNNL modified treatment seems to result in "cleaner" grain interiors, suggesting it is better at dissolving precipitates in the grain interior.

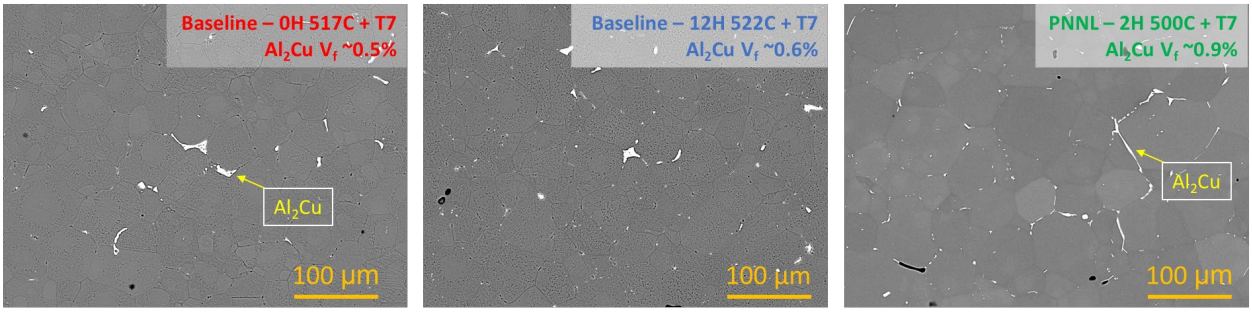

Figure II.1.7.5. SEM microstructures of A206 alloys solutionized and aged by: (a) the standard "0 h" method; (b) the standard "12 h" method; and (c) the PNNL 2 h method. Al_2Cu volume fractions calculated from these images are 0.5, 0.6, and 0.9 %, respectively. Source: PNNL.

Figure II.1.7.6 summarizes the hardness results obtained for various treatments. PNNL heat-treatment results in significantly higher hardness both in the as-solutionized and T7 conditions than do the furnace treatments at 450 and 475°C. In this case, the total processing time was similar for both treatments. However, furnace treatment fails in solutionizing the as-cast sample, as both solutionized and T7 hardness are far below those of the as-cast condition (54.5 ±1.2 HRB). Moreover, the two hardnesses are close to each other, indicating that

there are minimal Cu atoms in the solutionized state to cause any hardening during the aging. This is mostly because the furnace-solutionizing temperatures were considerably lower than the solvus temperature of 525°C of the ~4.6 wt% Cu alloy. PNNL heat-treatment also results in lower hardness than the as-cast state for the same reason. In PNNL heat-treatment case, however, there is a significant difference between the solutionized and aged states. This shows that PNNL heat-treatment is still able to dissolve Al_2Cu precipitates despite its temperature disadvantage and reprecipitate fine Al_2Cu during the aging.

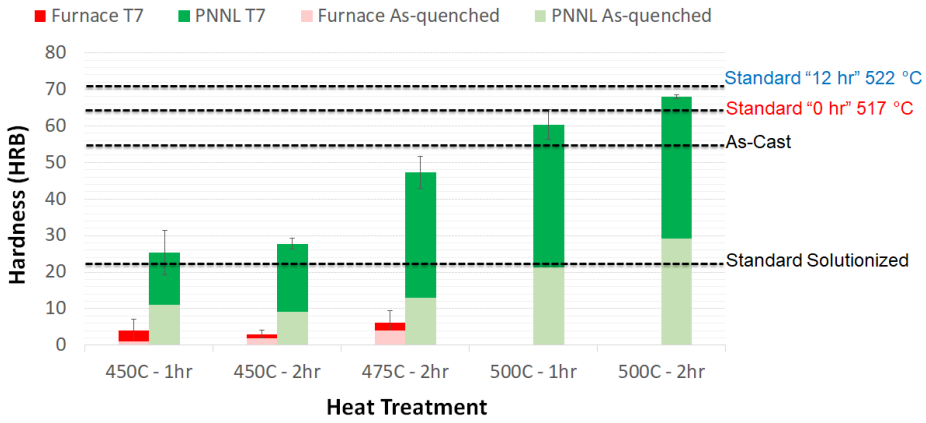

Figure II.1.7.6. Hardness plot summarizing the results of various heat treatments. Source: PNNL.

Conclusions

A benchtop setup has been constructed for the ultrasonic treatment of molten A356 Al alloy containing low (<0.1 wt. %) and high (0.9 wt. %) concentrations of Fe. Ultrasonic treatment in low Fe alloy resulted in slight refinement in sizes of dendrites and α-type ($Al_8Mg_3FeSi_6$) intermetallic phases. There was a slight increase in the sizes of dendrites and intermetallics with ultrasonication of the high-Fe alloy. In this case, precipitates were of β type (Al_5FeSi), which had needle-like morphologies. Formation of these precipitates was caused by the high-Fe content and/or, possibly, the slow cooling rate during casting, such that ultrasonic treatment at high temperatures (~620°C) was insufficient to break or transform these precipitates. A lower temperature ultrasonic treatment and/or higher power ultrasonic impulses are suggested as possible remedies. In a parallel set of experiments, an electrical heat-treatment method was developed at PNNL and applied to solutionization of as-cast A206 Al. The hardness and microstructure obtained by solution treatment and T7 aging were benchmarked against conventional treatments performed in a furnace. When compared to the standard practice, PNNL's method resulted in similar hardness and microstructure, but in about $1/6^{th}$ the solutionizing time and at a slightly lower temperature. For the same solutionizing times and temperatures below 500°C, the PNNL's modified heat-treatment method resulted in ~4 times higher hardness.

References

1. U.S. Geologic Survey (USGS), 2016, Minerals Yearbook 2015 – Volume I: Metals and Minerals, November 2016.
2. Richman, D., 2015, "Driving innovation with automotive Al," Drive Aluminum website. Available at: http://www.drivealuminum.org/research-resources/driving-innovation-with-automotive-aluminum-2/ (last accessed 10 December 2020).
3. Davis, J. R. (ed.), 1993, Aluminum and Aluminum Alloys – ASM Specialty Handbook, ASM International, Materials Park, OH, USA, p. 89.
4. Eskin, G. I., 1997, Principles of Ultrasonic Treatment: Application for Light Alloys Melt, Advanced Performance Materials, 4, pp. 223–232.
5. Davis, J. R. (ed.), 1993, Aluminum and Aluminum Alloys – ASM Specialty Handbook, ASM International, Materials Park, OH, USA, p. 291.

Acknowledgements

The technical contributions of PNNL staff supporting this research is gratefully acknowledged, in particular, Dr. Jens Darsell for his help in setting up the ultrasonic test capability, Dr. T. Mungole and Dr. M. Efe for performing the ultrasonic and heat-treatment experiments and associated analyses; Mr. A. Guzman for preparing the metallographic samples, and Mr. A. Schemer-Kohrn for performing the SEM imaging.

II.1.8 Room Temperature Stamping of High-Strength Aluminum Alloys (Pacific Northwest National Laboratory/Magna)

Aashish Rohatgi, Principal Investigator
Pacific Northwest National Laboratory
902 Battelle Boulevard
Richland, WA 99352
E-mail: aashish.rohatgi@pnnl.gov

Sarah Kleinbaum, DOE Technology Manager
U.S. Department of Energy
E-mail: sarah.kleinbaum@ee.doe.gov

Start Date: October 1, 2016 End Date: September 30, 2021
Project Funding: $1,425,000 DOE share: $1,000,000 Non-DOE share: $425,000

Project Introduction

This project addresses the challenge that high-strength Al sheet alloys possess limited formability at RT and are, therefore, difficult to stamp into structural components with complicated geometries. In other words, the sheet metal is unable to deform uniformly and instead cracks during RT forming/stamping. Warm/hot forming can increase the formability of Al, but it is expensive due to the added costs of heated dies, forming lubricants, lubricant clean-up, etc. Unlike hot-stamped steels that undergo austenite to martensite phase-transformation during quenching and achieve the high-strength at the end of the stamping process itself, the Al alloy matrix does not undergo such phase-transformation upon quenching. Hence, warm/hot forming results in lower post-formed strength such that heat-treatment, in addition to paint-bake, is needed (adding cost) to regain the strength. Thus, the use of an Al sheet is limited to lower strength Al alloys and/or simple-shapes (e.g., hood, deck lids, door inner, etc.) and many sheet components are still stamped in steel in the high-volume automotive industry. As such, the ability to form high-strength Al alloys cost-effectively (i.e., at RT), will expand Al use for structural components, as well (crash beams, B-pillars, etc.), which has the potential to result in significant lightweighting. By further incorporating mathematical models pertaining to precipitation kinetics in high-strength Al alloys, we aim to predict the YS evolution before and after the stamping process and identify a favorable zone to stamp the high-strength Al sheet akin to industrial processing timescales.

Objectives

This project aims to develop processing techniques that will overcome the formability limitations of high-strength Al alloys and enable RT forming. Eventually, this knowledge must be leveraged to fabricate an automotive component. Thus, the project objectives are to:

- Identify automotive components that, if formed out of high-strength Al, can provide lightweighting, relative to if they were made of high-strength steels.
- Develop constitutive relations and perform stamping simulations to determine the feasibility of stamping a selected component out of a high-strength Al alloy.
- Integrate microstructure and mechanical property models for the selected Al alloy:
  - Predict strength evolution during stamping and pre-/post-aging treatments using integrative modeling.
  - Establish a process routine based on predictive modeling for effective RT stamping.
- Fabricate and characterize the prototype component.

Approach

This project focuses on understanding the microstructure-formability-strength interplay in high-strength Al alloys with the expectation that microstructural control during processing could enable sufficient formability and strength in a prototypical automotive component. The project is structured to be performed in three phases. In the first, a door side impact beam was selected as the prototypical component for this project, and Al alloy AA7075 was selected as the high-strength alloy. In the second, forming simulations with the AA7075 were performed based on the design provided from an actual hot-stamped steel side impact beam. It was established from simulations that the selected design made of AA7075 is stampable. During the third phase, which began in FY 2019, strength evolution in the AA7075 was predicted during natural aging and under stamping/straining conditions. *In situ* and *ex situ* small-angle x-ray scattering (SAXS) and wide-angle x-ray scattering (WAXS) experiments were performed to quantify the evolution of microstructure (e.g., precipitation kinetics) during natural aging of the AA7075 sheet being used in the project.

As a part of our third phase efforts in FY 2020 and by using the data and analysis from prior years, stamping dies were fabricated and prototype side impact beams were stamped from AA7075 sheets. Prior to stamping, the blanks were heated in a hotbox furnace for solutionization purposes. After solutionization and quenching, blanks in two different tempers were stamped to the beam shape at RT in a 1000-ton forming press. The dies of the press were also at RT. The formed parts were then trimmed to the final shape. Two stamped and trimmed beams having two different initial tempers were cut into nine sections with length varying between 10 and 15 cm. These sections were then further cut into smaller sections according to the deformation observed in the form of surface protuberances and strain predictions from the simulations. Flat overhang pieces represented regions with no deformation, relatively flat side and outer walls represented regions with minimal deformation, and bent edges represented regions with a significant amount of deformation. Thickness strain and hardness were measured in each piece from each section. Hardness was measured by macro hardness (HRB: 1/16-in. Rockwell spherical indent, 100-kg load) by placing several indents (typically 4 to 8) at each measurement location. In the case of the bent regions, the hardness was measured on the concave side. The radii of such bent regions were measured to be in the range of 7-11 mm and therefore, the measured hardness values were corrected by subtracting 1.5 HRB per the guidance in ASTM E18 standard. Overall, about 250 hardness measurements were made on each beam and the data analyzed to determine the efficacy of the overall process to achieve T6 hardness without having been given a T6 temper heat-treatment. Finally, hardness data were correlated with the thickness measurements.

Parallel to the prototype fabrication and characterization experiments, microstructure and hardness evolution was monitored for sheet samples for the purpose of integrating the microstructure and mechanical property models. Sheets were solutionized at 480°C for 40 min., water quenched, and then aged to two different tempers (e.g., Tempers 1 and 2). Subsequently, tension samples cut with 0, 45, and 90-degree orientations with RD were deformed in tension at a constant strain-rate of 5×10^{-3} s^{-1} and at strains of 5, 10, and 15% and given a simulated “paint-bake” treatment of 180°C for ~20 min. For tension-tested samples, the hardness was acquired at the central-gauge region. Microstructure evolution and precipitate size in these samples were also monitored by SAXS measurements. SAXS with high-energy (13.5 keV) and high-brilliance x-ray beam of size 0.2 mm × 0.2 mm was performed to characterize the samples thinned down to ~150 μm during the complete aging experiment ($0 < t < 700$ hrs). SAXS was conducted at the 11-BM beamline facility housed at National Synchrotron Light Source (NSLS) at Brookhaven National Laboratory (BNL).

Results

Figure II.1.8.1 shows an example of two AA7075 stamped and trimmed side impact prototype beams having two different initial tempers that were successfully stamped at RT, validating the forming simulations performed in the previous phase. The 2.5 mm thick stamped Al beams weigh on average 897 g compared to 1449 g for the hot-stamped steel beam, corresponding to ~38% weight-saving over steel. If, to a first approximation, the tensile properties of the beam material are an indicator of the crash performance of the beam, preliminary tension data on coupons cut from the RT stamped AA 7075 beam is promising and shows somewhat higher specific strength compared to a hot-stamped 1.5 GPa steel. In other words, the lighter RT

stamped AA7075 beam is expected to possess a comparable, if not better, crash performance as the heavier steel beam although, full-scale impact/crash testing is necessary to confirm this.

While additional tension testing of the RT stamped Al beams is underway, the hardness distribution on the beams has been performed in greater detail. As described subsequently, hardness measurements in the as-stamped condition over the entire beam (for a given beam) are within 15% of the T6 temper hardness. The beams did not show any apparent surface defects, necks, or cracks and had surface finish comparable to the in-production steel beam that was used to design the Al prototype. Thus, the results show that high-strength Al alloys, specifically AA7075 in this case, can be formed into complex shapes (for structural components) at RT with the right conditioning of the blanks. While the absolute numbers for the weight savings are on the order of 0.5 kg per beam, it is easily seen that cumulative weight savings from multiple structural components made of high-strength Al and enabled by the current work, has the potential to yield considerable weight savings for the entire vehicle.

Figure II.1.8.1 also shows the hardness distribution on the two prototype beams (i.e., two different tempers) and the numbers represent the hardness values (Rockwell B scale) at the marked locations. A simple color scale is indicated to help visualize the hardness distribution. Colors and ranges in this scale are defined according to the whole range of hardness values measured on the beams. In each beam, the overall hardness values range from 81 to 92 HRB, where curved and bent regions have the highest hardness ranging between 85 and 92 HRB, relatively flat walls and sides range from 82 to 89 HRB, and undeformed regions have hardness between 81 and 84 HRB. Hardness measurements appear to be consistent for each beam as hardness values in each location match within ± 1 HRB for both beams. The similarly of hardness values also indicates that the RT stamping process produced repeatable mechanical property that appears to be independent of the starting temper of the blanks.

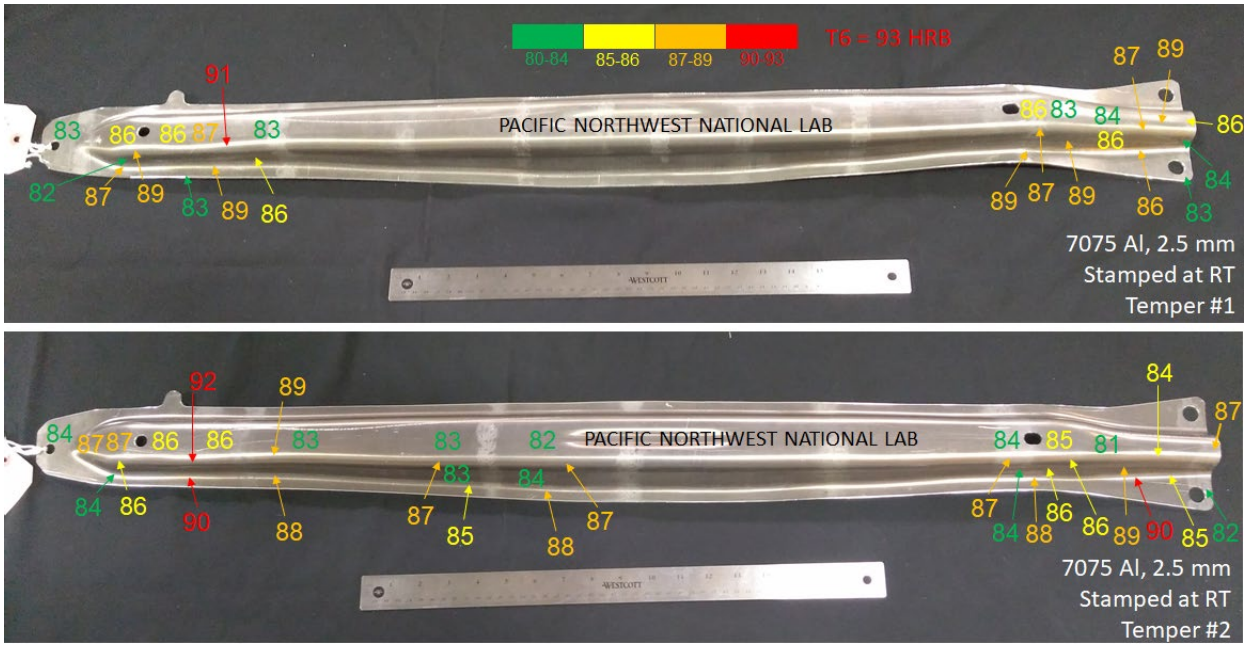

Figure II.1.8.1. Images and hardness distribution of the stamped prototype AA7075 side impact beams. Source: PNNL.

For the first beam (e.g., Temper 1), the average hardness was 86.3 ± 2.6 over the entire beam (i.e., 92% of the T6 hardness value of 93.0 ± 0.9). In the deformed regions, the average hardness was 87.0 ± 2.2 HRB, corresponding to 83% of the total measurements, while the average hardness in the undeformed regions was 82.8 ± 1.7 HRB, corresponding to the remainder 17% of the total 258 measurements. For the second beam (e.g., Temper 2), the average hardness was 85.6 ± 2.7 over the entire beam (i.e., 92% of the T6 hardness

obtained with artificial aging). In the deformed regions, the average hardness was 86.1 ± 2.6 HRB, corresponding to 86% of the total measurements while the average hardness in the undeformed regions was 82.6 ± 1.4 HRB, corresponding to the remaining 14% of the total 238 measurements.

Hardness results from these two beams are summarized in Figure II.1.8.2, which shows that > 80% of the measured values are within 10% of the T6 hardness and almost all the measured hardness values are within 15% of the T6 hardness. Hardness in the undeformed regions is slightly above the hardness obtained after natural aging while the hardness in deformed regions is close to the hardness obtained for natural aging and 10% tensile deformation. Finally, regions with the maximum hardness almost match the hardness of artificially T6 aged 7075. These results show the success of the RT stamping methodology, using natural aging and stamping, in meeting the T6 hardness requirements without a post-forming heat-treatment.

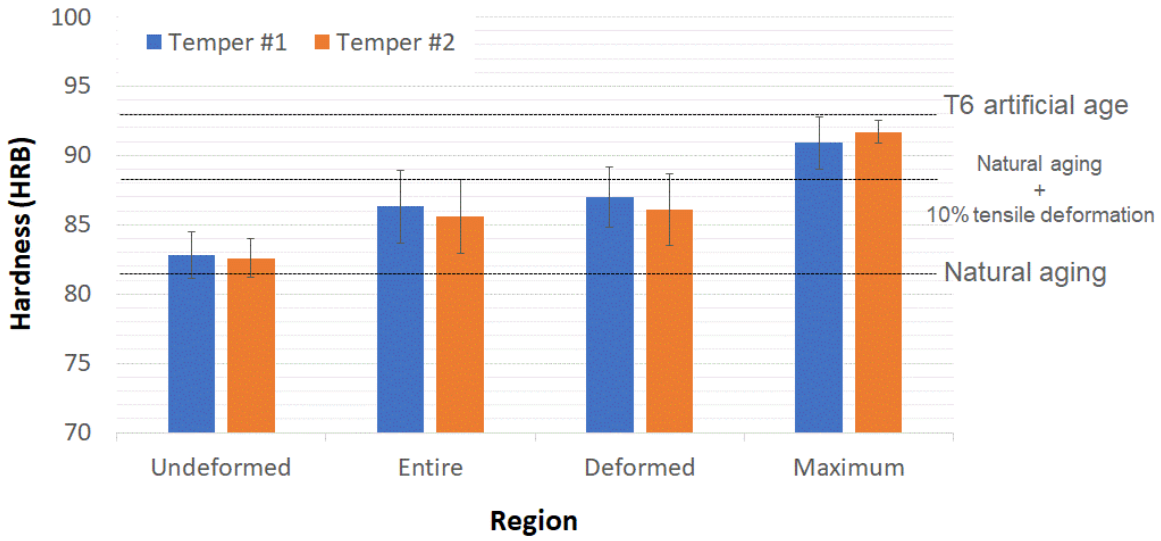

Figure II.1.8.2. Average hardness values obtained from different regions of the stamped beam and their comparison with the baseline treatments performed on the Al 7075 sheet. Source: PNNL.

Correlation of the hardness with the thickness strains for a given location reveals a rather complex relationship between these two parameters. Figure II.1.8.3 demonstrates a clear increase in hardness with strain in the regions that thicken (e.g., positive strain values on the x-axis) during stamping. Indeed, highest hardness values are observed in these regions. While the lowest values of hardness correspond to the undeformed regions of the beam, relationship between hardness and strains for the regions that undergo thinning (e.g., negative strain values on the x-axis) during stamping is unclear: the hardness data shows a larger scatter at lower thinning strains, but the hardness becomes almost independent of strain and reaches a steady value of ~87 HRB at the higher strains, as indicated by the trendlines in Figure II.1.8.3. Additional hardness measurements and on a larger number of beams per stamping condition will be necessary to confirm if the hardness is indeed strain-path (i.e., thickening versus thinning) dependent.

While hardness in most of the regions of the stamped beams reached the target T6-temper hardness value in the current work, microstructurally speaking, hardness is a function of the complex interactions between precipitates and dislocations that may evolve with time. For example, modeling work reported previously in this project indicated that the precipitation strengthening was controlled by Guinier-Preston (GP)-I and GP-II zones in the earlier (t ~ 10 hrs) and later stages (t ~ 100 hrs) of natural aging, respectively. Further, literature suggests that deformation may cause the precipitates to dissolve or change their sizes [3]. Therefore, understanding the interaction between precipitates and dislocation is necessary for both (1) design of the stamping process for optimum mechanical properties and without cracking, and (2) predicting the long-term performance of the stamped components.

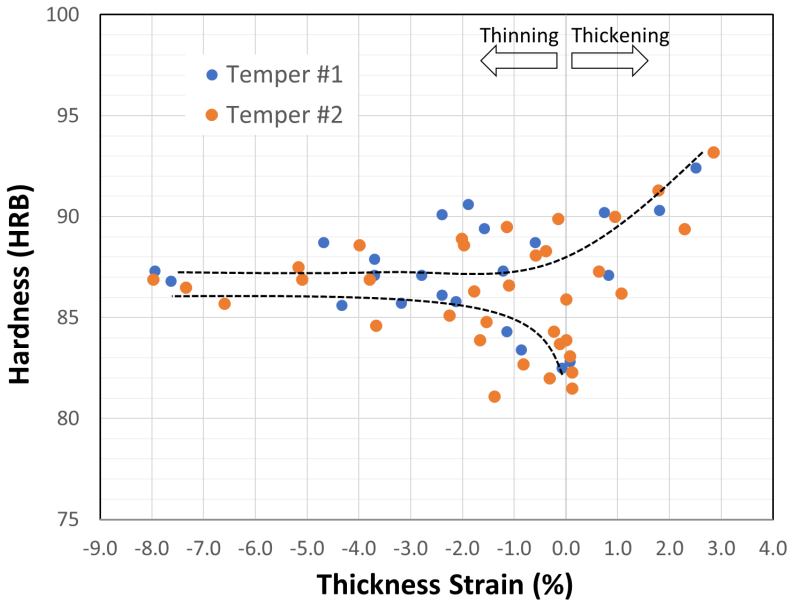

Figure II.1.8.3. Hardness vs thickness strain in the stamped beam. Each data point is average hardness with a typical ± 1 HRB standard deviation. Source: PNNL.

Controlled experiments on aged sheets show that mechanical behavior is highly dependent on aging condition, as observed in Figure II.1.8.4(a). For example, natural aging #1 shows a lower strength but a higher strain-hardening exponent of $n = 0.24$. However, serrations appear in the stress-strain curve because of the Portevin–Le Chatelier (PLC) effect, which is an indication of unstable plastic flow. On the other hand, natural aging #2 has a higher strength, lower strain-hardening exponent of $n = 0.22$, but show no indications of the PLC effect. It is evident that even a slight change in aging conditions can cause significant changes in the mechanical properties. Therefore, integration of the microstructure and mechanical behavior in models is important to optimize stamping.

Figure II.1.8.4(b) shows the hardness evolution in naturally aged and tensile deformed AA7075, where an unexpected fluctuating behavior is visible for all the samples. Although the hardness fluctuation range is quite small and, in fact, may be smaller than batch-to-batch property variation, they are remarkably similar in amplitude and frequency across multiple samples and may reveal interesting microstructural evolution. In fact, in a different set of samples that were tested in the x-ray beamline, Guinier-radius evolution during the post-deformation aging conditions, based on calculations from SAXS data, was also found to show a non-monotonic fluctuating behavior with time: the Guinier-radius increased from ~49 nm to 60 nm between 240 and 320 hrs, and then decreased back to ~54 nm at ~400 hrs. It is possible that GP-II zones (and likely η' precipitates) undergo dissolution/re-nucleation (or 're-growth') during natural aging (post-stamping) and lead to the observed fluctuations in their size and resulting hardness as shown in Figure II.1.8.4(b). These fluctuations indicate dynamically evolving microstructure and mechanical properties over a time scale that is short compared to the lifetime of the beams. An assessment of the long-term microstructure and property evolution is therefore needed to predict the lifetime performance of the stamped beams. Ongoing work comprises mechanical tests of the stamped beams under tension and bending, representing their mechanical behavior a few months after stamping.

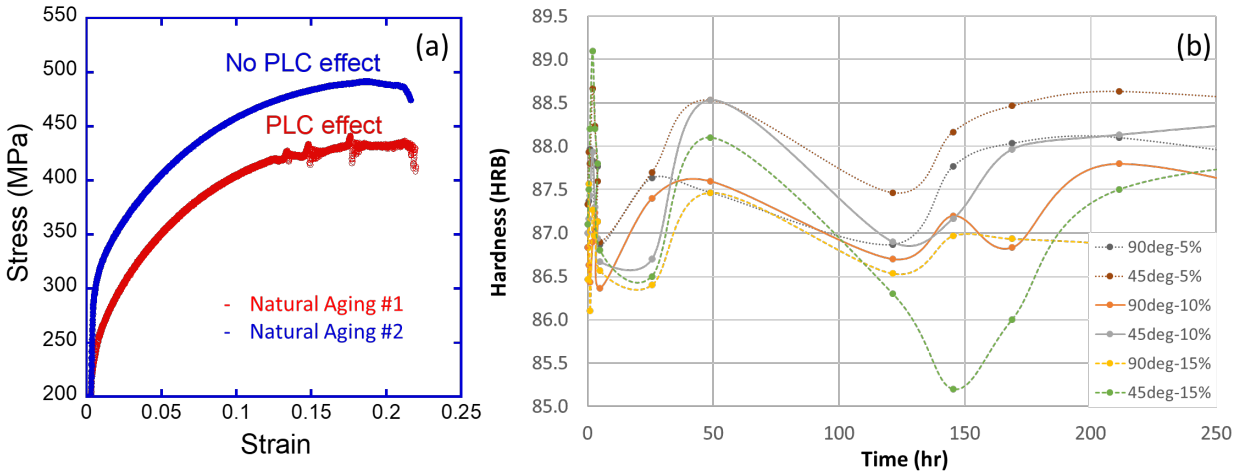

Figure II.1.8.4. (a) Engineering stress-strain curves for two sheet samples tested at different natural aging conditions. (b) Hardness evolution in AA7075 after being strained in two different orientations to different levels of strains. Each data point is an average of at least three hardness measurements with a typical variation of ± 0.5 HRB. Source: PNNL.

Conclusions

Based on the design of an in production hot-stamped steel beam, prototype side impact beams of AA7075 were successfully stamped at RT. The RT stamped Al beams were ~38% lighter than the baseline steel beam. Based on preliminary tension data, these lighter Al beams are expected to possess a comparable performance as the heavier steel beams although, full-scale testing is needed to confirm this. Extensive hardness measurements on different regions of the beams showed that more than 80% of the measured values were within 10% of the T6 hardness in the as-stamped condition (i.e., without the necessity of imparting a post-forming heat-treatment). To our knowledge, this is the first reported instance of such a structural component to be stamped in AA7075 at RT and achieving a near-T6 hardness without a need for post-forming T6 heat-treatment. With the careful control of the starting conditions of the blanks and the dies, it was possible to stamp the complex-shaped beam without any visible defects or cracks. The experiments also revealed two unexpected behaviors. First, correlation of the as-stamped hardness values with the corresponding thickness strains showed an apparent asymmetry viz. regions that thickened to a given strain showed greater hardness than those that thinned to the same strain. Second, hardness of aged and tensile deformed samples seemed to fluctuate with time and were mirrored, in a separate set of samples, by fluctuations in SAXS measurements of the precipitate sizes. While these observations are preliminary and deserve further investigation, they suggest a dynamic state-of-the-art microstructure in this alloy and highlight the importance of integrating microstructural and mechanical models. In the remaining work, the project will complete additional mechanical characterization of the prototype beams and the modeling efforts.

References

1. Berg, L. K., J. Gjønnes, V. Hansen, X. Z. Li, M. Knutson-Wedel, G. Waterloo, D. Schryvers, and J. R. Wallenberg, 2001, “GP-zones in Al-Zn-Mg alloys and their role in artificial aging,” *Acta Mater.*, Vol. 49, No. 17, pp. 3443–3451.

2. Deschamps, A., G. Fribourg, Y. Bréchet, J. L. Chemin, and C. R. Hutchinson, 2012, “*In situ* evaluation of dynamic precipitation during plastic straining of an Al-Zn-Mg-Cu alloy,” *Acta Mater.*, Vol. 60, No. 5, pp. 1905–1916.

3. Hutchinson, C. R., P. T. Loo, T. J. Bastow, A. J. Hill, J. da Costa Teixeira, 2009, “Quantifying the strain-induced dissolution of precipitates in Al alloy microstructures using nuclear magnetic resonance,” *Acta Mater.*, Vol. 57, pp. 5645–5653.

Acknowledgements

Technical contributions of the PNNL staff supporting this research is gratefully acknowledged. In particular, we are grateful to Dr. T. Mungole for developing mathematical models and securing synchrotron x-ray beamtimes; Dr. M. Efe for prototype characterization; Mr. K. Mattlin, Mr. M. Dahl, Mr. T. Roosendaal, and Mr. M. Rhodes in the Mechanical Testing Lab for their help in conducting heat treatments and mechanical tests; and Drs. M. Olszta and K. Kruska for their TEM analysis. We also acknowledge help from the beamline staff at the NSLS at BNL; namely, Dr. M. Fukuto and Dr. R. Li for conducting the SASX/WASX experiments and data analysis. This research used NSLS resources (11-BM), which is a DOE Office of Science User Facility operated for the DOE Office of Science by BNL under Contract No. DE-AC02-98CH10886. Finally, we would like to acknowledge the technical support provided by Mr. B. Kokosza and his team at Magna-Stronach Center for Innovation for stamping operation, technical discussions and support, and the technical staff at GM R&D—in particular, Mr. J. Carter and Dr. A. Sachdev, for their insightful comments, discussions, and providing the steel impact beam for this research, as well as providing information on lightweighting analyses for automotive components.

II.1.9 Graphene-Based Solid Lubricants for Automotive Applications (Argonne National Laboratory)

Anirudha V. Sumant, Principal Investigator
Argonne National Laboratory
9700 S. Cass Avenue
Lemont, IL 60439
E-mail: sumant@anl.gov

Tim Skszek, Co-Principal Investigator
Magna International, Inc.
750 Tower Drive
Troy, MI 48098
E-mail: tim.skszek@magna.com

Jerry L. Gibbs, DOE Technology Manager
U.S. Department of Energy
E-mail: jerry.gibbs@ee.doe.gov

Start Date: August 1, 2018 End Date: December 31, 2020
Project Funding: $650,000 DOE share: $640,000 Non-DOE share: $10,000

Project Introduction

Application of hot-stamped components can contribute up to 30–35% of the total mass of a typical passenger vehicle structure. Although most steel and Al sheet metal products are formed at RT, high-strength Al and UHSS alloys are processed at temperatures of 480°C and 930°C. Whereas RT metal stamping processes often include the use of water-based, oil-based, or solid lubricants to enable manufacture of an efficient design by reducing the coefficient of friction between the stamping blank and die surface and improves material formability, the use of such lubricants is not feasible here because oil- or water-based lubricants cannot survive the high operating conditions. The high coefficient of friction between the sheet metal blank and die surface during the forming operation results in a localized thinning condition that compromises design efficiency and structural performance. Therefore, it is of critical engineering importance to identify and develop lubricants that can perform at high temperatures. Engineering challenges include buildup on die surfaces, paint primer adhesion, effective sealants and structural adhesives, and environmental health/safety compliance.

Objectives

The objectives for the second year of this project are to:

- Demonstrate a reduction in the friction coefficient between a **7-xxx Al sheet** and a steel form die to enable cost-effective mass reduction of stamped Al safety components.
- Demonstrate a reduction in the friction coefficient between a **boron steel sheet** and a steel form die to enable cost-effective mass reduction of stamped ultra-high-strength automotive structural components.
- Demonstrate the ability to dispense a graphene-based lubricant in a cost-effective and environmentally safe manner.
- Demonstrate the ability to cost-effectively remove the die lubricant from the surface of the formed component part to ensure compatibility with secondary operations associated with adhesion of paint primer, sealants, and structural adhesives.

- Demonstrate that the die lubricant developed is “fit for use” in an industrial environment relative to environmental health/safety compliance.

Approach

Our approach to accomplishing the objectives involve the following three tasks and their subtasks:

- Pin-on-Disc Testing:
  - Determine the reduction friction and wear characteristics of various graphene-based solid lubricants applied to an Al sheet using a pin-on-disc test apparatus. Multiple solid lubricant coatings are applied to a **7xxx-series Al sheet** surface and tested at RT.
  - Determine the friction and wear characteristics of various graphene-based solid lubricants applied to boron steel sheet using a pin-on-disc test apparatus. Multiple solid lubricant coatings are applied to the **boron steel sheet** surface and tested at a RT.
- Develop a Large Area Coating Apparatus:
  - Characterize physical properties of graphene-based lubricant for dispensing application.
  - Develop and demonstrate means to efficiently dispense solid lubricant onto a die surface.
- Twist Compression Cup Testing:
  - Determine the reduction in friction coefficient associated with the use of a graphene-based die lubricant using the twist compression cup test apparatus. Evaluate the functional benefit of multiple solid lubricant die coatings when subjected to Al sheet materials at temperatures of **230°C and 480°C** and a steel sheet material temperature of **930°C.**

Figure II.1.9.1 illustrates the approach conceptually along with the relative timeline to accomplish the tasks.

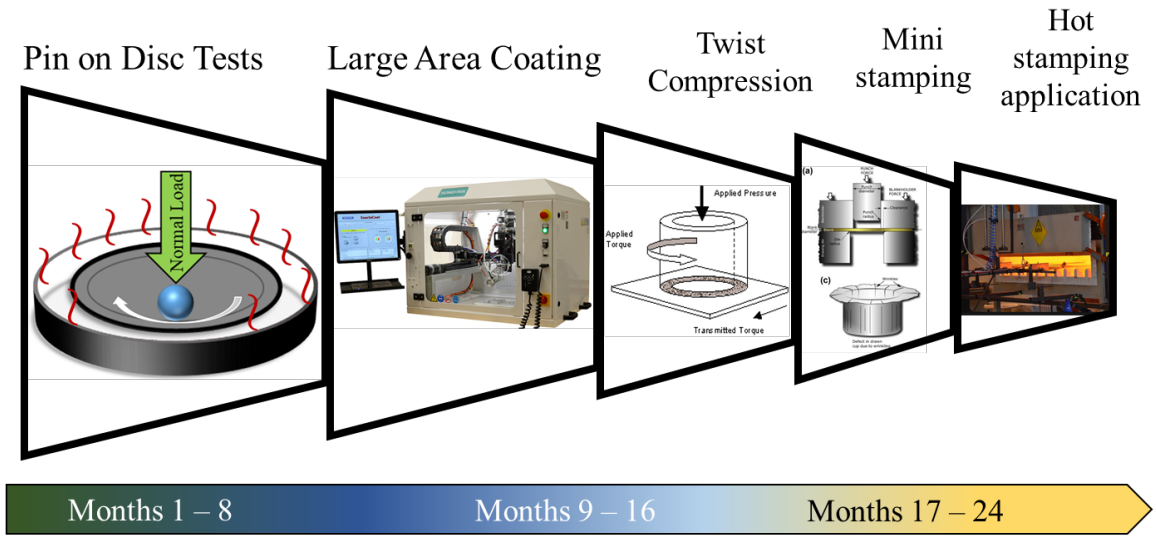

Figure II.1.9.1. Approach in the development of the lubricants [1]-[5]. Source: ANL.

Results

The pin-on-disc test results associated with various lubricant formulations were reported previously [6]. This report provides the results for the twist compression tests (TCTs) initiated in FY 2019 and completed in FY 2020 to evaluate the performance of the lubricants relative to an uncoated die surface, traditional lubricant. The TCT method includes coating the die cups with a graphene-based die lubricant and heating the coated die cup and sheet material to predetermined temperatures. The heated die cup and sheet material are inserted into

the test device and pressed against the sheet material to a predetermined load. The friction coefficient is recorded as the coated twist compression cup is rotated for a predetermined angular distance under load at a predetermined rate relative to the surface of the sheet material.

Graphene-based Development and TCT Results at 230 °C

The TCT results associated with the die cups coated with three graphene-based lubricant formulations are shown in Figure II.1.9.2. The coated die cups were preheated to 100°C and the Al sheet was preheated to 230°C prior to the transfer over to the TCT fixture. The friction coefficient associated with this series of TCTs ranged between 0.08 and 0.20 over a 45-mm sliding distance. This is in contrast to a commercial wax-based lubricant that revealed a friction coefficient of approximately 0.15 and an uncoated die cup that revealed a friction coefficient of approximately 0.37.

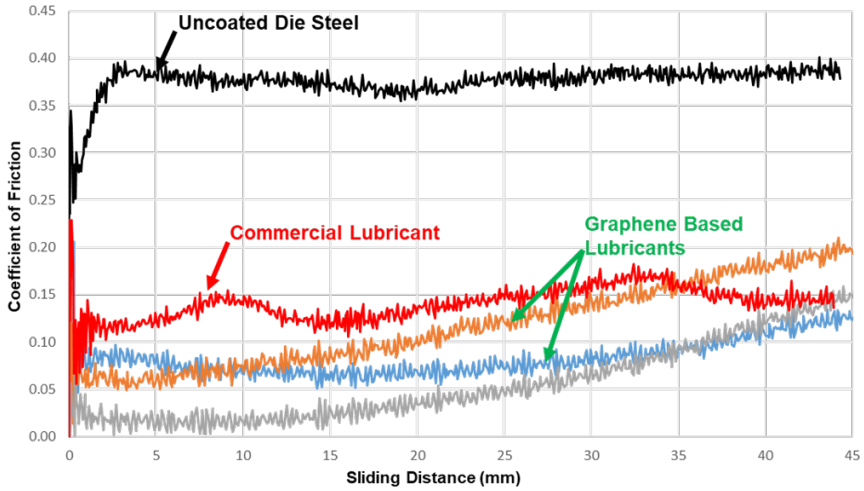

Figure II.1.9.2. Friction with three graphene-based lubricants developed for Al sheet preheated to 230 °C. Source: ANL.

Graphene-based Development and TCT Results at 480 °C

Minor modifications were made to the G and polymer mixture for use at 480°C, in terms of the percent of G and processing to sustain higher operating temperatures. The TCT results associated with the die cups coated with five graphene-based lubricant formulations are shown in Figure II.1.9.3. The coated die cups were preheated to 100°C and the Al sheet was preheated to 480°C prior to transfer to the TCT fixture. The friction coefficient associated this series of TCTs ranged between 0.05 and 0.15 over a 45-mm sliding distance. This is in contrast to a commercial wax-based lubricant that revealed a friction coefficient of approximately 0.25 and an uncoated die cup that revealed a maximum friction coefficient of approximately to 0.45.

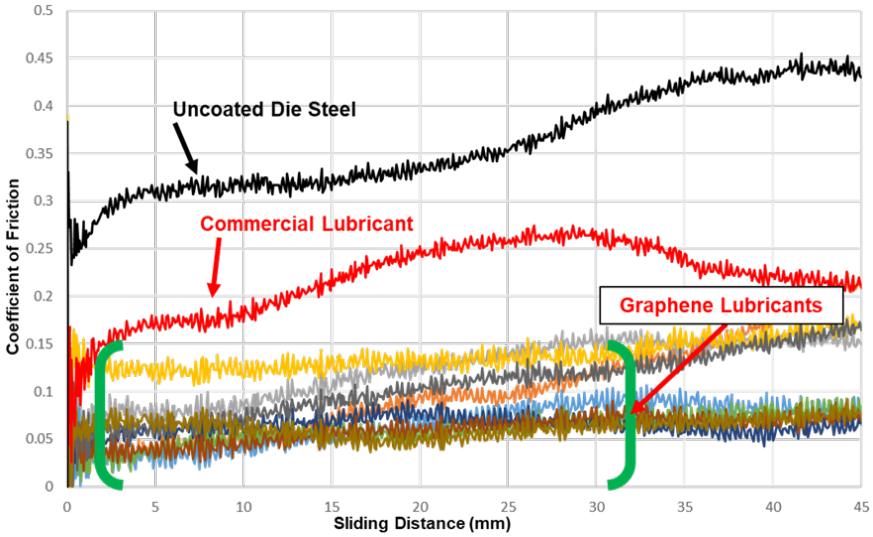

Figure II.1.9.3. Friction with five graphene-based lubricants developed for Al sheet preheated to 480 °C. Source: ANL.

Graphene-based Development and TCT Results at 930 °C

The literature reports that traditional oil- and wax-based lubricants are not effective at temperatures above 270°C. Boron-nitride lubricants are reported to reduce the friction coefficient at temperatures exceeding 1,000°C. Commercial use of boron-nitride as a die lubricant is limited due to issues associated with material cost, die buildup, and costs associated with removal of the coating from the sheet surface to enable adhesion of sealants, paint, and structural adhesive.

Minor modifications were made to the G and polymer mixture for use at 930°C, in terms of the percent of G and processing to sustain higher operating temperatures. The test results associated with the G-based solid lubricant-2 (SL2 formulation revealed *on par* performance with a commercially available boron-nitride high-temperature lubricant. The TCT results associated with the die cups coated with the SL2 graphene-based lubricant formulation is shown in Figure II.1.9.4. The coated die cups were preheated to 100°C and the boron steel sheet was preheated to 930°C prior to the transfer to the TCT fixture. The friction coefficient associated with the SL2 graphene-based die lubricant ranged between 0.07 and 0.10 over a 60-mm sliding distance. The advantages associated with the SL2 graphene-based die lubricant relative to the boron-nitride alternative include cost-reduction related to the material and removal of the lubricant from the surface of the enabled secondary operations. The disadvantage with the SL2 graphene-based lubricant formulation is the presence of ethanol, which imposes industrial safety concerns and prohibits use in an industrial high-temperature metal stamping environment. Further development activity included modification of G + polymer lubricant, addressing the need to reduce or eliminate the presence of ethanol.

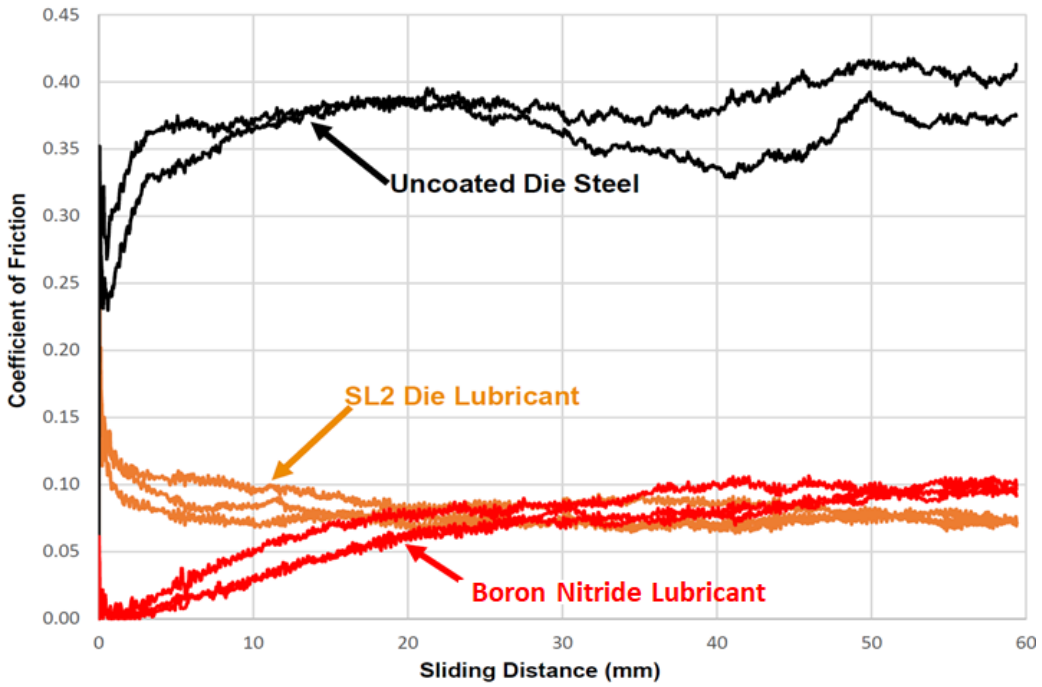

Figure II.1.9.4. Friction with G-based lubricants developed for use at 930°C. Source: ANL.

Minor modifications were made to the G and polymer mixture for use at 930°C, in terms of the percent of G and processing to reduce the presence of ethanol to near zero. The TCT results associated with the die cups coated with the graphene-based lubricants with near zero ethanol content are shown in Figure II.1.9.5. The friction coefficient associated with the G1 and G2 die lubricants ranged between 0.15 and 0.18 over a 60-mm sliding distance.

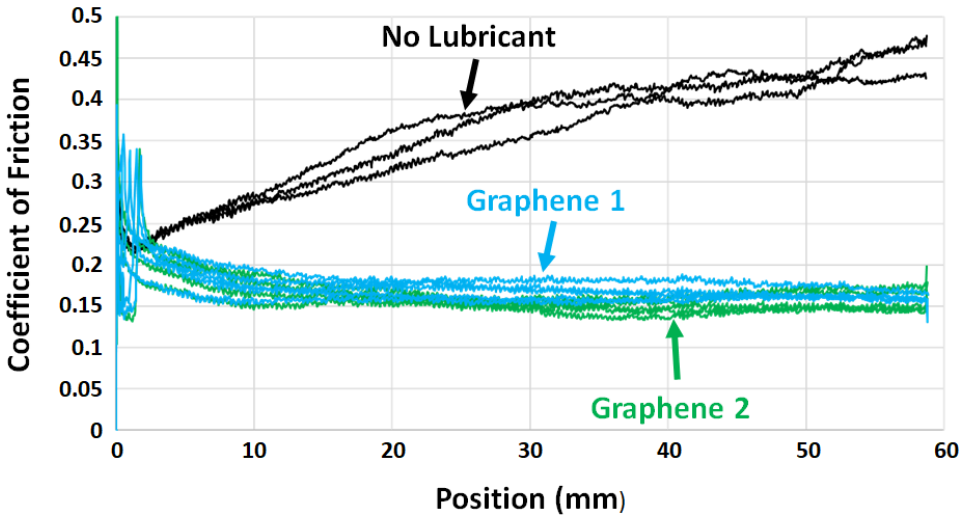

Figure II.1.9.5. Friction with graphene-based lubricants with reduced ethanol content for use at 930°C. Source: ANL.

Table II.1.9.1 provides a look at the ranges of friction that were observed in the three TCTs with the graphene-based lubricants.

Table II.1.9.1. Summary of Friction Observed in TCTs with Graphene-based Lubricants

Sheet Preheat Temperature	Friction Coefficient
230°C	0.08 – 0.20
480°C	0.05 – 0.15
930°C	0.07 – 0.20

Transfer and Removal of Die Lubricant

The surface of the TCT steel sheet samples were rinsed with purified water at 1,000-psi and analyzed to identify any transfer of lubricant during testing. Transfer of lubricant on the steel substrate may inhibit the adhesion of paint primer, sealants, and structural adhesives. Raman-spectroscopy was identified to be a reliable tool to map even minor traces of two-dimensional materials that may be on the surface of the substrate. The contact surface seen as a ring on the sheet material in Figure II.1.9.6(a) was mapped using Raman-spectroscopy and a representative Raman spectrum with no peaks for the vibrational modes of species in the lubricant is shown in Figure II.1.9.6(b). Multiple scans across several samples clearly show there is no transfer layer on the surface of the steel.

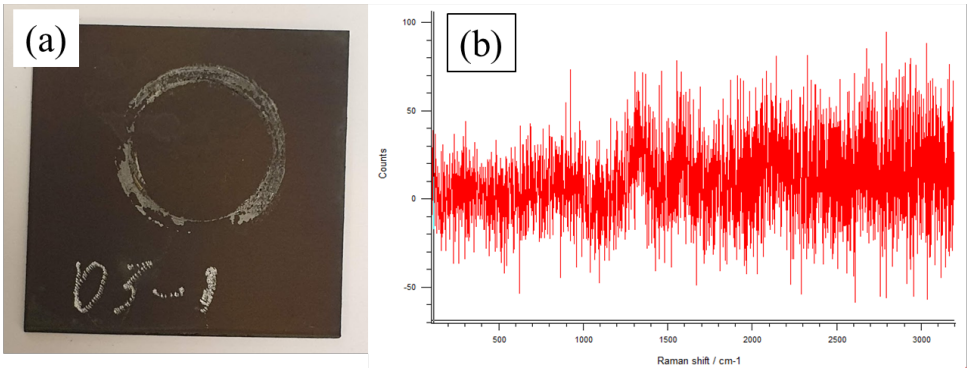

Figure II.1.9.6. Friction with graphene-based lubricants developed for use at 930°C. (a) Steel sample after TCT. (b) Raman spectra on the wear track. Source: ANL.

Large Area Coating and Evaluation of Coating Thickness

The feasibility of dispersing a water-based graphene/polymer lubricant onto a large area must be demonstrated to enable commercialization applications. To this end, a Sono-tek ultrasonication spray coater acquired and installed at ANL was used to dispense the lubricant onto an area about 300 mm × 300 mm. Figure II.1.9.7(a) shows the Sono-tek spray coating head dispensing the liquid carrying the solid material on to the substrate. Figure II.1.9.7(b) shows a close-up of the substrate with the G deposited. Figure II.1.9.7(c) shows the minute droplets of the solution just before evaporation of the liquid and depositing the solid contents on the substrate. A scratch was made on the substrate and the depth of the coating was measured using interferometry. Five such scratches were made on the four corners and one on the center. Another scratch was made at a random location. The average coating thickness measured on these six spots demonstrated a coating thickness within 10% variation demonstrating expected coating uniformity.

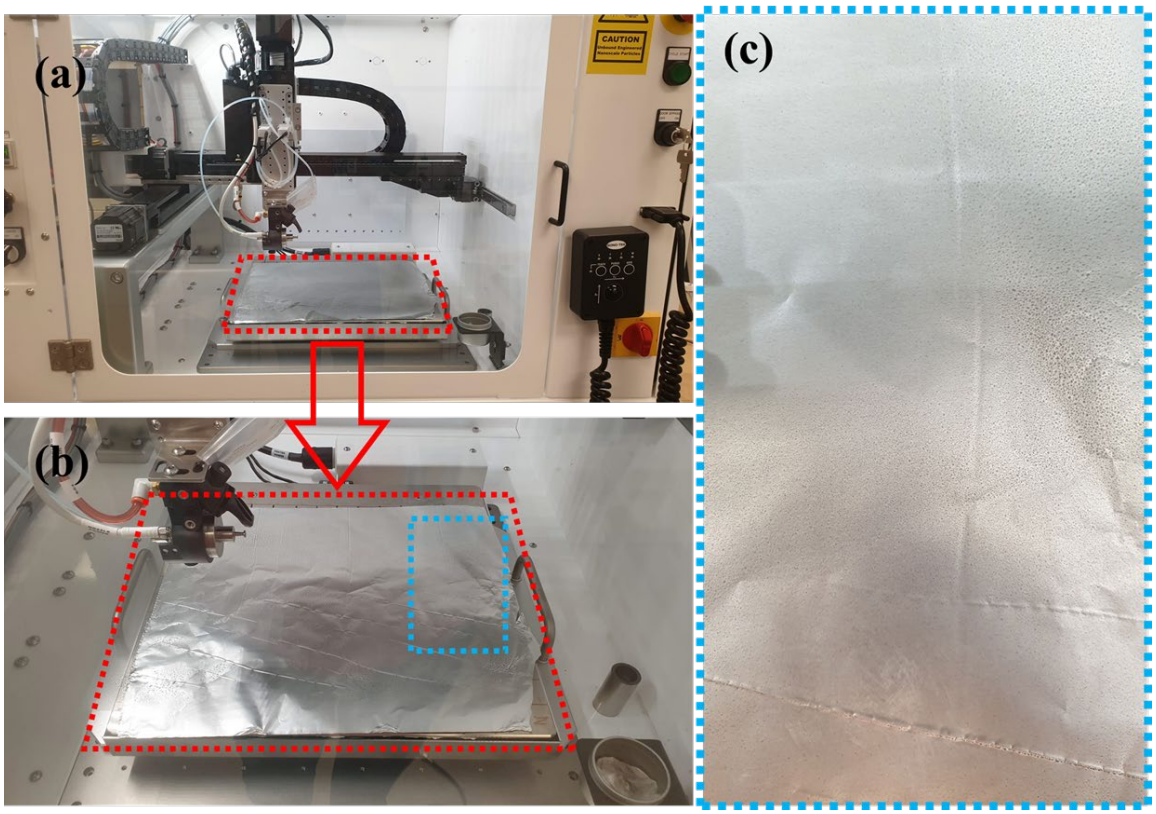

Figure II.1.9.7. Large area coater system demonstrating the feasibility of depositing the graphene-based lubricant on the substrate. (a) Sontek spray coating head. (b) G deposited on substrate. (c) Close-up of the droplets. Source: ANL.

Conclusions

Multiple potential lubricant combinations that have exceptional high-temperature performance have been identified, synthesized, and tested as follows:

- TCT was established as a reliable test method in which all the graphene-based lubricants were shown to outperform commercial lubricants.
- For the first time, graphene-based solid lubricants were shown to render lubrication at high temperatures—namely a 930°C steel sheet temperature in contact with a 100°C coated die surface.
- The Raman spectra test results indicate there was no detrimental transfer layers on the sheet surface after the TCT tests and high-pressure water rinse.
- Large area coating was shown to be feasible with a high degree of coating uniformity deposited.

Key Publications

1. Patent Disclosure ANL-19-016, 2019, Argonne National Laboratory, Chicago, IL, USA (submitted).

References

1. ANL native data used to generate the pin-on-disc image.
2. Sono-tek Inc. homepage, 2018, Available at: www.sono-tek.com (last accessed on 20 December 2020).
3. Gunderson, R., J. Hopkins, R. Main, and S. S. Malinowski, 2010, “Twist compression and four-ball test device redesign,” UM, Ann Arbor, MI, USA.

4. Qin, Y., W.A. Wan Nawang, and J. Zhao, 2015, "Forming of micro sheet metal components," in Qin, Y. (ed.). *Micromanufacturing Engineering and Technology*, *Second Edition*, Elsevier, Inc., New York, NY, USA. pp. 299–322. Available at: https://doi.org/10.1016/B978-0-323-31149-6.00013-X (last accessed on 20 December 2020).

5. Kahl, M., 2013, "Hot stamping goes mainstream," *Automotive World Megatrends Magazine*, 4 December 2013, pp. 59–61. Available at: https://www.automotiveworld.com/articles/hot-stamping-goes-mainstream/ (last accessed on 20 December 2020).

6. Sumant, A. V., and T. Skszek, 2019 "Graphene-based solid lubricants for automotive applications (Argonne National Laboratory)," *Materials 2019 Annual Progress Report*, DOE/EE-1990, Vehicle Technologies Office, Office of Energy Efficiency & Renewable Energy, Department of Energy, Washington, DC, USA. pp. 261–266.

Acknowledgements

ANL would like to acknowledge the excellent and productive collaboration with the Magna team and our University of Waterloo partners. The Magna team's support and suggestions during project planning, execution, and operation have been outstanding. Funding from DOE Technology Commercialization Grant TCF-17-13538.

II.1.10 Development of a Novel Magnesium Alloy for Thixomolding of Automotive Components (Oak Ridge National Laboratory)

Govindarajan Muralidharan, Co-Principal Investigator
Oak Ridge National Laboratory
1 Bethel Valley Road
Oak Ridge, TN 37831
E-mail: muralidhargn@ornl.gov

Bryan Macek, Co-Principal Investigator
Fiat Chrysler Automobiles U.S. LLC
1000 Chrysler Drive
Auburn Hills, MI 48326
E-mail: bryan.macek@FCA US LLCgroup.com

Nathan Sanko, Co-Principal Investigator
Leggera Technologies
87 Northpointe Drive
Orion Township, MI 48359
E-mail: nathan@leggaretech.com

Sarah Kleinbaum, DOE Technology Manager
U.S. Department of Energy
E-mail: sarah.kleinbaum@ee.doe.gov

Start Date: February 1, 2020 End Date: January 31, 2022
Project Funding: $300,000 DOE share: $150,000 Non-DOE share: $150,000

Project Introduction

Mg alloy die-castings are being increasingly used in the automobile industry as a means of providing cost-effective mass reduction, especially in systems where multiple components can be integrated into a single thin wall die-casting. However, there is only one die-caster in North America capable of producing die-castings of the size needed for instrument panel structures, liftgate inner panels, swing gate inner panels, and similar components, thus making it difficult to negotiate competitive pricing and creating a supply chain risk. Furthermore, there are several component quality restrictions in thin-walled Mg die-castings, including variability in dimensional accuracy, part-to-part variation in mechanical properties, and porosity in the final part, which has limited the continued growth of die-cast components in the automobile industry.

An alternative to die-casting is the process of thixomolding. Widely used in the electronics industry, the thixomolding process has begun to make inroads into the automobile industry (e.g., 2018 Jeep Wrangler spare tire carrier) as a competing process to die-casting for producing complex thin wall Mg components.

While the thixomolding process is somewhat similar to the die-casting process, it differs in at least one significant aspect. While the die-casting process relies on filling a mold at high speeds with the alloy in the completely molten state, the thixomolding process fills a mold with a thixotropic alloy in a semi-solid slurry state at a temperature between the liquidus and solidus temperatures. Ideally, the material should be ~30% to 65% solid rather than being completely liquid at the beginning of the injection process. Advantages of the thixomolding process include a finer grain structure, lower porosity, improved dimensional accuracy,

improved part-to-part consistency, improved mechanical properties, particularly ductility in the component, the ability to reduce wall thickness for mass savings, and longer tool life due to lower process temperatures.

Although thixomolding offers improved mechanical properties over die-cast Mg components, the mechanical properties obtained in the thixomolded parts are still not sufficient to broadly enable application in components where both strength and ductility are key requirements (e.g., crash critical components exposed to high-impact velocities and powertrain or chassis components subjected to high levels of cyclic loading). Currently, the mechanical properties are limited by the alloys being used, which are the same alloys used in the die-casting process. Thus, there is a need for the development of new alloys, which can achieve high-strength with improved ductility for use in components fabricated by the thixomolding process.

Objectives

The objective of this project is to develop a novel Mg alloy more suitable for thixomolded automotive structural components than current die-casting alloys. For this project, ORNL will assist Fiat Chrysler Automobiles U.S. LLC (FCA US LLC) and Leggera Technologies in the development of up to two new Mg alloys optimized for the thixomolding process with improved mechanical properties when compared to current die-casting alloys. The primary interest is in improving ductility and fatigue strength, as these are properties that are critical for use in body and chassis structural applications. Since good corrosion resistance is also desirable for this application, this property will also be considered when evaluating promising alloy compositions. Additionally, suitability for heat-treatment to further improve YS, tensile strength, and corrosion performance is of interest, since this capability is not available in current die-casting alloys.

Approach

In consultation with Leggera Technologies, FCA US LLC will establish the desired thixomolding processing parameters, target strength, ductility, and corrosion performance requirements of the new alloy. To understand the relationship between thixomolding process conditions, alloy composition, microstructure, and properties of the current alloys, ORNL will perform a baseline study of two industry-standard Mg alloys suitable for thixomolding in collaboration with industrial partners. In the initial phase of the work, ORNL has initiated microstructural characterization of an existing thixomolded component fabricated with AM60 using optical and SEM and X-ray microchemical analysis to understand the effect of alloy composition and processing conditions on the microstructural evolution during the thixomolding process and its effect on strength and ductility.

Based on correlations developed in this part of the work, the team will initiate new alloy development by identifying favorable microstructural characteristics for the target mechanical properties. ORNL will establish the feasibility of using computational thermodynamic models to predict the observed microstructure and to simulate the effect of selected alloying element additions on the solidification behavior. ORNL will also identify alloy compositions that have the potential to be successfully fabricated using the thixomolding process while having the desired microstructure in the final thixomolded component. Laboratory-scale heats will be fabricated at ORNL and the as-cast microstructure and tensile properties of the alloys will be evaluated to identify the required type and amount of alloying element additions. One or two alloys will be downselected for alloy ingot and chip production for use in the thixomolding process and a prototype component will be produced by Leggera Technologies. FCA US LLC will coordinate and complete material characterization tests for one new material from samples excised from the component produced by Leggera Technologies and will supervise computer-assisted engineering card development to support component modeling. Finally, FCA US LLC will conduct simulated component structural evaluation using the new properties developed for the computer-assisted engineering card.

Results

This project is a CRADA between ORNL, FCA US LLC, and Leggera Technologies. Since the project was initiated in the middle of February 2020, initial progress was hampered by COVID-19-related access restrictions at both ORNL and FCA US LLC facilities. Progress has been steady since the partial reopening at both facilities.

Microstructural analyses were initiated on samples culled from different regions in a component thixomolded from alloy AM60B (base nominal composition Mg-6% Al- 0.3%Mn, all in wt. %) [1]. Figure II.1.10.1(a) shows the typical microstructure observed in one of the regions obtained from the casting. Figure II.1.10.1(a) also shows the presence of nodules with an average diameter of approximately 50 µm accompanied by a fine two-phased microstructure. Based upon previous work [2],[3] and confirmed by X-ray microchemical analysis, it was inferred that these were primary α-Mg nodules surrounded by a fine eutectic microstructure. The region closest to the die-walls seems to be void of these nodules with almost all being distributed close to the central region of the component wall. Figure II.1.10.1(b) shows a higher magnification image of the fine two-phase eutectic microstructure surrounding the α-Mg nodules.

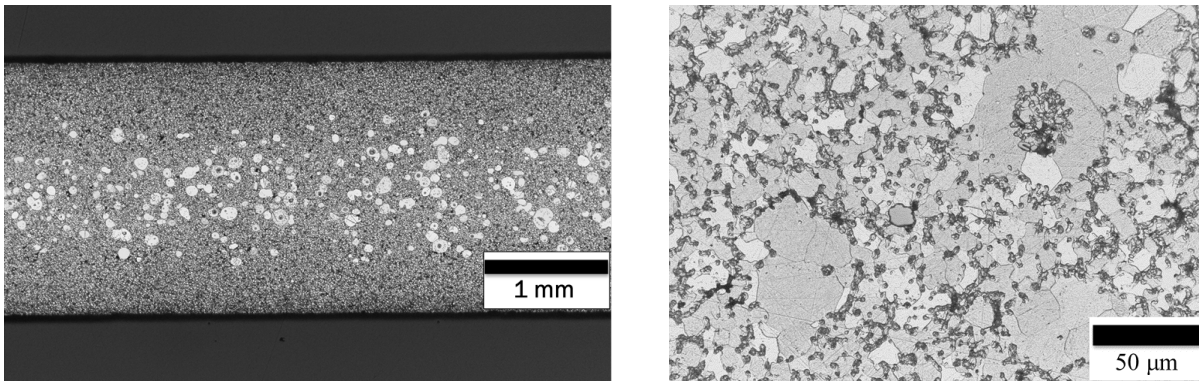

(a) (b)

Figure II.1.10.1. (a) Cross-sectional optical image of the wall of an AM60B thixomolded component. (b) A higher magnification image of a region shown in (a). Source: ORNL.

Figure II.1.10.2 shows secondary SEM images of an eqivalent region at two different magnifications. These images clearly show the presence of a bright area and a darker area in the region adjacent to the nodules.

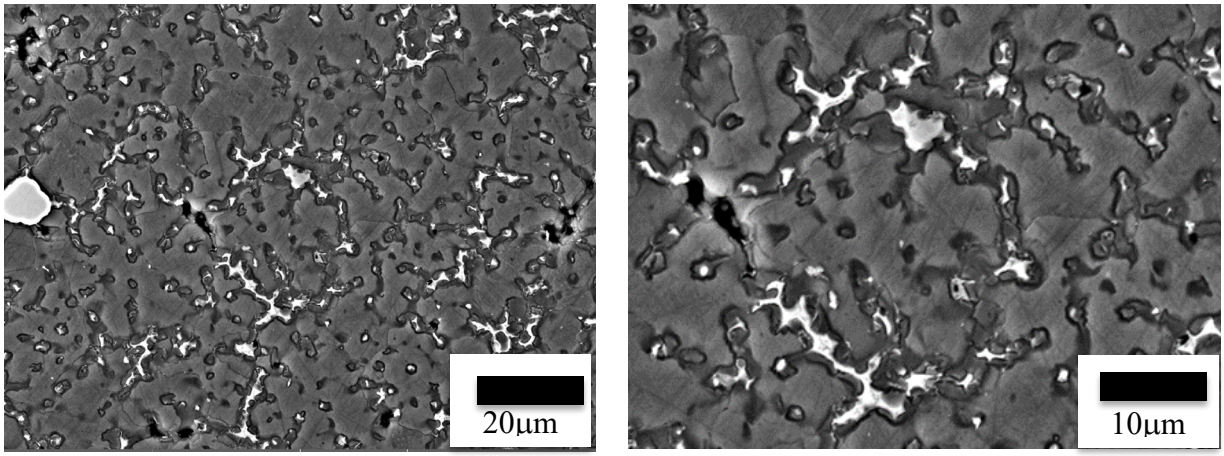

(a) (b)

Figure II.1.10.2. (a) A secondary electron image. (b) A higher magnification secondary electron image showing the fine eutectic microstructure in the region adjoining the nodules in the sample shown in Figure II.1.10.1. Source: ORNL.

Figure II.1.10.3 shows a secondary electron image along with Mg Kα, Al Kα, and Mn Kα X-ray maps from the corresponding region of the same sample shown in Figure II.1.10.1 and Figure II.1.10.2. Note the presence of a network of Al- and Mg-rich regions, as well as isolated particles that are rich in Al and Mn.

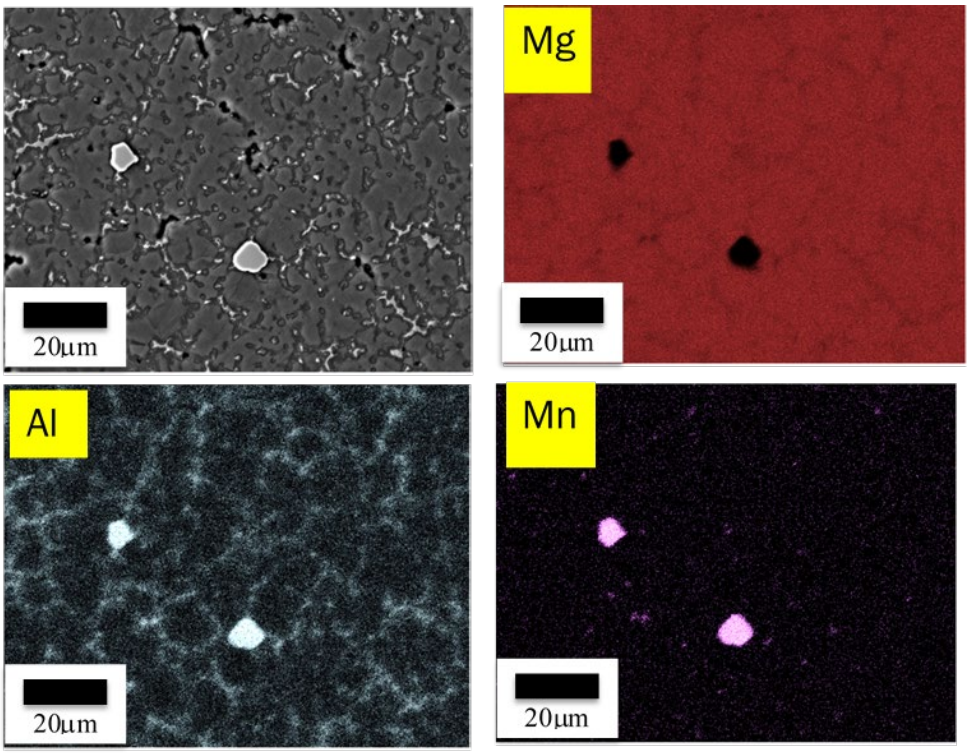

Figure II.1.10.3. Secondary electron image along with Mg Kα, Al Kα, and Mn Kα X-ray maps from the corresponding region of the sample. Source: ORNL.

Figure II.1.10.4 shows the results from the equilibrium phase diagram calculations for AM60B with a nominal composition of Mg-6.1Al-0.3Mn-0.18Zn-0.1Si all in wt% obtained using Thermo-Calc® Version 2020b and the TCMG5 database. Predictions show the potential for the presence of multiple second phases, in addition to the Mg solid solution phase with the $Al_{12}Mg_{17}$ phase being present in the largest amount.

Figure II.1.10.5 shows the predictions of phase fractions at the conclusion of solidification obtained using Scheil simulations. Figure II.1.10.5(b) shows the same data shown in Figure II.1.10.5(a) using an magnified y-axis scale emphasizing the minor phases. Note that in addition to the Hexagonal Close Packed Phase (HCP Mg), $Al_{12}Mg_{17}$ is shown to be present although at a significantly lower fraction. Minor phases predicted to form during solidification include the Al_8Mn_5 phase and the Mg_2Si phase. Comparison of predictions with experimental observations shown in Figure II.1.10.3 confirm the presence of $Al_{12}Mg_{17}$ and isolated particle-rich Al and Mn-rich inferred to be the Al_8Mn_5 intermetallic compound. Further analysis is in progress.

Figure II.1.10.6 shows the results from RT tensile tests on subsized tensile specimens machined from material culled from two different regions in the same casting. In tests conducted thus far, the measured 0.2% yield strengths range from approximately 122 to 150 MPa with strains to failure ranging from approximately 8 to 22%. Since component thicknesseses and distances from the injection point varied for these two locations, actual microstructures in these regions are being evaluated to obtain a better understanding of the microstructural features and defects (if any) that result in this variation in properties. Previous work on thixomolded AM60B has shown yield strengths in the range of 105 to 135 MPa [2], which is slightly lower but comparable to the values obtained in this study. Previous work showed elongation to failure of 5%, but the tensile specimen geometries are not specified in the previous work.

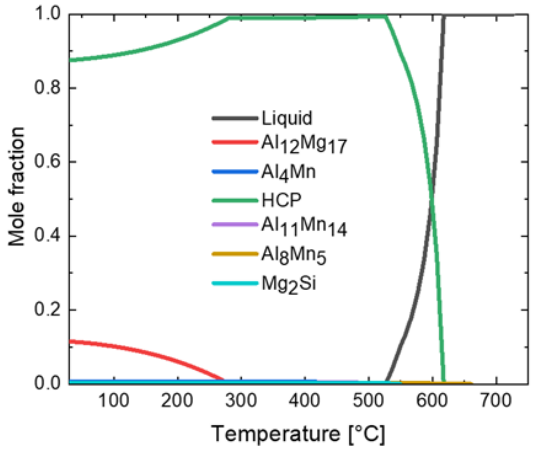

Figure II.1.10.4. Equilibrium phase diagram for AM60B nominal composition: Mg-6.1Al-0.3Mn-0.18Zn-0.1Si in wt% predicted using ThermoCalc™ version 2020b and the TCMG5 database. Source: ORNL.

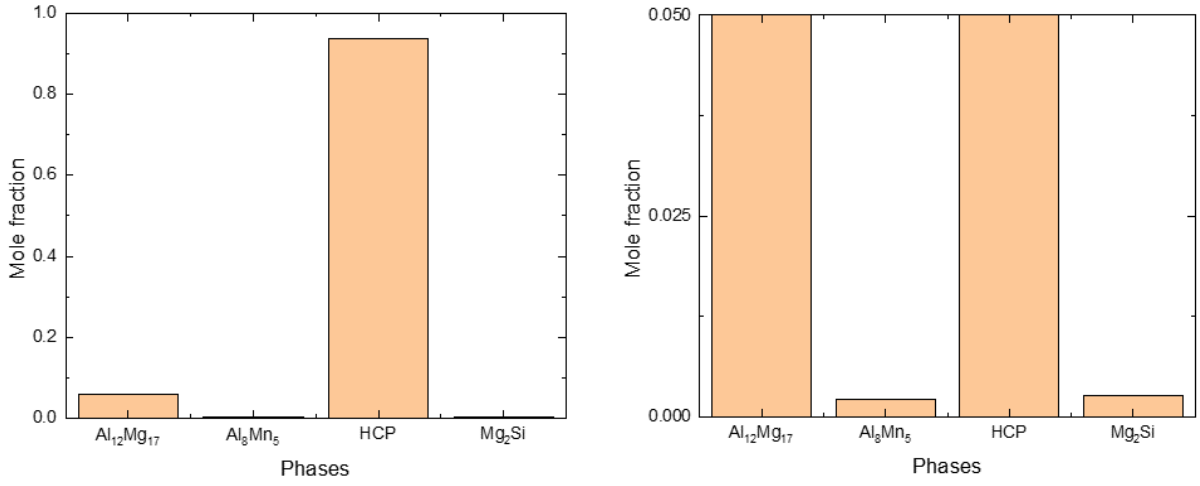

Figure II.1.10.5. (a) Predictions of phase mole fractions at the conclusion of solidification obtained using Scheil simulations. (b) Expanded y-axis showing minor phases. Source: ORNL.

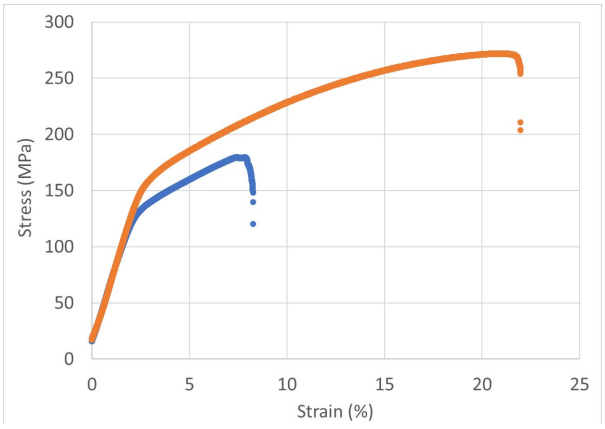

Figure II.1.10.6. Results from RT tensile tests on subsized specimens obtained from two different regions in the same casting. Source: ORNL.

In addition to experiments focused on characterizing material microstructure and materials properties, computational modeling is being used to evaluate the effect of different alloying elements on the liquidus temperatures, solidus temperatures, fractions of solids at processing temperatures, and fractions of different phases at RT. Predictions from these models will be combined with experimental correlations between microstructure and mechanical properties obtained from the work elucidated above to enable the identification of alloys with the potential to have improved mechanical properties.

Conclusions

Microstructural analyses and tensile testing have been initiated on samples culled from different regions in a thixomolded component cast using alloy AM60B. Experimentally observed microstructures compare well with thermodynamic predictions obtained using the Thermo-Calc 2020b and TCMG5 database. Tensile properties obtained using subsized specimens show good strength and ductility, but region-to-region variations occurred presumably due to variations in component thicknesses and cooling rates. Computational modeling is being used to evaluate the effect of different potential alloying elements on liquidus temperatures, solidus temperatures, fractions of solid at processing temperatures, and fractions of different phases at RT.

References

1. Luo, A. A., 2013, "Magnesium casting technology for structural applications," *J. Magnes. Alloy*, Vol. 1, pp. 2–22.
2. Esparza, J. A., W. C. Davis, and L. E. Murr, 2003, "Microstructure-property studies in friction-stir welded, thixomolded magnesium alloy AM60," *J. Mater. Sci.*, Vol. 38, pp. 941–952.
3. Patel, H. A., D. L. Chen, S. D. Bhole, and K. Sadayappan, 2010, "Microstructure and tensile properties of thixomolded magnesium alloys," *J. Alloys Compd.*, Vol. 496, No. 1–2, pp. 140–148.

Acknowledgements

The authors would like to acknowledge the support of R. Davies, S. Shukla, T. R. Muth, C. Carmichael, I. Stinson, and T. Geer from ORNL.

II.1.11 Laser Powder Bed Fusion Parameter Development for Novel Steel and Aluminum Powders Using *In Situ* Synchrotron Imaging and Diffraction (Argonne National Laboratory)

Aaron Greco, Co-Principal Investigator
Argonne National Laboratory
9700 S Cass Avenue
Lemont, IL 60349
E-mail: greco@anl.gov

Andrew Bobel, Co-Principal Investigator
General Motors
30470 Harley Earl Boulevard
RML 1-120, Research Metallurgical Laboratory
Warren, MI 48092
E-mail: andrew.bobel@gm.com

Sarah Kleinbaum, DOE Technology Manager
U.S. Department of Energy
E-mail: sarah.kleinbaum@ee.doe.gov

Start Date: October 1, 2019 End Date: September 30, 2021
Project Funding: $500,000 DOE share: $250,000 Non-DOE share: $250,000

Project Introduction

Weight reduction requirements in the automotive industry have led to an increased interest in the use of metal AM in vehicle body structures and powertrain components. Metal AM processes using LPBF and DED have been demonstrated as viable methods for producing these metallic components. The benefits of these technologies—including greater design flexibility, accuracy, part consolidation, and significant weight savings through topology-optimized design—are very attractive for automotive applications. Capturing the full value of AM for weight reduction will include not only optimized component design, but the use of unique low-cost additive materials, which will enable performance that would otherwise be impossible via current materials processing methods. The role of individual process parameters on the resulting microstructure and perceived material printability is unclear. This uncertainty translates to increased process-parameter development time for exploring multiple processing conditions.

Objectives

This project will address this issue through the unique combination of *in situ* X-ray imaging, temperature measurement, and phase-transformation diffraction monitoring at ANL during the laser additive process on these new materials. These unique capabilities will significantly accelerate the process-parameter development cycle using a scientifically motivated foundation. Specifically, the data generated will be used to validate CALPHAD alloy design modeling and create numerical models with sufficient fidelity to predict new AM lightweight alloys with properties that are better than existing alloys. This will greatly reduce the time taken from material conception to printing fully dense components in a manufacturing process that relies heavily on time-consuming trial-and-error iterative experimentation.

Approach

The proposed approach is to leverage ANL's unique facilities in ultra-high-speed synchrotron X-ray imaging of the metal LPBF process to guide and accelerate process optimization of manufacturing additive parts using innovative automotive-focused alloys identified and developed by GM. Recent successful efforts in measuring

and understanding the LPBF process at ANL include the *in situ* monitoring of melt pool dynamics, powder ejection, rapid solidification, phase-transformation, and defect formation in Ti-6Al-4V.

Task 1: Specimen and Powder Procurement

In this task, GM will identify and supply an additive powder and base-plate material with a unique alloy chemistry identified and developed by GM for the automotive market to ANL. GM will supply powder of the chosen alloy chemistry with a particle-size distribution suitable for the LPBF process to ANL. In addition, GM will prepare specimens to act as base plates for LPBF experiments of the same alloy chemistry. This task will be funded and performed by GM.

Task 2: Miniature Additive LPBF Builds

In this task, ANL will perform LPBF experiments at their Advanced Photon Source on the supplied additive alloys and base plates [1],[2], as shown schematically in Figure II.1.11.1(a) and the actual setup in Figure II.1.11.1(b). The purpose of this task will be to increase the print speed (i.e., minimize build time) while minimizing defect formation (e.g., porosity) for a range of process conditions. ANL will perform any final modifications to the supplied base plates (e.g., polishing) for use in the miniature laser powder bed system and will perform builds using the supplied powders. Builds will consist of laser scans that are 2 mm long using varied laser-parameter sets and powder-layer thicknesses. Each of the individual parameter sets identified will be tested and monitored using three different imaging capabilities at ANL: (1) ultra-high-speed dynamic X-ray imaging; (2) high-speed thermal imaging; and (3) high-speed XRD. The goal of this task is to couple the three imaging capabilities to fully understand the *in situ* dynamic phenomena—such as vapor depression dynamics, powder spatter, void formation/incorporation into the build, rapid solidification, and directional grain growth that occur during LPBF. X-ray imaging data that shows rapid solidification and spatter formation were generated, however, the results are not as conclusive as the porosity data. Moreover, available beam time has been severely limited due to the COVID pandemic which impacted the diffraction experiments. The following the diffraction experiments, the metallographic investigation will be conducted which would yield results relative to the directional grain growth.

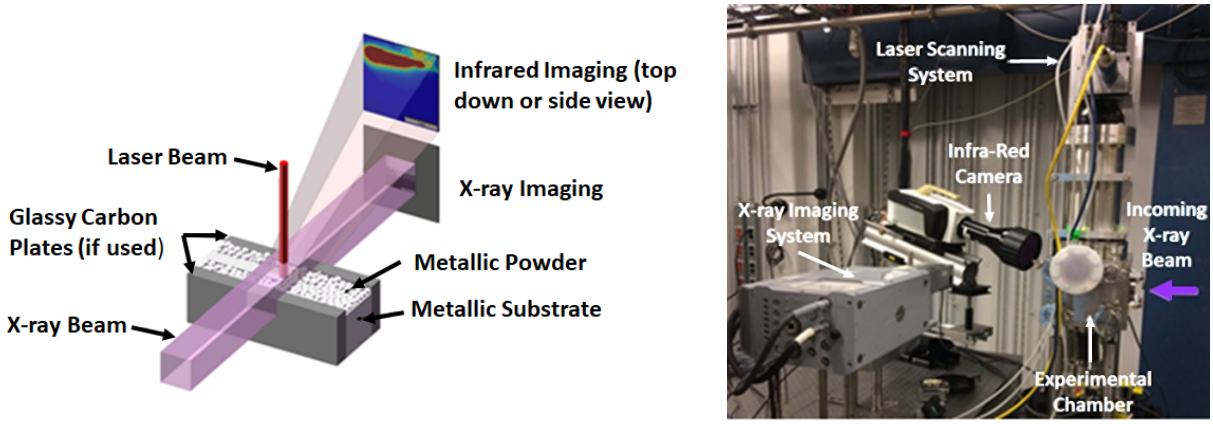

Figure II.1.11.1. (a) A schematic of the LPBF experimental setup. (b) A picture of the actual experimental setup installed in ANL's APS beamline [1]. Source: ANL.

Task 3: Image Analysis

In this task, ANL and GM will jointly post-process the high-speed image sets generated for each LPBF build. This task is critical because it will provide data needed to guide the selection of AM process parameters for the new alloys, guide AM process-model development, and stimulate future alloy designs. For example, the X-ray imaging can supply data, such as melt pool depth (into the subsurface) and shape during the build process, porosity formation and movement within the melt, resulting build-layer thickness, and defect concentration in the build. In addition, the infrared (IR) imaging will quantify temperature extremes experienced during the

LPBF's rapid heating and cooling cycles, will show melt pool size in the other two dimensions, will enable correlation with the microstructure observed in Task 4, and will provide requisite inputs for CALPHAD modeling that will be conducted at GM. These experiments will reveal the physical basis of the formation of different defects and develop new parameters and materials that solve the challenge of manufacturing nearly defect-free automotive parts.

Task 4: Microstructure Analysis

In this task, GM will perform microstructural analyses of the as-built laser-processed base plates and materials newly built-in Task 2. Task 4 will be funded and performed by GM. ANL will return the LPBF processed specimens to GM. GM will then use advanced metallographic techniques to prepare specimens to extract high-quality images and quantitative data on grains that span the nanometric- to micron-length scales. High-resolution SEM will be performed on the as-built samples to observe the resulting grain structure, intermetallic formation, and elemental segregation at locations throughout the laser-scan area. In addition, SEM will be used to verify the melt pool depths and resulting heat-affected zone produced by the laser-scan process. EBSD will be used to quantify micron-scale grains and determine grain size and shape, phase information, misorientation, orientation, and their distributions. Where necessary TEM will also be performed to identify nanoscale grain structure and precipitation within the as-built material. This task will identify the effects, such as columnar grain growth, of the laser parameters on as-built microstructures and drive new processing and alloy designs that avoid build failures, such as cracking and delamination.

Results

The team has completed Advanced Photon Source experiments on four alloy types: (1) AlTi; (2) AlSiCu; (3) FeCu; and (4) Fe393 as part of Task 1 and Task 2. However, more materials are planned for evaluation as soon as beam time becomes available. In the initial experiments, the laser power and scan speed were varied to determine the effect of printing parameters on the formation of porosity defects during the print. These experiments also used two types of printed and cast substrates—meaning that the sample flat was either fabricated by means of LPBF printing or casting of the corresponding alloys. Experiments were also conducted with and without the corresponding powders spread on the surface prior to the experiment to represent the powder bed. In total, over 100 experiments were performed and analyzed. The parameters of the experiments are shown in Table II.1.11.1.

Table II.1.11.1. List of Alloys and Laser Parameters Used for Testing

Materials Tested	Laser Power Tested (W)	Laser-Scan Speeds Tested (mm/s)
AlTi (on printed substrate)	260, 302, 395, 520	300, 800, 1000, 1300, 1600
AlTi (on cast substrate)	302, 520	300, 800, 1000, 1300
AlSiCu (on printed substrate)	260, 364, 520	800, 1300, 1400, 1600, 2000
AlSiCu (on cast substrate)	364, 520	800, 1300, 1400, 1600
FeCu (on printed substrate)	213, 348	40, 190, 300, 400, 500
Fe393 (on cast substrate)	208, 250, 400, 520	375, 470, 750, 940
Fe393 (on printed sustrate)	213, 348	300, 400, 700

The images shown in Figure II.1.11.2 are representative single frames from the *in situ* experiments. These frames were taken from the end of the test run after the laser completed its pass from left to right. The time scale of the images for these experiments is around 60,000 frames per second, although it can be varied significantly. The total imaging time ranges with material between 9 and 20 milliseconds. The image in Figure II.1.11.2(a) is representative of a test that results in the formation of significant porosity, while the image in Figure II.1.11.2(b) show that the conditions led to a better print with minimal porosity. In general, the solidification front in Figure II.1.11.2(b) is very near the surface region and there is little to no keyholing in this mode of laser operation.

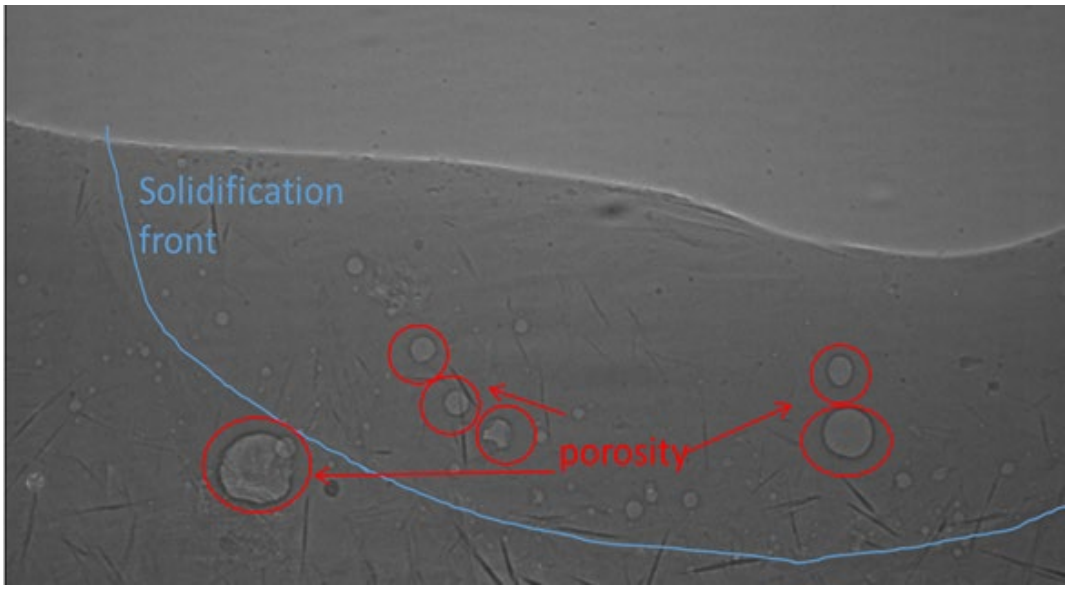

(a)

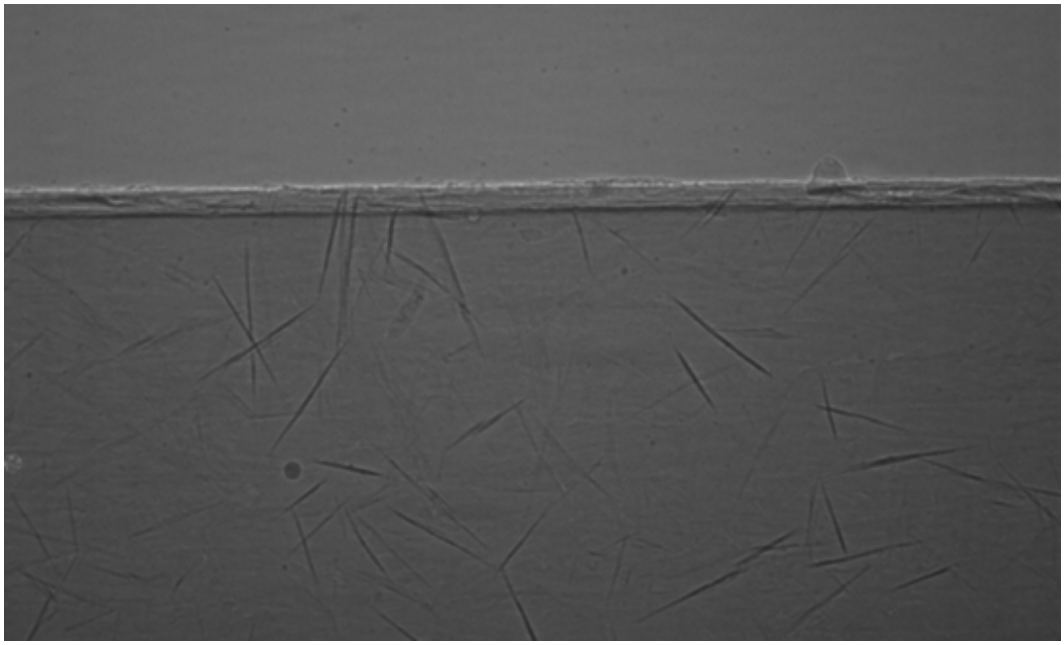

(b)

Figure II.1.11.2. Radiographic X-ray images representing a single frame from the *in situ* experiments after the laser has completed a pass on AlTi material (a) using 520 W and 300 mm/s showing porosity and (b) using 302 W and 800 mm/s showing minimal porosity. Source: ANL.

For each experiment, IR measurements were simultaneously taken to have correlation between top surface thermal condition and subsurface porosity. As an example, Figure II.1.11.3 shows a representative IR image during a similar experiment on 4140 steel. GM has designations for each set of laser conditions that are specific to each material and the set for this image is described as high-energy. All non-indigo regions represent an increase in temperature above the lowest measurable temperature of the camera. The blue and green particles that are not part of the main heated line are spatter from the scan which starts in the top left and moves to the bottom right. The large red area is the vapor depression of the laser at the middle of the scan.

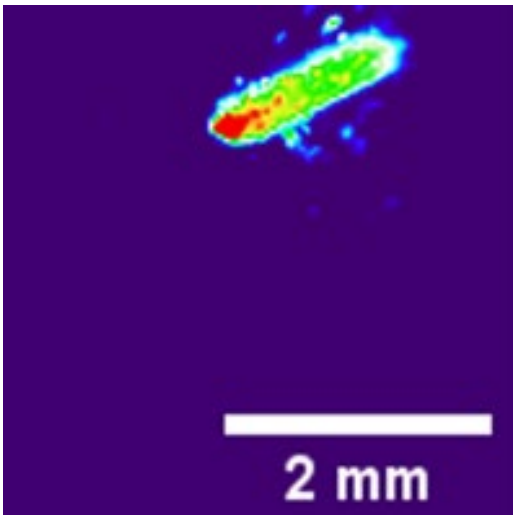

Figure II.1.11.3. An example of *in situ* IR data for 4140 steel under a high-energy set of laser conditions, specifically a laser power of 208 W and a speed of 300 mm/s. Source: ANL.

Conclusions

Through FY 2020, we have demonstrated that the x-ray based *in situ* experiment is effective at determining porosity formation for a given set of laser parameters. The experimental data, *in situ* x-ray radiographic images and corresponding *in situ* high-speed IR images, were collected for a set of AlTi, AlSiCu, FeCu, and Fe393 alloys. Future work will include microstructural analysis; together, these results will be utilized in CALPHAD modeling for additional insight into selection of appropriate laser parameters for respective alloys.

References

1. Gould, B., S. Wolff, N. Parab, C. Zhao, M. C. Lorenzo-Martin, K. Fezzaa, A. Greco, and T. Sun, 2020, "*In situ* analysis of laser powder bed fusion using simultaneous high-speed infrared and x-ray imaging," *JOM*, July 27, 2020. Available at: https://doi.org/10.1007/s11837-020-04291-5 (last accessed 1 December 2020).
2. Bobel, A., L. G. Hector, I. Chelladurai, A. K. Sachdev, T. Brown, W. A. Poling, and R. Kubic, 2019, "*In situ* synchrotron x-ray imaging of 4140 steel laser powder bed fusion," *Materialia*, Vol. 6 (June 1, 2019), Art. 100306. Available at: https://doi.org/10.1016/j.mtla.2019.100306 (last accessed 1 December 2020).

Acknowledgements

In addition to the PIs, the core project team also includes Dr. B. Gould, Materials Scientist, in the ANL Applied Materials Division and Dr. L. Hector Jr. of GM R&D. The team would also like to thank contributions from Mr. J. Singh, a DOE Science Undergraduate Laboratory Intern, and Dr. K. Fezzaa of the Advanced Photon Source. The authors would like to thank the Vehicle Technology Office for funding this project through the LightMAT consortium, and Ms. S. Kleinbaum for her guidance. This research used resources of the Advanced Photon Source, which is a DOE Office of Science User Facility operated for the DOE Office of Science by ANL under Contract No. DE-AC02-06CH11357.

II.2 Carbon Fiber & Polymer Composites

II.2.1 Integrated Computational Materials Engineering Predictive Tools Development for Low-Cost Carbon Fiber for Lightweight Vehicles (University of Virginia)

Xiaodong (Chris) Li, Co-Principal Investigator
University of Virginia
122 Engineer's Way
Charlottesville, VA 22904
E-mail: xl3p@virginia.edu

Leonid V. Zhigilei, Co-Principal Investigator
University of Virginia
Wilsdorf Hall, Room 303D
Charlottesville, VA 22904
E-mail: lz2n@virginia.edu

Adri van Duin, Co-Principal Investigator
Pennsylvania State University
240 Research Building East
University Park, PA 16802
E-mail: acv13@psu.edu

James W. Klett, Co-Principal Investigator
Oak Ridge National Laboratory
1 Bethel Valley Road
Oak Ridge, TN 37831
E-mail: klettjw@ornl.gov

Desmond Cook, Co-Principal Investigator
Solvay Composite Materials, Carbon Fibers
50 Akron Drive
Greenville, SC 29602
E-mail: desmond.cook@solvay.com

H. Felix Wu, DOE Technology Manager
U.S. Department of Energy
E-mail: felix.wu@ee.doe.gov

Start Date: October 1, 2017 End Date: March 31, 2021
Project Funding: $1,366,160 DOE share: $1,221,565 Non-DOE share: $144,595

Project Introduction

In response to consumer demand for fuel-efficient vehicles and stringent vehicle emission regulations, automotive manufacturers are searching for alternative lightweight, high-strength materials to replace conventional metal structures in vehicle designs. Even compared to high-strength metal alloys, CFRP composites are a promising alternative due to their superior strength-to-weight ratio. Recent estimates have predicted that automotive weight reductions of 50% or greater will be necessary, in addition to enhanced

engine and drivetrain efficiencies, to meet national and international emission standards [1],[2]. However, there are significant technical barriers that must be overcome to bring CFRP materials into widespread acceptance. CFRP materials are produced via a complex and expensive procedure and are often limited to small-scale production. A large portion of this cost is born by the precursor material preparation—51% of the total CF cost may be attributed to the precursor fibers [3],[4]. Therefore, this project aims to develop low-cost alternative precursors and processing techniques through the implementation of an ICME framework to evaluate precursor conversion kinetics. This framework will be used to down-select precursors for laboratory- and pilot-scale production to validate resulting CFRP material properties and process cost-savings.

Currently, the highest quality CFs are produced from polyacrylonitrile (PAN) precursors, which have a high C yield and ideal polymer structure for conversion into CFs with excellent mechanical properties. Typical yields are ~50% CF for the quantity of PAN precursor at the start of conversion. In literature, the highest quality commercially available CFs achieve strengths of up to 7 GPa (1000 ksi) [2],[5],[6]; however, PAN-derived CFs are expensive due to their high precursor cost- and energy-intensive processing, with costs of ~$11/lb subject to petroleum-price fluctuations. Although advanced manufacturing techniques may further lower the price toward $7/lb, PAN-derived fibers will likely remain too expensive for widespread adoption in the automotive industry [7],[8].

Therefore, the two most promising approaches to reduce the cost of CFs are to: (1) utilize new, low-cost precursors; and (2) reduce the energy requirements of CF processing. In FY 2019 of this work, Nylon 6 was identified as a promising low-cost alternative precursor, but the conversion into CF was energy intensive. Thus, in FY 2020 of this work, we applied the ICME framework and targeted experimentation to optimize the conversion to reduce its cost while maximizing mechanical performance. Laboratory-scale conversion of Nylon 6 into high-strength, low-cost CF was accomplished in FY 2020. This success in the lab conversion of Nylon 6 has raised the question of scalability to relevant continuous-scale fiber production, which will be the focus of work conducted in the remaining six-month extension of the project.

Objectives

The first objective is to develop, integrate, and demonstrate an ICME framework and evaluate alternative precursors for suitability to manufacture low-cost CF. This ICME framework will predict CF properties, such as load-to-failure, failure mode, stiffness/deflection, dynamic performance, and microstructures. It must be capable of minimum modeling-element accuracies within 15% of measured properties, which would enable design, development, and optimization of precursor chemistry and kinetics associated with the CF conversion process. The ICME framework will also include methodologies to simulate manufacturing processes, including variability from both process and material.

The second objective is to research, develop, manufacture, and demonstrate CF precursor technology and processing techniques, where CF is a material consisting of thin, strong multi-crystalline filaments of C used as a reinforcement material especially in resins, capable of achieving the requirements in Table II.2.1.1.

Table II.2.1.1. Project Parameters and Requirements

Parameter	Requirement	
Cost	≤ $5/pound	
Strength	≥ 250 Ksi	≥ 1.725 GPa
Modulus	≥ 25 Msi	≥ 172.5 GPa
Strain	≥ 1%	

Project performance was planned to span three federal fiscal year BPs. A six-month, no-cost extension was granted in response to the COVID-19 outbreak, extending the project through March 2021.

Approach

The ICME framework was developed and validated around PAN-based CFs during FY 2018, and it can predict the properties of PAN-based CF within 15% error. This critical accomplishment supports the reliability of the assembled framework, which was extended to analyze alternative precursors in FY 2019. The ICME framework is constructed from Reactive Force Field (ReaxFF) simulations [9],[10], which predict the fiber chemistry during conversion, and large-scale MD simulations, which elucidate polymer matrix/fiber mechanics and properties [11],[12]. This framework requires key input parameters (i.e., precursor chemistry, chemical structure, and conversion parameters) and validation points (i.e., fiber chemistry, gaseous products, and mechanical properties), which are supplied by experimentation. Furthermore, experimentation has identified new conversion steps, such as mixing additives within the polymer, alternative conversion treatments, which are, in turn, investigated by the ICME framework to elucidate the underlying chemical mechanisms. Thus, our project structure is optimized for closed-loop research feedback in which each group receives and passes along information and data to the next as we investigate and optimize the conversion of low-cost CF. The cyclic nature of running and refining the models with experimental data achieved significant results in FY 2020.

Results

At the conclusion of FY 2019, the project identified Nylon 6 as the most promising alternative precursor for low-cost CF; however, there were several critical challenges, which had to be addressed. First, converting Nylon 6 requires a lengthy conversion stage that is infeasible industrially. Second, Nylon 6 must also be treated in a bath, which is difficult to implement in a large-scale, continuous fashion. Last, alternative conversion techniques are relatively untested in a large-scale continuous-manufacturing environment. Each of these challenges was addressed in FY 2020 through application of the ICME framework.

Exploration of Alternative Precursors for Direct Carbonization

While Nylon 6 was the chosen precursor for the focus of experimental work, we continued to investigate other alternative precursors, such as blends of polyethylene (PE), mesophase pitch, and nylon, which would not require the long conversion step. An ideal precursor would not require oxidation at all and could, instead, be directly carbonized to reduce conversion costs. Thus, we completed atomistic ReaxFF simulations of the direct carbonization of a set of 26 polymer structures, as shown in Figure II.2.1.1, to unveil how these structures affected the carbonization process. Polymer density was one key factor, which helped to indicate the chance of successful conversion. A polymer with a density below 1.3 g/cm^3, which is indicated by the red line in Figure II.2.1.1, was not likely thermally stable enough to be directly carbonized.

The time evolution of the gas-molecule production and all C ring production during carbonization simulations at 2800 K was characterized, as observed in Figure II.2.1.1. The structural change of the polymers was then compared with oxidized PAN, poly(p-phenylene-2,6-benzobisoxazole) (PBO), and Nylon 6 to evaluate the relative improvement or lack thereof during carbonization. These structural changes, which promote the evolution of graphitic structure to rank the polymers based on their capacity for successful carbonization and conversion into CF, are being analyzed.

To support the computational exploration of alternative precursors and an experimental investigation of PE-based CF, we developed the ReaxFF CHONS (carbon-hydrogen-oxygen-nitrogen-sulfur) force field for the simulation of sulfonation of polyolefins, like PE, and for the carbonization of sulfonated polyolefins. The old version of the ReaxFF CHONS force field was parameterized for the sulfuric-acid solution with the CH_3-SO_3 bond and angle parameters, as observed in Figure II.2.1.3(a)–(c) and could describe the dehydrogenation and the functionalization of the O-containing and S-containing groups in the sulfonation process. However, the previous version had limited capability to capture the graphitic structure formation during the carbonization process. Thus, the ReaxFF CHON force field parameters for the carbonization chemistry were incorporated, as can be seen in Figure II.2.1.3(d)–(f) and the sulfonation and carbonization simulations were repeated using both versions of the force fields in the sequence described in Figure II.2.1.4. The new ReaxFF CHONS force field enabled lower onset temperatures for molecular chain cleavage, oxidation, and sulfonation, and the simulation temperatures are closer to experimental conversion temperatures, as shown in Figure II.2.1.3(a)-(f).

The results indicate the new ReaxFF CHONS force field is well-suited for characterizing the graphitic structure formation of sulfonated PE, while the chemistry of O-containing and S-containing groups during the carbonization process can also be well-traced. The energy barrier and chemical reaction pathways of the sulfonation of polyolefins still need to be benchmarked with the experimental results.

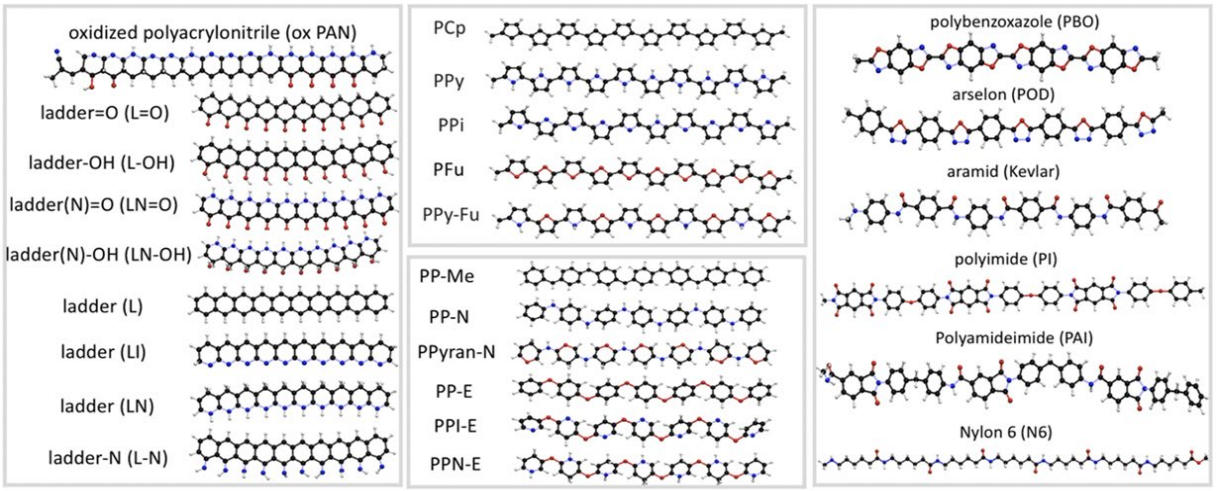

(a)

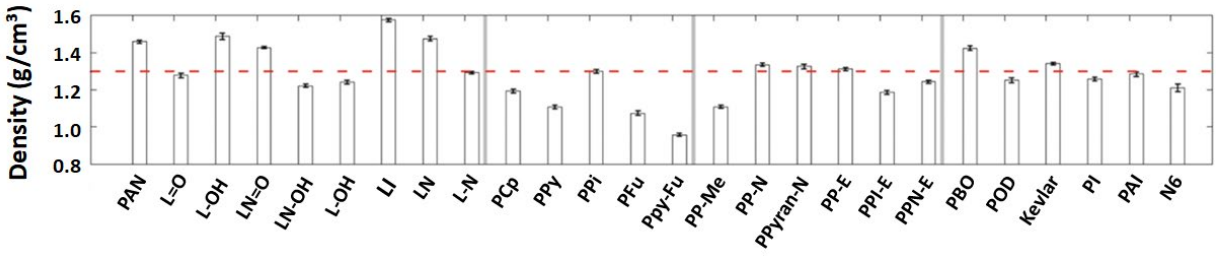

(b)

Figure II.2.1.1. Considered polymers and their densities: (a) the molecular structure of all considered polymers; and (b) the calculated densities of the polymer melts at RT and atmospheric pressure. A horizontal red line indicates density 1.3 g/cm³, the limit for thermal stability. Source: Pennsylvania State University.

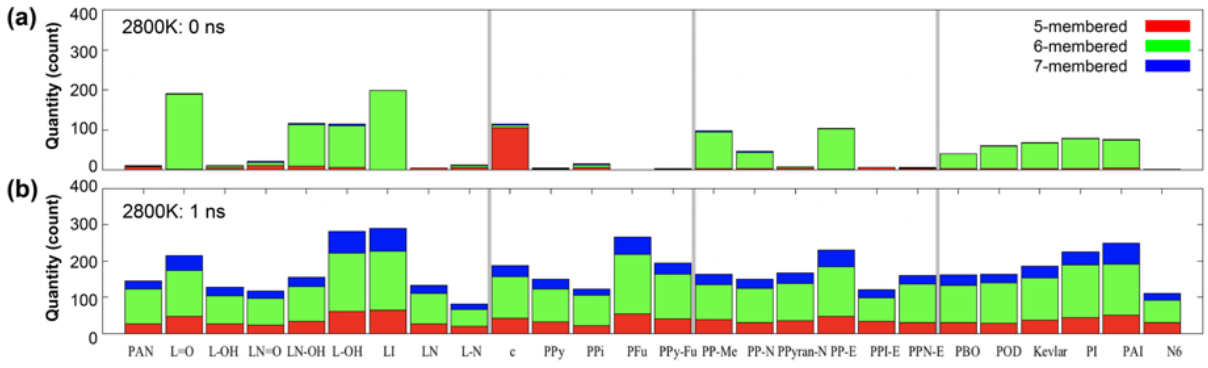

Figure II.2.1.2. The all C ring evolution. The quantity of the all C rings (5-/6-/7-membered rings) at a given time of the carbonization simulations for all considered polymers: (a) at the beginning of the carbonization simulations; and (b) after 1 ns. Source: Pennsylvania State University.

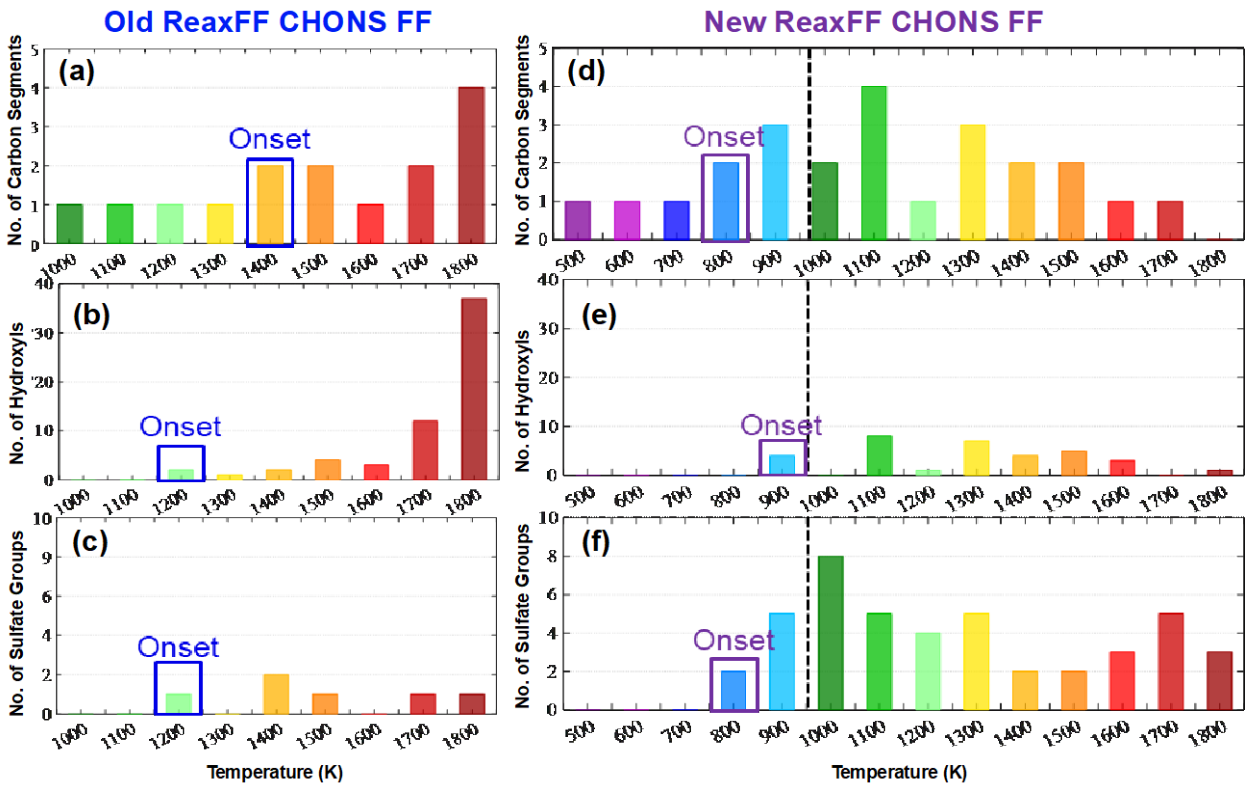

Figure II.2.1.3. A comparison between old and new versions of ReaxFF CHONS force fields applied to PE sulfonation at elevated temperatures: (a) a number of C segments; (b) a number of hydroxyl groups; (c) a number of sulfate groups with the old version ReaxFF CHONS force field; (d) a number of C segments; (e) a number of hydroxyl groups; and (f) a number of sulfate groups with the new version ReaxFF CHONS force field. Source: Pennsylvania State University.

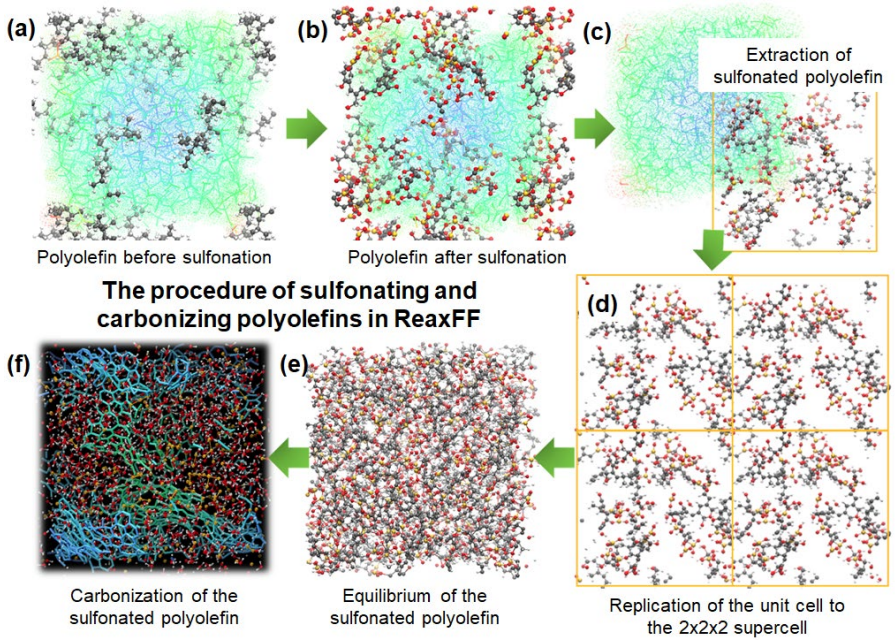

Figure II.2.1.4. Simulation snapshots representing CO production for samples with: (a) 2K/ps; and (b) 700 K/ps heating rate. Source: Pennsylvania State University.

ICME Characterization of Local CF Structure and Mechanical Property Relationships

We have successfully developed a novel approach within the ICME framework to generate complex CF structures, consisting of turbostratic, amorphous, and graphitic carbon, as well as nanovoids. Simulation of these structures elucidates the coupled structure and mechanical property relationships, which then inform the laboratory-scale synthesis and conversion of the fibers. Atomistic tensile test simulations of four computational samples (CF1, CF2, CF3, and CF4) were performed, as described in Table II.2.1.2. The four samples were generated by controlling the system under different compression levels prior to carbonization and with different hydrogenation rates. This variation in processing parameters led to different structural characteristics. For example, sample CF1 contained a large volume of nanovoids, which resulted in low strength and modulus. Furthermore, the strength and modulus were positively correlated to the degree of graphitization and a fraction of 6-membered rings, indicative of the desired CF structure.

Table II.2.1.2. Structural Characterization and Mechanical Properties of Four Large-Scale, Atomistic CF Models

Sample	Density (g/cm^3)	Degree of Graphitization (%)	Fraction of 6-Member Rings (%)	Volume Fraction of Voids (%)	Strength (GPa)	Tensile Strain (%)	Young's Modulus (GPa)
CF1	1.71	17.9	89.2	12.2	30.6	11.3	266.6
CF2	1.78	18.3	89	9.3	34.6	11.9	287.4
CF3	1.69	12.2	86.6	11.1	32.5	11.6	275.6
CF4	1.72	11.7	85.7	10.4	31.3	10.9	280.7

To fully understand the structure / property relationships, we divided the system into small cells, averaged the structural parameters in each cell, and calculated the correlation coefficients between several local structural parameters and mechanical properties. The results of the correlation analysis for sample CF2 are illustrated in Figure II.2.1.5(a), as well as a cross-sectional distribution of the atomic stress, which is shown in Figure II.2.1.5(b). The CF nanostructure can be represented by a mix of strong and soft regions. The strong regions are correlated with a higher density, an elevated fraction of sp2 carbon, a higher degree of graphitization, and a larger number of 6-member rings; thus, stress is localized in these regions during deformation. The soft regions are more deformable and are characterized by a higher potential energy and an elevated fraction of sp carbon. The fracture initiated in places with high localized stress surrounded by softer materials. We isolated the high stress structure as a percolating cluster, as observed in Figure II.2.1.5(c), of atoms with local atomic stress exceeding a certain threshold level, which was chosen so that the cluster extends through the whole computational sample. This high stress percolating cluster changes as the total strain increases during the deformation, and the transitory nature of the high stress cluster may be related to the high resilience of the CF against fracture.

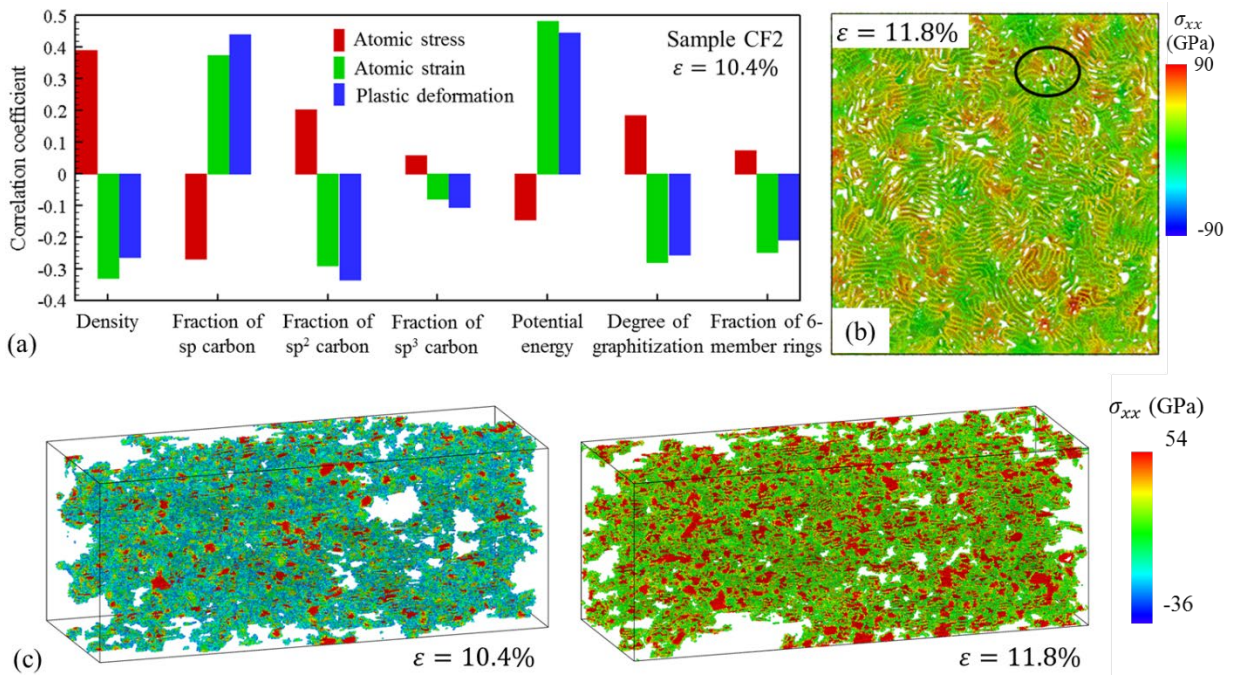

Figure II.2.1.5. (a) Correlation coefficients between the structural properties (i.e., density, fraction of sp, sp^2, and sp^3 C atoms, potential energy, degree of graphitization, and a fraction of 6-member rings) and the mechanical properties (i.e., local stress, strain, and an indicator for plastic deformation) in the deformed CF at a strain of ε = 10.4%. (b) Snapshot of a 3-nm-thick slice showing the cross-sectional distribution of atomic stress σ_{xx} at ε = 1.8%. The black circle outlines the region where the fracture starts. (c) Snapshots of the high stress percolating cluster extending along the system length at different strain levels. The results are shown for the CF2 sample. Source: University of Virginia.

This characterization, CF1 in particular, indicates that structural defects, like nanovoids, can adversely impact CF mechanical properties. The computational samples were found to have modulus values similar to the experimental values reported for PAN-based CF. However, the tensile strength and fracture strain exceed those experimental values by about an order-of-magnitude, suggesting that a substantial enhancement of the mechanical properties of the real/experimental CFs can be achieved through the elimination of the critical mesoscopic structural defects, such as voids, cracks, foreign inclusions, and surface defects. To better elucidate the effect of nanovoids on CF mechanical properties, a nanovoid with a diameter of 6 nm was created at the center of sample CF2, and the mechanical properties of the system were investigated through atomistic simulations of tensile testing, as observed in Figure II.2.1.6. Compared to the initial bulk sample, CF2, the presence of a nanovoid led to a decrease of tensile strength while the modulus remained stable, as shown in Figure II.2.1.6(a), and a fracture began at a strain level ~0.7% lower than in the void-free system, as can be seen in Figure II.2.1.6(b). Continuum-level finite element modeling was also performed to explore the stress distribution around the void, which can lead to the earlier onset of fracture from the surface of the void, as observed in Figure II.2.1.6(c). Although the creation of a nanovoid decreased the tensile strength and fracture strain, the values were still significantly higher than those measured in experiments. Such overestimation of the strength in computational CF samples can be attributed to the inability of atomistic modeling to reproduce the experimentally observed dimensions and spatial distribution of the mesoscopic voids and other critical defects which, as reported previously, can be orders of magnitude larger than the 6 nm simulated here.

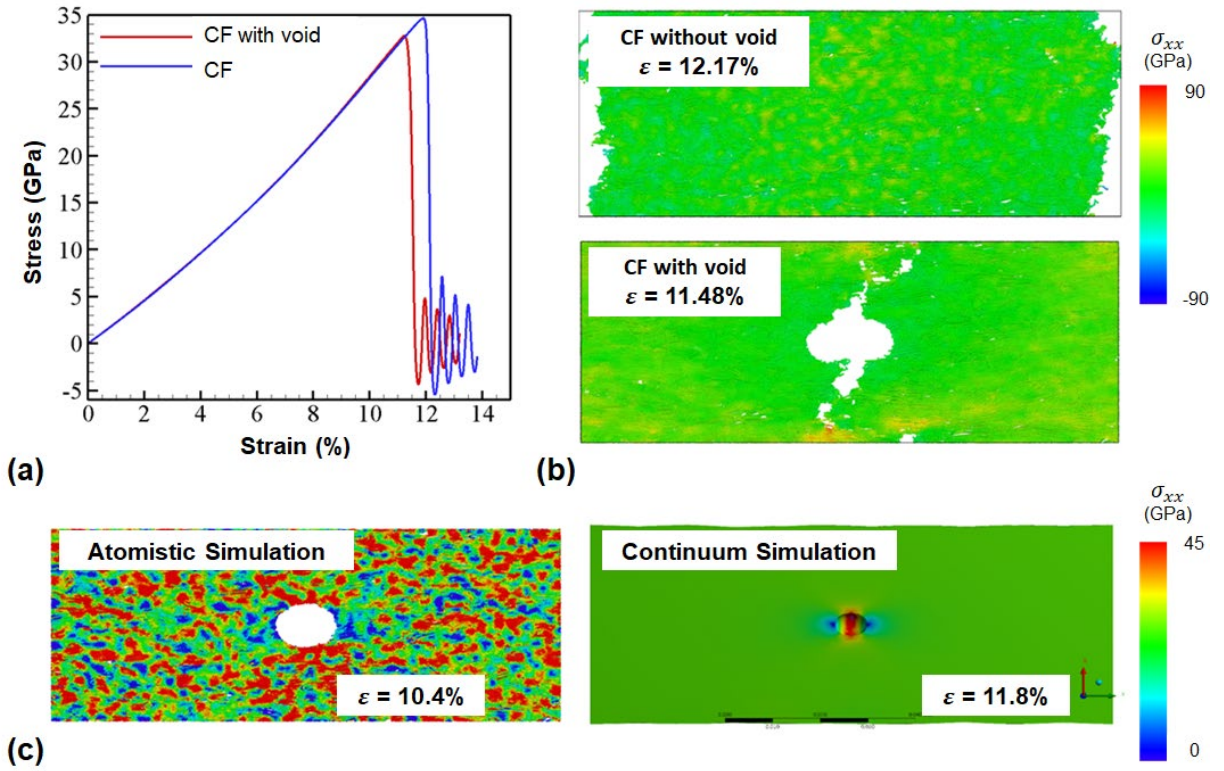

Figure II.2.1.6. (a) Stress-strain curves from atomistic tensile testing simulations performed for a void-free CF2 sample (blue line) and the same system, but with a 6 nm diameter nanovoid (red line). (b) Snapshots of the CF systems with (upper image) and without (lower image) the nanovoid. (c) Stress distribution in the CF2 system containing a void at ε = 10% predicted in the atomistic simulation (left) and continuum finite element modeling performed with ANSYS (right). Source: University of Virginia.

Optimization of Nylon 6 CF Conversion

Computational simulations under the ICME framework identified optimal CF densities, microstructure, conversion temperatures, and other parameters, which were translated to the laboratory-scale conversion of Nylon 6, the precursor downselected in FY 2019. Pilot-scale precursor Nylon 6 fibers were spun at the conclusion of FY 2019 courtesy of Hills, Inc., and Solvay Composites. These precursors were systematically studied, converted, and characterized over FY 2020. Nylon precursor is converted to CF via a multistage process.

The key challenge was to reduce the duration of the conversion procedure while maintaining target mechanical properties. We investigated alternative conversion methodologies and were able to successfully reduce the conversion time significantly. Alone, this reduction in conversion would severely weaken the CFs; however, the polymer microstructure can be regulated during conversion to maintain the target mechanical properties.

Nylon 6 is a very inexpensive precursor, especially compared to PAN, and the cost of precursor Nylon 6 can be as low as $0.45/lb. Furthermore, unlike PAN, Nylon does not require a high-temperature conversion, which provides additional energy and cost-savings. The key expense in nylon conversion is the lengthy conversion period; however, we demonstrated that with an alternative treatment, the conversion can be reduced significantly while retaining target mechanical performance. With this significant reduction in the manufacturing time, we predict that we can reduce the manufacturing costs of Nylon 6 CF will fall well below the $5/lb target to achieve all our target properties. Further savings may be possible and are being explored as we work to reduce the conversion time even further.

CF Quality Control and Scalability of CF Conversion

Having achieved the targeted performance and costs of Nylon 6 CF at a laboratory-scale, we next considered the obstacles to continuous industrial-scale production—namely, with respect to the implementation of alternative conversion procedures and treatments. The team is working with 4M CF and 4X Technologies to investigate the effect of large-scale treatment of nylon CFs to see if the conventional step can be eliminated. In the remaining six-month work period, we will also propose a design for continuous conversion treatments. The current laboratory-scale treatment is performed by placing the CF segments in a bath; however, we envision a pulley system capable of slowly feeding a continuous line of fiber in and out for treatment. The team will be working with Solvay Composites and Oshkosh to design a preliminary prototype and submit this design to Solvay to help translate the laboratory-scale conversion of Nylon 6 to larger scales. Pitch fibers were examined to investigate capability for micro-Raman characterization, and as this project ends, the team will continue focusing the work at Oak Ridge National Laboratory on the demonstration of the micro-Raman characterization of the CF, which will be helpful to qualify the effect key of processing parameters on the fiber microstructure.

A testbed system is under development for continuous bath treatment of Nylon 6 fiber, as shown in Figure II.2.1.7. The testbed system features variable bath parameters, including compatibility with various solutions, bath-temperature control, solution-turnover rate, and solution crossflow rate and characteristics. Some of the targeted data include fiber alignment, color, and conductivity, which will be used to add fidelity to subsequent fiber characterizations and to explore process optimization via ML. This testbed will be completed in the remaining six-month extension; remaining tasks include testing the continuous bath system, performing a pilot-scale conversion of the pilot-scale precursor fibers, and parametric optimization of continuous bath treatment parameters at the pilot-scale.

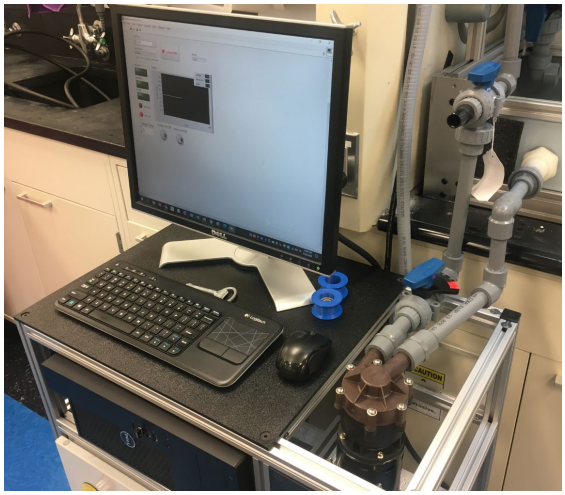

Figure II.2.1.7. View of the control station with LabView control and data logging program. All system functions are coordinated by an open-source programmable logic controller to ease transfer to industry. Source: University of Virginia.

Investigations continue on new methods of CF quality control via ML algorithms and optimization. Led by Oak Ridge National Laboratory, micro-Raman-spectroscopy was performed on cross-sections of fibers, as shown in Figure II.2.1.8(a). This technique maps fiber quality and heterogeneity by measuring the G/D band ratio (a ratio of the intensity of in-plane vibrations of sp2 bonded C atoms to out-of-plane vibrations). We hypothesize that variation in these G/D bands will correspond to structural variations as seen in Figure II.2.1.8(b). Indeed, the maps distinguish internal polymer microstructure, such as the presence of an outer shell of onion-skin-like layers and of radially oriented polymer layers in the fiber core. This finding strongly indicates that Raman-spectroscopy can be used to quantify and characterize CF quality and can be paired with ML algorithms to analyze the quantitative G/D band ratios to correlate fiber quality with fiber

processing parameters. To achieve this machine-learning-guided quality control in the remainder of the project, we will scan multiple CF converted via different processing steps and confirm the Raman-spectroscopy-indicated fiber quality with SEM, thermogravimetric analysis, etc. This wealth of information will be processed via ML algorithms to identify the optimal processing parameters to guide CF manufacturing.

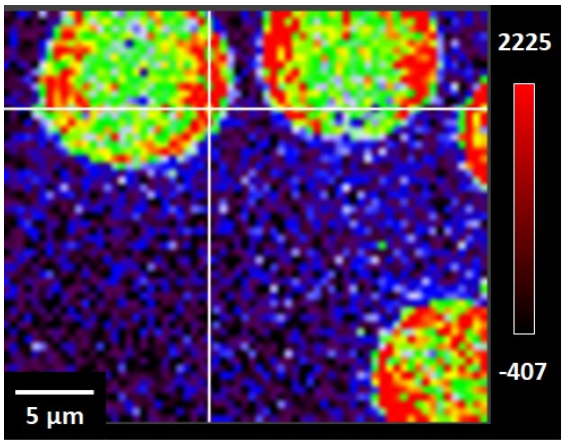

(a)

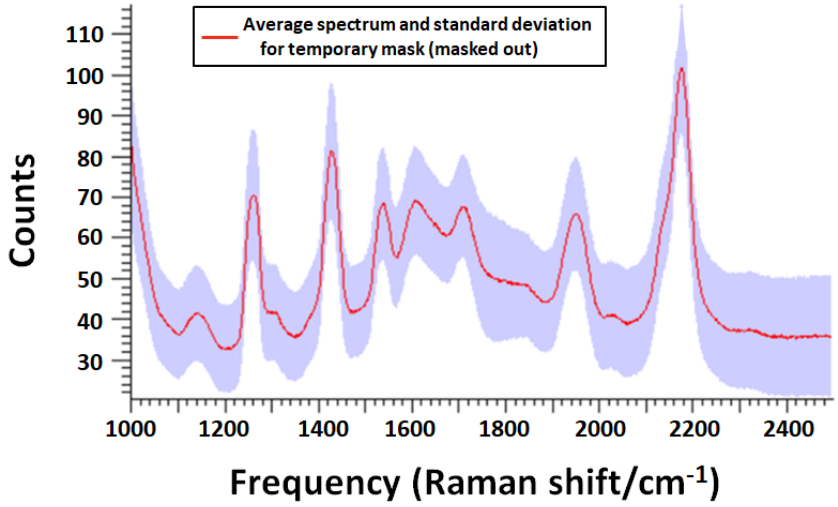

(b)

Figure II.2.1.8. (a) Micro-Raman mapping of CFs where the crosshair indicates the location of the spectra reading, (b) Raman spectra showing G/D bond peaks that can be used to quantify the structural variation of the fiber, indicated by the blue to red shading. Source: ORNL.

Last, to facilitate the technology transfer, we are preparing an ICME testbed software package. This package integrates all experimental data collected over the project and leverages ML algorithms to prescribe an optimal conversion recipe, including temperature and duration for stages of conversion. Currently, the ICME package is trained with 329 tests from 46 different recipes and 11 process variables. The objective of this package is to provide a quick reference tool for the CF industry, automotive industry, and vehicle technologies innovators to use to predict and optimize the properties of nylon CF; thus, we anticipate this package will accelerate adoption of nylon-based CF within the automotive industry.

Conclusions

We concluded FY 2020 having demonstrated successful achievement of our target metrics, including mechanical property and cost targets, with CF derived from Nylon 6. This accomplishment was achieved with the support of the ICME framework, which investigated the chemical mechanisms involved in conversion of Nylon and the microstructure-properties relationships inherent in these fibers. Furthermore, the ICME framework indicates that further optimization is possible with continued refinement of the fiber microstructure to reduce quantities of defects and pores to improve strength. With this guidance from the ICME framework, on a laboratory-scale, we controlled fiber microstructure and improved strength. We achieved a significantly reduced conversion of nylon fibers using alternative treatments. This collaborative effort has thus achieved significant accomplishments.

The remainder of the project will be devoted to addressing questions of Nylon 6 conversion scalability to larger, continuous-production scales, continued experimental and computational exploration of other alternative precursors, and optimization of the ICME framework. This ICME framework is built upon our success with ReaxFF simulations to uncover the underlying chemistries, atomistic simulations to investigate CF structure/property relationships, and laboratory-scale experimental CF conversion. However, over the 6-month extension period, we will package this wealth of data within a testbed software package, guided by ML, to present optimized Nylon CF conversion recipes and facilitate easy adoption of this technology within the CF and automotive industries. Importantly, we expect these tools, and the demonstration of Nylon-derived CF, will encourage the implementation of low-cost, high-strength CF within structural vehicular components to enable the manufacture of lightweight, energy-efficient vehicles.

Key Publications

Numerous manuscripts are currently in preparation or were recently submitted for publication. These manuscripts include: (1) “Cost-effective CF precursor selections of polyacrylonitrile-based blend polymers; carbonization chemistry and structural characterizations;” (2) “ReaxFF reactive force field study of carbonization condition effects on the structure of PAN/G nanocomposite derived CFs;” and (3) “Correcting single filament CF tensile test misalignment via stereoscopic computer vision imaging.” In addition, several publications detailing this research have been published:

1. Ashraf, C., A. Vashisth, C. E. Bakis, and A. C. T. van Duin, 2019, “Reactive molecular dynamics simulations of atomic oxygen impact on epoxies with different chemistries,” *J. Phys. Chem. C*, Vol. 123, pp. 15145–15156.
2. Gao, Z., J. Zhu, S. Rajabpour, K. Joshi, M. Kowalik, B. Croom, Y. Schwab, L. Zhang, C. Bumgardner, K. Brown, D. Burden, J. Klett, A. C. T. van Duin, L. Zhigilei, and X. Li, 2020, “Graphene-reinforced carbon fibers,” *Sci. Adv.*, Vol. 6, No. 17, Art. eaaz4191.
3. Joshi, K., M. I. Arefev, and L. V. Zhigilei, 2019, “Generation and characterization of carbon fiber microstructure in atomistic simulations,” *Carbon*, Vol. 152, pp. 396–408.
4. Kowalik, M., C. Ashraf, B. Damirchi, D. Akbarian, S. Rajabpour, and A. C. T. van Duin, 2019, “Atomistic scale analysis of the carbonization process for C/H/O/N-based polymers with the ReaxFF reactive force field,” *J. Phys. Chem. B*, Vol. 123, No. 25, pp. 5357–5367.
5. Kwon, H., S. Shabnam, A. C. T. van Duin, and X. Xuan, 2020, “Numerical simulations of yield-based sooting tendencies of aromatic fuels using ReaxFF molecular dynamics,” *Fuel*, Vol. 262, Art. 116545.
6. Mao, Q., S. Rajabpour, M. Kowalik, and A. C. T. van Duin, 2020, “Predicting cost-effective carbon fiber precursor: Unraveling the functionalities of oxygen and nitrogen-containing groups during carbonization from ReaxFF simulations,” *Carbon*, Vol. 159, pp. 25–36.
7. Ponomarev, I., A. C. T. van Duin, and P. Kroll, 2019, “A reactive force field for simulations of the pyrolysis of polysiloxanes into silicon oxycarbide ceramics,” *J. Phys. Chem. C*, Vol. 123, pp. 16804–16812.

8. Vashisth, A., M. Kowalik, J. C. Gerringer, C. Ashraf, A. C. T. van Duin, and M. J. Green, 2020, "ReaxFF simulations of laser-induced graphene (LIG) formation for multifunctional polymer nanocomposites," *ACS Appl. Nano Mater.*, Vol. 3, pp. 1881–1890.

9. Volkov, A. N., and L. V. Zhigilei, 2020, "Thermal conductivity of two-dimensional disordered fibrous materials defined by interfiber thermal contact conductance and intrinsic conductivity of fibers," *J. Appl. Phys.*, Vol. 127, Art. 065102.

10. Zhang, L., M. Kowalik, Z. Gao, C. Ashraf, S. Rajabpour, C. Bumgardner, Y. Schwab, B. Damirchi, J. Zhu, D. Akbarian, J. Klett, A. C. T. van Duin, and X. Li, 2019, "Converting PBO fibers into carbon fibers by ultrafast carbonization," *Carbon*, Vol. 159, pp. 432–442.

11. Zhu, J., Z. Gao, M. Kowalik, K. Joshi, C. Ashraf, M. Arefev, Y. Schwab, C. Bumgardner, K. Brown, D. Burden, L. Zhang, J. Klett, L. V. Zhigilei, A. C. T. van Duin, and X. Li, 2019, "Unveiling carbon ring structure formation mechanisms in polyacrylonitrile-derived carbon fibers," *ACS Appl. Mater. Interfaces*, Vol. 11, pp. 42288–42297.

12. Klett, J., Z. Gao, J. Zhu, S. Rajabpour, K. Joshi, M. Kowalik, Y. Schwab, L. Zhang, C. Bumgardner, B. Croom, D. Burden, K. Brown, Y. Murty, Q. Shi, B. Harmon, L. V. Zhigilei, A. C. T. van Duin, and X. Li, 2019, "Enhancement of Polyamid-6 derived carbon fibers with addition of graphene reinforcement," *Carbon Fibers and Their Composites and Applications Workshop*, 11–12 July 2019, ORNL, Oak Ridge, TN, USA.

13. Klett, J., L. Zhang, M. Kowalik, Z. Gao, J. Zhu, Y. Schwab, A. Chowdhury, B. Damirchi, C. Bumgardner, Y. Gu, Y. Murty, Q. Shi, B. Harmon, J. Batten, B. Epling, A. C. T. van Duin, and X. Li, 2019, "Conversion of poly(p-phenylene-2,6-benzobisoxazole) fibers to carbon fibers through processing optimization," *Carbon Fibers and Their Composites and Applications Workshop*, 11–12 July 2019, ORNL, Oak Ridge, TN, USA.

14. Kowalik, M., C. Ashraf, S. Rajabpour, B. Damirchi, D. Akbarian, Q. Mao, and A. van Duin, 2020, "Atomistic analysis of PBO carbonization process with ReaxFF reactive force field," *Bulletin of the American Physical Society*, 2–6 March 2020, Denver, CO, USA.

15. Li, X., 2019, "Graphene nanocomposites with exceptionally high-strength and toughness," *International Symposium on Clusters and Nanomaterials (Energy and Medicine)*, 3–7 November 2019, Richmond, VA, USA.

References

1. Mainka, H., O. Täger, E. Körner, L. Hilfert, S. Busse, F. T. Edelmann, and A. S. Herrmann, 2015, "Lignin – An alternative precursor for sustainable and cost-effective automotive CF," *J. Mater. Res. Technol.*, Vol. 4, No. 3, pp. 283–296.

2. Park, S.-J., and G.-Y. Heo, 2015, "Carbon fibers," In: Park, S.-J. (ed.), *Carbon*. Springer Science & Business Media, Berlin, Germany.

3. Brown, S. F, 2013, "Carbon fiber, light and strong, arrives where it's most needed," *New York Times*, 14 July 2013. New York, NY, USA. Available at: http://www.nytimes.com/2013/07/14/automobiles/carbon-fiber-light-and-strong-arrives-where-its-most-needed.html (last accessed 8 December 2020).

4. Warren, C. D., 2007, "The development of lower cost carbon fiber technologies for automotive applications," *Proceedings of The Global Outlook for Carbon Fiber*, 23–25 October 2007, San Diego, CA, USA.

5. Fitzer, E., 1989, "PAN-based carbon fibers-present state and trend of the technology from the viewpoint of possibilities and limits to influence and to control the fiber properties by the process parameters," *Carbon*, Vol. 27, No. 5, pp. 621–645.

6. Chen, J. C., and I. R. Harrison, 2002, "Modification of polyacrylonitrile (PAN) carbon fiber precursor via post-spinning plasticization and stretching in dimethyl formamide (DMF)," *Carbon*, Vol. 40, No. 1, pp. 25–45.

7. Pichler, D., 2016, "'Give us affordable carbon fiber!,'" *CompositesWorld*, 25 February 2016. Cincinnati, OH, USA. Available at: http://www.compositesworld.com/columns/give-us-affordable-carbon-fiber (last accessed 8 December 2020).

8. Rao, S., T. G. A. Simha, K. P. Rao, and G. V. V. Ravikumar, 2018, "Carbon composites are becoming competitive and cost-effective," *Infosys*, Bengaluru, India. Available at: https://www.infosys.com/engineering-services/white-papers/Documents/carbon-composites-cost-effective.pdf (last accessed 8 December 2020).

9. Senftle, T. P., S. Hong, M. M. Islam, S. B. Kylasa, Y. Zheng, Y. K. Shin, and C. Junkermeier, 2016, "The ReaxForce-Field: Development, applications, and future directions," *Npj. Comput. Mater.*, Vol. 2, Art. 15011.

10. Srinivasan, S. G., A. C. T. van Duin, and P. Ganesh, 2015, "Development of a ReaxFF potential for carbon condensed phases and its application to the thermal fragmentation of a large fullerene," *J. Phys. Chem. A*, Vol. 119, No. 4, pp. 571–580.

11. Joshi, K., M. I. Arefev, and L. V. Zhigilei, 2019, "Generation and characterization of carbon fiber microstructure in atomistic simulations," *Carbon*, Vol. 152, pp. 396–408.

12. Zhigilei, L. V., Z. Lin, and D. S. Ivanov, 2009. "Atomistic modeling of short pulse laser ablation of metals: Connections between melting, spallation, and phase explosion," *J. Phys. Chem. C*, Vol. 113, No. 27, pp. 11892–11906.

Acknowledgements

The PIs would like to recognize contributions from Co-PI R. Hathaway and collaborator J. Batten, who have provided valuable input and carbon materials to the team. This input has helped the project remain focused on industry production needs and key material requirements.

The PIs would also like to recognize the contributions from Co-PI B. Harmon, Q. Shi, D. Cook, J. Moskowitz, and V. Kumar at Solvay Composites. Mr. Harmon and Dr. Shi facilitated the pilot fiber production run at the conclusion of FY 2019 and provided guidance and feedback during the subsequent analysis and optimization during FY 2020. We would also like to thank Mr. Cook, Dr. Moskowitz, and Mr. Kumar for quickly onboarding as part of the project team and for their help critiquing the experimental and computational findings.

II.2.2 Integrated Computational Materials Engineering Predictive Tools for Low-Cost Carbon Fiber (Western Research Institute)

Jeramie J. Adams, Principal Investigator
Western Research Institute
3474 North Third Street
Laramie, WY 82072
E-mail: jeramie.adams@uwyo.edu

H. Felix Wu, DOE Technology Manager
U.S. Department of Energy
E-mail: felix.wu@ee.doe.gov

Start Date: October 1, 2017 End Date: July 31, 2021
Project Funding: $1,084,888 DOE share: $351,825 Non-DOE share: $733,063

Project Introduction

Significant weight reduction for vehicles would have several economic and environmental advantages—most notably, reduced fuel consumption and greenhouse gas emissions. Additional cascading benefits would include reductions in infrastructure costs and maintenance by virtue of less stress applied to vehicles, roads, and other transportation infrastructure, as well as far-reaching geopolitical impacts, such as improved national security, by reducing the dependency of the U.S. on foreign crude oil.

One such way to reduce the weight of vehicles, while not sacrificing strength and crashworthiness, is to replace traditional stress bearing metal components with lightweight advanced materials and composites, such as those made from comprising CF. These advanced materials can be engineered to have physical strength properties greater than steel at a fraction of the weight. By properly selecting materials and manufacturing protocols, very strong and flexible materials can be produced. This is why CFs are used to produce materials as diverse as the spaceship nosecones to shafts of fly-fishing rods. This gives validity to pursuing CFs for future development of lightweight vehicles.

One difficulty in the large-scale deployment of CF for the commercial vehicle industry is the availability of large quantities of CF with appropriate physical properties at a reasonable cost. To address these limitations, the U.S. Consortium for Affordable Carbon Fibers (CARE)—including academic, government, non-profit, and commercial entities—was assembled to study the feasibility of using large volume, low-cost natural resources to produce CFs of the appropriate quality and cost for use in the vehicle industry. Some of the most abundant natural resources are those from current biomass, such as sugars derived from agricultural sources, or those from ancient biomass, such as coal and petroleum. The results of a study on several different types of feedstocks, as well as blends of these feedstocks, will provide for a robust roadmap for potential materials, while also reducing economic risks that can arise by becoming too dependent on any one material, which may itself be subject to climatic, environmental, geopolitical, and, ultimately, market variations. Therefore, within this program, no particular preference was given to any one feedstock and CFs are being produced from coal-, petroleum-, and biomass-based feedstocks.

Objectives

The objective of this research is to investigate the current landscape of appropriate raw starting materials from petroleum-, coal-, and biomass-based feedstocks to derive precursors to produce low-cost CF materials for lightweight vehicles in the U.S. This objective is divided into two complementary parts:

1. Develop, integrate, and demonstrate a suite of ICME modeling tools that predict CF properties within 15% of measured properties. This will enable the design, development, and optimization of precursor

chemistry and molecular structure associated with conversion into CF and evaluate alternative precursors for their suitability to manufacture low-cost CF. The ICME models will also include methodologies to simulate the manufacturing processes, including variability from both process and material. All non-proprietary and non-business-sensitive public data and code—such as technical data used to support published journal articles or research code used for simulations—will be provided to the LightMat Consortium for curation and hosting.

2. Develop, manufacture, and demonstrate CF precursor technology and processing techniques where CF is a material consisting of thin, strong, multi-crystalline filaments of C used as a reinforcement material, especially in resins, and capable of achieving the requirements in Table II.2.2.1.

Table II.2.2.1. Project Parameters and Requirements

Parameter	Requirement
Cost	≤ $5/pound
Strength	≥ 250 Ksi
Modulus	≥ 25 Msi
Strain	≥ 1%

Approach

The approach will be to study readily available, large volume, feedstocks from biomass, coal, and petroleum to produce precursors of appropriate qualities that lend themselves to the production of CF with the appropriate physical properties and cost to be used in the commercial vehicle industry. The project will remove risk from this process by developing predictive models that can be used to guide the development of CF materials from new or blended feedstocks. To achieve this goal, a project team consortium was assembled including partners that have significant experience working with these different feedstocks, as well as experts in CF production, mechanical testing, and modeling from the molecular-, micro-, and macro-levels. The team chosen for this project comprises:

- Western Research Institute (WRI): Prime recipient
- Oak Ridge National Laboratory (ORNL): Subrecipient, funded by a field-work proposal (FWP)
- Grossman Group at Massachusetts Institute of Technology (GG-MIT): Subrecipient
- Southern Research Institute (SRI): Subrecipient
- University of Wyoming (UW): Subrecipient
- Advanced Carbon Products (ACP): Subrecipient
- Ramaco Carbon LLC (RAMACO): Subrecipient
- Solvay Composites (Solvay): Industrial advisor
- Koppers: Industrial advisor.

Each member of the consortium brings a unique and complementary necessary to build up fundamental scientific—and yet industrially relevant—understanding between the chemistry and molecular structure of different organic feedstocks and subsequent precursor formation, while following the production chain up through CF tow-level fabrication, mechanical characterization, and modeling. These individual aptitudes have been integrated using a database exploited by high-level data mining. Model inputs include DFT-assisted molecular dynamics, chemical and compositional characterization, morphology and mechanical CF data, CF processing parameters, tow-level epoxy mechanical information, ML, and computational methods to deliver state-of-the-art, holistic, and robust models. The strengths of each consortium member are necessary for the wide scope set forth in the project, while producing minimum overlap and duplication of efforts.
Figure II.2.2.1 shows a high-level depiction of the consortium organization and the primary strengths and responsibilities for each consortium member.

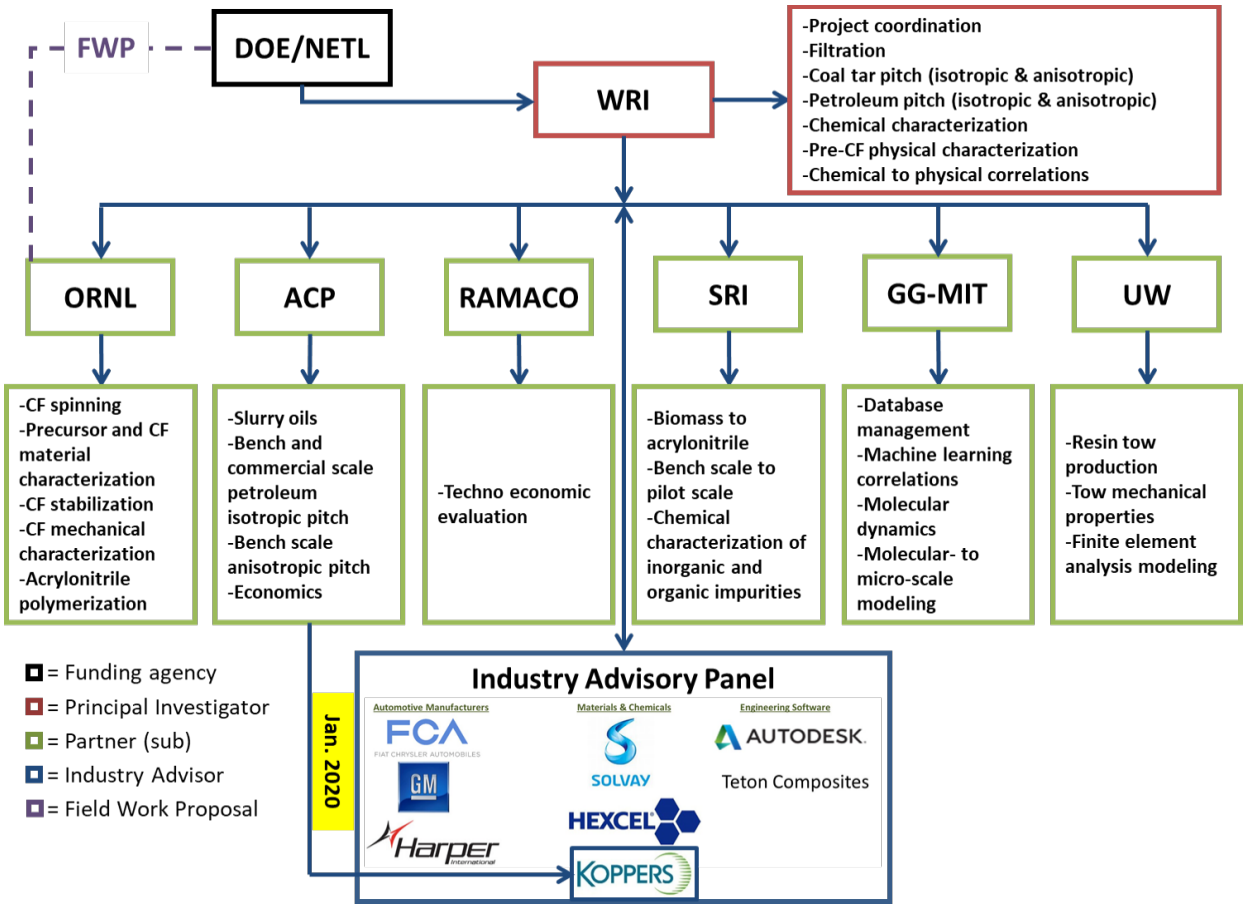

Figure II.2.2.1. Organization for the Consortium for Production of Affordable CFs in the U.S. Source: WRI.

The project is being conducted in three BPs.

BP1: CF Precursor Screening and Downselection

CF feedstocks and precursors were studied to down-select precursors capable of achieving the physical property goals at less than $5/lb. The project entered into a no-cost extension from October 2018 to December 2019 and all milestones were achieved by the end of the no-cost extension. CF produced from coal tar pitch (CTP), petroleum pitch (PP), and bio-based polyacrylonitrile (bio-PAN) met DOE's targets for BP1 for both mechanical properties and cost from the preliminary techno-economic analysis.

BP2: CF Tow-level Material System Properties and Analyses

Scale-up of acceptable candidates from BP1 was accomplished to produce larger batches of CF so that composite macro-level models will be created, and CF tow-level composites will be fabricated and tested at extreme temperatures for LD vehicle components to update micro-level and cost-estimate models. Micro-level models are being developed to optimize CF properties and production-engineering cost trade-off studies. The milestones for BP2 are shown in Table II.2.2.2.

Table II.2.2.2. Milestones for BP2

Title	Type	Milestone Description	Verification
Verify Macro-level FEMs	Tech	Check predictions against tow uniaxial creep and mechanical properties test data.	Accuracy is ± 15%
Micro-Level Models Validated	Tech	Check predictions against data.	Accuracy is ± 15%
CF Strength and Cost Goals Achieved	Go/No-Go	Check that higher volume precursor production retains CF performance.	Meets DOE strength goals at < $5/lb.
Establish CF Tow Strength-to-Weight Ratio	Tech	Establish strength-to-weight ratio with LD vehicle manufacturers to confirm weight savings.	30% to 50% < steel
Rank Precursors and CFs vs. DOE Goals	Tech	Use empirical data in ML tools to identify rank order precursor CF.	Confirm ML results match models

BP3: Validation and Transfer of Models and Data to DOE ICME Program

The most promising CF materials will be further evaluated for producibility and to improve macro-level models while building a comprehensive performance database up to the tow-level. Macro- and micro-level models will be integrated and validated for industry use. Models and data will be transferred to the DOE ICME program, and a final cost-estimate will be produced.

Results

Scaled-up batches of multifilament CF from bio-PAN and coal tar pitch mesophase (CTPM) were produced that met the desired DOE goals within error. A single filament spun CF from Koppers petroleum pitch mesophase (PPM) exceeded the strength and modulus goals; however, the elongation was below the target. Additional PPM processing has resulted in some improvements in the elongation. Table II.2.2.3 summarizes the CF properties for scaled-up CF precursors produced during BP2, and Figure II.2.2.2(a-f) provide images of the scaled-up multifilament samples for bio-PAN and CTPM.

Table II.2.2.3. CF Mechanical Property Data for Scaled-Up Precursors during BP2

Precursor	Strength (Ksi)	Modulus (Msi)	Strain (%)
Bio-PAN (1512 filament tow, 7.7 µm)	328.9 ± 54	30.0 ± 1.0	1.11 ± 0.15
CTP6M SP315+ (21 filament tow, 20 µm)	260 ± 28	24 ± 1.5	1.0 ± 0.14
CTP6M SP320 (single filament, 17.4 µm)	333.6 ± 57	34 ± 3.6	0.95 ± 0.12
PPM SP298 (single filament, 21 µm)	263 ± 102	56 ± 16.4	0.57 ± 0.11

(a)

(b)

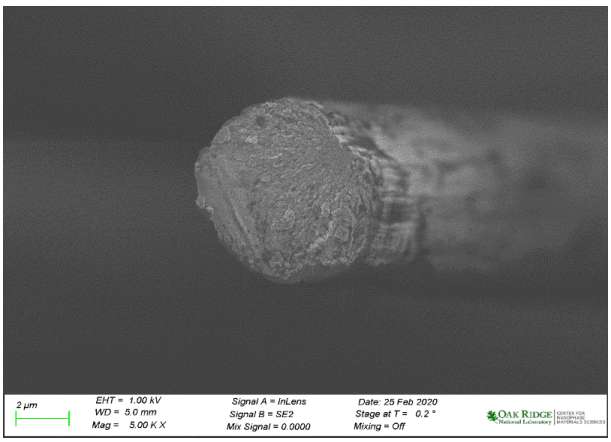

(c)

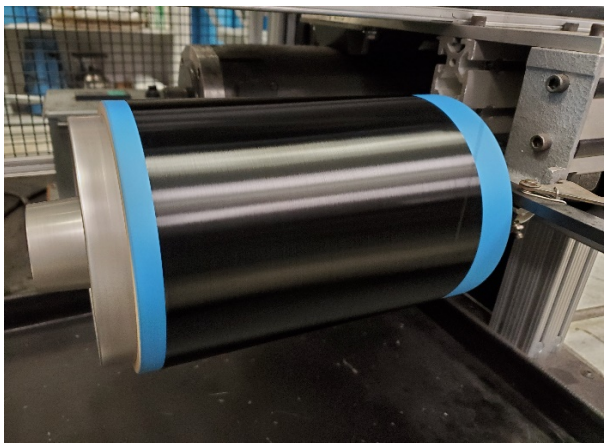

(d)

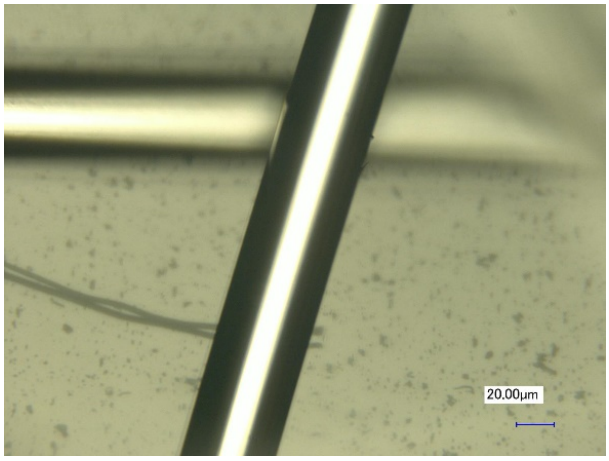

(e)

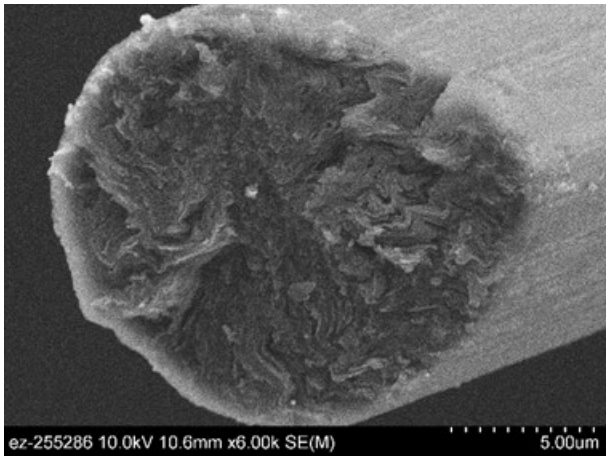

(f)

Figure II.2.2.2. (a) Multifilament fibers from bio-PAN. (b) A bio-PAN CF after stabilization and carbonization. (c) A SEM cross-section of a bio-PAN CF. (d) A spool of CTPM during multifilament melt-spinning. (e) A micrograph of smooth uniform CTPM fiber. (f) A cross-section of CTPM CF. Source: ORNL.

Significant advances were made in understanding pitch-based and bio-based acrylonitrile (bio-ACN) reactivity to produce precursor mesophase and bio-PAN, respectively, and the formation of CF from these materials. For pitch materials, the formation of covalent bonds between different aromatic molecules were investigated by different mechanisms to model the growth of larger aromatic mesogen molecules. The alignment of these molecules was investigated to show how molecular alignment along the fiber axis, as shown in Figure II.2.2.3(a-d), as well as increasing density, as shown in Figure II.2.2.4, produce a higher CF modulus. These results agree with experimental observations. CF production, through the processes of stabilization and carbonization, was also studied to understand how these processes impact atom connectivity within fibers to improve mechanical properties. Additional work was performed to understand the fundamental differences between CTPM and PPM molecule shape and aromatic ring substituents. Most PPM molecules contain methyl and small alkyl groups that affect aromatic growth and oxidation differently than CTPM molecules that are dominated by unsubstituted cata-condensed and peri-condensed polycyclic aromatic hydrocarbons. A summary of the computational developments for pitch-based micro-level is as follows:

1. An automated computational framework was developed to predict realistic possible molecules for aromatic growth during mesophase formation.
2. Insight into the role of small molecules generated during mesophase formation on aromatic growth.
3. A model was developed that shows and predicts the difference in self-assembly of the mesogen molecules between CTPM and PPM, due to the presence of methyl groups.
4. A model was developed that shows how increased connectivity in relation to ordering and density and selective oxidation during the spinning process is tied directly to the CF resulting modulus. This model helped to confirm BP1 results which showed that fully-isotropic CTP6 CF nearly met the DOE target.
5. Models were developed showing differences in the oxidation pathways between CTPM and PPM, which agreed with the experimental results.

Cross-sections of CF produced from CTP6 mesophase showed both radial- and random-wave morphologies with good alignment of aromatic domains in the direction of the CF length, as seen in Figure II.2.2.3. The morphologies of CFs are being studied to provide links to the failure modes for the fibers. Some of the failure modes which were established result from inadequate stabilization (hollow fibers), interfilament fusing (surface defects or partial melting of fibers along the axis of the fibers) from lower-SP mesophase, and porous fibers produced from high SP (>330°C) mesophase pitches, as seen in Figure II.2.2.4. For the high SP mesophase pitch, which must be spun at > 350°C, it is assumed that the high spinning temperature produces devolatilization within the precursor fibers, resulting in porous domains.

Coarse-grained molecular dynamic (CGMD) simulations were applied to simplify the ACN monomer molecules. This approach allows for convenient modeling of large covalently bonded structures that occur during polymerization to produce PAN units. These large molecular weight PAN units undergo further reactions during the CF process to produce ladder structures, and ultimately, a highly crosslinked network of ladder structures resulting in the final CF. Figure II.2.2.5(a-d) shows the CGMD simulations results at various stages of PAN CF production. This model was successfully used to predict the Young's modulus (e.g., 221 GPa) for a commercial Thornel T-300 PAN CF (e.g., 231 GPa) that was within the ± 15% targets.

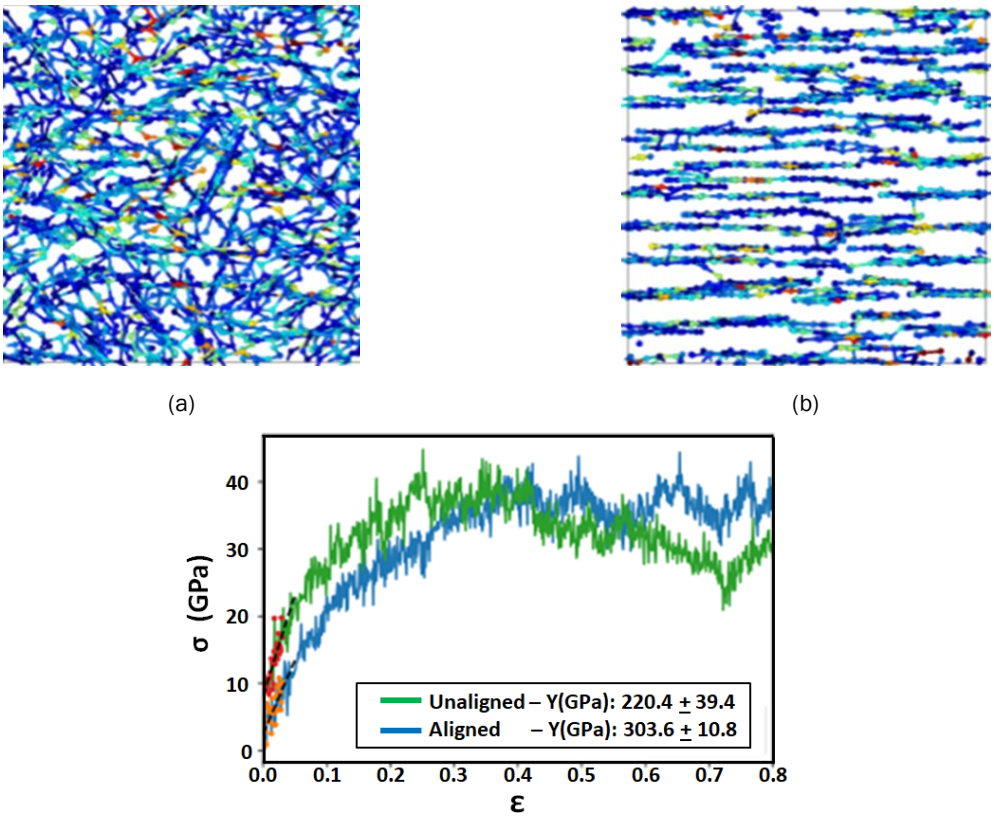

Figure II.2.2.3. Computational simulations of (a) unaligned aromatic molecules and (b) aligned aromatic molecules similar to alignment that occurs upon spinning. (c) A strain-stress analysis for these two systems with an insert showing that the Young's modulus (Y) of aligned system is 50% higher than the isotropic case.
Source: Massachusetts Institute of Technology.

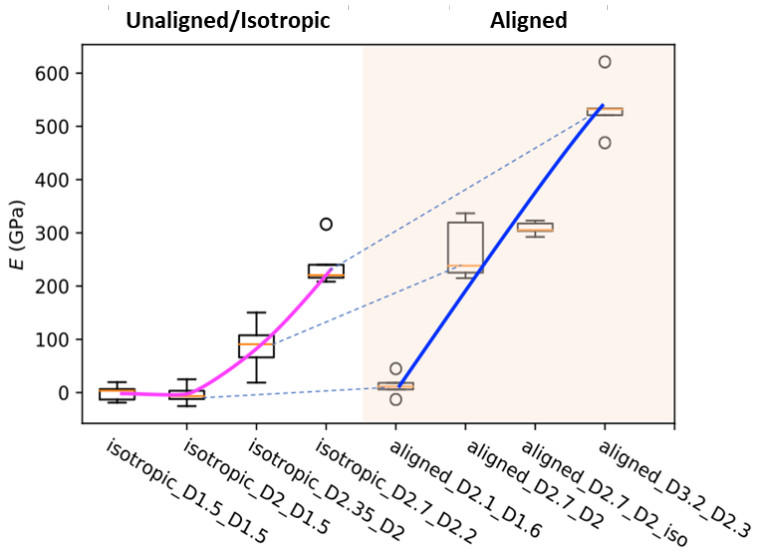

Figure II.2.2.4. Young's modulus for CFs processed under different conditions. The unshaded cases are unaligned (isotropic) fibers, while the shaded are aligned fibers. For each case, the Dx_Dy denotes the density under which the reactions underwent (Dx) and the final relaxed density (Dy). Source: Massachusetts Institute of Technology.

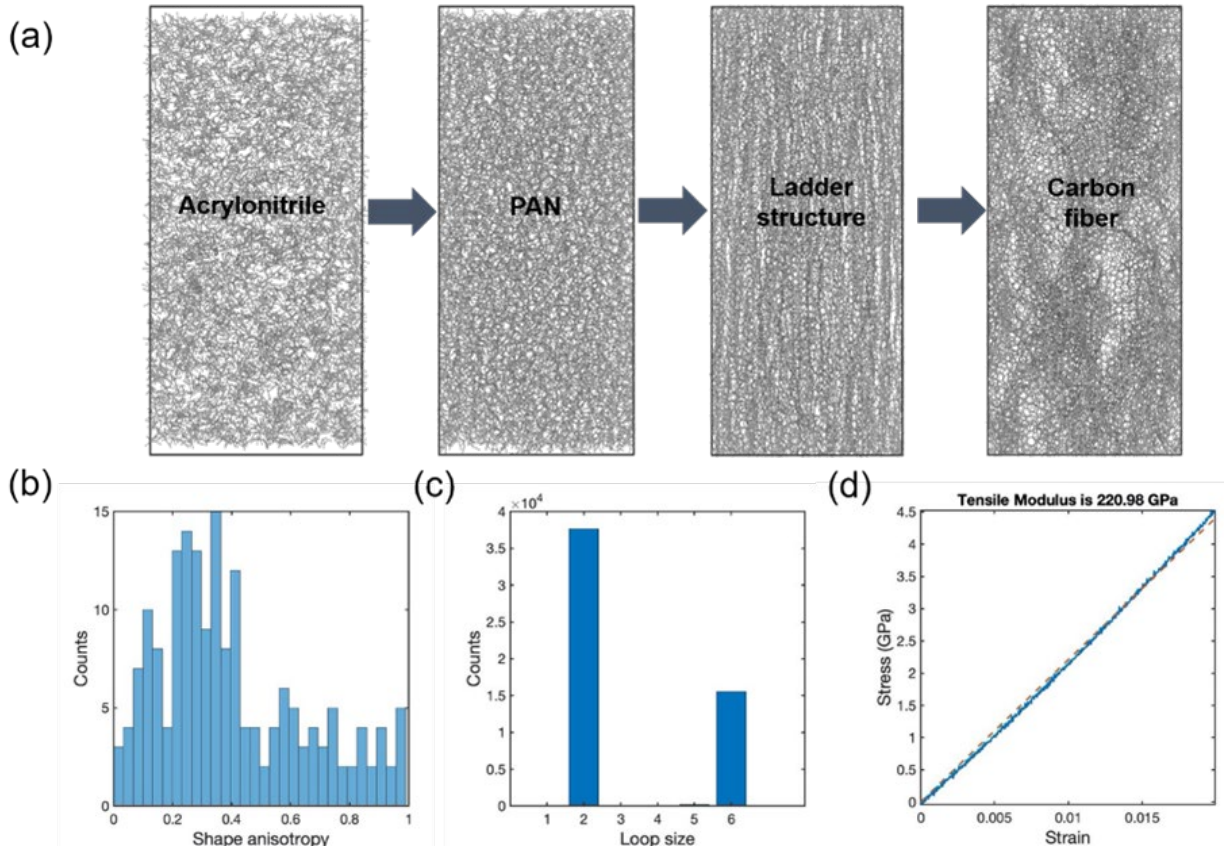

Figure II.2.2.5. (a) Microstructure evolution during the PAN-based CF synthesis captured by the CGMD simulations. (b) The distribution of the shape anisotropy of the ladder structures. (c) The counts of rings with different sizes in the CF system. (d) The stress-strain relationship of the simulated CF. Source: Massachusetts Institute of Technology.

Holistic ML approaches, which utilize all datasets for the given samples, are most appropriate when there is data available for large amounts of samples. The large number of samples are necessary to prevent overfitting of the data. However, this approach does not directly allow for easy discovery of direct cause and effect relationships. In this program, a new approach to ML was developed to handle the relatively narrow variety of samples and uncover direct causal relationships. These relationships are important because they can become the basis for understanding how to optimize precursor formulations to target specific CF properties. This new approach is considered a targeted approach where data are first analyzed by heat maps to identify strongly correlating data (e.g., positive or negative, Spearman or Pearson). After strongly correlating data is identified, it is used in the ML efforts. When this approach was applied, it shows that increasing methyl groups and the amount of 3–4 aromatic ring clusters decrease the softening point of the pitch. Conversely, higher molecular weight components in the pitch result in higher softening points. These specific features were determined from data obtained from Fourier transform infrared spectroscopy, fluorescence spectroscopy, and laser desorption ionization time-of-flight mass spectroscopy, and were all consistent with expectations.

Efforts placed a significant emphasis on developing reasonable assumptions for the techno-economic analysis from the literature and industry and integrating these with experimental data. Assumptions were made assuming a plant necessary to produce 10,000 kiloton per year of CF for all three feedstocks. For bio-PAN feed by-product, credits are applied, and for CTP by-product, distillates provide a credit as well. In the case of PP, a PP upgrading process, such as the one developed by ACP, assumes minimal by-product recovery due to recycle of distillates produced during the isotropic pitch and mesophase reactions. The analysis results in Table II.2.2.4 show that CF from bio-PAN, PP (from decant oil), and CTP all achieve DOE cost goals capable of being produced at less than $5/lb.

Table II.2.2.4. Results from the Techno-Economic Analysis for Scaled-Up Precursors during BP2

	Bio-ACN-PAN	PP	CTP
Feed Source - $/metric ton	$3,287	$300	$800
Total CF Cost - $/lb.	$4.86	$3.65	$3.86

Multiple types of tow-level commercial CF (pitch and PAN) were evaluated in epoxy molds to build and verify FEA models that captured key mechanical properties from single filament tests that were validated at the tow-level. The models were able to predict properties from the single CF very well and were usually within the ±15% goal. CF modulus was generally within ±5%, but strength had a wider deviation. Testing at the tow-level was performed according to the test matrix, as shown in Figure II.2.2.6.

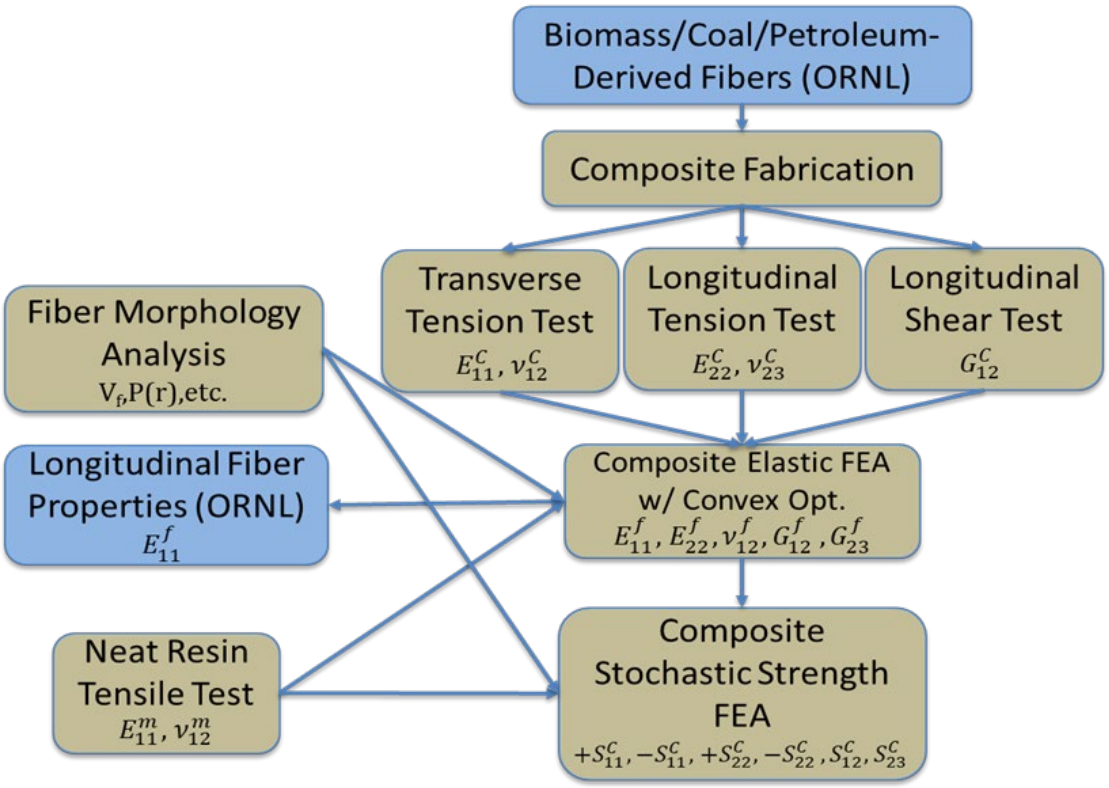

Figure II.2.2.6. Testing matrix developed and implemented at the University of Wyoming for characterizing tow-level CF properties with FEA. Source: University of Wyoming.

From the mechanical property data collected for tow-level bio-PAN CF, there is the expected significant in the strength-to-weight ratio compared to steel. Depending upon the type of steel (e.g., 1062 steel vs. 4340 steel), bio-PAN CF has a ratio that was 600–1,000% higher.

Delays due to COVID-19 caused the team to obtain a seven-month no-cost extension to complete BP2 activities.

Conclusions

Scaled-up CF from bio-, petroleum-, and coal-based feedstocks can be achieved at less than $5/lb. using current yields and assumptions to produce 10,000 kiloton per year. Achieving low-cost CF is a critical hurdle for incorporating more CF in vehicle parts. This is important since CF has a strength-to-weight ratio that is somewhere between 600–1,000% greater than steel, based on bio-PAN CF.

Scaled-up batches of bio-PAN and CTPM were successfully produced and spun into multifilament tows of CF, which meet DOE performance goals. CF produced from scaled-up batches of PPM exceeded strength and modulus properties; however, the material did not meet requirements for the elongation. Further work in BP3 will work to address the elongation issues for CF produced from PPM as well as explore a semi-scale-up CF production with bio-PAN and petroleum-based mesophase pitch precursors.

Many elements of a computational framework were developed to address key aspects of the broad CF production chain, beginning with an understanding of the feedstock molecules and the manipulations of these molecules to eventually produce CF. Significant advancements were achieved in modeling intermediate molecules (e.g., PP, CTP, bio-ACN) and precursor molecules (e.g., PPM, CTPM, bio-PAN) while also gaining understanding on the alignment of the precursor molecules during the CF production and the density of the resulting CF. Additional developments were made to model critical aspects for the transformation of precursor molecules during stabilization and carbonization. ML was applied to data for the different pitch and CF materials in a targeted approach to minimize overfitting and gain physical understanding of which chemical and compositional parameters most affect pitch properties and CF properties.

Key Publications

1. Annual Merit Review Meeting, June 3, 2020, “Consortium for the Production of Affordable Carbon Fibers (CPACF) in the U.S., ICME Predictive Tools for Low-Cost Carbon Fiber,” Project ID number: MAT125.
2. Annual Merit Review Meeting, June 11, 2019, “Consortium for the Production of Affordable Carbon Fibers (CPACF) in the U.S., ICME Predictive Tools for Low-Cost Carbon Fiber,” Project ID number: MAT125.
3. Annual Merit Review Meeting, June 19, 2018, “Consortium for the Production of Affordable Carbon Fibers (CPACF) in the U.S., ICME Predictive Tools for Low-Cost Carbon Fiber,” Project ID number: MAT125.

Acknowledgements

The Consortium for Affordable CFs in the U.S. would like to acknowledge DOE-EERE VTO Materials Technology Manager Dr. H. Felix Wu for his technical guidance. They would also like to acknowledge individuals who have contributed significantly to the technical success in several areas: L. Kearney at ORNL for CF spinning, mechanical properties testing, and ACN polymerization; N. Ferralis at MIT for spearheading the computational work at the molecular level, ML, and database; D. Malone at ACP for providing expert technical guidance on mesophase formation; K. Baig at WRI for analytical analysis, pitch filtration, and conversion of isotropic CTP to mesophase; S. McKinney, B. Johnston, and C. Muller at Koppers for providing CTP, PP, and PPM to the program; C. Atkins and J. Dietz at Ramaco Carbon, LLC, for providing the detailed techno-economic analysis; R. Fertig at UW for providing tow-level tests and FEA and other macro-level modeling; and A. Goyal at SRI for working to provide purified scaled-up batches of bio-ACN.

II.2.3 Ultralight Hybrid Composite Door Design, Manufacturing, and Demonstration (TPI Composites Inc.)

Nathan Gravelle, Principal Investigator
TPI Composites Inc.
373 Market Street
Warren, RI 02885
E-mail: ngravelle@tpicomposites.com

H. Felix Wu, DOE Technology Manager
U.S. Department of Energy
E-mail: felix.wu@ee.doe.gov

Start Date: December 1, 2015 End Date: March 31, 2020
Project Funding: $15,861.63 DOE share: $15,861.63 Non-DOE share: $0

Project Introduction

New corporate average fuel economy regulations require improved fuel efficiency of the future vehicle fleet. Weight reduction is key to achieving these targets. Replacing metal body and chassis components with CFRCs offer the most weight reduction potential at up to 70%. The introduction of the BMW i3 and i8 in 2014 required mass production processes to meet 20,000+ units per year. Preforming with high-pressure resin transfer molding (HP-RTM) has been implemented and meets rate, cost, and performance requirements. Our team members—Krauss-Maffei, Hexion, and Saertex®—were extensively involved in technology development (i.e., manufacturing, materials, and preforming) with BMW and brought this experience to our team, led by TPI, the vehicle OEM, and the University of Delaware Center for Composite Materials (UD-CCM). We will advance these technologies to develop an ultralight driver's side door for the vehicle with production rates of 80,000 units annually.

Objectives

The objectives for this project are to address the following targets and technology gaps:

- **Target:** Reduce part count and full-system weight by a minimum of 42.5%.

  Gap: Current materials and methods utilize steel as the main structural component, adding mass to the overall structure, thereby reducing the fuel efficiency of the vehicle.

- **Target:** Cost increase will not exceed $5 per pound of weight saved.

  Gap: One of the major materials at our disposal to decrease weight—CF—is upwards of $10–$15/lb. This material must be used judiciously to meet the cost targets.

- **Target:** Materials and processes will be demonstrated to meet the production rate and performance requirements (e.g., an approximate 4- to 5-minute cycle time is required to meet annual production rate).

  Gap: Standard composite manufacturing processes can produce these parts at a cycle time of about one-hour per part. New injection technologies and resin formulations provide possible faster cycle times.

Approach

Development of a vehicle body-in-white is a very complex and time-consuming process because various, often conflicting, functional requirements must be considered. Introducing new designs to reduce vehicle weight requires a system approach where new designs can be quickly iterated and refined to evaluate their performance. This is particularly true when metals are replaced with composite materials. Composite materials have significant potential to reduce weight when designs are fully optimized for parts consolidation and engineered properties using a variety of available material, fiber layups, and processing choices.

A typical automotive door is made from a combination of materials, including steel, plastic, and glazing. The structural materials are heavy, while the non-structural components do not contribute significantly to structural performance. Elements are joined together, which increases manufacturing and assembly costs and weight. We propose to replace all structural parts of the front driver's side door with continuous reinforced composites (with a weight savings of up to 60%), reduce part count and system weight through part consolidation, and evaluate alternative glazing materials. This approach has the potential to meet and exceed the goals of 42.5% system weight reduction as compared to the steel door baseline and to meet cost targets of $5 per pound weight saved. The team will take a systems approach to meet the targets as seen in the flow diagram in Figure II.2.3.1.

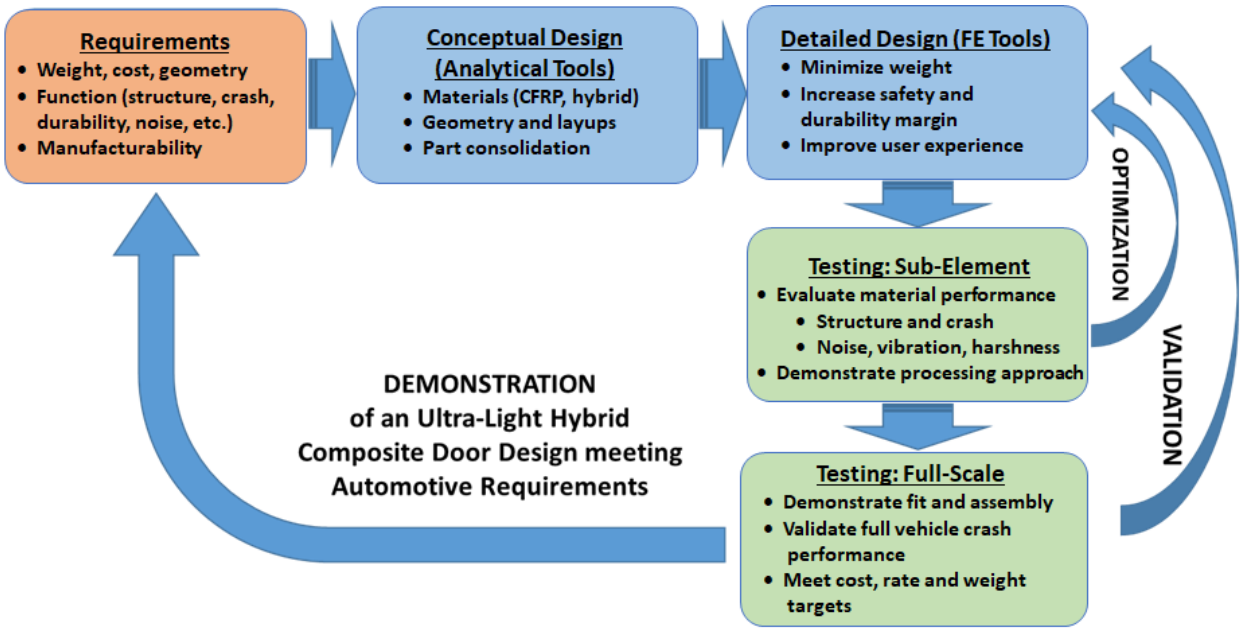

Figure II.2.3.1. Systems approach for reducing weight in complex automotive structures including the use of finite element tools for detailed design. Source: University of Delaware.

This approach relies on the use of computational engineering analysis and simulation tools combined with sub-element testing to rapidly develop and evaluate design changes while full-scale testing is used to proof out the final design. The program will define the design requirements (such as weight and cost targets), functional and topology constraints, and consider the ability to manufacture the door at the required rate and performance. Cost; structural; crash; NVH; and manufacturing simulations exist and will be utilized. These individual simulation tools are state-of-the-art, commercially available, and have been validated on numerous occasions. Conceptual designs will be evaluated at the sub-element level to evaluate material performance (i.e., structure; crash; and NVH) and to demonstrate that the processing approach meets rate and quality targets. Full-scale test articles will be manufactured to validate form, fit, function, and cost of all integrated structural and non-structural components. A small number of design iterations may be required to optimize the various configurations.

The approach will allow: (1) a shortened design cycle, resulting in reduced development time and costs; (2) elimination of trial-and-error process and part trials reducing tooling and manufacturing costs; and (3) an optimum door configuration at minimum weight leading to a more cost-competitive product. The overall approach will be demonstrated on a composite door solution for the vehicle, but it is also applicable to a wide variety of automotive components. The comprehensive systems approach for designing, manufacturing, and validating a complex ultra-lightweight composite automotive component using a validated, multidisciplinary design tool with a small number of manufactured components for validation will reduce risk to convert metal structures to composites.

Predictive engineering tools guide material and design downselection and are critical for eliminating trial-and-error and reducing cost and time. Figure II.2.3.2 shows the design environment the team will employ to evaluate the composite door structure.

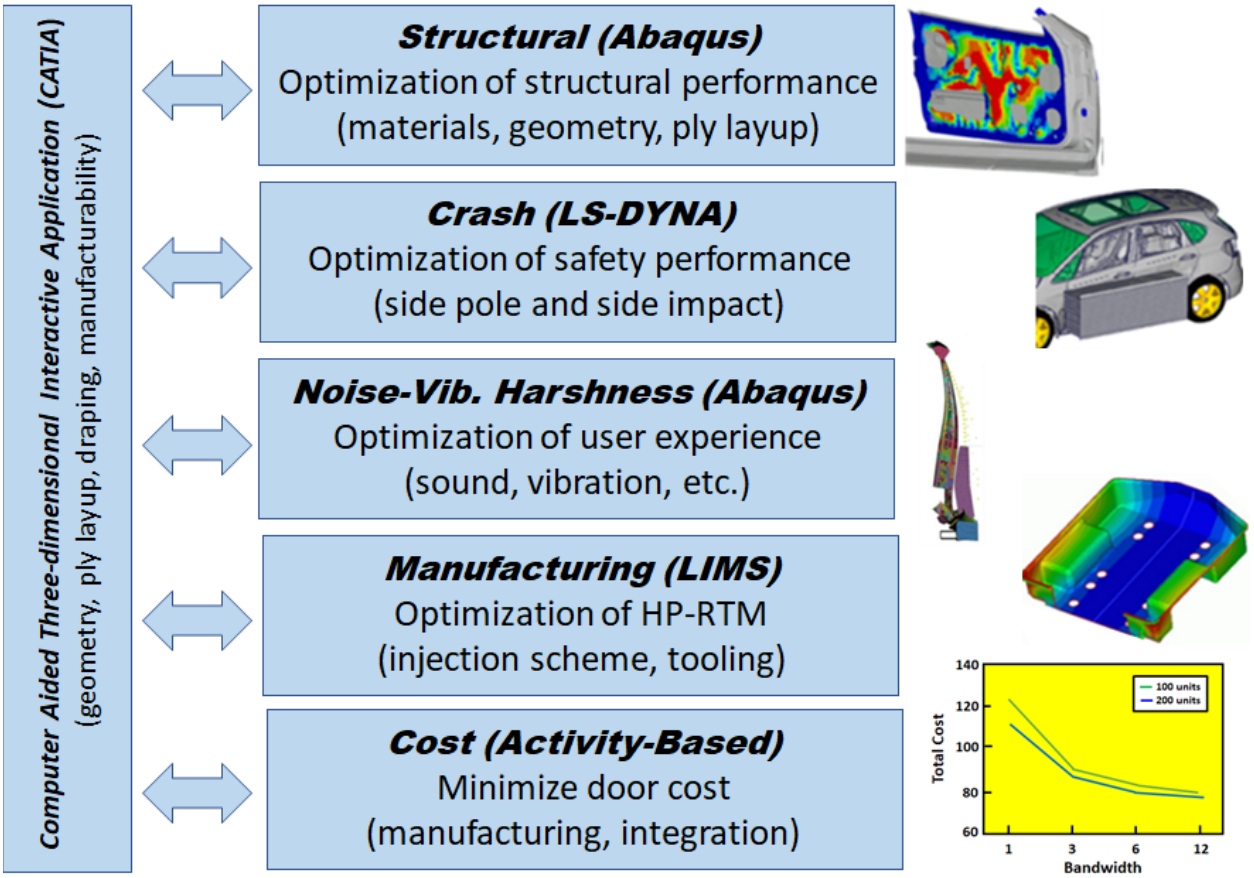

Figure II.2.3.2. Integrated predictive engineering environment and predictive engineering tools for the composite door development. Source: University of Delaware.

The existing vehicle steel door is used as a baseline and the ability to reduce part count with a composite structure will be investigated. Part consolidation reduces weight and cost because a smaller number of parts must be manufactured. Assembly time and associated labor costs can be significantly reduced as well. The HP-RTM process allows complex geometry part fabrication, which enables integration of features into one component. Figure II.2.3.3 illustrates the potential part count reduction of a steel door with an equivalent composite structure [1]. Part count reduction alone will not be able to meet our weight reduction goals of 42.5%, but in combination with hybrid and/or CFRC material replacement and lower weight window solutions, it will reduce the weight of the door structure to the required levels.

Our hybrid solution will evaluate a variety of material solutions, including glass and CFs. Fiber modulus and strength depend on the fiber selection with specific properties being the highest for CFs. Design solutions without cost consideration will use 100% CFs and provide the best structural performance at the lowest weight. A hybrid design will incorporate alternative fiber solutions at a lower cost and meet structural performance. Our optimal design will consider all options and will meet structural requirements and cost and weight targets.

Figure II.2.3.3. Composites allow part consolidation, further reducing cost and weight. Source: Composites World [1].

Crashworthiness will be evaluated using LS-DYNA, allowing simulation of the door and full vehicle under dynamic conditions. In particular, our team will consider the crash performance under side impact meeting Federal Motor Vehicle Safety Standard 214's protection requirements (other crash scenarios will be considered). The simulation will evaluate inward deflection as a function of time during impact for the baseline steel door and our composite door solution. A conservative design goal would require the composite solution to provide a deflection profile that stays below the transient intrusion levels of the steel baseline door. This would ensure the safety mechanisms (such as the side airbag) are able to be deployed in time and space and the passenger is protected in case of a side collision. UD-CCM has significant experience with crash predictions and, under a current NHTSA program, evaluates composites for a steel B-pillar replacement. Strain-rate-dependent material properties for composites are available; however, other properties for the HP-RTM resins and fibers may have to be determined using coupon and subscale element testing. The test data will provide the programs with a database of material properties for crash designs.

New resin materials are currently being developed at Hexion and will be optimized for this program. These resins (e.g., EPIKOTE™ 05475) and appropriate curing agents have low initial viscosity (e.g., below 100 centipoise) and allow rapid infusion of reinforcement during the injection phase of the HP-RTM process [2]. The rheology of the EPIKOTE™ resin with three different curing agents is discussed in Hillermeier *et al.* [2] and shows the ability to control the viscosity profile, while ensuring rapid cure without significant exothermic reaction of the polymer. Recent advances show full property translation and rapid (i.e., snap) cure in less than two minutes at elevated temperature. The low viscosity profile allows reduced injection pressure throughout the infusion cycle, relaxing the requirements of the preform, tool, mixer, and press. This, in turn, reduces preform distortion, cycle time, and capital cost.

Non-crimp fabrics provide the best fiber property translation and, using multiaxial systems, can be combined in a preform used in the production of large series vehicle components. These preforms are manufactured to the correct geometry and fiber layup, allowing rapid placement of the reinforcement into the HP-RTM tool. This enables minimum cycle time during the process, paired with the high-quality of the final product. It is important to optimize the preform to reduce scrap material and lower material cost. Our partner, Saertex, is the worldwide leader in tailor-made non-crimp fabric materials, and they will support the development of low-cost preforms for this program.

A key challenge of the HP-RTM is the design of the mold and preform to ensure full infusion of the polymer into the reinforcement. Tooling cost is a significant capital expense because applied pressures are high, and the tool is expected to last through the entire production run. UD-CCM is an expert in modeling the infusion behavior in liquid molding of hybrid preforms with complex geometry. The permeability and drapability of the

reinforcement, as well as the rheology of the resin, are key material properties and are needed to allow optimization of the injection port locations and resin pressure cycle during infusion processing. We will evaluate the feasibility of the proposed designs to be manufactured and optimize the mold features for successful infusion, eliminating any required tool changes due to resin infusion issues. The program will ensure manufacturability of the proposed concept with HP-RTM and use virtual process tools to optimize tooling and infusion approaches. Tooling cost for HP-RTM is a significant investment and can only be amortized over a large production run. Conventional RTM processing of prototypes with equivalent part properties will be conducted as part of our risk reduction strategy.

Results

Static Testing

A static header rigidity test was conducted in FY 2020 in accordance with the OEM test procedure, "Door System Upper Frame Rigidity Structural Test," dated January 2018. The objective of this test was to compare the header rigidity for the designed CF door and compare it with the baseline steel door. With the following exceptions and explanations, the test was successfully completed:

- All steel and CF doors were tested as-received.
- Clamping locations were determined by the R&D team.
- Load application locations were determined by the R&D team (250 kN at the B-pillar and 200 kN slightly away from the B-pillar).
- The load applicator was selected by the R&D team.
- Lasers were fixed to record movements of the load points during testing.

Figure II.2.3.4 shows the results of the header rigidity test, while Figure II.2.3.5 shows the test setup for the C and steel doors.

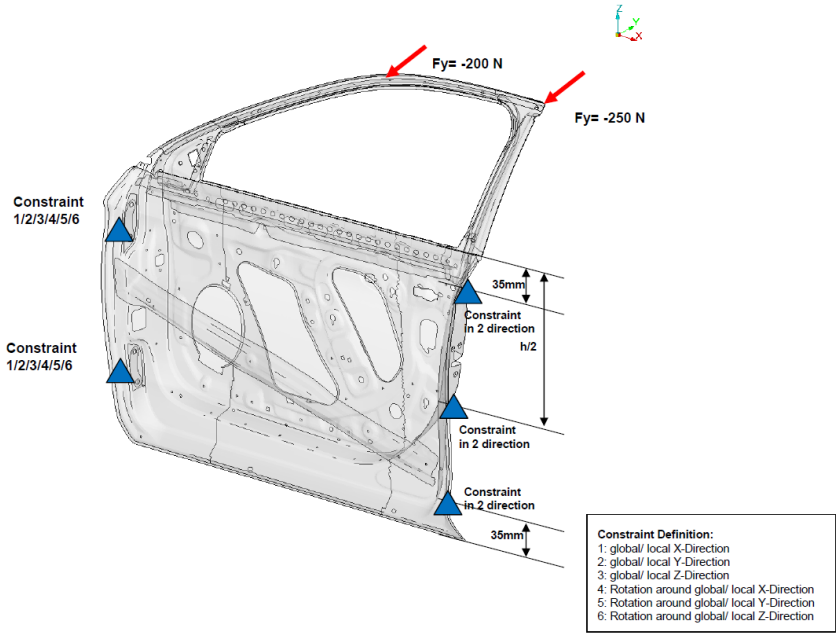

Figure II.2.3.4. Test specification for the header rigidity test. Source: TPI.

(a)

(b)

Figure II.2.3.5. Header test setup for the driver's side: (a) CF; and (b) steel door. Source: TPI.

Three steel and four CF doors were tested with the displacement measured at the load points. Table II.2.3.1 and Table II.2.3.2 show the displacement of these doors for the load at the B-pillar and at a location off-center from the B-pillar, respectively. Adequate care was taken in keeping the load locations the same for both doors.

Table II.2.3.1. Load at the B-Pillar (250 kN)

Type of Door	Displacement (mm)	Average (mm)	Stiffness (kN/mm)
Steel	5.20, 5.08, 5.09	5.12	48.8
CF	5.29, 5.08, 5.09, 5.91	5.34	46.8

Table II.2.3.2. Load at the Off-Center from the B-Pillar (200 kN)

Type of Door	Displacement (mm)	Average (mm)	Stiffness (kN/mm)
Steel	6.59, 6.47, 6.35	6.47	30.91
CF	5.50, 6.04, 5.71, 5.89	5.79	34.50

Based on the results shown in Table II.2.3.1 and Table II.2.3.2, the CF doors show a 4.1% lower stiffness as compared to the steel door at the B-pillar location. At a location a little offset from the B-pillar location, the stiffness measurement was 11.6% higher than that seen with the steel door. Also, the CF door shows a little more standard deviation in the measurements. This might be due to the variation coming from manufacturing. Overall, the experimental results indicate that CF design successfully met the header rigidity requirements as compared to the metal door assembly with a significantly lower mass.

Dynamic Testing

Test setup was conducted with metal doors to determine a baseline to compare with the composite designs. The impactor needed to be set at a height to produce significant side-body deflections but would not hit the bottom of the fixture. If the impactor were to have enough energy to allow the door to hit the bottom of the test setup, energy would be lost, invalidating the test. The test runs were run with the 3000 lb. impactor at 96, 72, 48, and 24 in., respectively. The 24 in. height was chosen because it did not show signs of floor impact and there were only eight total side-bodies for the testing. Four were used for the calibration of this test, as observed in Figure II.2.3.6 for a metal door. The composite doors were then tested at an impactor height of 24 in. The test setup and images of the damage to the composite door is shown in Figure II.2.3.7.

Figure II.2.3.6. Metal door after the impactor test at a height of 24 inches. Source: TPI.

Figure II.2.3.7. First composite door tested: (a) before the 24-in. impact; (b) after the 24-in. impact; (c) crushed ribs on impact beam; and (d) energy absorbed in crushing of "hats." Source: TPI.

Figure II.2.3.8 provides the data for the impact test load deflection and the impact test energy absorption showing the corrected force and the energy absorbed as a function of displacement for the composite and steel doors.

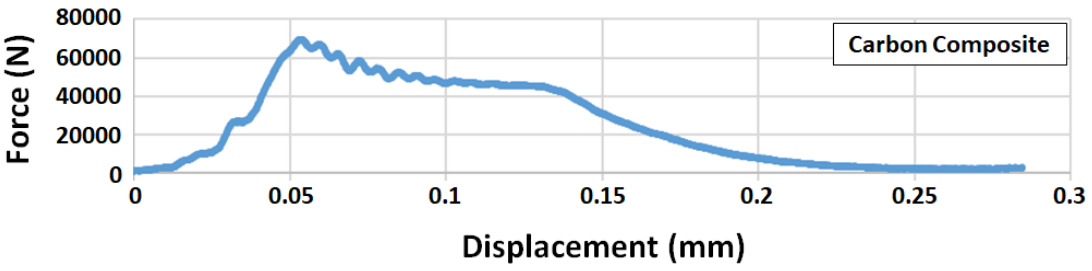

(a)

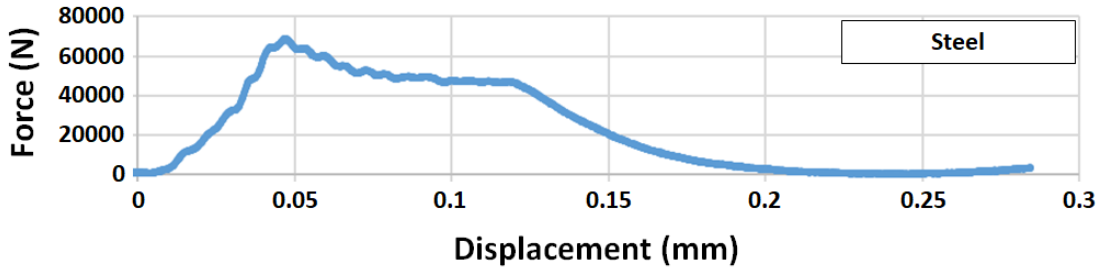

(b)

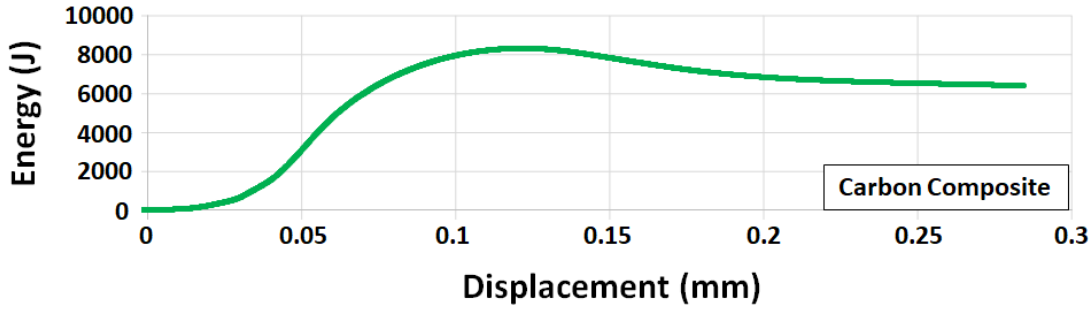

(c)

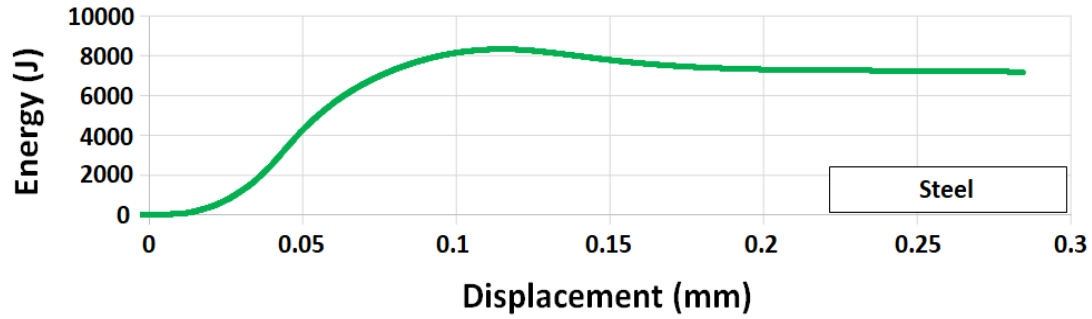

(d)

Figure II.2.3.8. Impact test load deflection and the impact test energy absorption curves for (a) the corrected force vs. displacement for the C composite door, (b) corrected force vs. displacement for the steel, (c) the energy absorbed vs. displacement for the C composited door, and (d) the energy absorbed vs. displacement for the steel door. Source: TPI.

Status to Target

The design solutions presented in this report represented a cost of $715 per door at a mass of 22.8 kg (or 50.2 lbs.) compared to the baseline door as depicted in the charts shown in Figure II.2.3.9 and Figure II.2.3.10. This represents a savings of 13.7 kg (or 30 lbs.) over the existing baseline door design. The cost increase of $138 per part and 30 lbs. of mass saved yields a $4.58 cost increase per pound of weight saved, exceeding the program targets. The total mass saved is 38% going from 36.5 kg to 22.8 kg. This target proves to be more difficult as the total mass of the door is included in this calculation. The window track and motor, latch, hinges, and other sub-assemblies represent 56% of the total mass of the door, and they are harder to lighten than the structure.

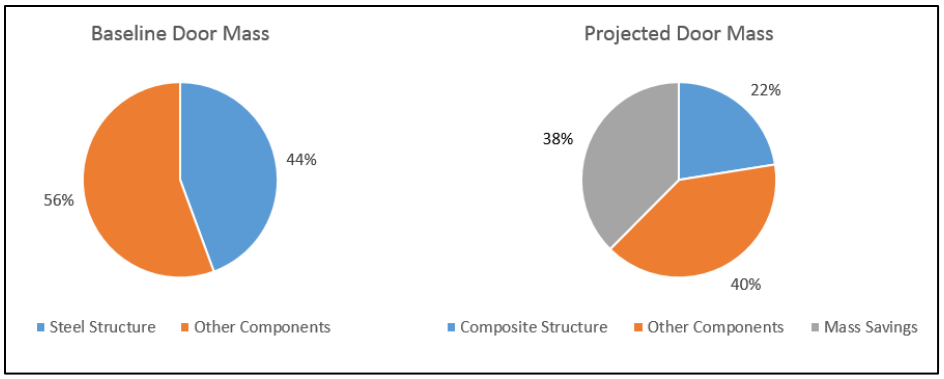

Figure II.2.3.9. Door mass breakdown. Source: TPI.

Component	Cost
Door Structure	$ 50.78
Inner Panel	$ 67.08
Door Mechanism	$ 57.33
Window system	$ 122.37
Sealing System	$ 21.92
Hinges	$ 9.92
Power System	$ 25.00
Molding System	$ 25.69
Mirror System	$ 46.45
Other	$ 150.00
TOTAL	$ 576.54

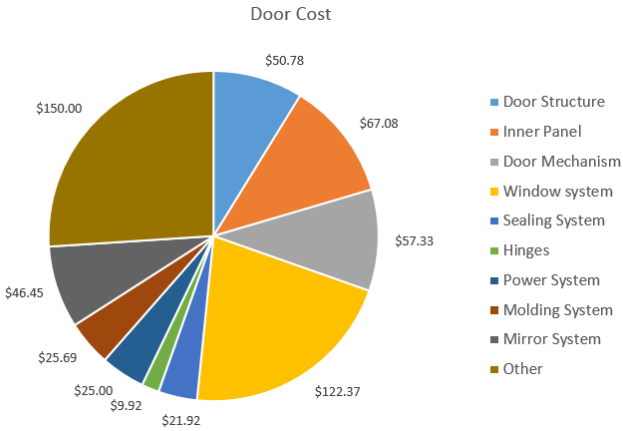

Component	Current Mass [kg]
Door Structure	16.2
Inner Panel	4.1
Door Mechanism	1.7
Window system	5.7
Sealing System	2.6
Hinges	1
Power System	1.1
Molding System	0.9
Mirror System	1.6
Other	1.6
TOTAL	36.5

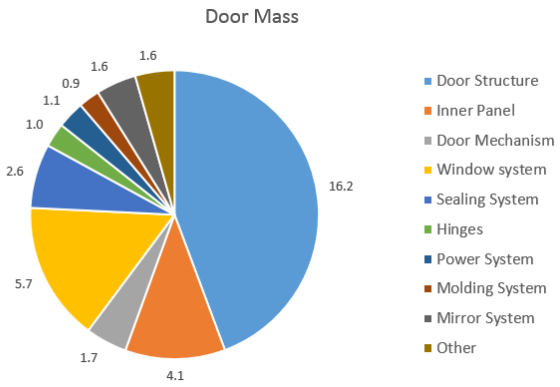

Figure II.2.3.10. Baseline costs and mass per door part. Source: TPI.

The optimized design as defined during the FY 2018 program yields a 38% mass save and a $5.47 cost increase per every pound saved. This is based on the input fiber, Zoltek Panex 35, at a cost of $7.75 per lb. The low-cost CF from ORNL has been commercialized and realized an input fiber cost of $4.75 per pound. If we were to utilize this fiber in place of NCF, we could then exceed the cost target even further, getting down to as low as $4.33 per pound saved, as shown in Table II.2.3.3.

Table II.2.3.3. Status to Target Based on Commercial CF and Developmental Low-Cost CF

Input CF Cost: $7.75/lb		Input CF Cost: $4.75/lb	
Optimized Design		ORNL Low-Cost CF Design	
Weight Reduction (lb.)	30.3	Weight Reduction (lb.)	30.3
% Reduction	38%	% Reduction	38%
Cost Increase	$165.72	Cost Increase	$131.13
Dollars/lb. saved	$5.47	Dollars/lb. saved	$4.33

Conclusions

We are close to the major goals of reducing part count and full-system weight by a minimum of 42.5% (38% achieved), the cost increase not exceeding $5 per pound of weight saved ($4.33 achieved with low-cost CF), and the materials and processes meeting the production rate and performance requirements. The mass targets were not met due to a high percentage of the doors mass is accounted for in the door other components. TPI was focused on the structural replacement of the door.

References

1. Sloan, J., 2012, "Auto composites quest: One-minute cycle time?," *Composites World* (August), Available at: http://www.compositesworld.com/articles/auto-composites-quest-one-minute-cycle-time (last accessed 3 December 2020).
2. Hillermeier, R., T. Hasson, L. Friedrich, and C. Ball, 2013, "Advanced thermosetting resin matrix technology for next-generation high-volume manufacture of automotive composite structures," *SAE Technical Paper* 2013-01-1176.

Acknowledgements

The author would like to acknowledge D. Ollett, our project manager at NETL. His support was directly related to the success of this program, and his guidance and direction kept us on the right path during this effort.

II.2.4 Functionally Designed Ultra-Lightweight Carbon Fiber-Reinforced Thermoplastic Composites Door Assembly (Clemson University)

Srikanth Pilla, Principal Investigator
Department of Automotive Engineering
Department of Materials Science and Engineering
Clemson University
4 Research Drive, Suite 340
Greenville, SC, 29607
E-mail: spilla@clemson.edu

H. Felix Wu, DOE Technology Manager
U.S. Department of Energy
E-mail: felix.wu@ee.doe.gov

Start Date: December 1, 2015 End Date: November 30, 2021 (applied 1-year no-cost extension)
Project Funding: $2,449,994 DOE share: $2,449,994 Non-DOE share: $0

Project Introduction

A promising route to achieve the 2025 Corporate Average Fuel Economy standards involves decreasing vehicular weight by incorporating lightweight materials, coupled with component redesign, to improve overall fuel efficiency. Indeed, one recent study indicates that the simple replacement of current metallic doorframes with CFRP composites can reduce the overall weight of the component by nearly 58% [1]. The objectives of this project are to achieve a weight reduction of at least 42.5% as compared to the baseline door structure at the cost of less than $5/lb., all while saving on energy metrics without compromising the fit, function, crash, and NVH requirements. The strategy for achieving these targets involves a holistic systems approach through the integration of unique designs, novel materials, manufacturing technologies, and joining/assembly of subsystems to ensure the developed technologies are ready for commercialization.

Objectives

The objective of this project is to reduce the weight of a door assembly by at least 42.5% compared to a baseline driver's side front door with an expected cost increase of less than $5/lb. in weight saved. A 2013 mid-sized sport utility vehicle's door from our OEM partner with an assumed production volume of 20,000 vehicles annually is the basis for design. These criteria will either meet or exceed the fit, function, crash, and NVH requirements of the baseline door..

The intent is to: (1) enable a radical redesign of the baseline door via a holistic systems approach through the integration of unique designs; (2) use novel materials to render the door 100% recyclable; and (3) investigate manufacturing technologies and joining/assembly of subsystems to ensure the developed technologies are ready for commercialization. The partner organizations listed in Table II.2.4.1 are providing highly leveraged knowledge expertise to ensure the success of this effort.

Table II.2.4.1. Project Participants

Universities	Industry Partners	Computation Partners
Clemson University	OEM	Altair Engineering
	Tencate, Lanxess	Core-Tech Systems (Moldex 3D)
University of Delaware	Krauss-Maffei, Trexel Inc.	MSC Software (Digimat)
	Proper Tooling	LS-DYNA

Approach

The project entails the use of a systems-level approach that begins with a systematic evaluation and benchmarking of the door and its sub-assemblies. In collaboration with our partnering companies and commercial suppliers, researchers are evaluating a variety of CF thermoplastic material forms for structural components (i.e., novel unidirectional and fabric prepregs, co-mingled fabrics, high-aspect-ratio discontinuous fibers, performance thermoplastic resins, novel fiber architectures, and localized reinforcements) and alternative solutions for glazing, trim, and other subcomponents. The initial focus involves creating the structural component and a materials database for all parts of the door structural assembly (i.e., outer shell, inner panel, carrier, and anti-intrusion beam[s]).

A two-phase integrated design and manufacturing optimization approach was adopted to obtain the optimal manufacturing process parameters of the thermoplastic materials and the optimal structural design parameters of the door. The Principal Investigators also conducted a top-level trade study to determine at least two candidate designs for optimization. The design parameters include: (a) thermoforming and injection-molding parameters (e.g., pressure, temperature); (b) fiber parameters (e.g., material, length, diameter, volume fraction); (c) matrix parameters (e.g., material, volume fraction); (d) structural wall thickness; and (e) material density distribution. The research team will use four analysis tools—Moldex3D, Digimat, and LS-DYNA Implicit and Explicit—to construct the manufacturing-to-response analysis pathway [2],[3],[4]. The team will fabricate a door based on this optimal design for testing in accordance with OEM performance requirements.

Results

Concept Development

The team's focus in the fifth fiscal year was on manufacturability of the final door concept based on draping and tooling inputs from our material supplier and tooling partner. To achieve this, the team made several modifications to all components with an emphasis on the structural components. The composite inner panel, our most critical piece, underwent several rounds of modifications. The three major modifications are highlighted in Figure II.2.4.1.

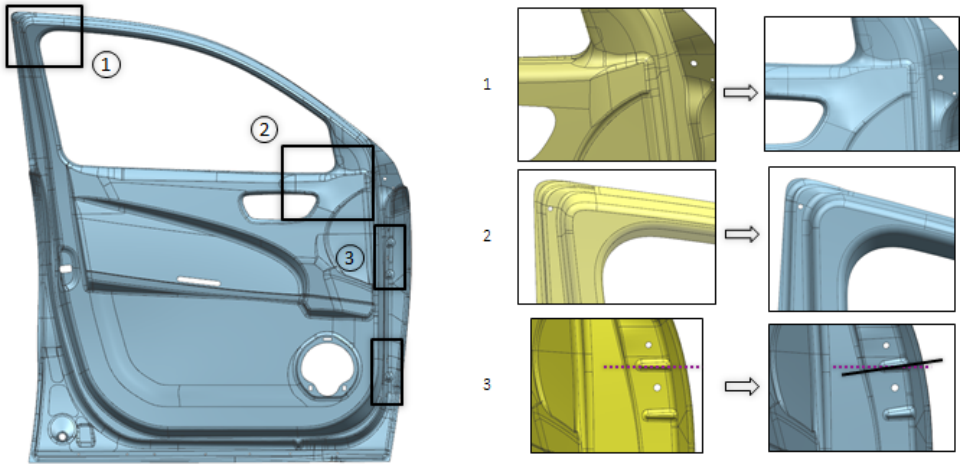

Figure II.2.4.1. Inner frame CAD modification at three locations (1,2,3). Source: Clemson University.

Similarly, significant computer-aided design (CAD) modifications were carried out on some of the mild steel and Al structural parts to improve manufacturability. Some examples include removing sharp corners and simplifying the surfaces to reduce shear stress in the metal during the drawing operation, as shown in Figure II.2.4.2.

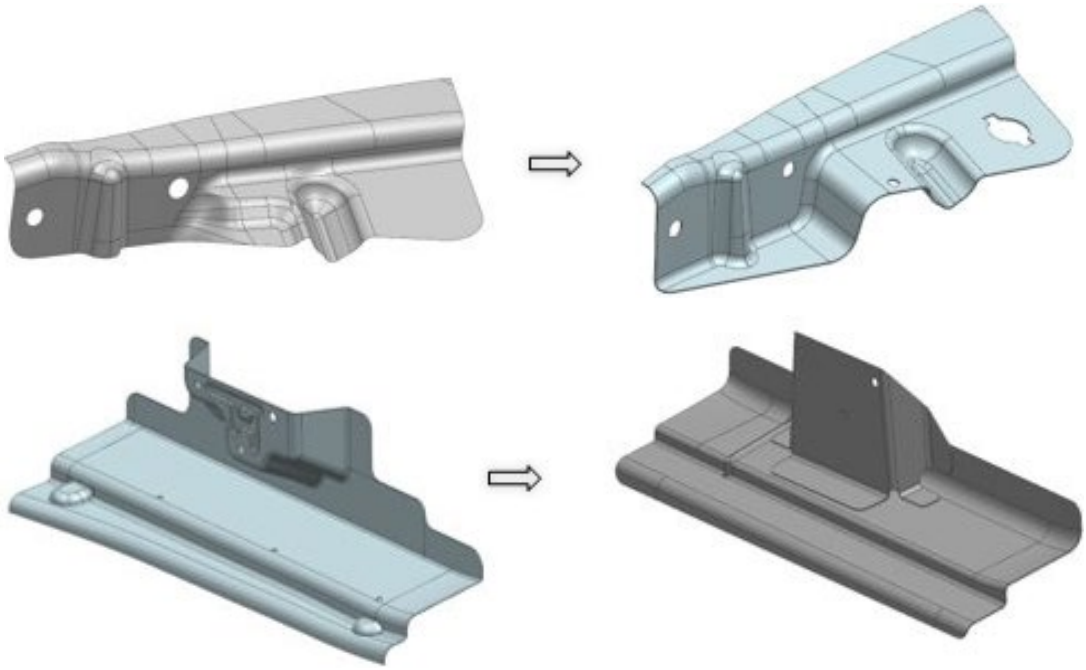

Figure II.2.4.2. Design change of anti-intrusion beam hinge side bracket and lower reinforcement. Source: Clemson University.

As a result of these changes, the team was able to achieve a 52% structural parts consolidation and a 45% structural weight consolidation due to innovative design strategic use of materials based on FEA and manufacturing simulation response, as illustrated in Figure II.2.4.3.

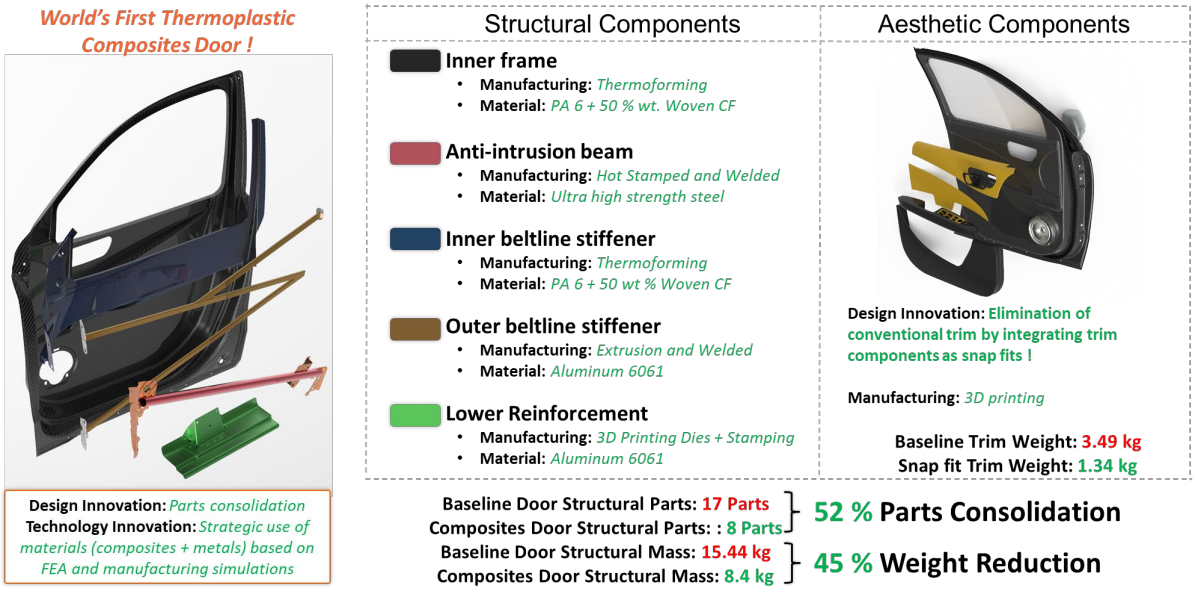

Figure II.2.4.3. Overview of final CAD for structural and aesthetic components. Source: Clemson University.

Summary of FEA Results

The team assessed the existing unidirectional (UD) + Woven ply design and decided to proceed with an entirely woven ply design having a uniform thickness of 3 mm for the inner panel and 2 mm for the inner beltline stiffener upon considering the geometric and thermoforming complexity of the inner panel. This configuration would greatly aid in simplifying the manufacturing effort by negating the need for equipment such as automated tape placement and simplifying material handling system while dramatically reducing tooling complexity.

The final door design is first optimized for linear static load cases, which represent daily use and misuse. These are: (1) door sag (two subcases); (2) sash rigidity (two subcases); (3) door over opening; (4) beltline stiffness; (5) outer panel stiffness; (6) mirror mount rigidity (two subcases); (7) speaker mount rigidity; and (8) window regulator stiffness. The composite door weight and deformation response under static loading is presented in Table II.2.4.2. The results are presented on the basis of the percentage relative difference between the baseline and the composite, where the negative sign indicates the reduction in the composite door response such as the mass or deformation from the target. The structural frame weight of the composite door is 45% lower than the target baseline weight while the total weight reduction achieved is 37%, which is a little short of DOE's target of 42%. The deformation response of the composite door under static loading is lower than the target baseline for the majority of the load cases. The two load cases where the composite door response is slighltly higher are mirror rigidity in X (+1%) and door over opening (+3%). However, these differences occur due to localized stress development near the hinges since the rigid body elements are used for modeling bolts. These differences can be easily eliminated during the door prototype fabrication by the usage of appropriate washers, therefore avoiding any major design change.

Table II.2.4.2. Static Performance of Composite Door

Serial No.	Target Category Subcase	Target (Unit)	% Relative Difference (Result – Target)/Target
1	Mass Target		
1.1	Structural Frame Weight	< Baseline (Kg)	-45%
1.2	Total Weight	< Baseline (Kg)	-37%
2	Frame Related		
2.1	Door Sag – Fully Open	< Baseline (mm)	-15%
2.2	Sash Rigidity at Point A	< Baseline (mm)	-10%
2.3	Sash Rigidity at Point B	< Baseline (mm)	-55%
2.4	Beltline Stiffness – IP	< Baseline (mm)	-79%
2.5	Window Regulatory (Normal)	< Baseline (mm)	-69%
2.6	Mirror Mount Rigidity in X	< Baseline (mm)	+1%
2.7	Mirror Mount Rigidity in Y	< Baseline (mm)	-67%
2.8	Door Over Opening	< Baseline (mm)	+3%
2.9	Speaker Mount Stiffness	< Baseline (mm)	-48%

The composite door was further tested under nonlinear load cases to evaluate crashworthiness. These load cases are: (a) the Federal Motor Vehicle Safety Standard S214S quasistatic pole test, as shown in Table II.2.4.3; and (b) the deformable barrier test (Insurance Institute for Highway Safety Side Impact Moving Deformable Barrier). The requirements for individual load cases were provided by the OEM partner. The performance of the composite door under the QSP test is compared with the baseline door in the contact force vs stroke plot, as presented in Figure II.2.4.4. The area under the curve of this plot gives the energy absorbed during pole impact. The total energy absorbed by the composite door (e.g., solid orange curve) is clearly higher

than that for the baseline door (e.g., solid black curve). Three OEM requirements exist for the QSP test: (i) an initial average crush requirement stroke under 6 inches (represented by a dashed green curve); (ii) an intermediate average crush requirement at under 12 inches (represented by a dashed blue curve); and (iii) a peak average crush requirement under 18 inches (represented by a dashed horizontal line). The initial average crush for the composite door is higher by 7% to the actual OEM requirement, and the intermediate crush (up to 12 inches) is higher than the actual OEM requirement by 81%. The composite door also satisfies the maximum peak crush requirement (e.g., the horizontal line in the plot) and is higher by 101%.

Table II.2.4.3. Results for the QSP Test

Results	% Above OEM Requirement
Initial Average Crush	7%
Intermediate Average Crush	81%
Peak Crush	101%

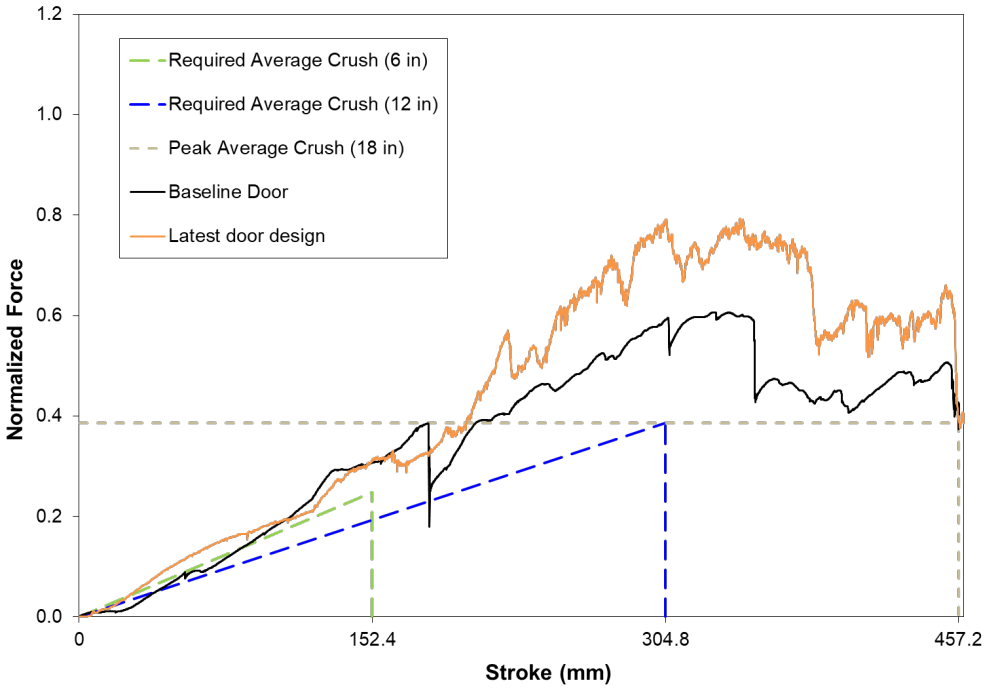

Figure II.2.4.4. Normalize force-displacement plot of baseline and composite door under the QSP test. Source: Clemson University.

To evaluate the performance of the door under deformable barrier load case, the team listed five key performance indicators after discussions with our OEM partner. A gauging matrix was further created to assess whether a composite door passed the OEM requirements or not. The gauging matrix is defined as: (a) successful (green) if the door response is better than the baseline; (b) tolerable (yellow) if the response is lower than the baseline, but is within the 10% margin; and (c) failure (red) if the response is below 10% from the baseline door. Table II.2.4.4 presents the composite door response compared to that of baseline target on five performance indicators, which are maximum intrusions at roof, near windowsill, at front door dummy hip and near door lower level and safety survival space. The highlighted response in green color shows that three intrusion indicators are in successful range while one intrusion criterion at door lower level is in tolerable range. The safety survival space which is indicative of the occupant space left after the impact is also measured which improved by 1% when compared with baseline target.

Table II.2.4.4. Results for Deformable Barrier Dynamic Load Cases Compared to Target Baseline Door

Key Performance Indicator	Target	Insurance Institute for Highway Safety Side Impact Moving Deformable Barrier (Response/Target)
Max Roof Intrusion		3%
Max Windowsill Intrusion		12%
Front Door Dummy HIP Intrusion		25%
Max Door Level Intrusion		4%
Safety survival space		1%
Gauging Metrics Green (Success) – Below Baseline target values (<b). Yellow (Tolerable) – More than Baseline values but smaller than 10 % difference (>b, <b+10%). Red (Failure) - More than 10% above Baseline value (>b+10%).		

Subcomponent Manufacturing, Modeling, and Testing

To correlate and verify the crash simulations results to real-world behaviors, a hat profile structure was manufactured with a pre-existing mold using Nylon 6 reinforced with 50 vol % woven CF supplied by our material partner, Lanxess. The forming setup, shown in Figure II.2.4.5(a), consists of two forming tools (e.g., the punch and die) and a blank holder apparatus accommodated in a thermal chamber. All forming tests were conducted on an Instron 5985 universal testing machine with a 250 kN 2580 series static load cell. Tests were performed using a crosshead speed of 5 kN/min until the preset load of 22 kN was reached. The entire set up—including the picture frame, composite material, and hat section tool—were placed in a furnace, thermocouples were placed on the punch, and the die, composite sheet, and furnace were heated. While cooling, the entire set up was cooled via forced convection until the composite material reached 100°C; then, liquid nitrogen was injected through Cu cooling channels in the tool to quench cool the part to RT. The intent of the quench cooling was to demonstrate the effect of cooling rate on the formation of residual stresses in the structure as shown in the graph of Figure II.2.4.5(b). The cooling channels were constructed in such a way that the composite part does not come into contact with the liquid nitrogen; any cooling seen on the material is due to conduction from the punch and the die.

The thickness variation and fiber orientations were experimentally measured after performing the thermoforming experiments and were compared with the numerical results. The thickness was measured at six different locations along the hat profile (or at three locations on each side) and the average thickness from the three experimental trials is presented in Figure II.2.4.6. The numerical thickness variation is predicted using a draping tool available in Altair Hyperworks software. A comparison between the measured thickness and the predicted thickness showed good agreement. Furthermore, the warp and weft tows of the composite sheet are referred to here as fibers in direction 1 and 2 initially 90° apart. These fibers of the composite sheet undergo reorientations as the sheet deforms to take the shape of the mold.

Figure II.2.4.7 shows a comparison of fiber orientations between the experiments and the simulation, where the change in angle between the two fiber directions was measured. The average fiber orientations from the three experimental trials were determined and compared with the numerical prediction, which showed good agreement. Next, the mechanical performance of the above thermoformed hat structure with the effect of residual stress was evaluated by carrying out a three-point bend test.

The hat structure samples were adhesively bonded to a 0.5 mm thick PA 6 woven composite plate using the Plexus MA 530 adhesive system, as shown in Figure II.2.4.8(a). The experimental setup for the quasistatic mechanical test of the hat structure is shown in Figure II.2.4.8(b), which consists of two supports with a support span of 119.3 mm and a punch. The three-point bend tests were performed on an Instron 5985 universal testing machine with a 10 kN 2580 series static load cell using a modified Instron 2810 series flexure fixture and a crosshead speed of 1 mm/min on three samples.

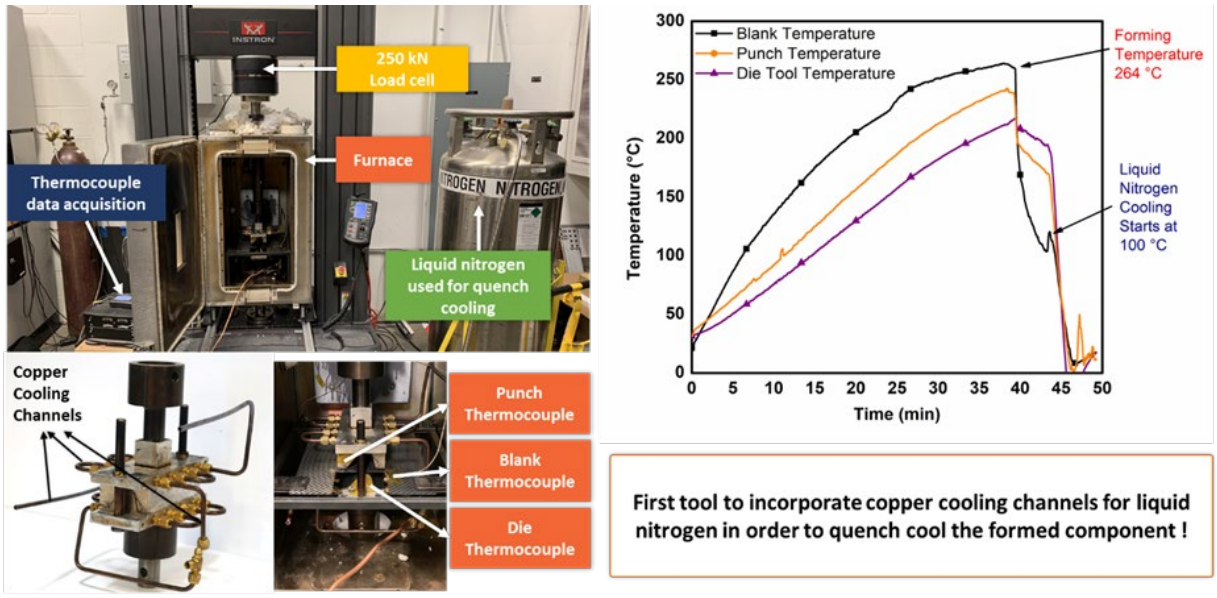

(a) (b)

Figure II.2.4.5. (a) Thermal chamber equipped with a thermocouple data acquisition system; and (b) liquid nitrogen cooling for thermoforming tests and thermoforming setup showing Cu cooling channels and thermocouple location.
Source: Clemson University.

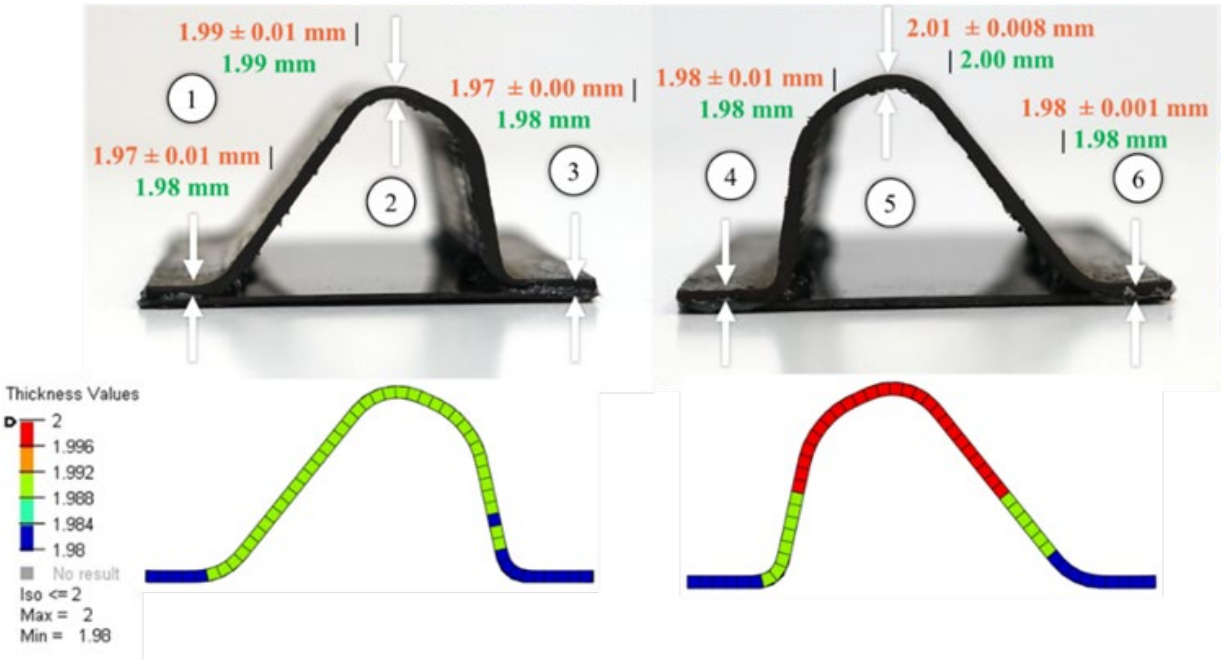

(a) (b)

Figure II.2.4.6. Thickness variation in the hat structure of: (a) Side 1; and (b) Side 2, which are represented as average thickness ± standard deviation. Predicted thickness from simulation measured for the three experimental forming trials.
Source: Clemson University.

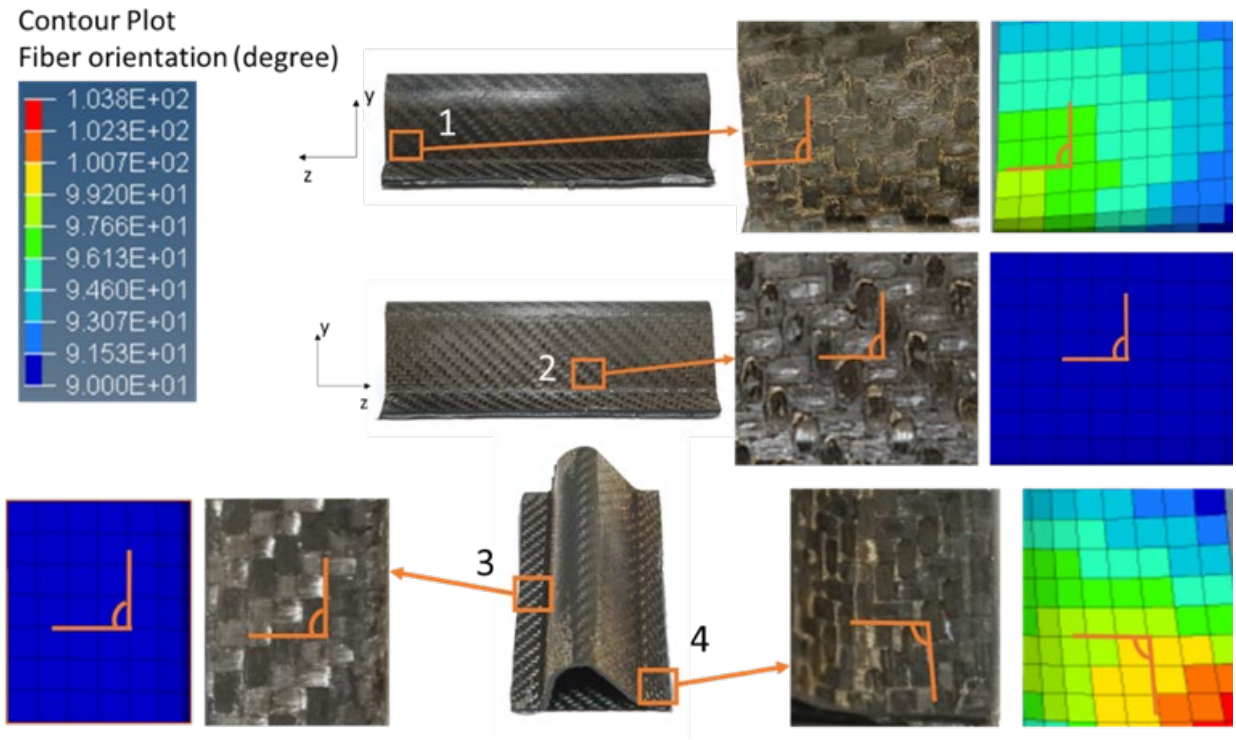

Figure II.2.4.7. Fiber orientation in degree as observed in thermoforming trials and simulation at marked locations of the hat structure. Source: Clemson University.

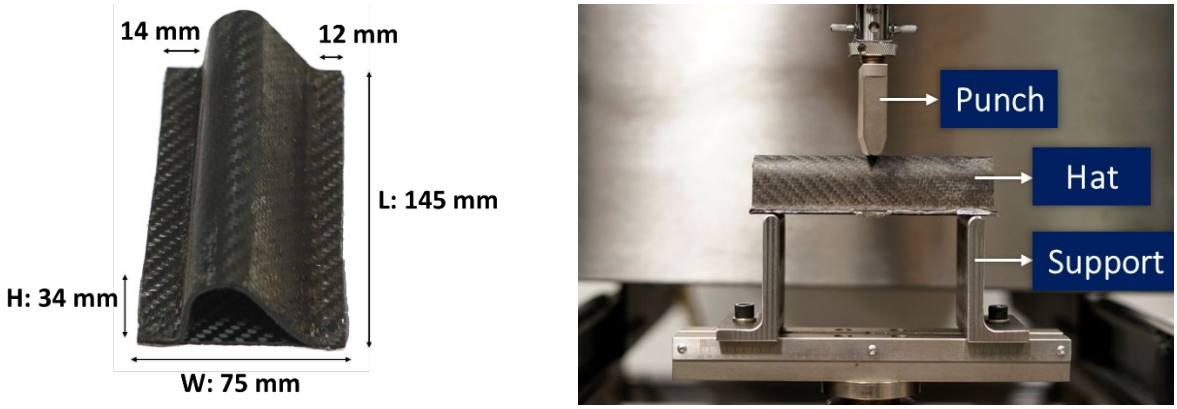

(a) (b)

Figure II.2.4.8. (a) Dimensions of the bonded hat section part; and (b) the experimental setup for the three-point bend test showing the hat structure, supports, and punch. Source: Clemson University.

The force-displacement responses obtained from the three-point bend tests are presented in Figure II.2.4.9(a). A consistent and repeatable linear stiffness zone and failure initiation at an approximate 6 mm deflection is observed among all three trials. Additionally, the location, time, and displacement at which crack initiation occurs is extremely consistent across the three samples. The trials show a slightly varied force-displacement response post 7 mm deflection, with trial 1 exhibiting a peak load of ~ 5877 MPa at a 10 mm deflection and trials 2 and 3 show a load of 5272 MPa ~ 4652 MPa at the same deflection. The final shape and deflection of the crack vary slightly across the three samples, with trial 1 showing the least amount of damage in terms of

crack diameter and deflection and trial 3 showing the most damage. The numerical three-point bend test under a quasistatic loading condition is carried out using LS-DYNA after mapping the thermoforming effects. The force-displacement response is compared with the mean experimental results in Figure II.2.4.9(b), which show very good agreement until the onset of damage. The large deformation is observed at the impact location of the hat structure when the numerical predictions are compared with the three experimental trials.

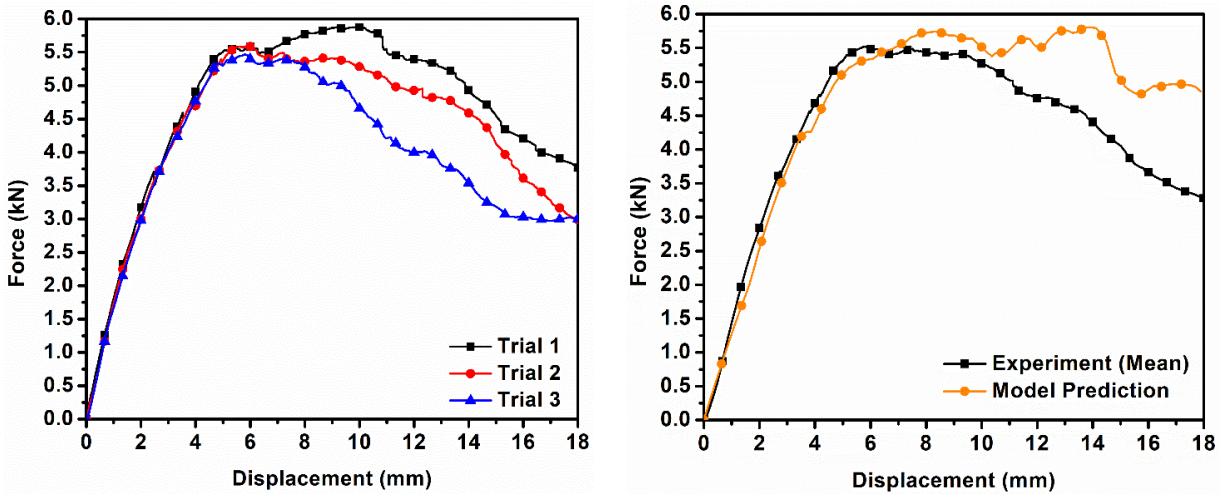

(a) (b)

Figure II.2.4.9. (a) Force-displacement plot of three experimental trials. (b) Force-displacement plot for the three-point bend test comparing experimental response with numerical prediction. Source: Clemson University.

Figure II.2.4.10(a) shows the side view, which closely matches the numerical prediction of deformation appearing in trial 3. Figure II.2.4.10(b) presents a top view of the hat structure along with the von-Mises stress contour and encircled regions (appearing in red) that show the damaged locations. The damage behavior is consistent with the experimental results. However, it should be noted that delamination failure and damage propagation, which requires a detailed damage modeling strategy, are not considered in the study.

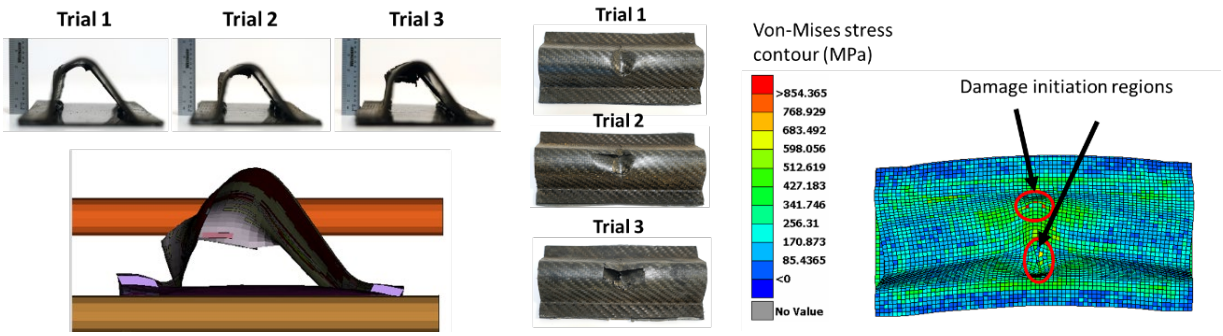

(a) (b)

Figure II.2.4.10. Deformation comparison between the experimental trials and the numerical simulations: (a) deformation side view showing a close match with experimental trial 3; and (b) top view comparison with stress contour plot. Encircled are the damage initiation locations on the structure. Source: University of Delaware.

Manufacturing of Door Components

As a result of COVID-19, the overall tooling effort has been delayed. Our tooling partner, Ventec, was unable to assist in a ventillator project. As such, a detailed tooling and manufacturing stratergy for all components were discussed with the material supplier, the tooling partner, and the team. With regards to the structural parts, the team would focus on the tooling and manufacturing of the smaller composite inner panel tool to implement simulated manufacturing stratergies and apply these learnings to the target composite inner panel part. Tooling and manufacturing of the steel anti-intrusion beam, Al outer beltline stiffener and Al lower reinforcement will be spearheaded by our OEM partner. The tooling strategy for each of the critical composite components is discussed below. The manufacturing for both strategies will begin with trials on PA 6 reinforced with 50 vol % glass fiber to optimize material handling, process conditions, and cost-savings.

The team is considering two strategies for the manufacturing of the inner beltline stiffener. In the first, a blank of 2 mm thickness will be pre-cut in the shape of the final part, as shown in Figure II.2.4.11(a). This pre-cut blank will be thermoformed to form the final part without the need of postprocessing operations. In the second, a 2-mm thick pre-consolidated composite sheet of dimensions 1240 × 860 mm will be used as a blank to thermoform the part, as shown in Figure II.2.4.11(b). A postprocessing process to cut out the trimline of the thermoformed part will be required in the second strategy. The team prefers the first strategy.

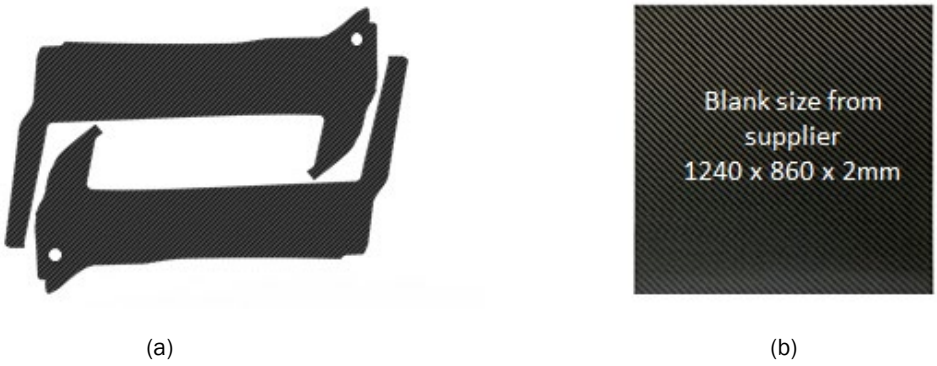

(a) (b)

Figure II.2.4.11. (a) Inner beltline stiffener blank strategy; and (b) the blank size (1240 × 860) obtained from the supplier. Source: Clemson University.

The compression molding tool will accommodate both strategies. The tool will be 1200 mm × 850 mm × 450 mm in size made up of 5000 series Al material with a B3 surface finish. The tool will have the capability to rapidly heat (e.g., 150°C) and cool for improved surface finish and reduced cycle time. An initial tool concept is shown in Figure II.2.4.12(a) and (b). For manufacturing, both the horizontal (from the injection molders) and vertical presses (from the OEMs) are being considered. The pin shaped cavity drivers shall be used to control the flow of material, as shown in the snapshots of simulation in Figure II.2.4.12(c) (e).

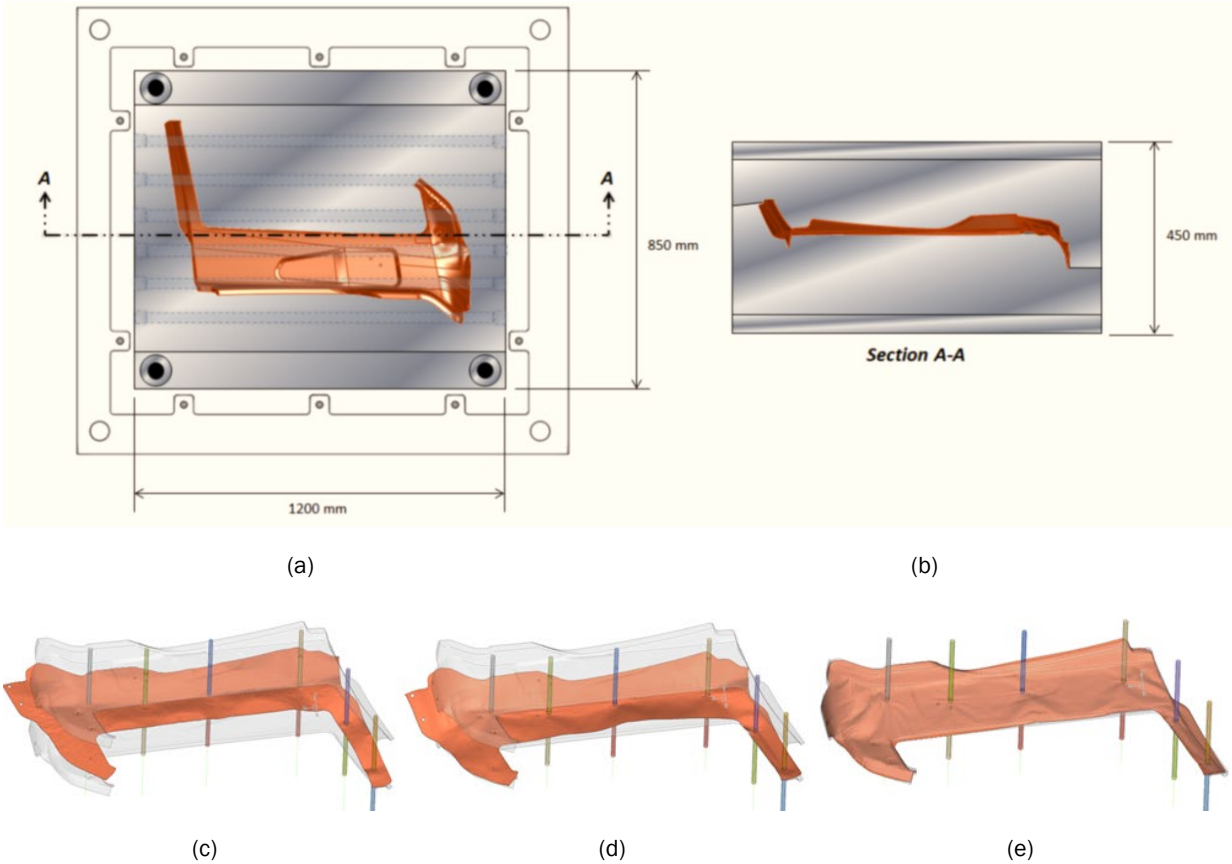

Figure II.2.4.12. (a) Initial tool concept of the inner beltline stiffener. (b) Thermoforming simulation of the inner beltline stiffener. (c) Before forming. (d) Cavity driver touch lower tool. (e) Tool closed condition. Source: Clemson University.

Composite Inner Frame

The size of the blank will be 1400 mm × 1540 mm × 3 mm made after the consolidation of three layers that are 1 mm thick, as shown in Figure II.2.4.13. The compression tool, as shown in Figure II.2.4.14(a) and (b), for the inner frame (1930 mm × 1780 mm × 1130 mm) will be machined with 5000 series Al and A2 high polish.). This tool will also have the capability to rapidly heat (e.g., 150°C) and cool for improved surface finish and reduced cycle time. The tool will consist of a cavity driver forming window, door sash, and some panel areas to control the material flow during the thermoforming process. A simulation of the thermoforming steps is illustrated in Figure II.2.4.14(c) through (e). The manufacturing strategy will begin with trials on PA 6 reinforced with ~ 50 vol % glass fiber to optimize the process conditions, specifically material handling, process conditions, and cost-savings.

After completing the draping simulations, a forming simulation was conducted to calculate the residual stress and accurate ply rotations from which the mechanical performance of the structure was re-evaluated. During these forming simulations, process parameters (i.e., blank holder force, punch velocity, and clamping forces) were determined, as shown in Figure II.2.4.14(c) through (e). The virtual optimization of these process parameters will be useful in minimizing the risks during the prototyping phase.

The blank will be held by a metallic frame using pneumatic grippers. The grippers will be controlled for the sequential release of the heated sheet, choreographed to properly form the inner panel. The concept is still under discussion with the material supplier. The snapshots of the initial simulation are shown in Figure II.2.4.14.

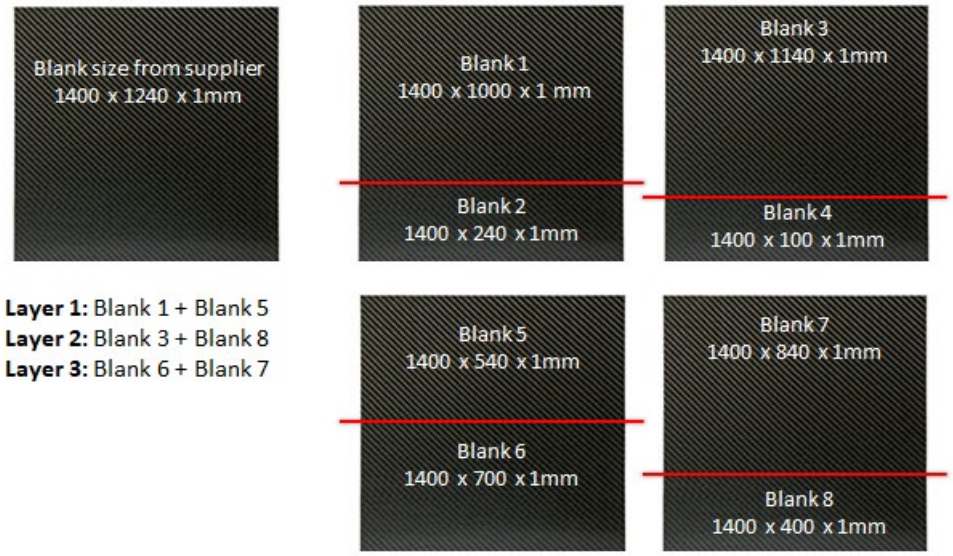

Figure II.2.4.13. Blank strategy for inner frame. Source: Clemson University.

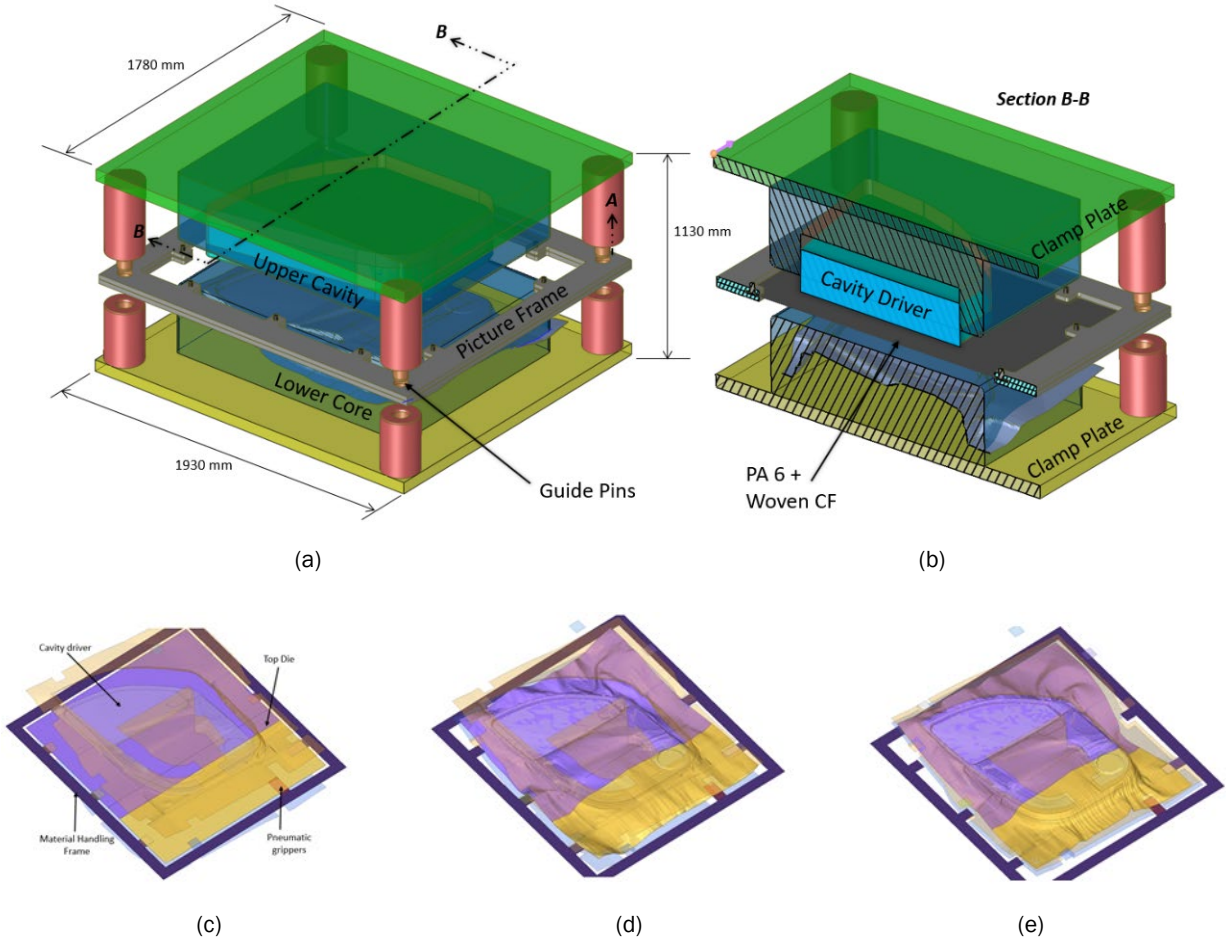

Figure II.2.4.14. (a) Initial tool concept of inner beltline stiffener. (b) Thermoforming simulation of inner beltline stiffener. (c) Before forming. (d) Cavity driver touch lower tool. (e) Tool closed condition. Source: Clemson University.

Cost Modeling Summary

The generative cost model and parametric cost model are developed to estimate the total cost of the door. The generative cost model is developed for the production version of the composites door that comprises both the UD and woven composite ply layup in the two structural parts inner panel and beltline stiffener. The developed cost model is based on the following assumptions: (a) the total cost is assumed to be a function of material, labor, equipment, tool, energy, and overhead cost; (b) the parameters identified for cost-estimation are independent of each other; (c) the data is collected and normalized using experience and literature review; (d) the rate of the overhead (e.g., 20% of the total cost) is assumed by experience; (e) the production volume per year is assumed to be around 80,000; (f) the cost of carry-over parts (~$181) is assumed to be constant; and (g) the number of workers working on each machine are assumed to be four. The total cost calculated for the latest design of the door is $935.26. The weight and cost of the door, made with UD and woven composite ply, are compared with a baseline steel door on a different component-level in Table II.2.4.5. The structural weight saved by the ultra-lightweight composite door is 45% as compared to the baseline door, while there is a cost increase of $4.02 for each lb. saved. Weight reduction of 47% is obtained for non-structural parts when compared with the baseline door with cost increase of $4.18/lb. saved. The other carry-over parts, such as the window frame and the seals, are not considered for weight reduction due to stringent constraints provided by the OEM partner on these parts. In addition, the cost of painting on the composite door was determined, which is higher by $32.79 than the baseline door. The total weight reduction achieved by the composite door is approximately 37% of the baseline door weight with the total cost increase of $5.40/lb. saved, which is slightly higher than DOE's target of $5/lb. saved. Cost of the material, tooling, equipment, labor, energy, building, maintenance, overhead, and capital were all considered to calculate the cost of each individual parts. It is observed that 46% of the total cost is the cost of the material itself while the overhead cost, labor cost, and tooling cost contribute 11%, 5%, and 4%, respectively. The cost distribution based on the individual door subsystems is presented in Figure II.2.4.15. The inner panel is the most expensive component of the car door with a cost of $391, which is 42% of the total cost.

Table II.2.4.5. Comparison of Weight and Cost Distribution of Composite Door (Production Version) with the Baseline Door

Results	Baseline Door Weight (kg)	Composite Door Weight (kg)	% Weight Reduction	$$/Lb-Saved
Door structural parts	15.44	8.44	45%	4.02
Door non-structural parts	9.37	4.97	47%	4.18
Other carry-over parts	6.29	6.29	0%	0
Total	31.1	19.7	36.66%	**5.40**

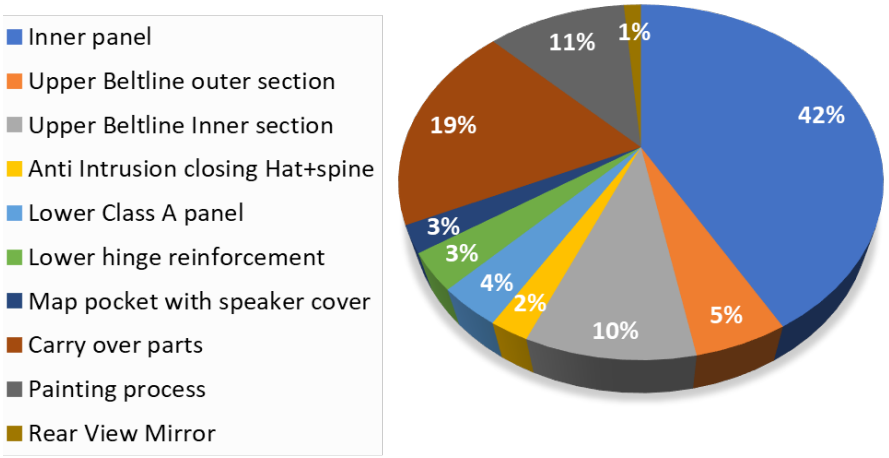

Figure II.2.4.15. Cost distribution of the individual parts of the door. Source: Clemson University.

The development of the generative cost model to estimate the total cost of the door was followed by the development of the parametric cost model to find how individual parameters influence the total cost. Parametric cost modeling is carried out in three steps: (i) development of a cost estimating relationships (CER); (ii) parameterization of the door design; and (iii) creating user interface to perform tradeoffs and estimate cost of individual parts. At first, individual parameters that influence the overall cost of the door were identified, which are electricity cost per kWh, scrap rate, mold life, equipment life, labor wage, production volume per year, overhead rate, and material cost. Then, a relationship between these parameters with the total cost is determined using mathematical and statistical tools. Assuming the normal distribution of the identified parameters when all are taken together to study overall variation in the door, it is found that the total cost of the door may vary between $873-$996, as presented in Figure II.2.4.16.

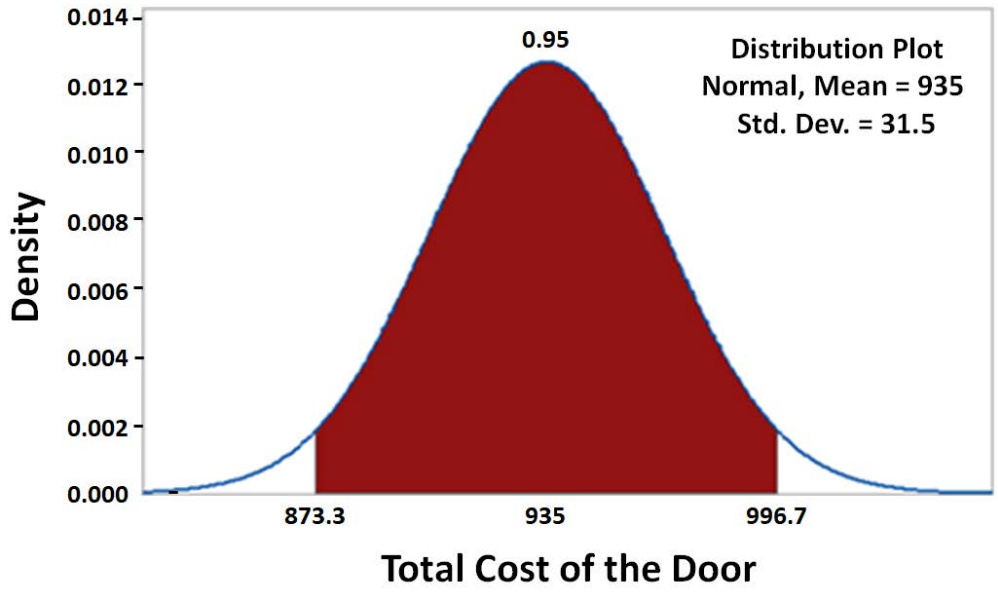

Figure II.2.4.16. Composite door manufacturing process. Source: Clemson University.

As a further cost saving strategy, the team also evaluated costs by adopting a glass fiber-based composite instead of a C composite system because the cost of the glass fiber is almost 1/10th of CF cost; therefore, glass fiber-based composite plies are considered for trials of thermoforming analysis. Keeping the same design, the total cost of a glass-based composite door is obtained as $805, while the weight reduction is 28%, which gives a cost increase of $0.21/lb. saved. The static performance of the glass fiber-based composite system is also evaluated, which lies in the tolerable range satisfying most of the static load cases. However, the glass fiber-based design needs to be further optimized for static and crash load cases. It can be concluded that the glass fiber-based composite system has a potential of reducing approximately 25% of the door weight while equally satisfying DOE's cost constraints.

Conclusions

The research focus during FY 2020 involved the finalizing of door design by employing an iterative processing that involved feedback from static and crash simulations, cost analysis, and manufacturing constraints, all while trying to comply with the aggressive weight targets. The final door design met and exceeded expectations from the viewpoint of static and crash targets. This was further validated by experimental tests performed on a subcomponent. A detailed overview of the tooling and manufacturing strategy was discussed in consultation with our material suppliers and tooling partners was presented. Lastly, from a cost perspective, the door was slightly above the cost targets primarily due to high input material costs, and strategies are being evaluated in order to meet this requirement. With the granting of the no-cost extension, the team will spend the early half of next year on tooling, manufacturing and the latter half on assembly and testing of the door.

Key Publications

1. Kothari, A.; A. Yerra, M. Limaye, S. A. Pradeep, G. Dalal, G. Li, S. Pilla, L. Fuessel, B. Haque, S. Yarlagadda, S. Malcolm, and D. I. Detwiler, 2020, "A finite element design study and performance evaluation of an ultra-lightweight carbon fiber reinforced thermoplastic composites vehicle door assembly," SAE Technical Paper 2020-01-0203.
2. Limaye, M.; S. A. Pradeep, S. Kothari, G. Li, and S. Pilla, 2020, "Thermoforming process induced structural performance of carbon fiber reinforced thermoplastic composite part through a novel manufacturing-to-response pathway," Society of Plastics Engineers ACCE Conference, 4-6 September 2020, Novi, MI, USA.

References

1. Kelly, J. C., J. L. Sullivan, A. Burnham, and A. Elgowainy, 2015, "Impacts of vehicle weight reduction via material substitution on life-cycle greenhouse gas emissions," *Environ. Sci. Technol.*, Vol. 49, No. 20, pp. 12535–12542.
2. Mi, H.-Y., X. Jing, J. Peng, L.-S. Turng, and X.-F. Peng, 2013, "Influence and prediction of processing parameters on the properties of microcellular injection-molded thermoplastic polyurethane based on an orthogonal array test," *J. Cell. Plast.*, Vol. 49, No. 5, pp. 439–458.
3. Chang, S. H. and S. S. Cheon, 2006, "In-plane directional mechanical properties of carbon fabric skins in sandwich structures after thermoforming," *Compos. Struct.*, Vol. 75, Nos. 1–4, pp. 577–581.
4. Yu, Y., J. Ye, Y. Wang, B. Zhang, and G. Qi, 2013, "A mesoscale ultrasonic attenuation FE model of composites with random-distributed voids," *Compos. Sci. Technol.*, Vol. 89, pp. 44–51.

II.2.5 Continuous Fiber, Malleable Thermoset Composites with Sub-1-minute Dwell Times: Validation of Impact Performance and Evaluation of the Efficacy of the Compression Forming Process (Mallinda LLC)

Philip Taynton, Co-Principal Investigator
Mallinda LLC
7270 Gilpin Way, Suite 180
Denver, CO 80229
E-mail: philip@mallinda.com

Leonard S. Fifield, Co-Principal Investigator
Pacific Northwest National Laboratory
902 Battelle Boulevard
Richland, WA 99352
E-mail: leo.fifield@pnnl.gov

Bo Song, Co-Principal Investigator
Sandia National Laboratories
1515 Eubank Boulevard SE
Albuquerque, NM 87123
E-mail: bsong@sandia.gov

Robert Norris Jr., Co-Principal Investigator
Oak Ridge National Laboratory
1 Bethel Valley Road
Oak Ridge, TN 37831
E-mail: norrisrejr@ornl.gov

H. Felix Wu, DOE Technology Manager
U.S. Department of Energy
E-mail: felix.wu@ee.doe.gov

Start Date: October 1, 2018 End Date: March 31, 2021
Project Funding: $1,000,000 DOE share: $500,000 Non-DOE share: $500,000

Project Introduction

Despite the significant impact that CF composite materials have on lightweighting, performance, and efficiency in the aerospace industry, adoption of these materials has been slow in high-volume industries, such as automotive. Two major barriers to adoption are cost and cycle time. Current approaches to thermoset composite part production are dependent on in-mold curing of thermosets, which is not optimal for high-volume, high-throughput production due to limitations and inefficiencies associated with the in-mold cure itself. In addition, ancillary activities, such as transport and the storage of shelf life limited uncured or B-staged prepreg materials, typically necessitate refrigerated transport and storage, which significantly impacts the cost and energy requirements associated with manufacturing. Furthermore, limited out-life means that trimmings cannot typically be used as they partially cure during initial production leading to high scrap rates (more than 20% is common). Finally, the need to cure in-mold drives cycle times to multiple minutes in the best cases, and from tens of minutes to hours in most cases. Furthermore, traditional thermoset composite materials and components are very problematic to recycle.

Mallinda is developing polyimine vitrimer prepreg composite materials that have excellent mechanical properties (e.g., 100-GPa tensile modulus, 1.7-GPa tensile strength, 2.4% elongation at break) and high operating temperatures (e.g., T_g >200°C). At scale, polyimine resins are anticipated to be commensurate in price with commodity epoxy resins. What distinguishes malleable thermoset prepreg from traditional thermoset prepreg materials is that they are fully cured during Mallinda's roll-to-roll production of prepreg laminate. This results in five key value-differentiating benefits. First, it simplifies manufacturing logistics by enabling ambient transportation and storage and by significantly extending out-life and shelf-life almost indefinitely. Second, elimination of autoclave curing reduces the cost and energy requirements to the customer. Third, scrap rates can be reduced as malleable thermoset prepreg materials are directly reusable. Fourth, the manufacturing consolidation step can be roughly 10 times faster than that of traditional thermosets because of the way the resin is already cured. Parts can be made via compression forming by the application of heat and pressure to quickly vitrify and consolidate a multilayer part, easily leading to less than three-minute cycle times. At a laboratory-scale, we have demonstrated a 20-second dwell time with room for further optimization. Finally, the closed-loop cradle-to-grave solution-based recyclability of malleable thermoset composites can also contribute significantly to the future of sustainable lightweight materials.

Technical background on vitrimers (also known as malleable thermosets) include:

- Recent major advances in polymer chemistry enable a paradigm shift in processing and the re-processing/recycling of advanced composite materials. Inexpensive compression molding with short cycle times, traditionally available for thermoplastic composites only, are now possible for the thermoset resins based on polyimine chemistry. One key feature of the proposed technology is the malleability of the thermoset polyimines, which allow for thermoplastic-like flow at elevated processing temperatures, but thermoset-like stability and strength at operating temperatures. The re-processability of these malleable thermoset materials (i.e., vitrimers) is attributable to the active exchange of covalent chemical bonds at elevated temperatures. Stress-relaxation studies have shown that below the glass transition temperature (T_g), malleable polyimine materials behave as traditional thermosets, while above the T_g, malleable behavior enables molding, welding, and repair [1],[2]. These novel and unique malleable properties allow for the facile forming and reforming of fabricated polyimine composite structures in a process analogous to metal compression forming. Another key feature of the polyimine system is intrinsic recyclability due to dynamic covalent chemistry that enables closed-loop recycling of both resin and filler material (e.g., fibers, ceramic) from the composite. The environmental and economic impact of recoverable resin from advanced composite scrap materials and end-of-life products is significant.
- Among other factors, composite material structural failures can be greatly affected by the constituents utilized (e.g., fibers, resins, fillers, etc.); loading levels of constituents; arrangement/architecture of constituents and interfaces; design, shape, joints, etc., involved in making final components; quality of each manufacturing step; and damage present at each stage of life. The malleable nature of vitrimer materials is projected to be advantageous for their use in automotive energy absorption applications.
- Despite the promise of malleable thermoset composites, large industry players (who are investing heavily in further optimization of incumbent thermoset-curing techniques) are reluctant to engage until the technology is fully validated. While Mallinda has validated the manufacturability of its resins by conducting full-scale prepreg production trials with a manufacturing partner, a few critical areas remain. These require experimental validation beyond the capabilities of Mallinda and existing third-party commercial-testing facilities. Fortunately, these capabilities can be found within the LightMAT network at PNNL, Sandia National Laboratories, and ORNL. Specifically, the ability to nondestructively characterize microscopic structural defects (such as voids and resin-rich areas) and to characterize high-speed impact performance are critical to the validation and adoption of these materials. Preliminary dynamic testing of Mallinda materials will demonstrate early performance and potential techniques for more extensive comparison of materials for specific application targets and requirements.

Objectives

The focus of this project is the development, optimization, and validation of malleable thermoset composite materials that exhibit manufacturing cycle times of three minutes or less, high-speed impact performance on par with incumbent technologies, and defect-free consolidation of three-dimensional (3D) parts.

Approach

To accomplish these objectives, the following LightMAT resources are included in this project:

1. Test machine for automotive crashworthiness. Principal Investigator: Robert Norris, ORNL.
2. Ultrasonic analysis of composite defects in 3D parts. Principal Investigator: Michael Larche, PNNL.
3. High-speed impact material characterization. Principal Investigator: Bo Song, SNL.

The following tasks will be accomplished at the industry partner (Mallinda) sites and will be funded by the industry partner (Mallinda) in fulfillment of the in-kind cost-match requirement:

1. Lab-scale development and optimization of malleable thermoset materials for a high-throughput compression forming automotive industry production environment.
2. Analysis of thermal-mechanical properties and performance of composite materials for development and validation purposes (including third-party validation of mechanical properties).
3. Automotive crashworthiness trials (including material synthesis and sample preparation).
4. High-speed-impact material characterization (including material synthesis and sample preparation).
5. Ultrasonic analysis of composite defects (including material synthesis and sample preparation).
6. Project management and reporting requirements.

The following tasks are being carried out at DOE sites and are funded by the DOE LightMAT consortium:

1. Automotive crashworthiness trials.
2. Ultrasonic analysis of composite defects.
3. High-speed-impact material characterization.

Results

During Year 2 of the project, the Mallinda team further advanced vitrimer-matrix composite technology, developing a final version of the material for the final phase of experimentation at the National Laboratory partner facilities in Year 3 of the project. COVID-19 did impact the progress of the project as it resulted in a four-month-long shutdown of the Mallinda facility, as well as having various impacts on the availability of partner facilities. As a result, the 24-month project was extended by six months to a new end date of March 31, 2021. Prior to this delay, the Mallinda team successfully demonstrated full-scale production of vitrimer-matrix composite prepreg, production of an automotive vehicle OEM demonstration part, recycling of a complete automotive component for recovery of both resin and fiber materials and completed a study of compression forming conditions for high-throughput part production.

The Mallinda team has produced and tested over 50 unique formulations in the development and scale-up of the high glass transition (Tg>120°C) resin system. The final formulation conformed to the requirements of an industrial hot-melt resin prepreg, exhibiting an initial viscosity less than 30,000 cPs and a pot life of >3 hours. Malinda's pilot reactor was able to produce 110 kg of the resin, while prepreg production was carried out at a private toll manufacturing partner facility, as pictured in Figure II.2.5.1.

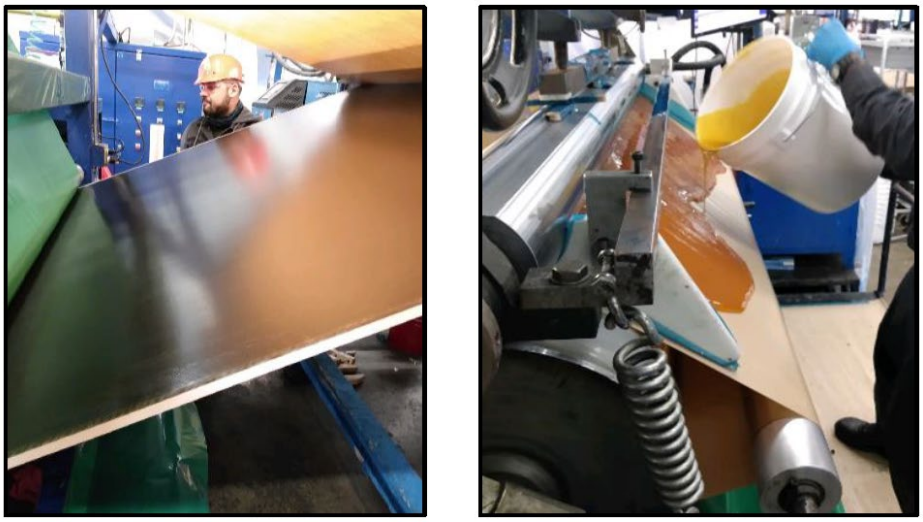

Figure II.2.5.1. Full-scale prepreg production using vitrimer resin. Source: Mallinda.

The prepreg material was produced to support production and recycling demonstrations of the vitrimer-matrix materials. The Mallinda team redesigned a high-volume automotive component provided by a North American OEM for demonstration of the mechanical, lightweighting, manufacturing, and recyclability advantages of using the vitrimer system. A seatback component was chosen, which is currently made using glass fiber mat thermoplastic. By using precured vitrimer prepreg, >40% weight savings and 100% recyclability was achieved without compromising the in-mold cycle time. Figure II.2.5.2 summarizes the advantages of the redesigned component.

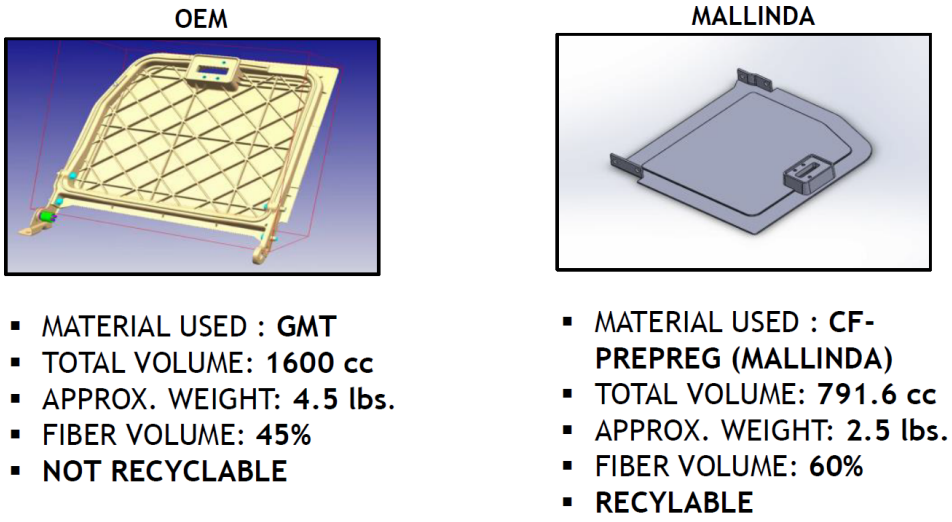

Figure II.2.5.2. Redesign of seatback component for manufacture using vitrimer prepreg. Source: Mallinda.

The Mallinda team partnered with Vistex Composites to create a custom mold and carry out pilot manufacturing of the seatback component. Figure II.2.5.3 shows the compression forming set up and summarizes the resulting component versus the OEM component. In Year 3 of this project, the test machine for automotive crashworthiness at ORNL will be used to evaluate the impact performance of both the OEM component and the Mallinda component.

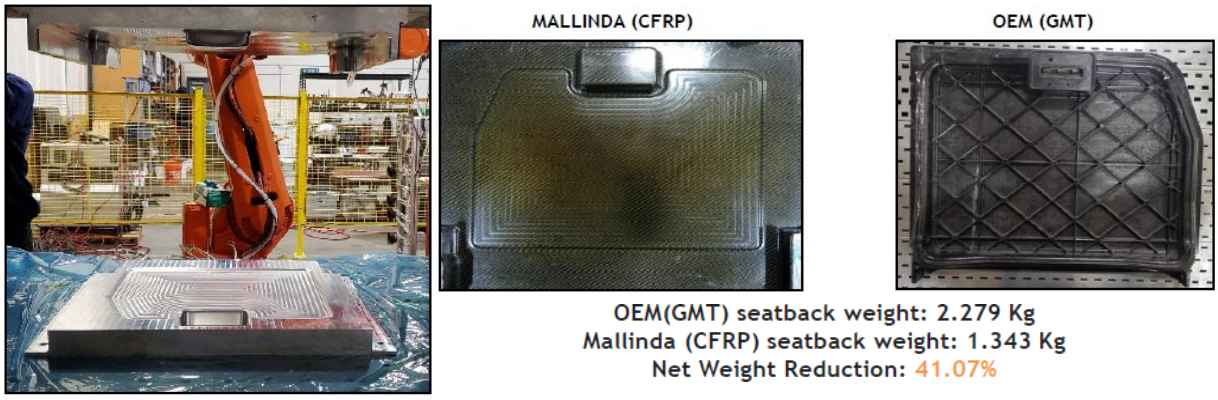

Figure II.2.5.3. Compression forming and resulting vitrimer prepreg component. Source: Mallinda.

During FY 2020, the Mallinda team conducted an optimization study of compression forming of precured prepreg vitrimer laminates. Temperature, time, and pressure were studied as independent variables and interlaminar shear strength was used to track the quality of the resulting interlaminar bonding. Through the study, conditions were identified that enabled both sub-three-minute and sub-one-minute in-mold times. In the next phase of the project, a similar sample set will be investigated via C-scan ultrasonic analysis, and cross-section microscopy to further investigate the dynamics of in-mold consolidation via vitrimeric chemical bond exchange. Using these conditions, a demonstration headlight housing automotive component was produced with an in-mold dwell of three minutes. The resulting demonstration video was published on youtube.com and mallinda.com and received coverage by industry publications, including *JEC Group* and *Composites World* websites. A screenshot from this demonstration is shown in Figure II.2.5.4.

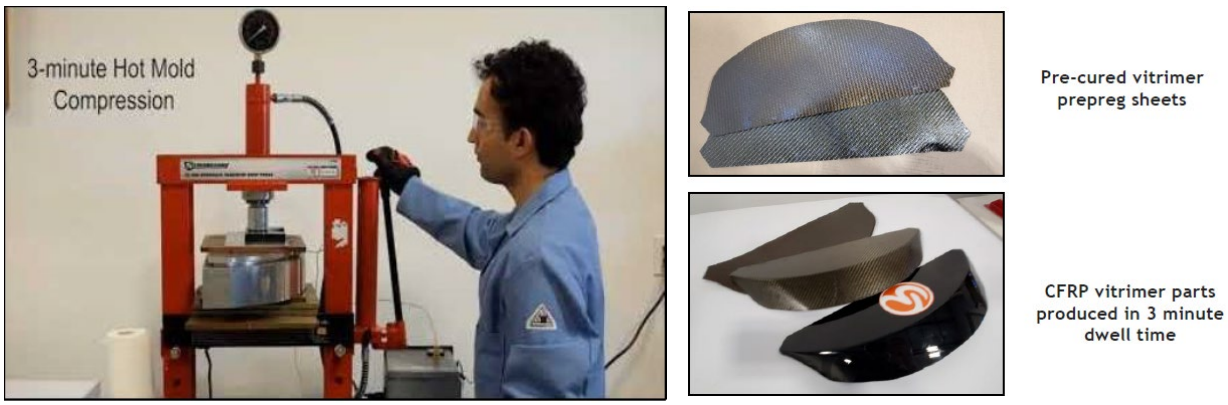

Figure II.2.5.4. Compression forming with <3-minute dwell time (left) and resulting vitrimer prepreg component (right). Source: Mallinda.

This headlight housing component was used to demonstrate the component-level recyclability of vitrimer-matrix composite materials. The component was immersed in a solution containing diamine monomers, which effectively depolymerized the vitrimer resin via dynamic bond exchange, allowing for the complete separation and recovery of both fiber and resin materials. A SEM energy-dispersive X-ray spectroscopy study of the recovered CF material revealed that the recycling process yielded pristine fiber, as can be seen in Figure II.2.5.5.

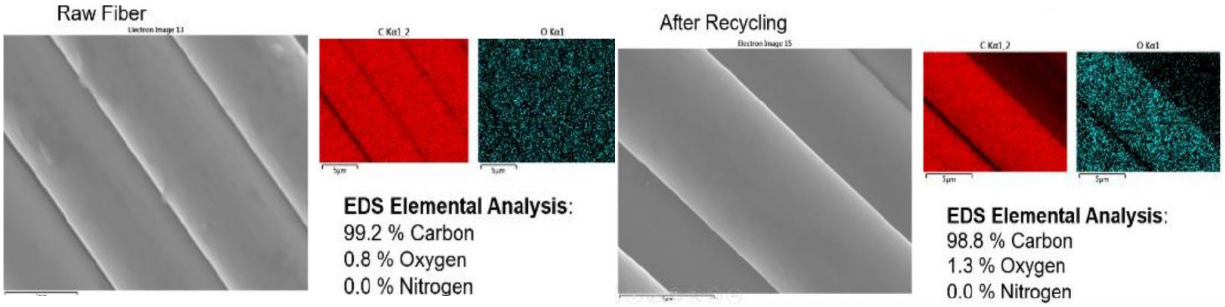

Figure II.2.5.5. SEM EDXS analysis of virgin and recovered CF material. Source: Mallinda.

Conclusions

The work carried out in Year 2 of this project established production demonstration, achieved sub-three-minute dwell times, and demonstrated component-level recyclability. 110 Kg of vitrimer resin was produced, and full-scale (sixty-inch wide) prepreg production was carried out to produce material for the production of an automotive seatback component. A redesign of the seatback using the novel resin enabled >40% weight reduction of the component while allowing for 3 minute in-mold time. It also enabled recyclability for the separation, recovery, and evaluation of pristine CF material.

Key Publications

1. Mallinda, 2020, "Vitrimer-matrix composite recycling," 28 February 2020, Available at: https://youtu.be/_X7xtq5UTlE (last accessed 20 December 2020).
2. Mallinda, 2020, "Precured Vitrimer-matrix prepreg: 3-minute in-mold dwell part production," 2 March 2020, Available at: https://youtu.be/EZeDaLgcfEA (last accessed 20 December 2020).
3. JEC Group, 2020, "Vitrimers promise to impact composites," 8 October 2020, Available at: http://www.jeccomposites.com/knowledge/international-composites-news/vitrimers-promise-impact-composites (last accessed 20 December 2020).
4. Composites World, 2020, "Vitrimers: The reprocessable thermoset," 28 September 2020, Available at: https://www.compositesworld.com/articles/vitrimers-the-reprocessable-thermoset (last accessed 20 December 2020).

References

1. Taynton, P., K. Yu, R. Shoemaker, Y. Jin, H. J. Qi, and W. Zhang, 2014, "Heat- or water-driven malleability in a highly recyclable covalent network polymer," *Adv. Mater.*, Vol. 26, pp. 3938–3942.
2. Taynton, P., H. Ni, C. Zhu, K. Yu, S. Loob, Y. Jin, H. J. Qi, and W. Zhang, 2016, "Repairable woven CF composites with full recyclability enabled by malleable polyimine networks," *Adv. Mater.*, Vol. 28, pp. 2904–2909.

II.2.6 Ultra-Lightweight, Ductile Carbon Fiber Reinforced Composites (Oak Ridge National Laboratory)

Vlastimil Kunc, Principal Investigator
Oak Ridge National Laboratory
1 Bethel Valley Road
Oak Ridge, TN 37831
E-mail: kuncv@ornl.gov

H. Felix Wu, DOE Technology Manager
U.S. Department of Energy
E-mail: felix.wu@ee.doe.gov

Start Date: October 1, 2018 End Date: December 31, 2022
Project Funding: $1,000,000 DOE share: $500,000 Non-DOE share: $500,000

Project Introduction

CFRP composites have a high-stiffness-to-weight ratio. Despite their lightweight and high stiffness, these composites are not suitable for dissipating energy because failure occurs with very little or no plastic deformation. In this project, we developed a scalable multi-material stereolithography (SLA) process and design approach for CFRP multiphase materials. Our proposed approach enabled the novel design of a three-dimensional (3D) lightweight cellular CFRP microlattice to reach the highest stiffness and damping pairs, a trade-off in the current state of CFRP. Hierarchical two-phase carbon fiber reinforced mesoscale lattice structures were fabricated using an AM system. Furthermore, the effect of unit-cell size on the structural response was studied, and the damping performance of the microlattice was obtained at small- and large-strain regimes via dynamic material analysis (DMA) and quasistatic cyclic compression tests, respectively. Using these measurements, the intrinsic and structural damping performances in terms of a damping figure of merit (FOM), defined as $E^{1/3}\tan\delta/\rho$, were analyzed. Finally, the $E^{1/3}\tan\delta/\rho$, from our microlattice was compared with the existing materials in a $E^{1/3}/\rho$ - $\tan\delta$ map to assess its damping performance.

Objectives

In this project, we solved the limitations in the brittleness in additively manufactured CFRP composite and harnessed the benefit of hierarchical architecture and size effects to create hybrid hierarchical materials that are simultaneous ultralight, strong, and tough. To achieve this, the following goals were accomplished:

1. Verified mechanical properties (e.g., compression, shear, tensile) in all directions through theoretical and numerical calculations and experimental testing of microlattice materials.
2. Printed hierarchical two-phase carbon fiber reinforced mesoscale lattice materials (e.g., < 500 kg/m^3), comprising microscale CF fillers and large-scale structural components.
3. Printed size effects of CF composite with varying length scales from micrometers to centimeters.
4. Demonstrated ultralight (e.g., < 200 kg/m^3) hierarchical CF composites with tailored energy absorption and high strain recovery (e.g., > 10%).

Approach

Our approach for the fabrication of CFRP, detailed below, is based on developing a new AM method to produce CFRP composites with a rationally designed dissipative phase. The hybrid material system allows the attainment of the upper bound of stiffness and damping pairs at low-density:

1. *Material preparation and development of multi-material 3D printing system.*

   To fabricate the lightweight cellular CFRP microlattice, an ultraviolet-curable CFRP composite was developed. The composite was made of an ultraviolet-sensitive resin, reinforced with ~70 μm CF. A high-energy ball mill was used to mix the monomer, photo-initiator, and CF. This resin mixture method ensured the uniform spatial distribution of the fibers. Incorporating the dissipative inclusion into prescribed sites within the CFRP struts was achieved via a multi-material AM system we developed, which prints viscous multi-material resins via a recoating process and a material-switching system. To print a structure, a computer-assisted drawing model was sliced into different groups of closely spaced images. These two-dimensional slices were subsequently digitized and sent to a digital micromirror device chip that projects an image at 405 nm wavelength through a series of lenses onto the corresponding photosensitive resin. This process initiates polymerization of the resin, converting it into a solid single layer part that has the same shape as the projected image. When the other materials needed to be fabricated in the same layer or the next layer, the transition stage moves the platform to the washing vat, and the previously printed part is cleaned by a cleaning dispenser. After cleaning, the platform moves to the other resin vat to print the next layer.

   For the size effect study, we synthesized another photosensitive resin consisting of trimethylolpropane triacrylate (TMPTA) with 0.0125 wt% photo absorber (Sudan 1) and 2 wt% photo-initiator (Phenylbis[2,4,6-trimethylbenzoyl] phosphine oxide). All of these chemicals were purchased from Sigma-Aldrich and used as-received.

2. *Testing methods including the small-strain DMA test and large-strain cyclic test.*

   Energy dissipation mechanisms can be generally categorized into intrinsic and structural damping [1]. To capture the intrinsic damping properties of the lightweight cellular CFRP microlattice, we performed small-strain DMA tests using the TA Instruments DMA 850. All tests were performed with a maximum strain of 0.05% to ensure that all fabricated samples were excited elastically at small strains. The results measured at 0.1 Hz were adopted here for a direct comparison of damping property ($\tan\delta$) obtained from small-strain DMA and quasistatic large-strain experiments because the frequency of the quasistatic compression tests is usually considered as < 0.1 Hz [1]. Structural damping properties were investigated by performing large-strain quasistatic cyclic compression tests using an INSTRON 5944 test frame. A strain-rate of 10^{-3}/s was adopted to ensure that all tests were performed in a quasistatic regime to suppress mass inertia effects. From the measured stress-strain hysteresis loop, we computed the effective modulus from a slope of a loading curve in the linear region, dissipated energy (ΔU) from the area within the stress-strain hysteresis loop, and stored energy (U) from the area under the loading curve. The last two measures were used to evaluate the damping performance of the microlattice via the loss coefficient (Ψ) defined as $\Psi = \Delta U/U$ [1]. This quantity was then converted to $\tan\delta$ via $\Psi = (\pi/2)\tan\delta$ [2],[3] for a direct comparison between the structural damping and intrinsic damping. Note that this conversion represents a quarter of a full cycle compressive loading-unloading response [2].

Results

1. *Mechanical property test and theoretical calculation for CFRP composite.*

   All mechanical tests of the CFRP microlattices have been performed and evaluated by theoretical analysis. Several samples were tested comprising different volume percent of CF; namely, 0 (i.e., pure Formlabs Rigid resin), 5, and 10 vol% CFRP. All samples were tested in the TD with respect to the print direction. This ensures that failure does not occur due to layer debonding. This treatment is critical because the properties of fiber-reinforced composites depend on the direction of the fibers. Since fiber-reinforced composites behave differently in tension and compression, elastic moduli for these loading

conditions were tested. Figure II.2.6.1 shows the test results for tensile, compressive, and shear modulus, respectively. The modulus is plotted against different volume fractions of CF loaded in the matrix resin. The red diamond in each plot represents the average value from the samples that were tested, and the error bars are positioned at one standard deviation. The addition of CFs to the matrix increased the modulus in all three cases. The measured tensile modulus of the pure matrix without CF reinforcement was slightly lower than the modulus claimed by a manufacturer, Formlabs Inc. This can be attributed to the change in printing systems, printing parameters, and post-curing techniques. The tensile modulus increased linearly with an increase in CF loading. The compressive modulus also increases in a similar manner but is lower than the tensile modulus due to the anisotropy presented in fiber-reinforced composites. This is because fibers under compressive loading fail via buckling, making them less stiff. Also, the error bars in all cases are close to the average value. This implies that the stiffness in the compressive direction is less susceptible to 3D-printing defects, such as porosity and layer adhesion. These defects were particularly evident in the measurement of shear modulus tests. As the CF loading increases, the shear modulus also increases less linearly, becoming prone to large errors due to print quality.

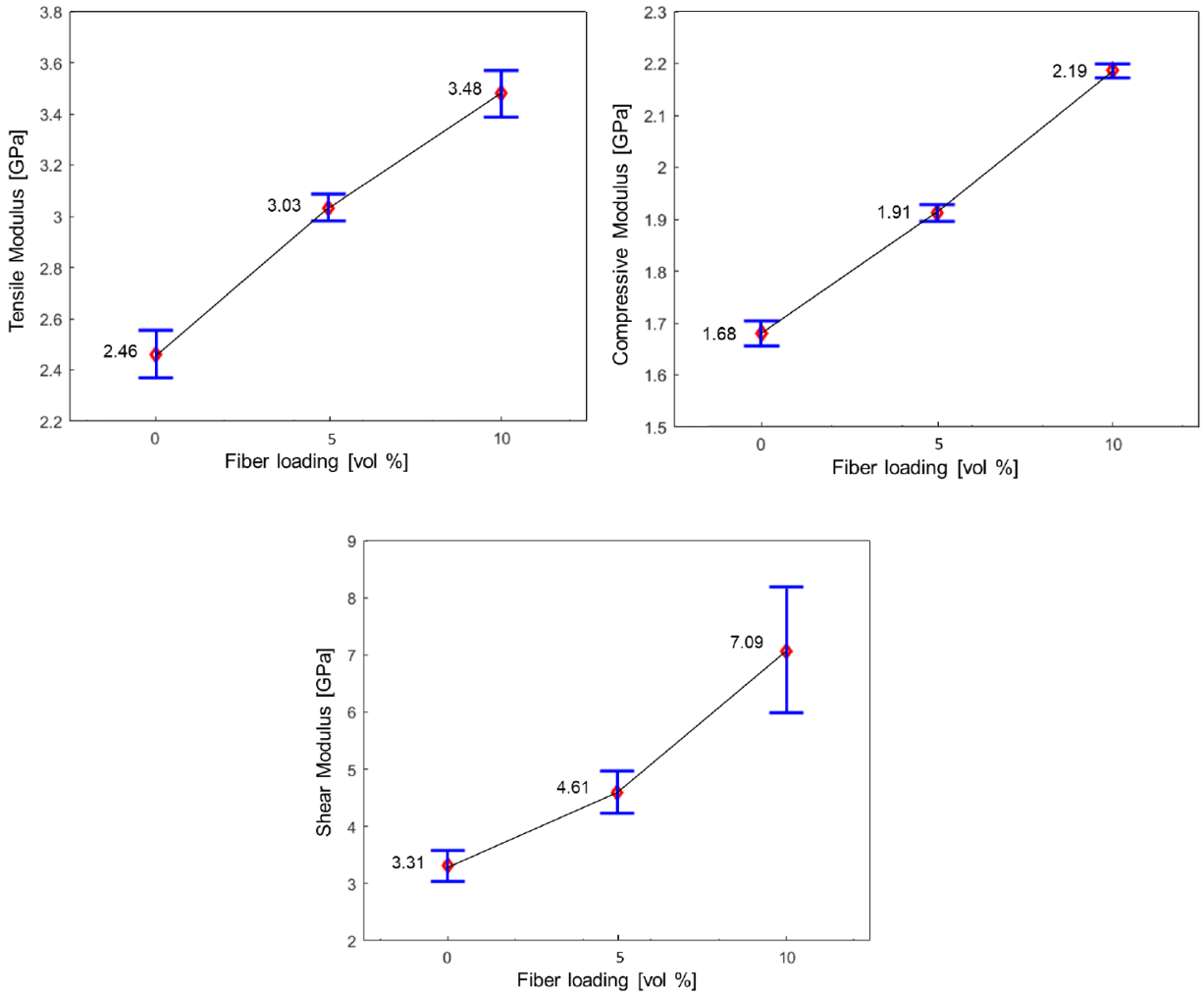

Figure II.2.6.1. Verified experimental results from the tensile, compressive, and shear test, respectively. Source: ORNL.

The stiffness in tensile, compressive, and shear directions increases linearly with an increase in fiber volume fraction. When compared to the theoretical bounds shown in Equations (1) and (2), the printed samples that were tested were close to the lower Reuss bound. This is attributed to several factors. The upper Voigt bound assumes an ideal case of continuous fiber reinforcement in the sample, perfect alignment, and perfect fiber-matrix adhesion. This is not the case in the samples tested. The fibers used for reinforcement here tested as short and discontinuous. The results obtained show higher stiffness when compared to other studies using SLA and fused deposition modeling techniques to 3D print CFRP composites. Our published paper details our new method on further improving the energy absorption, stiffness/density ratio and coverable strain employing a novel two-phase material design [4].

Theoretical bounds:

$$E_{upper} = fE_{CF} + (1 - f)E_{matrix} \quad (1)$$

$$\mathrm{E_{lower}} = \frac{\mathrm{E_{CF}\,E_{matrix}}}{\mathrm{fE_{matrix} + (1 - f)E_{CF}}} \quad (2)$$

where E_{CF} = Young's modulus of CF reinforcement, E_{matrix} = Young's modulus of matrix, and f = Volume fraction of CF.

2. *Printing hierarchical two-phase CF-reinforced mesoscale lattice materials (e.g., < 500 kg/m^3), comprising microscale CF fillers and large-scale structural components.*

Lightweight CFRP microlattices were developed consisting of periodically arrayed OT unit cells. The OT topology was chosen as a repeating unit-cell in the microlattices because its deformation mechanism is stretching-dominated, which gives rise to a favorable stiffness-to-weight ratio compared to stochastic bending-dominated cells [5],[6],[7]. The relative density of the microlattice, $\bar{\rho}$, is approximated by $\bar{\rho} = 6\pi\sqrt{2}(r/l)^2$, where r is the strut radius and l is the strut length [7],[8]. The density of the microlattice equals to the product of its relative density and the density of the base material. Figure II.2.6.2 shows as-fabricated two-phase CF-reinforced mesoscale lattice materials comprised of microscale CF fillers and large-scale structural components.

Figure II.2.6.3 shows the range of densities that have been fabricated and all achieved the densities below 500 kg/m^3. Unit cells having a range of relative densities (e.g., $\bar{\rho}$ ~ 4–30%) with a side length of 15 mm were fabricated using a projection micro-stereolithography system. The inset picture in Figure II.2.6.3 shows an OT unit-cell sample having $\bar{\rho}$ = 4%, density of 49.2 kg/m^3. The modulus is plotted against the density of the microlattice, where the solid triangle means the average value based on several testing results and the red line is the scaling power. The effective stiffness E of the octet microlattice is related to the virgin base materials by $E = (1/9)\bar{\rho}E_b$, where E_b is the stiffness of base material and $\bar{\rho}$ is the relative density of the OT structure. For example, the CFRP base material has a measured stiffness of 2.71 GPa; our 12% octet lattice has a measured stiffness of 32.2 MPa (compared to the theoretical 36.2 MPa).

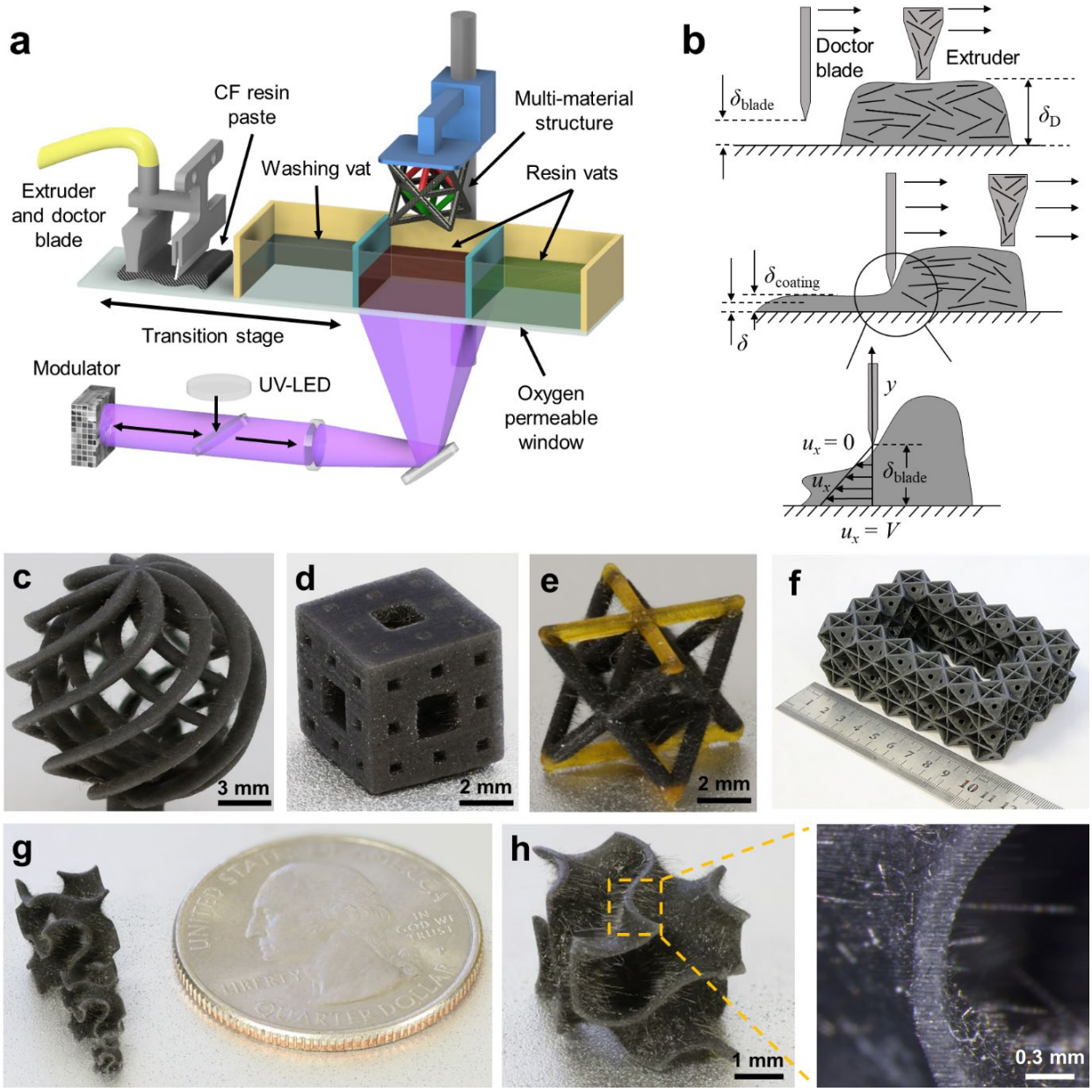

Figure II.2.6.2. As-fabricated two-phase CF-reinforced mesoscale lattice materials composed of microscale CF fillers and large-scale structural components. (a) Schematic of the multi-material projection micro-stereolithography process from a published paper on this work [4]. (b) Schematic of the recoating process. (c) and (d) Complex 3D structures fabricated by the system. (e) A multi-material OT unit-cell comprising CFRP and polyethylene glycol diacrylate resin. (f) A closed-cell lattice with a dimension over ten centimeters. (g) and (h) Gyroid 3D structure with a wall thickness of 150 μm and magnified area of the structure. Source: ORNL.

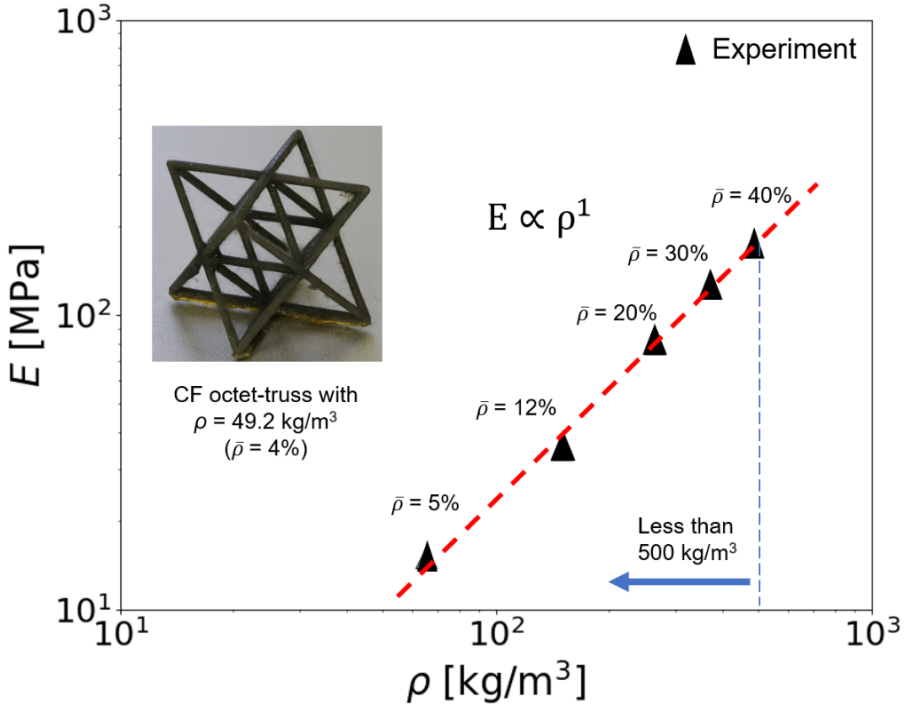

Figure II.2.6.3. Testing results for CFRP OT lattices material with different relative densities, where all achieved densities are below 500 kg/m³. Source: ORNL.

3. *Size effects of CF composite printed with varying length scales from micrometers to centimeters.*

   To study the size effect caused by boundary condition and topology in detail, our team first considered two stretch-dominated topologies—namely, iso-truss and reinforced square unit cells, as shown in Figure II.2.6.4. The rationale of this study is that the size effect is expected to be independent of the base material properties and to reveal similar relationships with the effective material properties across other stretch-dominated latticed structures, such as an OT lattice, which will be discussed later. While keeping the relative density (ρ/ρ_s = 10%) and the overall volume ($V_{\text{lattice}} = 40^3$ mm^3) constant, lattices with different numbers of cells were additively manufactured. The number of cells per side N_{cell} was varied from 1 to 5 for the iso-truss lattices and from 1 to 4 for the reinforced square lattices, as observed in Figure II.2.6.4(a) and (f). The base material chosen for these samples was TMPTA, which is relatively easy to fabricate as compared to using CFRP due to its lower viscosity and effortless curing conditions.

   The following results were measured from compressive stress-strain curves shown in Figure II.2.6.4(c) and (h) for the iso-truss and reinforced square lattices, respectively, shown in Figure II.2.6.4(b) and (g). In these figures, the curves start from zero strain and go to a strain in which any fracture occurs. Figure II.2.6.4(d), (e), (i), and (j) show the effective elastic modulus and YS as a function of N_{cell}, which are averaged values over the three repeats of each size with standard deviation indicated by error bars. For both topologies, the effective elastic modulus decreases with N_{cell} (generally N_{cell} >2), and a similar trend is also seen in the effective YS. This indicates a softening size effect in which samples comprising smaller unit cells are softer than those with larger ones. This softening size effect can be explained by the fact that stress distributions are concentrated differently near free and loaded edges for different sample sizes. The cells adjacent to these edges most likely carry more stress than those on the interior due to the stress concentration, and samples with a high N_{cell} (i.e., small unit cells) have lower theoretical peak stress than their counterparts, leading to lower values of properties. Material arrangements, defined by a strut orientation within a material, also contribute to different stress distributions for different topologies; however, this does not affect a general trend of the softening size effect.

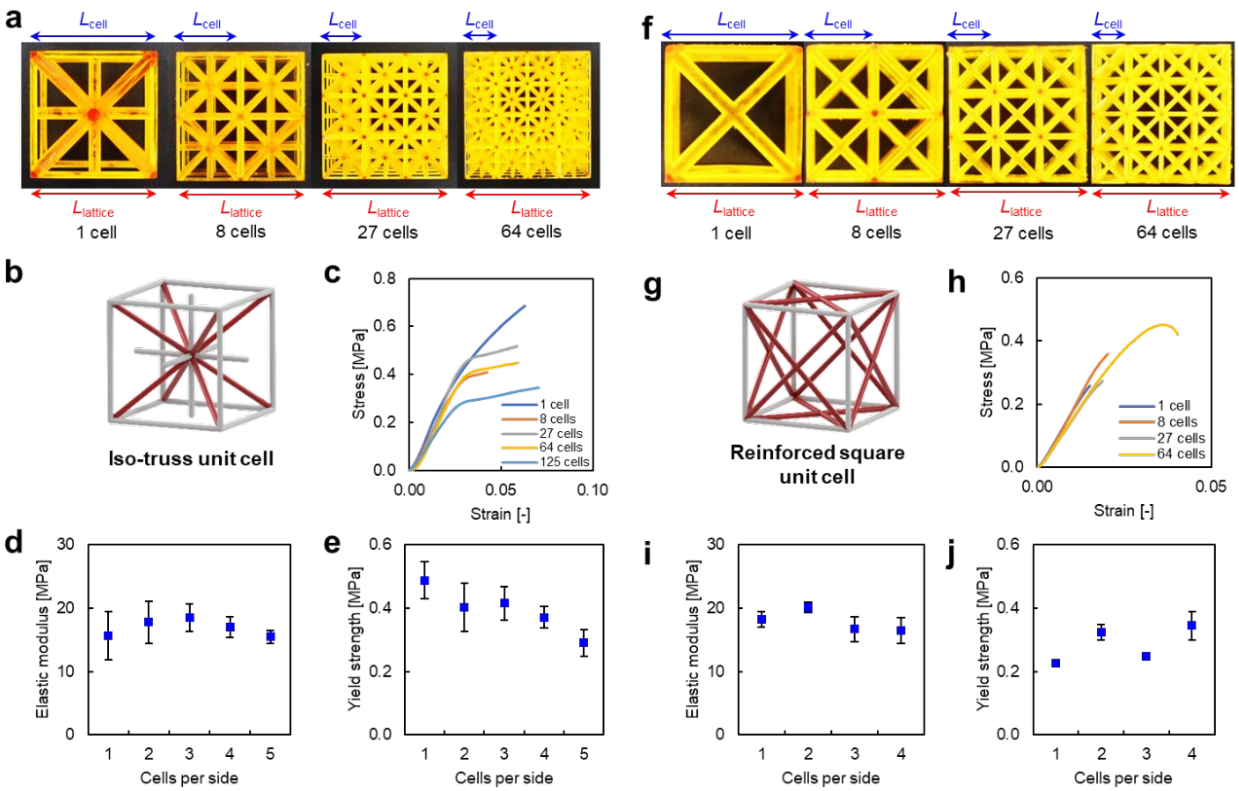

Figure II.2.6.4. (a) Iso-truss samples made of TMPTA. (b) 3D representation of iso-truss unit-cell. (c) Compressive stress-strain curves of iso-truss samples with different numbers of cells. (d) and (e) The effective elastic modulus and YS of iso-truss samples with different sizes. (f) Reinforced square samples made of TMPTA. (g) 3D representation of reinforced square unit-cell. (h) Compressive stress-strain curves of reinforced square samples with different numbers of cells. (i) and (j) The effective elastic modulus and YS of reinforced square samples with different sizes. Source: ORNL.

In addition, two distinct failure modes depending upon N_{cell} were observed for both topologies with a fixed relative density. For example, an iso-truss sample having N_{cell} of 1 clearly shows brittle-like failure; fracture is seen near a center node, and the corresponding stress-strain behavior reveals very little or no plastic deformation. On the other hand, similar samples made of N_{cell} equal to 2 or greater experience buckling failure of the constituent struts. A similar observation was seen in reinforced square lattice samples, but brittle-like failure persists with a higher N_{cell} as compared to that of the iso-truss samples. This implies that the size effect can lead to different failure modes due to different stress distributions within the material domain.

To discover material independency of the softening size effect, the effective material properties of OT lattice structures were investigated with different numbers of cells made of CFRP, as shown in Figure II.2.6.5(a). The relative density (ρ/ρ_s) of all samples was 0.10 approximated via $\rho/\rho_s = 6\pi\sqrt{2}(r/l)^2$, where r is the strut radius and l is the strut length. Samples with different sizes were realized by acquiring various N_{cell} ranging from 2 to 5, and the overall volume was 32,768 mm^3. The same compression tests described earlier were used to compute the effective material properties from compressive stress-strain curves shown in Figure II.2.6.5(b). Similar to the two topologies studied earlier, both effective elastic modulus and YS display the softening size effect with an increase in N_{cell}, as shown in Figure II.2.6.5(c) and (d). In addition, all samples showed brittle-like failure regardless of size.

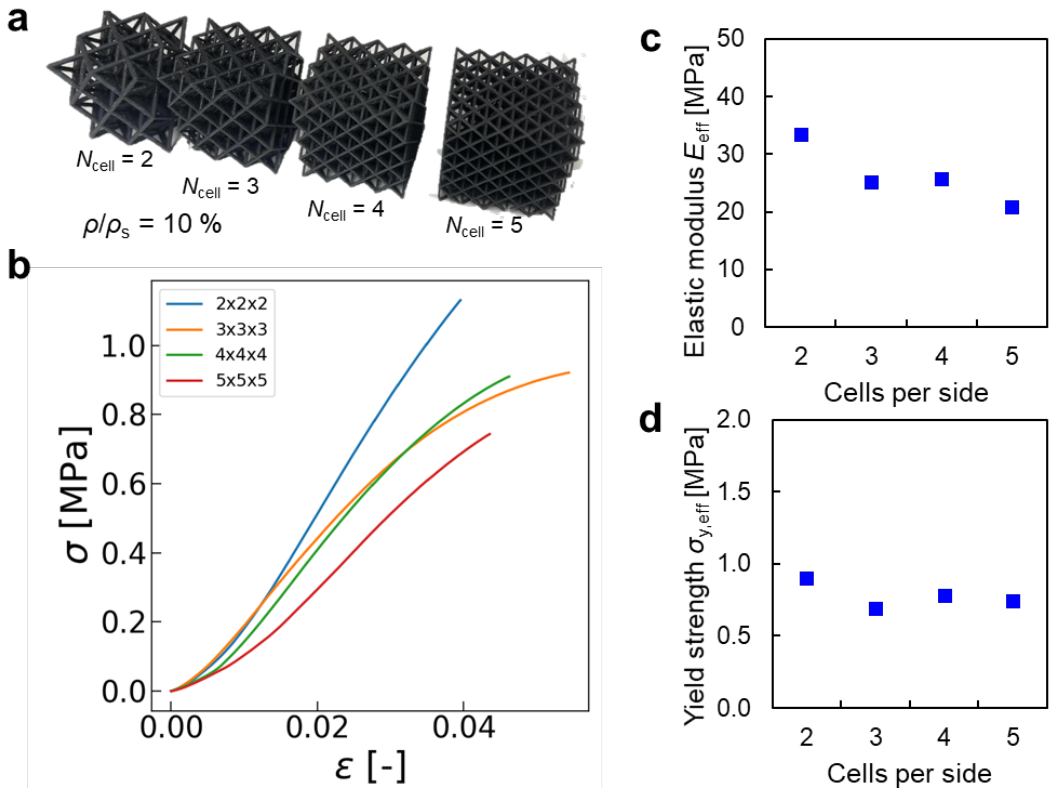

Figure II.2.6.5. (a) OT samples with different numbers of cells made of CFRP. (b) Compressive stress-strain curves of samples with different sizes. (c) Effective elastic modulus and (d) YS of OT samples as a function of the number of cells per side. Source: ORNL.

To have a better understanding of the material independency regarding the softening size effect, the effective elastic modulus and YS of the iso-truss (made of TMPTA) and OT samples (made of CFRP) were normalized by the corresponding base material properties and were fitted with a power law function, as illustrated in Figure II.2.6.6(a) and (b). As expected, a similar trend is seen for both material properties regardless of different base materials. Deviations in the magnitude of these normalized properties are most likely attributed to different topologies rendering different strut arrangements.

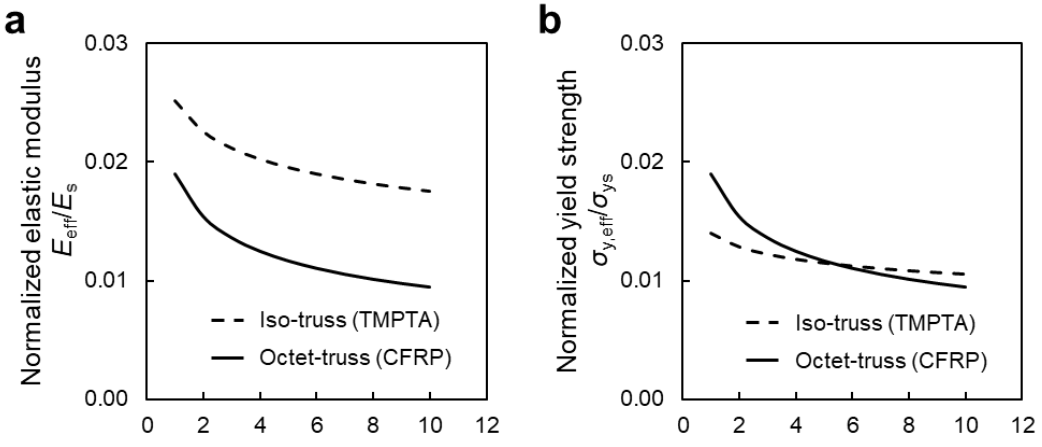

Figure II.2.6.6. Power law fitted normalized (a) elastic modulus, and (b) YS of iso-truss samples (made of TMPTA) and OT samples (made of CFRP). Source: ORNL.

4. *Demonstrated ultralight (e.g., < 200 kg/m³) hierarchical CF composites with tailored energy absorption and high strain recovery (e.g., > 10%).*

It is promising to use a two-phase composite layout to achieve high-stiffness-loss pair [2]. To design a lightweight structure, an OT cell was chosen as the blueprint topology because it is one of the stretch-dominated topologies capable of maintaining a constant specific stiffness at lower density compared to bending-dominated foams [5],[6]. This led to a design of a multi-material architecture, consisting of multiple OT unit cells made of CFRP and designed soft inclusion in selected out-of-plane struts, as shown in Figure II.2.6.7(a). The relative density ($\bar{\rho}$) of the architecture shown in Figure II.2.6.7(b) is 7% (density of 86.1 kg/m³). The soft inclusion ratio in a single Reuss strut, V_{soft}, is defined as the ratio of h to H. The relative density of the microlattice ($\bar{\rho}$) is defined approximately as $\bar{\rho} = 6\pi\sqrt{2}(r/l)^2$, where r is the strut radius and l is the strut length [5],[8]. As shown in Figure II.2.6.7(c), a SEM image was taken at the boundary, showing a desired separation between the two phases; in this figure, the top is CFRP whereas the soft phase is in the bottom.

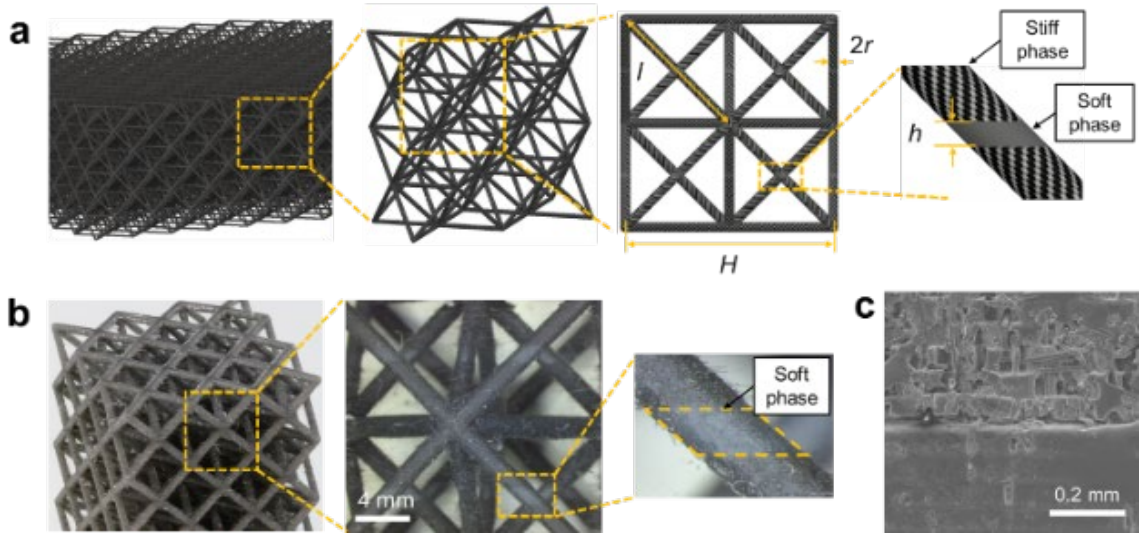

Figure II.2.6.7. Multi-material architecture. (a) Design of lightweight, stiff, high damping microlattice with two-phase materials incorporating CFRP and soft phase. (b) Fabricated lightweight cellular CFRP microlattice having $\bar{\rho}$ = 7% (density of 86.1 kg/m³) with V_{soft} = 9%. (c) SEM image showing the interface between the two phases. Source: ORNL.

Figure II.2.6.8 depicts the intrinsic damping property obtained from DMA tests of the samples having $\bar{\rho}$ = 7% with various soft phase ratios. The effective modulus (i.e., storage modulus) of the samples, shown in Figure II.2.6.8(a) is inversely proportional to V_{soft} and show an exponential relationship as a function of V_{soft} via $E = a^*\exp(bV_{soft}) + c^*\exp(dV_{soft})$. Conversely in Figure II.2.6.8(b), tanδ, representing intrinsic damping, is nonlinearly proportional to V_{soft} via $\tan\delta = a^*\exp(bV_{soft}) + c$. The computed FOM representing the effective stiffness-damping characteristics of the microlattice, reaches its peak when V_{soft} is equal to approximately 10%, as shown in Figure II.2.6.8(c). In this study, we only considered a single relative density since the intrinsic damping is invariant with respect to the relative density.

For the structural damping property, Figure II.2.6.9(a) and (b) show the measured stress-strain hysteresis loops of samples with $\bar{\rho}$ = 4 and 12% (e.g., with a density of 49.2 and 147.6 kg/m³) having V_{soft} = 20% in response to multicyclic compression (e.g., 30 cycles), confirming 10% or larger compression strain. Figure II.2.6.9(c) shows the evolution of the stress-strain hysteresis loops over different relative densities while holding V_{soft} constant. The dominant deformation mechanism at a low relative density (e.g., $\bar{\rho}$ = 4%) was elastic buckling of the constituent struts. However, this buckling response diminished with an increase in the relative density (e.g., $\bar{\rho}$ = 7%), and plastic yielding mechanism started to dominate at a higher relative density (e.g., $\bar{\rho}$ = 20%). For uniform V_{soft}, the effective modulus of the microlattice was

proportional to an increase in the relative density, as shown in Figure II.2.6.9(d). An increase in V_{soft} led to an improvement in the loss tangent (tanδ), as shown in Figure II.2.6.9(e). In addition, all samples exhibited the maximum FOM at specific V_{soft}, as shown in Figure II.2.6.9(f).

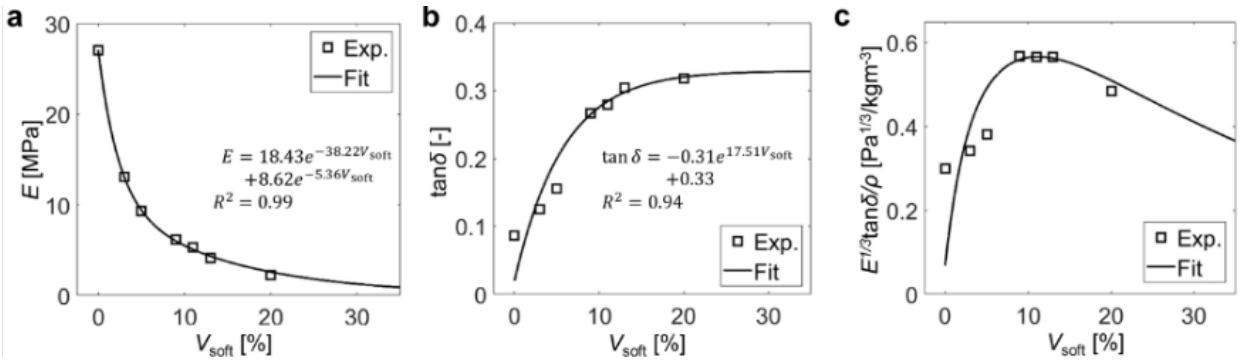

Figure II.2.6.8. Intrinsic damping properties of the lightweight cellular CFRP microlattice having a relative density of 7% with different soft phase ratios. (a) The effective modulus, E, as a function of the soft phase ratio V_{soft}. (b) Loss tangent (tanδ) as a function of V_{soft}. (c) Damping FOM as a function of V_{soft}. Solid lines in these figures represent the curve fit. Source: ORNL.

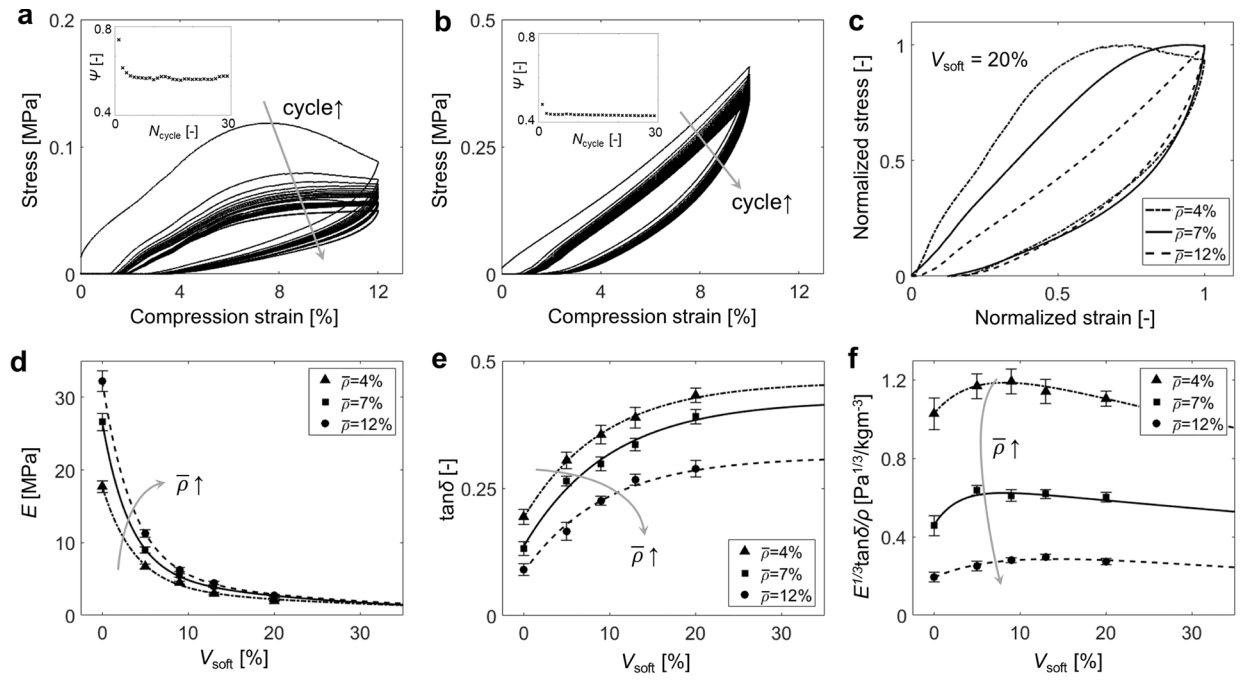

Figure II.2.6.9. Structural damping properties of the lightweight cellular CFRP microlattice obtained from large-strain quasistatic cyclic compression tests. (a) and (b) Hysteresis loops from multicyclic compression tests for 30 cycles and evolution of the loss coefficient with cycle number with compressive strains exceeding 10%. (a) Sample with $\bar{\rho}$ = 4% having V_{soft} = 20%. (b) Sample with $\bar{\rho}$ = 12% having V_{soft} = 20%. (c) Normalized stress-strain hysteresis loops of samples having V_{soft} = 20% with various $\bar{\rho}$. Elastic buckling behavior was observed for $\bar{\rho}$ = 4% and diminished with an increase in $\bar{\rho}$. (d) The effective modulus, E, as a function of V_{soft}, where the modulus was inversely proportional to an increase in V_{soft}, showing its asymptotic value. (e) Loss tangent (tanδ) as a function of V_{soft} showing that an increase in V_{soft} led to an improvement in loss tangent. (f) Damping FOM as a function of V_{soft} where FOM can be tuned to have a peak when V_{soft} is about 10%. Source: ORNL.

Tunability maps of the intrinsic and structural damping performance, shown in Figure II.2.6.10(a) and (b) respectively, were obtained by using the curve fit of experimentally determined FOM values. The FOM for both intrinsic and structural damping has its maximum at low relative densities and at the soft inclusion ratio of approximately 5–10%. Moreover, the performance of the stiffness-damping pair of the present CFRP microlattice was evaluated in a $E^{1/3}/\rho$—tanδ map against other existing materials, as illustrated in Figure II.2.6.11. The CFRP microlattice is superior to any CFRPs available by almost two orders of magnitude with respect to tanδ. Furthermore, the CFRP microlattice exhibits a relatively high specific stiffness per density similar to commercial CFRPs, technical ceramics and composites, and high damping properties comparable to that of elastomers.

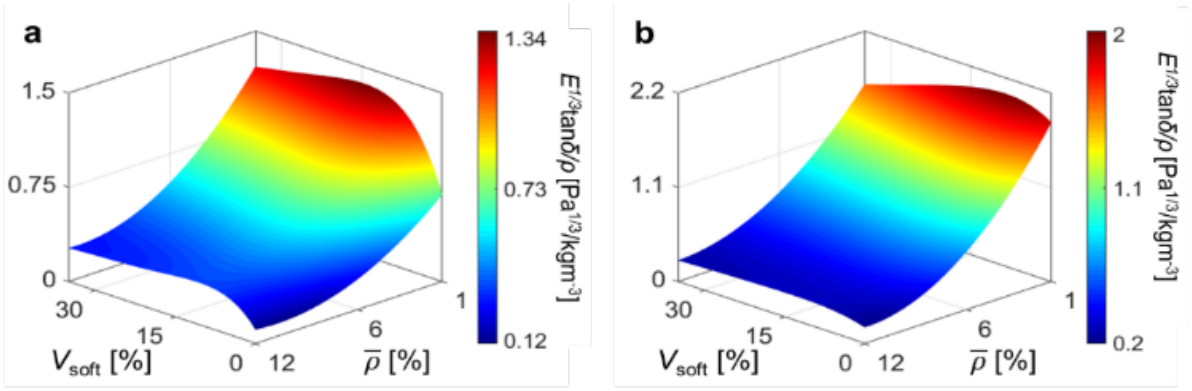

Figure II.2.6.10. Tunability maps for (a) intrinsic and (b) structural damping performance in terms of the damping FOM obtained from experimental measurement. Source: ORNL.

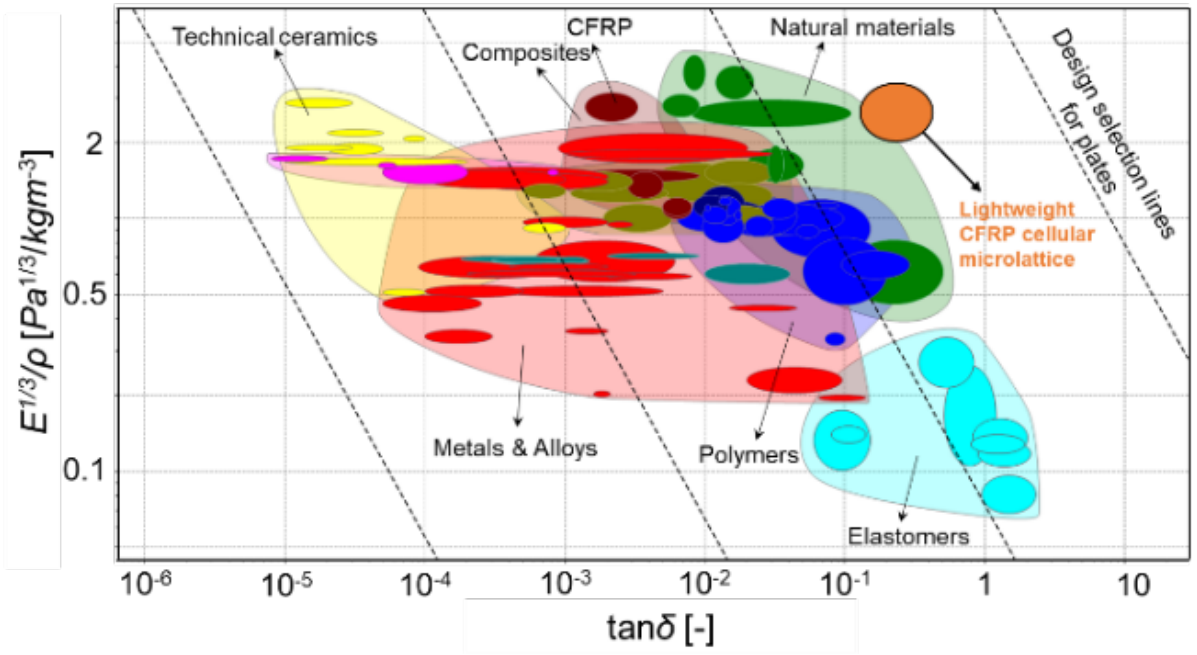

Figure II.2.6.11. Assessment of the lightweight cellular CFRP microlattice developed in this work. The orange ellipse represents the envelope of experimental results for an overall damping property. The CFRP microlattice exhibits similar stiffness as commercially available CFRP composites while providing high damping as similar to that of elastomers. Source: ORNL.

Conclusions

We developed a scalable multi-material SLA process capable of fabricating dissipative soft inclusions embedded in a viscous, highly loaded CF-reinforced resin. Our process was achieved by recoating the highly viscous resin with the uniformly thin film via the doctor blade and by multiple vats allowing two or more material selection, which is not limited to fabricate the CFRP composite, but can also be applied to other types of viscous resins. To demonstrate our technique, a lightweight cellular CFRP microlattice (e.g., < 200 kg/m^3) for high-stiffness-damping pairs was designed, fabricated, and investigated analytically and experimentally. We studied the base material properties and size effect of the designed lightweight lattices. Furthermore, through DMA tests and quasistatic cyclic compression tests at small and large strains, respectively, we observed that a small volume fraction of the soft phase was adequate to improve both intrinsic and structural damping performance with high strain recovery and some compensation in the effective stiffness (approximately 50% improvement in FOM). Tunability maps for the intrinsic and structural damping were also developed by using the experimental measurements for design usefulness in terms of FOM (e.g., $E^{1/3}\tan\delta/\rho$).

Key Publications

1. Xu, Z., C. Ha, R. Kadam, J. Jindahl, S. Kim, H. Wu, V. Kunc, and X. Zheng, 2020, "Additive manufacturing of two-phase lightweight, stiff and high damping carbon fiber reinforced polymer microlattices," *Addit. Manuf.*, Vol. 32, No. 1, Art. 101106.

References

1. Salari-Sharif, L., L. Valdevit, and T. A. Schaedler, 2014, "Energy dissipation mechanisms in hollow metallic microlattices," J. Mater. Res., Vol. 29, No. 16, pp. 1755–1770.
2. Lakes, R., 2009, *Viscoelastic Materials*. Cambridge University Press, New York, NY, USA.
3. Graesser, E., and Wong, C., 1992, "The relationship of traditional damping measures for materials with high damping capacity: A review," in: Kinra, V., and A. Wolfenden (eds.), *M^{3}D: Mechanics and Mechanisms of Material Damping*. ASTM International, West Conshoshocken, PA, USA. pp. 316–343.
4. Xu, Z., C. Ha, R. Kadam, J. Jindahl, S. Kim, H. Wu, V. Kunc, and X. Zheng, 2020, "Additive manufacturing of two-phase lightweight, stiff and high damping carbon fiber reinforced polymer microlattices," *Addit. Manuf.*, Vol. 32, No. 1, Art. 101106.
5. Deshpande, V. S., N. A. Fleck, and M. F. Ashby, 2001, "Effective properties of the OT lattice material," *J. Mech. Phys. Solids*, Vol. 49, No. 8, pp. 1747–1769.
6. Zheng, X., H. Lee, T. Weisgraber, M. Shusteff, J. DeOtte, E. Duoss, J. Kuntz, M. Biener, Q. Ge, J. Jackson, S. Kucheyev, N. Fang, and C. Spadaccini, 2014, "Ultralight, ultrastiff mechanical metamaterials," *Science*, Vol. 344, No. 6190, pp. 1373–1377.
7. Zheng, X., W. Smith, J. Jackson, B. Moran, H. Cui, D. Chen, J. Ye, N. Fang, N. Rodriguez, T. Weisgraber, and C. M. Spadacinni, 2016, "Multiscale metallic metamaterials," *Nat. Mater.*, Vol. 15, pp. 1100 –1106.
8. Dong, L., V. Deshpande, and H. Wadley, 2015, "Mechanical response of Ti-6Al-4V OT lattice structures," *Int. J. Solids Struct.*, Vol. 60–61, pp. 107–124.

Acknowledgements

This project was performed in collaboration with Prof. X. Zheng's group at the University of California—Los Angeles.

II.2.7 Carbon Fiber Technology Facility (Oak Ridge National Laboratory)

Merlin Theodore, Co-Principal Investigator
Oak Ridge National Laboratory
1 Bethel Valley Road
Oak Ridge, TN 37831
E-mail: theodorem@ornl.gov

Amit Naskar, Co-Principal Investigator
Oak Ridge National Laboratory
1 Bethel Valley Road
Oak Ridge, TN 37831
E-mail: naskarak@ornl.gov

Rich Davies, Co-Principal Investigator
Oak Ridge National Laboratory
1 Bethel Valley Road
Oak Ridge, TN 37831
E-mail: daviesrw@ornl.gov

H. Felix Wu, DOE Technology Manager
U.S. Department of Energy
E-mail: felix.wu@ee.doe.gov

Start Date: March 1, 2011 End Date: Project continuation evaluated annually
Project Funding: $1,000,000 DOE share: $1,000,000 Non-DOE share: $0

Project Introduction

In March 2009, DOE-EERE issued a competitive call for proposals to construct and operate a highly flexible, highly instrumented, Carbon Fiber Technology Facility (CFTF) for demonstrating and evaluating low-cost carbon fiber (LCCF) and new low-cost manufacturing technologies at a pilot-scale. Construction began in March 2011 and the CFTF was commissioned for operations in March 2013.

The CFTF offers a unique, highly flexible, highly instrumented CF processing line for demonstrating advanced technology scale-up and for producing market development volumes of prototypical CFs. The CFTF's unique capabilities, including the flexibility to process a range of feedstocks and product forms, are unmatched anywhere in the world. Designed to bridge what has been called the "valley of death" between laboratory research and commercial scale deployment of LCCF technologies, the CFTF fills a critical need for support for industrial competitiveness in the manufacture of CF in this nation. The objective of this project is to accomplish the safe and reliable operation of CFTF and to further DOE's objectives for large-scale LCCF commercialization. The CFTF supports EERE's efforts toward transitioning technologies to industry, specifically with respect to cost-effective CF for composite materials in high-volume energy applications.

The semi-production-scale CF facility can produce up to 25 tons of CF each year based on melt-spinning processing with the 24k polyacrylonitrile precursor in the tow format. In addition to a conventional conversion line, the CFTF has a melt-spun precursor fiber production line with a rated capacity of 65 tons per year. The 42,000-sq. ft. facility has the capacity for future expansion to include the addition of an advanced technology conversion line.

CF is a strong, stiff, lightweight material used as a reinforcement for polymer-based composites to enable improved product performance in many applications. However, its use in cost-sensitive, high-volume industrial applications is limited because of today's relatively high cost of production. Half of the cost in manufacturing lies in the precursor material, as seen in Figure II.2.7.1. Current methods for manufacturing CF and CFRC structures are slow and energy intensive. New, innovative manufacturing processes for low-cost precursor development and conversion technologies hold the key to reducing CF cost for energy applications.

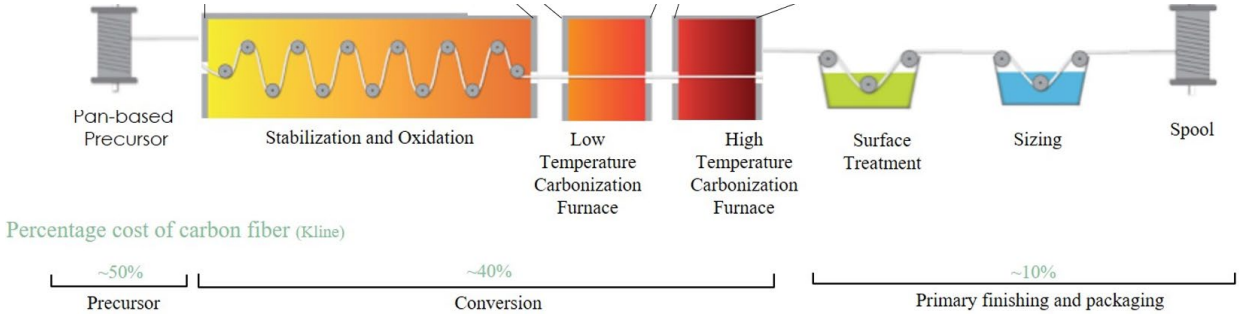

Figure II.2.7.1. CF manufacturing process and cost analysis. Source: ORNL.

ORNL operates DOE's unique CFTF and works with leading companies to overcome technology barriers to reduced cost CF manufacturing and realize the strength and energy saving benefits of these new materials. Because of its exceptional strength and low-density, CF is an enabling material for a number of applications, such as fuel-efficient automobiles, large wind-turbine blades, and lightweight compressed H or natural gas tanks. DOE is interested in increasing the availability and affordability of CF and CF composites to increase energy efficiency and product performance. The major obstacles to CF availability in high-volume industries are the high cost of CF relative to materials currently used, limited availability, and the lack of compatible materials and processes for manufacturing CF composites. In order for CF to achieve widespread use in vehicle and industrial markets, the cost of CF production must be reduced by 30 to 50%.

The high cost of commercially available CF is due largely to the high cost of specialty precursor materials and the energy- and capital-intensive nature of the conversion process. Responding to the need to reduce the cost- and energy-intensity of CF production to meet its long-term program goals, DOE-EERE issued a competitive solicitation in 2009 to all DOE National Laboratories to acquire a flexible capability for advanced research, development, and demonstration of CF production. ORNL was the successful proposer to build a semi-production-scale facility with capability to handle various feedstock materials, to integrate advanced energy-efficient conversion technologies, and to produce sufficient quantities of finished fiber to supply end users for R&D of improved composite manufacturing methods. The proposed capability was focused on four critical areas: (1) development of low-cost feedstocks (precursors); (2) development of more affordable feedstock-conversion methods; (3) integration of developed technologies into an industry-scalable demonstration facility to reduce risk of investment; and (4) development of CF composite material and processing technologies. The project objective will be addressed through the third task in the CFTF annual operating plan.

ORNL R&D efforts and the demonstration of converting textile-based precursor into textile-based C material at double the throughput in comparison to the conventional manufacturing process have resulted in a 33% and 41% reduction in embodied energy for precursor and embodied energy for the fiber as shown by the data in Figure II.2.7.2(a) and (b), respectively. Additionally, the fiber cost of manufacturing is reduced by 45% (i.e., $9.92/kg for the 2X capacity) as shown in Table II.2.7.1 [1].

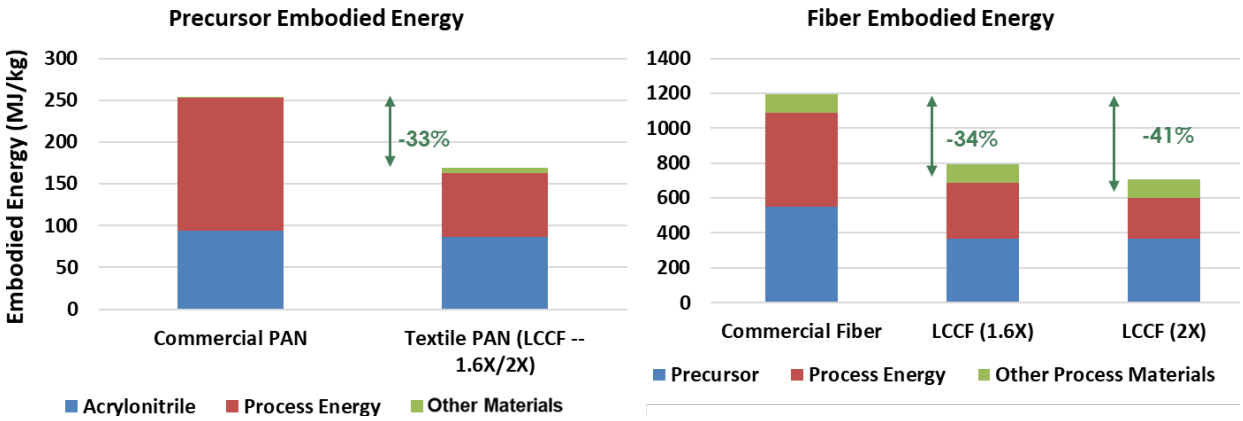

Figure II.2.7.2. Embodied energy for precursor and CF manufacturing. Source: ORNL.

Table II.2.7.1. Cost of Manufacturing for Textile CF Manufacturing

Parameter	Baseline	Heavy Textile Tow (1.6X Capacity)	Heavy Textile Tow (2X Capacity)
Estimated Precursor Cost	$3.63/kg.	$2.24/kg.	$2.24/kg.
Tow Size	50 K	457 K	457 K
Annual Production Volume	1,500 tons/yr.	2,400 tons/yr.	3,000 tons/yr.
Capital Investment	$58 M	$58 M	$58 M
Final Fiber Cost	$18.11/kg.	$11.19/kg.	$9.92/kg.

ORNL continues R&D efforts to further reduce the cost of CF using other alternative precursors or advanced processes. Table II.2.7.2 depicts a list of alternative precursors and advanced processes, along with their advantage and disadvantage for use, and the estimated reduction in cost and embodied energy.

Table II.2.7.2. Alternative Precursor and Advanced Conversion Processing Estimated Reduced Cost and Embodied Energy

Precursor/ Process	Advantage	Disadvantage	Conversion Yield	Cost	Energy
Standard PAN precursor	Strength, elongation, knowledge base, and fiber architecture.	Feedstock price, volatility, capital cost, energy, yield, and processing.	50%	0%	0%
Textile PAN precursor	Properties and knowledge base comparable to standard PAN. Energy consumption and cost reduced.	Capital cost and yield comparable to standard PAN precursor.	50%	-25%	-30%
Melt stable PAN precursor	Througput and energy in spinning, strength, elongation, and fiber architecture.	Same as standard PAN, but higher energy productivity and lesser knowledge base.	50%	-30%	-30%
Bio-PAN	Renewable; pricing decoupled from oil.	Knowledge base and scale.	TBD	TBD	TBD
Polyolefin precursor	Feedstock price and stability, spinning, yield, and fiber architecture.	Conversion process and equipment, knowledge base, and capital cost.	65–75%	-20%	-50%
Mesophase pitch-based precursor	Feedstock price and stability, spinning, yield, knowledge base, properties develop w/o stretching, moderate capital. **Pitch-based precursor offers the highest potential cost and energy reduction potential.**	Elongation, compression strength, and fiber strength.	80–85%	-70%	-70%
Lignin-based precursor	Feedstock price and stability, and renewable domestic feedstock.	Mechanical properties, yield, processing, and knowledge base.	35–45%	-50%	-40%
Recycled CF	Cost, energy, capital cost, yield, and fiber architecture (future).	Feedstock availability, fiber architecture (current), knowledge base, and risk.	N/A	-60%	-90%
Advanced conversion processing	Speed, energy, and capital cost.	Knowledge base and risk.	N/A	-25%	-50%

Preliminary estimations depicted in Figure II.2.7.3 show a significant reduction potential in coal pitch CF embodied manufacturing from a lower raw material embodied energy and higher process yield. Additionally, pitch CF potentially offers the lowest cost/stiffness among CF; hence, a compelling value in cost-sensitive, stiffness-driven, high-volume applications. ORNL will be initiating R&D efforts in other advanced fibers in the near future.

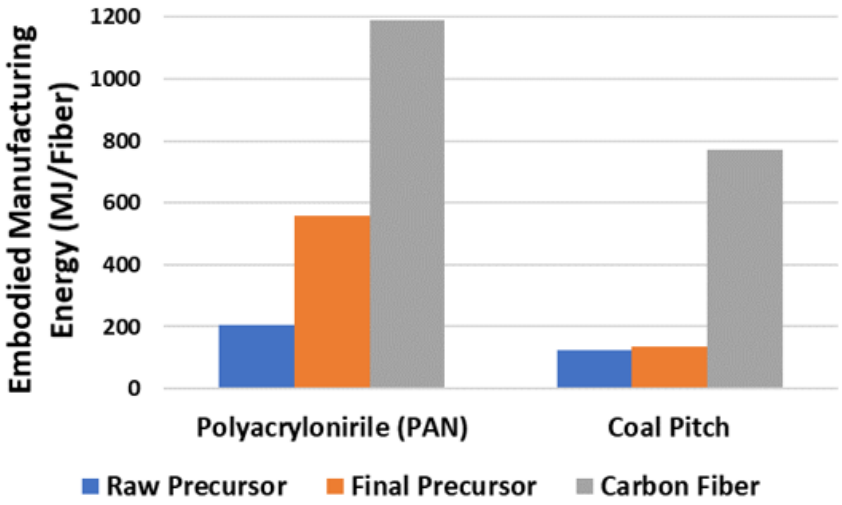

Figure II.2.7.3. Embodied energy for PAN and coal pitch precursor and CF manufacturing. Source: ORNL.

Objectives

The project's objective is to develop LCCF from alternative precursors and accomplish the safe and reliable operation of the CFTF to further DOE's objectives for large-scale commercialization of LCCFs. The tasks covered under these agreements are co-funded by the VTO and Advanced Manufacturing Office (AMO) in support of the efforts by DOE-EERE in transitioning technologies to industry. The CFTF serves as a national resource to assist industry in overcoming the barriers of CF cost, technology scaling, and product and market development. The CFTF is intended to be the bridge from R&D to deployment and LCCF commercialization. The CFTF is open for tours so that industry and others can see the technology and the process science being developed to produce LCCF with industry-appropriate mechanical properties from alternative precursor materials.

Approach

Currently, no commercial manufacturer exists for LCCF, so the CFTF plans to identify cost-effective alternative sources of precursors based on availability, C yield, cost, and spinnability. Once the chemistry of the precursor is developed and baseline properties of 250 Ksi tensile strength and 25 Msi modulus are met, a sufficient amount of material will be produced for scaling up to the next level at the CFTF. The CFTF staff will then develop process conditions for converting the precursor material into LCCF that will exceed baseline properties. Enough CF will be produced for deployment to industry to evaluate, thereby showcasing the quality of LCCF on a multitude of end-user platforms. This work is intended to produce industry demand for the technology. The CFTF staff continues to hold discussions with industrial partners that are interested in scaling the processes being developed at CFTF. The financial investment for industry to scale the technology is significant and, thus, not a subject for quick decision.

CFTF's integrated CF and its composites research portfolio, within the intricate ORNL ecosystem, shown in Figure II.2.7.4, was developed to maximize the impact in the U.S. economy. ORNL is the only National Laboratory that can deliver a multiscale strategic approach from precursor to part with technology readiness levels ranging from one through seven at handoff to collaborating partners. The vision was developed to drive innovation in R&D from precursor to part for structural and non-structural applications across various technology areas, especially automotive.

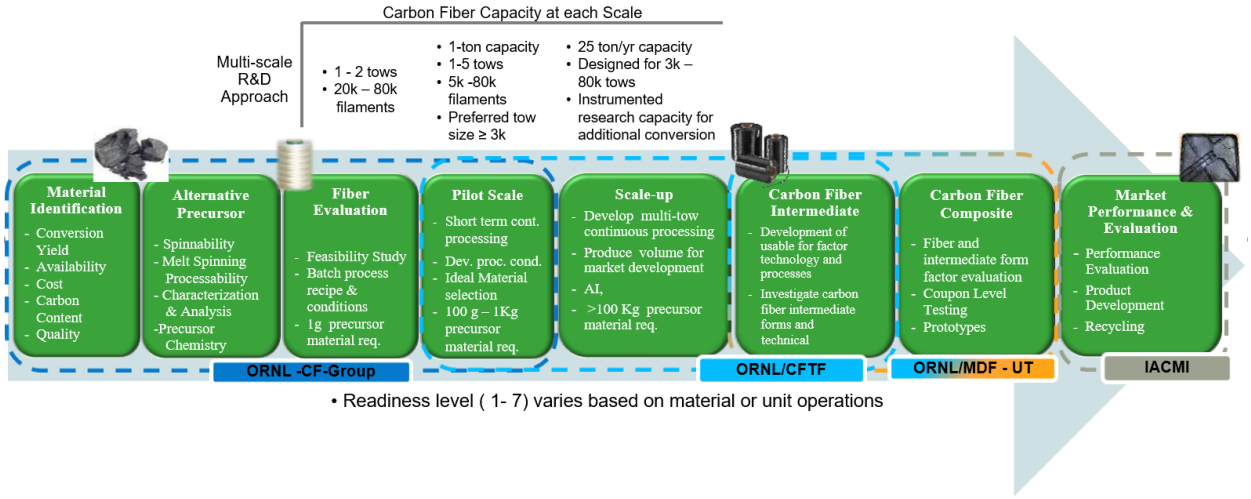

Figure II.2.7.4. Multiscale R&D approach. Source: ORNL.

CFTF's mission is to transition technology to industry for scaling, but many technical challenges remain that must be overcome to further reduce the risk for industry to implement the technology. These technical challenges are being addressed in collaboration with industry to reduce implementation risks. These challenges include handling the various form factors of fibers processed from the alternative precursors and developing appropriate sizing for LCCFs for specific composite applications. The CFTF continues to be a training ground for any technical staff involved in the production of CFs. Key strategies implemented by the project in FY 2020 supported by VTO were labeled under Task 3 of the CFTF annual operating plan with defined milestones. The milestones and their status at the end of FY 2020, as shown in Table II.2.7.3, were to investigate potential alternative CF precursors. This will allow for the selection of a candidate precursor not previously studied and an investigation of supplier-to-supplier variation effects in precursor chemistry, physical characteristics on product variability, and performance. This year the work was focused on pitch-based precursors and CFs.

Table II.2.7.3. Task 3 Milestones, Task Descriptions, and Status

Milestone	Title or Short Description	Original Plan	Revised Plan	Percent Complete
3.1	Demonstrate spinnability of pitch material in melt-blown or fully drawn precursor yarn form.	12/31/19	12/31/19	100%
3.2	Demonstrate spinnability of a minimum of two variations of pitch material into precursor.	03/31/20	03/31/20	100%
3.3	Evaluate and report the mechanical properties, microstructure, diameter, density, and stabilizing temperature of the pitch precursor(s).	06/30/20	09/30/20	100%
3.4	Demonstrate the ability to stabilize the pitch precursor in line through CFTF oxidation process. Determine the thermal profile of the stabilize precursor during DSC.	09/30/20	10/30/20	Moved to Q1 FY 2021 due to COVID-19 work from home policy

Results

Visitors/Tours

In FY 2020, the CFTF hosted 371 visitors, representing 183 organizations:

- For Quarter 1, the CFTF had 146 visitors, representing 115 organizations.
- For Quarter 2, the CFTF had 179 visitors, representing 31 organizations.
- For Quarter 3, the CFTF had 12 visitors, representing 24 organizations.
- For Quarter 4, the CFTF had 34 visitors, representing 13 organizations.

Precursor and CF Development

Three variations of pitch material from various sources (e.g., AR mesophase pitch, Cytec/L3 mesophase, and Rain Carbon, Inc. isotropic pitch) were identified and successfully melt-blown in a subscale custom melt-blowing system, as shown in Figure II.2.7.5, using the following steps. A single-screw extruder was used to push pitch melt material to an extruder-die head. The pitch precursors were blown with overpressure air into a collection box. The fibers were then oxidized, followed by carbonization. The thermal conductivity of all three mats of fibers was measured and found to be between 0.03 and 0.04 W/mK in-air. This is the thermal-resistance equivalent to the R-value of standard fiberglass insulation for home construction. This fiber could be used for insulation in the carbonized state and, if graphitized, potentially be used for composite reinforcement. The precursor processing conditions were developed for each type of pitch material. The data were then translated to the CFTF and used as baseline process conditions for precursor melt-blowing trials at scale.

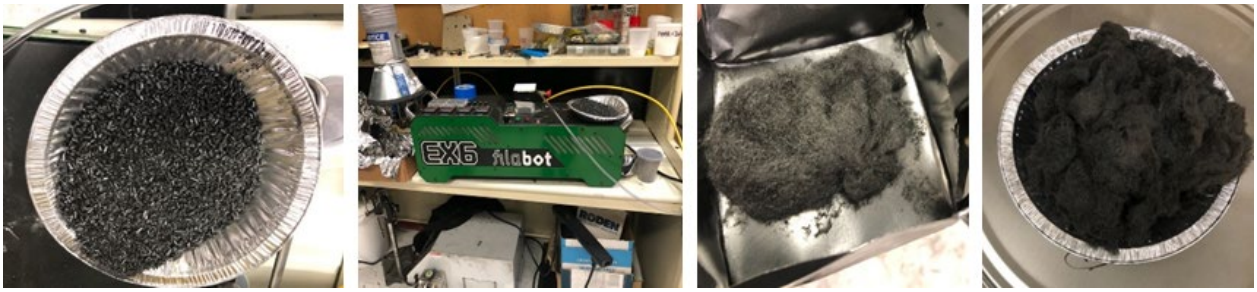

(a) (b) (c) (d)

Figure II.2.7.5. Melt-blow process: (a) mesophase pitch; (b) bench-scale melt blower; (c) melt-blown precursor; and (d) oxidized pitch. Source: ORNL.

Due to the availability of material required for at scale processing, only the Rain Carbon, Inc. isotropic pitch material was processed and developed at scale. While operating at a much larger scale, the system is very simple. As in the bench-scale system, a single-screw extruder was used also to push pitch precursor melt to an extruder-die head with hundreds of capillaries for extrusion into fiber. Multiple capillary temperatures were used for processing pitch material. Air overpressure was then used to grab the fiber and blow it onto a conveyor belt, as shown in Figure II.2.7.6. The material was successfully blown at scale after three trials.

Once melt-blown at scale, the pitch material was then stabilized and carbonized using an experimental design at bench-scale due to the limited amount of material produced. Stabilization and carbonization trials will resume at scale as larger quantities of material become available [1]. The fiber was stabilized, as shown in Figure II.2.7.7, and carbonized, as shown in Figure II.2.7.8, at a range of temperatures typical in CF oxidation (i.e., 200–300°C) and carbonization (1,000–3,000°C) processes long enough to produce a fully carbonized mat material, as observed in Figure II.2.7.9. Close examination of the oxidized and carbonized fiber bundles allowed the team to determine ideal processing temperatures for the material. The fiber bundles appeared to be a completely free bundle of fibers, with no sticking between them.

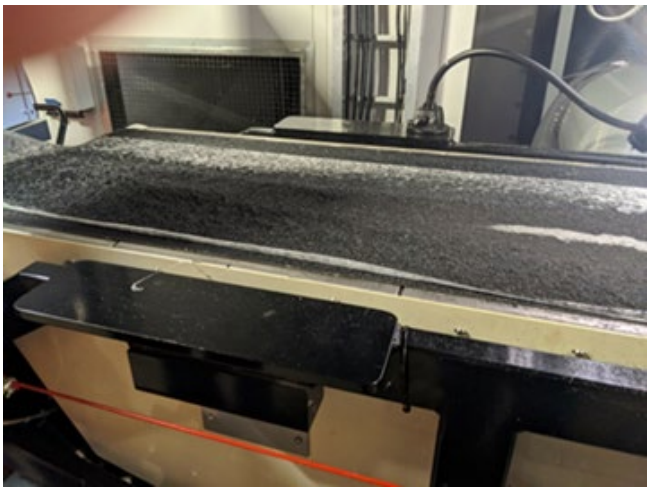

Figure II.2.7.6. Melt-blown pitch fiber on conveyor belt. Source: ORNL.

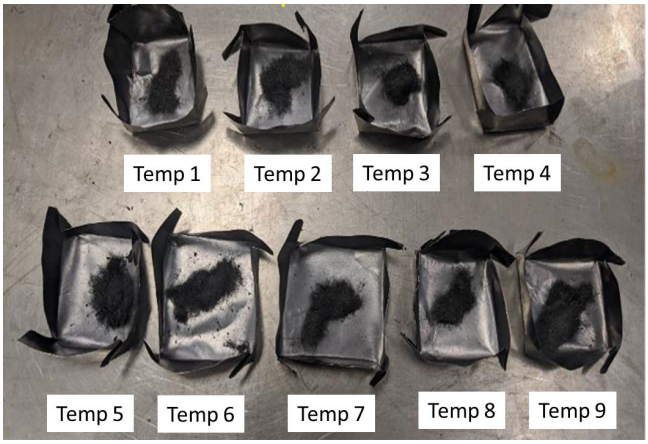

Figure II.2.7.7. Fibers bundles after oxidation at various temperatures. Source: ORNL.

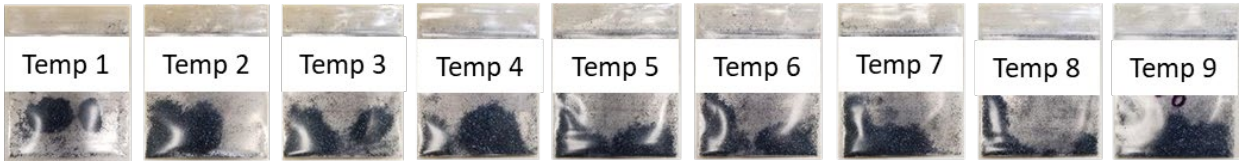

Figure II.2.7.8. Fibers bundles after carbonization. Source: ORNL.

Figure II.2.7.9. Fiber mat after carbonization. Source: ORNL.

These fiber mats were examined using optical microscopy for characterization, as observed in Figure II.2.7.10. In addition, single filaments suitable for fiber testing were pulled from the mat. These were mounted and tested on an Instron single filament testing machine at ORNL. As can be seen in Table II.2.7.4, the average strength was, as expected, relatively low, with an average of 184 MPa. The modulus was approximately 15 GPa, again as expected, low, being an isotropic pitch-based fiber. However, the goal of attaining a high strain to failure, > 1.5, was attained and is promising for a mat of fibers. It is anticipated this will increase significantly upon graphitization. The next steps are to fine-tune the process condition to narrow variation in properties.

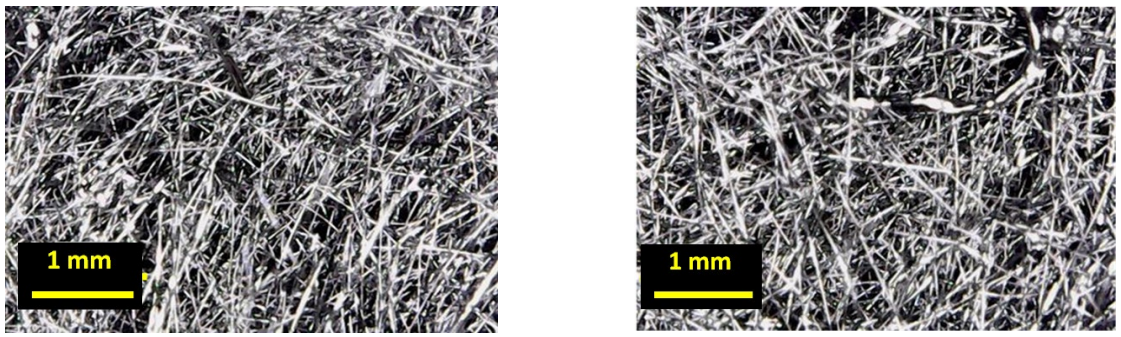

Figure II.2.7.10. Microscopy images of fibers. Source: ORNL.

Table II.2.7.4. Physical and Mechanical Properties of Pitch-Based CFs

	Tensile Stress at Max Force [GPa]	Maximum Force [N]	Modulus (Auto Young's) [GPa]	Displacement at Maxi Force [mm]	Diameter [mm]	Strain at Failure
1	0.107	0.135	11.71	0.162	0.04	0.638
2	0.225	0.057	17.72	0.333	0.02	1.312
3	0.207	0.118	12.69	0.719	0.03	2.832
4	0.330	0.114	23.92	0.444	0.02	1.750
5	0.064	0.029	– –	0.805	0.02	3.168
6	0.224	0.063	13.90	1.280	0.02	5.038
7	0.150	0.047	13.18	0.191	0.02	0.753
8	0.283	0.072	– –	0.800	0.02	3.150
9	0.159	0.032	17.29	0.408	0.02	1.608
10	0.159	0.072	12.12	1.016	0.02	3.999
11	0.120	0.046	– –	0.442	0.02	1.741
Maximum	0.330	0.135	23.92	1.280	0.04	5.038
Mean	0.184	0.071	15.32	0.600	0.02	2.363
Minimum	0.064	0.029	11.71	0.1262	0.02	0.638
Standard Deviation	0.08	0.04	4.15	0.35	0.01	1.39

Conclusions

Under the circumstances of the COVID-19 pandemic, facilities where the current project was being executed were not in operation or were in operation only for execution of COVID-19 projects for at least six months of the funding year. The team managed to obtain meaningful results and met four of the five milestones despite these circumstances. The team was able to demonstrate successful melt-blown pitch precursor at the bench-scale and in the scale-up facility that produced CF with good physical and mechanical properties. Two industry partners are interested in working with ORNL on developing pitch CFs and working mechanisms are in process to initiate the collaboration.

In FY 2020, CFTF team did not report the cost analysis on the accomplishments on textile-based CF research during the VTO annual merit review. The analysis was not completed at the time. However, the CFTF team demonstrated that the team was able to achieve all VTO metrics which are 250 Ksi tensile strength, 25 Msi tensile modulus, and $5/lb CF manufacturing cost using the textile-based precursor. Converting a textile-based precursor into CF at double the throughput reduced the CF manufacturing cost to $9.92/kg ($4.50/lb), with tensile strength and modulus above 400 Ksi and 35 Msi (up to 40 Msi), respectively. Manufacturing costs and energy can be further reduced with other alternative precursor such as pitch precursor.

Key Publications

1. Kumar, V., S. P. Alwekar, U. Vaidya, C. Blue, M. Theodore, V. Kishore, V. Kunc, and A. A. Hassen, "Large-Scale multi-material additive manufacturing of preforms with control microstructure for high-performance composites," ready to submit.
2. Kumar, V., N. Hiremath, P. S. Yeole, R. Spencer, K. M. M. Billah, M. Hasanian, M. Theodore, A. A. Hassen, A. Barnes, U. Vaidya, and V. Kunc, 2020, "Internal arcing and lightning strike damage in short carbon fiber-reinforced thermoplastic composites," *Compos. Sci. Technol.*, Vol. 201, Art. 108525.
3. Singh, D. K., A. Vaidya, V. Thomas, M. Theodore, S. Kore, and U. Vaidya, 2020, "Finite element modeling of the fiber-matrix interface in polymer composites," *J. Compos. Sci.*, Vol. 4, No. 2, Art. 58.
4. Yeole, P., S. Alwekar, N. Veluswary, S. Kore, N. Hiremth, U. Vaidya, and M. Theodore, 2020, "Characterization of textile-grade carbon fiber polypropylene composites," *Polym. Polym. Compos.*, June 2020. Available at: https://doi.org/10.1177/0967391120930109.
5. Hiremath, N., S. Young, H. Ghossein, D. Penumadu, U. Vaidya, and M Theodore, 2020, "Low-cost textile-grade carbon fiber epoxy composites for automotive and wind energy applications," *Compos. B. Eng.*, Vol. 198, Art. 108156.

References

1. Advanced Manufacturing Office 2020 Peer Review (virtual), June 2-3, 2020, Washington, DC, USA. Available at: https://www.energy.gov/eere/amo/maps/amo-2020-peer-review-presentations (accessed 20 December 2020).
2. Zoltek website, n.d., "Carbon fiber education center: How is carbon fiber made." Available at https://zoltek.com/carbon-fiber/how-is-carbon-fiber-made/ (accessed 20 December 2020).

Acknowledgements

The CFTF Team would like to acknowledge our DOE sponsors, Dr. H. Felix Wu, DOE VTO Technology Manager, J. Leong, DOE AMO Technology Manager; the ORNL Management/Team: C. Blue, M. Khaleel, Dr. V. Uday, E. Lara-Curzio, N. Gallejo, J. Klett, A. Blankenship, D. Garrett, T. Reagan, F. Crowson, K. Gaul, L. Lee, R. Strong, C. Daniel, and R. Davies for their sponsorship, contributions, and/or support of the ORNL CFTF program.

II.2.8 Close Proximity Electromagnetic Carbonization (Oak Ridge National Laboratory)

Felix L. Paulauskas, Principal Investigator
Oak Ridge National Laboratory
1 Bethel Valley Road
Oak Ridge, TN 37831
E-mail: paulauskasfl@ornl.gov

H. Felix Wu, DOE Technology Manager
U.S. Department of Energy
E-mail: felix.wu@ee.doe.gov

Start Date: October 1, 2015 End Date: September 30, 2020
Project Funding: $1,000,000 DOE share: $1,000,000 Non-DOE share: $0

Project Introduction

The goal of the close proximity electromagnetic (EM) carbonization (CPEC) project is to develop a novel carbonization technique to replace existing conventional low temperature carbonization (LTC) equipment in the CF industry. It is a joint development project fully funded by DOE, research carried out by ORNL (technical lead) and 4XTechnologies, LLC (formerly RMX Technologies). Preliminary work on EM carbonization was jointly conducted in 2013. This former work is the impetus of the CPEC project. This report covers the progress and final data obtained on the CPEC project during FY 2020.

The previous setup of CPEC-3 in earlier fiscal years produced low temperature CF from a polyacrylonitrile (PAN) precursor on a continuous single tow with direct EM radiation. The output fiber was measured to have a density of 1.5 g/cc or greater, and by November 2017 the final CF (after full carbonization) reached the milestone requirements for a tensile strength of at least 250 ksi, a modulus of at least 25 Msi and an ultimate strain of at least 1%. In the meantime, the modeling of the next iteration of the CPEC technology, CPEC-4, began and was completed in April 2018. For scalability and cost reasons, the design of CPEC-4 was entirely revised. As designed, CPEC-4 is capable of processing up to eight tows and works at a lower power per unit mass of material than the previous version.

During FY 2019, the major effort was focused on mitigating the negative impact of the delays in delivery of components for CPEC-4. Indeed, several suppliers were unable to honor the lead time they had promised. Unfortunately, the longest delay was in delivery of the generator, which is a critical element for commissioning the setup. This came in two separate deliveries: the first in March 2019 (delayed 8.5 months) and the second in June 2019 (delayed 11.5 months). This important delay reduced the time available to six months to complete the installation, test the performance of the equipment, commission the setup, and perform the experimental work.

At the end of FY 2019, an intense effort was dedicated to fix the technical issues discovered during the commissioning of the overall LTC processing system. Several experimental tests were conducted at this time. Finally, the conversion of oxidized PAN fiber was observed on a limited area of a static batch, but the antenna system failed; therefore, the design had to be revisited. Negotiations for a one-year extension of this project began in September 2019. This extension was approved on October 31, 2019.

At the beginning of FY 2020, the effort was dedicated to redesigning the non-reliable antenna fixture. The complexity of the system required a new material investigation/characterization as well as several assumptions. On October 31, 2019, DOE approved an extension of the period of performance and the effort dedicated to make CPEC-4 operational was split between a straight upgrade of the existing configuration with the

exploration of at least one other possibility. By the second quarter of FY 2020, the second configuration, named CPEC-4 Configuration #2, was determined to be potentially more reliable due to a shorter implementation delay. At the end of this project, all experimental results were achieved with CPEC-4 Configuration #2.

Objectives

The objective of the project is to develop a faster and more efficient carbonization process than the actual conventional process. The concept is to elevate the temperature of the material only and to increase the throughput by approximately 30%, while producing the same (or better) quality CF. Also, this technology is expected to reduce unit energy consumption of the LTC stage in kWh/kg by approximately 50%, which represents about a 5% cost-reduction of the overall CF manufacturing process. Physically, the CPEC technology could be scaled to a nameplate capacity of one annual metric ton and ORNL will demonstrate this capability by the end of the project.

Approach

The CPEC project is split into four major design and construction phases from preliminary work to completion with each phase related to a separate experimental setup as listed in Table II.2.8.1. All the tasks accomplished in FY 2020 are encompassed in Phase 4. The three main tasks accomplished in FY 2020 were the modeling of two possible configurations, construction of one of them, and experimental work completed for operation and data collection purposes. This technology was co-developed by ORNL and 4XTechnologies.

Table II.2.8.1. Phase Approach for CPEC-4

Phase	Name	Date	Status (Sept. 2020)	Description
1	CPEC-1	FY 2013	Completed	Demonstration of feasibility (static mode).
2	CPEC-2	FY 2016	Aborted	Upgrade of CPEC-1 (with automatic impedance matching); abandoned in favor of CPEC-2V.
	CPEC-2V	FY 2016	Completed	Optimization of the CPEC concept using a computational model.
3	CPEC-3	FY 2016	Completed	Physical construction of CPEC-2V (continuous process at lab-scale).
4	CPEC-4	FY 2017 FY 2019	Completed	Scale-up of CPEC-3 to a 1 ton/year furnace.

Results

Preliminary results were obtained with CPEC-4 Configuration #1 at the end of FY 2019 after substantial delays in its construction and setup implementation. Evidence of the carbonization effect was limited to an area of approximately 10 mm × 200 mm: on a static batch of eight tows, only one tow was partially carbonized. Unfortunately, during this test run, one subsystem related to the energy distribution failed causing serious damage and preventing further experimental work with the setup until repairs and modifications could be made to prevent further failures. Subsequently, the meeting with DOE on October 31, 2019, defined new goals for the project in FY 2020.

Prior to discussions with DOE Technology Manager, efforts were focused on the evaluation of solutions to repair the setup. The evaluation of the repair involved material, hardware, and supplier research, as well as computational electromagnetic modeling. After several iterations, the calculation time on the available hardware was determined to be too slow to allow for the successful completion of an effective parameter study before December 31, 2019. Specifications for the necessary hardware upgrades and software license renewal/update were determined in October 2020.

At the beginning of FY 2021, the goals during the last year of the project were redefined as follows:

1. Redesign the failing subsystem and upgrade the existing setup (e.g., Configuration #1).

2. Simultaneously design an alternative subsystem (e.g., Configuration #2).
3. Implement at least one of the two configurations.
4. Process and characterize the fiber.
5. Assess energy consumption by the system per mass unit of the processed fiber.

The information technology upgrade process began on November 4, 2019 and took more than a month to complete due to the hardware not being received until December 12, 2019. Upon completion of the upgrade, computational electromagnetic modeling solve times decreased by a factor of 3.8 (e.g., from approximately 10 days per run to 2.5 days), allowing procurement of long lead time parts to begin by early January 2020. By mid-February 2020, among a variety of possibilities, two main configurations were explored using computational electromagnetics modeling. Both require significant hardware modifications/upgrades to the experimental setup.

Hardware Configuration #1

The first configuration is designed for four or eight tows. Figure II.2.8.1 and Figure II.2.8.2 show the typical radiation pattern and tuning characteristics, respectively, which can be expected with Configuration #1. In Figure II.2.8.2, several configurations show favorable tuning opportunities. For a setup such as CPEC-4, a good tuning is at -20dB or lower. Marker 1 indicates a narrow band with 29dB, which is ideal, whereas Marker 2 shows a broader band with fair match at -17dB, which is still acceptable.

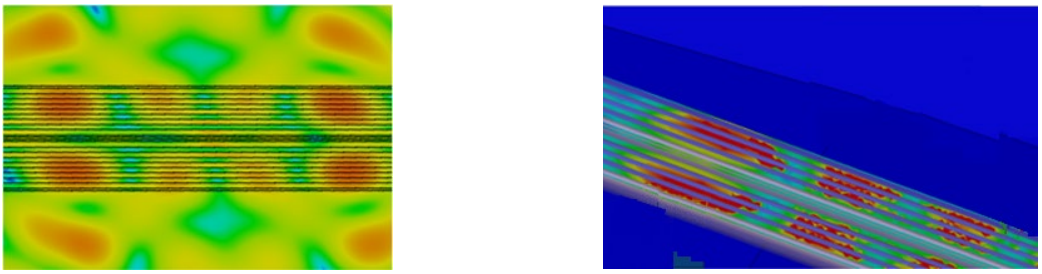

(a) (b)

Figure II.2.8.1. Computational electromagnetic modeling pictures of eight static tows validating the concept of the new design. (a) Example of EM field distribution achieved with the new design. (b) Corresponding theoretical energy deposition on the material. In this case, the thermal evaluation gives higher values than expected, which is not plausible. Additional models need to be processed for variable adjustment. Source: ONRL/4XTechnologies.

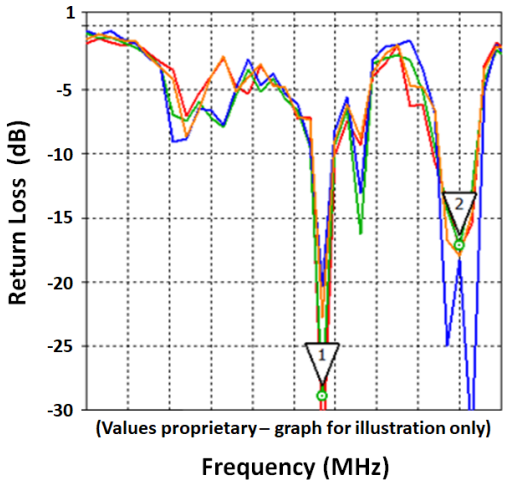

Figure II.2.8.2. Examples of theoretical values of S11 over a band of interest showing several configurations of favorable tuning opportunities. For a setup such as CPEC-4, a good tuning is at 20dB or lower. Marker 1 indicates a narrow bandwidth at 29dB, which is ideal, whereas marker 2 shows a broader band with a fair match at -17dB, which still acceptable. Source: ORNL/4XTechnologies.

At the time of the outbreak of the COVID-19 pandemic, the overall concept of this approach had been validated by CEM with one parameter remaining that needed to be fully explored to optimize the hardware geometry. At that time, even without a pandemic that creates delays in procurement, implementation of Configuration #1 would have required a lead time of several months due to material delivery, machining, and other technical challenges.

Hardware Configuration #2

A second solution was developed in parallel to the upgrade of the device that failed. In contrast to the previous approach, computational electromagnetic modeling work on this second configuration is focused on two tows, but the hardware was designed to handle at least four tows in compliance with the programmatic milestones.

Figure II.2.8.3 shows a model of the field distribution across the two tows that can be expected with Configuration #2. With this configuration, the intensity is mostly centered on the two tows only; it drops dramatically beyond the edges of the tows (not represented in the figure). The homogeneity of the process across four tows is ensured by the geometry of the system—symmetry is used to achieve this goal.

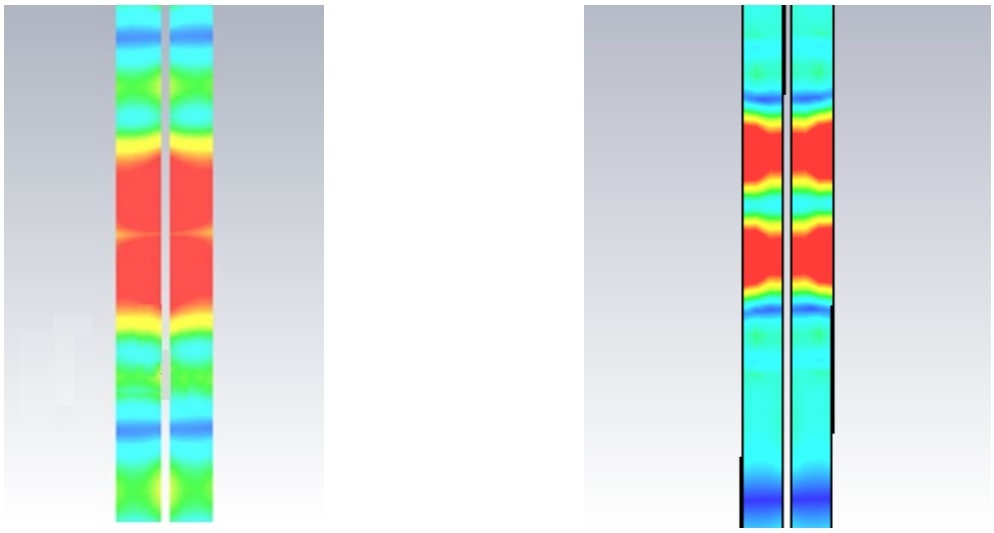

Figure II.2.8.3. These two pictures show two energy deposition patterns with Configuration #2 resulting from tuning modifications. The process will be adapted to four parallel tows. For export control reasons, dimensions and ratios have been distorted. Source: ORNL/4XTechnologies.

Prior to Configuration #2

For technical reasons, the implementation of Configuration #2 was given priority over Configuration #1. Furthermore, the construction of the Configuration #2 required fewer suppliers and was assessed to be faster to build. Dedication of the effort to the quickest solution was encouraged due to the COVID-19 pandemic.[6] The goal was to implement Configuration #2 within four to five weeks. Because of the internal and external constraints related to the pandemic, construction took almost eight weeks and was eventually completed on April 27, 2020. Implementation of Configuration #1 was planned to happen subsequently, but regrettably was not achievable within the limited timeline of this project.

Experimental Work

CPEC-4 Configuration #2 was in operation by the end of April. Approximately two weeks were needed for commissioning and preliminary tests. During the test phase, some unexpected behaviors were observed. Corrective operations were undertaken accordingly. First, experimental results were collected with one or two tows, around mid-May. The first test with four tows was conducted on June 9, 2020. Figure II.2.8.4 shows an example of the characteristics the fiber achieved with one of the first runs with the four tows. On the left of this plot, properties of the four tows as they come after LTC for slightly less than a minute with CPEC is displayed in the density range of 1.57 to 1.65g/cc. On the right, the same tows are conventionally carbonized at HTC with two sets of parameters (cluster of 8 points in the 1.78 – 1.82 g/cc range). With LTC fiber in the 100 – 200 ksi range and an associated final product (e.g., high-temperature carbonization (HTC) fiber) around 500 ksi for the tensile strength, this setup was able to provide remarkable fiber very quickly. Only the deviation of the density of the LTC fiber indicates that the process is not even, which tempered those first results. Nonetheless, despite this large deviation of the fiber, the HTC fiber shows a more homogeneous cluster. Additionally, the cluster of eight points represents two HTC conditions (not differentiated on this figure). One of these two conditions gives the core cluster, whereas the four other points make a more scattered cluster. This confirms that the process condition at HTC also impacts the properties of the final product.

[6] At the time of the decision, COVID-19 had already broken out in Southeast Asia and Western Europe, forcing global shutdown in several countries. The virus was already in the USA. Eventually, on March 30, 2020, Governor Lee (TN) issued executive order #22: “Stay home unless engaging in essential activities.”

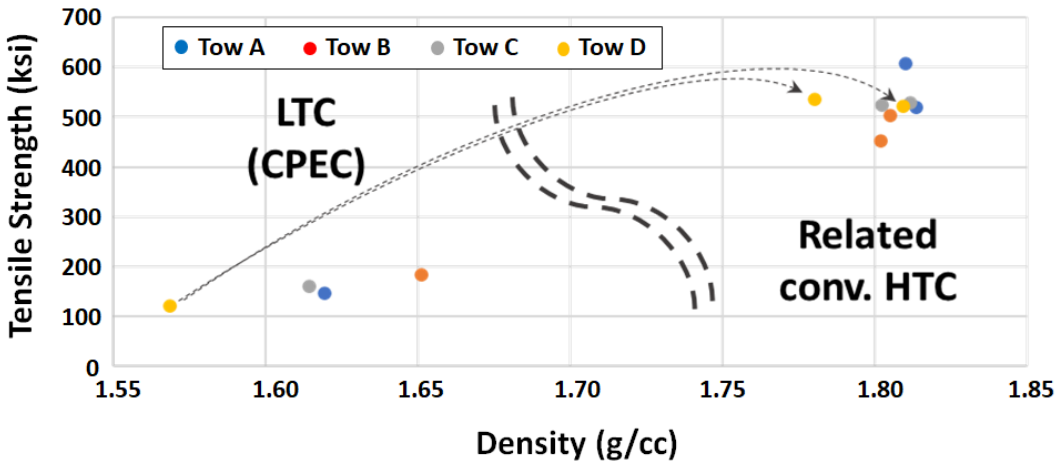

Figure II.2.8.4. Tensile strength vs. density of carbonized material correlating LTC and HTC by tow for CPEC-4 Configuration #2 fed with four tows (e.g., A, B, C, D) of industrial commodity grade oxidized PAN fiber with a density of 1.37 g/cc. Colors indicate the relation between LTC and HTC data. An example of this relation is shown by a set of two arrows on Tow D. Source: ORNL/4XTechnologies.

Various tests with different parameters were made. Among those, one of the most valuable is the residence time and its effect on the density and properties of the LTC and HTC fiber. Figure II.2.8.5 depicts two plots showing the mechanical properties of both LTC and HTC fiber. Two residence times were used—T1, which is significantly shorter than one-minute; and T2, which is slightly shorter than one-minute. Only three of the four tows were characterized.[7] In addition to confirming this system can produce fiber with good mechanical properties (e.g., tensile strength around 550 ksi and modulus at 30 Msi), these tests also confirmed that density is strongly correlated to the residence time. This correlation seems not to exist for the mechanical properties. A larger dataset with more parameters explored at HTC would be needed to be able to establish solid correlation based on the statistical measurements.

Figure II.2.8.6 shows the density of each tow as a function of the residence time. This parameter is essential to assess the advancement of the process. This test was run first with four tows, and a second with seven. For the second test, the three additional tows were inserted in the existing gaps between the four initial tows and the tested span of residence time was larger than with the four tows. With four tows, all residence times are shorter than a minute. With seven tows, the longest residence time is clearly above one-minute. Both plots show the same expected trend, with an increase of the density that reduces with the prolongation of the residence time. On average, the set with seven tows is less processed and shows a standard deviation smaller by 12% to 17%, as compared to the set with four tows at the same residence time. Nonetheless, it shows that the process of seven tows needs an increase of the residence time in a smaller ratio than the one of material insertion to achieve the same density: this seems especially true at the lowest residence time.[8] In other words, the ratio of the residence times between four or seven tows processed at equivalent density is much smaller than the ratio of material. This indicates that if low-density (e.g., 1.50 to 1.54 g/cc) is targeted, this process might have a higher throughput by increasing the amount of material and adjusting the residence time accordingly than by trying to decrease the amount of material and processing it faster. If higher densities after LTC are targeted (e.g., 1.65 g/cc and above), both ratios of throughput material and residence time tend to equalize[9] (i.e., at higher densities, the proportion of time increase matches the material increase, making no advantage of one parameter set over if the throughput is the only one parameter of consideration).

[7] Tow A was processed at LTC only. It was not processed at HTC due to equipment availability. It is expected this tow would have similar properties as Tow C, as shown in Figure II.2.8.4.

[8] This dataset shows that the progress of the process is in favor of material insertion over residence time reduction. The system can be considered overloaded when some of the tows are insufficiently processed or when the standard deviation of the density becomes large enough to affect the consistency of the final product.

[9] This is what the available dataset indicates. This would need to be confirmed with additional data.

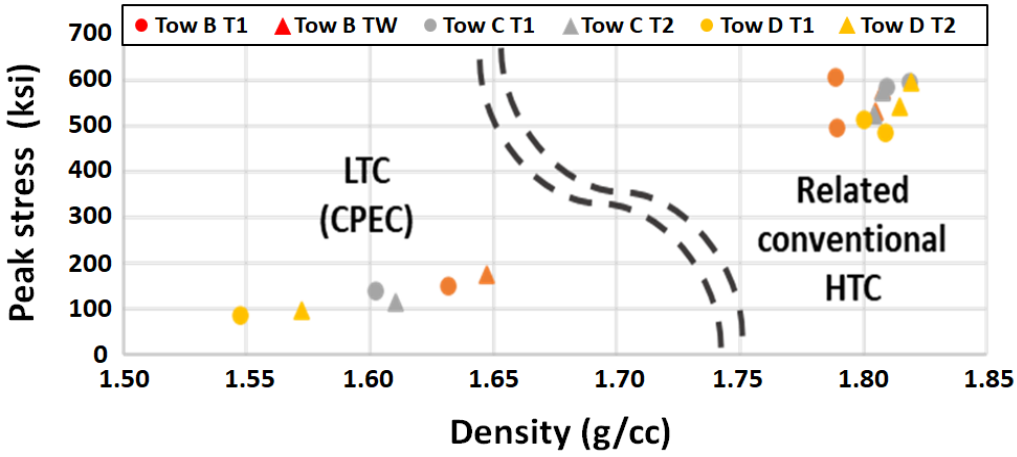

(a)

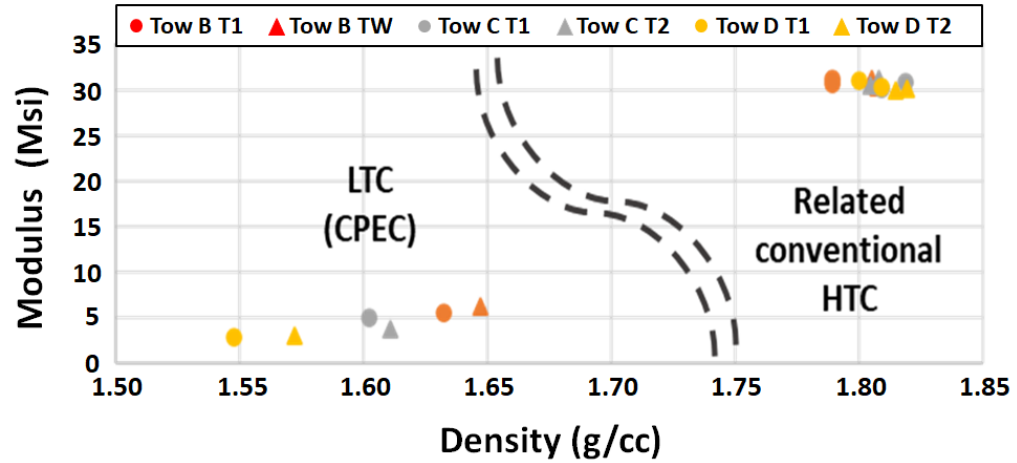

(b)

Figure II.2.8.5. Mechanical properties of three tows from a continuous run with CPEC-4 Configuration #2 with two residence times: T1 < T2 < 1min. Tow A, the fourth tow, was not characterized. The same precursor, same tow position, and same HTC conditions were used compare to the experimental run characterized in Figure II.2.8.4: (a) Plot "Peak stress vs. Density"; and (b) Plot "Modulus vs. Density" Effects of the residence time at LTC on the final CF product are minor. Source: ORNL/4XTechnologies.

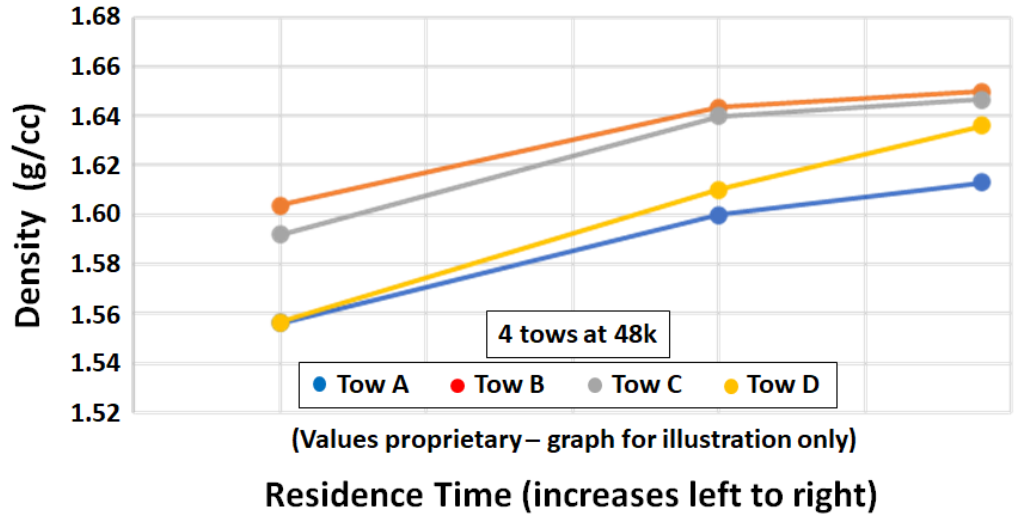

(a)

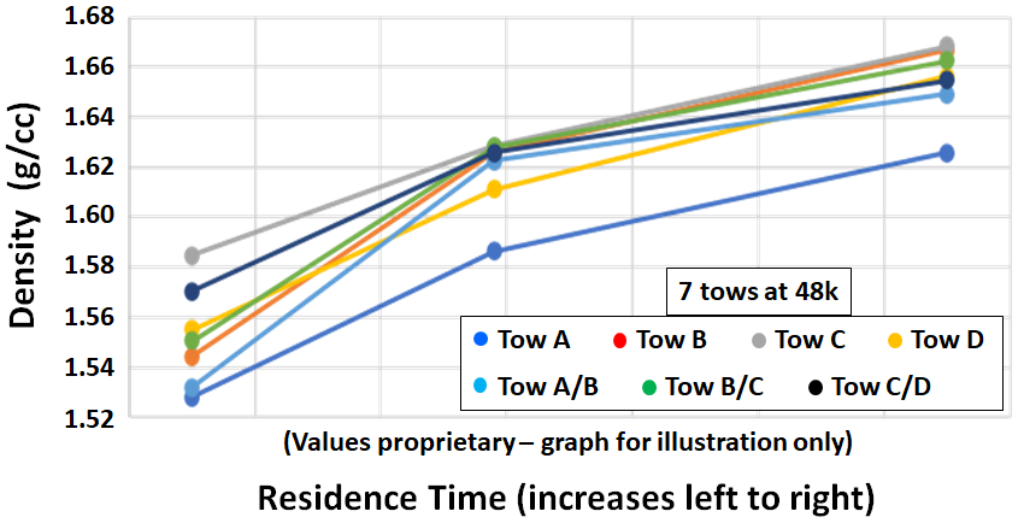

(b)

Figure II.2.8.6. Plots of density vs. residence time at the same power. Time axes do not cover the same span on both plots. (a) Run with four tows (A, B, C, D) where all residence times are shorter than a minute. Standard deviation is from 1.7% (longest residence time) to 2.4% (shortest residence time). (b) Run with seven tows (A/B, B/C, and C/D) were inserted between the four initial tows whose relative positions remained unchanged. Standard deviation is from 1.4% (longest residence time) to 2.0% (shortest residence time). Source: ORNL/4XTechnologies.

Energy Efficiency

The goal of this project is to demonstrate that an EM energy source can be more advantageous than conventional radiative furnaces used in industry. In this study, the performance of the CPEC technology was benchmarked with some data calculated by ORNL in 2012, as observed in Table II.2.8.2. With this calculated consumption of electricity, and in addition to initial capital investment, maintenance, and other additional costs, ORNL determined that the cost of conventional LTC and HTC represents 8% of the overall cost of CF in the industry, as observed in Table II.2.8.3. For this project, the value of 1.74 kWh/lb is used as a reference.

Table II.2.8.2. Energy Consumption Evaluation for a 13.5 m Long Industrial Conventional LTC Furnace [1]

Energy Consumption of Conventional Process	
Theoretical Furnace Characteristics	
Name Plate Capacity (mT/year)	1,500
Number of tows (50k filaments)	120
Length (m)	13.5
Process Parameters	
Temperature (°C)	700
Residence Time (s)	90
Line speed (m/min)	8.96
Estimated Unit Consumption (Industrial Conventional Process) 1.74 kWh/lb	

Table II.2.8.3. An 8% Cost Share Being Significantly Lower Than in Other Benchmark Studies [1],[2]

	Goss (1986)	Cohn (2001)	Kline (2004)	Harper (2011)	Trützschler (2012)	Das (2012)	2013 Paper
Precursor	34%	47%	51%	31%	51%	54%	54%
Pretreatment	3%			69%	49%	6%	1%
Stabilization	20%	16%	16%			13%	12%
Carbonization	23%	26%	23%			8%	21%
Surface Treatment	4%	2%	4%			3%	4%
Sizing	7%	2%				4%	4%
Winding	5%	3%	6%			9%	4%
Other	4%	4%	0%			3%	0%

The experimental setup was set to constant power (e.g., 2.8 kW), and run #1 (e.g., four tows) and run #2 (e.g., seven tows) are used as opportunities to measure electrical consumption. Except for the nitrogen purge and the oxidized PAN fiber, the only resource used by this process is electrical. Because this is an experimental prototype setup—the first of its kind—it is not optimized regarding two major aspects: (1) the efficiency of the process; and (2) the energy consumption of its subsystems. For both reasons, the energy efficiency analyses will be performed on several control volumes. The energy consumption of each subsystem is reported in Table II.2.8.4. Additionally, two experimental conditions are used to calculate the energy consumption per unit mass: Run #1 (e.g., four tows) and Run #2 (e.g., seven tows) and their multiple residence times, as described above, are the experimental runs of reference. Calculations of energy consumption per unit mass are recorded in Table II.2.8.5. Note that two values are lower than the 1.74 kwh/lb used as a reference for the performance of industrial conventional furnaces. Out of the 4 kW injected on the applicator and its dampers (e.g., 2.8 kW of EM energy, and 1.2 kW of conventional resistance heat), it is estimated that the main energy distribution is:

- 0.4 kW due to the cooling of critical parts.
- 0.6 kW dedicated to the warmup of the nitrogen, which is then exhausted.
- 3 kW for the process (e.g., chemical reaction), the effluents, and the losses through the outer surfaces of the setup.[10]

[10] Most of the outer surface of the setup is covered by a 4 in thick insulation. The surface of the insulation was measured to be 47 °C ± 5 °C. The non-insulated parts are at a much higher temperature (up to 300 °C for the uncovered flanges directly connected to the dampers). Losses through the outer surface of the setup are estimated to be 0.5 – 1 kW. This loss is partially due to the construction and is mitigable.

Table II.2.8.4. Energy Consumption of Each Control Volume

CPEC-4 Configuration #2 Control Volume	Energy Consumption (kW)	Comments
Applicator[1] – EM Energy Only	2.8	Most of the energy delivered to the applicator comes from the generator. It also has some conventional heaters and needs cooling as well (not included in this line).
Generator – Electrical Consumption	6.8	This includes the radio frequency energy delivered to the applicator. The efficiency of the generator is 41%.
Cooling	4	Cooling is used primarily for the generator.Minimal cooling is also used by the applicator. The available cooling system is significantly oversized[2] for this system.
Conventional Heaters	1.2	Conventional heaters are located in the dampers of the applicator. Their purpose is limited to prevent tar condensation inside the damper.

[1] The applicator is the part of the setup were the process occurs (i.e. processing chamber).
[2] The chilling system used for the setup was existent and repurposed for this project. The device used to control the temperature of the area portion of the applicator was oversized by a factor of ~10 (e.g., for the flow and the chilling capacity).

Table II.2.8.5. Energy Consumption Per Unit Mass as a Function of the Amount of Material, Residence Time, and Considered Control Volume

CPEC-4 Configuration #2 Efficiency (kWh/Lb) Per Given Control Volume								
Residence Time	Applicator EM Energy Only (2.8 kW)		Generator Elec. Consumption (6.8 kW)		Generator + Cooling Elec. Consumption (10.8 kW)		All System Elec. Consumption (12 kW)	
	Run #1 (4 Tows)	Run #2 (7 Tows)	Run #1 (4 Tows)	Run #2 (7 Tows)	Run #1 (4 Tows)	Run #2 (7 Tows)	Run #1 (4 Tows)	Run #2 (7 Tows)
T >> 1 min	5.4	3.1	13.1	7.5	20.7	11.8	23.0	13.2
T ~ 1 min	3.2	1.8	7.8	4.5	12.4	7.1	13.8	7.9
T < 1 min	2.7	1.5	6.5	3.7	10.4	5.9	11.5	6.6
T << 1 min	1.8	1.0	4.4	2.5	6.9	3.9	7.7	4.4

The dataset in Table II.2.8.5 shows that two values (**in red**) are lower than the value of the 1.74 kWh/lb referenced from Table II.2.8.3. This indicates that outperforming a conventional industrial furnace is possible with CPEC-4 Configuration #2 under the following conditions:

- **Maximization of the number of tows.** The efficiency per unit mass of converted material is proportional to the amount of material with the limitation of space and efficiency of conversion.
- **Reduction of the residence time.** The efficiency per unit mass of converted material is inversely proportional to the residence time. There is no real technical restriction aside from the mechanical properties of the material. The data in Figure II.2.8.6 shows that with four or seven tows, all densities are still above 1.50 g/cc. This indicates that there might be some possibility to reduce the residence time, especially with four tows, but this could be detrimental to the homogeneity of the process. Ultra-short residence times have not been tested.
- **Limitation of the calculation to the radio frequency power injected into the applicator.** If so, the energy consumption is reduced by 41.5% compared to conventional (e.g., 1.02 kWh/lb vs. 1.74 kWh/lb). Extension of the control volume to the generator reduces the efficiency significantly because its

conversion yield of electricity into EM energy is only 41% at the desired output power.[11] The remaining subsystems also require a significant amount of electricity (e.g., cooling and heating units consume 5.2 kW, which is 43.3% of the total). Both the cooling and heating units do not contribute directly to the process. The cooling units are used to protect the generator and its transmission line from overheating. The cooling units are significantly oversized: the temperature of the generator barely exceeds RT, whereas the transmission line does not exceed 45°C (e.g., far below its rated temperature). Additionally, some generators and transmission lines, especially those offering a better yield would need less cooling. On the other side, the system uses some conventional heaters. Located outside the processing cavity, their only function is to prevent the condensation of fumes/vapors in the radio frequency absorbing dampers at the fiber entry/exit areas. For safety reasons, the dampers were oversized. A reduction of their size is possible.

With its concept based on a 100% EM energy source, the applicator of the CPEC-4 Configuration #2 alone can operate with 41.5% less energy than a conventional 1500 t/year furnace. Because it is an experimental setup at lab-scale, almost all subsystems of CPEC-4 Configuration #2 offer multiple opportunities for energy savings and engineering optimization. Even without significant hardware modification, efficiency of the setup could be tested with more material at shorter residence time at different power levels to determine optimal operating parameters. All the data shown in this report was obtained while the setup is being used below its rated power. For example, the addition of an eighth tow with acceptable mechanical properties at constant control volume would be sufficient to reach 50% energy savings.

Conclusions

Over its last year, the LTC project made significant progress and all programmatic milestones were completed. Among a plurality of options, two major designs were modeled with the CEM and one was successfully implemented: CPEC-4 Configuration #2. The three major achievements are:

- Design and implementation of a new configuration for multiple tows processing (at least four tows).
- Operation of the experimental setup and production of several samples involving multiple tows (up to seven) with residence time shorter than a minute (compared to 90 s to 140 s usually observed with conventional processes).
- Production of CF all in the range of 450 – 600 ksi and 30 – 32 Msi for the tensile strength and modulus, respectively. These comfortably surpass the 250 ksi and 25 Msi values of programmatic milestones M14 and M15.

The experimental work showed that the consistency of the process is good along the tow. However, as designed, this experimental setup produces fiber with a standard deviation between tows around ~2% depending on the process parameters. Although all tows can be simultaneously carbonized and become LTC fiber within less than a minute, this deviation of process between tows indicates that CPEC-4 Configuration #2 still needs improvements. Nonetheless, the deviation of density between the tows has a limited impact on the mechanical properties of the final product (high-temperature CF), which is the ultimate criteria. This was verified with all the sets of CFs that were tested. This statement is especially true for the final density and the modulus, which seem to have a very low correlation with the density of the fiber after LTC using the CPEC-4 Configuration #2 process.

As is, CPEC-4 Configuration #2 is using EM energy as the sole energy source for the process. However, as designed, the hardware still needs some conventional heaters (i.e., mostly to prevent tar condensation inside the dampers, at the flanges, and to warm up the nitrogen purge). Additionally, the other subsystems that are needed may have poor energy yield. As a result, if the overall energy yield of the process is strongly dependent on the efficiency of the applicator, it is also a function of the energy efficiency of each subsystem. As is, the

[11] Generators exist on the market that offer conversion yields of at least 60%, but they do not offer some of the features or flexibility that were highly valuable for this experimental work.

prototype consumes 4.4 kW/lb. But if the control volume is limited to the 1.02 kWh/lb of EM energy responsible for the production of acceptable fiber within less than a minute, a reduction of 41.5% of energy can be observed compared with the value of 1.74 kWh/lb provided by a model of industrial furnace with a 1,500 metric ton name plate capacity, the thriftiest model of a benchmark.

At the end of this project, it has been demonstrated that a limited amount of EM energy (1.02 kW/lb) can produce acceptable CF with an LTC residence time shorter than one-minute. The CPEC-4 Configuration #2 is a stable prototype that still offers opportunities for optimization on both aspects: engineering and processing parameters. As examples: the generator has an energy yield of 41% in the conversion of electrical power into EM power, while the addition of an eighth tow could bring the EM energy to 50% of the energy needed by conventional processes. In addition to the reported results already achieved, those opportunities for improvement are strong evidence that CPEC and EM energy can be viable technologies for future LTC production.

Further Development

With the continual growth of the CF market, it is imperative to develop innovative carbonization technologies that provide improvements in economics, mechanical performance, or (ideally) both. The carbonization step of the overall CF conversion process includes two distinct stages. In the LTC stage, the fiber in processing experiences significant morphological changes (e.g., mass reduction by ~50%, almost total elimination of non-C atoms, initiation of the proto G structures, etc.). In the HTC stage the conversion of the material is finalized (e.g., mostly morphological rearrangement induced by the temperature). For the advancement of the CF conversion process, it is absolutely necessary to develop advanced technology for both stages of the carbonization step. For over 50 years, both carbonization stages have used the same conventional technologies, and no significant improvement in these conventional conversion technologies has been achieved over this period. Now that the LTC project has developed alternate technology for the first carbonization stage, it is necessary to proceed with development of new technology for HTC.

References

1. Das, S., and J. Warren, 2012, “Cost modeling of alternative carbon fiber manufacturing technologies – baseline model demonstration,” DOE, 5 April 2012, Washington, DC, USA.
2. Ellringmann, T., C. Wilms, M. Warnecke, G. Seide, and T. Gries, 2016, “Carbon fiber production costing: A modular approach.” *Text. Res. J.*, Vol. 86, No. 2, pp. 178–190.

Acknowledgements

This research was sponsored by DOE-EERE VTO, performed at ORNL, and managed by UT-Battelle, LLC, for DOE under contract DEAC05-00OR22725.

II.2.9 Self-Sensing Fiber-Reinforced Composites (Oak Ridge National Laboratory)

Christopher Bowland, Principal Investigator
Oak Ridge National Laboratory
1 Bethel Valley Road
Oak Ridge, TN 37831
E-mail: bowlandcc@ornl.gov

H. Felix Wu, DOE Technology Manager
U.S. Department of Energy
E-mail: felix.wu@ee.doe.gov

Start Date: October 1, 2019 End Date: September 30, 2021
Project Funding: $300,000 DOE share: $150,000 Non-DOE share: $150,000

Project Introduction

The project aims to demonstrate a scalable coating process to adhere nanoparticles to the surface of fibers and fabricate composites with *in situ* damage detection abilities and simultaneous mechanical performance enhancements. CF composites have the inherent problem of hiding damage within the structure with no visual indications on the surface. Therefore, a technique to monitor for damage or excessive stress on the composite is necessary to ensure its safety and avoid catastrophic failure. This capability will be desired in future transportation vehicle designs, such as in cargo and surveillance drones developed by Dronesat, LLC (Dronesat), the industrial partner on this project.

Prior work showed that SiC nanoparticles embedded in a thin polymer layer on the surface of CF can result in multifunctional composites that have increased mechanical performance and enhanced self-sensing behavior [1]. Specifically, the composite's interlaminar shear strength was improved, which demonstrates better adhesion between the fiber layers. This fiber-to-fiber adhesion is typically the weak property of fiber-reinforced composites and is the mechanism for composites to fail catastrophically. The nanoparticles also enhanced the electrical resistance change of the bulk composite structure when subjected to applied stress, thus giving it better structural health monitoring capabilities. The nanoparticle deposition technique utilizes a continuous feed-through process that is compatible with existing commercial CF processing lines, thus enabling potential commercial deployment. This prior work resulted in a patent-pending fiber-coating technology titled, "Carbon Fiber-Nanoparticle Composites with Electromechanical Properties" (non-provisional patent application number 16/280,268). Within this project, the prior work was leveraged to extend the fiber-coating process to another material system (i.e., titanium dioxide [TiO_2] nanoparticles on CF) to create composites with embedded active sensing abilities.

Working with Dronesat, this project also involved the design and initial fabrication of self-sensing composite components for a prototype drone. Dronesat has developed a tethered drone system for prolonged flight times. To improve drone safety, Dronesat wants to integrate sensing composites into their drones to detect damage before catastrophic failure. The ultimate result would reduce maintenance time by early detection of cracks or damage, thus mitigating costly effects of unexpected failures, which could result in vehicle loss. Materials that could detect damage and provide timely information about critical components—in particular, ducted fan blades, disks, open rotors, ducts, propellers, airframe, control surfaces, horizontal and vertical stabilizers, and wings—would be highly desirable for product safety. Dronesat collaborated with ORNL on this project to help integrate multifunctional composites into their structures, and Dronesat offers its drone system as a testbed to demonstrate the application of multifunctional composites in real-world scenarios. Dronesat has one of the most unique power infrastructure concepts for a drone in development that is positioning it to become a highly sought-after drone manufacturer. Safety is one of the biggest challenges in this type of drone market, so

Dronesat partnered with ORNL to integrate sensors that could solve some of the safety challenges. To meet these safety challenges, ORNL has further developed the nanoparticle coating process within this project to achieve improved mechanical and sensing performance.

Objectives

This research work aimed to demonstrate self-sensing CF composites that can be deployed in transportation vehicles using a patent-pending process developed at ORNL. The embedded nanoparticles result in multi-functionalities that increase mechanical performance and enhance self-sensing behavior through electrical resistance change of the bulk composite structure when subjected to applied stress, thus giving it better structural health monitoring capabilities. The specific objectives include homogeneously coating CF with nanoparticles using a continuous processing method, improving mechanical performance through interlaminar shear strength characterization, and enhancing sensing capabilities by utilizing nanoparticles with piezoresistive behavior.

Approach

To achieve the project objectives, nanoparticles were coated on CF using a continuous feed-through process to be able to generate a sufficient length of fiber to fabricate into composites. This process consists of a two-step coating process. The bare CF was first submerged into an aqueous suspension of TiO_2 nanoparticles with subsequent drying. These coated fibers were then dipped in a second coating bath with a commercially sourced aqueous epoxy sizing emulsion. Sizing is a typical coating that is applied to CF in industrial settings. This polymer layer is 100–200 nm and serves multiple functions. It enhances the adhesion between the fiber and the matrix, protects the fiber surface during composite fabrication, and aids in handling of the fibers. This project aimed to utilize the sizing layer as a carrier matrix for nanoparticles in that the sizing helped bond the nanoparticles to the fiber surface. The goal of the nanoparticles was to enhance the mechanical interlocking at the composite interphase to increase the interlaminar shear strength, as well as increase the piezoresistive response of the composites. This piezoresistive response was quantified by measuring the electrical resistance of composite beams during repeated strain cycles.

Results

The dip-coating procedure was successful in homogeneously dispersing TiO_2 nanoparticles on the surface of a CF tow and subsequently coating it with sizing as shown in Figure II.2.9.1(a) through (e). This process allowed the concentration of TiO_2 nanoparticles to be easily modified by changing the concentration of nanoparticles in the coating bath. The fibers and composites in the figures are designated by the concentration of nanoparticles in the solution bath (i.e., the “1-wt%” fibers were dip coated through a water bath with 1-wt% nanoparticles). Fibers were dip coated with 0.1 to 4-wt% nanoparticle mixtures. Using these various fibers, unidirectional composites were fabricated using a filament winding technique followed by compression molding during epoxy curing. The resulting composites were short beam shear tested to quantify the interlaminar shear strength as summarized in Figure II.2.9.2(a). For most composites, the nanoparticles enhanced the interlaminar shear strength with the most significant improvements in the 0.5 to 1.5 wt% composites as shown in Figure II.2.9.2(b). Overall, the best performing sample was the 1-wt% composites, which was 14.7% stronger than the composites with no nanoparticles.

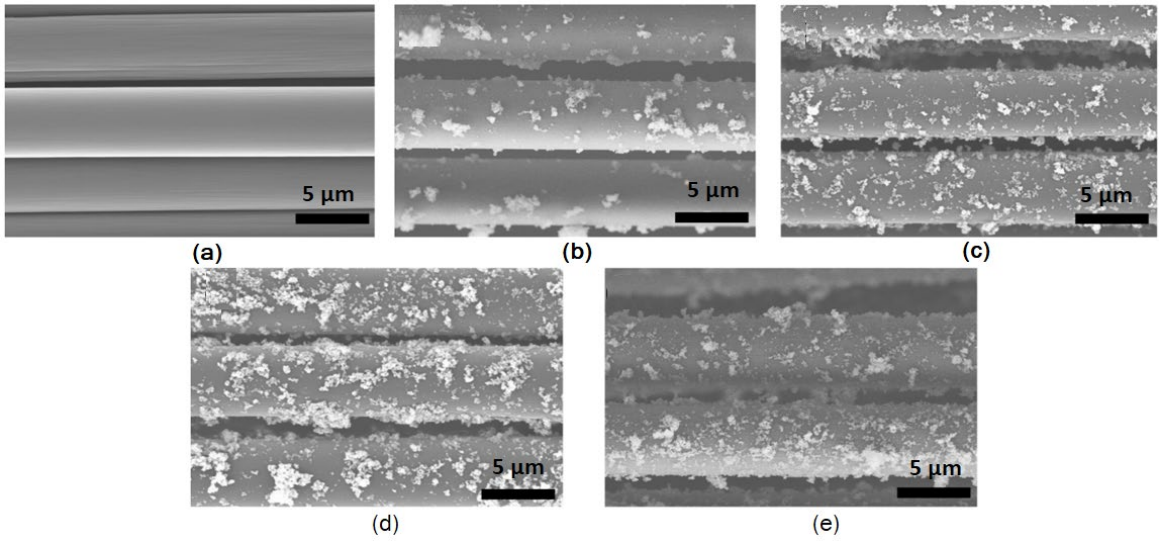

Figure II.2.9.1. SEM images of TiO_2 on CF after a dip-coating process with mixtures containing: (a) 0 wt%; (b) 1 wt%; (c) 2 wt%; (d) 3 wt%; and (e) 4 wt% TiO_2 nanoparticles [2]. Source: ORNL.

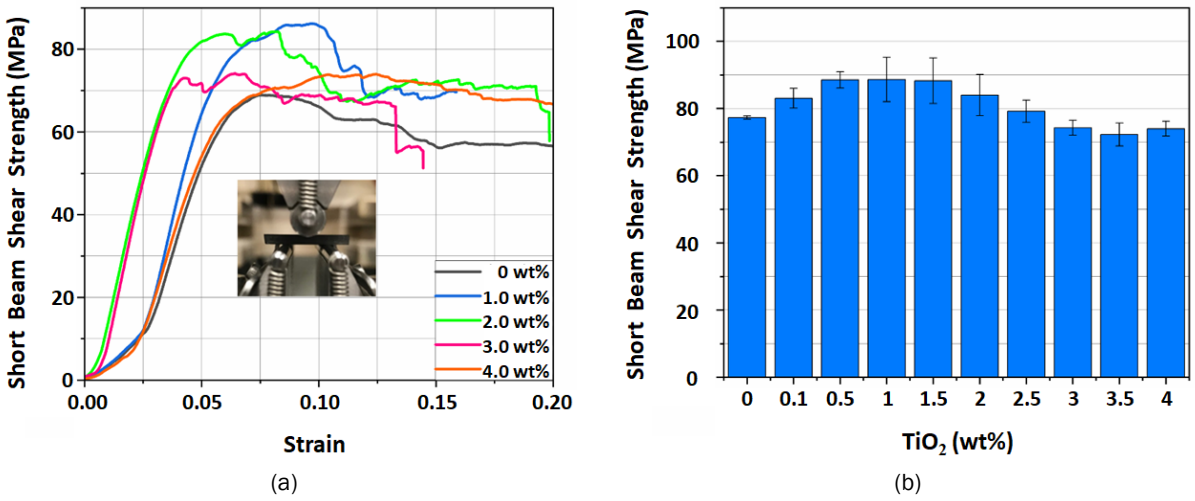

Figure II.2.9.2. Results of the interlaminar shear strength testing showing: (a) the representative strength vs. strain curves; and (b) the average strength values versus the nanoparticle concentration in the coating mixture. The error bars signify one standard deviation [2]. Source: ORNL.

To characterize the structural health monitoring capabilities of the composites, the unidirectional composites were electroded in an out-of-plane through-thickness configuration, as observed in Figure II.2.9.3(a) and placed in a dynamic mechanical analyzer using a single cantilever clamp. The composites were subjected to cyclic strain loading and unloading at different strain magnitudes, as shown in Figure II.2.9.3(b), while capturing the change in electrical resistance, as shown in Figure II.2.9.3(c). An overlay of the strain input and resulting electrical resistance change can be seen in Figure II.2.9.3(d).

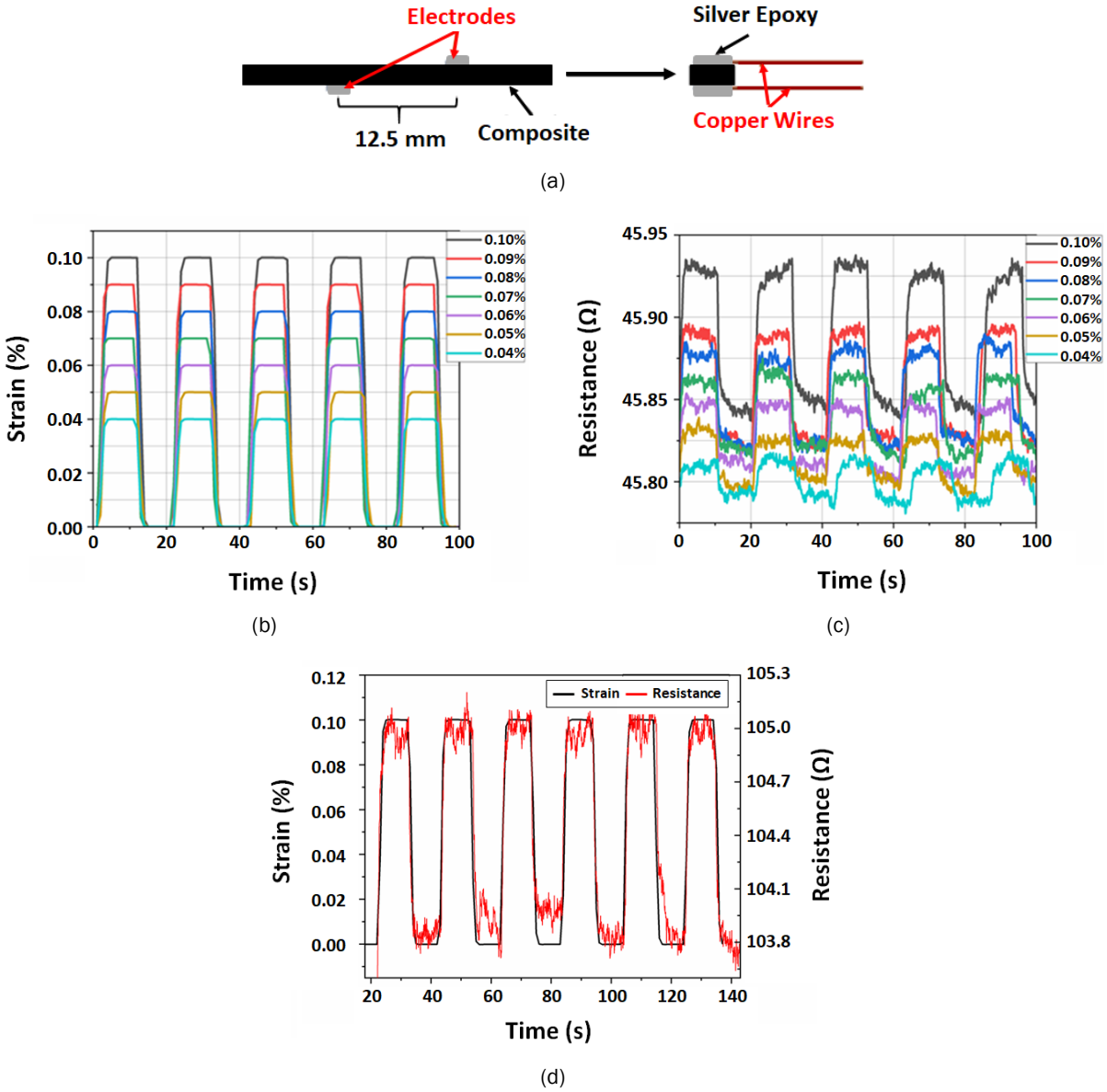

Figure II.2.9.3. (a) Electroded sample schematic in which the CFs run in the x-direction and the thickness is in the y-direction. (b) An overlay of the different strains placed on the composite beam. (c) Representative curves of the electrical resistance in response to the different strain cycles. (d) Overlap of a representative input strain and the electrical resistance response [2]. Source: ORNL.

At least 10 strain cycles were repeated for each strain level and the corresponding electrical resistance change was averaged over the 10 cycles to create the plot in Figure II.2.9.4(a), which shows the average electrical resistance change at each strain level for every composite. To quantify the structural health monitoring sensitivity, the gauge factor for each composite was calculated by dividing the relative electrical resistance change by the strain. The average gauge factor for each composite is shown in Figure II.2.9.4(b), where a larger value represents a better performing composite. This showed that the composites with 1–3 wt% nanoparticles exhibited enhanced structural health monitoring sensitivity. The best performing composites in terms of gauge factor was the 2.5 wt% composites with a gauge factor of 7.14, which equates to 186% increase in sensitivity as compared to the composites without nanoparticles.

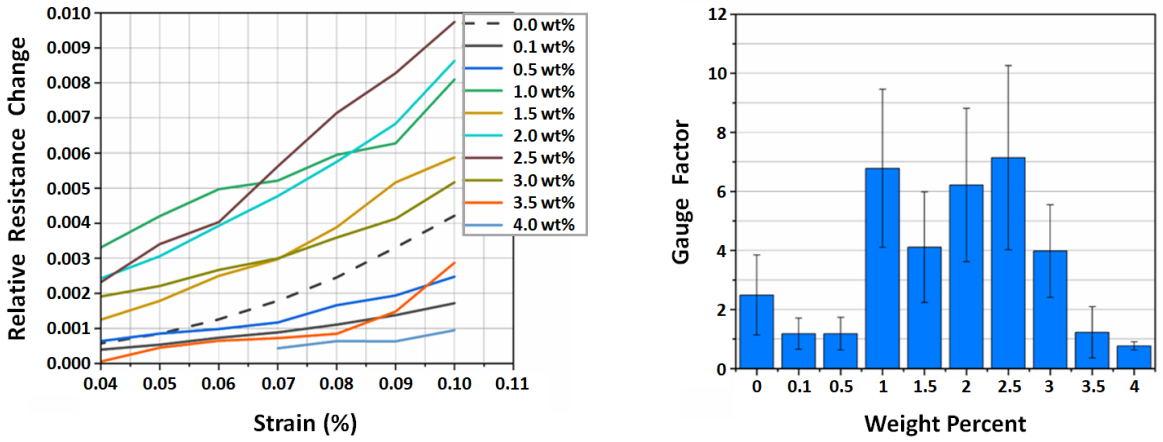

Figure II.2.9.4. (a) Relative resistance change versus percent strain. (b) Gauge factor for each composite averaged over all the strain levels tested. Error bars signify one standard deviation [2]. Source: ORNL.

The overall performance of the composites is summarized in Figure II.2.9.5, which plots both the interlaminar shear strength and gauge factor for each composite. The targeted area of the plot is the highlighted upper-right quadrant, which represents improvements in both mechanical and sensing performance as compared to the composites with no nanoparticles. As shown in Figure II.2.9.5, the composites with 1–2.5 wt% nanoparticles saw enhancements in both properties. The best performing sample was the 1 wt% composites with improvements of 14.7% and 172% in interlaminar shear strength and gauge factor, respectively, as compared to the composites with no nanoparticles.

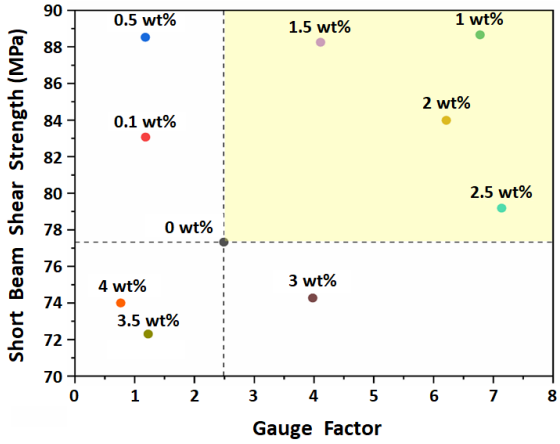

Figure II.2.9.5. Plot of the different composites showing the average interlaminar shear strength versus the average gauge factor. The dashed lines show the values for the composite without nanoparticles with the highlighted region signifying simultaneous improvements in both properties [2]. Source: ORNL.

The next step of the project was working with Dronesat to design the prototype components that could be made from the developed nanoparticle-enhanced composites. Figure II.2.9.6 shows one example of many parts that were designed by Dronesat. The example here shows the fan blade assembly with different viewpoints. The critical part of this assembly would be the point at which the blade is attached to the base. This attachment point is the most prone to failure, so it was targeted as an ideal location to place the sensing composites. These nanoparticle-enhanced composites would both enable sensing of this joint and offer increased strength to reduce composite failure. The implementation of these composites in the drone prototypes is ongoing work.

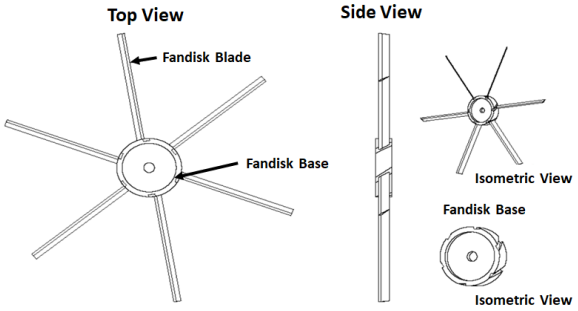

Figure II.2.9.6. Schematic design of the fan blade assembly prototype where the multifunctional composites will be integrated. Source: Dronesat.

Conclusions

This project demonstrated that the continuous fiber dip-coating process developed at ORNL could be used to homogeneously disperse TiO_2 nanoparticles on CF to produce multifunctional composites. The interlaminar shear strength was selected as the metric for mechanical performance. Most of the composites showed increased strength, and the highest performing composite was the 1-wt% nanoparticle composite, which showed a 14.7% increase. The structural health monitoring capabilities were evaluated by measuring the piezoresistive behavior of the composites and calculating the gauge factor for each composite. It was shown that composites with 1–3 wt% nanoparticles exhibited increased gauge factor with the highest performing sample being the 2.5-wt% composites, which had a 186% improvement. In comparing the performance of all the composites based on these two properties, the 1-wt% composite performed the best overall with 14.7% and 172% improvements in interlaminar shear strength and structural health monitoring sensitivity, respectively. Therefore, this project produced CF coated with TiO_2 nanoparticles using a continuous feed-through dip-coating process that significantly enhanced the multifunctional performance of the composites. This research downselected the nanoparticle concentrations to the best performing composites containing 1-wt% nanoparticles. This 1-wt% TiO_2 nanoparticle composite is now in the process of being scaled-up into prototype drone components for integration into Dronesat's novel drone system to create *in situ* sensing of the critical components of the drone.

Key Publications

1. Rankin, S. M., M. K. Moody, A. K. Naskar, and C. C. Bowland, 2021, "Enhancing functionalities in carbon fiber composites by titanium dioxide nanoparticles," *Compos. Sci. Technol.*, Vol. 201, Art. 108491.

References

1. Bowland, C. C., N. A. Nguyen, and A. K. Naskar, 2018, "Roll-to-roll processing of silicon carbide nanoparticle deposited carbon fiber for multifunctional composites," *ACS Appl. Mater. Interfaces*, Vol. 10, pp. 26576–26585.
2. Rankin, S. M., M. K. Moody, A. K. Naskar, and C. C. Bowland, 2021, "Enhancing functionalities in carbon fiber composites by titanium dioxide nanoparticles," *Compos. Sci. Technol.*, Vol. 201, Art. 108491.

Acknowledgements

The author would like to acknowledge S. Rankin and M. Moody for their work on this project as part of their ORNL internships, as well as A. Naskar for his supervision and assistance with this research.

II.2.10 Industrialization of Carbon Fiber Composite Wheels for Automobiles and Trucks (Oak Ridge National Laboratory)

Brian Knouff, Co-Principal Investigator
IACMI Scale-up Research Facility
Oak Ridge National Laboratory
1400 Rosa Parks Boulevard
Detroit, MI 48216
E-mail: knouffbj@ornl.gov

Michael Hayes, Co-Principal Investigator
ESE Industries
675 Ponce de Leon Avenue Northeast, Suite 8500
Atlanta, GA 30308
E-mail: m.hayes@ese-industries.com

H. Felix Wu, DOE Technology Manager
U.S. Department of Energy
E-mail: felix.wu@ee.doe.gov

Start Date: March 1, 2020 End Date: February 28, 2022
Project Funding: $1,000,000 DOE share: $500,000 Non-DOE share: $500,000

Project Introduction

ESE Carbon Company

ESE Carbon Company (ESE) is on track to be the second manufacturer in the world—and the first in North America—of one-piece CF composite wheels to market, behind Australia's Carbon Revolution. ESE has invested in this technology with an engineering team comprising experts in composite materials, mechanics, design, and manufacturing. With a prototype factory in Jasper, GA, which houses considerable capital investment including a computer numerical control machine, a tailored-fiber placement (TFP) machine, an autoclave, and an industrial robot.

ESE's current wheel design, named "E2," has passed two of the SAE's aftermarket (metal) wheel tests: one for cornering fatigue (SAE Recommended Practice J2530/J328) at a heavy sports utility vehicle wheel rating and another for curb impact (SAE Recommended Practice J175) at a heavy-sedan wheel rating. At the time of this effort, we will be bringing a revised design, "E2.1," into prototype production with the expectation of passing curb impact, radial/pothole impact (European AKLH_08), radial fatigue (SAE Recommended Practice J2530/J328), and biaxial fatigue (SAE Recommended Practice J2562) at heavy sports utility vehicle loads. In addition, ESE has taken an active role on the SAE Composite Wheels Task Force, which is charged with adopting and building upon the existing SAE standards for steel and AA wheels.

ESE brings considerable experience in wheel design and manufacturing with composite materials. The combination of its composite design and manufacturing know-how, knowledge of the wheel-specific design challenges, and understanding of the passenger vehicle wheel market are unique and unsurpassed in North America. ESE is interested in scaling from aftermarket sales to passenger car OEM's specification and to HD truck and military applications.

Oak Ridge National Laboratory

ORNL brings capabilities crucial to meeting the goals of the team, which has decades of experience in industrial composite automotive design and optimization, as well composite materials characterization and testing. We are interested in integrating LCCF into our materials portfolio, using ORNL's Manufacturing Science Group to provide materials testing and characterization, assist in process improvement, and aid in the virtual simulation including the use of high-performance computing.

ORNL Composite Materials Characterization and Modeling

The Composites Group is part of the Manufacturing Science Group at ORNL. Besides establishing leading-edge technologies in composites processing and testing, this group will lead the industry in composite design and optimization using state-of-the-art physical-simulation techniques.

Objectives

The primary objective of this project is to couple ESE's existing passenger car wheel design and manufacturing process with ORNL's expertise in materials characterization, composites processing, and computational methods to accelerate the current development phase and the subsequent commercialization phase. These phases are not sequential and may overlap.

Approach

The approach breaks down the work statement into different tasks performed over 24 months (plus a to be determined extension due to COVID-19), including deliverables by ORNL and our industrial partner. Each task will include a report summarizing the findings.

Phase 1—

Task 1: Baseline Materials Characterization (First Year)

ESE will manufacture flat panels using its proprietary process with current process parameters, while ORNL will provide characterization and testing. Baseline mechanical properties in both quasistatic loading and fully reversed fatigue testing will be generated.

Task 2: TFP Parametric Study (Initiate Month 4)

ESE's current TFP process was set up with the intent of maximizing throughput during ply construction while providing sufficient wheel performance. However, we do not have a good understanding of the tradeoffs between performance and efficiency. The impact of a better dispersed tow on productivity and properties, as well as infusion, is unknown. Other potential opportunities for optimization include TFP parameters such as stitch material, tension, and density and backing materials. ORNL will provide onsite consulting to help optimize the TFP and infusion/molding process parameters to maximize material properties and minimize cycle times, as well as provide ways to perform the stitching automatically. All parts will be made onsite at ESE with its molding process.

Task 3: Environmental Effects Study

ESE based its design on public domain data for a similar material system. The following environmental conditions are considered:

- Cold temperature, dry
- Room temperature, dry
- Elevated temperature, wet
- Elevated temperature, dry.

Primary concerns include dry RT performance for nominal conditions and for correlation with the SAE fatigue tests, all of which are performed at laboratory RT conditions, wet elevated temperature conditions experienced during service in hot climates or during track use, and the dry cold temperature impact performance. Coupon testing will be performed by ORNL at these conditions with specific temperature definitions to be determined.

ORNL will assist in the materials testing setup, and test materials after exposure to provide properties as per Task 1.

Task 4: Damage Tolerance Study

The primary performance and safety concerns for composite wheels are stiffness, fatigue life, thermal stability, and damage tolerance. The above tasks, in conjunction with the SAE wheel tests, will address all but the issue of damage tolerance. Topics of concern include both manufacturing variabilities and impact-induced damage. In the current task, ESE and ORNL will identify the highest priority concerns and design coupon study experiments to quantify the effects of these flaws. ESE will manufacture flat panels with intentional variabilities that are representative of those found in our prototype wheels.

Phase 2—

NOTE: Tasks 5 through 9 will include many iterations until the final design is approved by both ORNL and ESE which may also require re-testing with newly fabricated panels for verification.

Task 5: Design Analysis

Rerun simulations of cornering fatigue, radial fatigue, curb impact, and pothole impact to reassess E2.1 design with new test data for revised TFP plies and process parameters.

Task 6: Virtual Design Optimization

Optimize design with objectives (mass, strain, cost minimization), design variables (e.g., ply thickness, layup, materials) and design constraints (e.g., safety factors, strain allowables, stiffness).

Task 7: Revised Design Analysis

Reanalyze new design based on all results accumulated from this project to ensure it passes all necessary testing (including SAE).

The final deliverable from both parties will be a report addressing the objectives and deliverables. ORNL will provide this report to the Office of Scientific and Technical Information for open access.

Results

Due to the combination of the COVID-19 pandemic and the ORNL principal investigator getting ill and requiring major surgery (along with six weeks of short-term disability), progress has been delayed significantly. We are currently in Task 1 and have yet to begin Task 2.

Task 1. Baseline Materials Characterization

ESE's Flat-Panel Tool Development

ESE's flat-panel tools have long served as small-scale test beds for its wheel-production process. ESE recently shifted from a compression RTM process, wherein part of the tool moves using autoclave pressure toward a vacuum-assisted RTM process. Prior to being awarded the LightMAT project, ESE's flat-panel tooling had undergone several design iterations (e.g., flat-panel tool generations A to C) to test different panel thicknesses and tooling materials, as well as more accurate temperature monitoring. Attempting to validate process variables during the transition from compression RTM to fixed-tool RTM has also been a primary goal. These tools showed minor improvements in geometric consistency, but still lacked consistent infusion quality, demonstrating high void content, which was attributed primarily to an inability to fully remove air from the cavity. The tools also suffered from some ergonomic deficiencies and they were slow to operate.

Starting in 2019, ESE engaged third-party design consultation with both a composites manufacturer and two composites tool makers to develop an industry-tested solution. The feedback suggested that early tool designs focused too heavily on emulating wheel-tool function and porting location, which ultimately hampered quality. For example, the tools were ported such that injection occurred on a large face of the tool, and resin flowed through the thickness ("z-direction") and then turned to flow parallel to the primary plane of the tool/panel. Injection was also being performed manually using a caulk gun, so there was only crude control over injection pressure and rate. Finally, heating was performed in the autoclave, and ESE's experience in the development

of the E2 tool demonstrated the deficiencies of autoclave heating. It became clear that on-tool heating should be implemented with the flat-panel tool.

2020 (Year 1) Efforts

To address these issues, ESE built a new flat-panel tool, referred to as Tool D, in the first quarter of 2020. The new design incorporated better port locations on the edge, more ergonomic features and fasteners using clamps instead of bolts for faster cleaning and operation, and resistive on-tool heating and thermocouples to be controlled by a National Instruments control system. Overall quality was vastly improved by the new port locations but continued to fluctuate as different infusion techniques and fiber-stacking sequences were introduced. Specifically, infusion quality degraded as the fiber volume fraction (Vf) exceeded 50% and off-axis (e.g., 90°) fiber plies were introduced. Several different injection speeds and heating profiles were explored to reduce void content with little success. Though not yet confirmed, "race-tracking" of resin along the edges of the tool and around the center of the panel cavity was also suspected as a possible contributing factor. One experiment in which tacky tape was included on the edges of the outer plies to slow down the race-tracking resulted in improvement.

While running these experiments, ESE also reviewed the composites literature to better understand the fundamental mechanisms of void formation and how they relate to specific flow characteristics and techniques available to reduce void content. Clearly, higher pressure and better control of pressure and flow rate were necessary to further improve panel quality. To meet the demands of RTM, ESE custom-built a resin-metering pump capable of 250 psi and with precision metering down to fractions of a cubic centimeter. Work also began on design and construction of a custom high-precision press with an electromechanical actuator, which would allow the study of different sequences of applying mechanical pressure and actuating our tools—the emphasis being on facilitating very high-precision control with sufficiently high force. Up to this point, the tools had all been standalone, benchtop solutions. However, the higher infusion pressures attempted on Tool D quickly highlighted limitations with the tool: higher mechanical force was required to maintain tool closure, and the fastening system was not designed for such pressures. Longevity and consistency issues of the resistive heating elements also left question about the cause of imperfections.

In the summer of 2020, the high-precision press was completed, along with a further updated tool design, referred to as Tool E, which can now apply the desired mechanical force to accommodate higher infusion pressure while also creating larger panels to yield more testing coupons per panel. The press and tool are shown in Figure II.2.10.1. The tool also features integrated channels to accommodate fluid heating (e.g., pressurized water) provided by a newly installed Regloplas thermolator that is also integrated with the National Instruments control system. The heating system is accompanied by a chiller that facilitates cooling in an expedited and controlled way. Thermal control and evenness are much improved over the resistive heating it replaces. The use of a press to maintain tool closure also permits fewer fasteners for ease of operation. Combined with the controlled cooling functionality afforded by the chiller, the tool assembly time and overall cycle times have shortened drastically. ESE's move to more standard industrial practices have resulted in a leap forward in production speed.

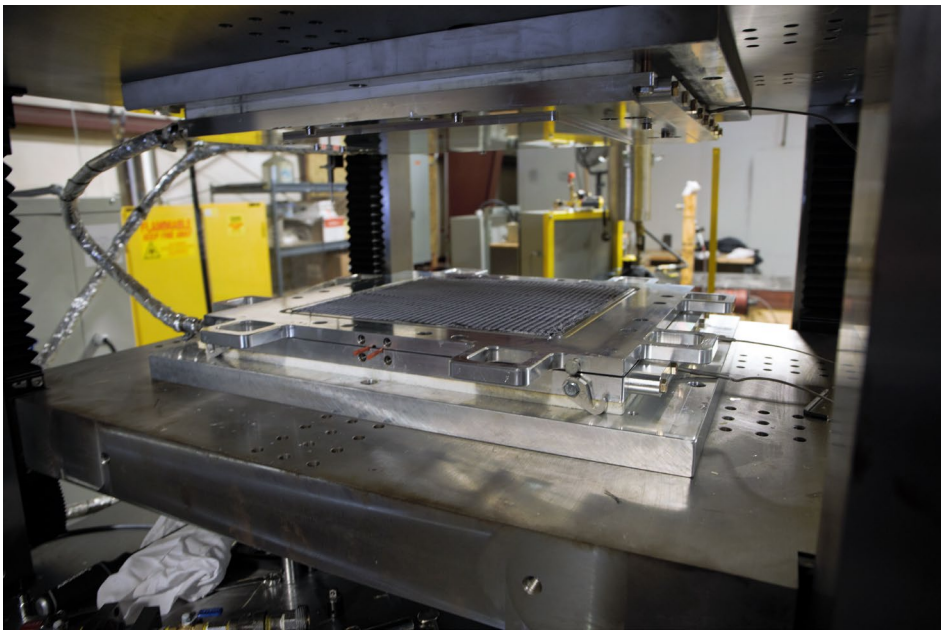

Figure II.2.10.1. Press and tool used to make the flat panels for testing. Source: ESE.

Results from the first batch of panels made using Tool E have been promising, as seen by the test panel in Figure II.2.10.2, albeit at low (e.g., < 50%) Vf thus far. For example, no signs of race-tracking have been observed. ESE is delivering a few of the initial panels to ORNL for some trial testing. However, ORNL has voiced concerns about testing these panels with all 0-degree plies due to the load required and the likelihood of tab or grip failures. ESE's standard panel thickness is 6.8 mm, which allows for an 8-ply (e.g., quasi-isotropic) layup at a Vf = 55% using 24k tow. Thus, ESE is currently working on a design for a 3.4 mm thick version of the tool. Thicker panels will be relegated to flexural testing, shear testing, and fatigue with quasi-isotropic or crossply layups, while the thinner panels will be used for quasistatic testing—and eventually, perhaps, fatigue testing—of unidirectional laminates to establish basic stiffness and strength parameters.

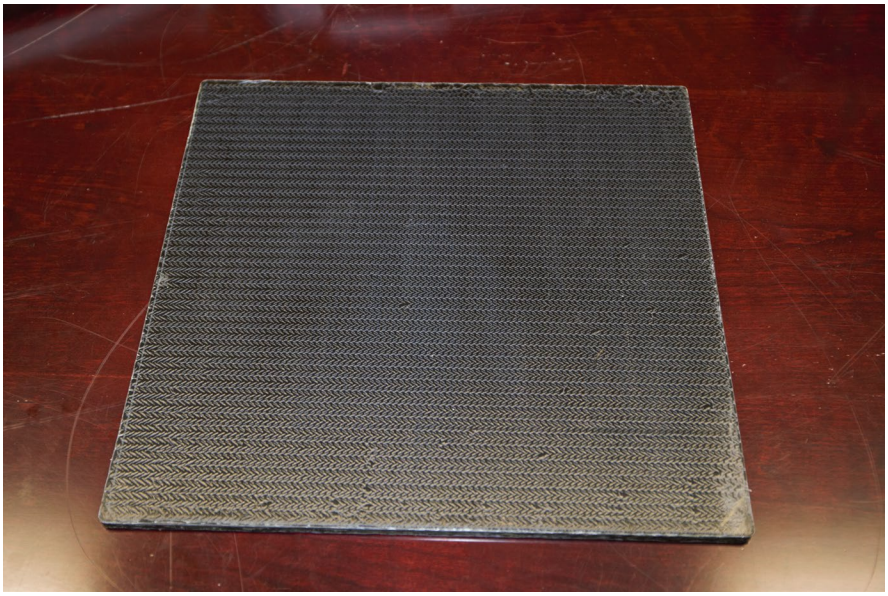

Figure II.2.10.2. Fully made panel for testing and close-up showing fiber architecture and good wet-out of the fibers. Source: ESE.

Conclusions

After trials on prototype tools, ESE has been able to improve flat-panel quality by changing the injection port location, tool sealing, actuation and by increasing injection pressure and control, which was enabled by switching from a standalone benchtop process to manufacturing in a press. Race-tracking of resin along ply boundaries remains a concern, and ESE is adjusting its next tool design to address this issue. Fabrication of 7-mm thick flat panels is being conducted successfully, and the panels are ready for testing at ORNL. ESE plans to begin work on another tool to accommodate a thinner (i.e., 3.4 mm) panel for testing unidirectional $[0]_4$ panels or crossply panels—e.g., $[0/90]_s$. Panels were fabricated and submitted to ORNL for testing in December 2020. As of January 20, 2021, they are being machined and tested using the layout in Figure II.2.10.3. Table II.2.10.1 shows the calculation of the flexure specimen lengths, which vary to obtain shear and longitudinal properties.

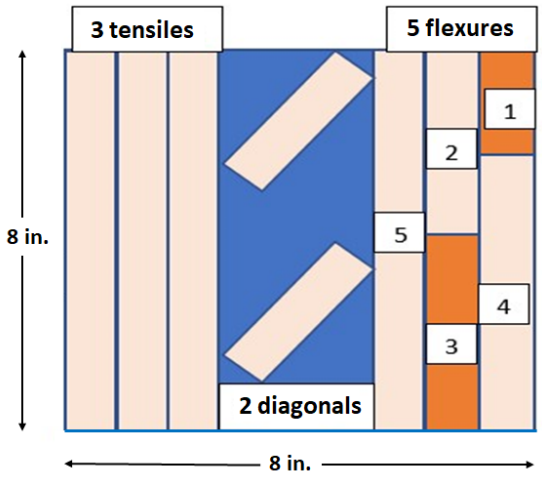

Figure II.2.10.3. Schematic of cutting diagram used to extract tensile and flexural samples from ESE plaques provided to ORNL for testing. Source: ORNL.

Table II.2.10.1. Calculated Flexure Specimen Lengths

Sample No.	Span-to-Thickness Ratio	Thickness, mm	Span, in.	Overhang, in.	Total Length, in.
1	4	7	1.1	.25 (each end)	1.65
2	8	7	2.2	.3	2.8
3	12	7	3.3	.35	4
4	18	7	5	.4	5.8
5	25	7	6.9	.5	7.9

Acknowledgements

The authors would like to thank D. Erdman and R. Lowden at ORNL for their assistance in setting up the testing equipment.

II.2.11 A Novel Manufacturing Process of Lightweight Automotive Seats – Integration of Additive Manufacturing and Reinforced Polymer Composite (Oak Ridge National Laboratory)

Vlastimil Kunc, Principal Investigator
Oak Ridge National Laboratory
1 Bethel Valley Road
Oak Ridge, TN 37831
E-mail: kuncv@ornl.gov

H. Felix Wu, DOE Technology Manager
U.S. Department of Energy
E-mail: felix.wu@ee.doe.gov

Start Date: February 21, 2020 End Date: February 20, 2022
Project Funding: $1,000,000 DOE share: $500,000 Non-DOE share: $500,000

Project Introduction

Developing a thinner, lighter weight seat offers multiple benefits to OEMs in terms of cost-savings from various aspects, including less material usage, more integrated processes, and compliance with Corporate Average Fuel Economy standards. For this reason, OEMs are focused on innovative opportunities for lightweight automotive seats. In this project, a novel manufacturing technology is being developed for a lightweight car seat that involves multiple novel composite manufacturing processes including large-scale AM, discontinuous reinforced composite, AM metal insert attachment, and topology optimization. The car seat back panel will be made with a tailored material microstructure, and hence, a more tailored performance. Design and distribution of the panel reinforcement ribs will be optimized via proven adaptive core optimization technology. The optimizations for the core structure will be based on computational stress analysis to maximize the stiffness and minimize the weight. AM metal inserts for the recliner connection will be integrated to the composite structure during the manufacturing process. All the seat components will be consolidated under pressure to form the final seat geometry in one shot. A database will be generated during the manufacturing process to enhance the quality control system using an artificial intelligence framework.

Objectives

The aim of this project is to develop a novel manufacturing technique to produce lightweight car seats by combining AM and conventional techniques. Note that the scope of the project will be limited to the primary structure of the seat assembly. This does not include any electric motors, sensors, actuators, or seat coverings that represent the bulk of the seat assembly mass. Instead, this project will focus on developing the AM and overmolding methods that not only apply to seat structures but would also be relevant to a broad range of structural applications across all vehicle subsystems. The newly developed materials and processes will allow for the following:

- Reduce the mass of the primary seat structure.
- Allow for new/smart seat designs via topology optimization, which cannot be achieved through any other conventional processing methods.
- Produce seats with improved performance.
- Allow for in line integration of sensing and smart systems through the AM process that will be used for process monitoring. The collected data will then be used within an artificial intelligence framework for discontinuous reinforced composite manufacturing processes in order to optimize processing conditions and part performance.

Approach

An innovative approach for seatback manufacturing to be developed for this project is illustrated in Figure II.2.11.1, which integrates three major manufacturing techniques: (1) Adaptive lattice structure generation; (2) AM preform with controlled deposition direction; and (3) Overmolding on metal inserts.

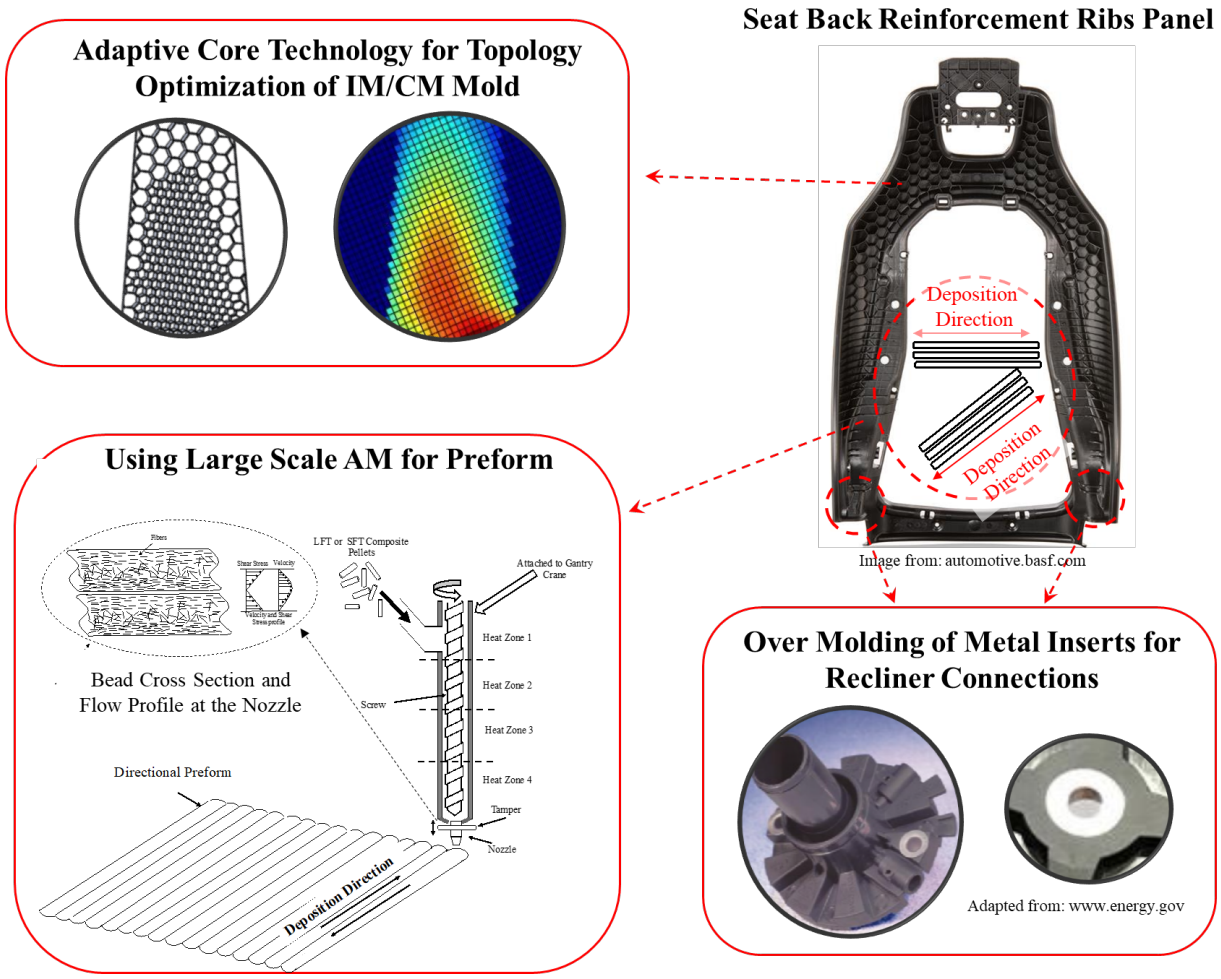

Figure II.2.11.1. An innovative approach for seatback manufacturing that integrates adaptive lattice structure generation, AM preform with controlled deposition direction, and overmolding on metal inserts. Source: ORNL.

Stage I: Topology Optimization of a Seatback Panel, Including Oak Ridge National Laboratory's (ORNL's) Recently Developed Adaptive Lattice Method

- In this stage, the design of the seatback frame is topologically optimized, including ORNL's recently developed adaptive lattice generation method [1]. Using this method, the structure with its lattice densities can be optimized based on a stress applied to the structure. The local density of the lattice cells is determined based on the stress profile. The infill geometry is mathematically generated using a circle packing algorithm.

Stage II: Manufacturing of the Seatback Panel Via Large-Scale AM

- In this stage, a large-scale AM system (i.e., capable of greater than 100 lb/h deposition rate and a size up to 20 ft × 8 ft × 6 ft) is used to form a preform of the seatback panel. The process is highly capable of producing preform with highly aligned fibers at the deposition direction. Optimization and control of the tool path (i.e., deposition direction) allows the fabrication of preforms with tailored microstructure and properties. The system also can be used to deposit multi-material to help reduce the weight of the seat

even further. As an example, the preform can be made from a reinforced thermoplastic for load-bearing areas where foams can be deposited at locations where there are no load-bearing requirements.

Stage III: Overmolding Process (Integration of the Seatback Panel Preform, Molding of the Reinforcement Features, and Placement of the Metal Inserts)

- In this stage, the AM preform manufactured in Stage I is transferred to a compression mold for consolidation under pressure. After placing the preform and the metal inserts for the recliner connection into the mold, the mold is heated up to the molding temperature. The extrusion compression molding process is then used to mold the reinforcement features for the seat. Extruded charges will be strategically placed on the top of the AM preform in the mold and then all components will be consolidated under pressure to form the final seat geometry in one shot.

Results

A car seat experiences multiple loading forces upon crash. A simulation has been performed on the assembly of car seat components for a frontal impact case, and a significant deflection has been observed. In a seatback frame, the safety belt is pulled while the bottom areas of the two frame sides are constraint. Figure II.2.11.2 shows an example of the boundary and load conditions applied to the part. Please note that due to proprietary information restrictions, the seatback image in Figure II.2.11.2 is from a different model made by a different company.

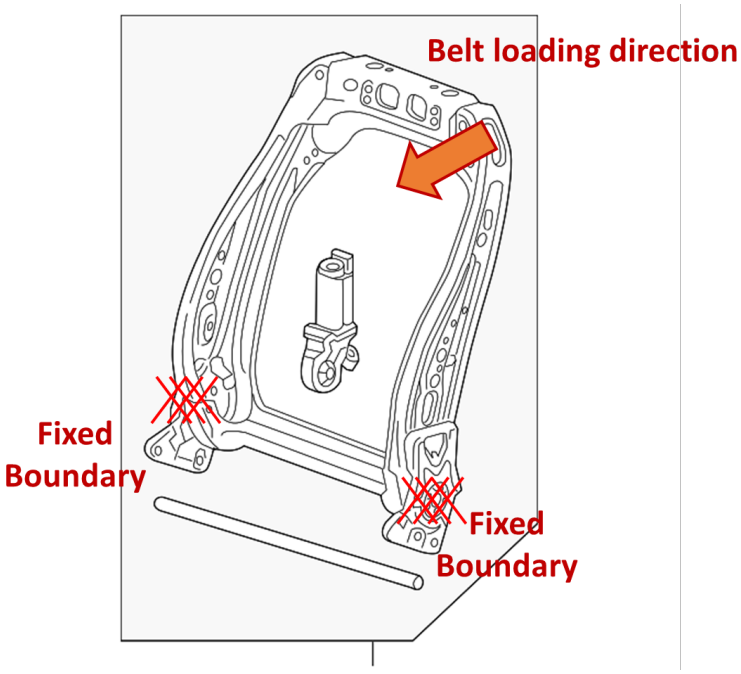

Figure II.2.11.2. Seatback frame and the BCs for a frontal impact. Source: GM. (Note: The original figure used in this work was not used due to proprietary information restrictions. The image used here is from a different model made by another company.)

A design space for the seatback was used for lattice optimization. Using the load and BCs, a finite element method was used to calculate the stress of a design space similar to the image in Figure II.2.11.3(a). The original figure used in this project has been removed due to proprietary information restrictions. A graded lattice design was generated based on the stress profile using ORNL's adaptive lattice generation method and is shown in Figure II.2.11.3(b). A finer lattice corresponds to a high stress area, while a coarse lattice corresponds to a low stress area. Although the adaptive lattice provides higher stiffness than a regular lattice with a uniform cell size, it does not provide enough stiffness for a bending load condition. Therefore, we moved away from an adaptive lattice for the panel design of a seatback.

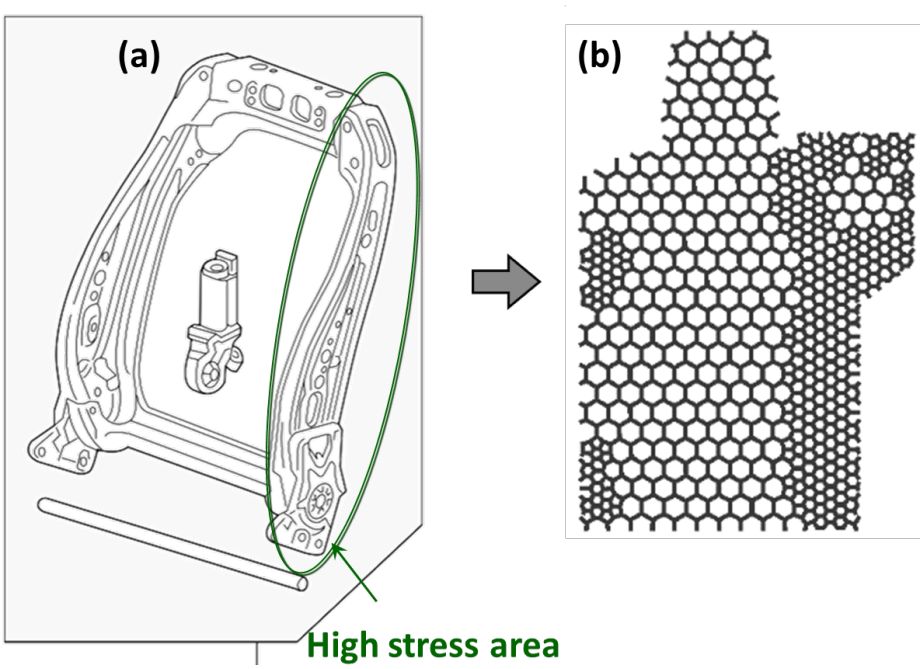

Figure II.2.11.3. (a) The side column where the seat belt is located is a high stress region for a fully solid design space where the frame is not a hollow object but a fully solid part. (b) The graded finer lattice structure for the side column where the seat belt is placed corresponds to a high stress area. The lattice structure does not provide enough bending stiffness for the seatback application. Source: GM/ORNL. (Note: The original image at (a) used in this work has been removed due to proprietary information restrictions. The image shown in (a) is from a different model made by another company.)

Using a topology optimization technique, a seatback structure with a reduced volume was obtained. The topology optimization utilized an iterative process between a finite element method calculation and the removal of volumes where stress levels are lower than the prescribed threshold. The stiffness of the topologically optimized part should remain high for the optimized structure. The results show a significant reduction (> 50%) for most of the locations, except for the left side column that requires the highest stiffness.

The deformation of a composite structure was obtained and compared with a current metal design as shown in Figure II.2.11.4(a) provided a concept of our analysis. As stated previously, the original figure used in this project has been removed due to proprietary information restrictions. The composite seatback in Figure II.2.11.4(b) shows a significantly larger deformation even if the entire volume of the design space was filled. Therefore, we have replaced a small portion in the left side column of the design space with a metal insert to increase the stiffness as shown in Figure II.2.11.4(c). If the seatback is made of a composite alone, the stiffness decreases significantly as compared to the metal frame, which necessitates the use of a metal insert. Where a simple metal insert is used, the stiffness increases by three times. A further optimization of the insert design is required.

The first design of the metal insert was a simple L-shape with a uniform thickness. With the metal insert, the stiffness increased to three times as compared to the seatback made of the composite alone. Nylon reinforced with 30 wt%. short CFs was used as the composite material for our analysis. This result indicates the necessity of further investigation/optimization of the metal insert. After multiple iterations between the design modifications and stress analyses/deflection predictions, an optimized design of a metal part was obtained as shown in Figure II.2.11.5. This optimized metal design results in only a small deflection while the current design has a large deflection for a similar weight, which provides a rough concept of the current and optimized designs as well as their corresponding weights and deflections.

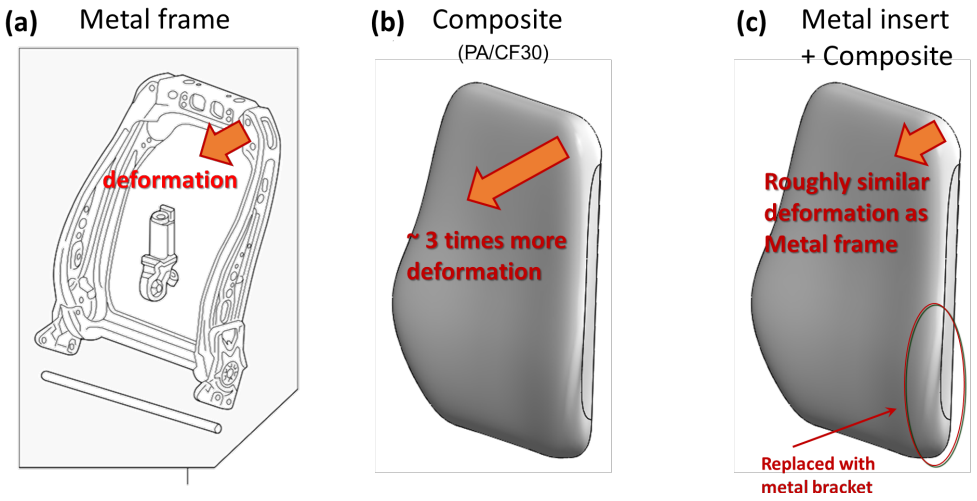

Figure II.2.11.4. Deformation of the seatback made of a metal (a) in comparison with a composite material alone (b) and a combination of a composite material and a metal insert (c). The designs have not been optimized in this stage. Sources: (a) GM; (b) and (c) GrabCAD.

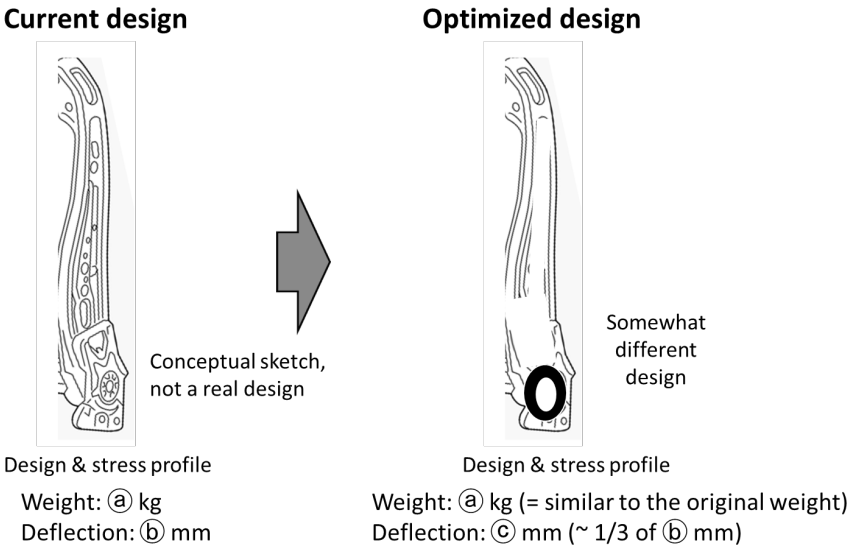

Figure II.2.11.5. A conceptual illustration of the current design and optimized design for the left side column of the frame where both designs have a similar weight, but the optimized design shows much less deflection as compared to the original design. Source: GM. (Note: The original figure and the exact numbers have been removed due to proprietary information restrictions. The image used here is from a different model made by another company.)

For composite overmolding onto the metal insert, the design was modified for better bonding between the metal portion and the composite portion. The new design mainly consists of three major parts. The first is the unitape part which is made of a polymer reinforced with unidirectional fibers and placed in a mold. The second is a long fiber thermoplastic made from AM preform. The preform design will be sliced with a controlled toolpath for high stiffness and 3D printed using the Big Area Additive Manufacturing system at ORNL. The third is a 3D-printed metal insert, which has a mesh structure on one side for strong mechanical bonding between the metal and the thermoplastic AM preform. This concept was submitted as an invention disclosure previously. A conceptual illustration (the original design is proprietary) of the optimized design for the composite overmolding onto the metal insert is shown in Figure II.2.11.6. The metal insert will be 3D-printed with a mesh structure on one side for better mechanical bonding between the metal and thermoplastic.

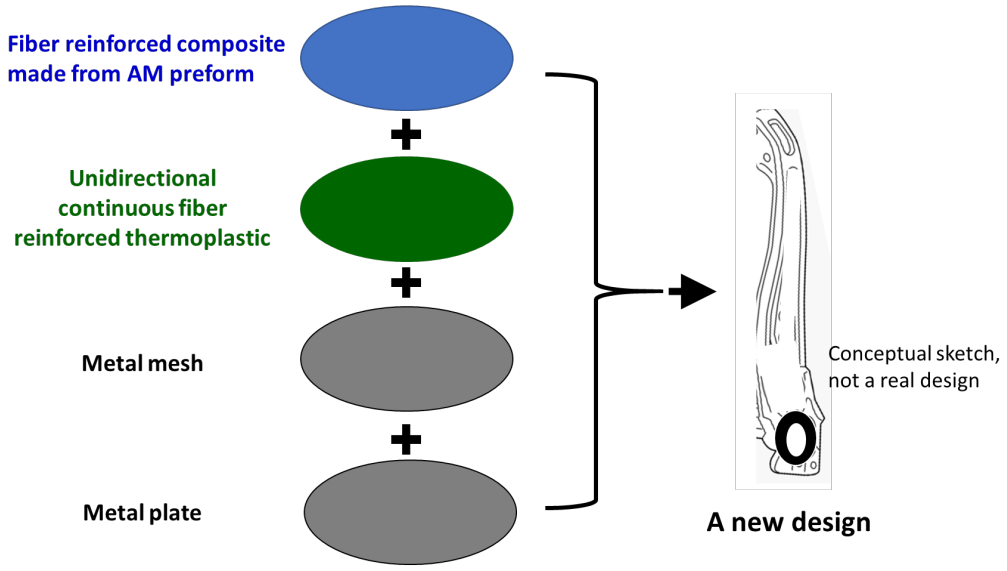

Figure II.2.11.6. The conceptual design of the iindividual components. The polymer composite will be overmolded with the metal insert and consists of two parts: a long fiber thermoplastic made from the AM preform and the unitapes. Source: ORNL.

Conclusions

In FY 2020, our team proposed a new design for a seatback subcomponent that integrates multiple novel manufacturing technologies, including metal 3D printing, polymer composite 3D printing to make a preform with a tailored directionality, and composite overmolding. Based on our computational simulations, this design shows far superior stiffness (e.g., larger than two times) than can be achieved with the current metal frame design.

We initially proposed a graded lattice design for the panel of a seatback. However, the lattice structure was not suitable for the bending conditions of a seatback. A classical topology optimization was used for a composite seatback design space. However, the stiffness from the seatback made of just the polymer composite alone showed much less stiffness than can be achieved by the current metal frame. Therefore, a metal insert with an AM mesh structure specifically designed for better bonding with the polymer composite was introduced, which showed roughly three times higher stiffness. The material for the metal insert is a maraging steel.

The new design, which is a significant improvement in performance over the conventional design, will demonstrate and verify a new manufacturing approach for integrating multiple novel manufacturing techniques. We will continue this project in FY 2021 and fabricate test coupons for mechanical performance measurement and further modify the design from the lessons learned during the experiments.

References

1. Kim, S., X. Chen, G. Dreifus, J. Lindahl, I. Kang, J.-H. Kim, M. Selim, D. Nuttall, A. Messing, A. Nycz, R. Minneci, K. Stephenson, J. C. Bowers, B. Braswell, R. B. Pipes, A. A. Hassen, and V. Kunc, 2017, "An integrated design approach for infill patterning of fused deposition modeling and its application to an airfoil," *Society for the Advancement of Material and Process Engineering (SAMPE) Conference*, 22–25 May 2017, Seattle, WA, USA.

Acknowledgements

This project was performed in collaboration with Ford Motor Company.

II.3 Multi-Material Joining

II.3.1 A Multiscale Computational Platform for Predictive Modeling of Corrosion in Al-Steel Joints (University of Michigan)

Mihaela Banu, Principal Investigator (2019–2021)
University of Michigan
2350 Hayward Street
Ann Arbor, MI, 48109
E-mail: mbanu@umich.edu

S. Jack Hu, Principal Investigator (2018–2019)
University of Michigan
2350 Hayward Street
Ann Arbor, MI, 48109
E-mail: jackhu@umich.edu

Sarah Kleinbaum, DOE Technology Manager
U.S. Department of Energy
E-mail: sarah.kleinbaum@ee.doe.gov

Start Date: January 24, 2019 End Date: December 31, 2021
Project Funding: $1,978,423 DOE share: $1,978,423 Non-DOE share: 0

Project Introduction

The goal of this project is to develop multiscale models for predicting the location and extent of corrosion and the impact of such corrosion on the performance of dissimilar materials joints. The selected joining technologies are RSW, self-piercing riveting (SPR), and rivet-welding that are applied to coupons made of AA 6022, 2.0-mm thick, and hot-dipped galvanized (HDG) high-strength low alloy (HSLA) 340 steel, 1.2-mm thick. The performance models will include joint strength and fatigue life predictions. These models will be validated by experiments with the goal of achieving strength and fatigue prediction accuracy within 10% of experiments.

Objectives

To achieve the project goal, three objectives are considered: (1) to develop the models at the microscale level starting from DFT and simulating the initiation of the corrosion; (2) to develop corrosion mesoscopic models by bridging the scales from atom to grain structure, with the mesoscale material properties being homogenized using uncertainty quantification; and (3) to develop finite element performance and fatigue life predictions by integrating models at different scales. These models will be validated as they are developed.

Approach

The multiscale models will integrate (1) the atomic-phase level modeling with new high-throughput DFT and calculation of phase diagram (CALPHAD) simulations; (2) the mesoscopic level modeling of corrosion evolution with a finite element model, material property homogenization, and uncertainty quantification; (3) the macro-level modeling of joint performance with experimental validations; and (4) the integrations of these models into a computational platform. The models will be validated by the experiments with the goal of achieving an accuracy in strength and fatigue life prediction within 10% of the experiments.

Results

Advancement in Understanding Corrosion Mechanism in Dissimilar Material Joints

The corrosion behavior of SPR and RSW joints were evaluated by cyclic corrosion testing following the General Motors GMW14872 standard, which reproduces the environmental conditions where a vehicle is exposed. One cycle includes three phases: (1) the Ambient Stage, consisting of eight hours of salt spray; (2) the Humid Stage, consisting of eight hours of humidity; and (3) the Dry-off Stage, consisting of eight hours of drying off. The joined SPR and RSW specimens were placed in a cyclic corrosion chamber at GM for induced corrosion at different durations: 1 cycle, 7 cycles, 14 cycles, 26 cycles, 48 cycles, 72 cycles, and 104 cycles. Based on the experimental observations, the corrosion mechanisms of SPR and RSW joints can be concluded as shown in Figure II.3.1.1(a) and (b), respectively.

Common corrosion development is observed in both joints. Specifically, some white corrosion product starts to appear and aggregate on the steel surface starting with the first cycle, followed by brown corrosion products that are apparent after the 14th cycle. As the corrosion duration increases, the layer of brown corrosion products become thicker. On the other hand, the Al becomes dull gray in the first cycle, demonstrating that the Al has been oxidized and is then covered by some white corrosion product observed after 14 cycles. The corrosion products on the surfaces were examined by performing energy-dispersive x-ray analysis. According to the mapping results, the white products on the Al surface mainly consist of Zn and Al oxides. While the brown products are mainly comprised of Fe and Zn oxides. Hence, the white corrosion product on the steel surface initially is the Zn oxide, which is the result of the HDG corrosion. When the steel substrate was exposed and corroded during the 14 cycles, the brown Fe oxides were generated. Zn and Fe oxides appeared on the Al surface in longer corrosion exposure, which comes from the steel surface since the joints are leaning on the holder in the test chamber with the steel on the top. Moreover, within the Al-steel overlapping area, it was observed that the Al is corroded and the most damaged zone is at the overlap end of the Al while the steel is protected.

After 48 cycles, pits start to be observed at the overlap end in the Al. As the corrosion proceeds, the pitted area spreads into the joints and, by 104 cycles, the whole piece of Al at the overlapping area becomes severely porous. According to the open-circuit potential measurements, the electrochemical potential of HDG is -1.03 V_{SCE}, AA 6022 is -0.74 V_{SCE}, and bare HSLA 340 is -0.70 V_{SCE}. Hence, at the overlapping area, HDG is corroded first when the salt solution penetrates the crevice. When HSLA 340 is exposed and the salt solution is present, a galvanic cell is generated, AA 6022 is corroded, but HSLA 340 is protected. A large number of pits in AA 6022 will significantly decrease the strength of the joint and stiffness.

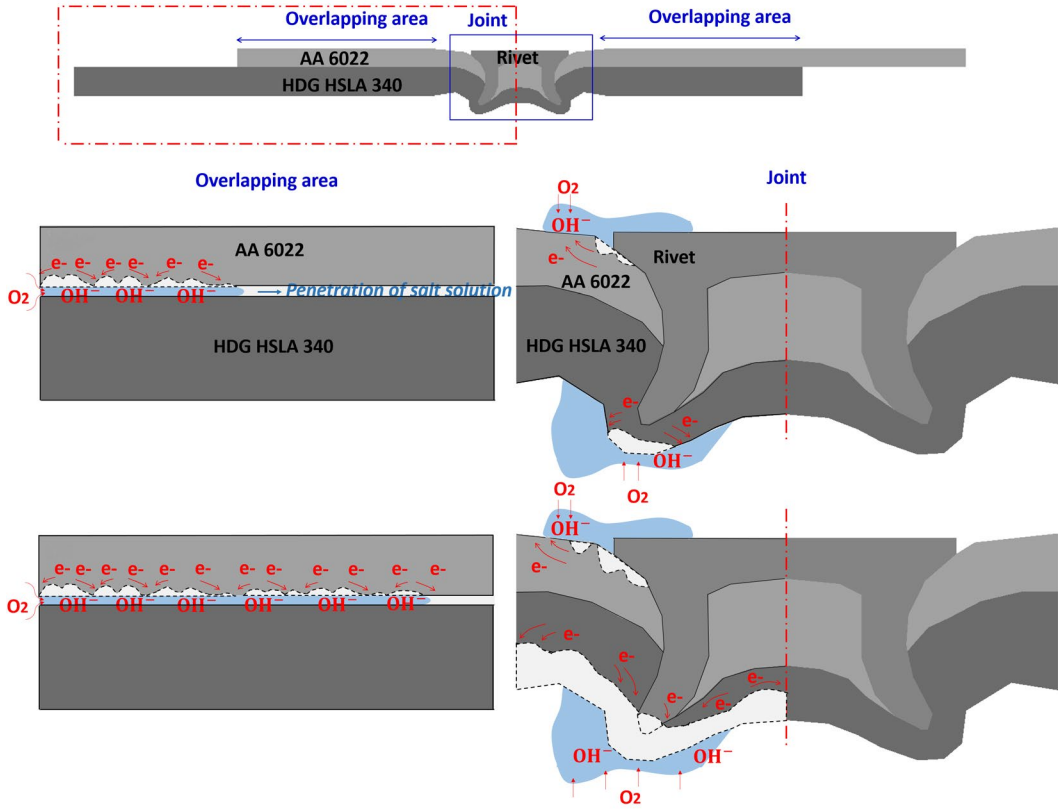

(a)

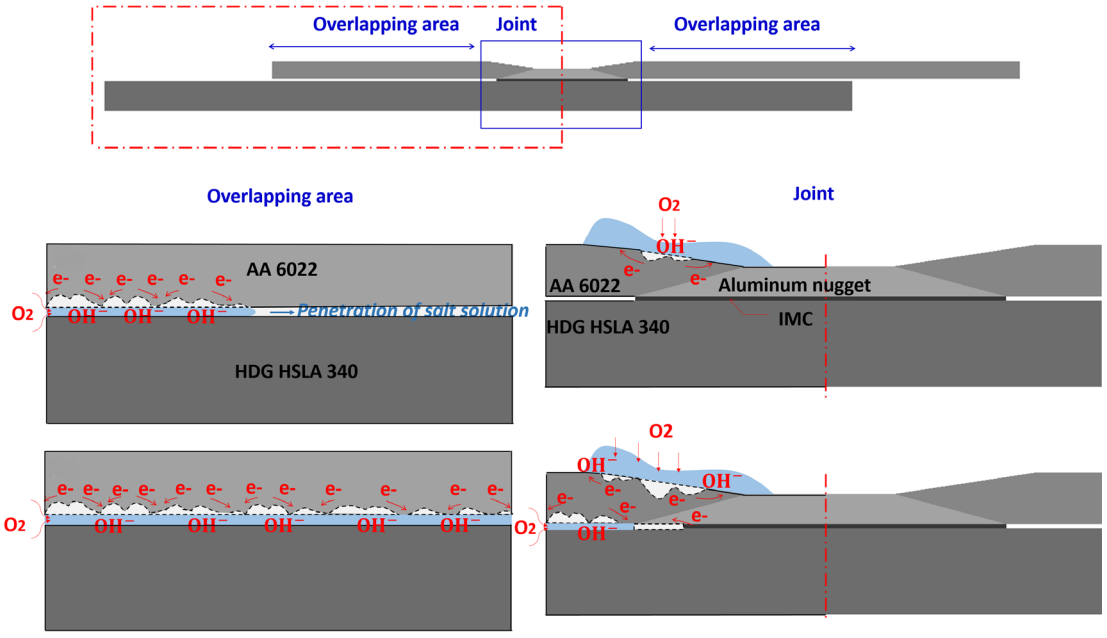

(b)

Figure II.3.1.1. The schematic of the corrosion mechanism of: (a) SPR Al-steel joints (top) with slight corrosion (26–72 cycles) (middle) and severe corrosion (≥ 104 cycles) (bottom); and (b) RSW Al-steel joints (top) with slight corrosion (14–48 cycles) (middle) and severe corrosion (72–104 cycles) (bottom). Source: University of Michigan.

Based on these microscopic investigations, the corrosion evolution in the SPR and RSW joints can be explained as follows:

- **For the SPR joints**, galvanic corrosion occurs at the Al-rivet coupling and Al-steel overlapping areas by attacking the AA 6022. The corrosion leaves a large number of pits on the AA 6022 surface which significantly affect the stiffness of the specimen. With slight corrosion (~72 cycles), the strength does not decrease since the interlock has not been affected; it occurs only under severe corrosion (≥104 cycles) in which the rivet will be exposed and corroded. As a result, the strength will decrease significantly.
- **For the RSW joints**, corrosion is observed on the rings of AA 6022 (e.g., indentation area). However, as corrosion proceeds, corrosion products on the surface prevent the salt solution from penetrating into the remaining AA 6022 (e.g., passive film). The detrimental corrosion is the galvanic corrosion that occurs at the Al-steel faying interface. The solution penetrates the overlapping area by first attacking the AA 6022 and then the intermetallic compound (IMC) layer. Strength decreases significantly when the IMC is corroded. Just like the SPR joints, pits are formed in AA 6022 at the overlapping area which results in the decrease of the stiffness of the joints. Since the crevice at the Al-steel interface is much larger, galvanic corrosion in the RSW joints is more severe than in the SPR joints; hence, the stiffness reduction is higher. Overall, SPR performs better at delaying the corrosion attack within the joints; hence, it retains the strength, stiffness, and energy absorbed until failure. Fundamental understanding of corrosion mechanisms in SPR and RSW enable an accurate formulation of the physics-based, data-driven approach used in building the multiscale models for prediction of the joining performance.

Prediction of the Corrosion Products and Their Physical and Mechanical Properties

At the atomic-scale: Models were developed for prediction of the IMCs formed during the joining process and their further transformation into corrosion products in the presence of electrolyte. A material database was created with the predicted results including: (1) IMCs formed during welding and corrosion of the Al-Fe joints; (2) elastic properties of all possible Al-Fe compounds; and (3) single crystal stress-strain curves of fcc-Al and bcc-Fe. Figure II.3.1.2 summarizes the material database content. The legend in the bottom left corner indicates the meaning of the Al inside, Al outside, Fe inside, and Fe outside referring to the material and the side of the fractured lap-shear coupons. The bottom right corner indicates the elastic properties of the intermetallic compounds. The error of prediction on the intermetallic compounds and the corrosion products is < 5% comparing with the experimental analysis done by Penn State University through scanning electronic microscopy, high-resolution TEM, and x-ray powder diffraction [1],[2].

By considering thermodynamic and kinetic effects, the corrosion products for a different number of corrosion cycles was predicted, which are summarized in Figure II.3.1.3.

In addition to the proposed DFT calculations and CALPHAD modeling to develop materials property databases, ML predictions were performed for the properties of interest. Additional materials properties were added to the database including: (1) stacking fault energies of dilute Al alloys; and (2) ideal shear strengths for dilute Al-based and dilute Fe-based alloys. The ideal shear strength together with elastic properties are key parameters to predict the critical resolved shear stress [3]. The SFE and ideal shear strengths are key parameters in defining the plastic behavior of the corrosion products —capital for modeling their behavior at the macroscale level. Figure II.3.1.4 summarizes the SFE of the corrosion products of Al-Fe joints in the coupled and uncoupled regions based on DFT calculations or ML. The ML values are labeled with a superscript * with the standard deviations in parentheses. The unperformed predictions are marked by “Null” or empty; and the green (low), yellow (middle), and red (high) color scale is used to mark the $\Delta\gamma$SFE data. For DFT-based first principles calculations of $Pt_{23}X$, the ‘pv’ or ‘sv’ after an atomic symbol X indicate that the p or s states are treated as valence states, respectively.

Cycles	Al Inside	Al Outside	Fe Inside	Fe Outside
1	Al	$Al(OH)_3$ $Ca_4Al_2(CO_3)(OH)_{12}.(H_2O)_5$	Zn	$Zn_5(OH)_8Cl_2(H_2O)$ Zn
7	$Al(OH)_3$ $Ca_4Al_2(CO_3)(OH)_{12}.(H_2O)_5$	$Al(OH)_3$ $Ca_4Al_2(CO_3)(OH)_{12}.(H_2O)_5$	$Fe_6(OH)_{12}(CO_3)$ ZnO $Zn_5(CO_3)_2(OH)_6$ $Zn_5(OH)_8Cl_2(H_2O)$	$Fe_6(OH)_{12}(CO_3)$ $Zn_5(CO_3)_2(OH)_6$ $Zn_5(OH)_8Cl_2(H_2O)$ ZnO
14	$Al(OH)_3$ $Ca_4Al_2(CO_3)(OH)_{12}.(H_2O)_5$	$Al(OH)_3$ $Ca_4Al_2(CO_3)(OH)_{12}.(H_2O)_5$	$Fe_6(OH)_{12}(CO_3)$ ZnO $Zn_5(CO_3)_2(OH)_6$ $Zn_5(OH)_8Cl_2(H_2O)$	$Fe_6(OH)_{12}(CO_3)$ $Zn_5(CO_3)_2(OH)_6$ $Zn_5(OH)_8Cl_2(H_2O)$ ZnO
26	$Al(OH)_3$ $Ca_4Al_2(CO_3)(OH)_{12}.(H_2O)_5$	$Al(OH)_3$ $Ca_4Al_2(CO_3)(OH)_{12}.(H_2O)_5$	$Fe_6(OH)_{12}(CO_3)$ ZnO $Zn_5(CO_3)_2(OH)_6$ $Zn_5(OH)_8Cl_2(H_2O)$	Fe_3O_4 ZnO γ–FeO(OH)
48	$Al(OH)_3$ $Ca_4Al_2(CO_3)(OH)_{12}.(H_2O)_5$	$Al(OH)_3$ $Ca_4Al_2(CO_3)(OH)_{12}.(H_2O)_5$	$Fe_6(OH)_{12}(CO_3)$ ZnO $Zn_5(CO_3)_2(OH)_6$	Fe_3O_4 ZnO γ–FeO(OH) α–FeO(OH)
72	$Al(OH)_3$ $Ca_4Al_2(CO_3)(OH)_{12}.(H_2O)_5$	$Al(OH)_3$ $CaCO_3$	$Fe_6(OH)_{12}(CO_3)$ ZnO $Zn_5(CO_3)_2(OH)_6$ Fe_3O_4	Fe_3O_4 ZnO γ–FeO(OH) α–FeO(OH)
104	$Al(OH)_3$ $Ca_4Al_2(CO_3)(OH)_{12}.(H_2O)_5$	$CaCO_3$ $Al(OH)_3$ Al_2O_3	$Fe_6(OH)_{12}(CO_3)$ ZnO Fe_3O_4	Fe_3O_4 ZnO γ–FeO(OH) α–FeO(OH)

(a)

Cycles	Al Inside	Al Outside	Fe Inside	Fe Outside
1	Uncorroded	Al	$Zn_5(OH)_8Cl_2(H_2O)$	ZnO $Zn_5(CO_3)_2(OH)_6$ $Zn_5(OH)_8Cl_2(H_2O)$ Zn
7	Uncorroded	$Al(OH)_3$ $Ca_4Al_2(CO_3)(OH)_{12}.(H_2O)_5$	$Fe_6(OH)_{12}(CO_3)$ ZnO $Zn_5(CO_3)_2(OH)_6$ $Zn_5(OH)_8Cl_2(H_2O)$ Zn	$Fe_6(OH)_{12}(CO_3)$ $Zn_5(CO_3)_2(OH)_6$ $Zn_5(OH)_8Cl_2(H_2O)$ ZnO
14	Uncorroded	$Al(OH)_3$ $Ca_4Al_2(CO3)(OH)_{12}.(H_2O)_5$	$Fe_6(OH)_{12}(CO_3)$ ZnO $Zn_5(CO_3)_2(OH)_6$ $Zn_5(OH)_8Cl_2(H_2O)$	$Fe_6(OH)_{12}(CO_3)$ $Zn_5(CO_3)_2(OH)_6$ $Zn_5(OH)_8Cl_2(H_2O)$ ZnO
26	Uncorroded	$Al(OH)_3$ $Ca_4Al_2(CO3)(OH)_{12}.(H_2O)_5$	$Fe_6(OH)_{12}(CO_3)$ ZnO $Zn_5(CO_3)_2(OH)_6$ $Zn_5(OH)_8Cl_2(H_2O)$	Fe_3O_4 ZnO γ-FeO(OH)
48	Uncorroded	$Al(OH)_3$ $Ca_4Al_2(CO3)(OH)_{12}.(H_2O)_5$	$Fe_6(OH)_{12}(CO_3)$ ZnO $Zn_5(CO_3)_2(OH)_6$	Fe_3O_4 ZnO γ-FeO(OH) α-FeO(OH)
72	Uncorroded	$Al(OH)_3$ $Ca_4Al_2(CO3)(OH)_{12}.(H_2O)_5$	$Fe_6(OH)_{12}(CO_3)$ ZnO $Zn_5(CO_3)_2(OH)_6$	Fe_3O_4 ZnO γ-FeO(OH) α-FeO(OH)

(b)

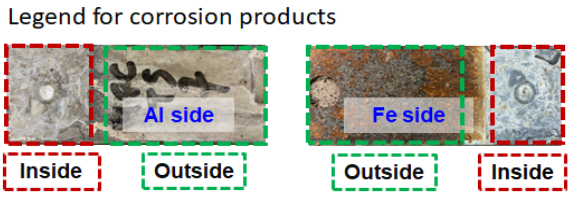

Predicted elastic properties:
B_0 - Bulk Modulus (GPa)
G_0 - Shear Modulus (GPa)
Y_0 - Young Modulus (GPa)
B_0/G_0 (>1.75 for ductile materials)
Poisson ratio
A^U- Anisotropic index (0 for isotropic single crystals)

(c)

IMCs	B_0	G_0	Y_0	Poisson	B_0/G_0	A^u
Al	77.8	20.9	57.5	0.377	3.73	0.329
	79	29	78	0.34		
Al_6Fe	106.6	53.0	136.4	0.287	2.01	0.694
$Al_{13}Fe_4$	125.6	76.7	191.2	0.247	1.64	0.163
Al_8Fe_5	141.8	73.3	187.6	0.279	1.93	0.001
Al_2Fe ($MoSi_2$-type)	154.7	115.8	278.0	0.201	1.34	0.812
Al_2Fe (structure 1)	134.3	79.8	199.8	0.252	1.68	0.147
Al_2Fe (structure 2)	136.9	83.3	207.8	0.247	1.64	0.134
AlFe	184.0	102.5	259.3	0.265	1.79	0.951
Al_5Fe_2 (structure 1)	132.6	87.8	215.8	0.229	1.51	0.177
Al_5Fe_2 (USPEX)	137.0	83.7	208.6	0.247	1.64	0.664
$AlFe_3$ (structure 1)	188.3	56.5	154.1	0.367	3.33	11.04
$AlFe_3$ (structure 2)	197.2	81.0	213.7	0.321	2.43	3.343
Fe	180.6	76.5	201.1	0.315	2.36	0.196
	173	87	223	0.29		

(d)

Figure II.3.1.2. The material database with 90% common material components in blue lettering for: (a) RSW and (b) SPR. Material database with predicted intermetallic compounds for: (c) SPR and (d) RSW joints and predicted elastic properties. Source: Penn State University.

Fe coupled	a	b	c	d	e	f	g	h	Al coupled	i	j	k	l
1	x								1	x			
7		x	x	x	x				7		x	x	
14		x	x	x	x				14		x	x	
26		x	x	x	x				26		x	x	
48		x	x	x					48		x	x	
72		x	x	x		x			72		x	x	
104		x	x			x			104		x	x	
Fe uncoupled									**Al uncoupled**				
1	x				x				1		x	x	
7		x	x	x	x				7		x	x	
14		x	x	x	x				14		x	x	
26			x			x	x		26		x	x	
48			x			x	x		48		x	x	
72			x			x	x	x	72		x		
104			x			x	x	x	104		x		x

Legends: a:Zn, b:$Fe_2(OH)_2(CO_3)$, c:ZnO, d:$Zn_5(CO_3)_2(OH)_6$, e:$Zn_5(OH)_8Cl_2(H_2O)$, f:Fe_3O_4, g:γ- FeOOH, h:α-FeOOH i:Al, j: $Al(OH)_3$, k: $Ca_4Al_2(CO_3)(OH)_{12}(H_2O)_5$, l: Al_2O_3

(a)

Fe coupled	a	b	c	d	e	f	g	h	Al coupled	i	j	k	l
1	x				x				1	x			
7		x	x	x	x				7	x			
14		x	x	x	x				14	x			
26		x	x	x	x				26	x			
48		x	x	x					48	x			
72		x	x	x					72		x	x	
104		x	x			x			104		x	x	
Fe uncoupled									**Al uncoupled**				
1	x		x	x	x				1	x			
7		x	x	x	x				7		x	x	
14		x	x	x	x				14		x	x	
26)			x			x	x		26		x	x	
48			x			x	x		48		x	x	
72			x			x	x	x	72		x	x	
104			x			x	x	x	104		x		x

Legends: a:Zn, b:$Fe_2(OH)_2(CO_3)$, c:ZnO, d:$Zn_5(CO_3)_2(OH)_6$, e:$Zn_5(OH)_8Cl_2(H_2O)$, f:Fe_3O_4, g:γ- FeOOH, h:α-FeOOH i:Al, j: $Al(OH)_3$, k: $Ca_4Al_2(CO_3)(OH)_{12}(H_2O)_5$, l: Al_2O_3

(b)

Figure II.3.1.3. Material databases with predicted corrosion products (blue if they can be formed) for the Fe coupled and uncoupled regions and the Al coupled and uncoupled regions under different corrosion cycles (indicated by integer numbers) for: (a) RSW joints; and (b) SPR joints. Source: Penn State University.

Li	Be											B	C
-2	33												
Null	Null												
Null	Null												
Na	Mg											Al	Si
-52	-8	←			$\Delta\gamma_{SFE}$ of $Al_{23}X$ from DFT or ML						→	0.0	-22
Null	-12* (23)	←			$\Delta\gamma_{SFE}$ of $Ni_{23}X$ from DFT or ML						→	-28	-27
Null	-6* (28)	←			$\Delta\gamma_{SFE}$ of $Pt_{23}X$ from DFT or ML						→	-15	-35
K	Ca	Sc_sv	Ti_pv	V_pv	Cr_pv	Mn_pv	Fe_pv	Co	Ni_pv	Cu_pv	Zn	Ga	Ge
-134	-66	-75	-73	-59	7	44	44	83	55	27	2	-19	-37
Null	-75* (2)	-74	-65	-70	-42	-24	-27	-21	0	-16	-23	Null	Null
Null	-69* (7)	-63	-60	-66	-19	-5	5	2	22	18	-5	Null	Null
Rb	Sr	Y_sv	Zr_sv	Nb_pv	Mo_pv	Tc_pv	Ru_pv	Rh_pv	Pd	Ag	Cd	In	Sn
	-146	Null	-114	-96* (7)	-64* (15)	-29* (12)	-17* (14)	12* (12)	35* (2)	15	-14	-36	-58
	Null	-106	-95	-92	-94	-80	-54	-29	-13	-31* (8)	Null	Null	Null
	Null	-122	-102	-105	-92	-43	-9	6	-7	-27	Null	Null	Null
Cs	Ba	La	Hf_pv	Ta_pv	W_pv	Re_pv	Os_pv	Ir	Pt	Au	Hg	Tl	Pb
		-191	-98	-94* (2)	-73* (5)	-41* (13)	-14* (13)	13* (5)	25* (1)	-2* (2)			-76
		Null	-84	-82	-88	-85	-60	-34	-9	-26* (3)			Null
		Null	-87	-98	-104	-61	-17	11	0	-26			Null

Figure II.3.1.4. Predicted values of relative $\Delta\gamma$SFE (mJ/m^2) in dilute $Al_{23}X$, $Ni_{23}X$, and $Pt_{23}X$ with respect to the values γSFE of Al, Ni, and Pt, respectively, by DFT-based calculations or ML. Source: Penn State University.

Prediction of the Corrosion Evolution and Material Loss

At the mesoscale level: Finite element (FE) models are used to study corrosion in the Al-steel joints and the evolution of the galvanic/crevice corrosion with the implementation of crystal microstructure of the anode (Al) and the precipitation of the corrosion product ($Al(OH)_3$). Based on the previously developed and partially validated model [2], the influences of various geometric and environmental couplings on the corrosion progression and material loss were studied. The mesoscale models are developed for prediction of the corrosion evolution in the joints and adjacent areas. The models include the effects of couplings in various geometric and environmental factors, such as: (1) uneven distribution of the electrolyte; (2) effects of roughness of Al coupon; (3) effects of crevice distance; (4) effects of Al crystal microstructure; and (5) synergetic effects of the combinations of couplings.

Thus, dissolution of metal (e.g., electrochemical submodel) and crack propagation (e.g., mechanical submodel) were coupled and simulated via the phase-field approach. The mesoscopic corrosion models bridge the atomistic model with the continuum scale models while taking accurate DFT calculations as the model inputs. The mesoscopic modeling accuracy for corrosion initiation and evolution was improved by modeling stress corrosion cracks (SCC) and grain microstructure obtained by EBSD. SCC modeling combines the slip dissolution model with a modified phase-field model, decohesion model based on H embrittlement mechanism, and a peridynamics model. The FE model is combined with data-driven models (e.g., Principal Component Analysis and Support Vector Machine - Python library RiskPy), deep learning and Sysweld—a commercial software for welding simulation. The results of the corrosion prediction at the mesoscale level for SPR joints is presented in Figure II.3.1.5. Two cross-section planes were used for measuring the mass loss surrounding the rivet with respect to the coupon position in the corrosion chamber, as shown in Figure II.3.1.5(a). The electrolyte was sprayed from the top of the chamber. The cross-sections for validation of the corrosion prediction with the experiments were designated: L-left, R-right, T-top, and B-Bottom. Prediction of the mass loss for L, R, T, and B cross-sections considering phase-field and grain microstructure determined using EBSD analysis are shown in Figure II.3.1.5(b). Quantification of the material loss in the experiments and simulation are compared in Figure II.3.1.5(c).

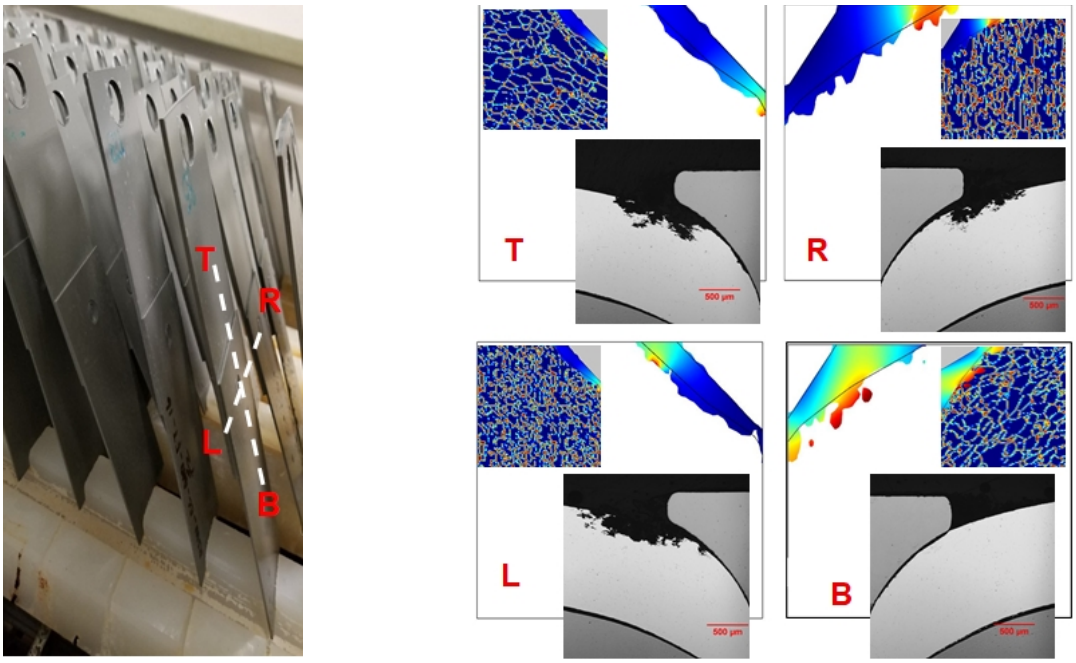

Figure II.3.1.5. Prediction of the corrosion evolution and material loss based on mesoscale modeling for SPR joints. (a) Cross-section planes for measuring the mass loss surrounding the rivet. (b) Prediction of the mass loss for different cross-sections. (c) Comparison of experimental and simulated material loss. Source: Simulation - University of Illinois Urbana-Champaign, Experiments - General Motors and University of Michigan.

A similar approach was considered for modeling the corrosion initiation and evolution in RSW joints. Because of the degradation of materials caused by corrosion, SCC crack propagation is significantly faster than the pure crack or pure corrosion case. However, the considerations of the microstructure led to improved prediction of the corrosion propagation because the pattern of the microstructure influences the crack trajectory. This model now has the capacity to simulate the type of microstructure that will be needed for a delayed corrosion growth, which can become an important design criterion for assembled multi-material parts. Thus, corrosion rates representing the speed of material loss with the number of the corrosion cycles were predicted using the same mesoscale model. As shown in Figure II.3.1.6, predicted results agree with the experimentally determined values and they are < 5% error comparing with the experiments. The experimental mass loss was calculated based on the SEM of the joints cross-sections and quantified using Image J software.

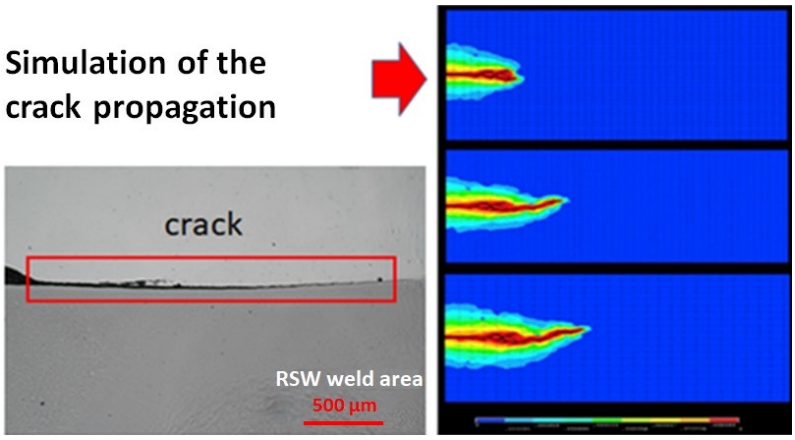

(a)

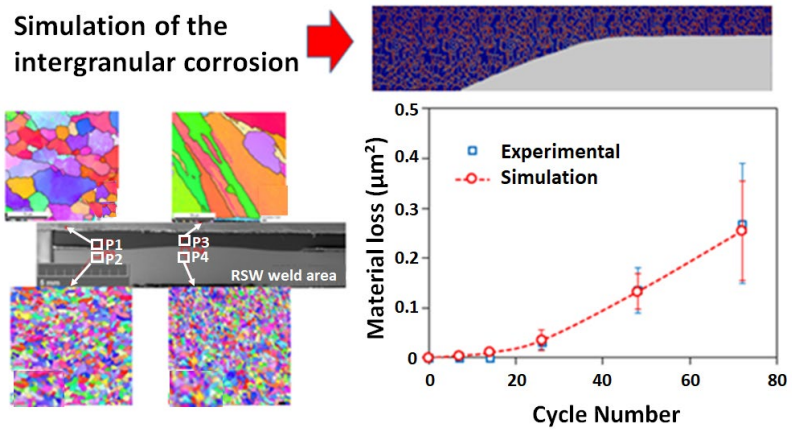

(b)

Figure II.3.1.6. (a) Crack propagation in RSW joints considering microstructure and (b) SCC for predicted vs. experimentally determined material loss vs. corrosion cycles for RSW joints. Source: Simulation - University of Illinois Urbana-Champaign, Experiments - General Motors and University of Michigan.

Prediction of the Joining Performance

At the mesoscale level: FE models were created to predict the mechanical performance of lap-shear joining configurations with different levels of corrosion similar to the corrosion induced experimentally. The FE models were created for the RSW and SPR joints which reproduce the lap-shear configuration used in the experiments as presented in the VTO's Materials 2019 Annual Progress Report [2]. The RSW model consists of four parts: Al coupon, high-strength low alloy steel coupon, and two zones characterizing the joint. These zones include: (1) a recrystallized zone where the temperature during joining of about 480°C recrystallizes the Al grain structure; and (2) an IMC zone formed by diffusion of Al in the steel and characterized by a composite structure of $Al_{13}Fe_4$, Al_2Fe_5, Al, and steel. The dimensions of each part were determined by measuring the experimental samples using microscopic imaging of the joint cross-section areas. In a similar way, the SPR model consists of an Al coupon, a high-strength low alloy steel coupon, and the rivet, which has tight contact with the Al and steel coupons. The key contribution in simulation of the RSW and SPR lap-shear tests under corrosion is the development of the constitutive material model, which is able to simulate changing the behavior of the interface from ductile to brittle by increasing the number of corrosion cycles. This behavior was predicted at the atomic-scale.

Thus, the Gurson-Tvergaard-Needleman (GTN) model was considered, which is a model for ductile fracture of materials with porosity. This model highlights the evolution of randomly distributed volume fractions of spherical voids in porous materials. According to the GTN model, local damage is caused by nucleation, growth, and subsequent coalescence of voids inside the materials; these three mechanisms result in a resistance loss, which, in turn, leads to progressive failure. The yield potential in the GTN model is expressed by defining the following: the von-Mises stress, porosity, equivalent tensile flow stress, critical porosity, final fracture porosity, ultimate porosity, total effective void volume fraction, hydrostatic stress, and void interaction parameters. The GTN parameters were identified through a data-driven approach combined with physical modeling by bridging the scales from the atomic level (mechanical properties of the intermetallic interface) to the mesoscale level (corrosion rates) to the macroscopic level. The lap-shear tests were simulated using the above-mentioned models for the RSW joints before corrosion and induced corrosion corresponding to 26 cycles, 48 cycles, and 72 cycles. The resulting force-displacement curves were used for calculating the maximum load capacity, the energy at failure, and the energy at the maximum load, and compared with the experimental values calculated on the average curves. These three parameters are defining the performance of the joints. The average experimental curve represents an average of five to seven replicates. The results for RSW before and after 26, 48, and 72 corrosion cycles are presented in Figure II.3.1.7. Lap-shear tests for 104 cycles were not recorded because their advanced corrosion led to an early failure of the joint right after their extraction from the corrosion chamber. Due to variation of the experimental RSW lap-shear results, a T-student statistical analysis was used to calculate prediction error. Based on this analysis, the prediction error of the joining performance is 4% as compared with the experiments.

As shown in Figure II.3.1.8, the difference in the corrosion evolution in SPR as compared with the RSW is that the corrosion products are developed at the interface between the rivet and Al on one hand and between the rivet and the steel on the other hand filling an existing gap of about 20 µm (presented in 2019 Report [2]). These corrosion products play the role of tightening the contact. Thus, to model this physical phenomenon, it was considered to have a static and a dynamic friction coefficient between the rivet and the Al, and between the rivet and the steel. This approach, together with the same constitutive material model considered in modeling RSW joints, were used for simulation of the lap-shear test applied to SPR before corrosion. Figure II.3.1.7 above shows very good agreement between the experimental and simulated fracture area. The simulation of the lap-shear applied to SPR after 26, 48, and 72 corrosion cycles are in progress and will be presented in next year's report.

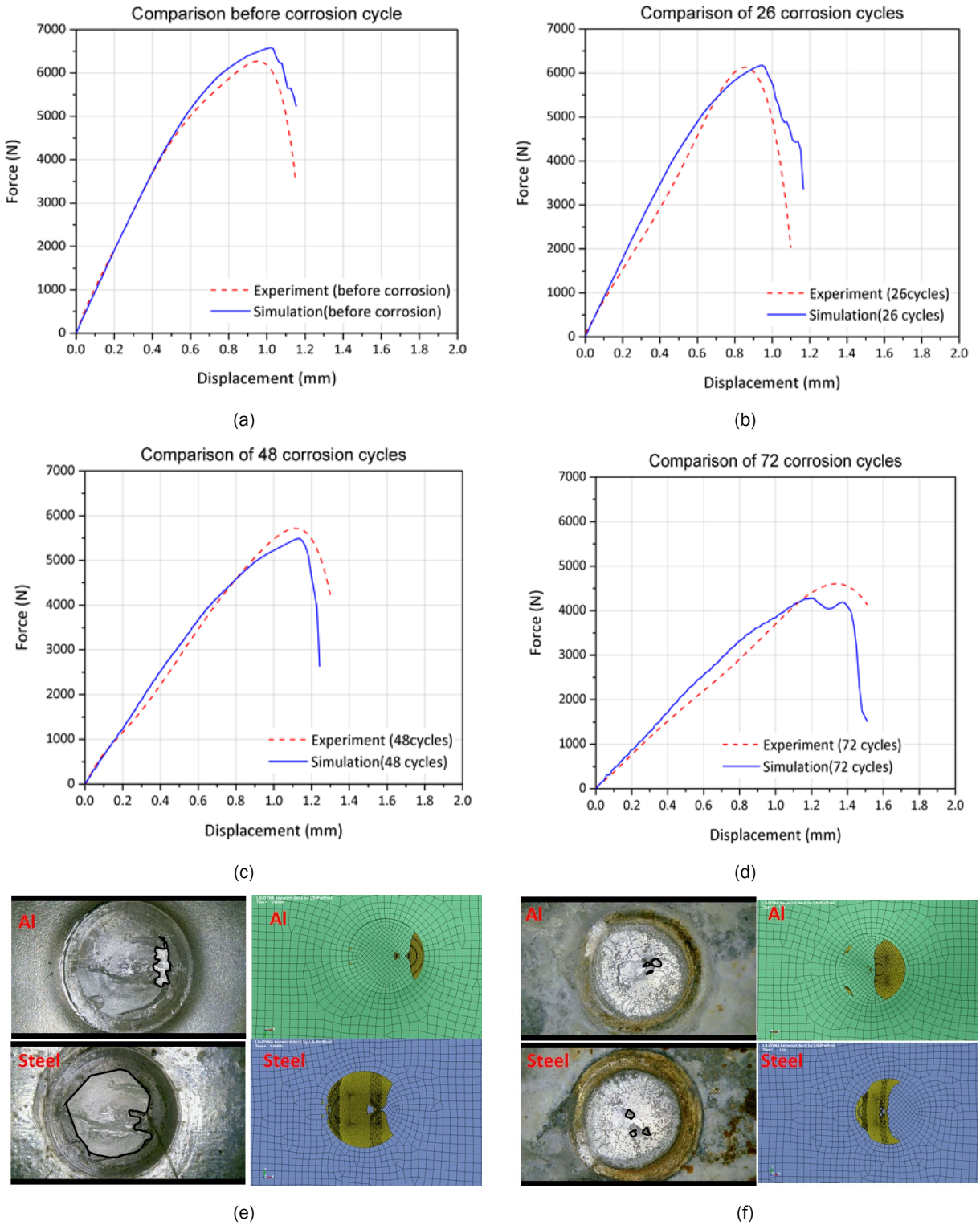

Figure II.3.1.7. Force-displacement curves obtained within the lap-shear tests applied to the RSW joints. Comparison between experiments and simulation for: (a) before corrosion; (b) 26 cycles of corrosion; (c) 48 cycles of corrosion; (d) 72 cycles of corrosion; (e) top view of the experimental fracture area vs. simulated fracture area for RSW joint before corrosion; and (f) top view of the experimental fracture area vs. simulated fracture area for RSW joint after 72 corrosion cycles. Source: University of Michigan.

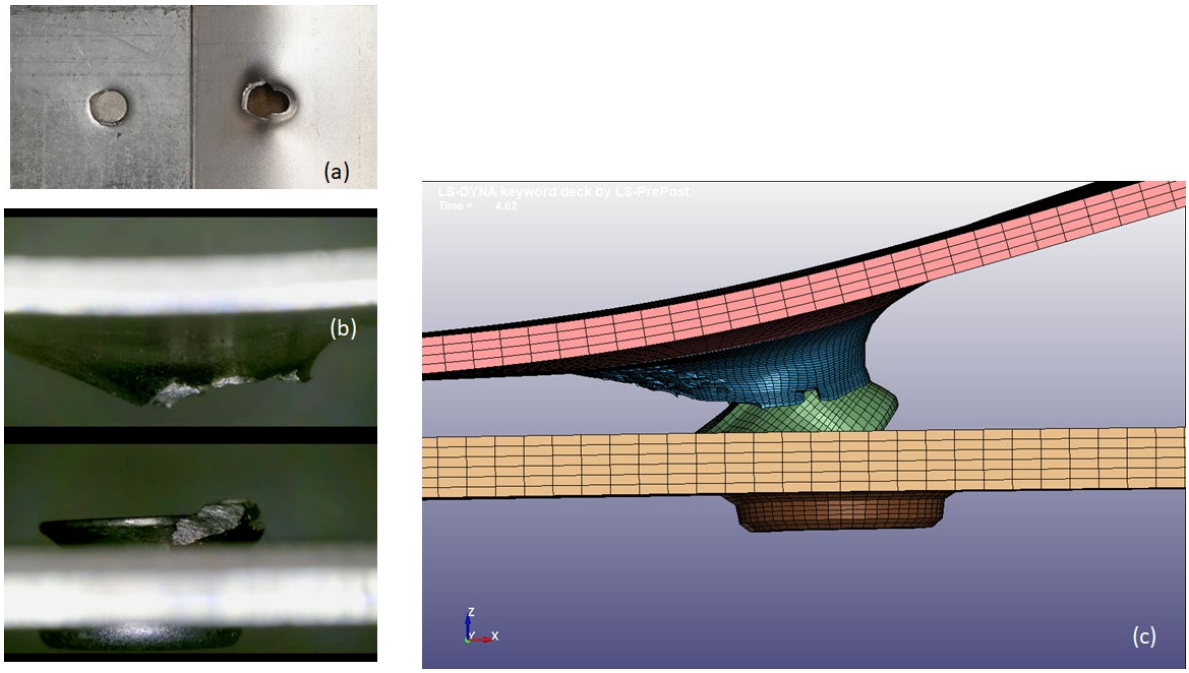

Figure II.3.1.8. Pullout fracture obtained from lap-shearing an SPR joint before corrosion: (a) top view of the fracture showing a circumferential fracture–experiment; (b) lateral view of the fracture showing a ductile fracture of Al substrate with portion of adherence on the rivet which determines a slight tilting of the rivet–experiment; and (c) LS-DYNA simulation of the fracture showing a ductile failure with a tilt of the rivet. Source: University of Michigan.

Conclusions

In the second year of this project, microscopic atomic modeling from DFT-based first principles calculations and phase-field modeling from CALPHAD approach were developed to predict welding and corrosion products and their mechanical properties (5% error prediction comparing with experiments). A material database with the property parameters of the IMC compounds and corrosion products was established. Mesoscopic corrosion models were developed based on the FE method and improved by incorporating SCC modeling and data-driven methods. Material loss and corrosion rates were predicted with an error of < 5% compared with the experiments. At the macroscopic level, FE models were built for simulation of lap-shear tests applied to RSW and SPR joints. The performance of the joints with and without corrosion compare well with results from experiments. An average of 4% error as compared with the experiments was achieved for the RSW joints. Simulation of the lap-shear tests applied to the SPR joints are in progress. Up to now, the failure fracture of SPR joints was successfully predicted showing that the model approaches that were developed for RSW and applied to SPR are providing a high accuracy of simulated results.

Key Publications

1. Wen, W., T. Liu, J. Simmer, B. Carlson (GM), S. J. Hu, and M. Banu, 2020, "Corrosion evolution in Al-steel dissimilar joints," *Proceedings of the ASME 2020, the 15th International Manufacturing Science and Engineering Conference, MSEC 2020*, 22–26 June 2020, Cincinnati, OH, USA.
2. Wang, K. F., S. L. Shang, Y. X. Wang, A. Vivek, G. Daehn, Z. K. Liu, and J. J. Li, 2020, "Unveiling non-equilibrium metallurgical phases in dissimilar Al-Cu joints processed by vaporizing foil-actuator welding," *Mater. Design*, Vol. 186, Art. 108306.
3. Chong, X. Y., S. L. Shang, A. M. Krajewski, J. Shimanek, W. H. Du, Y. Wang, J. Feng, D. Shin, A. M. Beese, and Z. K. Liu, 2021, "Exploring materials properties by machine-learning: Illustrated with stacking fault energy from first principles calculations in dilute Al-, Ni-, and Pt-based alloys," submitted to *Acta Mater*.

4. Liu, Z. K., 2020, "Computational thermodynamics and its applications," *Acta Mater*., Vol. 200, pp. 745–792.

5. Zheng, Z., P. Bansal, P. Wang, C. Shao, and Y. Li, 2020, "Corrosion modeling and prognosis of the Al-steel SPR joints," *Proceedings of the International Mechanical Engineering Congress & Exposition, IMECE 2020*, 15–19 November 2020, Portland, OR, USA.

References

1. Pan, B, H. Sun, S.-L. Shang, W. Wen, M. Banu, J. C. Simmer, B. E. Carlson, Z.-L. Zi-Kui Liu, and J. Li, 2020, "Understanding corrosion in aluminum/steel resistance spot welding and self-pierce riveting joints after salt sprays," *Corrosion Science* (submitted November 2020).

2. DOE-EERE, *VTO's Materials 2019 Annual Progress Report*, DOE/EE-1990, April 2020, Washington DC, USA.

3. Shang, S.-L., J. Shimanek, S. Qin, Y. Wang, A. M. Beese, and Z.-K. Liu, 2020, "Unveiling dislocation characteristics in Ni_3Al from stacking fault energy and ideal strength: A first principles study via pure alias shear deformation," *Phys. Rev. B*., Vol. 101, Art. 024102.

Acknowledgements

The authors would like to recognize the following individuals whose contributions to this project have been greatly appreciated:

- Co-PI Blair Carlson, Joseph Simmer, GM
- Co-PI Richard Chinoski, Henrob
- Weiling Wen, Tae Hwa Lee, and Tian Liu, UM
- Co-PI Jingjing Li, Shun-Li Shang, Zi-Kui Liu, Hui Sun, and Bo Pan, Pennsylvania State University
- Co-PI Chenhui Shao, Pingfeng Wang, and Yumeng Li, Post-Doc Zhuoyuan Zheng, and Graduate Students Yuquan Meng, Parth Bansal, and Yuhang Yang, University of Illinois Urbana-Champaign
- Co-PI Jack Hu, University of Georgia
- Co-PI Marco S. Pigazzini, Dandan Lyu, Livermore Software Technology Corporation.

II.3.2 Phase-Field Modeling of Corrosion for Next-Generation Aluminum-Magnesium Vehicle Joints (Worcester Polytechnic Institute)

Adam C. Powell, IV, Principal Investigator
Worcester Polytechnic Institute
100 Institute Road
Worcester, MA 01609
E-mail: acpowell@wpi.edu

Sarah Kleinbaum, DOE Technology Manager
U.S. Department of Energy
E-mail: sarah.kleinbaum@ee.doe.gov

Start Date: October 1, 2018 End Date: July 31, 2022
Project Funding (FY 2020): $750,952.49 DOE share: $528,047.09 Non-DOE share: $222,905.40

Project Introduction

The next frontier in vehicle body lightweighting could make extensive use of Mg alloy sheet for its outstanding stiffness and strength-to-weight ratio, with an AA sheet providing low-cost paintable Class A finish surfaces. Already, the Lincoln MKT and Chrysler Pacifica liftgates have used cast Mg inner and Al sheet outer components. Next-generation ultralight doors could likely use similar materials; however, corrosion of Al-Mg fusion welds must be addressed to consider widespread use of this material pair in a vehicle's body structure. Use of boron steel self-piercing rivets to join an A-Mg sheet would result in a severe corrosion issue.

FSW leads to significant grain refinement, second-phase refinement, homogenization, and densification; all characteristics known to have beneficial effects on the corrosion resistance of light metals. Al corrosion studies suggest grain refinement via equal-channel angular pressing improves corrosion resistance primarily via impurity breakup and homogenization leading to reduced microgalvanic current. Similarly, FSW in wrought Mg-Y RE and AA5083 Al alloys shows potential for improved corrosion resistance likely due to break down and dispersion of intergranular precipitates reducing the mass loss rate.

That said, there is no quantitative link between microstructure and corrosion performance. Closing this missing link in understanding will facilitate design of cost-effective processes for making robust joints whose geometry and microstructure reduce corrosion and joint failure, even when coatings fail.

Objectives

The objective of this project is to provide a quantitative link between FSW microstructure and corrosion performance. In particular, the team aims to develop and validate a grain-level phase-field model of microgalvanic corrosion, as well as coupled micromechanics model of mechanical failure, in FSW Al-Mg alloy joints to predict strength and fatigue lifetime of corroded joints within 10% of measured performance.

This project will develop the models using 6022 Al and ZEK100 Mg alloys, which were selected for the Magna- Fiat Chrysler Automobiles U.S. LLC ultralight door project. Test joints between these sheet materials will use diffusion-bonding and FSW. The team will attempt to validate the model using 7xxx-series Al alloys.

Approach

The phase-field corrosion model starts with an expression for free energy vs. composition in the metal, electrolyte, oxide, and hydroxide corrosion product phases, following the method of Pongsaksawad *et al.* [1]. This expression begins with a fit to thermodynamic data on the Al and Mg alloy systems, including the base metals and intermetallic compounds. The electrolyte is an aqueous solution with Al^{3+} and Mg^{2+} ions and dissolved O. Using a representation of the full Al-Mg system free energy function produces the correct compositions at phase boundaries and leads to correct chemical potential of both species at metal-electrolyte boundaries, which automatically creates electronically mediated microgalvanic corrosion reactions between the various phases.

Corrosion model validation begins with fabrication of diffusion-bonded and welded joints. Diffusion-bonded sheets of pure Mg and Al provide an ideal model system for understanding the fundamentals of galvanic corrosion. Diffusion-bonded alloy sheets deepen this understanding to include additional phases in each alloy. When the phase-field corrosion model is proven for diffusion-bonded couples, we will then try to use it to describe corrosion in a complex FSW microstructure.

Prediction of FSW microstructure is beyond the scope of this study. Instead, characterization techniques, such as SEM with EDS and EBSD, will produce maps of composition and grain orientation across a FSW joint. This includes using *in situ* FIB and plasma etching to expose and characterize multiple layers in a joint leading to a 3D microstructure, which will provide the initial condition for the corrosion model.

This project consists of four tasks with an end goal of a validated model of corrosion and mechanical failure:

1. Produce Diffusion-Bonded and Welded Coupons for Testing:
   Produce coupons with joints between pure and alloyed Mg and Al sheets by diffusion-bonding and/or friction-stir and/or fusion welding.
2. Conduct Corrosion and Mechanical Testing:
   Run accelerated corrosion tests and tensile and fatigue tests to determine corrosion morphology and its effect on mechanical performance of Mg-Al joints.
3. Characterize Welded Joints and Corrosion and Mechanical Test Samples:
   Use advanced characterization methods including SEM with EDS and EBSD, as well as small-angle neutron scattering, to understand the structure of corrosion products and fracture surfaces and provide input geometry/morphology as an initial condition for models.
4. Develop Corrosion and Mechanics Model:
   Use phase-field and crystal plasticity modeling based on PRISMS tools from the UM to build a grain-level model of corrosion and mechanical deformation of Mg-Al joints.

Results

Produce Diffusion-Bonded and Welded Coupons for Testing

Diffusion-Bonding

The diffusion-bonding technique reported previously had successfully bonded 6022 Al and ZEK100 Mg sheets with high-quality bonds. But attempts to bond pure Al and Mg sheets had not worked: the sheets bonded in parts, with splits between them. This year, extending bonding time from two hours to four hours at 395°C succeeded, and the method produced high-quality continuous diffusion bonds between pure Al and Mg sheets. Figure II.3.2.1(a) and (b) shows optical images of intermittent and continuous bonds produced with two and four hours of bonding, respectively.

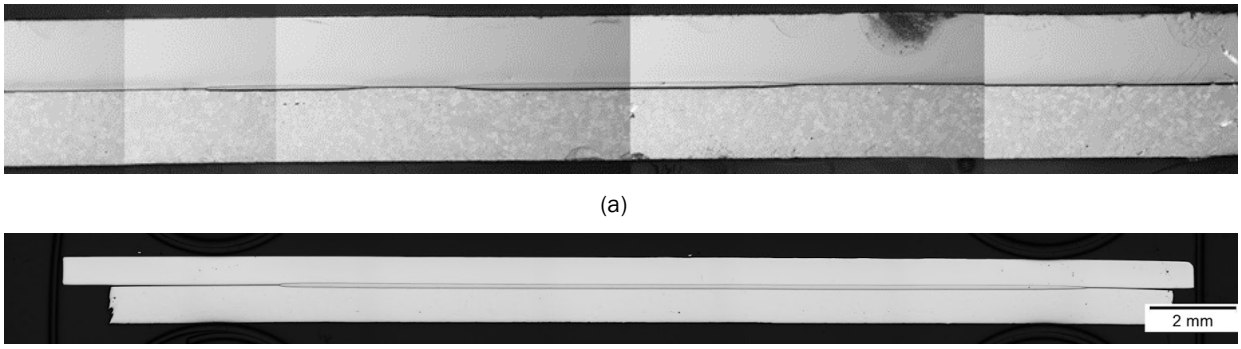

(a)

(b)

Figure II.3.2.1. (a) Diffusion-bonded pure Al-Mg sheets showing intermittent bond after two hours at 395°C. (b) Continuous bond after four hours at 395°C. Source: PNNL.

Friction-Stir Welding

Figure II.3.2.2(a) summarizes the welding process development. Power control modes enabled elimination of surface defects observed in rotation speed control modes. An aggressively triangular pin feature resulted in decrease of large root side defects on the advancing side as seen in the middle-bottom macrograph of Figure II.3.2.2(b). Consequently, the load-carrying capacity of the joints made with triangular tools are greater than that for cylindrical tools, as shown in the bar graph of Figure II.3.2.3 and line graph of Figure II.3.2.4(a). A DIC map shown in Figure II.3.2.4(b) collected during tensile testing shows strain concentrations and provides clues on load-carrying interfaces. The apparent intrusion of the Al matrix into the bottom Mg sheet formed a hook-like structure that may be responsible for mechanical reinforcement of the joint. Nevertheless, a simple structure-property simulation that we recently ran (results not shown here) shows mechanical reinforcement in the form of hook alone does not account for the total joint strength. Thus, metallurgical bonding via intermetallic compounds may be responsible for the remainder of joint strength.

It is important to note there is some variability in joint strength between samples extracted from different locations of the linear joint. The joint strength corresponding to 116 ± 20 N/mm was observed for the three samples tested. More detail regarding the weld zone can be found in the sections that follow.

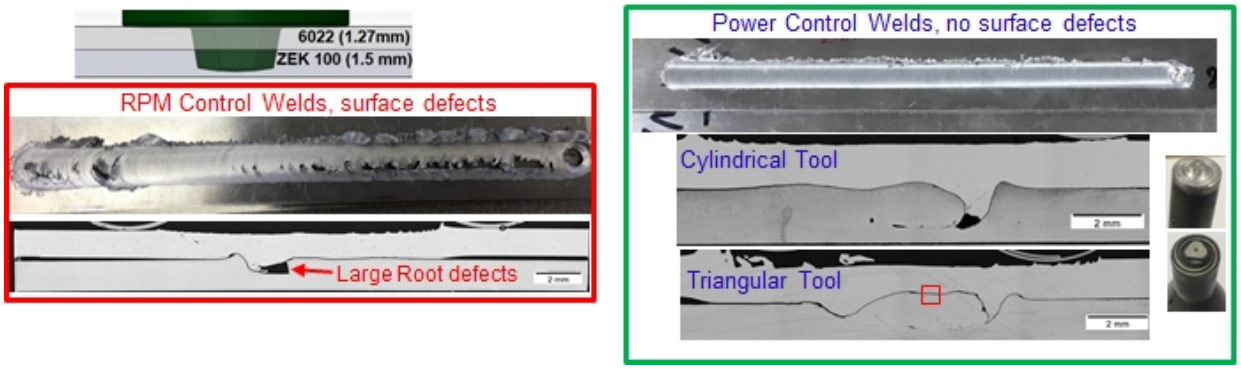

(a) (b)

Figure II.3.2.2. (a) Sheet, weld, and pin geometries at upper left and weld surface and cross-section with speed control at lower left. (b) Power control welds with cylindrical and triangular pin geometries. Source: PNNL.

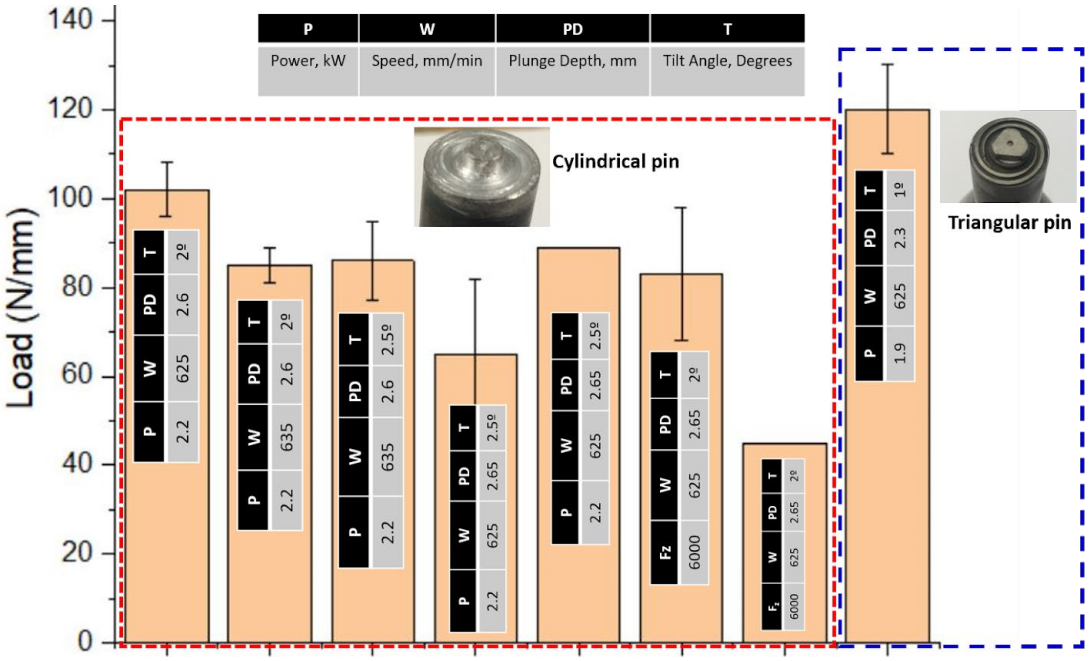

Figure II.3.2.3. FSW strength in load per unit weld length for several welding parameters and two tool features. Source: PNNL.

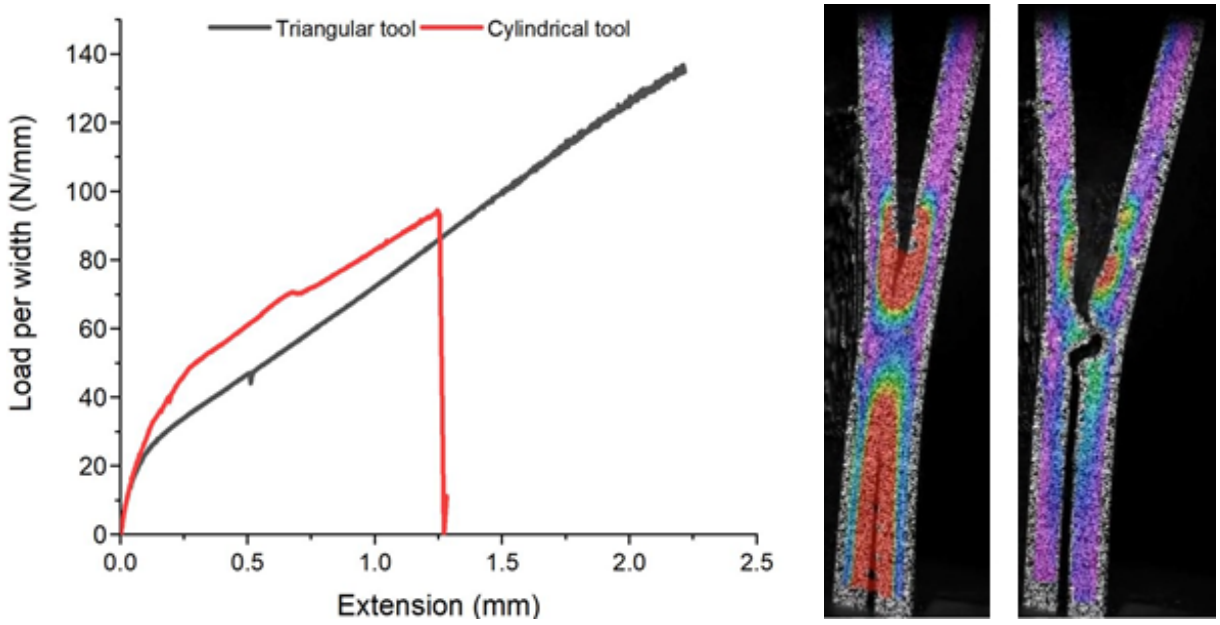

(a) (b)

Figure II.3.2.4. (a) Weld geometry (top) and preliminary optical characterization with the length direction from left to right. (b) Lap-shear test results. Source: PNNL.

Corrosion Testing

The corrosion team ran multiple sets of tests. The first is a galvanic corrosion baseline for FSW 6022 Al and ZEK100 Mg alloy sheets. Several samples were carefully cut from a weld with Al:Mg surface area ratios of 1:2, 1:1, and 2:1, as shown in Figure II.3.2.5(a). Cyclic corrosion testing following the Society of Automotive Engineers, SAE-J2334, standard resulted in higher corrosion with a higher Al-Mg surface area ratio as shown in Figure II.3.2.5(b). This is consistent with our hypothesis of cathodic polarization in the Al, with the water oxidation reaction $H_2O + ½O_2 + 2e^- \rightarrow 2OH^-$ limiting the overall galvanic corrosion reaction, anodic polarization, and mass loss $Mg \rightarrow Mg^{2+} + 2e^-$.

Second, galvanic corrosion testing using the American Society for Testing and Materials Standard Guide for Conducting and Evaluating Galvanic Corrosion Tests in Electrolytes, ASTM G71, with the apparatus shown in Figure II.3.2.6(a) showed pitting corrosion in the ZEK100 Mg alloy sheet, but little corrosion in 6022 Al. Figure II.3.2.6(b) shows pitting corrosion in Mg samples when Al and Mg were 8 cm and 4 cm apart at 1 V applied potential, with the closer samples showing higher corrosion. This is likely due to the higher electric field between them. Under these conditions, pit diameters measured 200-600 μm.

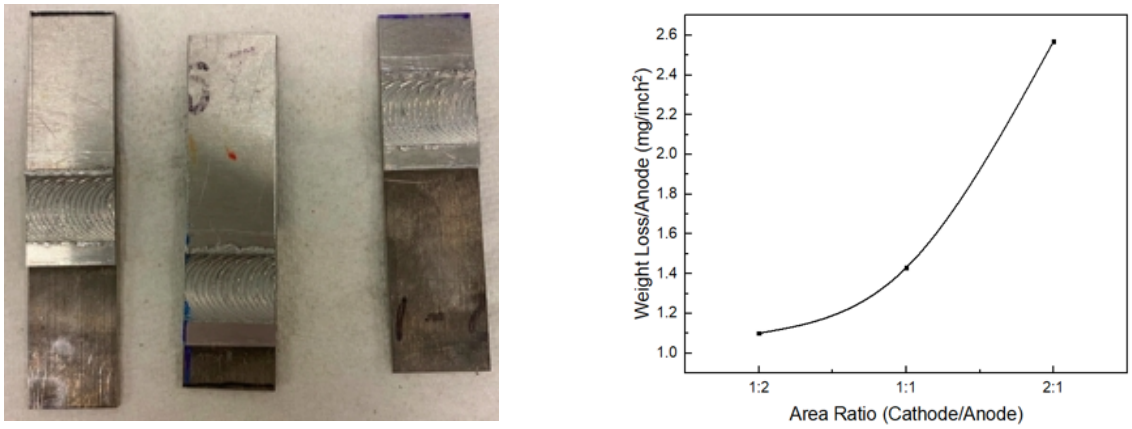

(a) (b)

Figure II.3.2.5. (a) Samples with Al:Mg area ratios of 1:1, 2:1, and 1:2. (b) Corrosion rate results from a cyclic corrosion testing test of 6022-ZEK100 Al and Mg alloy FSWs, showing increased corrosion rate with increasing Al:Mg surface area ratio. Source: WPI.

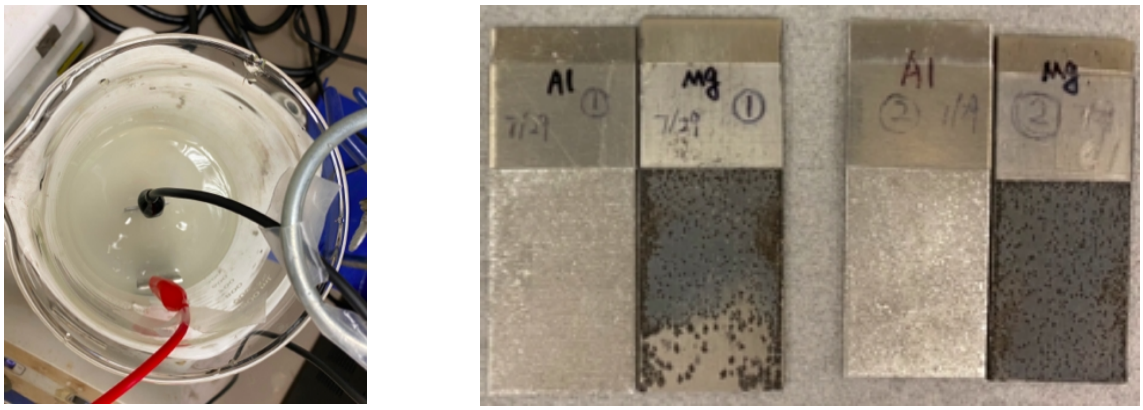

(a) (b)

Figure II.3.2.6. (a) Galvanic corrosion beaker with electrolyte, showing Al and Mg samples 4 cm apart. (b) Al and Mg specimens after one-hour corrosion at 1 V applied potential at 8 cm (left) and 4 cm (right) distance. Source WPI.

Third, a polished 6022 Al-ZEK100 Mg sheet FSW cross-section immersed in 0.1 M NaCl solution for one-hour showed filamentous corrosion in Mg. In literature, this occurs when Mg is at cathodic potential. It is not clear why Mg would be cathodic here; we will investigate Mg potential in the door challenge problem.

Characterize Welded Joints and Corrosion and Mechanical Test Samples

The team completed advanced characterization of weld joints and corrosion samples as follows:

- Characterization of welds and diffusion bonds with grain sizes, precipitate sizes, and compositions.
- Characterization of diffusion-bonded pure and alloy Mg-Al sheet, including interface separation in pure sheet bonds, with detailed analysis of precipitates in intermetallic layers.
- Neutron scattering of FSW Al-Mg joints determined nanoscale phase distributions including porosity.
- Microscopy and microanalysis (e.g., the large area in the EBSD and EDS maps) of FSW ZEK100/6022 joints showed that the Mg-Al interface is very sharp with no discernable intermetallic compounds at the interface, in addition to a decrease in grain size in the Al and Mg at the joint interface.
- Preliminary diffraction contrast microscopy, performed on two cylindrical samples cut from within a FSW joint, indicated that the Al component is suitable for XRD contrast tomography analysis of grain orientation.
- SEM analysis showed filamentous corrosion in Mg as described at the end of the prior section.
- Pit depth measurement using a wide-area 3D measurement system showed 30-50 µm pit depth in Mg and 0.5-2.5 µm pit depth in Al in ASTM G71 galvanic corrosion samples, as shown previously in Figure II.3.2.6(b).

In baseline FSW characterization, while the optical imaging shows a clear marking between the Mg/Al boundary in the nugget, this should not be confused with a lack of bonding. SEM imaging in Figure II.3.2.7(a) shows intimate bonding between the ZEK100 and 6022. The image and an EDS line scan in Figure II.3.2.7(b) seem to indicate the presence of a ~1-micron-thick intermediate layer between the two alloy layers. This is significantly thinner than the ~100 µm intermetallic layer observed during two hours of diffusion-bonding, which makes sense given the few seconds at high-temperature FSW. Preliminary FEA suggests that mechanical hooking alone cannot provide the strength observed in the joints. But while conditions of high-temperature are conducive to the formation of intermetallic compound, there is no distinct step or plateau in composition, as was observed in diffusion-bonding, so it remains unknown whether intermetallic compounds are present.

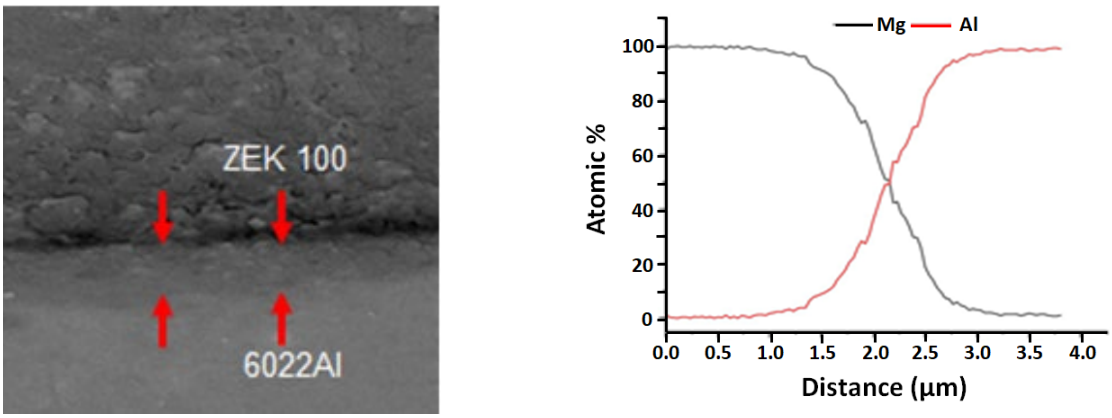

(a) (b)

Figure II.3.2.7. (a) SEM image showing intimate bonding at the interface of FSW samples from the region marked with a red square in the cross-section seen in Figure II.3.2.2(b). (b) EDS line scan results showing Mg and Al content across the interface. Source: PNNL

The Mg samples previously shown in Figure II.3.2.6(b) were analyzed using the measurement and analysis functions of a Keyence VR3000 instrument. Specifically, the height difference measurement function was employed to determine pit depths. For this, a reference plane is first chosen and is the blue square (e.g., Area #1) shown in Figure II.3.2.8(a) and (c). Next, nine pits were manually measured by drawing a circle in the pit regions as shown in Figure II.3.2.8(a) and (c) as colored shaded regions. Corresponding histograms of the measured pit depths are presented in Figure II.3.2.8(b) and (d), respectively. As a result of this data analysis, it was determined that the average pit depth with the corrosion product still in them was 17.2 µm with a standard deviation of measurements equally 9.3 µm. Removal of the corrosion product with an acid dip, as shown in Figure II.3.2.8(c), resulted in an average measured pit depth of 51.9 µm with a standard deviation of 8.2 µm. Thus, as a first attempt, quantitative pit depth measurements are in the range of 30-50 µm.

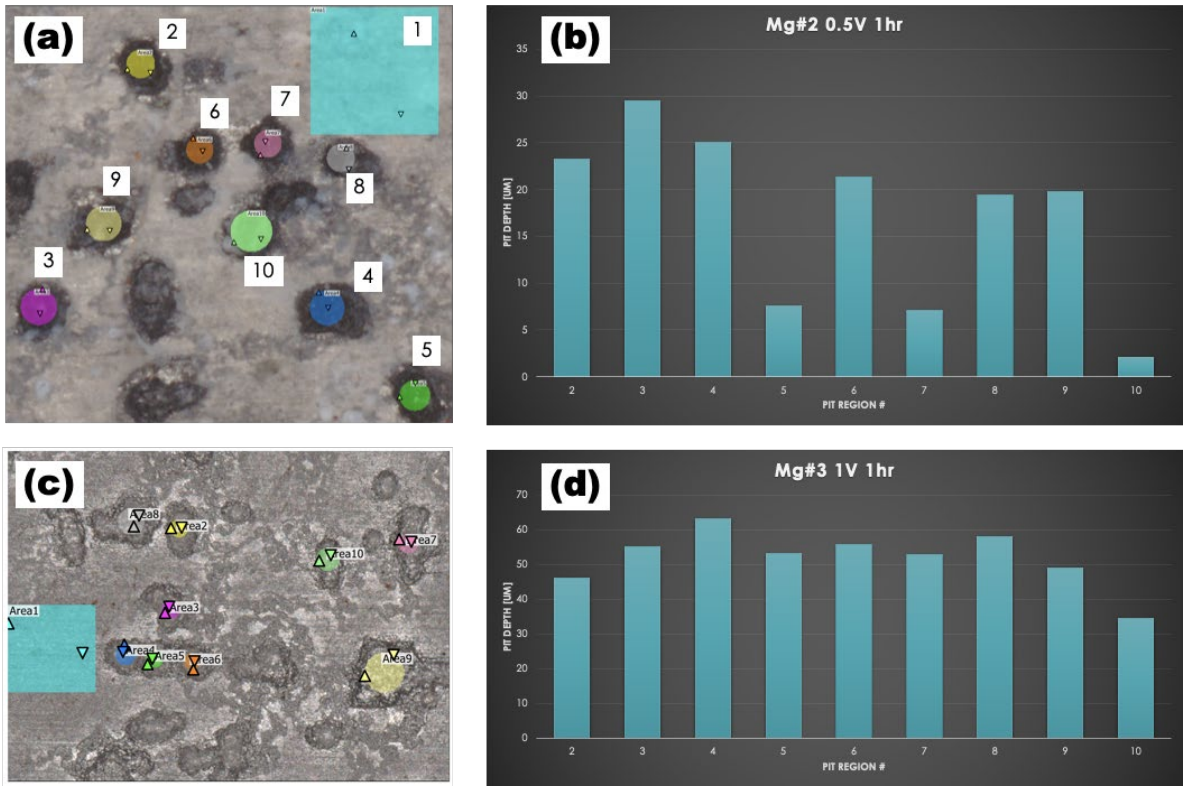

Figure II.3.2.8. (a) Manual selection of pit area where depth measurements were determined on sample Mg#2. Area 1 is the reference plane from which the height difference was determined for areas 2-10. (b) Histogram of quantitative pit depths measured from (a). Note the y-axis maximum scale is 35um. (c) Sample Mg#3 reference area (blue square) and pit areas 2-10. (d) Histogram of quantitative pit depths measured from (c). Note the y-axis maximum scale is 70um. Source: ORNL

Develop Corrosion Model

As mentioned above, the corrosion model is a Cahn-Hilliard phase-field model following the method of Pongsaksawad *et al.* [1]. A quaternary system is necessary to model water oxidation at the Al cathode, and at the anode either Mg dissolution as mentioned above, or passivation following: $Mg + 2OH^- \rightarrow Mg(OH)_2 + 2e^-$. This model ran to simulate galvanic and pitting corrosion in 2D with initial conditions shown in Figure II.3.2.9(a). In the galvanic corrosion simulations, although very high mobility, interface thickness, and domain size were adopted to reduce computation time, the results can still be qualitatively compared with galvanic corrosion experiments. Simulations started with equal amounts of Al and Mg metals. It was observed in the simulation that Mg dissolves with time, and a layer of $Mg(OH)_2$ is formed on the Mg surface as shown in Figure II.3.2.9(b), which indicates a high starting pH in the electrolyte. Note that due to the existence of Al^{3+} ions in the electrolyte, a small amount of Al deposition is observed in these simulations.

Figure II.3.2.9(b) shows the result of a simulation with high dissolved O concentration in the electrolyte and the same mobility in $Mg(OH)_2$ as the electrolyte; these conditions lead to growth of an $Mg(OH)_2$ passivation layer. Note also that the lower electric potential on the Mg side of the domain with a higher potential on the Al side indicates galvanic protection of the Al, which is expected.

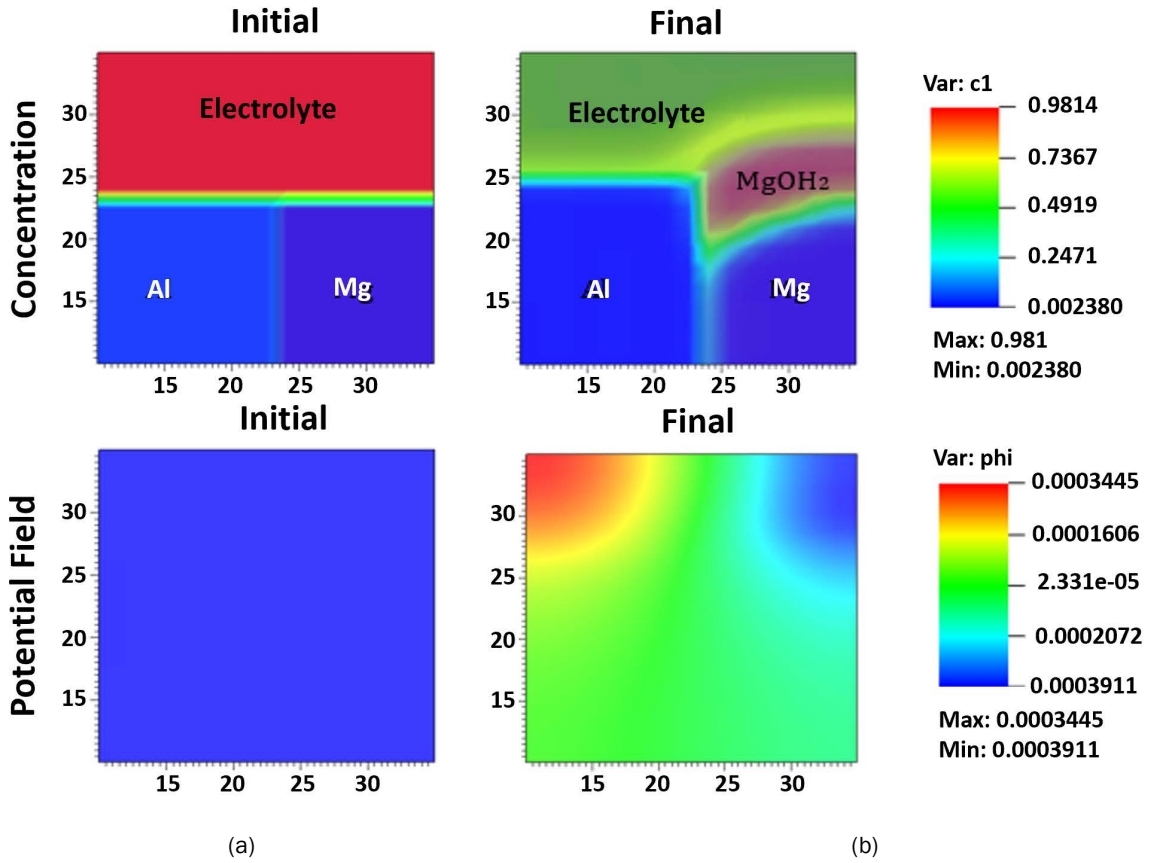

Figure II.3.2.9. Output of the model with initial conditions representing galvanic corrosion showing the spatial distribution of the C1 composition variable (top) and electrical potential (bottom): (a) at the start of the simulation, and (b) after the final timestep. Source: WPI.

Next, the physical material parameters were implemented, and pitting corrosion simulations were run for validation purposes as shown in Figure II.3.2.10(a), (b), and (c). The simulation domain size was set to 1460 × 2920 µm, and a symmetry axis along the right boundary was applied to reduce the computation time. A discussion of the evolution of a single pit with time follows. The initial domain presents a thin layer of $Mg(OH)_2$ on the Mg surface with a small opening to initiate corrosion. It was observed that the Mg starts to corrode from the opening and forms a small pit. Here, the initially described $Mg(OH)_2$ acts as a protective layer preventing corrosion of Mg underneath. This is similar to most pitting corrosion modeling studies, including those of Chadwick *et al.* [2], which used PRISMS-PF, and of Jafarzadeh *et al.* [3].

At the final simulation time of 3600 seconds, the pit depth is ~500 µm. As discussed previously, Mg corrosion pits measured 200-600 µm across, and had a roughly hemispherical profile at the edges, so the assumption of hemispherical pit geometry leads to 100-300 µm depth. The current model thus shows roughly correct morphology with a pit depth somewhat higher than measurements. Note that if individual pits start to form at various times, maximum pit depth is most relevant for comparison with the model. Also, this 2D geometry is equivalent to a groove rather than a pit; a 3D or axisymmetric model would predict slightly shallower depth. The team will continue to refine the model to bring it further into alignment with measurements.

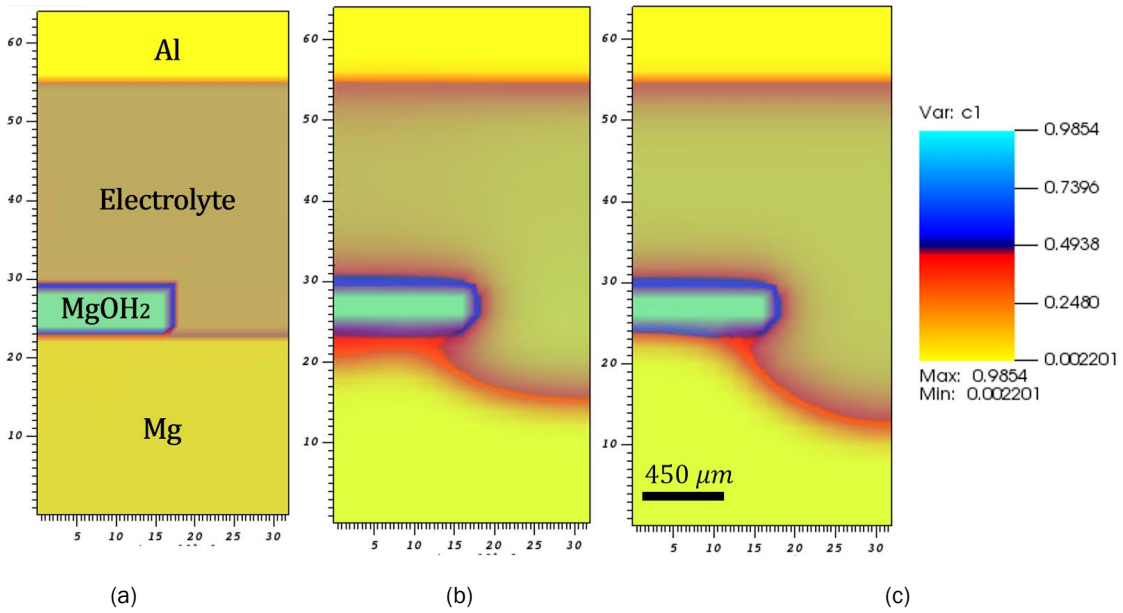

Figure II.3.2.10. Output of the model showing spatial distribution of the C1 composition variable with initial and BCs corresponding to pitting corrosion for: (a) the initial condition; (b) after 608 seconds; and (c) after 3600 seconds. Source: WPI.

Conclusions

This project team has successfully completed its first major tasks. Significant accomplishments include:

- The development of FSW through Al into Mg with repeatable strength at least 40% of the base ZEK100 sheet strength, which is likely suitable for the lightweight door challenge problem.
- The use of multiple testing methods (i.e., salt solution immersion, galvanic corrosion, cyclic corrosion testing) to characterize the mechanisms and rates of corrosion in the base metals, diffusion-bonded couples, and FSW joints.
- Advanced characterization of both baseline joints (i.e., diffusion bonds, FSW) and corroded base metals and FSW joints, with phase identification and 3D mapping of surface topography.
- A new Cahn-Hilliard phase-field formulation capable of modeling diffusion-bonding, microgalvanic corrosion, and pitting, with preliminary results comparable to observed passivation and pit formation.

The team will continue to develop this corrosion model and will work on a new model of combined corrosion and mechanical failure to build understanding and help to advance the lightweight goals described above.

References

1. Pongsaksawad, W., A. C. Powell, and D. Dussault, 2007, "Phase-field modeling of transport-limited electrolysis in solid and liquid states," *J. Electrochem. Soc.*, Vol. 154, No. 6, Art. F122.
2. Chadwick, A. F., J. A. Stewart, R. A. Enrique, S. Du, and K. Thornton, 2018, "Numerical modeling of localized corrosion using phase-field and smoothed boundary methods," *J. Electrochem. Soc.*, Vol. 165, No. 10, pp. C633–C646.
3. Jafarzadeh, S., Z. Chen, and F. Bobaru, 2019, "Computational modeling of pitting corrosion," *Corros. Rev.*, Vol. 37, No. 5, pp. 419–439.

Acknowledgements

This work was supported by DOE Contract DE-EE0008454.

II.3.3 A Hybrid Physics-Based Data-Driven Approach to Model Damage Accumulation in Corrosion of Polymeric Adhesives (Michigan State University)

Roozbeh Dargazany, Principal Investigator
Michigan State University
428 S. Shaw Lane, Room 3567
East Lansing, MI 48824
E-mail: roozbeh@msu.edu

Sarah Kleinbaum, DOE Technology Manager
U.S. Department of Energy
E-mail: sarah.kleinbaum@ee.doe.gov

Start Date: October 1, 2018 End Date: December 31, 2021
Project Funding: $680,856 DOE share: $636,866 Non-DOE share: $43,990

Project Introduction

Degradation of polymeric adhesives in dissimilar joints is a menace to electric and structural components of the automotive industry. Often in polymeric adhesives, failure occurs due to damage accumulated from discrete environmental sources—thermal degradation, oxidation, hydrolysis, radiation, and moisture—that are combined with progressive damage mechanisms, such as aging and fatigue. Because most damage mechanisms that lead to degradation act in parallel, estimation of the lifetime of a polymeric material becomes a significant reliability issue. No study currently exists that can simultaneously consider even two of these phenomena. Most current efforts are directed toward a single-phenomenon, single-model approach in which a model is developed to cover one specific damage mechanism. While this approach is advantageous in exploring single mechanisms, it is strongly inconclusive for degradation that occurs by multiple damage mechanisms. Our team plans to take a fresh perspective by designing a hybrid constitutive/data-driven approach that allows models of different damage mechanisms to be integrated into one model and then used to explore degradation-induced failure of polymeric adhesives. The theoretical-computational part of this work is divided into four research components as described in the Approach section below.

Objectives

The objective of this project is to develop and validate a model to predict degradation-induced failure in polymeric adhesives with respect to damage accumulated by different degradation and fatigue mechanisms within 10% of measured performance. Models of different damage mechanisms will be integrated into one platform and used to explore the degradation-induced failure of polymeric composites. Initially, the focus will be on modeling and coupling of viscoelasticity, thermo-oxidation, photo-oxidation, and moisture degradation. The platform output will be given to a neural network engine to calculate remaining service life. Using the neural network, a new fatigue-failure model will be developed that considers the effect of degradation.

Approach

This report covers our results for FY 2020 where our focus was on understanding, characterizing, and modeling individual degradation mechanisms. The modeling part of this project consists of four major tasks that focus on the multiscale modeling of each of the following damage mechanisms based on the substructural changes associated with them:

- **Vibration-induced** damage of adhesives, which is required to predict damage induced by deformation and vibration. The model is being developed based on Michigan State University's (MSU's) quasistatic [1] and viscoelastic [2] models. The vibration model will mainly be developed to describe the contribution of engine vibration to accumulative damage in adhesives.

- **Thermo-oxidative** degradation of adhesives, which is being modeled after MSU's recent micromechanical model [3],[4]. The proposed approach can be considered as one of the first attempts to micromechanically model the constitutive behavior of crosslinked polymers during thermo-oxidative degradation.
- **Hydrolysis** modeling, which is being modeled by combining two concepts: (1) mass uptake will be modeled using the Langmuir diffusion model [5] and (2) using mass uptake as a damage precursor, degradation will be modeled following the concept of network evolution [1].
- **Photo-oxidation**, which will be the next step after modeling thermo-oxidative aging. It will be modeled by advancing the concept of the thermo-oxidative degradation model [3]. The balance equations will be rewritten based on a new damage precursor: ultraviolet energy dosage.

Results

Vibration-Induced Damage

In recent years, elastomeric parts were reported to show significant damage accumulation, making fatigue lifetime prediction of great importance. This progressive damage causes three important features: (1) significant stress-softening during the first cycle; (2) increasing permanent set in the sample; and (3) stiffness reduction. In this study, we are only considering the effect of the number of cycles on stress-softening of material, and energy dissipation after the first cycle is not considered. However, the model is based on the modular platform [7].

Evolution of damage accumulation in the crosslinked network is derived based on the effect of force on the rate of chain scission and dissociation of bonds. To this end, the mechano-chemistry theory of history-dependent damage [8] is used to predict the number of active chains with a constant length. So, the probability distribution of chains with different lengths evolves during cyclic deformation, which results in non-uniform stress-softening in the material. The kinetics of irreversible chain scission can be represented as:

$$\frac{dN(n)}{d\tau} = -K_s N(n) \tag{1}$$

where K_s is the rate of chain scission in the active chains. Considering the experimentally established relationship between the lifetime of the material and its load, known as the Zhurkov formula, the rate of the surviving chains, K_s, can be written as:

$$K_s = nK_{s0}e^{\frac{\alpha\left(f(\lambda,n)-f(1,n)\right)}{k_BT}} \tag{2}$$

where K_{s0} is the Arrhenius rate factor, α is the activation length, and k_B and T are the Boltzmann constant and the absolute temperature, respectively. Moreover, $f(\lambda, n)$ is the entropic force of the chain with n segment at deformation λ. The activation force, $f(1, n)$, is considered to remove the effect of equilibrium-chain forces on the damage evolution. The rate multiplied by chain length, n, is used to consider the same rupture probability for each bond on the chain, which is sufficient for chain scission. The number of survived chains with n segment at time τ can be calculated by solving the kinetics equation. Thus, the evolution of the probability of the chain length in each direction during cyclic loading yields:

$$\overset{d_i}{\tilde{P}}(n) = P_0(n)\, e^{-C_s(n)\, j},\ C_s(n) = \int_{cycle} \exp\left[\frac{\alpha}{k_BT}\left(\mathcal{L}^{-1}\left(\frac{R\lambda^{d_i}}{n}\right) - f_a\right)\right]dt \tag{3}$$

To investigate the relevance of the concept of damage accumulation, the model was evaluated with a set of uniaxial tensile tests after 1, 1000, and 2000 loading-unloading cycles. A dumbbell-shaped specimen was elongated up to a deformation (stretch) level of 1.65, and then unloaded, which made up one complete uniaxial

tension cycle. This procedure was repeated thousands of times. Using six material parameters, the model was fitted to the first cycle of the tensile test. In addition, two material parameters of damage accumulation were calculated by only considering maximum stress after 10 and 4000 cycles. The model prediction was plotted against the experimental test in Figure II.3.3.1(a) for stress-stretch data and Figure II.3.3.1(b) for the maximum stress as a function of the number of loading cycles. As can be seen from Figure II.3.3.1, the model prediction has good agreement with the experiment.

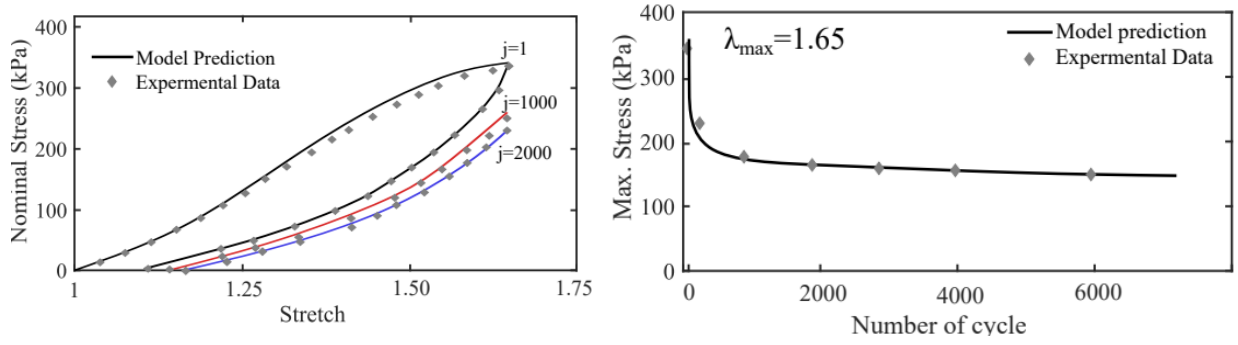

(a) (b)

Figure II.3.3.1. Comparison of the nominal stress-stretch curves of the model and experiment for: (a) the uniaxial tensile tests after 1, 1000, and 2000 cycles; and (b) the maximum stress as a function of number of loading cycles. Source: Michigan State University.

Thermo-Oxidative Degradation

Progress made in this area was a continuation of FY 2019 efforts and results are not sufficiently different from those results.

Constitutive Model

During aging, two types of chemical reactions occur—chain scission and crosslinking. Chain scission reactions break the chains and cause degradation of the original network. On the other hand, crosslinking reactions create a whole new polymer matrix. Accordingly, the strain energy of the polymer matrix, Ψ_M, at each stage of aging can be simply represented with respect to energies of the network at those two states, namely Ψ_0 and Ψ_∞, as:

$$\Psi_M(t,T,\mathbf{F}) = \rho(t,T)\Psi_0(\mathbf{F}) + \big(1-\rho(t,T)\big)\Psi_\infty(\mathbf{F}), \quad \text{where} \quad \rho(t,T) = A_1 \exp\left(-\tau_1 \exp\left(-\frac{E_{a1}}{RT}\right)t\right) + A_2 \exp\left(-\tau_2 \exp\left(-\frac{E_{a2}}{RT}\right)t\right) \qquad (4)$$

where $\rho(t,T)$ represents the weight of each state.

To validate the proposed model, predictions were benchmarked against experimental data specifically designed to capture the effects of thermo-oxidative aging causing failure of styrene-butadiene rubber (SBR), Dow Corning silicone, and polyurethane, as observed in Figure II.3.3.2(a, c, and d) along with a comparison of predicted values versus experimental values for the Mullins value as a function of aging, as shown in Figure II.3.3.2(b).

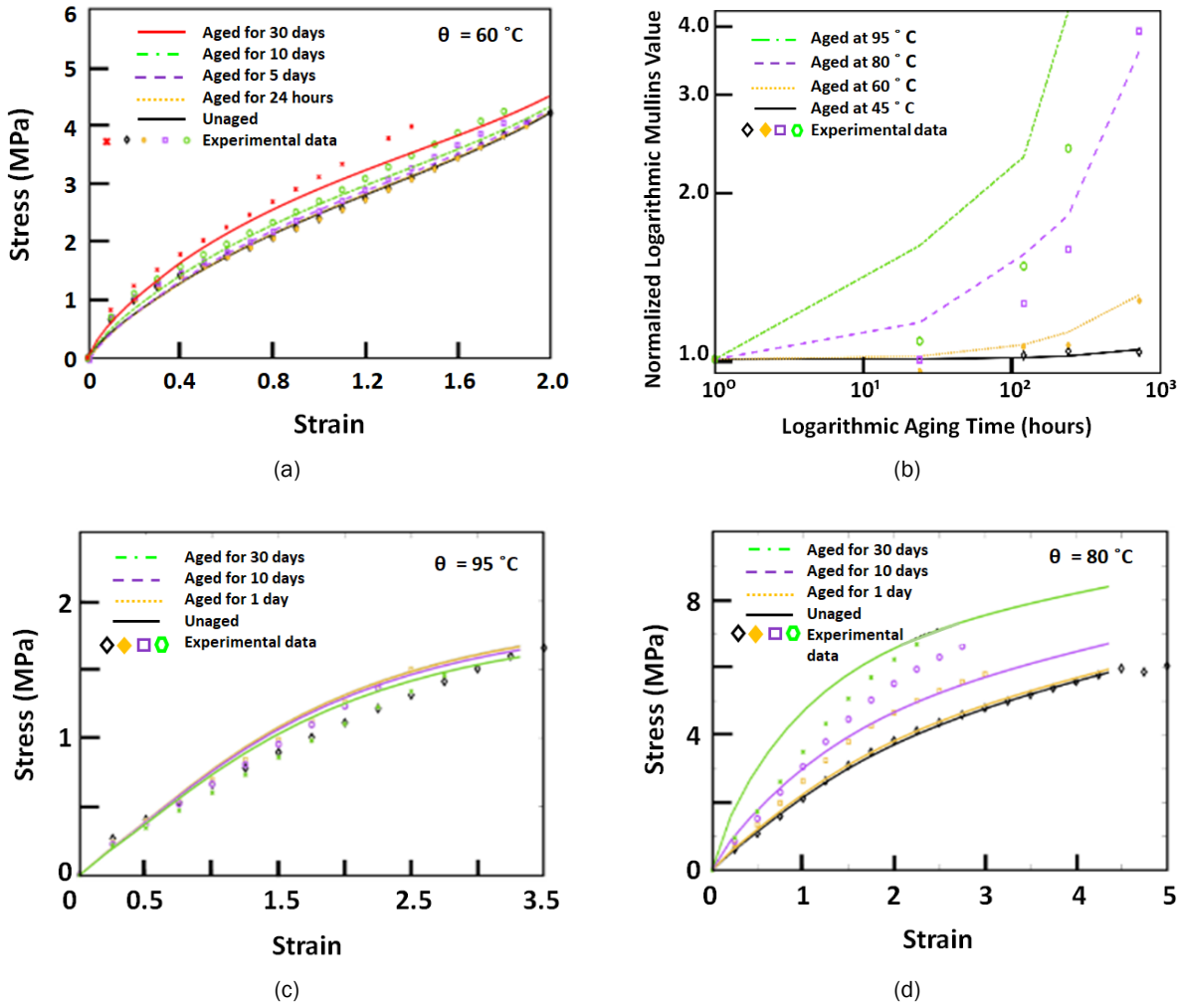

Figure II.3.3.2. Constitutive behavior of: (a) a failure of SBR; (b) Mullins effect for SBR; (c) a failure for Dow Corning silicone; and (d) a failure of polyurethane. Source: Michigan State University.

Hydrolysis and Hygrothermal

Adhesives can be exposed to hygrothermal aging, which is the combination of both heat and moisture, continually. Here, predictive models are needed to prevent catastrophic failure of the samples due to aging. So far, only a few phenomenological models can predict the effects of hydrolytic aging on rubber-like adhesives. To the best of our knowledge, there is no micromechanical model that accounts for inelastic behavior of elastomeric samples.

Experiment

The pilot-phase tests, which included failure and cyclic tests for Si- and polyurethane-adhesive variants, were completed in FY 2020. Samples of these materials were submerged in distilled water and seawater or aged at three humidity levels: 30%, 50%, and 80% relative humidity. Chemical tests were conducted on the aged materials along with Fourier Transform Infrared Spectroscopy and differential scanning calorimetry. Special mechanical tests, such as Dynamic Mechanical Analysis, was conducted on some of the submerged silicone samples. Similar tests were conducted on SBR samples to create a reference for the expected behavior and for training the model.

Constitutive Model

Damage in the polymer matrix should be described with respect to three independent variables—temperature (T), time (t), and deformation, given by the deformation gradient tensor (**F**). To describe the state of damage with respect to time, one can use the status of the matrix at time 0 and ∞ as the reference points and then define a shape function to interpolate the damage status at t. Representing the energy of the matrix in the virgin state by Ψ_0 and after indefinite aging time by Ψ_∞, the strain energy of the matrix Ψ_M at t can be approximated as:

$$\Psi_M(t,T,\mathbf{F}) = N(t,T)\Psi_0(\mathbf{F}) + N'(t,T)\Psi_\infty(\mathbf{F}), \quad \text{where} \quad N(t,T) = \exp\left(-\gamma \exp\left(-\frac{E_a}{RT}\right)t\right) \tag{5}$$

where $N(t,T)$ and $N'(t,T) = 1 - N(t,T)$ represent the weight of each state. To define the changes of the matrix in the course of hydrolytic aging, the matrix degradation needs to be described with respect to the shape function N and the energy states, Ψ_0, and Ψ_∞, as observed in Figure II.3.3.3.

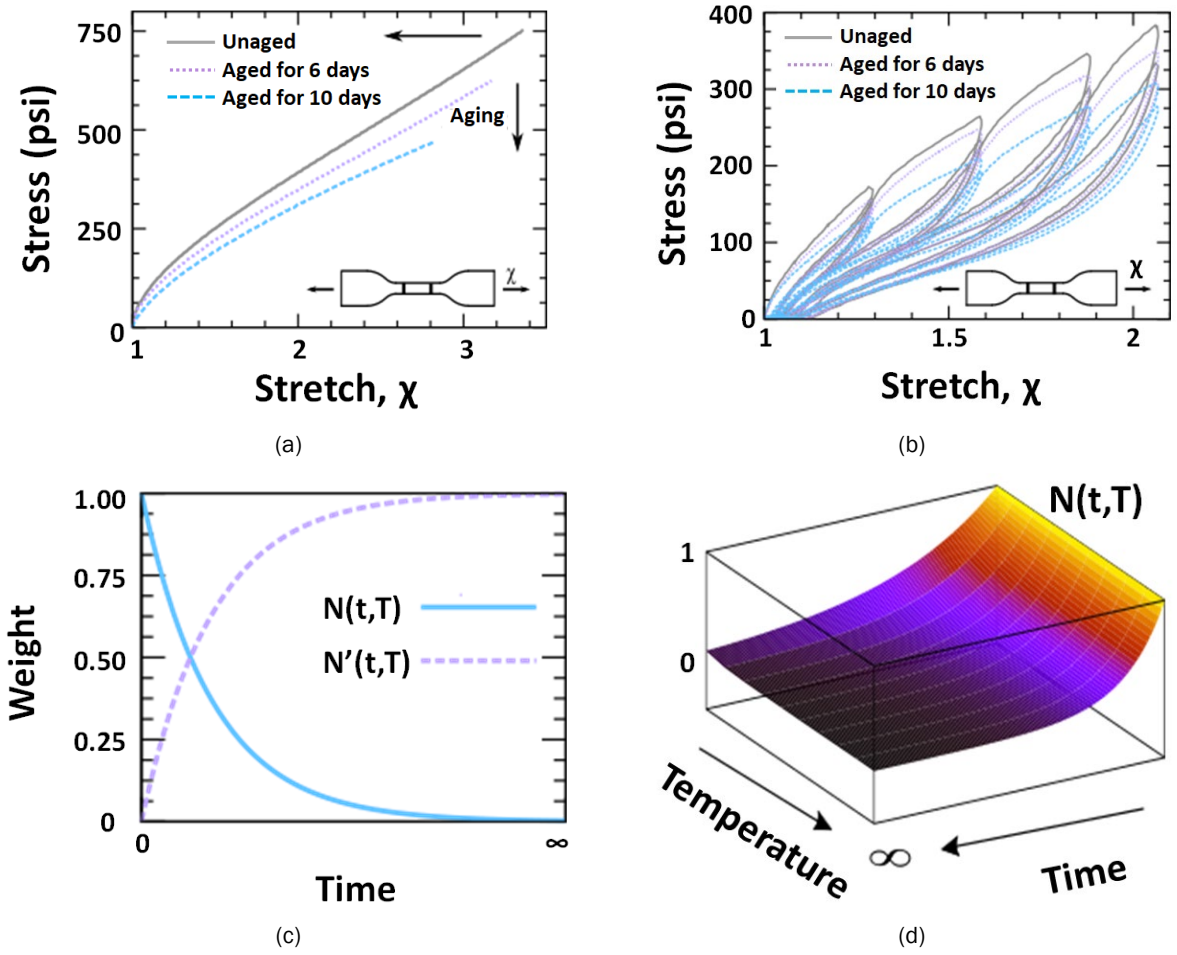

Figure II.3.3.3. Constitutive behavior of SBR samples at various aging times shown in: (a) failure; (b) cyclic tests that were performed at 60°C; (c) shape functions in one dimension using the Arrhenius function; and (d) the reconstructed surface of $N(t,T)$. Source: Michigan State University.

Hygrothermal damage can come from two parallel phenomena: (1) chain scission due to the presence of temperature; and (2) reduction of cross-links. This reduction can originate from two parts, the first is attributed to the attendance of water and the second is a result of the existence of O. Two assumptions were made to represent the strain energy on the polymer matrix. First, the damage-decay function can be similar to the water-uptake function; that is, the hygrothermal and hydrolysis damages are relevant to the amount of water that is absorbed by the samples. Second, each of the aging phenomena can be superimposed upon each other. The assumption is that a polymer matrix decomposes to two different networks: (1) a result of diffusion of O to the polymer matrix; and (2) the effect of water on the matrix. This network later decomposes into a morphed and deactivated subnetwork.

Once water attacks the matrix, two parallel phenomena occur: (1) reduction of the cross-links, which increases average chain length in the matrix, and (2) energy dissipation due to the reduction of polymer active agents. To this end, a fully attacked matrix, Ψ_∞, can be decomposed into two independent networks—namely, a newly morphed network, Ψ_m, and a deactivated network, Ψ_d,—as given below:

$$\Psi_\infty = (1-\beta)\Psi_T + \beta\Psi_w = (1-\beta)\Psi_T + \beta\left((1-\alpha)\Psi_d + \alpha\,\Psi_m\right),\ \beta = \theta RH\sqrt{t\exp\left(\frac{-E_b}{RT}\right)} \quad (6)$$

where Ψ_m and Ψ_d represent the energies of the morphed and deactivated networks, respectively. The morphed network results from the reduction of the un-attacked network cross-links; consequently, it has longer chains than the virgin matrix. A deactivated network results from a water attack on polymer chains.

To validate the proposed model, predictions were benchmarked against a set of new experimental data for black polyurethane specifically designed to capture the effects of deformation history, aging time, and aging temperature, as observed in Figure II.3.3.4(a-c) for varying relative humidity (RH).

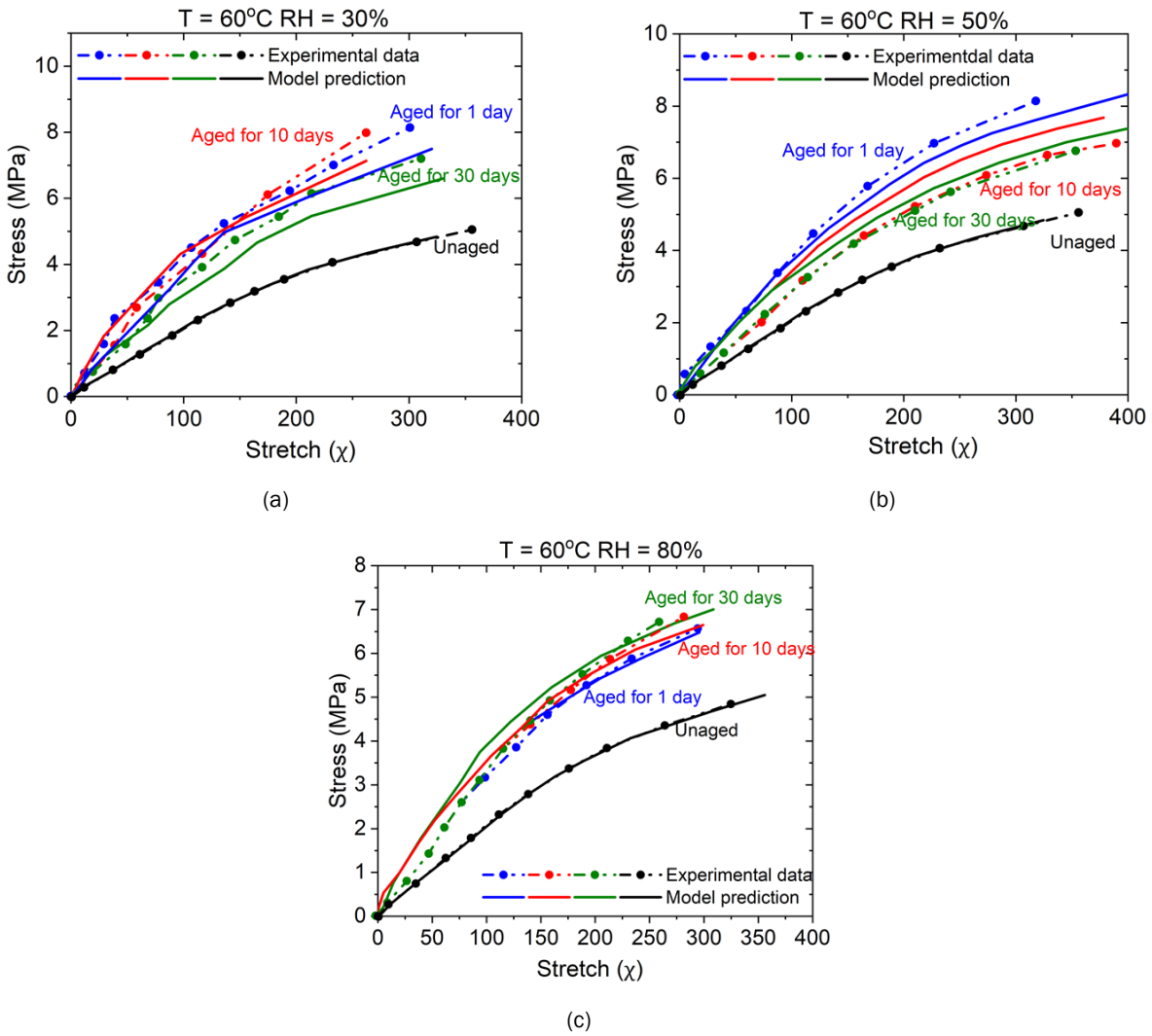

Figure II.3.3.4. Validation of model predictions for black polyurethane aged at (a) 30% RH, (b) 50% RH, and (c) 80% RH. Source: Michigan State University.

Photo-oxidation

One of the environmental conditions that has a harsh effect on the adhesive is ultraviolet radiation. The effect of this radiation on the polymer structure is similar to what has been seen in thermo-oxidation. Because temperature has a direct effect on photo-oxidation results, separating them seems to be challenging. Thus, for photo-oxidation, the goal is to find an add-on function to modify the thermo-oxidative model that can compensate for photo-oxidation effects.

Experiment

Photo-oxidative experiments were conducted with several other different conditions and durations. Other experiments, such as the permanent set, Fourier transform infrared spectroscopy, differential scanning calorimetry, and swelling tests were also conducted. Relaxation set along with dual-condition and temperature-jump experiments are currently underway, with projected completion times of the first batch being at the end of 2020. Some of the results of the experiments are presented in Figure II.3.3.5(a) for Dow Corning silicone and Figure II.3.3.5(b) black polyurethane.

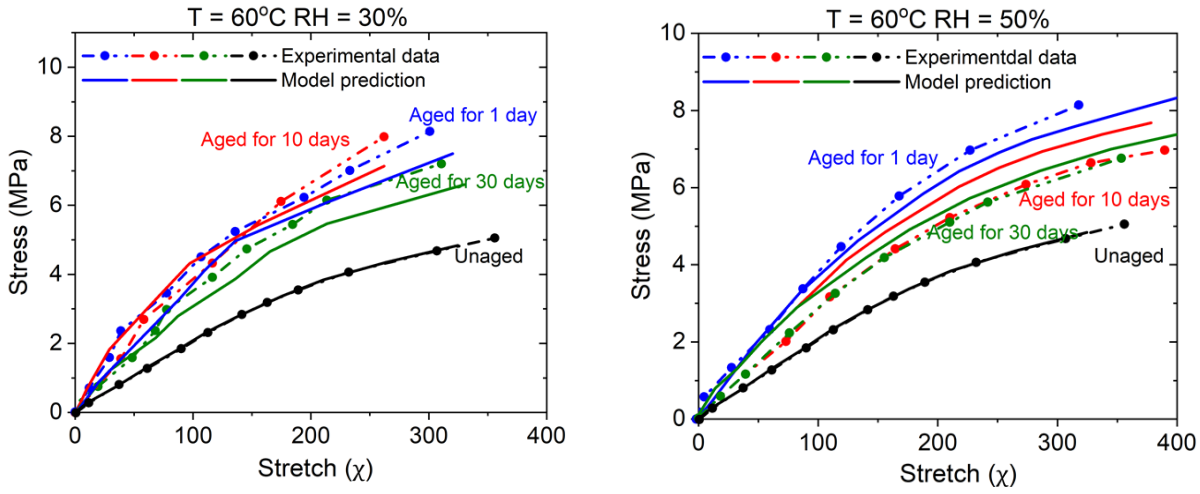

Figure II.3.3.5. Different parameter investigation achieved through: (a) a Dow Corning silicone tensile test; and (b) a black polyurethane-adhesive permanent set. Source: Michigan State University.

Constitutive Model

Photo-oxidative aging adds a set of chain scission and crosslinking to the thermo-oxidative process. Accordingly, it seems a reasonable approach to use the same dual-network hypothesis here as well. We also proposed a continuous network hypothesis that, for both relative end-to-end distance and cross-link density, is a function of time. Based on this idea, the effect of photo-oxidation reaction would be shown in the decay function as:

$$cr(t) = cr_0 - \left(cr_1 - \frac{cr_I}{2}\right)\left[1 - \exp\left(-\tau_1 e^{-\frac{E_1}{RT_{ref}}}\gamma^{\alpha}\left(\alpha_{T_1}\, t\right)\right)\right] + \left(cr_2 - \frac{cr_I}{2}\right)\left[1 - \exp\left(-\tau_2 e^{-\frac{E_2}{RT_{ref}}}\gamma^{\beta}\left(\alpha_{T_2}\, t\right)\right)\right] \quad (5)$$

$$\bar{r}(t) = R_0 - \left(R_{cr} - \frac{R_I}{2}\right)\left[1 - \exp\left(-\tau_1 e^{-\frac{E_1}{RT_{ref}}}\gamma^{\alpha}\left(\alpha_{T_1}\, t\right)\right)\right] + \left(R_{ch} - \frac{R_I}{2}\right)\left[1 - \exp\left(-\tau_2 e^{-\frac{E_2}{RT_{ref}}}\gamma^{\beta}\left(\alpha_{T_2}\, t\right)\right)\right] \quad (6)$$

To validate the proposed models, their predictions were benchmarked against experimental data, which were specifically designed to capture the effects of thermo-oxidative aging. The model predictions were in good agreement with the experimental data. The results of these tests can be seen in the stress-strain curves of Figure II.3.3.6(a-c) for three different temperatures.

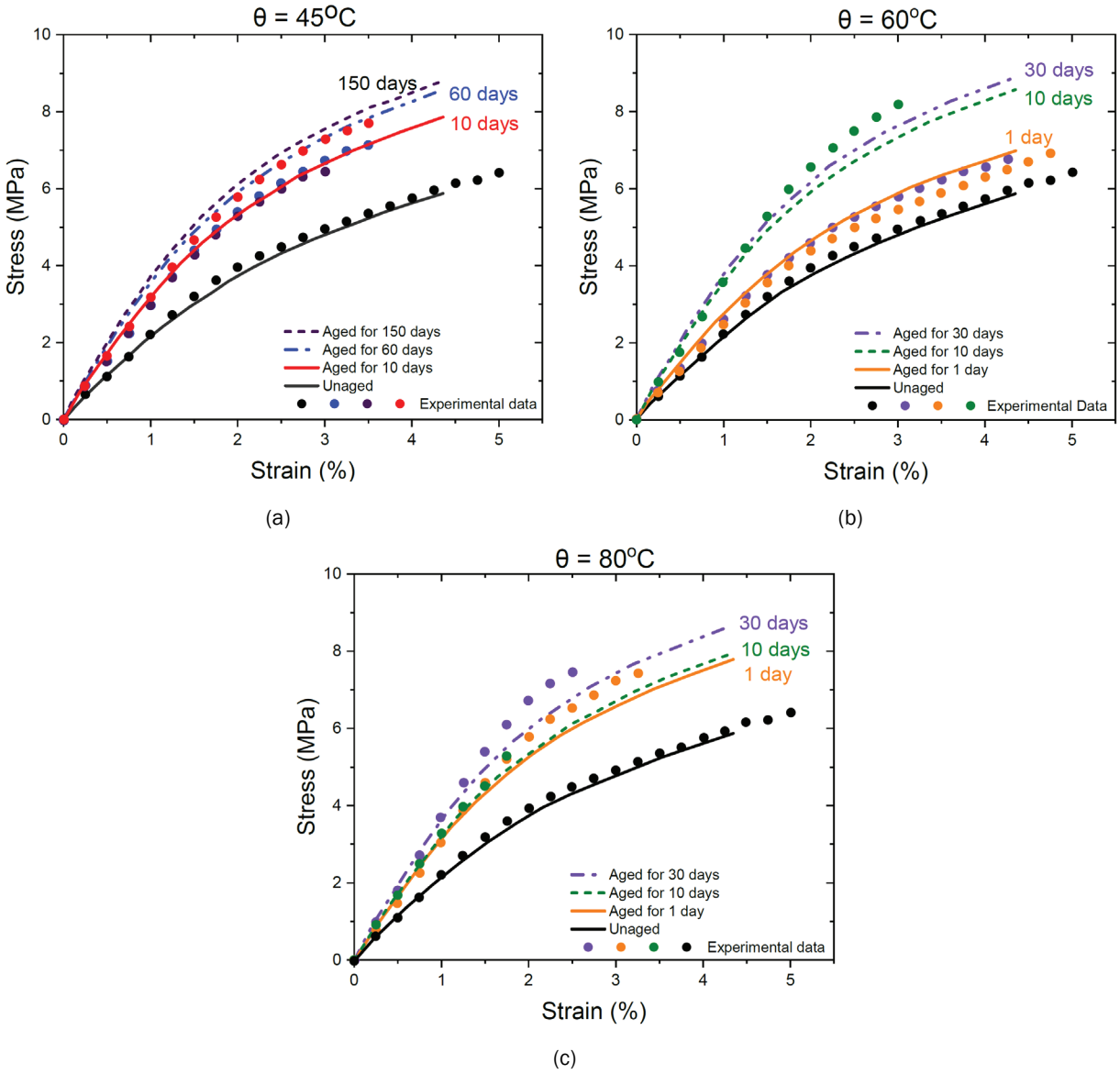

Figure II.3.3.6. Fitting predictions to experimental data for failure tests at (a) 45 °C, (b) 60 °C, and (c) 80 °C. Source: Michigan State University.

Conclusions

We developed an integrated experimental, computational, and analytical approach to understand and model the mechanisms of degradation in polymeric adhesives through a set of constitutive models that was supported by an extensive experimental program. This approach should provide predictive capabilities on the state of damage accumulation for cases in which degradation is induced by multiple parallel mechanical and environmental loads.

The proposed platform can also provide guidance for future durability research of compounds. The micromechanical concepts and modeling strategies employed in this project are evolving to reflect best practices to provide the most confidence in predicted results. In view of the experimental tests provided on different adhesives, most adhesives with crosslinked networks are highly susceptible to damage when environmental loads are combined with mechanical loads.

Key Publications

1. Morovati, V., and R. Dargazany, 2019, "Improved approximations of non-Gaussian probability, force, and energy of a single polymer chain," *Phys. Rev. E*, Vol. 99, Art. #052502.
2. Morovati, V., and R. Dargazany, 2019, "NET v1.0: A framework to simulate permanent damage in elastomers under quasistatic deformations," *Softwarex*, Vol. 10, Art. #100229.
3. Mohammadi, H., A. Bahrololoumi, Y. Chen, and R. Dargazany, 2019, "A micromechanical model for constitutive behavior of elastomers during thermo-oxidative aging," In: Huneau, B., J.-B. Le Cam, Y. Marco, and E. Verron, *Constitutive Models for Rubber XI: Proceedings of the 11th European Conference on Constitutive Models for Rubber (ECCMR 2019), Nantes, France, 25–27 June 2019*, pp. 542–547, CRC Press: New York.
4. Mohammadi, H., V. Morovati, E. Poshtan, and R. Dargazany, 2020, "Understanding decay functions and their contribution in modeling of thermal-induced aging of crosslinked polymers," *Polym. Degrad. Stabil.*, Vol. 175, Art. 109108.
5. Bahrololoumi, A., V. Morovati, E. A. Poshtan, and R. Dargazany, 2020, "A multiphysics constitutive model to predict quasistatic behavior: Hydrolytic aging in thin crosslinked polymers," *Int. J. Plast.*, Vol. 130, Art. 102676.

References

1. Dargazany, R., and M. Itskov, 2009, "A network evolution model for the anisotropic Mullins effect in carbon black filled rubbers," *Int. J. Solids Struct.*, Vol. 46, No. 16, pp. 2967–2977.
2. Khalili, L., V. Morovati, R. Dargazany, and J. Lin, 2017, "Micromechanical modeling of visco-elastic behavior of elastomers with respect to time-dependent response of single polymer chains," *Constitutive Models for Rubber X*, 28–31 August 2017, Munich, Germany, Vol. 10, Art. 523.
3. Mohammadi, H., and R. Dargazany, 2019, "A micromechanical approach to model thermo-oxidative aging in elastomers," *Int. J. Plast.*, Vol. 118, pp. 1–16.
4. Mohammadi, H., and R. Dargazany, 2018, "Micromechanical model for thermo-oxidative aging of elastomers," In: ASME 2018 International Mechanical Engineering Congress and Exposition, American Society of Mechanical Engineers, Art. V009T12A028–V009T12A028.
5. Carter, H. G., and K. G. Kibler, 1978, "Langmuir-type model for anomalous moisture diffusion in composite resins," *J. Compos. Mater.*, Vol. 12, No. 2, pp. 118–131.
6. Khalalili, L., A. I. Azad, J. Lin, and R. Dargazany, 2019, "Modular platform to model parallel inelastic mechanisms in rubber-like materials," *Rubber Chem. Technol.*, Vol. 92, No. 1, pp. 51–68.
7. Morovati, V., and R. Dargazany, 2019, "NET v1.0: A framework to simulate permanent damage in elastomers under quasistatic deformations," *Softwarex*, Vol. 10, Art. 100229.
8. Beyer, M. K., and H. Clausen-Schaumann, 2005, "Mechanochemistry: The mechanical activation of covalent bonds," *Chem. Rev.*, Vol. 105, No. 8, pp. 2921–2948.

Acknowledgements

We thank S. Kleinbaum, the DOE VTO Technology Manager, for her comments and suggestions on experimentation procedure and continuous feedback and Mr. J. Terneus from NETL for managing the progress of the project. This material is based on work supported by the DOE-EERE under Award Number DE-EE0008455. This report was prepared as an account of work sponsored by an agency of the U.S. Government. The views and opinions of authors expressed herein do not necessarily state or reflect those of the U.S. Government or any agency thereof.

II.3.4 High-Strength Steel-Aluminum Components by Vaporizing Foil-Actuator Welding (The Ohio State University)

Glenn Daehn, Co-Principal Investigator
Department of Materials Science and Engineering
The Ohio State University
295 Watts Hall
2041 College Road North
Columbus, OH 43210
E-mail: daehn.1@osu.edu

Anupam Vivek, Co-Principal Investigator
Department of Materials Science and Engineering
The Ohio State University
348 MacQuigg Labs
105 West Woodruff Avenue
Columbus, OH 43210
E-mail: vivek.4@osu.edu

Sarah Kleinbaum, DOE Technology Manager
U.S. Department of Energy
E-mail: sarah.kleinbaum@ee.doe.gov

Start Date: October 1, 2016 End Date: April 30, 2021
Project Funding: $289,948.40 DOE share: $4,702.04 Non-DOE share: $285,246.36

Project Introduction

This project aims to address the challenge of effectively welding dissimilar materials—high-strength steel and high-strength Al—for creating lightweight, multi-material automotive components. Traditional fusion-based welding between dissimilar combinations of Al and steel is difficult due to starkly disparate melting points. Also, their reactivity usually leads to the formation of brittle intermetallic compounds at the weld interface. Such joints are weak and cannot be implemented in crash-sensitive components. Structural adhesives and mechanical fasteners of various types, including self-piercing rivets, flow-drilled screws, friction element welds, and RIVTAC, are currently being used to address this issue. Solid-state welding techniques, like friction-stir and impact welding, offer an elegant alternative solution for joining dissimilar metals without the use of a third body, such as rivets. This project utilizes vaporizing foil-actuator welding (VFAW), an impact welding method developed at OSU [1]. Details on this process can be found in the Materials 2017, 2018, and 2019 Annual Progress Reports [2],[3],[4], as well as several journal articles published on this technology.

VFAW has demonstrated much success in welding a wide range of alloys, including Mg-Al, Al-Cu, Ti-Cu, bulk metallic glass-Cu, and Ni-Ti. In this project, the focus is on welding specific grades of steel and Al that are relevant to automotive subframes and developing the technology to a level at which it can be transitioned to an automotive supplier or an OEM. Besides the research on weldability of different material combinations and determination of ideal parameters through experiment and simulation, the project also includes design, production, and testing of a prototype subframe component, as well as production equipment. Robustness of the process for application in a serial production setting is demonstrated via robotic implementation.

Work in FY 2020 was focused on testing and optimizing the prototype weld head and automation work cell. Through collaboration with Magna and Coldwater Machine, the prototype weld head was constructed and

assembled. The weld head system is undergoing the optimization process through extensive welding tests at OSU and is close to being installed at Magna for final prototype production. The automation work cell was complete and tested to achieve fully automated VFAW joints.

Objectives

This project accelerated and focused the development of VFAW to produce an automotive component. At project completion, the technology will be ready for adoption within the R&D groups of Tier 1 and OEMs for assembly of mixed, advanced material bodies.

The overall objectives of the project are:

- A 20% weight reduction of the current all steel automotive component from a 2017 mid-size sedan at a cost premium of $3/lb-saved by developing a mixed material joining technology capable of high-volume production.
- The produced component that meets or exceeds the strength and durability of the incumbent component.
- A predictive modeling capability for relating process, structure, and property of VFAW joints.

The specific objectives for FY 2020 were:

- To construct, test, and optimize the prototype weld head system for maximum reproducibility.
- To produce a prototype Al-steel engine cradle using the weld head that meets automotive performance objectives of strength, durability in corrosion, durability in fatigue, and stiffness via subcomponent testing.
- To test and optimize an automation system achieving fully automated coupon feeding, foil feeding, vaporizing foil-actuator spot welding, and cleaning to show the potential for automation capability of the VFAW process.

Approach

The overall approach for this project is to perform coupon scale testing at OSU, develop welding systems and part fixtures at OSU and Coldwater, prototype-scale manufacture and testing at Magna, and process simulation at PNNL. Ashland, Arconic, Hydro, Novelis, and Magna are providing material. The pre-prototype welding heads and final welding head will be fabricated at Coldwater and tested at OSU. The final welding head, along with a capacitor bank, will be installed at Magna. Coupon data will be imported into the design of the prototype component, while simulated testing and design iterations will lead to the final part. Once the prototype design is released, Magna will produce subcomponents and perform the assembly at its prototype facility. The assembled prototypes will be tested for durability and corrosion performance.

Coupon Testing

The Al-steel combination was finalized as hot-rolled 4.2 mm thick AA5182-O and 2.2 mm thick high-strength low alloy (HSLA) 340, based on the screening results and actual material inventory at Magna's material supplier, Novelis. For this project, VFAW requires a 1 mm thick AA3003-H14 intermediate layer (interlayer). Standoff gaps between the interlayer and target were provided by dimpling the target sheet. Geometry of the preformed dimples was finalized based on the trials conducted to generate the strength and durability data used in the prototype design simulation. As the final welding parameters, two welds are required to create a weld: the first weld joins the interlayer with the pre-deformed target, and the second weld joins the Al flyer to the target at the pre-welded interlayer. A schematic of this process is shown in Figure II.3.4.1.

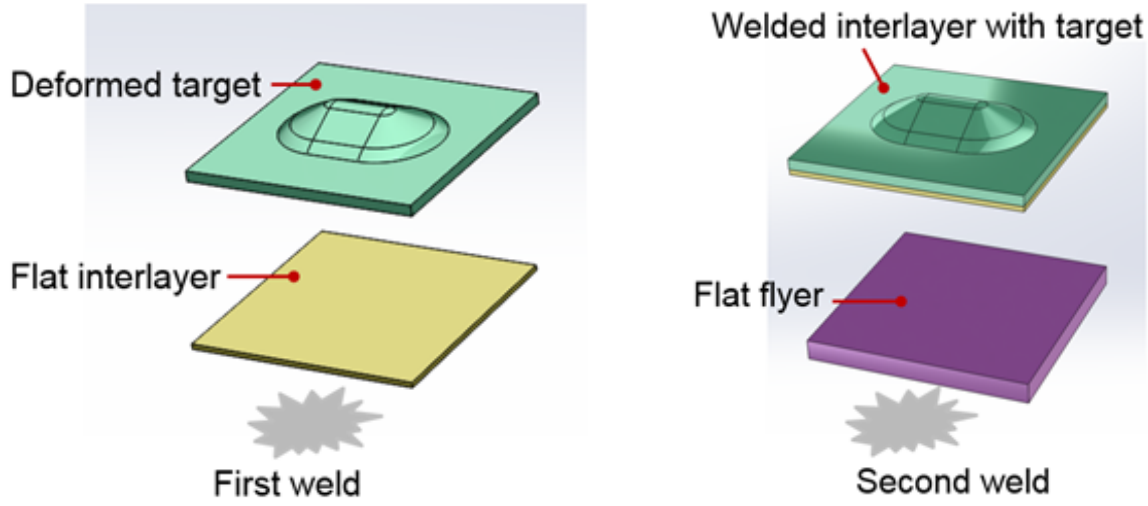

(a) (b)

Figure II.3.4.1. Illustrations of the two-shot VFAW showing: (a) the first shot welds the flat interlayer to the deformed target; and (b) the second shot welds the flyer to the welded flyer-target stack-up. Source: The Ohio State University.

Subcomponent Welding Test

Prior to prototype production, a steel subcomponent was tested in a lab environment. The subcomponent of 2.5 mm HSLA 340 was produced with welding dimples pre-deformed in a designed position, shown in Figure II.3.4.2(a). The pre-prototype weld head constructed in FY 2019 was used for welding. The setup is shown in Figure II.3.4.2(b).

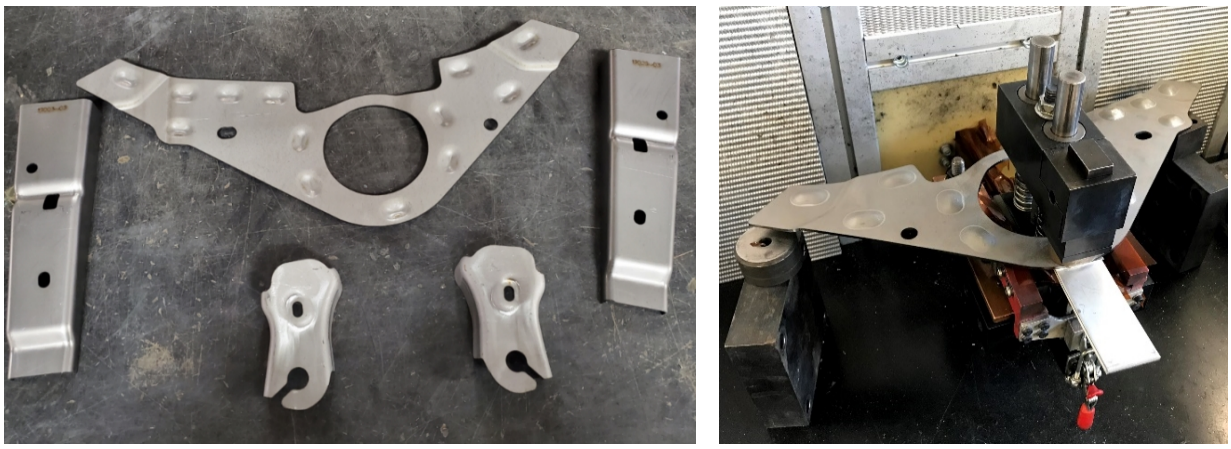

(a) (b)

Figure II.3.4.2. VFAW of subcomponent with: (a) stamped steel subcomponents; and (b) welding setup using pre-prototype fixture. Source: The Ohio State University.

Development of Prototype Weld Head

The weld head was designed and pre-prototyped in FY 2019, and construction was completed this year. Installed at OSU, the weld head is being validated and optimized through coupon-welding tests. Lap-shear tests were performed to determine weld quality. Current and voltage trace during welding was acquired using an oscilloscope as the reference system parameters. A noise-resistant chamber was constructed for the prototype weld head test.

Development of Automation Work Cell

Fully automated VFAW joints of 1 mm thick AA 5052 and 1 mm thick dual phase 590 steel coupons were created using the automation work cell, including hybrid samples with automated epoxy-adhesive dispersion and VFAW-only samples. Lap-shear tests were performed to validate the VFAW automation process.

Results

COVID-19 Impacts

The testing of the prototype welding tool, described next, was delayed due to COVID-19 related shutdowns in March 2020. Testing resumed at OSU in July 2020, and the overall project has been extended by six months to complete the remaining tasks of prototype production, testing, and cost analysis.

Prototype Weld Head Test

The new prototype weld head was set up inside of the sound-reduction chamber, shown in Figure II.3.4.3(a). A few coupons have been welded using the new system. Arcing issues are being addressed to make the system robust for prototype production. Vaporizing foil-actuator welds of 4.5 mm 5183 Al to 2 mm HSLA 340 steel coupons with clean surfaces and maximum shear loads higher than 16 kN, which is as good as the previous coupon testing results in a lab environment, were created under no-arcing condition, shown in Figure II.3.4.3(b). Current and voltage trace during discharge were obtained; they showed negligible difference from the previous system, indicating the new prototype weld head is valid in terms of inductance. Another technical hurdle that has been overcome through the trials thus far is connecting the weld head to the capacitor bank while maintaining mobility of the weld head. The 16 ft-long coaxial-cable assembly did not decrease the efficiency of the system in making welds at the same energy levels as the ones used when the welding tool was fastened directly to the capacitor bank terminals, as shown in Figure II.3.4.2(b) above.

(a) (b)

Figure II.3.4.3. Prototype weld head test: (a) the fixture during welding and (b) AA 5183-HSLA340 coupon welds created by the system. Source: The Ohio State University.

A schematic of VFAW prototype production assembly is shown in Figure II.3.4.4(a). The prototype weld head is to be mounted on a KUKA 6-axis welding robot, as shown in Figure II.3.4.4(b), to achieve the maximum maneuverability and flexibility, as well as to better accelerate the technology. With the engine cradle fixed with a holding fixture, shown in Figure II.3.4.4(c), the robot arm will precisely deliver the welding head to preset locations then achieve VFAW.

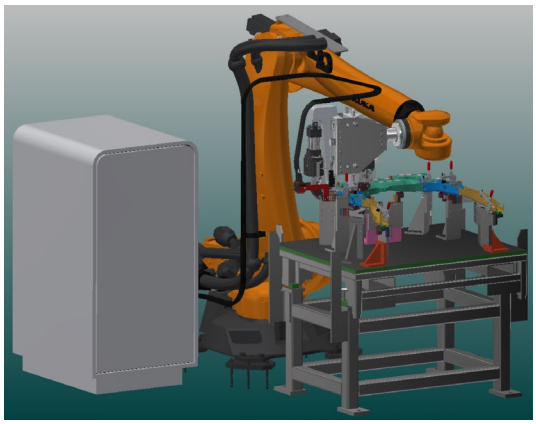

(a)

(b)

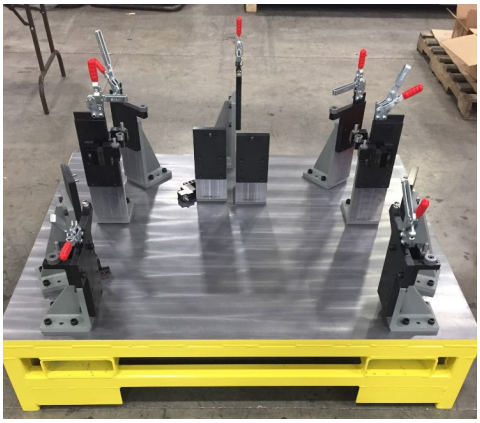

(c)

Figure II.3.4.4. Robotic prototype system: (a) a schematic of VFAW prototype production showing a 4.2kJ capacitor bank, robotic arm, prototype welding head, prototype components, and fixture table; (b) procured KUKA 6-axis welding robot; and (c) a holding fixture. Source: Magna.

Prototype Component Manufacture

The subcomponent production at Magna is complete. Several Zn and some steel dies were fabricated to stamp these components, and each component was checked against check fixtures to ensure part fit. Forty-nine different steel and Al subcomponents were stamped at Magna, including stamped and laser-cut steel and Al parts, shown in Figure II.3.4.5.

(a)

(b)

(c)

Figure II.3.4.5. Stamped and laser-cut steel and Al subcomponents. Source: Magna.

Subcomponent Welding Test

4.0 mm Al 5754 and 5.1 mm hot-rolled Al 5052 coupons were successfully welded to the subcomponent using a two-shot method, shown in Figure II.3.4.6. The subcomponent was tested with the pre-prototype system. During testing, it was proved that providing good support on the subcomponent is important to preserve the steel dimple from fracturing near the peak due to the welding process.

(a) (b)

Figure II.3.4.6. VFA-welded thick 5000 series Al coupon with HSLA 340 subcomponents: (a) steel side shows no damage; and (b) Al side shows successful welds of first weld (yellow) and second weld (blue). Source: The Ohio State University.

Test of Automation Work Cell

The automated pedestal system, as shown in Figure II.3.4.7, has been tested and used to create VFAW joints. A total of 40 samples with VFAW-only and 10 samples that combined VFAW with Pliogrip 4000, Ashland's one component, crash-toughened structural epoxy-adhesive, were created in a fully automated manner. While making the 40 VFAW-only samples, 16 samples failed to weld during the process. Conversely, only one sample failed to weld while making the 10 hybrid samples. All samples were made with 1 mm thick Al 5052 as the flyer and 1 mm thick dual phase 590 steel as the target.

The work cell is not stable enough in operation to be able to create hundreds of samples without intervention. The main issue is with the foil feeder, which is still struggling to dispense foils repeatably. A contributing factor is that the foil is being bent and dispensed at the same time, and this creates resistance to dispensing. There were also issues found with electrical arcing that contributed to some samples not welding. The final instability is in the coupon dispensing and is a result of the stack of coupons being dispensed too far. All these issues are fixable and would dramatically increase the stability of the system. Despite these issues, the system was still able to perform several welds in sequence before issues arose that required resetting the system. This means the samples produced still provide data on fully automated welds.

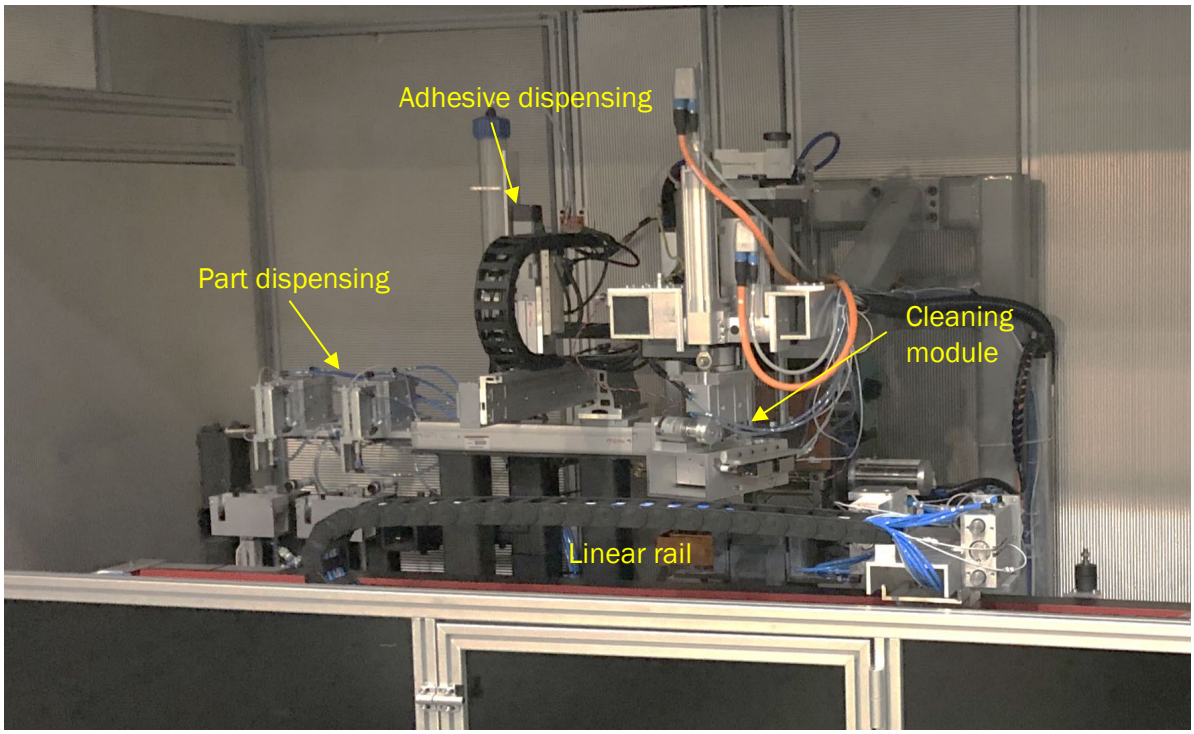

Figure II.3.4.7. Pedestal welder with automated part handling, adhesive dispense, and cleaning. Source: The Ohio State University.

The load-displacement curves for the hybrid VFAW samples are presented in Figure II.3.4.8. Only two samples had interfacial failure, and the rest of the samples yielded nugget tear-out. The data show good repeatability with maximum loads around 9 kN except for the one outlier (green line). These samples would still have the same variance in foil, so it appears the use of small amounts of adhesive around the joining perimeter can improve weld repeatability. The addition of adhesive produced higher strength than were seen in the VFAW-only samples. This was accomplished despite small amounts of the adhesive burning during the welding process. Hybrid welds were made with a lower energy level than VFAW-only welds to counteract increased air resistance from air trapped in the weld center.

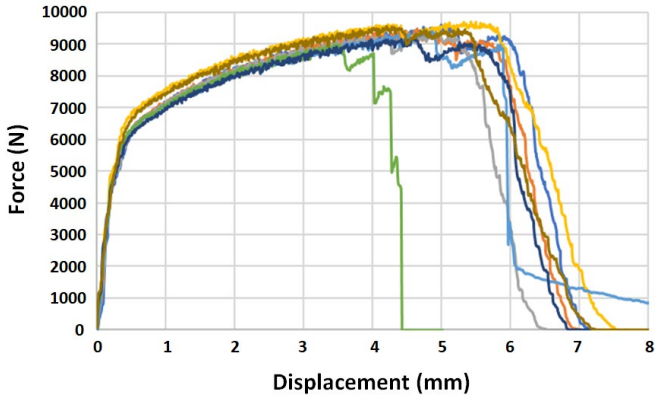

Figure II.3.4.8. Force vs. displacement curve for the hybrid VFAW samples. Source: The Ohio State University.

Conclusions

VFAW automation has been achieved with programmed foil feeding, part dispensing, adhesive feeding, and firing. VFAW of HSLA 340 steel and 5000-series Al has been moving from the lab environment to prototype production with a robot-mountable welding head. VFAW of a prototype subcomponent was validated.

Key Publications

1. Thurston, B. P., A. Vivek, B. S. Nirudhoddi, and G. S. Daehn, 2019, "Vaporizing foil-actuator welding," *MRS Bulletin*, Vol. 44, No. 8, pp. 637–642.
2. Sridharan, N., J. Poplawsky, A. Vivek, A. Bhattacharya, W. Guo, H. Meyer, Y. Mao, T. Lee, and G. Daehn, 2019, "Cascading microstructures in Al-steel interfaces created by impact welding." *Mater. Charact.*, Vol. 151, pp. 119–128.
3. Gupta, V., T. Lee, A. Vivek, K. S. Choi, Y. Mao, and X. Sun, 2019, "A robust process-structure model for predicting the joint interface structure in impact welding," *J. Mater. Process. Tech.*, Vol. 264, pp. 107–118.
4. Mao, Y., V. Gupta, B. Ufferman, A. Vivek, K. S. Choi, X. Sun, and G. S. Daehn, 2018, "On process, structure, property relationships in impact welding of Al 6061 and Steel 4130," *Eighth International Conference on High-Speed Forming*, May 14–15, 2018, Columbus, OH, USA.
5. Gupta, V., X. Sun, K. Choi, A. Vivek, Y. Mao, and G. Daehn. 2017, "A computational modeling approach to predict the interfacial characteristics obtained in high velocity impact welding of metals," *Materials Science & Technology 2017*, October 8–12, 2017, Pittsburgh, PA, USA.
6. Gupta, V., K. Choi, A. Vivek, Y. Mao, X. Sun, and G. Daehn, 2018, "Prediction of joint properties obtained in the high velocity impact welding of dissimilar metals," *TMS 2018 Annual Meeting & Exhibition*, March 11–15, 2018, Phoenix, AZ, USA.

References

1. Vivek, A., S. R. Hansen, B. C. Liu, and G. S. Daehn, 2013, "Vaporizing foil-actuator: A tool for collision welding," *J. Mater. Process. Tech.*, Vol. 213, No. 12, pp. 2304–2311.
2. DOE-EERE Vehicle Technologies Office, 2018, "Materials 2017 Annual Progress Report," DOE-EERE VTO Report No. DOE/EE-1711, May 2018.
3. DOE-EERE Vehicle Technologies Office, 2019, "Materials 2018 Annual Progress Report," DOE-EERE VTO Report No. DOE/EE-1827, April 2019.
4. DOE-EERE Vehicle Technologies Office, 2020, "Materials 2019 Annual Progress Report," DOE-EERE VTO Report No. DOE/EE-1990, April 2020.
5. Marker, M. C. J., B. Skolyszewska-Kühberger, H. S. Effenberger, C. Schmetterer, and K. W. Richter, 2011, "Phase equilibria and structural investigations in the system Al-Fe-Si," Intermetallics, Vol. 19, No. 12, pp. 1919–1929.

II.3.5 Corrosion Control in Carbon Fiber Reinforced Plastic (CFRP) Composite-Aluminum Closure Panel Hem Joints (PPG Industries, Inc.)

Brian Okerberg, Principal Investigator
PPG Industries, Inc.
Coatings Innovation Center
4325 Rosanna Drive
Alison Park, PA 15101
E-mail: okerberg@ppg.com

Sarah Kleinbaum, DOE Technology Manager
U.S. Department of Energy
E-mail: sarah.kleinbaum@ee.doe.gov

Start Date: October 1, 2016 End Date: September 30, 2020
Project Funding: $685,578 DOE share: $476,353 Non-DOE share: $209,225

Project Introduction

This project developed new coatings and adhesives, and established corrosion characterization techniques that enable CFRP/Al hem flange joints, which were designed to meet current specifications for mechanical performance, corrosion resistance, and appearance when cured between 150°C and 180°C. Critical success factors to achieve this goal include the development of novel coatings, adhesives, and/or joining geometries to fully isolate the inner panel from the outer panel in the joint while maintaining the ability to electrostatically paint the inner panel in the paint line. Extensive electrochemical and SCC testing was conducted to evaluate the corrosion performance of the new solutions and determine the appropriate accelerated test methods.

Objectives

The objective of this project was to develop new coatings, adhesives, and joint geometries, as well as to establish and validate corrosion characterization techniques that enable Ford Motor Company to implement lightweight closure panels based on a CFRP inner/Al outer joined by a hem flange.

Approach

The project was divided into three BPs. The first budget period focused on understanding the nature and extent of the corrosion problem resulting from the CFRP/Al joint. During the second budget period, formulation of prototype conductive primers, adhesives, and E-coats were completed. In the third budget period, coatings and adhesive formulations were finalized and scaled-up. Work on galvanic corrosion, SCC, and accelerated corrosion test methods was continued. Five liftgate assemblies incorporating CRFP/Al hem joints were produced using the prototype materials from PPG. The liftgate assemblies were tested by Ford and compared to laboratory test results and accelerated corrosion test results from OSU.

Results

TASK 1

Subtask 1.1.3: Effect of Galvanic Coupling on SCC Susceptibility

Repeat testing in-air of AA6111-T8-like material at the slower displacement rate of 4.50×10^{-8} in/sec confirm the results of previous testing and confirm that strain-rate is not influencing the results. Threshold stress intensity, K_{TH}, values for the repeat test were 21.7 and 23.7 MPa$\sqrt{m}$ as determined by both analysis methods (e.g., ASTM E1820 and E561/B646, respectively). The plot of load and crack length as a function of crosshead displacement and the stress intensity, K_R, curve measured for this test are shown in Figure II.3.5.1 and Figure II.3.5.2, respectively. The crack length is a measured voltage that is converted using a Johnson equation. It is common to see initial voltage changes at the start of a test that are not crack related, which is the reason for the decrease in load up to 0.25 mm displacement seen in Figure II.3.5.1. The measured values of

K_{TH} for -756 mV_{SCE} and -706 mV_{SCE} are close to the air K_{TH} values, indicating only mild SCC is occurring at these levels of polarization; however, since only one air test was conducted, normal scatter in experimental data may compensate for the small difference in K_{TH}. Anodic polarization greatly decreases SCC resistance, causing K_{TH} to fall to lower than an experimentally measurable value at -656 mV_{SCE}.

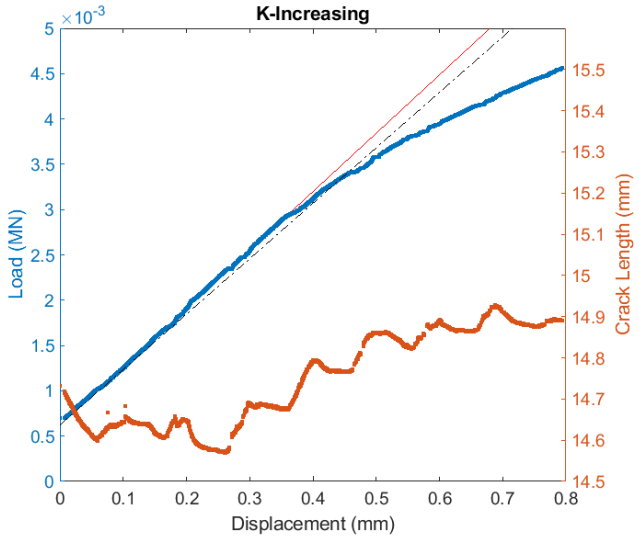

Figure II.3.5.1. SCC testing of AA6111-T8-like material in 3.5 wt% NaCl at the slower displacement rate of 4.50 x 10-8 in/sec. Source: The Ohio State University.

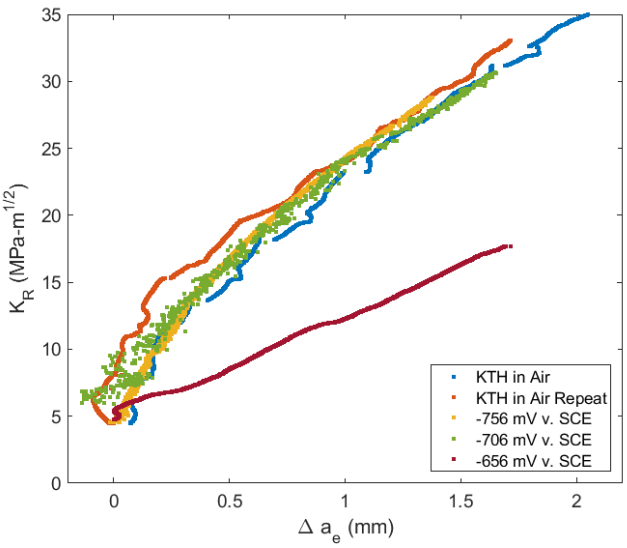

Figure II.3.5.2. Stress intensity (K_R) as a function of effective crack extension (Δa_e) for SCC testing of AA6111-T8-like material in 3.5 wt% NaCl at the slower displacement rate of 4.50 x 10-8 in/sec. Source: The Ohio State University.

The summary plot of K_{TH} (stress intensity as a function of effective crack elongation) as a function of polarization potential is illustrated in Figure II.3.5.3. Each "x" indicates that no cracking above the resolution limit occurred during the test segment, while the checkmarks indicate cracking at that potential and stress intensity. The red region is the range of measured K_{TH} behavior in-air.

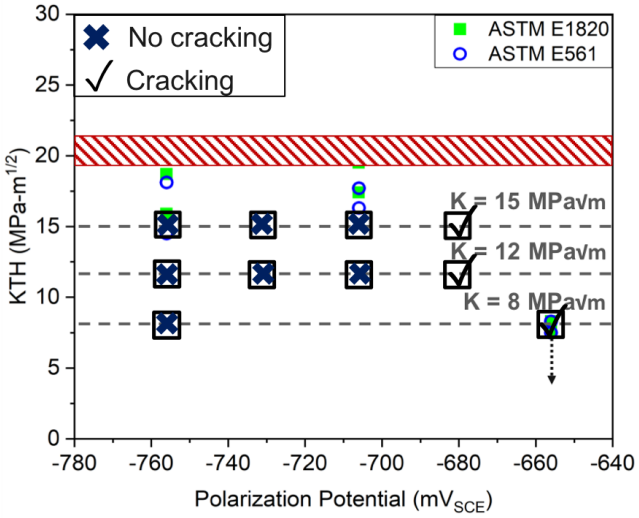

Figure II.3.5.3. Summary of results for constant K SCC testing superimposed on a plot of K_{TH} measured during slow rising displacement as a function of applied polarization potential for AA6111-T8-like in 3.5 wt% NaCl.
Source: The Ohio State University.

TASK 2

Subtask 2.3: Galvanic Characterization and Assessment

Localized corrosion mechanism in AA6XXX. The microscopic and electrochemical behavioral differences between AA6111 and AA6022 that led to enhanced activity in AA6111 at galvanic potentials were investigated. In this work, AA6111 and AA6022 have been potentiodynamically polarized from -10 to +150 $mV_{OCP,AA}$. Microstructures of AA6111 and AA6022 were recorded unpolarized and after polarization, as shown in Figure II.3.5.4 and Figure II.3.5.5, respectively. The presence of precipitates can be clearly distinguished and trenching around precipitates is noted upon polarization. The trenching appears to be more uniform in AA6022. The preferential dissolution of the matrix around precipitates is not currently well understood.

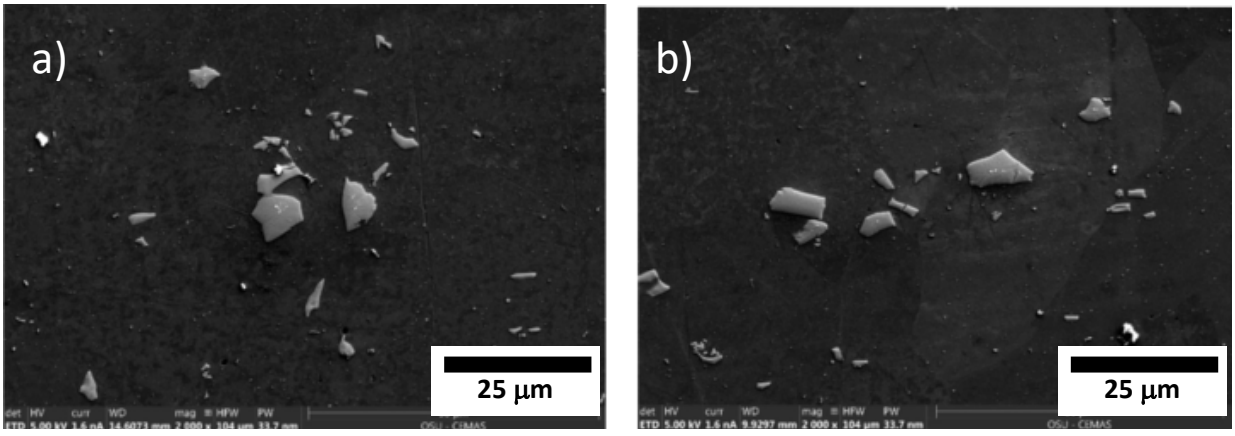

(a) (b)

Figure II.3.5.4. SEMs of finely polished unpolarized: (a) AA6111 and (b) AA6022. Source: The Ohio State University.

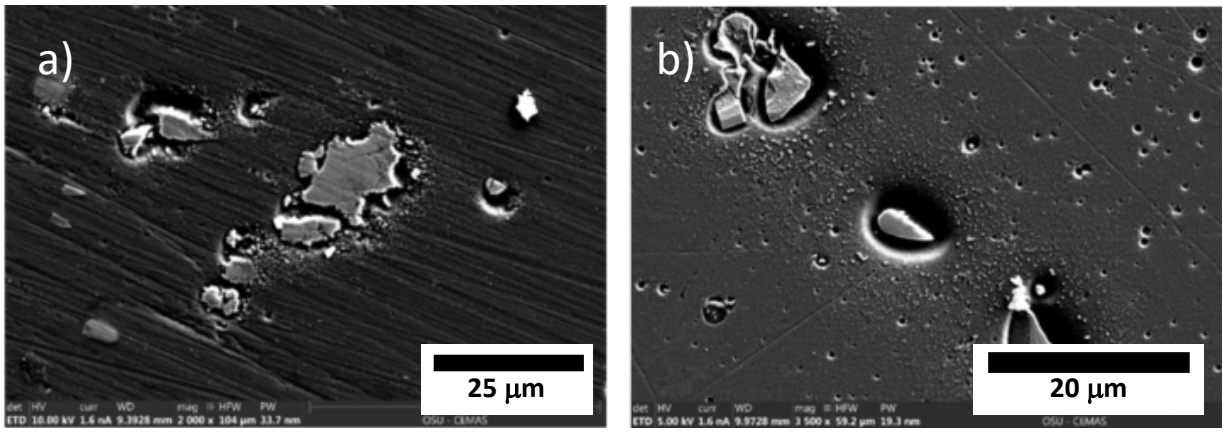

(a) (b)

Figure II.3.5.5. SEMs of polished and potentiodynamically polarized: (a) AA6111; and (b) AA6022.
Source: The Ohio State University.

L467 Ford-accelerated corrosion testing. Combinations of uncoated/e-coated AA6111-Twill CFRP, 6111-Random CFRP, 6022-Random CFRP, and 6111-Twill CFRP were tested for corrosion under accelerated conditions in accordance with Ford Corporate Engineering Test Procedure 00.00-L-467 for Cyclic Corrosion (L-467) for about 13 weeks. Galvanic currents flowing between components were measured using the zero-resistance ammeter mode of the potentiostat, and the data were plotted with respect to exposure time. Galvanic currents closely correspond to environmental changes in the chamber. The cycles include spraying (Phase I), high humidity (Phase II), half-time decay/drying (Phase III), and dry phase (Phase IV). Peaks in galvanic currents (e.g., starred points) occur during the spray cycle and during drying when the concentration of electrolyte increased thereby increasing the solution conductivity.

From Figure II.3.5.6, there is no significant difference in the galvanic currents measured in e-coated and uncoated coupons. The trend of e-coated coupons in Figure II.3.5.6(b) shows an increase in currents for three weeks, and then a decrease up to six weeks. One possible reason for this could be the formation of blisters around three weeks in combination with an accumulation of corrosion product or worn off e-coat in the blisters, restricting the solution flow leading to lowering of current up to six weeks. However, the increase in current after six weeks can be explained by flushing the accumulated matter away. A decrease in currents in these coupons could result from an accumulation of corrosion product or an increase in the ohmic potential drop due to coupon warping. Figure II.3.5.6 shows the distinction in corrosion susceptibility in different coupon combinations. AA6111-random exhibited the highest currents, whereas AA6022-Twill exhibited the lowest currents, which closely corresponds to the extent of damage observable in Figure II.3.5.7 and Figure II.3.5.8.

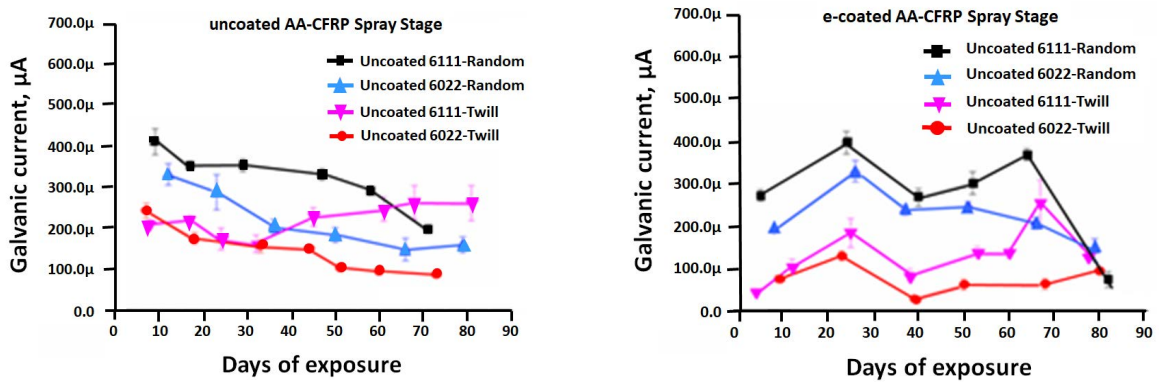

(a) (b)

Figure II.3.5.6. Galvanic current measurements during spray on: (a) uncoated coupons; and (b) e-coated coupons.
Source: The Ohio State University.

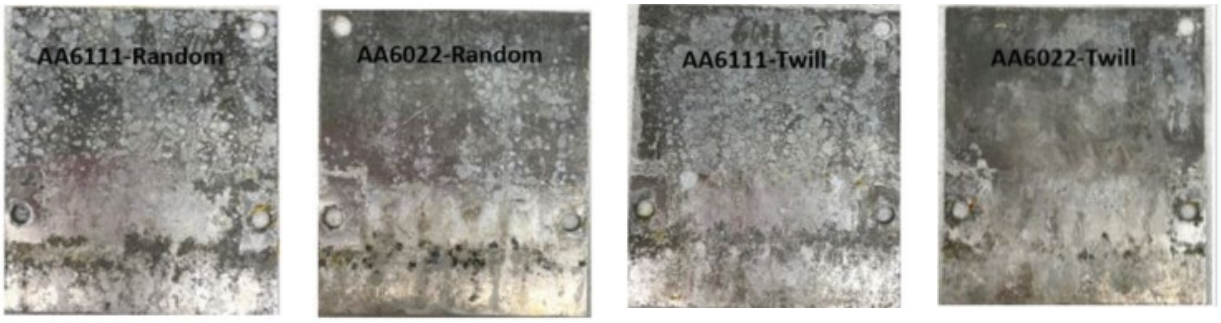

(a) (b) (c) (d)

Figure II.3.5.7. (a-d) Uncoated AA6xxx-CFRP coupons after 13-week exposure under L467 testing.
Source: The Ohio State University.

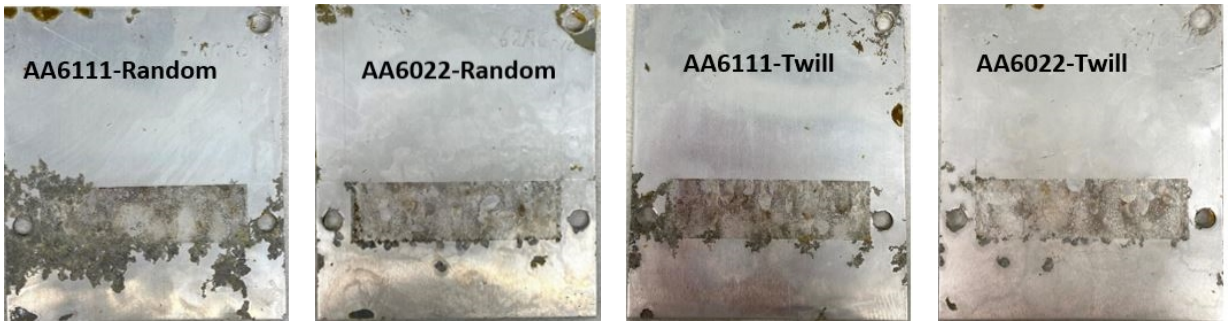

(a) (b) (c) (d)

Figure II.3.5.8. (a-d) E-coated AA6xxx-CFRP coupons after 13-week exposure under L467 testing.
Source: The Ohio State University.

CF-Reinforced Panel Analysis. The cathodic current densities observed during potentiodynamic polarization experiments have shown that surfaces of CFRP exhibit significant electrochemical activity, as shown in Figure II.3.5.9, indicating lack of complete polymer coverage on CFs. The cathodic current densities were not significantly different for CFRP-Twill and Random samples. However, in L-467 chamber accelerated corrosion testing and on-road testing, Al alloys coupled with CFRP-Random consistently exhibited greater corrosion than when coupled to CFRP-Twill, as observed in Figure II.3.5.10.

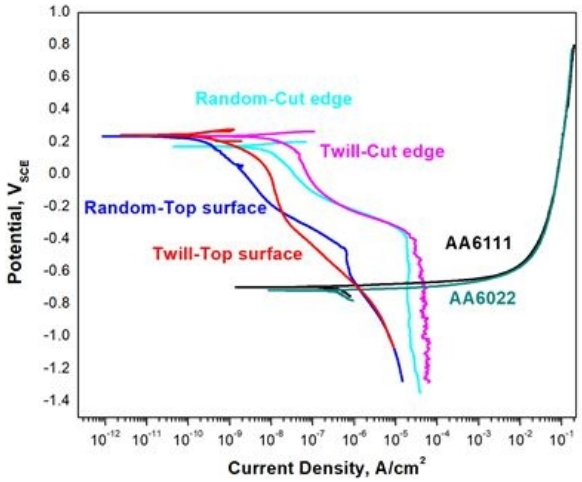

Figure II.3.5.9. Electrochemical activity of CFRP. Source: The Ohio State University.

(a) (b)

Figure II.3.5.10. Corrosion damage of Al coupled with CFRP. Source: The Ohio State University.

Subtask 2.4: Accelerated Corrosion Test Procedure Analysis/Development

Uncoated and e-coated AA6xxx-CFRP coupons were mounted on OSU buses during December 2018. On-bus on-road testing was carried out for 13 months. Figure II.3.5.11 and Figure II.3.5.12 show the corroded surfaces of uncoated and e-coated coupons, respectively, which show that the uncoated and e-coated AA6111-Random exhibited maximum corrosion susceptibility, whereas uncoated and e-coated AA6022-Twill exhibited minimum corrosion susceptibility. These observations match the results observed in L467 testing for 13 weeks, suggesting that the L467 chamber testing is suitable for simulating on-vehicle on-road test conditions for these coupons. The duration of tests can be altered to match the quantitative measurements of corrosion damage.

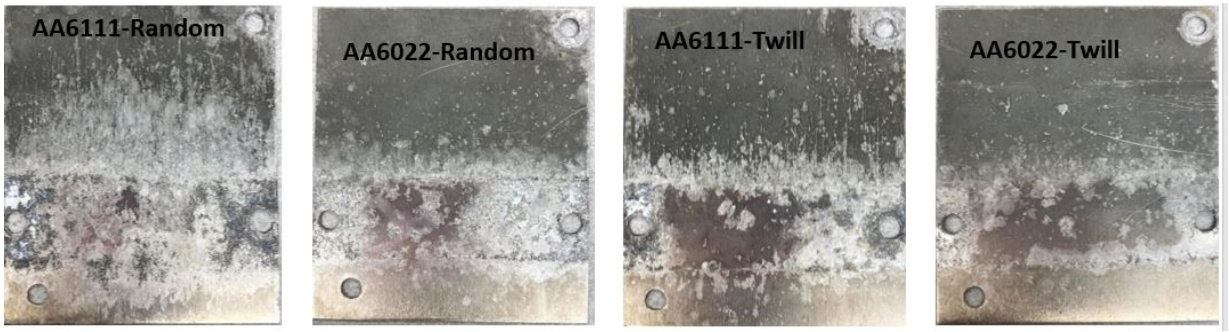

(a) (b) (c) (d)

Figure II.3.5.11. (a-d) Uncoated coupons after 13- month exposure in on-bus on-road testing.
Source: The Ohio State University.

(a) (b) (c) (d)

Figure II.3.5.12. (a-d) E-coated AA6xxx-CFRP coupons after 13- month exposure in on-bus on-road testing.
Source: The Ohio State University.

TASK 3

Subtask 3.1.3: Prototype Testing and Analysis

The prototype liftgates were tested using Ford's Corporate Engineering Test Procedure 00.00-R-343 Accelerated Corrosion testing protocol (R-343) at Michigan Proving Ground. The liftgates were inspected every three weeks to assess the progress of the test. Corrosion was noted on the hem flanges of all the prototypes, as shown in Figure II.3.5.13.

Figure II.3.5.13. Example of corrosion on CFRP-Al liftgate after 12 weeks of R-343 corrosion testing. Source: Ford.

To quantify corrosion, the liftgate hem flange on each vehicle was divided into segments and the number of segments that showed corrosion was counted and expressed as a percentage of the total, as can be seen in Figure II.3.5.14. The liftgates manufactured with the conventional adhesive (e.g., liftgates 5, 8, and 6) displayed less corrosion than those with the prototype adhesive (e.g., liftgates 4 and 9).

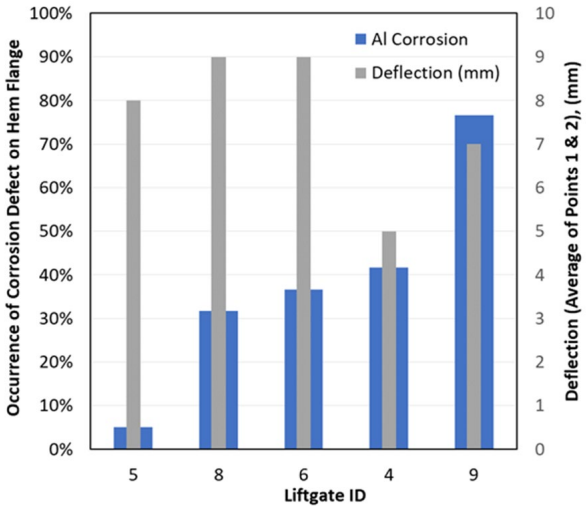

Figure II.3.5.14. Percent of liftgate perimeter that displayed corrosion after 12 weeks of R-343 corrosion testing, and deflection of liftgates after manufacturing. Source: Ford.

The adhesive's contribution to corrosion protection is expected to be small. However, secondary properties of the prototype adhesive may have played a role. From coupon testing, the prototype adhesive required less force to open and the adhesive cleanly pulled away from the conductive primer, as observed in Figure II.3.5.15. Poor adhesion would increase the likelihood of galvanic corrosion between the CFRP and the Al panels, as an electrolytic connection would more easily form between the two materials. Second, from coupon testing, it appears that the prototype adhesive does not flow as readily as the conventional adhesive. A smaller gap observed in samples with conventional adhesive implies better coverage of both the CFRP cathode and Al anode in the coupons, and likely the hems, as well.

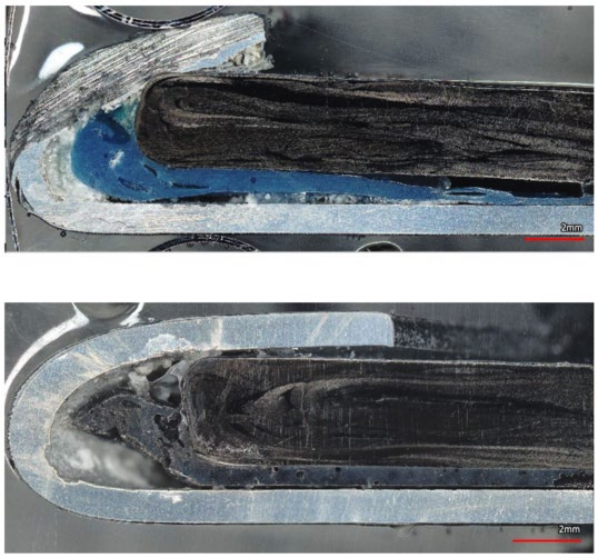

Figure II.3.5.15. Cross-section of CFRP-Al hem joint for both flexible (upper) and conventional (lower) adhesive. Source: Ford.

The reduced flow of the prototype adhesive may have led to less encapsulation of the ends of the CFRP inner panel leading to increased galvanic current. This is shown in Figure II.3.5.15 where cross-sections of a liftgate made with the prototype adhesive and conventional adhesive are both shown. The isolation between the Al and CFRP is significantly better with the conventional adhesive preventing a strong galvanic couple. The manual assembly of the liftgates may have also influenced the results. As a result, we rely on the results from the better controlled coupon studies, which suggest that the differences in flow and adhesion are factors in reduced corrosion performance of the liftgates made with the prototype adhesive.

The lower curing temperature and modulus of the flexible adhesive did lead to smaller part distortion after curing in laser-scanning measurements. Subsequent teardown and inspection of the liftgates suggests that the parts with the conventional adhesive may not have been sufficiently bonded, and thus, the benefits of the flexible adhesive may be under-represented.

Conclusions

The project team has completed the project. Our primary conclusions are as follows:

1. The differences in cathodic current densities between the CFRP-twill and random were not consistent with the increased corrosion observed for CFRP-random in L467 testing and remains under investigation.
2. AA6111 was not highly susceptible to SCC at freely corroding conditions, but the anodic polarization reduced the SCC resistance. Several challenges for measurements of galvanic currents during corrosion testing of overlap coupons were identified including the buildup of corrosion products, which restricted solution ingress, blisters trapping residual electrolyte, and CFRP-Al coupon warpage.
3. L-467 accelerated testing appears to be suitable to predict corrosion performance based on a comparison of overlap coupon corrosion results from on-bus road tests and L-467.
4. Galvanic-accelerated corrosion of Al in CFRP-Al closure panels was conclusively demonstrated in coupons and prototype closure panels.
5. Unexpected results were observed when testing materials at the prototype-scale. Despite reduced deflection when using low cure adhesives, increased corrosion was observed. Contributing factors may have included reduced adhesive/conductive primer layer adhesion and reduced flow of the adhesive.

Reduced flow may have prevented isolation of the CFRP from the Al outer. Manual hemming operations may have also contributed to variability.

Acknowledgements

This material is based on work supported by DOE-EERE under VTO Contract Number DE-EE0007760.

The project team would also like to acknowledge the work of Mr. S. Benton for his many years managing the project and wish him well in his retirement from PPG.

II.3.6 Corrosion Protection of Dissimilar Material and Joining for Next-Generation Lightweight Vehicles (Arconic Inc.)

Donald J. Spinella, Principal Investigator
Arconic Technology Center
100 Technical Drive
New Kensington, PA 15069
E-mail: dj.spinella@arconic.com

Sarah Kleinbaum, DOE Technology Manager
U.S. Department of Energy
E-mail: felix.wu@ee.doe.gov

Start Date: October 1, 2016 End Date: March 31, 2021
Project Funding: $2,223,288 DOE share: $1,648,180 Non-DOE share: $575,108

Project Introduction

The goal of the project is to demonstrate the use of RSRs to join steel to Al and Al to CFRP on a prototype-scale. This new technology is being developed by Arconic to leverage the existing automotive RSW infrastructure for high-performance joining of steel to Al and Al to CFRP.

When using this process to join an Al sheet to a steel sheet, a steel rivet is fed to a spot weld gun. The initial spot weld cycle heats the steel rivet, which is then forced through the Al sheet. Upon contact with the steel sheet, a RSW is made between the steel sheet and the rivet. An alternative is to use a pilot hole in the Al sheet and directly weld the rivet to the steel sheet while simultaneously mechanically locking the Al sheet. The process can be reversed by employing an Al RSR, if joining through steel, or CFRP and welding to an Al sheet.

Objectives

In this project, the joint strength and corrosion performance will be documented with and without adhesives between steel and the Al sheet, and Al and the CFRP sheet. The weld quality will be evaluated under different process conditions. The production viability will be evaluated with the feed system and integration of the feed system onto a robotic system.

Approach

The fourth year of this project focused on completing the corrosion studies initiated at both OSU and Honda. The last two program milestones, fabrication and testing of the demonstration articles were targeted for completion during FY 2020. Demonstrator fabrication was planned in two steps. The initial (Step 1) assemblies would be used to establish the design and verify the mechanical performance against Honda's predicted simulations. Any necessary changes would then be incorporated into the final demonstration pieces (Step 2). The Step 2 demonstrators would then be fabricated and assembled in late 2020 followed by testing at Honda in January 2021. The RSR pilot line and rivet delivery system (RDS) tested in the previous year will be employed for the fabrication of all demonstrators.

Results

Due to the COVID-19 pandemic all partners have experienced significant delays due to facilities closing and work from home restrictions. Throughout the year, the team has been continually accessing the situation and worked with DOE to minimize the delay and finalize the no-cost extension. While the original target date for completion of BP3 was June 30, this program will extend an additional nine months to March 31, 2021.

The majority of OSU work was in completing the corrosion analysis for the remaining samples and generating documentation for the annual report. OSU evaluated material stack-ups joined by RSR, SPR, and flow drill screw (FDS) according to ASTM B117, ASTM G85-A2, and cyclic corrosion testing (CCT-1) cabinet testing methods. Stack-ups were oriented with both the rivet or screw head facing up (e.g., directly facing salt spray during exposure), and down (e.g., not directly exposed to salt spray) to observe the effect of orientation. Samples were removed at 3, 21, and 32 days of exposure to assess the effect of exposure time on corrosion.

Serial cross-sectioning of material stack-ups after 32 days of exposure to ASTM B117, ASTM G85-A2, and CCT-1 revealed that each of the tests produced a different maximum depth of attack and total number of attack sites on the same material stack-up type. In general, the stack-up types suffering the most versus the least aggressive attack were consistent across the various corrosion tests. This can be seen in Table II.3.6.1, which shows the maximum depth recorded on each sample after 32 days of exposure to the three tests. Generally, CCT-1 had the largest maximum pit depths, followed by G85, and then B117, when examining a single stack-up type. Table II.3.6.1 also shows that the samples of the same type exposed to 32 days of G85 had a larger total number of attack sites than CCT-1 or B117.

Table II.3.6.1. Number of Attack Sites and Maximum Depth of Attack Measurements for Various Material Stack-Ups after 32 Days of Exposure to ASTM G85-A2, CCT-1, and ASTM B117

Joining Type Materials	ASTM G85-A2		CCT-1		ASTM B117	
	No. Attack Sites	Max Depth (mm)	No. Attack Sites	Max Depth (mm)	No. Attack Sites	Max Depth (mm)
RSR 5754-980	491	595	455	510	159	203
SPR 6013-590	-	-	621	827	178	483
RSR 6013-590	1350	612	593	726	815	351
RSR 6013-980	630	519	588	668	485	265
RSR Aural2-980	953	694	549	977	550	732
FDS 7055-980	793	1043	1112	905	550	732
RSR 7055-980	1040	930	1473	1339	640	1471

Figure II.3.6.1 shows the maximum depth on the Al sheet after 21 and 32 days of G85 exposure. RSR 5754-980 and RSR 6013-980 had similar attack depths after increased exposure time, and all other material stack-ups had increased corrosion depths after increased exposure. It can also be seen that the maximum depth was larger when the steel sheet is on top of the Al sheet (e.g., RSR in the flipped orientation, SPR and FDS in the regular orientation) after 21 days of G85 exposure. RSR 5754-980 and RSR 6013-980 did not show this increase in pit depth, as these two stack-ups have shown increased corrosion resistance when comparing maximum pit depth. This may imply that the time studied here was sufficient for the more corrosion-resistant alloys to reach their rate-limiting pit depth. Another observation made, which is not reflected in Figure II.3.6.1 is that after 21 days of exposure, the maximum depth was always located on the faying surface. After 32 days of exposure, there was only one case in which the maximum depth was found on the unmated surface (it was located on the faying Al surface in all other cases). All samples were tested in the orientation that places the faying surface down and away from direct exposure to the spray. Should they have been tested in the flipped orientation, it is highly likely that the faying surface would have suffered the deepest attack in all samples.

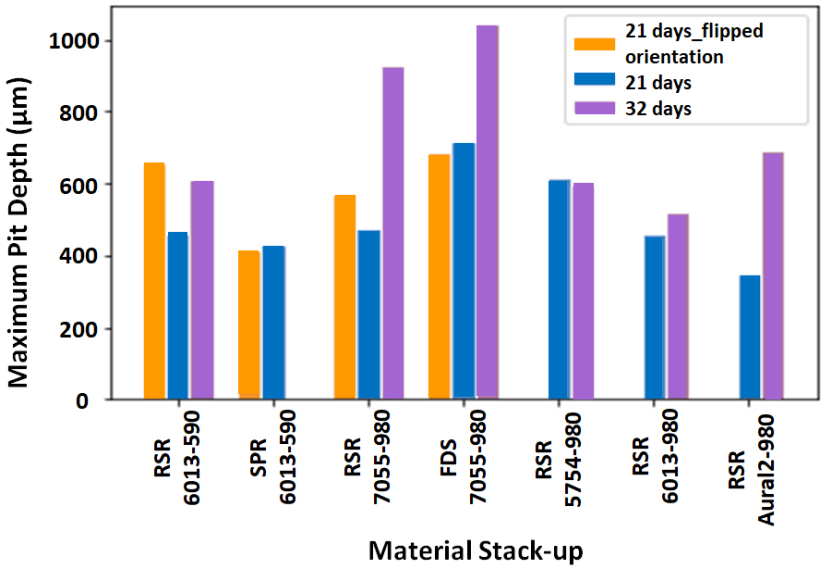

Figure II.3.6.1. Maximum pit depth of various material stack-ups after 21 and 32 days of G85 exposure. Source: The Ohio State University.

Figure II.3.6.2 shows the total number of corrosion sites observed on samples after 21 and 32 days of G85 exposure. Here, it is found that half the samples had a lower total number of attack sites after increased exposure time (e.g., 21 to 32 days). The most probable cause for this is pit coalescence. Along with the maximum depth and number of corrosion sites, Kolmogorov-Smirnov (K-S) testing was used to statistically determine the differences between depth distributions of two samples. This test determines if two datasets are statistically different based on a user-defined significance level. K-S testing was done on cumulative probability plots from 21 to 32 days of G85 exposure. Every sample's depth distributions were statistically different from 21 to 32 days. This agrees with the data as there are lower number of sites and increased depths after increased exposure time.

Testing is ongoing on a new tensile shear strength corrosion specimen geometry following the edge exposure guidelines Honda has established in another DOE-sponsored program. The samples were e-coated by Honda and are currently in corrosion testing. The samples will reach 100 cyclic corrosion cycles in December 2020 before they undergo mechanical and sectioning evaluation.

Honda fabricated approximately 16 demonstrators for the Step 1 assembly trials. The majority of the Step 1 demonstrators were produced with the intention to confirm the robotic cell programming and perform destructive testing to verify the process before the final pieces in Step 2 were commissioned. Both the RSR and RSW were produced with the same resistance welding gun. All RSR joining was conducted in the self-pilot mode (i.e., no pre-hole in the Al sheet). In terms of the conventional RSW joints between the steel sheets, the RDS was not enabled, so a rivet was not fed to the weld gun. After verifying the process, CenterLine, LTD assembled five Step 1 demonstrator components, as seen in Figure II.3.6.3, and shipped the component to Honda for testing. Honda reported good correlation between the empirical and predicted results. As a result, Step 2 demonstrators are expected to be fabricated by Honda in November 2020 and assembled by CenterLine LTD in December 2020 with testing following at Honda in January 2021.

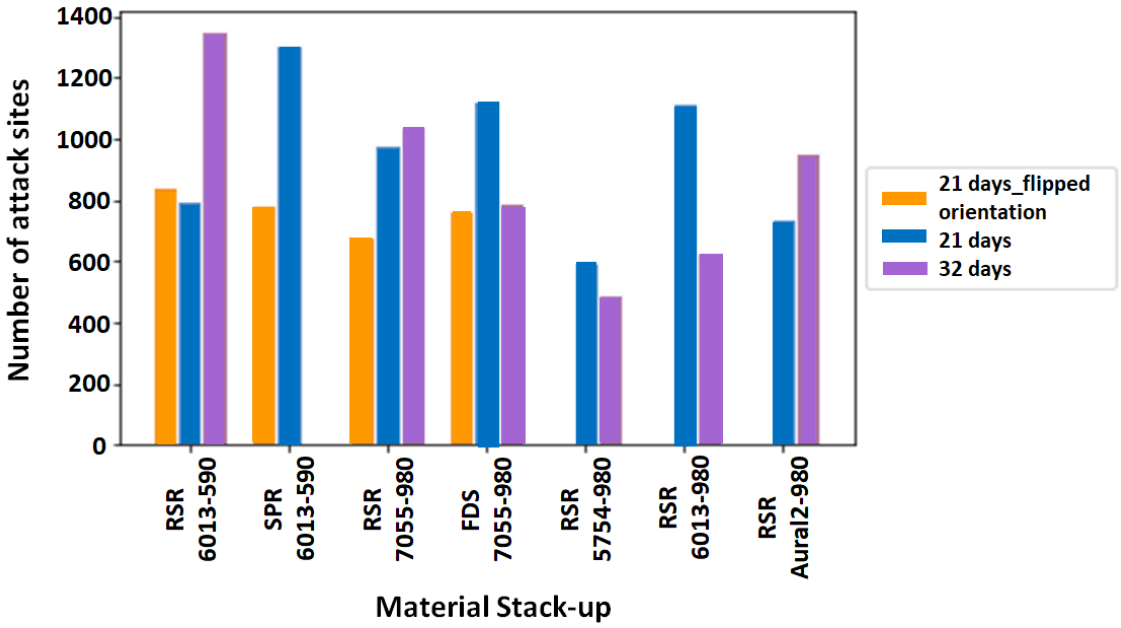

Figure II.3.6.2. Maximum pit depth of various material stack-ups after 21 and 32 days of G85 exposure. Source: The Ohio State University.

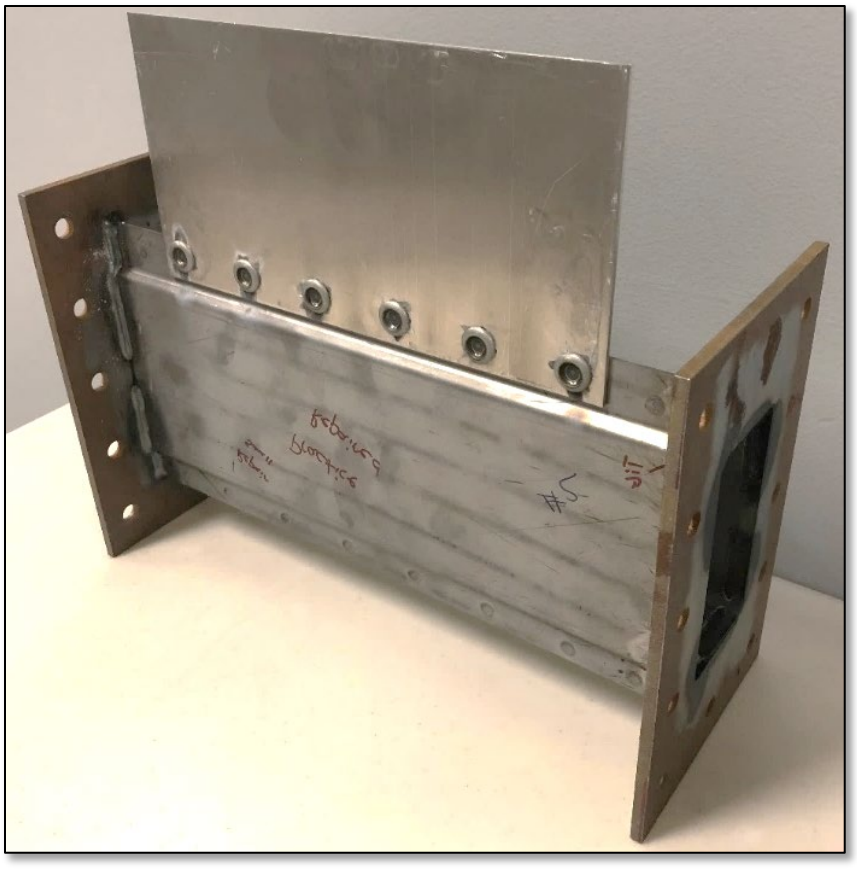

Figure II.3.6.3. Assembled Step 1 demonstrator prior to mechanical testing. Source: Honda.

Conclusions

Corrosion work under a variety of test protocols neared completion at both OSU and Honda, including joints between Al to steel and Al to CFRP. OSU completed additional testing of the joint orientation in the test chamber to characterize the corrosion performance under a variety of conditions. While the overall trends remained similar between the various joining technologies, the orientation can influence the aggressiveness of the galvanic corrosion pitting so special care must be taken when comparing technologies. K-S testing was performed on cumulative probability plots from 21 to 32 days of G85 exposure. It was found that in all samples evaluated, depth distributions were statistically different from 21 to 32 days, which agreed with the observation that pit depth increased as the number of pits decreased with an increase in exposure.

Honda is currently evaluating a new tensile shear strength corrosion specimen geometry following the edge exposure guidelines Honda has established in another DOE-sponsored program. This geometry minimizes the edge effect to increase the fidelity of the test coupon. The samples were e-coated by Honda and are in corrosion testing. The samples will reach 100 cyclic corrosion cycles in December 2020 before they undergo mechanical and sectioning evaluation.

Honda completed fabrication of the Step 1 demonstrators and CenterLine, LTD successfully assembled five pieces for mechanical testing. Each demonstrator contained six RSR and ten RSW joints, which were assembled using the same robotic gun and RDS system. All the RSR joints were produced using the self-piloting process (i.e., no holes were used in the top sheet of Al). Honda reported good correlation between the empirical and predicted results.

Step 2 demonstrators are expected to be fabricated by Honda in November 2020 and assembled by CenterLine, LTD in December 2020. The goal is to produce between 10 to 12 demonstrators with testing following in January 2021.

Key Publications

1. Spinella, D., 2020, “Resistance Spot Riveting Meets the Challenge of Joining Both Conventional and Multi-material Structures,” International Automotive Body Congress (IABC 2020), September 24, 2020.

References

1. ASTM International, 2018, *Standard Practice for Operating Salt Spray (Fog) Apparatus*, ASTM B117-18, West Conshohocken, PA, USA. Available at: https://doi.org/10.1520/B0117-18 (last accessed 20 December 2020).
2. ASTM International, 2018, *Standard Practice for Modified Salt Spray (Fog) Testing*, ASTM G85-11, West Conshohocken, PA, USA. Available at: https://doi.org/10.1520/G0085-11 (last accessed 20 December 2020).

II.3.7 Adhesive Bonding of Carbon Fiber Reinforced Plastic to Advanced High-Strength Steel (Oak Ridge National Laboratory)

Zhili Feng, Co-Principal Investigator
Oak Ridge National Laboratory
1 Bethel Valley Road
Oak Ridge, TN 37831
E-mail: fengz@ornl.gov

Kevin Simmons, Co-Principal Investigator
Pacific Northwest National Laboratory
902 Battelle Boulevard
Richland, WA 99352
E-mail: kl.simmons@pnnl.gov

Sarah Kleinbaum, DOE Technology Manager
U.S. Department of Energy
E-mail: sarah.kleinbaum@ee.doe.gov

Start Date: October 1, 2017 End Date: September 30, 2020
Project Funding: $600,000 DOE share: $600,000 Non-DOE share: $0

Project Introduction

Adhesive bonding is widely used in the automotive industry, primarily for structurally non-critical components. For structurally critical components, weld bonding that combines adhesive bonding and spot welds is more common for joining lightweight materials to meet performance requirements in body stiffness, crash and safety performance, and enhanced NVH characteristics. These lightweight materials include cases of joining AHSS to other AHSS alloys, or Al alloys to other Al alloys and fiber-reinforced polymers. Innovations in adhesive bonding would allow for the development of new and innovative designs of mixed materials—high-strength steels, non-ferrous metals, plastics, and composites—that provide more efficient assembly and weight reduction.

Purely adhesive-bonded joints historically suffer from limitations in peel strength, brittle cleavage failure, relatively low toughness, long-term aging degradation, and poor environmental performance. They also have low crack-arrest resistance in dynamic crash events under compressive load. For dissimilar material bonding, a few unique challenges must be addressed, including tailoring adhesives to provide strong bonding for two different materials, compatibility with mismatches in coefficients of thermal expansion, and the galvanic corrosion effect.

This multi-year early-stage R&D project plans to address several key aspects of adhesive bonding, including the effects of surface conditions of substrates and the effect of adhesive modulus, effects of adhesive chemistries. Overcoming each of these factors or their combination could lead to significant advancements in multi-material joining.

Objectives

This project focuses on the fundamentals of adhesive bonding of CFRP to AHSS. In concert with a parallel interface-by-design simulation task, innovative adhesive bonding concepts are identified and explored, and predictive tools are developed for adhesive bonding performance. The ultimate goal is to significantly improve the performance and productivity of adhesive bonding in high-volume autobody production to enable increased use of CFRP in multi-material body structures for weight reduction. ORNL and PNNL are working together on

this research to effectively use the complementary research capabilities, facilities, and technical knowledge of two National Laboratories to achieve the project goals.

Another primary objective of the R&D research is to establish a robust computational framework that can simulate the local strain concentration and damage growth toward high-fidelity strength evaluation. Through computational studies, the dependence of joint strength on adhesive layer geometric factors (e.g., overlap length, fillet size, thickness, surface modification) can be clarified to proactively design the adhesive joint interface.

Approach

Figure II.3.7.1 outlines the overall research approach and plan. It is organized into four major categories—key governing factors, methods to improve and innovations, interface/adhesive characterization, and joint properties. In recognizing the nature and risks associated with early-stage research, a phased approach was taken in proposed R&D. The first phase was a 12–18-month effort to explore the feasibility of the concept and ideas identified as promising. Based on the outcome from the first phase effort, promising alternatives were downselected for more comprehensive R&D in later phases of the project. Major R&D activities in FY 2020 are marked with red-outlined boxes in Figure II.3.7.1.

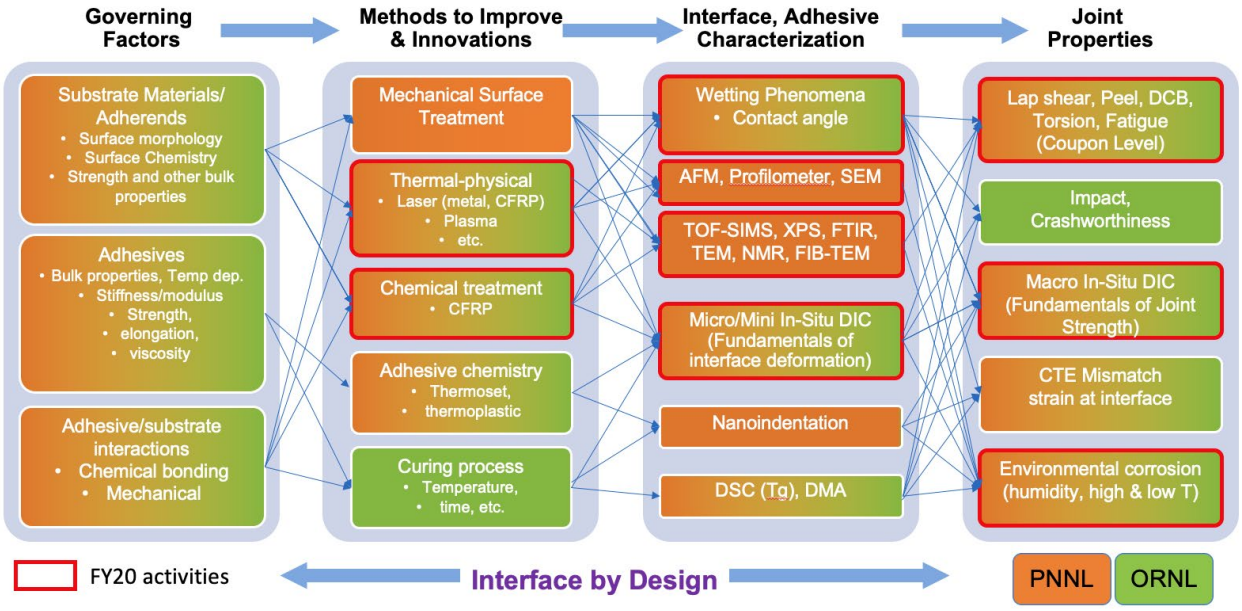

Figure II.3.7.1. Overall research plan. Source: ORNL.

Surface conditions (e.g., chemistry, roughness, morphology) are well-known to significantly influence adhesive bonding strength. Techniques that alter surface conditions (e.g., laser surfacing, mechanical abrasion) have demonstrated benefits; however, there is a lack of understanding of the surface condition and morphology most appropriate to improve bonding. With interface-by-design modeling tools, it is possible to proactively design surface conditions for bonding. This task took the designs and concepts from interface-by-design simulations and identified surface modification processes and methodologies to implement such interface design concepts to achieve improved bonding strength.

Mechanical testing capabilities provided full characterization of the substrate and adhesive materials. The testing also provided joint efficiency performance. With new real-time imaging techniques (such as DIC) for analysis, we were able to focus on understanding how fracture and failure are occurring.

During FY 2020, we focused on the improvement of adhesion between adhesive and thermoplastic CFRP polyphthalamide (PPA) surface to have strong adhesive bonding of thermoplastic CFRP(PPA) to bare DP980. First, our approaches included surface modifications and characterization of PPA resin only adherends, CFRP(PPA), and DP980 as follows:

- Gas/plasma treatment: preferred chemical functional groups on adherend surfaces
- Gas blown ion modification
- Chemical surface treatments (dip-coating, spray, etc.) (PNNL/ORNL)
- Core characterization methods used in this program—water contact angle; laser confocal profilometry; surface chemistry analysis by SEM; Fourier transform infrared spectroscopy; X-ray photoelectron spectroscopy; time-of-flight secondary ion mass spectrometry; etc.

Second, adhesive-bonded specimens were evaluated as follows:

- Mechanical testing of joints of treated samples (e.g., cross tensile pull, double cantilever beam, lap-shear)
- Bonding interface characterization—μ-DIC; nanoindentation; TEM; etc.

CFRP-steel adhesive bond was modeled by cohesive zone element and continuum element to accommodate the strain localization and large aspect ratio of the adhesive layer. Tensile test of miniature coupons was simulated by continuum-damage model to capture the fracture behavior accurately as validated by *in situ* high-resolution DIC technique. The DIC data served as input for cohesive zone modeling, which is commonly used in engineering applications for cost-effective predictions.

Results

Summary of Adhesives and Testing Materials for Adhesive Bonding

During FY 2020, efforts were focused on the improvement of adhesion between adhesive and thermoplastic CFRP(PPA) with 40% short CF surface to have strong adhesive bonding to bare DP980. Adhesive joint strength is a function of bond area and surface chemistry, and it varies with adhesive bond-line thickness. Adherend test geometries were cut by a water jet into 25.4 mm × 101.6 mm plaques and shear machined for DP980. Due to COVID-19 restrictions, researchers at National Laboratories had limited access, so downselection of adhesives was made as summarized in Table II.3.7.1. Epoxy-based adhesives from Dow, L&L Products, and 3M with different modulus were applied and thermally or RT cured according to the manufacturer's instructions. To protect business-sensitive information for each adhesive company, name and modulus of each adhesive are labeled as a numeric number and high, mid, or low based on the modulus category. This number for adhesive is consistent with the previous reporting [1]. Orientation of adherend pieces during bonding was maintained using engineered jigs. Bond-line thickness was initially controlled using glass spheres of a known diameter (i.e., 250 μm) in the bond-line. To avoid large bending during lap-shear tensile testing, a 12.7 mm overlap was used for the lap-shear coupon.

Table II.3.7.1. Summary of Various Adhesives with Different Modulus

Adhesive	Adhesive 1	Adhesive 8
Modulus	>2000 MPa	<1000 MPa
Modulus Label	High	Low

In previous work, the weak bonding interface was on TP-CFRP-PPA, so surface modification on the polymer surface was applied by laser and mechanical abrasion to study surface roughness and morphology effect to improve bonding strength. In FY 2020, surface modifications using plasma chemical treatment were studied so that chemical functional groups on the polymer surface would enhance adhesive bonding strength.

Plasma Treatment and Characterization of Adherends

Three different gases; air, nitrogen, and O were used to modify the adherend surfaces. Subsequently, we evaluated surface energy and wetting envelope changes with different plasma exposure time to find the optimum process conditions while achieving the maximum surface energy. The adherend surface energy is one of the important factors to have good wetting characteristics for adhesive bonding. In general, the higher the surface energy of the adherend, the better the wetting properties of the adhesive on the adherend surface. Even though different gases produce different surface functional groups, the ratios of polar components were the lowest in CFRP surfaces due to the relative stability of CFs in CFRP to plasma, as shown in Figure II.3.7.2. O reacted faster and produced a higher polar component and overall surface energy.

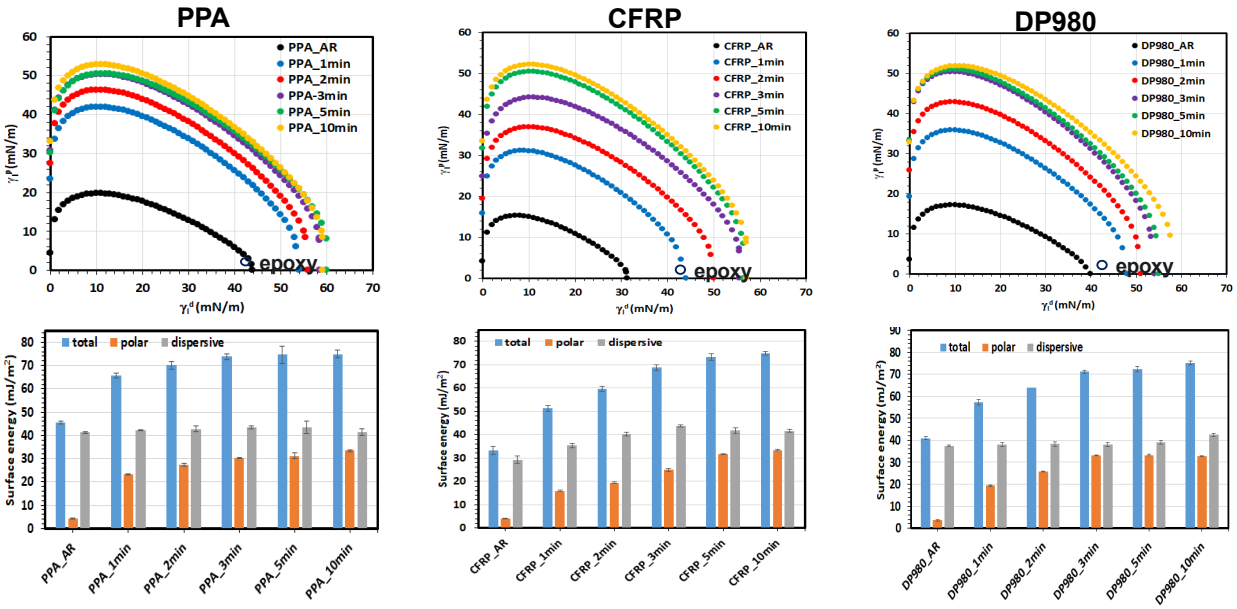

Figure II.3.7.2. Wetting envelopes (top) and the measured surface energy (bottom) of PPA, CFRP, and DP980 surfaces treated with 45 W O_2 plasma. Source: PNNL.

The stability of surface functional groups that are generated by the plasma treatment are important to have consistent joining strength. When we tested time-dependent decay of surface energy of O_2-plasma-treated surfaces, DP980 and PPA resin only surfaces showed faster decay than the TP-CFRP-PPA surface. The total surface energy decay was about 1.4 mJ/m^2/h for DP980 and 0.98 mJ/m^2/h for PPA alone, but it was 0.80 mJ/m^2/h for TP-CFRP-PPA. For TP-CFRP-PPA during the first 6 hours, the total surface energy was mainly maintained, as observed in Figure II.3.7.3. However, the total surface energy decayed quickly after 24 hours of exposure in-air. The primary decay from the surface comes from the polar component loss. This study provides information on the stability of functional groups on the surface, which is important for an automotive-production environment. An alternative method that has longer stability of the functional groups is required to improve bonding strength.

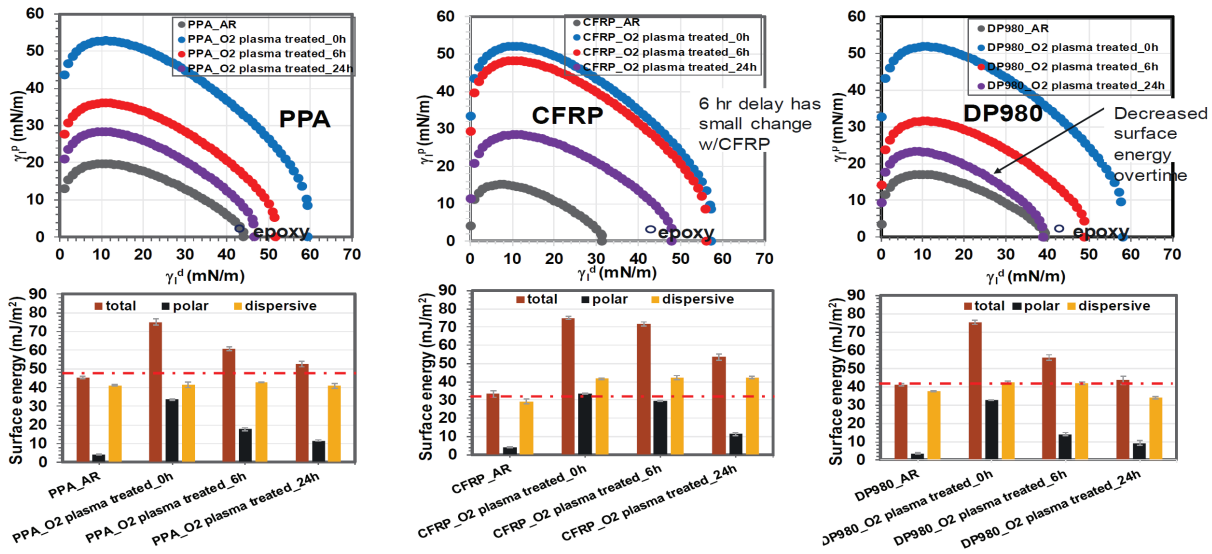

Figure II.3.7.3. Stability surface energy and wetting envelopes of O_2 plasma-treated surfaces with time. Source: PNNL.

Because of stability and potential contamination issues in plasma-treated samples, both ORNL and PNNL used their plasma equipment at each laboratory. Measured surface energies for O_2-plasma-treated adherends show similar values between the two laboratories, indicating good repeatability. Each laboratory next prepared adhesive-bonded samples to evaluate adhesive-bonded joint performance.

Adhesive bonding strength of plasma-treated samples was investigated and compared to the as-received TP-CFRP-PPA and bare DP980. High-modulus Adhesive 1 was used to bond tensile pull specimens (e.g., 25.4 mm wide, 38.1 mm long, with a 25.4 mm overlap) as illustrated in Figure II.3.7.4(a). Tensile pull tests were performed by threading pull rods directly into the backing blocks, with a cross-section of 2.54 cm × 3.81 cm connected to the specimens. Specimens were then pulled in tension at a constant rate of 1.27 mm/min until failure occurred. Figure II.3.7.4(b) summarizes the results for the tensile pull testing of N_2-plasma-treated specimens. The treatment of the CFRP side increases the tensile strength by 14%, while treating of the DP980 side results in lower values, a phenomenon which needs to be studied more.

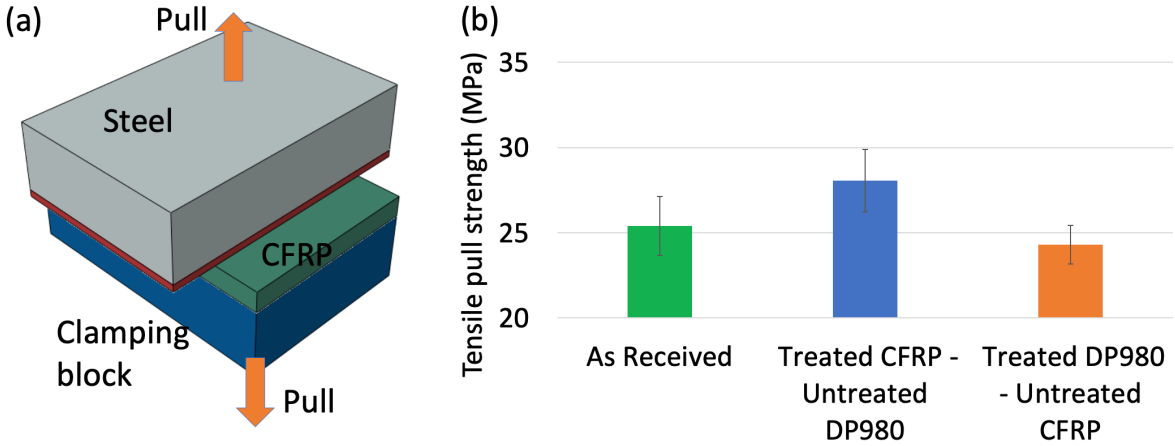

Figure II.3.7.4. (a) Schematic of tensile pull testing and (b) summary of tensile pull strength of as-received treated CFRP to untreated DP980, and treated DP980 to untreated CFRP. Source: PNNL.

Lap-shear tensile testing was conducted for as-received CFRP using Adhesive #1 and #8. Because all adhesive-bonded samples with Adhesive #1 failed at the CFRP, no further surface modification was made. However, weaker bonding strength with adhesive failure at the interface between CFRP and adhesive was found using Adhesive #8. O_2 plasma treatment was applied on the CFRP surface prior to bonding. Figure II.3.7.5 provides summary of averaged lap-shear peak failure load for three conditions (As-received TP-CFRP-PPA with adhesive 1, as-received TP-CFRP-PPA with adhesive 8, plasma-treated TP-CFRP-PPA with adhesive 8). Overall, higher moduli Adhesive #1 shows higher peak fracture load with the base TP-CFRP-PPA failure. For low modulus Adhesive #8, O_2 plasma treatment on CFRP surface greatly improved adhesive bonding strength (~83.3%) compared with as-received CFRP samples. Also, failure location was changed from mostly adhesive failure at CFRP surface to adhesive failure at bare DP980 surface (3 of 6 samples). This result indicates that O_2 plasma treatment is an effective method to modify thermoplastic surface. However, further surface treatment needs to be applied on the bare steel surface to further improve bonding strength.

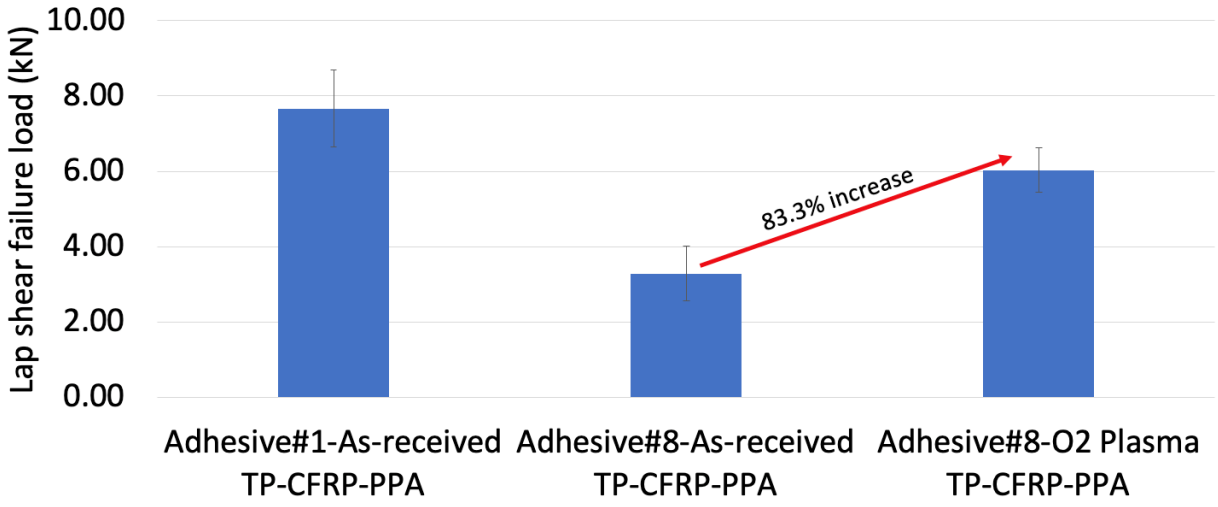

Figure II.3.7.5. Summary of lap-shear tensile testing of as-received and O_2-plasma-treated TP-CFRP-PPA using Adhesives 1 and 8. Source: ORNL

Interface-by-Design for Modeling of Adhesive Bonding

Figure II.3.7.6(a) shows the model configuration proposed for the mechanical performance study of the CFRP-AHSS adhesive joint. A continuum element zone is sandwiched between the two cohesive element zones to simulate the bulk adhesive-deformation and failure behavior. Various failure modes—such as cohesive failure, adhesive failure, and fracture jumping—can be captured by this simulation framework. Material properties—including shear modulus, YS, and tensile strength, as well as fracture energy—are quantified by a purposely designed and built high-resolution micro-DIC system at ORNL using miniature coupon (e.g., 25 mm long and 5 mm wide, with a 2 mm overlap) and an in-house load frame. Figure II.3.7.6(b) shows the computational load-displacement curve and experimental measurement of a steel-to-steel miniature coupon test as a basis. Shear-strain concentration is observed near the steel and adhesive interface in the lower inserted image of Figure II.3.7.6(b). The linear and nonlinear material behavior is well predicted by the continuum-damage model. With material properties calibrated from mesoscale modeling, the cohesive zone model shown in Figure II.3.7.6(c) was employed to predict failure behavior of adhesive joint as a further step toward component-scale modeling. As shown in Figure II.3.7.6(d), the failure path again appears at the bottom part of the adhesive layer due to the difference in the rigidity of the substrates. The load increases smoothly after reaching 80 N, and reaches a peak when the interfacial separation is about 0.02 mm.

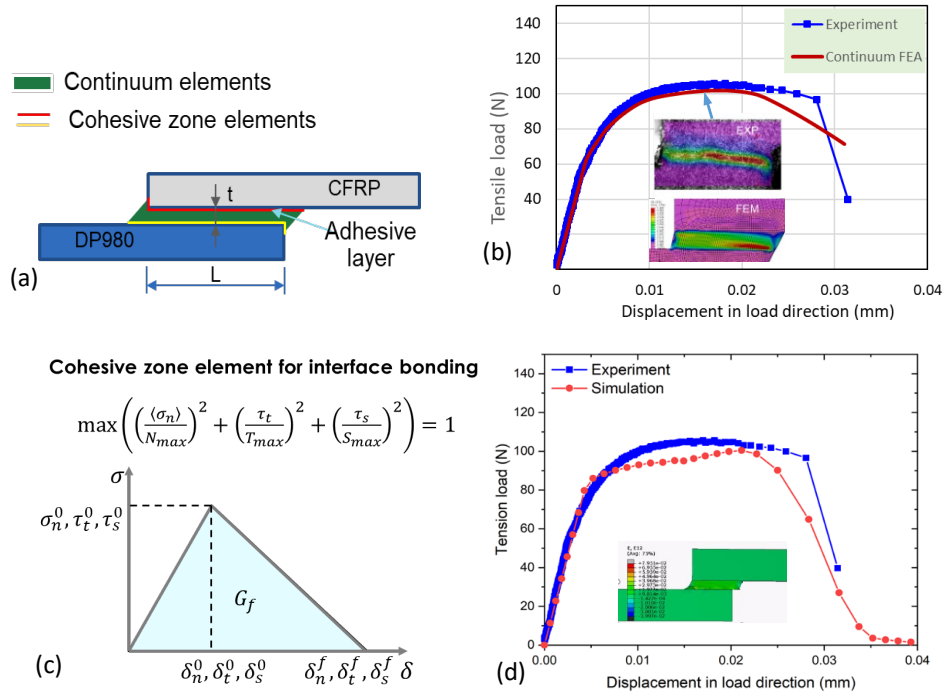

Figure II.3.7.6. Continuum-damage model and cohesive zone model: (a) schematic of modeling approach; (b) continuum element modeling of a miniature coupon; (c) cohesive zone model; and (d) cohesive zone model results. Source: ORNL

Conclusions

Plasma treatments have a significant, positive effect on the surface energy and wetting envelopes of all adherends. Plasma time limits are directly related to polar-surface reduction over time because they activate at the low depth of the surface (e.g., ~50 nm). Adhesive bonding performance was greatly improved after plasma treatment on the CFRP surface. A micro-DIC-informed computational model has been developed to accurately predict the damage evolution and load-displacement relationship of CFRP-steel adhesive joints.

Key Publications

1. Lim, Y. C., J. Chen, H. Huang, Y. Li, B. S. Lokitz, H. M. Meyer III, N. Nguyen, A. Sabau, Z. Feng, K. Simmons, W. Kuang, Y. Shin, G. Petrossian, L. Fifield, and A. Ortiz, 2020, "Adhesive bonding of carbon fiber reinforced polymers to dual phase 980 steel," *MS&T (Virtual Meeting)*, 2–6 November 2020. Keynote address.

2. Lim, Y. C., J. Chen, H. Huang, N. Nguyen, D. Warren, Z. Feng, K. Simmons, and L. Fifield, 2020, "Adhesive bonding of advanced high-strength steel to carbon fiber reinforced polymers (polyphthalamide)," *Adhesion Society 43rd Annual Meeting*, 23–26 February 2020, Charleston, SC, USA.

References

1. Feng, Z., K. Simmons, "Adhesive bonding of CF-reinforced polymer to advanced high-strength steels," U.S. Department of Energy, Vehicle Technology Office, Materials 2019 Annual Progress Report, pp. 495-502.

Acknowledgements

The Principal Investigators would like to recognize Y. C. Lim, J. Chen, H. Huang, Y. Li, W. Zhang, B. S. Lokitz, H. Meyer III, D. Warren, and X. Sun of ORNL; K. Simmons, W. Kuang, Y. Shin, G. Petrossian, L. Fifield, and A. Ortiz of PNNL; and our industry partners—DOW, L&L, 3M, and GM—for their support and assistance with this project.

II.3.8 Solid-State Joining of Magnesium Sheet to High-Strength Steel (Pacific Northwest National Laboratory)

Piyush Upadhyay, Co-Principal Investigator
Pacific Northwest National Laboratory
902 Battelle Boulevard
Richland, WA 99352
E-mail: piyush.upadhyay@pnnl.gov

Zhili Feng, Co-Principal Investigator
Oak Ridge National Laboratory
1 Bethel Valley Road
Oak Ridge, TN 37831
E-mail: fengz@ornl.gov

Sarah Kleinbaum, DOE Technology Manager
U.S. Department of Energy
E-mail: sarah.kleinbaum@ee.doe.gov

Start Date: October 1, 2017 End Date: September 30, 2020
Project Funding: $600,000 DOE share: $600,000 Non-DOE share: $0

Project Introduction

In a modern multi-material vehicle, lightweight materials such as Al and Mg alloys can be a challenge to join and attach to the underlying substructure, usually composed of steel. Even in Al- and Mg-intensive designs where entire substructures may be constructed of lightweight metals, there remains a need to join the substructure with other parts of the vehicle, such as the steel passenger safety cage. Joining methodologies available in the cost range relevant to automotive manufacturing include RSW, adhesives, linear fusion welding, hemming, clinching, bolting, and riveting. However, because of the highly dissimilar natures of the materials, Mg-to-steel joints are extremely problematic. Mg-to-steel joints simply cannot be fusion-welded due to the extreme differences in their melt temperatures. Additionally, no intermediate phases exist between a Mg and Fe system. Joining methods that require a large amount of plastic strain in the Mg component suffer from Mg's poor ductility at RT.

FSW and USW methods provide joining options that may be able to overcome some of the technical barriers preventing more robust and reliable joining of Mg-to-steel [1],[2],[3]. These methods involve creating a large degree of plastic deformation at the interface while at the same time delivering heat from frictional and plastic work. Both methods are solid-state, warm deformation technologies, and take advantage of the enhanced ductility of Mg and steel at elevated temperatures. There are several identified technical barriers:

1. Lack of understanding of the methods and processing conditions required to achieve robust joints.
2. Lack of comprehensive performance information on joints fabricated by FSW/USW methods (e.g., strength, fatigue, durability, crash performance).
3. Insufficient understanding of the feasible joint geometries.
4. For USW, lack of fundamental understanding of the response of materials and joint geometry to process variables (i.e., frequency, etc.).
5. Lack of understanding of the corrosion protection and mitigation strategies that will be necessary to implement for these joining methods.

Objectives

The overall goal of this project is to mature two types of solid-phase joining techniques—FSW and USW—by developing an understanding of the methods and processing conditions required to achieve robust joints between Mg and steel, thus integrating lightweight materials for multi-material vehicles.

Approach

The research approach in FY 2020 was guided to attain the following two goals, each associated with a milestone:

- Provide an evidence-based explanation of mechanism responsible for joining Mg-Fe immiscible systems using Friction-stir assisted Scribe Technique (FaST) and USW.
- Obtain mechanical performance dataset in various loading conditions for Mg-Fe joints to attract interest from industry sector for future collaborative work towards technology transfer.

The following subtasks were performed this year with an eye towards these two goals:

- Fabrication of Mg-Fe joints in different processing conditions, interface conditions, material composition, and loading conditions, as can be seen in Table II.3.8.1.
- Characterization of joined interface using progressively advanced techniques including SEM, TEM, and APT.
- Mechanical testing in different loading conditions.

Table II.3.8.1. Interface Conditions, Alloys Types, and Configurations Used to Make Mg-Fe Joints in FY 2020

Joining Method	Steel Surface	Mg	Fe	Joint Configuration
FaST	Zn-Coated and Bare	Pure Mg, AZ31, AZ80	DP590, Pure Fe	Lap-shear, T-peel, U-peel, Cross-tension, Micro tensile, Stitch vs. cut
USW		AZ31, AZ80, AZ61, Pure Mg	DP590, DP980, Pure Fe	Lap-shear, U-peel, Fatigue

Results

Joint Fabrication

FaST and USW joints were fabricated in various conditions for characterization and testing. Figure II.3.8.1 and Figure II.3.8.2 show various elements of joining including the setup, joined sample, and cross-sections for FaST and USW, respectively. The configurations indicated in Table II.3.8.1 were fabricated for both the joining methods. A SEM cross-section at joint interface shows bonded area for both the joints. TEM foils were extracted from the vicinity of the interface region, as can be seen in Figure II.3.8.1(b) and (c) for both the AZ31-DP590 and Pure Mg-DP590 welds, using a FIB lift-out technique. In FY 2020, most of the advanced characterization was concentrated on joint interface without the presence of Zn in the steel.

For FaST, in comparison to FY 2019 reporting, most of the joints investigated this year were made using smaller plunging depth (~40 μm of engagement) to minimize the contribution of mechanical hooking in joint strength. Thus, the characteristic steel hook feature is significantly reduced.

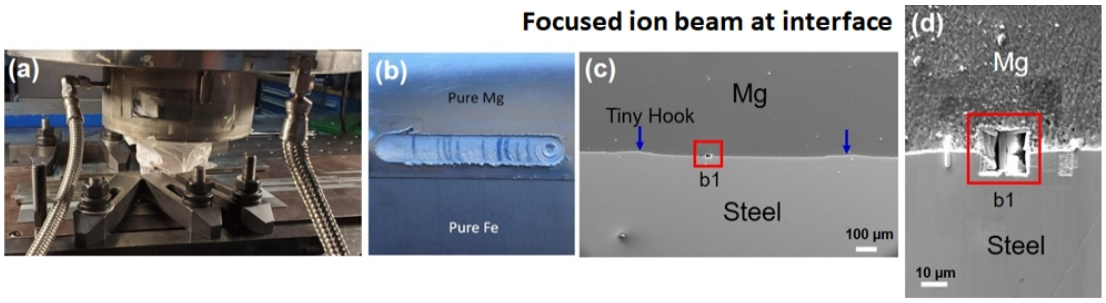

Figure II.3.8.1. (a) Welding setup used to produce Pure Mg- Pure Fe FaST joints. (b) FaST produced Pure Mg- Pure Fe joints. (c) A representative Mg/Steel joint. (d) An area from where samples were extracted for characterization. Source: PNNL.

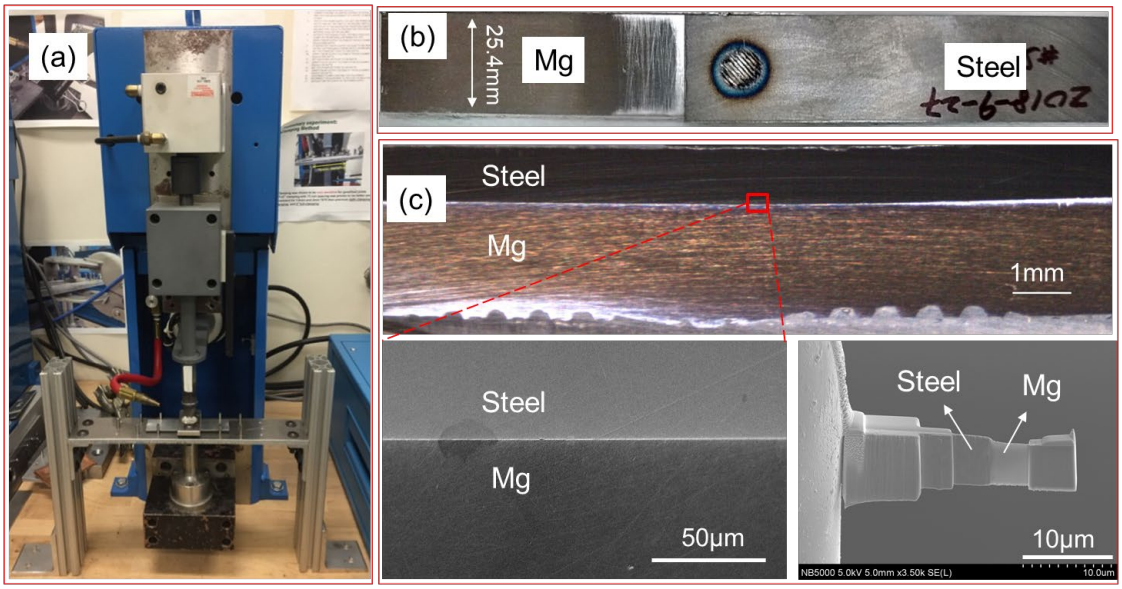

Figure II.3.8.2. (a) USW setup. (b) A representative Mg-steel joint. (c) A multiscale characterization. Source: ORNL.

To understand the fundamental joining mechanism resulting in bonding of the two immiscible systems, investigations were made to explore the possibility of joining Pure Mg to Pure Fe and DP590. After some adjustment of the welding parameters, typically involving the reduction of welding power, both processes were able to bond Pure Mg-Pure Fe and Pure Mg-DP590 material pairs. Lap-shear tests conducted on produced samples indicate that viable joints with an appreciable amount of interfacial strength is observed for all cases. For instance, a load-bearing capacity close to base Pure Mg was measured when FaST joints between Pure Mg and Pure Fe were tested. In the following section, insights gathered from advanced characterization methods are discussed that adds to our understanding of the joining mechanism of the immiscible systems with and without the presence of alloying elements at the interface.

Mg-Fe Bonded Interface and Characterization

In the case of FaST joining, the Mg and Fe systems immediately next to the bonded interface both contained recrystallized grain as shown in the TEM images of the interface for AZ31-DP590, Pure Mg-DP590, and Pure Mg-Pure Fe in Figure II.3.8.3. Severe plastic deformation due to the FSW pin on the Mg side and machining due to the cutter scribe on the steel side is responsible for this grain refinement. Ultrafine grains were observed towards the steel side. Grains of steel were refined from 8 ± 5 µm (base steel) to 200 ± 100 nm in the case of AZ31-DP590 joint, to 70 ± 15 nm for the Pure Mg-DP590 joint, and to 250 ± 100 nm for the Pure Mg-Pure Fe joint. The grain size appears to gradually increase with distance from the interface. Nevertheless, the refined grains span 37 ± 3 µm away from the interface, indicating the extent of the plastic deformation in steel beyond the observed scribe engagement.

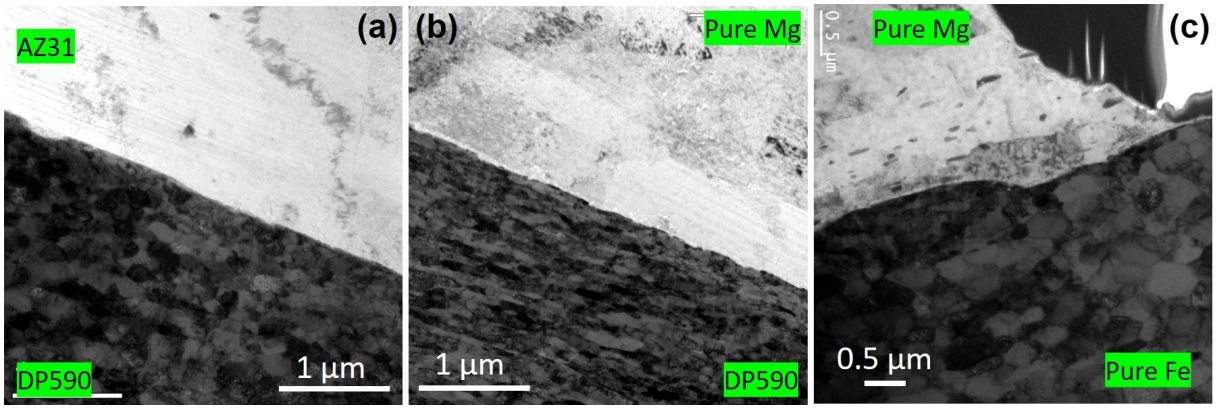

Figure II.3.8.3. High-magnification TEM images of the (a) AZ31-DP590 (left); (b) Pure Mg-DP590; and (c) Pure Mg- Pure Fe bonded interface revealing recrystallized grain structure around the bonded interface. Source: PNNL.

The Mg side, where conventional FSW occurred, also contained recrystallized and refined grains. However, the extent of grain refinement was much less than that seen on the steel side. The grain size was reduced from 20 ± 10 µm to 3 ± 2 µm. This could be associated with the comparatively high processing temperature in Mg, resulting in greater grain growth after recrystallization than in steel.

Recrystallization and grain refinement also occurred in the vicinity of the USW joints (e.g., ~30 µm thick adjacent to the joint interface) owing to the shear deformation and heating. Within this region, grain size reduced from 50 ~100 µm to less than 10 µm, as can be seen in Figure II.3.8.4(a). A higher magnification image in Figure II.3.8.4(b) shows fine Fe grains of around 1 µm size.

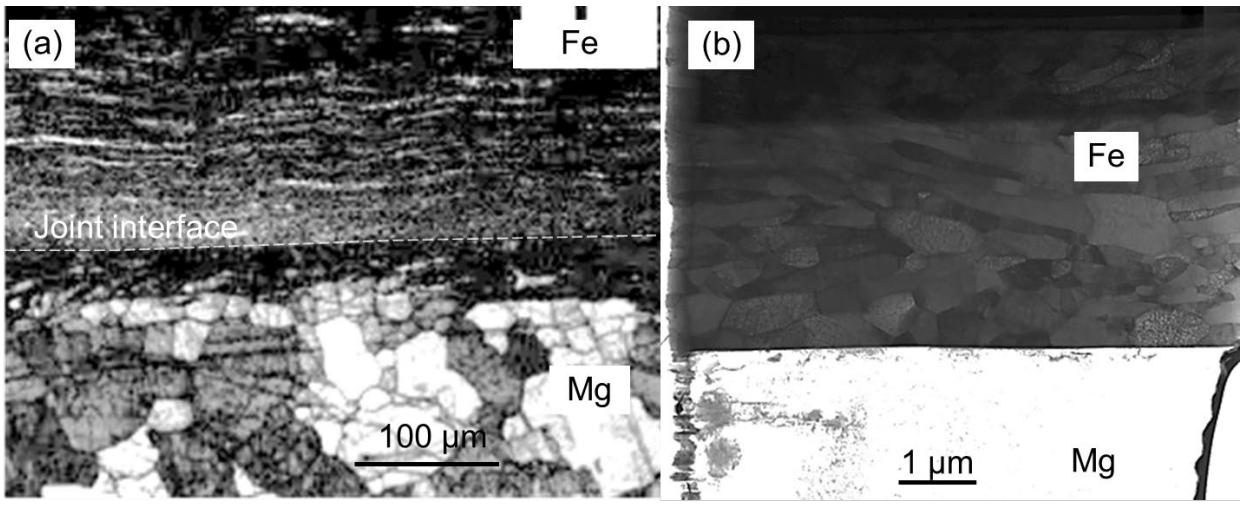

Figure II.3.8.4. (a) and (b) High-magnification images show the grain structures on the Mg and Fe sides adjacent to the joint interface. Source: ORNL.

STEM and EDS elemental maps at the interface and surrounding area for the AZ31-DP590 (uncoated) FaST joint are shown in Figure II.3.8.5. An iron-rich particle of approximately 100 nm size was observed about 400 nm away from the interface on the Mg side. This is a result of the scribing operation, similar to what has been routinely observed in macro cross-sections in previous FaST work [4]. Nevertheless, this is a first observation of nanosized stray steel particles in FaST joining. At the interface, a continuous, nanosized, Al-rich layer (~40 nm) was found, as seen in the high-magnification inset in Figure II.3.8.5. This suggests the formation of an intermetallic compound, which has been previously reported in butt joining of Mg/steel [5]. Al-rich chemistry around the stray steel particle on the Mg side shows that conditions are favorable for the

formation of Al/Fe intermetallic compound layer. Fe- and Al-rich peaks also matched indicating formation of an Al-Fe intermetallic compound at the interface [5]. An appreciable amount of O was also observed, especially on the Mg side and the interface region. From line scan in Figure II.3.8.5(b), the elemental gradient of Mg and O suggests the presence of MgO layer at the interface.

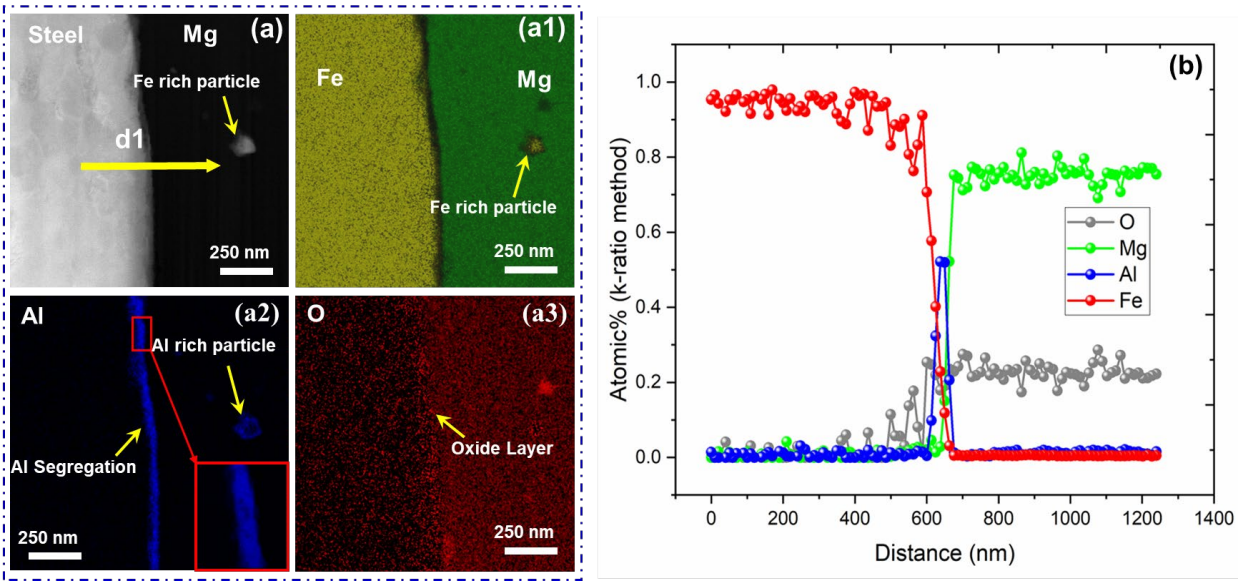

Figure II.3.8.5. (a) TEM imaging of the AZ31-DP590 FaST joint. Steel and Mg interface with Fe-rich particle in the Mg side identified with the small arrow (top left): (a1) Fe and Mg; (a2) Al; and (a3) O elemental EDS mapping is also shown. (b) Atomic% shows EDS line scan of various elements across the interface. Source: PNNL.

TEM observations for USW (e.g., AZ31- Bare DP590) were presented in the FY 2019 report. The joint interface had a submicron-thick layer with a high concentration of Al, Zn, and O. Similar element concentration at the interface was also observed in USW joints made with bare DP590 and AZ80, as seen in Figure II.3.8.6. Al and Zn are two major alloying elements in AZ31B and AZ80 (e.g., 3wt% Al and 0.9wt% Zn in AZ31B and 8.3wt% Al and 0.7wt% Zn in AZ80).

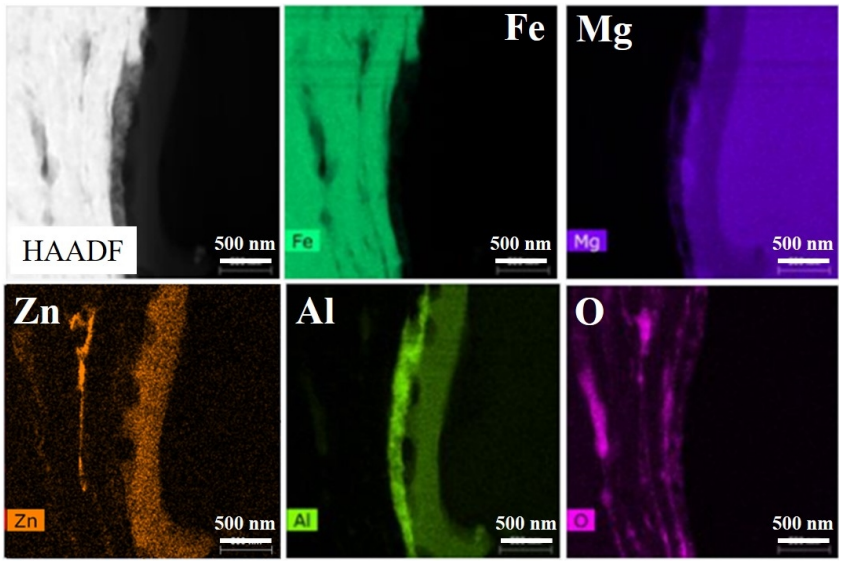

Figure II.3.8.6. HAADF image showing the interfacial morphology and EDS maps showing the chemical composition at the center of USW joints made with bare DP590 and AZ31B. Source: ORNL.

TEM with EDS elemental mapping of FaST-processed Pure Mg and DP590 steel is presented in Figure II.3.8.7. In the absence of Al, the interface layer has a distinct composition. An O-rich interfacial layer with profuse nanosized lumps was identified close to the interface on the Mg side. A high contrast view at the interface further reveals the nanosized lumps as darker spots marked with yellow arrows in the inset of Figure II.3.8.7(a). This layer is ~35 ± 5 nm thick and is present across the interface view field, as seen in the high-magnification inset in Figure II.3.8.7(c2). An EDS line scan also suggests formation of a nanosized oxide layer, as observed in Figure II.3.8.7(d1).

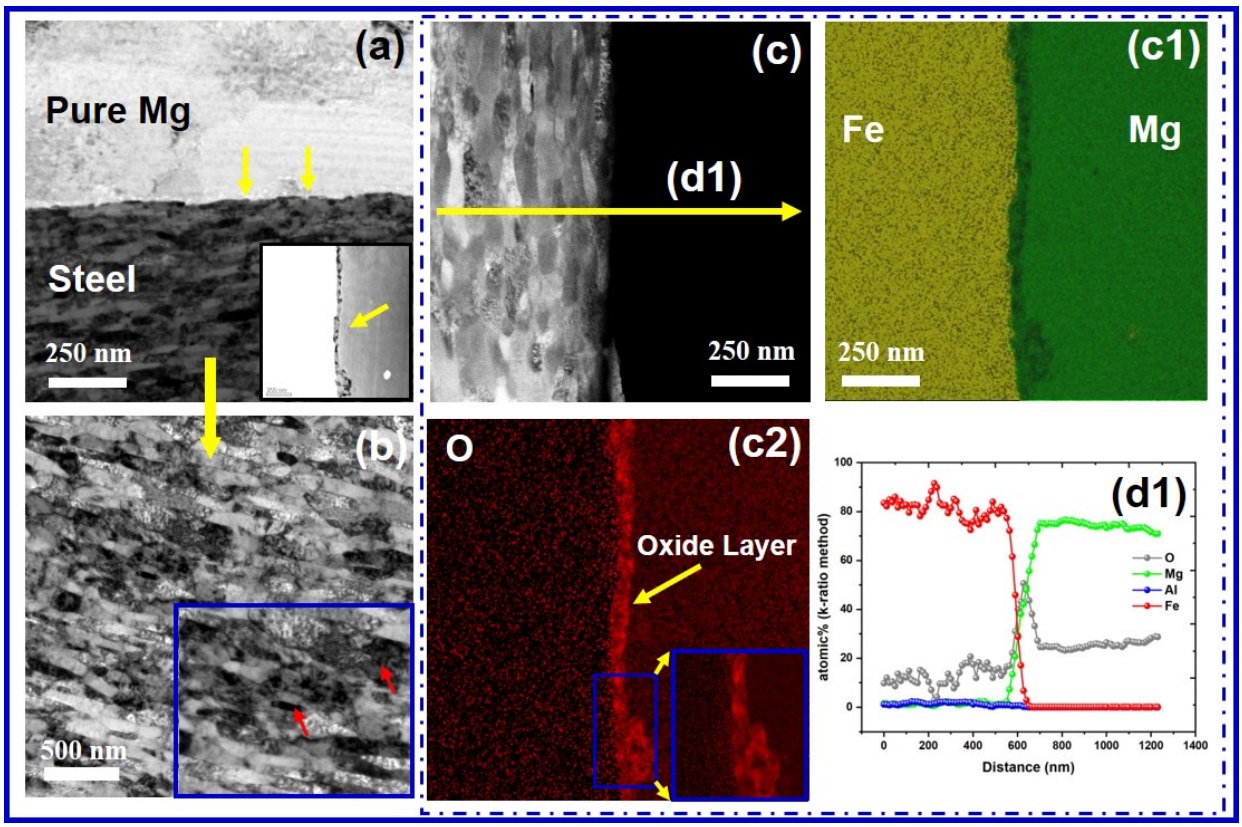

Figure II.3.8.7. TEM with EDS of a Pure Mg-DP590 joint: (a) Joint interface (inset: high contrast, HAADF image with oxide layer at the interface); (b) nanosized steel grains (inset: dislocations, marked by red arrows); (c) S/TEM image with location of EDS line scan; (c1) EDS mapping of Fe and Mg; (c2) EDS mapping of O (inset: high-magnification view); and (d1) line scan elemental analysis plot for Pure Mg-DP590. Source: PNNL.

For additional insight into the elemental diffusion mechanism, needle-shaped specimens were extracted from the interface region for APT. Figure II.3.8.8 and Figure II.3.8.9 show needle reconstruction of various elements. Figure II.3.8.8 shows needle reconstruction and elemental distribution for two USW joints of Pure Mg and Pure Fe in two controlled gas environment cases of Pure O in Figure II.3.8.8(a) and nitrogen as a shielding gas (e.g., < 1 vol % O) in Figure II.3.8.8(b). Oxides, Fe, and Mg were observed at the joint interfaces that are responsible for the joint formation between Pure Fe and Pure Mg. With a reduced amount of O in the nitrogen environment, a much thinner layer of O (e.g., ~8 nm) was formed. APT needle morphology for the Fe-Mg joint in Figure II.3.8.9(c2) and Figure II.3.8.9(c4) suggests a tenuous discreet region containing Fe, O, and Mg.

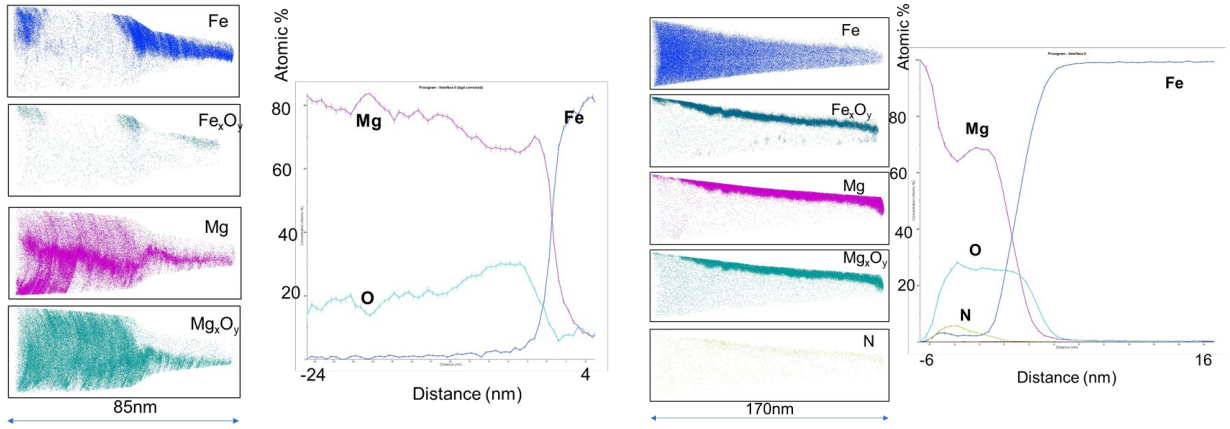

Figure II.3.8.8. APT chemical analysis of USW joints made with: (a) pure Mg in pure O; and (b) nitrogen shielding gas (<1 vol% O). Source: ORNL

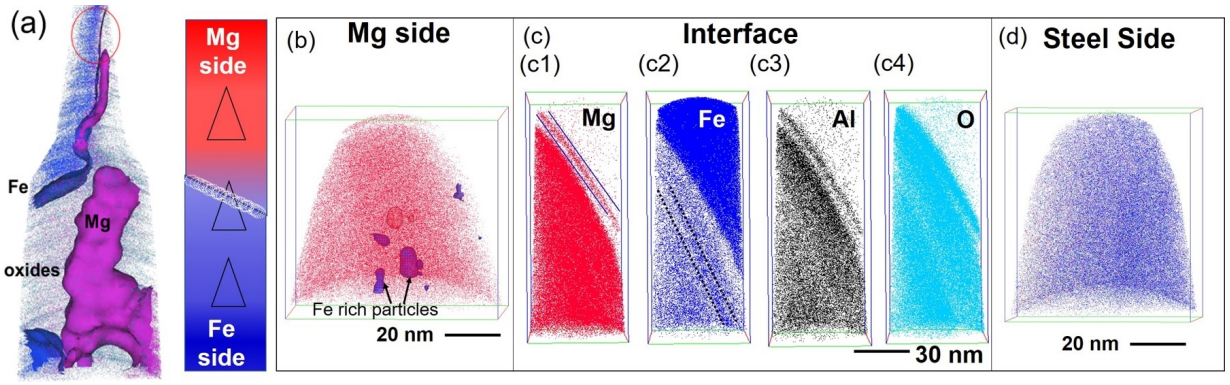

Figure II.3.8.9. (a) Compositional map for Pure Fe and Pure Mg USW joint. (b) APT results from the interfacial region of the FaST joint between AZ31 and DP590. (b) Reconstruction showing the Mg ion map from Mg alloy side, (c) reconstructions showing the Mg, Fe, Al, and O maps including the interface between the two alloys, and (d) DP590 steel side. Source: PNNL.

Similar observations were obtained independently for FaST joints as well. Figure II.3.8.9(b) shows the reconstruction depicting the Mg ions (red) from the needle made for FaST-processed AZ31 Mg alloy side (~1 µm away from the interface). A few discrete Fe-rich regions are evident in the reconstruction, as highlighted by the arrows in Figure II.3.8.9(b). These regions were mechanically transferred to the Mg side by the scribe action during the FaST process. The overall region on the Mg alloy side is enriched to ~10 at.% Fe, and the discrete regions are > 90% Fe. The APT results from the interfacial region confirmed the formation of a nanoscale Al-rich layer along with O enrichment at the interface. Note that the reconstructions of Mg, Fe, Al, and O in Figure II.3.8.9(c1-c4) show nanolayers of compositionally distinct regions depicting the mass transfer during the process.

Mechanical Testing

Lap-shear, fatigue, and U-peel tests were performed to evaluate the mechanical performance of the USW joints made with AZ31B and DP590 (both Zn-coated and non-coated). Figure II.3.8.10 shows the lap-shear and U-peel test results. With Zn coating on the steel side, the lap-shear strength reached around 7~8kN. The result of U-peel strength scattered between 0.35 kN and 0.65 kN. Without Zn coating, the lap-shear strength was about 5 kN and the U-peel strength was between 0.27 kN and 0.5 kN, roughly 60~70% of the lap-shear and the

U-peel strengths compared with the USW joints made with Zn coating. Overall, the U-peel results had more scatter in comparison to lap-shear tests. This is likely due to the pre-bent steel and Mg sheets undergoing relative displacement and rotation during ultrasonic vibration, resulting in slight misalignment of the U-peel joint coupons. The U-peel test was more sensitive to such misalignment. The fracture of all lap-shear and U-peel joint coupons occurred at the joint interface.

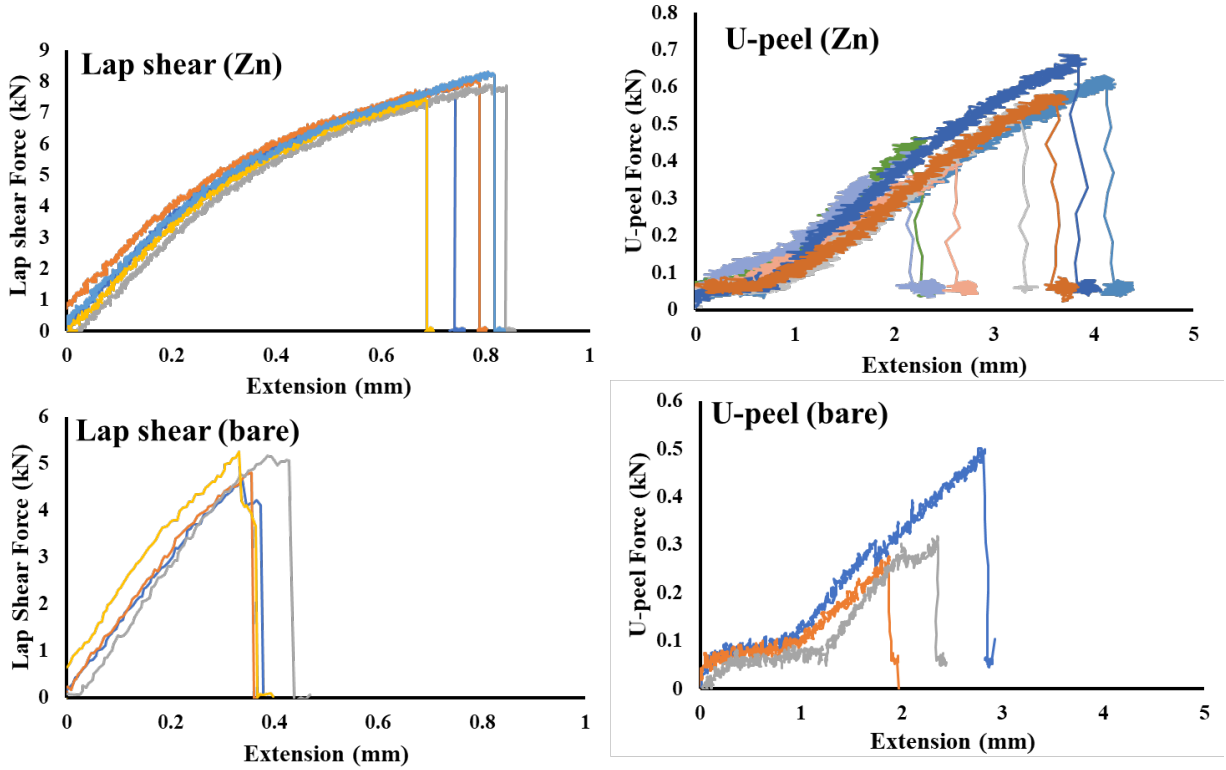

Figure II.3.8.10. Lap-shear and U-peel test results of USW joints made with AZ31B and DP590 (Zn-coated versus non-coated), Source: ORNL.

Figure II.3.8.11 summarizes the lap-shear strength of USW joints made of various Mg-Fe systems (e.g., 2-mm and 1 mm thick, respectively) as well as other dissimilar metal pairs. All joints were produced with an identical USW process condition (i.e., 3500W for 4 s). For Mg-Fe systems, the USW joints with Zn coating on the DP590 steel sides had the highest average strength at around 8 kN due to the formation of Mg-Zn intermetallic compounds. Without Zn, the average lap-shear strength of USW joints made of bare steel and different Mg alloys (i.e., AZ31B, AZ61, and AZ80) ranged from 3.5 kN to 5 kN. The alloying elements (i.e., Al and Zn) from the Mg alloy side, as well as the oxide layer at the interface, played a key role. For the USW joints made with bare steel and Pure Mg, the lap-shear strength was only 1.8 kN on the average. This lower strength was likely a result of an oxide layer that was observed at the interface. In addition, the same USW process condition was feasible to join other dissimilar metal pairs including DP980-AZ31B, DP590-Al5754, and AZ31B-Al5754. The average lap-shear strength and failure mode is shown in Figure II.3.8.12(a) and examples of interfacial and Mg failure are illustrated in Figure II.3.8.12(b) for reference.

Mechanical testing in several configurations was performed to understand joint strength of Mg-steel FaST joints. This included performing welds in lap-shear, T-Peel, Cross-tension, U-Peel, and miniature sample conditions. T-peel, U-Peel, and cross-tension datasets generated were provided to the interface-by-design team to serve as an input into evaluating the cohesive zone model coefficient. The full data set will be discussed in our upcoming final report.

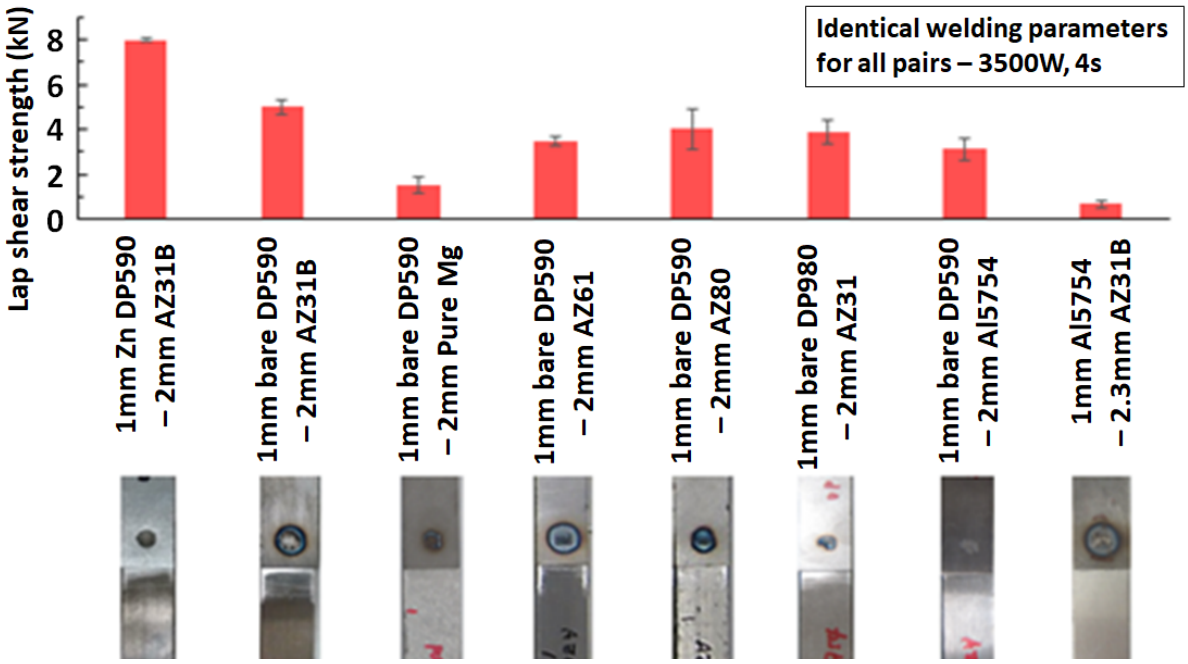

Figure II.3.8.11. An overview of lap-shear tensile strength for various Mg-Fe systems of joints produced by USW. All the joints were made using identical welding parameters. Source: ORNL.

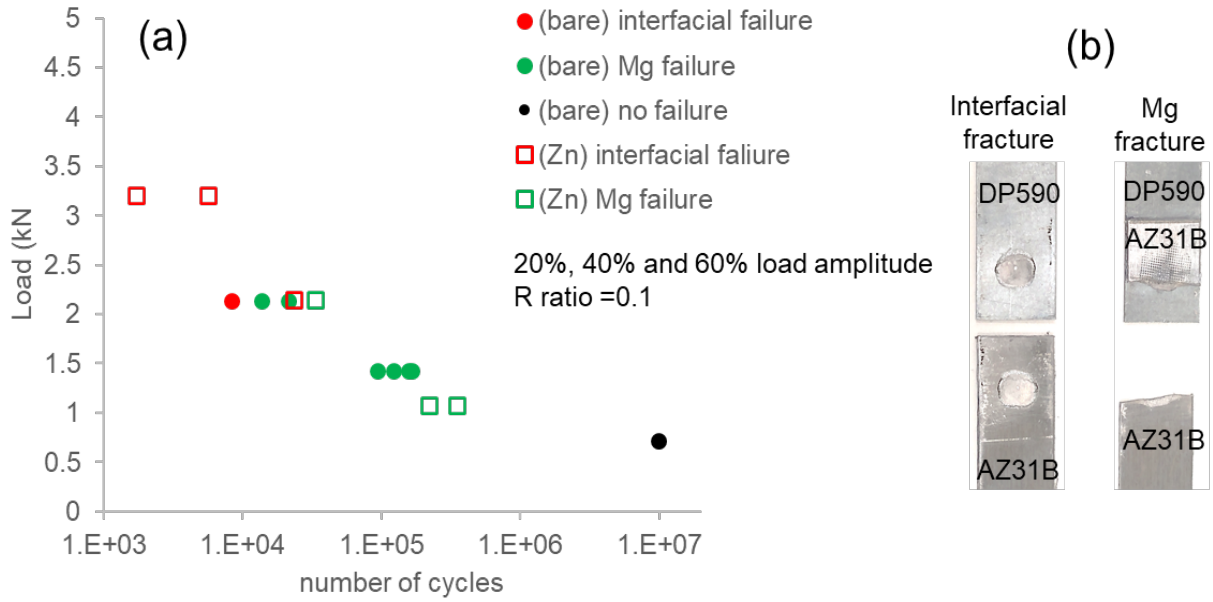

Figure II.3.8.12. (a) Results of HCF testing on Mg-steel USW samples with fracture modes and test samples illustrating an interfacial fracture. (b) A Mg fracture. Source: ORNL.

Miniature testing that was used to evaluate longitudinal joint strength of linear FaST joints and corresponding results are shown in Figure II.3.8.13(a) and Figure II.3.8.13(b) respectively. In the longitudinal direction, the interface strength was found to be 2.5 times greater at the joints central region as opposed to the whole weld sample (i.e., ~40N/mm^2 vs. ~110 N/mm^2). Given that the scribe engagement into the steel was minimized during the weld runs, the contribution of mechanical hooks can be assumed to be minimal. Thus, this increase can be attributed to an increased metallurgical bonding facilitated by higher deformation/strain in the central region as opposed to the edge of the joint.

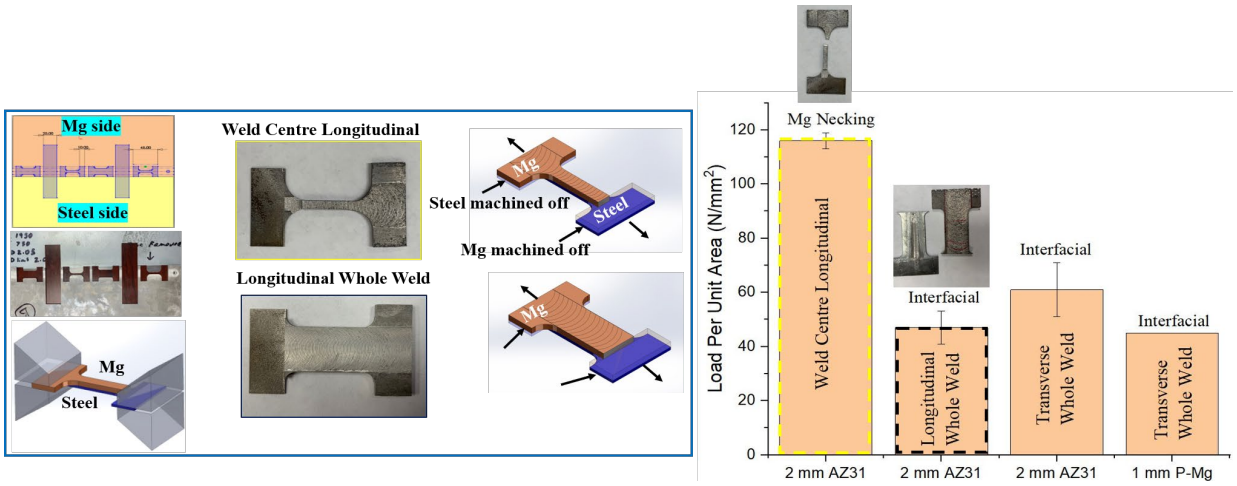

(a) (b)

Figure II.3.8.13. (a) Miniature sample extraction, grip setup, and picture of the miniature sample for longitudinal joint strength evaluation for FaST joints. (b) Load per unit area values obtained from miniature testing for the weld center, longitudinal whole weld, transverse whole weld, and Pure Mg cases. Source: PNNL.

A summary of load per unit weld length vs. extension obtained from lap-shear and cross-tension tests is shown in Figure II.3.8.14(a) and Figure II.3.8.14(b) respectively. The presence of Zn at the interface (e.g., from the Zn coating in the steel) resulted in a marked reduction in load-bearing capacity for all loading conditions.

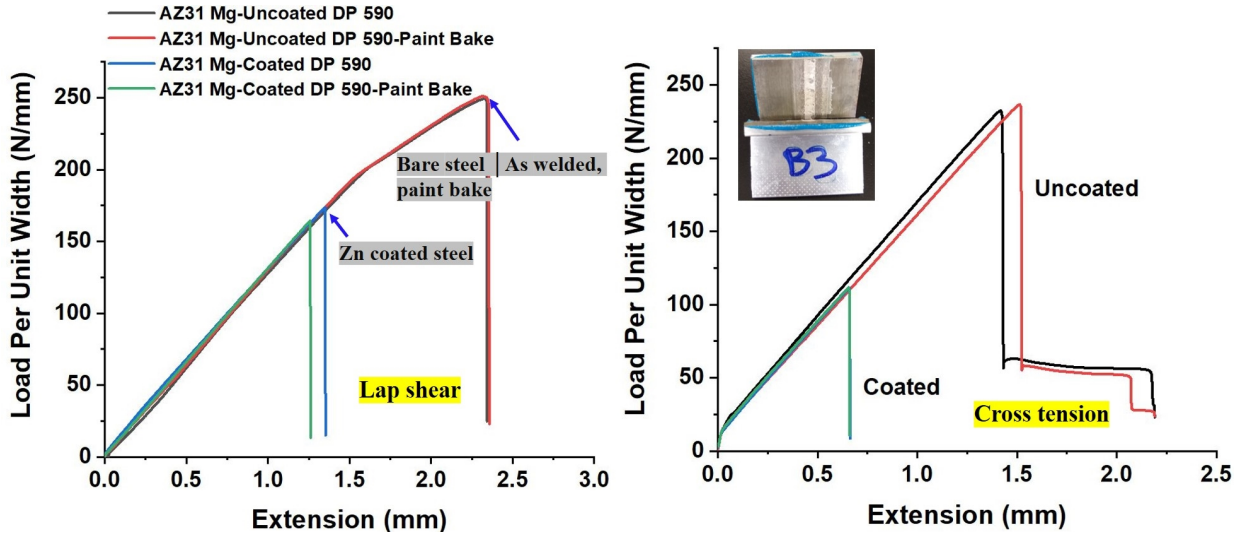

(a) (b)

Figure II.3.8.14. (a) Miniature sample extraction, grip setup, and picture of the miniature sample for longitudinal joint strength evaluation for FaST joints. (b) Load per unit area values obtained from miniature testing for the weld center, longitudinal whole weld, transverse whole weld, and Pure Mg cases. Source: PNNL.

Test results for joints made using two interface fracture conditions and two scribe lengths (SLs) of 0.3 and 0.35 are presented in Figure II.3.8.15. With the scribe length of 0.3 mm, the removal of Zn coating from steel resulted in a 3.5-fold increase in T-peel load-bearing capacity, as shown in Figure II.3.8.15(a), and a ~ 2-fold increase in cross-tension loading, as observed previously in Figure II.3.8.14(b). Four T-peel samples were

tested for each case while six to eight samples were tested for cross-tension testing. This effect of Zn coating on loading appears to interact with the scribe length used. For instance, when the engagement was deeper, SL = 0.35mm, removal of Zn resulted in only ~20% increase in T-peel loading prior to fracture, as observed in Figure II.3.8.15(a). However, in this case, the fracture occurred via the Mg sheet rather than at the interfacial point. The inset of Figure II.3.8.15(a) provides images at the fracture points captured during DIC.

Thus, the overall T-peel load-bearing capacity also decreased with increased engagement. This is an important discovery since this behavior is not readily observed in lap-shear testing. The scribe engagement—and thus, the hook height—needs to be significantly greater before a Mg sheet fracture is observed. This suggests that to maximize T-peel performance, the scribe engagement should be kept lower (with SL=0.30 mm in this case). An overall picture of load-bearing capacity in T-peel loading obtained over the course of this project is summarized in Figure II.3.8.15(b), which provides various cases including different SLs with and without Zn coatings, and stitch welds vs. cut weld sections. A wide range of ductility and load-bearing capacity has been observed. This data set, along with an already existing lap-shear data set, can serve as a baseline for designing Mg/steel joints for a prototype part.

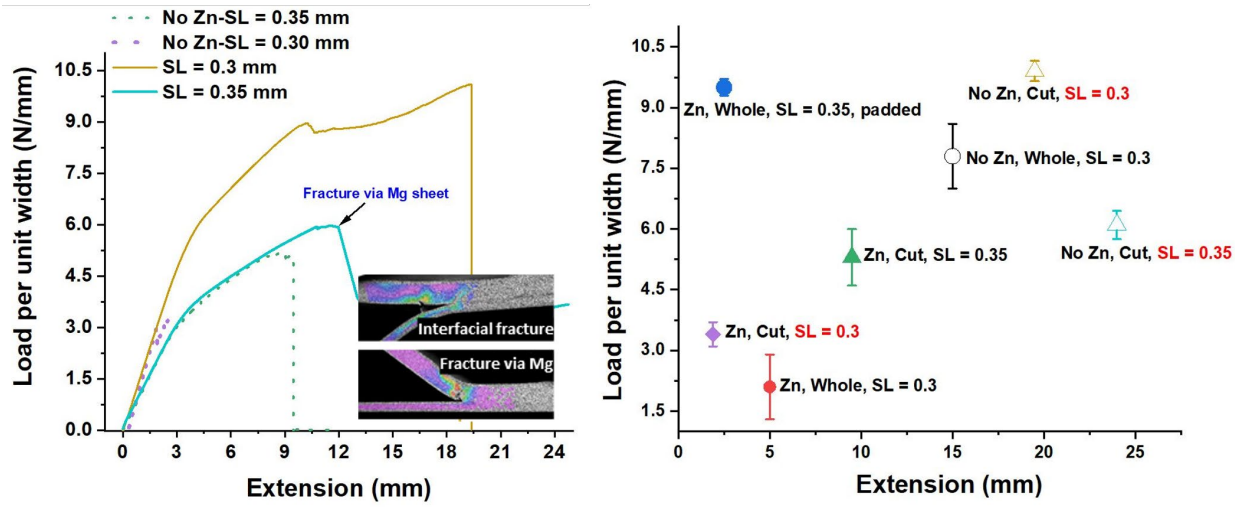

Figure II.3.8.15. (a) Load per unit width vs. extension curves for two interface conditions and scribe length with fracture modes shown in the inset. (b) A summary of T-peel load-carrying capacity for a variety of conditions where each data point contains data obtained from three or more samples. Source: PNNL.

Conclusions

This project aimed to develop an applied understanding of two solid-state joining techniques to overcome barriers in joining Mg-to-steel such that multi-material joints can be realized. In FY 2020, the project team at PNNL (evaluating FaST) and ORNL (evaluating USW) focused on the advanced characterization of Mg-Fe joint interface to understand joining mechanism and mechanical performance of joint in various loading conditions. In the case of AZ31-DP590, the joint interface was found to contain a nanoscale thin layer of Al/Fe intermetallic compound. Additionally, a complex oxide layer composed of Al/Mg or Fe was present. When Al is absent in the base material, the interface is marked by a segregation of nanoscale oxide, which may act as a bridging layer between the two immiscible system via lattice matching. Having performed a large set of mechanical testing for both the joining techniques in Mg-Fe systems, we have obtained a good understanding of the effects of welding parameters on mechanical performance of joints in various loading conditions.

Key Publications

1. Upadhyay, P., 2019, "Solid-state joining of Mg sheet to high-strength steel," *Annual Merit Review Meeting*, 10–13 June 2019, Arlington, VA, USA.
2. Chen, J., Lim, Y., Huang, H., Feng, Z., & Sun, X., 2019, "Ultrasonic welding of AZ31B Mg alloy," *MRS Bulletin*, Vol. 44, No. 8, pp. 630–636.
3. Chen, J., Lim, Y., Huang, H., Feng, Z., & Sun, X., 2019, "Ultrasonic Joining of Mg-to-Steel," AWS Professional Program, Nov. 2018, Atlanta, GA, USA.
4. Wang, T., D. Ramírez-Tamayo, X. Jiang, P. Kitsopoulos, W. Kuang, V. Gupta, E. Barker, and P. Upadhyaya, 2020, "Effect of interfacial characteristics on the mechanical performance of magnesium to steel joint obtained using FaST," *Mater. Des.*, Vol. 192, Art. 108697.
5. Chen, J., Y. C. Lim, D. Leonard, H. Huang, Z. Feng, and X. Sun, 2020, "*In situ* and post-mortem characterizations of ultrasonic spot-welded AZ31B and coated dual phase 590 steel joints," *Metals*, Vol. 10, No. 7, Art. 899.
6. Huang, H., J. Chen, Y. C. Lim, X. Hu, J. Cheng, Z. Feng, and X. Sun, 2019, "Heat generation and deformation in ultrasonic welding of magnesium alloy AZ31," *J. Mater. Process Technol.*, Vol. 272, pp. 125–136.

References

1. Jana, S., Y. Hovanski, and G. J. Grant, 2010, "FSLW of Mg alloy to steel: A preliminary investigation," *Metall. Mater. Trans. A*, Vol. 41, No. 12, pp. 3173–3182.
2. Patel, V. K., S. D. Bhole, and D. L. Chen, 2013, "Formation of zinc interlayer texture during dissimilar ultrasonic spot welding of Mg and high-strength low alloy steel," *Mater. Des.*, Vol. 45, pp. 236-40.
3. Wang, T., H. Sidhar, R. S. Mishra, Y. Hovanski, P. Upadhyay, and B. Carlson, 2017, "Friction-stir scribe welding technique for dissimilar joining of Al and galvanized steel," *Sci. Technol. Weld. Joi.*, Vol. 23, No. 3, pp. 249–255.
4. Chen, J., C. L. Yong, D. Leonard, H. Huang, Z. Feng, and X. Sun, 2020, "*In situ* and post-mortem characterizations of ultrasonic spot-welded AZ31B and coated dual phase 590 steel joints," *Metals*, Vol. 10, No. 7, Art. 899.
5. Kasai, H., Y. Morisada, and H. Fujii. 2015, "Dissimilar FSW of immiscible materials: Steel/magnesium," *Mater. Sci. Eng. A*, Vol. 624, pp. 250–255.

Acknowledgements

At PNNL, welding and data analysis activities were supported by H. Das in association with T. Wang. Mechanical testing and characterizations were performed by T. Roosendaal, E. Nickerson, and O. Angel. A. Guzman performed sample preparation. Advanced characterization work was performed by X. Ma and B. Gwalani. J. Chen and Y. C. Lim performed and characterized the USW at ORNL.

II.3.9 Mechanical Joining of Thermoplastic Carbon Fiber-Reinforced Polymer to Die-Cast Magnesium (Pacific Northwest National Laboratory)

Keerti Kappagantula, Co-Principal Investigator
Pacific Northwest National Laboratory
902 Battelle Boulevard
Richland, WA 99352
E-mail: keertisahithi.kappagantula@pnnl.gov

Yong Chae Lim, Co-Principal Investigator
Oak Ridge National Laboratory
1 Bethel Valley Road
Oak Ridge, TN 37831
E-mail: limy@ornl.gov

Sarah Kleinbaum, DOE Technology Manager
U.S. Department of Energy
E-mail: sarah.kleinbaum@ee.doe.gov

Start Date: October 1, 2017 End Date: September 30, 2020
Project Funding: $550,000 DOE share: $550,000 Non-DOE share: $0

Project Introduction

Existing methods for joining Mg alloys to CFRCs are challenged in varying degrees by corrosion, strength, surface treatment requirements, compatibility with high-volume production or being too application specific. As part of the Joining Core Program, a task on joining Mg to CFRC has been established to address these challenges. PNNL and ORNL have combined forces in the areas of process development, materials characterization, and materials testing in an effort to identify new and promising technologies for joining Mg to CFRC.

Four Mg/CFRC joining processes were screened initially in this project: friction-stir interlocking (FSI), friction self-piercing riveting (FSPR), overcasting Mg over CFRC, and ultrasonic joining. Downselection was performed by the DOE Technology Manager based on the evaluation criteria submitted by the team at the end-of-year project-review meeting held at ORNL on October 10, 2018. The projects selected for continued development in FY 2019 were FSI, conventional bolting, and FSPR. Techniques investigated within this project are now centered on new methods for creating robust mechanical interlocking between Mg and CFRC.

Objectives

The objectives of the FSI, FSPR, and bolting methods explored in this task include the development of new techniques for joining Mg to thermoplastic (TP) or thermoset (TS) CFRC, improvement of joint performance compared to existing dissimilar joining techniques, and minimization of Mg corrosion using different mitigation strategies.

Approach

In the FSI task, a new variation to FSI, known as FSI-Spot, was demonstrated at a viable proof-of-concept level for joining Mg (AZ31B) to CFRC plates using Mg (AZ31B) interlocks. Lap-shear testing was performed to determine the mechanical performance of the joints. Additionally, scanning electrochemical cell microscopy (SECCM) testing was performed to evaluate the effect of thermomechanical processing on the corrodibility of the Mg members joined using the FSI-Linear process developed in FY 2018 and FY 2019.

In the FSPR and bolting tasks, corrosion of Mg-CFRC joints was studied, and corrosion mitigation methods for the joints were also investigated. It was challenging to measure the corrosion damage specific to the dissimilar joint due to massive general corrosion of Mg occurring simultaneously during ASTM B117 salt spray exposure. Therefore, a systematic and new approach to studying corrosion on Mg/CFRC joints was developed.

Results

Method 1: FSI (PNNL Lead)

In FY 2020, we examined the corrosion behavior of the thermoplastic CFRC plates joined to Mg plates using the FSI-Linear process developed in the previous project years. The polarization behavior was determined using the SECCM method developed by the corrosion task in the joining core program. Mg/CFRC joints made using the FSI-Linear process were polished and three specific locations in the cross-section were identified as locations of interest, as shown in Figure II.3.9.1(a). Location 1 is at the interface of the Mg plate and Mg interlock and corresponds to the thermomechanically processed region where the Mg interlock is friction-stir welded to the Mg plate during the FSI-Linear process. Location 2 is in the interior of the Mg interlock, which was not processed during joint manufacturing. Location 3 is an unprocessed region in the Mg plate adjacent to the Mg/CFRC interface that experienced high-temperature variations and is near the cathodic CFRC. The corrosion potential at Location 1 was seen to be significantly lower than that at Locations 2 and 3 as seen in Figure II.3.9.1(b) indicating that the processed region was less prone to corrosion compared to the joint locations where the Mg components (plate, interlock) were not processed.

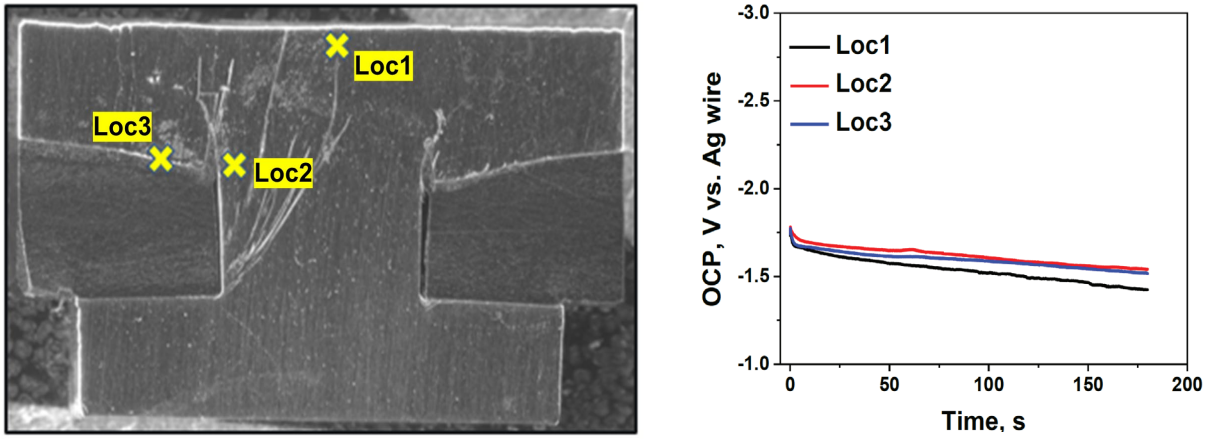

(a) (b)

Figure II.3.9.1. (a) Optical micrograph of the Mg/CFRC FSI-Linear joint cross-section showing the three locations of interest at which SECCM testing was performed to evaluate (b) the effects of thermomechanical processing on Mg corrosion. Source: PNNL.

In FY 2020, we also showed proof-of-concept for joining Mg to CFRC plates using a new variant of the previously used FSI process known as the FSI-Spot process. Mg/CFRC joints made with the FSI-Linear process, where the FSW tool was run along the line of interlocks (rivets), showed less-than-optimal joint strength owing to the high deflection observed in the CFRC adjoining the Mg rivet. Temperature monitoring during joining showed that the heat generated due to the continuous joining process may be too high for the CFRC. We then explored modifying the FSI-Linear process to a spot joining process to minimize heat generation such that CFRC does not experience high deflection, leading to low strength joints. As shown in Figure II.3.9.2 during the FSI-Spot process, a rivet is used to mechanically interlock two plates that are to be joined. The rivet head is formed via severe plastic deformation of a solid shank enabled by heat generated from friction and plastic deformation. The deforming rivet head forms a metallurgical bond with the underlying metal sheet during the joining process. Holes with a 5 mm diameter and a center-to-center spacing of 15 mm

were pre-drilled on Mg and CFRC sheets initially before joining them and aligned in the lap arrangement, as shown in Figure II.3.9.2(a). Solid shanks of Mg rivets with a matching diameter of 5 mm were inserted through the aligned holes in the joint assembly and extended 2–3 mm above the surface of the top sheet to allow sufficient material availability to form a rivet.

Surface appearance of the Mg/CFRC FSI-Spot joint as a function of rotation rate, plunge speed, and surface appearance is shown in Figure II.3.9.2(b). A wide-parameter window was observed where defect-free runs were obtained for the Mg/CFRC FSI-Spot joints. At a tool plunge speed of 780 mm/min, the riveting process was completed in about 0.23 s. Two conditions resulted in joints made outside the defect-free parameter window, as shown in Figure II.3.9.2(b). At a relatively high tool rotation rate of 1950 RPM and tool plunge speed of 450 mm/min, a portion of the Mg rivet head remained adhered to the concave surface of the tool due to excessive heat input. On the other hand, an incomplete rivet surface was observed for process conditions corresponding to low rotation rate (1000 RPM) and high plunge speed (780 mm/min) (a cold run) plausibly owing to the heat generated during the thermomechanical joining process being insufficient to form the Mg rivet head.

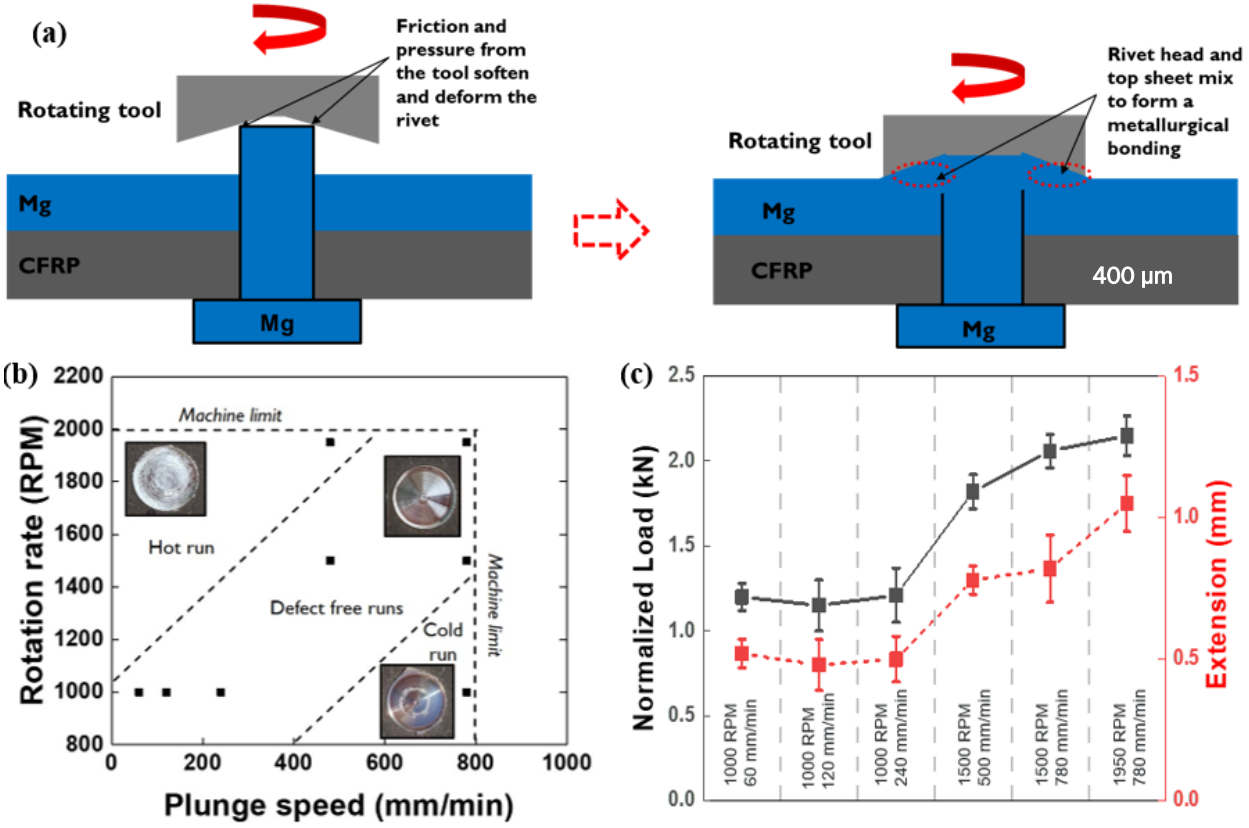

Figure II.3.9.2. (a) Schematics for the FSI-Spot process set up. (b) Parameter window for FSI-Spot processed Mg/CFRC sheets. (c) Normalized load and extension at failure of Mg/CFRC FSI - Spot joints with different parameters. Source: PNNL.

Lap-shear tensile tests were performed on the FSI-Spot riveted Mg/CFRC joints. Results showed that normalized load at failure ranged from ~1.2 to 2.2 kN, while the extension ranged from ~0.5 to 1.1 mm as shown in Figure II.3.9.2(c). All joints fractured in a brittle manner through the CFRC with the fractures possibly initiating from defects in CFRC resulting from drilling the holes prior to the joining process. The difference in load and extension is strongly associated with the extent of deflection generated in the CFRC sheet because of the FSI-Spot process. Joints where CFRC demonstrated lower deflection (i.e., manufactured at higher rotation rate and plunge speed) led to higher load-bearing capacity and extension at failure.

Figure II.3.9.3 shows cross-sections of riveted Mg/CFRC joints and optical microscopy images corresponding to FSI-Spot samples manufactured with tool rotation rate/plunge speed of 1000 RPM/60 mm/min and 1950 RPM/780 mm/min, respectively. For both runs, the rivet head and Mg sheet were mixed, forming a fully bonded interface. The mixing region was larger for the joint manufactured at a tool rotation rate of 1000 RPM and plunge speed of 60 mm/min, as can be seen from Figure II.3.9.3(a), compared to the joint manufactured at a rotation rate of 1950 RPM and plunge speed of 780 mm/min. This implies that the effect of plunge speed increasing from 60 to 780 mm/min overweighs the effect of rotation rate increment from 1000 to 1950 RPM on heat generation and resultant plasticized deformation zone.

In addition, deflection of the CFRC reduced from ~0.65 to ~0.37 mm with the increase in plunge speed from 60 to 780 mm/min, as evident from Figure II.3.9.3(a) and Figure II.3.9.3(b). Both observations may be associated with the FSI-Spot process duration of these two runs. As the plunge speed was increased from 60 mm/min to 780 mm/min, the process time decreased from 3 s to 0.23 s. Even though higher temperatures were recorded at the rivet head for the 780 mm/min sample, there may not have been sufficient time for the higher heat generated at 1950 RPM to penetrate the joint, thereby resulting in a smaller mixed region at the Mg sheet and rivet head interface, as well as smaller CFRC deflection.

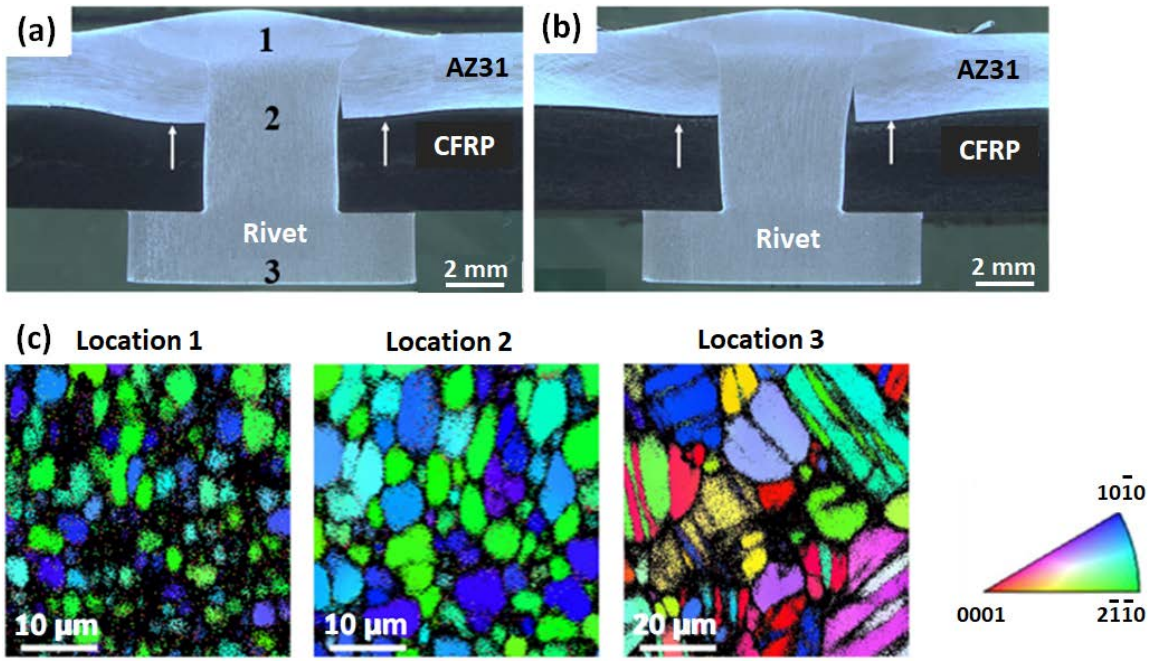

Figure II.3.9.3. Cross-sections of riveted Mg/CFRC joints with: (a) a rotation rate of 1000 RPM and plunge speed of 60 mm/min showing three locations at which subsequent EBSD analysis was performed; (b) a rotation rate of 1950 RPM and a plunge speed of 780 mm/min (note the deflection of the bottom of the CFRC sheet is labeled by white arrows); and (c) EBSD maps at different locations on the thermomechanically processed Mg interlock cross-section in (a). Source: PNNL.

Figure II.3.9.3(c) shows EBSD imaging analysis of the Mg/CFRC FSI-Spot joint, manufactured at a tool rotation rate of 1000 RPM and a plunge rate of 60 mm/min. A gradient in microstructural evolution from the rivet head (e.g., thermomechanically processed region) at Location 1 to the rivet bottom (base rivet material) at Location 3 was observed. The FSI-Spot process generated a significantly refined, with an average grain size of 2.6 ± 1.7 µm, and strongly textured microstructure within the AZ31B Mg rivet head. Conversely, the rivet bottom remained coarse-grained (e.g., average grain size of 15 ± 5 µm) with extensive twins. In the transition region at Location 2 adjacent to the thermomechanically processed region, both the grain size (e.g., 7.2 ± 4.6 µm) and the texture strength were intermediary to those seen in the rivet head and rivet base regions. Grain refinement may be attributed to two primary factors: (1) severe plastic strain, which facilitates the grain

subdivision process by dislocation slip and twinning; and (2) temperature rise, which assists in the dynamic recrystallization to form fine grains during the short processing period.

Method 2: FSI Conventional Bolting (ORNL Lead)

This task demonstrated the proof-of-concept for mitigating the damage created by drilling holes in the composite, and the proof-of-concept for electrochemical isolation of the joint components to reduce the galvanic corrosion of Mg joined with steel fasteners and CFRC. To mitigate damage in the CFRC, the inside of the hole was coated with a very low viscosity resin that is compatible with the CFRC polymer matrix and has a surface affinity to permeate into the microcracks of the composite. Working with 3M, a custom-designed polymer was identified for this purpose. A three-step isolation method for bolted joints was also developed. In the first step, the polymer infiltrates the microcracks, blunting the crack tip and reducing microcrack propagation. The crack-filling polymer also provides electrochemical isolation of the CFRC. A separate epoxy designed to adhere to Mg was "painted" onto the surface of the Mg as the second step for the places where the steel washers and the composite will be in contact with the Mg substrate. For the third step, polytetrafluoroethylene (PTFE) insulating tape with a high-service temperature (>326°C) was applied to the steel bolt for electrical isolation and corrosion protection. Figure II.3.9.4(a) illustrates the schematic of an as-bolted condition without any protection (control) and Figure II.3.9.4(b) illustrates the condition protected by the three-step isolation method. Based on feedback from OEMs, thicker thermoset CFRC (4 mm thick, 20 ply, +45/-45-degree stacking sequence) and AZ31B (3.29 mm thick) plates more representative of applications where bolts would be placed were used to evaluate corrosion performance of bolted Mg-CFRC joints. The standard lap-shear specimen was modified due to the larger bolt size (Φ12.7 mm) and the length was increased to still allow for a square overlap, leading to a 38.1 mm × 114.3 mm coupon size.

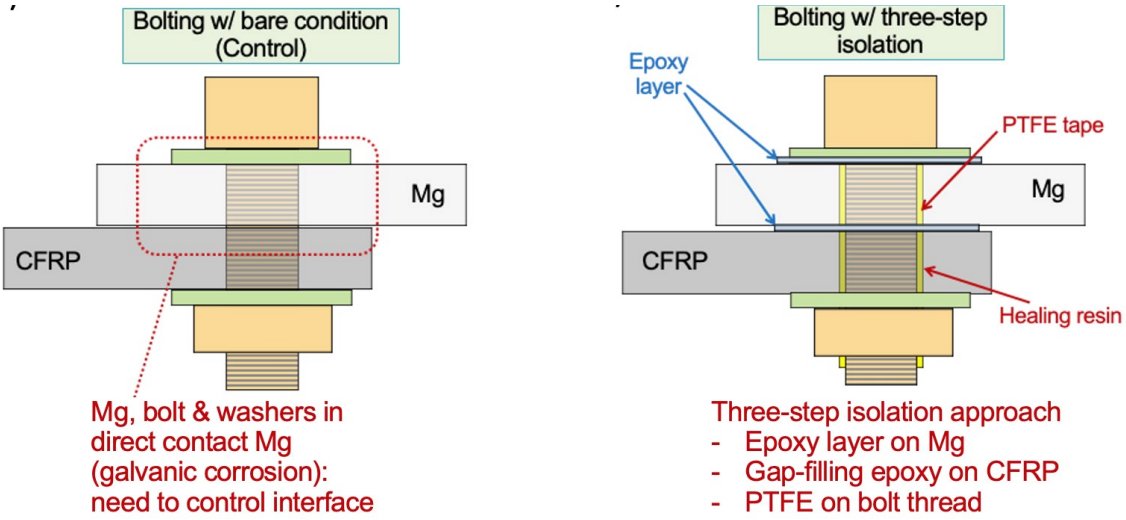

Figure II.3.9.4. Cross-sectional schematic of: (a) bolt joints with no insulation (control); and (b) 3-step isolation applied bolted joints. Source: ORNL.

In FY 2019, as a proof-of-concept, we successfully demonstrated that the three-step isolation technique significantly reduced galvanic corrosion of Mg alloy under 24-h exposure in 0.1-M NaCl solution. In FY 2020, a standard ASTM B117 salt spray exposure was used with longer exposure times for both the control case and the three-step isolation method. This allows automotive and transportation industry companies to see where this technology is now and to compare it with other relevant methods. Figure II.3.9.5summarizes lap-shear tensile failure load for both cases with different exposure times. As expected, lap-shear peak failure load for the control case significantly decreased with increasing exposure time, as seen in Figure II.3.9.5(a). At 438-h exposure, only 10.3% of joint strength remained. In addition, the fracture mode for non-corroded bolt joints

(control) was net shear failure. As the corrosion exposure time increased, the failure location was initiated and failed within a corrosion ditch (e.g., red arrows on fractography) on Mg alloy surface. Also, the bolt was not significantly corroded due to sacrificial anode effect (i.e., Mg alloy was galvanically corroded). For three-step isolation case, the peak failure load from lap-shear tensile testing was gradually decreased with increasing salt spray exposure time, as shown in Figure II.3.9.5(b). At 438-h exposure, 77.9% of the pristine bolted jointed strength was retained. Also, failure mode was consistently net shear failure mode due to limited galvanic corrosion of Mg alloy surface. In addition, the bolt head corroded with increasing corrosion exposure times, due to the absence of sacrificial anode effect, indicating electrochemical isolation between bolt and Mg alloy. Therefore, three-step isolation shows more general corrosion of bolt and Mg alloy rather than the galvanic corrosion observed in the control case. To fully protect the entire joint from both general and galvanic corrosion, support from the coating industry to surface coat the mechanical fasteners (bolts, nuts, and washers) and Mg alloy will be required.

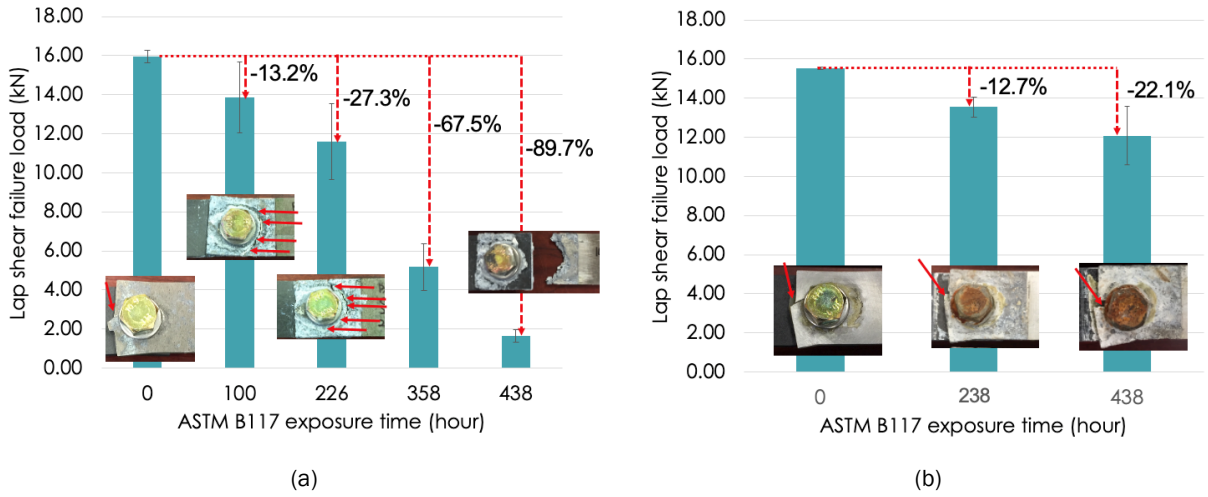

Figure II.3.9.5. Comparison of lap-shear failure load after salt spray exposure (ASTM B117) for: (a) the baseline bolt joints without isolation control case; and (b) the 3-step isolation bolted joints. Source: ORNL.

Method 3: Friction Self-Piercing Riveting (ORNL Lead)

The FSPR process uses a rotating piercing rivet to generate localized frictional heating during the process. The frictional heating softens the CFRC to facilitate the piercing of a steel rivet. The frictional heating further increases the local ductility of Mg to avoid cracking issues commonly associated with SPR of Mg alloys. Table II.3.9.1 and Figure II.3.9.6(a) show the mechanical performance of Mg-thermoset CFRC FSPR joints evaluated in lap-shear, cross-tension, and fatigue respectively. The lap-shear coupons were 25.4 mm wide and 101.6 mm long, whereas cross-tension coupons were 50 mm wide and 150 mm long. Fatigue life (R=0.1, frequency=20 Hz) was studied at different peak loads. Because no open literature exists for fatigue life of Mg/CFRC with the same test coupon dimension, we compared our results with the fatigue life of resistance spot-welded AZ31B-AZ31B with the similar average peak failure load (~5.12 kN) for spot-joined samples [1]. Fatigue life for FSPR joints was longer than the fatigue life of resistance spot-welded Mg joints in that spot-welded Mg joints developed cracks at less than E+06 cycles while FSPR joints did not show crack initiation until after E+07 cycles. To study how a crack initiates and propagates in dissimilar material joints, non-contact optical DIC was used during the fatigue testing process. Figure II.3.9.6(b) presents a series of DIC images on the backside of the FSPR joint during fatigue testing. As can be seen, the higher strain was found at the periphery of the FSPR joint during testing because of stress concentration at the joint. Additional strain was developed at the side of the Mg alloy due to cyclic tension and compression during fatigue. The crack was initiated around the rivet joint after 1 million cycles and continuously grew and propagated into the lateral direction, leading to a final failure at the Mg alloy. Several factors, including material properties (i.e., thickness, stiffness, and strength), specimen size, riveting force, cyclic load level, and residual stress, affect the

fatigue life of the joints. For FSPR joints, there are large differences in material properties (i.e., higher stiffness and strength for CFRC than the AZ31B), so the weaker material (Mg alloy) failed. Residual stress also affects fatigue life, but it is quite challenging to measure Mg/CFRC alloy joints due to complex geometry and different material combinations. Therefore, more efforts are needed to develop the measurement technique for residual stress measurement.

Table II.3.9.1. Summary of Mechanical Joint Performances of FSPR Joints

Material Combination (Mechanical Testing)	Peak Failure Load (kN)	Failure Location
TP CFRP-AZ31B (Lap-shear)	3.07 ± 0.19	Base TP CFRP
TS CFRP-AZ31B (Lap-shear)	5.18 ± 0.12	AZ31B pullout
Weld-bonded (FSPR + adhesive) TS CFRP-AZ31B (Lap-shear)	8.89± 0.81	Cohesive (for adhesive) + AZ31B pullout (for FSPR)
TS CFRP-AZ31B (Cross-tension)	2.81±0.11	AZ31B pullout

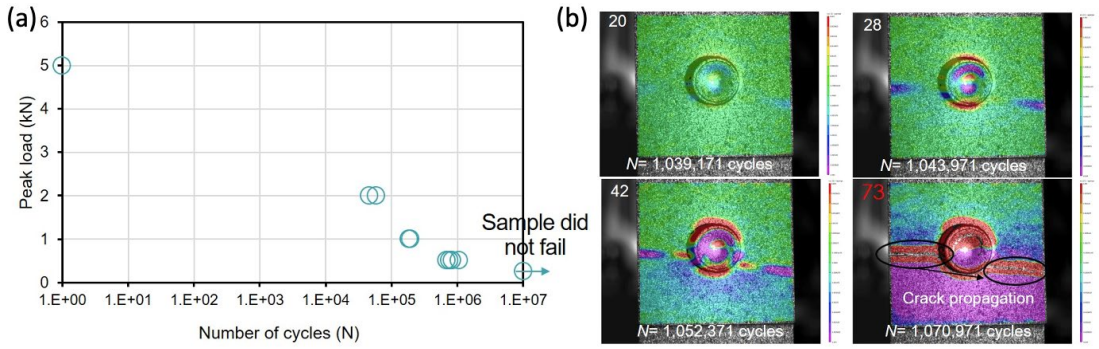

Figure II.3.9.6. (a) Stress vs number of cycles for TS CFRC-AZ31B FSPR joints; and (b) sequential DIC images on the backside of the FSPR joint during fatigue testing showing crack initiation and propagation for final failure. Source: ORNL.

After achieving good mechanical joint performance of the FSPR joints, the focus was on a quantitative corrosion study of dissimilar joints and mitigation approaches. A new methodology was developed to quantitatively study galvanic corrosion, which is the most significant issue for Mg alloy in the actual FSPR joints. As presented in Figure II.3.9.7(a), the rivet head and side sections of AZ31B in the FSPR joints were selectively exposed in 0.1 M NaCl solution. The mass loss rate of AZ31B at the exposure areas on AZ31B in the FSPR joints was measured and used to calculate the galvanic current using Faraday's law as:

$$I = \frac{m}{t}\frac{Fz}{M} \quad (1)$$

where, I is a galvanic current, $\frac{m}{t}$ is a mass loss rate (g/s), F is Faraday's constant (96500 C/mole), z is a charge of ion (z=+2 for Mg), and M is a molecular mass (24.3 g/mole for pure Mg). Figure II.3.9.7(b) summarizes the calculated galvanic current for the FSPR joints with different 0.1-M NaCl immersion times. Initially, the galvanic current was nearly constant up to 100-hour exposure time, and then gradually decreased, indicating that Mg dissolution decreased over time. The main cause of reduced Mg dissolution would be the increased ohmic drop from the corrosion products that accumulate between the dissolving Mg surface and NaCl solution. This selective exposure test permits quantification of a galvanic attack for the dissimilar material joints and can be used to verify the effectiveness of corrosion mitigation methods being developed by ORNL on Mg galvanic corrosion.

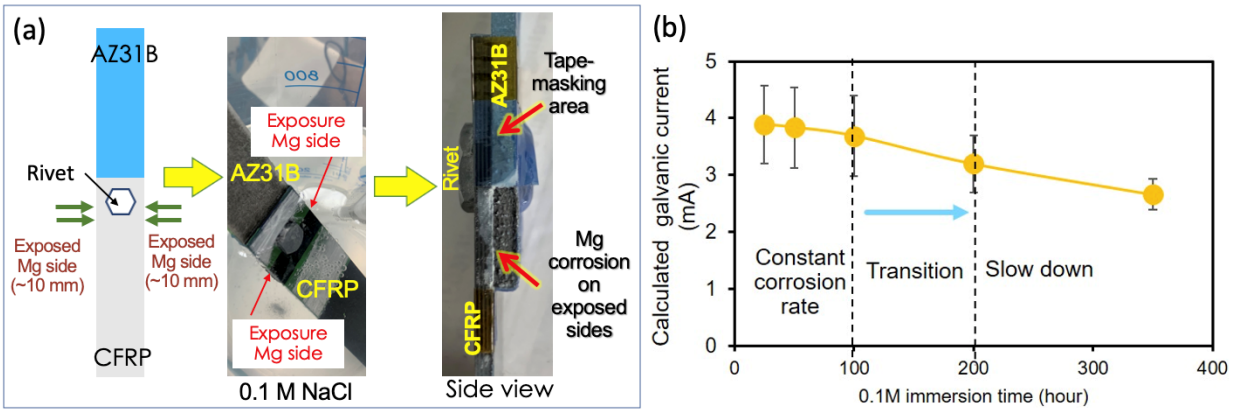

Figure II.3.9.7. (a) Selective corrosion exposure testing for quantification of mass loss of Mg alloy in FSPR joints. (b) Calculated galvanic current for FSPR joints as a fuction of 0.1M NaCl immersion times. Source: ORNL.

Conclusions

In FY 2020, the conclusions from the research activities performed in the Mg-CFRC joining task are summarized below:

1. FSI-Linear joint corrosion performance revealed that the thermomechanically processed region may be prone to higher corrosion rate based on the SECCM testing. Additionally, a novel FSI-Spot joining process was developed and proof-of-concept was demonstrated for successfully joining Mg to CFRC using this process.
2. Three-step isolation bolted joints effectively reduced galvanic corrosion for Mg and retained ~80% of the original joint strength after 438 hours of ASTM B117 exposure.
3. FSPR has been successfully used to join CFRC to Mg with good mechanical joint performances. Novel methodology to quantify galvanic corrosion of Mg alloy in the FSPR joints was developed (selective exposure approach).

Key Publications

1. Wang T., P. Upadhyay, M. Reza, E. Rabby, X. Li, L. Li, A. Soulami, and K.S. Kappagantula, 2020, "Joining of thermoset carbon fiber reinforced polymer and AZ31 magnesium alloy sheet via friction-stir interlocking," *Int. J. Adv. Manuf. Tech.,* Vol. 109, No. 3–4, pp. 689–698.
2. Whalen S. A., T. Skszek, N. R. Overman, V. Joshi, J. T. Darsell, P. Upadhyay, and K. S. Kappagantula, 2019, "Solid-Phase Processing of Magnesium Alloys," *MS&T 2019*, 3 October 2019. Portland, OR, USA.
3. Wang T., K. S. Kappagantula, P. Upadhyay, S. A. Whalen, and W. Choi, "Joining Dissimilar Materials via Rotational Hammer Rivet Technique," *TMS 2020*, 23–27 February 2020, San Diego, CA, USA.
4. Wang T., S. A. Whalen, P. Upadhyay, and K. S. Kappagantula, 2020, "Joining Dissimilar Materials via Rotational Hammer Riveting Technique," *Magnesium Technology*, Brian, J. (ed.), Springer Nature, New York, NY, USA: pp. 207–212.
5. Wang T., L. Li, M. Pallaka, H. Das, S. A. Whalen, A. Soulami, and P. Upadhyay, 2020, "Mechanical and microstructural characterization of AZ31 magnesium-carbon fiber reinforced polymer joint obtained by friction-stir interlocking technique." *Mater. Des.*, in press. Available at: https://doi.org/10.1016/j.matdes.2020.109305.

6. Wang T., P. Upadhyay, S. A. Whalen, and K. S. Kappagantula, "Joining of magnesium to carbon fiber reinforced polymers using friction-stir interlocking technique," *MS&T 2020, Portland, Oregon*, September 30, 2019.

7. Das, H., T. Wang, M. Pallaka, P. Upadhyay, and K. Kappagantula, "Component-scale performance of friction-stir interlocked magnesium/carbon fiber reinforced composites," in preparation.

8. M. Pallaka, V. Prabhakaran, H. Das, T. Wang, P. Upadhyay, and K. Kappagantula, "Corrosion behavior of magnesium/carbon fiber reinforced composite joints manufacturing via friction-stir interlocking," in preparation.

9. Lim, Y. C., J. Jun, D. N. Leonard, Y. Li, J. Chen, M. P. Brady, Z. Feng, "Study of galvanic corrosion and mechanical joint properties of AZ31B and carbon fiber reinforced polymer joined by friction self-piercing riveting," in preparation.

10. Jun, J., Y. C. Lim, Y. Li, C. D. Warren, and Z. Feng, "Mitigation of galvanic corrosion in bolted AZ31B and Carbon Fiber Reinforced Epoxy using electric isolation by epoxy resin and polymer tape," in preparation.

11. Lim, Y. C., J. Jun, D. N. Leonard, Y. Li, J. Chen, M. P. Brady, and Z. Feng, "Dissimilar joining of carbon fiber reinforced composite to magnesium alloy by friction self-piercing riveting process," AWS professional program, 2020 (Virtual due to COVID 19). Accepted for presentation.

12. Warren, C.D., J. Jun, Y.C. Lim, and Z. Feng, "Effect of surface coating and PTFE tape insulation on galvanic corrosion of AZ31B bolt-joined with CFRP," *MS&T Conference*, 2–6 November 2020 (Virtual). Accepted for presentation.

13. Lim, Y. C., J. Jun, D. N. Leonard, Y. Li, J. Chen, M. P. Brady, and Z. Feng, "Characterizations of corrosion tested CFRC-AZ31B joint by friction self-pierce riveting process," *MS&T Conference*, 2–6 November 2020 (Virtual). Accepted for presentation.

14. Lim, Y. C., J. Chen, J. Jun, D. N. Leonard, M. P. Brady, C. D. Warren, and Z. Feng, 2020, "Mechanical and corrosion assessment of friction self-piercing rivet joint of carbon fiber-reinforced polymer and magnesium alloy AZ31B," *J. Manuf. Sci. Eng*. Accepted for publication.

15. Lim, Y., J. Jun, J. Chen, M. Brady, D. Leonard, C. Warren, J. Chen, and Z. Feng, 2020, "Corrosion study on CFRP-AZ31B spot-joined by friction self-pierce rivet," *TMS Coatings and Surface Engineering for Environmental Protection II*, 23–27 February 2020, San Diego, CA, USA. (Invited).

References

1. Behravesh S. B., H. J. Jahed, S. Lambert, "Characterization of magnesium spot welds under tensile and cyclic loadings," *Mater. Des*., Vol. 32, 2011, pp. 4890–4900.

2. Acharya, M. G., A. N. Shetty, "The corrosion behavior of AZ31 alloy in chloride and sulfate media – A comparative study through electrochemical investigations," *J. Magnes. Alloy.,* Vol. 7, 2019, pp. 98–112.

Acknowledgements

The Co-PI at PNNL would like to express appreciation for T. Wang, H. Das, M. R. Pallaka, P. Upadhyay, D. Graff, A. Guzman, L. Li, A. Soulami, T. Roosendaal, and R. Seffens for their efforts with this project. The Co-PI at ORNL would like to express appreciation for J. Chen, J. Jun, Y. Li, H. Huang, L. Donovan, M. P. Brady, R.R. Lowden, D. Erdman III, D. Warren (retired 2020), and Z. Feng for their efforts. The Co-PIs at PNNL and ORNL also acknowledge BASF for providing materials.

II.3.10 Interface-by-Design for Joining of Dissimilar Materials (Oak Ridge National Laboratory)

Xin Sun, Co-Principal Investigator
Oak Ridge National Laboratory
1 Bethel Valley Road
Oak Ridge, TN 37831
E-mail: sunx1@ornl.gov

Ayoub Soulami, Co-Principal Investigator
Pacific Northwest National Laboratory
902 Battelle Boulevard
Richland, WA 99352
E-mail: ayoub.soulami@pnnl.gov

Sarah Kleinbaum, DOE Technology Manager
U.S. Department of Energy
E-mail: sarah.kleinbaum@ee.doe.gov

Start Date: October 1, 2017 End Date: September 30, 2020
Project Funding: $1,025,000 DOE share: $1,025,000 Non-DOE share: $0

Project Introduction

Further weight reduction of automotive body structures depends on the industry's ability to assemble multiple lightweight materials, including CF-reinforced composites, Mg alloys, Al alloys, and AHSSs reliably and cost-effectively. Because of their extreme disparities in physical properties, such as melting temperature, thermal conductivity, and thermal expansion coefficient, dissimilar materials pose a serious challenge for traditional joining process development. There is a lack of fundamental understanding on the interfacial bond formation mechanisms for the different dissimilar materials pairs to enable process development.

Objectives

With the recent advancements in high-performance computing and high-throughput experiments at various materials length scales, this project aims to establish a scientific framework for designing the hierarchical interfacial features and the associated chemical and thermomechanical kinetic pathways to achieve them.

Approach

For each set of material interfaces, the interfacial characteristics at different length scales are simulated with multiscale material processing models and the results will be experimentally validated and calibrated with associated experiments at the corresponding scales. The calibrated model parameters at a lower length scale will be hierarchically passed to a higher length scale to predict the robust processing parameter windows with quantitative confidence. Once the hierarchical multiscale interfacial modeling framework is established, it can be used to inversely design the dissimilar materials interface and the associated welding process and parameters, thereby accelerating the development and deployment of dissimilar materials joining technologies.

In FY 2020, the interface-by-design project has progressed on two parallel tasks on model development for (1) joining a Mg alloy to a Zn-coated AHSS using the ultrasonic spot welding (USW) method; and (2) joining a Mg alloy to an uncoated AHSS using friction assisted stir technology. The first task is performed using the ICME approach, in which a comprehensive multiscale modeling framework has been established to study and predict the weld interface microstructure and bonding strength under different welding process conditions (e.g., a process-microstructure-properties relation). The framework starts with a coupled thermomechanical-

diffusion FE model of the USW process to quantify the heat generation, cooling, and diffusion between Mg and coated steel, in which the different process parameters such as welding time, input power, clamping force, vibration frequency, and magnitude are explicitly considered. The predicted temperature and chemical composition at the joining interface are taken as inputs to the solidification model for calculating the interface microstructure using the CALPHAD method in the commercial package Thermo-Calc, as well as predicting the microstructure morphology using the phase-field method. The final microstructure is then converted into the micromechanical FE model, where each individual phase and interface are explicitly modeled, and their mechanical properties are obtained from literature or evaluated from atomic-scale MD simulations. The final microstructure-based FE model of the joint interface is tested under various loading conditions to evaluate the bonding strength, providing guidance to the welding method development. In addition, a modal analysis tool was further developed and validated toward component-level USW to evaluate the weld performance when making multiple joints.

The second task focuses on modeling joining a Mg alloy to an uncoated AHSS using FSW. To understand the bonding mechanism of the interface and joint performance, characterization techniques were used along with computational modeling. A complex-variable finite element method (ZFEM) approach was developed to determine the cohesive law parameters to mechanically characterize the interface obtained in dissimilar FSW joints. A crystal plasticity theory-based model was also developed to understand the effect of microstructure on the joint performance. Low-length scale characterizations, such as SEM images, EBSD analysis, and nanoindentation data, are used as input in the crystal plasticity model.

Results

Task 1.1. Multiscale Modeling for USW of Mg Alloy to Zn-Coated AHSS

Mg- to Zn-coated AHSS USW is sensitive to welding process conditions, such as different temperature and chemical composition. This is shown by the SEM characterization results in Figure II.3.10.1.
Figure II.3.10.1(a) shows the weld interface in the center of the bonding area where the temperature is the highest and the Zn coating is at a minimum due to ultrasonic vibration-induced scratching. A uniform interface layer containing Mg dendrites and Mg/Mg-Zn eutectic phases is observed in this region. In contrast, the temperature is lower near the edge of the weld, which results in a heterogeneous interface layer microstructure, as shown in Figure II.3.10.1(b), and contains a thick unreacted Zn layer, a layer of uniform Mg-Zn intermetallic and a layer of eutectic phases. The difference in the interface microstructure results in different bonding strength, which is assessed by the multiscale modeling framework, discussed below.

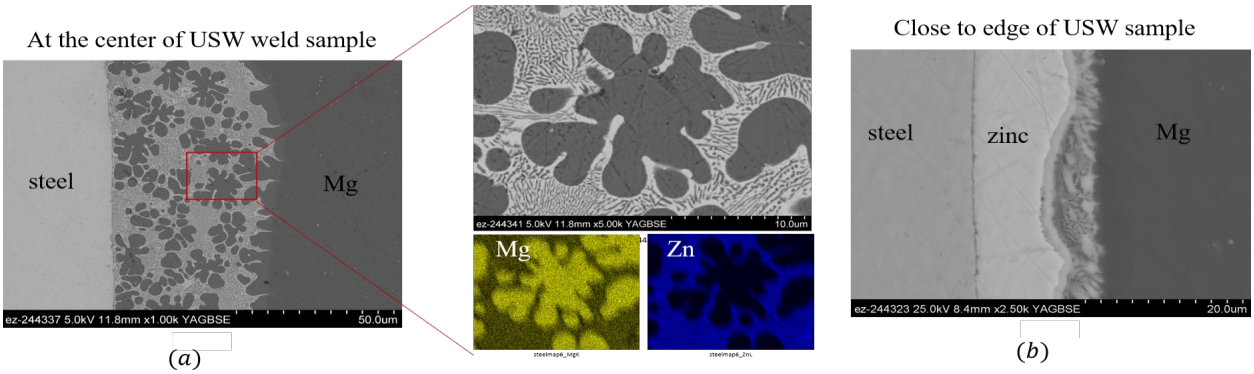

Figure II.3.10.1. SEM result of the Mg-Zn-coated steel USW interface at weld spot (a) center, and (b) close to the edge.
Source: ORNL.

The macroscopic process model was created using the commercial FE package, ABAQUS, which is illustrated in Figure II.3.10.2(a). The Mg and steel plates were clamped by sonotrode horns. A 200-µm-thin layer of a Zn foil was sandwiched between the two plates to mimic the increased Zn coating on the steel surface at the Mg-steel interface. The "hard" frictional contact condition was applied to model the interaction between two substrates and between substrate-sonotrodes. Ultrasonic vibrations were applied to the sonotrodes in the TD with pre-described frequency and magnitude. As shown in Figure II.3.10.2(a), the temperature increased at the Mg-AHSS interface due to frictional heating, and the temperature gradient through-thickness was large due to significant difference in thermal diffusivity of Mg and steel. The Zn layer was squeezed under the clamping and rubbing, resulting in less Zn distributed in the center with more distributed to the edges, as shown in Figure II.3.10.2(b). As discussed later, less Zn at the interface forms a stronger bonding interlayer, while the partially dissolved thick Zn layer leads to premature failure. Therefore, the bond area can be estimated based on the distribution of Zn content at the interface. Figure II.3.10.2(c) shows the temperature history at the center of the Mg-Zn interface along with the predicted bond area at weld time t = 2 s and t = 4 s, respectively. The bond area at t = 4s expanded almost four times from 2 s and more uniform mixing of Mg and Zn can be seen near the center of the interface. The joining zone showed an oval shape with the major axis in the longitudinal direction, which is caused by limited heat conduction in the width direction. The experimentally observed bond areas are also shown in Figure II.3.10.2(c), which compared well with the simulation in both bond size and shape.

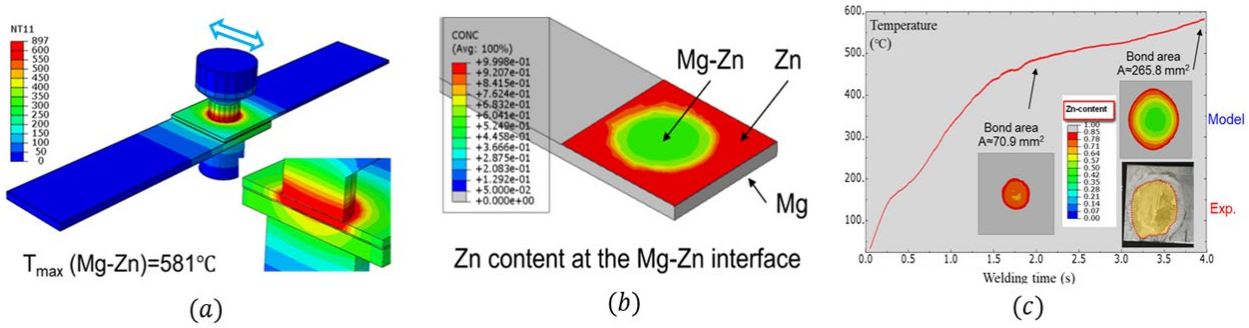

Figure II.3.10.2. (a) Macroscopic FE model of the USW process, color contour corresponding to the temperature after USW for 4 seconds. (b) Distribution of Zn after 4 seconds of USW process under a welding power of 3500 W and a clamping pressure of 60 psi. (c) Temperature evolution and bond area. Source: ORNL.

During USW simulation, the diffusion between the Mg substrate and the Zn coating was computed by coupling the process model and Fick's diffusion model. Diffusion from Zn to Fe was not experimentally observed; therefore, it was ignored. The diffusion coefficient of Zn with respect to Mg is a function of temperature, which was obtained from the microdiffusion model that was developed in FY 2019. Figure II.3.10.3(a) shows the computed relationship between the diffusion coefficient and the temperature. A higher temperature results in higher Zn diffusivity, and the highest diffusivity occurs when Zn concentration is about 30%. Figure II.3.10.3(b) shows the simulated temperature history at the center and edge of the weld spot. At the center, the temperature reached a peak of ~600°C after 4 seconds of ultrasonic vibration, while the edge had a peak temperature of only ~300°C. The difference in local temperature and Zn-Mg distribution led to the formation of a different interface microstructure. At the center, the high peak temperature and low Zn content led to a rather uniform mixing of 60% Mg and 40% Zn. Based on this result and the cooling profile in Figure II.3.10.3(b), the solidification process was computed using the CALPHAD method (Thermo-Calc), which is shown in Figure II.3.10.3(c). The formation of Mg and Mg-Zn phases was predicted at the end of the cooling stage. To obtain the morphology of the interface microstructure, phase-field simulation was conducted using an in-house code, and the predicted microstructure is shown in Figure II.3.10.3(d). The predicted result is consistent with the experiment characterization in Figure II.3.10.1(a), showing promise for the model. In contrast, at the edge region, the peak temperature was 300°C lower and the Zn content was much higher, which led to a partially dissolved Zn layer from the Thermo-Calc DICTRA diffusion calculation. Currently,

the phase-field model only considers the Mg and Mg-Zn phases, and multilayer microstructure at the edge was handled differently as described later.

To assess the bonding strength between the Mg and steel sheet, the predicted interface microstructure was subjected to mesoscale mechanical simulations using FE modeling. To construct the FE model, the predicted microstructure in Figure II.3.10.3(d) above was first converted into a FE mesh by converting each voxel into an eight-node linear brick element (C3D8). Then, a layer of steel was introduced by assigning elements close to the left edge to have properties of steel. Such assignment is consistent with experimental observations that the steel region has a clear and flat interface from the eutectic interlayer. Next, the interface between neighboring elements that belonged to different material phases were identified, and the cohesive elements layer with the traction-separation law was created to model the interface bonding/debonding/sliding behaviors. The final microstructure contains steel, Mg, Mg-Zn phases, and interfaces between steel/Mg, steel/Mg-Zn and Mg/Mg-Zn. Here, only the steel and Mg phase had mechanical data available from literature (e.g., Johnson-Cook plasticity and damage model and model parameters).

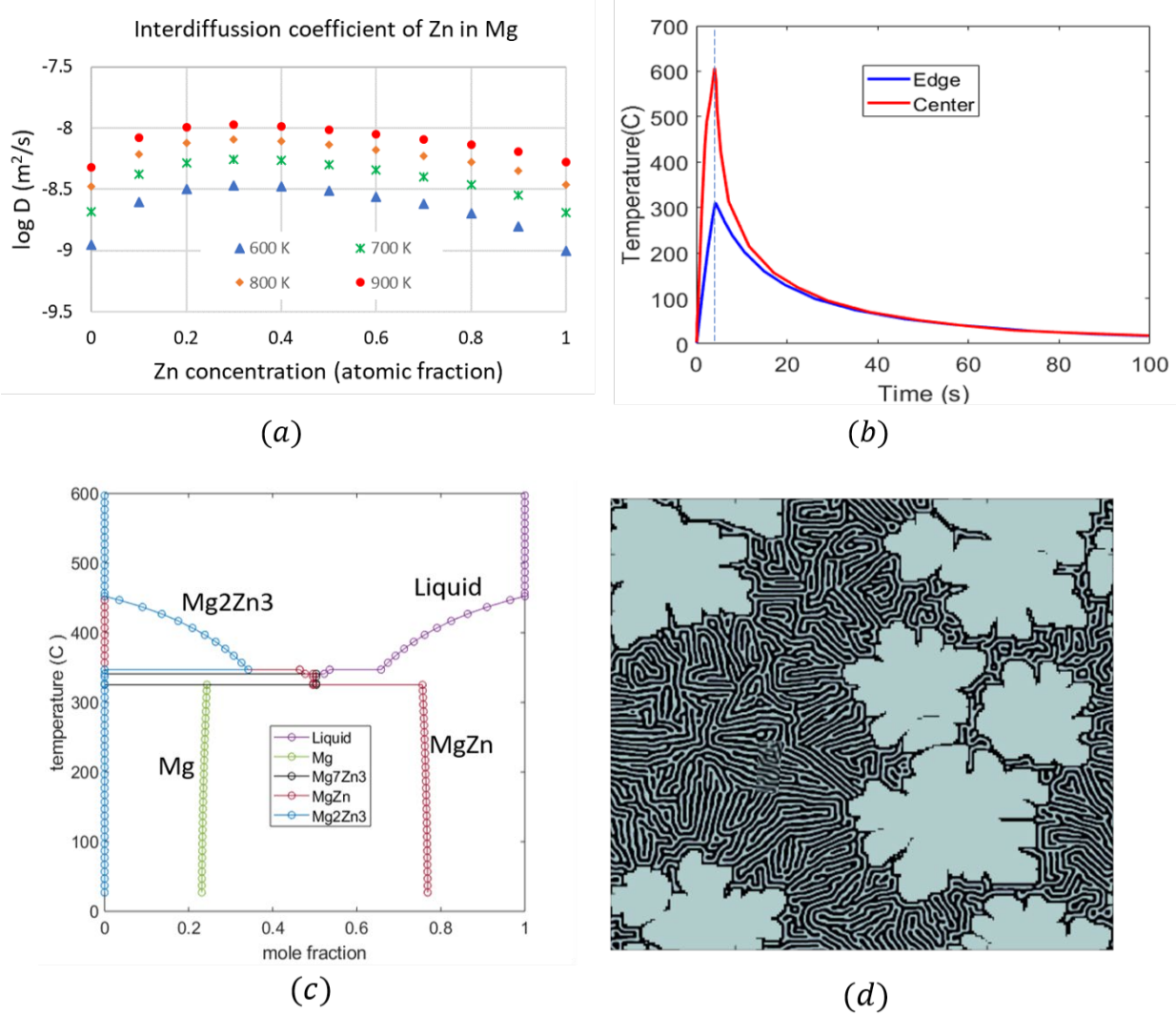

Figure II.3.10.3. (a) Interdiffusion coefficient map constructed for various conditions. (b) Temperature evolution result from process modeling. (c) Thermo-Calc prediction of the solidification process at the center of the USW weld spot. (d) Predicted morphology of the interface microstructure using the phase-field method. Source: ORNL.

To estimate the mechanical properties of the Mg-Zn intermetallic phase and the interfaces, MD simulations were conducted using open-source package LAMMPS based on existing modified embedded atom method potentials. Figure II.3.10.4(a) through (c) illustrates MD simulation results for the pure Mg-Zn phase, the Mg/Mg-Zn interface, and the Fe/Mg-Zn interfaces, respectively. The MD simulation was conducted under tensile loading (along vertical direction) at RT with all surfaces set to be periodic. Figure II.3.10.4(d) plots the tensile stress-strain curves from the MD simulations. Due to the intrinsic extremely small-time step ($\leq 10^{-15}s$) constraint of MD simulations, the MD simulation was based on extremely high strain rates on initially defect-free crystal structures which resulted in very high stress in all cases. To estimate a reasonable strength under a normal strain-rate, the pure Mg was also tested and serves as a reference to normalize all MD computed stress-strain curves. As observed from MD simulations, the Mg-Zn intermetallic exhibited very limited plasticity and showed a brittle fracture behavior. Therefore, it was modeled with an elastic law with a brittle failure criterion in the microstructural FE model. All interfaces were set to have corresponding failure strength based on the MD simulation predictions.

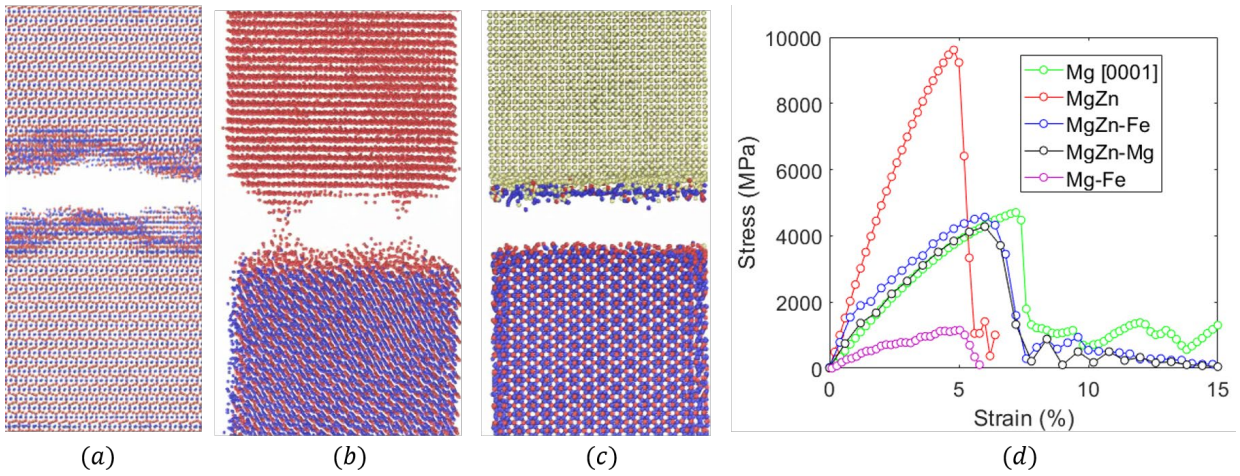

Figure II.3.10.4. MD simulation of: (a) a pure Mg-Zn intermetallic phase; (b) a Mg/Mg-Zn interface; and (c) a Fe-Mg-Zn interface under tensile loading. (d) MD simulation predicted stress-strain curves. Source: ORNL.

Figure II.3.10.5(a) through (c) shows the FE simulation predicted USW interface behavior at the weld center under applied tensile load (along the horizontal direction) and shear loading (on the left and right edge in the vertical direction), respectively. In tensile loading, cracks first nucleated in the eutectic region between the dendrites where stress concentration was shown. However, once the cracks propagated to the Mg dendrites, they are arrested due to the high ductility of Mg. While the crack in the eutectic was hindered, a new crack near the steel-eutectic interface formed and propagate along with the interface, leading to the failure of the joint between the steel and eutectic interlayer. Under applied shear deformation, a crack nucleated directly at the steel-eutectic layer interface and propagated along with the interface, as shown in Figure II.3.10.5(c). This is consistent with the lap-shear experiment result where debonding between steel and the interlayer at the interfaces were observed. To estimate the joint strength at the edge region of the weld spot, a pure Zn layer and a $MgZn_2$ intermetallic layer were introduced to the microstructure in Figure II.3.10.5(d), resulting in a FE model shown in Figure II.3.10.5(d). This model consisted of a steel layer (green), a pure Zn layer (yellow), a $MgZn_2$ layer (orange), and the eutectic regions. The mechanical properties of Zn were obtained from the literature in the form of the Johnson-Cook plasticity and damage model. The properties of $MgZn_2$, as well as the corresponding new interfaces, were estimated from the MD simulation following a similar methodology as discussed above. Figure II.3.10.5(e) and (f) showed the tension and shear simulation results of the edge region microstructure, respectively. In both cases, the failure occurred in the Zn region at a low stress level. This is because Zn has much lower strength and ductility and acted as a weak spot in the weld interface.
Figure II.3.10.5(g) and (h) compare the stress-strain curves from the FE simulation for the center and edge region under tension and shear conditions, respectively. The edge region showed a much lower strength in both

cases due to premature failure in the Zn layer. These results suggest that bonding strength in the center and edge of the USW weld spot varies significantly. It also explains the observed trend of an increase in joint strength with welding time and welding power: sufficient heat generation is required to fully dissolve the Zn coating and avoid a pure Zn layer in the microstructure to cause a weak joint.

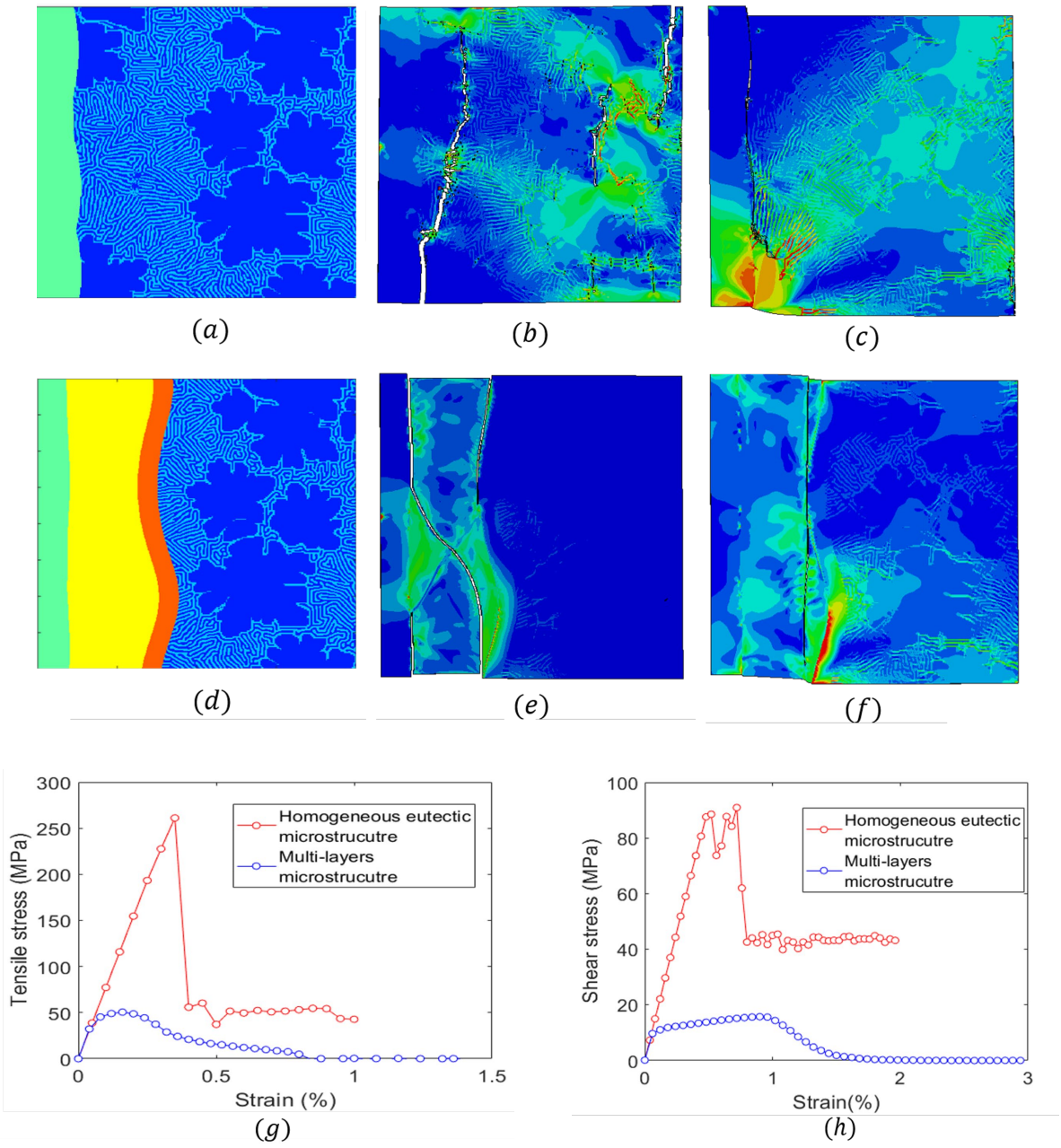

Figure II.3.10.5. (a) FE model of interface microstructure at the center region of the USW weld spot, the simulation results under tension and shear loading condition are shown in (b) and (c), respectively. (d) FE model of interface microstructure at the edge region of the USW weld spot, the simulation results under tension and shear loading condition are shown in (e) and (f), respectively. (g) and (h) compares the FE simulation predicted stress-strain curves for tension and shear tests, respectively. Source: ORNL.

With the proposed modeling framework, more USW process parameters were searched for the ideal process window providing guidance to optimize the USW design. To demonstrate, the bond area under various processing conditions was investigated. The focus of this study was the clamping load (p = 30~80 psi) and the vibration amplitude (u_0 = 5~20 μm). Figure II.3.10.6 shows the window of the bond status at two different welding times. The size of the bond area was normalized by dividing a unit square inch area and plotted as circles in the figure. For USW at 2 s shown in Figure II.3.10.6(a), no bond was formed at the initial condition (p = 30 psi, u_0 = 20 μm), as well as at the final condition (p = 80 psi, u_0 = 5 μm). Larger clamping load and vibration amplitude were needed to create a necessary bond area within the short welding time, which is important from a production efficiency perspective. For the case of USW at 4 s shown in Figure II.3.10.6(b), the larger bond area was expected at the same clamping and vibration condition. Especially, the welds made at p>60 psi and u_0=20 μm achieved nearly 100% bonding at the Mg-Zn interface. This process window provides a path for joining at locations which require a lower clamping load or sonotrode force to avoid ultrasonic-induced crack and bond failure. Other welding conditions, such as sheet thickness and sonotrode size, can be investigated similarly using the developed computational framework to guide the USW application.

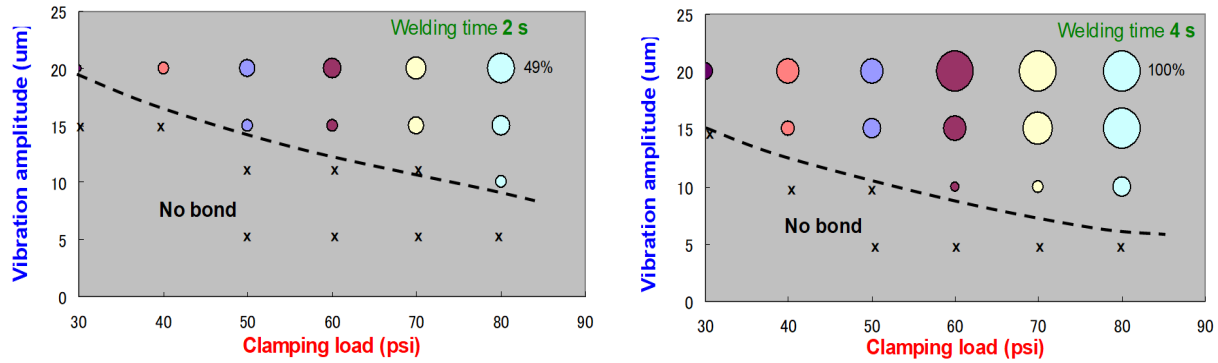

(a) (b)

Figure II.3.10.6. Process windows of Mg/Zn-coated steel USW at (a) a welding time of 2 s, and (b) a welding time of 4 s. Source: ORNL.

Task 1.2. Development of Modal Analysis Tool for USW

Depending on the component geometry and vibration frequency, the sonotrode vibration may not deliver the acoustic energy properly or can even pose a detrimental effect on the sheet material and existing welds. In this study, a modal analysis tool was developed for USW based on the steady state dynamics and mechanical load derived from thermomechanical simulation of the USW process. By predicting relative motion and shear stress at the faying surface, the coupon length and weld spacing were identified as two major factors that affect the welding reliability and joint quality in multiple USW welds. Figure II.3.10.7(a) shows a schematic of the USW of AA6061 with the sonotrode vibrating in longitudinal direction. The sheets were welded without any restraint such that the ends can move freely. The dependence of interfacial vibration and joint quality on extension length L was investigated. The wavelength λ of the ultrasonic wave propagation in the material can be calculated as 252 mm. Figure II.3.10.7(b) shows the vibration mode predicted at the condition of extension length equal to a quarter λ. The clamped location by the sonotrode appeared to be a node position where the top sheet can hardly vibrate against the bottom sheet. The relationship between the interfacial vibration amplitude and the extension length is shown in Figure II.3.10.7(c). It is clear that the vibration amplitude is very low at certain critical lengths (L= λ /4, 3λ /4, …). In such a case, more heat will be generated on the top sheet surface, resulting in severe plastic deformation and weak bond as shown by the experiments as depicted in Figure II.3.10.7(d). The variation of the joint strength of the Al ultrasonic weld with respect to extension length L has a good correlation with interfacial vibration, which is necessary to clean the faying surface and soften the material for mechanical interlocking. In actual welding, the node position or node line of the sheet should be avoided to facilitate a reliable bond.

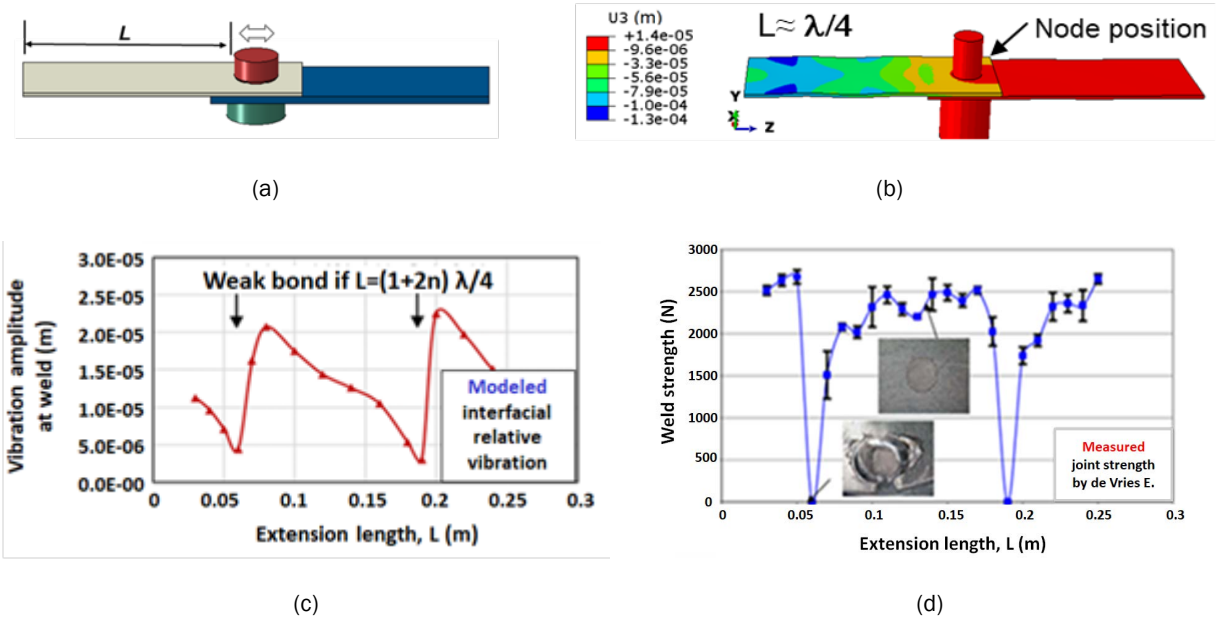

Figure II.3.10.7. Modal analysis of vibration amplitude and experimental results of AA6061-T6 USW: (a) USW setup and definition of extension length L; (b) predicted longitudinal vibration at condition L equal to a quarter wavelength; (c) dependence of interfacial vibration on extension length; and (d) dependence of joint strength on extension length. Source: ORNL.

The multi-spot joining of Mg to Mg, as shown in Figure II.3.10.8(a), was analyzed by the modal analysis tool. The effect of weld spacing on ultrasonic joining performance was investigated. The length of the top sheet was 5 in. which was half the wavelength of the Mg material. For welding at Location 3 with the spacing of a = 1 in., the interfacial shear stress induced at previous welds, as observed in Figure II.3.10.8(b), are much higher than the lap-shear strength of a USW joint. Thus, bond failure could occur especially when the existing welds are not strong enough. Figure II.3.10.8(c) is a bar chart that summarizes the peak shear stress recorded in the sheets when joining a spot weld. All cases except for a = 1.25 in. will generate a detrimental stress wave during sequential spot welding. Figure II.3.10.8(d) is a validation example for a = 1.0 in. showing the debonding phenomenon at Weld 1 and Weld 2. The imprint of the sonotrode tip at Weld 2 is smaller than the other two locations which indicates that heat generation was smaller, resulting in a weak bond. In another case, as shown in Figure II.3.10.8(e), the weld locations were offset by ½ in. while keeping the weld spacing as 1 in. Predicted vibration amplitude at Weld 2 was small as confirmed by the indent mark. Shear stress induced by USW at Weld 3 is close to 50 MPa which may again break the bond at the weakest location. During the welding experiment, the bond at Weld 1 survived after Weld 3 while the bond/failure status at Weld 2 was unknown. After the completion of all four spot welds, a nondestructive examination by ultrasound was conducted to reveal the bond area of each weld. As shown in Figure II.3.10.8(f), the full screen height map indicates that Weld 2 has failed during subsequent USW. The major reason of this failure can be attributed to the weak bond from low vibration amplitude and heat generation at the faying surface.

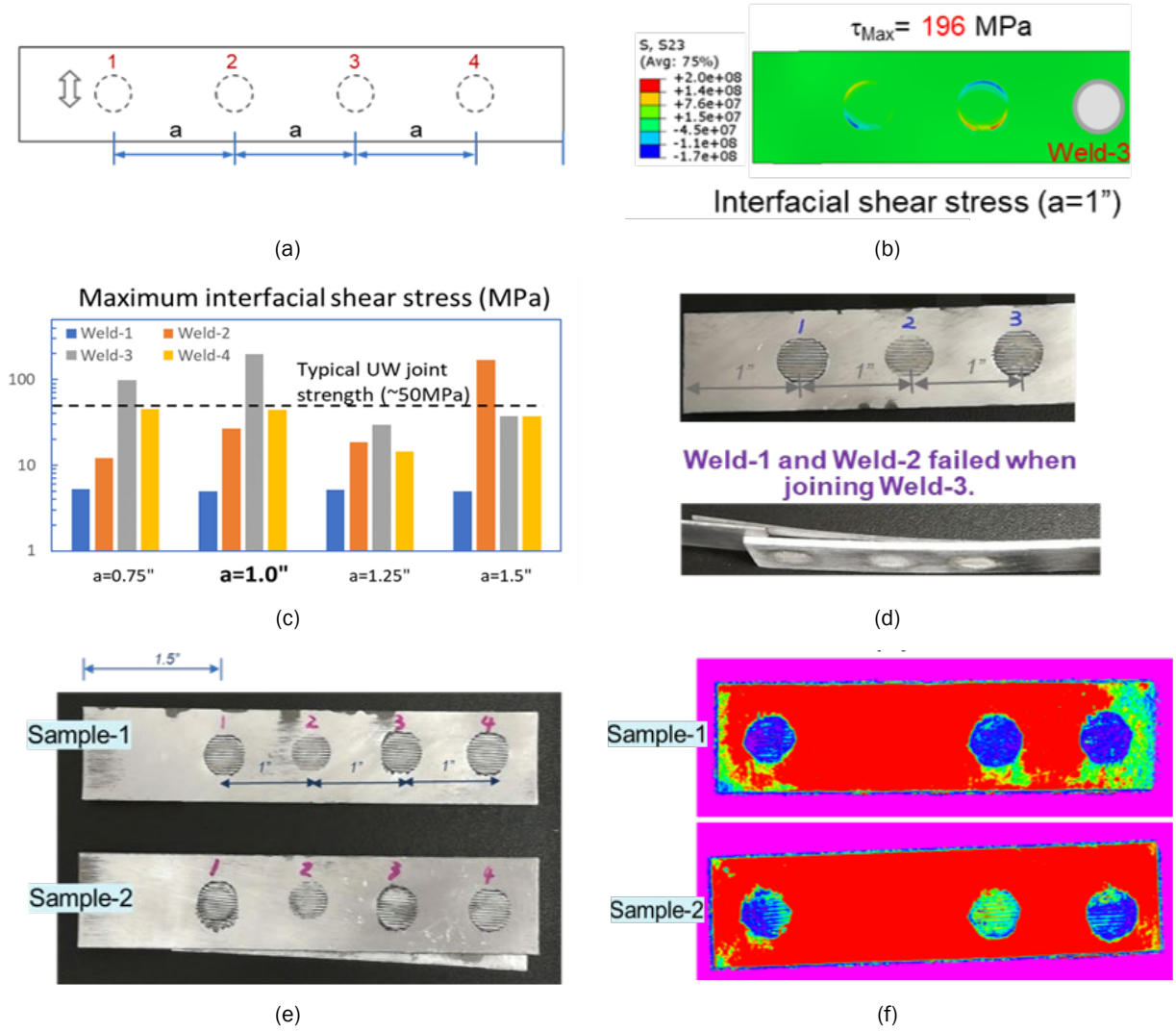

Figure II.3.10.8. Predicting shear stress in multi-spot AZ31 USW and experimental validation: (a) Configuration of weld spots; (b) Shear stress induced by welding at Location 3; (c) Peak shear stress induced by each weld; (d) Failure of existing welds due to ultrasonic vibration; (e) Welded samples with first weld location approximately 1.5 in. away from edge; and (f) Full screen height map with red color indicating for gap and blue color for bond. Source: ORNL.

Task 2.1. Development of ZFEM Model for FSW of Mg Alloy to Uncoated AHSS

The structural performance prediction of a mechanical joint requires characterization of the interface resulting from the joining process. Some techniques to obtain the parameters for a cohesive law place restriction on the test geometries and require the existence of analytical solutions. In addition, these techniques use a global response (load-displacement curve) to describe a local material property, resulting in uncertainties on the adopted model. Other techniques, such as hybrid inverse techniques, use full-field kinematic measurements from a suitable test geometry obtained using the DIC procedure and an inverse FE analysis to identify the cohesive parameters by solving an optimization problem. The ZFEM method computes highly accurate estimates of arbitrary shape, material, or loading sensitivities. These gradients will be used in gradient-based optimization algorithms for determination of the specific numerical values that govern interfacial behavior. For FSW Mg-AHSS joints, these parameters determine the behavior of a traction-separation law.

Task 2.1.1. Optimization Framework

An optimization framework was developed where experimental data is used in conjunction with ZFEM simulations to obtain the material parameters that govern the interfacial behavior of a joint. Figure II.3.10.9(a) depicts the optimization framework. First, experimental data containing reaction force, P^{DIC}, and the DIC obtained strain fields, ϵ^{DIC}, was generated. Then, a ZFEM simulation was run with an initial guess of the parameters to be optimized, θ. From this hypercomplex simulation the traditional FE outputs were obtained (reaction forces and strain fields) with their derivatives with respect to the material parameters in question. The numerical and experimental load and strain fields were compared, and a residual was computed. With the derivatives, a gradient of the residual was computed allowing the minimization routine for a faster search of the global minimum. The process was repeated until a minimum was found. This minimum corresponds to a set of material parameters that best recreate the behavior that was seen experimentally.

Task 2.1.2. Validation Tests of ZFEM Framework for FSW

Three tests were conducted to validate the ZFEM-based optimization framework. The first test was based on a tensile study where the material parameters to be retrieved were the YS, σ_y, and the nonlinear exponent, n from a Ramberg-Osgood material law that describes the behavior of the material. Figure II.3.10.9(b) contains a three-dimensional representation of the residual function. Thirteen iterations were needed to converge to the minimum of this function. The values of the YS and nonlinear exponent corresponding to the minimum are σ_y = 322.58 MPa and n = 688. Then using these values, strain fields and a stress-strain curve are generated, as shown in Figure II.3.10.9(b). The experimental and computational results are in excellent agreement.

The second test is based on a double cantilever beam (DCB) geometry and the material parameters that govern the interfacial behavior of the joint were obtained. The complex-valued cohesive model, herein referred to as Z- Park–Paulino–Roesler (ZPPR), was used to recreate the debonding process in the ZFEM simulations and to obtain sensitivities with respect to the fracture parameters. Figure II.3.10.10(a) shows the experimental set up used for the DCB experiment and the region for which the DIC data will be obtained. A corresponding FE mesh was created with a layer of cohesive elements between the two plates. The initial guess of cohesive parameters for this problem was ϕ_{n_0} = 350 N/m and σ_{max} = 10 MPa. Where ϕ_{n_0} and σ_{max} are the fracture energy and maximum cohesive traction in Mode-I loading, respectively. Figure II.3.10.10 shows the residual function and the steps taken by the nonlinear optimization algorithm. A comparison of the experiment against the computational force-displacement curves for the initial (educated guess) and optimized parameters is shown in Figure II.3.10.10(b). The results are in excellent agreement, verifying the use of the method to retrieve adhesive material parameters.

As a last step, the optimization algorithm was applied to a T-peel sample that was obtained from an FSW sheet of dissimilar materials: AZ31 Mg alloy and HDG DP590 steel. Figure II.3.10.11(a) shows an SEM image of the welded interface. The mechanical interlock that manifests as a hook feature on either side of the weld was kept minimal to ensure interfacial failure. This allows one to characterize the interfacial behavior using a cohesive zone model as shown with the DCB example. Figure II.3.10.11(b) shows the FE model and an image from the T-peel test. The welded interface (green zone) was reproduced using a ZPPR cohesive zone model. An additional layer of cohesive elements (black zone) with very low interfacial properties (fracture toughness and maximum cohesive traction) was added to the right of the welded region to avoid penetration between the plates. In this case, three mode-I cohesive parameters will be retrieved from the optimization procedure. The mode-I fracture toughness, ϕ_n, the maximum cohesive traction in the normal direction, σ_{max} , and the initial slope indicator (from the ZPPR cohesive model), λ_n. An initial educated guess was made for these parameters, ϕ_n = 1000 N/m, σ_{max} = 15 MPa, and λ_n = 0.5. Then, after 37 iterations of the nonlinear optimization algorithm, a set of optimized parameters was obtained: ϕ_n = 1928 N/m, σ_{max} = 16.2 MPa, and λ_n = 0.454. Figure II.3.10.11(c) shows a comparison of the experimental and ZFEM load-displacement curves. The results are in excellent agreement.

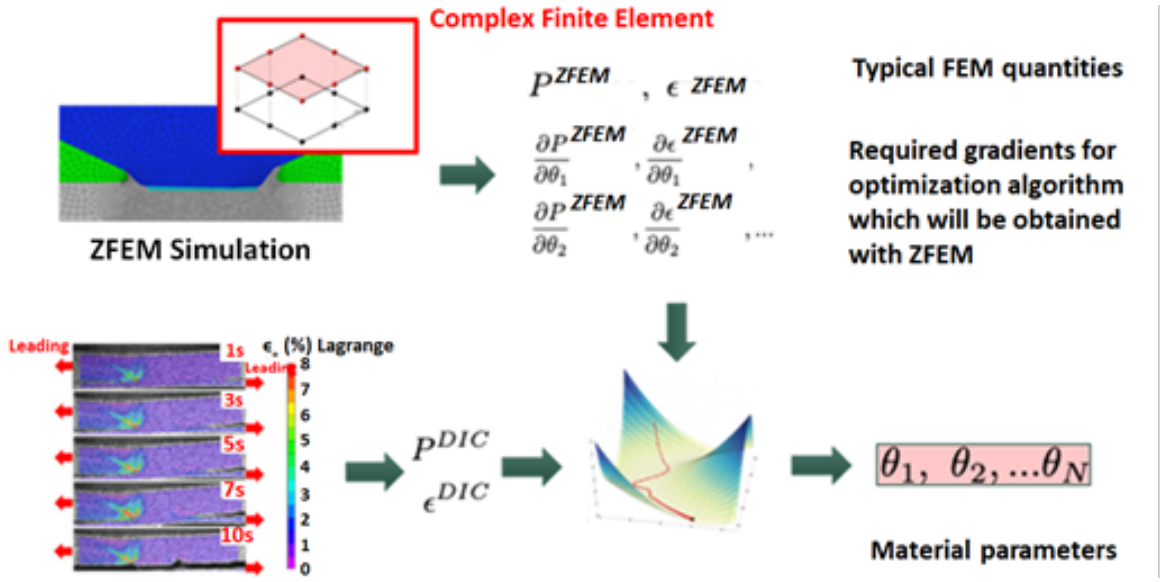

(a)

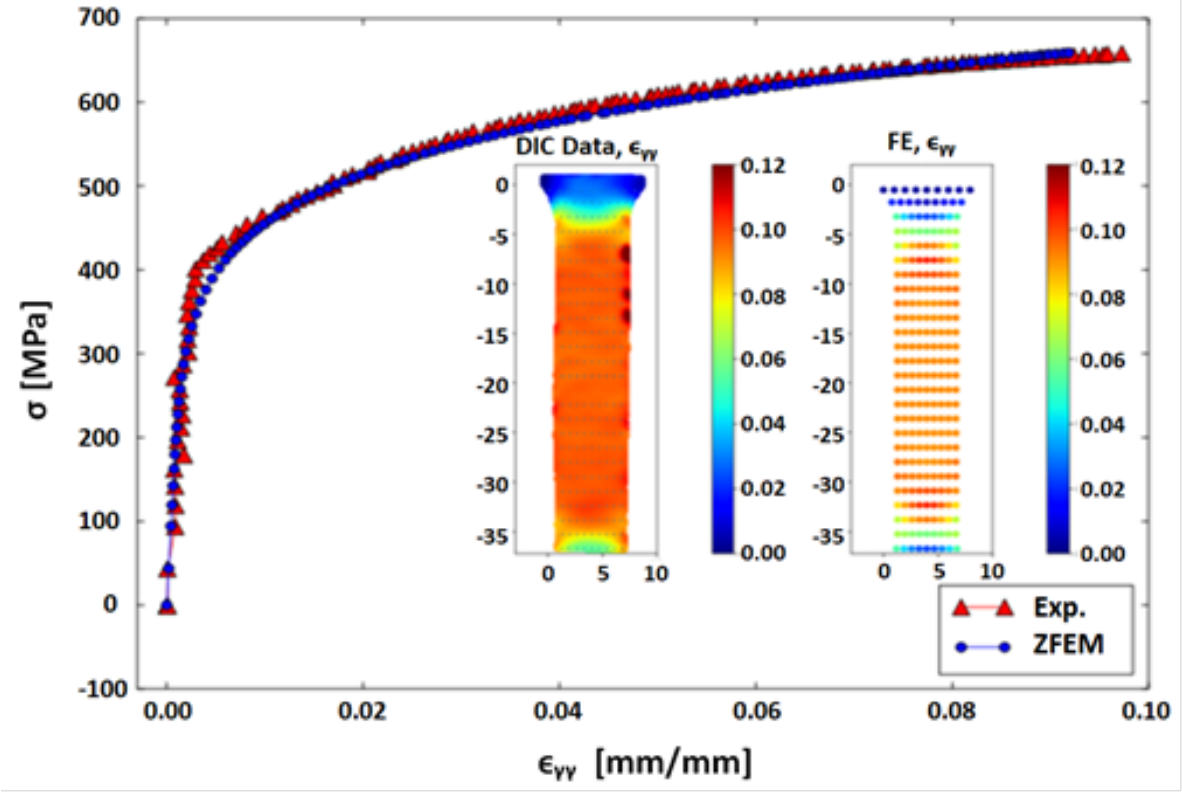

(b)

Figure II.3.10.9. (a) Optimization flowchart and (b) Tensile test optimization results. Source: PNNL.

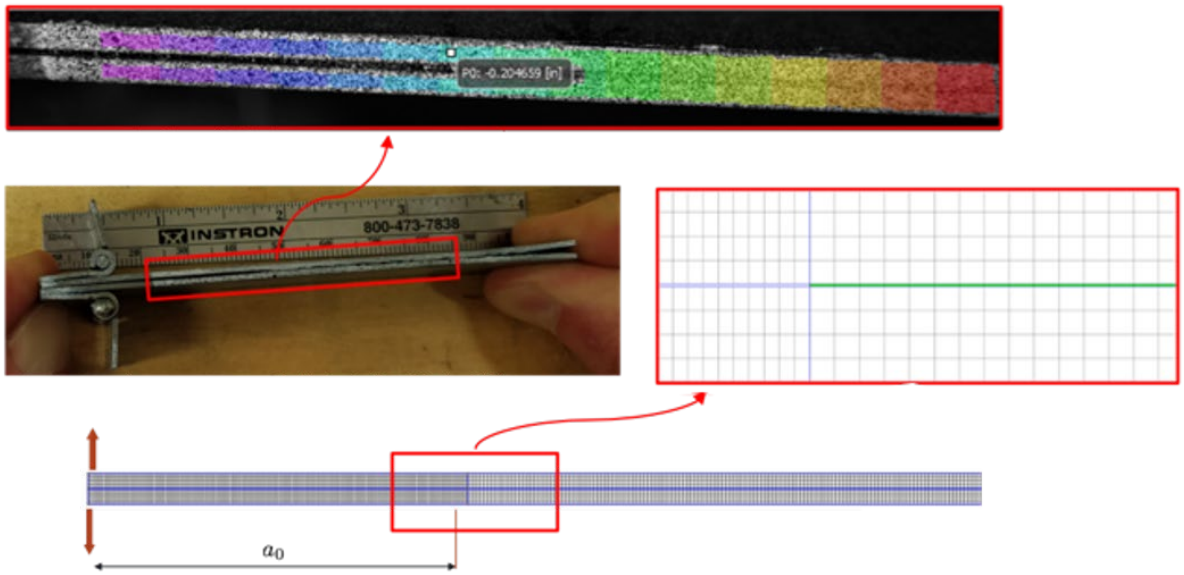

(a)

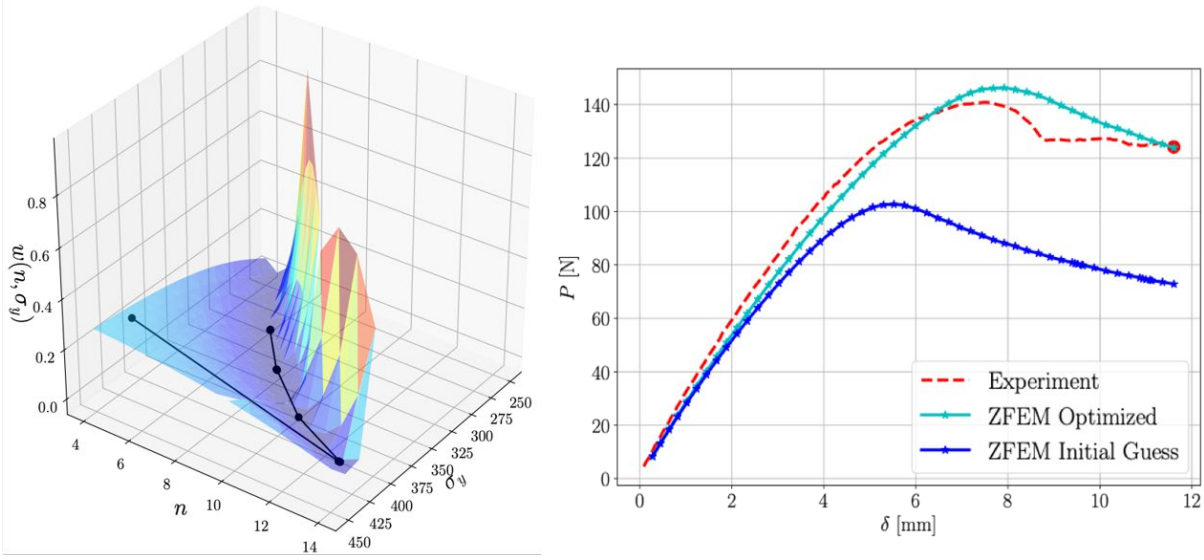

(b)

Figure II.3.10.10. (a) DCB experimental set up, DIC data, and corresponding FE mesh. (b) DCB optimization results. Source: PNNL.

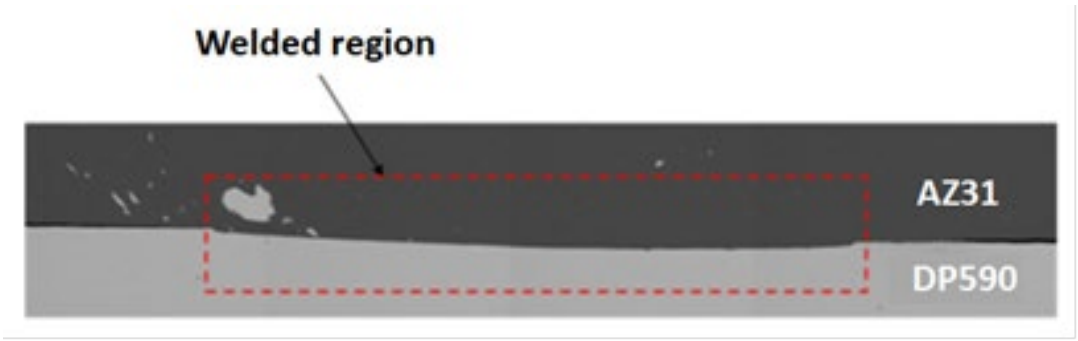

(a)

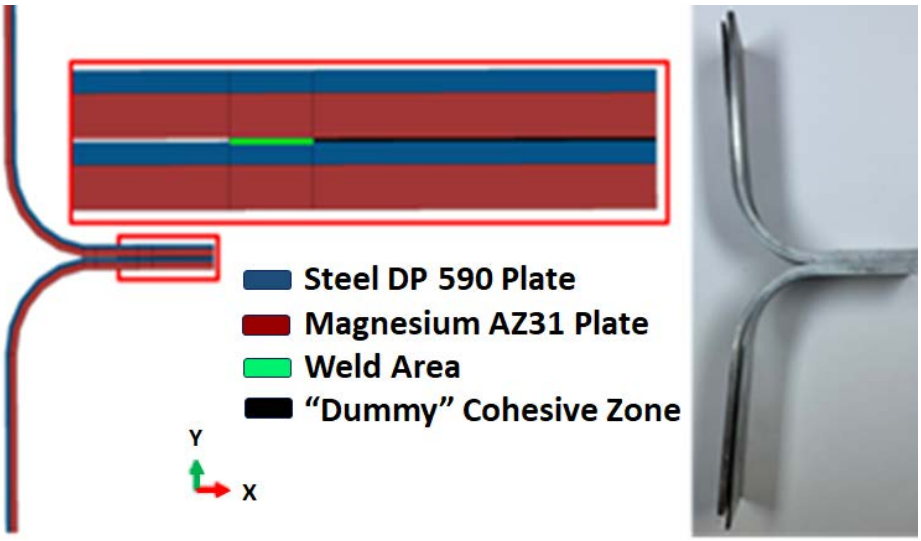

(b)

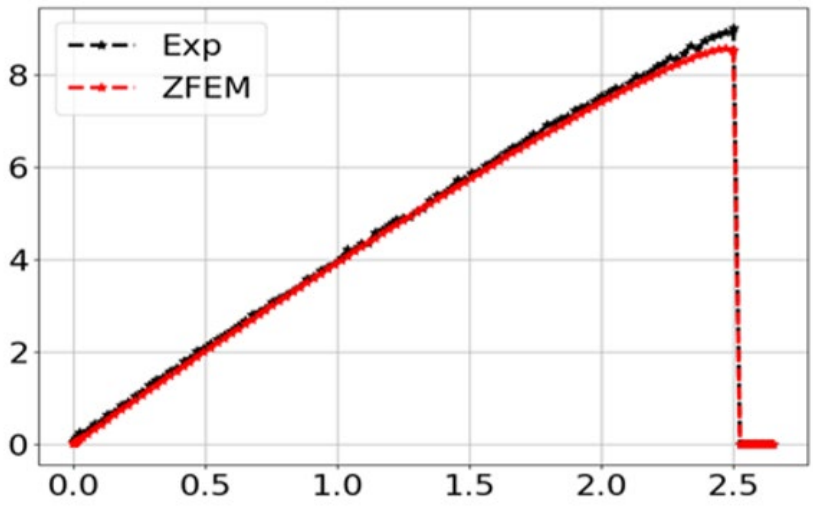

(c)

Figure II.3.10.11. (a) SEM image of the welded interface. (b) FE model and an image from the T-peel test. (c) Comparison of the experimental and ZFEM load-displacement curves. Source: PNNL.

Task 2.2. Extraction of Stress-Strain Curves using Nanoindentation Data

Nanoindentation test offers the advantages of a surface-based measurement in providing the statistically representative local property variation for different regions. In this work, local stress-strain properties of AZ31 and DP590 near the interface were calculated based on the load-depth curves obtained from a nanoindentation test. Figure II.3.10.12(a) shows the SEM image of an FSW joint. Large-sized hooks and rather thick interlayer are observed in the figure. Nanoindentation tests were performed on two different regions (i.e., "inside" and "outside" of the hook) of the three different materials (e.g., steel, Mg, interlayer). For example, indent marks and the corresponding load-depth curves obtained from the tester for Mg outside of the hook are presented in Figure II.3.10.12(b) and (c), respectively.

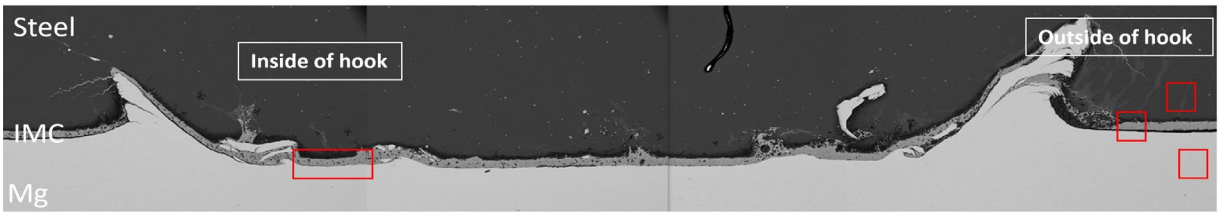

(a)

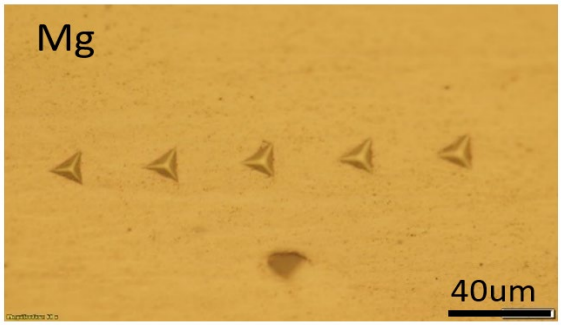

(b)

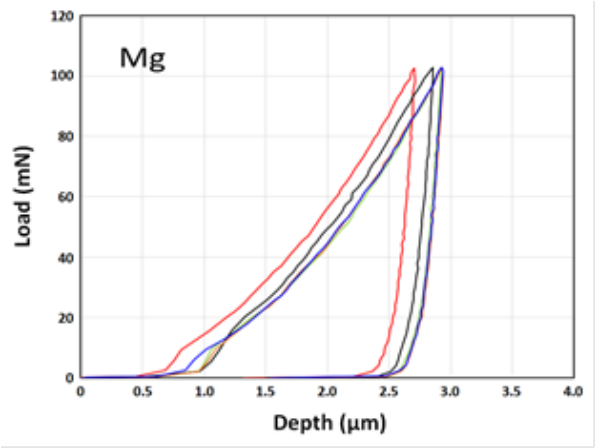

(c)

Figure II.3.10.12. (a) SEM image of the interface of the friction-stir weld joint between the AZ31 and bare DP590 steel, (b) examples of indent marks, and (c) obtained load-depth curves from AZ31 outside of the hook. Source: PNNL.

Cheng *et al.* [1] proposed an inverse method to calculate stress-strain curves from the nanoindentation load-depth curves. This method is shown schematically in Figure II.3.10.13(a). Based on this method, five stress-strain curves for each region were calculated and then averaged. The resulting average stress-strain curves for six different regions are compared in Figure II.3.10.13(b). For each material, the strength difference between the "inside" and the "outside" of the hook was observed, which is due to severe microstructural change inside the hook during the welding process. Interestingly, steel and interlayer materials show higher strength level inside of the hook than outside, whereas Mg shows softer strength inside of the hook. Microstructural observation using EBSD is planned to understand this opposite behavior of steel and Mg that occurred during the welding process. The results obtained from this work can be used as input data for the crystal plasticity FE model.

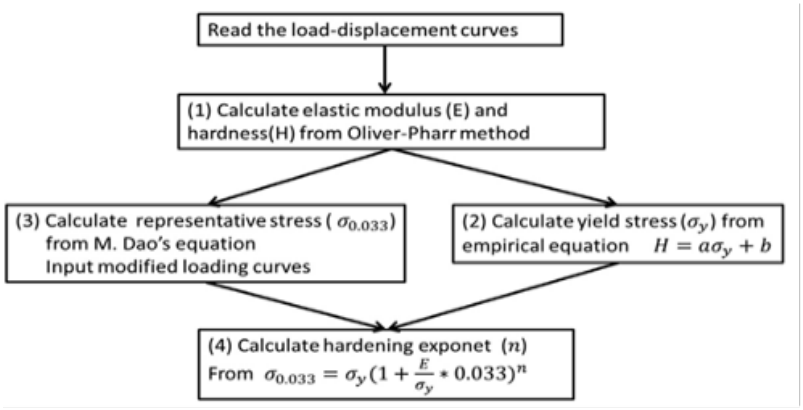

(a)

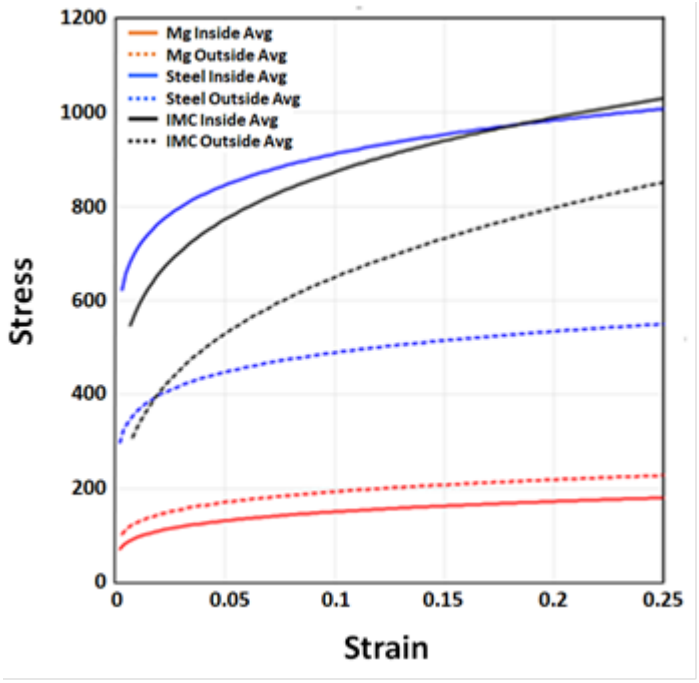

(b)

Figure II.3.10.13. (a) Algorithm for stress-strain curve estimation from nanoindentation test data. (b) Estimated average stress-strain curves for different regions. Source: PNNL.

Task 3. Microstructural-based Modeling of Joint between AZ31 and Bare DP590 using FSW

In this task, a joint between AZ31 and bare DP590 steel is modeled using a phenomenological crystal plasticity formulation on the mesoscale. Crystal plasticity parameters are calibrated using the experimental results. Interfacial bonding between two metals is modeled using a cohesive zone model. The microstructural information was obtained using high-resolution SEM and TEM images. Figure II.3.10.14(a) shows a TEM image of the interface of FSW joint between AZ31 and bare DP590 steel. The steel grains are much finer than the AZ31 grains. A 3D representative volume element (RVE) shown in Figure II.3.10.14(b) was built using a reference of this TEM image. The RVE has a cubical shape with the side of the cube measuring 10 µm. One-half of the RVE has AZ31 grains with the average size of 2 µm and the other half has DP590 steel grains with an average size of 0.2 µm.

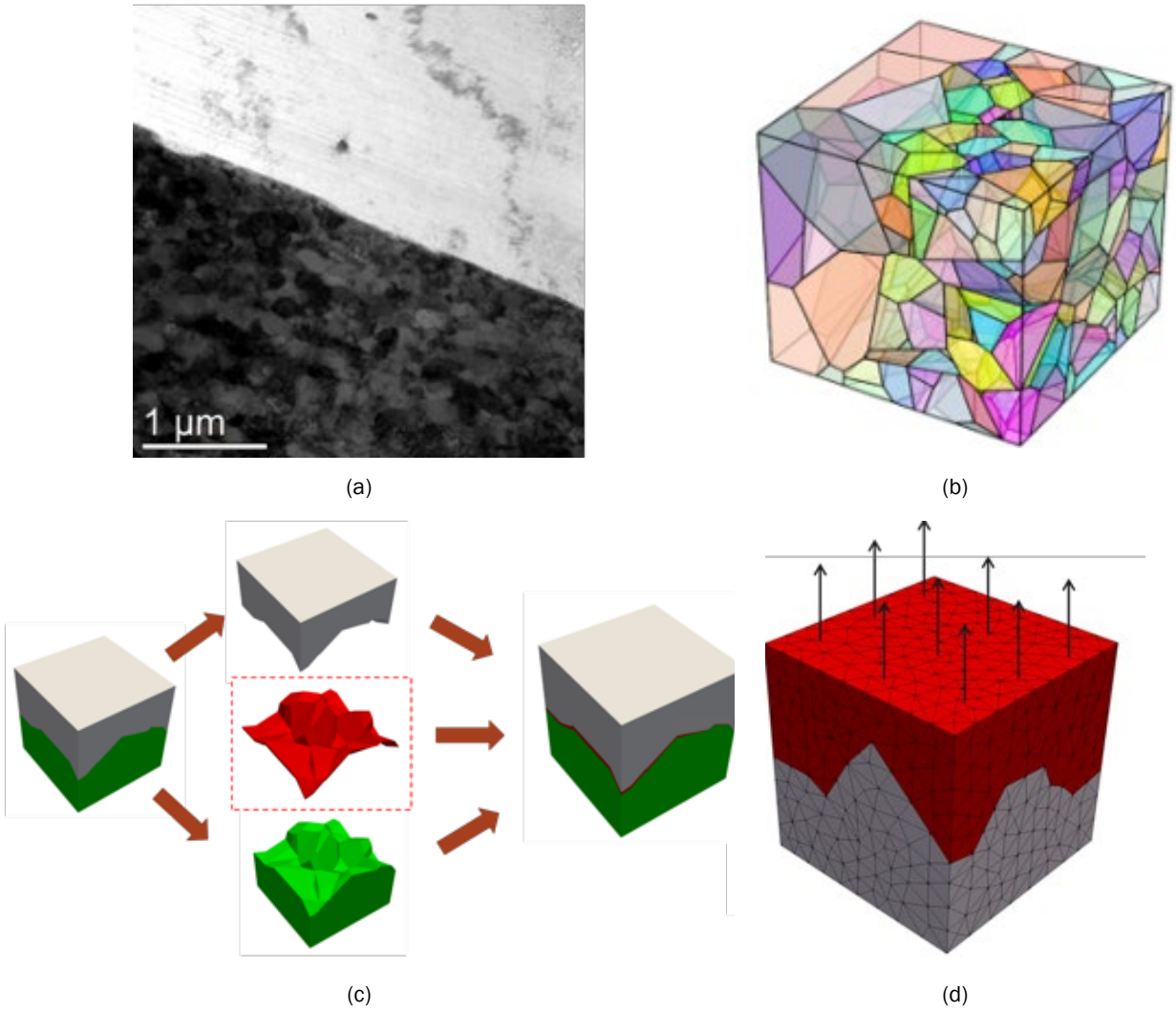

Figure II.3.10.14. (a) TEM image of the interface of FSW joint between AZ31 and bare DP590 steel. (b) A 0.01 mm^3 RVE. One-half of the RVE contains DP590 grains and the other half contains AZ31 grains. (c) A schematic diagram showing the insertion of cohesive elements (shown in red) at the joint interface. (d) BCs and load on the RVE. Source: PNNL.

Once the RVE was meshed with tetrahedral second-order elements using open-source software Gmsh, the boundary where AZ31 and DP590 steel grains meet is identified using in-house MATLAB scripts. The RVE is separated at this boundary and the cohesive elements are inserted before putting the RVE back together. This process is shown in Figure II.3.10.14(c). These cohesive elements represent the bonding between both metals. Once the stress in the cohesive elements reaches a certain value, the damage starts in those elements that degrade their load-bearing capacity. This degradation continues until their load-bearing capacity reaches zero at which point the interface fails and a crack is formed. The resulted RVE is applied with BCs and loadings that will mimic the uniaxial tensile test as shown in Figure II.3.10.14(d). The symmetry boundary condition is used for three orthogonal faces: $x = 0$, $y = 0$, and $z = 0$. The uniform displacement of 0.5 µm is applied on the top surface of RVE while keeping the remaining two vertical faces flat all the time. Finally, simulations are carried out with the help of open-source nonlinear FEM solver WARP3D.

The stress-strain response was obtained by postprocessing the data from the FEM simulations and is shown in Figure II.3.10.15(a). The orange line is the stress-strain response of the RVE with the interface modeled using

cohesive elements incorporating the damage model. This response is compared with the stress-strain response obtained from the RVE without any damage model shown as a blue line. The joints load-bearing capacity decreases as cohesive elements start to fail. Figure II.3.10.15(b) through (d) shows the spatial distribution of displacement in loading direction, mises stress, and strain in loading direction across the RVE under uniaxial tensile load, respectively.

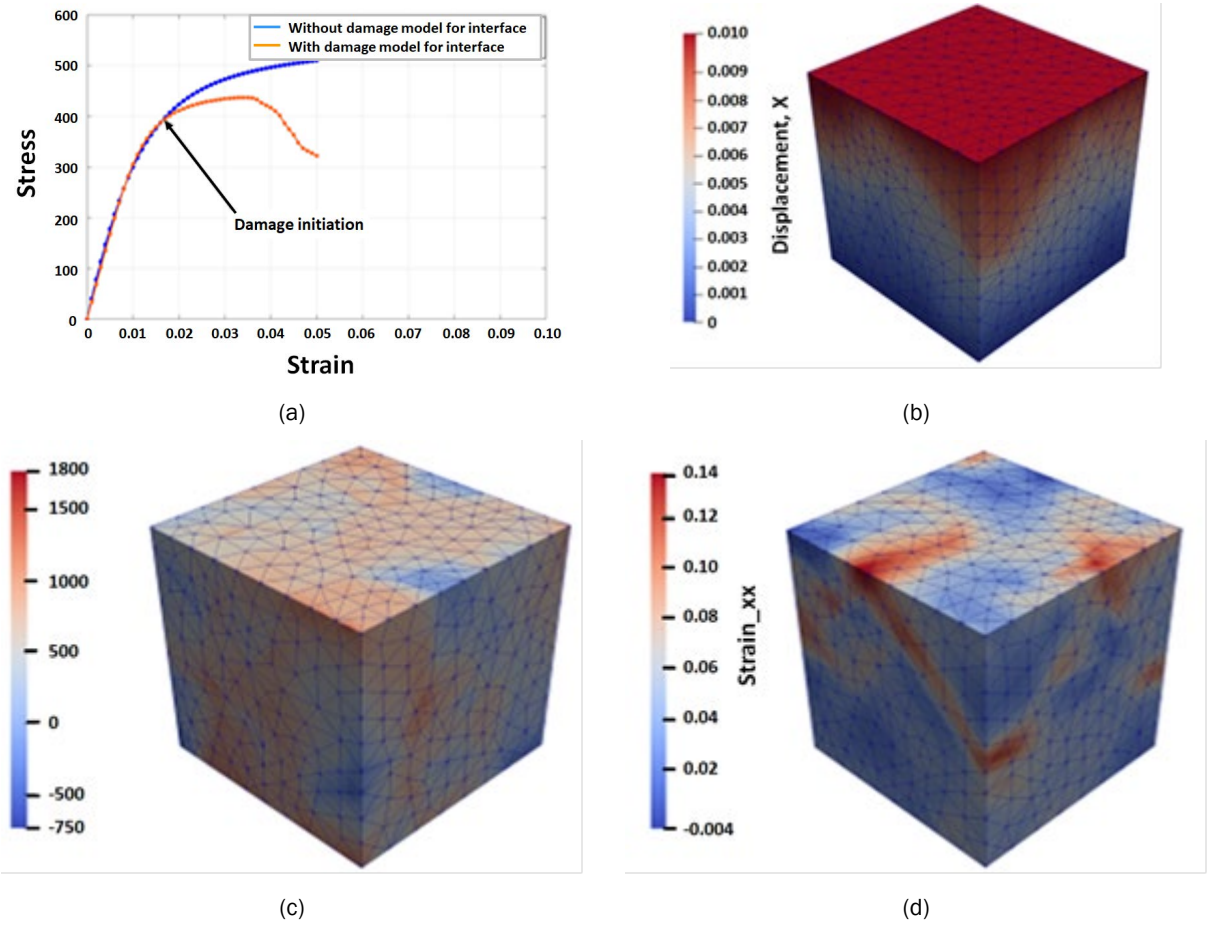

Figure II.3.10.15. (a) Stress-strain response of the RVE under uniaxial tensile loading for with and without the damage model for the interface. For RVE model with damage, the distribution of: (b) displacement in loading direction; (c) mises stress; and (d) strain in loading direction across the RVE are also plotted. Source: PNNL.

Conclusions

A comprehensive modeling framework for the USW process of joining a Mg alloy to Zn-coated steel is developed by integrating multiple metallurgy and mechanics models across different length scales. The model provides a fundamental understanding in the formation of the underlying interface microstructure and bonding strength. The full dissolution of the Zn coating is key to enhancing the bond strength, while insufficient heat generation or welding time would result in weak Zn and catastrophic failure. The bond area was predicted for various clamping loads and vibration amplitudes to establish a processing window for ultrasonic joining of the dissimilar materials. The developed multiscale model provides a high-throughput predictive modeling tool that can be applied to the interface design of other material pairs, 2T/3T stack-ups, and sheet thicknesses.

In addition, a modal analysis tool has been developed to predict the relative motion and shear stress at the faying surfaces of the materials joined by USW. The numerical model was employed to study the effect of coupon geometry and weld spacing on joining performance at single/multiple spot level. Hot spots in the USW

of lightweight materials can be screened by numerical model to avoid the crack occurrence and bond failure. Computational models as such can be used to design the spot weld configuration and clamping fixtures to enable multi-spot welding at the component-level.

For FSW modeling of a Mg alloy to uncoated steel, an optimization method was developed to retrieve the interfacial parameters of a joint. The method combines full-field kinematic DIC data and a ZFEM to minimize the mismatch between experimental and computational results by solving a nonlinear optimization problem. A key ingredient in this method is the computation of derivatives using the ZFEM method. The approach was verified with an adhesively bonded DCB and a T-peel specimen from an FSW. Furthermore, a microstructure-based model was developed to simulate the joint between dissimilar metals. The crystal structure of both metals was different. The interface bonding between the metals was modeled using cohesive elements. The material parameters were obtained using lower length scale experiments, such as SEM, TEM, and nanoindentation. The model can predict the mechanical response of the joint under different loading conditions and give insight about local damage behavior at the interface of the joint.

Key Publications

1. Cheng, J., X. H. Hu, X. Sun, A. Vivek, G. Daehn, and D. Cullen, 2020, "Multiscale characterization and simulation of impact welding between immiscible Mg/steel alloys," *J. Mater. Sci. Technol.*, Vol. 59, pp. 149–163.
2. Cheng, J., X. H. Hu, and X. Sun, 2020, "Molecular dynamics study on interface formation and bond strength of impact-welded Mg-steel joints," *Comput. Mater. Sci.*, Vol. 185, Art. 109988.
3. Huang, H., J. Chen, Y. C. Lim, Z. L. Feng, X. H. Hu, J. H. Cheng, and X. Sun, 2019, "Heat generation and deformation in ultrasonic welding of magnesium alloy AZ31," *J. Mater. Process. Technol.*, Vol. 272, pp. 125–136.
4. Huang, H., J. Chen, J. Cheng, Y. C. Lim, X. H. Hu, Z. L. Feng, and X. Sun, 2020, "Surface engineering to enhance heat generation and joint strength in dissimilar materials AZ31 and DP590 ultrasonic welding," *Int. J. Adv. Manuf. Tech.*, minor revision.
5. Xiong, L. H., J. Cheng, A. Chuang, D. Singh, X. H. Hu, and X. Sun, 2020, "Synchrotron experiment and simulation studies of magnesium-steel interface manufactured by impact welding," (submitted).
6. Ramírez-Tamayo, D., A. Soulami, V. Gupta, D. Restrepo, A. Montoya, and H. Millwater, 2020, "A complex-variable cohesive finite element subroutine to enable efficient determination of interfacial cohesive material parameters," (submitted).
7. Cheng, J., H. Huang, J. Chen, D. Leonard, X. H. Hu, Z. Feng, and X. Sun, 2021, "Predicting joint interface microstrucutre of Mg/Zn-coated steel ulstrasonic welded sample," (In preparation).
8. Huang, H., Y. Li, J. Chen, J. Cheng, X. H. Hu, Z. L. Feng, and X. Sun, 2021, "Modal analysis of ultrasonic welding to enable multi-spot lightweight materials joining," (In preparation).
9. Li, Y., J. Cheng, H. Huang, J. Chen, X. H. Hu, Z. L. Feng, and X. Sun, 2021, "Process window of Mg alloy and Zn-coated steel ulstrasonic welding," (In preparation).
10. Ramírez-Tamayo, D., A. Soulami, V. Gupta, D. Restrepo, A. Montoya, E. Nickerson, T. Roosendaal, K. Simmons, G. Petrossian, and H. Millwater, 2021, "A complex-variable finite element method-based inverse methodology to extract constitutive parameters," (80% completed).
11. Ramírez-Tamayo, D., A. Soulami, V. Gupta, D. Restrepo, A. Montoya, E. Nickerson, T. Roosendaal, K. Simmons, G. Petrossian, and H. Millwater, 2021 "Characterization of a FaST joint using kinematic field data and a complex-variable finite element formulation," (50% completed).

References

1. Cheng, G., K. S. Choi, X. Hu, and X. Sun, (2016) "Determining individual phase properties in a multiphase Q&P using multiscale indentation tests," *Mater. Sci. Eng. A*, Vol. 652, pp. 384–395.

Acknowledgement

The Principal Investigators would like to recognize X. Hu, H. Huang, J. Cheng, J. Allen, J. Chen, Y. C. Lim, D. Cullen and Z. Feng of ORNL and S. Kulkarni, K. S. Choi, H. Das, P. Upadhay, and T. Roosendaal from PNNL, D. Ramírez-Tamayo and Professor H. Millwater from University of Texas San Antonio, and A. Vivek and G. Daehn from OSU.

II.3.11 Solid-State Body-in-White Spot Joining of Aluminum to Advanced High-Strength Steel at a Prototype-Scale (Oak Ridge National Laboratory)

Zhili Feng, Co-Principal Investigator
Oak Ridge National Laboratory
1 Bethel Valley Road
Oak Ridge, TN 37831
E-mail: fengz@ornl.gov

Eric Boettcher, Co-Principal Investigator
Honda R&D Americas, Inc.
21001 State Route 739
Raymond, OH 43067
E-mail: eboettvher@oh.hra.com

Sarah Kleinbaum, DOE Technology Manager
U.S. Department of Energy
E-mail: sarah.kleinbaum@ee.doe.gov

Start Date: November 1, 2014 End Date: June 30, 2020
Project Funding: $50,000 DOE share: $0 Non-DOE share: $50,000

Project Introduction

This project focuses on developing and demonstrating two emerging solid-state, friction-heating-based spot joining processes—friction bit joining (FBJ), and friction-stir spot welding (FSSW)—to join AHSS to high-strength Al alloys (HSA alloys) from the coupon scale to the prototype part level. Application of these joining processes to HSA and AHSS in the body-in-white (BIW) production environment requires further R&D to address a number of technical obstacles (i.e., joint performance, productivity, maintaining consistency of joint quality under expected dimensional variations of stamped and/or formed parts, and cost-effectiveness).

The project consists of two phases. During Phase 1, both FBJ and FSSW methods were developed and evaluated at a coupon scale. Furthermore, because corrosion management is a primary concern for the joining of dissimilar materials, both FBJ and FSSW were combined with adhesive bonding as an isolation approach to protect the spot joint from galvanic corrosion. Finally, an integrated computational welding engineering modeling framework, developed by the project team over the years, is being adopted, refined, and applied. The purpose of the integrated computational welding engineering model is to refine and optimize the solid-state joining process, understand microstructure changes in the weld region and their effects on the strength/properties of an individual joint, and optimize joinability and joint performance at the prototype assembly level.

During Phase 2, FBJ was selected as the “winning” process for further development using prototype-scale BIW assembly level joining. Hardware of the winning joining process is being integrated with an assembly line welding robot. Prototype BIW subsystems, selected by the OEM, will be welded and assembled with the robotic joining system to evaluate and validate the production readiness of the joining technology for high-volume mass production BIW assembly. Al-steel joints, at both the coupon scale and the prototype-scale, will be tested and characterized to determine performance of the joints in accordance with the requirements in the funding opportunity announcement and a set of process and performance criteria from the OEM, Tier 1 supplier, and industry partners. The project assembled an excellent project team composed of automotive

manufacturers and auto part suppliers to carry out the proposed process R&D: engineering testing, joining system integration, and eventual commercialization and implementation.

The project is led by ORNL with participation from Honda R&D Americas, Alcoa, DOW Chemical, L&L Products, Cosma Engineering, G-NAC, MegaStir Technologies, Brigham Young University, and OSU.

Objectives

This project aims to develop, mature, and validate near-production readiness of a solid-state spot joining technology to join prototype-scale automobile BIW subsystems made of AHSS and 7000/6000 series HSA alloys to meet the dissimilar metal joining challenges in high-volume mass production.

The project focuses on spot joints—the most common form of joints in BIW structures of high-volume production vehicles. Thus, it enables the broadest insertion of lightweight materials in BIW and has the highest potential as a joining technology to support the reduction of petroleum consumption, environmental, and economic impacts in the transportation sector.

Approach

FBJ is a newly invented solid-state joining process particularly suitable for dissimilar materials. FBJ creates a metallurgical-bonded spot joint in two or more sheets of dissimilar metals through a combination of frictional drilling and bonding action of a high-strength consumable joining bit. FSSW is a derivative of the FSW process. A rotating fixed-pin tool is plunged into the upper sheet with normal force to generate frictional heat. The heated and softened material adjacent to the tool deforms plastically and a solid-state bond is made between two dissimilar metals, such as Al and steel. After critical review of both processes by project teams, FBJ was downselected for Phase 2.

The development of joining technology must be coupled with corrosion management, which is critical for automotive applications, especially for any joint between dissimilar materials. An adhesive was applied at all proposed contact locations between HSA and AHSS components to serve as an insulator. The solid-state joining techniques, adhesive bonding, and combination of the two were initially assessed using laboratory-scale coupons.

During Phase 2, FBJ was selected for further development using prototype-scale BIW assembly level joining. The main objective in Phase 2 is to demonstrate the FBJ process in a controlled production environment. A new FBJ welding head will be designed, manufactured, and integrated with a robot system along with fixtures for coupons and demonstration parts. Coupons and demonstration parts produced by the prototype FBJ welding cell will be further tested and evaluated for mechanical and corrosion performance. Prototype BIW subsystems, selected by the OEM, will be welded and assembled with the robotic joining system to evaluate and validate production readiness of the joining technology for high-volume mass production BIW assembly. Al-steel joints, at both the coupon and prototype scales, will be tested and characterized to determine the performance of the joints in accordance with the requirements in the funding opportunity announcement and a set of process and performance criteria from the OEM, Tier 1 supplier, and industry partners.

Results

Prototype FBJ Work Cell and Demonstration Part Joining

In FY 2020, Mazak MegaStir, Brigham Young University, Honda R&D America, and ORNL worked as a team to develop and execute the R&D plan in Phase 2. The main accomplishment is the design of an improved FBJ welding head based on the learnings of the FBJ technology in Phase I, the requirements of automated robotic assembly cell typical in a high-volume autobody assembly production line, and the prototype-scale BIW component selected for the project demonstration. Largely due to COVID-19-related difficulties, the team experienced significant delays with slower than expected progress toward the successful completion of the project.

The new FBJ welder was optimized for functionality and for meeting the weight requirement for attachment to the robot welding system. Figure II.3.11.1 shows the new FBJ welder attached to a Fanuc Robotic arm for fully automated robotic FBJ and joining/assembly cell, including fixtures for FBJ coupons.

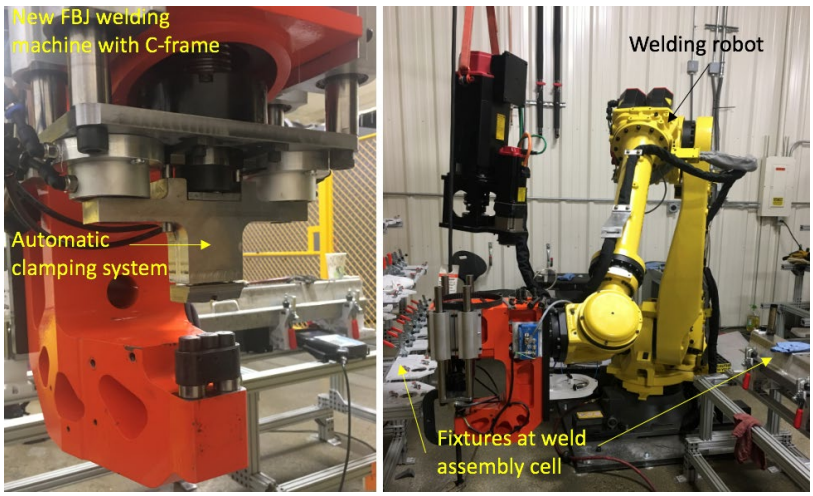

Figure II.3.11.1. Integrating a new FBJ welding head with a robotic system and fixtures at a welding assembly cell for the demonstration phase. Source: ORNL

More extensive system tests, adjustments, and refinements (e.g., automatic clamping system, automated joining bit feed system, data acquisition, feedback) has been continued for the prototype-scale BIW component assembly. Coupon-level lap-shear and cross-tension FBJ trials yielded satisfactory results that were consistent with Phase I development results in terms of joint strength. After satisfying lap-shear and cross-tension joint strength with the new FBJ system, T-peel coupon testing was developed and all samples met the joint strength criteria (1.5 kN), as summarized in Table II.3.11.1, indicating a good repeatability of new FBJ welding system.

Table II.3.11.1. Summary of T-peel Testing Results

Sample	Peak Failure Load (kN)	Elongation at Failure (mm)
1	2.0	14.37
2	1.87	16.64
3	1.72	10.59
4	1.88	11.71
5	2.03	20.98
6	1.78	20.62
7	1.77	15.26
8	1.66	12.39
9	1.71	14.55
10	1.92	18.15
Average ± STDEV	1.83 ± 0.13	15.53 ± 3.57

The joining/assembly cell including fixtures necessary for joining and assembly of the prototype-scale BIW components has been constructed, as shown in Figure II.3.11.2. The prototype-scale BIW components with different lengths (e.g., 650, 950, 1150 mm) were spot-welded with multiple joints after adjustment and refinement of new FBJ system (e.g., automatic clamping system, automated joining bit feed system, data

acquisition, feedback). Figure II.3.11.3 shows the new FBJ system with the prototype-scale 7xxx Al (on the top) and AHSS (on the bottom) parts mounted on the fixture and final assembled component parts 1150 mm long with 28 FBJ welds on each side. Figure II.3.11.4 presents an example of the 950 mm long high-strength Al-steel component parts with different FBJ weld pitch distances (e.g., 50, 100, 900 mm) assembled by the new FBJ system at the MegaStir facility. These parts were sent to ORNL to study thermal distortion of the parts during simulated paint baking conditions. For a next step, the FBJ process will be combined with an adhesive to make weld-bonded component parts. Due to COVID19, ORNL researchers have limited access to conduct research. In addition, because shelf life of retained adhesive in the weld-bonded parts is a great concern under long exposure in temperature and humid, the team needs to coordinate a schedule for thermal distortion measurement and mechanical joint performance at ORNL.

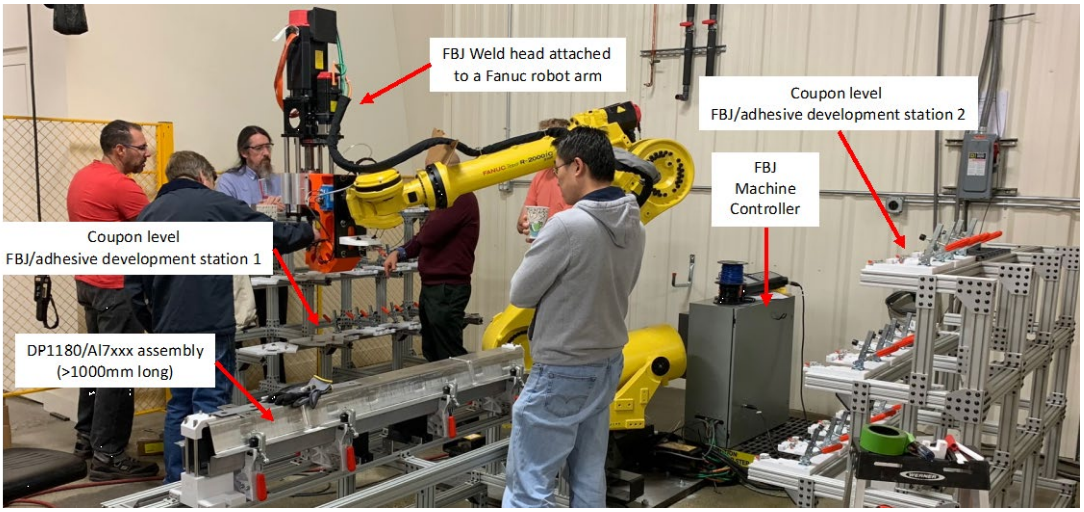

Figure II.3.11.2. New FBJ welding head on Fanuc robot and work cell fixtures for coupons and prototype parts at Mazak MegaStir. Source: ORNL.

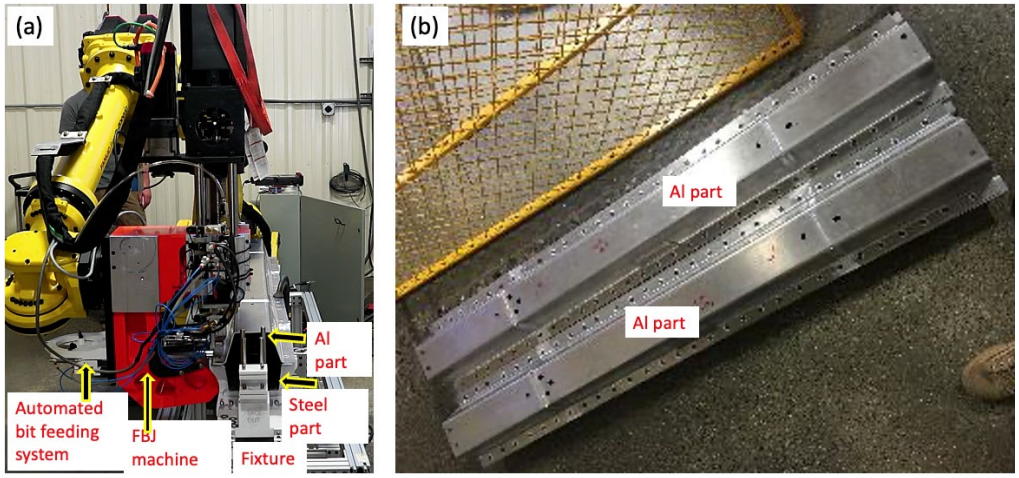

Figure II.3.11.3. (a) Welding head on Fanuc robot and work cell fixtures at Mazak MegaStir for multiple spot welding of component Al-steel parts. (b) Demonstrated prototype part 1150 mm long. Source: ORNL.

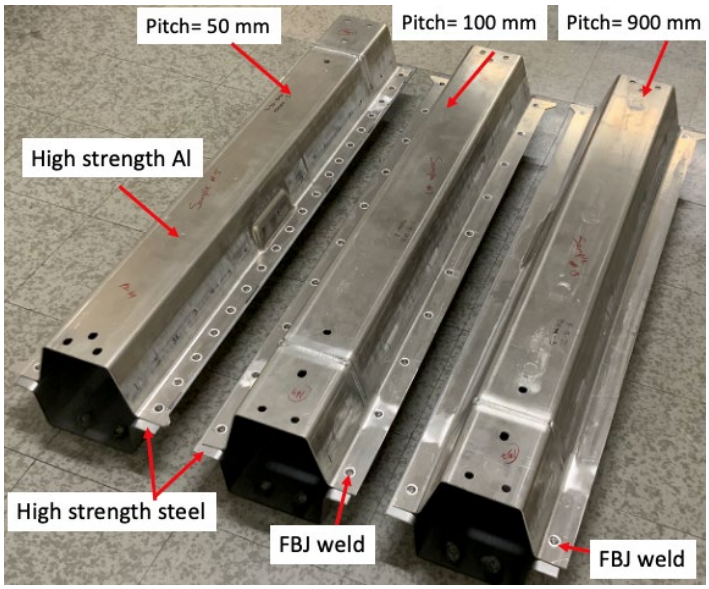

Figure II.3.11.4. Demonstrated prototype parts 950 mm long with different FBJ weld pitches (e.g., 50, 100, 900 mm) received at ORNL. Source: ORNL.

Conclusions

A new FBJ welder was designed, manufactured, and integrated with a robotic system. FBJ coupons, including lap-shear, cross-tension, and T-peel configuration, were produced by the newly integrated FBJ machine, and their joint strength exceeded the OEM requirement. Design of the FBJ weld cell was finalized and integrated with the robotic-mounted new FBJ machine and weld fixtures for final demonstration. Prototype parts that consist of high-strength Al and AHSS were successfully assembled with multiple welds by the new FBJ welding system and cell.

Acknowledgements

The Principal Investigators would like to thank the following individuals for their contributions to this work:

- Oak Ridge National Laboratory: Y. C. Lim, H. Huang, and Y. Wang
- Honda R&D Americas: E. Boettcher and A. Seid
- Brigham Young University: M. Miles, T. Berg, and S. Wood
- MegaStir: D. Fleck, B. Johnson, and R. Steel
- The Ohio State University: W. Zhang
- DOW Chemical: M. Mansour and G. Hayes
- L&L Products: D. Kosal and S. Crump
- Cosma Engineering: A. Srilatha, C. Shi, and E. Ashmore
- G-NAC: E. Yousey, S. Wakameda, N. Weisenberger, and R. Clark
- Alcoa: R. Long, D. Spinella, and D. Bergstrom.

II.3.12 Corrosion Mechanisms in Magnesium-Steel Dissimilar Joints (Pacific Northwest National Laboratory and Oak Ridge National Laboratory)

Vineet V. Joshi, Co-Principal Investigator
Pacific Northwest National Laboratory
902 Battelle Boulevard
Richland, WA 99352
E-mail: vineet.joshi@pnnl.gov

Donovan N. Leonard, Co-Principal Investigator
Oak Ridge National Laboratory
1 Bethel Valley Road
Oak Ridge, TN 37831
E-mail: leonarddn@ornl.gov

Sarah Kleinbaum, DOE Technology Manager
U.S. Department of Energy
E-mail: sarah.kleinbaum@ee.doe.gov

Start Date: October 1, 2019 End Date: September 30, 2020
Project Funding: $600,000 DOE share: $600,000 Non-DOE share: $0

Project Introduction

FSSW and USW methods are being investigated as viable techniques to join Mg-to-steel for light weighting of vehicles. Both involve creating a large degree of plastic deformation at an interface while delivering heat from frictional and plastic work-dissipation mechanisms. This creates unique microstructural and mechanical features at joint interfaces that enhance joint strength. Despite the potential success of these processes, their application is limited because of the poor corrosion resistance of Mg. Mg inherently corrodes at a faster rate than steel, and because Mg is the most anodic of the structural materials, it is susceptible to galvanic corrosion and corrodes severely when interfaced with steel. To mitigate and decrease the corrosion in these joints, we not only need to understand the design of the joints, but also the impact of the microstructural features at the interface on the corrosion rate. Such considerations will also provide baseline information for understanding and optimizing protective coatings for Mg-steel joints, which will be needed in automotive service.

Objectives

The objective of this work is to understand and quantify galvanic corrosion of Mg in FSSW and USW joints. This information can then be used to provide a basis to optimize joint design and process conditions to achieve high-quality joints that minimize susceptibility to galvanic corrosion to the extent possible (i.e., coatings will still be needed). The joints to be studied are Mg alloy, AZ31B, joined to a dual phase steel, DP590, with and without a Zn coating.

Approach

Both macro- and microgalvanic corrosion behavior was analyzed as a function of weld type, process parameters, and materials pairing of AZ31B to DP590 steel, with and without a Zn coating. Multiple exposure and characterization methods were applied and complemented with computational assessment. To allow a systematic evaluation of corrosion, two types of corrosion attack pronounced in FSSW and USW lap joints were considered: Mg external and weld lap/gap corrosion, as described in Figure II.3.12.1. The weld inside the gap functions as a solid current path and a corrosion interface in Mg external and weld lap/gap corrosion cases, respectively. The corroding interfaces in each case are summarized in Table II.3.12.1.

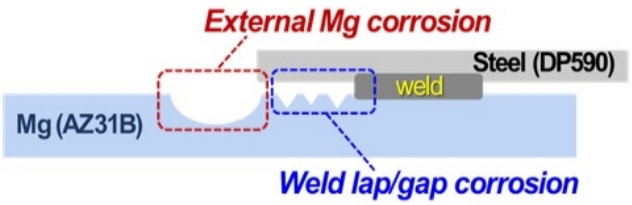

Figure II.3.12.1. Two types of corrosion attack for external Mg and weld lap/gap corrosion cases are schematically illustrated for a weld lap joint of Mg (AZ31B) and steel (DP590). Source: ORNL.

Table II.3.12.1. Related Corrosion Interfaces in Contact with Electrolyte for Each Corrosion Case

Location	External/ Mg Corrosion	Weld Lap/ Gap Corrosion
Mg	O	O
Weld	X	O
Steel	O	O
O: contact with corrosive electrolyte		
X: no contact		

Mg anode and cathode, steel or Zn, were specifically defined by tape-masking for macro-galvanic corrosion experiments, as shown in Figure II.3.12.2(a). The tape-masked specimens were then immersed in 0.1 M NaCl solution to corrode the Mg anode with a reference saturated calomel electrode (SCE), also placed to monitor corrosion potential. The galvanic corrosion volumes are schematically illustrated for the joint specimens in Figure II.3.12.2(b). For simple quantitative comparison, corrosion depth, representing the distance between the original and corroded Mg boundaries, was used. Corrosion rate for the configurations were determined using the experimental configuration, as shown in Figure II.3.12.2(a). Corresponding Tafel plots of the two materials and conductivity of the solution were used as input for the multiphysics model using COMSOL.

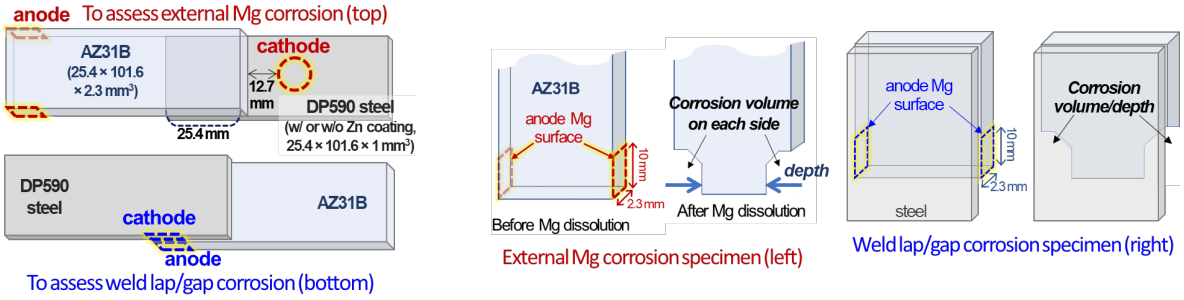

(a) (b)

Figure II.3.12.2. Corrosion exposure for USW and FSSW joint specimens shown as (a) the anode and cathode areas schematically described for both external Mg and weld lap/gap corrosion cases and (b) the illustrations of corrosion volume/depth for each corrosion case. Source: ORNL.

Materials characterization of the as-joined and post-corrosion samples was accomplished using correlative multilength-scale microscopy and microanalysis and X-ray computed tomography (CT). Complementing this work, microgalvanic behavior was studied at the Mg-steel joints by SECCM [1],[2]. Measurement protocol was optimized for SECCM measurement for the microscopic corrosion study to map the entire area across the interface of a welded joint. In the welded Mg-steel joint sample, corrosion measurements were done across the interface in the direction of Mg side to steel side to map out the entire area.

Results

The corrosion depths are compared for different FSSW (or FSW) and USW Mg-steel weld lap joints after the external Mg corrosion exposure in Figure II.3.12.3(a). For the steel cathode where the Zn layer was removed, the corrosion depth was greater in USW than in the FSSW specimens. This result could imply that the weld microstructure evolved by FSSW exhibited a higher resistance than that by USW, leading to a reduction of Mg galvanic corrosion. In a USW joint specimen, the single Mg corrosion depth associated with the Zn cathode where the Zn layer on steel was not removed, was much shallower than the corrosion depths produced by steel cathodes, highlighting the effect of Zn in reducing galvanic corrosion in this external Mg corrosion case. The four photos of corroded Mg in USW and FSSW joints, as shown in the bottom portion of Figure II.3.12.3(a), clearly show the lower corrosion volumes (i.e., related with shallow corrosion depth in steel cathode FSSW and Zn cathode USW specimens).

The Mg corrosion depths are compared for the weld lap/gap corrosion exposure in Figure II.3.12.3(b). Overall, the corrosion depths in USW joints were greater with a steel cathode than with a Zn cathode. As an example, two photos of corroded USW specimens in the right side of Figure II.3.12.3(b) are provided. These results indicate that Zn coating on steel can reduce Mg galvanic corrosion in the weld joints for both the external and weld lap/gap exposure cases. Note that the impact of welding method (USW or FSSW) for each corrosion experiment was not consistent because the corrosion depth was greater for FSSW in the weld lap/gap exposure but greater for USW in the external exposure. At this moment, more corrosion depth data from FSSW are needed to confirm this trend further. The corrosion potentials measured at the end of immersion are plotted in Figure II.3.12.3(c) for the same USW and FSW specimens presented in Figure II.3.12.3(a) for their corrosion depths. All measured corrosion potentials were higher than the corrosion potentials of Mg alone, which ranges typically from -1.55 to -1.6 V_{SCE} . The measured corrosion potentials were higher in the specimens with greater corrosion depths, indicating that Mg corrosion loss is closely related with the degree of galvanic polarization. In addition to the macroscopic galvanic corrosion described above, galvanic corrosion of joint cross-sections was also studied to better understand how the microstructure produced during joining influences corrosion response and the type of corrosion product. Cross-sections of FSSW joints of both Zn-coated and Zn-removed DP590 joined to AZ31 were immersed in a 0.1 M NaCl solution for 30 minutes. Optical micrographs clearly show that the thermomechanical affected zone, the nugget region, and the unjoined AZ31 all had different corrosion responses after immersion (not shown).

To better understand and correlate these experimental observations, three-dimensional multiphysics modeling was performed. The configuration shown in Figure II.3.12.2(a) was used for the simulations (not shown) and, for purposes of clarity, a three-dimensional view of corrosion of Mg over time is visualized in Figure II.3.12.4(a). As was observed in the experiments, after over 80 h, Mg is lost around the corners and edge of the bar. The reaction is concentrated where the Mg is closest to the steel. The U-shape on top of the bar corresponds to what is observed experimentally. Mg is lost very quickly under the front of the bar, where it touches the steel, making a pit. In the areas where Mg has been corroded away, the reaction is concentrated into a smaller area, increasing the rate at which Mg is lost. Projection views of Mg corrosion over time, corresponding to Figure II.3.12.4(a), where projection on the Mg is defined as top, side, and front view, are defined in Figure II.3.12.4(b). The side view allows us to see the Mg eaten away, forming a pit under the joint (e.g., side view, t = 80 h, on the right side of Figure II.3.12.4).

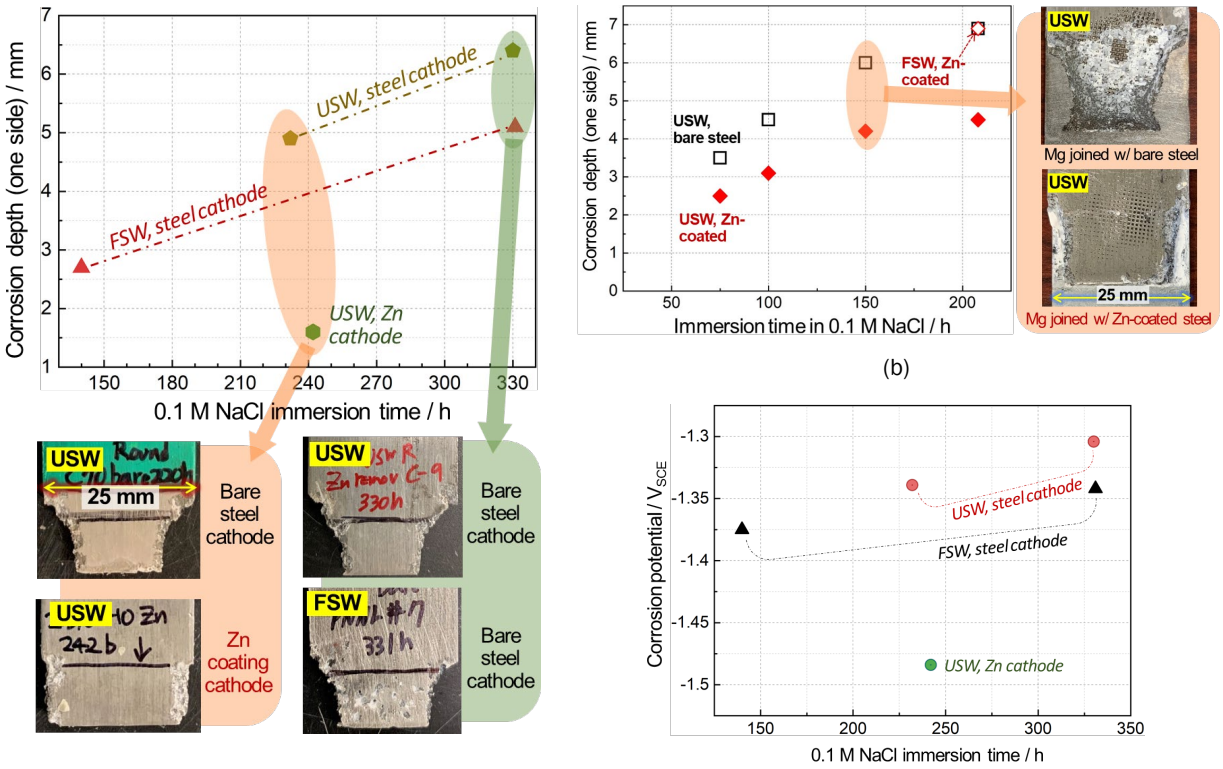

Figure II.3.12.3. Corrosion depth measured for USW and FSSW specimens with steel or Zn cathode (a) after the external corrosion exposure and (b) the weld lap/gap exposure described in Figure II.3.12.2. The four photos on the bottom in (a) and the two photos on the right in (b) are post-corrosion specimens corresponding to the data points in the shaded regions. For USW specimens, a round sonotrode (Φ = 10 mm) was used for the joining process. (c) Corrosion potentials measured from the same USW and FSSW joint specimens presented in (a). Source: ORNL.

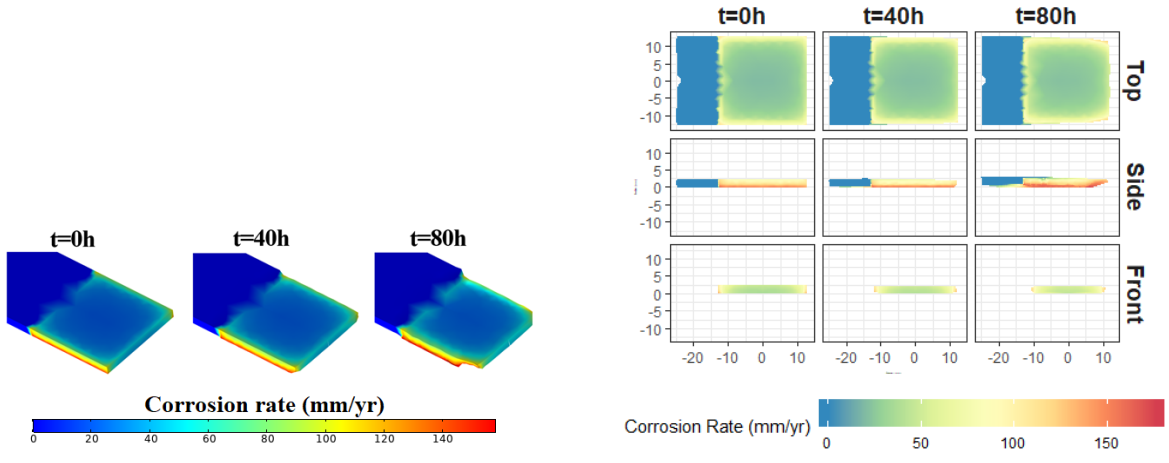

Figure II.3.12.4. Corrosion depth in Mg measured using COMSOL simulations: (a) isometric view of the measured corrosion rate for up to 80 h; and (b) projection views of Mg corrosion over time corresponding to simulations of (a), for which projection on the Mg is defined as top, side, and front view. Source: ORNL.

Another conclusion from the macroscopic galvanic corrosion studies described above was the influence of the Zn layer on reduction of Mg galvanic corrosion. X-ray microscopy and CT were used on both the FSSW and USW joints to image the Zn layer and nondestructively observe if the layer was present or delayered along a 2–3 cm length of FSSW specimens, as shown in Figure II.3.12.5(a-g). In the FSSW sample, spherical features on the surface of the ringed region where the tool head makes contact with AZ31 during joining were observed, but it was unclear how these features evolved and whether they were related to Zn delayering at the interface. First, a cross-section of the sample was studied with SEM energy-dispersive X-ray spectroscopy to determine that the spherical features were composed of a eutectic composition of Mg and Zn metal (not shown). Energy-dispersive X-ray spectroscopy phase maps showed that the spherical particle on the surface was tethered to a ~70 µm wide, ~3 mm long Mg/Zn eutectic feature, which originated from the AZ31/DP590 interface.

However, this polished cross-section was just one plane of a 3-cm long joint region, and the question of how Zn delayering progressed along the length of the joint was still unanswered. To answer this question, an X-ray microscope and CT were used to nondestructively observe the joint interface and entirety of the Mg and DP590 layers above and below the joint interface. Both the isosurface and AZ31/Zn-coated DP590 sample cross-sections can be seen in Figure II.3.12.5 as a function of length down the joint. The spherical Mg/Zn feature and the tether to the joint interface were also resolved in the X-ray CT data and surprisingly subsurface Zn delamination was also observed. This subsurface delamination detail could help understand how the rotation of the scribe played a role in the delamination and would have been difficult to observe holistically if just conventional metallographic cross-sectional analysis was used.

To identify the effect of different phases on corrosion behavior, localized microscopic electrochemical-measurement protocols were established using SECCM. We were able to get the line profile and imaging data (open-circuit potential [OCP], Tafel, and EIS at fixed frequencies) on welded DP590-AZ31 steel, as shown in Figure II.3.12.6(a) through (c). Similar studies were performed on pure Mg-to-steel joint samples and AZ80-to-steel samples (not shown). SECCM can map the localized galvanic potentials and impedance across the different phases of the Mg-steel interface. The newly established protocols were successfully employed on steel and Mg substrates to demonstrate instrument capability.

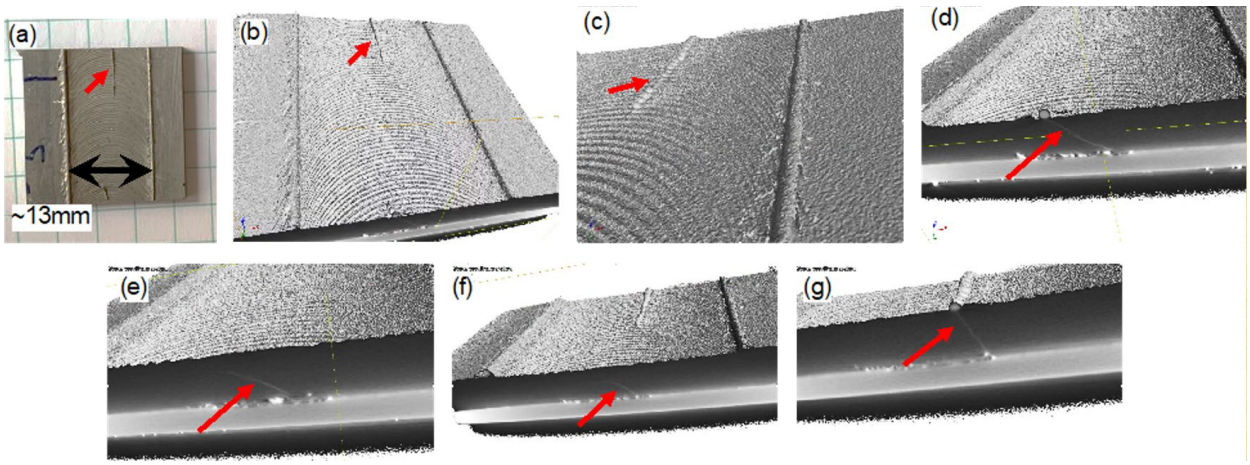

Figure II.3.12.5. (a) AZ31 surface after FSW joining and the resulting ~13 mm wide tool head contact region. (b–f) Frames from an X-ray CT animation showing the FSSW joint's isosurface and Mg/Zn spherical surface features. Red arrows denote Zn layer delamination from the joint interface and the position in the AZ31 layer where it resided. (g) X-ray CT micrograph of the Mg/Zn eutectic spherical surface feature, shown by a red arrow in (a), and how this exact feature is tethered to the joint interface below the surface. Source: ORNL.

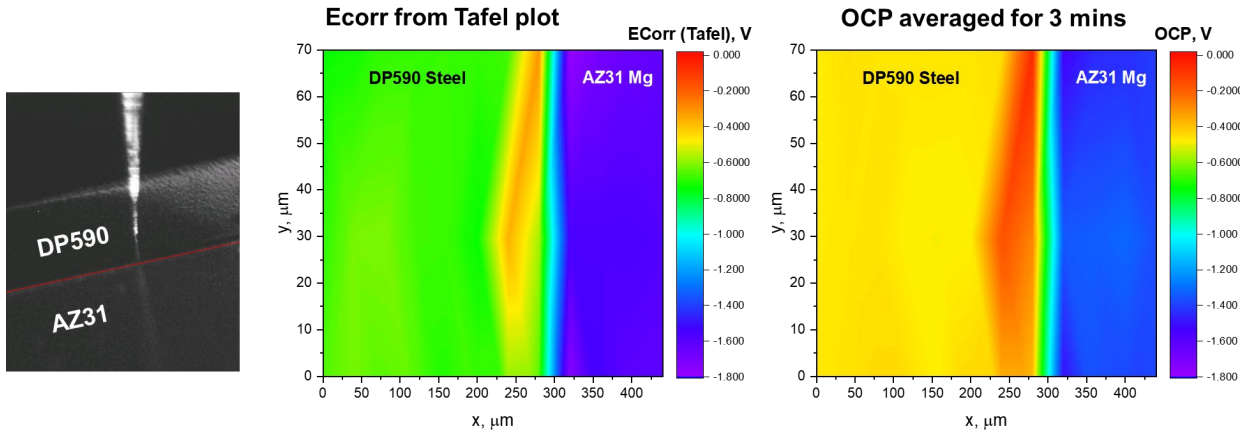

Figure II.3.12.6. (a) Two-dimensional image scan of localized corrosion across steel-Mg interface where the SECCM probe and interface region measurements were conducted. (b) The distribution of corrosion potential (Ecorr). (c) Averaged OCP values measured across a 450 µm x 70 µm interfacial region determined from Tafel plot and OCP measurement, respectively. Source: ORNL.

We are able to identify the gradient in galvanic potentials across steel-Mg interfaces, as shown in Figure II.3.12.6, and the formation of cathodic regions that are rich in O at the Mg-steel interface. The potential values measured using conventional OCP measurement are in line with the values determined using Tafel plot at each point during the scan. This technique produced reliable results; this was further confirmed by measuring sample surface resistance using two different independent techniques, current-voltage and EIS at the same location. In both cases, measured surface resistance was very similar. Additionally, the galvanic potential measurement by the SECCM technique on separate Mg and steel samples was comparable to values reported in the literature. The system was able to uniquely measure the differences in Ecorr as a function of location of SECCM probe on the sample. Discrete Ecorr values, measured locally, can represent characteristic microstructural features, such as crystal orientation, second-phase, particles, and precipitates.

Conclusions

In this work, our team implemented combined experimental and modeling efforts to understand and reduce corrosion of uncoated Mg-steel joints through weld-parameter and joint design optimization by successfully:

1. Establishing exposure protocols to quantify macroscale galvanic attack of Mg-steel joints and confirmed reduced galvanic attack by Zn coating on the steel.
2. Developing evaluation protocols to gain insights on microgalvanic behavior in Mg-steel joints by a novel SECCM technique and local galvanic current grading in AZ31B in advance of the AZ31B-steel interface observed.
3. Employing multilength-scale microscopy and microanalysis to compare pre- and post-corrosion Mg-steel joint microstructures.
4. Validating a COMSOL model that predicts corrosion rates for different joint configurations.
5. Initiating X-ray CT of USW and FSSW joints and showing the benefits of its nondestructive nature, ability to resolve features >15 µm, high-throughput, and usefulness when downselecting samples for further microscopy and microanalysis with higher-resolution electron microscopy techniques.

Key Publications

1. Jun, J., J. Chen, Y. C. Lim, M. Brady, D. Leonard, and Z. Feng, 2020, "Corrosion behavior of ultrasonic-welded AZ31B and dual phase steel with and without galvanize layer," *TMS Coatings and*

Surface Engineering for Environmental Protection II, 23–27 February 2020, San Diego, CA, USA. (Invited).

2. Jun, J., *et al.*, 2021, "Galvanic corrosion of AZ31B joined with dual phase steel with and without Zn layer by ultrasonic- and friction-stir-welding," in preparation for journal publication in 2021.
3. Kalsar, R., V. Prabhakaran, O. A. Marina, and V. V. Joshi, 2020, "Measurement of corrosion potentials across the interfaces using SECCM," in preparation.

References

1. Yule, L. C., C. L. Bentley, G. West, B. A. Shollock, and P. R. Unwin, 2019, "Scanning electrochemical cell microscopy: A versatile method for highly localized corrosion related measurements on metal surfaces." *Electrochim. Acta*, Vol. 298, pp. 80–88.
2. Ebejer, N., A. G. Güell, S. C. S. Lai, K. McKelvey, M. E. Snowden, and P. R. Unwin. "Scanning electrochemical cell microscopy: A versatile technique for nanoscale electrochemistry and functional imaging." *Annu. Rev. Anal. Chem.*, Vol. 6, pp. 329–351.

Acknowledgements

At Pacific Northwest National Laboratory (PNNL), the authors recognize the exceptional contributions of Alasdair Crawford and Vilayanur V. Viswanathan, who performed the COMSOL modeling work. The authors also recognize Rajib Kalsar, Venkateshkumar Prabhakaran, and Olga A. Marina, who performed the SECCM work. At ORNL, the authors like to recognize Jay Jun, who led the aqueous corrosion studies and designed the corrosion assessment protocols, and Mike Brady, who provided guidance on Mg corrosion testing and interpretation. We also acknowledge the joining expertise, knowledge and samples supplied by Piyush Upadhyay (PNNL, FSW) and Jian Chen (ORNL, USW).

II.3.13 Prediction of Al-Steel Joint Failure (Pacific Northwest National Laboratory)

Kyoo Sil Choi, Principal Investigator
Pacific Northwest National Laboratory
902 Battelle Boulevard
Richland, WA 99352
E-mail: kyoosil.choi@pnnl.gov

Sarah Kleinbaum, DOE Technology Manager
U.S. Department of Energy
E-mail: sarah.kleinbaum@ee.doe.gov

Start Date: December 1, 2018 End Date: March 31, 2021
Project Funding: $500,000 DOE share: $500,000 Non-DOE share: $0

Project Introduction

GM has developed a RSW process for joining Al to steel for several different joint configurations (i.e., alloys and material thicknesses). For RSW, one of the common metrics for an acceptable joint is for the weld nugget to remain on the lower sheet upon completion of a destructive tensile test. This is referred to as button pullout failure mode. Conversely, an unacceptable RSW failure occurs through the nugget at the interface between the two materials, referred to as an interface failure. As process development efforts to determine viable process parameters for any new joint configuration can be very intensive, predictive models for the process could significantly reduce these efforts. This project was proposed and initiated with the objective to develop a model that could predict failure mode of the weld coupon under various destructive test configurations. Destructive test configurations included typical configurations used in the automotive industry for RSW—including lap-shear, coach-peel, and cross-tension. Additionally, automotive components are often painted and subsequently processed through a paint-bake process. This exposes the RSW to additional thermal history, which has been demonstrated to have an effect on the joint failure mode.

Objectives

While the overall objective of this project is to develop a validated FE model that can predict the failure mode of Al to steel RSW, there are four more detailed objectives to support this effort as follows:

1. Fabrication and Destructive Testing of Al to Steel Spot Weld Coupons. This a GM-led effort that involved creating weld coupons in five joint configurations. Post-weld destructive testing included lap-shear, coach-peel, and cross-tension tests. In addition, microhardness testing and metallography were included.
2. Detailed Characterization of the Al to Steel RSW Joints. This is a PNNL-led effort focused on microstructural characterization and local material property measurement. Outputs from this effort are inputs to the FE model.
3. Weld Joint Simulation Finite Element Modeling. This is a PNNL-led effort toward the development of FE models to simulate the three destructive test configurations using material property data inputs.
4. Validation. These efforts will be performed to determine the accuracy of the developed model. By comparing failure modes of the actual samples versus the model prediction and analyzing discrepancies, additional model refinement activities will be performed to improve the accuracy of the model.

Approach

The approach taken for this project is similar to other simulation development efforts, involving test coupon creation, characterization of the RSW (input data for the model), model creation, and then an iterative validation and model refinement process. A more detailed description of the approach follows:

- Fabrication and Destructive Testing of Al to Steel Spot Weld Coupons:
  - RSW coupons were created in multiple joint configurations to allow for a range of input conditions for the model. Five unique weld joint configurations were created that included a single Al alloy in a single thickness and three HDG steel alloys in three different thicknesses.
  - Destructive testing of the coupons was performed in three common test configurations used by the automotive industry for characterizing RSW joint performance. These included lap-shear, coach-peel, and cross-tension tensile testing. The failure mode and load-displacement curve output from these tests are used for model validation efforts.
- Joint Characterization:
  - It was anticipated that local material properties at a fine resolution would be required as inputs to the FE model to enable accurate model output and failure mode prediction. The approach taken was first to involve a process of ranking and then selecting test methods to generate local material property data. Cost and alignment of the test method output to model input needs were the most important criteria. Test methods were selected for creating input data or for use as validation data.
  - Joint characterization was then performed with prioritization based on model input needs.
- Simulation Development:
  - FE models for coach-peel, cross-tension, and lap-shear tensile testing were developed. Information from optical and SEM images were used to generate the FE models with various geometric features observed near the weld nugget. The intermetallic compound (IMC) layer was modeled using solid elements to represent the damage since the fracture parameter is rather easily defined for solid elements.
  - FE models for uniaxial tensile testing were also developed to determine the fracture strain level of Al alloy under tension. To consider the stress-triaxiality dependency of the fracture strain of Al, FE models for limiting dome-height tests will be developed, which is expected to provide the fracture strain level under higher stress-triaxiality range.
- Validation:
  - Load-displacement data from simulations for multiple joint and test coupon configurations will be generated. Using data generated from the destructive testing and joint characterization efforts, the accuracy of the model will be assessed and opportunities for improvement will be identified. In an iterative fashion, model refinements and output reassessed for accuracy.

Results

In the last quarter of FY 2019, plans were made regarding experimentation and testing to support the modeling efforts. Decisions were made to focus on nano-hardness testing, from which load-displacement curves could be converted into stress-strain curves to develop an understanding of local material properties in and around the weld nuggets and into the base material. Multiple conversion methods were available, including some that were available in the literature and others that testing suppliers had internal to their organizations. It is also noted that there are multiple nano-hardness tip geometries available, including spherical, flat-ended, and a Berkovich pyramidal tip. These tips are also available in a range of diameters.

In FY 2020, efforts to perform the nano-hardness testing and convert the data into stress-strain curves were initiated. Initial efforts focused on performing the tests in the Al and steel base material. The objective of this work was to test the validity/capability of converting the nano-hardness test load-displacement curve into a stress-strain curve. Early measurement efforts were performed with Berkovich tips and some peculiarities were observed in the load-displacement curves from the time of contact on the coupon surface to shortly thereafter. For early curve conversion activities, this data was omitted, but even so, there was poor correlation of the predicted stress-strain curves in the base material generated from the nano-hardness testing versus the stress-strain curves generated from traditional tensile testing procedures. Issues were identified with the nano-hardness tester, but even after rectification of the issues, the correlation was inadequate. Figure II.3.13.1 shows a comparison of the calculated stress-strain curves versus those generated from the macro-tensile tests. The data for the Al base material is shown in Figure II.3.13.1(a), whereas Figure II.3.13.1(b)displays the results from the steel. The orange lines (upper lines) are the data from the macro-tensile tests. As can be seen, the correlation is relatively poor. The calculated curves shown in Figure II.3.13.1 were generated using the Cheng method [1].

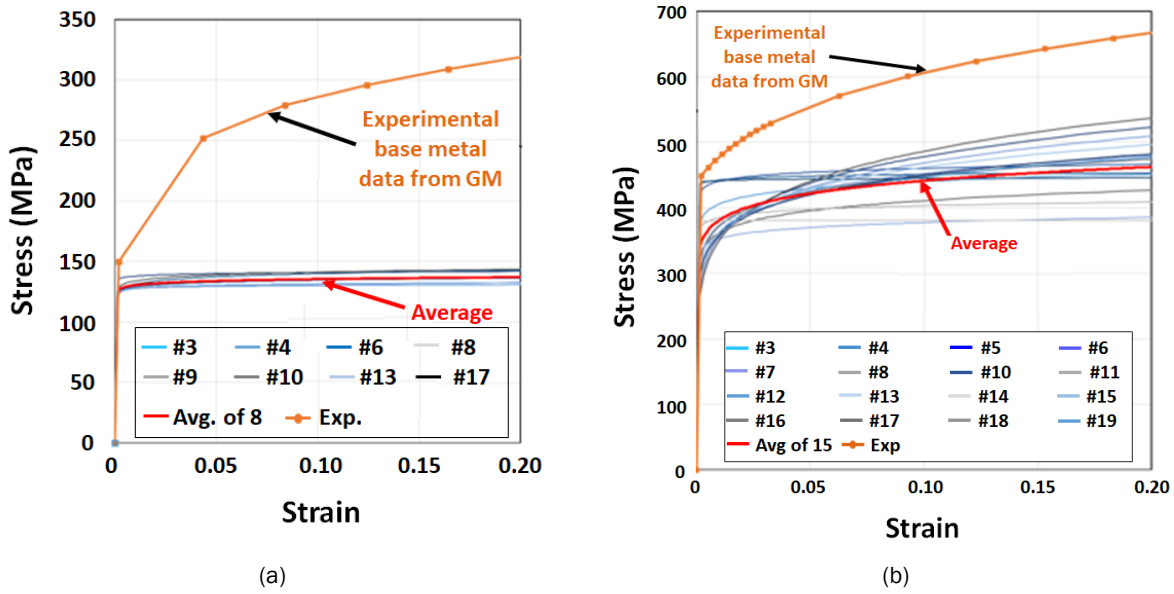

Figure II.3.13.1. Calculated stress-strain curves for (a) Al and (b) steel base materal vs. experimental data. Source: GM/PNNL.

Based on these results, a significant effort was initiated to understand the source(s) of the discrepancies between the calculated curves and the experimental data. The following lists the approaches that were taken:

1. Varying the nano-hardness test point spacing to understand if there were any effects of one test site affecting data in the subsequent tests.
2. Varying the hardness tip diameter to understand if there were size effects.
3. Varying the nano-hardness tip type.
4. Considering variation in macro-tensile data in transverse versus parallel to the RD.
5. Investigating other nano-hardness to stress-strain curve conversion methods [2],[3],[4],[5].
6. Performing additional machine calibration processes with multiple material systems/calibration blocks.
7. Consulting experts in the field.
8. Creating a FE model of the nanoindentation process.

In summary, some methods and approaches resulted in better accuracy than others, but no single method resulted in a universal solution with accuracy level acceptable to the team. The conclusion was that while accuracy could be generated for specific conditions, accuracy was dependent on a lot of the factors noted above with no universal solution discovered. Unfortunately, the details of each of these activities and their results are much more than can be discussed in a summary report.

Based on the results of the previous efforts, the team decided to take an alternate approach for converting microhardness data into stress-strain curves could be developed. Various stress-strain curves for the steels and Al alloy were available with the corresponding hardness values from GM's property characterization test. Approximate relationships between the hardness and the yield and ultimate strength were determined from these test data, and then used to predict the stress-strain curves from the hardness values. Results of this modeling are shown in Figure II.3.13.2, where predicted curves are overlaid onto the macro-tensile test data from previous testing completed at GM for the base materials used in the RSW coupons. The graph in Figure II.3.13.2(a) shows the results for the Al in the various paint-baked conditions and the data in Figure II.3.13.2(b) are for the steel alloys.

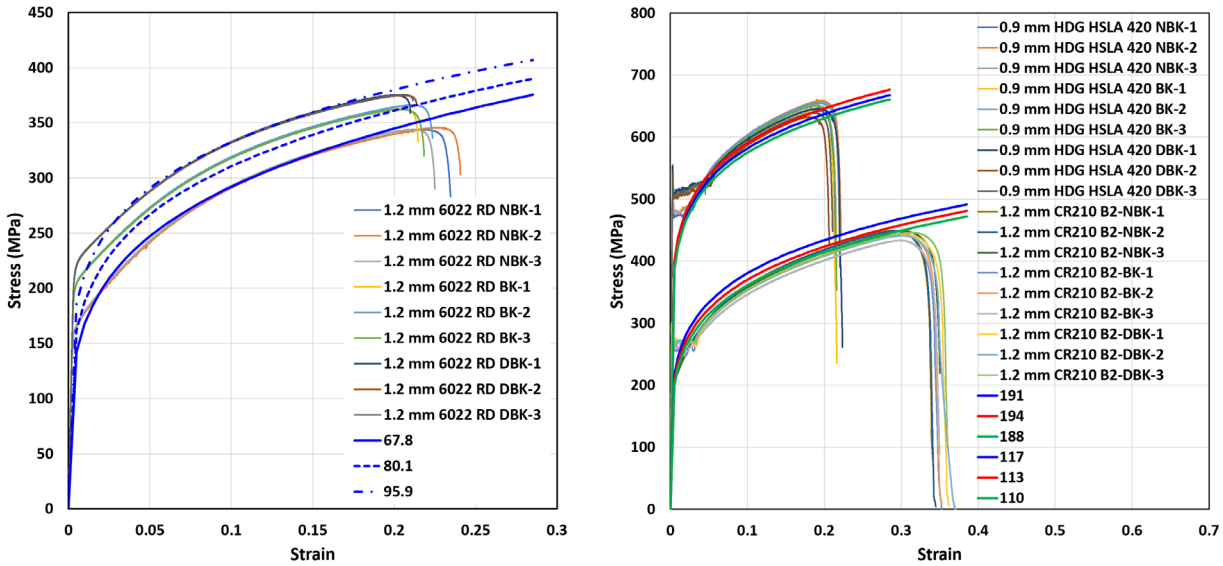

(a) (b)

Figure II.3.13.2. Calculated stress-strain curves of (a) Al and (b) steel base materal from the simple PNNL developed model. Source: PNNL/GM.

In the graphs, the predicted stress-strain curves are line correlating to the numbered lines (e.g. 67.8) in the legends. The numbers represent the measured hardness of the material. Other acronyms include, NBK, BK, DBK, and RD, which represent no bake, single bake, double bake, and parallel to rolling direction. As can be seen there is good correlation between the actual data and the predicted data. As a result, the team decided to apply the internally developed method to generate input data for the modeling efforts.

In the latter part of FY 2020, model validation efforts were initiated. These efforts focused on simulating the traditional macro-tensile tests first to help determine the validity of the hardness to tensile test stress-strain curve conversion process. This effort initially demonstrated that the shape and fracture strain of the tensile curves matched between the previously completed tests and simulation, but the failure modes of the weld samples (i.e., coach-peel, cross-tension, lap-shear) was not correctly captured due to their complicated stress state near the crack initiation region. This effort indicated that stress-triaxiality needed to be considered, and after considering this input, the failure modes could be better matched between test and simulation. This led to an effort to perform limited-dome-height to generate actual data. Additional validation efforts were then

performed by further simulating the failure mode during the cross-tension, coach-peel, and lap-shear tests for one of the joint configurations. The model could correctly predict failure mode (button pullout or interface failure), but only if the input fracture strength of the IMC was near 1000 MPa. Literature values for the bond strength of Al are in the range of 50 – 100 MPa. [6] Model results and correlation to the actual cross-tension and coach-peel tests than the lap-shear tests are in Figure II.3.13.3. Correlation between the model and lap-shear tensile test failure mode was less accurate.

With reasonable success in being able to simulate the fracture mode, time-based simulations were created for further model validation efforts. These time-based models were created to simulate the load-displacement curves of the three different destructive tests. Similar trends were observed in that greater accuracy (e.g., load at failure) could be achieved with the cross-tension and coach-peel tests versus the lap-shear tests. To generate accurate results, the fracture strength of the IMC needed to be adjusted further and fracture criterion considered. Figure II.3.13.4 shows examples of the model versus experimental result for the cross-tension test.

While it has been shown that the model can generate accurate simulations of the fracture modes, it was necessary to adjust inputs such as the IMC fracture strength, failure criterion, and level of stress-triaxiality (and/or mesh size) dependency of the Al fracture strains. Future efforts will focus on developing an understanding of the need to adjust inputs and collecting additional data as inputs to the model.

While significant progress has been made on the modeling efforts, experimentation related to gathering validation data has been delayed by COVID-19 and resulting laboratory closures. Planned experimentation includes performing DIC during destructive testing of coach-peel coupons. This has not impacted progress on modeling efforts to date. DIC experimentation is in process.

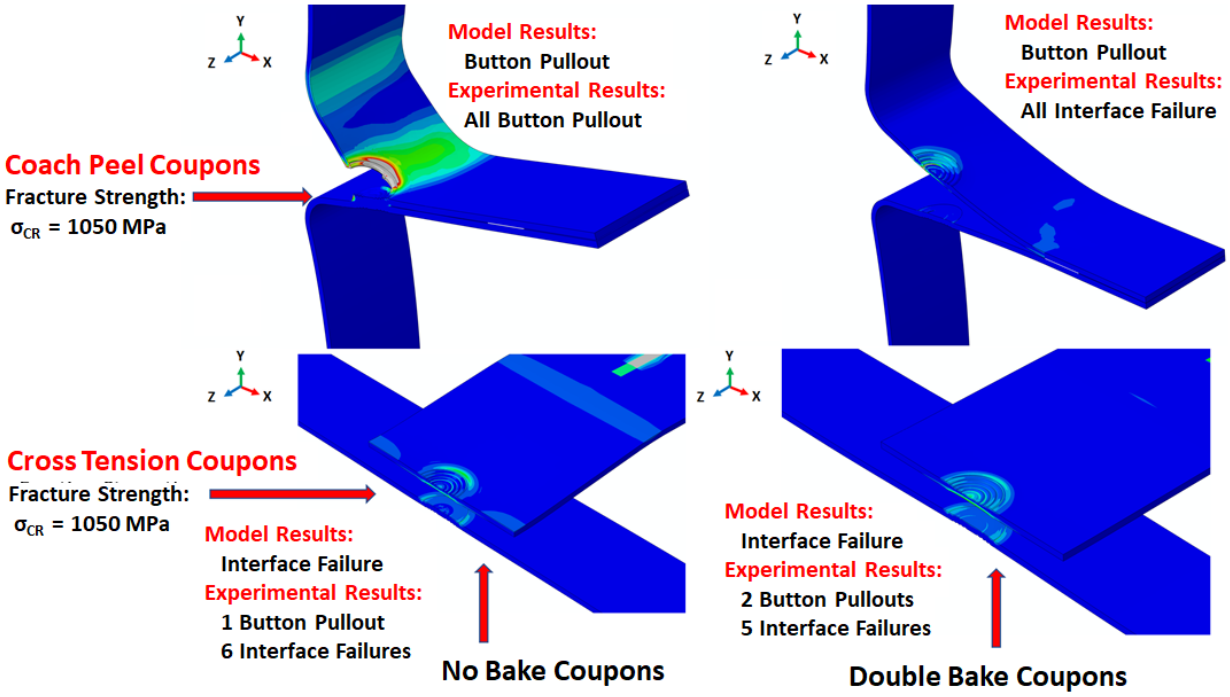

Figure II.3.13.3. Model validation results for simulation of no bake and double bake coupons showing coach-peel and cross-tension failure modes. Source: PNNL.

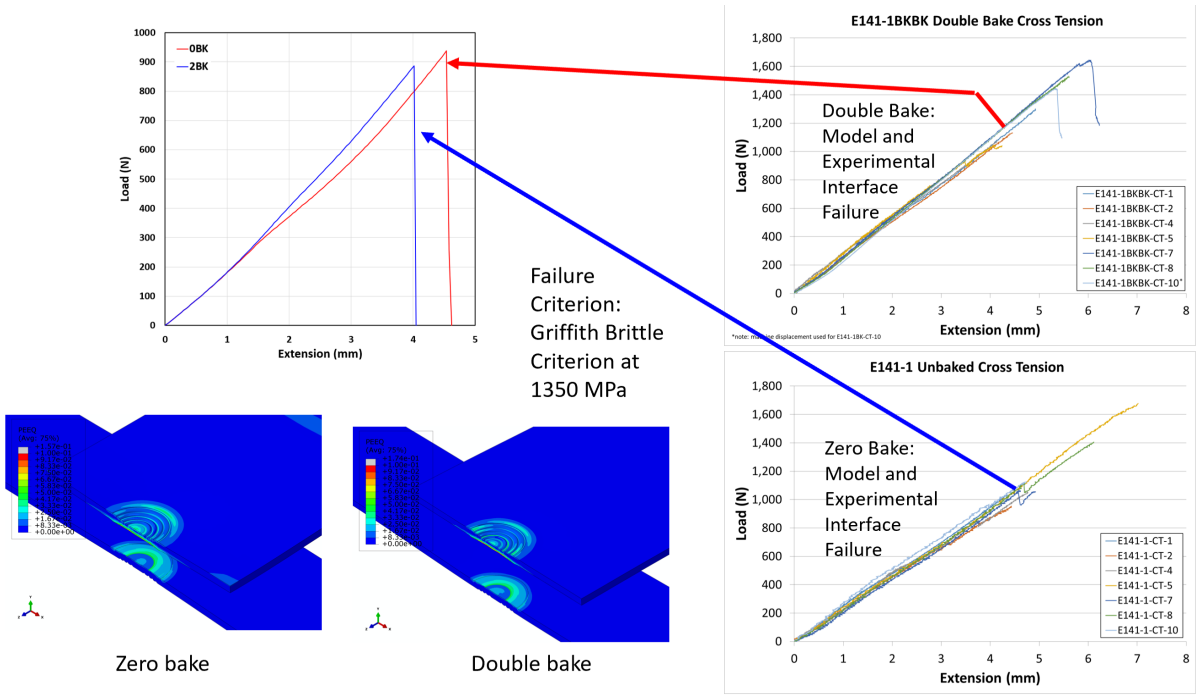

Figure II.3.13.4. Model validation results of load-displacement curve simulation. Source: PNNL.

Conclusions

The following conclusions are made for the FY 2020 progress:

- Nano-hardness testing and resulting conversion of load-displacement curves to stress-strain curves appeared to have the most promise to develop local material property data at high-resolution.
- Obtaining accurate stress-strain curves from nano-hardness load-displacement curves (by comparing base material tests versus GM macro-tensile test data) was much more difficult than anticipated. The success of various conversion methods found in literature appears to be very application specific and not universal. No one method generates data accurate enough for what was needed.
- PNNL developed an alternative approach that converted local microhardness data into stress-strain curves that had better accuracy for the conditions in this project.
- A means of obtaining local material properties of the IMC layer has not been identified due to the very thin nature of the IMC (<10 µm). As such, assumptions on its properties are inputs to the model.
- Initial model validation efforts (e.g., single joint configuration) indicate that failure mode can be predicted correctly about 70% of the time by using PNNL's developed method to determine local stress-strain curves from microhardness data and assumptions on IMC material properties. The least accuracy is with the lap-shear configuration, which also displays the most variable failure modes. This indicates that local variations resulting from the weld process (not modeled) may have a more significant effect on the lap-shear test. Additionally, more accurate fracture strains for Al under shearing load (i.e., under lower stress-triaxiality range) may be required to improve the prediction from simulations.
- To achieve correlation between the actual and simulated failure modes, IMC strength is assumed to be higher than what is likely to be reality (> 1000 MPa). Investigations into this difference are ongoing.
- To help understand the observed differences, full time-based simulations were performed for the various tensile test configurations. These models are very computationally intensive and were performed on GM's high-performance, multiprocessor computer. Similar observations were made for accuracy versus tensile tests (i.e., coach-peel and cross-tension results demonstrated better correlation).

References

1. Cheng, G., K. S. Choi, X. Hu, and X. Sun, X., 2016, "Determining individual phase properties in a multiphase Q&P using multiscale indentation tests," *Mat. Sci. Eng. A*, Vol. 652, pp. 384–395.
2. Dao, M., N. Chollacoop, K. J. Van Vliet, T. A. Venkatesh, and S. Suresh, 2001, "Computational modeling of the forward and reverse problems in instrumented sharp indentation," *Acta Mater.*, Vol. 49, pp. 3899–3918.
3. Cao, Y. P., and J. Lu, 2004, "A new method to extract the plastic properties of metal materials from an instrumented spherical indentation loading curve," *Acta Mater.*, Vol. 52, pp. 4023–4032.
4. Tabor, D., *Hardness of Metals*, Clarendon Press, Oxford, UK, 1951.
5. KLA, Inc. Measuring stress-strain curves of metals by nanoindentation, U.S. Patent #10288540.
6. Brown, T. W., and D. R. Sigler, 2016, *Faying interface mechanical properties of aluminum-to-steel welds as determined by microtensile testing*, Proprietary GM Internal Research Report.

Acknowledgements

The author would like to thank and recognize the following team members for their valuable input, including N. Overman who provided material science expertise, as well as experimental direction; W. Kuang and X. Ma for nano-hardness testing and insight; C. Smith for project management; and S. Riechers for atomic force microscopy testing and input. Additionally, all team members would like to thank GM and their team, specifically W. Cai, A. Haselhuhn, and B. Carlson, for their valuable insight, guidance, and providing test coupons and data.

(This page intentionally left blank)

U.S. DEPARTMENT OF
ENERGY

Office of
ENERGY EFFICIENCY &
RENEWABLE ENERGY

For more information, visit:
energy.gov/eere/vehicles

DOE/EE-2336 June 2021